LIQUID CRYSTALS BEYOND DISPLAYS

LIQUID CRYSTALS BEYOND DISPLAYS

CHEMISTRY, PHYSICS, AND APPLICATIONS

Edited by

Quan Li
Liquid Crystal Institute
Kent, OH

WILEY

A JOHN WILEY & SONS, INC., PUBLICATION

Copyright © 2012 by John Wiley & Sons, Inc. All rights reserved

Published by John Wiley & Sons, Inc., Hoboken, New Jersey
Published simultaneously in Canada

No part of this publication may be reproduced, stored in a retrieval system, or transmitted in any form or by any means, electronic, mechanical, photocopying, recording, scanning, or otherwise, except as permitted under Section 107 or 108 of the 1976 United States Copyright Act, without either the prior written permission of the Publisher, or authorization through payment of the appropriate per-copy fee to the Copyright Clearance Center, Inc., 222 Rosewood Drive, Danvers, MA 01923, (978) 750-8400, fax (978) 750-4470, or on the web at www.copyright.com. Requests to the Publisher for permission should be addressed to the Permissions Department, John Wiley & Sons, Inc., 111 River Street, Hoboken, NJ 07030, (201) 748-6011, fax (201) 748-6008, or online at http://www.wiley.com/go/permission.

Limit of Liability/Disclaimer of Warranty: While the publisher and author have used their best efforts in preparing this book, they make no representations or warranties with respect to the accuracy or completeness of the contents of this book and specifically disclaim any implied warranties of merchantability or fitness for a particular purpose. No warranty may be created or extended by sales representatives or written sales materials. The advice and strategies contained herein may not be suitable for your situation. You should consult with a professional where appropriate. Neither the publisher nor author shall be liable for any loss of profit or any other commercial damages, including but not limited to special, incidental, consequential, or other damages.

For general information on our other products and services or for technical support, please contact our Customer Care Department within the United States at (800) 762-2974, outside the United States at (317) 572-3993 or fax (317) 572-4002.

Wiley also publishes its books in a variety of electronic formats. Some content that appears in print may not be available in electronic formats. For more information about Wiley products, visit our web site at www.wiley.com.

Library of Congress Cataloging-in-Publication Data:

Liquid crystals beyond displays : chemistry, physics, and applications /
edited by Quan Li, Liquid Crystal Institute, Kent, OH.
pages cm
Includes bibliographical references and index.
ISBN 978-1-118-07861-7
1. Liquid crystals–Research. 2. Optoelectronic devices–Research. I. Li, Quan, 1965- editor of compilation.
QC173.4.L55L55 2012
530.4′29–dc23
2011052325

Printed in the United States of America

10 9 8 7 6 5 4 3 2 1

CONTENTS

Preface vii

Contributors ix

1. **Liquid Crystal Lasers** 1
   Hideo Takezoe

2. **Self-Organized Semiconducting Discotic Liquid Crystals for Optoelectronic Applications** 29
   Chenming Xue and Quan Li

3. **Magnetic Liquid Crystals** 83
   Rui Tamura, Yoshiaki Uchida, and Katsuaki Suzuki

4. **Ferroelectric Liquid Crystals for Nonlinear Optical Applications** 111
   Yongqiang Zhang and Jesús Etxebarria

5. **Photo-Stimulated Phase Transformations in Liquid Crystals and Their Non-Display Applications** 157
   C. V. Yelamaggad, S. Krishna Prasad, and Quan Li

6. **Light-Driven Chiral Molecular Switches or Motors in Liquid Crystal Media** 213
   Yan Wang and Quan Li

7. **Liquid Crystal-Functionalized Nano- and Microfibers Produced by Electrospinning** 251
   Jan P. F. Lagerwall

8. **Functional Liquid Crystalline Block Copolymers: Order Meets Self-Assembled Nanostructures** 285
   Xia Tong and Yue Zhao

9. **Semiconducting Applications of Polymerizable Liquid Crystals** 303
   Mary O'Neill and Stephen M. Kelly

10. Liquid Crystals of Carbon Nanotubes and Carbon Nanotubes in Liquid Crystals **341**
Giusy Scalia

11. Liquid Crystals in Metamaterials **379**
Augustine M. Urbas and Dean P. Brown

12. Ferroelectric Colloids in Liquid Crystals **403**
Yuriy Reznikov

13. Fact or Fiction: Cybotactic Groups in the Nematic Phase of Bent Core Mesogens **427**
Bharat R. Acharya and Satyendra Kumar

14. Lyotropic Chromonic Liquid Crystals: Emerging Applications **449**
Heung-Shik Park and Oleg D. Lavrentovich

15. Liquid Crystal-Based Chemical Sensors **485**
Jacob T. Hunter and Nicholas L. Abbott

16. Polymer Stabilized Cholesteric Liquid Crystal for Switchable Windows **505**
Deng-Ke Yang

17. Liquid Crystals for Nanophotonics **525**
Timothy D. Wilkinson and R. Rajesekharan

Index **569**

PREFACE

Liquid crystals (LCs) were discovered more than 100 years ago, however the renaissance of research and development activities during the last quarter of 20th century led to the successful commercialization of LC devices for information displays. Currently the global market of LC displays (LCDs) stands more than $100 billion annually. Though the LCDs ubiquitous in our daily life seem mature, there is still considerable interest in the development of 3D-displays using LCs. Nevertheless parallel to this development, nowadays there is an unprecedented growth of interest for non-display applications of LCs during the 1st decade of 21st century. Consequently the research and development of LCs are moving rapidly beyond displays and evolving into entirely new scientific frontiers, opening broad avenues for versatile applications such as lasers, photovoltaics, light-emitting diodes, field effect transistors, nonlinear optics, biosensors, switchable windows, and nanophotonics. These fields, which gain extensive attentions of physicists, chemists, engineers, and biologists, are of a most engaging and challenging area of contemporary research, covering organic chemistry, materials science, bioscience, polymer science, chemical engineering, material engineering, electrical engineering, photonics, optoelectronics, nanotechnology, and renewable energy.

This book does not intend to exhaustively cover the field of LCs beyond displays, as it is extremely difficult to do so within a single book. Instead, the book focuses on the recent developments of most fascinating and rapidly evolving areas related to the theme. The chapters span the following topics: LC lasers (Chapter 1), self-organized semiconducting discotic LCs (Chapter 2), magnetic LCs (Chapter 3), ferroelectric LCs for nonlinear optical applications (Chapter 4), photo-stimulated phase transformations in LCs (Chapter 5), light-driven chiral molecular switches or motors in LC media (Chapter 6), LC functionalized nano- and microfibers produced by electrospinning (Chapter 7), functional LC block copolymers (Chapter 8), semiconducting applications of polymerizable LCs (Chapter 9), LCs of carbon nanotubes and carbon nanotubes in LCs (Chapter 10), LCs in metamaterials (Chapter 11), ferroelectric colloids in LCs (Chapter 12), cybotactic groups in the nematic phase of bent core mesogens (Chapter 13), lyotropic chromonic LCs: emerging applications (Chapter 14), LC-based chemical sensors (Chapter 15), LCs for switchable windows (Chapter 16), and LCs for nanophotonics (Chapter 17). In each chapter, the state-of-the-art along with future potentials in the respective fields has been discussed and highlighted by the leading experts.

I hope this book is not only to introduce fundamental knowledge, illustrative examples, and successful applications beyond displays, but also to stimulate more

interest for further development in this realm of research, wishing the interdisciplinary actions of physicists, chemists, engineers, and biologists can bring grateful values to push the LCs research forward in the 21st century. For graduate students, researchers, and scientists from other fields who want to get involved in LCs, this book is anticipated to serve as a beginners' guide. For established researchers, this book is expected to provide insights into knowledge beyond their expertise. I sincerely hope this book can generate interest to readers and help researchers to spark creative ideas.

I would like to express my gratitude to Jonathan Rose at John Wiley & Sons, Inc. for inviting us to bring this exciting field of research to a wide audience, and to all our distinguished contributors for their dedicated efforts. Also I am indebted to my wife Changshu, my sons Daniel and Songqiao for their great support and encouragement.

QUAN LI
KENT, OHIO

August 2011

CONTRIBUTORS

Nicholas L. Abbott, Department of Chemical and Biological Engineering, University of Wisconsin, Madison, WI, USA

Bharat R. Acharya, Platypus Technologies, Madison, WI, USA

Dean P. Brown, Materials and Manufacturing Directorate, Air Force Research Laboratory WPAFB, OH, USA

Jesús Etxebarria, Department of Condensed Matter Physics, University of the Basque Country, Bilbao, Spain

Jacob T. Hunter, Department of Chemical and Biological Engineering, University of Wisconsin, Madison, WI, USA

Stephen M. Kelly, Department of Physics and Chemistry, University of Hull, UK

Satyendra Kumar, Department of Physics, Kent State University, Kent, OH, USA

Jan P. F. Lagerwall, Graduate School of Convergence Science and Technology, Seoul National University, Gyeonggi-do, Korea

Oleg D. Lavrentovich, Liquid Crystal Institute, Kent State University, Kent, OH, USA

Quan Li, Liquid Crystal Institute, Kent State University, Kent, OH, USA

Mary O'Neill, Department of Physics and Chemistry, University of Hull, UK

Heung-Shik Park, Liquid Crystal Institute, Kent State University, Kent, OH, USA

S. Krishna Prasad, Center for Soft Matter Research, Bangalore, India

R. Rajesekharan, Electrical Engineering Division, University of Cambridge, Cambridge, UK

Yuriy Reznikov, Institute of Physics, National Academy of Sciences of Ukraine, Kyiv, Ukraine

Giusy Scalia, Department of Nanoscience and Technology, Seoul National University, Gyeonggi-do, Korea

Katsuaki Suzuki, Graduate School of Human and Environmental Studies, Kyoto University, Kyoto, Japan

Rui Tamura, Graduate School of Human and Environmental Studies, Kyoto University, Kyoto, Japan

Hideo Takezoe, Department of Organic and Polymeric Materials, Tokyo Institute of Technology, Tokyo, Japan

Xia Tong, Department of Chemistry, University of Sherbrooke, Québec, Canada

Yoshiaki Uchida, Graduate School of Human and Environmental Studies, Kyoto University, Kyoto, Japan

Augustine M. Urbas, Materials and Manufacturing Directorate, Air Force Research Laboratory WPAFB, OH, USA

Yan Wang, Liquid Crystal Institute, Kent State University, Kent, OH, USA

Timothy D. Wilkinson, Electrical Engineering Division, University of Cambridge, Cambridge, UK

Chenming Xue, Liquid Crystal Institute, Kent State University, Kent, OH, USA

Deng-Ke Yang, Chemical Physics Interdisciplinary Program and Liquid Crystal Institute, Kent State University, Kent, OH, USA

C. V. Yelamaggad, Center for Soft Matter Research, Bangalore, India

Yongqiang Zhang, Micron Technology, Inc., Longmont, CO, USA

Yue Zhao, Department of Chemistry, University of Sherbrooke, Québec, Canada

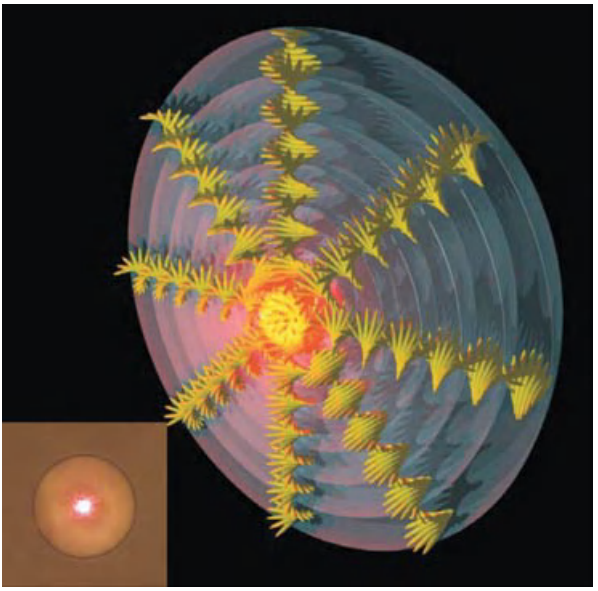

FIGURE 1.21 Helical structure in a CLC microdroplet. Image of microdroplet in a lasing condition is also shown [76].

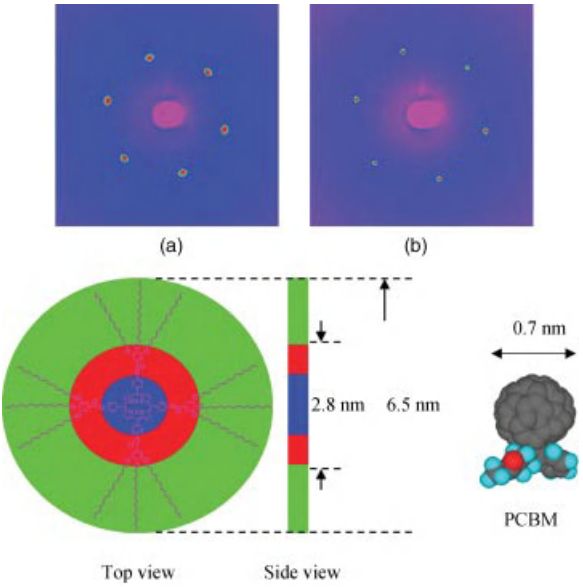

FIGURE 2.20 Top: Synchrotron XRD patterns from homeotropic monodomain of material **35** (a) and the blend of **35** (b) with $PC_{61}BM$ in an 8-μm-thick glass cell. Bottom: Calculated geometric dimensions of porphyrin **35** and 3D ChemDraw spacing-filling model of fullerene derivative $PC_{61}BM$ and the schematic representations of homeotropically aligned architecture of the blend of **35** and $PC_{61}BM$. Reproduced with permission from ref. 110.

Liquid Crystals Beyond Displays: Chemistry, Physics, and Applications, Edited by Quan Li.
© 2012 John Wiley & Sons, Inc. Published 2012 by John Wiley & Sons, Inc.

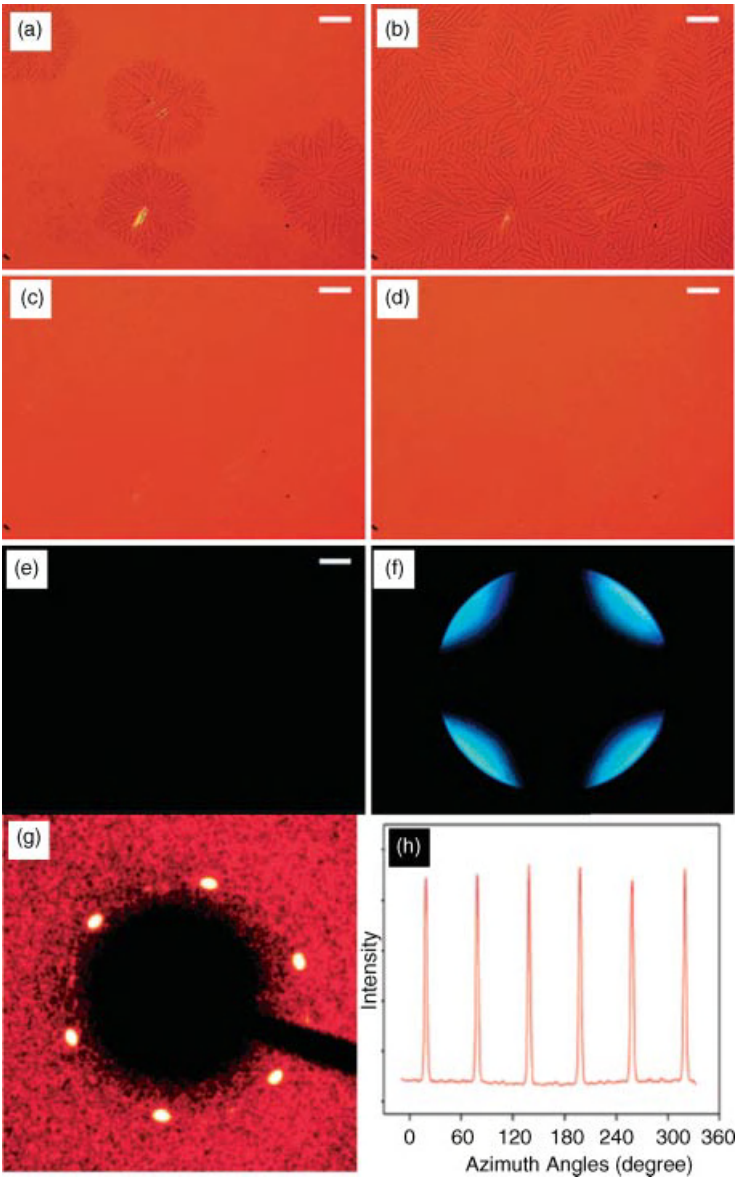

FIGURE 2.32 Formation of homeotropic texture on a macroscopic scale via slow cooling of the 1.8 μm cell with **33**. Slow cooling induces selective nucleation and growth of homeotropic domain (parts (a) and (b) at 121.0°C) and hence yields uniform homeotropic columnar orientation at lower temperatures ((c) 113.0°C and (d) 75.0°C), confirmed by both (e) optical texture under crossed polarizers and (f) conoscopic image at 75.0°C. Optical images were taken at (a–d) 70° and (e) 90° angles between polarizers. The scale bar corresponds to 50 μm. (g) X-ray 2D pattern for the Col_h phase at 75.0°C of **33**. (h) The azimuthal scan of the peak in (g) shows equally spaced six peaks with uniform intensity distribution. Reproduced with permission from ref. 77(a).

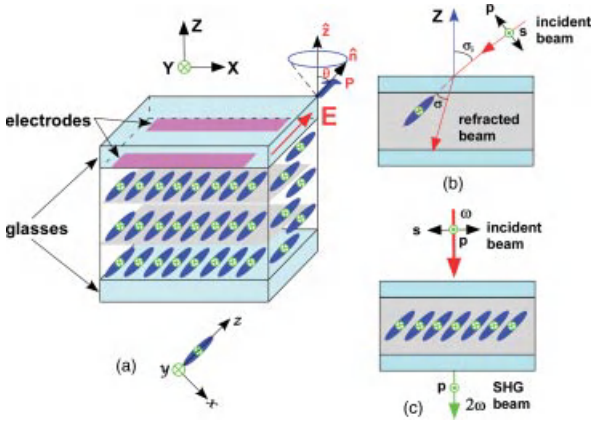

FIGURE 4.8 Schematic illustration of (a) a homeotropically aligned FLC cell with the spontaneous polarization P parallel to the polar axis which is the Y-axis in the XYZ coordinate system and the y-axis in the xyz molecular coordinate system, (b) SHG experiments using phase matching method, and (c) SHG experiments using Maker fringe method at normal incidence. In (b), the phase matching is achieved by rotating the cell around the polar axis, θ is the tilt angle, σ_i is the incident angle, and σ is the angle between the optical propagation direction and the FLC molecule director $\hat{n}$.

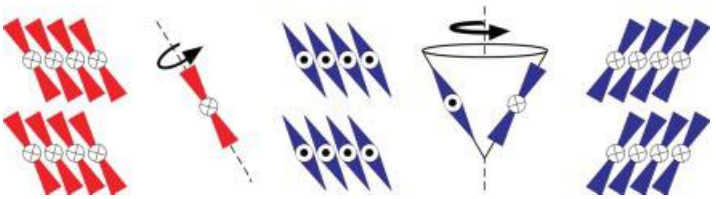

FIGURE 4.15 Switching by molecular rotation around the long axis (left) changes both chirality and polarity, while switching on the tilt cone (more common, right) only changes polarity with retention of chirality.

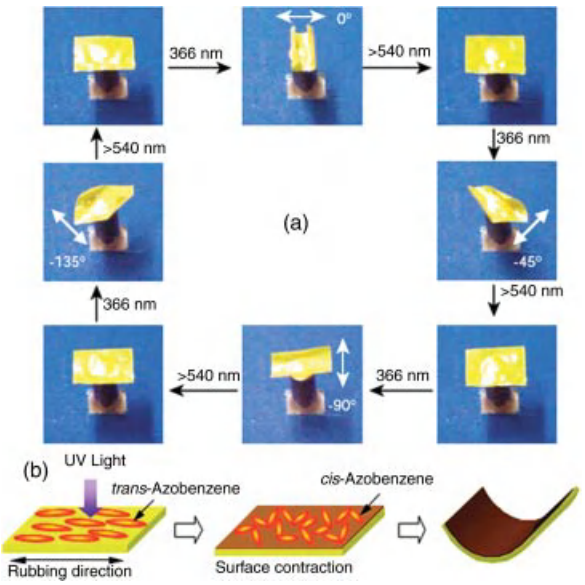

FIGURE 5.30 (a) Demonstration of photocontraction of a cross-linked polymer liquid crystal containing azobenzene, in which the bending direction of the film is manipulated by the orientation of linearly polarized light in the UV region (inducing contraction) and visible light (recovery of the original shape). Reprinted with permission from ref. 100, Copyright 2003, Nature publishing group. (b) Schematic to illustrate the proposed mechanism governing the photocontraction. Reprinted with permission from ref. 90, Copyright 2006, John Wiley & Sons.

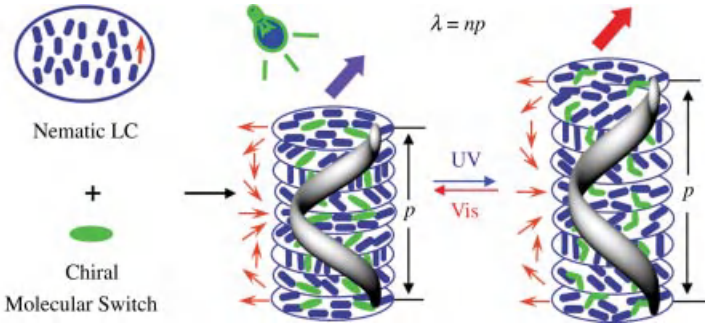

FIGURE 6.1 A schematic mechanism of the reflective wavelength of light-driven chiral molecular switch or motors in achiral nematic LC media reversibly and dynamically tuned by light.

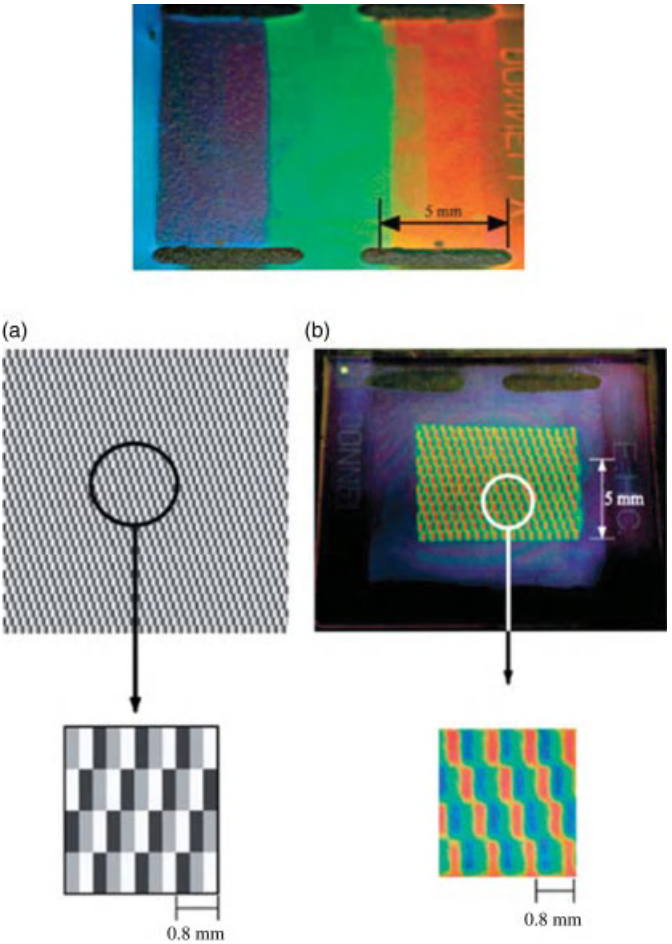

FIGURE 6.9 Changes in the reflection color of the CLC consisting of chiral azobenzene **9** and non-photoresponsive chiral dopant **10** in E44 by varying UV irradiation time: 0 s (left), 4 s (middle), and 10 s (right) (top); (a) gray mask and (b) red–green–blue (RGB) patterning of the CLC obtained by UV irradiation for 10 s through the gray mask at 25°C. Used with permission from Ref. [43].

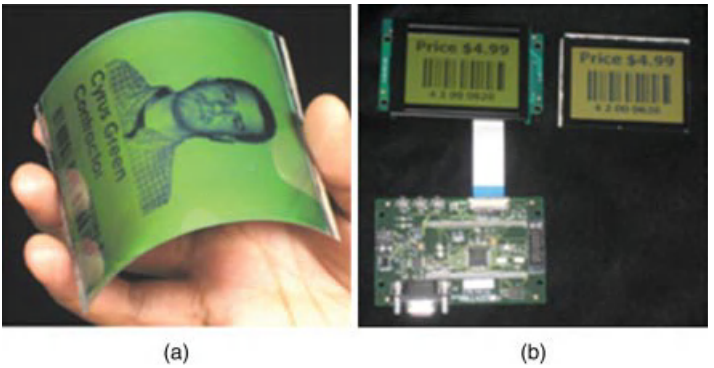

FIGURE 6.11 A flexible optically addressed photochiral display (A); a conventional display attached bulky and costly electronics compared with an optically addressed display with the same image without the added electronics (B). Used with permission from Ref. [47].

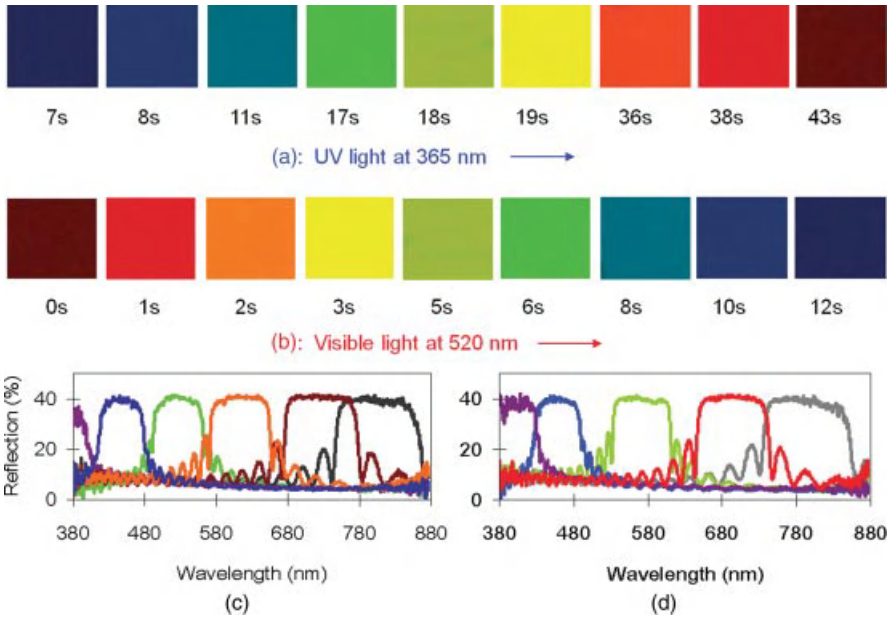

FIGURE 6.14 Reflection color images of 6.5 wt% chiral switch **2** in commercially available achiral LC host E7 in 5 μm thick planar cell. A: upon UV light at 365 nm (5.0 mW/cm^2) with different time; B: reversible back across the entire visible spectrum upon visible light at 520 nm (1.5 mW/cm^2) with different time. The colors were taken from a polarized reflective mode microscope. Reflective spectra of 6.5 wt% chiral switch **2** in LC E7 in a 5 μm thick planar cell at room temperature. C: under UV light at 365 nm wavelength (5.0 mW/cm^2) with different time (3 s, 8 s, 16 s, 25 s, 40 s, and 47 s, from left to right). D: under visible light at 520 nm wavelength (1.5 mW/cm^2) with different time (2 s, 5 s, 9 s, 12 s, and 20 s, from right to left). Used with permission from Ref. [39].

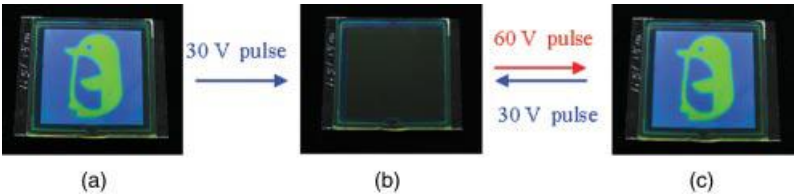

FIGURE 6.15 Images of 5 μm thick homeotropic alignment cell with 4 wt% chiral switch **2** in LC host E7. (*See text for full caption.*)

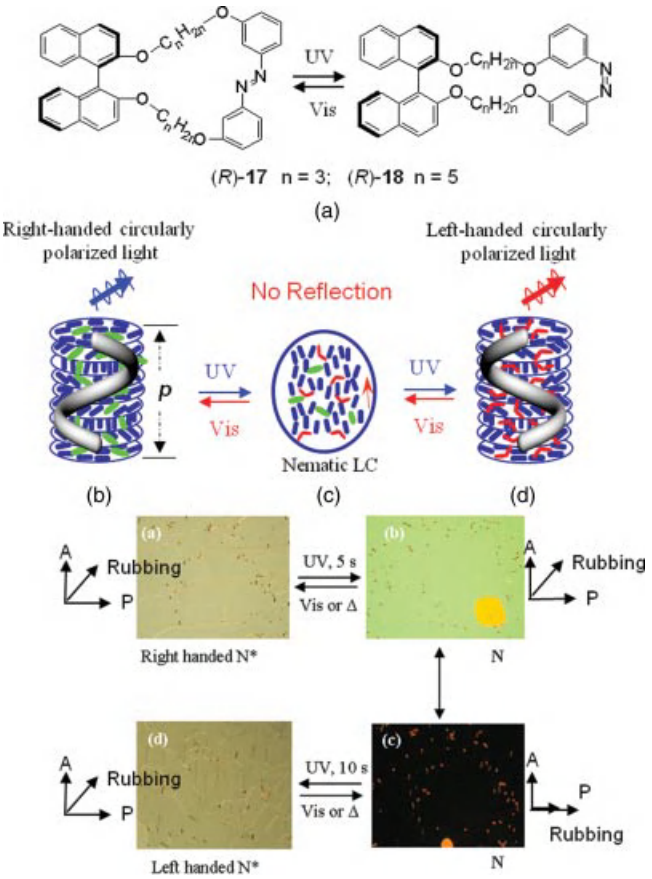

FIGURE 6.16 Top: Molecular structures of chiral cyclic azobenzenes (*R*)-**17** and (*R*)-**18** (A). Middle (B–D): Schematic mechanism of reflection wavelength tuning and handedness inversion of light-driven chiral molecular switch or motor in achiral nematic LC media reversibly and dynamically tuned by light. Bottom: Polarized optical photomicrographs of a planar aligned N* film containing 10 wt% (*R*)-**17** in ZLI-1132 at room temperature, showing reversible phase transitions occurring by light irradiation of the sample inside a 5 μm cell: (a) oily streak texture of the N* phase before irradiation; (b) N phase obtained by exposure of the sample to UV irradiation; (c) extinguishing orientation of the N cell by rotation between crossed polarizers; (d) regeneration of the oily streak texture of the N* phase upon continued irradiation (bottom–right). Used with permission from Ref. [56].

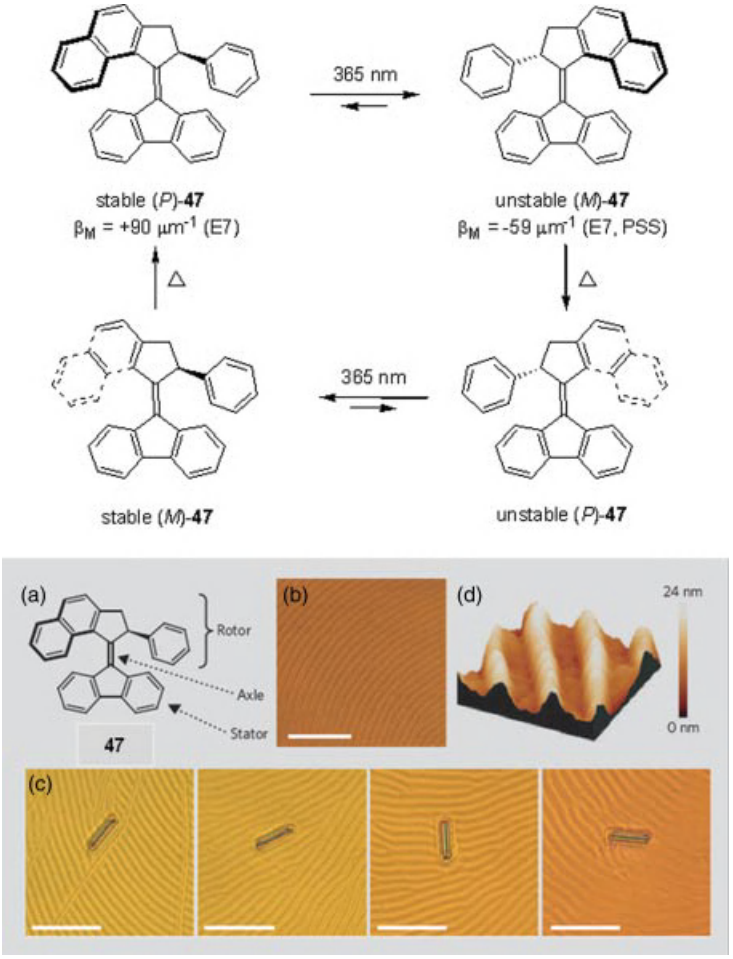

FIGURE 6.27 Features of a light-driven molecular motor: (a) Molecular structure of chiral motor **47**. (b) Polygonal texture of a LC film doped with 1 wt% chiral motor **47**. (c) Glass rod rotating on the LC during irradiation with ultraviolet light. (*See text for full caption.*)

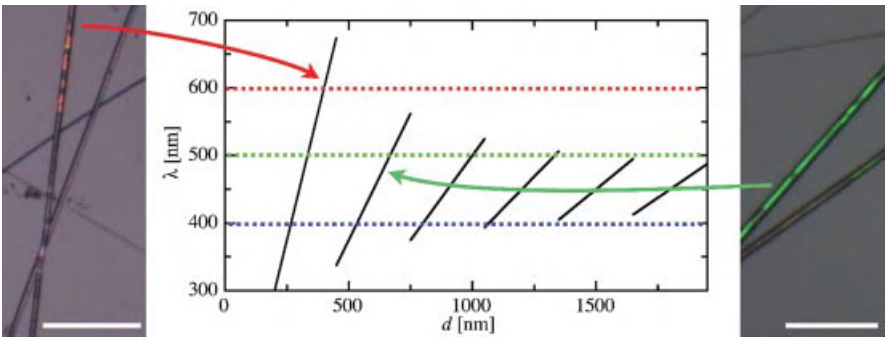

FIGURE 7.13 The confinement of the cholesteric liquid crystal **mixture 1** inside thin cylindrical fibers forces the director helix to expand or compress from its natural pitch, leading to a reflection color λ that depends on the inner fiber diameter d, as illustrated in the center diagram (black curve). (*See text for full caption.*)

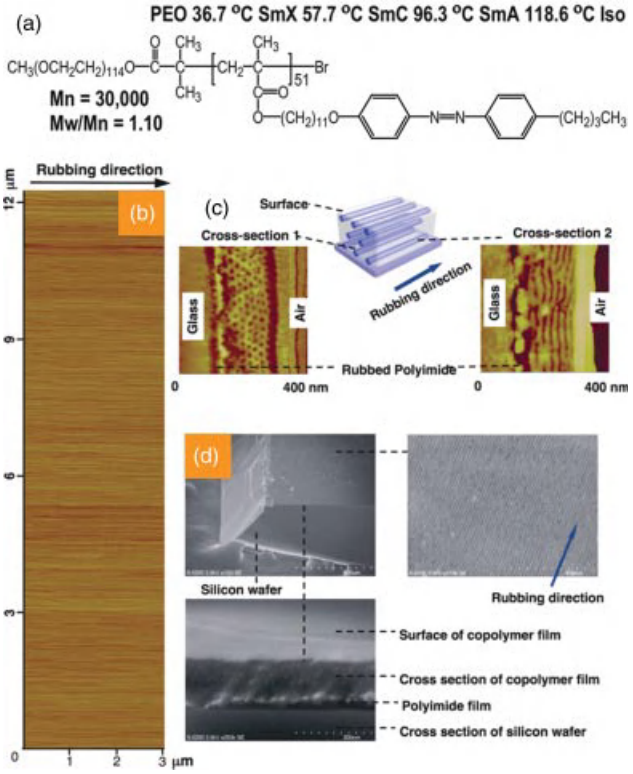

FIGURE 8.1 (a) Chemical structure and phase transition temperatures of the LC diblock copolymer. (*See text for full caption.*)

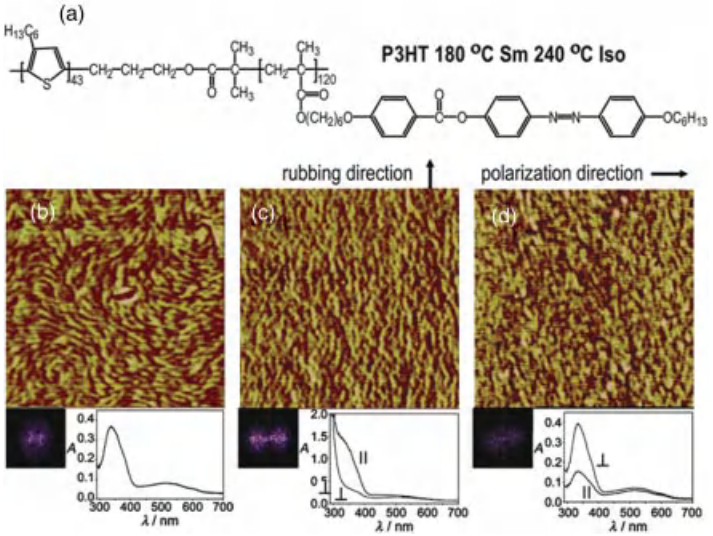

FIGURE 8.4 (a) Chemical structure and phase transition temperatures of the LC diblock copolymer. (*See text for full caption.*)

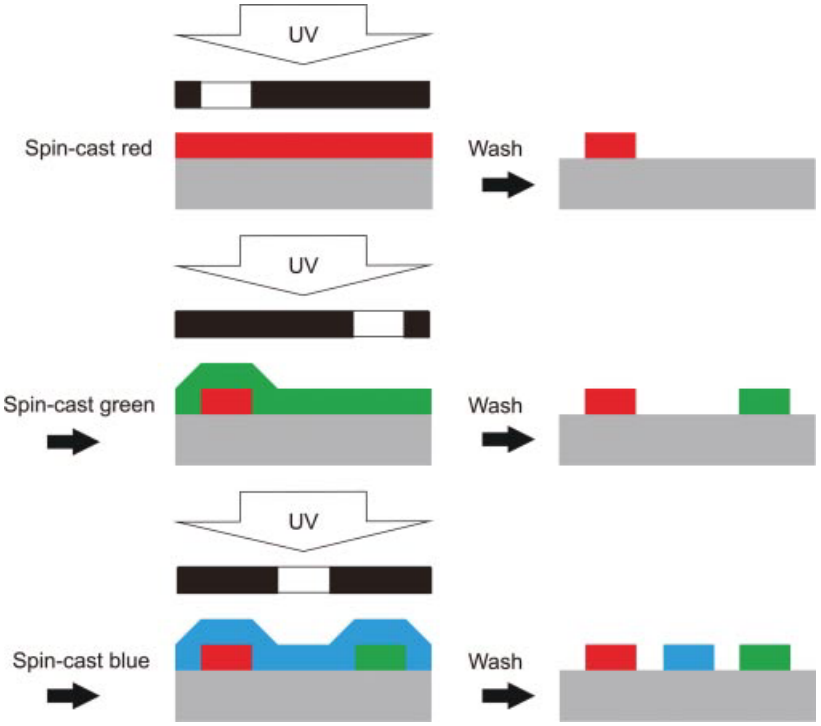

FIGURE 9.16 Photolithographic process to produce a red, green, and blue pixellated OLED. After patterned irradiation with ultraviolet light, the sample is washed with the solvent used for deposition, so that the unexposed regions are removed.

FIGURE 9.18 A prototype OLED with a red, green, and blue pixel on the same substrate fabricated by sequential spin-coating and polymerization of the materials **20**, **5** blend, **5** and **19** onto a PEDOT:PSS film covering a patterned indium tin oxide (ITO) substrate. (*See text for full caption.*)

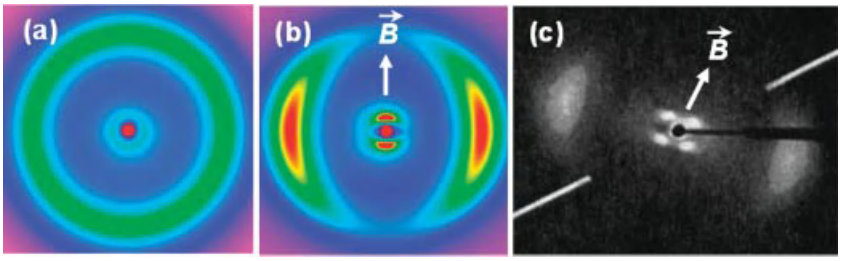

FIGURE 13.4 Two dimensional X-ray diffraction pattern from (a) isotropic and (b) nematic phases of 4-cyano-4′-pentylbiphenyl (5CB) and (c) cybotactic smectic C phase of nematic phase of bis-(4′-n-octyloxybenzal)-2-chlor1o,4-phenylenediamine. (*See text for full caption.*)

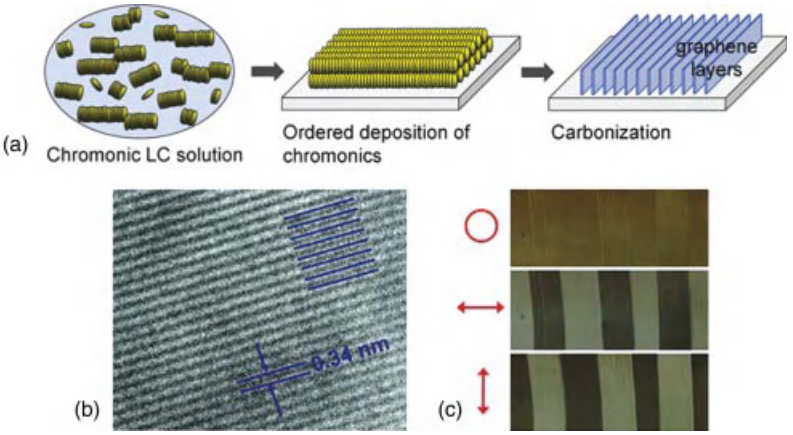

FIGURE 14.19 Schematic diagram illustrating the formation of vertically aligned graphene layer arrays (a). HR-TEM image showing the full fringe field in *Z*-axis projection, indicating vertical grapheme layer orientation (b). (*See text for full caption.*)

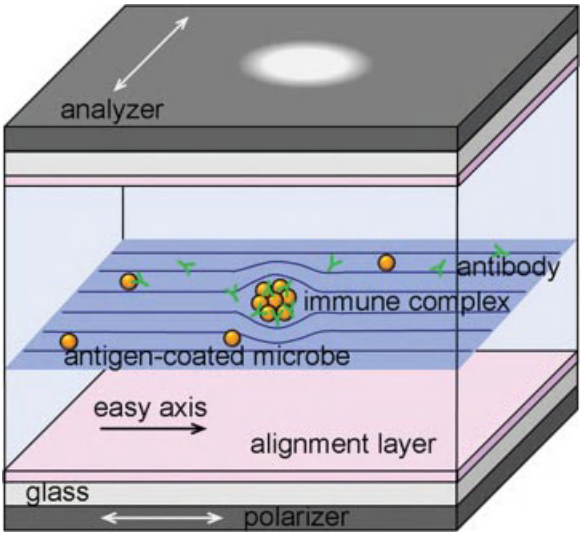

FIGURE 14.20 The scheme of the LCLC biosensor for the detection of immune complexs. (Redrawn from Shiyanovskii et al. [37].)

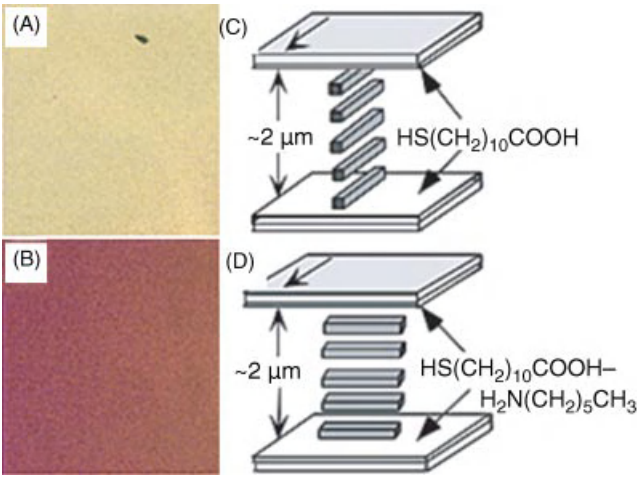

FIGURE 15.11 (A) and (B) Interference color of a film of nematic 5CB supported on a SAM formed from $HOOC(CH_2)_{10}SH$ before (A) and after (B) exposure to n-$H_2N(CH_2)_5CH_3$. (C) Schematic illustration of the orientation of the LC in contact with a carboxylic acid monolayer that is consistent with interference colors shown in panel (A). The bold arrow indicates the direction of deposition of gold onto the substrate. (D) Schematic illustration of the orientation of the LC in contact with the hexylamine-reacted carboxylic acid monolayer that is consistent with the interference colors shown in panel (B). Reprinted with permission from Shah and Abbott [28]). Copyright 2003 American Chemical Society.

FIGURE 16.3 Photographs of green house with liquid crystal switchable window in Cleveland Botanic Garden. Photo courtesy of Cleveland Botanic Garden.

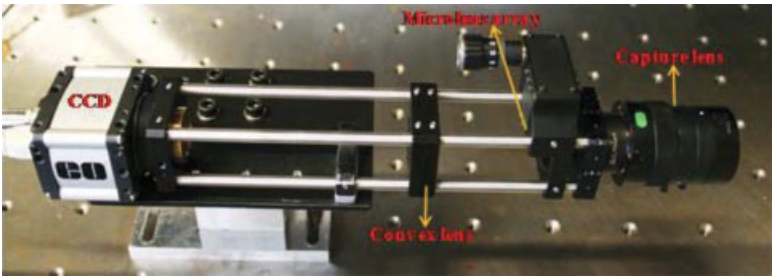

FIGURE 17.37 The 3D vision sensor camera stage developed.

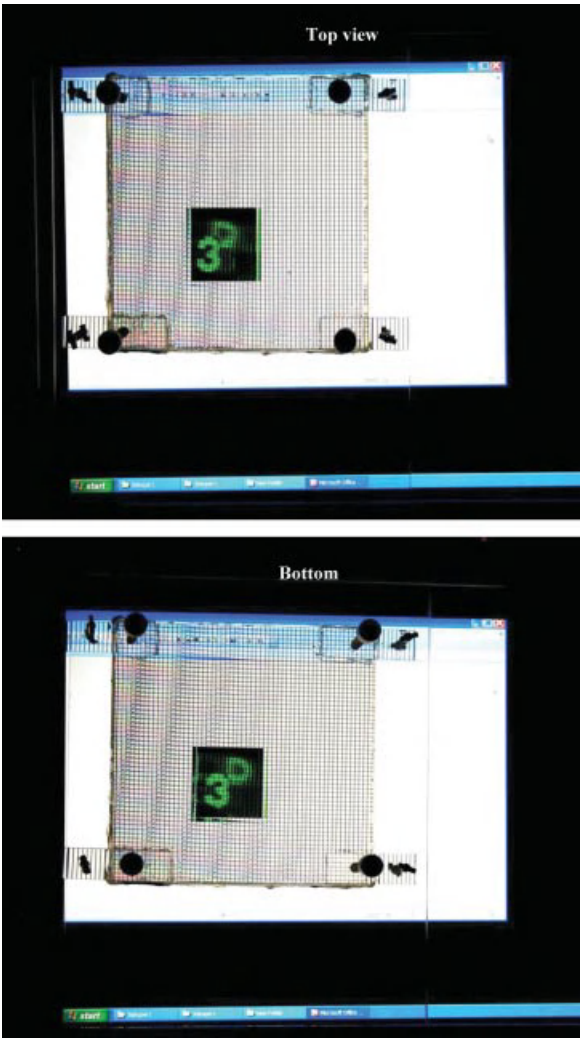

FIGURE 17.39 The reconstructed 3D image in the developed 3D display from all the elemental images viewed from top and bottom.

CHAPTER 1

Liquid Crystal Lasers

HIDEO TAKEZOE

Department of Organic and Polymeric Materials, Tokyo Institute of Technology, Tokyo, Japan

1.1 INTRODUCTION

Liquid crystals (LCs) have fluidity and a long-range orientational order. These properties enable us to use LCs as display materials. Another important property is a positional order. The periodicity is in the range not only of the molecular length periodicity like in smectic LCs but also of visible light wavelength. The latter generally arises from chirality, and in many cases results in helical structures. The most well-known example is cholesteric LCs (CLCs), in which the local structure is nematic and the director rotates to form a helical structure with the helical axis perpendicular to the director. The media that have periodic structures in the optical wavelength are called photonic crystals. Hence, we can call CLC a one-dimensional (1D) photonic crystal. Like an energy gap for electrons propagating in periodic crystal structures, a stop band emerges at the edges of the first Brillouin zone in CLCs. Within the stop band, light dampens and cannot propagate. When the light propagation is limited along any direction, we call it the photonic bandgap (PBG) [1, 2]. In this chapter, the stop band is called PBG in a broad sense.

The dispersion relation between angular frequency ω and wavenumber k *in vacuo* is given by $\omega = ck$, where c is the velocity of light (Figure 1.1a). In CLCs, the refractive index changes periodically, so the incoming light to the helix undergoes reflection if the light wavelength coincides with the optical pitch (structural pitch multiplied by an average refractive index), that is, Bragg reflection. Helical periodic structure makes the reflection very unique; that is, only a circularly polarized light (CPL) with the same handedness as the helix is reflected and another CPL with opposite handedness just passes through. This is called selective reflection. Such light propagation characteristics along the helical axis are rigorously solved, giving an analytical solution [3]. The dispersion relation thus obtained is shown in Figure 1.1b. Another unique feature compared with the other periodic structure is the sinusoidal

Liquid Crystals Beyond Displays: Chemistry, Physics, and Applications, Edited by Quan Li.
© 2012 John Wiley & Sons, Inc. Published 2012 by John Wiley & Sons, Inc.

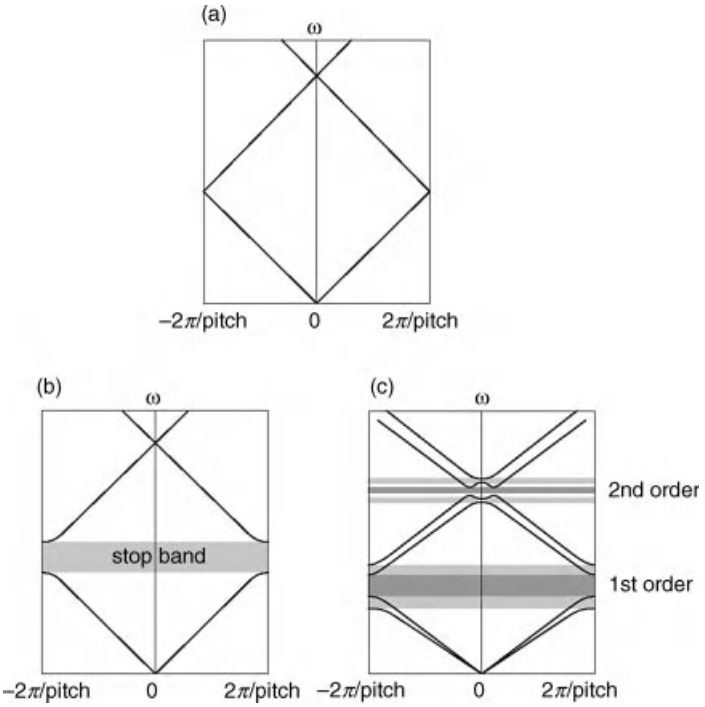

FIGURE 1.1 Dispersion relation (a) *in vacuo*, (b) in CLC at normal incidence, and (c) in CLC at oblique incidence. At oblique incidence, higher order reflection and total reflection regions are recognized.

change of the refractive index. Because of this, only the first-order Bragg reflection takes place (Figure 1.1b). For oblique incidence of light with respect to the helical axis, the periodic structure is no more than sinusoidal, so higher order reflections occur [4]. In addition, total reflection band(s) emerges, where light with any polarization states is reflected [5]. The dispersion relation (Figure 1.1c) calculated by the 4×4 matrix method [6] clearly reveals such behaviors. The emergence of higher order reflections and total reflection can be brought about by deforming the sinusoidal helical structure, for example, by applying an electric field. Such optical properties are similarly observable in other helical LC phases such as chiral smectic C^* (SmC^*) and twist grain boundary (TGB) phases.

Because of the selective reflection in visible wavelength regions, it is a natural question how the emission from dye molecules existing inside the helical structure is affected by the Bragg condition. Actually, Kogelnik and Shank [7] studied possible distributed feedback (DFB) lasers. Namely, lasing may occur if emitted light is confined in a DFB cavity made of CLC. The lifetime of the luminescence from dyes embedded in CLCs was also examined [8, 9]. The first observation of lasing from CLC was reported by Il'chishin et al. in 1980 [10]. They even showed the lasing wavelength tuning by temperature. However, it took almost two decades to be paid

much attention from other groups until Kopp et al. [11] reported a CLC microlaser. For historical details, please refer to an article by Bartolino and Blinov [12].

Let us consider efficient lasing conditions. In an isotropic medium, the rate R of photon emitted from an excited molecule is described by Fermi's golden rule:

$$R_{\mathrm{iso}} \sim M_{\mathrm{iso}} |E \cdot \mu|^2 \tag{1.1}$$

where M_{iso} is the density of state (DOS), μ is the transition dipole moment, and E is the electric field. In isotropic media, M is independent of the polarization and the radiation direction. In anisotropic media, the emission depends on the orientation of transition dipole moment μ with respect to the polarization of light, that is, E. When emission occurs from the excited CLC molecules, light propagates as one of the two eigenmodes E_1 and E_2. Then, emission rate for eigenmode E_i (R_i) is described as

$$R_i \sim M_i |E_i \cdot \mu|^2 \tag{1.2}$$

where M_i is the DOS associated with the eigenmode E_i. The fluorescent molecules embedded in CLCs have a certain degree of the nematic order, resulting in an anisotropic orientation distribution of the transition dipole moment. Hence to have large R_i, it is profitable that μ is parallel to the polarization of the eigenmode E_i. Now the other factor to have large R_i is DOS M, which is defined as

$$M = \left| \frac{\mathrm{d}}{\mathrm{d}\omega} \mathrm{Re}(k) \right| \tag{1.3}$$

Figure 1.2 shows a simulated transmittance spectrum and DOS (M). DOS shows maxima at the PBG edges where group velocity approaches to zero.

1.2 TYPES OF LASERS

There are several types of CLC microlasers. DFB lasers and defect mode lasers are the most popular ones, which will be described later. For more detail on these modes, please refer to a review by Kopp et al. [13]. In this chapter, we do not include random lasing and lasing from artificial structures such as grating.

1.2.1 DFB CLC Lasers

When light propagates in periodic media with the same periodicity as the light wavelength, the light suffers reflection due to the PBG. Hence, if CLC is doped with dyes, emitted light within the PBG is confined and amplified in CLC, and finally lasing results. This type of cavity without using mirrors is called DFB cavity. Lasers using DFB cavities are called DFB lasers. The DFB cavity is widely

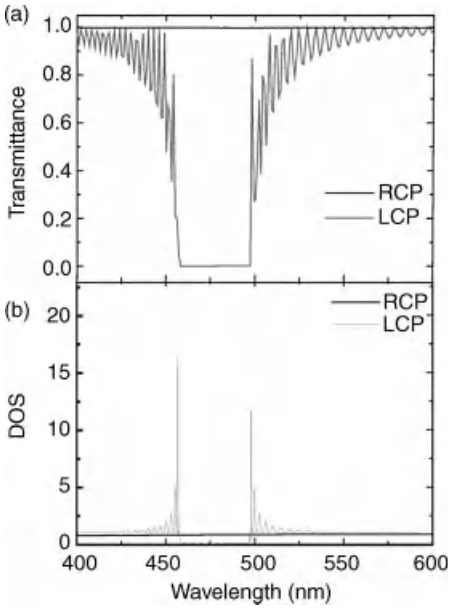

FIGURE 1.2 Simulated transmittance spectrum and DOS spectrum for R- and L-CPL to left-handed CLC at normal incidence [79].

used in semiconductor lasers, in which active materials are on substrates with periodic refractive index changes. Since CLCs themselves spontaneously form DFB cavity, this is the simplest CLC microlaser structure. Namely, instead of fabricating layer-by-layer structures consisting of high and low refractive indices as in semiconductor lasers, the refractive indices in CLC change due to the helical structure of the dielectric ellipsoid. This is a great advantage of CLC microlasers compared with semiconductor lasers, in which the fabrication of microstructure is necessary.

Dowling et al. [14] predicted that DFB lasing occurs at the edge of PBG for 1D periodic structures with sufficiently large refractive index modulation. They demonstrated that the photon group velocity approaches zero near the band edge of a 1D photonic bandgap structure. This effect implies an exceedingly long optical path length in this structure, and the photon dwell time for incident waves at the band edge is significantly increased. M in Eq. (1.3) is the absolute inverse slope of the dispersion relation or reciprocal form of group velocity. Since the emission rate R is proportional to DOS, the emission rate reaches maximum when group velocity falls to almost zero, which is realized at the edges of PBG, as shown in Figure 1.2b. Thus, low-threshold and mirrorless CLC laser is realized at the edges of PBG, where DOS gives maxima.

Experimentally, two major structures are possible in CLC microlasers; the helical structure is perpendicular or parallel to substrates. The former is rather easy to be fabricated by using substrate surfaces treated with planar alignment agents.

Homeotropic alignment surfaces give orientation with helical axis parallel to the surface. However, the orientation of helical axis to a particular direction is not easy.

Optical eigenmodes at the edges of PBG are linearly polarized in CLCs; they are perpendicular and parallel to the local director at the higher and lower energy edges, respectively. According to Eq. (1.2), R_i is larger at the lower energy edge, so lasing preferably occurs at the lower energy edge [15]. A simple theoretical description of the spontaneous emission as a function of wavelength in terms of the order parameter S for the transition dipole moment of the dye in the CLCs is as follows [16]:

$$\left\langle |E \cdot \mu|^2 \right\rangle = \frac{2}{3}\frac{\rho_i^2 - \frac{1}{2}}{\rho_i^2 + 1} S_{\text{dye}} + \frac{1}{3} \tag{1.4}$$

Here, ρ_i is the ellipticity of polarization state. Figure 1.3a shows calculated $\left\langle |E \cdot \mu|^2 \right\rangle$ in CLCs with the local director of the order parameter $S = 1.0$, 0.5, 0.2, 0, and -0.5 for the incidence of left circularly polarized light as a function of wavelength. Near the edges of photonic bandgap, the variation in $\left\langle |E \cdot \mu|^2 \right\rangle$ occurs sharply, because the polarization states of the eigenmode with the same handedness as the CLC's

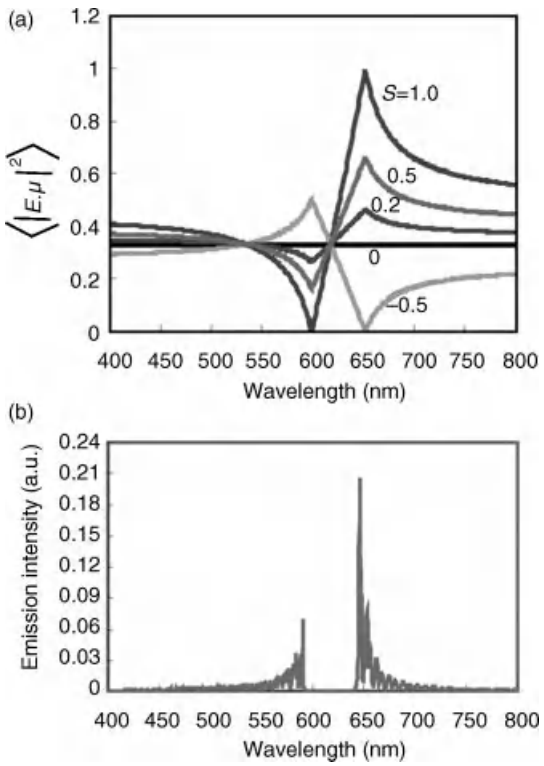

FIGURE 1.3 (a) Calculated $\left\langle |E \cdot \mu|^2 \right\rangle$ against wavelength for several S values. (b) Emission rate as a function of wavelength for $S = 0.5$.

structure is linearly polarized along the local director of the CLC. Particularly, at the low-energy edge of photonic bandgap, the value of $\left\langle |E \cdot \mu|^2 \right\rangle$ is high because the polarization direction is parallel to the local director of the CLC. However, at the high-energy edge of PBG, the $\left\langle |E \cdot \mu|^2 \right\rangle$ value is low because the polarization direction is perpendicular to the local director of the CLC. Then, the emission rate R_i (Eq. (1.2)) takes the highest value at the low-energy edge, as shown in Figure 1.3b.

1.2.2 Defect Mode Lasing

By doping semiconductors with donor or acceptor, donor or acceptor level is introduced within energy gaps. Similarly, addition or removal of extra dielectric material locally inside the photonic crystal produces donor or acceptor level [17]. DOS at such defect levels is much higher than that at PBG edges, so defect mode lasing is very important to realize low-threshold lasing. Many types of defect mode have been studied in 1D [13, 14, 18], 2D [19], and 3D [20, 21] photonic structures. These can be produced by removing or adding material or by altering the refractive index of one or a number of elements in 1D, 2D, and 3D PCs. Introducing a quarter-wavelength space in the middle of a layered 1D sample produces a defect in the middle of PBG. Such a defect is widely used to produce high-Q laser cavities [13].

Five kinds of configurations are suggested to generate a defect mode in CLCs (Figure 1.4): (1) the creation of a phase jump without any spacing layer in CLCs [22–24] and in smectic LCs [25], (2) the introduction of an isotropic spacing layer in the middle of the CLCs [26, 27], (3) the introduction of an anisotropic spacing layer in the middle of the CLCs [28, 29], (4) combination of (1) and (2) [30], and (5) the local deformation of the helix in the middle of the CLC layer [31].

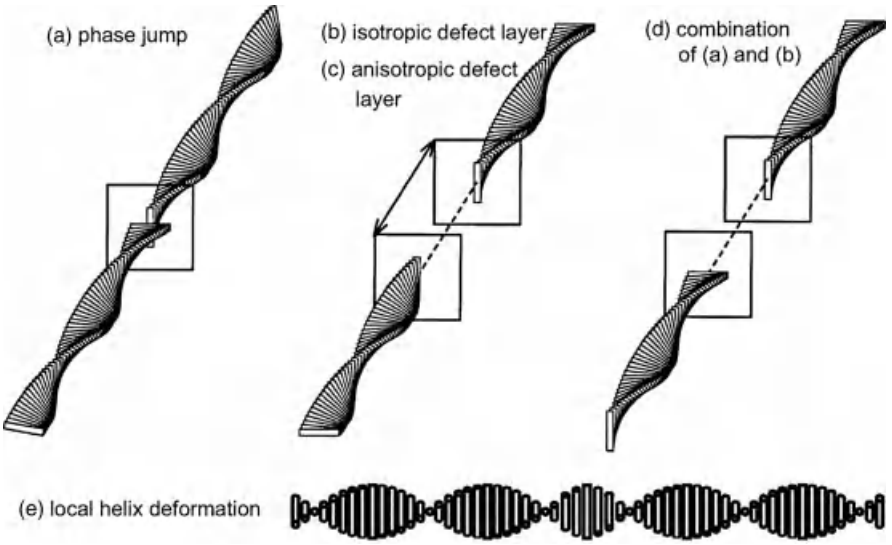

FIGURE 1.4 Five kinds of defect structures in CLCs.

The defect mode 1, that is, a chiral twist defect, can be created by rotating one part of the CLC [22, 23], as shown in Figure 1.4a. Changing the chiral twist angle from 0° to 180° tunes the defect wavelength from high- to low-wavelength PBG edge. By twisting one part of the CLC by 90°, a defect mode can be generated at the center of PBG due to the phase shift $\pi/2$ of electromagnetic wave inside the photonic bandgap. The defect mode 2 can be produced in a CLC structure by introducing isotropic layer between two CLC layers in order to destroy the helical periodicity of CLCs, as shown in Figure 1.4b [26]. For the thickness of the isotropic defect layer that generates the phase shift $\pi/2$, a defect mode can be generated at the center of PBG. This condition is expressed as

$$d = (2i + 1)\frac{\lambda}{4 \cdot n} \tag{1.5}$$

where d is the thickness of a defect layer, i is an integer, λ is the wavelength of the defect mode, and n is the refractive index of the defect layer.

Let us show one example of defect mode lasing of type 2 [27]. Figure 1.5 shows the simulation of transmittance and DOS in a CLC laser with a thin isotropic layer (0.54 μm thick poly(vinyl alcohol) (PVA) film) as an isotropic defect layer. A sharp defect level is observed, where highest DOS is obtained. Lasing was observed at

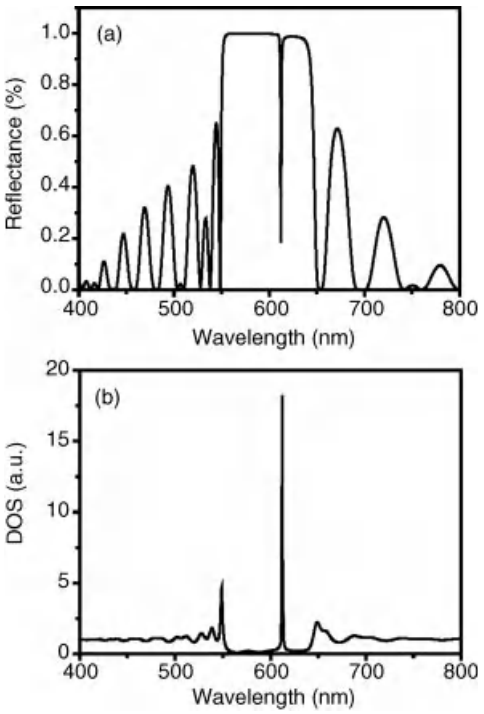

FIGURE 1.5 (a) Simulated transmittance spectrum and (b) DOS spectrum for CLC with an inserted isotropic defect layer [27].

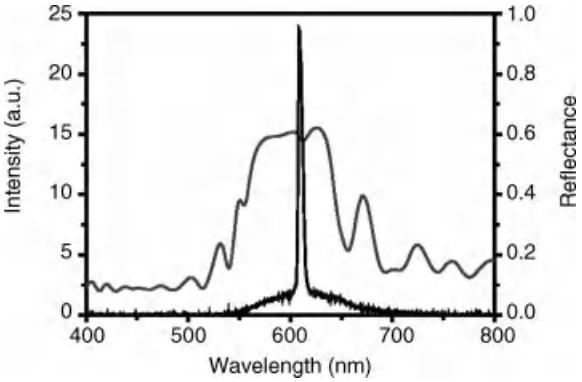

FIGURE 1.6 Lasing spectrum at the defect state together with a transmittance spectrum [27].

the defect wavelength, as shown in Figure 1.6. Since the device is composed of polymer CLC and PVA, one can peal out the film from the substrate as a freestanding film of 5.5 μm thickness.

1.3 LOWERING THRESHOLD

One of the ultimate goals of CLC microlasers is continuous wave (cw) lasing. For this purpose, the lasing threshold must be essentially zero. Many efforts have been made from various points of view. These efforts are classified into three groups: (1) improved cavity structures, (2) improved excitation conditions, and (3) improved materials. For (1), (1a) utilizing a single output window and (1b) utilizing defect mode were examined. For (2), (2a) excitation at the PBG edge by CPL and (2b) excitation at a higher energy (shorter wavelength) side of an absorption band were used. For (3), (3a) utilizing highly ordered dyes, (3b) utilizing CLCs with higher anisotropy of refractive indices, (3c) utilizing Förster energy transfer, and (3d) developing new dyes were examined.

1.3.1 Lowering Threshold by Improved Cavity Structures

Amemiya et al. [32] introduced polymeric CLC (PCLC) reflection layers for excitation light (PCLC pump substrate) as well as for outcoupled light (PCLC laser substrate), as shown in Figure 1.7, and succeeded in reducing the threshold by a factor of 2 (Figure 1.8). Matsuhisa et al. [33] used multiple inorganic layers for the similar purpose and obtained lower lasing threshold than the normal cell. It is known that the defect mode has an advantage to have higher DOS, as shown in Figure 1.5. Actually, Schmidtke et al. [23] and Ozaki et al. [24] demonstrated low-threshold defect mode lasing by using a phase jump in CLCs. As shown in Figure 1.9, the threshold in defect mode lasing is more than one order of magnitude smaller than that in the PBG edge lasing. The other group also obtained the similar results [27].

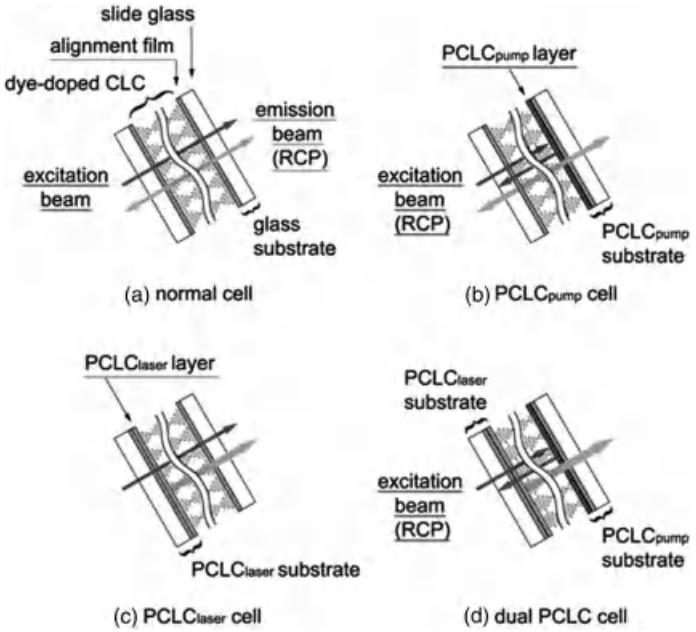

FIGURE 1.7 Some kinds of cell structures: (a) simple CLC cell, (b) CLC cell with PCLC layer for reflecting excitation light, (c) CLC cell with PCLC layer for reflecting emitted light, and (d) CLC with PCLC layers for reflecting both excitation and emitted light [32].

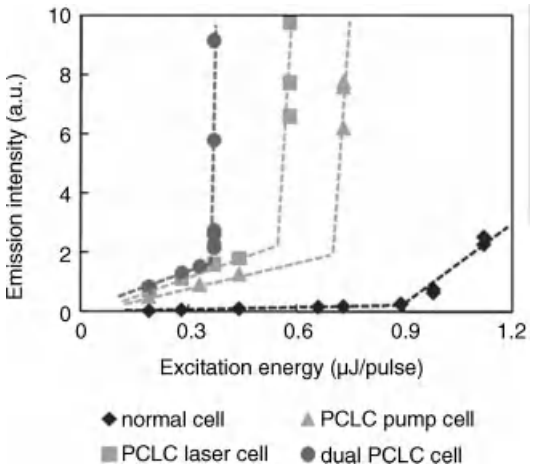

FIGURE 1.8 Threshold behavior for four cell geometries illustrated in Figure 1.7.

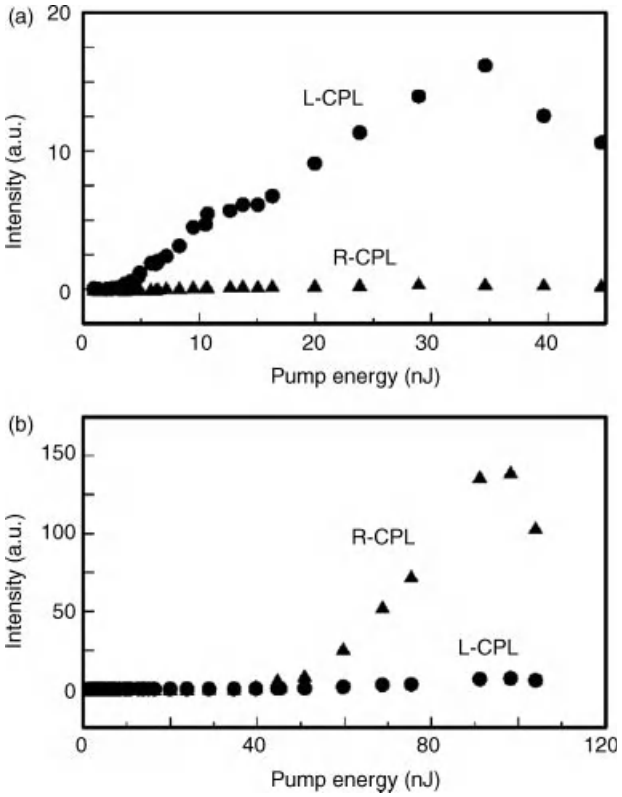

FIGURE 1.9 Threshold behavior for (a) defect and (b) DFB modes [23].

1.3.2 Lowering Threshold by Improved Excitation Conditions

If the dwell time at the excitation wavelength is long, efficient use of excitation energy can be achieved [34]. This condition can be realized by the excitation using CPL of the same handedness as the CLC helix at the first minimum of the subsidiary oscillation in the higher energy side of the reflection band [35]. Figure 1.10 shows the result in a dye-doped right-handed CLC (R-CLC). At 532 nm, R-CPL excitation gives lower threshold than left-handed CPL (L-CPL) excitation. Surprisingly, the threshold also depends on the excitation wavelength. Although the reason is not clear, it was confirmed using three different dyes that excitation at higher energy side of absorption bands gives lower threshold [36].

1.3.3 Lowering Threshold by Improved Materials

The efforts for lowering threshold have been made also from materials sides. As host materials, CLCs with higher anisotropy of the refractive index are more profitable. This is because PBG width is proportional to the anisotropy, and wider PBG gives

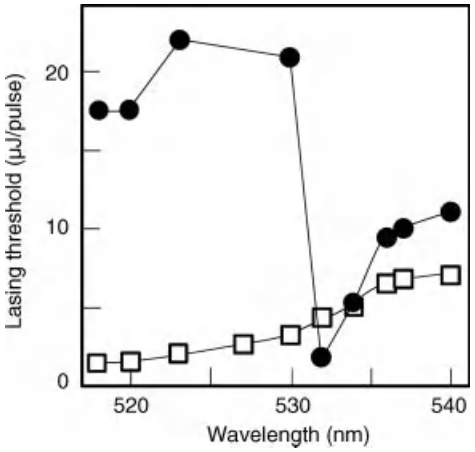

FIGURE 1.10 Lasing threshold as a function of wavelength for R- and L-CPL incidence to right-handed CLC cell [35].

higher DOS at the edges. This was experimentally confirmed by using three CLC hosts with different anisotropies of the refractive index [37]. The development of dyes is also important; first, highly ordered dyes are preferable because of Eq. (1.2) [15, 38]. As shown in Figure 1.3, the higher the order parameter S of dyes, the higher the DOS at the lower energy edge of PBG. In this sense, poly(phenylene vinylene) with triptycene groups is interesting, since S increases with increasing dye concentration. It is also known that the use of appropriate energy transfer between dye molecules (Förster couples) is possible to reduce the threshold. Reabsorption of the emitted light is a serious problem because it is one of the losses for lasing. In this sense, the use of energy transfer is one of the solutions to avoid reabsorption [39, 40]. Figure 1.11 shows the absorption and emission spectra of three dyes and threshold behaviors in the mixture systems containing two of these dyes. In both cases, the threshold is lower when the excitation through energy transfer is used compared with that by direct excitation.

So far, most of researchers have used commercially available dyes. Uchimura et al. [41] systematically synthesized pyrene and anthracene derivatives and evaluated the lasing characteristics. They found that one of the pyrene derivatives (Figure 1.12) shows a threshold as low as 1/20 of that in a commercial dye DCM. It was found that the threshold becomes lower with increasing luminous efficiency and radiative decay rate, as shown in Figure 1.12. We also need to systematically study the stability of dyes against light excitation. In this respect, it is important to have dyes showing low lasing threshold to minimize damage as well.

Recently, Wei et al. [42] used oligofluorene as a red-emitting dye and showed the superiority compared with a commercial DCM. Moreover, glassy CLC containing this dye is temporally stable compared with fluid CLC, lasing emission from which decays with time. Glassy state is important to realize robust sustainable lasing devices.

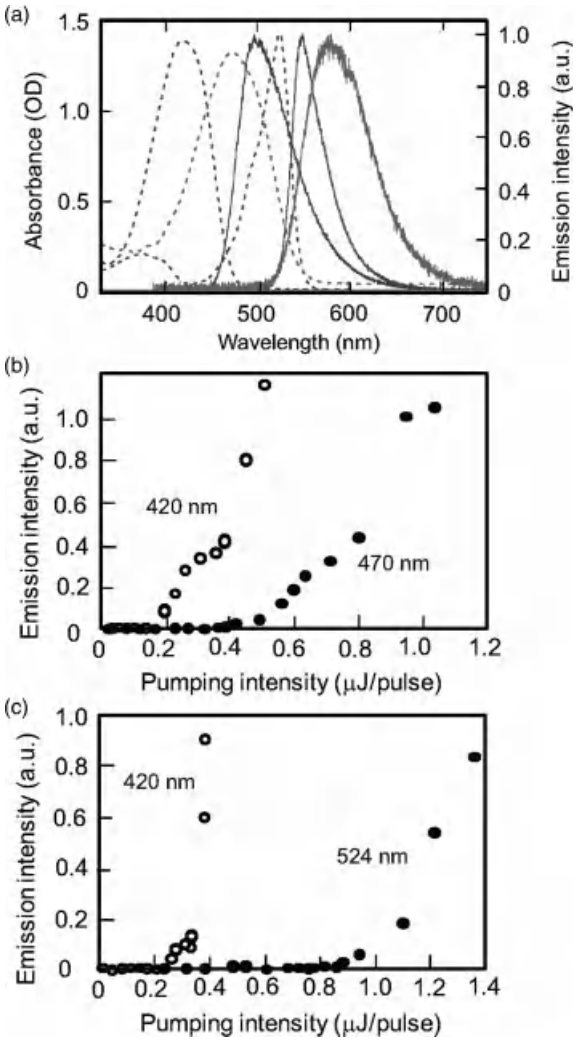

FIGURE 1.11 (a) Absorption (dotted curves) and emission (solid curves) spectra of dyes used as two kinds of Förster couples. Coumarin (C153), DCM, and pyrromethene (PM580) with increasing wavelength of the absorption peaks. Lasing threshold for direct and indirect (energy transfer) excitations to CLC cell with (b) C153 and DCM and (c) C153 and PM580 [39].

1.4 TUNABILITY

Wavelength tunability is one of the most attractive features in CLC lasers. Since the DFB lasing occurs at either or both of the edges of PBG, most of the cases at the lower energy edge, tuning of lasing wavelength is possible by tuning the helical pitch. There are many factors influencing the helical pitch: (1) temperature, (2) electric field, and (3) light irradiation. For polymer samples, (4) mechanical strain can also be used.

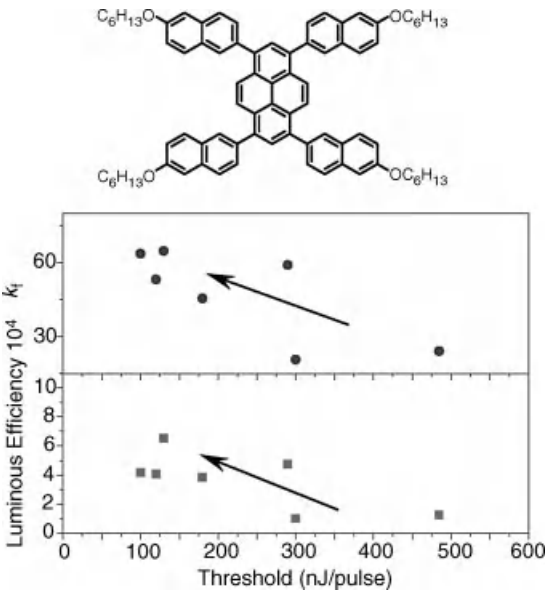

FIGURE 1.12 Relationship between luminous efficiency, radiative decay rate, and lasing threshold. The chemical structure of a pyrene derivative is also shown at the top.

In addition, (5) spatial tuning is a practical method for wavelength tuning, and (6) multiple lasing is also interesting.

1.4.1 Thermal Tuning

It is well known that the helical pitch in CLCs sensitively varies with temperature. Hence, thermal tuning was achieved by many scientists [38, 43] even from the very beginning [10]. Quite wide range of tuning like 30–60 nm is possible using single dye containing CLCs. However, the tuning is not really continuous because of the surface pinning of molecules. For the alignment with the helical axis perpendicular to the surface, surfaces have to be homogeneously treated. Since the molecular orientation at surfaces is fixed, number of pitch is quantized to be multiple numbers of half a pitch. The neighboring band edge wavelength λ and $\lambda + \Delta\lambda$ is given by

$$\frac{nd}{\lambda} - \frac{nd}{\lambda + \Delta\lambda} = \frac{1}{2}$$

where n is an average refractive index. Figure 1.13 shows the result using $d = 9\,\mu\text{m}$, $n = 1.66$, and $\lambda = 600\,\text{nm}$; $\Delta\lambda$ is 12.3 nm [43]. The discreteness can be reduced by using thick cells, but essential discreteness remains. To achieve real continuous tenability, devices with helical axis parallel to the surface were examined [44, 45]. Principally, thermal tuning in SmC* cavity must be continuous [46].

A different method for continuous wavelength tuning was examined by Morris et al. [47]. They used two different chiral dopants that exhibit opposing dependences

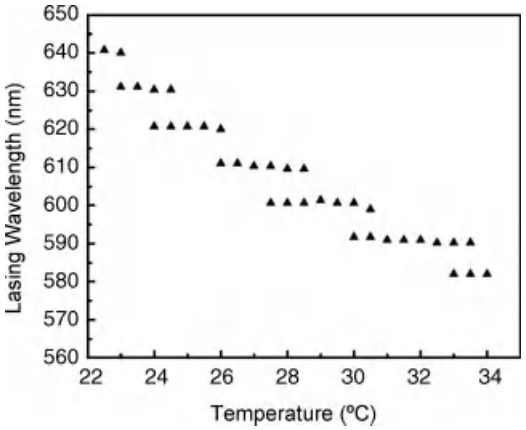

FIGURE 1.13 Temperature dependence of lasing wavelength in a CLC DFB laser [43].

of the natural pitch on temperature. Tuning over 15 nm was achieved using a 10 μm thick cell. However, the reason of the tunability in a cell, where the molecules at both surfaces are fixed, is not clear. Moreover, the cell quality might not be good judging from the wide lasing emission peak (~2 nm). Thermal tuning is also possible by using temperature-dependent chiral dopant solubility; that is, solubility of chiral dopant increases with increasing temperature, resulting in shorter pitch. Figure 1.14 shows the result [48]. Tuning over 60 nm was achieved.

1.4.2 Electric Field Tuning

It is also well known that helical pitch can be tuned by applying an electric field and is finally unwound under sufficient field strength. However, again surface pinning effect

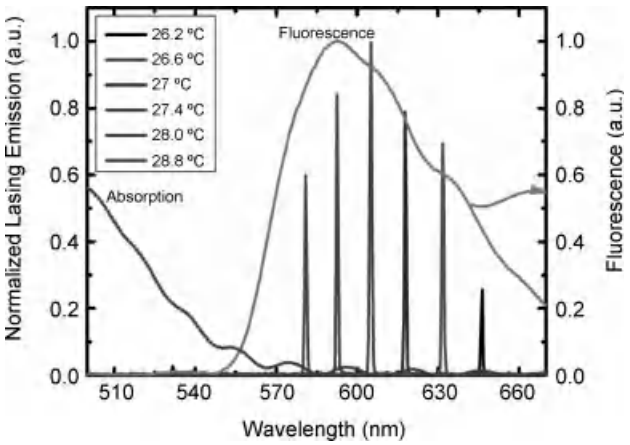

FIGURE 1.14 Lasing wavelength tuning as a function of temperature using temperature-dependent solubility of chiral dopant [48].

prevents the tuning of the helical pitch in cells with the helical axis perpendicular to substrates. Yoshida et al. [44] prepared wedge cells with the helical axis parallel to substrates and examined the tunability of lasing wavelength by applying an electric field. The field strength linearly depends on the position. Using such cells, position-dependent lasing wavelength variation over 100 nm was obtained. Electrotunable liquid crystal lasers are also possible using SmC* cells, since the surface pinning effect is negligible [46, 49].

Electrotunability of the lasing wavelength of the defect mode was also demonstrated using a layer of nematic liquid crystal (NLC) inserted into dielectric multilayers [18] and CLC layers [50]. This is based on the fact that the wavelength of defect modes continuously changes with the refractive index of the defect layer [26]. By applying an electric field, LC molecules change the orientation, resulting in effective refractive index, as shown in Figure 1.15a. Figure 1.15b is one of the results of electrotuning using defect mode lasing [51].

Another type of electrotuning was also demonstrated by Lin et al. [52]. They used CLC with negative dielectric anisotropy. By applying dc fields along the helical axis, the selective reflection band shifts toward shorter wavelength side. By applying an electric field of 150 V, lasing emission shifted by 15 nm. The field-dependent helical pitch was attributed to electrohydrodynamical effect. Similar but different

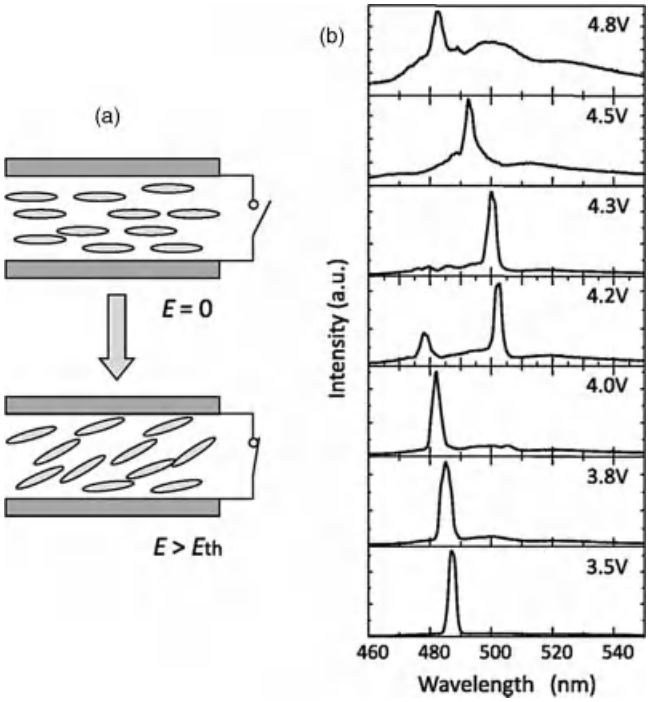

FIGURE 1.15 (a) Orientational change by applying an electric field. (b) Electric field-dependent lasing wavelength tuning of a defect mode using an anisotropic defect layer [79].

observation was made by Park et al. [53]. The sample used was NLCs embedded in helical polymer networks consisting of photopolymerizable CLC. With increasing electric field, transmittance spectra and color viewed from the substrate surface normal were blue shifted. The lasing emission was observed. However, the lasing peak does not show any wavelength shift but just becomes weak. In the absence of a field, lasing occurs toward the normal direction parallel to the helical axis. Surprisingly, however, under the field application, lasing emission is generated to any angle up to at least 70° with almost the same intensity as that in the normal direction. This phenomenon was interpreted as a spatial undulation of helical axis by Helfrich effect [54].

1.4.3 Phototuning

Several methods have been employed for wavelength tuning by light irradiation. Chanishvili et al. [55] prepared dye-doped CLCs. The photoexcitation of samples allows laser emission at about 400 nm. Phototransformation is induced by ultraviolet (UV) light irradiation in the structure of chiral molecules, leading to the change in the helical pitch (selective reflection peak) from 370 to 410 nm after 15 min irradiation. Since this process is irreversible, one or some compositions of chiral molecule mixture (Merck, ZLI-811) seem to be decomposed. In this sense, this is not real tunability.

A more practical method was proposed by Furumi et al. [56]. They used cholesteryl iodine, cholesteryl nonanoate, and cholesteryl oleyl carbonate as a host. UV irradiation at 254 nm resulted in continuous changes in the helical pitch from 550 to 720 nm depending on UV exposure energy. This phenomenon was attributed to photolysis reaction of the cholesteryl iodide. Lasing experiment using dye-doped samples reveals phototuning of laser wavelength over a 100 nm wavelength range.

Azomolecules are commonly used for phototuning of physical parameters. Lin et al. [57] used a chiral molecule with an azo linkage. Upon the irradiation of UV (350 nm) light for up to 20 min, selective reflection band becomes short over 100 nm. After 20 min UV irradiation, the photoisomerization from *trans* to *cis* forms occurs almost completely. The back-photoisomerization to *cis* is achieved by heating. Using a dye-doped system, the lasing wavelength was tuned over 100 nm by controlling the UV irradiation time.

1.4.4 Mechanical Tuning

CLCs are noncompressive media, so compression does not affect the helical pitch. For CLC films, however, mechanical strain to CLC films with the helical axis along the film normal can induce the variation in pitch. Experiments have been performed using CLC elastomers [58]. Since the directors at surfaces are fixed, the helical pitch linearly changes with the compression rate. Using dye-doped CLC elastomers, red, green, and blue lasing emission was observed. The experiments were performed using biaxial strain, so uniform thickness change and associated uniform helix compression were achieved. If uniaxial strain is exerted, we obtain a deformed helix

with shorter pitches. Since the refractive index change is not sinusoidal, it would be possible to observe higher order reflection. The experiment has not been performed so far.

1.4.5 Spatial Tuning

As mentioned above, a variety of external stimuli have been employed to control the helical pitch of CLCs. However, tunability is generally restricted within a narrow wavelength range at most 100 nm, and none of them supply tunability over the whole visible range. Chanishvili et al. [59, 60] and Huang et al. [61, 62] fabricated CLC structures with a spatial helical pitch gradient and tried to achieve lasing over a wide wavelength range. The former group used spatial gradient of chiral molecules, whereas the latter group used temperature gradient along the cell surface. Finally, Chanishvili et al. succeeded in obtaining position-dependent lasing emission over the whole visible range. Unfortunately, however, there was a window, where lasing was not possible [60]. Moreover, six or more kinds of dyes were necessary for wide-band lasing. On the other hand, Huang et al. [61] introduced temperature gradient across the cell and used temperature-dependent chiral dopant solubility to obtain the spatial-dependent pitch. Since they used reactive monomers as a host and polymerized, the pitch gradient was stable. However, the tuning range was only 50 nm because of the use of single dye. Later, they succeeded in expanding the tunable range to about 100 nm [62].

Narrow tunable range partly originates from emission bandwidth of the dye used. Actually, Chanishvili et al. [60] achieved a wide tunable range by using six or more dyes. Sonoyama et al. [63] used two dyes, coumarin and DCM, and succeeded in obtaining a wide tunable range covering the whole visible range without a wavelength window showing no lasing. Important points are summarized in Figure 1.16: (1) introduction of pitch gradient by temperature gradient, (2) introduction of concentration gradient of two dyes, and (3) energy transfer between two dyes. The emission band of coumarin dyes largely overlaps with the absorption band of DCM dyes, so efficient energy transfer is expected. Pumping light is absorbed by coumarin. The gradients in both pitch and dye concentration are important; at the shorter pitch region, emission of coumarin covers this region, so the region must be rich in coumarin. In the longer pitch region, on the contrary, the wavelength corresponds to the emission of DCM. Hence, this region must be rich in DCM. But at the same time, a certain amount of coumarin is also necessary to absorb pumping light. Finally, they succeeded in obtaining lasing emission covering the whole visible range from 470 to 670 nm by translating the cell with respect to a pumping beam, as shown in Figure 1.17 [63].

Another important effort was to make the lasing device temporally stable. Manabe et al. [64] used photopolymerizable CLCs and fixed the position-dependent pitch and dye concentration gradients by UV irradiation. Although the pitch slightly blue shifted by polymerization, position-dependent lasing over a full visible range was preserved. Photopolymerized CLC lasers with a helical axis lying within a substrate and with a pitch gradient were also fabricated [44]. In this case, the pitch gradient was

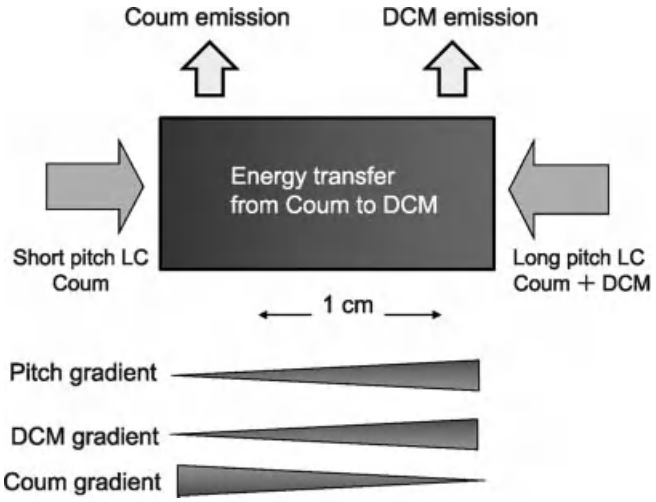

FIGURE 1.16 Gradients of pitch and dye concentration in a CLC cell for spatial lasing wavelength tuning.

realized by applying an electric field across wedged cells. These works opened the door of opportunity for a practical application as disposable dye lasers of a film form.

1.4.6 Multimode Lasing

We sometimes observed multiple lasing in (1) defect mode lasing from a thick defect layer [65], (2) simultaneous lasing of edge mode and defect mode [28], and (3) simultaneous lasing at both edges of PBG in single dye system [15] and (4) a Förster couple system [40]. However, the wavelength range of multiple lasing emission is limited within a very narrow range. Recently, Wang and Lin [66] obtained simultaneous nine lasing peaks around a 600–675 nm range. They prepared CLCs doped with chiral dopant exceeding the dissolving limit. As temperature increases, solubility increases and the helical pitch becomes shorter. The special uniformity of the dissolved chiral dopant depends upon the sample heating and cooling rates; that is, by increasing the cooling rate, the number of defects and domains increases, causing a multiple lasing.

To achieve wide-range simultaneous multiwavelength lasing such as red (R), green (G), and blue (B), a much sophisticated method to form wide-range multiple reflection bands is demanded. Ha et al. succeeded in obtaining RGB multiple reflection bands using multilayered structures of single-pitch CLC layers together with Fibonaccian defect [67] or isotropic defect layers [68], and then in RGB simultaneous lasing [69]. In order to explain the phenomenon, one of the key facts in CLC selective reflection is the cell thickness-dependent PBG width; the PBG width becomes broader and the reflectance decreases with decreasing sample thickness, as shown in Figure 1.17. Actually CLC with one-pitch (1*P*) thickness displays low

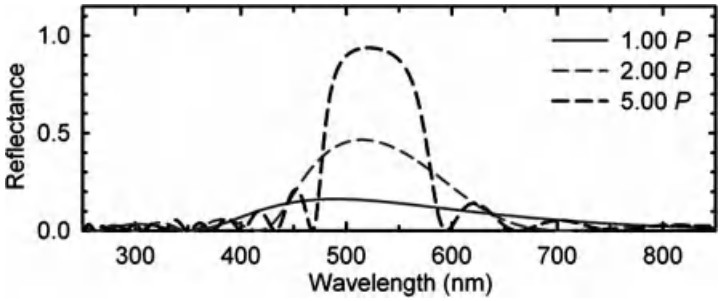

FIGURE 1.17 Selective reflection spectra in CLC cells with different thicknesses, 1, 2, and 5 pitch thick [78].

reflectance of 16% but the reflection band extends from 350 to 850 nm. If we insert isotropic defect layers, several reflection bands due to the defect mode may emerge within the wide PBG region. High reflectance can be achieved by increasing the number of CLC layers and defect layers alternately assembled. This is the fundamental idea of RGB or white light reflector [68].

They used PVA as a defect layer and constructed structures M_n = CLC/PVA/CLC/···/CLC/PVA/CLC, where n stands for the number of CLC layers, as shown in Figure 1.18a. In Figure 1.18b are shown simulated (lower) and experimental (upper) reflection spectra for M_1, M_2, M_3, and M_4 systems [68]. These reflection spectra clearly indicate the presence of multiple PBGs from the multi-CLC systems. The agreement between experimental and calculated spectra is satisfactory. The physical parameters such as CLC and PVA film thicknesses obtained by theoretical fittings using the Berreman 4×4 matrix agreed with those experimentally obtained [68].

By using a dye-doped NLC sandwiched by M_4 layers with PCLC (1.5P/0.56 μm thick), simultaneous RGB lasing was achieved [69]. The same dye system as in Ref. 63 was used: coumarin and DCM. The excitation wavelength was 420 nm corresponding to the absorption peak of coumarin. As shown in Figure 1.19, the increase of

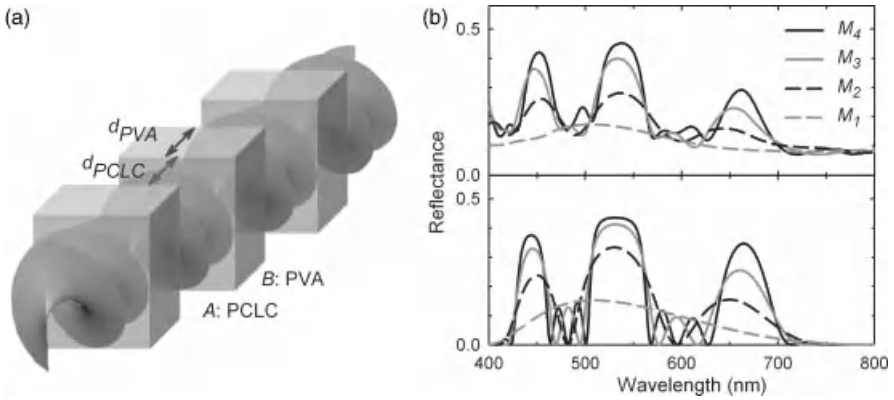

FIGURE 1.18 (a) Multistacked structures of CLC and PVA layers. (b) Experimental (upper) and simulated (lower) reflection spectra in four different multilayered cells [78].

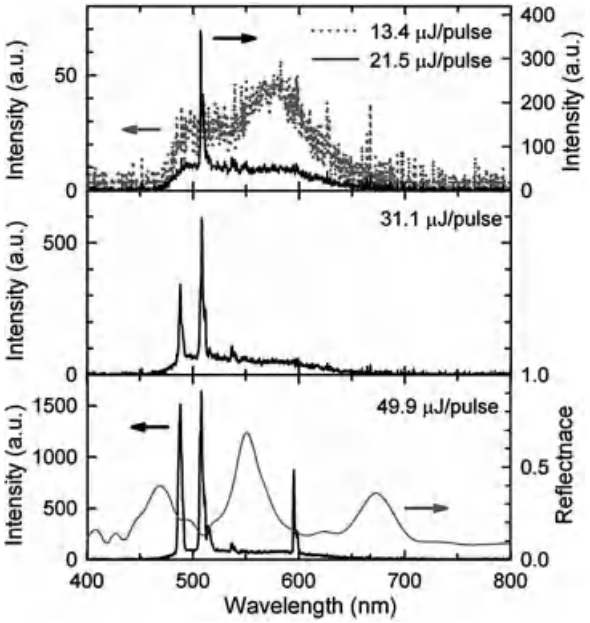

FIGURE 1.19 Multiple lasing emission spectra under different excitation powers. A reflection spectrum is also shown [78].

the pumping energy results in lasing at 508 nm (greenish, G) and 488 nm (bluish, B), and finally simultaneous RGB lasing emissions including 595 nm (reddish, R) light. This is unique as simultaneous RGB lasing occurs in a single resonator using single-pitched CLC with a single gain medium by a single optical pumping. Furthermore, each emission color of such lasings could be controlled by adjusting mixing ratios of two fluorescence dyes in the gain medium and optical pumping energies.

1.5 3D LC LASERS

Every LC laser mentioned so far has 1D cavity. One of the 3D structures whose periodicity could be in the visible range is obtained in the blue phase (BP). The first lasing using a dye-doped BP was reported by Cao et al. [70]. They actually observed different lasing peaks from three directions. Despite relatively low lasing threshold, the problem of using BP is always the temperature range of the phase. This problem was solved by Kikuchi et al. [71] by polymer stabilization. Using this technique, BP temperature range becomes 60 K including room temperature, although BP temperature range is usually only 1 K or so. Using such polymer-stabilized BP, lasing action was confirmed over 40 K [72].

Two types of 3D LC resonators have been reported by Humar et al. [73]. Both utilize liquid crystal droplets suspended in polymer matrices such as polydimethylsiloxane. Polymer dispersions of NLC droplets have been studied extensively in the

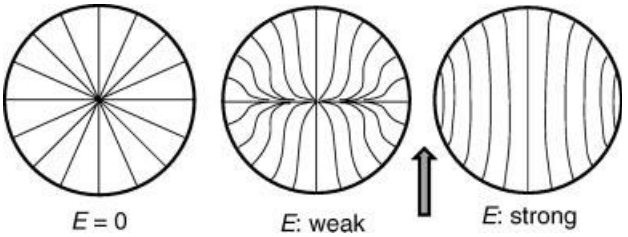

FIGURE 1.20 Director map of a NLC microdroplet embedded in polymer solution: (a) in the absence of an electric field, (b) under a weak electric field, and (c) under a strong electric field.

past, but individual droplets have never been considered as tunable optical resonators. The first one is a microresonator of dye-doped NLC droplets of about 10 μm diameter [73]. The microscope observation under crossed polarizers certifies the radial orientation of the NLC director, as shown in Figure 1.20a. When the NLC droplet was illuminated at the edge by a focused laser beam, a bright spot was observed at the other edge. In between, a light ring along the circumference of the microcavity was clearly visible. These observations clearly indicate whispering gallery modes (WGMs). Actually, they succeeded in observing spectra of WGMs circulating in a LC droplet. From the line width (about 0.055 nm), Q factor of the order of 12,000 was obtained. Lasing has not been reported using WGMs of this droplet. However, lasing capability using WGMs is well known in other systems [74], so lasing in LC WGMs is surely possible. Moreover, by deforming the sphere slightly, highly unidirectional lasing action would be possible [75], while lasing emission of WGMs of perfect sphere always emits tangentially. Another important aspect of the WGMs from LC microdroplets is tunability. By applying an electric field, director orientation in the droplet changes as shown in Figure 1.20b and c. Linear and reversible electrical tuning was obtained, and the tuning range could be over 40 nm by choosing proper LC materials.

The second type of 3D LC resonator was formed by using CLC droplet [76]. By using glycerol, the director is parallel to the interface of the droplet. Then, the formation of 3D helical structure with radial helical axes could be imagined (Figure 1.21). Lasing condition is the same as that in 1D DFB CLC lasers. Although the size of microdroplets cannot be controlled, lasing wavelength is uniquely defined by the helical pitch. An important point is that only dyes located at the center of droplets contribute to the lasing action (Figure 1.21), because the light emitted at the center is confined three dimensionally due to the radial helical axes; omnidirectional lasing emission occurs toward all the radial directions. Temperature-dependent helical pitch can also be used for tuning the laser light wavelength as in 1D DFB CLC lasers. A number of applications of the cholesteric onion microlasers were suggested by the authors [76]. One of the questions that still remained is polarization of laser light. The lasing emission is neither linearly nor circularly polarized. This could be due to the existence of many defects like in BP. Moreover, surface boundary condition of planar alignment does not define director orientation on the spherical surface. This is one of the future problems.

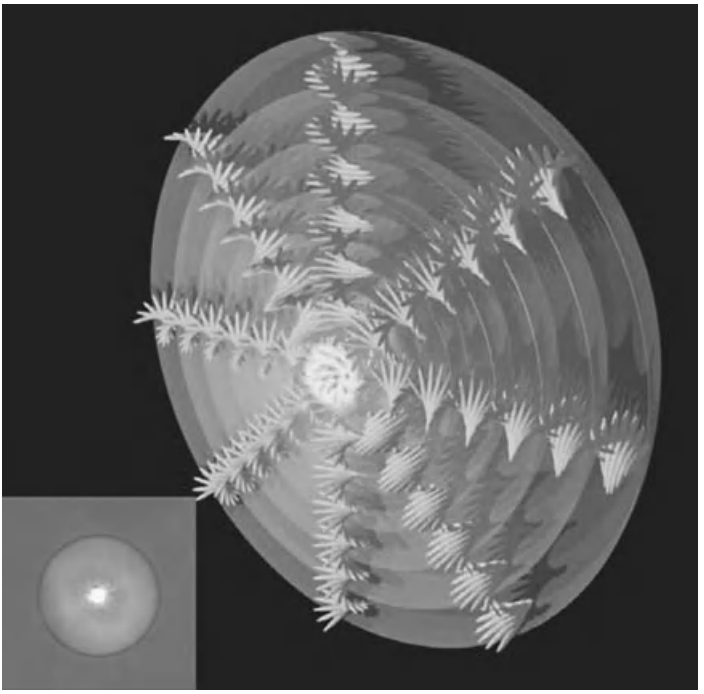

FIGURE 1.21 Helical structure in a CLC microdroplet. Image of microdroplet in a lasing condition is also shown [76]. (*See the color version of this figure in Color Plates section.*)

1.6 CONCLUSIONS

It has been more than three decades since the first observation of CLC laser emission in 1980 [10]. This field has been expanding rapidly particularly since Kopp et al. published a paper [11]. In this chapter, I focused on the most typical LC lasers, CLC microlasers. First, I described two kinds of CLC microlasers, DFB and defect mode lasers. Next, extensive efforts to lower the lasing threshold were summarized. They are classified into three kinds of improvements, that is, cavity structures, excitation conditions, and materials. Then, methods for tuning lasing wavelength, which is the most important feature of CLC lasers, were described. We can use variations in temperature, electric field, and light irradiation. Mechanical strain for polymer samples, spatial tuning for wide wavelength tuning, and multiple lasing over a wide wavelength range were also described. The readers may also refer recent review article [77]. Tunability is not only for wavelength, but also possible for polarization and directions, which I did not included in this chapter. Please refer to Ref. 78 for these tunabilities. 3D lasing is the most recent topic and provides us with promising devices. Much more application areas can be expected in 3D lasers such as telecommunications, optical computing, imaging devices, apparel and decoration, sensors, and biological imaging [76].

REFERENCES

1. E. Yablonovitch. Inhibited spontaneous emission in solid-state physics and electronics. *Phys. Rev. Lett.* **1987**, *58*, 2059–2062.
2. S. John. Strong localization of photons in certain disordered dielectric superlattices. *Phys. Rev. Lett.* **1987**, *58*, 2486–2489.
3. H. L. De Vries. Rotatory power and other optical properties of certain liquid crystals. *Acta Crystallogr.* **1951**, *4*, 219–226.
4. H. Takezoe, K. Hashimoto, Y. Ouchi, M. Hara, A. Fukuda, and E. Kuze. Experimental study on higher order reflection by monodomain cholesteric liquid crystals. *Mol. Cryst. Liq. Cryst.* **1983**, *101*, 329–340.
5. H. Takezoe, Y. Ouchi, M. Hara, A. Fukuda, and E. Kuze. Experimental studies on reflection spectra in monodomain cholesteric liquid crystal cells: total reflection, subsidiary oscillation and its beat or swell structure. *Jpn. J. Appl. Phys.* **1983**, *22*, 1080–1091.
6. D. W. Berreman. Optics in stratified and anisotropic media: 4×4 matrix formulation. *J. Opt. Soc. Am.* **1972**, *62*, 502–510.
7. H. Kogelnik and C. V. Shank. Coupled-wave theory of distributed feedback lasers. *J. Appl. Phys.* **1972**, *43*, 2327–2335.
8. R. Dreher and H. Schomburg. Prolongation of fluorescence decay time by structural changes of environment of emitting molecule. *Chem. Phys. Lett.* **1974**, *25*, 527–530.
9. M. Hara, H. Takezoe, A. Fukuda, E. Kuze, Y. Kaizu, and H. Kobayashi. Influence of cholesteric Bragg reflection of spontaneous emission from the inside of the helical structure. *Mol. Cryst. Liq. Cryst.* **1985**, *116*, 253–263.
10. I. P. Il'chishin, E. A. Tikhonov, V. G. Tishchenko, and M. T. Shpak. Generation of a tunable radiation by impurity cholesteric liquid crystals. *JETP Lett*. **1980**, *32*, 24–27.
11. V. I. Kopp, F. Fan, H. K. M. Vitana, and A. Z. Genack. Low-threshold lasing at the edge of a photonic stop band in cholesteric liquid crystals. *Opt. Lett.* **1998**, *23*, 1707–1709.
12. R. Bartolino and L. M. Blinov. Liquid crystal microlasers (introductory notes) In: L. M. Blinov and R. Bartolino, Eds., *Liquid Crystal Microlasers*, Transworld Research Network, Kerala, 2010, Chapter 1.
13. V. I. Kopp, Z.-Q. Zhang, and A. Z. Genack. Lasing in chiral photonic structures. *Prog. Quant. Electron.* **2003**, *27*, 369–416.
14. J. P. Dowling, M. Scalora, M. J. Bloemer, and C. M. Bowden. The photonic band edge laser: a new approach to gain enhancement. *J. Appl. Phys.* **1994**, *74*, 1896–1899.
15. K.-C. Shin, F. Araoka, B. Park, Y. Takanishi, K. Ishikawa, Z. Zhu, T. M. Swager, and H. Takezoe. Advantages of highly ordered polymer-dyes for lasing in chiral nematic liquid crystals. *Jpn. J. Appl. Phys.* **2004**, *43*, 631–636.
16. J. Schmidtke and W. Stille. Fluorescence of a dye-doped cholesteric liquid crystal film in the region of the stop band: theory and experiment. *Eur. Phys. J. B* **2003**, *31*, 179–194.
17. E. Yablonovitch, T. J. Gmitter, R. D. Meade, A. M. Rappe, K. K. Brommer, and J. D. Joannopoulos. Donor and acceptor modes in photonic band structure. *Phys. Rev. Lett.* **1991**, *67*, 3380–3383.
18. R. Ozaki, T. Matsui, M. Ozaki, and K. Yoshino. Electrically color-tunable defect mode lasing in one-dimensional photonic-band-gap system containing liquid crystal. *Appl. Phys. Lett.* **2003**, *82*, 3593-1–3593-3.

19. O. Painter, P. K. Lee, A. Scherer, A. Yariv, J. D. O'Brien, P. D. Dapkus, and I. Kim. Two-dimensional photonic band-gap defect mode laser. *Science* **1999**, *284*, 1819–1821.
20. S. G. Johnson and J. C. Joannopoulos. Three-dimensionally periodic dielectric layered structure with omnidirectional photonic band gap. *Appl. Phys. Lett.* **2000**, *77*, 3490-1–3490-3.
21. K. M. Ho, C. T. Chan, and C. M. Soukoulis. Existence of a photonic gap in periodic dielectric structures. *Phys. Rev. Lett.* **1990**, *65*, 3152–3155.
22. V. I. Kopp and A. Z. Genack. Twist defect in chiral photonic structures. *Phys. Rev. Lett.* **2002**, *89*, 033901-1–033901-4.
23. J. Schmidtke, W. Stille, and H. Finkelmann. Defect mode emission of a dye doped cholesteric polymer network. *Phys. Rev. Lett.* **2003**, *90*, 083902-1–083902-4.
24. M. Ozaki, R. Ozaki, T. Matsui, and K. Yoshino. Twist-defect-mode lasing in photo-polymerized cholesteric liquid crystal. *Jpn. J. Appl. Phys.* **2003**, *42*, L472–L475.
25. H. Hoshi, K. Ishikawa, and H. Takezoe. Optical second-harmonic generation enhanced by a twist defect in ferroelectric liquid crystals. *Phys. Rev. E* **2003**, *68*, 020701(R)-1–020701 (R)-3.
26. Y.-C. Yang, C.-S. Kee, J.-E. Kim, and H. Y. Park. Photonic defect modes of cholesteric liquid crystals. *Phys. Rev. E* **1999**, *60*, 6852–6854.
27. S. M. Jeong, N. Y. Ha, Y. Takanishi, K. Ishikawa, and H. Takezoe. Defect mode lasing from a double-layered dye-doped polymeric cholesteric liquid crystal films with a thin rubbed defect layer. *Appl. Phys. Lett.* **2007**, *90*, 261108-1–261108-3.
28. M. H. Song, B. Park, K.-C. Shin, T. Ohta, Y. Tsunoda, H. Hoshi, Y. Takanishi, K. Ishikawa, J. Watanabe, S. Nishimura, T. Toyooka, Z. Zhu, T. M. Swager, and H. Takezoe. Effect of phase retardation on defect-mode lasing in polymeric cholesteric liquid crystals. *Adv. Mater.* **2004**, *16*, 779–783.
29. M. H. Song, N. Y. Ha, K. Amemiya, B. Park, Y. Takanishi, K. Ishikawa, J. W. Wu, and H. Takezoe. Defect-mode lasing with lowered threshold in a three-layered hetero-cholesteric liquid-crystal structure. *Adv. Mater.* **2006**, *18*, 193–197.
30. J. Schmidtke and W. Stille. Photonic defect modes in cholesteric liquid crystal films. *Eur. Phys. J. E* **2003**, *12*, 553–564.
31. T. Matsui, M. Ozaki, and K. Yoshino. Tunable photonic defect modes in a cholesteric liquid crystal induced by optical deformation of helix. *Phys. Rev. E* **2004**, *69*, 061715-1–061715-4.
32. K. Amemiya, T. Nagata, M. H. Song, Y. Takanishi, K. Ishikawa, S. Nishimura, T. Toyooka, and H. Takezoe. Enhancement of laser emission intensity in dye-doped liquid crystals with single-output window. *Jpn. J. Appl. Phys.* **2005**, *44*, 3748–3750.
33. Y. Matsuhisa, R. Ozaki, Y. Takao, and M. Ozaki. Linearly polarized lasing in one-dimensional hybrid photonic crystal containing cholesteric liquid crystal. *J. Appl. Phys.* **2007**, *101*, 033120-1–033120-4.
34. V. A. Belyakov. Low threshold DFB lasing in chiral LC at diffraction of pumping wave. *Mol. Cryst. Liq. Cryst.* **2006**, *435*, 43–69.
35. Y. Matsuhisa, Y. Huang, Y. Zhou, and S.-T. Wu. Low-threshold and high efficiency lasing upon band-edge excitation in a cholesteric liquid crystal. *Appl. Phys. Lett.* **2007**, *90*, 091114-1–091114-3.

36. Y. Wang, T. Manabe, Y. Takanishi, K. Ishikawa, G. Shao, A. Orita. J. Otera, and H. Takezoe. Dependence of lasing threshold power on excitation wavelength in dye-doped cholesteric liquid crystals. *Opt. Commun.* **2007**, *280*, 408–411.
37. M. G. Chee, M. H. Song, D. Kim, H. Takezoe, and L. J. Chung. Lowering lasing threshold in chiral nematic liquid crystal structure with different anisotropies. *Jpn. J. Appl. Phys.* **2007**, *46*, L437–L439.
38. F. Araoka, K.-C. Shin, Y. Takanishi, K. Ishikawa, H. Takezoe, Z. Zhu, and T. M. Swager. How doping a cholesteric liquid crystal with polymeric dye improves an order parameter and makes possible low threshold lasing. *J. Appl. Phys.* **2003**, *94*, 279–283.
39. K. Sonoyama, Y. Takanishi, K. Ishikawa, and H. Takezoe. Lowering threshold by energy transfer between two dyes in cholesteric liquid crystal distributed feedback lasers. *Appl. Phys. Exp.* **2008**, *1*, 032002-1–032002-3.
40. M. Chambers, M. Fox, M. Grell, and J. Hill. Lasing from a Forster transfer fluorescent dye couple dissolved in a chiral nematic liquid crystals. *Adv. Funct. Mater.* **2002**, *12*, 808–810.
41. M. Uchimura, Y. Watanabe, F. Araoka, J. Watanabe, H. Takezoe, and G. Konishi. Development of laser dyes to realize low threshold in dye-doped cholesteric liquid crystal lasers. *Adv. Mater.* **2010**, *22*, 4473–4478.
42. S. K. H. Wei, S. H. Chen, K. Dolgaleva, S. G. Lukishova, and R. W. Boyd. Robust organic lasers comprising glassy-cholesteric pentafluorene doped with a red-emitting oligofluorene. *Appl. Phys. Lett.* **2009**, *94*, 041111-1–041111-3.
43. K. Funamoto, M. Ozaki, and K. Yoshino. Discontinuous shift of lasing wavelength with temperature in cholesteric liquid crystal. *Jpn. J. Appl. Phys.* **2003**, *42*, L1523–L1525.
44. H. Yoshida, Y. Inoue, T. Isomura, Y. Matsuhisa, A. Fujii, and M. Ozaki. Position sensitive, continuous wavelength unable laser based on photopolymerizable cholesteric liquid crystals with an in-plane helix alignment. *Appl. Phys. Lett.* **2009**, *94*, 093306-1–093306-3.
45. G. Strangi, V. Barna, R. Caputo, A. de Luca, C. Versace, N. Scaramuzza, C. Umeton, and R. Bartolino. Color-tunable organic microcavity laser array using distributed feedback. *Phys. Rev. Lett.* **2005**, *94*, 063903-1–063903-4.
46. M. Kasano, M. Ozaki, and K. Yoshino. Electrically tunable waveguide laser based on ferroelectric liquid crystal. *Appl. Phys. Lett.* **2003**, *82*, 4026–4028.
47. S. M. Morris, A. D. Ford, and H. J. Coles. Removing the discontinuous shifts in emission wavelength of a chiral nematic liquid crystal laser. *J. Appl. Phys.* **2009**, *106*, 023112-1–023112-4.
48. Y. Huang, Y. Zhou, C. Doyle, and S.-T. Wu. Tuning the photonic band gap in cholesteric liquid crystals by temperature-dependent dopant solubility. *Opt. Express* **2006**, *14*, 1236–1242.
49. M. Ozaki, M. Kasano, T. Kitasho, D. Ganzke, W. Hasse, and K. Yoshino. Electro-tunable liquid-crystal lasers. *Adv. Mater.* **2003**, *15*, 974–977.
50. M. H. Song, B. Park, S. Nishimura, T. Toyooka, I. J. Chung, Y. Takanishi, K. Ishikawa, and H. Takezoe. Electrotunable non-reciprocal laser emission from a liquid-crystal photonic device. *Adv. Funct. Mater.* **2006**, *16*, 1793–1798.
51. M. H. Song, B. Park, K.-C. Shin, T. Ohta, Y. Tsunoda, H. Hoshi, Y. Takanishi, K. Ishikawa, J. Watanabe, S. Nishimura, T. Toyooka, Z. Zhu, T. M. Swager, and H. Takezoe. Lasing characteristics of a dye-doped nematic liquid crystal layer sandwiched by two polymeric cholesteric liquid crystals. *Proc. SPIE* **2004**, *5518*, 66–76.

52. T.-H. Lin, H.-C. Jau, C.-H. Chen, Y.-J. Chen, T.-H. Wei, C.-W. Chen, and A. Y.-G. Fuh. Electrically controllable laser based on cholesteric liquid crystal with negative dielectric anisotropy. *Appl. Phys. Lett.* **2006**, *88*, 061122-1–061122-3.
53. B. Park, M. Kim, S. W. Kim, W. Jang, H. Takezoe, Y. Kim, E. H. Choi, Y. H. Seo, G. S. Cho, and S. O. Kang. Electrically controllable omnidirectional laser emission from a helical-polymer network composite film. *Adv. Mater.* **2009**, *21*, 771–775.
54. W. Helfrich. Electrohydrodynamic and dielectric instabilities of cholesteric liquid crystals. *J. Chem. Phys.* **1971**, *55*, 839–842.
55. A. Chanishvili, G. Chilaya, and G. Petriashvili. Phototunable lasing in dye-doped cholesteric liquid crystals. *Appl. Phys. Lett.* **2003**, *83*, 5353–5355.
56. S. Furumi, S. Yokoyama, A. Otomo, and S. Mashiko. Phototunable photonic bandgap in a chiral liquid crystal laser device. *Appl. Phys. Lett.* **2004**, *84*, 2491–2493.
57. T.-H. Lin, Y.-J. Chen, C.-H. Wu, A. Y.-G. Fuh, J.-H. Liu, and P.-C. Yang. Cholesteric liquid crystal laser with wide tuning capability. *Appl. Phys. Lett.* **2005**, *86*, 161120-1–161120-3.
58. H. Finkelmann, S. T. Kim, A. Munoz, P. Palffy-Muhoray, and B. Taheri. Tunable mirrorless lasing in cholesteric liquid crystalline elastomers. *Adv. Mater.* **2001**, *13*, 1069–1072.
59. A. Chanishvili, G. Chilaya, G. Petriashvili, R. Barberi, R. Bartolino, G. Cipparrone, A. Mazzulla, and L. Oriol. Lasing in dye-doped cholesteric liquid crystals: two new tuning strategies. *Adv. Mater.* **2004**, *16*, 791–795.
60. A. Chanishvili, G. Chilaya, G. Petriashvili, R. Barberi, R. Bartolino, G. Cipparrone, A. Mazzulla, R. Gimenex, L. Oriol, and M. Pinol. Widely tunable ultraviolet–visible liquid crystal laser. *Appl. Phys. Lett.* **2005**, *86*, 051107-1–051107-3.
61. Y. Huang, L.-P. Chen, C. Doyle, Y. Zhou, and S.-T. Wu. Spatially tunable laser emission in dye-doped cholesteric polymer films. *Appl. Phys. Lett.* **2006**, *89*, 111106-1–111106- 3.
62. Y. Huang, Y. Zhou, and S.-T. Wu. Spatially tunable laser emission in dye-doped photonic liquid crystals. *Appl. Phys. Lett.* **2006**, *88*, 111107-1–111107-3.
63. K. Sonoyama, Y. Takanishi, K. Ishikawa, and H. Takezoe. Position-sensitive cholesteric liquid crystal dye laser covering a full visible range. *Jpn. J. Appl. Phys.* **2007**, *46*, L874–L876.
64. T. Manabe, K. Sonoyama, Y. Takanishi, K. Ishikawa, and H. Takezoe. Toward practical application of cholesteric liquid crystals to tunable lasers. *J. Mater. Chem.* **2008**, *18*, 3040–3043.
65. M. H. Song, B. Park, Y. Takanishi, K. Ishikawa, S. Nishimura, T. Toyooka, and H. Takezoe. Lasing from thick anisotropic layer sandwiched between polymeric cholesteric liquid crystal films. *Jpn. J. Appl. Phys.* **2005**, *44*, 8165–8167.
66. C.-T. Wang and T.-H. Lin. Multi-wavelength laser emission in dye-doped photonic liquid crystals. *Opt. Express* **2008**, *16*, 18334–18339.
67. N. Y. Ha, Y. Takanishi, K. Ishikawa, and H. Takezoe. Simultaneous RGB reflections from single-pitched cholesteric liquid crystal films with Fibonaccian defects. *Opt. Express* **2007**, *15*, 1024–1029.
68. N. Y. Ha, Y. Ohtsuka, S. M. Jeong, S. Nishimura, G. Suzaki, Y. Takanishi, K. Ishikawa, and H. Takezoe. Fabrication of a simultaneous red–green–blue reflector using single-pitched cholesteric liquid crystals. *Nat. Mater.* **2008**, *7*, 43–47.

69. N. Y. Ha, S. M. Jeong, S. Nishimura, G. Suzaki, K. Ishikawa, and H. Takezoe. Simultaneous red, green, blue lasing emission in a single-pitched cholesteric liquid-crystal system. *Adv. Mater.* **2008**, *20*, 2503–2507.
70. W. Cao, A. Munoz, P. Palffy-Muhoray, and B. Taheri. Lasing in a three-dimensional photonic crystal of the liquid crystal blue phase II. *Nat. Mater.* **2002**, *1*, 111–113.
71. H. Kikuchi, M. Yokota, Y. Hisakado, H. Yang, and T. Kajiyama. Polymer-stabilized liquid crystal blue phases. *Nat. Mater.* **2002**, *1*, 64–68.
72. S. Yokoyama, S. Mashiko, H. Kikuchi, K. Uchida, and T. Nagamura. Laser emission from a polymer-stabilized liquid-crystalline blue phase. *Adv. Mater.* **2006**, *18*, 48–51.
73. M. Humar, M. Ravnik, S. Pajk, and I. Musevic. Electrically tunable liquid crystal optical microresonators. *Nat. Photon.* **2009**, *3*, 595–600.
74. V. Snadoghdar, F. Treussart, J. Hare, V. Lefevre-Seguin, J.-M. Raimond, and S. Haroche. Very low threshold whispering-gallery-mode microsphere laser. *Phys. Rev. A.* **1996**, *54*, R1777–R1780.
75. Q. J. Wang, C. Yan, N. Yu, J. Unterhinninghofen, J. Wiersig, C. Pflugl, L. Diehl, T. Edamura, M. Yamanishi, H. Kan, and F. Capasso. Whispering-gallery mode resonators for highly unidirectional laser action. *Proc. Natl. Acad. Sci. USA* **2010**, *107*, 22407–22412.
76. M. Humar and I. Musevic. 3D microlasers from self-assembled cholesteric liquid-crystal microdroplets. *Opt. Express* **2010**, *18*, 26995–27003.
77. H. Coles and S. Morris. Liquid-crystal lasers. *Nat. Photon.* **2010**, *4*, 676–685.
78. H. Takezoe, N. Y. Ha, M. H. Song, S. M. Jeong, and B. Park. Tuning laser light from liquid crystal lasers. In: L. M. Blinov and R. Bartolino, Eds., *Liquid Crystal Microlasers*, Transworld Research Network, Kerala, 2010, Chapter 4.
79. H. Takezoe. Photonic devices using liquid crystal; nanostructures. In: H. Hosono, Y. Mishima, H. Takezoe, K.J.D. Mackenzie, Eds., *Nanomaterials -from research to applications-*, Elsevier, London, 2006, Chapter 4.

CHAPTER 2

Self-Organized Semiconducting Discotic Liquid Crystals for Optoelectronic Applications

CHENMING XUE and QUAN LI
Liquid Crystal Institute, Kent State University, Kent, OH, USA

2.1 INTRODUCTION

Why are almost all of the leaves on earth green? Because they have a superior light harvesting material, i.e., chlorophyll, to efficiently absorb sunlight for photochemical reactions. This material evolved to be the best for the above purpose since it was produced after hundreds of millions of years' natural selection. Interestingly, the key component of chlorophyll is porphyrin, a disc-like aromatic molecule with a large π-conjugated system. In many cases, when large π-conjugated aromatic cores are linked with flexible aliphatic peripheral substituents, a discotic liquid crystalline (DLC) phase may appear. Since the work of Chandrasekhar on the hexaesters of benzene published in 1977 [1], DLC materials have been investigated intensively, especially over the last decade. Successful commercialization of DLC materials has been accomplished in Fuji "Wide-View" (WV) optical compensation films [2, 3]. Apart from the use in display, they have been widely and deeply investigated starting from structure–properties to structure–device performance relationships.

In recent decades, there has been increasing attention in the research field of organic electronics for device applications such as photovoltaic devices (PVD), light-emitting-diodes (LEDs), field-effect transistors (FETs), memory elements, and sensors. Particularly in the area of developing organic photovoltaic devices for reducing the demand of fossil fuels in the world, this research has been expected to create cheap, flexible thin films to replace the expensive and not easily processable inorganic materials. Among the diverse new materials for organic semiconductors, conjugated liquid crystals (LCs) hold a particular promise due to their extraordinary

Liquid Crystals Beyond Displays: Chemistry, Physics, and Applications, Edited by Quan Li.
© 2012 John Wiley & Sons, Inc. Published 2012 by John Wiley & Sons, Inc.

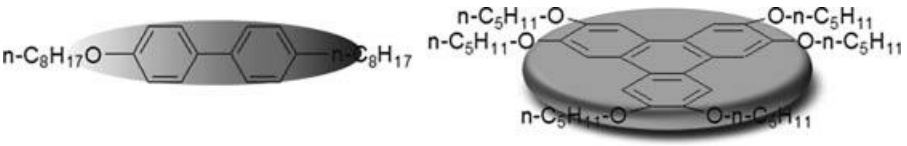

FIGURE 2.1 Schematic drawing of some prototype calamitic (left) and discotic (right) liquid crystal molecules.

abilities of self-organization and self-healing that can remove structural defects, such as grain boundaries, which are detrimental to charge transport. By thermal annealing, the spontaneous formation of large single domains could be achieved [4, 5]. Among these conjugated LCs, discotic molecules are well known for their disc-like molecular shape, different from their rod-like (calamitic) counterparts as shown in Figure 2.1 [6]. Owing to this particular type of molecular shape, quite different phase symmetry, direction of charge transport, and extent of π-orbital overlap have been observed. For discotic molecules, there is more than one assembling state in LC phase depending on the type of lattice (Figure 2.2) [7]. The least ordered mesophase formed by disc-like molecules is the nematic (N_D) phase (a). The N_D phase is analogous to the nematic phase formed by rod-like molecules and is characterized by the presence of only orientational order where the mesogens align with their principal axes along one direction. More common phases exhibited by disc-like molecules are

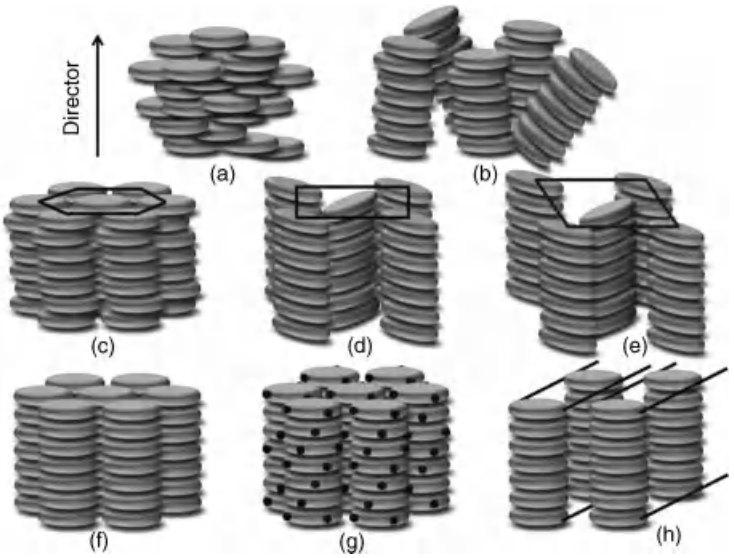

FIGURE 2.2 Schematic drawings of common mesophases of disc-shaped molecules: (a) discotic nematic, (b) columnar nematic, (c) hexagonal columnar, (d) rectangular columnar, (e) columnar oblique, (f) columnar plastic, (g) columnar helical, and (h) columnar lamellar phase.

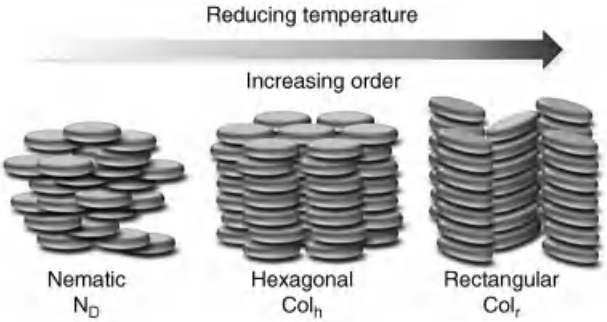

FIGURE 2.3 The phases formed by disc-like molecules are distinguished by the degree of positional order and symmetry, and they may be rearranged from one mesophase to another upon temperature change.

columnar phases, in which the disc-like molecules stack into columns. Columnar phases show a rich poly-mesomorphism, which are generally classified according to their symmetry, the degree of ordering within the column, and the orientation of the discs with respect to the columnar axis [8, 9]. Apart from the columnar nematic phase (b) showing different directors of orientational order of columns, other columnar phases show identical orientational order plus positional order. Among them, a hexagonal columnar (Col_h) phase (c) and a rectangular columnar (Col_r) phase (d) with tilted columns are the two most common types of columnar phases. However, more ordered phases such as columnar oblique (Col_{ob}) (e), columnar plastic (Col_p) (f), columnar helical (g), and columnar lamellar (h) mesophases are not as common. For the same molecule, when temperature changes they may transfer from one mesophase to another with variant ordered states. For example, one can make a distinction between the least ordered N_D phase, Col_h phase, and Col_r phase when temperature decreases as shown in Figure 2.3. These different mesophases can be experimentally characterized by the combined use of techniques. For textural observation, we can use polarizing optical microscopy (POM); for thermal analysis, we can use differential scanning calorimetry (DSC); and for molecular packing structures determination, we can use X-ray diffraction (XRD).

The particular two-dimensional chemical structure of discotic molecules brings new features. First of all, within columns the adjacent disc-like molecules have a much larger orbital overlap than calamitics. As a result, the band width reaches a value as high as 1.1 eV, close to that of graphite (*ca.* 1.0–1.4 eV) [10]. Secondly, the large orbital overlap between stacked disc-like molecules results in high values of the charge carrier mobility (μ) in their liquid crystalline mesophases, which can be 0.2–1.3 $cm^2 V^{-1} s^{-1}$ [11–14]. Thirdly, in the discotic columnar mesophase, the exciton diffusion length in discotics is able to exceed 70 nm [15], which is much higher than that of most conventional conjugated polymers (*ca.* 10–20 nm).

In this chapter, progress in the research field of DLC materials is comprehensively outlined. First, charge transport measurements of DLCs are briefly introduced. Second, molecular structures of most typical DLCs and novel systems are

presented. Third, as the supramolecular alignment of DLC is critically controlled by the processing methods, important techniques are described. In the last part, a general introduction of most important optoelectronic applications of DLCs are demonstrated.

2.2 CHARGE TRANSPORT AND MEASUREMENTS IN DLCs

2.2.1 Charge Transport in DLC Semiconductors

For organic semiconducting materials in a conjugated system, π-orbital wave functions of adjacent carbon atoms overlap and the electrons occupying such orbitals become relatively delocalized. Figure 2.4 clearly shows this fundamental but essential molecular electronic feature. Each conjugated carbon atom in the sp^2 hybridization of a molecule forms 3 σ-bonds from the overlapping of hybridized $2s$, $2p_x$ and $2p_y$ valence atomic orbitals; the fourth $2p_z$ orbital is perpendicular to the σ-bond plane and laterally overlaps to form the π-bonds. σ-Bond is strong and the energy difference between the occupied bonding orbital (σ) and the unoccupied antibonding orbital (σ^*) is quite large. π-Bond is weaker than σ-bond, and it has a much smaller energy difference between the highest occupied molecular π-orbital (HOMO) and the lowest unoccupied molecular orbital (LUMO). The

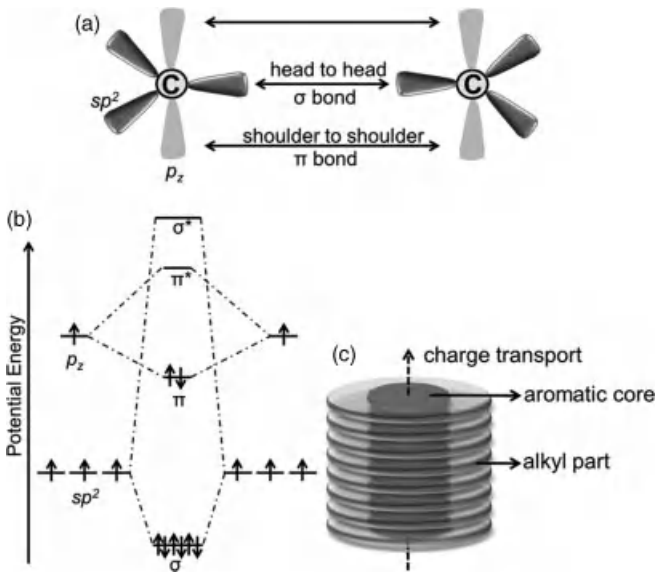

FIGURE 2.4 (a) Schematic illustration of σ-bond and π-bond formation between two sp^2 hybridized carbons. (b) An orbital energy-level diagram for the C–C bond formation between two sp^2 hybridized carbons. (c) Schematic representation of the organization of discotic molecules into an one-dimensional conducting column.

corresponding lower band gap energy determines the semiconducting properties of a molecule. For semiconducting materials, the forming energy of band gaps is in the range of 1.5–3 eV.

Compared with inorganic semiconductors, organic semiconductors are cheap, easy to process, excellent for casting large films, and capable of being deposited on flexible substrates such as plastics. Although it is generally recognized that the charge transport mobility is not as high as inorganic semiconductors, great efforts are being made and the mobilities are catching up.

Electron and hole transport in organic semiconductors occurs via π–π coupling between the HOMO and LUMO orbitals respectively of neighboring sites. In discotic columnar mesophases, the charge carrier mobility was relatively high since the cores of the conjugated aromatic systems self-organize into long-range ordered, π-orbital overlapped columnar structures (inter-core distances of about 3.5 Å), providing pathways to facilitate charge carrier transport between adjacent molecules (in Figure 2.4c). Generally speaking, charge-carrier mobility in such discotic columns can reach from 10^{-3} to $1.0\,cm^2\,V^{-1}\,s^{-1}$. For the charge mobilities less than $0.1\,cm^2\,V^{-1}\,s^{-1}$ in DLC semiconductors, a one-dimensional hopping process was postulated [16, 17]. For the carrier mobilities more than $0.1\,cm^2\,V^{-1}\,s^{-1}$, a band-like charge transport that involves the formation of conduction bands across several molecules was proposed [18]. Discotic columns can be considered as one-dimensional conducting molecular wires/belt because of the anisotropic conducting behavior in the columnar mesophase, in which the charges transport along the aromatic cores. Furthermore, the peripheral chains (usually flexible alkyls) linking to the rigid core form an insulating hydrocarbon matrix prohibiting charge carriers from transporting between columns. Depending on the ionization potential or electron affinity, the discotic molecules can transport either positive holes or negative electrons or both under certain conditions [19]. Based on the charge transport property, such DLC semiconducting materials can be classified as three types: *p*-type, *n*-type or ambipolar.

2.2.2 Measurements of Charge Mobility

The charge carrier mobility is a key parameter in determining the performance of a semiconducting material. In the past decades, various techniques have been developed to determine the charge mobility value and the most widely used ones are briefly described below.

2.2.2.1 Time of Flight (TOF) Charge mobilities in organic materials were first measured with the TOF technique by Kepler [20] and Leblanc [21]. In this technique as shown in Figure 2.5, one organic layer of a few micrometers thick is sandwiched between two electrodes with known inter-distance. Charges are generated by irradiating a laser pulse with energy greater than or equal to the band gap towards materials in the proximity of one electrode. The generated holes or electrons migrate across the organic material layer to the second electrode under an applied electric field depending on the polarity of the applied bias and the corresponding electric field

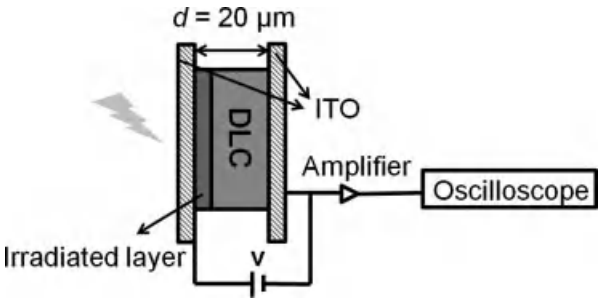

FIGURE 2.5 Schematic representation of the TOF experiment.

(in the range of 10^4–$10^6\,\mathrm{V\,cm^{-1}}$). The current at that electrode is recorded as a function of time, which enables one to study the mobility by measuring the transient time [22]. The mobility (μ) of the holes or electrons is estimated as:

$$\mu = \frac{v}{F} = \frac{d}{Ft} = \frac{d^2}{Vt}$$

where v is the velocity, F is the electric field, d is the distance between the electrodes, t is the averaged transient time, and V is the applied voltage.

Generally, a sharp signal is obtained in the case of ordered materials while in disordered systems a broader signal occurs because of the distribution of transient times for charges passing across the material. This is mostly due to shallow trapping often caused by structural defects in the materials which cause variations of mobilities. It has been revealed that the mobility decreases with the reduction of molecular order from crystal, liquid crystal to isotropic phase [23].

Measurements of the TOF technique for DLCs exhibit values usually on the order of $10^{-3}\,\mathrm{cm^2\,V^{-1}\,s^{-1}}$, while a value as high as $0.2\,\mathrm{cm^2\,V^{-1}\,s^{-1}}$ has also been reported [24]. Because imperfections in the columnar arrangement can have a negative influence on charge carrier transport and a lower limit value will show up, self-organized molecules possessing a degree of order as high as possible within the inter-electrode gap are desired.

2.2.2.2 Pulse-Radiolysis Time-Resolved Microwave Conductivity (PR-TRMC) In the PR-TRMC technique, the sample (bulk material) is first excited by a pulse of highly energetic electrons (in the MeV range) to create a low density of free charge carriers. As shown in Figure 2.6, charge carriers are created by using nanosecond-duration pulses of ionizing radiation from a Van de Graaff accelerator [25]. New generated charge carriers, induced by the pulse, will increase the conductivity of the sample, then a frequency dependent deviation of the microwave power can be detected. The change of conductivity $\Delta\sigma$ is expressed as [26]:

$$\Delta\sigma = e\sum \mu N_{\mathrm{e-h}}$$

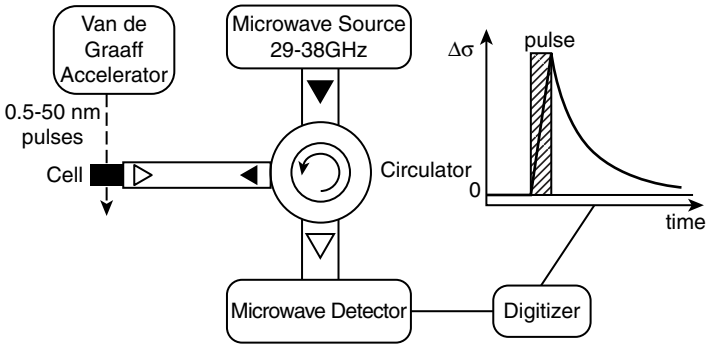

FIGURE 2.6 Schematic illustration of the PR-TRMC experimental setup.

where $\Sigma\mu$ is the sum of hole and electron mobilities and N_{e-h} is the density of generated electron–hole pairs. From PR-TRMC measurements, the sum of positive and negative charge-carrier mobilities: $\Sigma\mu = \mu(+) + \mu(-)$ is yielded and it is not possible to separate the positive and negative carriers. This N_{e-h} value is calculated as follows: a ratio of the amount of energy density transferred to the material by the energy required to create one electron–hole pair is first obtained, then this ratio is further multiplied by a survival probability because during the standing of the pulse there is possible charge recombination.

PR-TRMC is a contact-free technique which is not affected by space-charge effects. It requires no electrode deposition onto the sample and the interference of the electrode can be excluded. Moreover, the charges are directly generated in the bulk and the charges trapped by structural defects or impurities are not responsive. Therefore, the mobility of intrinsic charge carriers can be determined even for multi-domain samples without alignment. Because PR-TRMC measurement of the mobility shows local-wise character which is over a short range (a few molecules) and on a nanosecond timescale, the resulting intrinsic AC mobility value for the bulk is considered to be the upper limit for a sample at low field. On the contrary, in TOF technique the DC measurements probing a macroscopic range are generally smaller since the charge carriers are crossing structural defects and interacting with impurities. Thus, depending on the degree of order in the sample, AC and DC mobility values deviate above a threshold frequency. A class of DLC materials hexahexylthiotriphenylene (HHTT) have been used as reference compounds to validate the PR-TRMC technique [27], and with this technique, mobility values as high as $1.1\,cm^2\,V^{-1}\,s^{-1}$ have been achieved in a discotic hexabenzocoronene (HBC) derivative [28].

2.2.2.3 Space-Charge-Limited Current (SCLC) The charge mobility behavior can be characterized by the SCLC technique, in which an organic layer is sandwiched between two electrodes. The charge transport is bulk dependent but not contact dependent. Ohmic contacts are assumed. In this technique, when the organic layer's intrinsic electrostatic potential equals that of the electrode, the injection of additional charges can be prevented, the current density is closest to that of the

injecting electrode, and the obtained mobility value is the maximum [29, 30]. In this technique, when neglecting diffusion contributions, the current density J can be expressed as:

$$J = \frac{9}{8}\varepsilon_0\varepsilon_r\mu\frac{V^2}{L^3}$$

where ε_r denotes the dielectric constant of the organic material, V is the applied bias voltage, and L is the device thickness. At high electric fields, the field-dependence of the mobility has to be considered. Generally, the electrodes are chosen based on when electrons or holes can be injected at low voltage.

Normally when traps are present, the J–V curve becomes complex, exhibiting a linear regime where transport is injection-limited. Then a sudden increase for an intermediate range of applied biases appears, and at last the V^2-dependence of the trap-free SCLC regime is reached.

2.2.2.4 FET Electrical characteristics measurement in a FET configuration can also provide the carrier mobilities. Horowitz has pointed out that the I–V (current–voltage) expressions derived for inorganic transistors in the linear and saturated regimes are ready to be applied to organic field-effect transistors (OFETs) [31]. The expressions are listed below:

in the linear regime,

$$I_{SD} = \frac{W}{L}\mu C(V_G - V_T)V_{SD}$$

in the saturated regime,

$$I_{SD} = \frac{W}{2L}\mu C(V_G - V_T)^2$$

I_{SD} and V_{SD} are the current and voltage bias between source and drain, V_G is the gate voltage, V_T is the threshold voltage at which the current starts to rise, C is the capacitance of the gate dielectric, W and L are the width and length of the conducting channel respectively, and μ is the carrier mobility.

In FETs, the charges transport within a very narrow channel (no more than a few nanometers wide) at the interface between the organic semiconductor and the dielectric [32, 33]. There are many factors influencing the charge transport, for example, the structural defects in the organic layer at the interface, the surface topology and polarity of the dielectric, the presence of defects at the interface depending on the structure of the gate dielectric surface materials, and contact resistance at the source and drain metal/organic interfaces [34–36]. The dielectric constant of the gate insulator also affects the mobility; the carrier mobility decreases with increasing dielectric constant due to polarization (electrostatic) effects across the interface [37, 38].

When the above methods are compared, different results are found for an identical sample. The charge mobility determined by the TOF method is often found to be lower than the PR-TRMC value. This is because TOF mobility is measured over relatively thick samples (usually tens of microns) on a millisecond or microsecond timescale and therefore is more susceptible to defects and grain boundaries. Nevertheless, TOF experiments lead to higher mobility values over OFET and SCLC techniques, which yield one order of magnitude lower. This discrepancy is because the carrier injection efficiency is lower between the metal electrodes and the organic material in both SCLC and OFET devices [39].

Furthermore, charge transport behavior in DLC materials with multiscale conformational dynamics were computationally investigated [40]. From that, fundamental understanding of the relationship between the mechanism of charge transport and structures of the active organic materials, including chemical composition and supramolecular organization, has been well established, which is critical for improving device performance [41]. By improving molecular organization, the mobility of charge carriers along molecular stacks can be significantly enhanced. Therefore, to facilitate efficient charge transport, developing ordered self-assembling materials with defined structures is highly desired.

2.3 DISCOTIC MOLECULAR SYSTEMS

For the DLCs, the structure is the most significant and direct factor influencing the supramolecular assembly, which leads to multiple morphologies, properties, and functionalities. To develop novel functional DLC materials and/or to improve the performance of devices using these materials, understanding the structural effects and structure–property relationships is fundamental. To improve the semiconducting properties of DLCs, creating versatile DLC materials is a key issue. A typical DLC molecule is a model having a rigid aromatic core surrounded by multiple flexible side chains. With organic synthesis, the main driving force to the structural diversity, it is feasible for researchers to vary the nature of the central core and the peripheral substituents. Increasing the DLC core size, which enhances the π-orbital overlap within the columnar structure, is one of the most successful designing strategies that have been widely accepted to achieve high charge-carrier mobility. To further strengthen the π–π stacking of molecules, various ways have been explored to enhance the inter-disc correlation within the columns, for example, introducing hydrogen bonding and dipole–dipole interactions. On the other hand, flexible chains on the periphery of discotic molecules help introduce liquid crystalline properties and processability (solubility). When the chain length and structure change (e.g., with branches or/and heteroatoms), the resulting phase behavior and alignment will be altered. On all accounts, by varying molecular structures, DLC materials with good thermal and chemical stability as well as desirable electronic properties (appropriate HOMO and LUMO energy levels) can be obtained. In this section, the molecular structures of common DLC materials will be presented.

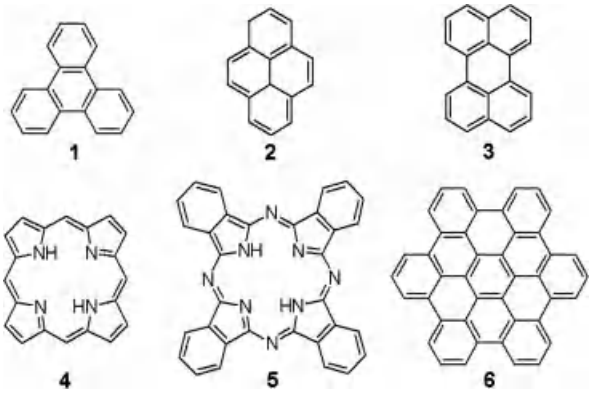

FIGURE 2.7 Typical aromatic structures for discotic cores.

2.3.1 General DLC Molecules with High Charge Mobility

Most discotic molecules have rigid large-aromatic cores. The typical core structures varying from small size to large size are listed in Figure 2.7 in the order: benzene [2, 42], triphenylene [43], pyrene [44], perylene [12], porphyrin [45], phthalocyanine [46], and hexabenzocoronene [47].

Benzene is the smallest and the first used aromatic core for discotic mesogen [48]. Since researchers have discovered that larger aromatic cores tend to form more efficient π-stacks, extending the sizes of the conjugated cores has become one important way to develop new discotic mesogens. In 1982 Simon and co-workers first discussed the idea of using discotic liquid crystals as quasi-one-dimensional conductors [49]. In the early 1990s, researchers successfully generated photo-induced charge carriers in chemically pure DLC molecules and measured the mobility by PR-TRMC or TOF technique. In 1993, Adam et al. managed to measure photo-induced charge-carrier mobility of $1 \times 10^{-3}\,\mathrm{cm^2\,V^{-1}\,s^{-1}}$ in the columnar phase of hexapentyloxytriphenylene **7** by TOF technique (Figure 2.8) [22]. Further in 1994, they discovered one DLC material hexahexylthiotriphenylene showing a decent charge carrier mobility (holes μ_+) of *ca.* $0.1\,\mathrm{cm^2\,V^{-1}\,s^{-1}}$ [50]. From these studies, valuable information of charge transport in DLCs was accomplished for the first time, via examining the nature of charge carriers and observing charge transport along the column axis. After that, the major focus of research on DLCs has proceeded from the beginning studies of structure–property relationship to the advanced improvement of charge transport, in order for developing new systems for various practical applications with higher mobilities.

Triphenylene derivatives as shown in Figure 2.8 are typical DLC materials. Their properties are significantly influenced by the nature of the substituents. For example, a strong tuning effect in the order within the columnar phase of discotic triphenylenes is achieved by varying only one of the lateral chains on the aromatic core, resulting in dramatic changes of phase behavior and photophysical properties [51, 52]. A systematic charge mobility study of triphenylene-based DLC molecules indicated

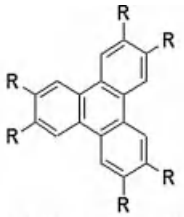

7 R = OC_5H_{11} **8** R = OC_4H_9

9 R = OC_6H_{13} **10** R = OC_7H_{15} **11** R = SC_6H_{13}

FIGURE 2.8 Molecular structures of disc-like triphenylene derivatives.

that the charge transport properties are strongly correlated with the order in the mesophases. For DLC **7** in the Col_h phase, carrier mobilities (holes) of the order of $10^{-3}\,cm^2\,V^{-1}\,s^{-1}$ were measured [22]. For a smaller homolog **8**, approximately an order of magnitude increase in the hole transport was observed suggesting the existence of more ordered plastic columnar phase [53]. Compared with the analog compounds **9**, **10** with longer-side chains, the shorter-side chain derivatives **7**, **8** have better π-orbital interactions of the cores, resulting in higher mobilities [54]. Interestingly, even a higher hole mobility value ($1 \times 10^{-1}\,cm^2\,V^{-1}\,s^{-1}$) has been found in DLC **11** with higher mesophase order when the alkyl chains connect to the core via sulfur. These DLC molecules provide generally higher charge mobility values than those with the chains linking either directly or via oxygen to the cores [50].

In addition, compound **11** has been used to show the correlation between the carrier mobility and molecular order of DLC materials, as displayed in Figure 2.9. During cooling, **11** exhibits phase transitions from isotropic to Col_h phase, to the more ordered columnar helical phase, and eventually to the crystal phase below 40°C. In the isotropic liquid phase, a low charge mobility value of $1 \times 10^{-4}\,cm^2\,V^{-1}\,s^{-1}$ is measured because there is no columnar order. When order increases, the value rises to $5 \times 10^{-3}\,cm^2\,V^{-1}\,s^{-1}$ in the Col_h phase and further to $0.1\,cm^2\,V^{-1}\,s^{-1}$ in the columnar helical phase. Furthermore, although in the crystalline phase charge-carrier mobility could not be determined by the TOF technique due to the trapping sites at grain boundaries, the sum of the one-dimensional charge-carrier mobilities (about $0.4\,cm^2\,V^{-1}\,s^{-1}$) has been derived from the PR-TRMC technique [23]. By combining the results of both techniques (TOF and PR-TRMC), an elevation in mobility by more than three orders of magnitude has been achieved during transitions from mesophase to crystalline phase. This result is a common feature of a number of different discotic materials and is attributed to the more ordered packing of molecules.

For organic semiconductors, a vast majority of the known discotic mesogens are relatively rich in electrons, which are better for transporting holes (*p*-type) than electrons (*n*-type). For discotic triphenylene derivatives, earlier studies have reported that the majority of them were *p*-type semiconductors and the electron mobility was much smaller than the hole mobility, indicating the major charge carriers are holes. However, recent research has discovered that by improving the purity of materials, ambipolar charge transport (for both electron and hole) in the columnar phases of **7**

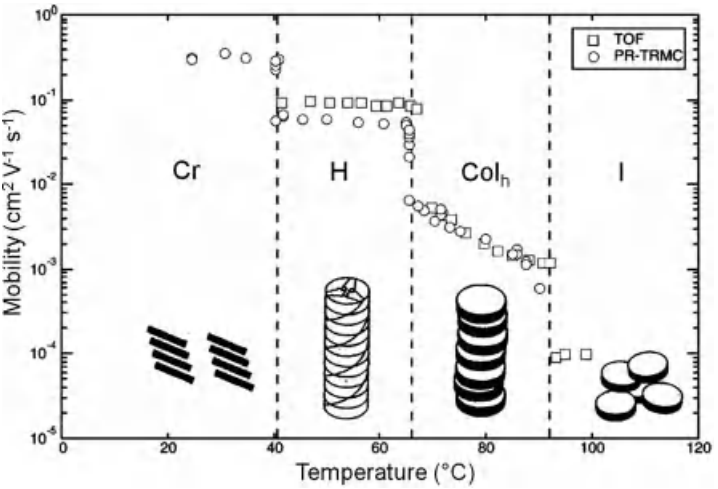

FIGURE 2.9 The charge-carrier mobility in different phases of **11** measured by TOF (μ_h; squares) and sum of one-dimensional intracolumnar mobility $\Sigma\mu_{1D}$ (open circles) estimated by PR-TRMC experiments while cooling the sample from its isotropic phase. Cr: crystalline phase; H: helical columnar phase; Col$_h$: hexagonal columnar phase; I: isotropic phase.

and **11** could be obtained [55, 56]. This is important because electron-transporting materials (electron acceptors) with high mobility are essential for solar cells, bipolar transistors and organic light-emitting diodes (OLEDs). For example, a layer of *n*-type semiconducting material sandwiched between the cathode and the emission layer enhances the performance of LEDs by facilitating the electron injection. More efforts have been devoted to synthesizing and characterizing electron-deficient (*n*-type) discotic molecules recently as *n*-type materials are highly desired but are fewer compared to the large number of electron-rich (*p*-type) ones. From the molecular structural point of view, connecting electron-withdrawing peripheral groups onto a *p*-type discotic core or modifying aromatic core structures to be electron-deficient (e.g., with heteroatoms) are feasible ways. **12** is one example of *n*-type DLC materials built up with hexaazatriphenylene as core structure connected by electron-withdrawing carbonyl substituents (Figure 2.10) [98]. Meanwhile, substitution of electron-withdrawing groups can lower the LUMO and HOMO levels in π-conjugated systems, which reinforces electron mobility.

Lehmann et al. reported that DLC hexaazatrinaphthylene (HATNA) **13** with an electron-deficient core showed charge carrier mobilities of $0.3\,cm^2\,V^{-1}\,s^{-1}$ by PR-TRMC measurements and demonstrated the electron-deficient character for **13** by cyclic voltammetry [57]. Hexaazatriphenylene **14** is another DLC example with an electron-deficient aromatic heterocyclic core. When it was blended in films with a donor material poly(3-hexylthiophene) (P3HT), the photo-induced electron transfer process has been investigated and Meijer et al. determined it as an electron-acceptor [58]. As a matter of fact, electron transport in the columnar mesophase

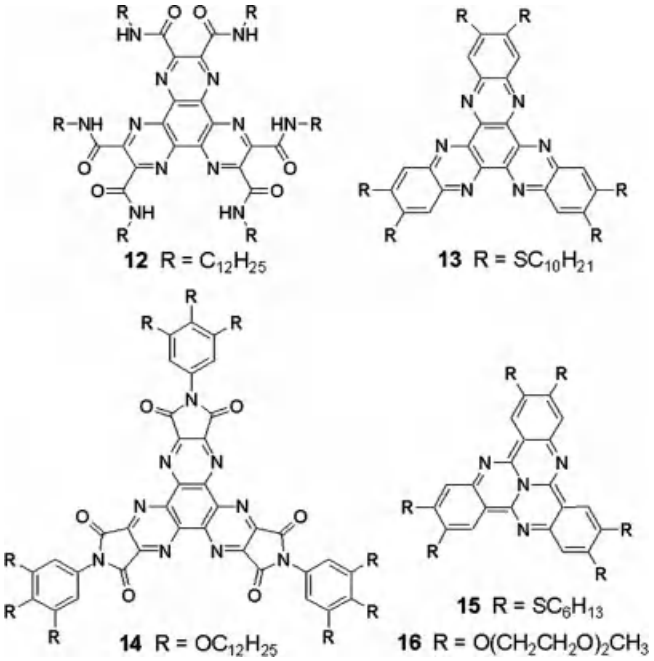

FIGURE 2.10 Molecular structures of triphenylene derivatives with various modifications **12–16**.

was first evidenced in an electron-deficient thioether substituted tricycloquinoxaline derivative **15** (Figure 2.10) [59], which was similar to triphenylene core in shape. Conductivity of about $2.9 \times 10^{-5}\,\mathrm{S\,m^{-1}}$ in the columnar phase was obtained and later when replacing the hexylthio side chains with ethyleneoxy chains (**16**), the conductivity reached to an even higher value of $1.1 \times 10^{-3}\,\mathrm{S\,m^{-1}}$.

Among the *n*-type DLC materials, one class showing particularly high charge mobilities are the perylene derivatives shown in Figure 2.11, which are often functionalized with substituents at the imide N atoms. Perylene diimide (PDI) compounds have strong optical absorption and excellent thermal, chemical, and photochemical stability. They are widely used as pigments and dyes in industry. Recently, discotic mesogens of PDIs rose as an attractive *n*-type DLC semiconductor. Due to their photoconductivity and *n*-type semiconducting properties, these materials have significant applications in prototype devices such as solar cells, OLEDs, and OFETs. In recent reviews by Würthner [60] and Langhals [61], details have been discussed in synthesis, supramolecular self-assembly and spectral properties of PDI derivatives and related compounds. For PDI derivatives with relatively short N-substituents, they are crystalline solids with high melting points. When substituents at the two imide nitrogen atoms increase to a sufficient length, liquid crystalline phases (e.g., **17–20**) may appear. When operated under nitrogen atmosphere, **18** in thin-film transistors showed a field-effect mobility as high as $0.6\,\mathrm{cm^2\,V^{-1}\,s^{-1}}$ [62]. As the first reported perylene-based DLC compound for charge transport mobility by PR-TRMC

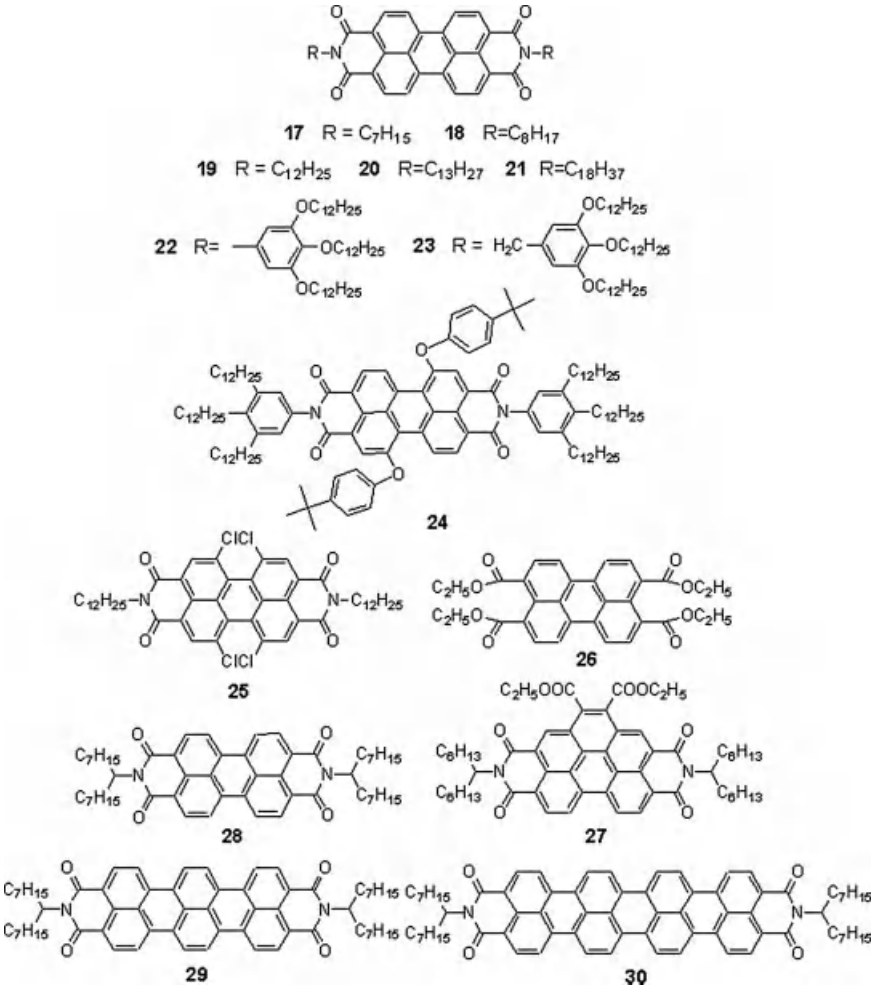

FIGURE 2.11 Molecular structures of perylene derivatives **17–30**.

method, **21** illustrated mobilities of 0.1 $cm^2 V^{-1} s^{-1}$ and 0.2 $cm^2 V^{-1} s^{-1}$ in the liquid crystalline and crystalline phases, respectively [63]. When the substituted chains further become branched, for example, compound **22**, which bears trialkoxyaryl substituents at N atoms, the LC mesophase can enter room temperature with a wide transition range from room temperature to 373°C [64]. When an additional CH_2 spacer was introduced between the tri(alkoxy)phenyl group and the imide nitrogen atom in the molecule **23**, the clearing point was reduced to 226°C, making it easy to process from the melt. Under ambient conditions, it is intriguing to find that this compound shows an electron mobility of 1.3 $cm^2 V^{-1} s^{-1}$, even higher than that of amorphous silicon [12]. In order to further induce mesomorphism, modification of PDI cores at bay positions was considered by researchers. For example, when a bulky

substituent was introduced to the bay area (scaffold) of the molecule **24**, the isotropization temperature further decreased to 283°C. Also, charge transport properties were enhanced for tetrachloro-substituted perylene bisimide **25**, comparing to a non-substituted analog compound at bay positions [65]. DLC PDIs were used in OLEDs because of their strong emission in columnar mesophases. Red light emission by combining electron-deficient **26** with electron-rich triphenylene **17** in a bilayer OLED device was demonstrated by Destruel et al., since fluorescence in the columnar mesophase of perylene tetraester compound **26** was discovered [66]. Another example of an OLED was reported by combining columnar LC **27** having strong electron-withdrawing substituents with benzoperylene triesters, which yielded a red color emission [67].

Since larger aromatic cores may bring highly ordered supramolecular organizations which enhance charge carrier mobilities, extended PDI aromatic cores along the long molecular axis have led to the investigations of terrylene diimides (TDI) and quaterrylene diimides (QDI). With identical branched substituents connected to the cores, **28**, **29** and **30** were synthesized [68]. When core size enlarges from **28** to **30**, the isotropization temperature increases from 130°C to $>$500°C. Although **28** and **29** directly melt from a crystalline state to the isotropic liquid without forming any LC mesophase, **30** with the largest aromatic core is able to form hexagonal columnar phases above 188°C.

Porphyrin has a larger aromatic core and the macrocycle has 26 π electrons. The heterocyclic macrocycles are composed of four modified pyrrole subunits connecting at their α carbon atoms via methine units. Porphyrins are important natural materials: two well-known porphyrins are chlorophyll, an important component in green leaves, and heme, the pigment in red blood cells. For applications, incorporating porphyrin derivatives into photovoltaic devices is highly attractive because of their unique light harvesting ability which has been proved by efficient photosynthesis in green leaves, which evolves by hundreds of million years' natural selection. Moreover, porphyrins are becoming more and more important in science and technology owing to their thermal stability, excellent charge transport ability due to large π-stacks, and photochemical properties. Phthalocyanine has a similar core structure to porphyrin but with four phenyl group combining to pyrrole units and the carbon bridge units changing to nitrogen atoms. When π-electron-rich macrocycles of porphyrins and phthalocyanines are substituted at the periphery by alkyl chains, they tend to self-assemble and form columnar mesophases which have received much attention [49, 69–74]. In fact, porphyrin and phthalocyanine derivatives were the first DLCs samples investigated for the charge transport by PR-TRMC method [75, 76]. As studies have revealed that the substituting chain structures and metal ions have influences on phase transition temperatures, mesophase ranges, and carrier mobilities, the liquid crystalline properties and charge transport ability can be tuned by desirable molecular structures via versatile synthesis.

Recent research on DLC porphyrin derivatives has provided some important supplements to self-organized charge transport materials for photovoltaic devices. Our group has designed and synthesized some porphyrin-based DLCs (e.g., **31–35** as shown in Figure 2.12) which combine easy synthesis, high chemical purity, and

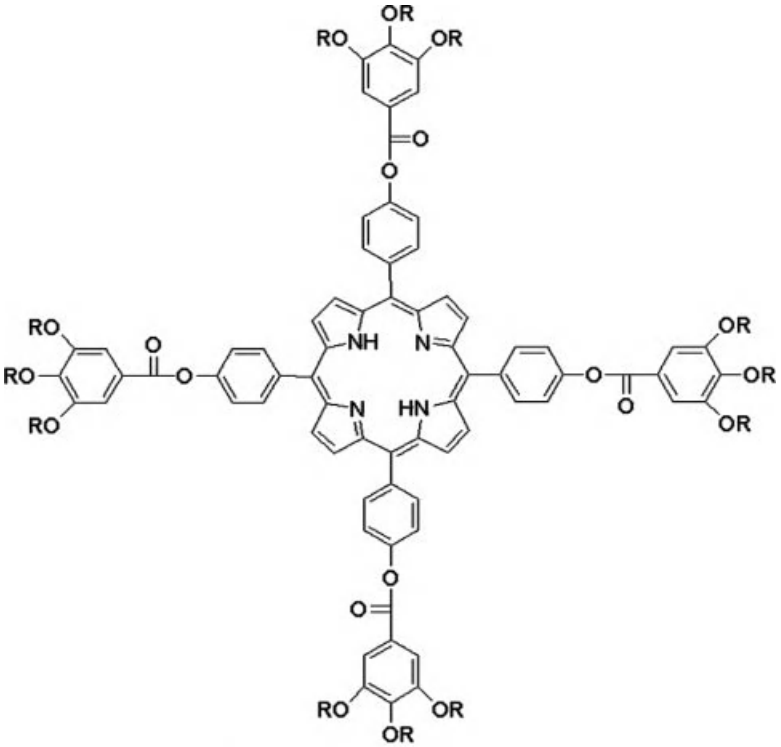

31 R = $C_{12}H_{25}$ **32** R = $C_{14}H_{29}$

33 R = $C_{16}H_{33}$ **34** R = $(CH_2)_{10}C_4F_9$ **35** R = $C_{15}H_{31}$

FIGURE 2.12 Molecular structures of DLC porphyrin derivatives **31–35**.

unique self-aligning properties, together with a wide DLC temperature range for their mesophase, extending even to room temperature [77]. It is intriguing to point out that they are able to spontaneously form defect-free large-area monodomain films with homeotropic alignment. This is beneficial to potential photovoltaic applications [78]. Moreover, we have achieved solution processable bilayer- and bulk-heterojunction solar cells based on **31–32** and the resulting power conversion efficiency achieved under ambient conditions appears to be higher than any other reported solar cells using columnar DLC materials [79].

For phthalocyanines, early charge-carrier mobility measurements of **36**, **37** (in Figure 2.13) have been carried by PR-TRMC, revealing charge mobility values over $0.1\,cm^2\,V^{-1}\,s^{-1}$ [75]. For **37** when it is combined with electron-deficient peripheral alkylsulfonyl substituents, it exhibited a first reduction potential value of about -0.14 V versus the saturated calomel electrode (SCE), which indicated this material as a potential air-stable *n*-type semiconductor [80]. Bushby et al. recently reported high hole mobility ($\sim 0.2\,cm^2\,V^{-1}\,s^{-1}$) in the Col_r phase of an octaalkyl phthalocyanine **38** [81].

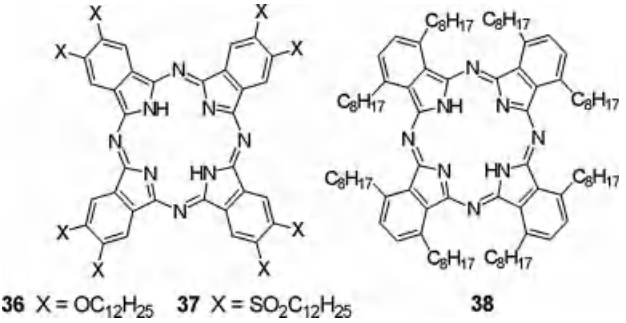

FIGURE 2.13 Molecular structures of phthalocyanines **36–38**.

When the aromatic core is further extended, a planar aromatic molecule HBC **6** forms, consisting of 13 fused six-membered aromatic rings. HBCs and their larger derivatives usually possess sixfold (D_{6h}) symmetry and stack with an average rotational degree of 30° in their columnar phases. K. Müllen's group has extensively investigated this class of materials [82]. HBCs are attractive materials for semiconducting applications such as OFETs and solar cells [83], because they have planar aromatic discogens with large π orbitals, forming highly ordered columnar mesostructures not only presenting a large mesophase range that extends to room temperature [84], but also providing outstanding charge carrier mobility values reaching $0.38\,\mathrm{cm^2\,V^{-1}\,s^{-1}}$ [26]. For the corresponding crystalline phase, charge mobility values can exceed $1.1\,\mathrm{cm^2\,V^{-1}\,s^{-1}}$ [28].

HBC derivatives have also been developed. Since a theoretical prediction has pointed out that molecules of threefold symmetry (e.g., triangular shaped polycyclic aromatic hydrocarbons (PAHs)) with a helical packing structure and 60° as rotation angle would form optimal local arrangement for higher charge mobilities [85], DLC triangle-shaped **39**, **40** in Figure 2.14 were synthesized, reporting improved photovoltaic performance in comparison to the other HBCs [86].

Furthermore, C. Nuckolls et al. reported a contorted HBC derivative **41** with stable columnar mesophase [87]. It formed LC films in OFETs, exhibiting relatively high

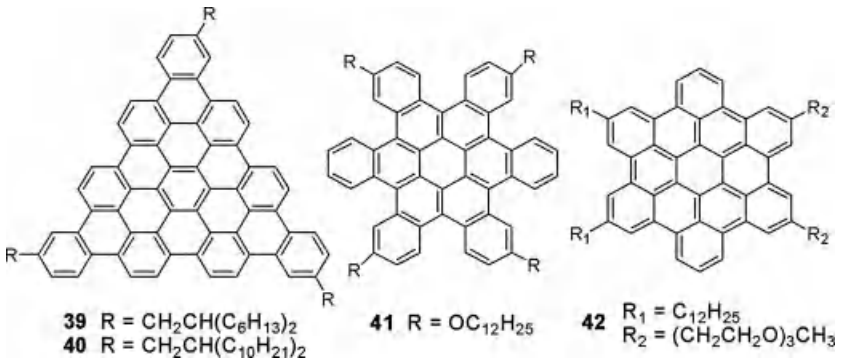

FIGURE 2.14 Molecular structures of modified HBCs **39–42**.

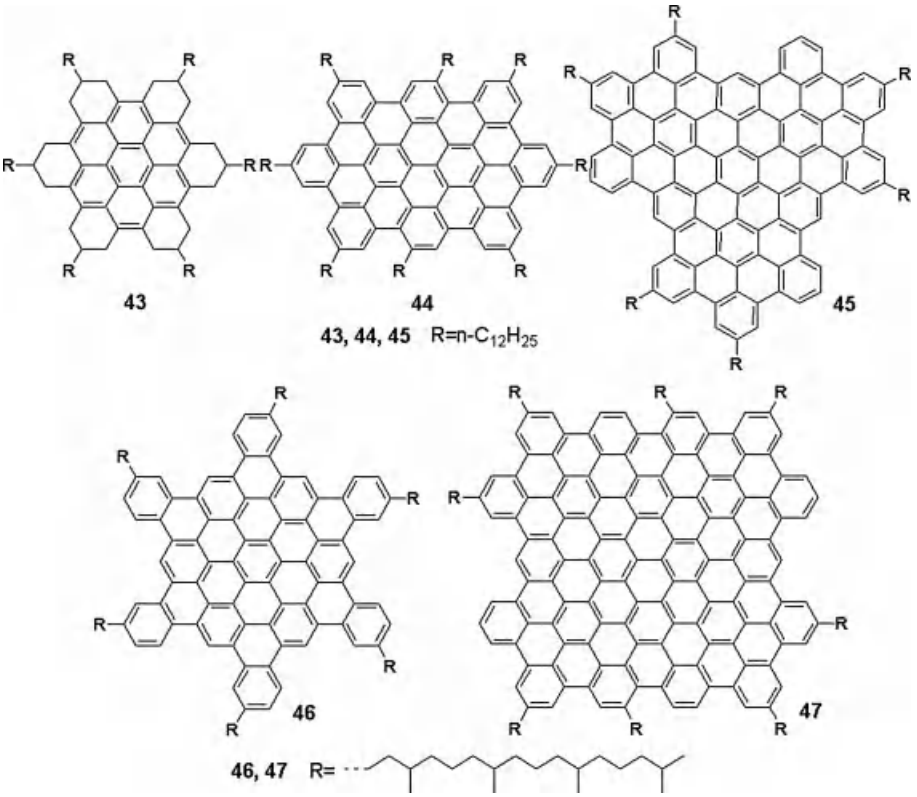

FIGURE 2.15 Chemical structures of disc-like PAHs of various core diameters: **43** (*ca.* 1.0 nm), **44** (*ca.* 1.6 nm), **45** (*ca.* 1.9 nm), **46** (*ca.* 2.0 nm), and **47** (*ca.* 2.3 nm).

carrier mobilities and current modulation ($\mu = 0.02\,\mathrm{cm^2\,V^{-1}\,s^{-1}}$; on–off current ratio of 10^6:1). A gemini-shaped HBC derivative **42** was created by Aida et al. This structure has two hydrophobic dodecyl chains on one side and two hydrophilic triethylene glycol chains on the other [88]. Its solution cast films exhibited a hole mobility of about $1.0 \times 10^{-4}\,\mathrm{cm^2\,V^{-1}\,s^{-1}}$.

For further improving the charge transport properties of these materials, the HBC derivatives with even larger PAHs was synthesized, and some of the resulting DLC materials provided high charge mobilities [89]. In Figure 2.15, the PAH rings contain a larger number of aromatic carbons varying from 24 to 132 [89–92]. They are like graphite structures. With these compounds, a relationship between the sizes of the conjugated aromatic cores and the corresponding charge transport abilities has also been discussed [83].

Apart from the satisfying charge transport properties, DLC PAH materials have also exhibited excellent optical properties which are important for applications in photovoltaic devices, because absorbing sunlight efficiently over a large range of wavelengths, in other words, matching the sun flux spectrum is highly desired.

This target can be achieved by extending the aromatic core of PAH as the maximum absorption peak shifts prominently when the size of aromatic cores increases. There is an empirical formula from experimental results: $\lambda_{max} = 280 + 2n$, where n is the number of carbon atoms in the aromatic core. After the absorption peaks red shift, together with the broadened peaks, a wider coverage to sunlight could be achieved [83].

On the other hand, although large PAH structures show advantages for various applications, there are problems of purifying these molecules with very big aromatic cores. The traces of impurities are charge trapping sites which destroy free charges and the mobility values could be undervalued from experimental results. Additionally, not all of these graphites like PAH rings are planar. In recent years, with further modification to the structures of HBC cores, some of the novel multi-aromatic compounds are ring bent and became non-planar [93].

Apart from the above commonly known DLC materials, a few other cores like coronene, decacyclene, and rufigallol are also used. With appropriate substituents, the corresponding materials exhibit charge transport in their DLC mesophase [94–96].

2.3.2 H-Bond Assisted DLCs

Introducing intermolecular hydrogen bond may be an efficient way to enhance mesophase order and charge transport in DLC materials. It can anchor the molecules in DLC columns. For example, peripheral functionalized triphenylene derivative $C_{18}H_6(OC_6H_{13})_4(OCH_2CONHR)_2$ containing amide groups at the 2,7-positions, which have H-bond interactions with adjacent molecules in columnar stacks, has been synthesized. As shown in Figure 2.16, the intermolecular hydrogen bonds

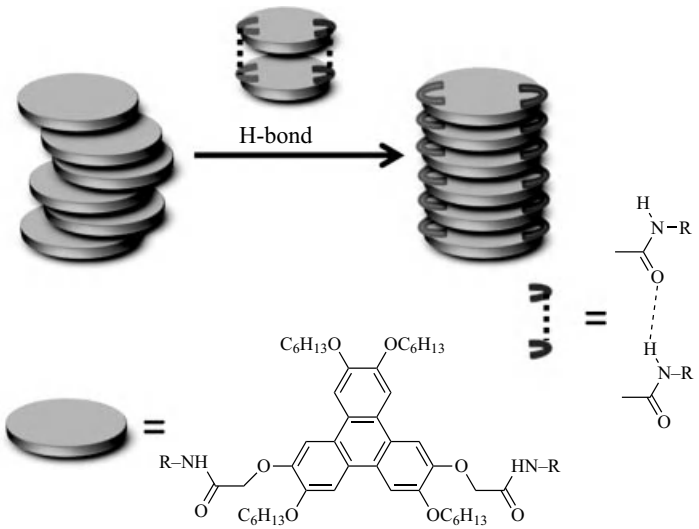

FIGURE 2.16 Hydrogen bonds anchor the columnar organization resulting in more ordered Col_h mesophase and organic gel.

stabilize the columnar organization and lead to an ordered mesomorphic and organic gel state [97]. For other examples, Gearba et al. reported a short interdisc distance of 3.18 Å for **12** which is the smallest value ever found in the columnar phase, due to the presence of intermolecular hydrogen bonding. As a result, an enhanced $\Sigma\mu_{1D}$ mobility up to $2.0 \times 10^{-2}\,cm^2\,V^{-1}\,s^{-1}$ in the columnar mesophase of hydrogen bonded hexaazatriphenylene **12** was found [98]. Due to the presence of intracolumnar hydrogen bonding, an interesting discovery of benzotristhiophene derivative **48** having a temperature independent charge mobility ($2.0 \times 10^{-2}\,cm^2\,V^{-1}\,s^{-1}$) in two hydrogen bonded thermotropic hexagonal columnar mesophases was reported (Figure 2.17), even across phase transition between the two mesophases [99].

Attributed to the highly ordered columnar hexagonal plastic phase that was induced by the intermolecular hydrogen bonding of the 1,3,5-benzenetrisamide with three pendant hexaalkoxytriphenylene groups, a high charge mobility of $0.2\,cm^2\,V^{-1}\,s^{-1}$ was reported [100]. Reported by Kato et al., even by mixing with hydrogen-bonded fibers forming physical gelation of molecules, molecular fluctuations in the columnar phase was suppressed successfully and a threefold enhancement in the hole mobility of **9** was obtained [101].

Similarly, dipole–dipole interactions can also be applied to the design of self-assembled discogens. For example, hexaalkoxydibenzo[a,c]phenazines (HDBP)

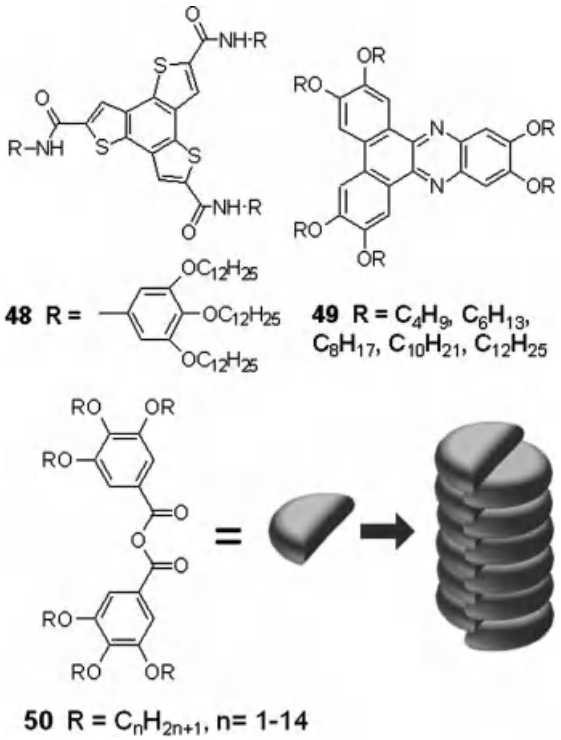

FIGURE 2.17 Chemical structures of **48–50**, and schematic columnar stacks of **50**.

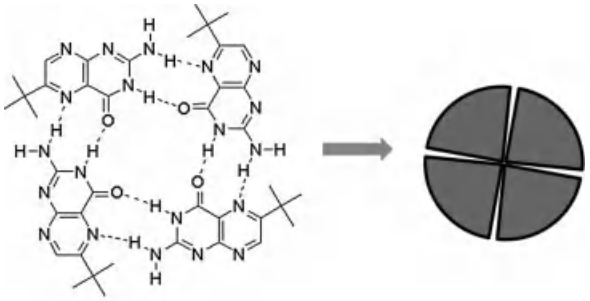

51

FIGURE 2.18 Cyclic disk-like aggregation structure **51** composed of four hydrogen-bonded self-assembled folic acid derivatives (pterin molecules).

49 possess stable hexagonal mesophases in a fairly broad temperature range and can form homeotropically aligned films [102]. 3,4,5-Trialkoxybenzoic anhydride **50** forms a columnar mesophase with geared interdigitation through polar junctions among molecules (Figure 2.17) [103].

Furthermore, by using hydrogen-bonding interactions, supramolecular self-assembled discogens forming disc units in a columnar phase have been obtained, for example **51** in Figure 2.18. This provides a way to create larger molecular discogens for potentially improving charge carrier mobilities. Kato et al. have recently reviewed many other examples of mesogenic H-bonded systems, and useful applications of the resultant supramolecular structures have been highlighted [104, 105].

2.3.3 DLCs with Partially Perfluorinated Periphery

In recently reported research, there is an interesting concept in the design of discotic semiconductors using peripheral polyfluorinated alkyl chains, although there is enormous previous research in fluorinated calamitic liquid crystals [106]. For DLC materials, fluorinated substituents are expected to create an inert "mantle" around the discotic core that effectively increases the columnar phase stability. As the melting point becomes higher, one dimensional charge transport is improved because of the reduced intercolumnar interactions. For polyfluoroalkyl triphenylenes **52**, it is shown that introduction of polyfluoroalkyl groups favors the formation of spontaneous homeotropic alignment (Figure 2.19) [107]. Also, other DLC molecules with partially perfluorinated alkyls such as porphyrin **34** [77(b)] and HBC **53** [108] have been obtained. They are expected to not only become more stable in DLC phase, but also show better alignment and reduce lateral conduction, and hence improve one-dimensional charge carrier mobilities.

2.3.4 Incorporating Fullerenes into DLCs

It is known that fullerene and its analogs are one of the most important families of organic semiconductors. In the past years, numerous electron donor–acceptor

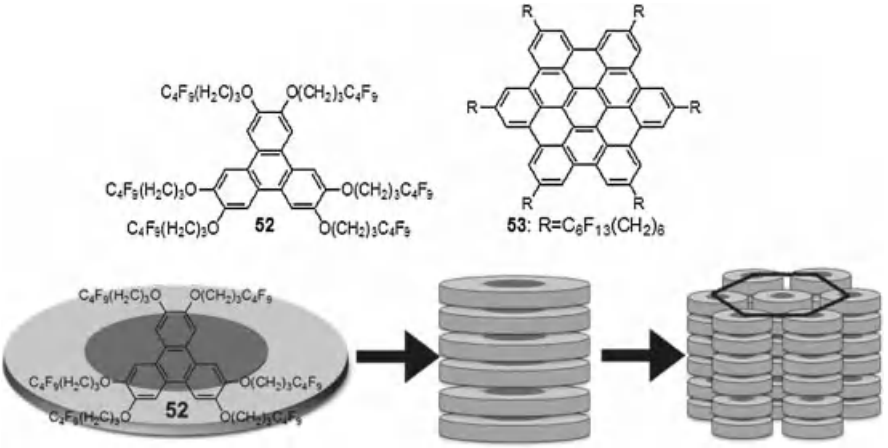

FIGURE 2.19 Top: Chemical structures of **52** and **53**. Bottom: Schematic drawing of homeotropically aligned columnar structures of fluorinated triphenylene **52**.

complexes with fullerene as the electron acceptor core have been synthesized to demonstrate the electron transfer process. In organic photovoltaics (OPVs), the formation of a bicontinuous interpenetrating network from donor and acceptor components as a result of self-organization on the nanometer scale is one key issue for efficient carrier transport of the separated charges. The use of fullerene combined with liquid crystals to form a self-organized phase can be an important approach to improve device performance [109].

Of all the donor–acceptor blends, the porphyrin–fullerene blend is an attractive combination since fullerene is an excellent electron acceptor, and porphyrin is a superior electron donor. Recently, it was found that the blend of porphyrin and $PC_{61}BM$ (a fullerene derivative) can self-organize into a highly ordered thin film by thermal annealing as shown in Figure 2.20 [110]. The hexagonal columnar phase of porphyrin with $PC_{61}BM$ at interstices of the columns has been proposed as the molecular arrangement or it is possible that $PC_{61}BM$ is sandwiched between two porphyrin cores because of the strong π-donor and π-acceptor interaction. Regardless of the packing arrangement, a homeotropically aligned columnar architecture of the porphyrin and $PC_{61}BM$ complex has been proved by XRD. This is very important for OPV applications because such a molecular arrangement can provide an efficient path for electrons and/or holes along the columnar axis where the light harvesting molecules are arranged with the largest area toward the incident light.

Besides, the C_{60} unit can be connected to electron donor molecules by covalent bonding. One example of phthalocyanine–C_{60} dyad **54** (a mixture of isomers, details see Ref. 111) by connecting $PC_{61}BM$ and phthalocyanine derivative designed for heterojunction OPV cells was reported by Geerts et al. (Figure 2.21) [111]. The dyad exhibited a LC phase at room temperature.

Moreover, intermolecular interaction is another way that links fullerene to electron donor molecule. Guldi et al. observed a very strong electronic communication through

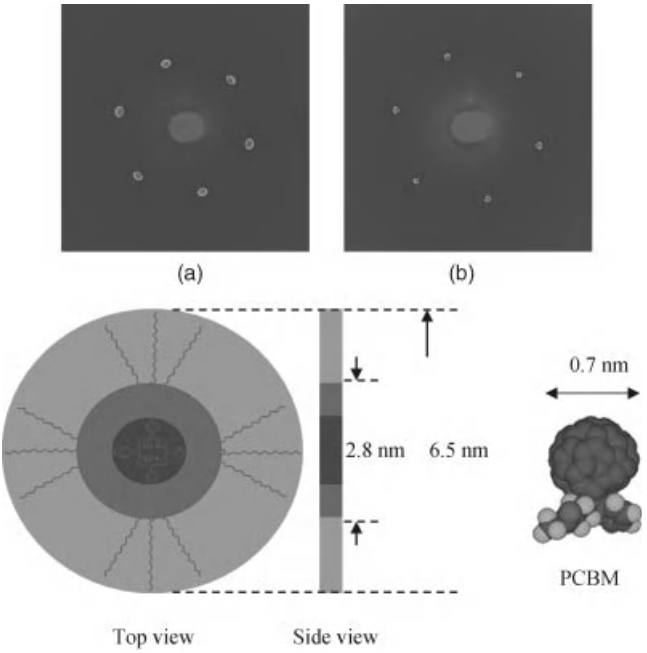

FIGURE 2.20 Top: Synchrotron XRD patterns from homeotropic monodomain of material **35** (a) and the blend of **35** (b) with $PC_{61}BM$ in an 8-μm-thick glass cell. Bottom: Calculated geometric dimensions of porphyrin **35** and 3D ChemDraw spacing-filling model of fullerene derivative $PC_{61}BM$ and the schematic representations of homeotropically aligned architecture of the blend of **35** and $PC_{61}BM$. Reproduced with permission from ref. 110. (*See the color version of this figure in Color Plates section.*)

hydrogen bonds between porphyrin and C_{60} forming **55** in Figure 2.22 [112], which exhibited a longer-lived formation of radical-ion-pair state (~10 μs in THF) compared to that of the similar covalent C_{60} conjugates (~1 μs in THF) [113]. It showed an even higher lifetime of 2.02 μs [114] for the photogenerated radical-ion pair due to the

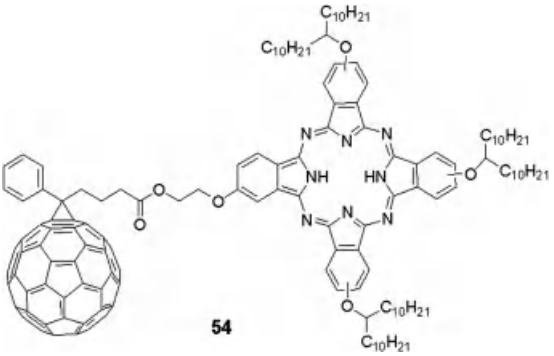

FIGURE 2.21 Chemical structure of phthalocyanine–C_{60} dyad **54**.

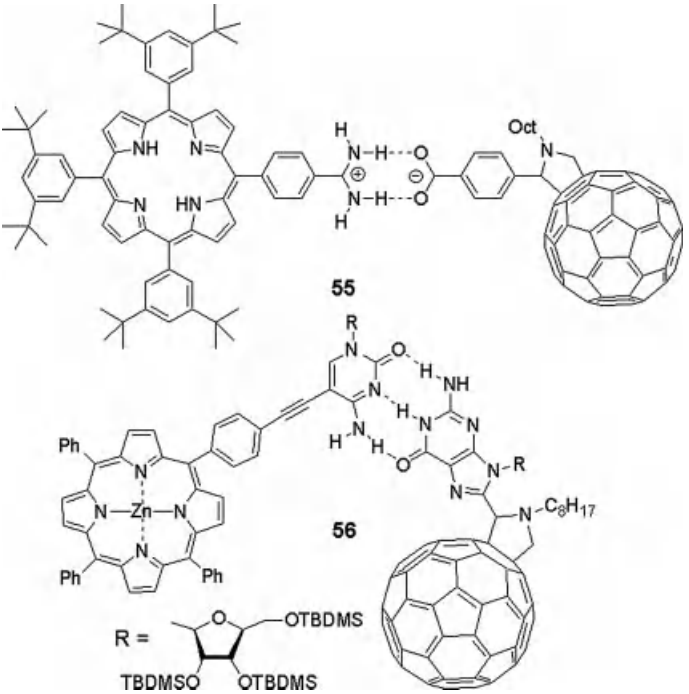

FIGURE 2.22 Chemical structure of the fullerene-based hydrogen-bonded donor–acceptor ensembles **55** and **56**.

stronger Watson–Crick hydrogen bonding in **56** [115–118]. Later, phthalocyanine has also been incorporated into this kind of structure [119].

2.3.5 Incorporating Metal Elements into DLCs

Metal elements can be combined together with organic materials through metal–electron pair coordination and they have an important impact on organic semiconducting materials. On one hand, liquid crystal phases can be induced by the presence of a metal complex. The effect of a metal enhances the mesophase behavior of the material. In the area of photovoltaic cells, researchers clearly want to mimic chlorophyll to have its light-harvesting and electron-transfer properties. The liquid crystal property of this kind of metal–porphyrin complex was first reported by Bruce's group [120]. On the other hand, the metal ion can also change the electronic property of the material and affect the charge transport along the column. For example, metalations of the porphyrins will change the molecular energy and alter the absorption as well as photoemission spectrum. Many metallo-porphyrins or phthalocyanines coordinated with transition metal complexes have been reported, presenting attractive photovoltaic effect [75, 121]. Ohta et al. found ambipolar charge transport (a negative charge mobility of $2.4 \times 10^{-3}\,\mathrm{cm^2\,V^{-1}\,s^{-1}}$ and a positive

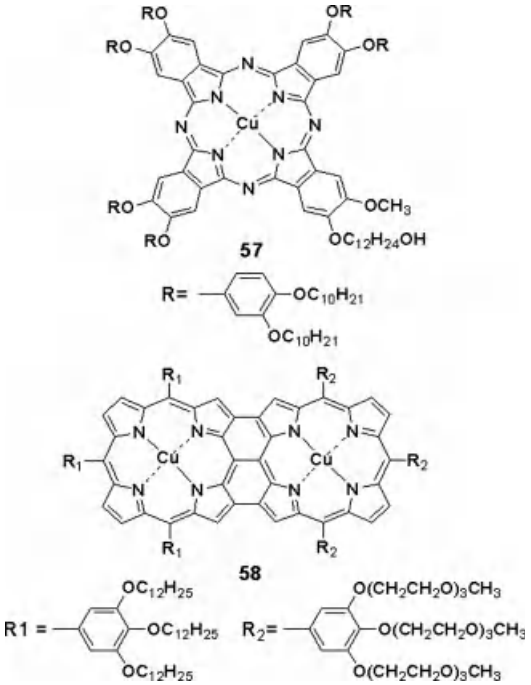

FIGURE 2.23 Molecular structure of porphyrin derivative **57** and dimer **58**.

mobility of $2.2 \times 10^{-3}\,cm^2\,V^{-1}\,s^{-1}$) in the Col_h of a Cu-phthalocyanine compound **57** [122]. Cook et al. recently reported a high hole mobility of $0.2\,cm^2\,V^{-1}\,s^{-1}$ in the Col_r phase of an octaalkyl phthalocyanine **38** [123]. Higher mobility values as high as $0.7\,cm^2\,V^{-1}\,s^{-1}$ were reported in the columnar phase of phthalocyanine metallomesogens [124].

Aida et al. recently synthesized a fused metalloporphyrin dimer **58** (Figure 2.23) bearing hydrophobic (alkyl) and hydrophilic (triethylene glycol) chains in the periphery and reported its self-organization into a room-temperature columnar phase. High electron mobilities were found for the LC film of **58** ($0.27\,cm^2\,V^{-1}\,s^{-1}$ at 16°C) [125].

Apart from common transition metals, porphyrin complexes with lanthanide ions (Eu^{3+}, Tb^{3+}, Dy^{3+}, and Sm^{3+}) [126, 127] have been studied (Figure 2.24). They exhibit unique optical properties. For example, they exhibit line-like emission bands and relatively long luminescence lifetimes [128–131]. Recently, holmium(III) Ho^{3+} porphyrin complexes **59** have been developed, which present the Col_h phase and have an extended lifetime of excited state [132].

Not only porphyrin but also other mesogens can coordinate with lanthanide ions forming DLC structures, showing intriguing properties, for example, phthalocyanine **60** (Figure 2.24) [133] and N-aryl based Schiff bases (Figure 2.25) [134].

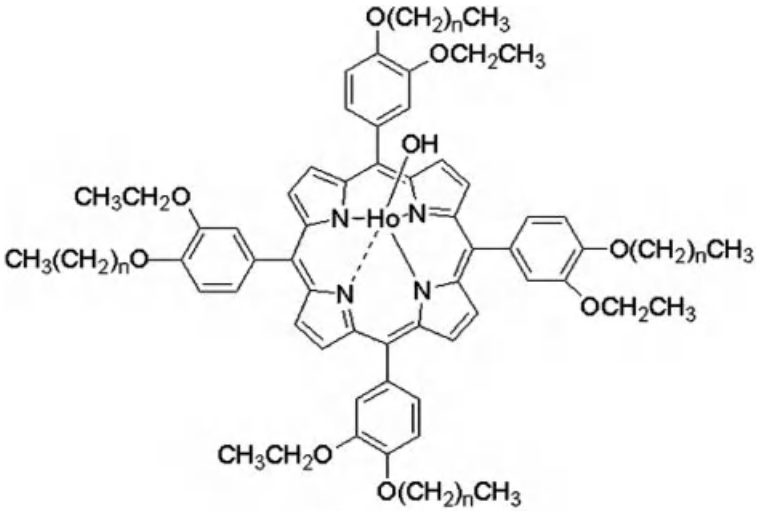

59 n = 11, 13, 15

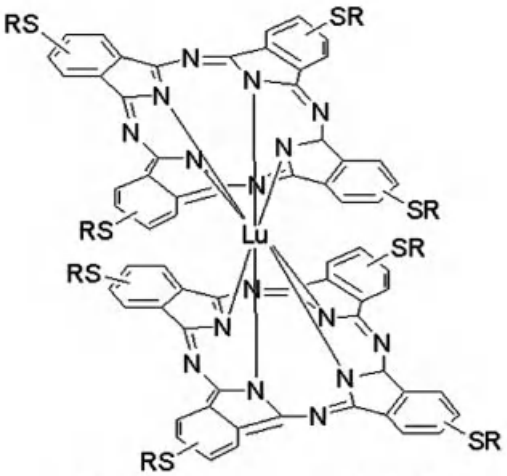

60 R = C_nH_{2n+1} n = 6, 8, 10, 12, 16

FIGURE 2.24 Molecular structure of holmium porphyrin complexes **59** and phthalocyanine complex **60**.

2.3.6 Incorporating Gold Nanoparticles (GNPs) in DLCs

Very recent studies revealed that doping gold nanoparticles into the columnar phase does not disturb the nature of the columnar mesophase (only alter the transition temperatures), but improves charge transport behavior significantly. For the DLC material 2,3,6,7,10,11-hexakis-hexyloxy-triphenylene, the presence of 1% (w/w) of

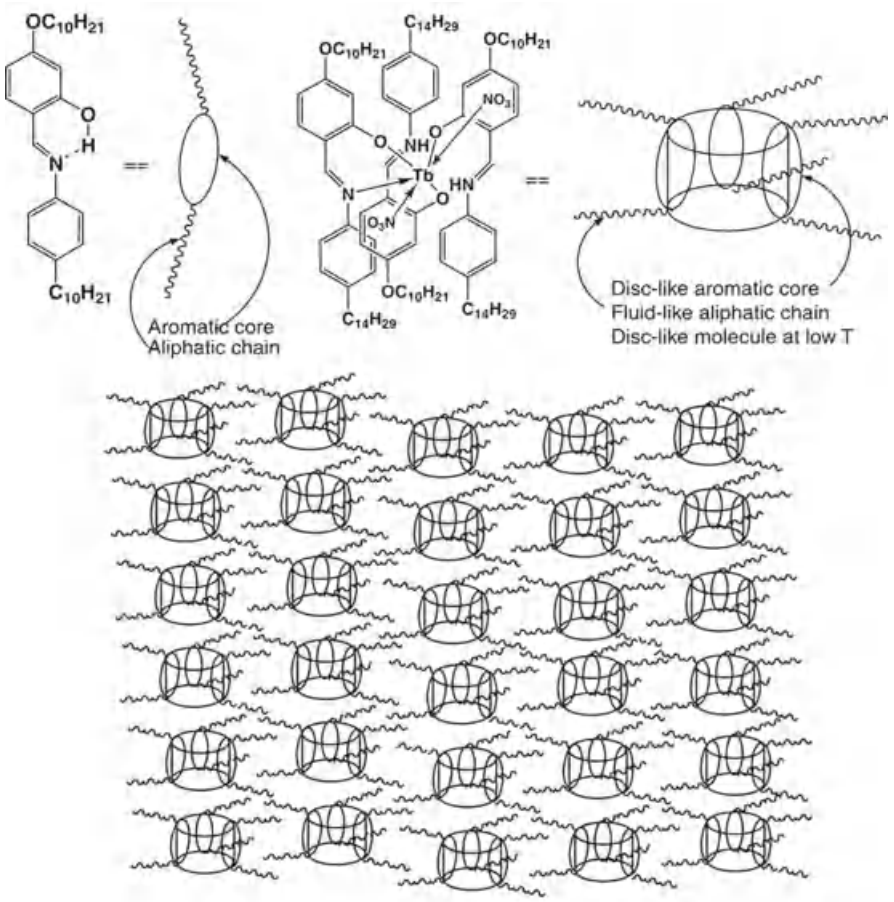

FIGURE 2.25 Molecular model of the ligand and complex in disc-like form, which can organize in columnar phase. Reproduced with permission from ref. 134.

methylbenzene thiol coated gold nanoparticles increases the conductivity of the discotic liquid crystal by about two orders of magnitude [135].

For more research on incorporating gold nanoparticles into the supramolecular order of DLCs, Kumar's group has synthesized GNP stabilized by simple alkanethiols, and dispersed them into the columnar matrix of different DLCs. Thermophysical properties of these nanocomposites have been studied and the columnar phases of DLCs could well-disperse the nanoparticles in their matrices. However, discotic nematic liquid crystal did not disperse well the nanoparticles and there was macroscopic phase separation [136, 137]. Remarkably, there is a dramatic increase in DC conductivity of DLC hexaheptyloxytriphenylene (H7TP) by more than 10^6 times upon doping with 1% triphenylene-GNP (TP-GNP) [138]. The GNP doped molecular stacking columnar structure is shown in Figure 2.26. Similarly, carbon nanotubes

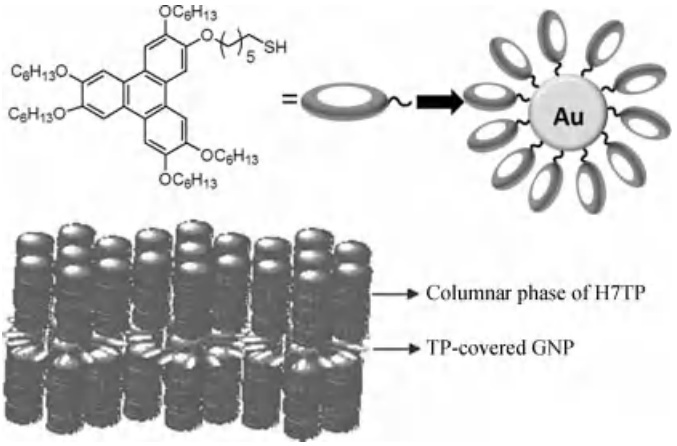

FIGURE 2.26 A schematic diagram illustrating TP-GNP structure and its arrangement in the inter domain spacing formed between the discotic columns. Reproduced with permission from ref. 138.

have also been mixed into DLC mesophases. As a result, LC nanocomposites with broad mesophase ranges and different electronic properties may potentially be important for many device applications, such as photoconductors, light-emitting diodes, photovoltaic solar cells, sensors, thin-film transistors [139].

2.4 ALIGNMENT OF DLC MATERIALS IN ACTIVE SEMICONDUCTING LAYERS

For DLC materials, one key issue determining charge-carrier mobility is the order of the molecules in columns. Therefore, efforts have been devoted to discover processes leading to highly ordered monodomain thin-films of DLC materials. The charge transport mechanism in columnar phase is one fundamental point to know, which indicates DLCs are quasi one-dimensional semiconductors and charges travel much faster along the columnar stacks than between columns. This implies that molecules must be appropriately aligned in a column to form a tunnel that the current can go through. According to the aligning direction of DLC molecules on a substrate surface, homeotropic alignment (or "face-on" orientation) means columns are perpendicular to the surface and planar alignment (or "edge-on" orientation) means columns are parallel to the surface have been defined. The models are shown in Figure 2.27. The first alignment is preferred by solar cells, OLED devices and the second is for OFET devices. In such devices, the conducting columns are usually generated as defect-free long-range ordered thin (a few tens of nanometers) films to fill the gap between the anode and the cathode. Although numerous discotic molecules that can self-organize into columnar structures have been synthesized, controllable molecular orientation either forming homeotropic or planar alignment onto a substrate is difficult. Conventional techniques used for alignment of calamitic

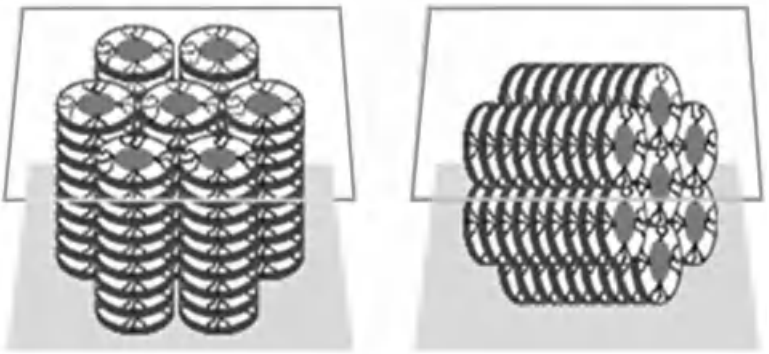

FIGURE 2.27 Schematic representation of the homeotropic (left) and planar (right) orientations of a discotic columnar mesophase.

LC phases are not useful for the highly viscous columnar LC materials [140]. Therefore, new device fabrication techniques are in strong demand for organizing discotic molecules, forming homeotropic or planar alignment.

2.4.1 Homeotropic Alignment

A "face-on" alignment of the columnar mesophase sandwiched between two substrates can generally be generated by thermal annealing. Various examples such as triphenylene, phthalocyanine, porphyrin, and hexabenzocoronene DLCs have exhibited such an alignment in their columnar mesophases in relatively thick films (even a few micrometers) when the material is confined between two substrates and slowly cooled from their isotropic state. For example, a systematic study of one DLC triphenylene derivative on various substrates revealed that the homeotropic alignment is thermodynamically favored in the columnar phases [141]. It is noteworthy that a slower cooling rate is more favored because the high viscosity of the columnar mesophase often quickly promotes multidomains and prevents the perfect homeotropic alignment over a large area. In recent years, the development of homeotropically aligned DLC materials has become more comprehensive for the influences of different parameters such as molecular structures and surface interactions. For example, by incorporating heteroatoms in the flexible side chains or by introducing groups with larger sterical hindrance on to the mesogenic core, the isotropic melt viscosity of mesogens has decreased. Thus, developing novel ways for various DLCs to obtain homeotropic alignment has been one attractive research topic. Researchers have used mixed molecules forming self-organized DLCs for high-efficiency organic photovoltaics [142]. A face-on oriented bilayer heterojunction formed by two types of discotic molecules was reported (Figure 2.28) [143]. These designed molecules have specific properties, e.g., selective solubility, low degree of miscibility, controllable transition temperatures, and room temperature hexagonal columnar liquid crystallinity.

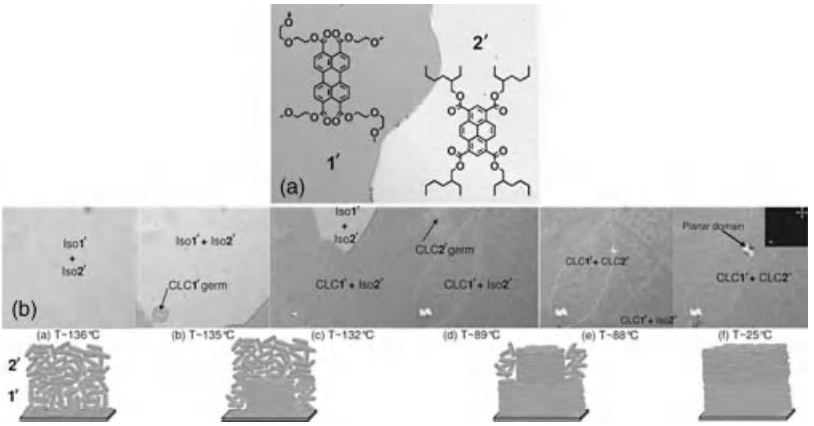

FIGURE 2.28 (a) Schematic structure of the two compounds **1′** (where only one of the two regioisomers is sketched) and **2′**. Their low degree of miscibility is shown by a contact preparation between coverslip and glass slide in the isotropic liquid phase. Observation performed by bright field microscopy. The image size is 440 μm × 325 μm. (b) Growth by thermal annealing of a homeotropically oriented open bilayer (cooling rate: 5°C/min) observed by differential interference contrast microscopy. In a preliminary step, both compounds **1′** and **2′** have been sequentially deposited by spin-coating before (a) being heated up to their isotropic liquid phase (Iso**1′** and Iso**2′**, respectively). (b and c) Nucleation of the compound **1′** in the columnar liquid-crystalline phase (CLC**1′**) with a dendritic texture, while the upper layer (compound **2′**) is still in its isotropic liquid phase (Iso**2′**). (d and e) Growth of CLC**2′** above CLC**1′**. Note the apex angle of the CLC**2′** growing domain of ≈120° characteristic of a face-on alignment. (f) Both layers exhibit a homeotropic alignment, as confirmed in the inset by the lack of birefringence between crossed polarizers. The layer thicknesses are approximately 350 and 200 nm for compounds **1′** and **2′**, respectively. The image size is 715 μm × 650 μm. Reproduced with permission from ref. 143.

An effective method to obtain homeotropic alignment is to modify the affinity of molecules by changing the chemical nature of the side chains to the substrate surface such as polyimide, ITO, and cetyltrimethylammonium bromide (CTAB)-coated glass substrates. Partially perfluoroalkyl groups were used as the peripheral chains for triphenylene mesogens, promoting homeotropic alignment in the hexagonal columnar phase [144]. Porphyrin derivative **34** with partially perfuoronated alkyl chains on peripheral [77(b)] can form homeotropic alignment on various substrates as well, which is more important as it has a larger π-conjugated system, together with other advantages of porphyrin (Figure 2.29). On the other hand, there are reports demonstrating homeotropic alignment of columnar mesophase on surfaces with certain nature or treatment. For example, Pisula et al. reported spontaneous homeotropic alignment of branched long alkyl chain-substituted HBC derivatives on ITO substrates [145]. There were reports on the formation of homeotropically aligned open films of a hexagonal columnar phase on discotic phthalocyanine derivatives deposited on ITO substrates treated by either UV, ozone or nitrogen plasma [146, 147]. Geerts et al. also demonstrated a method of using a polymer sacrificial layer to induce

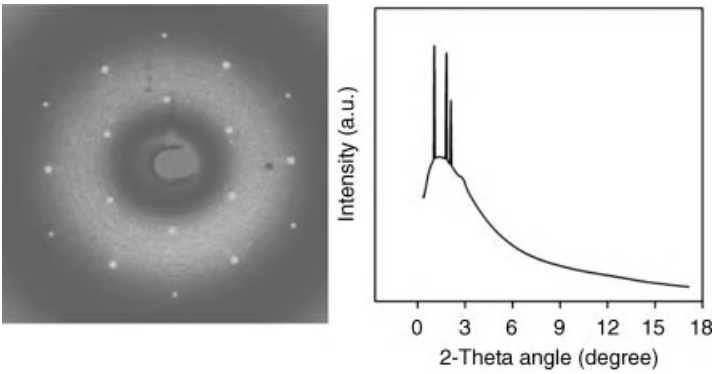

FIGURE 2.29 Synchrotron X-ray diffraction pattern (left) and X-ray intensity versus diffraction angle plot (right) obtained from homeotropic monodomain of sandwiched sample **34** with an 8 μm gap at 126°C. Reproduced with permission from ref. 77(b).

homeotropic alignment of the columnar LC films, as shown in Figure 2.30. In their method, homeotropic alignment of phthalocyanine is imposed by thermally annealing the confined LC film with a top polymer layer that is later removed by washing with a selective solvent [148]. Moreover, ordered porous alumina templates have been introduced to prepare homeotropically aligned nanowires of a triphenylene discotic compound, reported by Steinhart et al. [149]. One interesting observation was about introducing homeotropic alignment of corannulene-based DLC molecular columns by applying an electric filed, considering that most known DLCs so far were

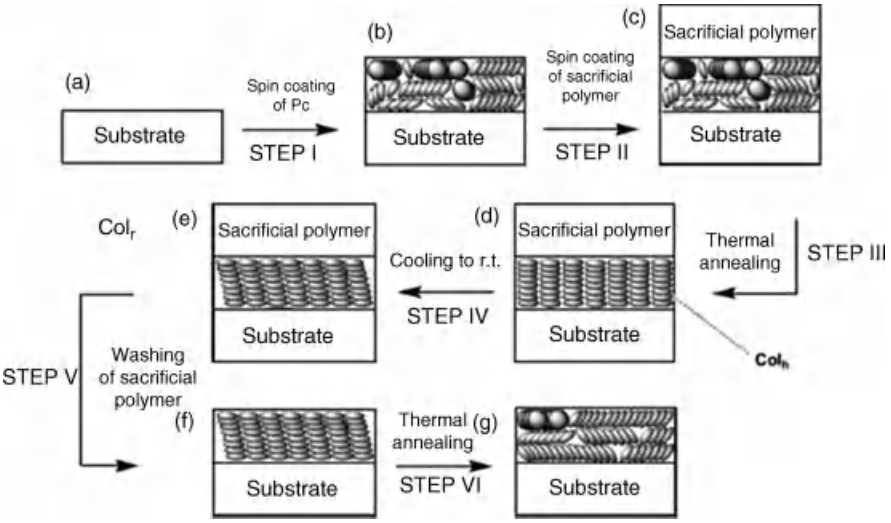

FIGURE 2.30 Fabrication process of homeotropically aligned thin films of phthalocyanine derivative. The last step serves only to demonstrate the function of the sacrificial layer. Reproduced with permission from ref. 148.

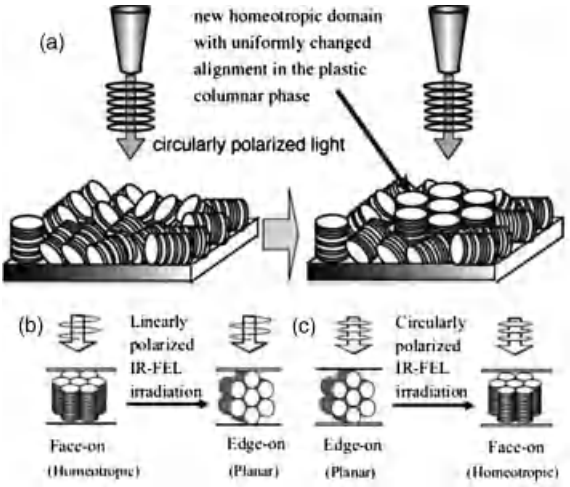

FIGURE 2.31 (a) Schematic representations of alignment change of **8** with the circularly polarized IR irradiation. Reproduced with permission from ref. 152. Alignment change of **9**: (b) infrared irradiation with linearly polarized light and (c) irradiation with circularly polarized light. Reproduced with permission from ref.151.

not responsive to the applied electric field in their columnar mesophases [150]. Furthermore, alignment change of the discotic liquid crystal domains induced by infrared irradiation was recently investigated for the hexagonal columnar phase of hexahexylthiotriphenylene, as shown in Figure 2.31 [151, 152]. The results imply that polarized infrared irradiation is a potential technique for alignment of DLC semiconductors: circular polarized one is for homeotropic alignment and linear polarized one is for planar alignment.

Additionally, Kang et al. have investigated some porphyrin-based DLCs for their alignment behavior which preferred homeotropic alignment. In thinner cells ($<10\,\mu m$), there was even more uniform homeotropic alignment. The example of compound **33** is shown in Figure 2.32. The control of orientational order of columns was found to be achieved by varying the film thickness, thermal annealing process, and mechanical shearing [77].

2.4.2 Planar Alignment

Discotic columns with planar alignment are very important for applications in OFETs. To improve device performance, a well-ordered and uniaxially aligned thin layer of discotic columns exhibiting high charge-carrier mobility is required. Technically, to achieve planar alignment of organic discotic semiconducting molecules, various approaches such as applying aligned polytetrafluoroethylene (PTFE) layers, zone casting, Langmuir–Blodgett (LB) films, self-assembled monolayers (SAM), pulsed infrared irradiation, and magnetic field have been developed. Among these methods, while some of them are employed for solid state materials, the use of an aligned PTFE layer and zone casting offers a way for solution samples: by spin

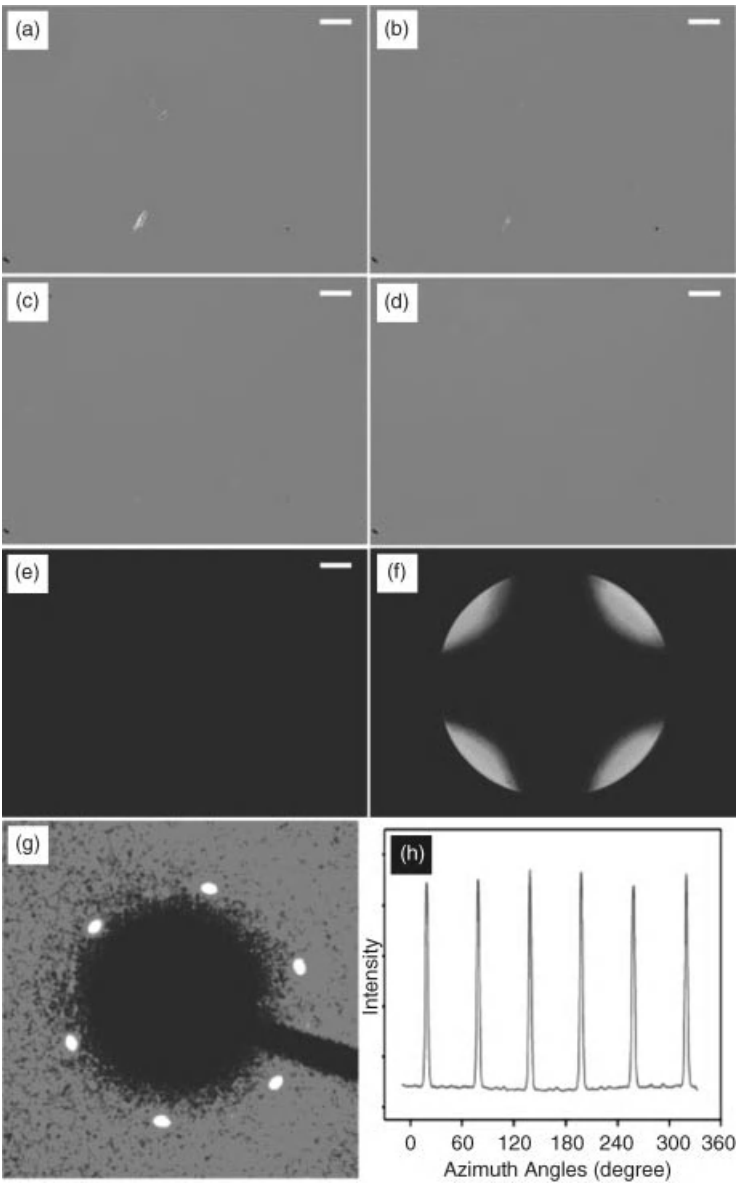

FIGURE 2.32 Formation of homeotropic texture on a macroscopic scale via slow cooling of the 1.8 μm cell with **33**. Slow cooling induces selective nucleation and growth of homeotropic domain (parts (a) and (b) at 121.0°C) and hence yields uniform homeotropic columnar orientation at lower temperatures ((c) 113.0°C and (d) 75.0°C), confirmed by both (e) optical texture under crossed polarizers and (f) conoscopic image at 75.0°C. Optical images were taken at (a–d) 70° and (e) 90° angles between polarizers. The scale bar corresponds to 50 μm. (g) X-ray 2D pattern for the Col_h phase at 75.0°C of **33**. (h) The azimuthal scan of the peak in (g) shows equally spaced six peaks with uniform intensity distribution. Reproduced with permission from ref. 77(a). (*See the color version of this figure in Color Plates section.*)

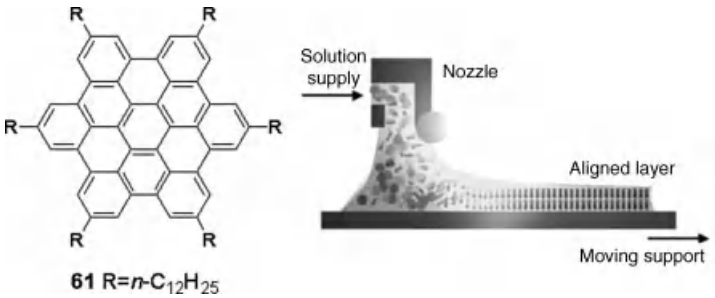

FIGURE 2.33 Schematic presentation of the zone-casting technique on **61** displaying homogeneous film formation lying in the zone-casting direction. Reproduced with permission from ref. 155.

coating the material onto an aligned PTFE layer, Zimmermann et al. first reported the "edge-on" orientation of a triphenylene compound in its hexagonal plastic columnar phase [153]. Furthermore, PTFE-coated surfaces were later applied for aligning other materials like HBCs. Friend et al. reported planar alignment of an HBC derivative on rubbed-PTFE layer and obtained field-effect mobility as high as $0.5 \times 10^{-3}\,cm^2\,V^{-1}\,s^{-1}$, even without an annealing step [154]. With zone-casting (Figure 2.33) films of discotic HBC **61**, Müllen et al. reported higher FET device performance (on-off ratio of 10^4 and a field-effect mobility of $\sim 5 \times 10^{-3}\,cm^2\,V^{-1}\,s^{-1}$) [155, 156].

Using the Langmuir–Blodgett film technique is another frequently applied method for fabricating ultrathin ordered layers of discotic molecules. In this technique, amphiphilic molecules can "edge on" align at the air–water interface, which is thereafter effectively transferred to a solid substrate by vertical dipping and raising of the substrate (Figure 2.34) [157]. When spread at the air–water interface, DLC materials such as triphenylenes, phthalocyanines, and HBCs that have been partially functionalized with hydrophilic side chains are reported to form well-ordered Langmuir monolayers [158–160].

For other approaches, Räder et al. have reported a soft-landing method in which matrix-assisted laser desorption/ionization (MALDI) mass spectrometry can produce ordered structures of organic macromolecules at surfaces [161]. Application of a strong magnetic field (20 T) was used to produce large-area monodomain films of discotic HBC molecules, by which constructed solution-processed FETs exhibited charge-carrier mobilities up to $10^{-3}\,cm^2\,V^{-1}\,s^{-1}$, significantly higher than that of unaligned material [162]. A. Calo et al. demonstrated a viable method to yield highly oriented DLC films by controlling the entangled phenomena of dewetting and electromigration in DLC films. This approach provides a powerful tool for aligning DLC in a bottom-electrode device channel which is potentially useful for stabilizing and optimizing the device performance of other classes of mesogenic organic semiconductors in ultrathin film devices [163].

Recently, there have been extensive reports of DLC materials with potentially attractive properties. Development of a suitable processing technique aligning DLCs in the highly ordered arrangement is critical in optimizing their desirable properties

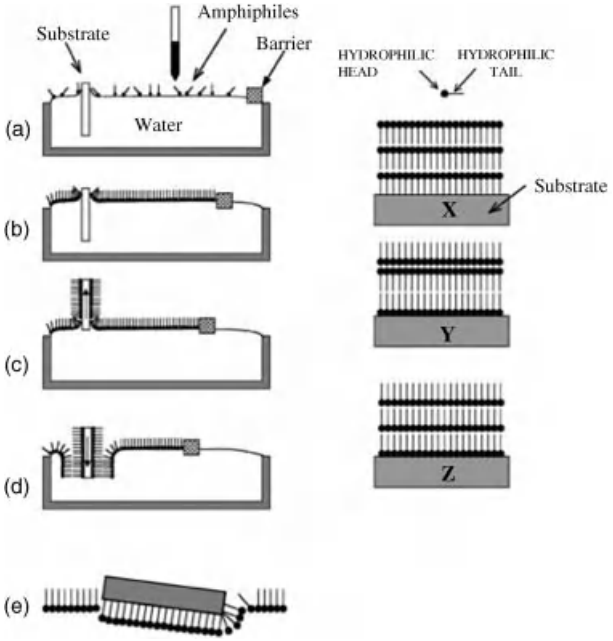

FIGURE 2.34 The Langmuir–Blodgett technique. Left side: A, deposition of the amphiphiles on the water subphase with a solid substrate sub-merged; B, by action of the barrier the monolayer is compressed; C, by pulling out the substrate vertically a monolayer is transferred to both sides of the substrate; D, a multilayered structure is built up by repeated up and down strokes of the substrate; E, transfer of monolayer by horizontal lifting (Schaefer method). Right side: examples of different types of multilayer structures (X, Y, and Z) which can be built up by the LB technique. Reproduced with permission from ref. 157.

in practical electronic devices. This is an urgent task that encourages researchers recently and it is expected that DLCs will have an excellent performance in optoelectronics in the near future.

2.5 APPLICATIONS OF SELF-ASSEMBLED DLCs

Although practical useful discotic nematic liquid crystals have been used in commercial applications for the development of an optical compensator film for improving the view angle of liquid crystal displays (LCDs) [2, 3, 164], there has been a rapidly growing research interest in the recent decade for non-display applications in various molecular electronic devices, such as solar cells, OLEDs and OFETs.

2.5.1 Solar Cells

Solar cells (also known as photovoltaic cells) allow the conversion of light energy into electrical energy. During the past years, organic photovoltaic cells consisting of

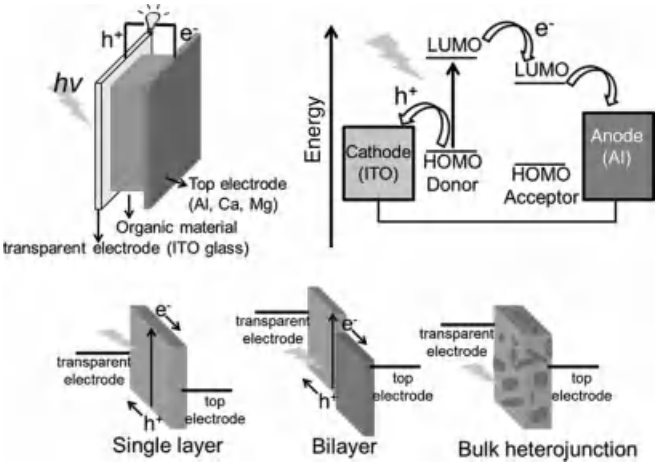

FIGURE 2.35 Top: Schematic diagram of an organic solar cell (heterojunction) (left) and the corresponding energy-level diagram showing charge separation and transport (right). Bottom: Three types of organic layer structures.

semiconducting thin films sandwiched between two electrodes have been developed. A model is shown in Figure 2.35. Unlike inorganic semiconductors where free electron hole pairs are photoinduced, organic semiconductors generate excitons (bound hole–electron pairs) by photoabsorption. After generation, the excitons move by hopping between neighboring sites. The transport efficiency is limited by the diffusion length (the distance over which the excitons can travel without recombination). For organic semiconductors, exciton diffusion lengths are usually of 10–20 nm. The performance of a solar cell device critically depends on several factors such as absorption of incident light, exciton diffusion length, charge separation, and charge collection at the electrodes [165]. In solar cells, the UV–Visible absorption capability of the materials is very important, as it directly relates to the quantity of photons that the device can capture from the sun to form excitons. Most organic semiconducting materials possess a high absorption coefficient ($\alpha > 10^5$ cm^{-1}), meaning thin layer can work efficiently for absorbing light. Equally important are the relative energy levels of the donor and acceptor materials because the energy gap between HOMO of the donor and LUMO of the acceptor determines the efficient charge separation at the interface of donor–acceptor, as well as the potential output (open-circuit voltage) of the device. Once an exciton reaches the donor–acceptor interface, a polaron pair forms: the electron promoted in the LUMO level of the excited donor transfer to the lower LUMO level of the acceptor, with the hole remaining in the HOMO level of the donor. Generally in organic semiconducting materials, by overcoming the intrinsic exciton-binding energy, charge separation will occur at the donor–acceptor interface and this is the major source of free charges: electrons and holes. Furthermore, to generate current the dissociated electrons and holes have to move to their corresponding electrodes under a built-in electric potential created by connecting two electrodes. In such a device, when electrons

flow from the low-work-function electrode to the high-work-function electrode for equalizing the Fermi energies of the two electrodes, a built-in electric field forms. Because this built-in electric field can pull the photo-induced charge carriers (electrons and holes) to their corresponding electrodes, a current and a voltage may appear. For improving energy conversion efficiency, single layer, bilayer, and bulk heterojunction (BHJ) cells were developed one by one in history (Figure 2.35). In the case of heterojunction devices, two organic semiconducting materials with different electron affinities (LUMO) or ionization potentials (HOMO) are combined together to provide sufficient contact area.

Discotic columns as an active semiconducting layer in OPV cells have a number of advantages over other organic materials. Apart from the easy solution and/or melt processing into large-area thin films on flexible substrates, the highly ordered columnar mesophase of DLCs offers large exciton diffusion length and high charge-carrier mobilities, which are both key parameters for the device efficiency. Moreover, the large π-conjugated aromatic cores of DLCs can be particularly attractive because of their absorption capabilities over the entire solar spectrum. Calculations based on the absorption coefficient of organic materials reveal that a film thickness of 50–100 nm is often required to absorb up most of the incident light. Experiments have shown that an exciton can diffuse only around 5–40 nm in most organic semiconductors before recombination. Highly ordered homeotropically aligned DLC films support efficient transport of charge carriers in relatively thick films (up to a few 100 nm), preventing the possible recombination during their journey to the electrodes. Thus, the high intrinsic charge-carrier mobilities reported for several discotic materials have highlighted their potentials for solar cell applications.

Good discotic materials for photovoltaic applications should have certain prerequisites such as (i) high absorption over the wavelengths of the solar spectrum, (ii) exhibiting spontaneous homeotropic alignment in their columnar mesophase, and (iii) energy levels matching well with the electron acceptors and anode materials to facilitate charge separation and transport. Among the most promising columnar discotics that have been investigated so far for solar cell applications, there are DLC materials such as porphyrin, phthalocyanine, HBC, triphenylene, and perylene derivatives. The first DLC film having a photovoltaic effect was published in 1990 by Gregg et al., who sandwiched a porphyrin DLC layer between ITO-coated glass electrodes [166]. Years later, Petritsch et al. reported photovoltaic performance in a bilayer cell composed of a DLC donor–acceptor pair: a phthalocyanine derivative as an electron donor and a perylene derivative as an electron acceptor [167]. A milestone improvement in photovoltaic performance by combining a *p*-type discotic HBC molecule (hexaphenyl-substituted hexabenzocoronene) with an *n*-type perylene molecule (*N*,*N*′-bis(1-ethylpropyl)-3,4,9,10-perylenebis dicarboximide) in a BHJ device, achieving a maximum external quantum efficiency of more than 34% and a power conversion efficiency around 2% under monochromatic illumination of 490 nm was reported by Schmidt-Mende et al. [143]. It is due to the self-assembled DLC HBC and perylene compounds stacking along the π-system that the high efficiency of photoinduced charge transfer can be achieved. Recently, bilayer and BHJ solar cells by solution processing of discotic porphyrin donors with C_{60} or

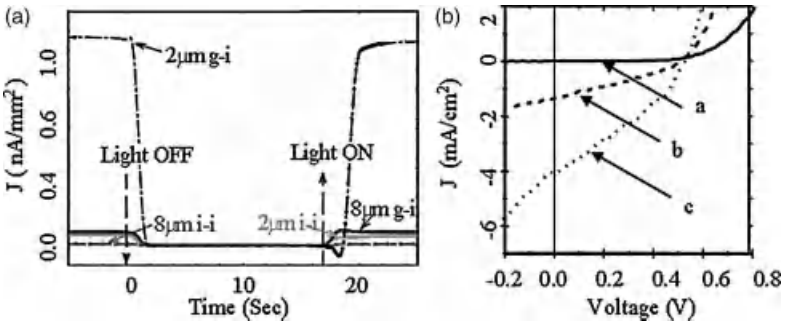

FIGURE 2.36 *J–V* characteristics of the bulk heterojunction cell. (a) Time dependences of the induced currents in normalized current density per 1 mm^2 area in 3 homeotropically aligned thin-film cells (g-i: gold–ITO; i-i: ITO–ITO electrode pairs). The light source was a mercury lamp. The area of the cell was measured directly. (b) *J–V* characteristics of the bulk-heterojunction solar cells based on 3 (a: in the dark; b: under illumination of AM 1.5 G, 100 mW cm^{-2}; c: cooling to room temperature after heating the cell to 145°C, then under illumination of AM 1.5 G, 100 mW cm^{-2}). Reproduced with permission from ref. 78.

$PC_{61}BM$ acceptors were fabricated [78, 79]. In Figure 2.36, the BHJ PV cell formed from a 1:1 (w/w) blend of a DLC porphyrin electron donor (**31**) and $PC_{61}BM$ electron acceptor presented a power conversion efficiency (PCE) of 0.22%, where the ITO anode was coated with a conducting polymer poly(3,4-ethylenedioxythiophene) (PEDOT) and the cathode was Ca/Al. Upon post annealing, which lead to a better alignment of the porphyrin, the PCE increased to 0.712%.

2.5.2 OLEDs

The reverse of a solar cell configuration is the OLED device. Generally, OLEDs generate light by electroluminescence. The basic structure of an OLED is presented in Figure 2.37.

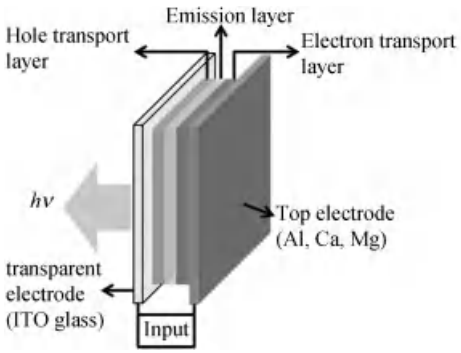

FIGURE 2.37 Schematic diagram of an OLED device. Electrons introduced at the metal electrode (cathode) recombine with holes introduced at the ITO electrode (anode) to emit light.

Sandwiched between two electrodes lies a thin film of stacked organic semiconductors, consisting of three sub-layers: a hole transport layer, an emission layer, and an electron transport layer. In many cases, an electron-transporting layer and a light-emitting layer are combined together into one layer. On one side, the low-work-function electrode such as Al or Mg injects electrons into the LUMO of the electron-transporting material. On the other side, a thin film of the transparent ITO deposited onto the substrate usually serves as the anode which injects holes into the HOMO of the hole-transporting material. Under a voltage across the OLED, electrons and holes transport through their corresponding layers and recombine at the interface (emission layer), and then light is emitted.

The key properties for OLEDs are efficient charge transport and light emission. As excellent charge transport was evidenced in the columnar mesophases, DLC materials have caught attention for OLED application. After Wendorff et al. first pointed out the potential use of columnar discotics for applications in single-layer OLEDs, shortly Bacher et al. reported bilayer OLEDs composing low-molar-mass polymeric discotic triphenylene compounds [168–170].

For typical OLED bilayer example, in Figure 2.38(a) a red organic light emitting device made from DLC materials, the *p*-type 2,3,6,7,10,11-hexabutoxytriphenylene

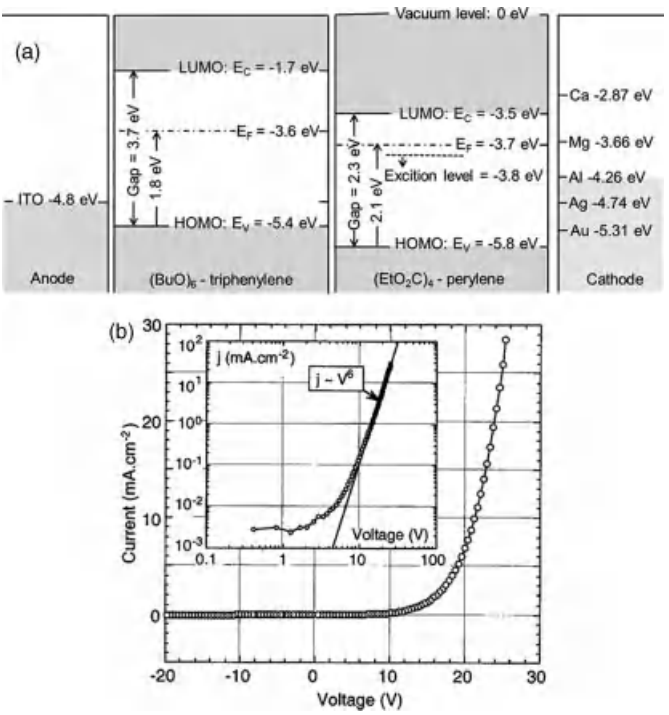

FIGURE 2.38 (a) Band diagram of OLED made of stacked triphenylene and perylene layers. (b) Current density–voltage characteristics of the electron-luminescence device. Reproduced with permission from ref. 171.

and *n*-type fluorescent tetraethylperylene-3,4,9,10-tetracarboxylate was reported by Nguyen et al. [171]. The typical OLED device structure is composed of ITO/triphenylene hexaether/perylene tetraester/aluminium. Electrons are injected from the aluminium cathode into the perylene layer and holes are injected from the ITO anode into the triphenylene layer. Then the charge recombination occurs in the perylene layer close to the heterojunction, emitting a red light (615 nm). In Figure 2.38(b), the current density was discovered to reach the maximum of 28 mA cm^{-1} at 26 V, while at 28 V a luminance maximum as 45 cd m^{-1} was reported when the light was turned on at 16 V. Furthermore, Destruel et al. reported red, green, and blue light by combining highly fluorescent and electron-deficient discotic perylene derivative with an electron-rich triphenylene (as hole transport material) in a bilayer/multilayer OLED devices [66, 172].

2.5.3 OFETs

In FET devices controlled by an electric field, the current can flow along a semiconductor path (channel). Electrons can move along this path by continually putting electrons in one end (the source electrode) and moving out at the other (the drain electrode). An OFET can be fabricated in either top- or bottom-contact configuration (Figure 2.39). In top-contact form, the drain and source electrodes are deposited on top of the semiconducting layer, while in bottom-contact form the electrodes are positioned under the active layer. By inputting a voltage through a control electrode called the gate, which is often a highly doped silicon substrate, a large variation in the current flow from the source to the drain can be achieved. In a typical OFET device, a thin organic semiconducting film forms ohmic contacts (negligible resistance) to the drain and source electrodes. For the electrodes,

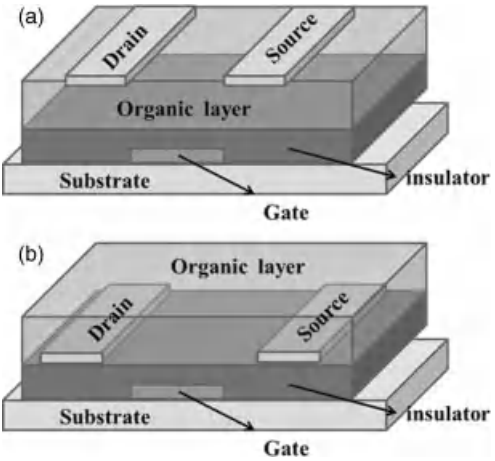

FIGURE 2.39 OFET device configurations: (a) Top-contact device, with source and drain electrodes deposited onto the organic semiconducting layer. (b) Bottom-contact device, with organic semiconductor deposited onto prefabricated source and drain electrodes.

commonly Au is used and vacuum deposition is used for fabrication. If there is no gate voltage applied, the organic semiconductor, which is intrinsically undoped, will not show any charge carriers.

Here is an example of a typical OFET device based on the zone-casting technique. Figure 2.40 shows an OFET device constructed using aligned **61** with top contacts of 25 μm channel length which exhibits saturation mobilities up to $5 \times 10^{-3}\,cm^2\,V^{-1}\,s^{-1}$ [155]. The on-off ratio was 10^4 and the turn-on voltage was ~15 V.

When a voltage is applied to the gate electrode, a thin layer of accumulated charge at the semiconductor–dielectric interface forms, resulting in a current flow between source and drain electrodes. They can be potentially used for thin film transistor applications in active matrix displays, sensors, smart cards, and radiofrequency identification tags [173].

In recent years, dramatic improvement of OFETs has been achieved and high-performance DLC materials for OFET applications have been demonstrated, such as derivatives of HBCs, phthalocyanines, and perylenes [174]. Armstrong et al. fabricated bottom-contact transistors based on a discotic Cu-phthalocyanine derivative on silicon substrates with the LB alignment technique, showing a field mobility value of $10^{-2}\,cm^2\,V^{-1}\,s^{-1}$ [175]. Much higher field-effect mobility (as high as

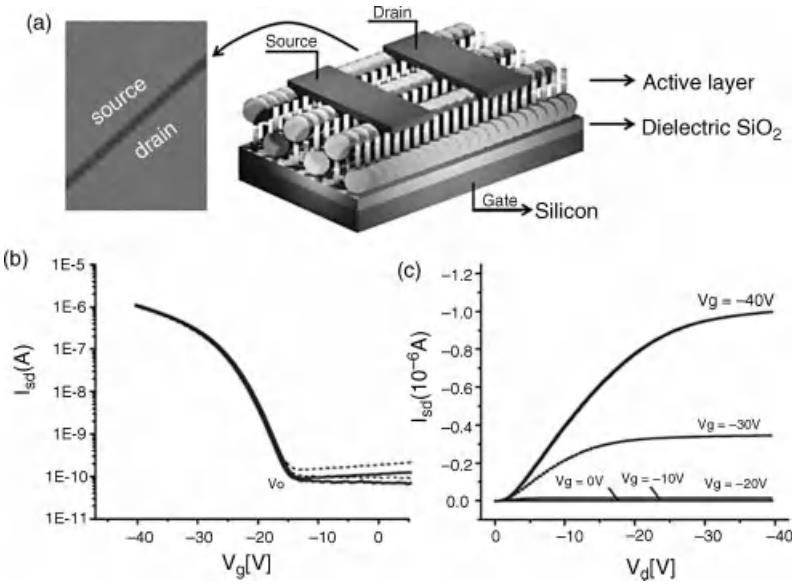

FIGURE 2.40 (a) Schematic presentation of the top-contact device configuration (channel length $L = 25$ mm, width $W = 1.6$ mm, and depth $d = 200$ nm) onto a 20 nm thick zone-cast **62** aligned film. A 200 nm SiO_2 dielectric gate and an n-doped silicon substrate as a gate electrode were used in this device configuration. (b) Transfer characteristics (gate voltage $V_g = -40$ V). (c) Current–voltage (*I–V*) output characteristics. Both dependences are measured along the columnar alignment. V_d: drain voltage; I_{sd}: source–drain current. Reproduced with permission from ref. 155.

2.1 $cm^2 V^{-1} s^{-1}$) with perylene diimide **19c** by annealing at an adequate temperature (140°C) after device fabrication can be achieved [176]. One significant drawback of semiconducting perylene diimide derivatives is that they lack stability under ambient conditions in air. However, this problem can be fixed by introducing substitution of fluoroalkyl chains in the imide substituents which improves the air stability of perylene diimide organic semiconductors [177]. For more information about applications of DLC materials, see reference [178].

2.6 CONCLUSIONS AND OUTLOOK

In this chapter, the principles of DLC materials have been comprehensively introduced. When focusing on the columnar phases of DLCs, it has become evident that the electronic delocalization of intracolumn molecules has introduced prominent features: (1) low band gap and low reorganization energies; (2) large exciton diffusion length; and (3) high charge carrier mobility. Until now the research activities on these materials have been primarily focused on synthesis and processing of new materials. The overall objectives of the research on DLCs are to achieve the following purposes: (1) introducing functionalities through various molecular structures and supramolecular assemblies; (2) processing alignments to satisfy performance requirements in devices; and (3) increasing order of defect-free DLC mesophase to improve charge transport. In recent years, other impressive achievements have been made. A number of perspectives of new and exciting research are being explored, for example, the control of supramolecular order, the miscibility and the morphology of discotic blends, the use of helical columnar structures for generating large non-linear optical responses, the combination of charge transport with magnetic properties, and the incorporation of columnar structures in membranes.

In summary, the self-organized DLCs are very powerful functional materials for many applications, particularly for energy production and charge migration purposes. Publications and patents of recent decades indicate that there will be a continuous tremendous interest in creating a new generation of organic semiconducting DLCs. For future investigations, there will be considerable efforts to uncover the full potential of discotic semiconductors for not only improving their device performances, but also bringing them to the consumer market for the benefit of societal needs.

ACKNOWLEDGMENTS

The preparation of this chapter benefited from the support to Quan Li by the Ohio Board of Regents under its Research Challenge program, the Department of Energy (DOE DE-SC0001412), the Air Force Office of Scientific Research (AFOSR FA9550-09-1-0193 and FA9550-09-1-0254), the Department of Defense Multidisciplinary University Research Initiative (AFOSR MURI FA9550-06-1-0337 and FA9550-12-1-0037), and the National Science Foundation (NSF IIP 0750379).

REFERENCES

1. S. Chandrasekhar, B. K. Sadashiva, and K. A. Suresh. Liquid crystals of disk-like molecules. *Pramana* **1977**, *7*, 471–480.
2. S. Kumar and S. K. Varshney. A room-temperature discotic nematic liquid crystal. *Angew. Chem. Int. Ed.* **2000**, *39*, 3140–3142.
3. M. Okazaki, K. Kawata, H. Nishikawa, and M. Negoro. Polymerizable discotic nematic triphenylene derivatives and their application to an optically anisotropic film. *Polym. Adv. Technol.* **2000**, *11*, 398–403.
4. V. de Cupere, J. Tant, P. Viville, R. Lazzaroni, W. Osikowicz, W. R. Salaneck, and Y. H. Geerts. Effect of interfaces on the alignment of a discotic liquid−crystalline phthalocyanine. *Langmuir* **2006**, *22*, 7798–7806.
5. A. J. J. M. van Breemen, P. T. Herwig, C. H. T. Chlon, J. Sweelssen, H. F. M. Schoo, S. Setayesh, W. M. Hardeman, C. A. Martin, D. M. de Leeuw, J. J. P. Valeton, C. W. M. Bastiaansen, D. J. Broer, A. R. Popa-Merticaru, and S. C. J. Meskers. Large area liquid crystal monodomain field-effect transistors. *J. Am. Chem. Soc.* **2006**, *128*, 2336–2345.
6. D. Demus. One century liquid crystal chemistry: from Vorlander's rods to disks, stars and dendrites. *Mol. Cryst. Liq. Cryst.* **2001**, *364*, 25–91.
7. S. Kumar. Self-organization of disc-like molecules: chemical aspects. *Chem. Soc. Rev.* **2006**, *35*, 83–109.
8. C. Tschierske. Micro-segregation, molecular shape and molecular topology partners for the design of liquid crystalline materials with complex mesophase morphologies. *J. Mater. Chem.* **2001**, *11*, 2647–2671.
9. C. Tschierske. Liquid crystalline materials with complex mesophase morphologies. *Curr. Opin. Colloid Interface Sci.* **2002**, *7*, 69–80.
10. X. Crispin, J. Cornil, R. Friedlein, K. K. Okudaira, V. Lemaur, A. Crispin, G. Kestemont, M. Lehmann, M. Fahlman, R. Lazzaroni, Y. Geerts, G. Wendin, N. Ueno, J.-L. Bredas, and W. R. Salaneck. Electronic delocalization in discotic liquid crystals: a joint experimental and theoretical study. *J. Am. Chem. Soc.* **2004**, *126*, 11889–11899.
11. J. M. Warman, M. P. de Haas, G. Dicker, F. C. Grozema, J. Piris, and M. G. Debije. Charge mobilities in organic semiconducting materials determined by pulse-radiolysis time-resolved microwave conductivity: π-bond-conjugated polymers versus $\pi-\pi$ stacked discotics. *Chem. Mater.* **2004**, *16*, 4600–4609.
12. Z. An, J. Yu, S. C. Jones, S. Barlow, S. Yoo, B. Domercq, P. Prins, L. D. A. Siebbeles, B. Kippelen, and S. R. Marder. High electron mobility in room-temperature discotic liquid-crystalline perylene diimides. *Adv. Mater.* **2005**, *17*, 2580–2583.
13. B. A. Jones, M. J. Ahrens, M.-H. Yoon, A. Facchetti, T. J. Marks, and M. R. Wasielewski. High-mobility air-stable *n*-type semiconductors with processing versatility: dicyanoperylene-3,4:9, 10-bis(dicarboximides). *Angew. Chem. Int. Ed.* **2004**, *43*, 6363–6366.
14. H. Iino, Y. Takayashiki, J.-I. Hanna, and R. J. Bushby. Fast ambipolar carrier transport and easy homeotropic alignment in a metal-free phthalocyanine derivative. *Jpn. J. Appl. Phys. Part 2* **2005**, *44*, 1310–1312.
15. D. Markovitsi, S. Marguet, J. Bondkowski, and S. Kumar. Triplet excitation transfer in triphenylene columnar phases. *J. Phys. Chem. B* **2001**, *105*, 1299–1306.

16. N. Boden, R. J. Bushby, J. Clements, B. Movaghar, K. J. Donovan, and T. Kreouzis. Mechanism of charge transport in discotic liquid crystals. *Phys. Rev. B* **1995**, *52*, 13274–13279.
17. K. Kohary, H. Cordes, S. D. Baranovskii, P. Thomas, S. Yamasaki, F. Hensel, and J.-H. Wendorff. One-dimensional hopping transport in disordered organic solids. II. Monte Carlo simulations. *Phys. Rev. B* **2001**, *63*, 094202.
18. L. J. Lever, R. W. Kelsall, and R. J. Bushby. Band transport for discotic liquid crystals. *Phys. Rev. B* **2005**, *72*, 035130.
19. J. Zaumseil and H. Sirringhaus. Electron and ambipolar transport in organic field-effect transistors. *Chem. Rev.* **2007**, *107*, 1296–1323.
20. R. G. Kepler. Charge carrier production and mobility in anthracene crystals. *Phys. Rev.* **1960**, *119*, 1226–1229.
21. O. H. Leblanc. Hole and electron drift mobilities in anthracene. *J. Chem. Phys.* **1960**, *33*, 626–627.
22. D. Adam, F. Closs, T. Frey, D. Funhoff, D. Haarer, H. Ringsdorf, P. Schuhmacher, and K. Siemensmeyer. Transient photoconductivity in a discotic liquid crystal. *Phys. Rev. Lett.* **1993**, *70*, 457–460.
23. A. M. Van de Craats, J. M. Warman, M. P. De Haas, D. Adam, J. Simmerer, D. Haarer, and P. Schuhmacher. The mobility of charge carriers in all four phases of the columnar discotic material hexakis (hexylthio) triphenylene: combined TOF and PR-TRMC results. *Adv. Mater.* **1996**, *8*, 823–826.
24. W. Pisula, M. Zorn, J. Y. Chang, K. Müllen, and R. Zental. Liquid crystalline ordering and charge transport in semiconducting materials. *Macromol. Rapid Commun.* **2009**, *30*, 1179–1202.
25. J. M. Warman and A. M. Van de Craats. Charge mobility in discotic materials studied by PR-TRMC. *Mol. Cryst. Liq. Cryst.* **2003**, *396*, 41–72.
26. A. M. van de Craats and J. M. Warman. The core-size effect on the mobility of charge in discotic liquid crystalline materials. *Adv. Mater.* **2001**, *13*, 130–133.
27. J. M. Warman, M. P. de Haas, G. Dicker, F. C. Grozema, J. Piris, and M. G. Debije. Charge mobilities in organic semiconducting materials determined by pulse-radiolysis time-resolved microwave conductivity: π-bond-conjugated polymers versus π–π stacked discotics. *Chem. Mater.* **2004**, *16*, 4600–4609.
28. A. M. Van de Craats, J. M. Warman, A. Fechtenkötter, J. D. Brand, M. A. Harbison, and K. Müllen. Record charge carrier mobility in a room-temperature discotic liquid crystalline derivative of hexabenzocoronene. *Adv. Mater.* **1999**, *11*, 1469–1472.
29. P. W. M. Blom, M. J. M. deJong, and J. J. M. Vleggaar. Electron and hole transport in poly (p-phenylene vinylene) devices. *Appl. Phys. Lett.* **1996**, *68*, 3308–3310.
30. D. Fichou. *Handbook of Oligo- and Polythiophenes*, Wiley-VCH, Weinheim, New York, 1999.
31. G. Horowitz. Organic field-effect transistors. *Adv. Mater.* **1998**, *10*, 365–377.
32. G. Horowitz. Organic thin film transistors: from theory to real devices. *J. Mater. Res.* **2004**, *19*, 1946–1962.
33. A. Dodabalapur, L. Torsi, and H. E. Katz. Organic transistors: two-dimensional transport and improved electrical characteristics. *Science* **1995**, *268*, 270–271.
34. P. V. Pesavento, R. J. Chesterfield, C. R. Newman, and C. D. Frisbie. Gated four-probe measurements on pentacene thin-film transistors: contact resistance as a function of gate voltage and temperature. *J. Appl. Phys.* **2004**, *96*, 7312–7324.

35. C. Goldmann, S. Haas, C. Krellner, J. P. Pernstich, D. J. Gundlach, and B. Batlogg. Hole mobility in organic single crystals measured by a "flip-crystal" field-effect technique. *J. Appl. Phys.* **2004**, *96*, 2080–2086.

36. V. Podzorov, S. E. Sysoev, E. Loginova, V. M. Pudalov, and M. E. Gershenson. Single-crystal organic field effect transistors with the hole mobility ~8 cm^2/V s. *Appl. Phys. Lett.* **2003**, *83*, 3504–3506.

37. A. F. Stassen, R. W. I. de Boer, N. N. Iosad, and A. F. Morpurgo. Influence of the gate dielectric on the mobility of rubrene single-crystal field-effect transistors. *Appl. Phys. Lett.* **2004**, *85*, 3899–3901.

38. J. Veres, S. D. Ogier, S. W. Leeming, D. C. Cupertino, and S. M. Khaffaf. Low-*k* insulators as the choice of dielectrics in organic field-effect transistors. *Adv. Funct. Mater.* **2003**, *13*, 199–204.

39. B. Domercq, J. Yu, B. R. Kaafarani, T. Kondo, S. Yoo, J. N. Haddock, S. Barlow, S. R. Marder, and B. Kippelen. A comparative study of charge mobility measurements in a diamine and in a hexaazatrinaphthylene using different techniques, *Mol. Cryst. Liq. Cryst.* **2008**, *481*, 80–93.

40. A. Troisi, D. L. Cheung, and D. Andrienko. Charge transport in semiconductors with multiscale conformational dynamics. *Phys. Rev. Lett.* **2009**, *102*, 116602.

41. F. C. Grozema and L. D. A. Siebbeles. Mechanism of charge transport in self-organizing organic materials. *Int. Rev. Phys. Chem.* **2008**, *27*, 87–138.

42. J. Y. Chang, J. R. Yeon, Y. S. Shin, M. J. Han, and S. K. Hong. Synthesis and characterization of mesogenic disk-like benzenetricarboxylates containing diacetylenic groups and their polymerization. *Chem. Mater.* **2000**, *12*, 1076–1082.

43. A. N. Cammidge and H. Gopee. Macrodiscotic triphenylenophthalocyanines. *Chem. Commun.* **2002**, 966–967.

44. A. Hayer, V. de Halleux, A. Koehler, A. El-Garoughy, E. W. Meijer, J. Barbera, J. Tant, J. Levin, M. Lehmann, J. Gierschner, J. Cornil, and Y. H. Geerts. Highly fluorescent crystalline and liquid crystalline columnar phases of pyrene-based structures. *J. Phys. Chem. B* **2006**, *110*, 7653–7659.

45. J. E. Kroeze, R. B. M. Koehorst, and T. J. Savenije. Singlet and triplet exciton diffusion in a self-organizing porphyrin antenna layer. *Adv. Funct. Mater.* **2004**, *14*, 992–998; H. Eichhorn. Mesomorphic phthalocyanines, tetraazaporphyrins, porphyrins and triphenylenes as charge-transporting materials. *J. Porphyrin Phthalocyanines* **2000**, *4*, 88–102.

46. B. Cabezon, M. Nicolau, J. Barbera, and T. Torres. Synthesis and liquid-crystal behavior of triazolephthalocyanines. *Chem. Mater.* **2000**, *12*, 776–781;J. F. van der Pol, E. Neeleman, J. W. Zwikker, R. J. M. Nolte, W. Drenth, J. Aerts, R. Visser, and S. J. Picken. Homologous series of liquid-crystalline metal free and copper octa-*n*-alkoxyphthalocyanines. *Liq. Cryst.* **1989**, *6*, 577–592;K. Ohta, L. Jacquemin, C. Sirlin, L. Bosio, and J. Simon. Influence of the nature of the side chains on the mesomorphic properties of octasubstituted phthalocyanine derivatives. *New J. Chem.* **1988**, *12*, 751–754; D. Guillon, A. Skoulios, C. Piechocki, J. Simon, and P. Weber. The crystal and molecular structure of a reentrant nematogen: 4-cyanophenyl-3-methyl-4′-(4″-*n*-undecyloxy cinnamoyloxy) benzoate (11 CPMCB). *Mol. Cryst. Liq. Cryst.* **1983**, *100*, 275–284;L. Dulog and A. Gittinger. Octaalkyl esters of 2,3,9,10,16,17,23,24-(29H, 31H)-phthalocyanineoctacarboxylic acid: a new homologous series of discotic liquid crystals. *Mol. Cryst. Liq. Cryst.* **1992**, *213*, 31–42;S. Sergeyev, E. Pouzet, O. Debever, J. Levin, J. Gierschner, J. Cornil, R. Gomez-Aspe, and Y. H. Geerts. Liquid crystalline

octaalkoxycarbonyl phthalocyanines: design, synthesis, electronic structure, self-aggregation and mesomorphism. *J. Mater. Chem.* **2007**, *17*, 1777–1784.

47. J. Wu, M. D. Watson, L. Zhang, Z. Wang, and K. Müllen. Hexakis(4-iodophenyl)-*peri*-hexabenzocoronene: a versatile building block for highly ordered discotic liquid crystalline materials. *J. Am. Chem. Soc.* **2004**, *126*, 177–186.
48. A. N. Cammidge and R. J. Bushby.In: D. Demus, J. W. Goodby, G. W. Gray, H. W. Spiess, and V. Vill,Eds., *Handbook of Liquid Crystals, vol. 2B*, Wiley-WCH, Weinheim, 1998.
49. C. Piechocki, J. Simon, A. Skoulios, D. Guillon, and P. Weber. Discotic mesophases obtained from substituted metallophthalocyanines. Toward liquid crystalline one dimensional conductors. *J. Am. Chem. Soc.* **1982**, *104*, 5245–5247.
50. D. Adam, P. Schuhmacher, J. Simmerer, L. Haussling, K. Siemensmeyer, K. H. Etzbach, H. Ringsdorf, and D. Haarer. Fast photoconduction in the highly ordered columnar phase of a discotic liquid crystal. *Nature* **1994**, *371*, 141–143.
51. J. A. Rego, S. Kumar, and H. Ringsdorf. Synthesis and characterization of fluorescent, low-symmetry triphenylene discotic liquid crystals: tailoring of mesomorphic and optical properties. *Chem. Mater.* **1996**, *8*, 1402–1409.
52. A. Kettner and J. H. Wendorff. Modifications of the mesophase formation of discotic triphenylene compounds by substituents. *Liq. Cryst.* **1999**, *26*, 483–487.
53. J. Simmerer, B. Glusen, W. Paulus, A. Kettner, P. Schuhmacher, D. Adam, K.-H. Etzbach, K. Siemensmeyer, J. H. Wendorff, H. Ringsdorf, and D. Haarer. Transient photoconductivity in a discotic hexagonal plastic crystal. *Adv. Mater.* **1996**, *8*, 815–819.
54. H. Bengs, F. Closs, T. Frey, D. Funhoff, H. Ringsdorf, and K. Siemensmeyer. Highly photoconductive discotic liquid crystals: structure–property relations in the homologous series of hexa-alkoxytriphenylenes. *Liq. Cryst.* **1993**, *15*, 565–574.
55. H. Iino, J. Hanna, C. Jager, and D. Haarer. Fast electron transport in discotic columnar phase of triphenylene derivative, hexabutyloxytriphenylene. *Mol. Cryst. Liq. Cryst.* **2005**, *436*, 217–224.
56. H. Iino, Y. Takayashiki, J. Hanna, R. J. Bushby, and D. Haarer. High electron mobility of 0.1 $cm^2 V^{-1} s^{-1}$ in the highly ordered columnar phase of hexahexylthiotriphenylene. *Appl. Phys. Lett.* **2005**, *87*, 192105.
57. M. Lehmann, G. Kestemont, R. Gomez Aspe, C. Buess-Herman, M. H. J. Koch, M. G. Debije, J. Piris, M. P. de Haas, J. M. Warman, and M. D. Watson. High charge-carrier mobility in p-deficient discotic mesogens: design and structure–property relationship. *Chem. Eur. J.* **2005**, *11*, 3349–3362.
58. K. Pieterse, P. A. van Hal, R. Kleppinger, J. A. J. M. Vekemans, R. A. J. Janssen, and E. W. Meijer. An electron-deficient discotic liquid-crystalline material. *Chem. Mater.* **2001**, *13*, 2675–2679.
59. N. Boden, R. C. Borner, R. J. Bushby, and J. Clements. First observation of an *n*-doped quasi-one-dimensional electronically-conducting discotic liquid crystal. *J. Am. Chem. Soc.* **1994**, *116*, 10807–10808.
60. F. Würthner. Perylene bisimide dyes as versatile building blocks for functional supramolecular architectures. *Chem. Commun.* **2004**, *14*, 1564–1579.
61. H. Langhals. Control of the interactions in multichromophores: novel concepts. Perylene bisimides as components for larger functional units. *Helv. Chim. Acta.* **2005**, *88*, 1309–1343.
62. P. R. L. Malenfant, C. D. Dimitrakopoulos, J. D. Gelorme, L. L. Kosbar, T. O. Graham, A. Curioni, and W. Andreoni. N-type organic thin-film transistor with high field-effect

mobility based on a *N,N*-dialkyl-3,4,9,10-perylene tetracarboxylic diimide derivative. *Appl. Phys. Lett.* **2002**, *80*, 2517–2519.

63. C. W. Struijk, A. B. Sieval, J. E. J. Dakhorst, M. van Dijk, P. Kimkes, R. B. M. Koehorst, H. Donker, T. J. Schaafsma, S. J. Picken, and A. M. van de Craats. Liquid crystalline perylene diimides: architecture and charge carrier mobilities. *J. Am. Chem. Soc.* **2000**, *122*, 11057–11066.
64. F. Würthner, C. Thalacker, S. Diele, and C. Tschierske. Fluorescent *J*-type aggregates and thermotropic columnar mesophases of perylene bisimide dyes. *Chem. Eur. J.* **2001**, *7*, 2245–2253.
65. Z. Chen, M. G. Debije, T. Debaerdemaeker, P. Osswald, and F. Würthner. Tetrachloro-substituted perylene bisimide dyes as promising *n*-type organic semiconductors: studies on structural, electrochemical and charge transport properties. *Chem. Phys. Chem.* **2004**, *5*, 137–139.
66. I. Seguy, P. Destruel, and H. Bock. An all-columnar bilayer light-emitting diode. *Synth. Met.* **2000**, *111*, 15–18.
67. S. Alibert-Fouet, S. Dardel, H. Bock, M. Oukachmih, S. Archambeau, I. Seguy, P. Jolinat, and P. Destruel. Electroluminescent diodes from complementary discotic benzoperylenes. *Chem. Phys. Chem.* **2003**, *4*, 983–985.
68. F. Nolde, W. Pisula, S. Müller, C. Kohl, and K. Müllen. Synthesis and self-organization of core-extended perylene tetracarboxdiimides with branched alkyl substituents. *Chem. Mater.* **2006**, *18*, 3715–3725.
69. J. W. Goodby, P. S. Robinson, B.-K. Teo, and P. E. Cladi. The discotic phase of uroporphyrin octa-*N*-dodecyl ester. *Mol. Cryst. Liq. Cryst.* **1980**, *56*, 303–309.
70. C. Y. Liu and A. J. Bard. Optoelectronic properties and memories based on organic single-crystal thin films. *Acc. Chem. Res.* **1999**, *32*, 235–245.
71. Q. D. Zhao, M. Yu, T. F. Xie, L. L. Peng, P. Wang, and D. J. Wang. Photovoltaic properties of a ZnO nanorod array affected by ethanol and liquid-crystalline porphyrin. *Nanotechnology* **2008**, *19*, 245706.
72. K. Ohta, N. Ando, and I. Yamamoto. Discotic liquid crystals of transition metal complexes: 22. Synthesis and mesomorphism of octa-alkoxy-substituted tetraphenylporphyrin derivatives and their copper(II) complexes. *Liq. Cryst.* **1999**, *26*, 663–668.
73. H. Miwa, N. Kobayashi, K. Ban, and K. Ohta. Synthesis, spectroscopy, electrochemistry, and mesomorphism of triple-decker porphyrins consisting of two cerium ions and three 5, 15-diarylporphyrins. Bull. *Chem. Soc. Jpn.* **1999**, *72*, 2719–2728.
74. T. Nakai, K. Ban, K. Ohta, and M. Kimura. Discotic liquid crystals of transition metal complexes. Part 32. 1. Synthesis and liquid-crystalline properties of doubledeckers and tripledeckers based on cerium complexes of bis- and tetrakis(3,4-dialkoxyphenyl) porphyrin. *J. Mater. Chem.* **2002**, *12*, 844–850.
75. P. G. Schoten, J. M. Gorman, M. P. deHaas, M. A. Fox, and H. L. Pan. Charge migration in supramolecular stacks of peripherally substituted porphyrins. *Nature* **1991**, *353*, 736–737.
76. P. G. Schoten, J. M. Gorman, M. P. deHaas, J. F. van der Pol, and J. W. Zwikker. Radiation-induced conductivity in polymerized and nonpolymerized columnar aggregates of phthalocyanine. *J. Am. Chem. Soc.* **1992**, *114*, 9028–9034.
77. (a) S. W. Kang, Q. Li, B. D. Chapman, R. Pindak, J. O. Cross, L. Li, M. Nakata, and S. Kumar. Microfocus X-ray diffraction study of the columnar phase of porphyrin-based

mesogens. *Chem. Mater.* **2007**, *19*, *5657-5663;* (b) X. Zhou, S. W. Kang, S. Kumar, and Q. Li. Self-assembly of discotic liquid crystal porphyrin into more controllable order nanostructure mediated by fluorophobic effect. *Liq. Cryst.* **2009**, *36*, 269–274.

78. L. Li, S. W. Kang, J. Harden, Q. Sun, X. Zhou, L. Dai, A. Jakli, S. Kumar, and Q. Li. Nature-inspired light-harvesting liquid crystalline porphyrins for organic photovoltaics. *Liq. Cryst.* **2008**, *35*, 233–239.
79. Q. Sun, L. Dai, X. Zhou, L. Li, and Q. Li. Bilayer-and bulk-heterojunction solar cells using liquid crystalline porphyrins as donors by solution processing. *Appl. Phys. Lett.* **2007**, *91*, 253505.
80. B. Tylleman, G. Gbabode, C. Amato, C. Buess-Herman, V. Lemaur, J. Cornil, R. Gómez Aspe, Y. H. Geerts, and S. Sergeyev. Metal-free phthalocyanines bearing eight alkylsulfonyl substituents: design, synthesis, electronic structure, and mesomorphism of new electron-deficient mesogens. *Chem. Mater.* **2009**, *21*, 2789–2797.
81. H. Iino, J. Hanna, R. J. Bushby, B. Movaghar, B. J. Whitaker, and M. J. Cook. Very high time-of-flight mobility in the columnar phases of a discotic liquid crystal. *Appl. Phys. Lett.* **2005**, *87*, 132102.
82. V. S. Iyer, M. Wehmeier, J. D. Brand, M. A. Keegstra, and K. Müllen. From hexa-*peri*-hexabenzocoronene to "Superacenes". *Angew. Chem. Int. Ed.* **1997**, *36*, 1604–1607.
83. M. G. Debije, J. Piris, M. P. de Haas, J. M. Warman, Z. Tomovic, C. D. Simpson, M. D. Watson, and K. Müllen. The optical and charge transport properties of discotic materials with large aromatic hydrocarbon cores. *J. Am. Chem. Soc.* **2004**, *126*, 4641–4645.
84. M. Kastler, F. Laquai, K. Müllen, and G. Wegner. Room-temperature nondispersive hole transport in a discotic liquid crystal. *Appl. Phys. Lett.* **2006**, *89*, 252103.
85. X. Feng, V. Marcon, W. Pisula, M. R. Hansen, J. Kirkpatrick, F. Grozema, D. Andrienko, K. Kremer, and K. Müllen. Towards high charge-carrier mobilities by rational design of the shape and periphery of discotics. *Nat. Mater.* **2009**, *8*, 421–426.
86. X. Feng, M. Liu, W. Pisula, M. Takase, J. Li, and K. Müllen. Supramolecular organization and photovoltaics of triangle-shaped discotic graphenes with swallow-tailed alkyl substituents. *Adv. Mater.* **2008**, *20*, 2684–2689.
87. S. Xiao, M. Myers, Q. Miao, S. Sanaur, K. Pang, M. L. Steigerwald, and C. Nuckolls. Molecular wires from contorted aromatic compounds. *Angew. Chem. Int. Ed.* **2005**, *44*, 7390–7394.
88. Y. Yamamoto, G. Zhang, W. Jin, T. Fukushima, N. Ishii, A. Saeki, S. Seki, S. Tagawa, T. Minari, K. Tsukagoshi, and T. Aida. Ambipolar-transporting coaxial nanotubes with a tailored molecular graphene–fullerene heterojunction. *PNAS* **2009**, *106*, 21051–21056.
89. Z. Tomovic, M. D. Watson, and K. Müllen. Superphenalene-based columnar liquid crystals. *Angew. Chem. Int. Ed.* **2004**, *43*, 755–758.
90. C. D. Simpson, J. S. Wu, M. D. Watson, and K. Müllen. From graphite molecules to columnar superstructures—an exercise in nanoscience. *J. Mater. Chem.* **2004**, *14*, 494–504.
91. M. D. Watson, M. G. Debije, J. M. Warman, and K. Müllen. Peralkylated coronenes via regiospecific hydrogenation of hexa-*peri*-hexabenzocoronenes. *J. Am. Chem. Soc.* **2004**, *126*, 766–771.
92. V. S. Iyer, K. Yoshimura, V. Enkelmann, R. Epsch, J. P. Rabe, and K. Müllen. A soluble C_{60} graphite segment. *Angew. Chem. Int. Ed.* **1998**, *37*, 2696–2699.

93. X. J. Zhang, X. X. Jiang, K. Zhang, L. Mao, J. Luo, C. Y. Chi, H. S. O. Chan, and J. S. Wu. Synthesis, self-assembly, and charge transporting property of contorted tetrabenzocoronenes. *J. Org. Chem.* **2010**, *75*, 8069–8077.

94. U. Rohr, C. Kohl, K. Müllen, A. Craats, and J. Warman. Liquid crystalline coronene derivatives. *J. Mater. Chem.* **2001**, *11*, 1789–1799.

95. K. Hirota, K. Tajima, and K. Hashimoto. Physicochemical study of discotic liquid crystal decacyclene derivative and utilization in polymer photovoltaic devices. *Synth. Met.* **2007**, *157*, 290–296.

96. H. K. Bisoyi and S. Kumar. Room-temperature electron-deficient discotic liquid crystals: facile synthesis and mesophase characterization. *New J. Chem.* **2008**, *32*, 1974–1980.

97. Y. F. Bai, K. Q. Zhao, P. Hu, B. Q. Wang, and Y. Shimizu. Synthesis of amide group containing triphenylene derivatives as discotic liquid crystals and organic gelators. *Mol. Cryst. Liq. Cryst.* **2009**, *509*, 802–818.

98. R. I. Gearba, M. Lahmann, J. Levin, D. A. Ivanov, M. H. J. Koch, J. Barbera, M. G. Debije, J. Piris, and Y. H. Geerts. Tailoring discotic mesophases: columnar order enforced with hydrogen bonds. *Adv. Mater.* **2003**, *15*, 1614–1618.

99. A. Demenev, S. H. Eichhorn, T. Taerum, D. F. Perepichka, S. Patwardhan, F. C. Grozeme, L. D. A. Siebbeles, and R. Klenkler. Quasi temperature independent electron mobility in hexagonal columnar mesophases of an H-bonded benzotristhiophene derivative. *Chem. Mater.* **2010**, *22*, 1420–1428.

100. I. Paraschiv, K. de Lange, M. Giesbers, B. van Lagen, F. C. Grozema, R. D. Abellon, L. D. A. Siebbeles, E. J. R. Sudholter, H. Zuilhof, and A. T. M. Marcelis. Hydrogen-bond stabilized columnar discotic benzenetrisamides with pendant triphenylene groups. *J. Mater. Chem.* **2008**, *18*, 5475–5481.

101. N. Mizoshita, H. Monobe, M. Inoue, M. Ukon, T. Watanabe, Y. Shimizu, K. Hanabusa, and T. Kato. The positive effect on hole transport behaviour in anisotropic gels consisting of discotic liquid crystals and hydrogen-bonded fibres. *Chem. Commun.* **2002**, 428–429.

102. C. W. Ong, J. Y. Hwang, M. C. Tzeng, S. C. Liao, H. F. Hsu, and T. H. Chang. Dibenzo [a,c]phenazine with six-long alkoxy chains to probe optimization of mesogenic behavior. *J. Mater. Chem.* **2007**, *17*, 1785–1790.

103. K. Kishikawa, S. Furusawa, T. Yamaki, S. Kohmoto, M. Yamamoto, and K. Yamaguchi. Novel superstructure of nondiscoid mesogens: uneven-parallel association of half-disk molecules, 3,4,5-trialkoxybenzoic anhydrides, to a columnar structure and its one-directionally geared interdigitation. *J. Am. Chem. Soc.* **2002**, *124*, 1597–1605.

104. T. Kato, N. Mizoshita, and K. Kanie. Hydrogen-bonded liquid crystalline materials: supramolecular polymeric assembly and the induction of dynamic function. *Macromol. Rapid. Commun.* **2001**, *22*, 797–814.

105. T. Kato. Hydrogen-bonded liquid crystals: molecular self-assembly for dynamically functional materials. In: Molecular self-assembly, a comprehensive summary of mesogenic hydrogen bonded systems. *Struct. Bond.* **2000**, *96*, 95–146.

106. M. Hird. Fluorinated liquid crystals—properties and applications. *Chem. Soc. Rev.* **2007**, *36*, 2070–2095.

107. N. Terasawa, H. Monobe, K. Kiyohara, and Y. Shimizu. Strong tendency towards homeotropic alignment in a hexagonal columnar mesophase of fluoroalkylated triphenylenes. *Chem. Commun.* **2003**, 1678–1679.

108. B. Alameddine, O. F. Aebischer, W. Amrein, B. Donnio, R. Deschenaux, D. Guillon, C. Savary, D. Scanu, O. Scheidegger, and T. A. Jenny. Mesomorphic hexabenzocoronenes bearing perfluorinated chains. *Chem. Mater.* **2005**, *17*, 4798–4807.

109. A. Escosura, M. V. Martínez-Díaz, J. Barberá, and T. Torres. Self-organization of phthalocyanine-[60]fullerene dyads in liquid crystals. *J. Org. Chem.* **2008**, *73*, 1475–1480.

110. X. Zhou, S.-W. Kang, S. Kumar, R. R. Kulkarni, S. Z. D. Cheng, and Q. Li. Self-assembly of porphyrin and fullerene supramolecular complex into highly ordered nanostructure by thermal annealing. *Chem. Mater.* **2008**, *20*, 3551–3553.

111. Y. H. Geerts, O. Debever, C. Amato, and S. Sergeyev. Synthesis of mesogenic phthalocyanine–C_{60} donor–acceptor dyads designed for molecular heterojunction photovoltaic devices. *Beilstein J. Org. Chem.* **2009**, *5*, 49.

112. L. Sánchez, M. Sierra, N. Martín, A. J. Myles, T. J. Dale, J. Rebek, W. Seitz, and D. M. Guldi. Exceptionally strong electronic communication through hydrogen bonds in porphyrin–C_{60} pairs. *Angew. Chem. Int. Ed.* **2006**, *45*, 4637–4641.

113. H. Imahori, H. Yamada, D. M. Guldi, Y. Endo, A. Shimomura, S. Kundu, K. Yamada, T. Okada, Y. Sakata, and S. Fukuzumi. Comparison of reorganization energies for intra- and inter-molecular electron transfer. *Angew. Chem. Int. Ed.* **2002**, *41*, 2344–2347.

114. J. L. Sessler, J. Jayawickramarajah, A. Gouloumis, T. Torres, D. M. Guldi, S. Maldonado, and K. J. Stevenson. Synthesis and photophysics of a porphyrin–fullerene dyad assembled through Watson–Crick hydrogen bonding. *Chem. Commun.* **2005**, 1892–1894.

115. H. Yamada, H. Imahori, Y. Nishimura, I. Yamazaki, T. K. Ahn, S. K. Kim, D. Kim, and S. Fukuzumi. Photovoltaic properties of self-assembled monolayers of porphyrins and porphyrin–fullerene dyads on ITO and gold surfaces. *J. Am. Chem. Soc.* **2003**, *125*, 9129–9139.

116. H. Imahori and Y. Sakata. Donor-linked fullerenes: photoinduced electron transfer and its potential application. *Adv. Mater.* **1997**, *9*, 537–546.

117. N. Watanabe, N. Kihara, Y. Forusho, T. Takata, Y. Araki, and O. Ito. Photoinduced intrarotaxane electron transfer between zinc porphyrin and fullerene in benzonitrile. *Angew. Chem. Int. Ed.* **2003**, *42*, 681–683.

118. H. Imahori, M. E. El-Khouly, M. Fujitsuka, O. Ito, Y. Sakata, and S. Fukuzumi. Solvent dependence of charge separation and charge recombination rates in porphyrin–fullerene dyad. *J. Phys. Chem. A* **2001**, *105*, 325–332.

119. T. Torres, A. Gouloumis, D. Sanchez-Garcia, J. Jayawickramarajah, W. Seitz, D. M. Guldi, and J. L. Sessler. Photophysical characterization of a cytidine–guanosine tethered phthalocyanine–fullerene dyad. *Chem. Commun.* **2007**, 292–294.

120. D. W. Bruce, D. A. Dunmur, L. S. Santa, and M. A. Wali. Mesomorphic metalloporphyrins showing calamitic mesophases. *J. Mater. Chem.* **1992**, *2*, 363–364.

121. H. N. Tsao, W. Pisula, Z. Liu, W. Osikowicz, W. R. Salaneck, and K. Müllen. From ambi- to unipolar behavior in discotic dye field-effect transistors. *Adv. Mater.* **2008**, *20*, 2715–2719.

122. H. Fujikake, T. Murashige, M. Sugibayashi, and K. Ohta. Time-of-flight analysis of charge mobility in a Cu-phthalocyanine-based discotic liquid crystal semiconductor. *Appl. Phys. Lett.* **2004**, *85*, 3474.

123. H. Iino, J. Hanna, R. J. Bushby, B. Movaghar, B. J. Whitaker, and M. J. Cook. Very high time-of-flight mobility in the columnar phases of a discotic liquid crystal. *Appl. Phys. Lett.* **2005**, *87*, 132102.

124. K. Ban, K. Nishizawa, K. Ohta, A. M. Craats, J. M. Warman, I. Yamamoto, and H. Shirai. Discotic liquid crystals of transition metal complexes 29: mesomorphism and charge transport properties of alkylthio-substituted phthalocyanine rare-earth metal sandwich complexes. *J. Mater. Chem.* **2001**, *11*, 321–331.

125. T. Sakurai, K. Shi, H. Sato, K. Tashiro, A. Osuka, A. Saeki, S. Seki, S. Tagawa, S. Sasaki, H. Masunaga, K. Osaka, M. Takata, and T. Aida. Prominent electron transport property observed for triply fused metalloporphyrin dimer: directed columnar liquid crystalline assembly by amphiphilic molecular design. *J. Am. Chem. Soc.* **2008**, *130*, 13812–13813.

126. M. Xiao and P. R. Selvin. Quantum yields of luminescent lanthanide chelates and far-red dyes measured by resonance energy transfer. *J. Am. Chem. Soc.* **2001**, *123*, 7067–7073.

127. S. I. Klink, L. Grave, D. N. Reinhoudt, and F. C. J. M. van Veggel. A systematic study of the photophysical processes in polydentate triphenylene-functionalized Eu^{3+}, Tb^{3+}, Nd^{3+}, Yb^{3+}, and Er^{3+} complexes. *J. Phys. Chem. A* **2000**, *104*, 5457–5468.

128. W. D. Horrocks and M. Albin.In: S. J. Lippard,Ed., *Progress in Inorganic Chemistry*, John Wiley & Sons, 1984.

129. K. Binnemanns. Lanthanides and actinides in ionic liquids. *Chem. Rev.* **2007**, *107*, 2592–2614.

130. C. Piguet, J. C. G. Bünzli, B. Donnio, and D. Guillon. Thermotropic lanthanidomesogens. *Chem. Commun.* **2006**, 3755–3768.

131. B. Donnio, D. Guillon, R. Deschenaux, and D. W. Bruce.In: J. A. McCleverty and T. J. Meyer, Eds., *Comprehensive Coordination Chemistry II*, vol. *7*, Elsevier, Oxford, UK, 2003.

132. M. Yu, Y. J. Zhang, J. H. Shi, G. F. Liu, and H. J. Zhang. Holmium porphyrin compound liquid crystals: synthesis and properties. *Solid State Sci.* **2009**, *11*, 2016–2022.

133. D. Atilla, N. Kilinc, F. Yuksel, A. G. Gurek, Z. Z. Ozturk, and V. Ahsen. Synthesis, characterization, mesomorphic and electrical properties of tetrakis(alkylthio)-substituted lutetium(III) bisphthalocyanines. *Synth. Met.* **2009**, *159*, 13–21.

134. N. V. S. Rao, T. D. Choudhury, R. Deb, M. K. Paul, T. R. Rao, T. Francis, and I. I. Smalyukh. Fluorescent lanthanide complexes of Schiff base ligands possessing *N*-aryl moiety: influence of chain length on crossover (calamitic to discotic) phase behavior. *Liq. Cryst.* **2010**, *37*, 1393–1410.

135. L. A. Holt, R. J. Bushby, S. D. Evans, A. Burgess, and G. Seeley. A 10^6-fold enhancement in the conductivity of a discotic liquid crystal doped with only 1% (w/w) gold nanoparticles. *J. Appl. Phys.* **2008**, *103*, 063712.

136. S. Kumar and V. Lakshminarayanan. Inclusion of gold nanoparticles into a discotic liquid crystalline matrix *Chem. Commun.* **2004**, 1600–1601.

137. D. Vijayaraghavan and S. Kumar. Self-assembled superlattices of gold nanoparticles in a discotic liquid crystal. *Mol. Cryst. Liq. Cryst.* **2009**, *508*, 101–114.

138. S. Kumar, S. K. Pal, P. S. Kumar, and V. Lakshminarayanan. Novel conducting nanocomposites: synthesis of triphenylene-covered gold nanoparticles and their insertion into a columnar matrix. *Soft Matter* **2007**, *3*, 896–900.

139. H. K. Bisoyi and S. Kumar. Carbon nanotubes in triphenylene and rufigallol-based room temperature monomeric and polymeric discotic liquid crystals. *J. Mater. Chem.* **2008**, *18*, 3032–3039.

140. S. H. Eichhorn, A. Adavelli, H. S. Li, and N. Fox. Alignment of discotic liquid crystals. *Mol. Cryst. Liq. Cryst.* **2003**, *397*, 47–58.

141. J. K. Vij, A. Kocot, and T. S. Perova. Order parameter, alignment and anchoring transition in discotic liquid crystals. *Mol. Cryst. Liq. Cryst.* **2003**, *397*, 231–244.

142. L. Schmidt-Mende, A. Fechtenkotter, K. Müllen, E. Moons, R. H. Friend, and J. D. MacKenzie. Self-organized discotic liquid crystals for high-efficiency organic photovoltaics. *Science* **2001**, *293*, 1119–1122.

143. O. Thiebaut, H. Bock, and E. Grelet. Face-on oriented bilayer of two discotic columnar liquid crystals for organic donor–acceptor heterojunction. *J. Am. Chem. Soc.* **2010**, *132*, 6886–6887.

144. N. Terasawa, H. Monobe, K. Kiyohara, and Y. Shimizu. Strong tendency towards homeotropic alignment in a hexagonal columnar mesophase of fluoroalkylated triphenylenes. *Chem. Commun.* **2003**, 1678–1679.

145. W. Pisula, Z. Tomovic, B. El Hamaoui, M. D. Watson, T. Pakula, and K. Müllen. Control of the homeotropic order of discotic hexa-*peri*-hexabenzocoronenes. *Adv. Funct. Mater.* **2005**, *15*, 893–904.

146. R. I. Gearba, D. V. Anokhin, A. I. Bondar, W. Bras, M. Jahr, M. Lehmann, and D. A. Ivanov. Homeotropic alignment of columnar liquid crystals in open films by means of surface nanopatterning. *Adv. Mater.* **2007**, *19*, 815–820.

147. E. Charlet, E. Grelet, P. Brettes, H. Bock, H. Saadaoui, L. Cisse, P. Destruel, N. Gherardi, and I. Seguy. Ultrathin films of homeotropically aligned columnar liquid crystals on indium tin oxide electrodes. *Appl. Phys. Lett.* **2008**, *92*, 024107.

148. E. Pouzet, V. D. Cupere, C. Heintz, J. W. Andreasen, D. W. Breiby, M. M. Nielsen, P. Viville, R. Lazzaroni, G. Gbabode, and Y. H. Geerts. Homeotropic alignment of a discotic liquid crystal induced by a sacrificial layer. *J. Phys. Chem. C* **2009**, *113*, 14398–14406.

149. M. Steinhart, S. Zimmermann, P. Goring, A. K. Schaper, U. Gosele, C. Weder, and J. H. Wendorff. Liquid crystalline nanowires in porous alumina: geometric confinement versus influence of pore walls. *Nano Lett*. **2005**, *5*, 429–434.

150. D. Miyajima, K. Tashiro, F. Araoka, H. Takezoe, J. Kim, K. Kato, M. Takata, and T. Aida. Liquid crystalline corannulene responsive to electric field. *J. Am. Chem. Soc.* **2009**, *131*, 44–45.

151. H. Monobe, K. Awazu, and Y. Shimizu. Alignment control of a columnar liquid crystal for a uniformly homeotropic domain using circularly polarized infrared irradiation. *Adv. Mater.* **2006**, *18*, 607–610.

152. H. Monobe, H. Hori, Y. Shimizu, and K. Awazu. Alignment control of columnar liquid crystals for uniformly homeotropic domain with circularly polarized infrared irradiation. *Mol. Cryst. Liq. Cryst.* **2007**, *475*, 13–22.

153. S. Zimmermann, J. H. Wendorff, and C. Weder. Uniaxial orientation of columnar discotic liquid crystals. *Chem. Mater.* **2002**, *14*, 2218–2223.

154. A. M. van de Craats, N. Stutzmann, O. Bunk, M. M. Nielsen, M. Watson, K. Müllen, H. D. Chanzy, H. Sirringhaus, and R. H. Friend. Meso-epitaxial solution-growth of self-organizing discotic liquid-crystalline semiconductors. *Adv. Mater.* **2003**, *15*, 495–499.

155. W. Pisula, A. Menon, M. Stepputat, I. Lieberwirth, U. Kolb, A. Tracz, H. Sirringhaus, T. Pakula, and K. Müllen. A zone-casting technique for device fabrication of field-effect

transistors based on discotic hexa-peri-hexabenzocoronene. *Adv. Mater.* **2005**, *17*, 684–689.

156. W. Pisula, M. Kastler, D. Wasserfallen, T. Pakula, and K. Müllen. Exceptionally long-range self-assembly of hexa-peri-hexabenzocoronene with dove-tailed alkyl substituents. *J. Am. Chem. Soc.* **2004**, *126*, 8074–8075.
157. T. Bjornholm, T. Hassenkam, and N. Reitzel. Supramolecular organization of highly conducting organic thin films by the Langmuir–Blodgett technique. *J. Mater. Chem.* **1999**, *9*, 1975–1990.
158. O. Y. Mindyuk and P. A. Heiney. Structural studies of Langmuir films of disc-shaped molecules. *Adv. Mater.* **1999**, *11*, 341–344.
159. P. Smolenyak, R. Peterson, K. Nebesny, M. Torker, D. F. O'Brien, and N. R. Armstrong. Highly ordered thin films of octasubstituted phthalocyanines. *J. Am. Chem. Soc.* **1999**, *121*, 8628–8636.
160. N. Reitzel, T. Hassenkam, K. Balashev, T. R. Jensen, P. B. Howes, K. Kjaer, A. Fechtenkotter, N. Tchebotareva, S. Ito, and K. Müllen. Langmuir and Langmuir–-Blodgett films of amphiphilic hexa-peri-hexabenzocoronene: new phase transitions and electronic properties controlled by pressure. *Chem. Eur. J.* **2001**, *7*, 4894–4901.
161. H. J. Räder, A. Rouhanipour, A. M. Talarico, V. Palermo, P. Samorì, and K. Müllen. Processing of giant graphene molecules by soft-landing mass spectrometry. *Nat. Mater.* **2006**, *5*, 276–280.
162. I. O. Shklyarevskiy, P. Jonkheijm, N. Stutzmann, D. Wasserberg, H. J. Wondergem, P. C. M. Christianen, A. P. H. J. Schenning, D. M. de Leeuw, Z. Tomovic, J. Wu, K. Müllen, and J. C. Maan. High anisotropy of the field-effect transistor mobility in magnetically aligned discotic liquid-crystalline semiconductors. *J. Am. Chem. Soc.* **2005**, *127*, 16233–16237.
163. A. Calo, P. Stoliar, M. Cavallini, S. Sergeyev, Y. H. Geerts, and F. Biscarini. Monolayer control of discotic liquid crystal by electromigration of dewetted layers in thin film devices, *J. Am. Chem. Soc.* **2008**, *130*, 11953–11958.
164. K. Kawata. Orientation control and fixation of discotic liquid crystal. *Chem. Rec.* **2002**, *2*, 59–80.
165. T. L. Benanti and D. Venkataraman. Organic solar cells: an overview focusing on active layer morphology. *Photosynth. Res.* **2006**, *87*, 73–81.
166. B. A. Gregg, M. A. Fox, and A. J. Bard. Photovoltaic effect in symmetrical cells of a liquid crystal porphyrin. *J. Phys. Chem.* **1990**, *94*, 1586–1598.
167. K. Petritsch, R. H. Friend, A. Lux, G. Rozenberg, S. C. Moratti, and A. B. Holmes. Liquid crystalline phthalocyanines in organic solar cells. *Synth. Met.* **1999**, *102*, 1776–1777.
168. T. Christ, B. Glusen, A. Greiner, A. Kellner, R. Sander, V. Stumpflen, V. Tsukruk, and J. H. Wendorff. Columnar discotics for light emitting diodes. *Adv. Mater.* **1997**, *9*, 48–51.
169. I. H. Stapff, V. Stümpflen, J. H. Wendorff, D. B. Spohn, and D. Möbius. Multi-layer light emitting diodes based on columnar discotics, *Liq. Cryst.* **1997**, *23*, 613–617.
170. A. Bacher, I. Bleyl, C. H. Erdelen, D. Haarer, W. Paulus, and H. W. Schmidt. Low molecular weight and polymeric triphenylenes as hole transport materials in organic two-layer LEDs. *Adv. Mater.* **1997**, *9*, 1031–1035.
171. I. Seguy, P. Jolinat, P. Destruel, J. Farenc, R. Mamy, H. Bock, J. Ip, and T. P. Nguyen. Red organic light emitting device made from triphenylene hexaester and perylene tetraester. *J. Appl. Phys.* **2001**, *89*, 5442–5448.

172. T. Hassheider, S. A. Benning, H. S. Kitzerow, M. F. Achard, and H. Bock. Color-tuned electroluminescence from columnar liquid crystalline alkyl arenecarboxylates. *Angew. Chem. Int. Ed.* **2001**, *40*, 2060–2063.

173. H. Sirringhaus. Device physics of solution-processed organic field-effect transistors. *Adv. Mater.* **2005**, *17*, 2411–2425.

174. Y. Shimizu, K. Oikawa, K. Nakayama, and D. Guillon. Mesophase semiconductors in field effect transistors. *J. Mater. Chem.* **2007**, *17*, 4223–4229.

175. S. Cherian, C. Donley, D. Mathine, L. LaRussa, W. Xia, and N. Armstrong. Effects of field dependent mobility and contact barriers on liquid crystalline phthalocyanine organic transistors. *J. Appl. Phys.* **2004**, *96*, 5638–5643.

176. S. Tatemichi, M. Ichikawa, T. Koyama, and Y. Taniguchi. High mobility *n*-type thinfilm transistors based on *N, N*-ditridecyl perylene diimide with thermal treatments. *Appl. Phys. Lett.* **2006**, *89*, 112108.

177. R. Schmidt, J. H. Oh, Y. S. Sun, M. Deppisch, A. M. Krause, K. Radacki, H. Braunschweig, M. Konemann, P. Erk, Z. Bao, and F. Wurthner. High-performance air-stable *n*-channel organic thin film transistors based on halogenated perylene bisimide semiconductors. *J. Am. Chem. Soc.* **2009**. *131*, 6215–6228.

178. Q. Li,Ed., *Self-organized Organic Semiconductors: From Materials to Device Applications*, John Wiley & Sons, New Jersey, 2011.

CHAPTER 3

Magnetic Liquid Crystals

RUI TAMURA, YOSHIAKI UCHIDA, and KATSUAKI SUZUKI
Graduate School of Human and Environmental Studies, Kyoto University, Kyoto, Japan

3.1 INTRODUCTION

Paramagnetic liquid crystals (PLCs) have been considered to become novel advanced soft materials that can combine the optical and electrical properties of conventional liquid crystals (LCs) with the magnetic and electronic properties of paramagnetic compounds [1–3]. The PLCs are classified into two categories: the majority were metal-containing LCs (metallomesogens) with permanent spins originating from transition (d-block) or lanthanide (f-block) metal ions in the mesogen core [3, 4], while only a few all-organic radical liquid-crystalline (LC) materials were prepared, most likely due to the difficulty in the molecular design and synthesis which must satisfy the molecular linearity or planarity necessary for the existence of LC phases (rod-like or disk-like molecules, respectively) as well as the radical stabilization [1, 5–7]. Moreover, endowing the PLCs with chirality is expected to result in the emergence of unconventional magneto-electric [8–10] or magneto-optical [11–13] properties, intriguing magnetic interactions and so on in the chiral LC state.

Thus, the research on chiral and achiral PLCs is being explored in the context of the following objectives or expectations:

(1) Realization of the paramagnetic anisotropy ($\Delta\chi_{para}$)-controlled molecular orientation in the chiral and achiral LC phases by weak magnetic fields, e.g. (i) application to Freedericksz transition between the planar and perpendicular molecular alignments in achiral LC phases [14], (ii) application to the unwinding of the helical superstructure in chiral LC phases, and (iii) application to ionic LCs unsuitable for the orientation control by applied electric fields.

(2) Utilization as magnetically anisotropic chiral and achiral LC spin-probes or chiral and achiral spin-labeled LC molecules to observe the dynamic behavior

Liquid Crystals Beyond Displays: Chemistry, Physics, and Applications, Edited by Quan Li.
© 2012 John Wiley & Sons, Inc. Published 2012 by John Wiley & Sons, Inc.

of chiral and achiral diamagnetic LCs or to determine the microscopic molecular orientation in chiral and achiral PLC phases, respectively, by electron paramagnetic resonance (EPR) spectroscopy.

(3) Verification of the generation of unique intermolecular spin–spin interactions in the PLC phases in the presence or absence of applied magnetic fields.

(4) Observation of the influence (magneto-electric effects) of applied electric fields on the magnetic properties in the ferroelectric LCs (FLCs) (Eq. 3.1) and vice versa (Eq. 3.2).

$$M = \chi^{\mathrm{m}} H + \chi^{\mathrm{me}} E \tag{3.1}$$

$$P = \chi^{\mathrm{e}} E + \chi^{\mathrm{me}'} H \tag{3.2}$$

where M is the magnetization, H is the applied magnetic field, E is the applied electric field, P is the polarization, χ^{m} is the magnetic susceptibility, χ^{e} is the electric susceptibility, and χ^{me} and $\chi^{\mathrm{me}'}$ are the magneto-electric susceptibilities.

(5) Crystal engineering for the preparation of molecular magnetic materials with different magnetic properties from a given compound; formation of supercooled glassy phases or crystal polymorphs by cooling the LC phases.

(6) Observation of unique spin crossover or luminescence phenomena.

(7) Observation of magneto-chiral dichroism (MChD).

For objective 1, the larger the magnetic anisotropy ($\Delta\chi$), the weaker the critical magnetic field (H_{c}). This is because the H_{c} necessary for the alignment of LC molecule is inversely proportional to the square root of $\Delta\chi$ (Eq. 3.3) [15].

$$H_{\mathrm{c}} = \pi d^{-1}\ k^{1/2} (\Delta\chi)^{-1/2} \tag{3.3}$$

where d represents the cell thickness and k is the elastic constant. For objective 2, there had been no precedent for a magnetically anisotropic chiral or achiral all-organic radical LC compound with a geometrically fixed spin unit in the core portion until the first PROXYL type of chiral LC compounds **1** were prepared by the present authors [16] (Figure 3.1). For objective 3, there was no report on the observation of appreciable magnetic interactions in PLCs until our recent finding of inhomogeneous magnetic interactions ($\bar{J} > 0$) generated in the LC phases of compounds **1** under weak magnetic fields [17, 18]. For objective 4, such FLCs, if available, would need to exhibit both magnetic and electric ordering in the LC state [8–10]. As the typical examples of objective 5, Nakatsuji et al. observed the change in magnetic behavior between the original crystalline phase and the supercooled solid phase formed by cooling from the isotropic phase with respect to an all-organic PLC compound (see Section 3.5.1) [19], while Veciana et al. prepared a single-molecule magnet (SMM) with two different relaxation processes by controlling the cooling rate from the

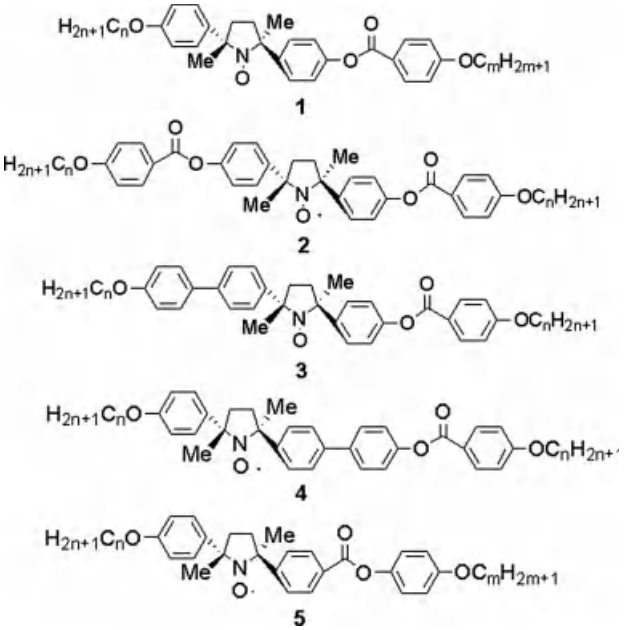

FIGURE 3.1 PROXYL type of LC compounds **1–5**.

LC phase of a double-decker terbium complex (see Figure 3.11) [20]. Objective 6 has become one of the current topics in the research field of metallomesogens (see Sections 3.4.1.3 and 3.4.2.2). In the case of objective 7, Rikken et al. observed MChD in luminescence from an optically active paramagnetic Eu(III) complex in solution [11, 12] and in the enantiopure single crystal of a molecule-based ferromagnet composed of $[Mn(II)Cr(III)(C_2O_4^{2-})_3]^-$ and $[N(CH_3)(n\text{-}C_3H_7)_2(s\text{-}C_4H_9)]^+$ [13]. However, MChD has not been observed yet in a chiral LC phase with magnetic ordering.

In this chapter, we first focus on the magnetic susceptibility anisotropy (or simply, magnetic anisotropy) of LCs that are relevant to the alignment of both diamagnetic and paramagnetic LC molecules by magnetic fields. Then magnetic properties of known paramagnetic metallomesogens and the first-generation of all-organic radical LCs are surveyed. In Section 3.5.3, our works on the second-generation of chiral all-organic radical LCs carried out in relation to the above objectives (2 and 3) are described briefly.

3.2 MAGNETIC ANISOTROPY ($\Delta\chi$) OF LCs

Similar to the molecular dielectric anisotropy ($\Delta\varepsilon$), $\Delta\chi$ is obtained by subtracting the magnetic susceptibility component ($\chi_\perp$) perpendicular to the molecular long axis from the component ($\chi_\parallel$) parallel to the same axis (Figure 3.2 and Eq. 3.4).

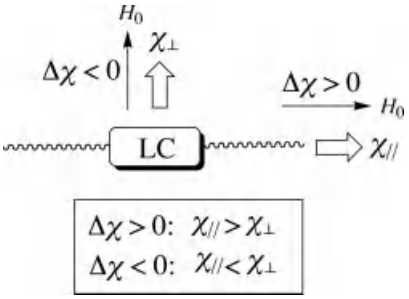

FIGURE 3.2 Magnetic anisotropy ($\Delta\chi$) of LCs.

Furthermore, $\Delta\chi$ comprises a paramagnetic component ($\Delta\chi_{para}$) (Eq. 3.5) and a diamagnetic component ($\Delta\chi_{dia}$) (Eq. 3.6). Although χ_{para} and χ_{dia} are always positive and negative, respectively, $\Delta\chi_{para}$ and $\Delta\chi_{dia}$ become positive or negative, depending on the magnitude of the respective $\chi_\perp$ and $\chi_\parallel$ values. Therefore, the overall molecular magnetic anisotropy ($\Delta\chi_{overall}$) is the sum of $\Delta\chi_{para}$ and $\Delta\chi_{dia}$ (Eq. 3.7) [2, 3]. If $\Delta\chi_{overall}$ is positive (or negative), the molecular long axis or the director becomes parallel (or perpendicular) to the applied magnetic field (H_0), when the applied field is larger than H_c (Figure 3.2). Such is a driving force for molecular alignment by magnetic fields.

$$\Delta\chi = \chi_\parallel - \chi_\perp \tag{3.4}$$

$$\Delta\chi_{para} = \chi_{para\,\parallel} - \chi_{para\,\perp} \tag{3.5}$$

$$\Delta\chi_{dia} = \chi_{dia\,\parallel} - \chi_{dia\,\perp} \tag{3.6}$$

$$\Delta\chi_{overall} = \Delta\chi_{para} + \Delta\chi_{dia} \tag{3.7}$$

3.3 DIAMAGNETIC LCs

Diamagnetism resides in all atoms. Particularly aromatic rings show a strong diamagnetic effect in an applied magnetic field. Therefore, the diamagnetic rod-like LC molecules orient themselves such that the axis with the most negative χ_{dia} is perpendicular to the magnetic field. Since $|\chi_{dia\,\perp}|$ is usually larger than $|\chi_{dia\,\parallel}|$ with respect to organic LC molecules, the $\Delta\chi_{dia}$ becomes positive and the molecules orient with the director parallel to the magnetic field (Figure 3.2). For organic LCs, the magnitude of the $\Delta\chi_{dia}$, which is produced by two diamagnetic phenyl groups, is approximately $+50 \times 10^{-6}$ emu mol^{-1} [21]. Accordingly, a relatively strong magnetic field (>0.2 T) is necessary to align diamagnetic LCs, depending on the type of LC phases [22].

3.4 PARAMAGNETIC METALLOMESOGENS

Transition metal-containing metallomesogens which have the ligand-coordinated metal-complex structures with a number of long alkyl chains show nematic, smectic, or columnar mesophases [23], while lanthanide-containing LCs usually exhibit smectic or columnar mesophases with high viscosity due to their high and variable coordination numbers [24–26].

3.4.1 d-Block Metal Complexes

3.4.1.1 Magnetic Anisotropy A number of paramagnetic rod-like metallomesogens containing 3d transition metal ions, such as VO(IV) ($3d^1$), Fe(III) ($3d^5$), Cu(II) ($3d^9$) and Ni(II) ($3d^8$), were synthesized and their magnetic properties were fully characterized (e.g., Figure 3.3) [2, 27–31]. Since the magnitude of the $\Delta\chi_{para}$ arising from the 3d orbital is as small as 20–90 $\times 10^{-6}$ emu mol^{-1} and comparable to that of the $\Delta\chi_{dia}$ of organic ligands, the $\Delta\chi_{para}$ and the $\Delta\chi_{dia}$ work cooperatively or competitively to determine the direction of the molecular alignment by magnetic fields [22, 32].

3.4.1.2 Intermolecular Magnetic Interactions It should be emphasized that the McConnell type strong ferromagnetic interactions necessary for effective intermolecular spin–spin exchange are not expected for paramagnetic rod-like LC phases

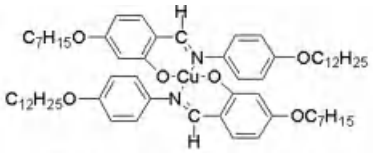

C 122.0 SmC 133.0 SmA 161.0 I

$\Delta\chi_{para} = -84.36 \times 10^{-6}$ cm^3/mol

$\Delta\chi_{dia} = 72.42 \times 10^{-6}$ cm^3/mol

$\Delta\chi_{overall} = -11.94 \times 10^{-6}$ cm^3/mol

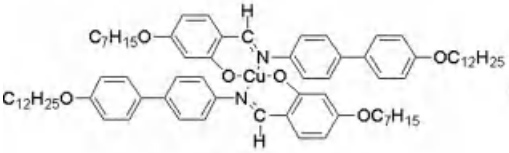

C 180.0 SmC 275.0 I

$\Delta\chi_{para} = -66.81 \times 10^{-6}$ cm^3/mol

$\Delta\chi_{dia} = 120.20 \times 10^{-6}$ cm^3/mol

$\Delta\chi_{overall} = 53.39 \times 10^{-6}$ cm^3/mol

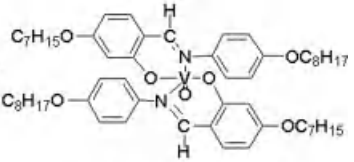

C 151.0 SmA 176.8 I

$\Delta\chi_{para} = 16{,}82 \times 10^{-6}$ cm^3/mol

$\Delta\chi_{dia} = 72.42 \times 10^{-6}$ cm^3/mol

$\Delta\chi_{overall} = 89.24 \times 10^{-6}$ cm^3/mol

FIGURE 3.3 Transition metal-containing metallomesogens and their magnetic anisotropy.

due to their dynamic behavior characterized by fast molecular rotation (10^{10}–$10^{11}\,s^{-1}$) around the molecular long axis [1], although theoretical considerations on the existence and dynamics of ferromagnetic LCs were presented [33, 34]. At present, no appreciable intermolecular ferromagnetic interaction has been observed in the LC state of rod-like d-block metallomesogens.

Interestingly, however, Jin et al. explicitly observed room temperature (RT) ferromagnetism generated in a diamagnetic discotic LC phase of tetra(2-decyltetradecyloxy)phthalocyanine derivative **6** intercalated with Fe(III)-phthalocyanine [Fe(III)Pc] over the range of magnetic field of ±2000 Oe (Figure 3.4), whereas Fe(III)Pc itself showed only a paramagnetic nature at RT. Outside of this range of magnetic field or at molar ratios of Fe(III)Pc to **6** of greater than 1/45, the hysteretic magnetization–magnetic field (*M–H*) curves characteristic of ferromagnetism disappeared and instead linear diamagnetic response was noted. The origin of the RT ferromagnetism observed in weak magnetic fields was ascribed to the magnetic interactions between the conductive spins in **6** and the localized spins in Fe(III)Pc in the LC state, based on EPR spectroscopy and SQUID magnetization measurements in the temperature range of 4.3–353 K [35].

3.4.1.3 Spin Crossover Spin crossover materials display labile electronic configurations switchable between the high spin and low spin states in response to external stimuli such as temperature, pressure, light, and magnetic field, showing distinct changes in magnetism, color, and structure [36]. The first single material combining spin crossover and LC behavior was a Fe(III) metallomesogen (low spin state $S = 1/2$; high spin state $S = 5/2$) exhibiting both properties not synchronously in different temperature intervals (Figure 3.5a) [37]. Later, synchronous spin crossover and LC transition have been devised for Fe(II) ($S = 0$; $S = 2$) (Figure 3.5b) [38] and Co(II) ($S = 1/2$; $S = 3/2$) metallomesogens (Figure 3.5c) [39].

3.4.1.4 SMM To fabricate SMMs with self-organized ordering, Rogez and Donnio et al. endowed the SMM Mn_{12} cluster molecule with LC properties [40]. The obtained two $[Mn_{12}O_{12}L_{16}(H_2O)_4]$ compounds which showed stable mesophases with 3D (cubic) or 1D (random mesh smectic) positional order between −11.5

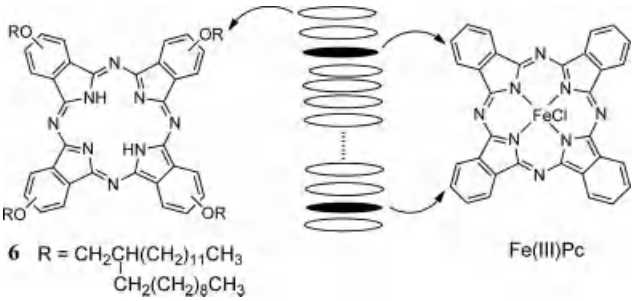

FIGURE 3.4 LC columnar structure of diamagnetic **6** intercalated with Fe(III)Pc.

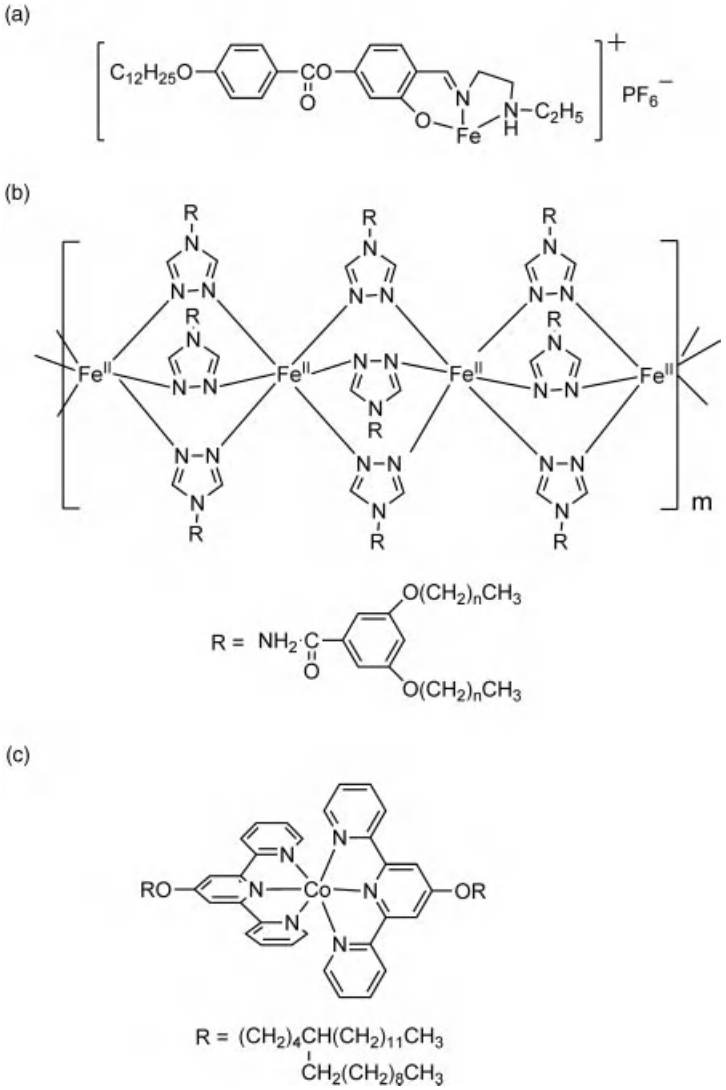

FIGURE 3.5 Metallomesogens showing spin crossover: (a) Fe(III) ($S = 1/2$; $S = 5/2$), (b) Fe(II) ($S = 0$; $S = 2$), and (c) Co(II) ($S = 1/2$; $S = 3/2$).

and 150.0°C or between 40.5 and 150.0°C, respectively, behaved as SMMs with the blocking temperature below 8 K (Figure 3.6).

3.4.1.5 Ferroelectricity To develop ferroelectric metallomesogens, several chiral transition metal-containing LC materials showing a SmC* phase were prepared. Among them, Cu(II) and VO(IV) metallomesogens with analogous chiral bis (salicylideneaniline) ligands were paramagnetic (Figure 3.7) [27, 29, 31]. However,

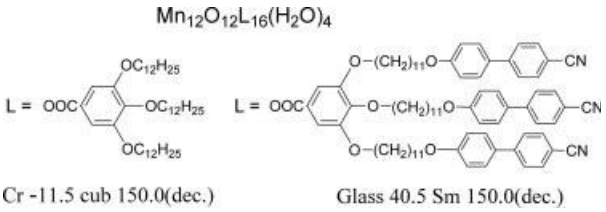

FIGURE 3.6 SMM Mn_{12} cluster molecules showing LC properties at high temperatures.

they did not show any noteworthy optical and electric properties, compared with usual organic ferroelectric LCs. For example, the ferroelectric Cu(II)-mesogen **7** showed a spontaneous polarization Ps($-10°$) of 38 nC cm^{-2} at 100°C and a long optical response time [$\tau(-10°)$] of 8.5 ms, while its organic ligand itself exhibited better ferroelectricity with a slightly higher Ps($-10°$) of 41 nC cm^{-2} and a shorter $\tau(-10°)$ of 1.1 ms than **7** [31]. No magnetic property was reported for these paramagnetic chiral metallomesogens.

Meanwhile, chiral VO(IV) and Cu(II) β-diketone complexes **8** showed a RT columnar mesophase that underwent ferroelectric switching (Figure 3.8), although the Ps could not be evaluated [41, 42].

3.4.2 f-Block Metal Complexes

At present, no appreciable intermolecular ferromagnetic interaction has been observed in the LC state of f-block metallomesogens.

3.4.2.1 Magnetic Anisotropy Not a few examples of rod-like metallomesogens containing 4f rare earth metal ions, such as Pr(III), Nd(III), Tb(III), Dy(III), and Er(III), have been documented (Figure 3.9) [24–26]. Due to the large anisotropy of the 4f orbital arising from the spin–orbital coupling, the magnitude of the $\Delta\chi_{para}$ is as large as 810–5550 $\times 10^{-6}$ emu mol^{-1} and prevails over that of the $\Delta\chi_{dia}$ of organic ligands [24, 43–47]. Accordingly, the molecular alignment by magnetic fields should be $\Delta\chi_{para}$-controlled. However, the intrinsic high viscosity of rod-like f-block metallomesogens (SmA or columnar phases) brought about by the

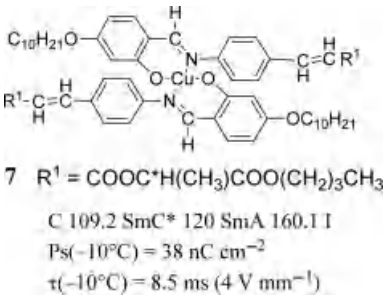

FIGURE 3.7 Ferroelectric metallomesogen **7**.

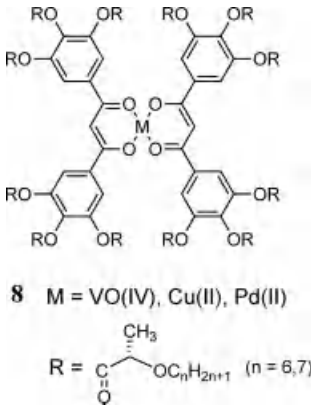

FIGURE 3.8 Switchable columnar metallomesogens **8**.

ligand-coordinated metal-complex structure generally renders the response to weak magnetic fields difficult and raises the phase transition temperature; a strong applied magnetic field (>1.2 T) is necessary even for the molecular alignment in the SmA phase during the cooling process from the isotropic phase and the crystal-to-LC phase transition generally occurs at a high temperature ($>100°$C). Therefore, these rod-like metallomesogens exhibiting SmA or columnar phases are not always appropriate materials for investigating the alignment of LC molecules by magnetic fields.

Recently Galyametdinov and Binnemans et al. reported the first example of lanthanidomesogens (La(III), Nd(III), Eu(III), and Yb(III)) that can exhibit a low viscous nematic (N) phase over a wide temperature range between ca. 100°C and ca. 140°C after the appearance of the SmA phase during the heating process (Figure 3.10). However, the electrical switching of the N phase of the pure lanthanide complex was not possible. The preparation of a lanthanide complex showing a stable N phase at room temperature is anticipated (see Section 3.4.2.2) [48].

3.4.2.2 Luminescence Galyametdinov and Binnemans et al. observed linearly polarized luminescence by exciting the homogeneously aligned SmA phase of the paramagnetic Eu(III) complex mesogen **9** in a 5 μm-thick sandwich cell with UV-irradiation (Figure 3.10) [48, 49]. However, the radiationless deactivation was dominant at the temperatures at which the N phase is stable (108–142°C). Therefore, it is anticipated that the linearly polarized luminescence can be observed in concert

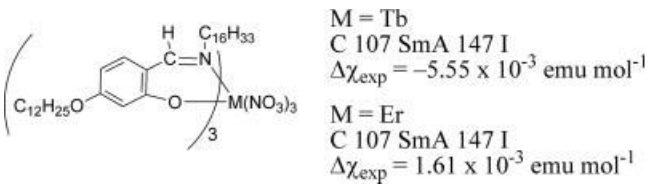

FIGURE 3.9 Rare earth metal-containing LCs and their magnetic anisotropy.

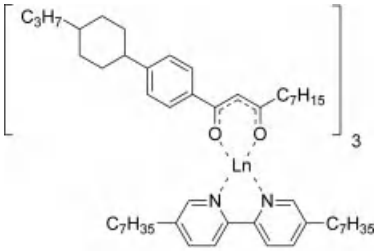

9 Ln = Eu(III)

FIGURE 3.10 Lanthanidomesogen **9** exhibiting an N phase.

with electrical or magnetic switching of the aligned N phase of a pure lanthanide complex at room temperature.

3.4.2.3 SMM Veciana et al. prepared a SMM with two different relaxation processes by controlling the cooling rate from the LC phase of a double-decker terbium complex **10** (Figure 3.11) [20].

3.5 ALL-ORGANIC RADICAL LCs

All-organic rod-like LC materials with a stable radical unit, which can benefit from the low viscosity and small molecular size, may show unique intermolecular magnetic interactions owing to the swift coherent collective properties of organic molecules in the LC state, although their $\Delta\chi_{para}$ is considered to be too small to control the molecular orientation by magnetic fields due to the p-orbital origin.

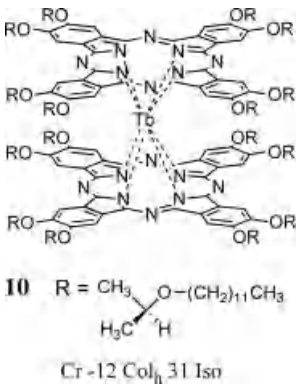

FIGURE 3.11 SMM double-decker terbium complex **10** showing LC properties at high temperatures.

3.5.1 First-Generation of Rod-Like All-Organic Radical LCs

Only a few all-organic radical LC compounds have been prepared, most likely because the geometry and bulkiness of the radical-stabilizing substituents are detrimental to the stability of LCs, which requires molecular linearity or planarity [1]. Although several achiral rod-like organic LCs with a stable nitroxyl group (DOXYL or TEMPO group) as the spin source were prepared (Figure 3.12), their molecular structures were limited to those containing the nitroxyl group within the terminal alkyl chain, away from the rigid core, and hence allowed the free rotation of the nitroxyl moiety inside the molecule, resulting in a decrease in the $\Delta\chi_{para}$ as well as the $\Delta\varepsilon$ of the whole molecule. All attempts to prepare monomeric or polymeric LC compounds with a nitroxyl unit as part of the rigid core were unsuccessful. The molecular structures and magnetic properties of such first-generation of all-organic nitroxyl radical LCs and the objectives of individual studies are briefly summarized below.

Dvolaitzky et al. synthesized chiral racemic and achiral compounds **11**–**13** to use them as a LC spin-probe for EPR spectroscopic study. Racemic **13** showed stable smectic phases such as SmA, SmC, and SmE [50–52]. Their temperature dependence of the χ was not measured.

With the aim of measuring the magnetic properties of a LC structure at low temperatures, Finkelmann et al. prepared chiral racemic radical polymer **14** which can retain the LC structure in the supercooled glassy phase [53]. By means of a

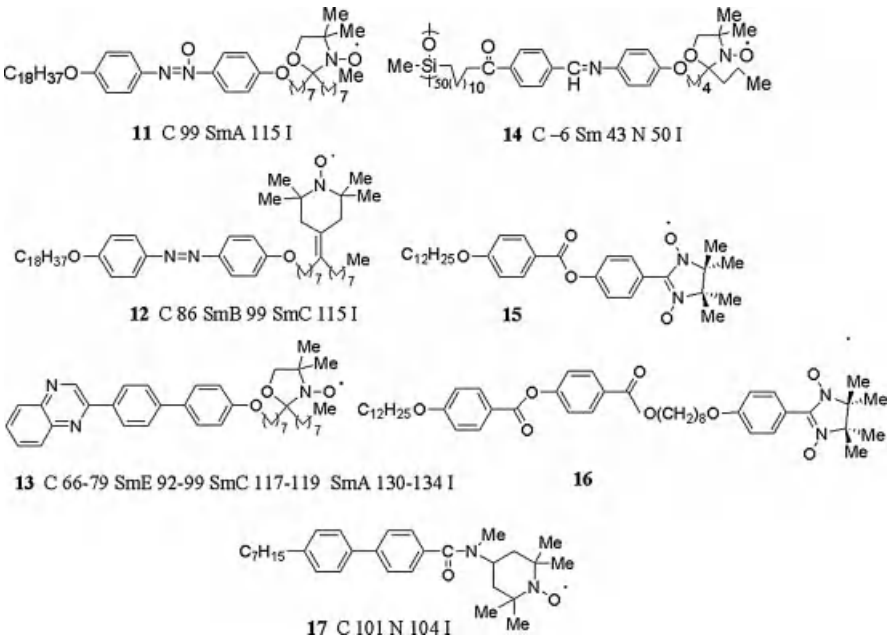

FIGURE 3.12 First-generation of rod-like all-organic radical LC compounds **11**–**17**.

Faraday balance, the temperature dependence of the χ was measured in the temperature range from 6 to 350 K, in which the crystal-to-LC-to-liquid phase transition occurred. Consequently, during the heating process in this temperature range, **14** showed no molecular orientation; no appreciable change in χ was observed at the crystal-to-LC phase transition temperature. This is most likely due to the high viscosity of the polymer material. It is desirable to measure the temperature dependence of the χ during the cooling process from the isotropic phase on a SQUID susceptometer.

Greve et al. synthesized the first LC compounds **15** and **16** bearing an α-nitronyl nitroxide (α-NN) structure as a spin source at the terminal position in the molecule [54]. They showed a highly viscous monotropic LC phase in the narrow temperature range from 36 to 39°C during the heating process. The temperature dependence of the χ was not measured.

To prepare a supercooled glassy material and crystal polymorphs in the applied magnetic fields and to observe the change in the magnetic behavior accompanying the alteration in the solid-state structure, achiral LC compound **17** was synthesized by Nakatsuji et al. [19]. Although **17** showed the N phase within a narrow temperature range of 3° during the heating process, a distinct increase in χ was observed at the crystal-to-LC transition temperature. The difference in the magnetic behavior between the heating and cooling processes was also observed; **17** showed antiferromagnetic interactions according to a singlet–triplet model at low temperatures before the thermal phase transition during the heating process of the crystals, while the magnetic behavior obeyed the Curie–Weiss law during the cooling process from the isotropic phase (Eq. 3.8).

$$\chi_{\text{para}} = \frac{C}{T - \theta} \tag{3.8}$$

where C is the Curie constant, T is the temperature, and θ is the Weiss temperature.

3.5.2 Discotic All-Organic Radical LCs

Use of π-delocalization of an unpaired electron is an alternative method to stabilize the radical species. Based on this methodology, the cation-radical charge-transfer salts **18a** and **18b** with semiconductivity were prepared from the corresponding tetraphenylbipyranylidene or tetraphenylbithiopyranylidene derivative and tetracyanoquinodimethane (TCNQ) by Saeva et al. and Strzelecka et al., respectively (Figure 3.13) [55, 56]. The salt **18a** showed a discotic LC phase over a wider temperature range and a lower clearing point than the neutral tetraphenylbipyranylidene, while the salt **18b** showed a SmA phase. The magnetic susceptibility measurement of **18b** by the Faraday method indicated that there were no interacting spins between the donor and the acceptor in the LC phase, while the weak antiferromagnetic behavior characteristic of interacting spins was observed below the crystal-to-LC transition point of 120°C.

Nakatsuji et al. successfully prepared the first stable discotic all-organic radical LC compounds **19** and **20**, which have a nitroxide unit (TEMPO or PROXYL group) at the peripheral position in the molecule and showed an enantiotropic columnar

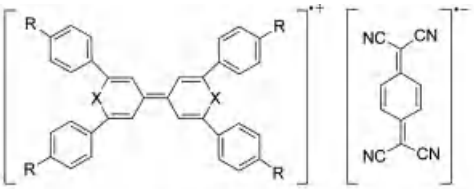

18a X = O, R = $C_{12}H_{25}$ C 11 D_1 34 D_2 242.5 (dec)
18b X = S, R = $OC_{12}H_{25}$ C 120 SmA 154 I

FIGURE 3.13 LC charge-transfer complexes **18**.

phase over a wide temperature range (Figure 3.14). Weak antiferromagnetic interactions were observed in the crystalline, LC, and supercooled phases by measuring the temperature dependence of the χ in the temperature range between 2 and 300 K [57].

Recently, Julia and Velasco et al. successfully synthesized the discotic radical compound **21**, which has a stable tris(2,4,6-trichlorophenyl)methyl radical structure as a spin source in the core of LC molecule (Figure 3.15). They observed distinct antiferromagnetic interactions in the columnar LC phases by measuring the temperature dependence of the χ in the temperature range between 2 and 400 K [58].

3.5.3 Second-Generation of Rod-Like All-Organic Radical LCs

3.5.3.1 Molecular Design and Synthesis To examine the several possibilities anticipated for PLCs in Section 3.1, the second-generation of chiral nitroxide molecules that could satisfy the following four mandatory requirements were designed.

Spin source: Among persistent or stable organic free radicals such as nitroxides [59], verdazyls [60, 61], thioaminyls [62], a certain hydrazyl [63], phenoxyls [64, 65], and carbon-centered radicals [58, 66], a nitroxyl group, which serves as the spin source of nitroxides and possesses a large electric dipole moment (ca. 3 Debye) and known principal g-values (g_{xx}, g_{yy}, g_{zz}) should be the best spin source,

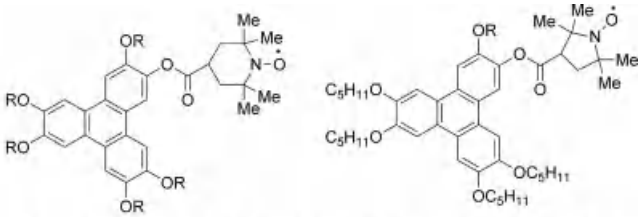

19a R = C_5H_{11} I 169.1 Col_h –60 > **20** I 153.1 Col_h Col_{rp} –60>
19b R = C_6H_{13} I 147.8 Col_h –60 >

FIGURE 3.14 Discotic nitroxide radical LC compounds **19** and **20**.

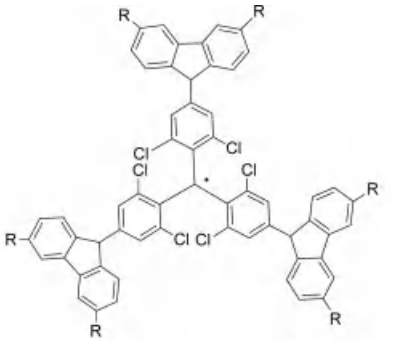

21 R = $COC_{17}H_{35}$ I 78 Col_h 14 Col_r –43>

FIGURE 3.15 Discotic triphenylmethyl radical LC compound **21**.

because (i) the dipole moment is large enough for the source of the Ps and (ii) the principal *g*-values are useful to determine the direction of molecular alignment in the LC phase by EPR spectroscopy (Figure 3.16a).

High thermal stability: A 2,2,5,5-tetraalkyl-substituted pyrrolidine-1-oxy (PROXYL) structure is stable enough for repeated heating and cooling cycles below 150°C in the air.

Molecular structure: (a) To avoid the free rotation of the nitroxyl group inside the molecule so as to maximize the $\Delta\chi_{para}$ and $\Delta\varepsilon$, a geometrically fixed chiral cyclic nitroxide unit should be incorporated into the rigid core of LC molecules. (b) To obtain a slightly zigzag molecular structure and a negative $\Delta\varepsilon$ advantageous for the appearance of a SmC* phase, a trans-2,5-dimethyl-2,5-diphenylpyrrolidine-1-oxy (PROXYL) skeleton in which the electric dipole moment orients to the molecular short axis is the best choice (Figure 3.16b).

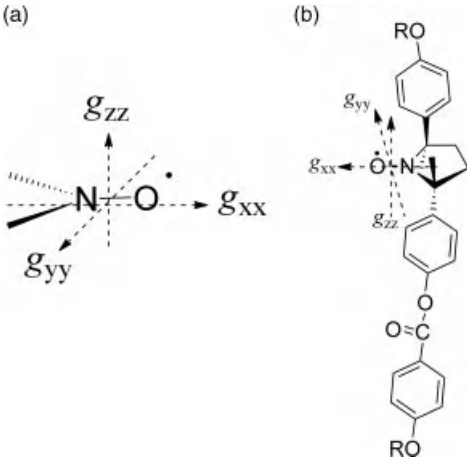

FIGURE 3.16 Principal *g*-values of a nitroxide molecule.

Chirality: Since both chiral and achiral LCs are required for comparison of their optical and magnetic properties in various phases, the molecules should be chiral and both enantiomerically enriched and racemic samples need to be available.

According to the above requirements, structurally different five LC compounds (**1**–**5**) with a negative $\Delta\varepsilon$ were prepared in both enantiomerically enriched and racemic forms (Figure 3.1) [5–7, 16, 67–70].

3.5.3.2 Characterization of LC Phases Individual LC phase types of compounds **1**–**5** were determined by means of differential scanning calorimetry (DSC), hot-stage polarized optical microscopy (POM), and variable temperature X-ray diffraction (VT-XRD) analysis under random or homogeneous planar boundary conditions [16, 67–70].

Compounds **1**–**4** showed chiral (or achiral) N* (N) and/or SmC* (SmC) phases (Figure 3.17a) [16, 67, 68], while compounds **5** possessing the partially modified molecular structures of **1** exhibited a different sequence of LC phases, N* (N), SmA* (SmA) and SmC* (SmC) (Figure 3.17b) [69, 70]. This difference in the LC phase change can be explained in terms of the difference in the direction of molecular dipole moment between **1** and **5** [70]. It is noteworthy that compounds **1** showed the LC phases over a wide range of temperature between ambient temperature and 90°C, particularly on the cooling run.

3.5.3.3 Magnetic Properties Since the magnetic properties such as $\Delta\chi$-controlled molecular orientation and magnetic interactions in all-organic PLC phases have been fully characterized for the first time by using the various LC phases of compounds **1**, these experimental results are described in detail.

Magnetic Anisotropy and Magnetic-Field-Induced Molecular Alignment In Section 3.4, it has been stated that rod-like metallomesogens with high viscosity are not always appropriate for the investigation on the alignment of LC molecules by magnetic fields. In contrast, LC compounds **1** with low viscosity, low phase transition temperature, and known principal g-values of the nitroxide moiety are considered to be a good candidate for the studies on the $\Delta\chi$-controlled molecular orientation by weak magnetic fields, albeit its small $\Delta\chi_{para}$. Therefore, we determined whether the magnetic-field-induced molecular alignment in the LC phases of **1** was dominated by the $\Delta\chi_{para}$ or $\Delta\chi_{dia}$, by the quantitative evaluation of the $\Delta\chi_{para}$ and $\Delta\chi_{dia}$ values of **1** and then evaluated the approximate magnitude of H_c for each LC phase of **1** by EPR spectroscopy and by POM observation under variable magnetic fields [71].

First, the temperature-dependent $\Delta\chi_{para}$ value of compound **1a** ($m = n = 13$) was calculated to be -1.7×10^{-6} emu mol^{-1} at 300 K from the g-value obtained by EPR spectroscopy, while the temperature-independent $\Delta\chi_{dia}$ value was calculated to be $+6.5 \times 10^{-5}$ emu mol^{-1} from the experimental molar magnetic susceptibility of (±)-**1a** measured on a SQUID magnetometer. Thus, $|\chi_{dia}|$ has turned out to be 30 times larger than $|\chi_{para}|$; the molecular alignment of **1a** by magnetic field is definitely $\Delta\chi_{dia}$-controlled.

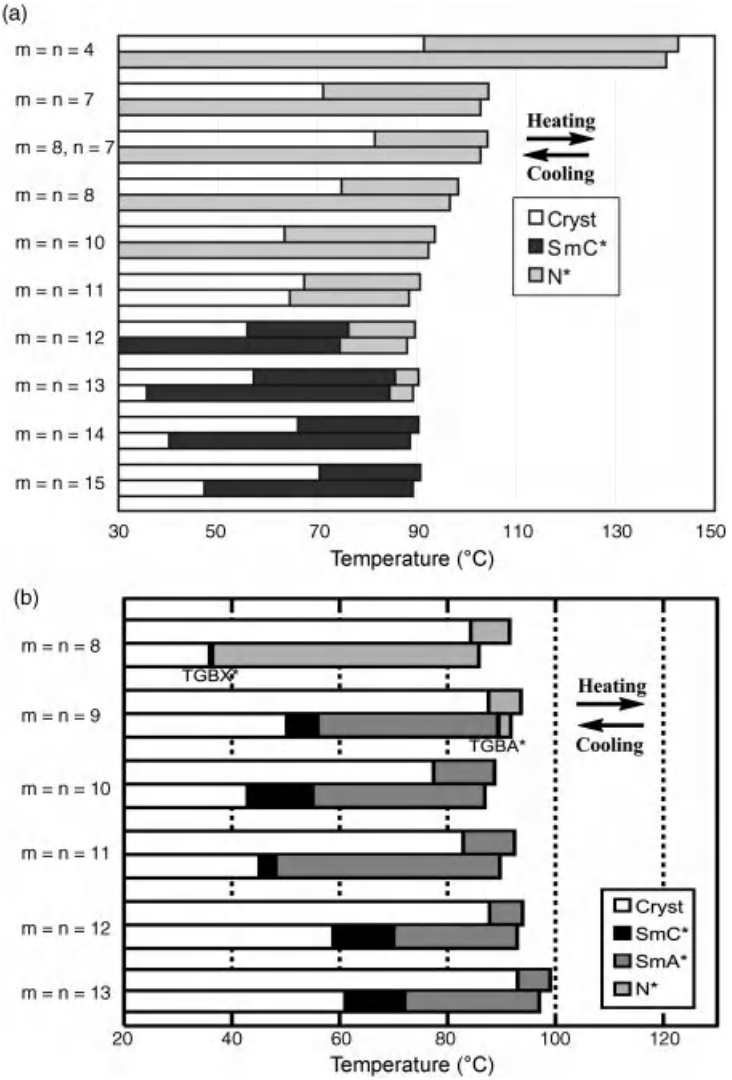

FIGURE 3.17 LC behavior of (a) (2S,5S)-**1** and (b) (2S,5S)-**5**.

Next, to identify the direction of molecular alignment in the bulk LC state under a weak magnetic field, the temperature dependence of the experimental g-value (g_{exp}) of (±)-**1a** was measured at a magnetic field of 0.33 T by EPR spectroscopy (Figure 3.18). During the heating process, the g_{exp} of (±)-**1a** was constant at around 2.0065 in the crystalline state, then increased at the crystal-to-SmC phase transition, became constant at around 2.0068 in the SmC phase, then decreased abruptly to 2.0058 at the SmC-to-N phase transition, and finally returned to the level (~2.0065) of the crystalline state in the isotropic phase. During the cooling process, the g_{exp} of (±)-**1a** was constant at around 2.0065 in the isotropic phase, then decreased at the

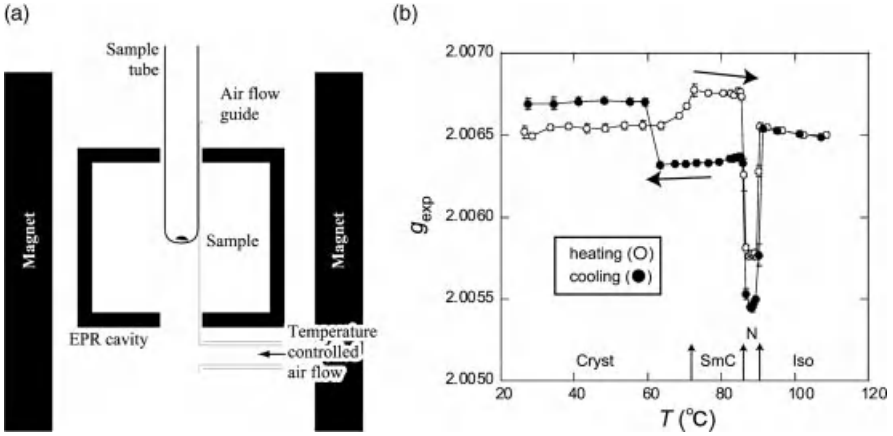

FIGURE 3.18 EPR spectroscopy of (±)-**1a** ($m = n = 13$). (a) Experimental setup and (b) temperature dependence of the g-value measured through the first heating (white circles) and cooling (black circles) processes. *Source*: Ref. 71 – Reproduced by permission of The Royal Society of Chemistry.

Iso-to-N phase transition, became constant at around 2.0055 in the N phase, then increased to 2.0063 at the N-to-SmC phase transition, and finally increased to 2.0067 in the crystalline state.

From these results and the calculated principal g-values ($g_{iso} = 2.00632$, $g_{\parallel} = 2.00540$, $g_{\perp} = 2.00678$) of **1a**, it is concluded that (i) in the N phase the majority of molecules align their long axis along the applied magnetic field of 0.33 T (Figure 3.19a), whereas in the SmC phase during the heating process the molecular short axis is almost parallel to the field (Figure 3.19b), most likely due to the viscous layer structure and the natural homeotropic anchoring effect by quartz surface, and (ii) that the molecular alignment in each LC phase is influenced by that

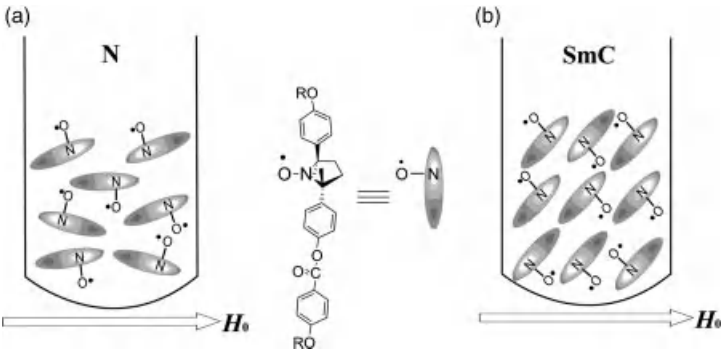

FIGURE 3.19 Molecular alignment in the LC phases of (±)-**1a** under a weak magnetic field (0.34 T). (a) N phase during both heating and cooling processes and (b) SmC phase during the heating process.

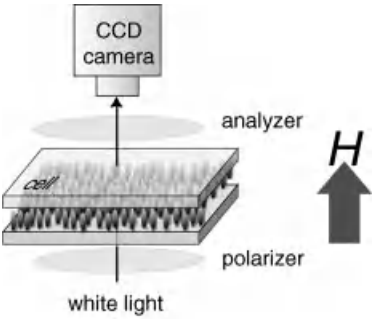

FIGURE 3.20 Experimental setup for the polarized optical microscopy observation of (±)-**1a** under variable magnetic fields applied perpendicular to the cell surface. *Source*: Ref. 71 – Reproduced by permission of The Royal Society of Chemistry.

in the preceding LC phase, although the molecular orientation modes are quite different between the N and SmC phases.

To evaluate the H_c for each LC phase of (±)-**1a**, we observed the texture change by POM observation under variable magnetic fields. Figure 3.20 shows the experimental setup. The direction of applied magnetic fields is perpendicular to the LC cell surface. The inner glass surface in the sandwich cell with 40 μm thickness was neither chemically nor physically treated. The random texture of the N phase gradually became dark with the increasing magnetic field until 0.5 T, resulting in the complete homeotropic orientation of molecules at 1.0 T, whereas the random texture of SmC phase scarcely changed below 1.0 T, largely changed between 1.0 T and 1.5 T, and finished the change at less than 2.0 T to show a Schlieren texture [71], which is similar to the SmC Schlieren texture of (±)-**1** observed under alternative homeotropic boundary conditions [14]. Accordingly, it has been concluded that the smectic layer planes became parallel to the glass plates at 2.0 T. Furthermore, no texture change was noted for N* and SmC* phase of (2S,5S)-**1a** below 5 T using the same experimental setup.

Thus, the H_c of each LC phase turned out to be largely affected by the superstructure; H_c(N) (<1.0 T) $<$ H_c(SmC) (<2.0 T) $<$ H_c(N*, SmC*) (>5.0 T).

Inhomogeneous Intermolecular Magnetic Interactions As mentioned in Section 3.4.1.2, the possibility of a ferromagnetic rod-like LC material has been considered unrealistic due to the inaccessibility of long-range spin–spin interactions between rotating molecules in the LC state. Nevertheless, it is interesting to know whether and how LC domains can help to induce magnetic interactions in low viscous all-organic radical LC phases in which order coexists with fluidity.

Interestingly, we observed a nonlinear relationship (S-curve) between the applied magnetic field (H) and the observed magnetization (M) in chiral and achiral LC phases of **1** (Figure 3.21), which implies the generation of an unusual magnetic interaction in the LC phases under applied magnetic fields [17, 18]. Such a nonlinear paramagnetic magnetization (NPM) was not observed in the crystalline phases of the

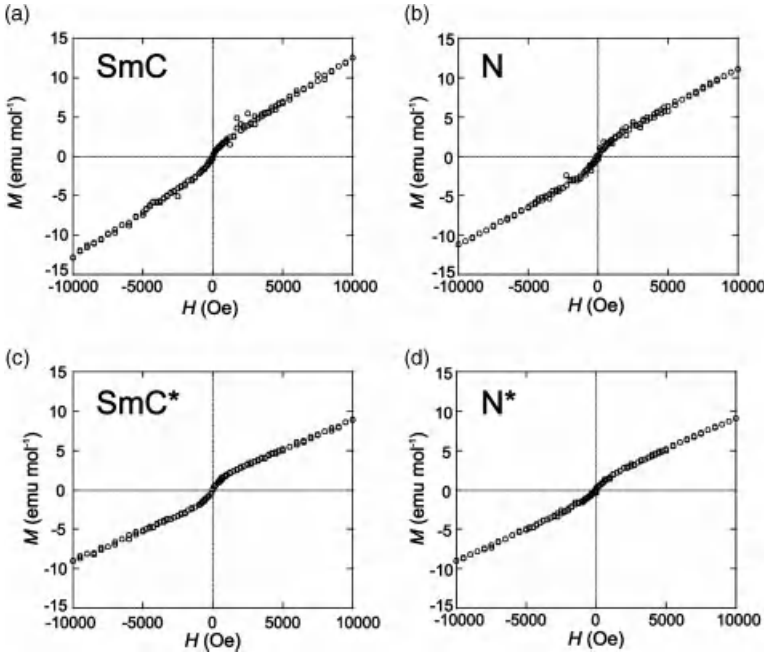

FIGURE 3.21 Magnetic field (H) dependence of molar magnetization (M) at 77°C for (a) the SmC phase of (±)-**1a**, (b) the N phase of (±)-**1b** ($m = n = 8$), (c) the SmC* phase of (2S,5S)-**1a** (88% ee), and (d) the N* phase of (2S,5S)-**1b** (96% ee). *Source*: Ref. 18 – Reprinted with permission from the American Chemical Society.

same compounds, which showed a usual linear relationship indicating a paramagnetic nature and no contamination of magnetic impurities in the sample. The in-depth investigation on the magnetic properties of LC compounds **1** strongly suggested that the generation of a sort of spin glass (SG)-like inhomogeneous magnetic interactions (the average spin–spin interaction constant $\bar{J} > 0$) induced by weak magnetic fields in the various LC phases of compounds **1** is responsible for the observed NPM; the magnitude of magnetic interactions depended on the LC phase type, or the superstructure (Figure 3.22) [18]. Furthermore, it was concluded that (i) the molecular reorientation effect arising from the simple molecular magnetic anisotropy ($\Delta\chi$) has nothing to do with the NPM or the unusual magnetic interactions observed in the LC phases of **1** and instead (ii) the origin of such strong SG-like inhomogeneous magnetic interactions, which has been referred to as positive 'magneto-LC effects', can be interpreted in terms of the anisotropic spin–spin dipole interactions induced in the anisotropic LC superstructure under magnetic fields.

In this study, we could indicate that EPR spectroscopy is the much better means than SQUID magnetization measurement to measure the temperature dependence of the χ_{para} for organic nitroxide radical LC materials at high temperatures. This is due to the following four reasons: (i) The χ_{para} can be derived from the Bloch equation (Eq. 3.9) by

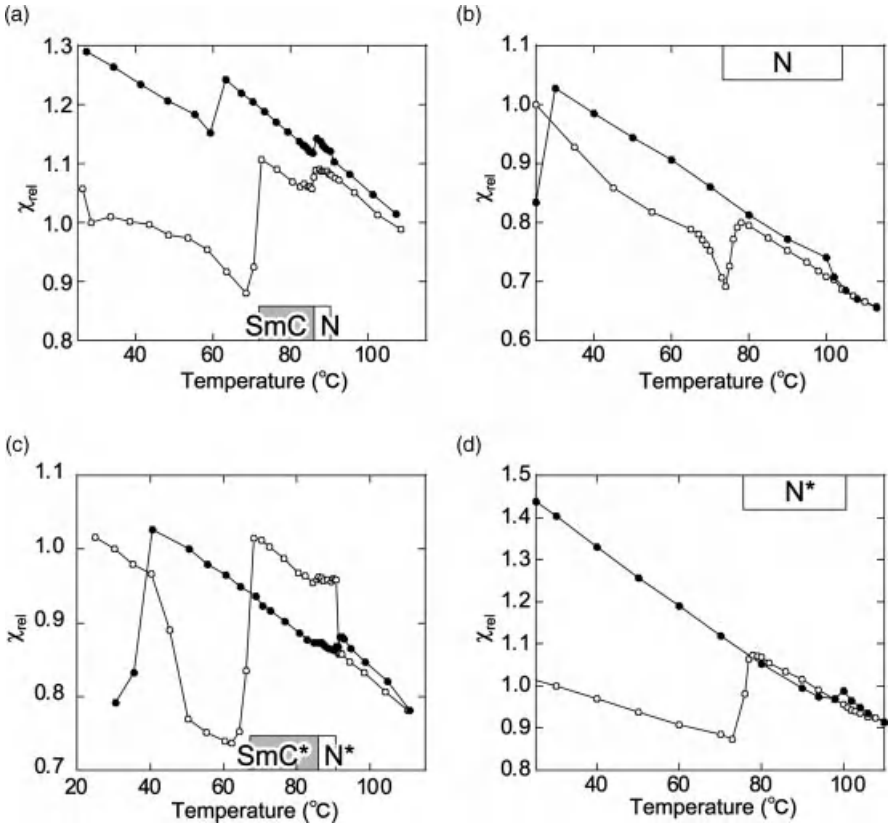

FIGURE 3.22 Temperature dependence of relative paramagnetic susceptibility (χ_{rel}) for (a) (±)-**1a**, (b) (±)-**1b**, (c) (2S,5S)-**1a** (88% ee), and (d) (2S,5S)-**1b** (96% ee) at a magnetic field of 0.33 T. Open and filled circles represent the first heating and cooling runs, respectively. The LC temperatures shown in a box refer to the first heating process. *Source*: Ref. 18 – Reprinted with permission from the American Chemical Society.

using the parameters obtained from the EPR differential curves, such as maximum peak height (I'_m and $-I'_m$), g-value (g), and peak-to-peak line width (ΔH_{pp}).

$$\chi_{para} = \frac{2\mu_B g I'_m \ \Delta H_{pp}^2}{\sqrt{3} h v H_1} \tag{3.9}$$

where μ_B is the Bohr magnetron, h is Planck's constant, v is the frequency of the absorbed electromagnetic wave, and H_1 is the amplitude of the oscillating magnetic field. Accordingly, the temperature dependence of relative paramagnetic susceptibility (χ_{rel}), which is defined as

$$\chi_{rel} = \frac{\chi_{para}}{\chi_0} \tag{3.10}$$

where χ_0 is the standard paramagnetic susceptibility, e.g., at 30°C in the heating run (Eq. 3.10), can be actually used (Figure 3.22). (ii) Treatment of the χ_{dia} term is totally unnecessary. (iii) The experimental error is very small even at such high temperatures. (iv) The analysis of microscopic magnetic interactions such as spin–spin dipole and exchange interactions is also feasible.

Furthermore, these radical LC droplets floating on water were uniformly attracted by a permanent magnet and moved freely on water under the influence of this magnet (Figure 3.23), whereas the crystallized particles of the same compounds never responded to the same magnet. The response of the LC droplets to the magnet also varied depending on the LC phase type, that is, the extent of the magnetic interaction ($\bar{J}$). These results indicate that the LC phase domain can help to induce magnetic interactions under applied magnetic fields [17, 18].

This unique magnetic attraction will find use in the development of the metal-free magnetic soft materials usable at ambient temperature, such as a magnetic LC carrier for the magnetically targeted drug-delivery system or an MRI contrast agent [72].

3.5.3.4 Ferroelectricity It is known that when a SmC* phase is confined to a thin sandwich cell with a gap smaller than the pitch of the helical superstructure, an unwinding of the helix occurs and a bistable, ferroelectric device is formed (Figure 3.24) [14, 73]. Consequently, Ps is generated in the sandwich cell in which ferroelectric switching occurs by changing the polarity of the electric field. The ferroelectric properties of the SmC* phase of each sample are characterized by measuring the Ps, the optical response time of bistable switching to an applied electric field, and the tilt angle.

The SmC* phases of (2S,5S)-**1**–**5** indeed exhibited ferroelectricity in a planar anchoring thin sandwich cell (4 μm thickness) (Table 3.1) [67–70]. The ferroelectric properties of (2S, 5S)-**1** deserve attention; e.g., for (2S, 5S)-**1a**, a Ps value of 24 nC cm^{-2}, an optical response time (τ_{10-90}) of 0.213 ms and a layer tilt angle (θ) of 29° were recorded. The FLC data of (2S, 5S)-**1a** were superior to those of (2S, 5S)-**2**–**5** [67–70] and the typical chiral metallomesogen **7** (Figure 3.7); **7** showed a higher Ps value of 38 nC cm^{-2} with a θ of 23° than (2S, 5S)-**1a**, but the optical response was very slow ($\tau_{10-90} = 8.5$ ms) due to the high viscosity (Table 3.1) [31].

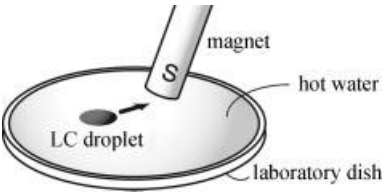

FIGURE 3.23 Schematic representation of the experimental setup for observing the attraction by a permanent magnet (maximum 0.5 T) of a paramagnetic LC droplet on water in a shallow laboratory dish. *Source*: Ref. 18 – Reprinted with permission from the American Chemical Society.

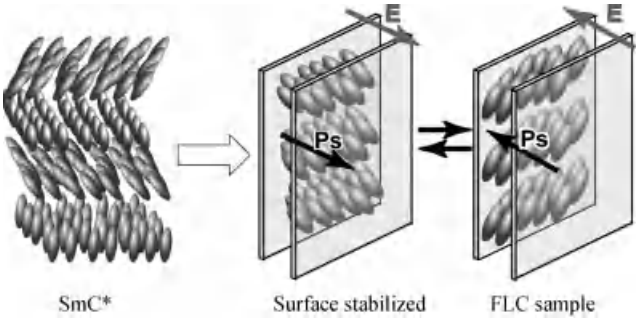

FIGURE 3.24 Ferroelectric switching in a thin sandwich cell.

TABLE 3.1 Comparison of ferroelectric properties

(2S,5S) $m=n=13$ [*ee* (%)]	Spontaneous polarization Ps(−10°) [nC cm^{-2}]	Response time $\tau_{10-90}(-10°)$ [ms]	Viscosity $\eta(-10°)$ [mPa s]	Tilt angle $\theta(-10°)$ [°]
1 [88]	24 (74°C)	0.213	73.0	29
2 [91]	36 (116°C)	–[a]	–	42
3 [91]	21 (137°C)	–[a]	–	38
4 [91]	12 (142°C)	–[a]	–	36
5 [86]	3.7 (85°C)	0.465	49.2	19
7	38 (100°C)	8.5	1870	23

[a] Unable to measure.

Furthermore, second-harmonic generation (SHG) was clearly observed by Kogo and Takezoe et al. under a phase-matching condition in the SmC* phase of (2S,5S)-**1a** loaded into an LC cell (20 μm thickness), validating the existence of ferroelectricity. The effective second-order nonlinear optical (NLO) constant was evaluated to be a 4.8×10^{-2} pm V^{-1}, 3 orders of magnitude smaller than that of quartz known as a standard NLO material [74].

3.6 CONCLUSIONS

The magnetic properties of two different types of paramagnetic LC materials, d- and f-block metallomesogens and all-organic radical LCs, were briefly surveyed.

For objective 1 listed in Section 3.1, lanthanide complexes showing a stable N phase at room temperature is most promising and their emergence is strongly anticipated.

In the context of objectives 2–4, noteworthy is the first observation of unique SG-like inhomogeneous intermolecular magnetic interactions ($\bar{J}>0$) in the LC state under weak magnetic fields of the second-generation of rod-like all-organic chiral

radical LC compounds **1** that can show thermally stable chiral and achiral rod-like LC phases such as N* and/or SmC* and N and/or SmC phases, respectively. Furthermore, the ferroelectric properties of the SmC* phases of **1** were fully characterized in a sandwich cell; a nitroxyl group proved to act as the sufficient source of the macroscopic electric dipole that can be evaluated as Ps. Such chiral all-organic radical LCs with low viscosity showed faster ferroelectric switching than chiral metallomesogens with high viscosity. The next step is the control of magnetic properties of ferroelectric PLCs of **1** by electric fields (and vice versa). In addition, it is of great advantage to use EPR spectroscopy and SQUID magnetization measurement as the tool for observing and evaluating the microscopic and macroscopic dynamic behaviors of the LC materials, respectively. Particularly, EPR spectroscopy has proved to be an excellent tool in place of SQUID magnetization measurement for measuring the temperature dependence of the χ_{para} for organic nitroxide radical LC phases at high temperatures. Thus, such second-generation of all-organic chiral radical LC compounds would open up a new research field of LC materials.

In terms of objective 3, another notable finding is the observation of RT ferromagnetism in a diamagnetic discotic LC phase of **6** intercalated with paramagnetic Fe(III)Pc under weak magnetic fields. This result would provide general guidelines for the fabrication of ferromagnetic discotic LCs.

As far as objectives 6 and 7 are concerned, the molecular design of sophisticated metallomesogens aiming for each desired function would be necessary.

The research on PLCs is in its infancy. Hence, PLCs would gradually become fascinating dynamic magnetic functional materials as these objectives can be achieved step-by-step. Therefore, it is envisaged that sooner or later PLCs would emerge as an important subfield of liquid crystal science at its own right.

ACKNOWLEDGMENTS

We acknowledge Professor Takeji Takui, Professor Hiroyuki Nohira, Dr. Yoshio Aoki, Professor Hideo Takezoe, Dr. Yoshio Shimbo, Ms. Reiri Kogo, Professor Jun Yamauchi, Dr. Yohei Noda, Dr. Naohiko Ikuma and Dr. Satoshi Shimono for their collaboration.

REFERENCES

1. P. Kaszynski. Liquid crystalline radicals: an emerging class of organic magnetic materials. In: P. M. Lahti, Ed., *Magnetic Properties of Organic Materials*, Marcel Dekker, New York, 1999.
2. K. Griesar and W. Haase. Magnetic properties of transition-metal-containing liquid crystals. In: P. M. Lahti, Ed., *Magnetic Properties of Organic Materials*, Marcel Dekker, New York, 1999.
3. D. Dunmur and K. Toriyama. Magnetic properties of liquid crystals. In: D. Demus, J. Gooby, G. W. Gray, and S. V. Vill, Eds., *Physical Properties of Liquid Crystals*, Wiley-VCH, Weinheim, 1999.

4. J.-L. Serrano. *Metallomesogens: Synthesis, Properties, and Applications*, Wiley-VCH, Weinheim, 1996.
5. R. Tamura. Organic functional materials containing chiral nitroxide radical units. In: G. I. Likhtenshtein, J. Yamauchi, S. Nakatsuji, A. I. Smirnov, and R. Tamura, Eds., *Nitroxides: Application in Chemistry, Biomedicine, and Materials Science*, Wiley-VCH, Weinheim, 2008.
6. R. Tamura, Y. Uchida, and N. Ikuma. Paramagnetic all-organic chiral liquid crystals. *J. Mater. Chem.* **2008**, *18*, 2872–2876.
7. R. Tamura, N. Ikuma, and S. Shimono. Preparation and magnetic properties of all-organic radical liquid crystals. In: H. S. Nalwa, Ed., *Soft Nanomaterials*. Volume 1, American Scientific Publishers, CA, 2009.
8. W. Eerenstein, N. D. Mathur, and J. F. Scott. Multiferroic and magnetoelectric materials. *Nature* **2006**, *442*, 759–765.
9. C. N. R. Rao and C. R. Serrao. New routes to multiferroics. *J. Mater. Chem.* **2007**, *17*, 4931–4938.
10. C. Felser, G. H. Fecher, and B. Balke. Spintronics: a challenge for materials science and solid-state chemistry. *Angew. Chem. Int. Ed.* **2007**, *46*, 668–699.
11. G. L. J. A. Rikken and E. Raupach. Observation of magneto–chiral dichroism. *Nature* **1997**, *390*, 493–494.
12. G. L. J. A. Rikken and E. Raupach. Enantioselective magnetochiral photochemistry. *Nature* **2000**, *405*, 932–935.
13. C. Train, R. Gheorghe, V. Krstic, L.-M. Chamoreau, N. S. Ovanesyan, G. L. J. A. Rikken, M. Gruselle, and M. Verdaguer. Strong magneto–chiral dichroism in enantiopure chiral ferromagnets. *Nature Mater.* **2008**, *7*, 729–734.
14. I. Dierking. *Textures of Liquid Crystals*, Wiley-VCH, Weinheim, 2003.
15. D. Dunmur and K. Toriyama. Elastic properties. In: D. Demus, J. Gooby, G. W. Gray, and S. V. Vill, Eds., *Physical Properties of Liquid Crystals*, Wiley-VCH, Weinheim, 1999.
16. N. Ikuma, R. Tamura, S. Shimono, N. Kawame, O. Tamada, N. Sakai, J. Yamauchi, and Y. Yamamoto. Magnetic properties of all-organic liquid crystals containing a chiral five-membered cyclic nitroxide unit within the rigid core. *Angew. Chem. Int. Ed.* **2004**, *43*, 3677–3682.
17. Y. Uchida, N. Ikuma, R. Tamura, S. Shimono, Y. Noda, J. Yamauchi, Y. Aoki, and H. Nohira. Unusual intermolecular magnetic interaction observed in an all-organic radical liquid crystal. *J. Mater. Chem.* **2008**, *18*, 2950–2952.
18. Y. Uchida, K. Suzuki, R. Tamura, N. Ikuma, S. Shimono, Y. Noda, and J. Yamauchi. Anisotropic and inhomogeneous magnetic interactions observed in all-organic nitroxide radical liquid crystals. *J. Am. Chem. Soc.* **2010**, *132*, 9746–9752.
19. S. Nakatsuji, M. Mizumoto, H. Ikemoto, H. Akutsu, and J. Yamada. Preparation and properties of organic radical compounds with mesogenic cores. *Eur. J. Org. Chem.* **2002**, 1912–1918.
20. M. Gonidec, F. Luis, A. Vilchez, J. Esquena, D. B. Amabilino, and J. Veciana. A liquid-crystalline single-molecule magnet with variable magnetic properties. *Angew. Chem. Int. Ed.* **2010**, *49*, 1623–1626.
21. H. J. Müller and W. Haase. Magnetic susceptibility and the order parameters of some 4,4′-disubstituted biphenyl cyclohexanes. *J. Phys. (Paris)* **1983**, *44*, 1209–1213.

22. M. I. Boamfa, M. W. Kim, J. C. Maan, and T. Rasing. Observation of surface and bulk phase transitions in nematic liquid crystals. *Nature* **2003**, *421*, 149–152.
23. S. A. Hudson and P. M. Maitlis. Calamitic metallomesogens: metal-containing liquid crystals with rodlike shapes. *Chem. Rev.* **1993**, *93*, 861–885.
24. K. Binnemans and C. Gröller-Walrand. Lanthanide-containing liquid crystals and surfactants. *Chem. Rev.* **2002**, *102*, 2303–2345.
25. E. Terazzi, S. Suarez, S. Torelli, H. Nozary, D. Imbert, O. Mamula, J.-P. Rivera, E. Guillet, J.-M. Benech, G. Bernardinelli, R. Scopelliti, B. Donnio, D. Guillon, J.-C. G. Bunzli, and C. Piguet. Introducing bulky functional lanthanide cores into thermotropic metallomesogens: a bottom-up approach. *Adv. Funct. Mater.* **2006**, *16*, 157–168.
26. C. Piguet, J.-C. G. Bunzli, B. Donnio, and D. Guillon. Thermotropic lanthanidomesogens. *Chem. Commun.* **2006**, 3755–3768.
27. M. Marcos and J. L. Serrano. Paramagnetic nematic liquid crystals. *Adv. Mater.* **1992**, *3*, 256–257.
28. M. Maracos, J. L. Serrano, T. Sierra, and M. J. Gimenez. Paramagnetic chiral smectic C materials: a new class of ferroelectric liquid crystals. *Angew. Chem. Int. Ed.* **1992**, *31*, 1471–1472.
29. K. Griesar, Y. Galyametdinov, M. Athanassopoulou, I. Ovchinnikov, and W. Haase. Paramagnetic liquid crystalline nickel(II) compounds. *Adv. Mater.* **1994**, *5*, 381–384.
30. P. J. Alonso, M. Maarcos, J. Martinez, J. L. Serrano, and T. Sierra. EPR study of a chiral metallomesogens: bis(N-[4″-((2S)-2-chloropropoxy)phenyl], 4-(4′-*n*-decyloxybenzoyloxy)salicylaldimine)copper(II). *Adv. Mater.* **1994**, *6*, 667–670.
31. R. Iglesias, M. Marcos, J. L. Serrano, T. Sierra, and M. A. Perez-Jubindo. Ferroelectric behavior of chiral bis(salicylideneaniline) copper(II), vanadium(IV), and palladium(II) liquid crystals. *Chem. Mater.* **1996**, *8*, 2611–2617.
32. I. B. Yu, Y. Galyametdinov, A. Prosvirin, K. Griesar, E. A. Soto-Bustamante, and W. Haase. Correlation between magnetic properties and molecular structure of some metallo-mesogens. *Liq. Cryst.* **1995**, *18*, 231–237.
33. M. Buivydas. Some conditions of ferromagnetic liquid crystal existence. *Phys. Status Solidi B* **1991**, *168*, 577–581.
34. E. I. Kats and V. V. Lebedev. Some properties of ferromagnetic liquid crystals. *Mol. Cryst. Liq. Cryst.* **1991**, *209*, 329–337.
35. C. H. Lee, Y.-W. Kwon, D. H. Choi, Y. H. Geerts, E. Koh, and J.-I. Jin. High-temperature ferromagnetism of a discotic liquid crystal dilutely intercalated with Iron(III) phthalocyanine. *Adv. Mater.* **2010**, *22*, 4405–4409.
36. A. B. Gaspar, M. Seredyuk, and P. Gütlich. Spin crossover in metallomesogens. *Coord. Chem. Rev.* **2009**, *253*, 2399–2413.
37. Y. Galyametdinov, V. Ksenofontov, A. Prosvirin, I. Ovchinnikov, G. Ivanova, P. Gütlich, and W. Haase. First example of coexistence of thermal spin transition and liquid-crystal properties. *Angew. Chem. Int. Ed.* **2001**, *40*, 4269–4271.
38. T. Fujigaya, D.-L. Jiang, and T. Aida. Switching of spin states triggered by a phase transition: spin-crossover properties of self-assembled iron (II) complexes with alkyl-tethered triazole ligands. *J. Am. Chem. Soc.* **2003**, *125*, 14690–14691.
39. S. Hayami, R. Moriyama, A. Shuto, Y. Maeda, K. Ohta, and K. Inoue. Spin transition at the mesophase transition temperature in a cobalt (II) compound with branched alkyl chains. *Inorg. Chem.* **2007**, *46*, 7692–7694.

40. E. Terazzi, C. Bourgogne, R. Welter, J.-L. Gallani, D. Guillon, G. Rogez, and B. Donnio. Single-molecule magnets with mesomorphic lamellar ordering. *Angew. Chem. Int. Ed.* **2008**, *47*, 490–495.
41. J. Barberá, R. Iglesias, J. L. Serrano, T. Sierra, M. R. de la Fuente, B. Palacios, M. A. Pérez-Jubindo, and J. T. Vázquez. Switchable columnar metallomesogens. New helical self-assembling systems. *J. Am. Chem. Soc.* **1998**, *120*, 2908–2918.
42. J. L. Serrano and T. Sierra. Switchable columnar metallomesogens. *Chem. Eur. J.* **2000**, *6*, 759–766.
43. Y. Galyametdinov, M. A. Athanassopoulou, K. Griesar, O. Kharitonova, E. A. Soto-Bustamante, L. Tinchurina, I. Ovchinnikov, and W. Haase. Synthesis and magnetic investigation on rare-earth-containing liquid crystals with large magnetic anisotropy. *Chem. Mater.* **1996**, *8*, 922–926.
44. K. Binnemans, Y. G. Galyametdinov, R. Van Deun, D. W. Bruce, S. R. Collinson, A. P. Polishchuk, I. Bikchantaev, W. Haase, A. V. Prosvirin, L. Tinchurina, I. Litvinov, A. Gubajdullin, A. Rakhmatullin, K. Uytterhoeven, and L. Van Meervelt. Rare-earth-containing magnetic liquid crystals. *J. Am. Chem. Soc.* **2000**, *122*, 4335–4344.
45. V. S. Mironov, Y. G. Galyametdinov, A. Ceulemans, and K. Binnemans. On the magnetic anisotropy of lanthanide-containing metallomesogens. *J. Chem. Phys.* **2000**, *113*, 10293–10303.
46. Y. G. Galyametdinov, W. Haase, L. Malykhina, A. Prosvirin, I. Bikchantaev, A. Rakhmatullin, and K. Binnemans. Synthesis, mesomorphism, and unusual magnetic behavior of lanthanide complexes with perfluorinated counterions. *Chem. Eur. J.* **2001**, *7*, 99–105.
47. Y. G. Galyametdinov, W. Haase, B. Gorderis, D. Moors, K. Driesen, R. Van Deun, and K. Binnemans. Magnetic alignment study of rare-earth-containing liquid crystals. *J. Phys. Chem. B* **2007**, *111*, 13881–13885.
48. Y. G. Galyametdinov, A. A. Knyazev, V. I. Dzhabarov, T. Cardinaels, K. Driesen, C. Görller-Walrand, and K. Binnemans. Polarized luminescence from aligned samples of nematogenic lanthanide complexes. *Adv. Mater.* **2008**, *20*, 252–257.
49. K. Binnemans. Lanthanide-based luminescent hybrid materials. *Chem. Rev.* **2009**, *109*, 4283–4374.
50. M. Dvolaitzky, J. Billard, and F. Poldy. Notes des Membres et Correspondants et Notes Présentées ou Transmises par Leurs Soins, *C. R. Acad. Sci.* **1974**, *279C*, 533–535.
51. M. Dvolaitzky, C. Taupin, and F. Poldy. Nitroxides piperidiniques – Synthese de nouvelles sondes paramagnetiques. *Tetrahedron Lett.* **1976**, *18*, 1469–1472.
52. M. Dvolaitzky, J. Billard, and F. Poldy. Smectic E, C and A Free Radicals, *Tetrahedron* **1976**, *32*, 1835–1838.
53. J. Allgaier and H. Finkelmann. Synthesis and magnetic properties of mesogenic side-chain polymers containing stable radicals. *Macromol. Chem. Phys.* **1994**, *195*, 1017–1030.
54. S. Greve, V. Vill, and W. Friedrichsen. Novel nitronyl nitroxides: synthesis and properties. *Z. Naturforsch.* **2002**, *57b*, 677–684.
55. F. D. Saeva, G. A. Reynolds, and L. Kaszczuk. Liquid-crystalline cation-radical charge-transfer systems. *J. Am. Chem. Soc.* **1982**, *104*, 3524–3525.

56. H. Strzelecka, V. Gionis, J. Rivory, and S. Flandrois. Liquid crystalline organic conductors. *J. Phys.* **1983**, *44(C3)*, 1201–1206.

57. C. V. Yelamaggad, A. S. Achalkumar, D. D. S. Rao, M. Nobusawa, H. Akutsu, J. Yamada, and S. Nakatsuji. The first examples of discotic radicals: columnar mesomorphism in spin-carrying triphenylenes. *J. Mater. Chem.* **2008**, *18*, 3433–3437.

58. S. Castellanos, F. Lopez-Calahorra, E. Brillas, L. Juliá, and D. Velasco. All-organic discotic radical with a spin-carrying rigid-core showing intracolumnar interactions and multifunctional properties. *Angew. Chem. Int. Ed.* **2009**, *48*, 6516–6519.

59. H. G. Aurich. Nitroxides. In: S. Patai and Z. Rappoport,Eds., *Nitrones, Nitronates and Nitroxides*, John Wiley and Sons, New York, 1989.

60. F. A. Neugebauer. Hydrazidinyl radicals: 1,2,4,5-tetraazapentenyls, verdazyls, and tetrazolinyls. *Angew. Chem. Int. Ed.* **1973**, *12*, 455–464.

61. N. Azuma, K. Ishizu, and K. Mukai. Magnetic-properties of verdazyl free-radicals. VII. π-Bridged verdazyl biradicals with triplet ground-state. *J. Chem. Phys.* **1974**, *61*, 2294–2296.

62. Y. Miura. Synthesis and chemical behaviors of persistent thioaminyl and related radicals. *Rev. Heteroatom Chem.* **1990**, *3*, 211–232.

63. S. Goldschmidt and K. Renn. Bivalent nitrogen: α, α-diphenyl-beta-trinitrophenylhydrazyl (IV. Announcement on amine oxidation). *Berichte der Deutschen chemischen Gesellschaft* **1922**, *55*, 628–643.

64. K. Mukai, K. Ueda, K. Ishizu, and Y. Deguchi. ESR studies of the anomalous phase transition in crystalline galvinoxyl radical. *J. Chem. Phys.* **1982**, *77*, 1606–1607.

65. K. Awaga, T. Saugano, and M. Kinoshita. Ferromagnetic intermolecular interactions in a series of organic mixed-crystals of galvinoxyl radical and its precursory closed shell compounds. *J. Chem. Phys.* **1986**, *85*, 2211–2218.

66. O. Armet, J. Veciana, C. Rovira, J. Riera, J. Castaner, J. Molins, J. Rius, C. Miravitlles, S. Olivella, and J. Brichfeus. Inert carbon free-radicals. 8. Polychlorotriphenylmethyl radicals: synthesis, structure, and spin-density distribution. *J. Phys. Chem.* **1987**, *91*, 5608–5616.

67. N. Ikuma, R. Tamura, S. Shimono, Y. Uchida, K. Masaki, J. Yamauchi, Y. Aoki, and H. Nohira. Ferroelectric properties of paramagnetic, all-organic, chiral nitroxyl radical liquid crystals. *Adv. Mater.* **2006**, *8*, 477–480.

68. N. Ikuma, R. Tamura, K. Masaki, Y. Uchida, S. Shimono, J. Yamauchi, Y. Aoki, and H. Nohira. Paramagnetic FLCs containing an organic radical component. *Ferroelectrics* **2006**, *343*, 119–125.

69. Y. Uchida, R. Tamura, N. Ikuma, S. Shimono, J. Yamauchi, Y. Aoki, and H. Nohira. Synthesis and characterization of novel all-organic liquid crystalline radicals. *Mol. Cryst. Liq. Cryst.* **2007**, *479*, 213–221.

70. Y. Uchida, R. Tamura, N. Ikuma, J. Yamauchi, Y. Aoki, and H. Nohira. Synthesis and characterization of novel radical liquid crystals showing ferroelectricity. *Ferroelectrics* **2008**, *365*, 158–169.

71. Y. Uchida, R. Tamura, N. Ikuma, S. Shimono, J. Yamauchi, Y. Shimbo, H. Takezoe, Y. Aoki, and H. Nohira. Magnetic-field-induced molecular alignment in an achiral liquid crystal spin-labeled by a nitroxyl group in the mesogen core. *J. Mater. Chem.* **2009**, *19*, 415–418.

72. C. Kumar, Ed., *Magnetic Nanomaterials*, Wiley-VCH, Weinheim, 2009.
73. S. T. Lagerwall. *Ferroelectric and Antiferroelectric Liquid Crystals*, Wiley-VCH, Weinheim, 1999.
74. R. Kogo, F. Araoka, Y. Uchida, R. Tamura, K. Ishikawa, and H. Takezoe. Second harmonic generation in a paramagnetic all-organic chiral smectic liquid crystal. *Appl. Phys. Express* **2010**, *3*, 041701.

CHAPTER 4

Ferroelectric Liquid Crystals for Nonlinear Optical Applications

YONGQIANG ZHANG

Micron Technology, Inc., Longmont, Colorado, USA

JESÚS ETXEBARRIA

Department of Condensed Matter Physics, University of the Basque Country, Bilbao, Spain

4.1 INTRODUCTION

4.1.1 Overview of Nonlinear Optical Materials (NLO) and Electro-Optic (EO) Materials

NLO materials have become increasingly indispensable to today's EO technology. Electro-optics involve these two important technologies (electronics and photonics), and the interdisciplinary field requires expertise from many fields such as mathematics, physics, chemistry, material science, electrical, and optical engineering. Electrons perform information functions in electronic devices, while photons are capable of performing the same functions in photonic devices at much faster speed but without production of too much heat. EO devices provide a means of converting information from the electronic domain to the photonic domain or vice versa. They have been widely used in telecommunication systems, and are particularly attractive in emerging optical computing applications.

Since the discovery of second harmonic generation (SHG) in inorganic materials in 1961 [1], a variety of inorganic crystalline materials including lithium niobate ($LiNbO_3$), potassium niobate ($KNbO_3$), potassium titanyl phosphate ($KTiOPO_4$), and potassium dihydrogen phosphate (KH_2PO_4), etc., have been successfully developed. Today's EO and NLO commercial markets are completely dominated by inorganic crystalline materials (mainly lithium niobate) because some of them have been found as superior NLO and EO materials for a variety of devices including modulators, parametric oscillators, optical switches, etc. Lithium niobate is today's benchmark

Liquid Crystals Beyond Displays: Chemistry, Physics, and Applications, Edited by Quan Li.
© 2012 John Wiley & Sons, Inc. Published 2012 by John Wiley & Sons, Inc.

in commercial EO technology because of its excellent performance in telecommunication applications. While inorganic crystals have the advantages of being well characterized, they have evident disadvantages such as shock sensitivity, high cost, and poor processability.

Compared with inorganic crystalline materials, organic materials show superior versatility, flexibility, durability, facile fabrication, and processability. It is possible to design organic materials using molecular engineering and thereby tailor the properties for a specific NLO and EO application because of the availability of a very wide range of chemical structural modifications in organic molecules. Moreover, organic materials show much smaller reduced half-wave voltages ($v_\pi = \lambda/(n^3 r_{\text{eff}})$, n is the refractive index) and much larger figures-of-merit ($n^7 r_{\text{eff}}^2/\varepsilon$ for EO modulators and $n^3 r_{\text{eff}}/\varepsilon$ for photorefractive applications) than inorganic materials because of their large effective EO coefficients, (r_{eff}) and small dielectric constants (ε). For example, the figure-of-merit ($n^3 r_{\text{eff}}/\varepsilon$) for a typical organic single crystal (optimized stilbene) is 5300 pm/V, while for inorganic lithium niobate it is only 11 pm/V [2]. There are also concerns for organic NLO materials, such as environmental stability, photochemical stability, mechanical strength, and performance at low and high temperatures.

Significant and dramatic advancement has been made for organic NLO materials in past decades. The field of organic NLO materials has been reviewed by many authors in numerous excellent review papers [3–15] and book chapters [16, 17]. Enormous data are available and meaningful insights have been gained through a comprehensive range of reviews on newly emerging organic NLO materials. On the basis of their nature, organic NLO materials are classified into six different categories: (i) single crystals [12, 14], (ii) metal-organic hybrids [5, 9, 12], (iii) Langmuir–Blodgett (LB) films [16, 17], (iv) self-assembled systems [9–12], (v) liquid crystals, and (vi) poled polymers [3, 4, 6, 7, 13, 15]. Each type of material has its own advantages and disadvantages.

Organic single crystals consisting of organic conjugated molecules carrying strong electron donors and electron acceptors exhibit very large NLO coefficients and excellent figures-of-merit, but they are mechanically soft, difficult to design and process with precision, and almost impossible to process into optical quality films. Growing large-size single crystals is usually difficult. LB films and self-assembled multilayers exhibit very large SHG activity and possess high degree of molecular orientation and precise control of film thicknesses and layer architectures. However, these NLO materials, particularly LB films, are soft and have very unstable structures. Although sometimes self-assembled multilayers are also included into metal-organic hybrids, herein metal-organic hybrids denote only organometallic complexes including compounds with covalent bonds between metal atoms and other elements or with coordination bonds between metal ions and organic ligands. These types of complexes include at least one metal atom or ion in their molecules and exhibit large molecular hyperpolarizabilities (β) owing to the existence of two special types of charge-transfer transitions, metal-to-ligand and ligand-to-metal. The incorporation of transition metals into organic molecules favors crystallization, thereby facilitating to grow large-size single crystals of organometallic compounds. Like other organic

chromophore compounds, organometallics incorporating strong chromophores can be used in five other categories.

Poled polymers [3, 4, 6] are among the most important organic NLO materials, and their macroscopic nonlinearities are generally realized by the electric field poling technique. To maintain a stable polar alignment in the thermodynamically unstable poled state, it is essential to utilize either high glass-transition temperature (T_g) polymers with NLO chromophores as pendants or cross-linked polymers with NLO chromophores locked in the polymer network. They can be easily processed into thin films by spin-coating and be readily integrated with silicon very-large-scale integration (VLSI) technology. Over the past decade, considerable effort and progress have been made on these materials from the viewpoint of EO activity, with current values of EO coefficients up to approximately 500 pm/V and of optical losses under 2 dB/cm. Thermal and photochemical stability have been also greatly improved. However, how to make one material possess all of the aforementioned properties remains problematic, let alone the challenge of addressing other properties such as solubility, shrinkage, adhesion, and mechanical stress.

Liquid crystals (LCs), particularly ferroelectric liquid crystals (FLCs) [18] as a special type of organic NLO material, are very appealing for NLO applications. FLCs possess thermodynamically stable intrinsic polar order, and their polar direction can be controlled via ferroelectric (FE) switching under an external electric field, enabling fabrication of more complex devices. Furthermore, as in LC displays, FLC materials can be readily integrated with silicon VLSI technology, allowing for hybrid technologies utilizing the FLCs' NLO properties.

4.1.2 Scope of This Chapter

Although LCs have been known to scientists for over one hundred years, it was only in the late 1960s that LCs began to be used in display applications. Today LCs have proven extremely valuable in commercial display products such as TVs, automobile gauges, road signs, watches, and computer displays. It was not until 1980s that LCs started to be recognized as potential NLO materials. For many decades, predominant LC molecules have been variants on simple rod shapes (Figure 4.1a). Several new types of LC molecules have been developed in the past three decades, such as disc molecules (Figure 4.1b) [19], bent-core (BC) (banana-shaped) molecules (Figure 4.1c) [20], and H-shaped twin molecules (Figure 4.1d) [21], which exhibit novel and potentially valuable properties that conventional rod-shaped calamitic LCs cannot possess. For instance, banana liquid crystals and H-shaped dimesogens exhibit larger NLO coefficients than rod-shaped NLO FLCs, and discotic LCs have been widely used for organic photovoltaics and other organic semiconductor devices [22].

In this chapter we focus on the NLO applications of LCs, particularly FLCs. The early developments on rod-shaped FLCs and their SHG and Pockels effects were reviewed in several papers and book chapters [23–26]. Herein we focus on fascinating new developments on H-shaped dimesogens and bent-core mesogens. We will also discuss miscellaneous NLO LC materials and their ferroelectricity-related

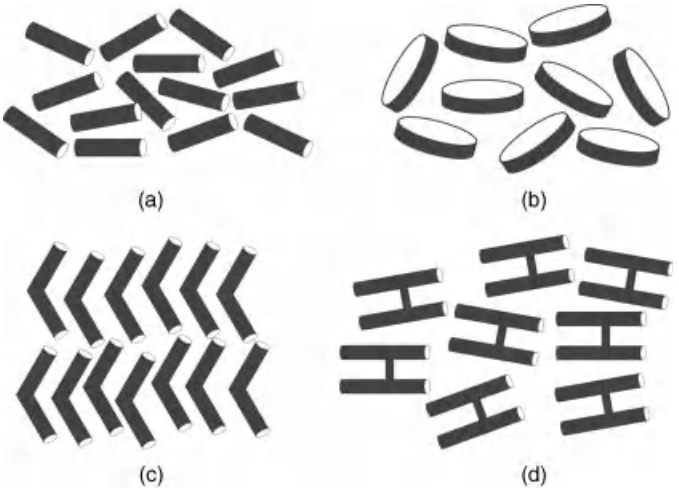

FIGURE 4.1 Different shaped liquid crystals: (a) conventional rod-shaped LCs, (b) disc-shaped LCs, (c) banana-shaped LCs, and (d) H-shaped twin LCs.

behaviors. Some important rod-shaped FLCs and their polymeric versions will be included in this chapter for comparison with other types of NLO FLC materials. The cross-linked polymeric versions of rod-shaped FLCs and their NLO applications will be highlighted since these pyroelectric polymers formed via photo-induced *in situ* polymerization are thermally and mechanically stable enough to be used for EO devices (e.g., waveguides). Cross-linked polymerization in these materials helps maintain the macroscopic nonlinearity via locking the chromophores into polymer networks. It should be pointed out that this chapter is by no means comprehensive and does not cover all the known FLC materials. Our idea is instead to give the readers a summary of this area and also an overview of the exciting new advances in NLO FLCs and their potential industrial applications by selectively choosing some targets. Owing to the limitation of the available literature and our knowledge, we apologize to all those who are not mentioned in this chapter, but have made contributions to the research and development of this subfield.

4.2 FUNDAMENTALS

4.2.1 Ferroelectricity in LCs

Ferroelectrics are a subgroup of pyroelectrics which show a non-vanishing spontaneous polarization at zero electric field. The distinguishing feature between a ferroelectric and a pyroelectric is that the direction of the spontaneous polarization (P) for a ferroelectric can be switched by an external electric field (E), yielding a typical single hysteresis loop (Figure 4.2) [27]. Both ferroelectrics and pyroelectrics are useful for NLO and other applications (e.g., ferroelectric RAM for computers [28]).

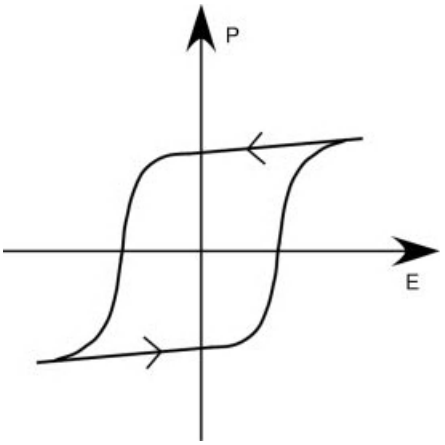

FIGURE 4.2 A typical single hysteresis loop for ferroelectrics.

Liquid crystals, as a state of matter between liquid and solid, uniquely combine both long range order (as in crystals) and mobility (as in liquids) in the same material. The order leads to the anisotropy of LC molecules on both molecular and supermolecular levels, and the mobility enables LC molecules to respond easily to external stimuli. LCs self-assemble into macroscopically ordered structures which can be classified into four major categories based on the orientational or positional orders of their molecules: nematic (N), smectic (Sm), columnar (Col), and cubic mesophases. Nematic mesophases have only long range orientational order, smectic mesophases exhibit one-dimensional (1D) positional order and form 2D layered structures, columnar mesophases (also called modulated layer mesophases) possess 2D positional order and form tube-like 1D structures, and cubic mesophases [29, 30] have 3D-ordered structural organization. Note that the shapes of the molecules are not exactly related to the types of mesophases formed. For example, linear rod-shaped (e.g., polycatenar mesogens [31]), disc-shaped molecules [32], and molecules without specific shape or with a spherical shape [33, 34] all can organize as nematic, smectic, columnar, and 3D-ordered mesophases. The most common smectic phases formed by rod-shaped LC molecules are the smectic A (SmA) phase with their molecular long axes (i.e., the director) parallel to the layer normal, and the smectic C (SmC) phase with the director tilted with respect to the layer normal.

The incorporation of chirality into LC systems leads to the formation of helical superstructures in nematic phases (e.g., cholesteric phases, N*) and tilted smectic phases (e.g., SmC* phases) and can also induce whole new classes of chiral phases such as blue phases (BP*), twist grain boundary phases (TGB*), and 3D-ordered mesophases [35]. The non-tilted chiral SmA* phase exhibits the electroclinic effect under an external electric field, while chirality induces polar order in the tilted chiral smectic LC phases (e.g., SmC* and SmC_A* phases). The two tilted chiral phases possess spontaneous polarizations and show FE and antiferroelectric (AF) switching under surface-stabilized conditions upon the application of an external electric field. Hence, the SmC* phase is also called the ferroelectric phase, while the SmC_A* phase

is similarly called the antiferroelectric phase. There also exist some intermediate chiral subphases (denoted as $SmC_{1/n}{}^*$, $n > 2$) between ferro- and antiferroelectric phases [36], which exhibit ferrielectric switching behavior under surface-stabilized conditions with the applied electric field and are therefore called ferrielectric phases.

FLCs are a natural and compelling candidate for NLO and EO applications due to the lack of inversion symmetry. Although the helix causes the vanishment of the spontaneous polarization for bulk materials at zero field, the FLCs exhibit bistable FE switching under surface-stabilized conditions. Traditional FLCs are composed of chiral rod-shaped molecules that possess a net electric-dipole moment perpendicular to the director and parallel to the layer plane. Because of the way in which molecules pack together, the minimum energy state is one in which all the molecules point on average in the same direction locally. However, dipole–dipole interactions in bulk materials favor the escape of macroscopic polarity by the formation of helical supermolecular structures. Such bulk materials are not so interesting for NLO applications. The discovery of the surface-stabilized ferroelectric liquid crystal (SSFLC) by Clark and Lagerwall [37] triggered not only the development of FLC-based displays but also the research of FLCs as NLO materials. It should be noted that FLC materials can be generated either from the pure chiral materials (e.g., one chiral compound or a mixture of several chiral compounds) possessing the SmC^* phase or by doping an achiral SmC host with a small percentage of one or more rod-shaped chiral compounds.

In a surface-stabilized cell with a bookshelf geometry, the FLC molecules self-assemble into parallel layers (Figure 4.3). Within each sheet the director is tilted away from the layer normal by the tilt angle θ that is characteristic of the particular liquid crystal mixture and which depends on temperature. The net molecular dipole moments are within the layers and perpendicular to the director. The FLC molecules can switch on a smectic cone between two stable states upon the application of an electric field, thereby yielding a single hysteresis loop for ferroelectricity (Figure 4.4) [38].

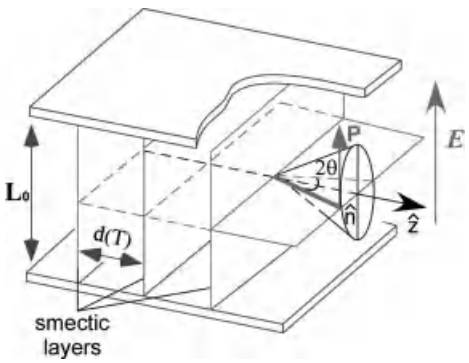

FIGURE 4.3 A bistable FLC cell with a bookshelf geometry showing that the director $\hat{n}$ is tilted away from the layer normal $\hat{z}$ by the tilt angle θ. The net molecular dipole moments P are within the layers and perpendicular to the director. $d(T)$ is the layer spacing.

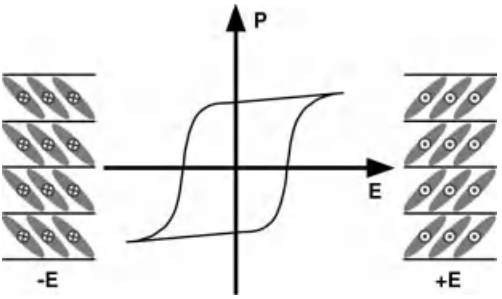

FIGURE 4.4 An ideal bistable FLC cell showing a typical single hysteresis loop (ferroelectricity) and two bistable FE states.

The antiferroelectric liquid crystals (AFLCs) are also important for NLO applications since the AF ground state can be switched to the two FE states, which show NLO activity, under an external electric field. The AFLC (SmC_A^*) phase is monostable and has three important states: one ground-state AF state and two field-induced FE states (Figure 4.5). Therefore, the field-induced switching among the three states exhibits a typical double hysteresis curve with a zero polarization at zero field.

The $SmC_{1/3}^*$ ferrielectric phase in the non-helical model has four FE states, and the field-induced switching yields a triple hysteresis curve (Figure 4.6) with a nonzero spontaneous polarization at zero field. In the bulk materials, the $SmC_{1/3}^*$ phase exhibits a vanishing spontaneous polarization at zero field due to the formation of the helical superstructure [39], which is also similarly found in the SmC^* case. Hence, many bulk LC materials exhibiting the SmC^*, $SmC_{1/3}^*$ or in general $SmC_{1/n}^*$ phases should be precisely called neither ferro- or ferrielectric nor pyroelectric but helielectric [40]. When the electric field is above the threshold for unwinding the helix (i.e., $E > E_{th}$), the spontaneous polarization reappears to enable FE switching on a smectic cone between the two complete FE states.

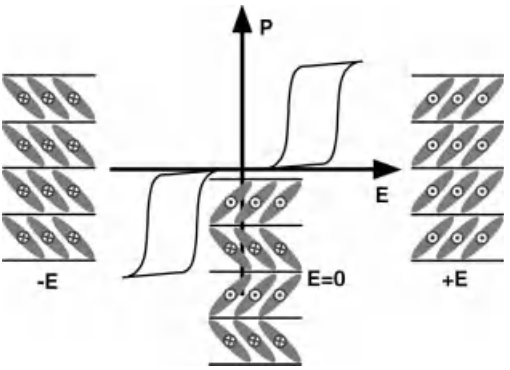

FIGURE 4.5 An ideal surface-stabilized AFLC cell showing a double hysteresis curve (antiferroelectricity), and one ground-state AF state and two FE states.

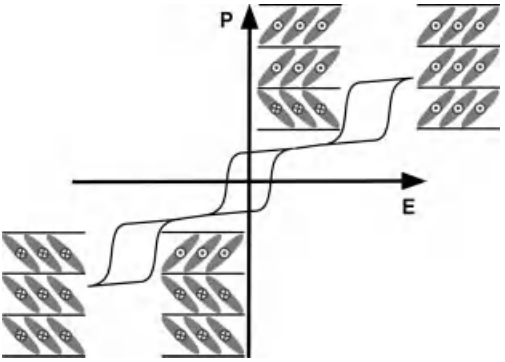

FIGURE 4.6 An ideal surface-stabilized ferrielectric cell showing a triple hysteresis curve (ferrielectricity) and four FE states.

The vanishing spontaneous polarization at zero field in the SmC^* phase should be distinguished from that in the SmC_A^* phase. The former will exhibit non-zero spontaneous polarization (i.e., ferroelectricity) unless the helix forms at zero field, while the latter phase will exhibit zero spontaneous polarization (i.e., antiferroelectricity) whether the helix forms at zero field or not since the opposite dipoles between the adjacent layers cancel each other out. The threshold voltage for the switching of an AFLC is about one order of magnitude larger than that of a FLC. These indicate that ferroelectricity in the SmC^* phase is strongly dependent on cell conditions. A bistable cell enables a SmC^* material to behave as a proper and real FLC (Figure 4.4).

When an FLC, AFLC, or ferrielectric liquid crystal is polymerized *in situ* under their field-induced FE states, macroscopic polar order is locked into cross-linked polymer networks. The removal of the electric field may not influence the macroscopically polar structures of these polymers. However, the high viscosity of the polymers makes it impossible to reverse the spontaneous polarization by applying an external electric field. These polymers, therefore, are pyroelectrics rather than ferroelectrics. They should be precisely called pyroelectric liquid crystal polymers (PLCPs).

We have discussed the importance of chirality to ferroelectricity in LCs. The introduction of chirality, in fact, is not the only way to realize ferroelectricity in LCs. Takezoe and Watanabe stated that it is possible to induce ferroelectricity by reducing the symmetry to C_n or C_{nv} in a LC system [41]. Four different molecular systems were proposed: (i) polar uniaxial nematic LC with $C_{\infty v}$ symmetry, (ii) polar biaxial nematic LC with C_{1v} (C_s) symmetry, (iii) polar uniaxial SmA LC with $C_{\infty v}$ symmetry, and (iv) polar biaxial smectic LC with C_{2v} symmetry. The discovery that achiral bent-core (banana-shaped) molecules form macroscopic polarity by Niori et al. [42] in 1996 supports the feasibility of the fourth molecular system. Most bent-core molecules form AF phases (see Section 4.3.3 for details). Polar ordering was reported in aromatic polyesters exhibiting nematic phases [43], but the high viscosity of the polymers prevents field-driven FE switching. These materials are pyroelectrics rather than ferroelectrics. In contrast, strong SHG at zero field and the reversal of the

polarization under a field were observed in the thermotropic or lyotropic cholesteric phase of a α-helical polypeptide [44], indicating the first proper ferroelectricity in nematic LCs (also see Section 4.3.4).

4.2.2 Microscopic to Macroscopic Nonlinearity

As in other organic materials, the nonlinearity in a bulk FLC material also results from that of individual molecules. The dipole polarization μ of an isolated organic molecule under an external electric field can be written as:

$$\mu = \mu_0 + \varepsilon_0(\alpha_{ij}E_j + \beta_{ijk}E_jE_k + \gamma_{ijkl}E_jE_kE_l + \cdots) \tag{4.1}$$

where μ_0 is the permanent dipole moment of the molecule, α_{ij} is the linear molecular polarizability, and β_{ijk} and γ_{ijkl} are the first and second hyperpolarizabilities, respectively. The subscripts i, j, and k refer to a molecule-based coordinate system, and E is the applied electric field. Symmetry requires that all terms of even order in the electric field vanish for a molecule with an inversion center.

The macroscopic polarization P of a bulk nonlinear material under an external electric field E can be expressed as:

$$P = P_0 + \varepsilon_0(\chi^{(1)}_{IJ}E_J + \chi^{(2)}_{IJK}E_JE_K + \chi^{(3)}_{IJKL}E_JE_KE_L + \cdots) \tag{4.2}$$

where P_0 is the spontaneous polarization, and $\chi^{(n)}$ is the nonlinear optical susceptibility of nth order. IJK is the coordinate system of the bulk material. As in the molecular case, a bulk material with an inversion center possesses zero even-order susceptibilities. This also indicates that a centrosymmetric bulk material does not exhibit second-order susceptibility even if the molecules constituting it do possess second-order non-zero hyperpolarizability β_{ijk}. Therefore, enabling bulk materials to possess macroscopic second-order nonlinearities has an indispensable requisite that their non-centrosymmetric nonlinear molecules are arranged in such a manner that the bulk materials do not have a center of symmetry.

The NLO coefficient d_{IJK} is an important parameter in the case of SHG. d_{IJK} is related to $\chi^{(2)}$ by:

$$d^{(-2\omega,\omega,\omega)}_{IJK} = \frac{1}{2}\chi^{(-2\omega,\omega,\omega)}_{IJK} \tag{4.3}$$

Building a relationship between microscopic (β) and macroscopic (d) nonlinear properties helps not only understand the measured values for bulk organic materials but also design new types of molecules and bulk materials. According to the most simple oriented-gas model [45], all contributions to the optical nonlinearity due to intermolecular interactions are neglected except for local-field corrections, and therefore, only intramolecular interactions are considered. Thus a simple relation between the NLO coefficients d_{IJK} for frequency doubling and molecular hyperpolarizabilities β_{ijk} is described as:

$$d_{IJK} = N f_I^{(2\omega)} f_J^{(\omega)} f_K^{(\omega)} \sum_{ijk}^{3} \cos\theta_{Ii} \cos\theta_{Jj} \cos\theta_{Kk} \beta_{ijk} \tag{4.4}$$

where θs are the angles between molecular charge-transfer axes ijk and the reference system IJK, respectively, and the f factors are local-field corrections at different frequencies. Note that this equation assumes that there is only one symmetry equivalent position in the unit cell.

The f factors at different frequencies are often calculated within the simple approximation of the Lorentz model:

$$f_I^{(2\omega,\omega)} = \frac{(n_I^{(2\omega,\omega)})^2 + 2}{3} \tag{4.5}$$

The principal indices n_I are for light with frequencies 2ω and ω.

According to the orientated gas model [45], the EO coefficients r_{IJK} for the Pockels effect are similarly related to the molecular hyperpolarizabilities β_{ijk} through:

$$r_{IJK} = -N \frac{4}{n_I^2 n_J^2} f_I^{(\omega)} f_J^{(\omega)} f_K^{(0)} \sum_{ijk}^{3} \cos\theta_{Ii} \cos\theta_{Jj} \cos\theta_{Kk} \beta_{ijk} \tag{4.6}$$

The f factors are similarly calculated by:

$$f_I^{(0)} = \frac{\varepsilon_I + 2}{3} \tag{4.7}$$

where ε_I is the dielectric constant along the principal I axis. Here the β terms are calculated for the EO process instead of SHG.

Note that the hyperpolarizabilities in Eqs. (4.4) and (4.6) are different ($\beta = \beta(-2\omega;\omega,\omega)$ in Eq. (4.4) and $\beta = \beta(-\omega;\omega,0)$ in Eq. (4.6)), though both are related to each other. In the simplest approach (two-level model) [45], the hyperpolarizabilites for SHG and EO effect are given by:

$$\beta(-2\omega;\omega,\omega) = \frac{\beta_0}{(1 - 4(\lambda_0^2/\lambda^2))(1 - (\lambda_0^2/\lambda^2))} \tag{4.8}$$

$$\beta(-\omega;\omega,0) = \frac{(3 - (\lambda_0^2/\lambda^2))\beta_0}{3(1 - (\lambda_0^2/\lambda^2))^2} \tag{4.9}$$

where

$$\beta_0 = \frac{3\mu_{\mathrm{eg}}^2 \lambda_0^2 \Delta\mu}{2\varepsilon_0 h^2 c^2} \tag{4.10}$$

Here, μ_{eg} is the element of matrix of the electric-dipole operator between the excited and ground state, λ_0 is the charge-transfer transition wavelength, $\Delta\mu$

is the difference between the excited and ground-state dipole moments, and ε_0 is the vacuum permittivity. Note that β_0 for similar chromophores can be readily computed by using Eq. (4.8) and the published data of $\beta = \beta(-2\omega; \omega, \omega)$, measured by Cheng et al. [46] at the fundamental wavelength of $\lambda = 1907$ nm using electric field induced second harmonic (EFISH) technique.

These authors [46] reported the hyperpolarizabilities of more than one hundred compounds that were carefully measured in solution using the EFISH technique at a fundamental wavelength of 1907 nm. They found a remarkable dependence of the experimental β values and the charge-transfer transition wavelength λ_0. For a given type of molecule (e.g., disubstituted benzene or stilbene derivatives), β_0 depends mainly on λ_0 without any further reference to the details of the donor and acceptor. Figure 4.7 shows β_0 as a function of the resonance wavelength (λ_0) in solution for some benzenes and stilbenes. These two families are the prototypical NLO chromophores with one and two aromatic rings and have already been incorporated into many LC molecules.

4.2.3 SHG and Pockels Effect in LCs

4.2.3.1 SHG Measurements SHG is a NLO process in which photons in a laser beam interacting with a material generate new photons with twice the frequency. SHG is, therefore, called frequency doubling. In addition to its use in high-resolution imaging in biological and medical science, another important

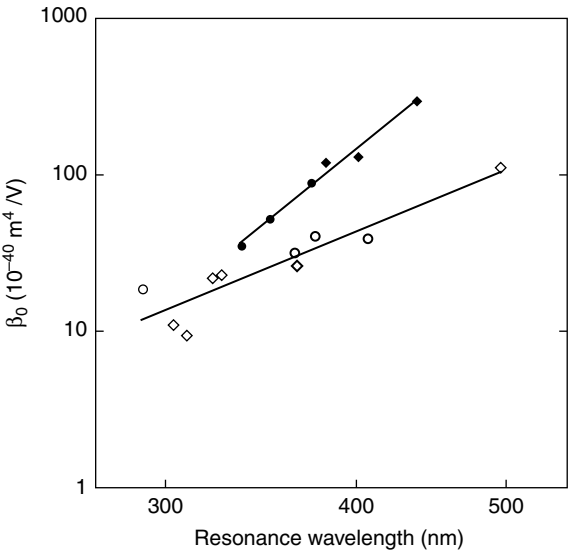

FIGURE 4.7 Log–log plot of the dependence of the zero-frequency hyperpolarizability on the resonance wavelength in solution for disubstituted benzenes (open circles) and stilbenes (closed circles). The straight lines are empirical relations between β_0 and λ_0, with $\beta_0 = 2.01 \times 10^{-9}\lambda_0^{3.97}$ for the benzenes and $\beta_0 = 6.19 \times 10^{-19}\lambda_0^{7.83}$ for the stilbenes. β_0 is expressed in 10^{-40} m^4/V and λ_0 in nm. Note that the β_0 data are adopted from reference [46].

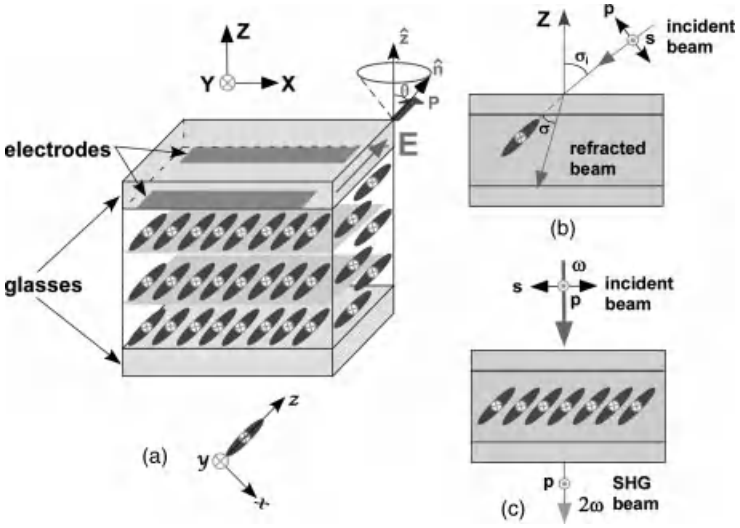

FIGURE 4.8 Schematic illustration of (a) a homeotropically aligned FLC cell with the spontaneous polarization P parallel to the polar axis which is the Y-axis in the XYZ coordinate system and the y-axis in the xyz molecular coordinate system, (b) SHG experiments using phase matching method, and (c) SHG experiments using Maker fringe method at normal incidence. In (b), the phase matching is achieved by rotating the cell around the polar axis, θ is the tilt angle, σ_i is the incident angle, and σ is the angle between the optical propagation direction and the FLC molecule director $\hat{n}$. (*See the color version of this figure in Color Plates section.*)

application in industry is to generate a green laser with the wavelength of 532 nm using the readily available Nd:YAG laser with the wavelength of 1064 nm.

For a FLC material with a C_2 symmetry axis along the polar Y-axis direction (Figure 4.8a), the only non-zero components of the contracted susceptibility **d** tensor in the XYZ coordinate system are given by

$$\mathbf{d} = \begin{pmatrix} 0 & 0 & 0 & d_{14} & 0 & d_{16} \\ d_{21} & d_{22} & d_{23} & 0 & d_{25} & 0 \\ 0 & 0 & 0 & d_{34} & 0 & d_{36} \end{pmatrix} \tag{4.11}$$

The number of independent d_{ij} coefficients is reduced to four (d_{22}, d_{21}, d_{23}, and d_{14}) with $d_{21} = d_{16}$, $d_{23} = d_{34}$, and $d_{14} = d_{25} = d_{36}$ according to Kleinman symmetry. For a material with a C_{2v} point group, only three independent coefficients (d_{22}, $d_{21} = d_{16}$, $d_{23} = d_{34}$, and $d_{14} = d_{25} = d_{36} = 0$) remain (see the SmC_aP_F structure with a C_{2v} axis symmetry in Section 4.3.3) upon the application of Kleinman symmetry.

To determine the d_{ij} coefficients, SHG is measured for different combinations of polarizations of the fundamental and second harmonic lights. Measurements are generally performed in homeotropic cells. A horizontal electric field, parallel to the cell surface, is usually applied to align this type of cell (Figure 4.8a). Different interaction lengths are employed because the SHG signal also depends on the phase

mismatch between the lights at 2ω and ω [47]. To change the interaction length, the cell can be measured at different angles of incidence (Figure 4.8b), or different cells with various thicknesses can be used at normal incidence (Figure 4.8c). Very often FLCs present the favorable condition of phase matching, when the SHG intensity is the largest [48]. Typically this happens for an *ee-o* process (i.e., generation of a 2ω photon with ordinary (o) polarization from two ω photons with extraordinary (e) polarization). The effective susceptibility d_{eff} for this process is expressed as

$$d_{eff} = d_{21}\cos^2\sigma + d_{23}\sin^2\sigma + d_{25}\sin(2\sigma) \tag{4.12}$$

where σ is the angle between the FLC director and the refracted beam (Figure 4.8b) at which the phase matching condition is achieved.

For a FLC material possessing strong absorption, the data process is cumbersome, and the approach proposed by Herman and Hayden for absorbing materials is followed [49].

In addition to the above measurements in homeotropic cells, the d_{ij} coefficients can be also measured in planar aligned cells with quasi-bookshelf (QBS) geometry, where the smectic layers are essentially perpendicular to the glass surface [50].

4.2.3.2 Pockels Effect Measurement The Pockels effect, also called Pockels EO effect, consists in the change of the refractive indices of a given material upon the application of an electric field. The Pockels effect depends on the material's macroscopic susceptibility $\chi^{(2)}$. The induced index change varies linearly with the applied electric field. Pockels cells are widely used in a variety of scientific and technological areas, particularly in fiber-optic communications.

For a FLC material with a C_2 symmetry axis along the polar *Y*-axis direction (Figure 4.8a), the only non-zero components of the **r** tensor in the *XYZ* coordinate system are given by

$$\mathbf{r} = \begin{pmatrix} 0 & r_{12} & 0 \\ 0 & r_{22} & 0 \\ 0 & r_{32} & 0 \\ r_{41} & 0 & r_{43} \\ 0 & r_{52} & 0 \\ r_{61} & 0 & r_{63} \end{pmatrix} \tag{4.13}$$

The number of independent r_{ij} coefficients is reduced to four (r_{22}, r_{12}, r_{32}, and r_{41}) with $r_{12} = r_{61}$, $r_{32} = r_{43}$, and $r_{41} = r_{52} = r_{63}$ if Kleinman symmetry is fulfilled. For a material with a C_{2v} point group, only three independent coefficients (r_{22}, $r_{12} = r_{61}$, $r_{32} = r_{43}$, and $r_{41} = r_{52} = r_{63} = 0$) are left upon the assumption of Kleinman symmetry.

Although the Pockels effect has been extensively investigated in polymeric materials, and many methods are developed to measure r_{ij} coefficients for poled polymeric films [2], reports on FLC materials including PLCPs are relatively limited. Hult and co-workers adopted a crossed-polarizer method to measure the EO

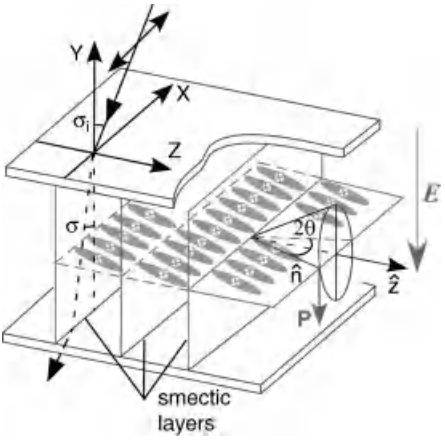

FIGURE 4.9 A surface-stabilized FLC cell with a bookshelf structure utilized for EO measurements. θ is the tilt angle, σ_i is the incident angle, σ is the angle of refraction, the Z-axis is parallel to the layer normal, the incident polarized light propagates in the XY plane, and the polar direction is parallel to the electric field with both of them perpendicular to the cell surface.

coefficient $(r_{22} - r_{12})$ of a PLCP in a surface-stabilized FLC cell with a bookshelf geometry (Figure 4.9) [51].

4.3 NLO AND EO LC MATERIALS

4.3.1 Rod-Shaped NLO LCs

4.3.1.1 LC Monomers The discovery that all chiral tilted smectic phases exhibit a spontaneous polarization by R.B. Meyer and co-workers [52], followed by a ground-breaking work on SSFLCs [37], led to extensive investigations of SmC* materials. The first NLO work in FLCs was reported in 1981 by Vtyurin et al. [53] who performed the SHG measurement of a Schiff-base FLC, **DOBAMBC**. Phase matched SHG work on **DOBAMBC** was reported in 1985 by Shtykov et al. [54], giving the effective coefficient of $d_{\text{eff}} = 0.0008$ pm/V (Table 4.1). Six years later Ozaki et al. [55] confirmed the above measurement and also found that a commercial FLC mixture including phenylpyrimidine-based components, **ZLI3654**, exhibited a d_{eff} value of 0.005 pm/V, almost one order of magnitude larger than that of **DOBAMBC**. Although Liu et al. [56] reported that another commercial FLC mixture having phenyl benzoates, **SCE9**, exhibited a similar d_{eff} value of 0.0037 pm/V, it was the first report to measure all four individual d_{ij} coefficients of a FLC. An interesting FLC with a chiral chloro group, **3M2CPOOB**, was found to have similar NLO coefficients to **SCE9** [57]. Since the aforementioned FLC materials contain neither an electron donor nor an electron acceptor along the FLC polar axis in their molecules, small NLO coefficients are expected.

According to the oriented-gas model (see Eqs. (4.4) and (4.6)), the NLO and EO coefficients of materials are closely related to the molecular hyperpolarizabilities.

TABLE 4.1 Representative rod-shaped NLO FLC monomers[a] and their properties

FLCs	P_s (nC/cm^2)	d_{ij} (pm/V)
DOBAMBC 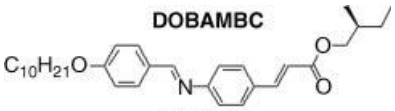	−3 [58]	$d_{eff} = 0.0008$ [54] $d_{eff} = 0.0011$ [55]
ZLI3654	−29 [58]	$d_{eff} = 0.005$ [55]
SCE9	+33.6 [58]	$d_{eff} = 0.0037$ [56] $d_{21} = 0.0026$ $d_{22} = 0.027$ $d_{23} = 0.073$ $d_{25} = 0.0009$
3M2CPOOB 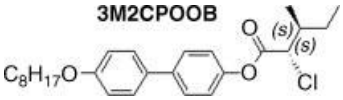	−200 [57]	$d_{eff} = 0.01$ [55] $d_{21} = 0.021$ [57] $d_{22} = 0.009$ $d_{23} = 0.053$ $d_{25} = 0.023$
W314 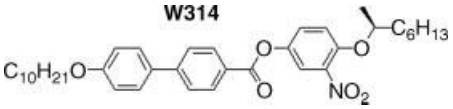	−420 (60°C) −560 (25°C) [58]	$d_{eff} = 0.23$ [61] $d_{21} = 0.08$ $d_{22} = 0.63$ $d_{23} = 0.63$ $d_{25} = 0.16$
Roche1 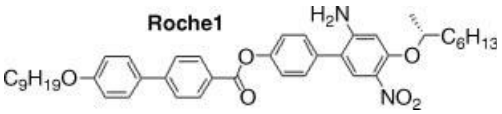	350 (120°C) 750 (50°C) [62]	$d_{eff} = 0.78$ [62] $d_{21} = 0.13$ $d_{22} = 5.0$ $d_{23} = 1.46$ $d_{25} = 0.49$

[a] The chirality (R or S configuration in the chiral centers) of the FLC molecules determines the sign of polarizations and is ambiguous in many papers, and we give the chrality of these molecules unambiguously according to the original literature.

The increase of the molecular hyperpolarizability will definitely enhance the NLO and EO coefficients if materials have similar polar order parameters. The factors influencing the molecular hyperpolarizability have been well established for organic chromophore materials: (i) charge separation between the donor and acceptor of a molecular chromophore, and (ii) the distance between the charge-separated species. To enhance the molecular hyperpolarizability of a FLC, incorporation of a strong chromophore, which carries both a strong donor and a strong acceptor and has two of them bridged by a highly π-conjugated linkage, into the FLC molecules along the polar direction instead of the director orientation is necessary. Such structural modifications without killing the SmC* phase, particularly in rod-shaped molecules, are a big challenge.

One of the most important NLO FLCs, (o-nitroalkoxy)phenyl 4′-alkoxylbiphenyl-4-carboxylate (**W314**), was successfully synthesized in 1991 by the Walba's group [58], on the basis of careful analysis of the Boulder Model for the polar order in FLCs and elegant design of molecules [59, 60]. **W314** possesses a spontaneous polarization ($-560\,\mathrm{nC/cm^2}$ at room temperature) [58], and SHG measurements exhibited the d_{eff} value of 0.23 pm/V with the largest coefficients of $d_{22} = d_{23} = 0.63$ pm/V [61]. This is over a 40-fold increase over the d_{eff} coefficient of **ZLI3654**.

It should be mentioned that **W314** does not contain any laterally substituted donor along the polar direction, which may weaken charge separation induced by the strong electron acceptor (NO_2). Realizing that the 4-nitroaniline unit might be a promising NLO functional group possibly incorporated into an FLC molecule along its polar direction, Schmitt et al. designed and synthesized a four-ring compound (**Roche1**) including both a laterally substituted amino group and a nitro group to create a strong NLO chromophore perpendicular to the molecular long axis. **Roche1** exhibited a phase sequence of *Cr-SmC*-SmA*-Iso* and the largest spontaneous polarization ($350\,\mathrm{nC/cm^2}$ at 120°C and $750\,\mathrm{nC/cm^2}$ at 50°C) ever reported for rod-shaped NLO FLCs [62]. SHG measurements of **Roche1** exhibited the largest coefficient of $d_{22} = 5.0$ pm/V reported for conventional rod-shaped FLCs. These values indicate that **Roche1** molecules show a perfect combination of chirality, NLO activity, and SmC* mesogenicity. Other reports on the SHG of rod-shaped FLCs existed [63–66] but the measured NLO coefficients were relatively smaller than those in **W314** and **Roche1**.

As shown in Table 4.1, the NLO coefficient from **DOBAMBC** to **Roche1** increased by about five thousand times because the 4-nitroaniline unit was incorporated into the molecules of **Roche1** along its polar direction. In contrast, although **DOBAMBC** possesses a highly conjugated chromophore along the molecular long axis, its NLO coefficient was extremely small. This clearly indicates that the incorporation of a chromophore along the polar direction is essential to achieve strong NLO strength. Note that an FLC with a large spontaneous polarization does not always show large NLO coefficients (**SCE9** vs. **3M2CPOOB**), because the spontaneous polarization is related to the molecular dipole, while the NLO coefficients depend on the molecular hyperpolarizability. For FLCs with small NLO coefficients, the d_{22} coefficients along the polar direction are smaller than the d_{23} coefficients, indicating the absence of functional groups with strong hyperpolarizabilities along their polar direction. This further supports the importance of a strong chromophore along the polar direction in FLC molecules.

4.3.1.2 LC Polymers One way to improve the thermal and mechanical properties of FLC monomers is to build polymers from them. The improvement in the thermal and mechanical stability can be useful for NLO applications.

FLC polymers can be classified into three categories: side-chain polymers, main-chain polymers, and cross-linked polymers. Zentel et al. [67] reported the first side-chain FLC polymers with a methylsiloxane backbone (Table 4.2), which exhibited a spontaneous polarization of $430\,\mathrm{nC/cm^2}$. Based on the modified version of **W314**

TABLE 4.2 Representative LC polymers and their properties

LC Polymers	P_s (nC/cm^2)	d_{ij} or r_{ij} (pm/V)
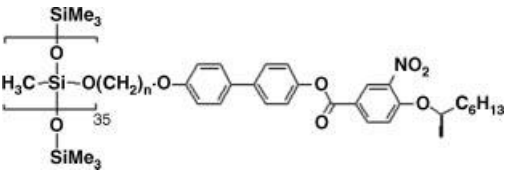	430 [67]	
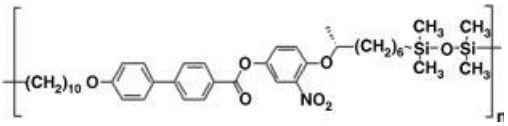	621 (25°C) [68]	
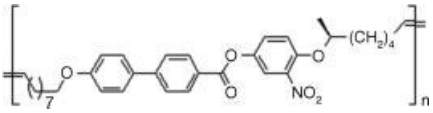	−639 (25°C) [69]	$d_{22} > 0.6$ (est.)
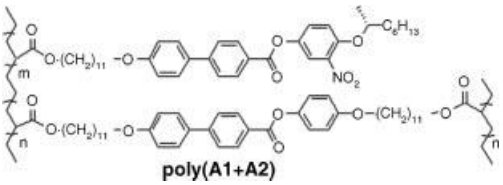 poly(A1+A2)	−25 (75°C) [71]	$r_{22} - r_{12} =$ 0.15 [71] $d_{21} = 0.040$ $d_{22} = 0.15$ $d_{23} = 0.048$ for an analogue [72]
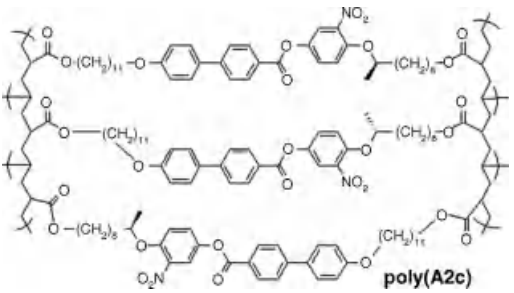 poly(A2c)	−175 for **A2c** [51]	$r_{22} - r_{12} =$ 15–35 [51]

with double bonds incorporated into the two chain termini of **W314**, Walba et al. [68] synthesized a main-chain FLC polymer using a tetramethyldisiloxane unit as a linkage, which showed a spontaneous polarization of ~600 nC/cm^2 at room temperature. Later they used the same monomer to synthesize a series of novel main-chain FLC oligomers [69] by acyclic diene metathesis (ADMET) polymerization using a Grubbs' catalyst [70]. It is interesting to note that these oligomers exhibited enantiotropic SmC* phases with very broad phase ranges. The spontaneous polarization and tilt angle for one of them were measured to be 639 nC/cm^2 and 34° (Table 4.2), respectively, at 70°C. Unfortunately, neither SHG nor Pockels effect was

measured for these compounds. However, on the basis of their monomeric analogue **W314**, the d_{22} and d_{23} coefficients of these compounds were expected to be more than 0.6 pm/V.

By incorporating the acrylate moiety into the chain termini of **W314**, the Hult group successfully developed a series of the mono- and bi-functional acrylate FLC monomers [50, 51, 71]. *In situ* photo-induced polymerization of these monomers alone, or co-polymerization of their respective mixtures or their mixtures with bi-functional cross-linking agents in cells generated a variety of completely or partially cross-linked pyroelectric LC polymeric films (e.g., **poly(A1 + A2)** and **poly(A2c)**) which possess good NLO and EO properties (Table 4.2). This technique has an obvious advantage that pyroelectric polymers possessing a uniform optic axis, and thermal and mechanical stability, are efficiently produced in a relatively easy way. A series of papers on these types of polymeric materials have been published, which cover the range of their syntheses [51, 71, 72], SHG and EO measurements [50, 51, 71–73], and waveguide devices [74–76]. The waveguide loss in these devices was reported to be 1.07 ± 0.95 dB/cm, which meets the requirement for NLO devices. Although the partially cross-linked polymer (**poly(A1 + A2)**) and its analogues exhibited smaller EO and NLO coefficients [71, 72], a completely cross-linked polymer (**poly(A2c)**) was shown to give a relatively large EO coefficient ($r_{22} - r_{12} = 15$–35 pm/V) [51]. This value makes the new material interesting for NLO and EO devices.

4.3.2 H-Shaped Ferroelectric Dimesogens

The incorporation of a strong chromophore into a FLC molecule along its polar axis, i.e., perpendicular to the molecular long axis, is essential to achieve strong NLO strength. Although a wide range of NLO chromophores [77] are available for molecular tailoring via organic synthesis, the simple rod-shape of conventional FLC molecules limits our ability to incorporate correctly oriented strong NLO chromophores while retaining the SmC* phase. Large laterally substituted functional groups including donors, acceptors, and π-conjugated linkages on the central core, will influence the molecular packing, thereby inhibiting the formation of the smectic layers. A new approach to making strong NLO FLCs was pioneered by the Walba's group [21], based on a novel molecular structure. Instead of using a conventional rod-shaped molecule, a pair of rod-shaped molecules are connected in a side-by-side "H" dimer configuration by a π-conjugated azo linkage. This configuration forces the strong chromophore to orient along the polar direction of the FLC material, producing larger NLO and EO coefficients. Another advantage of this structure is that a wider range of chromophores can be accommodated along the polar direction without significantly influencing the molecular packing to form the smectic layers.

The first H-shaped twin mesogens (also called fused twins) were reported by Malthete and co-workers [78] in 1975, which include a 1,4,5,8-tetrasubstituted naphthalene central core and exhibited a nematic phase. Later, several types of H-shaped twin mesogens containing a methylene group [79], sulfur groups (e.g., S, SO, and SO_2) (Table 4.3) [80], or substituted and unsubstituted 1,4-phenylene

TABLE 4.3 Representative H-Shaped Dimesogens and Their Properties

H-Shaped Twin Mesogens	Phases (T/°C) and P_s (nC/cm^2)	d_{ij} or r_{ij} (pm/V)
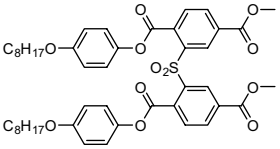	Cr-139-N-151-I [80]	
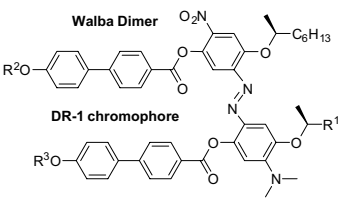 **WD1**: $R^1 = C_6H_{13}$, $R^2 = R^3 =$ (Z,Z)-9,12-octadecadienyl **WD2**: $R^1 = C_4H_8CH{=}CH_2$, $R^2 = C_{10}H_{21}$, $R^3 = C_8H_{16}CH{=}CH_2$	**WD1:** X-72-SmA*-74-Iso; I-74-SmA*-40-SmB*-25-X $P_{ext} = +65$ (25°C) [21] **WD2:** X-97-I; I-88-SmC*-65-X [82]	$r = 5$ for an analogue [83]
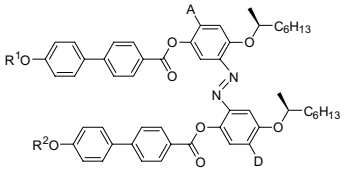 **DTC2368**: D = A = H, $R^1 = R^2 = C_{11}H_{22}SiMe_2CH_2SiMe_3$ **DTC2372**: D = NEt_2, A = NO_2, $R^1 = C_{10}H_{21}$, $R^2 = C_9H_{18}CH{=}CH_2$	**DTC2368**: Cr-74-SmC*-157-SmA*-174-I; I-170-SmA*-155-SmC*-8-gSmC* $P = +86$ (120°C) **DTC2372:** Cr-73-SmC*-78-I; I-73-SmC*-14-gSmC* $P = +70$ (60°C) [84]	**DTC2372:** $d_{22} = 17$ (1.064 μm) [84] $d_{21} = 1.5$ (1.6 μm) $d_{22} = 4.5$ (1.6 μm) $d_{23} = 1.8$ (est.) $d_{25} = 0$ (est.) [85]

segments [81] as lateral bridges, were reported by different groups. Although some of these compounds formed the SmC phase, these are unsuitable for NLO applications since these bridges are not conjugated linkages allowing for charge separation between a donor and an acceptor. It was the Walba's group who first incorporated a strong disperse red-1 chromophore, DR-1, into an H-shaped twin molecule (Table 4.3) [21]. However, the first reported two azo-bridged molecules exhibited the SmA* or SmB* phases instead of the desired SmC* phase [21]. The SmC* phase was generated by doping **WD1** into an achiral SmC host in a range of 20–60 wt% of **WD1**.

The extrapolated polarization was measured using these SmC* mixtures. The introduction of terminous double bonds into the carbon chain of the azo-bridged

dimer molecule induced a thermodynamically unstable monotropic SmC* phase (**WD2** in Table 4.3). ADMET polymerization of this dimer monomer using a Grubbs' catalyst produced a main-chain FLC polymer possessing an enantiotropic SmC* phase [82]. The spontaneous polarization was not measured due to the high viscosity of the polymer. Note that neither of the aforementioned H-shaped twin mesogens were investigated by SHG or Pockels effect experiments. Very recently, an analogue possessing an opposite DR-1 chromophore dipole orientation and a SmA* phase was reported to give an extrapolated coefficient of $r \approx 5$ pm/V [83].

Zhang et al. found that the replacement of the dimethylamino group in the Walba dimer with a diethylamino group induced the SmC* phase (Table 4.3). A series of dimers were reported to exhibit the thermodynamically stable enantiotropic SmC* phase in a broad phase range [84]. A single polarization peak was observed in surface-stabilized cells upon the application of a triangular wave voltage, suggesting FE switching. SHG measurements of a dimer using Maker fringe method gave the extrapolated d_{22} coefficient of 17 pm/V at 1064 nm, more than three times as large as that for the best calamitic NLO FLC, **Roche1** [62]. The d_{22} value is obviously resonance-enhanced due to the strong absorption of DR-1 chromophore at the second harmonic wavelength of 532 nm. SHG measurements at the longer incident wavelength of 1600 nm (i.e., much less resonance-enhanced) gave the values of $d_{22} = 4.5$ pm/V and $d_{21} = 1.5$ pm/V [85]. It is interesting to note that the d_{22} coefficients for the mixtures of **DTC2372** in the host **DTC2368** are linearly related to the mole fractions of **DTC2372**.

H-shaped dimesogens not only possess larger NLO coefficients than rod-shaped materials, but also achieve good alignment in both homeotropic cells with coplanar electrodes (Figure 4.10a and b) and planar cells (Figure 4.10c) with buffed polyimide (PI) or nylon alignment layers. These are interesting characteristics for NLO and EO applications.

4.3.3 BC LCs

4.3.3.1 Introduction Since bent-core mesogens are a very special type of mesogen, and possess quite distinct properties from other types of mesogens previously reported, herein we give them a more detailed introduction and discussion. In 1996 Niori et al. presented a paper [42] where the existence of polar liquid crystal

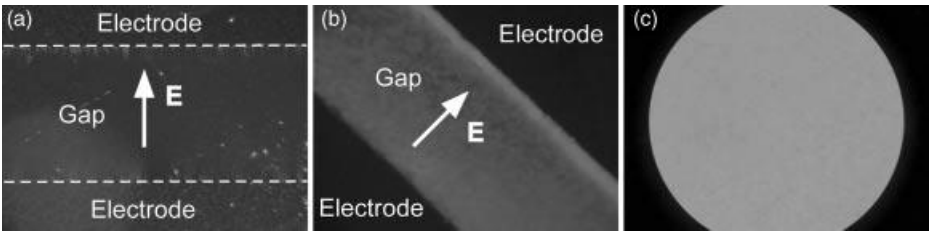

FIGURE 4.10 Textures of compound **DTC2372** between crossed polarizers (a and b) in a homeotropically aligned cell (2 μm thickness, 70°C, DC voltage of 1200 V across the gap of 100 μm) and (c) a planarly aligned cell (70°C) with PI alignment layers at both sides. (a) Polarizers along the indicatrix axes, and (b) the cell in (a) was rotated by about 45°.

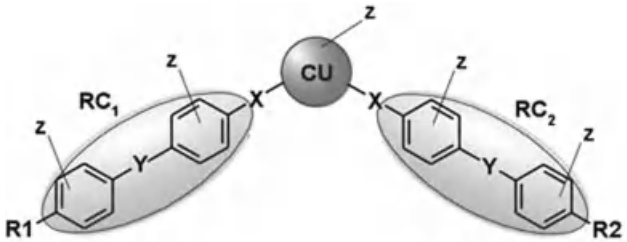

FIGURE 4.11 The general molecular structure of a bent-core molecule. The different constituents are: CU central unit, RC_1 and RC_2 linear rigid cores which can be the same or different, X and Y linking groups, Z lateral substituents, and R_1 and R_2 terminal chains.

phases in materials formed by achiral molecules was proven. Until then, structural polarity and molecular chirality had been unequivocally linked to each other. The studied compounds contain a bent-shape molecular core. For that reason, those materials were called BC LCs or banana-shaped mesogens.

A typical mesogenic BC molecule is shown in Figure 4.11 [86]. From the structural point of view, the molecule is conformed by a bent central unit, two rod-like wings, and linking groups. The bending angle is normally close to 120°. Terminal chains are usually alkyl or alkoxy flexible chains, as in normal calamitic molecules. This modification of the molecular geometry, apparently ingenuous, of a rod-like molecule brings about, apart from conventional phases such as N, SmA or SmC, completely new mesogenic structures. The new mesophases were initially named as B followed by a number. This nomenclature has been presently abandoned, at least in part, and has been substituted by another less ambiguous and more descriptive classification.

Figure 4.12 is a diagram where the common way to represent BC molecules depending on the point of view is shown. In a rigid model, the molecule is conveniently described as a bow with a long axis (the string n) and a short axis (the arrow b). Furthermore, a tilted smectic layer of achiral BC molecules is a chiral structure, and the same happens with some columnar stackings [87, 88]. This fact is represented with diagrams with different colors (red (−) and blue (+)) for opposite chirality.

There are lots of molecular arrangements characteristic of BC LCs: smectic [88], undulated [89], and columnar phases of rather different types [90, 91]. In addition, there are biaxial nematic organizations [92] (though microscopically they seem to be SmC cybotactic nuclei [93, 94]), isotropic-like dark conglomerate phases [95, 96], and more specific structures such as B_4 [97, 98], B_5 [99] or B_6 [100, 101]. In this

FIGURE 4.12 Schematic representation of an isolated bent-core molecule (left). When the molecule is placed in a tilted smectic layer, the structure becomes chiral, and opposite chirality is represented by different colors (right).

chapter we will focus our attention only on the B_2 (or SmCP) phases. For the reader interested in more details we refer to reviews on the subject of BC LCs. In references [102, 103] an enlightening description of the banana phases can be found. Another extensive and well-documented review [20] gives special attention to structure–property relationship and chirality-related phenomena. Some functionalities of these materials are also well surveyed [104].

4.3.3.2 SmCP Phases The most peculiar characteristics of BC LCs derive precisely from their anomalous molecular shape. The molecules are forced to adopt a compact packing arrangement that restricts their rotational freedom around the main molecular director (the string of the bow n) and, to minimize the excluded volume, molecules tend to stack in with parallel bent directions (see the banana bunch in Figure 4.13). In the SmCP phases, molecules are arranged in layers with a non-null tilt angle and each layer has identical polar order. Depending on the orientation of the tilt and molecular dipole directions in adjacent layers, there are four basic SmCP phases [88] (see Figure 4.14). The layer chirality alters from layer to layer in the SmC_sP_A (synclinic antiferroelectric) and SmC_aP_F (anticlinic ferroelectric) phases, giving rise to racemic structures. The other two variants SmC_aP_A (anticlinic antiferroelectric) and SmC_sP_F (synclinic ferroelectric) are homochiral. If we extend the correlation to more than two layers there are more possible tilt-polarization combinations. They can also be described as a repetition of stacks of the four different basic structures as described before, including information on the interface between the stacks. These suprastructures are designated as $[SmC_sP_F]_aP_s$ or $[SmC_sP_F]_aP_A$ [105]. The multi-layer stacking structure $[SmC_sP_F]_aP_s$ was induced from dark conglomerate phases by an external electric field and was also used to reasonably explain FE switching in a columnar phase [106].

FIGURE 4.13 In a bunch of bananas, the packing is more compact if the bent directions are parallel to each other.

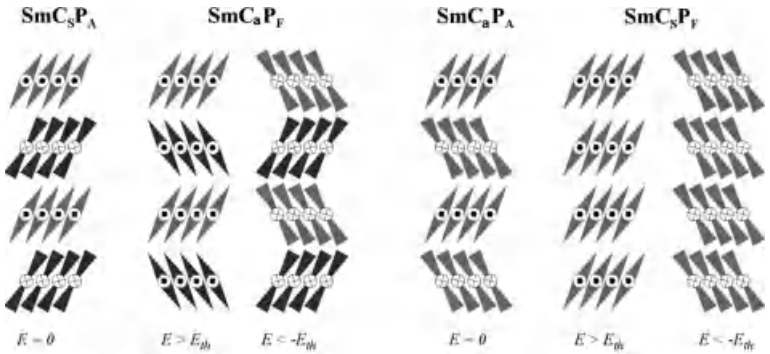

FIGURE 4.14 From left to right: SmC_sP_A, SmC_aP_F, SmC_aP_A, and SmC_sP_F states. The first two are racemic and consist of layers with opposite chirality, and the last two are homogeneously chiral structures. As indicated, an electric field above a threshold value E_{th} can transfer SmC_sP_A to SmC_aP_F, and SmC_aP_A to SmC_sP_F via switching on a smectic cone.

An electric field parallel to the layers can induce a polarization reorientation. The switching can be either around the smectic cone or along the long molecular axis (Figure 4.15). The kind of switching depends on factors such as the field frequencies, field intensity, or material viscosity. In most cases of practical interest, the first kind of switching (right) takes place and the chirality of the layers is kept in the process [88, 107]. In this situation a SmC_sP_A structure is changed to SmC_aP_F and SmC_aP_A is switched to SmC_sP_F. Recently, a new type of switching mode involving both switching modes (Figure 4.15) in the same molecule was reported in the columnar (i.e., modulated smectic) phase formed by the BC molecule with a bulky carbosilane terminous [108].

The ground-state FE phases (i.e., SmC_aP_F and SmC_sP_F) for bent-core molecules are rare and also difficult to identify [109]. A chiral BC compound **P8OPIMB6*** was unambiguously confirmed to be a ground state ferroelectric (SmC_aP_F) by both EO switching and zero-field SHG experiments [110]. It was later found that the appearance of ferroelectricity or antiferroelectricity for these type of homologues shows even–odd behavior [111]. Most BC compounds show ground-state AF phases (i.e., SmC_aP_A and SmC_sP_A). It has been suggested [112] that the ground-state AF behavior takes place because the end chains in $SmCP_A$ structures are essentially

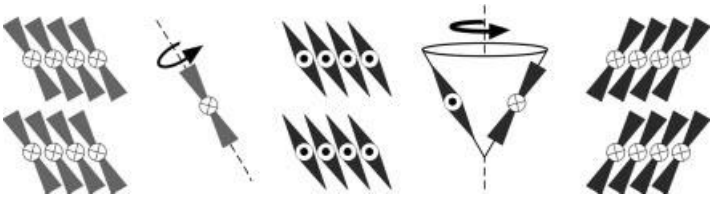

FIGURE 4.15 Switching by molecular rotation around the long axis (left) changes both chirality and polarity, while switching on the tilt cone (more common, right) only changes polarity with retention of chirality. (*See the color version of this figure in Color Plates section.*)

parallel, permitting out of layer fluctuations. This supplies a favorable entropic contribution, which is absent in $SmCP_F$ variants, to the free energy. From the viewpoint of NLO, we will be especially interested in the FE states. In the following we will concentrate on the two FE structures (SmC_aP_F and SmC_sP_F), no matter how they are generated, spontaneously or induced by an electric field.

4.3.3.3 Qualitative Aspects of NLO Properties of BC SmCP Phases

Soon after its discovery, SmCP structures were pointed out as candidates with potentialities in the field of electronic nonlinear optics [113–115]. Among the NLO properties, we include both SHG and electronic EO (Pockels) effect. Intuitively these capabilities can be understood in terms of two reasons: (a) the packing conditions derived from the molecular shape, and (b) the molecular geometry itself, which allows for a significant electronic response at molecular level along the polar axis and results in a relatively high molecular hyperpolarizability.

SmCP structures are known to exhibit high spontaneous polarization P_s. In fact, the degree of polar stereocontrol achievable in these phases is much better than that in poled polymers or calamitic SmC^* phases. The P_s values (in the range of 500–1000 nC/cm^2) in these materials imply that, typically, more than one half of the molecular dipoles are oriented along the polar axis. In contrast, only a few percent of chromophores are aligned in poled polymers, or ~20% in conventional FLCs.

The second point is illustrated in Figure 4.16, where a simplified model for a NLO BC molecule is presented. It is assumed that the NLO activity arises from two one-dimensional β-units integrated in the wings of the molecule. The β-units are simple donor–acceptor groups linked by a conjugated electronic system. As can be seen, there is always a molecular β response along the short axis (b), which macroscopically implies the existence of an important net component of NLO activity along the polarization direction. On the other hand, it is well known that to attain a high NLO response, the distance that allows for valid interaction between donors and acceptors must be as long as possible. In contrast to rod-like molecules, BC molecules can incorporate into their wings large β functional arrays, involving strong donor and acceptor groups with two or more conjugated aromatic rings between, without critically damaging its mesogenic character. In summary, due to their outstanding molecular shape, BC molecules are allowed simultaneously to have an inherently or field-induced FE character and large components of β along the macroscopic polar axis.

4.3.3.4 The Second-Order Susceptibility and EO Tensors

The above ideas will now be elaborated in a more quantitative manner. If the NLO activity is assumed to be mainly driven by the longitudinal hyperpolarizability β_l along the lateral structures in Figure 4.17, the molecular hyperpolarizability tensor $\boldsymbol{\beta}$ is given in reduced notation by [116],

$$\boldsymbol{\beta} = \begin{pmatrix} 0 & 0 & 0 & 0 & 0 & 0 \\ 0 & \beta_{yyy} & \beta_{yzz} & 0 & 0 & 0 \\ 0 & 0 & 0 & \beta_{yzz} & 0 & 0 \end{pmatrix} \tag{4.14}$$

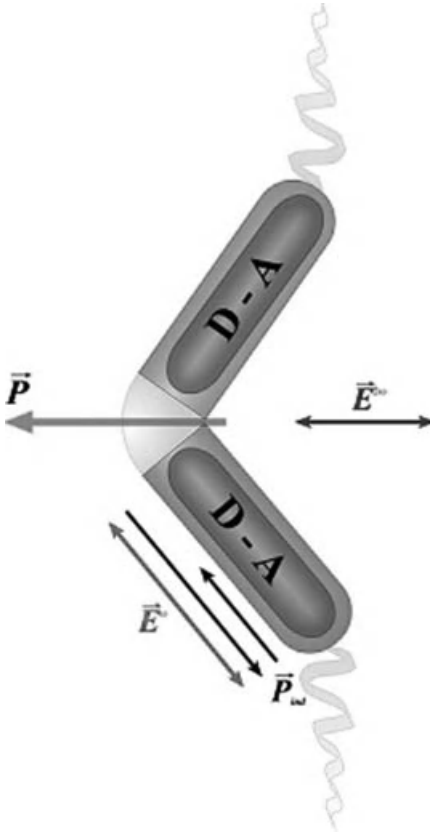

FIGURE 4.16 In BC molecules donor–acceptor (D-A) groups can be large since they can be integrated into the molecules without spoiling their mesogenic character. Moreover, there is always a nonlinear response along the polarization direction (red arrow).

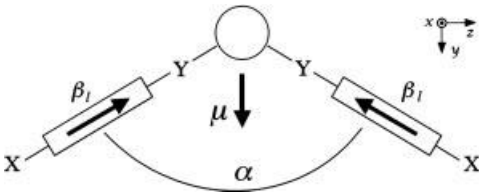

FIGURE 4.17 Schematic representation of the chemical structure of an average BC molecule. X and Y represent donor and acceptor groups, respectively, which are connected to each other through a conjugated spacer. β_{yzz} and β_{yyy} are assumed to be the dominant hyperpolarizability coefficients, with the rest being negligible. The whole tensor can be considered to arise from a unique one-dimensional hyperpolarizability β_l directed longitudinally along the wings of the molecule.

where

$$\beta_{yzz} = 2\beta_l \cos(\alpha/2)\sin^2(\alpha/2)$$
$$\beta_{yyy} = 2\beta_l \cos^3(\alpha/2) \tag{4.15}$$

Here β_l is the longitudinal hyperpolarizability for frequency doubling, i.e., $\beta_l = \beta_l(-2\omega;\omega,\omega)$.

The macroscopic second-order susceptibility tensor will be obtained using Eqs. (4.4) and (4.5). In the SmC_sP_F structure, the four independent d_{ij} coefficients (see Eq. (4.11) in Section 4.2.3.1) can be expressed in the XYZ frame of Figure 4.8a as:

$$d_{22} = d, \quad d_{21} = D\sin^2\theta + D'\cos^2\theta,$$
$$d_{23} = D\cos^2\theta + D'\sin^2\theta, \quad d_{14} = \frac{D+D'}{2}\sin 2\theta \tag{4.16}$$

where θ is the tilt angle, and the rest of the symbols are given by

$$D = Nf^3\langle\cos\Psi\rangle\beta_{yzz}, \quad D' = Nf^3\langle\cos\Psi\sin^2\Psi\rangle\beta_{yyy}, \quad d = Nf^3\langle\cos^3\Psi\rangle\beta_{yyy} \tag{4.17}$$

Here the same local-field factor f has been assumed for ω and 2ω lights, and Ψ is the angle between the macroscopic polarization and the molecular short axis (b). The introduction of this angle is a simple way to incorporate into our model some molecular disorder, which is modeled as rotation around the director (n). In terms of Ψ, P_s is given by

$$P_s = N\mu_{\mathbf{b}}\langle\cos\Psi\rangle \tag{4.18}$$

μ_b is the molecular dipole moment component along the b direction.

For the SmC_aP_F structure, Eq. (4.16) remains valid with the exception of the coefficients $d_{14} = d_{25} = d_{36} = 0$.

If the perfect molecular order is assumed ($\Psi = 0$ and the thermal averages are equal to 1 or 0), further simplification is achieved. In this context, $D' = 0$, and D and d are related to each other (see Eqs. (4.16) and (4.17)) via the bending angle, $D/d = \tan^2(\alpha/2)$. If $\alpha = 120°$ then $D/d = 3$.

The above equations allow an idea of the d coefficients if some rather general assumptions are made and the microscopic parameters (β_l and μ_b) are known. We will return to this point in Section 4.3.3.6.

The electronic contribution to the **r** tensor will similarly be obtained using Eqs. (4.6) and (4.7). In the SmC_sP_F structure, the four independent d_{ij} coefficients (see Eq. (4.13) in Section 4.2.3.2) can be similarly given by:

$$r_{22} = r, \quad r_{12} = R\sin^2\theta + R'\cos^2\theta,$$
$$r_{32} = R\cos^2\theta + R'\sin^2\theta, \quad r_{41} = \frac{R+R'}{2}\sin 2\theta \tag{4.19}$$

where R, R' and r are proportional to D, D' and d, respectively, with the same proportionality constant, i.e., $R/D = R'/D' = r/d = K$, with

$$K = -\frac{4f^0\beta_l(-\omega;\omega,0)}{(n^\omega)^4 f^{\omega'}\beta_l(-2\omega';\omega',\omega')} \tag{4.20}$$

Here ω and ω' are the frequencies of the light which are modulated and doubled in the EO and SHG processes, respectively.

4.3.3.5 SHG and EO Properties on Presently Known BC LCs So far most experimental tests have been focused on the determination of the **d** coefficients through measurements of SHG. The first results found in materials of the **P-n-O-PIMB** family were very promising, reporting **d** coefficients in the range of 10–50 pm/V [115–117], almost within the range needed for applications. However, subsequent measurements on these and other materials [118–121], did not confirm these data, the new **d** values being about one order of magnitude lower. The reasons for the disparities are still unclear. In this regard it is interesting to point out that the experiments are not easy to perform, and problems with the sample alignment or the quantitative analysis of the raw data must be in the origin of the discrepancies.

As shown in Table 4.4, all materials have AF ground states and were transformed into the $SmCP_F$ phases under field. The tilt angles are about 45°. The form of the **d** full tensor can be obtained from Eqs. (4.11) and (4.16) for the SmC_sP_F case. In all cases the coefficient D' was found to be small, with $D' \approx 0.1D$. For the SmC_aP_F variant the same equation applies with $d_{14} = d_{25} = d_{36} = 0$.

It should be noted that all compounds, perhaps with the exception of compound **8**, exhibit SHG efficiencies not large enough for NLO applications. The explanation for this fact as well as for the slight differences among these compounds can be understood in terms of the molecular structures. For example, the azo and imine groups (compounds **1–3**) allow for a more delocalized charge distribution between donors and acceptors. In contrast, compounds **4–7** only contain ester groups, which significantly cut the electronic conjugation and, consequently, their efficiencies are lower.

Compound **8** is different [122]. In one of the wings of this molecule there are a strong acceptor, α-cyano cinnamate (–CH=CH(CN)COO–), and a piperazine moiety (donor), connected via an azo (–N=N–) bridge, which preserves the conjugation. This material is the first BC liquid crystal specifically designed for NLO applications. There is significant enhancement in the SHG response which proves the basic efficacy of the synthesis design.

In comparison to SHG, electronic EO effects have been investigated comparatively less in these materials. These studies are very interesting because they directly prove the performance of the compounds for the construction of ultra-fast EO modulators. However, the experiments are difficult because it is necessary to handle high-frequency electric fields for the samples. The magnitude of the effect is measured through the EO **r** tensor. Up to now, the highest EO coefficients found are in the range of 10 pm/V achieved for a 40 MHz driving voltage in the material **P8OPIMB6*** [123].

TABLE 4.4 *D* and *d* Coefficients (pm/V) for SHG in $SmCP_F$ Compounds[a]

Bent-core Mesogen	D or d (pm/V)
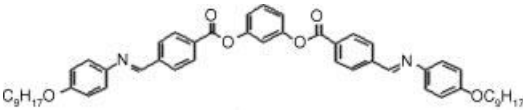	**1**: D = 6, d = 3.8 SmC_aP_F [119]
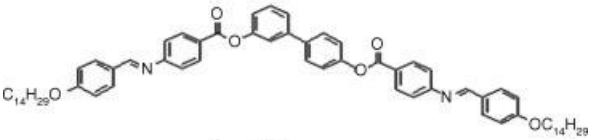	**2**: D = 8, d = 4 SmC_aP_F [121]
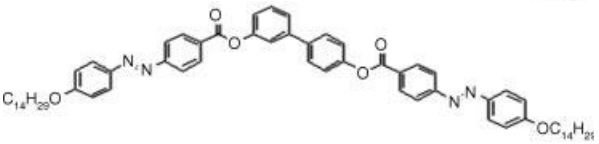	**3**: D = 6.1, d = 3.3 SmC_sP_F [121]
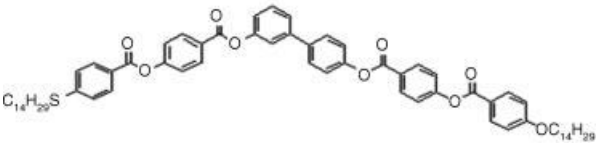	**4**: D = 2, d = 1.8 SmC_sP_F [119]
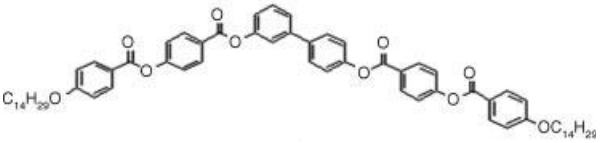	**5**: D = 2, d = 1.2 SmC_sP_F [121]
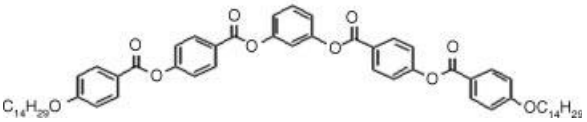	**6**: D = 3.1, d = 1.8[b] SmC_sP_F
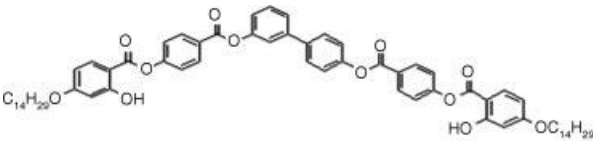	**7**: D = 1.9, d = 1 SmC_sP_F [119]
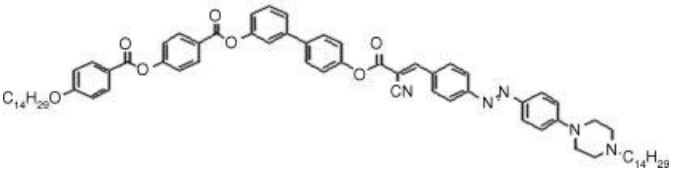	**8**: D = 17, d = 8[c] SmC_sP_F [122]

[a] Measurements were performed at the fundamental light wavelength of 1064 nm except for compound 8. SmC_aP_F and SmC_sP_F denote field-induced FE structures in spite of the ground-state AF structures.
[b] Unpublished results.
[c] Extrapolated from a 50% mixture at 1600 nm.

Now the question is to find out to what extent these **d** or **r** values can still be improved. We will try to answer this question in the next section where we analyze what we can possibly expect about the optimum NLO properties of these materials.

4.3.3.6 Limits of the SHG and EO Responses in BC LCs To find an estimate of the maximum NLO coefficients of any material we have to consider the limits of the molecular hyperpolarizabilities for a given molecular shape, some important structural parameters such as the degree of polar order or the density of molecules, and the refractive indices. The first parameter has the strongest influence on the NLO performance and depends on the nature of the donor and acceptor groups. We will restrict our disccusion to this point since for BC LCs there are no clear possibilities of influencing the rest of the factors by means of chemical design.

As has been pointed out before, in a one-dimensional donor–π-electron–acceptor system, the β values depend on the strength of the donor and acceptor and on the extension of the conjugation length. However, at least for aromatic-ring systems, the highest β per unit length is attained for two or three connecting rings. On the other hand, it is dubious to be able to maintain the mesogenic character of a BC molecule by attaching NLO moieties with arbitrary length to it. Trying to be realistic, we will consider the possibility of integrating NLO groups with only one or two aromatic rings into the BC LC molecules.

We have shown how to obtain the hyperpolarizability values for benzene- and stilbene-based chromophores (see Section 4.2.2 for details). Here we will show how to transfer these values to LCs. A similar study has been carried out by two groups [29, 37] for several organic solids. Upon transferring the data, however, it should be noted that in the bulk structure a red shift $\Delta\lambda$ in λ_0 is normally observed, i.e., $\lambda_0(\mathrm{LC}) = \lambda_0 + \Delta\lambda$. Empirically, it is found $\Delta\lambda \approx 50$ nm. Using this correction, the SHG and EO hyperpolarizabilities can be computed from Eqs. (4.8) and (4.9) at the desired wavelengths. Finally, from the knowledge of some structural parameters the full tensors **d** and **r** can be obtained using Eqs. (4.16)–(4.17) and (4.19)–(4.20), respectively.

To reach the limits of the NLO responses it is interesting to take advantage of the resonance enhancement. In accordance with this idea, the wavelength for operation should be near (but not just at) the absorption wavelength. Empirically, a good compromise is a wavelength about 100 nm away from the absorption peak, i.e., $\lambda_c = \lambda_0 + \Delta\lambda + 100$ nm. The d and r values obtained in this way are considered to be optimized for SHG and EO effect respectively.

The SHG and EO hyperpolarizabilities are obtained from Eqs. (4.8) and (4.9) at $\lambda = \lambda_c$, and the rest of the parameters needed in the calculations (see Eqs. 4.16–4.20) will be typical values of BC LCs. Specifically, we have used for all compounds $N = 9 \times 10^{26}$ molecules/m^3 (compound **1** in Table 4.4), $\theta = 45°$, $n^{\omega} = n^{2\omega} = 1.52$, and $\varepsilon = 5$. The degree of molecular order is estimated as $\langle \cos \Psi \rangle \approx 0.64$ from typical P_s and μ_b data (see Eq. (4.18)), and $\langle \cos^3 \Psi \rangle \approx 0.45$ (assuming a Gaussian distribution for Ψ). The results for the maximum D and R values are shown in Figures 4.18 and 4.19, respectively. The non-zero individual coefficients of the tensors are somewhat smaller. They are: $d_{22} = d \approx 0.24D$ ($r_{22} \approx 0.24R$), and $d_{21} \approx 0.55D$ ($r_{12} \approx 0.55R$).

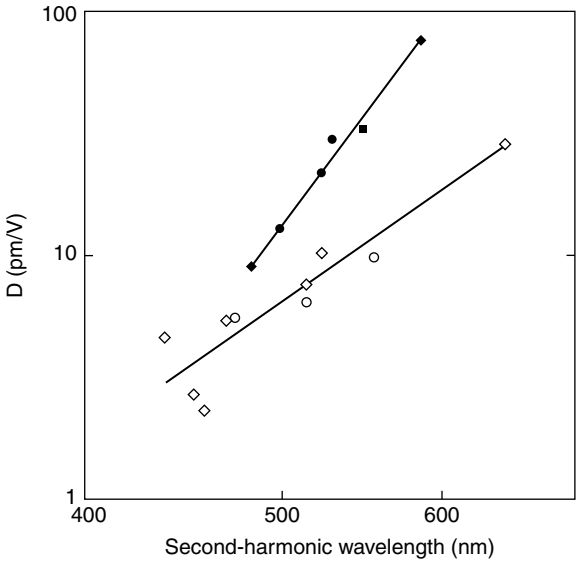

FIGURE 4.18 Log–log plot of the dependence of the D coefficient for SHG on the operating wavelength for the second-harmonic light $\lambda_c = \lambda_0 + 150\,\text{nm}$. Open circles represent BC molecules with disubstituted benzenes as NLO active groups. Closed circles are the same for the stilbene case. The straight lines are empirical relations between D and λ_c, $D = 2.58 \times 10^{-15}\lambda_c^{5.70}$ for the benzenes and $D = 1.99 \times 10^{-29}\lambda_c^{11.0}$ for the stilbenes. D is expressed in pm/V and λ_c in nm.

The predicted SHG efficiencies are moderate but not huge. Clearly an inevitable dilution effect of the NLO response takes place upon integrating relatively small NLO moieties into large BC LC molecules. More specifically, benzene chromophores are less likely to generate bent-core materials with stronger SHG strength, since the d coefficients are not better than those of some commercially available inorganic crystals such as $LiNbO_3$. Stilbene derivatives are better, though, obviously, more difficult to achieve in the sense that it may be problematic to maintain the mesogenic character of a molecule with two relatively long chromophores. If only one active group is introduced into one of the molecular wings, the coefficients shown in Figure 4.18 should be halved. In the case of stilbene derivatives, the SHG efficiencies are still good. Regarding the EO effect, the materials seem even more promising. The optimized r values are rather high (Figure 4.19), and there is still a large margin for improvement starting from the currently available materials. Coefficients about $r = 50\,\text{pm/V}$ for modulation of visible or near IR light seem feasible.

Clearly these values should be enough for applications. However, to determine whether these compounds can be used in practice, other issues must also be considered. For example, one of the key points is the ease of processability of the materials to fabricate different devices. In this sense, BC molecules present some problems to align, and certainly they are more difficult to handle than classical LCs.

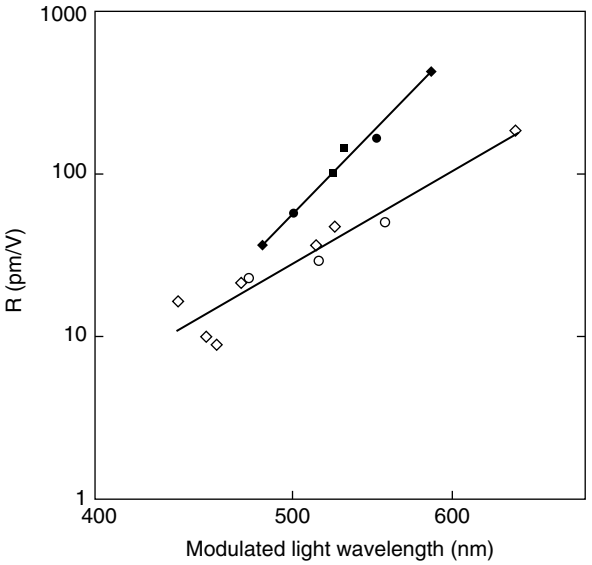

FIGURE 4.19 Log–log plot of the dependence of the R coefficient for the EO effect on the operating wavelength of the modulated light $\lambda_c = \lambda_0 + 150\,\text{nm}$. Open circles represent BC molecules with disubstituted benzenes as active groups. Closed circles are the same for the stilbene case. The straight lines are empirical relations between R and λ_c, $R = 8.42 \times 10^{-19}\lambda_c^{7.23}$ for the benzenes and $R = 7.19 \times 10^{-33}\lambda_c^{12.6}$ for the stilbenes. R is expressed in pm/V and λ_c in nm.

In this respect, some aligning methods have been applied with some success, such as the application of an AC electric field in a direction parallel to the plane of the (uncoated) substrates [1 1 0] or simply shearing the sample [1 2 4]. However, the alignment of BC molecules is still at the research stage. Another problem to solve is the temperature range of the mesophases. In this regard, some progress has been made, and more and more structures are being reported to exhibit the SmCP phase transition close to room temperature. On the other hand, irrespective of the mesophase temperature ranges, the mesogenic structures can be "frozen" at room temperature using the technique of *in situ* photopolymerization [125–127], if the BC molecules are incorporated into photo-induced polymerizable groups such as acrylate or methacrylate. This approach offers the additional advantage of improving the mechanical properties and locking the FE order in the pyroelectric polymer without the necessity of any external electric field. In this respect, stable SHG has been demonstrated at room temperature for a homeotropically aligned $SmCP_F$ film prepared under these conditions [128]. Alternatively, some materials show a high tendency to freeze the $SmCP_F$ layer structures with polar order into the glassy ordered states at room temperature [19, 20, 129]. Likewise, other macromolecular designs such as polymers [130–134], Langmuir–Blodgett films [135–137], or sol–gel materials [138] can also be explored for BC mesomorphic structures.

In summary, we have shown that the bent molecular shape is appropriate for the correct design of NLO materials. Structures are possible with large efficiencies both in SHG and EO processes. Some improvements have been achieved, but more design and synthetic work are still required to approach the theoretical potentialities of these materials. Moreover, applications require other important points to be addressed. Many strategies are at hand but the problems to be solved are far from being trivial. Research in this area is a challenging task for the near future.

4.3.4 Miscellaneous LC NLO Materials

In addition to rod-shaped chiral FLCs, H-shaped chiral ferroelectric dimesogens, and BC achiral polar mesogens, there are other interesting LC materials which show polar order and NLO activities (Table 4.5). The incorporation of chirality into disc-shaped molecules led to ferroelectricity in the tilted columnar phases as was realized by Helfrich [139, 140] and Scherowsky [141, 142]. It was reported that the polar order is perpendicular to the columns and the tilted molecules can be switched by the applied electric field. Hennrich et al. [143] recently reported that an achiral octopolar C_3-symmetric liquid crystal exhibited SHG activity at zero field, which was as strong as found in poled-polymer systems. This work indicated that this compound spontaneously assembles into a non-centrosymmetric supramolecular polar structure in the LC phases. An octopolar-based SiO_2 solid-state hybrid composite was later found to show quadratic NLO activity in a non-resonant SHG experiment [144].

Switchable polar columnar phases were reported to be formed by two types of achiral molecules: BC polycatenar molecules [145, 146] and urea derivatives linearly linked by hydrogen bonding [147, 148]. The former umbrella-like polycatenar compound exhibited three columnar phases, Col_h, Col_hP_A, and Col_X phases. The Col_h phase is paraelectric, and the Col_hP_A phase is axially polar and switchable under an external electric field with a spontaneous polarization of $\sim$250 nC/cm^2. The Col_h–Col_hP_A phase transition involves the transformation from flat discs to cones for the shape of the columnar building blocks. The urea derivatives exhibited two columnar phases, Col_h and Col_r. Although polar switching was observed in both the systems, the absence of SHG signal at zero field indicated that neither of them is truly FE. The former has a ground-state AF organization in the Col_hP_A phase, while for the latter, the polar structure along the column was readily induced by cooperative interaction between the polarization and the applied electric field. The single hysteresis loop observed in both systems is due to the slow relaxation of the field-induced FE states to the ground-state apolar supramolecular structures. Takezoe et al. recently have reviewed different types of switchable polar columnar phases in a highlight paper [149].

Baena et al. [150] reported the first metal-containing FLCs (i.e., ferroelectric metallogens) with the molecules consisting of a planar central core and four tails, namely three achiral ones and one chiral one. This complex can be also regarded as an H-shaped dimesogen with the palladium atom as the lateral bridging group. SHG measurements [151] of this complex exhibited a small effective coefficient of

TABLE 4.5 Special Types of NLO LC Materials and Their Properties

Polar Mesogens	Phases (T/°C), P_s (nC/cm^2), and d (pm/V)
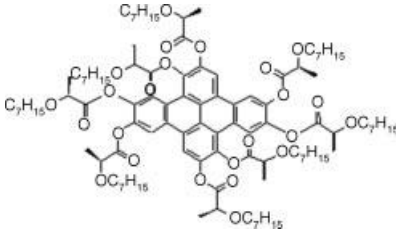	$P_s = 180$ [140]
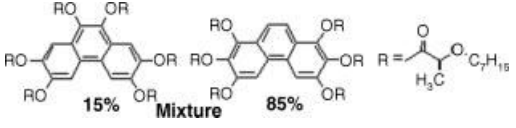	Cr-68-Col-74-Iso; Iso-66-Col-∼45-Cr $P_s = 54$ [142]
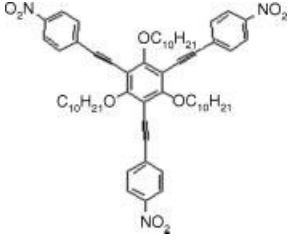	Cr_1-40-Cr_2-59.5-Col_h-68.5-N_D-112-Iso [143]
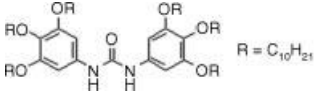	Cr-80-X-82-Col_r-139-Col_h-168-Iso Iso-164-Col_h-137-Col_r-74-Cr $P_s = \sim 250$ [145, 146]

(*continued*)

TABLE 4.5 (*Continued*)

Polar Mesogens	Phases (T/°C), P_s (nC/cm^2), and d (pm/V)
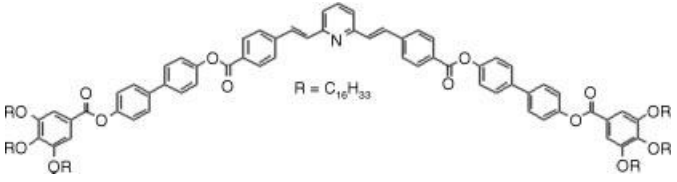	Cr-58-Col$_X$-90-Col$_h$P$_A$-123-Col$_h$-174-Iso [147, 148]
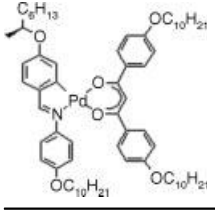	Cr-114.4-SmA*-118.4-Iso; Iso-118-SmA*-111-SmC*-89-Cr [150] $P_s = -29$ $d_{eff} = 0.047$ [151]

$d_{eff} = 0.047$ pm/V probably due to the lack of an electron acceptor along the direction normal to the molecular long axes.

Despite usually found in the smectic or columnar phases, polar order can also appear in the nematic phase. The Watanabe's group [43, 152] reported that a commercially available aromatic copolyester (also called Vectra), consisting of 4-hydroxybenzoic acid (*p*-HBA) and 6-hydroxy-2-naphthoic acid (HNA) in a molar ratio of 73/27, exhibited strong SHG at zero field in its nematic phase. It was shown that dipole–dipole interaction exists in this biaxial polymer with C_s symmetry. However, owing to the high viscosity of this material, the macroscopic polarity cannot be reversed even with a strong electric field, suggesting that Vectra is pyroelectric rather than ferroelectric. Another interesting polar nematic material is α-helical polypeptide. This chiral polymer has been found to form macroscopically polar order along the helical axis in the thermotropic and lyotropic cholesteric phases [44, 153, 154]. The polarization in this peptide can be reversed with the applied electric field, indicating that the material is truly a proper ferroelectric. To the best of our knowledge, this polymer is the first known nematic ferroelectric.

4.4 CONCLUSIONS AND FUTURE PROSPECTS

We have given an overview of FLC NLO materials and their efficiencies in SHG and the Pockels effect. Like poled polymers, FLCs are a promising alternative to inorganic crystals since their polar direction can be easily controlled with the applied electric field, and the LC film technology can be readily integrated with silicon VLSI technology on a large area and volume. As we discussed, real ferroelectricity is very difficult to achieve for LCs owing to strong dipole–dipole interaction in macroscopically polar superstructural organizations. So far there are only three types of materials: surfaced-stabilized bistable chiral FLCs, ground-state chiral bent-core SmC_aP_F materials, and a nematic α-helical polypeptide, which can be properly called ferroelectrics. However, as long as non-centrosymmetric superstructures can be achieved for LC materials, they are still interesting for NLO and EO applications. Hence, in this chapter we have discussed the helielectric SmC^* materials, cross-linked pyroelectric LC polymers, polar nematic materials, field-induced polar banana materials with ground-state AF organization (e.g., SmC_sP_A and SmC_aP_A) and ground-state dark conglomerate phases (e.g., BC materials with silane termini), octopolar LC materials, field-induced polar discotic materials, and field-induced polar polycatenar materials with hexagonal columnar phases. Most of these materials do not possess SHG activity at zero field, but strong SHG and even polarization switching in some cases were observed upon field application.

Although relatively good alignment can be readily achieved for rod-shaped NLO FLCs, their NLO optical susceptibilities ($\chi^{(2)}$) are too small for commercial applications. BC materials are much better, but their alignment is poor, particularly in planar cells. H-shaped twin mesogens can achieve good alignment in both homeotropic and planar cells, and larger NLO activity should be obtained by incorporating stronger

chromophores along the polar direction without influencing the SmC* phase. Thus, they could be promising candidates to penetrate commercial NLO and EO markets. Certainly the development of new types of NLO LC materials with special properties is also necessary.

Large nonlinear optical susceptibilities ($\chi^{(2)}$) are not the only requirement for applications in devices. Nalwa et al. in a book chapter [155] have listed 10 possible characteristics for an ideal NLO material: (1) large nonlinear figure-of-merit for frequency conversion, (2) high laser damage threshold, (3) fast optical response time, (4) wide phase matchable angle, (5) architectural flexibility for molecular design and morphology, (6) ability to process into crystals or thin films, (7) optical transparency, (8) ease of fabrication, (9) nontoxicity and good environmental stability, and (10) high mechanical strength and thermal stability. None of the single LC (or other types) materials could possess all of the above properties. Hence, the choice of materials for specific applications will depend on the particular properties required, and some trade-offs are certainly necessary. During the past decades, substantial progress has been made to enhance the EO activity of poled polymeric materials, reduce their EO losses, and improve their thermal and photochemical stability. In comparison to poled polymers, the NLO efficiency of LCs is relatively small. Incorporating strong chromophores into H-shaped twin molecules or bent-core molecules seems to be a good way to enhance the NLO activity in LC materials. To improve thermal and photochemical stability, cross-linked polymers should be used, and photochemically sensitive functional groups should be avoided as much as possible. EO loss will be a less critical issue since a normal pyroelectric LC polymer already has losses under 2 dB/cm [76]. Integration of these properties together into single materials, devices, or systems is a challenging task which will definitely lead to a bright future for NLO LC materials.

ACKNOWLEDGMENTS

YQZ would like to thank Micron Technology Inc. for its support and approval to write this chapter. JE would like to thank the generous support from MICINN-FEDER of Spain-UE (Project MAT 2009-14636-C03) and the Basque Country Government (Project GIC10/45). The authors would like to sincerely thank Veronica Cepak and Chris Walker for taking on the burden of carefully reading the manuscript, as well as Mike O'Callaghan for his comments on parts of the manuscript.

REFERENCES

1. P. A. Franken, A. E. Hill, C. W. Peters, and G. Weinreich. Generation of optical harmonics. *Phys. Rev. Lett.* **1961**, *7*, 118–119.
2. C. Bosshard and P. Günter. Electro-optical effects in molecular crystals and polymers. In: H. S. Nalwa and S. Miyata, Eds., *Nonlinear Optics of Organic Molecules and Polymers*, CRC Press, Inc., Boca Raton, FL, 1997.

3. L. R. Dalton, P. A. Sullivan, and D. H. Bale. Electric field poled organic electro-optic materials: state of the art and future prospects. *Chem. Rev.* **2010**, *110*, 25–55.
4. S. R. Marder. Organic nonlinear optical materials: where we have been and where we are going. *Chem. Commun.* **2006**, 131–134.
5. B. J. Coe. Switchable nonlinear optical metallochromophores with pyridinium electron acceptor groups. *Acc. Chem. Res.* **2006**, *39*, 383–393.
6. D. M. Burland, R. D. Miller, and C. A. Walsh. Second-order nonlinearity in poled-polymer systems. *Chem. Rev.* **1994**, *94*, 31–75.
7. P. A. Sullivan and L. R. Dalton. Theory-inspired development of organic electro-optic materials. *Acc. Chem. Res.* **2010**, *43*, 10–18.
8. O. Ostroverkhova and W. E. Moerner. Organic photorefractives: mechanisms, materials, and applications. *Chem. Rev.* **2004**, *104*, 3267–3314.
9. P. Innocenzi and B. Lebeau. Organic–inorganic hybrid materials for non-linear optics. *J. Mater. Chem.* **2005**, *15*, 3821–3831.
10. S. Yitzchaik and T. J. Marks. Chromophoric self-assembled superlattices. *Acc. Chem. Res.* **1996**, *29*, 197–202.
11. O. R. Evans and W. Lin. Crystal engineering self-organized porphyrinic materials ring of NLO materials based on metal-organic coordination networks. *Acc. Chem. Res.* **2002**, *35*, 511–522.
12. C. M. Drain, A. Varotto, and I. Radivojevic. Self-organized porphyrinic materials. *Chem. Rev.* **2009**, *109*, 1630–1658.
13. J. Luo, X.-H. Zhou, and A. K.-Y. Jen. Rational molecular design and supramolecular assembly of highly efficient organic electro-optic materials. *J. Mater. Chem.* **2009**, *19*, 7410–7424.
14. T. P. Radhakrishnan. Molecular structure, symmetry, and shape as design elements in the fabrication of molecular crystals for second harmonic generation and the role of molecules-in-materials. *Acc. Chem. Res.* **2008**, *41*, 367–376.
15. L. R. Dalton, W. H. Steier, B. H. Robinson, C. Zhang, A. Ren, S. Garner, A. Chen, T. Londergan, L. Irwin, B. Carlson, L. Fifield, G. Phelan, C. Kincaid, J. Amend, and A. Jen. From molecules to opto-chips: organic electro-optic materials. *J. Mater. Chem.* **1999**, *9*, 1905–1920.
16. J.-M. Lehn. From molecular to supramolecular nonlinear optical properties, In: *Materials for Nonlinear Optics. ACS Symposium Series*, vol. 455, 1991 (Chapter 28).
17. J. M. Hoover, R. A. Henry, G. A. Lindsay, M. P. Nadler, S. F. Nee, M. D. Seltzer, and J. D. Stenger-Smith. Langmuir–Blodgett multilayers of fluorinated, main-chain chromophoric, optically nonlinear polymers. In: *Macromolecular Assemblies in Polymeric Systems. ACS Symposium Series*, vol. 493, 1992 (Chapter 9).
18. S. T. Lagerwall. *Ferroelectric and Antiferroelectric Liquid Crystals*, Wiley-VCH, Germany, 1999.
19. S. Chandrasekhar, B. K. Sadashiva, and K. A. Suresh. Liquid crystals of disc-like molecules. *Pramana* **1977**, *9*, 471–480.
20. R. A. Reddy and C. Tschierske. Bent-core liquid crystals: polar order, superstructural chirality and spontaneous desymmetrisation in soft matter systems. *J. Mater. Chem.* **2006**, *169*, 907–961.

21. D. M. Walba, D. J. Dyer, T. Sierra, P. L. Cobben, R. Shao, and N. A. Clark. Ferroelectric liquid crystals for nonlinear optics: orientation of the disperse red 1 chromophore along the ferroelectric liquid crystal polar axis. *J. Am. Chem. Soc.* **1996**, *118*, 1211–1212.
22. S. Sergeyev, W. Pisula, and Y. H. Geerts. Discotic liquid crystals: a new generation of organic semiconductors. *Chem. Soc. Rev.* **2007**, *36*, 1902–1929.
23. M. Trollsås, F. Sahlén, P. Busson, J. Örtegren, U. W. Gedde, A. Hult, M. Lindgren, D. Hermann, P. Rudquist, L. Komitov, B. Stebler, and S. T. Lagerwall. The influence of the molecular structure on the second-order nonlinear optical properties of pyroelectric liquid crystalline polymers. In: *Organic Thin Films. ACS Symposium Series*, vol. 695, 1998 (Chapter 23).
24. D. M. Walba, M. B. Ros, N. A. Clark, R. Shao, K. M. Johnson, M. G. Robinson, J. Y. Liu, and D. Doroski. Ferroelectric liquid crystals designed for electronic nonlinear optical applications. In: *Materials for Nonlinear Optics. ACS Symposium Series*, vol. 455, **1991** (Chapter 32).
25. J.-C. Dubois, P. L. Barny, P. Robin, V. Lemoine, and H. Rajbenbach. Properties of side chain liquid crystal and amorphous polymers. Applications to non-linear optics. *Liq. Cryst.* **1993**, *14*, 197–213.
26. M. Schadt. Linear and non-linear liquid crystal materials, electro-optical effects and surface interactions. Their application in present and future devices. *Liq. Cryst.* **1993**, *14*, 73–104.
27. W. Känzig. Ferroelectrics and antiferroelectrics. In: F. Seitz, T. P. Das, D. Turnbull, and E. L. Hahn,Eds., *Solid State Physics*, vol. 4, Academic Press, 1957.
28. Jj. F. Scott. *Ferroelectric Memories*, Springer, New York, 2000.
29. T. Kato, N. Mizoshita, and K. Kishimoto. Functional liquid-crystalline assemblies: self-organized soft materials. *Angew. Chem. Int. Ed.* **2006**, *45*, 38–68.
30. C. Tschierske. Micro-segregation, molecular shape and molecular topology – partners for the design of liquid crystalline materials with complex mesophase morphologies. *J. Mater. Chem.* **2001**, *11*, 2647–2671.
31. H.-T. Nguyen, C. Destrade, and J. Malthécte. Phasmids and polycatenar mesogens. *Adv. Mater.* **1997**, *9*, 375–378.
32. S. Kumar. *Chemistry of Discotic Liquid Crystals: From Monomers to Polymers*, CRC Press, Taylor & Francis Group, Boca Raton, FL, 2011.
33. C. Tschierske. Liquid crystal engineering – new complex mesophase structures and their relations to polymer morphologies, nanoscale patterning and crystal engineering. *Chem. Soc. Rev.* **2007**, *36*, 1930–1970.
34. X. H. Cheng, S. Diele, and C. Tschierske. Molecular design of liquid-crystalline block molecules: semifluorinated pentaerythritol tetrabenzoates exhibiting lamellar, columnar, and cubic mesophases. *Angew. Chem. Int. Ed.* **2000**, *39*, 592–595.
35. B. Pansu. Are surfaces pertinent for describing some thermotropic liquid crystal phases? *Mod. Phys. Lett. B* **1999**, *13*, 769–782.
36. H.-T. Nguyen, J. C. Rouillon, P. Cluzeau, G. Sigaud, C. Destrade, and N. Isaert. New chiral thiobenzoate series with antiferroelectric mesophases. *Liq. Cryst.* **1994**, *17*, 571–583.
37. N. A. Clark and S. T. Lagerwall. Submicrosecond bistable electro-optic switching in liquid crystals. *Appl. Phys. Lett.* **1980**, *36*, 899–901.

38. T. Ikeda, T. Sasaki, and K. Ichimura. Photochemical switching of polarization in ferroelectric liquid-crystal films. *Nature* **1993**, *361*, 428–430.
39. I. Dierking. *Textures of Liquid Crystals*, Wiley-VCH, Germany, 2003.
40. A. G. Duranda and P. Martinot-Lagardea. Physical properties of ferroelectric liquid crystals. *Ferroelectrics* **1980**, *24*, 89–97.
41. H. Takezoe and J. Watanabe. Ferroelectricity in liquid crystals, *Mol. Cryst. Liq. Cryst.* **1999**, *328*, 325–332.
42. T. Niori, T. Sekine, J. Watanabe, T. Furukawa, and H. Takezoe. Distinct ferroelectric smectic liquid crystals consisting of banana shaped achiral molecules. *J. Mater. Chem.* **1996**, *6*, 1231–1233.
43. T. Watanabe, S. Miyata, T. Furakawa, H. Takezoe, T. Nishi, A. Migita, M. Sone, and J. Watanabe. Nematic liquid crystals with polar ordering formed from simple aromatic polyester. *Jpn. J. Appl. Phys.* **1996**, *35*, L505–L507.
44. B. Park, Y. Kinoshita, H. Takezoe, and J. Watanab. Ferroelectricity in the lyotropic cholesteric phase of poly L-glutamate. *Jpn. J. Appl. Phys.* **1998**, *37*, L136–L138.
45. C. Bosshard, K. Sutter, P. Petre, J. Hulliger, M. Flörsheimer, P. Kaatz, and P. Günter. *Organic Nonlinear Optical Materials*, Gordon and Breach, Basel, Switzerland, 1995.
46. L. T. Cheng, W. Tam, S. H. Stevenson, G. R. Meredith, G. Rikken, and S. R. Marder. Experimental investigations of organic molecular nonlinear optical polarizabilities. 1. Methods and results on benzene and stilbene derivatives. *J. Phys. Chem.* **1991**, *95*, 10631–10643.
47. J. Jerphagnon and S. K. Kurtz. Maker fringes: a detailed comparison of theory and experiment for isotropic and uniaxial crystals. *J. Appl. Phys.* **1970**, *41*, 1667–1681.
48. F. Zernike and J. E. Midwinter. *Applied Nonlinear Optics*, Wiley, New York, 1973.
49. W. N. Herman and L. M. Hayden. Maker fringes revisited: second-harmonic generation from birefringent or absorbing materials. *J. Opt. Soc. Am. B* **1995**, *12*, 416–427.
50. D. S. Hermann, P. Rudquist, S. T. Lagerwall, L. Komitov, B. Stebler, M. Lindgren, M. Trollsås, F. Sahlen, A. Hult, U. W. Gedde, C. Orrenius, and T. Norin. Second-harmonic generation in a novel crosslinked pyroelectric liquid crystal polymer (PLCP). *Liq. Cryst.* **1998**, *24*, 295–310.
51. M. Trollsås, C. Orrenius, F. Sahlén, U. W. Gedde, T. Norin, A. Hult, D. Hermann, P. Rudquist, L. Komitov, S. T. Lagerwall, and J. Lindström. Preparation of a novel cross-linked polymer for second-order nonlinear optics. *J. Am. Chem. Soc.* **1996**, *118*, 8542–8548.
52. R. B. Meyer, L. Liebert, L. Strzelecki, and P. Keller. Ferroelectric liquid crystals. *J. Phys. Lett.* **1975**, *36*, 69–71.
53. A. N. Vtyurin, V. P. Ermaeov, B. I. Ostrovskii, and V. F. Shabanov. Study of optical second harmonic generation in ferroelectric liquid crystal. *Phys. Status Solidi B* **1981**, *107*, 397–402.
54. N. M. Shtykov, M. I. Barnik, L. A. Beresnev, and L. M. Blinov. A study of a ferroelectric liquid crystal using second optical harmonic generation. *Mol. Cryst. Liq. Cryst.* **1985**, *124*, 379–390.
55. M. Ozaki, M. Utsumi, T. Gotou, Y. Morit, K. Daido, Y. Sadohara, and K. Yoshino. Static and dynamic properties of optical second harmonic generation in ferroelectric liquid crystal. *Ferroelectrics* **1991**, *121*, 259–274.

56. J. Y. Liu, M. G. Robinson, K. M. Johnson, and D. Doroski. Second-harmonic generation in ferroelectric liquid crystals. *Opt. Lett.* **1990**, *15*, 267–269.

57. K. Yoshino, M. Utsumi, Y. Morita, Y. Sadohara, and M. Ozaki. Second harmonic generation in ferroelectric liquid crystals and their mixtures. *Liq. Cryst.* **1993**, *14*, 1021–1032.

58. D. M. Walba, M. B. Ros, N. A. Clark, R. Shao, M. G. Robinson, J. Y. Liu, K. M. Johnson, and D. Doroski. Design and synthesis of new ferroelectric liquid crystals. 14. An approach to the stereocontrolled synthesis of polar organic thin films for nonlinear optical applications. *J. Am. Chem. Soc.* **1991**, *113*, 5471–5474.

59. D. M. Walba, M. B. Ros, N. A. Clark, R. Shao, K. M. Johnson, M. G. Robinson, J. Y. Liu, and D. Doroski. An approach to the design of ferroelectric liquid crystals with large second order electronic nonlinear optical susceptibility. *Mol. Cryst. Liq. Cryst.* **1991**, *198*, 51–60.

60. D. M. Walba, H. A. Razavi, A. Horiuchi, K. F. Eidman, B. Otterholm, R. C. Haltiwanger, N. A. Clark, R. Shao, D. S. Parmar, M. D. Wand, and R. T. Vohra. Evolution of the Boulder model for the molecular origins of the polarization in ferroelectric liquid crystals. *Ferroelectrics* **1991**, *113*, 21–36.

61. J. Y. Liu, M. G. Robinson, K. M. Johnson, D. M. Walba, M. B. Ros, N. A. Clark, R. Shao, and D. Doroski. The measurement of second-harmonic generation in novel ferroelectric liquid crystal materials. *J. Appl. Phys.* **1991**, *70*, 3426–3430.

62. K. Schmitt, R.-P. Herr, M. Schadt, J. Fünfschilling, R. Buchecker, X. H. Chen, and C. Benecke. Strongly non-linear optical ferroelectric liquid crystals for frequency doubling. *Liq. Cryst.* **1993**, *14*, 1735–1752.

63. A. Taguchi, Y. Ouchi, H. Takezoe, and A. Fukuda. Angle phase matching in second harmonic generation from a ferroelectric liquid crystal. *Jpn. J. Appl. Phys.* **1989**, *37*, L997–L999.

64. K. Kajikawa, T. Isozaki, H. Takezoe, and A. Fukuda. Mirrorless microcavity spontaneously formed in ferroelectric liquid crystals. *Jpn. J. Appl. Phys.* **1992**, *31*, L679–L681.

65. B. Park, M. Lim, J.-H. Lee, J.-H. Kim, and S.-D. Lee. Nonlinear optical anisotropy associated with polar ordering in ferroelectric liquid crystals. *Ferroelectrics* **1996**, *179*, 231–240.

66. M. Stanley, S. E. Day, D. A. Dunmur, and M. Grayson. Comparison of modelling and experimental values of non-linear optical coefficients of SCE13(*). *Ferroelectrics* **1996**, *179*, 249–256.

67. H. Kapitza, R. Zentel, R. J. Twieg, C. Nguyen, S. U. Vallerien, F. Kremer, and C. G. Willson. Ferroelectric liquid crystalline polysiloxanes with high spontaneous polarization and possible applications in nonlinear optics. *Adv. Mater.* **1990**, *2*, 539–543.

68. P. Keller, R. Shao, D. M. Walba, and M. Brunet. The first high polarization ferroelectric main chain liquid crystalline polymers. *Liq. Cryst.* **1995**, *18*, 915–918.

69. D. M. Walba, P. Keller, R. Shao, N. A. Clark, M. Hillmyer, and R. H. Grubbs. Main-chain ferroelectric liquid crystal oligomers by acyclic diene metathesis polymerization. *J. Am. Chem. Soc.* **1996**, *118*, 2740–2741.

70. R. H. Grubbs, S. J. Miller, and G. C. Fu. Ring-closing metathesis and related processes in organic synthesis. *Acc. Chem. Res.* **1995**, *28*, 446–452.

71. M. Trollsås, F. Sahlén, U. W. Gedde, A. Hult, D. Hermann, P. Rudquist, L. Komitov, S. T. Lagerwall, B. Stebler, J. Lindström, and O. Rydlund. Novel thermally stable polymer materials for second-order nonlinear optics. *Macromolecules* **1996**, *29*, 2590–2598.

72. C. Artal, M. B. Ros, J. L. Serrano, N. Pereda, J. Etxebarría, C. L. Folcia, and J. Ortega. SHG characterization of different polar materials obtained by in situ photopolymerization. *Macromolecules* **2001**, *34*, 4244–4255.

73. M. Lindgren, D. S. Hermann, J. Örtegren, P.-O. Arntzen, U. W. Gedde, A. Hult, L. Komitov, S. T. Lagerwall, P. Rudquist, B. Stebler, F. Sahlén, and M. Trollsås. Second-harmonic light generation in pyroelectric liquid-crystal polymers. *J. Opt. Soc. Am. B* **1998**, *15*, 914–922.

74. V. S. U. Fazio, S. T. Lagerwall, V. Zauls, S. Schrader, P. Busson, A. Hult, and H. Motschmann. Nonlinear optical properties of a channel waveguide produced with crosslinkable ferroelectric liquid crystals. *Eur. Phys. J. E* **2000**, *3*, 245–251.

75. V. S. U. Fazio, S. T. Lagerwall, P. Busson, A. Hult, and H. Motschmann. Phase-matched second-harmonic generation in a ferroelectric liquid crystal waveguide. *Appl. Phys. Lett.* **2000**, *77*, 319–321.

76. V. S. U. Fazio, V. Zaulsc, S. Schraderc, P. Busson, A. Hult, S. T. Lagerwall, and H. Motschmann. Enhanced phase-matched second-harmonic generation in a ferroelectric liquid crystal waveguide. *Mol. Cryst. Liq. Cryst.* **2001**, *368*, 293–302.

77. T. Verbiest, S. Houbrechts, M. Kauranen, K. Clays, and A. Persoons. Second-order nonlinear optical materials: recent advances in chromophore design. *J. Mater. Chem.* **1997**, *7*, 2175–2189.

78. J. Malthete, J. Billard, and J. Jacques. Tetrabenzoates of mesomorphic naphthalenetetrol. *C. R. Acad. Sci., Paris C* **1975**, *281*, 333–335.

79. A. C. Griffin, S. F. Thames, and M. S. Bonner. Effect of molecular structure on mesomorphism. Two series of novel methylene-bridged liquid crystal. *Mol. Cryst. Liq. Cryst.* **1977**, *34*, 135–139.

80. H. Dehne, A. Roger, D. Demus, S. Diele, H. Kresse, G. Pelzl, W. Wedler, and W. Weissflog. Sulphur ligated siamese twin mesogens. *Liq. Cryst.* **1989**, *6*, 47–62.

81. W. Weissflog, D. Demus, S. Diele, P. Nitschke, and W. Wedler. From laterally branched mesogens to novel twin molecules. *Liq. Cryst.* **1989**, *5*, 111–122.

82. D. M. Walba, L. Xiao, K. Keller, R. Shao, D. Link, and N. A. Clark. Ferroelectric liquid crystals for second order nonlinear optics. *Pure Appl. Chem.* **1999**, *71*, 2117–2123.

83. D. M. Walba, E. Garcia, J. Niessink-Trotter, M. Richard, R. Shao, M. Nakata, and N. A. Clark. *ILCC2008*, Jeju, Korea, abstracts I, p. 228.

84. Y. Zhang, J. Martinez-Perdiguero, U. Baumeister, C. Walker, J. Etxebarria, M. Prehm, J. Ortega, C. Tschierske, M. J. O'Callaghan, A. Harant, and M. Handschy. Laterally azo-bridged H-shaped ferroelectric dimesogens for second-order nonlinear optics: ferroelectricity and second harmonic generation. *J. Am. Chem. Soc.* **2009**, *131*, 18386–18392.

85. J. Martinez-Perdiguero, Y. Zhang, C. Walker, J. Etxebarria, C. L. Folcia, J. Ortega, M. J. O'Callaghan, and U. Baumeister. Second harmonic generation in laterally azo-bridged H-shaped ferroelectric dimesogens. *J. Mater. Chem.* **2010**, *20*, 4905–4909.

86. C. Y. Yelamaggad, M. Mathews, S. A. Nagamani, D. S. S. Rao, S. K. Prasad, S. Findesein, and W. Weissflog. A novel family of salicylaldimine-based five-ring symmetric and non-symmetric banana-shaped mesogens derived from laterally substituted resorcinol: synthesis and characterization. *J. Mater. Chem.* **2007**, *17*, 284–298.

87. G. Heppke and D. Moro. Liquid crystals – chiral order from achiral molecules. *Science* **1998**, *279*, 1872–1873.

88. D. R. Link, G. Natale, R. Shao, J. E. Maclennan, N. A. Clark, E. Körblova, and D. M. Walba. Spontaneous formation of macroscopic chiral domains in a fluid smectic phase of achiral molecules. *Science* **1997**, *278*, 1924–1927.

89. D. A. Coleman, J. Fernsler, N. Chattham, M. Nakata, Y. Takanishi, E. Körblova, D. R. Link, R. Shao, W. G. Jang, J. E. Maclennan, O. Mondainn-Monval, C. Boyer, W. Weissflog, G. Pelzl, L. C. Chien, J. Zasadzinski, J. Watanabe, D. M. Walba, H. Takezoe, and N. A. Clark. Polarization-modulated smectic liquid crystal phases. *Science* **2003**, *301*, 1204–1211.

90. J. Watanabe, T. Niori, T. Sekine, and H. Takezoe. Frustrated structure induced on ferroelectric smectic phases in banana-shaped molecular system. *Jpn. J. Appl. Phys.* **1998**, *37*, L139–L142.

91. J. Szydlowska, J. Mieckowski, D. Matraszek, D. W. Bruce, E. Gorecka, D. Pociecha, and D. Guillon. Bent-core liquid crystals forming two- and three-dimensional modulated structures. *Phys. Rev. E* **2003**, *67*, 031702.

92. B. R. Acharya, A. Primak, and S. Kumar. Biaxial nematic phase in bent-core thermotropic mesogens. *Phys. Rev. Lett.* **2004**, *92*, 145506.

93. C. Keith, A. Lehmann, U. Baumeister, M. Prehm, and C. Tschierske. Nematic phases of bent-core mesogens. *Soft Matter* **2010**, *6*, 1704–1721.

94. A. G. Vanakaras and D. J. Photinos. Thermotropic biaxial nematic liquid crystals: spontaneous or field stabilized? *J. Chem. Phys.* **2008**, *128*, 154512.

95. J. Ortega, C. L. Folcia, J. Etxebarria, N. Gimeno, and M. B. Ros. Interpretation of unusual textures in the B2 phase of a liquid crystal composed of bent-core molecules. *Phys. Rev. E* **2003**, *68*, 011707.

96. L. E. Hough, M. Spannuth, M. Nakata, D. A. Colemanm, C. D. Jones, G. Dantlgraber, C. Tschierske, J. Watanabe, E. Körblova, D. M. Walba, J. E. Maclennan, M. A. Glaser, and N. A. Clark. Chiral isotropic liquids from achiral molecules. *Science* **2009**, *325*, 452–456.

97. J. Thisayukta, J. Watanabe, and H. Takezoe. Study on helical structure of the B-4 phase formed from achiral banana-shaped molecule. *Jpn. J. Appl. Phys.* **2001**, *40*, 3277–3287.

98. L. E. Hough, H. T. Jung, D. Krüerke, M. S. Heberling, M. Nakata, C. D. Jones, D. Chen, D. R. Link, J. Zasadzinski, G. Heppke, J. P. Rabe, W. Stocker, E. Körblova, D. M. Walba, M. A. Glaser, and N. A. Clark. Helical nanofilament phases. *Science* **2009**, *325*, 456–460.

99. J. Svoboda, V. Novotna, V. Kozmin, M. Glogarova, W. Weissflog, S. Diele, and G. Pelzl. A novel type of banana liquid crystals based on 1-substituted naphthalene-2,7-diol cores. *J. Mater. Chem.* **2003**, *13*, 2104–2110.

100. D. Shen, S. Diele, G. Pelzl, I. Wirth, and C. Tschierske. Designing banana-shaped liquid crystals without Schiff's base units: m-terphenyls, 2,6-diphenylpyridines and V-shaped tolane derivatives. *J. Mater. Chem.* **1999**, *9*, 661–672.

101. S. Kang, M. Tokita, Y. Takanishi, H. Takezoe, and J. Watanabe. Structure of a B6-like phase formed from bent-core liquid crystals determined by microbeam X-ray diffraction. *Phys. Rev E* **2007**, *76*, 042701.

102. G. Pelzl, S. Diele, and W. Weissflog. Banana-shaped compounds – a new field of liquid crystals. *Adv. Mater.* **1999**, *11*, 707–724.

103. H. Takezoe and Y. Takanishi. Bent-core liquid crystals: their mysterious and attractive world. *Jpn. J. Appl. Phys.* **2006**, *45*, 597–625.

104. J. Etxebarria and M. B. Ros. Bent-core liquid crystals in the route to functional materials. *J. Mater. Chem.* **2008**, *18*, 2919–2926.

105. C. Keith, G. Dantlgraber, R. A. Reddy, U. Baumeister, and C. Tschierske. Ferroelectric and antiferroelectric smectic and columnar liquid crystalline phases formed by silylated and non-silylated molecules with fluorinated bent cores. *Chem. Mater.* **2009**, *19*, 694–710.

106. Y. Zhang, U. Baumeister, C. Tschierske, M. J. O'Callaghan, and C. Walker. Achiral bent-core molecules with a series of linear or branched carbosilane termini: dark conglomerate phases, supramolecular chirality and macroscopic polar order. *Chem. Mater.* **2010**, *22*, 2869–2884.

107. M. Nakata, R. Shao, J. E. Maclennan, W. Weissflog, and N. A. Clark. Electric-field-induced chirality flipping in smectic liquid crystals: the role of anisotropic viscosity. *Phys. Rev. Lett.* **2006**, *96*, 067802.

108. Y. Zhang, M. J. O'Callaghan, U. Baumeister, and C. Tschierske. Bent-core mesogens with branched carbosilane termini: flipping suprastructural chirality without reversing polarity. *Angew. Chem. Int. Ed.* **2008**, *47*, 6892–6896.

109. D. M. Walba, E. Korblova, R. Shao, J. E. Maclennan, D. R. Link, M. A. Glaser, and N. A. Clark. A ferroelectric liquid crystal conglomerate composed of racemic molecules. *Science* **2000**, *288*, 2181–2184.

110. M. Nakata, D. R. Link, F. Araoka, J. Thisayukta, Y. Takanishi, K. Ishikawa, J. Watanabe, and H. Takezoe. A racemic layer structure in a chiral bent-core ferroelectric liquid crystal. *Liq. Cryst.* **2001**, *28*, 1301–1308.

111. S. K. Lee, S. Heo, J. G. Lee, K.-T. Kang, K. Kumazawa, K. Nishida, Y. Shimbo, Y. Takanishi, J. Watanabe, T. Doi, T. Takahashi, and H. Takezoe. Odd-even behavior of ferroelectricity and antiferroelectricity in two homologous series of bent-core mesogens. *J. Am. Chem. Soc.* **2005**, *127*, 11085–11091.

112. C. Keith, R. A. Reddy, M. Prehm, U. Baumeister, H. Kresse, J. L. Chao, H. Hahn, H. Lang, and C. Tschierske. Layer frustration, polar order and chirality in liquid crystalline phases of silyl-terminated achiral bent-core molecules. *Chem. Eur. J.* **2007**, *13*, 2556–2577.

113. F. Kentischerk, R. Macdonald, P. Warnik, and G. Heppke. Second harmonic generation (SHG) investigations of different phases of banana shaped molecules. *Liq. Cryst.* **1998**, *25*, 341–347.

114. S. W. Choi, Y. Kinoshita, B. Park, H. Takezoe, T. Niori, and J. Watanabe. Second-harmonic generation in achiral bent-shaped liquid crystals. *Jpn. J. Appl. Phys.* **1998**, *37*, 3408–3411.

115. R. Macdonald, F. Kentischer, P. Warnick, and G. Heppke. Antiferroelectricity and chiral order in new liquid crystals of nonchiral molecules studied by optical second harmonic generation. *Phys. Rev. Lett.* **1998**, *81*, 4408–4411.

116. F. Araoka, B. Park, Y. Kinoshita, K. Ishikawa, H. Takezoe, J. Thisayukta, and J. Watanabe. Evaluation of the first-order hyperpolarizability tensor of bent molecules by means of hyper-Rayleigh scattering method. *Jpn. J. Appl. Phys.* **1999**, *38*, 3526–3529.

117. F. Araoka, J. Thisayukta, K. Ishikawa, J. Watanabe, and H. Takezoe. Polar structure in a ferroelectric bent-core mesogen as studied by second-harmonic generation. *Phys. Rev. E* **2002**, *66*, 021705.

118. J. A. Gallastegui, C. L. Folcia, J. Etxebarria, J. Ortega, I. De Francisco, and M. B. Ros. Determination of the second order susceptibility tensor in banana-shaped liquid crystals. *Liq. Cryst.* **2002**, *29*, 1329–1333.

119. J. Ortega, J. A. Gallastegui, C. L. Folcia, J. Etxebarria, N. Gimeno, and M. B. Ros. Second harmonic generation measurements in aligned samples of liquid crystals composed of bent-core molecules. *Liq. Cryst.* **2004**, *31*, 579–584.

120. C. L. Folcia, I. Alonso, J. Ortega, J. Etxebarria, I. Pintre, and M. B. Ros. Achiral bent-core liquid crystals with azo and azoxy linkages: structural and nonlinear optical properties and photoisomerization. *Chem. Mater.* **2006**, *18*, 4617–4626.

121. I. C. Pintre, N. Gimeno, J. L. Serrano, M. B. Ros, I. Alonso, C. L. Folcia, J. Ortega, and J. Etxebarria. Liquid crystalline and nonlinear optical properties of bent-shaped compounds derived from 3,4′-biphenylene. *J. Mater. Chem.* **2007**, *17*, 2219–2227.

122. I. C. Pintre, J. L. Serrano, M. B. Ros, J. Martinez-Perdiguero, I. Alonso, J. Ortega, C. L. Folcia, J. Etxebarria, R. Alicante, and B. Villacampa. Bent-core liquid crystals in a route to efficient organic nonlinear optical materials. *J. Mater. Chem.* **2010**, *20*, 2965–2971.

123. M. Rickard, M. Nakata, H. Takezoe, J. Watanabe, and N. A. Clark. Electronic electro-optic phase modulation using bent-core liquid crystals. *Appl. Phys. Lett.* **2005**, *87*, 261115.

124. A. Jakli, S. Rauch, D. Lotzsch, and G. Heppke. Uniform textures of smectic liquid-crystal phase formed by bent-core molecules. *Phys. Rev. E* **1998**, *57*, 6737–6740.

125. C. D. Keum, A. Kanazawa, and T. Ikeda. Novel cross-linked organic materials with pronounced spontaneous polarization based on bis-dipolar molecules. *Adv. Mater.* **2001**, *13*, 321–323.

126. A. C. Sentman and D. L. Gin. Polymerizable bent-core mesogens: switchable precursors to ordered, polar polymer materials. *Angew. Chem. Int. Ed.* **2003**, *42*, 1815–1819.

127. J. Barbera, N. Gimeno, L. Monreal, R. Piñol, M. B. Ros, and J. L. Serrano. SmCP-networked films obtained by in situ photopolymerization of neat reactive banana-shaped liquid crystals. *J. Am. Chem. Soc.* **2004**, *126*, 7190–7191.

128. J. A. Gallastegui, C. L. Folcia, J. Etxebarria, J. Ortega, N. Gimeno, and M. B. Ros. Fabrication and nonlinear optical properties of monodomain polymers derived from bent-core mesogens. *J. Appl. Phys.* **2005**, *98*, 083501.

129. S. Rauch, C. Selbmann, P. Baukt, H. Sawade, G. Heppke, O. Morales-Saavedra, M. Y. Young, and A. Jakli. Glass forming banana-shaped compounds: vitrified liquid crystal states. *Phys. Rev. E* **2004**, *69*, 021707.

130. C. Keith, R. A. Reddy, and C. Tschierske. The first example of a liquid crystalline side-chain polymer with bent-core mesogenic units: ferroelectric switching and spontaneous achiral symmetry breaking in an achiral polymer. *Chem. Commun.* **2005**, 871–873.

131. X. Chen, K. K. Tenneti, C. Y. Li, Y. Bai, X. Wan, X. Fan, Q. F. Zhou, L. Rong, and B. S. Hsiao. Side-chain liquid crystalline poly(meth)acrylates with bent-core mesogens. *Macromolecules* **2007**, *40*, 840–848.

132. C. Keith, G. Dantlgraber, R. A. Reddy, U. Baumeister, M. Prehm, H. Hahn, H. Lang, and C. Tschierske. The influence of shape and size of silyl units on the properties of bent-core liquid crystals – from dimers via oligomers and dendrimers to polymers. *J. Mater. Chem.* **2007**, *17*, 3796–3805.

133. S. Demel, C. Slugovc, F. Stelzer, K. Fodor-Csorba, and G. Galli. Alternating diene metathesis polycondensation (ALTMET) – a versatile tool for the preparation of perfectly alternating AB copolymers. *Macromol. Rapid Commun.* **2003**, *24*, 636–641.

134. E. J. Choi, J. C. Ahn, L. C. Chien, C. K. Lee, W. C. Zin, D. C. Kim, and S. T. Shin. Main chain polymers containing banana-shaped mesogens: synthesis and mesomorphic properties. *Macromolecules* **2004**, *37*, 71–78.

135. L. Zou, J. Wang, V. J. Beleva, E. E. Kooijman, S. V. Primak, J. Risse, W. Weissflog, A. Jakli, and E. K. Mann. Langmuir monolayers of bent-core molecules. *Langmuir* **2004**, *20*, 2772–2780.

136. J. Wang, L. Zou, W. Weissflog, A. Jakli, and E. K. Mann. Anisotropy in Langmuir layers of a bent-core liquid crystal. *Langmuir* **2006**, *22*, 3198–3206.

137. A. R. Geivandov, S. P. Palto, S. G. Yudin, L. M. Blinov, G. Pelzl, and W. Weissflog. Ferro- and antiferroelectric properties of Langmuir–Blodgett films composed of mesogenic bent-core molecules. *Ferroelectrics* **2006**, *344*, 247–254.

138. O. G. Morales-Saavedra, E. Rivera, J. O. Flores-Flores, R. Castañeda, J. G. Bañuelos, and J. M. Saniger. Preparation and optical characterization of catalyst free SiO_2 sonogel hybrid materials. *J. Sol-Gel Sci. Technol.* **2007**, *41*, 277–289.

139. H. Bock and W. Helfrich. Ferroelectrically switchable columnar liquid crystal. *Liq. Cryst.* **1992**, *12*, 697–703.

140. H. Bock and W. Helfrich. Two ferroelectric phases of a columnar dibenzopyrene. *Liq. Cryst.* **1995**, *18*, 387–399.

141. G. Scherowsky and X. H. Chen. New switchable columnar liquid crystals. *Liq. Cryst.* **1994**, *17*, 803–810.

142. G. Scherowsky and X. H. Chen. Ferroelectric switching in columnar phases of novel chiral discotic liquid crystals. *J. Mater. Chem.* **1995**, *5*, 417–421.

143. G. Hennrich, A. Omenat, I. Asselberghs, S. Foerier, K. Clays, T. Verbiest, and J. L. Serrano. Liquid crystals from C_3-symmetric mesogens for second-order nonlinear optics. *Angew. Chem. Int. Ed.* **2006**, *45*, 4203–4206.

144. V. Torres-Zúñiga, O. G. Morales-Saavedra, G. Hennrich, J. O. Flores-Flores, and R. Ortega-Martínez. Morphology, linear and nonlinear optical response of octopolar chromophores embedded in a silica sonogel matrix. *Mol. Cryst. Liq. Cryst.* **2010**, *527*, 1–11.

145. E. Gorecka, D. Pociecha, J. Mieczkowski, J. Matraszek, D. Guillon, and B. Donnio. Axially polar columnar phase made of polycatenar bent-shaped molecules. *J. Am. Chem. Soc.* **2004**, *126*, 15946–15947.

146. E. Gorecka, D. Pociecha, J. Matraszek, J. Mieczkowski, Y. Shimbo, Y. Takanishi, and H. Takezoe. Polar order in columnar phase made of polycatenar bent-core molecules. *Phys. Rev. E* **2006**, *73*, 031704.

147. K. Kishikawa, S. Nakahara, Y. Nishikawa, S. Kohmoto, and M. Yamamoto. A ferroelectrically switchable columnar liquid crystal phase with achiral molecules: superstructures and properties of liquid crystalline ureas. *J. Am. Chem. Soc.* **2005**, *127*, 2565–2571.

148. Y. Okada, S. Matsumoto, Y. Takanishi, K. Ishikawa, S. Nakahara, K. Kishikawa, and H. Takezoe. Polarization switching in a columnar liquid crystalline urea as studied by optical second-harmonic generation interferometry. *Phys. Rev. E* **2005**, *72*, 020701(R).

149. H. Takezoe, K. Kishikawa, and E. Gorecka. Switchable columnar phases. *J. Mater. Chem.* **2006**, *16*, 2412–2416.

150. M. J. Baena, P. Espinet, M. B. Ros, J. L. Serrano, and A. Ezcurra. Improved properties of ferroelectric liquid crystals from palladium β-diketone complexes. *Angew. Chem. Int. Ed.* **1993**, *32*, 1203–1205.

151. P. Espinet, J. Etxebarría, C. L. Folcia, J. Ortega, M. B. Ros, and J. Serrano. Second harmonic generation with metal-containing ferroelectric liquid crystals. *Adv. Mater.* **1996**, *8*, 745–748.

152. M. Koike, C.-C. Yen, Y. Liu, H. Tsuchiya, M. Tokita, S. Kawauchi, H. Takezoe, and J. Watanabe. Unusual nematic liquid crystal with polar C_s symmetry formed from aromatic polyesters with head−tail character. *Macromolecules* **2007**, *40*, 2524–2531.

153. J. Watanabe, Y. Hirose, M. Tokita, T. Watanabe, and S. Miyata. Polar structure in polypeptide cholesteric liquid crystals evidenced from observation of second-harmonic generation due to the helicoidal cavity effect. *Macromolecules* **1998**, *31*, 5937–5939.

154. C.-C. Yen, M. Tokita, B. Park, H. Takezoe, and J. Watanabe. Spontaneous organization of helical polypeptide molecules into polar packing structure. *Macromolecules* **2006**, *39*, 1313–1315.

155. H. S. Nalwa, T. Watanabe, and S. Miyata. Organic materials for second-order nonlinear optics. In: H. S. Nalwa and S. Miyata, Eds., *Nonlinear Optics of Organic Molecules and Polymers*, CRC Press, Boca Raton, FL, 1997.

CHAPTER 5

Photo-Stimulated Phase Transformations in Liquid Crystals and Their Non-Display Applications

C. V. YELAMAGGAD and S. KRISHNA PRASAD
Centre for Soft Matter Research, Bangalore, India

QUAN LI
Liquid Crystal Institute, Kent State University, Kent, OH, USA

5.1 INTRODUCTION

The anisotropy of molecular shape is the prime factor responsible for the formation of liquid crystalline phases [1–3]. Manipulating this anisotropy by altering the chemical structure of the molecules has been the traditional way of stabilizing/destabilizing liquid crystal (LC) phases [4–7]. While this has been very efficient and has resulted in a wide variety of organic molecules exhibiting rich mesomorphic behavior, the possibility to control the anisotropy by a non-chemical external means has always been attractive. The modification in the shape of the molecules owing to conformational change driven by photoisomerization of certain systems responsive to light of a particular wavelength, called *actinic light*, has served this need very well. Photochemical pathways have the advantage over thermal and catalytic methods of giving mixtures rich in energetically unstable isomers. Photoisomerization is a photochemical process leading to an isomerization of a certain chemical entity, either by bond rotation, skeletal rearrangement, or atom/group-transfer [8] in chemical compounds. A number of organic compounds such as azobenzenes, stilbenes, alkenes are good examples of photoisomerizable molecular systems, which are also called photochromic/photoactive/photoresponsive compounds.

Liquid Crystals Beyond Displays: Chemistry, Physics, and Applications, Edited by Quan Li.
© 2012 John Wiley & Sons, Inc. Published 2012 by John Wiley & Sons, Inc.

The organization of the chapter is as follows. We start with a brief introduction to the phenomenon of photoisomerization [8–20]. Section 5.2 gives a survey of the diverse photoinduced phase transitions (PIPT) observed in liquid crystalline systems involving achiral as well as chiral materials, nematic, smectic, columnar, and blue phases; a detailed account of certain unique behavior of these photo-stimulated transformations [21–26, 28–30, 36–38, 41, 42, 46–48, 53, 54, 59, 60, 63–89, 101–211] is provided in Section 5.3. The chapter concludes with a note on two specific non-display applications based on the ability of light to induce large changes in the properties of liquid crystals, and which have attracted tremendous attention [27, 31–35, 39, 40, 43–45, 49–52, 55–58, 61, 62, 90–100, 212–219].

5.2 SURVEY OF PHOTOINDUCED PHASE TRANSFORMATION IN LIQUID CRYSTALS

Over the last four decades, a number of light-driven isothermal phase transitions have been reported in LCs due to reversible structural change in the constituent photo-responsive component(s). Among a variety of photoresponsive systems known, azobenzenes, viz., azobenzene and its derivatives, have been extensively used to bring about such phase transitions. This is not only because of the ability of azobenzenes to exhibit fast, efficient, and fully reversible photoisomerization, but also their isomerization is one of the cleanest photoreactions ever known where side-products are not formed even with innumerable isomerization cycles [9–12]. For these reasons and also for the fact that majority of the results presented in this chapter employ azobenzenes to bring about photo-driven effects, we mainly consider the studies involving azobenzenes for the following discussions.

5.2.1 Photoisomerization

The elucidation of the isomerization mechanism in azobenzene has been substantially debated in the literature [13–20] and the latest semiclassical dynamics simulation suggests that the photoisomerization of *trans*-azobenzene follows an inversion-assisted rotation path [20]. Azobenzene may exist as two geometric isomers, the *trans* and the *cis* form, also referred to as E and Z forms, respectively. These two configurations differ in the direction of the central bonds as shown in Figure 5.1. In the energetically more stable E state the two bonds linking the azobenzene group to the aromatic rings are parallel, resulting in an elongated shape of the molecule. In the metastable Z state the molecules adopt a bent conformation. The two isomers also differ in their absorption spectra. The absorption spectrum of E-azobenzene exhibits a maximum at around 350 nm due to the π–π^* electronic transition and another at around 440 nm due to the n–π^* transition (Figure 5.2). The attractive feature, at least from the point of view of the present studies, is that the two forms are inter-convertible by the use of *actinic light*. Typically the absorption of one light quantum of radiation in the UV region ($\sim$350 nm) results in the $E \rightarrow Z$ transformation accompanied by changes in electronic spectra of the

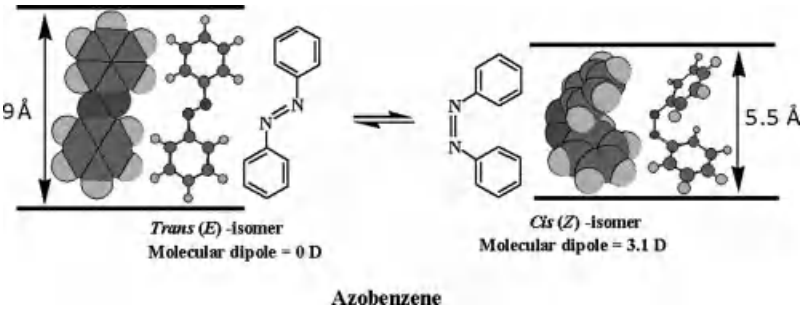

FIGURE 5.1 A facile photoinduced geometric isomerization of azobenzene about the azo bond, converting the *trans* (*E*) molecule into *cis* (*Z*) isomer. Note that the *cis*-isomer thermally reverts to the stable *trans* state. Also shown are the cylindrical and space filling models of energy minimized *E* and *Z* forms of azobenzene molecule to signify extremely large changes in conformation (shape), size (length), and molecular dipole (polarity).

material, the phenomenon being called photochromism. On the other hand, the *Z* isomer can be converted back to the *E* isomer by shining visible light (∼440 nm). Since the *E* isomer is energetically more stable than the *Z* isomer, the back conversion also occurs spontaneously, through a process known as *thermal*

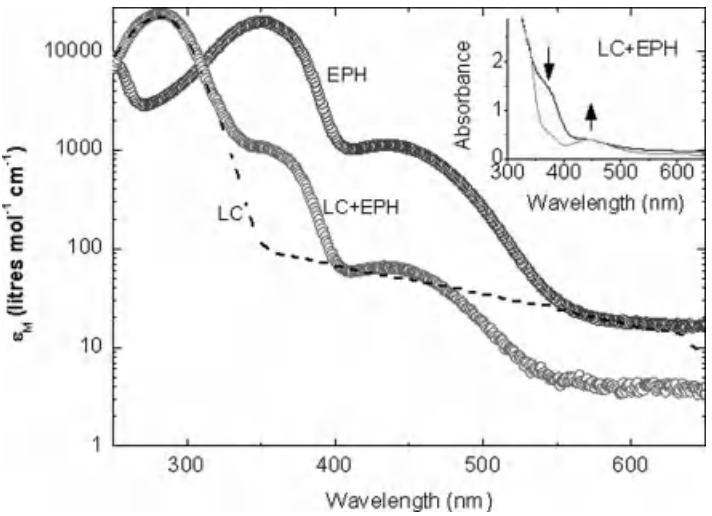

FIGURE 5.2 Molar absorptivity (ε_M) spectra for a typical azobenzene, EPH, and its mixture (5 wt%) with a nematic LC obtained using 0.1 mM/l solutions with 1,4-dioxane as a solvent. The peaks around 360 nm correspond to the π–π^* transition of the *trans* isomer of EPH. The higher wavelength (∼450 nm) peak in both the materials is due to the n–π^* transition of the *cis* isomer of EPH. The 280 nm peak seen for the mixture arises from the biphenyl moieties present in the parent LC, as confirmed by its spectrum. The inset shows the effect of photoisomerization on the relative concentration of *trans* and *cis* isomers, with the absorption for the former decreasing (indicated by down arrow), and the latter increasing (up arrow) [ref. 179].

back relaxation (TBR). Temperature, host environment, type of dye, and excitation wavelength are among the parameters, which play a decisive role in the character of photoisomerization.

5.2.2 PIPT and Related Phenomena

LC phase transitions are generally known to come about when the external parameters such as temperature, concentration, and pressure are varied. However, in recent years, irradiation with light of suitable wavelength—the photon action—has been recognized as another important stimulus that induces LC phase transitions [21–27]. In fact, it has been proven that actinic light serve as a fascinating tool to study condensed matter from a new dimension where the LC phases are stabilized/modulated through the photoisomerization of the constituent photoisomerizable molecules. From this viewpoint, the most important property that changes as a result of the photo-driven isomerization is the shape (geometry/conformation) of the molecule [see for example, refs. 9, 14, 19, 20]. Several extensive review articles on the topic of photoinduced phase transition (PIPT) in LCs exist in the literature [21–27]. Such light-driven transitions and closely related phenomena have been experimentally demonstrated since 1970s [28–34] where either photochromic molecules which themselves are mesomorphic or photoactive guest–LC host composites have been used [21–88, 180]. In general, apart from azobenzenes, other photoresponsive molecules such as stilbenes [29, 30, 63–65], azoxybenzenes [66–68], spiropyrans [63–65, 69], fulgides [63–65, 70, 71], diarylethenes [63–65, 72–78, 211], azabipyridines [79], butadienes [80, 81, 134, 135, 144, 155], menthanes [82, 83], and axially chiral azo compounds [65, 84–88] have been utilized to generate photoresponsiveness in LCs. Chart 5.1A and B depict the molecular structures of such photoactive organic compounds and their respective isomers/products formed after irradiation with *actinic light*.

As mentioned earlier, of all the known photoactive systems, azobenzene and its derivatives have attracted by far the most attention; specifically, besides being used as a dopant, the azobenzene core has been utilized in the design and synthesis of both low molar mass and polymeric LCs. The approach wherein azobenzene (or its derivative) is employed as a dopant/one of the pendant moieties in a copolymer, provides an invaluable opportunity to design different guest–host combinations, and thereby to engineer (at least to some extent) various properties such as order parameter, birefringence, color, viscosity, and polarity of the resulting photoresponsive system. In the following, we discuss about the various general aspects of photoinduced effects on LCs with special emphasis on phase transitions and related phenomena.

5.2.3 Photoinduced Nematic to Isotropic Phase Transition

Photoinduced phase transition resulting in the disordering of the nematic (N) LCs has attracted much attention from both fundamental and technology viewpoints [21–27, 31–62, 95–103, 163, 167, 168, 171, 173–177, 179, 180, 212]. In

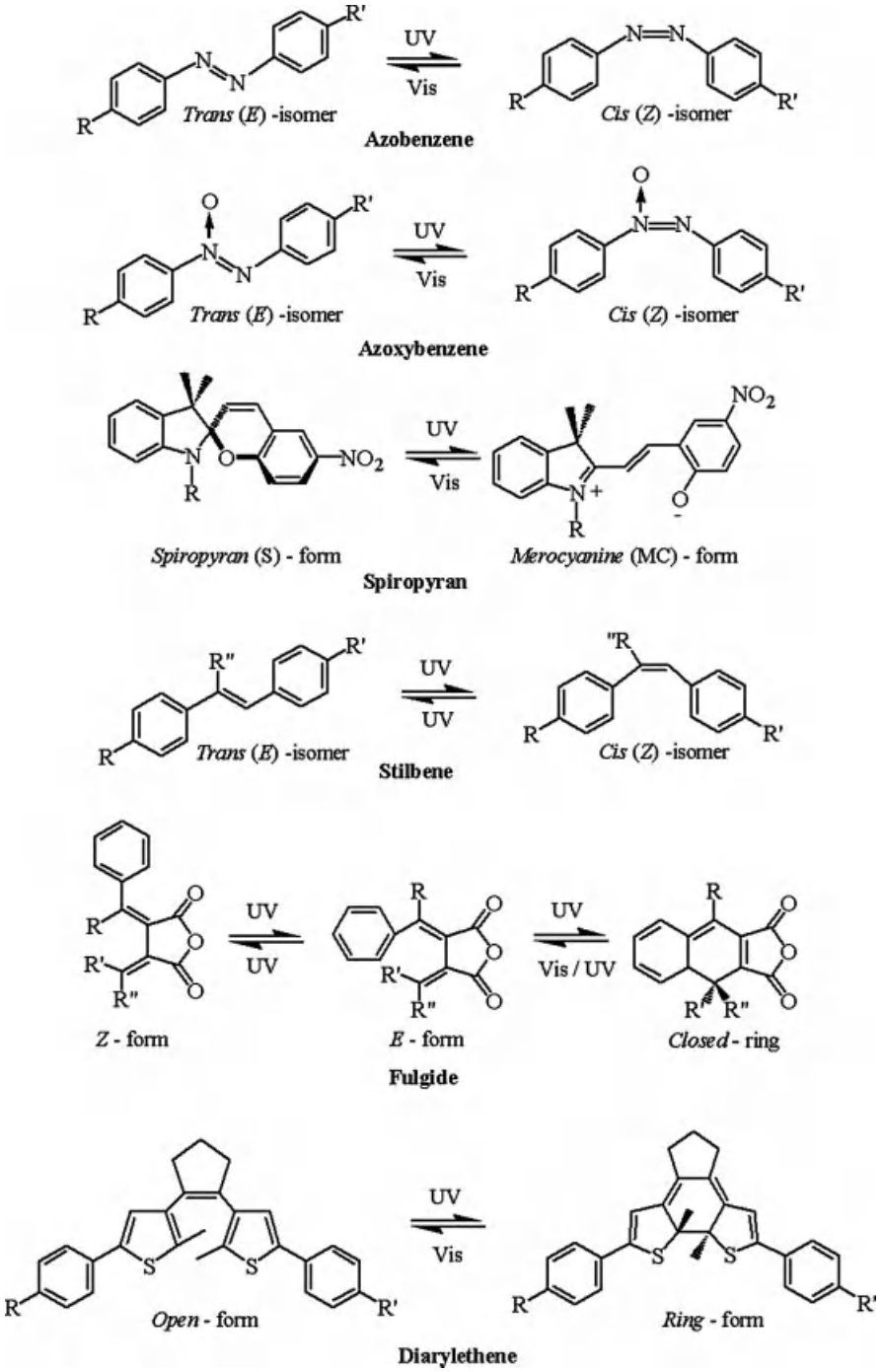

CHART 5.1A Molecular structures of photoactive compounds and their isomers/products formed after their illumination with light of suitable wavelength [refs. 21–23, 27, 63–65].

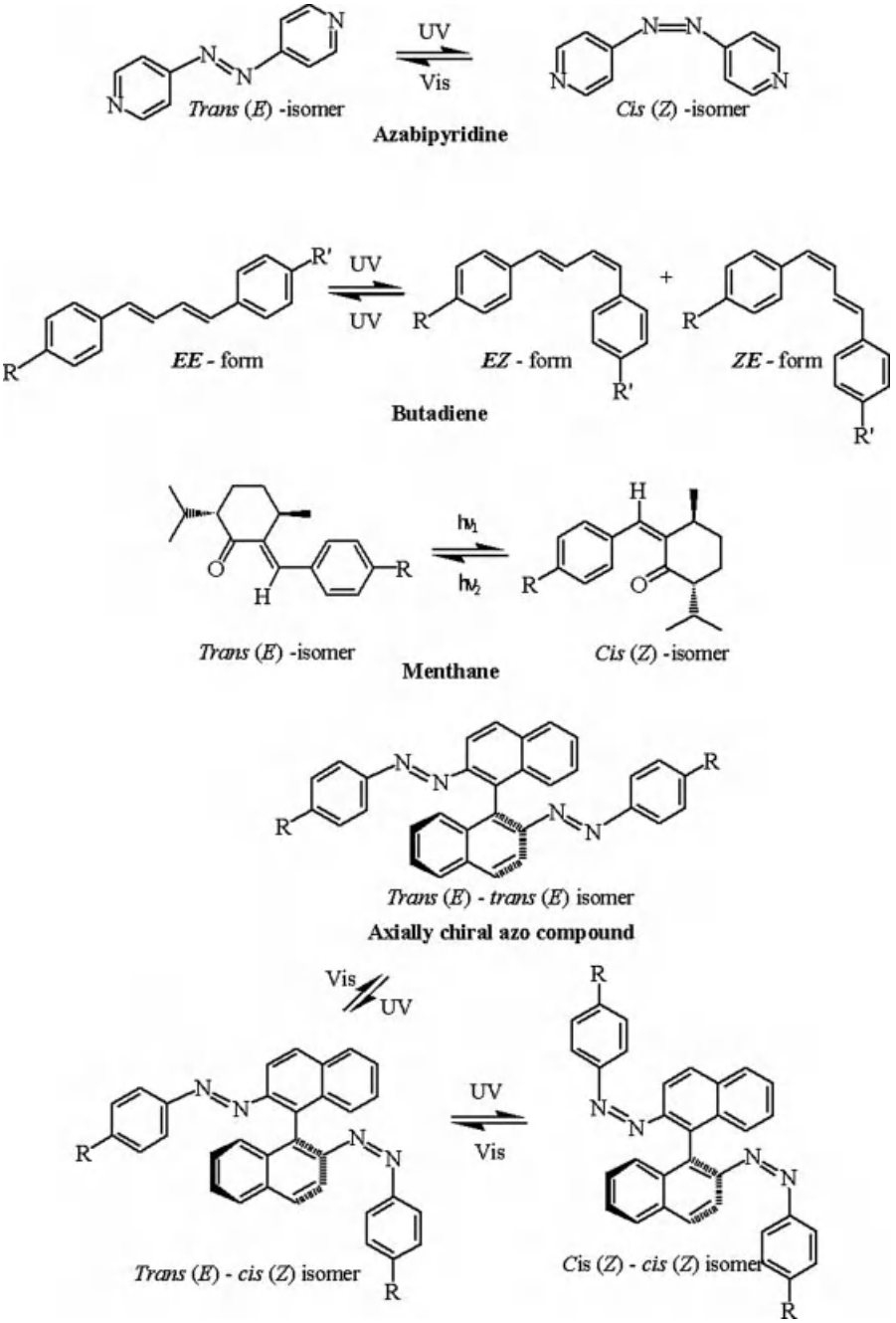

CHART 5.1B Molecular structures of photoactive compounds and their isomers/products formed after their illumination with light of suitable wavelength [refs. 21–23, 27, 63–65].

particular, the nematic-to-isotropic (N-I) transition is one of the most well-studied photoinduced isothermal phase transitions, which is generally seen in systems derived from azobenzene [11–42]. As mentioned earlier, the photoactive azobenzene, after substituting with suitable groups, can itself be mesomorphic or chemically attached to the liquid crystal molecule or used as a dopant to a LC host material. In such systems, the *E* form of the azobenzene dopant, as it is rod-like, is favorable for the stabilization of the liquid crystalline phase. On the other hand, the reduced shape anisotropy and the length of *Z* form is less in favor of liquid crystallinity. For example, the length of the *E* isomer of 4,4′-dipentylazobenzene, deduced from MM2 computations of CS Chem Draw 3D (version 5) program, is about 2.3 nm, whereas the *Z* isomer is nearly half of it, being about 1.1 nm as shown in Figure 5.3. It is this combination of dramatic change in the shape and length of the molecule in association with the high photochemical stability of azobenzenes that lies at the heart of the phenomenon of photoinduced transitions. In fact, the *Z* form with a striking bent-shape acts like an "*impurity*" and therefore destabilizes the liquid crystalline phase. Hence, photoisomerization from the *E* to the *Z* form causes, in general, a lowering of the transition temperature. If, for instance, the material containing the photoactive azobenzene derivative exhibits a N-I transition and the UV irradiation is done in the nematic phase, the gradual lowering of the transition temperature (T_{NI}), due to the accumulation of *cis*-isomers, could induce a transition to the isotropic phase. It must be emphasized that this transition is photochemical in nature and not driven by a change in temperature and therefore is an *isothermal* phase transition. Further, the photoinduced transitions in liquid crystalline materials generally employ one-photon excitation of the azobenzene group. However, recently, a photo-driven phase transition has been accomplished through two-photon

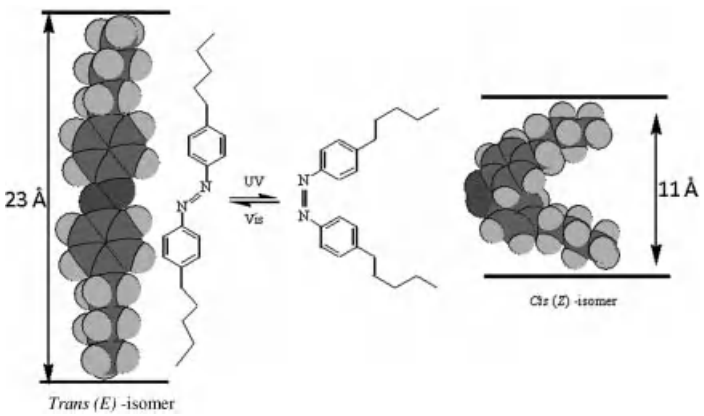

FIGURE 5.3 Molecular structures and the space filling models of *E*–*Z* isomers of 4,4′-dipentylazobenzene. Note that the *trans*-isomer possess rod-like geometry while the *cis*-isomers attain bent-conformation and as a result the length, and the shape anisotropy of the molecule gets reduced considerably.

excitation [89]. Such a two-photon driven *trans–cis* isomerization has the added advantage of controlling the location and spatial extent of a photo-stimulated structural distortion and expected to hold the promise for advanced opto-electronic and photonic applications.

5.2.4 Characterization of Liquid Crystal to Isotropic Phase Transition Using Polarizing Optical Microscope

Given the fact that in contrast to the isotropic phase the LC phases have a finite birefringence, polarizing optical microscopy (POM) can be used as a convenient probe to visualize the photoinduced isothermal LC-I transition. An example of such an observation for a system exhibiting photo-driven nematic-to-isotropic transition (see the following section for details) is shown in Figure 5.4. The sample in the N phase placed between crossed polarizers was illuminated uniformly with UV radiation except in the central region. The region that received the radiation underwent the photoinduced isothermal transition and therefore appears dark indicating the isotropic phase while the central masked portion, which is unirradiated, stays in the birefringent nematic state. Liquid crystals are elastically soft materials. If a small portion of LC molecules changes its orientation in response to an external stimulus, the other LC molecules tend to follow the change. Upon photoisomerization, the induced bent form of the photoactive molecules introduces a local region of higher orientational entropy (disorder) compared to the regions of the host (rod-like non-photoactive) molecules. If the generated disorder is large enough, the formation of the isotropic phase domains at the irradiated sites appears as dark regions under the microscope. The sphere of influence of the azobenzene molecules could become very large making the entire sample undergo the photoinduced transition from the nematic to the isotropic phase. It may be noted that the boundaries of the phases are quite sharp (except for a slight birefringence change between the middle and the edges, owing to slight light leakage) and if not illuminated with 450 nm light, it remains so

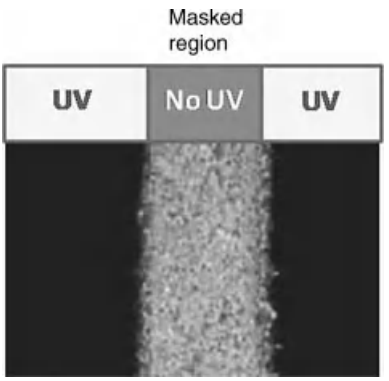

FIGURE 5.4 Photomicrograph demonstrating the isothermal nematic–isotropic transition driven by UV light.

until the thermal back relaxation occurs. A question that arises is why the boundaries should be sharp? The sample is a fluid and therefore why the azobenzene molecules converted into their *cis* state by UV light cannot disperse uniformly and results in an overall reduction of the order parameter rather than transforming the illuminated region to the isotropic phase? The reason must be the nematic potential. The molecules in regions containing the *Z* isomers and having undergone the transition to the nematic state should climb the nematic potential to reach the unirradiated region. The potential produces a barrier, which prevents an easy diffusion, thus creating a sharp boundary between the illuminated and non-illuminated regions.

The accumulated results indicate that the critical intensity at which the N-I transition occurs depends on several factors including the chemical nature of photoactive molecules [21–62, 180]. In fact, this was indicated in one of the earlier reports on photo-driven N-I phase transition [32] where a small amount of azobenzene or its derivative, 4-*n*-butyl-4′-methoxyazobenzene (**BMAB**), was doped in a standard nematic LC, 4-cyano-4′-*n*-pentylbiphenyl (**5CB**) (see Chart 5.2). In these binary mixtures showing photo-driven N-I transition, the *trans–cis* isomerization was found to be nearly linear with the reaction time. A parameter termed as amplification by the authors was better for **BMAB** than for the unsubstituted azobenzene. In the last four decades a number of single component low molar mass/polymeric and guest–host nematic LCs exhibiting photoinduced N-I transition have been investigated with a view to understand the structure–property correlations. In fact, the odd–even feature exemplified in dimers has been recently highlighted for the purpose of examining photoinduced effects [26, 139–144, 177]. In a later section we point out how the length and parity of the spacer is a powerful control parameter to alter the behavior of the N-I transition specifically.

Thus, it is quite apparent that different azobenzene derivatives have been used in accomplishing the photoinduced N-I transition. However, azoxybenzene compounds, which are stable and exhibit mesomorphism analogous to azobenzenes,

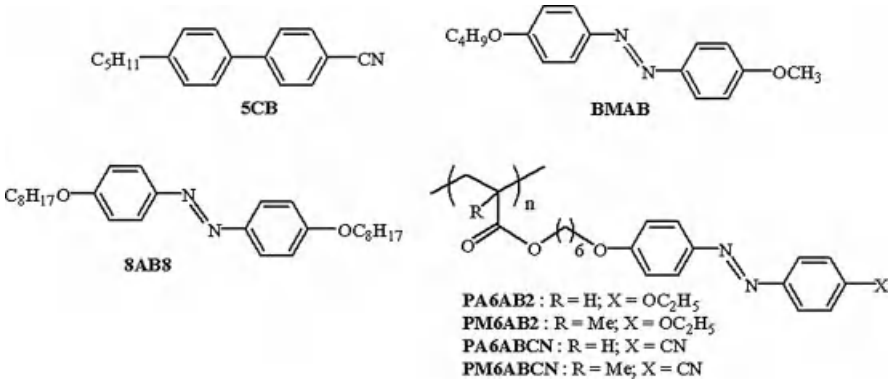

CHART 5.2 Molecular structures of nematic host LC (**5CB**), photoactive LC monomeric azobenzenes (**BMAB** and **8AB8**), and photoactive LC side-chain polymers (**PA6AB2**, **PM6AB2**, **PA6ABCN**, and **PM6ABCN**) used in early important studies [refs. 32 and 35].

have also been demonstrated to be effective for such photoinduced transitions [66–68]. One such study [68] involved a room temperature nematic LC made of 4-*n*-butyl-4′-methoxyazoxy-benzene and 4-*n*-butyl-4′-heptanoylazoxybenzene. The results revealed that in less than a minute a moderate UV intensity can bring about *trans–cis* isomerization with nearly equal amounts of both isomers present. It was also observed that a *cis* concentration of 12% is enough to lower the N-I transition from 70°C to room temperature highlighting the importance of azoxybenzene compounds. As we shall discuss briefly in the concluding section, photoinduced N-I transition has been well used in optical storage (holography) applications [31–35, 39, 40, 43–45, 49–52, 55–58, 61, 62, 212] as well as in devising soft actuators [27, 90–103, 213–219].

5.2.5 Photoinduced Nematic to Chiral Nematic Phase Transition

Appearance of chiral order in achiral materials has always been fascinating [104, 105]. In LCs, an entire class of materials, referred as banana mesophases, has seen an enormous activity owing to such a feature [104, 106–109]. In general several approaches to realize absolute asymmetric synthesis employing a chiral stimulus are known [110, 111]. Especially attractive, from the present context, is the usage of circularly polarized light (CPL) for this purpose. In fact, the conversion between achiral nematic (N) to chiral nematic (N^*) phases by CPL in guest–host composites has been achieved, where the guest systems (dopants) are racemic photochemical organic compounds [63–65, 111–117]. Indeed, the initial work on reversible photo-resolution of metal-complexes [118–121] and bridgehead imine [122] made it possible to use this novel phenomenon in the LC field with the early demonstration by Suarez and Schuster in 1995 [112]. For realizing N-N^* transition, a photoactive racemic compound, referred to as "racemic (optical) trigger", is dissolved in the host nematic LC and the system is irradiated with CPL, resulting in enantiodifferentiation as enantiomers of the racemic dopant absorb CPL with different probability. For example, Huck et al. [116] demonstrated the transition from N to N^* phase using the overcrowded racemic **alkene** [116] in a nematic host, 4′-(pentyloxy)-4-biphenyl-carbonitrile (**5OCB**) and irradiation by CPL at 313 nm (see Figure 5.5). It was noted that the transition was due to the chiral enrichment of the enantiomer (***M***)-**alkene**, and that the handedness of the helix of the N^* phase directly corresponds to that of the dopant. Restoration to the racemic nematic state was obtained upon illumination with unpolarized light.

The reverse N^*-N phase transition is achieved by photoracemization caused by illumination with unpolarized light. As mentioned above, Suarez and Schuster [112] used a chiral bicyclic ketone substituted with an exocyclic double bond as a dopant in a nematic LC namely, *trans*-1-*n*-heptyl-4-(p-cyano)phenylcyclohexane (Chart 5.3), to generate the N^* phase. Irradiation of the sample causes racemization of the chiral dopant. As the concentration of racemic component increases (with increasing irradiation), the helical pitch of the N^* phase increases, and finally it transforms to the N phase. Likewise, a photoswitchable donor–acceptor substituted, inherently dissymmetric compounds, (***M***)-**alkene-1** and (***P***)-**alkene-2** (Figure 5.6) have also

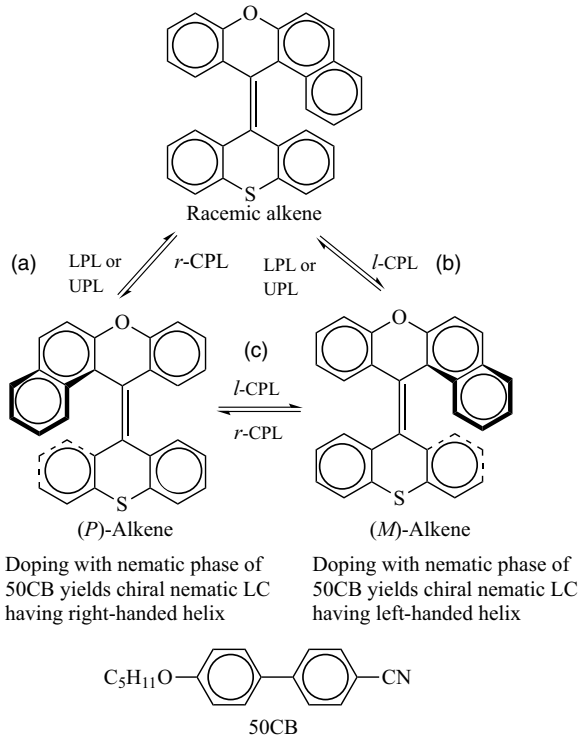

FIGURE 5.5 Photoinduced effects on an overcrowded alkene optical trigger dissolved in a nematic LC (**5OCB**): (a or b) resolution of racemic **alkene** into (***P***)-**alkene** or (***M***)-**alkene** and vice versa (racemization); (c) interconversion of enantiomeric (***P***) and (***M***) forms [ref. 116]. Here, the N-N* transition is achieved by illuminating the N phase of a binary system composed of a guest photoactive racemic compound, and the host nematic LC; the reverse (N*-N) phase transition is accomplished by illuminating the N* phase with the unpolarized light. (LPL: linearly polarized light; UPL: unpolarized light; r-CPL: right handed-circularly polarized light; l-CPL: left handed-circularly polarized light).

been shown to be very effective chiral guest molecules in the light-assisted reversible N*-N phase transitions [115]. It may be worth noting that the enantiodifferentiation has been observed in dimers [123, 124], bent-core molecules [125], columnar mesomorphs [126], and polymeric materials [127–129].

5.2.6 Photoinduced Transitions Involving Smectic and Blue Phases

Analogous to the aforementioned reversible I-N and N-N* transitions, a number of other remarkable photoinduced phase transitions involving interconversion of LC phases or their transformation to isotropic phase have been observed in a variety of systems. Yet again, the azobenzene chromophore has been incorporated in majority of the photo-functional materials. The observed phase transitions are smectic

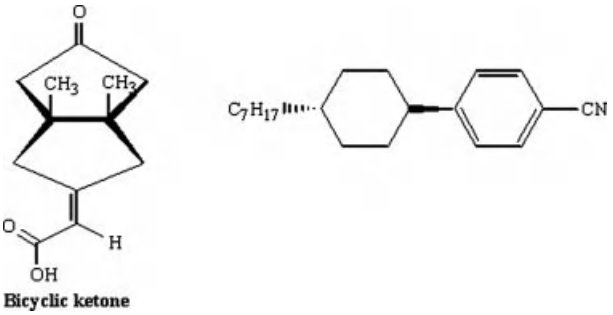

CHART 5.3 Molecular structures of the guest optically active bicyclic ketone and the host nematic LC, *trans*-1-*n*-heptyl-4-(p-cyano)phenylcyclohexane used to demonstrate the N*-N phase transition [ref. 112].

A (SmA)-to-isotropic (I) (SmA-I); SmA-N; SmA-to-crystal (Cr) state (SmA-Cr); SmA-N*; SmA-blue phase (BP) (SmA-BP); blue phase I (BP-I)-to-blue phase II (BPII) (BPI-BPII); BPII-to-blue phase III (BPII-BPIII); BPIII-I; N*-BPII; N*-BPI/BPII; smectic Q (SmQ)-to-SmQ (SmQ-SmQ); SmQ-I; chiral smectic C (SmC*)-to-I (SmC*-I); N*-I; SmC*-SmA; SmA-N*; SmC*-N*; columnar (Col)-to-I (Col-I). First we give an overview of photo-stimulated transformation of these sequences and then describe some specific examples in detail.

As is well known, the photolysis of photoactive LCs suppresses their clearing as well as LC–LC transition temperatures due to light-induced disordering of the system [21–26]; in fact, in certain cases, even the intensity of the microscope lamp source is sufficient to bring about such transitions [130–132]. Examples of photoactive compounds [131, 132] showing such effects and presenting the mesophases SmA, SmC*, twist grain boundary (TGB), N* and BP are given in Chart 5.4A. The photo illumination–temperature phase diagram was presented to show effect on, for example, the SmC*-N*-I phase sequence. The shifts in the LC–LC phase transition temperatures are found to depend on the imposed illumination and the

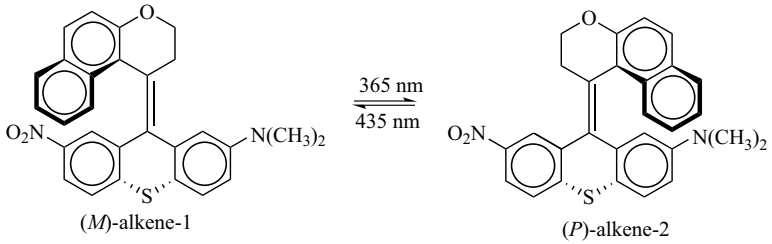

FIGURE 5.6 Light-assisted interconversion of (***M***)-**alkene-1** and (***P***)-**alkene-2**; the N*-N transition is achieved by irradiating the N* phase of a binary system consisting of a guest (***M***)-**alkene-1** and the host nematic LC **5OCB**; the N* phase is regained if the N phase is illuminated with 435 nm light [ref. 115].

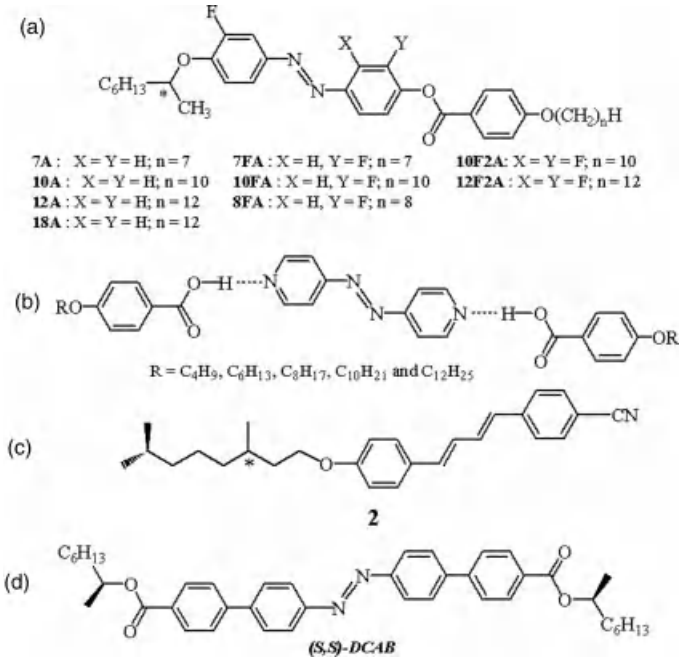

CHART 5.4 (A) General molecular structure of some optically active azobenzene-based monomeric LCs employed to study light-induced effect on (i) LC phase sequences involving SmA, SmC*, TGB, BP, and N* phases and (ii) spontaneous polarization of the SmC* phase [refs. 131–133]. (B) General molecular structure of supramolecular LC motifs formed by 4,4-bipyridine and alkoxybenzoic acids through H-bond association exhibiting photoinduced SmA-Cr transition [refs. 22, 79]. (C) Molecular structure of a chiral LC derived from 1,4-diphenylbutadiene core showing photoassisted SmA-BPI and SmA-N* transitions [ref. 135]. (D) Molecular structure of an optically active azobenzene-based atypical LC exhibiting reversible photoinduced SmQ_L-SmQ_H and SmQ_H-I transitions [ref. 138].

sample thickness; this is obvious given the fact that the rate of conversion from *trans* to *cis* isomers depends on the penetration depth of the incident light. Besides, the photo-modulation of the spontaneous polarization of the SmC* phase, has been established for some of these compounds [131]. Further, in one of such dimers (**18A** in Chart 5.4A), a continuous decrease in SmC* to TGBA (TGB phase having SmA blocks) phase transition temperature with the increase in the UV light intensity has been observed recently [133].

Light-stimulated SmA-I transition has been observed in a monomeric rod-like LC **BC-12** (Fig. 5.7) where the diphenylbutadiene core is substituted with a cyano group and a dodecyloxy tail [134]. A thin film of SmA phase, upon irradiation with 360 nm light at 120°C, transforms into an isotropic liquid state. This process was found to be thermally irreversible; that is, the isotropic state directly transforms into the crystalline state. The experimental results evidence that the photoinduced SmA-I transition is due to the conversion of *trans* (*EE*) isomers to the *cis* (*EZ* and *ZE*)

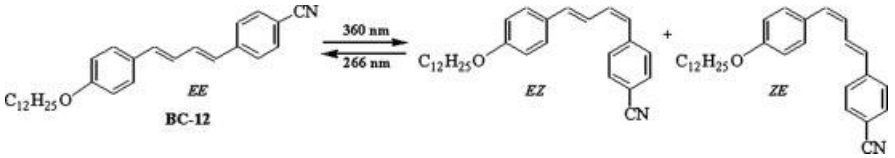

FIGURE 5.7 Light-stimulated interconversion of trans (*EE*) isomer to the *cis* (*EZ* and *ZE*) isomers of 1,4-diphenylbutadiene smectic LC **BC-12**. The SmA phase enriched with rod-like *EE* isomers, upon irradiation, transforms into isotropic liquid state due to formation of bent-shape *EZ* and *ZE* isomers [ref. 134].

isomers (Figure 5.7). Interestingly, irradiation at room temperature of the photoinduced isotropic phase with 266 nm laser, results in the generation of the system exhibiting the thermal behavior analogous to that of the *EE* isomers of **BC-12**. Such a transition has also been observed in photoactive chiral dimers which we discuss in a later section. It is worth mentioning here that the photoinduced SmA-Cr transition has been observed in supramolecular complexes formed by interacting 4-*n*-alkoxybenzoic acids with the bifunctional acceptor 4,4′-bipyridine via hydrogen bonding (Chart 5.4B) [22, 79]. Thus, a transition from the lessordered structure to highordered state occurs upon photolysis, which is, in fact, the reverse scenario when compared with other generally observed photoinduced transitions where photolysis causes a reduction in the ordering of the system. We shall describe a special case of photo-driven ordering between LC phases in a later section.

More recently, chiral LC **2** (Chart 5.4C) derived from this 1,4-diphenylbutadiene chromophore has been confirmed to show photoinduced isothermal phase transition from layered structure, SmA phase, to N* and BP depending upon the extent of photoisomerization [135]. The focal-conic fan texture of SmA phase illuminated at 13°C below the clearing point T_I with 360 nm light for 200 s, transforms into a stable oily streak texture of the N* phase. Under further irradiation, the latter pattern remains unaltered suggesting the attainment of the photostationary state; HPLC analysis shows the presence of 6% of *cis* isomers. Whereas, upon irradiation of the SmA phase at $T_I - 7$°C for 100 s yields the BP with striking platelet texture, a feature characteristic of BPI/BPII; however, based on the observation that the selective reflection wavelength λ_{max} shows strong time dependence, the phase is considered as BPI. If the SmA phase formed during the heating cycle is exposed to 360 nm light for 100 s, the BP appears with the selective reflection band at 510 nm; in fact, blue shift of the λ_{max} occurs if the phase is continuously irradiated. The occurrence of BPI in the photoirradiated films of SmA phase has been attributed to the presence of higher amounts of *cis* isomers. This is quite remarkable given the fact that photoinduced occurrence of the BP had not been reported earlier in any single component LCs. However, it may be noted here that photoinduced generation of BPs/conversion from one BP to another BP/transition from BP to isotropic liquid state has been observed in some mixtures consisting of different photoactive nematic hosts and photoinsensitive chiral components [67]. For example, irradiating the N* phase of one of the mixtures with 365 nm light at room temperature, BPII is formed while heating and BPI and

BPII were stabilized during the cooling cycle; this study is the first to illustrate the generation of BPs by the action of light. In another mixture, the photoinduced transitions from one BP to another have been observed; that is, when BPI is exposed to UV light for 2, 3, and 4 min, transitions to BPII, BPIII, and the isotropic phase occurs, respectively. In fact, modulation of the BP selective reflection with low levels of UV and visible light has also been established [67] in this study. The observed phenomena have been ascribed to changes in refractive indices as well as that of the helical pitch. In this context, it is worth mentioning that a photoinduced deformation in the BP structure has been demonstrated in chiral LC mixtures consisting of chiral nematic LC, chiral dopant (**S811**), and azobenzene compound namely, 4-dodecyloxy-4′-methoxyazobenzene [136, 137]. Irradiating the BP phase with 473 nm light, deformation in the cubic unit cell of the phase occurs with the shift in the photonic band gap. Changes in the crystal structure and platelet pattern of the BP have been established using the Kossel diffraction diagram technique.

Recently, photoinduced effects on smectic Q (SmQ) phase(s) have been revealed in an atypical chiral azobenzene compound, abbreviated as **(*S,S*)-DCAB**, where the azo-linkage bridges two biphenyl rings covalently as shown in Chart 5.4D [138]. This study is noteworthy since the SmQ phase, a chiral structure having 3D ordering, is photo-modulated, a feature that can be applied to photocontrollable switching devices. This compound exhibits two SmQ phases that were assessed based on the optical textural observations and thermodynamic property studies. The low temperature SmQ (SmQ_L) phase upon irradiating with UV light of 365 nm transforms into high temperature SmQ (SmQ_H) phase; while, the SmQ_H phase goes to isotropic state upon illumination. Upon switching off the UV light, the reverse transitions I-SmQ_H and SmQ_H-SmQ_L occur. The *trans–cis* isomerization of **(*S,S*)-DCAB** molecules responsible for these transitions is evidenced by electronic absorption spectra obtained in solutions with THF.

A number of light-driven transitions in photoresponsive dimers [139–144, 180] have been reported in the last decade. As mentioned earlier, odd–even effect on the phase transitional behavior, originating as a result of the spacer parity variation, is a very prominent and important feature of LC dimers; that is, the rod-like and kinked conformations of the odd- and even-members, respectively, virtually determine their thermal properties [180]. Given the fact that the photoinduced transitions largely depend on the shape of the photoactive component, the odd–even dimers exhibit interesting photoinduced phase behavior. For example, several light-driven isothermal phase transitions have been observed in single component dimers **D-4** to **D-21** (Chart 5.5A) that are made by joining cholesterol and azobenze segments through a flexible spacer [140–143]. The SmA and N^* phases formed by such dimers transform into the isotropic phase upon irradiation with 365 nm light [140]. Notably, a hypsochromic shift occurs in the selective reflection wavelength (λ_{max}) of the equilibrium N^* phase when it is exposed to UV light; the magnitude of the shift depends on the irradiation energy, temperature, and the length of alkyl tail of the azobenzene segment. These properties have been exploited in a rewritable full color image recording in photon mode [140]. The shift could be due to the isomerization-driven approach to the isotropic phase or as the authors speculate, the bent *cis* form

(a)

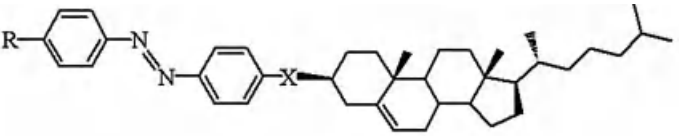

R	X	Azobenzene dimers (D-1 to D-21)
n-C_mH_{2m+1}	$OOC(H_2C)_8(C{=}C)_2(CH_2)_8COO$	**D-4** (m = 4), **D-5** (m = 7), **D-6** (m = 12), **D-7** (m = 14) and **D-8** (m = 16)
H	$OOC(H_2C)_8(C{=}C)_2(CH_2)_8COO$	**D-9**
H	$OOC(CH_2)_nCOO$	**D-10** (n = 20), **D-11** (n = 6), **D-12** (n = 7), **D-13** (n = 8), **D-14** (n = 9), **D-15** (n = 10), **D-16** (n = 11), **D-17** (n = 12), **D-18** (m = 13) & **D-19** (n = 14)
n-C_7H_{15}	$OOC(CH_2)_nCOO$	**D-20** (n = 7) and **D-21** (n = 8)

(b)

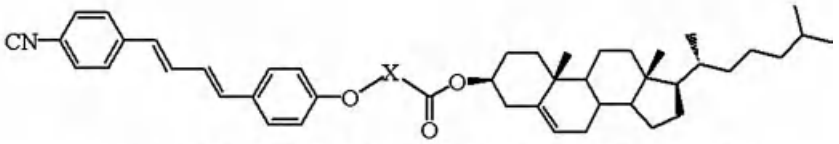

D-22: X = $-O(CH_2)_8O-$; **D-23**: X = $-O(CH_2)_{11}O-$; **D-24** : X = $-O(CH_2)_{12}O-$

CHART 5.5 (A) General molecular structure of chiral azobenzene-based LC dimers exhibiting various reversible photoinduced transitions [refs. 140–143]. (B) General molecular structure of photoactive dimers derived from 1,4-diphenylbutadiene showing light-induced SmA-N* and N*-I phase transitions [ref. 144].

has a smaller λ_{max}. These photosensitive dimers have also been employed as dopants with a dicholesteryl ester to realize a stable glassy N* state [140]. In these materials, irradiating the SmA phase with 366 nm light, the system first transforms to the N* phase and with continued illumination changes to the isotropic phase; and thus, SmA-N* and N*-I transitions have been observed [142]. In another dimer, exhibiting SmC*, SmA, and N* phases, a direct photoinduced transition from the SmC* phase to isotropic phase occurs without passing through other two phases [143] and thus, the SmC*-I transition has been observed. The percentage of *cis* isomer required for SmC*-I, SmA-N*, and SmA-I transition were estimated with the help of HPLC to be 30%, 6%, and 19%, respectively. It must be mentioned here that the effect of photoisomerization on the order parameter (spontaneous polarization) and dynamics (response time) has been investigated in the SmC* [145–152], antiferroelectric SmC* (SmC_A*) [153, 205], and chiral smectic I (SmI*) [154] phases on their approach to SmA and SmC* phases, respectively. These studies show that polarization diminishes and the response becomes faster upon photoisomerization.

Photoinduced SmA-N* and N*-I transitions were seen in analogous dimers **D-22** to **D-24** (Chart 5.5B) comprising non-azobenzene chromophore, viz., 1,4-diphenyl-butadiene core linked to cholesterol segment through an oxyalkoxycarbonyloxy (carbonate) spacer [144]. In these compounds, modulation of the reflection color of the N* film over the entire visible range has been achieved. The color images could be stored by rapidly quenching the irradiated film to 0°C. Recently, such observations have been made with the N* phase formed by LC trimers also [155].

A photoinduced reversible SmC*-N* phase transition under the influence of an applied electric field has been reported in mixtures consisting of an achiral smectic C (SmC) liquid crystal (4-hexyloxyphenyl-4-octyloxybenzoate: **HOPOOB**), chiral dopant [4-(methyl-heptyloxycarbonyl)phenyl 4-hexyloxybenzoate: **S811**], and azobenzene derivative (4-diethyl-aminoazobenzene) as a dopant in 3–7 wt% concentration (Chart 5.6) [156]. The SmC* phase formed upon cooling the N* phase held under the influence of a DC electric field shows uniform unidirectional layer alignment in the entire region of the rubbed cell. Upon reversing the polarity of the field, molecules tilt with respect to rubbing direction; further, the photolysis of this state gives rise to N* phase where the molecules tend to orient along the rubbing direction and in the absence of UV light, the N* phase transforms into SmC* phase. Thus, the photoassisted control of smectic layer alignment/switching, which appears to hold promises in fabricating display, optical memory, and optical grating devices, is achieved.

5.2.7 Photoinduced Transitions Involving Columnar Phase

From the foregoing discussion, it is quite evident that a variety of PIPT have been established using different photoresponsive LC motifs mostly of rod-like shape (calamitics). However, it is quite surprising that there is hardly any such study on disk-like (discotic) molecules [157], despite the fact that a number of photoactive discotics have been designed and synthesized [158–161]. Very recently, Norikane

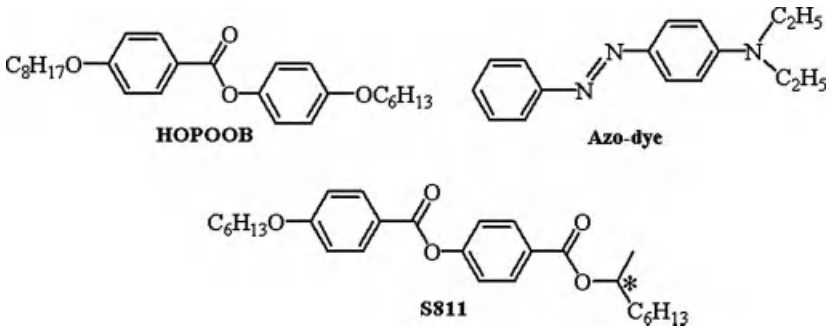

CHART 5.6 Molecular structures of a liquid crystal (**HOPOOB**), chiral dopant (**S811**), and azo dye used to demonstrate reversible SmC*-N* phase transition under the influence of an applied electric field [ref. 156].

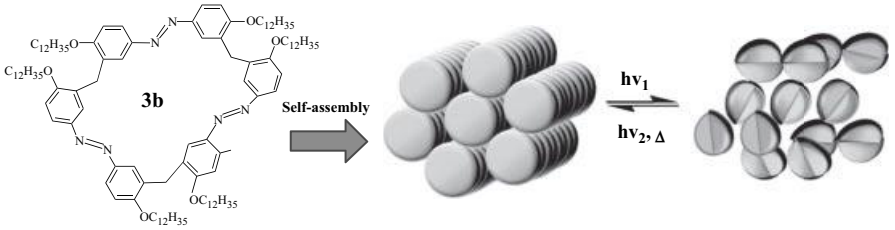

FIGURE 5.8 Schematic representation of self-assembly of photoactive discotic **3b** into columnar LC structure which upon photolysis transforms into isotropic phase due to *trans–cis* isomerism where the flat disks fold-up leading to the destabilization of columnar organization. Note that when the thermal relaxation from *cis* to *trans* isomers occurs, the isotropic liquid state transforms into the Col phase [ref. 162].

and coworkers [162] reported photoassisted transition from the Col to the isotropic phase in a macrocyclic compound **3b** comprising three fused-azobenzene mesogenic segments (Figure 5.8). Upon photolysis, the room temperature Col phase of the compound transforms into isotropic liquid where nonplanar (bent) molecules formed due to their *E–Z* isomerism destabilize the stacking of the molecules in columns; this process is reversible due to thermal back relaxation and quite sensitive to even small fractions of *Z*-isomer.

5.3 DETAILED ACCOUNT OF PIPT IN SPECIFIC SYSTEMS

In the following sections, we will look at the influence of certain parameters on the light-driven transitions. Specifically, we describe how parameters such as surface fields, elevated pressure, anisotropy reducing component, magnitude of orientational order, and electric field have a bearing on the photoinduced N-I transition. Also elaborated are the phenomena of dynamic self-assembly of a layered phase, tilt susceptibility of chiral smectic system, and primary and secondary photo ferroelectric effects in an antiferroelectric LC. Finally, a description of PIPT in systems composed of bent-core molecules is given.

5.3.1 Surface Fields

The importance of surface forces in controlling the dynamics is well known. For example, the Freedericksz transition with a well determined threshold requires proper surface forces and the relaxation to the equilibrium conditions is governed by the nature of the surface. The influence of such surface forces on PIPT, especially its dynamics, has been studied by confining the liquid crystalline material in networks. The employed networks were of two different types: a rigid polymer matrix and a fragile network of hydrogen-bonded aerosil particles. This section describes the results of these measurements wherein the sample is subjected to a restricted geometry.

5.3.1.1 Aerosil-LC A convenient way of creating a confined geometry is to disperse aerosil particles in a liquid crystal medium [164]. These silica particles of ~7 nm diameter and capped with hydrophilic or hydrophobic agents, form in the presence of a fluid medium—such as nematic—a fragile network of hydrogen bonds. The concentration or density as it is termed in these systems, of the aerosil particles, is given by $\rho_a = m_a/V_{LC}$, where m_a is the mass of aerosil and V_{LC} is the volume of LC material. ρ_a controls the strength of such a network, which could span from the soft to the rigid gel regime. The voids (the regions enclosing the LC molecules) define the scale of confinement, and thus ρ_a becomes the control parameter of the restricted geometry. Unlike the standard cell in which the surface–LC interactions arise only at the two bounding plates, the aerosil LC system results in such interactions in the "bulk" of the material also and therefore serves to enhance the influence on the static and kinetic characters of PIPT. LCM3, used as the host substance in the results to be described below consisted of 3.3 wt% of EPH in 4-*n*-heptyl-cyanobiphenyl (**7CB**). Figure 5.9 shows the differential scanning calorimeter (DSC) scans [167] obtained across the I-N transition for LCM3 and a soft gel composite ($\rho_a = 0.03$ g/cm^3) at a cooling rate of 1°C/min. While LCM3 exhibits a single peak, the aerosil mixture shows a twin-peak profile, more clearly seen at a cooling rate of 0.3°C/min (see inset of Figure 5.9). The observation of such a two-peak profile in an aerosol–LC composite has been associated [163, 167] with the development of nematic order from the isotropic phase through a two-step process. It is caused [165] due to a crossover from a random-dilution regime, where the silica gel couples to the scalar part of the nematic order parameter, to a random-field regime (occurring at a lower

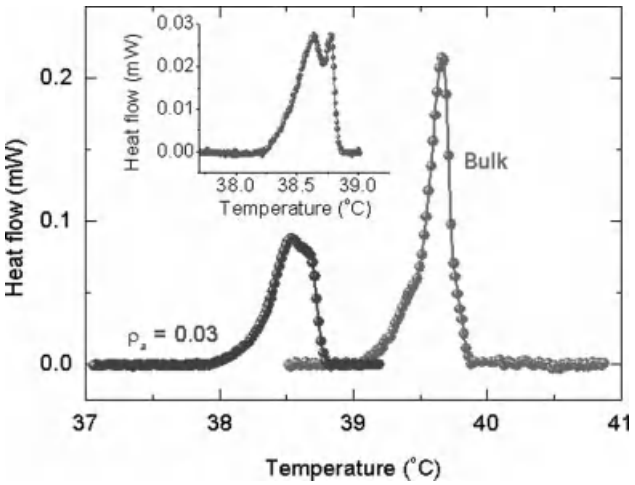

FIGURE 5.9 DSC scans at a rate of 1 K/min in the bulk and aerosil composites (aerosil concentration, $\rho_a = 0.03$ g/cm^3) of **7CB** + 3.3% EPH LC mixture, in the vicinity of the N-I transition. Notice the single peak of the bulk material gets split into two for the aerosil composite, a feature that is clearer when the cooling rate is reduced to 0.3 K/min, as shown in the inset [ref. 167].

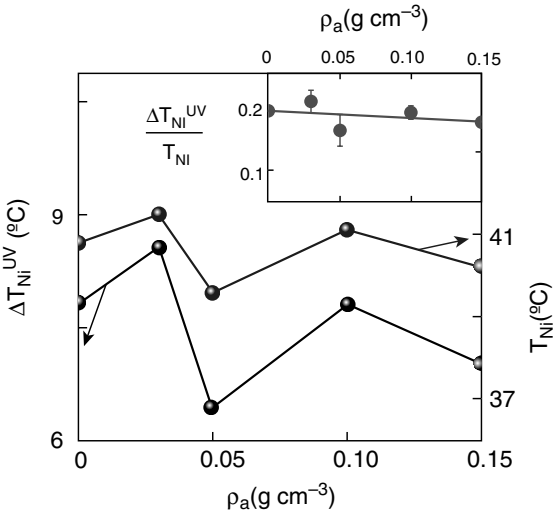

FIGURE 5.10 Influence of the aerosil composition on the transition temperature T_{NI} and the UV-induced shift in the transition temperature $\Delta T_{NI}{}^{UV}$. The inset shows that the ratio of the two parameters is only weakly dependent on the aerosil concentration. The line drawn through the data points is a fit to a straight line and the error bars indicate 95% confidence limit [ref. 167].

temperature), in which the coupling induces distortions in the director field. It should also be noted that the high temperature peak is much sharper compared to the low temperature peak. Since the high temperature peak is due to the appearance of the nematic domains in the isotropic phase, having a weak coupling to the aerosil network, its thermal signature is weaker than the low temperature peak. Upon isomerization of the photoactive component, the signature of this two-step process becomes prominent in the thermal and temporal variation of the dielectric constant of the sample, and also the temperature difference between the two steps increases. Surprisingly, just like T_{NI}, ΔT_{NI}, the photoinduced shift in T_{NI}, also varies non-monotonically with the aerosil density (see Figure 5.10). These results favor the random-field model in which the quenched LC is simply distributed randomly in space [166, 167]. The gel network also affects the kinetics of the photoinduced as well as the back relaxation process. The associated time scale again has a non-monotonic dependence on the aerosol density (Figure 5.11).

5.3.1.2 Polymer Matrix In comparison to the aerosil-LC case discussed above, LC sample dispersed in a polymer matrix (referred to as a polymer dispersed liquid crystal-PDLC system) forms a different kind of confinement. Unlike in the case of the aerosil-LC, the confining matrix of the polymer is more rigid and therefore the LC–surface interactions, which are again present not only at the bounding plates but also at each LC–polymer interface, should be stronger. The PDLC sample employed was composed of a photocurable prepolymer (Norland NOA65) and a LC mixture

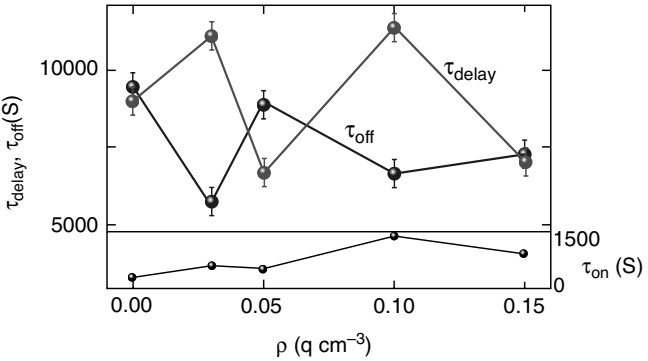

FIGURE 5.11 Dependence of the τ_{delay} and τ_{off}, the delay in the initial response and the total time taken to complete the back relaxation, respectively when the UV is switched off, on the aerosil composition. The response time τ_{on} for the photoinduced transition is shown in the bottom panel. Notice that all the responses vary non-monotonically with the aerosil composition [ref. 167].

(Merck-E7 + 5% EPH, referred to here as **LC4**) in the ratio of 62:38; we refer to the polymerized sample as **PLC**. Figure 5.12 shows the TBR process for the **LC4** and **PLC** samples [168]. The main difference in the behavior of the two samples was the substantial time delay (~2000 s) between the time of switch off, and the instant at which there is an abrupt decrease in sample response marking the onset of the I-N transition, typical of unconfined samples (including the **LC4** system), but absent for the **PLC** sample. However, after the abrupt variation further change in the response occurs at the same rate in both the cases. This behavior can be explained by applying the fact [169] that nematic order is known to persist at the surface even after the bulk has transformed into the isotropic phase. When UV is switched off this surface nematic order would promote the return of the photoinduced isotropic to the nematic phase in the bulk. While for the **LC4** sample the surface order is present only at the two substrate surfaces, for the polymer-based samples the presence of the polymer matrix provides "virtual surfaces" even in the bulk, at each LC–polymer interface, causing an acceleration of TBR and reduction of the delay time. Once the bulk starts recovering the N phase, the effect of the surface diminishes and therefore after the delay period the behavior of the two samples is quite similar. Owing to these features the total TBR time is twice as fast for the **PLC** sample in comparison to that for the **LC4** (see inset of Figure 5.12).

5.3.2 Influence of Anisotropy Reducing Component

Octadecane and other such similar long chain alkanes have only flexible units and thus *per se* are not favored to support the formation of liquid crystalline phases. Even when added to materials that already exhibit liquid crystalline phases they try to destabilize the liquid crystallinity [170]; at low concentrations (as it was the case in

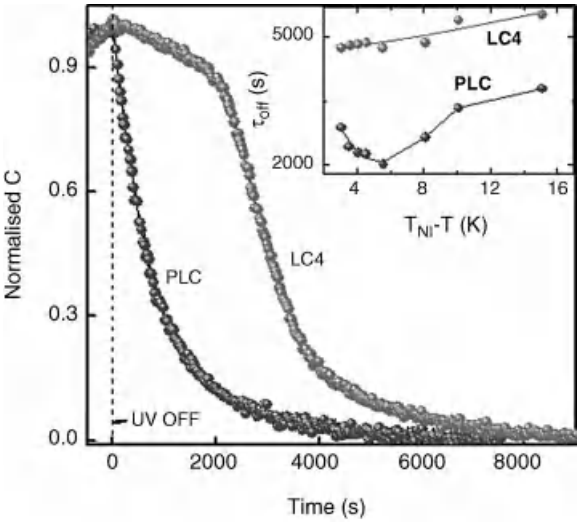

FIGURE 5.12 The thermal back relaxation processes for **LC4** and **PLC** samples probed as a function of the normalized sample capacitance *C*. After the UV is switched off, the **LC4** sample responds slowly and exhibits a substantial time delay between the time at which the UV is switched off and the instant at which there is an abrupt decrease in *C*, marking the onset of the I-N transition. In contrast the **PLC** sample, with the polymer matrix, responds instantaneously and has no time delay. The inset shows the dependence of τ_{off} as a function of reduced temperature for the two samples. Reprinted with permission from ref. 168, Copyright 2003, American Institute of Physics.

our experiments), the small biphasic region suggests that the structural incompatibility between the LC system and the alkane is still tolerable on a macroscopic scale. In the isotropic phase, due to the preference of the alkane molecules to exist in the coil-form, there would be less difference between the local order in the vicinity of the alkane and that of the entire medium. On the other hand, in the N phase the alkane molecules are forced to deviate from the coil-form to be compatible with the environment. But given an opportunity to deviate from this situation, the alkane molecules may hinder the liquid crystalline molecules in the vicinity from achieving nematic order. For the temperature-dependent transition, such an influence will lower the transition temperature, a feature generally observed for liquid crystalline mixtures containing alkanes. In the case of photoinduced transition, the process is an isothermal one. Thus a possibility is that in the absence of any isomerization-driven torques (e.g., presence of radiation to facilitate reverse isomerization) the local disorder of the alkane molecules will retard the relaxation of the system from the photoinduced isotropic phase, thereby increasing TBR by an order of magnitude [171]. Further, the length of the alkane employed also has a significant effect: a factor of 8 increase in TBR is seen when *n*, the number of carbon atoms in the alkane, is increased from 16 to 24 [172]; in contrast, the time duration for the photo-driven N-I process is hardly affected (see Figure 5.13).

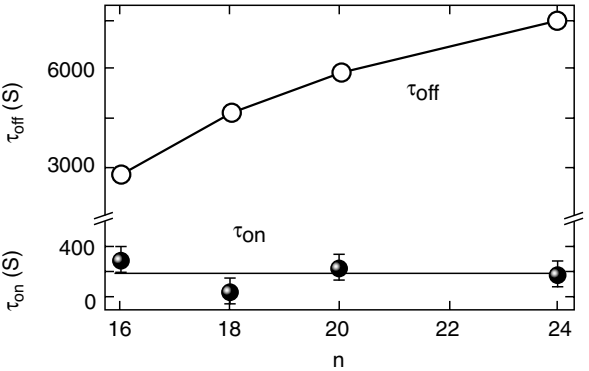

FIGURE 5.13 Influence of the length of the alkane, characterized by n, the number of carbon atoms in its chain, on the response times for the UV-on (τ_{on}) and UV-off (τ_{off}) processes at a fixed relative temperature of 20°C with respect to the clearing point. The ternary composite employed has the primary mixture consisting of hexyloxy cyanobiphenyl doped with 5 wt% EPH, to which the alkane is added at a concentration of 2.5 wt%. The lines are merely guide to the eye [ref. 171].

5.3.3 Influence of the Orientational Order

The orientational order of the nematic phase can be expected to govern the kinetics of the thermal back relaxation. However, contrary to expectations, τ_{off} exhibits [173] a non-monotonic variation with temperature having a pronounced reduction in the finite ΔT_{NI} region bracketed by the two transition temperature without ($T_{no\text{-}UV}$) and with UV ($T_{with\text{-}UV}$). Treating $\delta\varepsilon$, the difference in the dielectric anisotropy ε_a ($=\varepsilon_{\parallel} - \varepsilon_{\perp}$) between the equilibrium and photo-stimulated situations, as a good measure of the orientational order a simple correlation between τ_{off} and $\delta\varepsilon$ has been found (see Figure 5.14):

$$\tau_{off} = A + B \exp\left(\frac{-W}{K_B T}\right) - C\,\delta\varepsilon \tag{5.1}$$

5.3.4 Acceleration of TBR by an External Field

As discussed in previous sections, TBR, marking the recovery of the state existing before the photo-stimulation, is a slow process, extending from a few tens of minutes to days. Illuminating the sample with another radiation, typically in the blue region of the visible spectrum, is an established method of reducing this time scale. Now, we describe a recent finding [174] wherein an applied electric field can drastically alter the photoinduced thermal behavior and also accelerate the return to the equilibrium state. The fixed frequency dielectric constant data obtained for a planar sample in the absence of an electric field (except for the probing field) and when DC voltages of different magnitude are applied to a material with a positive ε_a are shown in

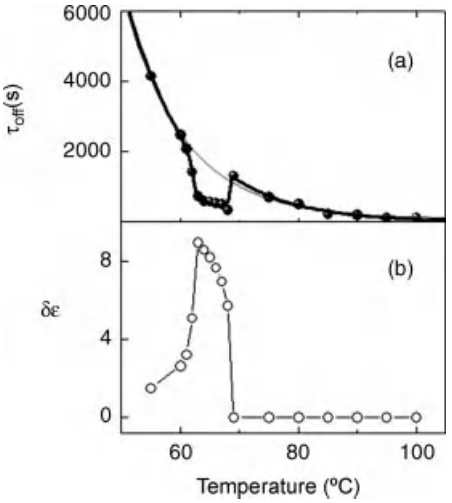

FIGURE 5.14 Thermal variation of the response time (a) τ_{off} and (b) $\delta\varepsilon$, the difference in the dielectric anisotropies for the no-UV and with-UV. The thick line in (a) is a fit to Eq. (5.1) and the thin line represents Arrhenius behavior [ref. 173].

Figure 5.15a. It should be noted that owing to $+\varepsilon_a$, the applied voltage, above a Freedericksz threshold (2 V for the sample used) causes a reorientation of the molecules from the planar to the homeotropic configuration. As the voltage is increased, ΔT_{NI}, the UV-induced shift in the transition temperature, is diminished to the extent that above a certain voltage there is no shift at all [174], resulting in an interesting temperature–voltage *phase diagram* (inset of Figure 5.15a). The striking influence of the field on TBR is shown in Figure 5.15b: τ_{delay} reduces by two orders of magnitude and τ_{off} by a factor of about 20 [174]. In a later section, we shall show that the observed behavior is universal and applicable to transitions involving different LC phases and discuss the possible reasons.

5.3.5 Effect of Elevated Pressure

Pressure being a thermodynamic variable, it can be expected that subjecting the sample to elevated pressures influences PIPT. Such studies demonstrated [175–177] the feature that application of pressure reduces ΔT_{NI}, even leading to complete absence of such a shift above a certain pressure. It was also found that P_o, the pressure at which such suppression takes place, can be tuned by I_{UV}, the magnitude of the actinic light intensity: P_o increases as the intensity is increased. Further, both ΔT and P_o vary strongly with I_{UV} at low intensities but have a limiting type of behavior for higher values of I_{UV}. This trend is qualitatively similar to the variation of ΔT_{NI} with I_{UV} at room pressure. The behavior of P_o is also similar to that of the dependence of the *E–Z* isomer conversion efficiency on I_{UV}. Pressure also strongly alters the kinetics of the photoinduced transition and its reversal. For quantitative description of the observation, we define four periods τ_1 and τ_3 as the delay times, and τ_2 and τ_4 as the

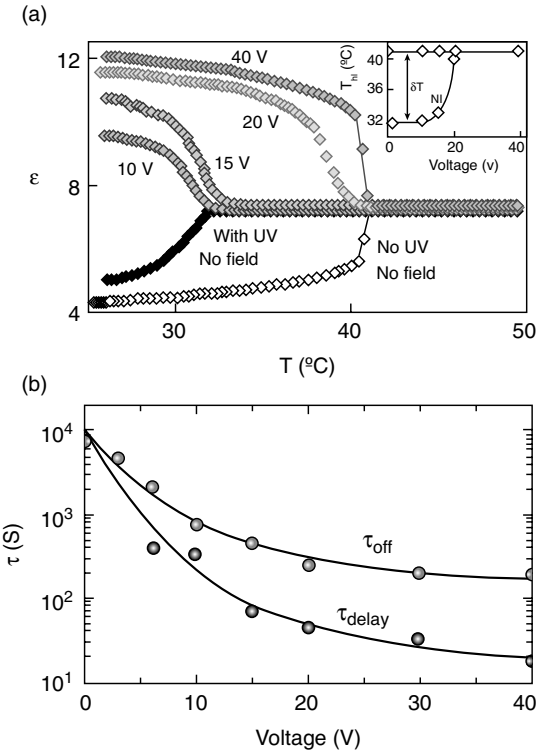

FIGURE 5.15 (a) Influence of the electric field (with the voltages indicated against each data set) on the dielectric constant behavior across the N-I transition in the presence of the UV radiation (filled circles). For comparison, temperature dependence of the dielectric constant ε obtained without the UV radiation (open symbol) is also plotted. Due to the positive dielectric anisotropy of the sample the application of the electric field reorients the molecules from the surface determined planar to the high-field driven homeotropic orientation. As a consequence ε decreases across the N-I transition unlike in the field-off case. For the sake of convenience of presentation, the data in the isotropic phase has been matched between different sets. Inset: Temperature–voltage phase diagram obtained without (open circle) and with UV radiation (filled circle). Notice that there is no UV-induced diminution in the transition temperature for voltages > 20 V. (b) Voltage dependence of the two time scales τ_{delay} (■) and τ_{off} (□) associated with the relaxation process, with the lines describing fit to an exponential function [ref. 174].

response times associated with the UV light being switched on and subsequently off. With increasing pressure, while the UV-on times, τ_1 and τ_2, show a moderate increase, τ_3 and τ_4 connected with the recovery of the equilibrium phase, exhibit an exponential decrease.

A standard nematic host (**8OCB**) doped with $n = 4$–11 homologues of a dimeric azobenze series [α,ω-bis(4′-*n*-butylazobenzene-4-oxy) alkane, BBAOA for short] as guests, has shown that the parity and length of the dimers affects the static and kinetic

characters of PIPT [177]. For example, not only the transition temperature T_{NI} but the shift ΔT_{NI}, also exhibits an alternation with the parity of the spacer in the dimer molecule. Figure 5.16a and b depicts the pressure dependence of the N-I phase boundary in the absence of, and upon UV illumination for the **M4** and **M5** mixtures (the numeral indicates the number of methylene units in the spacer of the photoactive compound). Although ΔT_{NI} diminishes with increasing pressure and finally vanishes for both the mixtures, P_o is substantially different. Indeed its value alternates with the parity of the spacer in the dimer, with the sign of alternation opposite to that of ΔT_{NI} (see Figure 5.16c).

Now, let us look at the possible reasons for the features observed in the high-pressure experiments. Isothermal measurements [178] suggest a decrease in the transition volume with increasing pressure. Consequently, with pressure there should be a reduction of the intermolecular space available for the azobenzene molecule to take a bent shape, which manifests as an opposition by the system for the formation of

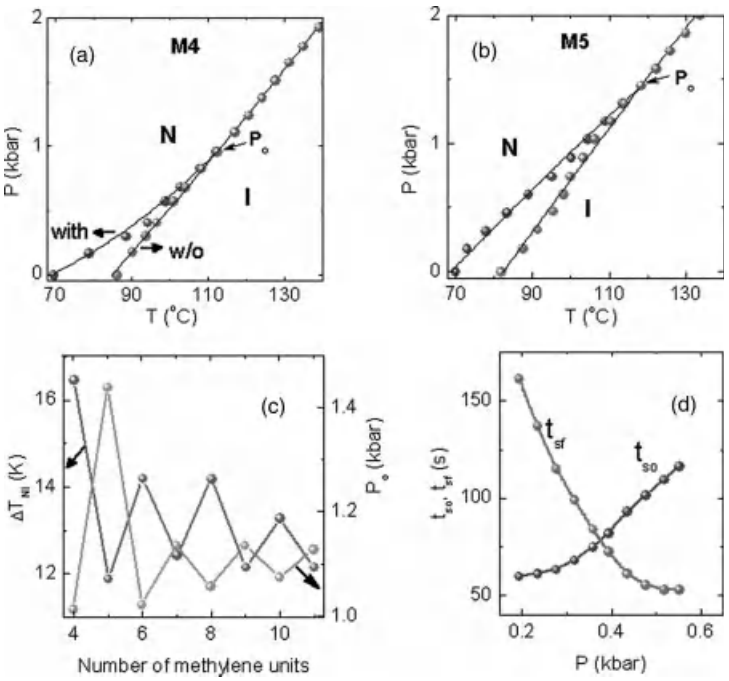

FIGURE 5.16 Pressure–temperature phase diagrams showing the N-I phase boundary obtained in the absence of (red symbols, without) and with UV radiation (blue symbols, with), for the representative mixtures **M4** (a) and **M5** (b), respectively. The photoinduced shift ΔT_{NI} decreases with increasing pressure becoming zero at a pressure of P_o. (c) Odd–even dependence of ΔT_{NI} and P_o on the spacer length of the dopant dimeric molecule. (d) Dependence of the total time (delay + response time) for the UV-on (t_{so}) and UV-off (t_{sf}) processes on the applied pressure at a constant reduced temperature of $T_{red} = 5°C$ for the mixture **M4** [ref. 177].

the Z isomers. As a result, the magnitude of ΔT_{NI}, dependent on the concentration of the Z isomers also becomes smaller as the pressure is increased and finally vanishes. This effect can be overcome, at least to a certain extent, by increasing I_{UV} thereby forcing the E–Z isomerization, leading to at least a partial restoration of the photoinduced shift in the transition temperature [176]; the balance between these two opposing forces decides the value of P_o for a certain I_{UV}. This fine balance between the opposing influences of the energy pumped and the pressure on the photoisomerization, can also explain the pressure dependence of the kinetics; the total (delay + response) switch off duration t_{sf} decreases with increasing pressure, whereas the total switch on duration t_{so} increases moderately (see Figure 5.16d). The odd–even effect on ΔT_{NI} caused by the parity of the spacer can be understood as follows. The E conformers of the even and odd spacers have respectively a somewhat elongated shape and a significantly bent shape (see Figure 5.17). Upon isomerization, whereas the even members assume a "Z" shape, the odd members take a "C" shape. This difference in the shape causes the projected length of the photoactive dopant to exhibit an alternation with n, the magnitude of the alternation being much larger for the E conformers than for the Z conformers [179, 180]. The larger change in the dimension of the even member dimers results in a larger value of ΔT_{NI} corresponding to their odd counterparts.

In the previous sections, we considered the influence of photoisomerization on the N-I transition. Next we consider achiral as well as chiral systems possessing smectic phase(s). Generally, a phase transition caused by the E–Z isomerization results in a reduction of the ordering of the medium, i.e., the transformation is an order to disorder transition. Further, as a rule, the photoinduced phase would in any case occur

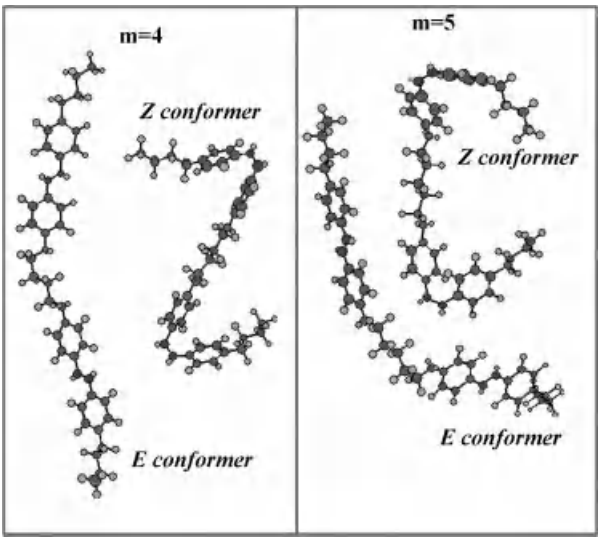

FIGURE 5.17 Minimum energy configurations in the E and Z conformer states for representative even ($m = 4$) and odd ($m = 5$) spacer dimer molecules.

in the thermal cycle. Exceptions to these features were found in the recent experimental results, as discussed in the following.

5.3.6 Dynamic Self-Assembly of the Smectic Phase

The phenomenon of reentrance has attracted a great deal of attention in a variety of condensed matter systems such as multicomponent systems, superconductors, solid ferroelectrics, and liquid crystals. A phase is said to be reentrant if it occurs both above and below another phase when a thermodynamic field like, e.g., temperature or pressure is varied. Perhaps the earliest example is of the nicotine system investigated by Hudson [181, 182]. In liquid crystals, the first such example was reported in a binary phase diagram at atmospheric pressure [183] later for a single component material at high pressures [184], and subsequently at room pressure [185, 186]. Since then a number of single-/multi-component materials have been reported to exhibit the reentrant sequence, either at atmospheric or at elevated pressures. The studies to be described below were on the reentrant nematic phase seen in a temperature–concentration binary phase diagram: specifically, for certain compositions, the system containing a photoactive guest component exhibits a nematic−smectic A−reentrant nematic ($N-SmA-N_{re}$) phase sequence on cooling from the isotropic phase. Upon UV illumination, the SmA and the high temperature N phases transform into N and isotropic phases respectively, as indeed expected, since photoisomerization can result in the "melting" of the phase, or in other words, transformation to a lessordered state. The N_{re} phase, however, transforms to a more ordered state, viz., the SmA phase [187]. Even more exotic behavior was observed [188, 189] for a mixture which did not exhibit the SmA phase in the absence of UV radiation. The self-assembly to the layered phase occurred with the UV radiation acting as a stimulant and existed only as long as the radiation was present.

The self-assembly of the layer structure in the above two cases (of dynamic character in the second one) has been explained using a combination of the photo-driven nanophase segregation mechanism [190] and the frustrated spin-gas model [191], the essentials of which are given in the following. In the equilibrium situation (absence of UV radiation) the photoactive molecules, in their rod-like *E* form are easily accommodated into the smectic layers. In contrast, the photoinduced *Z* isomers having a bent form not compatible with the shape of the host molecules are expelled to a region between the host molecule layers creating *nanophase segregation*. The frustrated spin-gas model [191] was essentially proposed to explain the reentrant behavior in materials, such as the host compound in the above-mentioned studies [188, 189] in which the molecules have a strong terminal polar group. Frustration is introduced by considering the possible terminal dipole configurations of a triangular lattice of the molecules. Relative stability of the SmA or the N (N_{re}) phase is compared by looking at the contributions of the dipole triplet to the free energy. In such a scenario, in the absence of the photoisomerization-driven segregation the molecules are free to liberate along the director direction, which promote the N or the N_{re} phase. The nanophase segregation due to photoisomerization will, in the segregated layers of the photoactive *Z* isomers in their bent form, create an alien

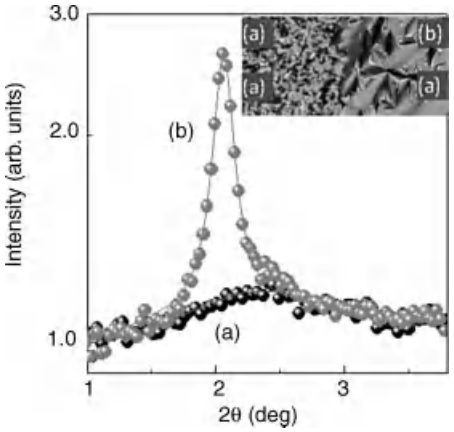

FIGURE 5.18 X-ray diffraction profiles of the (a) equilibrium N_{re} and (b) photoinduced SmA phases. As expected the N_{re} phase shows a broad and diffuse peak whereas the SmA has an intense and sharp profile. The lines are fits to a Lorentzian expression. The inset shows the corresponding polarizing microphotographs in the two phases: (a) N_{re} and (b) SmA [ref. 188].

atmosphere for the host rod-like molecules, thus disfavoring libration. Consequentially a layered arrangement as in the SmA phase is favored, as indeed established by X-ray (Figure 5.18) and magnetic field driven Freedericksz transition experiments (Figure 5.19). The texture changes seen under a polarizing microscope when the material transforms from the equilibrium N_{re} to the photoinduced SmA phase are shown in the inset of Figure 5.18, providing a clear support for the photo-driven layered structure. The photostabilization of the SmA phase allows one to map novel temperature–UV intensity (T–I_{UV}) phase diagrams, such as the one shown in Figure 5.20, with the critical intensity (I_c) needed to photoinduce the SmA increasing

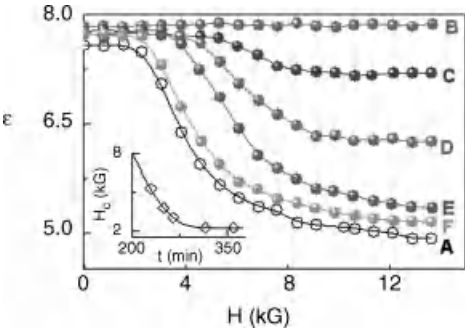

FIGURE 5.19 The magnetic field dependence of the sample dielectric constant in the photoinduced SmA (curve B) to the equilibrium N_{re} (curve A) phases. The time lapse profiles C–F show the behavior during the thermal back relaxation of the system after the UV beam is switched off. The temporal variation of the critical Freedericksz threshold field H_c during this relaxation is shown in the inset [188].

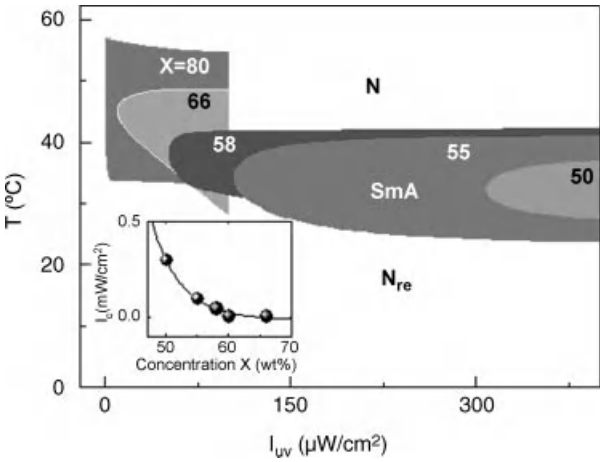

FIGURE 5.20 Partial temperature–UV intensity (I_{UV}) phase diagrams for various concentrations (X in wt%) of the non-smectic component in the host (non-photoactive) mixture, but with a fixed (4 wt%) concentration of the UV-active compound, to demonstrate the photostabilization of the SmA phase in systems ($X = 50$–66) lacking it in the absence of UV light; the filled area represents the thermal range of the SmA phase, whereas N and N_{re} phases exist above and below it respectively. For comparison, the diagram for $X = 80$ is also shown for which the SmA exists in the thermal cycle and its range increases with UV intensity. Inset: As X decreases the critical UV intensity (I_c) needed to induce the SmA phase increases drastically [ref. 189].

drastically as the concentration of the non-smectic component in binary non-photoactive host decreases (see inset of Figure 5.20). It may be pointed out that the UV intensity, used as a variable here, is a non-thermodynamic quantity, but mimics, in a limited sense, the role of a thermodynamic parameter like, for example, pressure. Also, it is worth noting here that these phase diagrams are obtained under non-equilibrium conditions as the existence of the SmA phase is dynamically driven.

As stated earlier, an applied electric field has been reported to accelerate the relaxation of the Z isomers to their E form, and consequent recovery of the equilibrium phase. The effect of the electric field is not specific to the N phase [174] or even to LC materials [192]. Here we quote an example of the reentrant system. Unique temperature–electric field phase diagrams of a liquid crystal exhibiting isotropic–nematic–smectic A–reentrant nematic sequence, mapped using light transmission as probe reveal that the electric field influences all the transitions, but the effect is maximum on the equilibrium reentrant nematic to the photoinduced smectic A transition [193]. Temporal measurements performed under non-equilibrium conditions to study the dynamics of both the photochemical and the back relaxation processes across the different transitions, show that the electric field is indeed observed to accelerate the thermal back relaxation in each case; especially the recovery of the reentrant phase is hastened by three orders of magnitude in time. A schematic diagram representing the molecular arrangement for

the photo-driven process across the three transitions, N-I, SmA-N, and N_{re}-SmA is given in Figure 5.21.

Now we look at the possible causes for the observed acceleration. While simple dielectric or flexoelectric coupling can be ruled out as the possible cause for the electric field-determined acceleration of the recovery of the *E* isomers, the electrode polarization as the reason may still be operative in the N-I as well as the reentrant cases. However, the different magnitudes of acceleration for the different transitions in the same system, and also that the values are non-monotonical with temperature indicates that there could be other influences also. It is perhaps that the electric field directly influences the azobenzene molecule itself with the host molecules hardly playing any role.

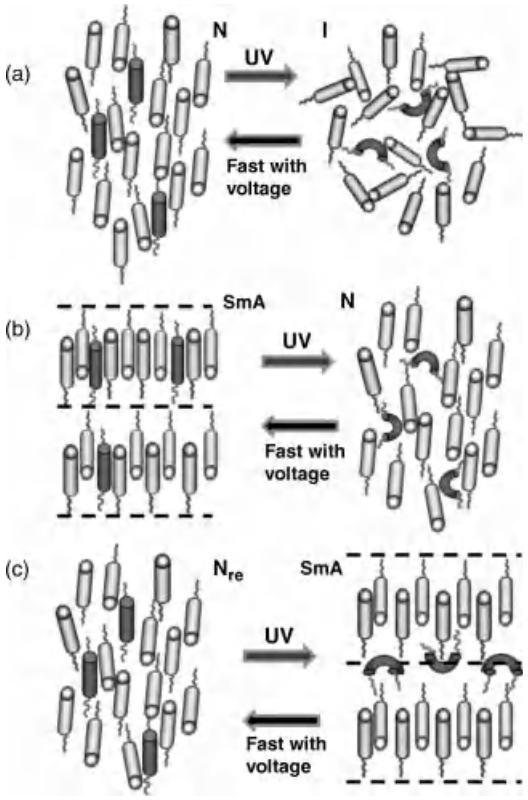

FIGURE 5.21 Schematic representation of the molecular arrangements in the equilibrium (left panels) and photo-driven (right panels) states. Notice especially the nanophase segregation in the photo-stimulated SmA phase (panel c). The cyan objects stand for the host non-photoactive molecules with a cyano termination. The red-straight objects are the azobenzene (EPH) molecules in their *E* form, which upon isomerization assume a bent form (bent red objects). The left pointing arrows emphasize the fact that the application of an electric field accelerates the return of the equilibrium phase owing to a swift back relaxation of the *Z* isomers to their *E* form, which otherwise is a very slow process.

A theoretical model that is under consideration in this regard is the density-functional-theory-based calculation [194], which proposes the possibility to induce the isomerization of azobenzene in the gas phase by an electric field; this model has been used to explain electric field-induced isomerization of an azobenzene derivative on the gold surface by a scanning tunnelling microscope (STM) tip [195]. The theory considers that in the presence of an electric field, the potential-energy surface related to a reaction path can be deformed, thus leading to an effective lowering of the isomerization barrier. Such an effect is argued to depend on the orientation of an intrinsic dipole moment (if present) and also on the polarizability of the molecule. The essential point is that application of an electric field reduces the potential barrier between the *E* and *Z* isomers and therefore favors a quicker return of the photoactive molecule to the equilibrium form. Qualitatively this theory can explain the influence of the electric field on the static as well as dynamic properties that have been observed in our experiments. A point that should however be emphasized is that the actual electric field in our experiments is (even at the highest voltage of 20 V) three orders of magnitude smaller than in the STM experiments. It is possible that the anisotropic ordering of the LC environment lower the actual field required.

5.3.7 Tilt Susceptibility Behavior Across SmA-SmC$_\alpha^*$ Transition

The SmC phase is the tilted analogue of the SmA phase having the director at an angle to the layer normal direction. Investigations on this phase, especially when composed of chiral molecules (SmC*) have attracted much attention since the phase displays ferroelectric properties. A variant of the SmC* phase, called as the antiferroelectric SmC* or SmC$_A^*$ phase, was reported in 1989 in which the molecules in neighboring layers are tilted from the smectic layer normal in almost opposite directions [196]. Subsequently, other sub-phases like the ferrielectric SmC$_\gamma^*$ and SmC$_\alpha^*$ phases have been discovered [for reviews on the antiferroelectric smectic and sub-phases see 197, 198]. Resonant X-ray scattering experiments [199] have established that the SmC$_\alpha^*$ phase has a short-pitched incommensurate helical structure extending over a few layers. Investigations on the effect of light in a system exhibiting the SmA-SmC$_\alpha^*$ phase transition using dielectric spectroscopy show that at any given reduced temperature, $T - T_c$ (T_c is the SmA-SmC$_\alpha^*$ transition temperature) the UV light enhances the magnitude of the tilt fluctuations [200, 201]. This is the opposite of the effect induced by ordering fields such as electric or magnetic fields [202]. Figure 5.22 presents the dielectric absorption spectra at a fixed temperature after the UV radiation is turned on: with elapsing time, the soft mode relaxation frequency f_s connected with softening elastic opposition to tilt fluctuations increases while the strength of the mode ε_a decreases before reaching a photostationary state in about a few minutes. The detailed temporal behavior of these two parameters brings out the influence of the magnitude of the UV intensity (see Figure 5.23). The variation of f_s with time is not the same at all UV intensities, with two different regions demarked by a critical intensity I_{cr}. For $I_{UV} < I_{cr}$ (region I), f_s decreases monotonically with elapsed time. In region II, with $I_{UV} > I_{cr}$, f_s diminishes immediately after the UV is on, but reverses its trend after a certain time interval; the time at which the reversal is seen decreases for

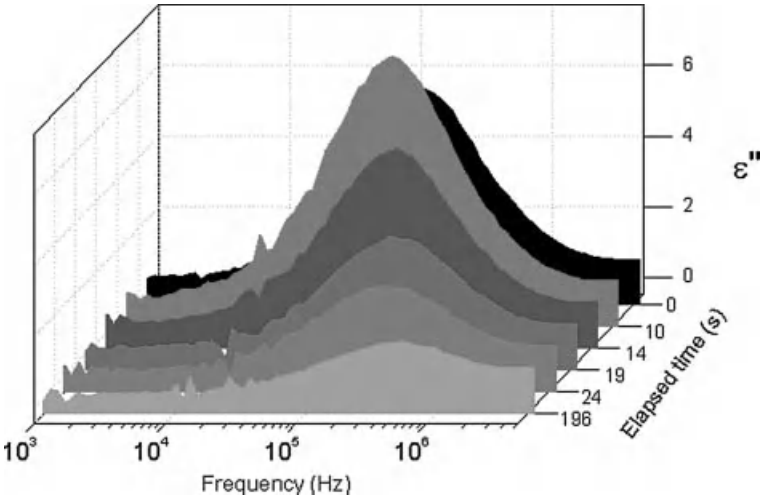

FIGURE 5.22 Dielectric loss spectra taken in the SmC_a^* phase (1°C below the transition, obtained before $t = 0$) and at elapsed times (indicated against each curve, in seconds) after the UV illumination is turned on. Notice that on UV illumination, initially the relaxation frequency (~peak frequency of the profiles) shifts to a lower value ($t = 10$ s) scan and then to higher values, reaching a limiting value for longer time scales [ref. 201].

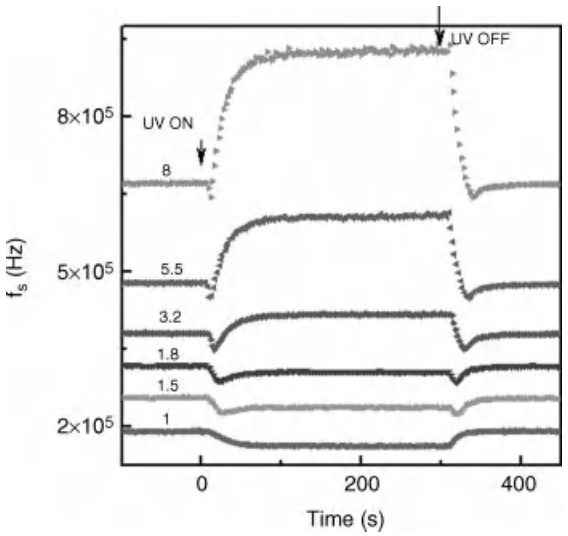

FIGURE 5.23 Evolution of the soft mode relaxation frequency (f_s) in the SmC_a^* phase as a function of time for UV-on and subsequent UV-off situations. The number mentioned above each dataset indicates the intensity of the UV light (in mW/cm^2) employed. For the sake of clarity the data sets have been shifted by arbitrary amounts in the vertical direction. It may be noted that before UV-on the f_s values coincide for all data sets [ref. 201].

higher intensities. Concomitant changes are seen in the dielectric strength. Comparing this behavior with the well-known thermal variation of these parameters [201], such a reversal in the trend signifies the photoinduced and isothermal SmA-SmC$_\alpha$* transition. Owing to the striking similarity between the thermal and I_{UV} dependence of the relaxation parameters, the latter data have been analyzed in terms of the equations of a Landau model for the thermal SmA-SmC* transition, expressing f_s as

$$f_s = \text{const} + A_1^{\pm}(I_{UV} - I_{cr})^{\gamma} \tag{5.2}$$

Here, $A_1^{\pm}$ represents the amplitudes above and below I_{cr}, the critical intensity to induce the isothermal transition which plays the role of transition temperature for the case of the thermal transition. In the thermal case, the exponent γ describes the critical behavior of the susceptibility near a critical point, having values dependent on the universality class to which the transition belongs: 1.24 for the 3D Ising and 1.316 for the 3D XY. The fitting to Eq. (5.2), shown as solid line in Figure 5.24 yields $\gamma = 1.23 \pm 0.04$, which within error bar is in agreement with the theoretically prediction for the Ising model [203]. It is worthwhile to recall that the specific heat data analyzed using correction-to-scaling terms seemed to favor the XY model, although description with the Ising model could not be unambiguously precluded [204]. In our opinion, the third possibility of the measured exponent being an effective one due to the crossover from mean field ($\gamma = 1$) to 3D XY ($\gamma = 1.316$) regimes, cannot also be ruled out. A caveat that should be added concerning the photo-driven transition data is that there is no *a priori* rule to say that the photoinduced isothermal transition should behave the same way as a thermal transition.

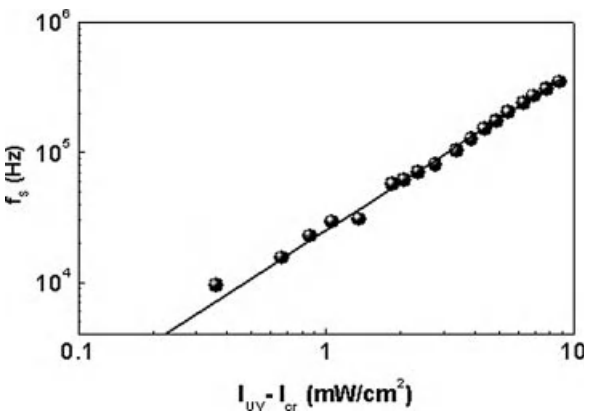

FIGURE 5.24 Double logarithmic plot of the UV intensity dependence of the saturated values of the relaxation frequency, with the slope of the straight line (a fit to Eq. (5.2)) yielding $\gamma = 1.23 \pm 0.04$ and a critical intensity I_c value of 1.2 ± 0.1 mW/cm^2 [ref. 201].

5.3.7.1 Polarization-Tilt Coupling in an Antiferroelectric System The better known of the smectic C antiphases, is the antiferroelectric smectic C (SmC_A^*) phase [196]. In this phase, the molecules in the neighboring layers are tilted from the smectic layer normal in almost opposite directions; in contrast the tilt is synclinic in the SmC^* phase. Generally, the SmC^* phase intervenes between the SmA and SmC_A^* phases. But in certain materials there can be a direct transition from the Sm-A to the SmC_A^* phase. A detailed study on the effect of photoisomerization in a binary mixture (referred to as AFM hereafter) composed of TFMHPOBC and 5% by weight of the guest UV-active dopant EPH has been reported [205]; this system exhibits a direct transition from the SmA to the SmC_A^* phase. The two-peak sample current response to an applied triangular wave characteristic of the SmC_A^* phase is employed to determine the electric polarization (P_s) as a function of temperature in the absence of and upon illuminating the sample with $I_{UV} = 4\,mW/cm^2$. The gross trend of the temperature dependence of P_s remains the same with and without UV. However, two distinguishing differences result from photoisomerization: (i) there is a reduction in T_c (the SmA-SmC_A^* transition temperature) and (ii) the saturated value of P_s seen well below T_c is substantially lower than without UV. The first feature, routinely seen for PIPT as discussed above, is labeled as *secondary photoferroelectric effect* [150]. Even after taking care of the reduction in the transition temperature, a large (30%) diminution in P_s found experimentally (Figure 5.25) should be accounted for. We suggest that this may be associated with a change in the polar ordering and/or the transverse molecular dipole moment and refer to it as *primary photoferroelectric effect* (PPE), and in the following look for possible causes. In ferroelectric as well as antiferroelectric LC systems the tilt angle of the molecules (θ) with respect to the layer normal is the primary order parameter and the electric polarization P_s is a secondary order parameter. Owing to a strong coupling between these two parameters, the primary photoclinic (light-driven tilt of the molecules) effect, although

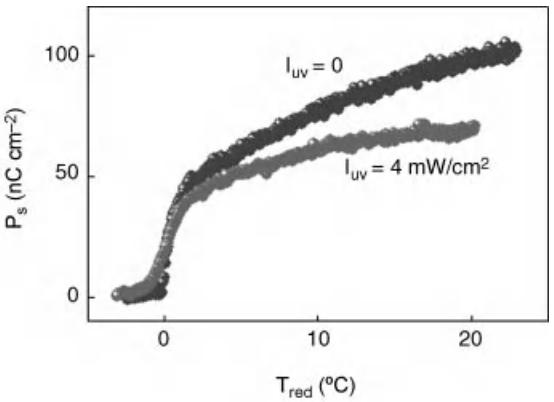

FIGURE 5.25 Dependence of the spontaneous polarization (P_s) on reduced temperature in the absence of UV (top curve) and when the sample is illuminated with $I_{UV} = 4\,mW/cm^2$ (bottom curve) for the antiferroelectric AFM mixture exhibiting PPE [ref. 205].

can be expected to be the cause for PPE, is not borne out by the experiments. The nanophase segregation mechanism, described above, is a possibility, but ruled out however, owing to the fact that upon UV illumination the maximum observed increase in layer spacing, and the consequent change in the dipole moment/unit volume is too small to account for the measured decrease in P_s. We suggested [205] that the cause lies in photoisomerization altering the coupling between P_s and θ, which turns out to be true when the data is analyzed in terms of a generalized mean field model [206]. This model incorporated a 6th order term in θ to account for the possibility of first order transition and a biquadratic coupling term $-\Omega P_s^2\theta^2/2$ to bring in transverse quadrupolar ordering (which is non-chiral in character). With terms relevant for the present case, the free energy is written as

$$F = F_o + \frac{a}{2}\theta^2 + \frac{b}{4}\theta^4 + \frac{c}{6}\theta^6 + \frac{P_s^2}{2\chi} - CP_s\theta - \frac{\Omega}{2}P_s^2\theta^2 - P_sE \tag{5.3}$$

yielding a simple relation between P_s and θ,

$$P_s = \frac{C\theta}{1/\chi - \Omega\theta^2} \tag{5.4}$$

Here a, b, and c are the usual Landau coefficients with only the parameter a having a temperature dependence, χ is the susceptibility, C and Ω are the bilinear and biquadratic coupling coefficients between P_s and θ, and E is the applied electric field. In this model an all important parameter $\beta \propto C/\Omega$ dictates the temperature dependence of the P_s/θ ratio.

The polarization dependence on tilt angle with and without UV illumination is given in Figure 5.26, along with the fitting done using Eq. (5.4). To be noted is the

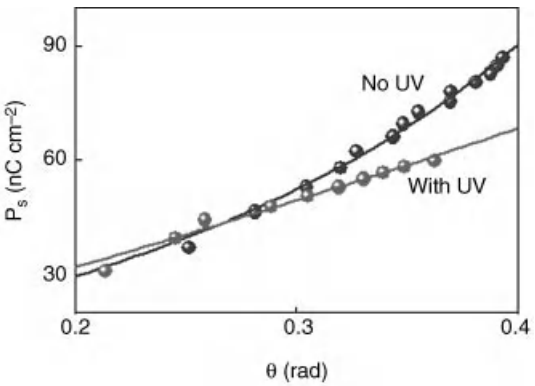

FIGURE 5.26 Tilt angle dependence of polarization in the absence of and upon shining UV. Notice that the no UV data has a significant curvature, whereas the data obtained with UV is nearly linear. The fit to Eq. (5.4) (shown as solid lines) describes the data well in both cases [ref. 205].

feature that while the data collected without UV has a significant curvature, under UV illumination it is highly linear (In fact, a fit done to the expression for a straight line yields only a slightly poorer fit.). The C and Ω values obtained from the best fit of the data to Eq. (5.4) are $4.4 \pm 0.1 \times 10^7\,\mathrm{V\,m^{-1}}$ and $8.2 \pm 0.4 \times 10^{10}\,\mathrm{N\,m^2\,C^{-2}}$ for the no UV data set and $5.2 \pm 0.2 \times 10^7\,\mathrm{V\,m^{-1}}$ and $1.8 \pm 0.1 \times 10^{10}\,\mathrm{N\,m^2\,C^{-2}}$ for the data with UV illumination; these values are of the same order of magnitude as for other ferroelectric liquid crystals [205, 206]. The photoisomerization influences the non-chiral coefficient Ω (factor of 4 decrease) more than the chiral coefficient C ($\sim$17% increase), resulting in an increase of the ratio C/Ω by a factor of 5. In other words, UV illumination reduces the non-chiral aspect of the P_s–θ coupling, thus supporting the qualitative change in the behavior of the P_s vs. θ data from non-linear trend to a linear one as shown in Figure 5.26. These observations are further supported by the UV-intensity dependence of the thermal variation of the dielectric strength [207]. From a molecular level of view, it may be suggested that mutual steric interactions, and consequent mutual orientation directions of the steric dipoles of the guest photoactive molecules and the host non-photoactive molecules, are perhaps responsible for the experimental features.

5.3.7.2 A System with Bent-Core Molecules Contrary to the earlier thinking, ferroelectricity has been observed in liquid crystals made of entirely achiral molecules, having a bent or banana shape [106–109]. The origin of spontaneous polarization in these systems is believed to be a combination of the following factors. These molecules have a highly polar character, are arranged in smectic layers in such a way that the dipoles point along a common direction within the layer and are tilted with respect to the layer normal. These factors can give rise to chiral layer symmetry, although the molecules themselves are achiral. Here again, the polarization P_s as well as the response time τ decrease upon photoisomerization of the guest EPH molecules in a host bent-core system; upon switching off the UV illumination, a rapid recovery to the equilibrium values is also observed (see Figure 5.27a) [208]. While ruling out the lowering of the transition temperature and the nanophase segregation mechanism as the cause for the reduction in P_s and τ (the response time), the results have been explained by considering the EPH molecules to remain in the smectic layer, even in the presence of the UV radiation. Since there is no additional volume cost, unlike for the host bent-core PHDBB molecules, the polar axis of the bent EPH molecules within one layer could point in either direction compared to the polar axis of the smectic layer. The antiferroelectric character of such an arrangement reduces the polar character of the layer, thereby reducing P_s values. In the tilt plane, i.e., the plane normal to twofold symmetry axis, the two Z molecules within one smectic layer can adopt a synclinic geometry. The disposition of the EPH molecules in this manner can perhaps be thought of as a "local racemization" (see Figure 5.27b). The behavior of the response time can also be explained with the above concept.

Photoinduced effect on the chiral azobenzene-based banana-shaped LCs (Figure 5.28) involving the N*-I transition and shift in selective reflection band position of the N* phase has been reported very recently [209]. A blue shift in the selective reflection band occurs when *cis*-isomers exist in low population; for a higher

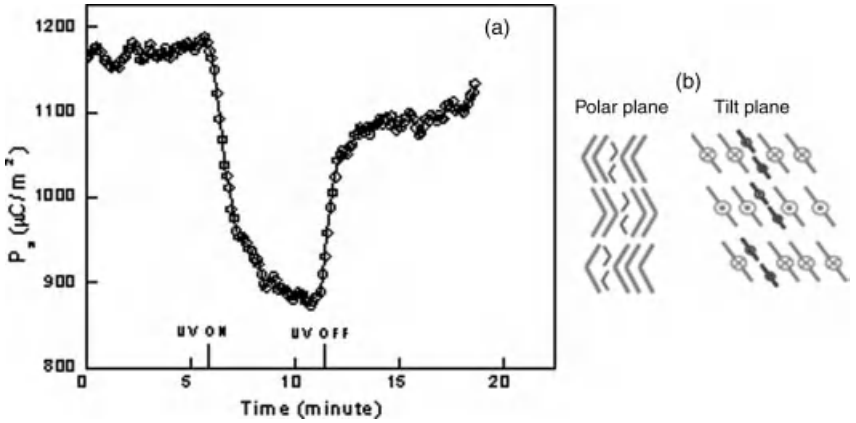

FIGURE 5.27 (a) Time dependence of the polarization upon UV illumination and subsequent switch OFF. The sample is kept at 4°C below the B_2–Iso transition temperature. The time required for substantial change in the value seems to be comparable for both illumination and switch OFF processes. (b) Polar plane and tilt plane views of the bent-core host (red structures) and rod-like photoactive guest molecules (blue entities) in their *Z* form. In the right panel, crosses indicate polarization direction pointing towards, and the crosses, away from the reader. Reprinted with permission from ref. 208, Copyright 2001, American Institute of Physics.

cis population isothermal transition to isotropic phase occurs. Using these materials as chiral dopants in the standard nematic mixture E7, their helical twisting power (HTP), given by $\beta = 1/PC$ (where P is the helical pitch length, and C is the concentration of a chiral dopant) has been determined. The β values for *trans* isomers of **1** and **2** were found to be 4.5 μm^{-1} and 3.3 μm^{-1}, respectively. A further lowering of β value was observed when *cis*-isomers are formed upon irradiation and thus, a light-induced hypsochromic shift results in the selective reflection band of the

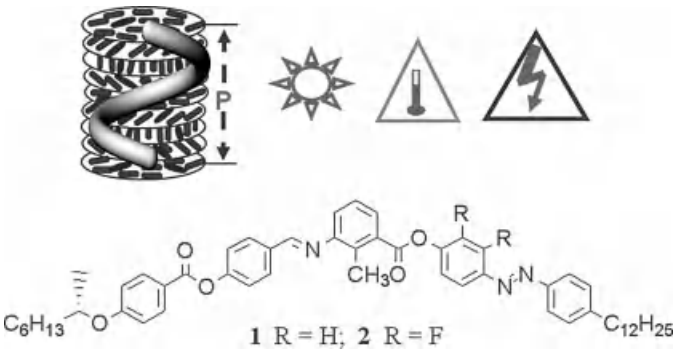

FIGURE 5.28 A schematic representation of chiral nematic (N*) phase with a photoresponsive, as well as thermally and electrically addressable, pitch *P*, composed of photosensitive optically active azobenzene-based banana-shaped compounds **1** and **2** [ref. 209].

N^* phase. These results are in agreement with the fact that a photoinduced shift in the N^* pitch can also occur due to the difference in twisting ability of the *trans* and *cis* isomers of photochromic chiral additives [210], as also seen by others [140, 211]. Indeed, such photoinduced effects involving the shift in the selective reflection band of the N^* phase have also been reported for a variety of photoactive compounds/dopants [21–27, 63–65, 78, 84–88, 140, 210, 211].

5.4 APPLICATIONS

5.4.1 Holography

Several photoactive polymeric LCs exhibiting N-I transitions have been examined in the context of dynamic holography phenomenon as it holds an immense promise in real-time image processing, phase conjugate mirrors, and other optical communication applications [31, 32, 49–52]. In particular, the important characteristics, viz., thermal stability of the stored information, resolution sensitivity, and storage capability have been evaluated; the high performance of these photoactive polymeric LC as a holographic recording medium has been revealed. Besides, a variety of low molar mass LCs [55–58] and LC/polymer composites [39, 40] have also been studied extensively in the context of both static and dynamic holographic gratings. However, it must be remarked here that Wendorff et al. pioneered the production of holograms in LC copolymers containing azobenzene moieties and mesogenic groups [33, 34, 61, 62].

Following the report of holographic device by Wendorff's group [33, 34], Ikeda and coworkers [35] demonstrated the potentials of N-I transition in optical image storage application by showing fast photochemical change (200 μs) both in low molar mass (**BMAB** and **8AB8**) and polymeric (**PA6AB2**) nematic LCs (see Chart 5.5B). In this demonstration, the nematic phase of polymeric LCs, covered with a photomask, is made to undergo photoinduced N-I transition; the illuminated regions transform to the isotropic liquid phase, while the unexposed remain in the N phase. The sample then taken to the glass state retains the stored pattern, even though reverse isomerization (*cis–trans*) occurs, pointing to the fact that no phase transition takes place in the glass environment. This feature has been ascribed to the fact that while the segmental motions of polymer chains are possible, no macroscopic ordering (necessary for the isotropic liquid state to return to the equilibrium N phase) is realized. Following this different types of azobenzene–low molar mass LC composites [43, 44], azobenzene–polymeric LCs [45], polymeric LCs [49], and copolymers [50] have been prepared and their response were investigated.

The dual frequency feature of some nematogens has been exploited to create an optical storage device. The nematic phase of such materials exhibits a crossover frequency f_c at which the dielectric anisotropy ε_a $(=\varepsilon_{\parallel} - \varepsilon_{\perp})$ changes sign: from being positive for $f < f_c$ to negative for $f > f_c$. Hence upon application of an electric field the molecules would feel a positive dielectric torque if $f < f_c$ and a negative torque if $f > f_c$. In other words, above a certain magnitude of the electric field, the so-called Freedericksz threshold, the director prefers to be along or perpendicular to the

electric field in the two cases, allowing the orientation (homeotropic/planar) to be controlled by the field itself, instead of appealing to surface forces. It has been demonstrated that such a configurational switching can be achieved at a constant frequency by illuminating the sample with actinic light [212]. The principle behind such a device is the substantial increase in the dielectric relaxation frequency f_R (and thus indirectly in the crossover frequency f_c), induced by the radiation (see Figure 5.29a). These changes are associated with strong changes in the transmitted intensity of the liquid crystal cell, which can be exploited to realize a photonic addressable device in which the bright and dark states are achieved without letting the material to transform to the isotropic phase, a highly desirable aspect particularly in view of enhancing the chemical stability of the liquid crystalline substance employed. Figure 5.29b is an optical storage device that is realized using this phenomenon. The sample was illuminated with UV light of 10 mW/cm^2 intensity through a standard pattern (1951 USAF resolution pattern positive target) while maintaining a high frequency voltage across the cell.

5.4.2 Soft Actuators

In recent times, the photoinduced N to I transformation has been also used in developing soft actuators derived from liquid crystalline elastomers (LCEs) [27, 90–95, 213, 214]. The possibility of coupling between orientational order and mechanical properties in

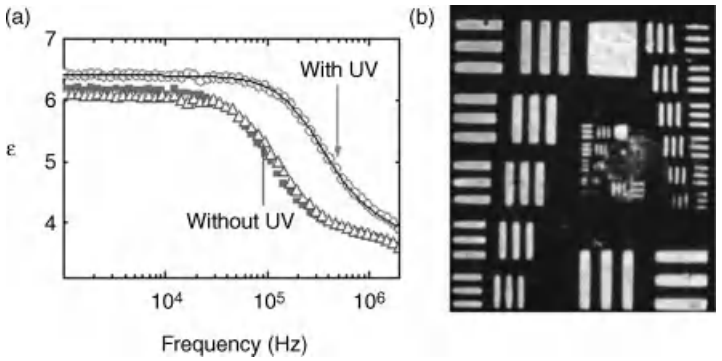

FIGURE 5.29 (a) Dielectric dispersion scans taken in the nematic phase exhibiting the dual frequency character before (open triangles), and with steady-state UV radiation (open circles). Notice that the relaxation frequency (indicated by the arrows) is higher for the UV-on case. After the radiation is switched off, the original value is recovered, as shown by the data indicated with filled squares. For the sake of clarity, the solid line representing the fit to the Havriliak–Negami equation is shown only for the UV-on data. (b) Optical storage device realized using the dual frequency principle. The sample was kept at room temperature and illuminated with UV radiation through a photomask (a standard 2″ 1951 USAF resolution pattern positive target). The dark regions are where the molecules are in the homeotropic alignment caused by the passing of the UV and the bright regions are where the radiation is masked. Reprinted with permission from ref. 212, Copyright 2005, American Institute of Physics.

LCEs, pointed out by de Gennes [91, 92], has potential application as artificial muscles and mechanically tunable optical elements [215]. In fact, experimentally, a spontaneous contraction along the director axis of the nematic LCE films upon heating towards the N-I transition has been observed [93]. Notably, the deformation in the shape up to 300% has been achieved in nematic LCE films derived from side-chain siloxane polymers [94]. Developing on the concept of photomechanical effects of a monolayer consisting of polyamides [216], large and reversible deformation of LCEs driven by actinic light have been demonstrated; the gradient of the cross-linking density, polarization direction of actinic light, the initial alignment of the LC molecules, etc. are found to control the associated motions of such LCE films [95, 100, 217]. Detailed mechanical characterization of such films has also been performed recently [218].

The occurrence of this photomechanical effect has been attributed to the decrease in the order parameter caused by *trans–cis* isomerization. For example, Ikeda's group [95–98] has accomplished photoinduced three-dimensional deformation of the azobenzene-based nematic LCEs swollen in suitable solvents or heated above their T_g in air. They have been successful in developing a single film capable of repeatedly bending precisely along the directed direction [27, 90, 99]. An example of such a photochemical effect is shown in Figure 5.30. Likewise, a number of investigations

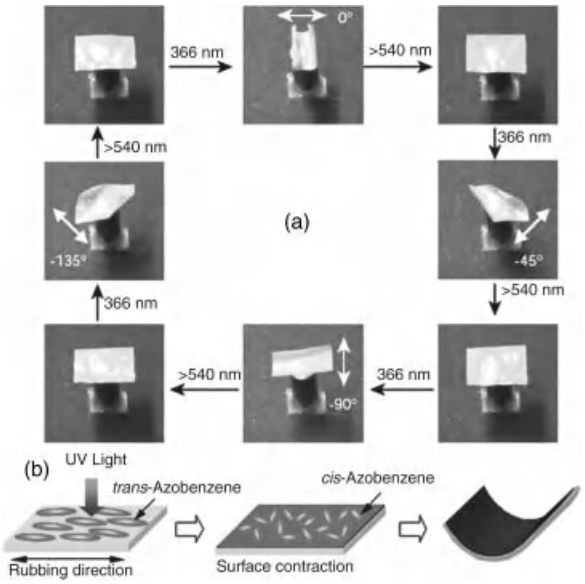

FIGURE 5.30 (a) Demonstration of photocontraction of a cross-linked polymer liquid crystal containing azobenzene, in which the bending direction of the film is manipulated by the orientation of linearly polarized light in the UV region (inducing contraction) and visible light (recovery of the original shape). Reprinted with permission from ref. 100, Copyright 2003, Nature publishing group. (b) Schematic to illustrate the proposed mechanism governing the photocontraction. Reprinted with permission from ref. 90, Copyright 2006, John Wiley & Sons. (*See the color version of this figure in Color Plates section.*)

have been reported to show that the LCEs derived from azobenzene moiety, in response to the illuminated light, exhibit remarkable changes in shape and volume where the light energy directly transforms into the mechanical energy. Photoswitchable ferroelectric LCEs have also been realized paving the way to control the shape changes through optical (isomerization) as well as electric (Piezo effect) means in addition to the more established thermal path [219].

5.5 SUMMARY AND OUTLOOK

Over the years, analogous to the parameters such as temperature, concentration of the solvent, and pressure, the significance of light of specific wavelength (actinic light) in driving liquid crystal phase transitions has been well demonstrated. Caused by the ability of light to alter/stabilize a particular thermodynamic phase via the photoisomerization, and consequent shape change of the constituent molecules, such a phenomenon provides an interesting tool to investigate condensed matter from a new dimension. A beautiful illustration of nature utilizing such photoinduced effects is that of the retinal protein rhodopsin that enables vision. In the artificial world this effect is perhaps best demonstrated by studies involving photosensitive organic molecules. This has resulted in a number of photoactive materials, for example, azobenzene or its derivatives, being employed either in pure form or as a guest component in guest–host mixtures, to investigate the stimulus provided by the photoresponsive part on the response of the entire system. In liquid crystalline systems, a diverse variety of photoinduced phase transitions have been observed involving achiral as well as chiral materials, nematic, smectic, columnar, and blue phases. A detailed account of these photo-stimulated, but isothermal transformations provided in this chapter illustrates their significance in both basic research and applied sciences. Given the fact that phase transition among the mesophases and their transition to isotropic phase bring about the changes in their optical properties effectively, the usage of light-driven phase transitions for such purposes continues to be a fascinating field of exploration. Notably, in recent years, the effects of parameters such as surface fields, electric field, elevated pressure, anisotropy reducing component, and magnitude of orientational order on the photoinduced nematic–isotropic transition have been well studied to signify their importance in technological aspects. Likewise, dynamic self-assembly of a layered phase induced and stabilized by actinic light, tilt susceptibility of chiral smectic system, primary and secondary photo ferroelectric effects in an antiferroelectric LC, etc. focusing on the static and dynamic properties highlight the fact that the actinic light can be used as a new tool to study phase transitions and the associated critical phenomena that could also bring about effects that are not seen in equilibrium situations. Most importantly, two applications originating from the photoisomerization, viz., optical storage and photomechanical effect have been well verified. In addition, several non-display applications can be expected to emerge, provided new photochromic molecules and photo-induced phase transitions with promising static and dynamic features evolve.

REFERENCES

1. S. Chandrasekhar, *Liquid Crystals*, 2nd Edition, Cambridge University Press, 1994.
2. P. G. de Gennes and J. Prost. *The Physics of Liquid Crystals*, Oxford University Press, Oxford, 1994.
3. D. Demus, J. W. Goodby, G. W. Gray, H.-W. Spiess, and V. Vill. *Handbook of Liquid Crystals*, *Vol. 1*: *Fundamentals,* Wiley-VCH, Germany, 1998.
4. D. Demus. One hundred years of liquid-crystal chemistry: thermotropic liquid crystals with conventional and unconventional molecular structure. *Liq. Cryst.* **1989**, *5*, 75–110.
5. C. Tschierske. Liquid crystalline materials with complex mesophase morphology. *Curr. Opin. Colloid Interface Sci.* **2002**, *7*, 69–80.
6. C. Tschierske. Micro-segregation, molecular shape and molecular topology – partners for the design of liquid crystalline materials with complex mesophase morphologies. *J. Mater. Chem.* **2001**, *11*, 2647–2671.
7. J. W. Goodby, I. M. Saez, S. J. Cowling, V. Gortz, M. Draper, A. W. Hall, S. Sia, G. Cosquer, S.-E. Lee, and E. P. Raynes. Transmission and amplification of information and properties in nanostructured liquid crystals. *Angew. Chem. Int. Ed.* **2008**, *47*, 2754–2787.
8. IUPAC. *Compendium of Chemical Terminology,* 2nd Edition (the "Gold Book"). Compiled by A. D. McNaught and A. Wilkinson. Blackwell Scientific Publications, Oxford, 1997. XML on-line corrected version: http://goldbook.iupac.org (2006-) created by M. Nic, J. Jirat, B. Kosata; updates compiled by A. Jenkins. ISBN 0-9678550-9-8. doi: 10.1351/goldbook.
9. H. Rau. Photoisomerization of azobenzenes. In: F. J. Rabeck,Ed., *Photochemistry and Photophysics*, vol. *2*, CRC Press, Boca Raton, FL, 1990, Chapter 4.
10. N. Tamai and H. Miyasaka. Ultrafast dynamics of photochromic systems. *Chem. Rev.* **2000**, *100*, 1875–1890.
11. T. Ishikawa, T. Noro, and T. Shoda. Theoretical study on the photoisomerization of azobenzene. *J. Chem. Phys.* **2001**, *115*, 7503–7512.
12. K. G. Yager and C. J. Barrett. Novel photo-switching using azobenzene functional materials. *J. Photochem. Photobiol. A: Chem.* **2006**, *182*, 250–261.
13. H. Rau, In: H. Dürr and H. Bouas-Laurent,Eds., *Photochromism – Molecules and Systems*, vol. *1*, Elsevier, Amsterdam, 1990, Chapter 4, and references cited therein.
14. H. Stegemeyer. On the mechanism of photochemical cis–trans isomerization. *J. Phys. Chem.* **1962**, *66*, 2555–2560.
15. M. Dumont, S. Hosotte, G. Froc, and Z. Sekkat. Orientational manipulation of chromophores through photoisomerization. *Proc. SPIE* **1994** *2042*, 2–13.
16. I. Lednev, T. Q. Ye, R. Hester, and J. Moore. Femtosecond time-resolved UV-visible absorption spectroscopy of trans-azobenzene in solution. *J. Phys. Chem.* **1996**, *100*, 13338–13341.
17. T. V. Galstyan, B. Saad, and M. M. Denariez-Roberge. Excitation transfer from azo dye to nematic host during photoisomerization. *J. Chem. Phys.* **1997**, *107*, 9319–9325.
18. N. Biswas and S. Umapathy. Resonance Raman study of the solvent dynamics for ultrafast charge transfer transition in 4-nitro-4′-dimethylamino-azobenzene. *J. Chem. Phys.* **2003**, *118*, 5526–5536.

19. C. R. Crecca and A. E. Roitberg. Theoretical study of the isomerization mechanism of azobenzene and disubstituted azobenzene derivatives. *J. Phys. Chem. A* **2006**, *110*, 8188–8203.
20. Y. Douab, Y. Hua, S. Yuanac, W. Wua, and H. Tang. Detailed mechanism of trans–cis photoisomerization of azobenzene studied by semiclassical dynamics simulation. *Mol. Phys.* **2009**, *107*, 181–190.
21. T. Ikeda. Photomodulation of liquid crystal orientations for photonic applications. *J. Mater. Chem.* **2003**, *13*, 2037–2057.
22. S. Das and R. Davis. Photoresponsive liquid crystals. *Proc. Indian Natl. Sci. Acad.* **2003**, *69A*, 109–122.
23. Y. Yu and T. Ikeda. Alignment modulation of azobenzene-containing liquid crystal systems by photochemical reactions. *J. Photochem. Photobiol. C: Photochem. Rev.* **2004**, *5*, 247–265.
24. S. K. Prasad, G. G. Nair, K. L. Sandhya, and D. S. Shankar Rao. Photoinduced phase transitions in liquid crystalline systems. *Curr. Sci.* **2004**, *86*, 815–823.
25. S. K. Prasad, G. G. Nair, G. Hegade, K. L. Sandhya, D. S. Shankar Rao, C. V. Lobo, and C. V. Yelamaggad. Photoinduced effects in nematic liquid crystals. *Phase Transitions* **2005**, *78*, 443–455.
26. S. K. Prasad, G. G. Nair, and D. S. S. Rao. Photoinduced phase transitions. *Liq. Cryst.* **2009**, *36*, 705–716.
27. H. Yu and T. Ikeda. Photocontrollable liquid-crystalline actuators. *Adv. Mater.* **2011**, *23*, 2149–2180.
28. E. Sackmann. Photochemically induced reversible color changes in cholesteric liquid crystals. *J. Am. Chem. Soc.* **1971**, *93*, 7088–7090.
29. W. E. Haas, K. F. Nelson, J. E. Adams, and G. A. Dir. UV-imaging with nematic chlorostilbenes. *J. Electrochem. Soc.* **1974**, *121*, 1667–1669.
30. K. F. Nelson, W. E. Haas, and J. E. Adams. Identification of the UV irradiation product in nematic chlorostilbene imaging processes. *J. Electrochem. Soc.* **1975**, *122*, 1564–1565.
31. G. Pelzl. Transformation of nematic into isotropic phase by photochemical isomerization. *Z. Chem.* **1977**, *17*, 294–295.
32. S. Tazuke, S. Kurihara, and T. Ikeda. Amplified image recording in liquid crystal media by means of photochemically triggered phase transition. *Chem. Lett.* **1987**, 911–914.
33. M. Eich, J. H. Wendorff, B. Reck, and H. Ringsdorf. Reversible digital and holographic optical storage in polymeric liquid crystals. *Macromol. Chem. Rapid Commun.* **1987**, *8*, 59–63.
34. M. Eich and J. H. Wendorff. Erasable holograms in polymeric liquid crystals. *Macromol. Chem. Rapid Commun.* **1987**, *8*, 467–471.
35. T. Ikeda and O. Tsutsumi. Optical switching and image storage by means of azobenzene liquid-crystal films. *Science*, **1995**, *268*, 1873–1875.
36. O. Tsutsumi, T. Shiono, T. Ikeda, and G. Galli. Photochemical phase transition behavior of nematic liquid crystals with azobenzene moieties as both mesogens and photosensitive chromophores. *J. Phys. Chem. B* **1997**, *101*, 1332–1337.
37. A. Shishido, O. Tsutsumi, A. Kanazawa, T. Shiono, and T. Ikeda. Distinct photochemical phase transition behavior of azobenzene liquid crystals evaluated by reflection-mode analysis. *J. Phys. Chem. B* **1997**, *101*, 2806–2810.

38. A. Shishido, O. Tsutsumi, A. Kanazawa, T. Shiono, T. Ikeda, and N. Tamai. Rapid optical switching by means of photoinduced change in refractive index of azobenzene liquid crystals detected by reflection-mode analysis. *J. Am. Chem. Soc.* **1997**, *119*, 7791–7796.
39. S. Kurihara, T. Ikeda, and S. Tazuke. Photochemically induced isothermal phase transition in liquid crystals. Effect of interaction of photoresponsive molecules with matrix mesogens. *Mol. Cryst. Liq. Cryst.* **1990**, *178*, 117–132.
40. C. Ruslim and K. Ichimura. *Z*-Isomers of azobenzenes highly compatible with liquid crystals. *Chem. Lett.* **1998**, 789–790.
41. C. H. Legge and G. R. Mitchell. Photo-induced phase transitions in azobenzene-doped liquid crystals. *J. Phys. D: Appl. Phys.* **1992**, *25*, 492–499.
42. J.-H. Sung, S. Hirano, O. Tsutsumi, A. Kanazawa, T. Shiono, and T. Ikeda. Dynamics of photochemical phase transition of guest/host liquid crystals with an azobenzene derivative as a photoresponsive chromophore. *Chem. Mater.* **2002**, *14*, 385–391.
43. S. Kurihara, T. Ikeda, T. Sasaki, H.-B. Kim, and S.Tazuke. Time-resolved observation of isothermal phase transition of liquid crystals triggered by photochemical reaction of dopant. *J. Chem. Soc., Chem. Commun.* **1990**, 1751–1752.
44. S. Kurihara, T. Ikeda, T. Sasaki, H.-B. Kim and S. Tazuke. Time-resolved observation of isothermal transition of liquid crystals induced by photoisomerization of azobenzene dopant. *Mol. Cryst. Liq. Cryst.* **1991**, *195*, 251–263.
45. T. Ikeda, T. Sasaki, and H.-B. Kim. Intrinsic response of polymer liquid crystals in photochemical phase transition. *J. Phys. Chem.* **1991**, *95*, 509–511.
46. H.-K. Lee, A. Kanazawa, T. Shiono, and T. Ikeda. All-optically controllable polymer/liquid crystal composite films containing the azobenzene liquid crystal. *Chem. Mater.* **1998**, *10*, 1402–1407.
47. S. Xie, A. Natansohn, and P. Rochoni. Recent developments in aromatic azo polymers research. *Chem. Mater.* **1993**, *5*, 403–411.
48. O. Tsutsumi, Y. Demachi, A. Kanazawa, T. Shiono, T. Ikeda, and Y. Nagase. Photochemical phase-transition behavior of polymer liquid crystals induced by photochemical reaction of azobenzenes with strong donor–acceptor pairs. *J. Phys. Chem. B* **1998**, *102*, 2869–2874.
49. O. Tsutsumi, T. Kitsunai, A. Kanazawa, T. Shiono, and T. Ikeda. Photochemical phase transition behavior of polymer azobenzene liquid crystals with electron-donating and accepting substituents at the 4, 4′-positions. *Macromolecules* **1998**, *31*, 355–359.
50. T. Sasaki, T. Ikeda, and K. Ichimura. Time-resolved observation of photochemical phase transition in polymer liquid crystals. *Macromolecules* **1992**, *25*, 3807–3811.
51. M. Hasegawa, T. Yamamoto, A. Kanazawa, T. Shiono, and T. Ikeda. A dynamic grating using a photochemical phase transition of polymer liquid crystals containing azobenzene derivatives. *Adv. Mater.* **1999**, *11*, 675–677.
52. T. Yamamoto, M. Hasegawa, A. Kanazawa, T. Shiono, and T. Ikeda. Phase-type gratings formed by photochemical phase transition of polymer azobenzene liquid crystals: enhancement of diffraction efficiency by spatial modulation of molecular alignment. *J. Phys. Chem. B* **1999**, *103*, 9873–9878.
53. M. Hasegawa, T. Yamamoto, A. Kanazawa, T. Shiono, and T. Ikeda. Photochemically induced dynamic grating by means of side chain polymer liquid crystals. *Chem. Mater.* **1999**, *11*, 2764–2769.

54. T. Yamamoto, M. Hasegawa, A. Kanazawa, T. Shiono, and T. Ikeda. Holographic gratings and holographic image storage via photochemical phase transitions of polymer azobenzene liquid crystal films. *J. Mater. Chem.* **2000**, *10*, 337–342.
55. R. Ortler, C. Brauchle, A. Miller, and G. Riepl. Reversible holographic-optical data storage in cholesteric liquid-crystalline siloxanes. *Macromol. Chem. Rapid Commun.* **1989**, *10*, 189–194.
56. G. P. Wiederrecht, B. A. Yoon, and M. R. Wasielewski. High photorefractive gain in nematic liquid crystals doped with electron donor and acceptor molecules. *Science* **1995**, *270*, 1794–1797.
57. G. P. Wiederrecht, B. A. Yoon, W. A. Svec, and M. R. Wasielewski. Photorefractivity in nematic liquid crystals containing electron donor–acceptor molecules that undergo intramolecular charge separation. *J. Am. Chem. Soc.* **1997**, *119*, 3358–3364.
58. T. Sasaki, A. Katsuragi, and K. Ohno. Spontaneous polarization vector reorientation photorefractive effect in dye-doped ferroelectric liquid crystals. *J. Phys. Chem. B* **2002**, *106*, 2520–2525.
59. F. Simoni, F. Bloisi, and L. Vicari. Transient amplitude grating in polymer dispersed liquid crystals. *Mol. Cryst. Liq. Cryst.* **1992**, *223*, 169–179.
60. T. Ubukata, T. Seki, and K. Ichimura. Surface relief gratings in host–guest supramolecular materials. *Adv. Mater.* **2000**, *12*, 1675–1678.
61. J. H. Wendorff and M. Eich. Nonlinear optical phenomenon in liquid crystalline side chain polymers. *Mol. Cryst. Liq. Cryst.* **1989**, *169*, 133–166.
62. K. Anderle and J. H. Wendorff. Holographic recording, using liquid crystalline side chain polymers. *Mol. Cryst. Liq. Cryst.* **1994**, *243*, 51–75.
63. B. L. Feringa, W. F. Jager, and B. de Lange. *Organic materials for reversible optical data storage. Tetrahedron* **1993**, *49*, 8267–8310.
64. B. L. Feringa, R. A. van Delden, N. Koumura, and E. M. Geertsema. Chiroptical molecular switches. *Chem. Rev.* **2000**, *100*, 1789–1816.
65. R. Eelkema and B. L. Feringa. Amplification of chirality in liquid crystals. *Org. Biomol. Chem.* **2006**, *4*, 3729–3745.
66. A. Chanishvili, G. Chilaya, G. Petriashvili, and D. Sikharulidze. Light induced effects in cholesteric mixtures with a photosensitive nematic host. *Mol. Cryst. Liq. Cryst.* **2004**, *409*, 209–218.
67. A. Chanishvili, G. Chilaya, G. Petriashvili, and P. J. Collings. Trans–cis isomerization and the blue phases. *Phys. Rev. E* **2005**, *71*, 051705-1–051705-5.
68. D. Aronzon, E. P. Levy, P. J. Collings, A. Chanishvill, G. Chilaya, and G. Petriashvili. Trans–cis isomerization of an azoxybenzene liquid crystal. *Liq. Cryst.* **2007**, *34*, 707–718.
69. S. Kurihara, T. Ikeda, S. Tazuke, and J.-e. Seto. Isothermal phase transition of liquid crystals induced by photoisomerization of doped spiropyrans. *J. Chem. Soc., Faraday Trans.* **1991**, *87*, 3251–3254.
70. H. Allinson and H. F. Gleeson. Dielectric permittivity properties of a fulgide dye guest–host liquid crystal. *Liq. Cryst.* **1995**, *19*, 421–425.
71. H. Allinson and H. F. Gleeson. Variations in the elastic constants of a fulgide-doped liquid crystal system. *J. Mater. Chem.* **1995**, *5*, 2139–2144.
72. M. Irie, K. Sakemura, M. Okinaka, and K. Uchida. Photochromism of dithienylethenes with electron-donating substituents. *J. Org. Chem.* **1995**, *60*, 8305.

73. M. Irie and K. Uchida. Synthesis and properties of photochromic diarylethenes with heterocyclic aryl groups. *Bull. Chem. Soc. Jpn.* **1998**, *71*, 985–996.

74. T. Yamaguchi, T. Inagawa, H. Nakazumi, S. Irie, and M. Irie. Photoswitching of helical twisting power of a chiral diarylethene dopant: pitch change in a chiral nematic liquid crystal. *Chem. Mater.* **2000**, *12*, 869–871.

75. C. Denekamp and B. L. Feringa. Optically active diarylethenes for multimode photoswitching between liquid-crystalline phases. *Adv. Mater.* **1998**, *10*, 1080–1082.

76. K. Matsuda and M. Irie. Diarylethene as a photoswitching unit. *J. Photochem. Photobiol. C: Photochem. Rev.* **2004**, *5*, 169–182.

77. H. Tian and S. Yang. Recent progresses on diarylethene based photochromic switches. *Chem. Soc. Rev.* **2004**, *33*, 85–97.

78. K. Rameshbabu, A. Urbas, and Q. Li. Synthesis and characterization of thermally irreversible photochromic cholesteric liquid crystals. *J. Phys. Chem. B* **2011**, *115*, 3409–3415.

79. V. A. Mallia, M. George, and S. Das. Photochemical phase transition in hydrogen-bonded liquid crystals. *Chem. Mater.* **1999**, *11*, 207–208.

80. R. Brettle, D. A. Dunmur, N. J. Hindley, and C. M. Marson. Synthesis of new liquid crystalline compounds based on 1,4-diarylbuta-1,3-dienes. *J. Chem. Soc., Perkin Trans. 1* **1993**, 775–781.

81. S. Das, S. Varghese, and N. S. S. Kumar. Butadiene-based photoresponsive soft materials. *Langmuir* **2010**, *26*, 1598–1609.

82. M. N. Pivnenko, V. V. Vashchenko, A. I. Krivoshey, L. A. Kutulya, and J. W. Goodby. New chiral ether derivatives of 2-arylidene-p-menthane-3-ones as components of induced ferroelectric systems. *Mol. Cryst. Liq. Cryst.* **2001**, *364*, 557–565.

83. T. G. Drushlyak, A. Kutulya, N. S. Pivnenko, N. I. Shkolnikov, and V. V. Vashchenko. New chiral esters, diastereomeric 2-(4-carboxybenzylidene)-p-menthane-3-one derivatives, as components of LC systems with induced helical structure. *Mol. Cryst. Liq. Cryst.* **2001**, *364*, 691–701.

84. Q. Li, L. Green, N. Venkataraman, I. Shiyanovskaya, A. Khan, A. Urbas, and J. W. Doane. Reversible photoswitchable axially chiral dopants with high helical twisting power. *J. Am. Chem. Soc.* **2007**, *129*, 12908–12909.

85. T. J. White, R. L. Bricker, L. V. Natarajan, N. V. Tabiryan, L. Green, Q. Li, and T. J. Bunning. Phototunable azobenzene cholesteric liquid crystals with 2000 nm range. *Adv. Funct. Mater.* **2009**, *19*, 3484–3488.

86. L. Green, Y. Li, T. White, A. Urbas, T. Bunning, and Q. Li. Light-driven molecular switches with tetrahedral and axial chirality. *Org. Biomol. Chem.* **2009**, *7*, 3930–3933.

87. T. J. White, R. L. Bricker, L. V. Natarajan, V. P. Tondiglia, L. Green, Q. Li, and T. J. Bunning. Electrically switchable, photoaddressable cholesteric liquid crystal reflectors. *Opt. Express* **2010**, *18*, 173–178.

88. J. Ma, Y. Li, T. White, A. Urbas, and Q. Li. Light-driven nanoscale chiral molecular switch: reversible dynamic full range colour phototuning. *Chem. Commun.* **2010**, *46*, 3463–3465.

89. T. V. Truong, C.-Y. Chen, N. V. Tabiryan, and Y. Ron Shen. Phase transition induced by two-photon absorption in azobenzene liquid crystals. *J. Opt. Soc. Am. B* **2007**, *24*, 2623–2626.

90. Y. Yu and T. Ikeda. Soft actuators based on liquid-crystalline elastomers. *Angew. Chem. Int. Ed.* **2006**, *45*, 5416–5418.

91. P.G. de Gennes. Possibilities offered by polymer crosslinking in the presence of a liquid crystal. *Phys. Lett. A* **1969**, *28*, 725–726.

92. P. G. de Gennes, M. Hebert, and R. Kant. Artificial muscles based on nematic gels. *Macromol. Symp.* **1997**, *113*, 39–49.

93. I. Kundler and H. Finkelmann. Director reorientation via stripe-domains in nematic elastomers: influence of cross-link density, anisotropy of the network and smectic clusters. *Macromol. Chem. Phys.* **1998**, *199*, 677–686.

94. S. M. Clarke, A. Hotta, A. R. Taj-bakhsh, and E. M. Terentjev. Effect of cross-linker geometry on equilibrium thermal and mechanical properties of nematic elastomers, *Phys. Rev. E* **2001**, *64*, 061702-1–061702-8.

95. H. Finkelmann, E. Nishikawa, G. G. Pereira, and M. Warner. A new opto-mechanical effect in solids. *Phys. Rev. Lett.* **2001**, *87*, 015501.

96. P. M. Hogan, A. R. Tajbakhsh, and E. M. Terentjev. UV manipulation of order and macroscopic shape in nematic elastomers. *Phys. Rev. E* **2002**, *65*, 041720.

97. M.-H. Li, P. Keller, B. Li, X. Wang and M. Brunet. Light-driven side-on nematic elastomer actuators. *Adv. Mater.* **2003**, *15*, 569–572.

98. T. Ikeda, M. Nakano, Y. Yu, O. Tsutsumi, and A. Kanazawa. Anisotropic bending and unbending behavior of azobenzene liquid-crystalline gels by light exposure. *Adv. Mater.* **2003**, *15*, 201–205.

99. Y. Yu, M. Nakano, A. Shishido, T. Shiono, and T. Ikeda. Effect of cross-linking density on photoinduced bending behavior of oriented liquid-crystalline network films containing azobenzene. *Chem. Mater.* **2004**, *16*, 1637–1643.

100. Y. Yu, M. Nakano, and T. Ikeda. Directed bending of a polymer film by light. *Nature* **2003**, *425*, 145.

101. M. Kondo, Y. Yu, and T. Ikeda. How does the initial alignment of mesogens affect the photoinduced bending behavior of liquid-crystalline elastomers? *Angew. Chem. Int. Ed.* **2006**, *45*, 1378–1382.

102. M. Camacho-Lopez, H. Finkelmann, P. Palffy-Muhoray, and M. Shelley. Fast liquid-crystal elastomer swims into the dark. *Nat. Mater.* **2004**, *3*, 307–310.

103. K. D. Harris, R. Cuypers, P. Scheibe, C. L. van Oosten, C. W. M. Bastiaansen, J. Lub, and D. J. Broer. Large amplitude light-induced motion in high elastic modulus polymer actuators. *J. Mater. Chem.* **2005**, *15*, 5043–5048.

104. M. M. Green, R. J. M. Nolte, and E. W. Meijer,Eds., *Topics in Stereochemistry*, *Vol. 24*: *Materials-Chirality*, Wiley-VCH, New York, 2003.

105. J. J. L. M. Cornelissen, A. E. Rowan, R. J. M. Nolte, and N. A. J. M. Sommerdijk. Chiral architectures from macromolecular building blocks. *Chem. Rev.* **2001**, *101*, 4039–4070.

106. R. A. Reddy and C. Tschierske. Bent-core liquid crystals: polar order, superstructural chirality and spontaneous desymmetrisation in soft matter systems. *J. Mater. Chem.* **2006**, *16*, 907–961.

107. H. Takezoe and Y. Takanishi. Bent-core liquid crystals: their mysterious and attractive world. *Jpn. J. Appl. Phys.* **2006**, *45*, 597–625.

108. A. Jakli, C. Bailey, and J. Harden, Physical properties of banana liquid crystals. In: A. Ramamoorthy,Ed., *Thermotropic Liquid Crystals. Recent Advances*, Springer, Netherlands, 2007, Chapter 2.

109. D. R. Link, G. Natale, R. Shao, J. E. Maclennan, N. A. Clark, E. Korblova, and D. M. Walba. Spontaneous formation of macroscopic chiral domains in a fluid smectic phase of achiral molecules. *Science* **1997**, *278*, 1924–1927.

110. M. Avalos, R. Babiano, P. Cintas, J. L. Jimenez, J. C. Palacios and L. D. Barron. Absolute asymmetric synthesis under physical fields: facts and fictions. *Chem. Rev.* **1998**, *98*, 2391–2404.

111. R. Maria Tejedor, L. Oriol, J. L. Serrano, and T. Sierra. Chiral photochemical induction in liquid crystals. *J. Mater. Chem.* **2008**, *18*, 2899–2908.

112. M. Suarez and G. B. Schuster. Photoresolution of an axially chiral bicyclo[3.3.0]octan-3-one: phototriggers for a liquid-crystal-based optical switch. *J. Am. Chem. Soc.* **1995**, *117*, 6732–6738.

113. M. Zhang and G. B. Schuster. Photoracemization of optically active 1,l′-binaphthyl derivatives: light-initiated conversion of cholesteric to compensated nematic liquid crystals. *J. Phys. Chem.* **1992**, *96*, 3063–3067.

114. K. S. Burnham and G. B. Schuster. A search for chiral photochromic optical triggers for liquid crystals: photoracemization of 1,1′-binaphthylpyran through a transient biaryl quinone methide intermediate. *J. Am. Chem. Soc.* **1998**, *120*, 12619–12625.

115. B. L. Feringa, N. P. M. Huck, and H. A. van Dorenl. Chiroptical switching between liquid crystalline phases. *J. Am. Chem. Soc.* **1995**, *117*, 9929–9930.

116. N. P. M. Huck, W. F. Jager, B. de Lange, and B. L. Feringa. Dynamic control and amplification of molecular chirality by circular polarized light. *Science* **1996**, *273*, 1686–1688.

117. K. S. Burnham and G. B. Schuster. Transfer of chirality from circularly polarized light to a bulk material property: propagation of photoresolution by a liquid crystal transition. *J. Am. Chem. Soc.* **1999**, *121*, 10245–10246.

118. K. L. Stevenson, J. F. Verdieck, Partial photoresolution. Preliminary studies on some oxalato complexes of chromium (III). *J. Am. Chem. Soc.* **1968**, *90*, 2974–2975.

119. K. L. Stevenson. Partial photoresolution. III. Tris(acetylacetonato) chromium(III) system. *J. Am. Chem. Soc.* **1972**, *94*, 6652–6654.

120. B. Norden. Optical activity developed by preferential racemization of one enantiomer in racemic Cr(III) $(ox)_3^{3-}$ induced by irradiation with circularly polarized light. *Acta Chem. Scand.* **1970**, *24*, 349–351.

121. B. Norden. Optical activity in racemic chromium(III) tartrate solution induced by circularly polarized irradiation. *Chem. Lett.* **1977**, *13*, 355–362.

122. J. G. Radziszewski, J. W. Downing, M. Jawdosiuk, P. Kovacic, and J. Michl. 4-Azahomoadamant-3-ene: spectroscopic characterization and photoresolution of a highly reactive strained bridgehead imine. *J. Am. Chem. Soc.* **1985**, *107*, 594–603.

123. N. Tamaoki and M. Wada. Dynamic control of racemization rate through *E–Z* photoisomerization of azobenzene and subsequent partial photoresolution under circular polarized light. *J. Am. Chem. Soc.* **2006**, *128*, 6284–6285.

124. M. Mathews and N. Tamaoki. Reversibly tunable helicity induction and inversion in liquid crystal self-assembly by a planar chiroptic trigger molecule. *Chem. Commun.* **2009**, 3609–3611.

125. S.-W. Choi, T. Izumi, Y. Hoshino, Y. Takanishi, K. Ishikawa, J. Watanabe, and H. Takezoe. Circular-polarization-induced enantiomeric excess in liquid crystals of an achiral, bent-shaped mesogen. *Angew. Chem. Int. Ed.* **2006**, *45*, 1382–1385.

126. F. Vera, R. M. Tejedor, P. Romero, J. Barberá, M. B. Ros, J. L. Serrano, and T. Sierra. Light-driven supramolecular chirality in propeller-like hydrogen-bonded complexes that show columnar mesomorphism. *Angew. Chem. Int. Ed.* **2007**, *46*, 1873–1877.

127. L. Nikolova, T. Todorov, M. Ivanov, F. Andruzzi, S. Hvilsted, and P. S. Ramanujam. Photoinduced circular anisotropy in side chain azobenzene polyesters. *Opt. Mater.* **1997**, *8*, 255–258.

128. L. Nedelchev, A. Matharu, L. Nikolova, S. Hvilsted, and P. S. Ramanujam. Propagation of polarized light through azobenzene polymer films. *Mol. Cryst. Liq. Cryst.* **2002**, *375*, 563–575.

129. R. M. Tejedor, L. Oriol, J. L. Serrano, F. Partal Urena, and J. J. L. Gonzalez. Photoinduced chiral nematic organization in an achiral glassy nematic azopolymer. *Adv. Funct. Mater.* **2007**, *17*, 3486–3492.

130. J. Garcia-Amoros, A. Szymczyka, and D. Velasco. Nematic-to-isotropic photo-induced phase transition in azobenzene-doped low-molar liquid crystals. *Phys. Chem. Chem. Phys.* **2009**, *11*, 4244–4250.

131. G. Joly, A. Anakkar, M. Ismaili, P. Cluzeau, N. Isaert, and H. T. Nguyen. Chiral azobenzene liquid crystals under illumination: thickness influence and spontaneous polarization variations. *Ferroelectrics* **2002**, *277*, 67–74.

132. G. Joly, A. Anakkar, and H. T. Nguyen. Light induced shifts of ferroelectric mesophase transitions. *Liq. Cryst.* **1999**, *26*, 1251–1255.

133. Y. Boussoualem, M. Ismaili, J. M. Buisine, C. Binet, G. Joly, and H. T. Nguyen. Dielectric and electro-optical properties of a photosensitive liquid crystal. *Liq. Cryst.* **2009**, *36*, 899–905.

134. R. Davis, V. A. Mallia, and S. Das. Reversible photochemical phase transition behavior of alkoxy-cyano-substituted diphenylbutadiene liquid crystals. *Chem. Mater.* **2003**, *15*, 1057–1063.

135. R. K. Vijayaraghavan, S. Abraham, D. S. Shankara Rao, S. K. Prasad, and S. Das. Light induced generation of stable blue phase in photoresponsive diphenylbutadiene based mesogen. *Chem. Commun.* **2010**, *46*, 2796–2798.

136. H.-Y. Liu, C.-T. Wang, C.-Y. Hsu, and T.-H. Lin. Optically tuneable blue phase photonic band gaps. *Appl. Phys. Lett.* **2010**, *96*, 121103-1–121103-3.

137. H.-Y. Liu, C.-T. Wang, C.-Y. Hsu, and T.-H. Lin. Photonic bandgaps controllable blue phase liquid crystal. *Proc. SPIE* **2011**, *7955*, 795506-1–795506-6.

138. T. Yamamoto, I. Nishiyama, and H. Yokoyama. Photo-control of chirality-induced liquid-crystalline 3D structures. *Ferroelectrics* **2008**, *365*, 39–47.

139. C. V. Yelamaggad, G. Shanker, U. S. Hiremath, and S. K. Prasad. Cholesterol-based nonsymmetric liquid crystal dimers: an overview. *J. Mater. Chem.* **2008**, *18*, 2927–2949.

140. N. Tamaoki, Y. Aoki, M. Moriyama, and M. Kidowaki. Photochemical phase transition and molecular realignment of glass-forming liquid crystals containing cholesterol/azobenzene dimesogenic compounds. *Chem. Mater.* **2003**, *15*, 719–726.

141. V. A. Mallia and N. Tamaoki. Photoresponsive vitrifiable chiral dimesogens: photothermal modulation of microscopic disordering in helical superstructure and glass-forming properties. *J. Mater. Chem.* **2003**, *13*, 219–224.

142. V. A. Mallia and N. Tamaoki. Photochemically driven smectic–cholesteric phase transition in an inherently photoactive dimesogen. *Chem. Mater.* **2003**, *15*, 3237–3239.

143. V. A. Mallia and N. Tamaoki. Photoactive dimesogen having different pathways of light driven phase transitions at different temperatures. *Chem. Commun.* **2004**, 2538–2539.

144. S. Abraham, V. A. Mallia, K. V. Ratheesh, N. Tamaoki, and S. Das. Reversible thermal and photochemical switching of liquid crystalline phases and luminescence in diphenylbutadiene-based mesogenic dimers. *J. Am. Chem. Soc.* **2006**, *128*, 7692–7698.

145. T. Ikeda, T. Sasaki, and K. Ichimura. Photochemical switching of polarization in ferroelectric liquid-crystal films. *Nature* **1993**, *361*, 428–430.

146. H. G. Walton and H. J. Coles. Photomechanically induced phase transitions in ferroelectric liquid crystals. *Ferroelectrics* **1993**, *147*, 223–240.

147. A. Langhoff and F. Giesselmann. Kinetics of the photoferroelectric effect in chiral smectic-C liquid crystals studied by time-resolved measurements of spontaneous electric polarization and director tilt angle. *Chem. Phys. Chem.* **2002**, *3*, 424–432.

148. L. Komitov, C. Ruslim, and K. Ichimura. Light-induced changes of the spontaneous polarization in ferroelectric liquid crystal phase. *J. Nonlinear Opt. Phys. Mater.* **2000**, *9*, 151–156.

149. L. M. Blinov, M. V. Kozlovsky, M. Ozaki, and K. Yoshino. Photochromism of azo dyes and effect of liquid crystalline ordering on its efficiency and kinetics. *Mol. Cryst. Liq. Cryst. Sci. Technol. Sect. C: Mol. Mater.* **1996**, *6*, 6235–6252.

150. A. Langhoff and F. Giesselmann. Thermodynamics of the photoferroelectric effect in smectic-C^* liquid crystals. *J. Chem. Phys.* **2002**, *177*, 2232–2237.

151. L. Dinescu, K. E. Maly, and R. P. Lemieux. Design of photonic liquid crystal materials: synthesis and evaluation of new chiral thioindigo dopants designed to photomodulate the spontaneous polarization of ferroelectric liquid crystals. *J. Mater. Chem.* **1999**, *9*, 1679–1686.

152. R. P. Lemieux. Photoswitching of ferroelectric liquid crystals using photochromic dopants. *Soft Matter* **2005**, *1*, 348–354.

153. K. Shirota and I. Yamaguchi. Optical switching of antiferroelectric liquid crystal with azo dye using photochemically induced SmC_A^*-SmC^* phase transition. *Jpn. J. Appl. Phys., Part 2* **1997**, *36*, L1035–L1037.

154. H. J. Coles, H. G. Walton, D. Guillon, and G. Poetti. Photomechanically induced phase transitions in ferroelectric liquid crystals. *Liq. Cryst.* **1993**, *15*, 551–558.

155. R. K. Vijayaraghavan, S. Abraham, H. Akiyama, S. Furumi, N. Tamaoki, and S. Das. Photoresponsive glass-forming butadiene-based chiral liquid crystals with circularly polarized photoluminescence. *Adv. Funct. Mater.* **2008**, *18*, 2510–2517.

156. T. Matsui, K. Nakayama, M. Ozaki, and K. Yoshino. Photoinduced layer alignment control in ferroelectric liquid crystal with N^*–C^* phase transition doped with photochromic dye. *Appl. Phys. Lett.* **2000**, *76*, 1228–1230.

157. For a recent general review on discotic liquid crystals see: S. Kumar. *Chemistry of Discotic Liquid Crystals: From Monomers to Polymers*, CRC Press, Boca Raton, FL, 2010.

158. Y. Shimizu, A. Kurobe, H. Monobe, N. Terasawa, K. Kiyohara, and K. Uchida. Calamitic and discotic mesophases formed by kinetically controlled rod–disc alternation of molecular shape in a triphenylene–azobenzene mesogenic system. *Chem. Commun.* **2003**, 1676–1677.

159. S. Yagai, T. Nakajima, K. Kishikawa, S. Kohmoto, T. Karatsu, and A. Kitamura. Hierarchical organization of photoresponsive hydrogen-bonded rosettes. *J. Am. Chem. Soc.* **2005**, *127*, 11134–11139.

160. C. S. Pecinovsky, E. S. Hatakeyama, and D. L. Gin. Polymerizable photochromic macrocyclic metallomesogens: design of supramolecular polymers with responsive nanopores. *Adv. Mater.* **2008**, *20*, 174–178.

161. E. Westphal, I. H. Bechtold, and H. Gallardo. Synthesis and optical/thermal behavior of new azo photoisomerizable discotic liquid crystals. *Macromolecules* **2010**, *43*, 1319–1328.

162. Y. Norikane, Y. Hirai, and M. Yoshida. Photoinduced isothermal phase transitions of liquid-crystalline macrocyclic azobenzenes. *Chem. Commun.* **2011**, *47*, 1770–1772.

163. C. V. Lobo, S. K. Prasad, and C. V. Yelamaggad. Experimental investigations on weakly polar liquid crystal–aerosil composites. *J. Phys.: Condens. Matter.* **2006**, *18*, 767–776.

164. G. S. Iannacchione. Review of liquid-crystal phase transitions with quenched random disorder. *Fluid Phase Equilib.* **2004**, *222–223*, 177–187.

165. M. Caggioni, A. Roshi, S. Barjami, F. Mantegazza, G. S. Iannacchione, and T. Bellini. Isotropic to nematic transition of aerosil-disordered liquid crystals, *Phys. Rev. Lett.* **2004**, *93*, 127801-1–127801-4.

166. G. S. Iannacchione, C. W. Garland, J. T. Mang, and T. P. Rieker. Calorimetric and small angle X-ray scattering study of phase transitions in octylcyanobiphenyl-aerosil dispersions. *Phys. Rev. E* **1998**, *58*, 5966–5981.

167. V. Jayalakshmi, G. G. Nair, and S. K. Prasad. Effect of aerosil dispersions on the photoinduced nematic–isotropic transition. *J. Phys.: Condens. Matter.* **2007**, *19*, 226213-1–226213-12.

168. K. L. Sandhya, S. K. Prasad, and G. G. Nair. Enhanced dynamic response of the photoinduced nematic–isotropic transition in a polymer matrix. *Appl. Phys. Lett.* **2003**, *83*, 2707–2709.

169. K. Miyano. Wall-induced pretransitional birefringence: a new tool to study boundary aligning forces in liquid crystals. *Phys. Rev. Lett.* **1979**, *43*, 51–54.

170. H. Orendi and M. Ballauff. Complete phase diagrams of mixtures of a nematic liquid crystal with n-alkanes. *Liq. Cryst.* **1989**, *6*, 497–500.

171. G. G. Nair, S. K. Prasad, and G. Hegde. Influence of a long-chain alkane on the photoinduced nematic–isotropic transition. *Phys. Rev. E* **2004**, *69*, 021708-1–021708-6.

172. G. Hegde, S. K. Prasad, and G. G. Nair. Unpublished work.

173. V. Jayalakshmi, G. G. Nair, and S. K. Prasad. Kinetics of the thermal back relaxation time of the photoinduced nematic–isotropic transition. *Phys. Rev. E* **2007**, *75*, 031710-1–031710-6.

174. S. K. Prasad, G. G. Nair, and V. Jayalakshmi. Electric-field-assisted acceleration of the photostimulated nematic–isotropic transition. *Adv. Mater.* **2008**, *20*, 1363–1367.

175. S. K. Prasad, D. S. S. Rao, and P. Jeyagopal. Effect of pressure on the photoinduced nematic–isotropic phase transition. *Phys. Rev. E* **2001**, *64*, 011706-1–011706-4.

176. S. K. Prasad, V. K. Gupta, D. S. S. Rao, and C. V. Lobo. Effect of pressure on the dynamics of the photostimulated orientational ordering transition in a liquid crystal. *Phys. Rev. E* **2005**, *72*, 021705-1–021705-6.

177. V. K. Gupta, D. S. S. Rao, C. V. Lobo, S. K. Prasad, U. S. Hiremath, and C. V. Yelamaggad. High pressure investigations of the photo-stimulated orientational ordering transition in a liquid crystal with photoactive dimeric molecules. *Thermochim. Acta* **2006**, *440*, 205–211.

178. R. V. Tranfield and P. J. Collings. High-pressure measurements in a homologous series of liquid crystals. *Phys. Rev. A* **1982**, *25*, 2744–2749.

179. G. G. Nair, S. K. Prasad, and C. V. Yelamaggad. Opto-dielectric effect on a nematic liquid crystal doped with a photoactive azo mesogen. *J. Appl. Phys.* **2000**, *87*, 2084–2089.

180. S. Krishna Prasad, K. L. Sandhya, G. G. Nair, U. S. Hiremath, and C. V. Yelamaggad. Spacer parity dependence of photoinduced effects in liquid-crystalline dimers. *J. Appl. Phys.* **2002**, *92*, 838–841.

181. C. S. Hudson. Die gegenseitige loslichkeit von nikotin in wasser. *Z. Physik. Chem.* **1904**, *47*, 113–115.

182. For an exhaustive survey of reentrance in a variety of systems see: T. Narayanan and A. Kumar. Reentrant phase transitions in multicomponent liquid mixtures. *Phys. Rep.* **1994**, *249*, 135–218.

183. P. E. Cladis. New liquid-crystal phase diagram. *Phys. Rev. Lett.* **1975**, *35*, 48–51.

184. P. E. Cladis, R. K. Bogardus, W. B. Daniels, and G. N. Taylor. High-pressure investigation of the reentrant nematic bilayer smectic-A transition. *Phys. Rev. Lett.* **1977**, *39*, 720–723.

185. F. Hardouin, G. Sigaud, M. F. Achard, and H. Gasparoux. Enantiotropic nematic reentrant behaviour at atmospheric pressure in a pure compound. *Phys. Lett. A* **1979**, *71*, 347–349.

186. N. V. Madhusudhana, B. K. Sadashiva, and K. P. L. Moodithaya. *Curr. Sci.* **1979**, *48*, 613–614.

187. S. K. Prasad and G. G. Nair. Effects of photo-controlled nanophase segregation in a re-entrant nematic liquid crystal. *Adv. Mater.* **2001**, *13*, 40–43.

188. S. K. Prasad, G. G. Nair, and G. Hegde. Dynamic self-assembly of the liquid crystalline smectic A phase. *Adv. Mater.* **2005**, *17*, 2086–2091.

189. S. K. Prasad, G. G. Nair, and G. Hegde. Nonequilibrium liquid crystalline layered phase stabilized by light. *J. Phys. Chem. B* **2007**, *111*, 345–350.

190. Y. Lansac, M. A. Glaser, N. A. Clark, and O. D. Lavrentovich. Photocontrolled nanophase segregation in a liquid-crystal solvent. *Nature* **1999**, *398*, 54–57.

191. A. N. Berker and J. S. Walker. Frustrated spin-gas model for doubly reentrant liquid crystals. *Phys. Rev. Lett.* **1981**, *47*, 1469–1472.

192. X. Tong, M. Pelletier, A. Lasia, and Y. Zhao. Fast cis–trans isomerization of an azobenzene derivative in liquids and liquid crystals under a low electric field to the photoinduced N–I transition. *Angew. Chem. Int. Ed.* **2008**, *47*, 3596–3599.

193. S. Sridevi, S. K. Prasad, and G. G. Nair. Electric-field-dictated phase diagram and accelerated dynamics of a reentrant nematic liquid crystal under photostimulation. *Phys. Rev. E* **2009**, *80*, 021703-1–021703-9.

194. G. Fuchsel, T. Klamroth, J. Dokic, and P. Saalfrank. On the electronic structure of neutral and ionic azobenzenes and their possible role as surface mounted molecular switches. *J. Phys. Chem. B* **2006**, *110*, 16337–16345.

195. M. Alemani, F. Moresco, M. V. Peters, S. Hecht, K.-H. Rieder, and L. Grill. Electric field-induced isomerization of azobenzene by STM. *J. Am. Chem. Soc.* **2006**, *128*, 14446–14447.

196. A. D. L. Chandani, E. Gorecka, Y. Ouchi, H. Takezoe, and A. Fukuda. Antiferroelectric chiral smectic phases responsible for the trislable switching in MHPOBC. *Jpn. J. Appl. Phys.*, C Part 2 **1989**, *28*, L1265–L1268.

197. S. T. Lagerwall. *Ferroelectric and Antiferroelectric Liquid Crystals*, Wiley-VCH, Weinheim, 1999.

198. I. Musevic, R. Blinc, and B. Zeks. *The Physics of Ferroelectric and Antiferroelectric Liquid Crystals*, World Scientific, Singapore, 2000.

199. See e., g., P. Mach, R. Pindak, A. M. Levelut, P. Barois, H. T. Nguyen, C. C. Huang, and L. Furenlid. Structural characterization of various chiral smectic-C phases by resonant X-ray scattering. *Phys. Rev. Lett.* **1998**, *81*, 1015–1018.

200. S. K. Prasad, K. L. Sandhya, and Y. S. Negi. Photoinduced effects in the vicinity of the smectic-C_α^*–smectic-A transition. *Phys. Rev. E* **2002**, *65*, 031718-1–031718-4.

201. S. K. Prasad, K. L. Sandhya, D. S. S. Rao, and Y. S. Negi. Time-resolved measurements of the dynamics of the photoinduced smectic-C_α^*–smectic-A transition. *Phys. Rev. E* **2003**, *67*, 051701-1–051701-5.

202. S. K. Prasad, S. M. Khened, V. N. Raja, S. Chandrasekhar, and B. Shivakumar. Dielectric studies in the vicinity of the A-C^* transition. *Ferroelectrics* **1993**, *138*, 37–49.

203. C. Bagnuls and C. Bervillier. Nonasymptotic critical behaviour from field theory at $d = 3$: the disordered-phase case. *Phys. Rev. B* **1985**, *32*, 7209–7231.

204. K. Ema, M. Ogawa, A. Takagi, and H. Yao. Crossover from XY critical to tricritical behaviour of heat capacity at the smectic-A–chiral-smectic-C liquid-crystal transition. *Phys. Rev. E* **1996**, *54*, R25–R28.

205. G. G. Nair, G. Hegde, S. K. Prasad, C. V. Lobo, and Y. S. Negi. Photoinduced effects in the vicinity of the smectic-A–smectic-C_A^* transition: polarization, tilt angle, and response time studies. *Phys. Rev. E* **2006**, *73*, 011712-1–011712-8.

206. T. Carlsson, B. Zeks, C. Filipic, A. Levstik, and R. Blinc. Thermodynamic model of ferroelectric chiral smectic C^* liquid crystals. *Mol. Cryst. Liq. Cryst.* **1988**, *163*, 11–72.

207. G. G. Nair, G. Hegde, S. K. Prasad, and Y. S. Negi. Investigations of the opto-dielectric effects in the vicinity of the smectic-A–smectic-C_A* transition. *J. Phys.: Condens. Matter.* **2006**, *18*, 9415–9425.

208. G. G. Nair, S. K. Prasad, U. S. Hiremath, and C. V. Yelamaggad. Effect of light on the polarization of a banana-shaped achiral compound doped with a photoactive azobenzene material. *J. Appl. Phys.* **2001**, *90*, 48–52.

209. M. Mathews, R. S. Zola, D. -ke Yang, and Q. Li. Thermally, photochemically and electrically switchable reflection colors from self-organized chiral bent-core liquid crystals. *J. Mater. Chem.* **2011**, *21*, 2098–2103.

210. S. Pieraccini, S. Masiero, A. Ferrarini, and G. P. Spada. Chirality transfer across length-scales in nematic liquid crystals: fundamentals and applications. *Chem. Soc. Rev.* **2011**, *40*, 258–271.

211. T. van Leeuwen, T. C. Pijper, J. Areephong, B. L. Feringa, W. R. Browne, and N. Katsonis. Reversible photochemical control of cholesteric liquid crystals with a diamine-based diarylethene chiroptical switch. *J. Mater. Chem.* **2011**, *21*, 3142–3146.

212. G. Hegde, G. G. Nair, S. K. Prasad, and C. V. Yelamaggad. A photodriven dual-frequency addressable optical device. *J. Appl. Phys.* **2005**, *97*, 093105-1–093105-6.

213. M. H. Li and P. Keller. Artificial muscles based on liquid crystal elastomers. *Phil. Trans. R. Soc. A* **2006**, *364*, 2763–2777.

214. D. K. Shenoy, D. L. Thomsen, A. Srinivasan, P. Keller, and B. R. Ratna. Carbon coated liquid crystal elastomer film for artificial muscle applications. *Sens. Actuators A* **2002**, *96*, 184–188.

215. H. Finkelmann, S. T. Kim, A. Munoz, P. Palffy-Muhoray, and B. Taheri. Tunable mirrorless lasing in cholesteric liquid crystalline elastomers. *Adv. Mater.* **2001**, *13*, 1069–1072.

216. H. S. Blair, H. I. Pague, and J. E. Riordan. Photoresponsive effects in azo polymers. *Polymer* **1980**, *21*, 1195–1198.

217. C. L. van Oosten, D. Corbett, D. Davies, M. Warner, C. W. M. Bastiaansen, and D. J. Broer. Bending dynamics and directionality reversal in liquid crystal network photoactuators. *Macromolecules* **2008**, *41*, 8592–8596.

218. M. Kondo, R. Miyasato, Y. Naka, J. Mamiya, M. Kinoshita, Y. Yu, C. J. Barrett, and T. Ikeda. Photomechanical properties of azobenzene liquid-crystalline elastomers. *Liq. Cryst.* **2009**, *36*, 1289–1293.

219. P. Beyer and R. Zentel. Photoswitchable smectic liquid-crystalline elastomers. *Macromol. Rapid Commun.* **2005**, *26*, 874–879.

CHAPTER 6

Light-Driven Chiral Molecular Switches or Motors in Liquid Crystal Media

YAN WANG and QUAN LI

Liquid Crystal Institute, Kent State University, Kent, OH, USA

6.1 INTRODUCTION

Thorough understanding and/or mimicking nature's art of expressing and augmenting chirality from microscopic to mesoscopic levels remains elusive. However, the ubiquitous bio-molecular self-assembly into helical structures such as the double helix of DNA, α-helix of peptides, and the elegant colors of butterfly wings, bird feathers, and beetle exoskeletons [1–4] has inspired chemists to develop novel materials not only to reveal the structure–property correlation but also to explore their usage in diverse technological applications. The foremost objective of such studies has been the design and synthesis of chiral molecular systems capable of yielding complex large scale helical structure originating from the manifestation of chirality in the constituent molecules through non-covalent supramolecular interactions. Among the self-organized supramolecular systems, liquid crystals (LCs) represent a promising class of materials which might exhibit stable supramolecular helical organizations if the mesogens are chiral. The fascinating helical superstructure of chiral nematic LCs, i.e., cholesteric LCs (CLCs), undoubtedly is a striking example of such self-organization owing to its unique property of selective reflection of light and its consequent potential applications. However, large scale production of chiral LCs with desired properties is discouraging because of the high cost of chiral starting materials, synthetic difficulties and purification challenges, etc. The search for alternative ways of obtaining chiral nematic phase has led to the observation that when small quantities of chiral materials, i.e., chiral dopants, are dissolved in an achiral nematic LC (NLC), this results in a chiral nematic phase. One of the hallmarks of such systems is the amplification of molecular chirality by the anisotropic medium. To further elaborate its scope and add another dynamic quality to the LC system, the

Liquid Crystals Beyond Displays: Chemistry, Physics, and Applications, Edited by Quan Li.
© 2012 John Wiley & Sons, Inc. Published 2012 by John Wiley & Sons, Inc.

incorporation of switchable chiral dopants capable of shape change under the influence of external stimuli has attracted tremendous attention in the recent years. Such dopants are known as chiral molecular switches or motors [5], where molecules should own bistable structures, normally two isomers, which can be driven easily to convert from one state to another by various external stimuli [6]. Thereby the handedness or/and pitch length of the induced helical organization by chiral molecular switches or motors can be tuned and controlled. Compared with molecular switches or motors driven by electric and magnetic field, heat, chemical or electrochemical reaction, those capable of being driven by light possess advantages of ease addressability, fast response time, and potential for remote control in a wide range of ambient environment. Hence, the subject of this chapter is confined to the use of light as the controlling stimulus to accomplish dynamic reflection wavelength changes including the inversion of helical handedness in induced cholesteric LCs. The LC materials can be applied not only in novel LC photo displays but also in various non-display photonic applications, such as optical switches, optical storage, optical computing, and energy-saving devices. Effective materials for molecular switches or motors with chiral component(s) are being sought comprehensively as viable dopants for LCs in order to achieve complete light-driven systems for the applications above.

In this chapter, we will focus on light-driven chiral molecular switches or motors in LC media for the induction and manipulation of photoresponsive cholesteric LC system and their consequent applications.

6.2 PHOTORESPONSIVE CHOLESTERIC LIQUID CRYSTALS

Historically, chiral nematic LCs were called cholesterics because the first materials observed exhibiting this phase were cholesterol derivatives. Nowadays this is not the case and there exist many different types of chiral materials that exhibit chiral nematic (cholesteric) phase and most of them have no resemblance to cholesterol whatsoever. Cholesteric LCs have similar orientational order as nematics but differ from the fact that the molecules are locally oriented in a plane which rotates around a perpendicular direction (called helical axis) that repeats itself within a length called pitch. The pitch characterizes the distance across the helical axis where the director in each "plane" completes a full 360° rotation. For this reason, cholesterics may be picturized as a layered structure where the layer separation corresponds to half pitch, which is easily observed in the "finger print" texture of cholesterics.

As will be discussed later, the light reflections as well as any other applications are directly related to the pitch. Ever since the first application of cholesterics was discovered, being able to tune the pitch has been a major goal, as it would allow dynamic change in the system, for example, continuously changing the wavelength of reflected light. However, a direct tuning has always been an issue. Perhaps the easiest and most widely used manner is by taking advantage of photoresponsive CLC materials where light-driven molecules suffer structure change under irradiation leading to change in the helical superstructure and therefore a shift in the pitch length.

There are three basic methods to obtain photoresponsive cholesteric LCs. The first way, also the most direct way, is to use photoresponsive chiral mesogens which can furnish the chiral nematic LC phase [7]. However, this method has a major problem that the pitch in such single molecular system is usually tuned over a relatively narrow range and cannot match its physical properties required for device applications, so it is considered as the oldest but not a very useful strategy. The second way is to photosensitize either nematic LC host/system or chiral doped LCs, i.e., dope both chiral molecules and achiral photoresponsive molecules in a nematic host, or dope both photoresponsive achiral/chiral molecules and non-photoresponsive chiral molecules in a nematic host. This method uses the photoresponsive cholesteric LC with more than one dopant in the nematic host, which makes the CLC system more complicated and may alter the desired physical properties of LC host. It is worth noting here that commercial LC blends are often composed of many components. The third and most commonly used method is to dope a small amount of photoresponsive chiral trigger molecules (light-driven chiral dopant) into an achiral nematic LC host, which can self-organize into a helical superstructure. The changes of concentration or shape of chiral dopant upon light irradiation can easily induce pitch change (Figure 6.1). When the chiral dopant and the LC host are mixed together, they will self-organize into a helical superstructure, i.e., CLC phase, and most of the LC properties will not change significantly if the amount of the trigger dopant is small. Currently the third strategy is being studied widely, and the most important aspect of this method is that it is the chiral dopant on which the sign and the magnitude of the CLC pitch strongly depend. Regardless of the method of how the cholesteric phase is obtained, when light propagates through the CLC medium, it selectively reflects light of specific wavelength according to Bragg's law. The average wavelength λ of the selective reflection is defined by $\lambda = np$, where p is the pitch length of the helical structure and n is the average refraction index of the LC material. Hence by varying the pitch length of the CLCs upon light irradiation, the wavelength of the reflected light can be tuned, providing opportunities as well as

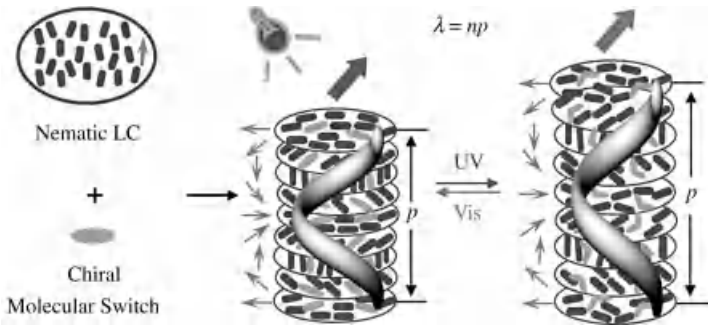

FIGURE 6.1 A schematic mechanism of the reflective wavelength of light-driven chiral molecular switch or motors in achiral nematic LC media reversibly and dynamically tuned by light. (*See the color version of this figure in Color Plates section.*)

challenges in fundamental science that are opening the door for many applications such as tunable color filters, tunable LC lasers, optically addressed displays, and biomedical applications.

6.2.1 Helical Twisting Power of Chiral Dopants

As discussed above, while the cholesteric LC phase can be observed in single component molecular system, these materials are mostly formed by adding a chiral dopant to an achiral nematic LC host/system. When a chiral dopant is dispersed into a nematic LC media, the system self-organizes into a unique helical superstructure. The ability of a chiral dopant to twist an achiral nematic phase is expressed by the equation: $\beta = (pc)^{-1}$ where β is helical twisting power (HTP), p is the pitch length of the helical structure, and c is the concentration of the chiral dopant in LC. Different dopant molecules have different capability to twist the NLC. Therefore, HTP is an important parameter for the applications of CLC systems.

So far, many different techniques have been developed to quantitatively measure the HTP of different dopant materials. However, there are two conventional techniques that are widely used nowadays. One is spectroscopic method, and the other is the Grandjean–Cano method [8–11]. The spectroscopic technique is mainly based on the unique reflection wavelength, which is governed by the equation: $\lambda = np$. Typical NLC host has an average refractive index that is around 1.6. Thus pitch length can be obtained by measuring the reflection wavelength of CLC. With known concentration c, β can be easily calculated here according to the equation: $\beta = (pc)^{-1}$. The non-spectroscopic technique is usually based on a wedge cell, where the alignment is planar and substrates are rubbed parallel. The total twist inside the cell must be a multiple of half pitch in order to follow the boundary conditions. Thus the pitch is discrete and only certain pitch lengths are allowed. As the cell thickness change in the wedge cell, more half pitch turns are formed, but only when the cell gap and the boundary conditions allow it, as shown in Figure 6.2. This arrangement produces disclination lines between areas that contain a different number of layers. The disclination lines of CLCs in the wedge cell can be observed through a polarizing optical microscope. The pitch can be determined according to the equation: $p = 2R\tan\theta$, where R represents the distance between the Grandjean lines and θ is the wedge angle of wedge cells.

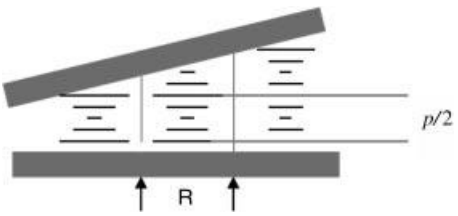

FIGURE 6.2 Schematic illustration of a Grandjean–Cano wedge cell for the HTP measurement of cholesteric LC. Disclination lines are pointed out with arrows and the thickness change between two domains is marked $p/2$.

The inverse of pitch proportionately increases with increasing the concentration of the chiral dopant and HTP value.

6.3 LIGHT-DRIVEN MOLECULAR SWITCHES OR MOTORS AS DOPANTS

Chiral dopants for LC research have been developed mainly for two different purposes. The first purpose focuses on the development of chiral dopants with persistent shape, and the research mainly aims at achieving high HTP and investigation of the interaction between chiral dopant and LC host molecules [12–14]. Another purpose, currently attracting more attention, is to develop switchable chiral dopants, whose shapes are changed by external stimulus such as light or heat [15–18]. Such molecular switches can act much as an electronic "on and off" switch under light-driven condition. These molecules can exist in at least two stable states and the equilibrium of the transition between these two states can be achieved upon light irradiation as shown in Figure 6.3. Moreover, light-driven switching requires that the photoresponsive molecule employed as chiral dopant either reverses its intrinsic chirality or forms different switching states capable of inducing the helical superstructure including handedness inversion of cholesteric helix upon light irradiation.

Many different molecular switchable systems based on azobenzene, spiropyran, fulgide, diarylethene, etc. have been developed [19, 20]. These chiral molecular switches can be applied as bistable dopants for switching in LC media to create different helicity and pitch length in cholesteric states. As mentioned above, a variety of external stimuli, including pH, pressure, magnetic field, solvent, chemical reactions, electric field, heat, and light can induce the switching process [21]; however, heat and light are most commonly applied for these LC systems due to their non-destructive, reversible nature. Light especially has advantages over other stimuli, and can be used at selected wavelengths, distinct polarizations, and different intensities as well as for remote, spatial, and temporal controls. Moreover, the use of photoresponsive chiral dopants in optically addressed displays would require no drive electronics or control circuitry and can be made flexible. Furthermore, it gives the possibility of laser and mask applications, as the radiation pattern and intensity distribution can be accurately controlled. As a result, most of the molecular switches are designed as light-driven switches, which are doped into an LC media to achieve the change in helical pitch or order upon irradiation with the appropriate wavelength of light. Light-driven chiral switches or motors doped in LC media can be classified and distinguished by the different radiation triggered processes.

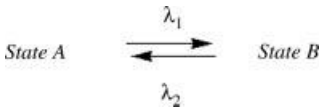

FIGURE 6.3 Schematic representation of a light-driven bistable switch.

The first report on modulation of CLC properties by doping photoresponsive materials was reported by Sackmann in 1971 [22], where azobenzene was chosen as the photo trigger molecule. After that initial study, many molecular switches or motors were applied as light-controlled dopants in LC media. All these switches or motors exist as bistable structures; however, molecules with bistable states cannot necessarily be used as chiral dopants. As a result, the molecules that are regarded as light-driven chiral molecular switches or motors in LCs should possess the following properties. First and foremost, the chiral switch or motor must be soluble in LC host. It must maintain light stability as well as light sensitivity in the host material. The switch or motor must have an adequately high HTP to induce a Bragg reflection since its high concentration can often lead to phase separation, coloration, and alter the desired physical properties of the LC host. The excitation and relaxation in the host material must be tunable with fatigue resistance. Accordingly, many molecular switches or motors have been developed especially over the past decade and are widely used as light-driven chiral dopants in LC media to induce the photoresponsive CLCs, which are illustrated and discussed in the following sections.

6.3.1 Chiral Azobenzenes as Dopants

Azobenzenes have the unique feature of reversible *trans–cis* isomerization upon light irradiation, which can cause the large conformational and polarization changes intramolecularly. The *trans*-form of azobenzene has a rod-like structure that can stabilize the LC superstructure, whereas its *cis*-form is bent-like structure and generally destabilizes the LC superstructure by generating disorder in the aligned systems. This property has been used in photochemical orientation of nematic films [23–25], pitch change in cholesterics [23–29], and phase transitions from nematic to isotropic states [30]. The dopant containing an azobenzene core which effects a change in cholesteric pitch upon irradiation was first reported in 1971 [22]. However, the azobenzene moiety is still the most widely used photoactive bistable group in LC research today because of its easy synthesis and having a good compatibility with LC phase especially in its *trans*-form (its elongated structure). Besides, due to the dramatic difference of molecular geometry of *trans*- and *cis*-forms, the HTPs of these states typically have large difference, which in turn makes a large change of the cholesteric pitch.

Generally in a CLC mixture containing chiral azobenzene, the HTP of chiral azobenzene dopant depends on its molecular structure, the nature of chirality, and the interaction with host molecules [31]. It is interesting that azobenzene with axial chirality usually shows much more efficient ability to induce the cholesteric LC phase than azobenzene with tetrahedral chirality. For example, the highest HTP (β) values reported for azobenzenes with tetrahedral chirality are around $15\,\mu m^{-1}$ [31–36], whereas azobenzenes with axial chirality can have β value over $300\,\mu m^{-1}$ [36–39] (Figure 6.4).

It is known that the *trans*-isomer of chiral azobenzene normally shows more efficient cholesteric induction than its *cis*-form, whereas even small amounts of its *cis*-forms can destabilize the LC phase into an isotropic phase. For example, Li et al.

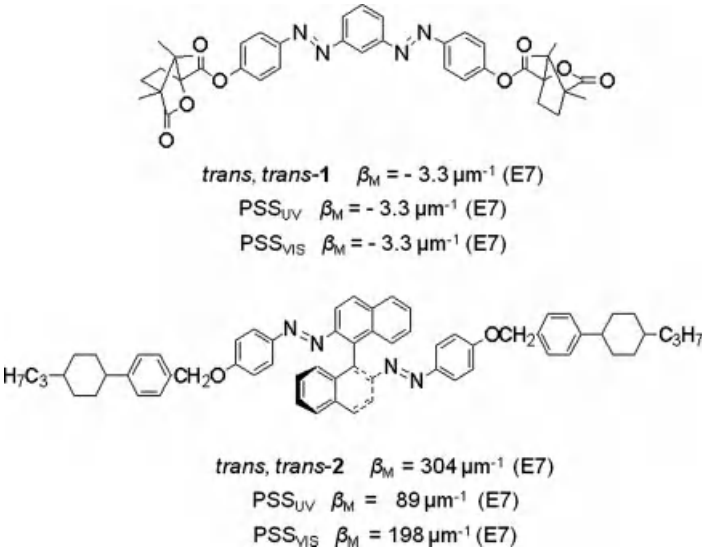

FIGURE 6.4 Molecular structures of chiral azobenzenes **1** and **2**, and their associated HTPs.

reported chiral azobenzene **3** with tetrahedral chirality as a mesogenic dopant in nematic LC 5CB (Figure 6.5) [40]. As expected, its HTP is low, which is approximately 13 μm^{-1}. The chiral mesogenic dopant **3** needs to dope 25 wt% into an achiral nematic 5CB (or K15) to induce phase chirality with characteristic fingerprint texture (Figure 6.5A). Within 10 s under UV irradiation, this sample transits to isotropic phase as evidenced by a texture change as shown in Figure 6.5B. This experiment exhibited that the conversion from *trans* to *cis* configuration of the

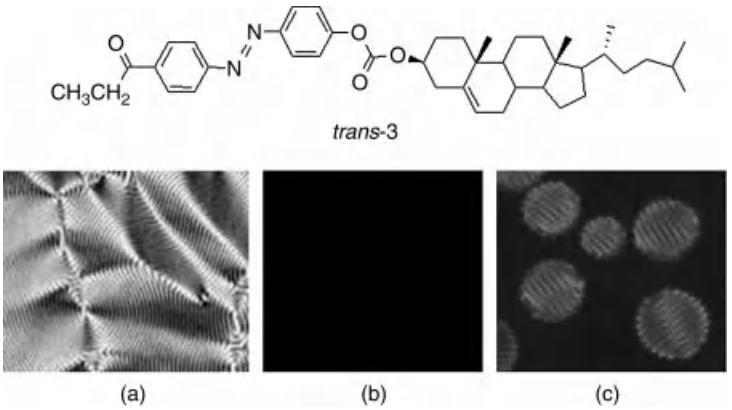

FIGURE 6.5 Crossed polarized optical micrograph of the mixture of 25 wt% **3** in an achiral nematic LC host 5CB on cooling at 38.9°C (A: before UV irradiation; B: after UV irradiation for 10 s; C: 20 s after removal of UV light at isotropic phase). Used with permission from Ref. [40].

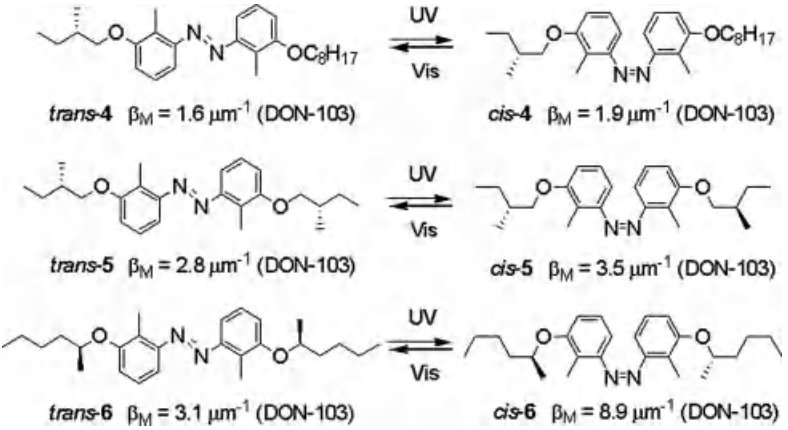

FIGURE 6.6 Azobenzenes **4–6** with tetrahedral chirality.

chiral dopant resulted in destabilization of the LC phase of the mixture. Removal of UV light immediately led to reverse process of chiral nematic domain formation from isotropic phase appearing as droplet nucleation followed by coalescence (Figure 6.5C). The reversion to the original polygonal fingerprint texture in Figure 6.5A was reached within approximately 2 h at room temperature in the dark.

However, Ichimura et al. reported that the *cis*-forms of chiral azobenzenes **4–6** exhibited higher "intrinsic" HTPs than their corresponding *trans*-isomers (Figure 6.6) [41, 42], which might result from the *cis*-isomers having a more rod-like shape compared with their *trans*-forms.

As mentioned above, HTP value of *trans*-chiral azobenzene is usually larger than that of its *cis*-chiral azobenzene. The combination of chiral azobenzene and non-photoresponsive chiral compound in nematic LC host can provide some interesting mechanisms for photochemical control of the helical structure such as phototuning helical pitch in any direction longer or shorter, phase transition between nematic and cholesteric phase, and handedness change of helical superstructure. Kurihara et al. reported photo-controlled switching of the photoresponsive CLCs consisting of chiral azobenzene (*S*)-**7** and non-photoresponsive chiral dopant (*S*)-**8** or its enantiomer (*R*)-**8** (Figure 6.7) [35]. Chiral azobenzene (*S*)-**7** induced a left-handed helix from an achiral nematic E44 whereas (*S*)-**8** and (*R*)-**8** induce a left- and right-handed helix, respectively. Figure 6.7a shows transmittance spectra of the CLC mixture of 17 wt% (*S*)-**7** and 16 wt% (*S*)-**8** in nematic LC E44 before and after UV irradiation, where the selective reflection wavelength was red-shifted upon UV irradiation. Contrary to the result shown in Figure 6.7a, the selective reflection of the CLC mixture composed of 5 wt% (*S*)-**7** and 28 wt% (*S*)-**8** in nematic LC E44 was blue-shifted upon UV irradiation. The results demonstrated that the helical pitch can be tuned and controlled in both directions to longer and shorter wavelengths by the combination of light-driven chiral switch or motor and non-photoresponsive chiral material as co-chiral dopant.

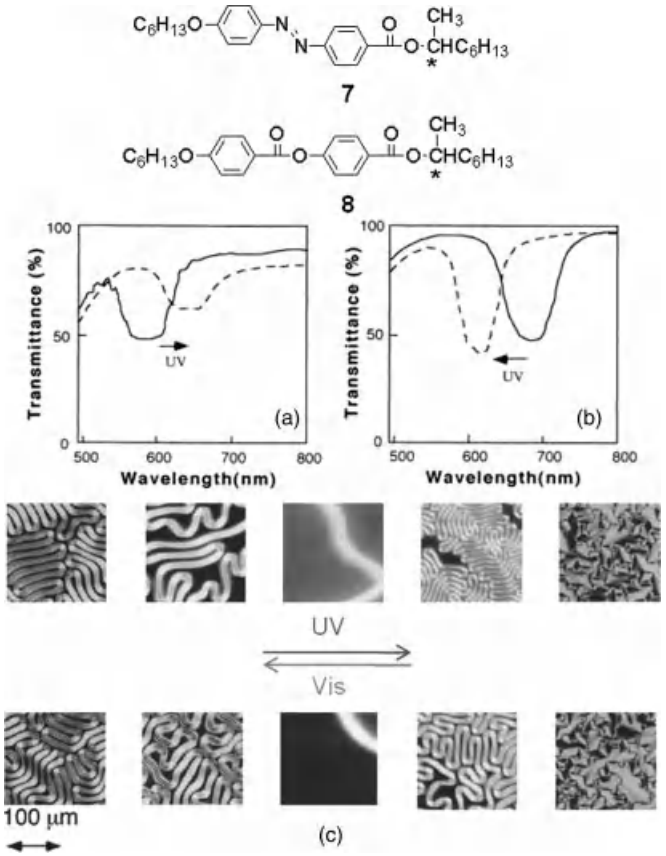

FIGURE 6.7 Top: Molecular structures of chiral azobenzene **7** and non-photoresponsive chiral dopant **8**. Middle (a and b): Transmittance spectra of the mixtures consisting of photoresponsive chiral dopant **7** and non-photoresponsive chiral dopant **8** in nematic LC E44 before (solid lines) and after (dotted lines) UV irradiation [a: (*S*)-**7**/(*S*)-**8**/E44 17:16:67 in wt%; b: (*S*)-**7**/(*R*)-**8**/E44 5:28:67 in wt%]. Bottom (c): Polarized optical micrographs of 11.6 wt% (*S*)-**7** and 8.4 wt% (*R*)-**8** in E44 upon UV and visible light irradiation at 30°C. The LC mixture was in a 5 μm glass cell without any alignment treatment. Used with permission from Ref. [35].

Kurihara et al. reported a combination of chiral azobenzene **9** and non-photoresponsive chiral compound **10** with LC host E44 to provide an effective photochemical modulation of the helical structure of CLCs (Figure 6.8) [43]. Non-photoresponsive chiral compound **10** was used for adjusting the initial reflection wavelength. Figure 6.9 (top) shows the colors reflected from the resulting CLC with different UV irradiation time. Before UV irradiation, the CLC was purple, and it turned to green, and then gradually to red with increasing irradiation time. The color could also be adjusted by varying the light intensity with a gray mask, as seen in Figure 6.9a and b. The resolution of the color patterning was estimated to be

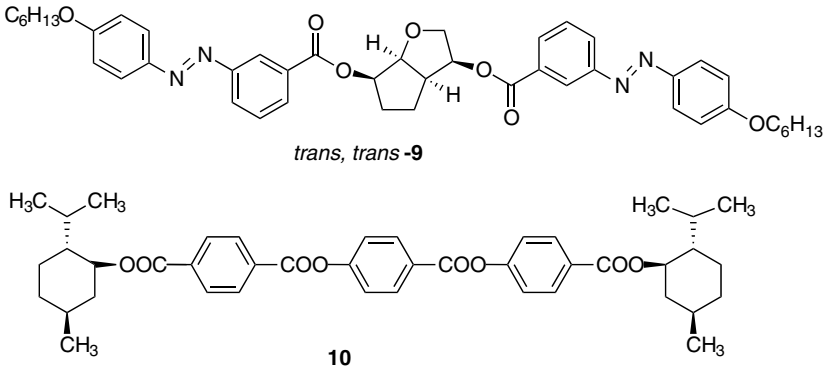

FIGURE 6.8 Molecular structures of chiral azobenzene **9** and non-photoresponsive compound **10**.

70–100 μm by patterning experiments with the use of a photomask. The limitation of the resolution may be related to the diffusion of the low-molecular-weight compounds.

As mentioned previously, azobenzene with axial chirality usually induces short pitch cholesteric LCs due to high HTP. Many efforts were made to obtain a photo-controllable visible light reflector by doping axially chiral azobenzenes into a nematic LC media [44, 45]. The reflection wavelengths can be changed reversibly by photoisomerization of these azobenzenes [37, 38], normally red-shift upon UV irradiation and blue-shift upon visible light irradiation. Li et al. reported four reversible photoswitchable axially chiral azo dopants **11–14** with high HTPs as shown in Figure 6.10 [46]. These light-driven chiral switches were found suitable for dopants in nematic host for applications in novel optical addressed displays, i.e., photodisplay. For example, an image was created on the display cell filled with chiral switch **11**-based CLC using UV light with a negative photo mask made of 10 mil PET placed on the top of the cell and exposed to UV light (637 $\mu W/cm^2$ at $\lambda_{max} = 365$ nm) for 20 min. Depending on the optical density of the mask, certain areas were exposed with different intensities of light, resulting in an image composed of a variety of colors due to the various shifts in pitch length. Figure 6.10 (bottom) shows the photo of an original image (A), the negative mask (B), and the resulting image on the display cell (C). The light-driven switches in LC media were sufficiently responsive to an addressing light source that a high resolution image with gray scale could be imaged in a few seconds of irradiation time. It was further found that an image could be retained on the screen at room temperature for 24 h before being thermally erased. The high solubility of these materials in nematic host is also of commercial interest for stability in display applications.

A flexible optically addressed photochiral display is shown in Figure 6.11A [47, 48]. This photochiral display is also based on reversibly photoswitchable axially chiral azobenzene **11** with high HTP and the ability for molecular conformational changes upon light irradiation [46]. This display is flexed and based on flexible cholesteric LC display technology [49, 50]. As shown in Figure 6.11, two identical displays were

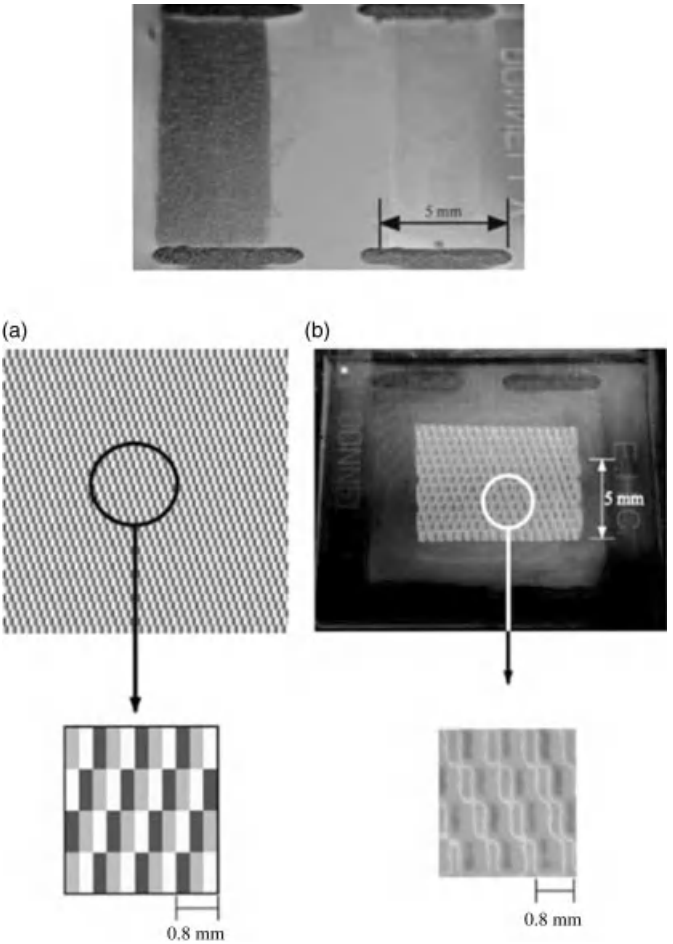

FIGURE 6.9 Changes in the reflection color of the CLC consisting of chiral azobenzene **9** and non-photoresponsive chiral dopant **10** in E44 by varying UV irradiation time: 0 s (left), 4 s (middle), and 10 s (right) (top); (a) gray mask and (b) red–green–blue (RGB) patterning of the CLC obtained by UV irradiation for 10 s through the gray mask at 25°C. Used with permission from Ref. [43]. (*See the color version of this figure in Color Plates section.*)

driven by different energies. One is electrically addressed with the standard multiplexing electronics, while the other one is optically addressed. Relatively, the overall size of the display module is reduced in case of the light-driven one and the cost can potentially be saved up to six times compared to the cost of the electric-driven one. The simplification of the final product can make markets such as security badges, small point of sale advertisements, and other applications that require a very low cost module that is updated infrequently now possible. It is worth noting here that the photo display device can display a high resolution image without the need of attached drive and

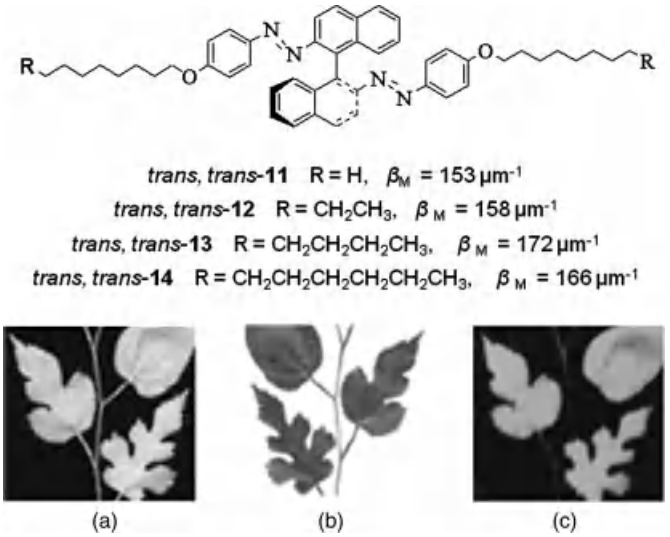

FIGURE 6.10 Top: Molecular structures of light-driven switches **11–14** with axial chirality. Bottom: Illustration of an optically addressed image with negative photo mask [A: regular photograph of the original digital image; B: negative photo mask made of PET; C: image optically written on the display cell]. Used with permission from Ref. [46].

control electronics, substantially reducing the cost of the display unit for use in applications where paper is currently used.

Phototuning reflection wavelength over 2000 nm was demonstrated by White et al. in an azobenzene-based CLC consisting of a high HTP axially chiral azobenzene **11** (Figure 6.12) [51]. Phototuning range and rate are compared as a function of chiral dopant concentration, light intensity, and thickness. CLCs composed of **11** maintain

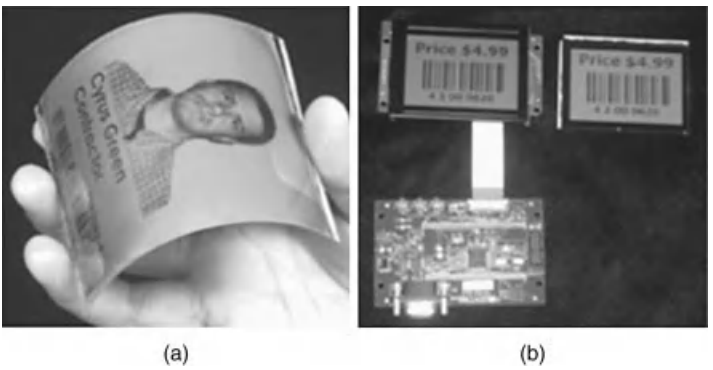

FIGURE 6.11 A flexible optically addressed photochiral display (A); a conventional display attached bulky and costly electronics compared with an optically addressed display with the same image without the added electronics (B). Used with permission from Ref. [47]. (*See the color version of this figure in Color Plates section.*)

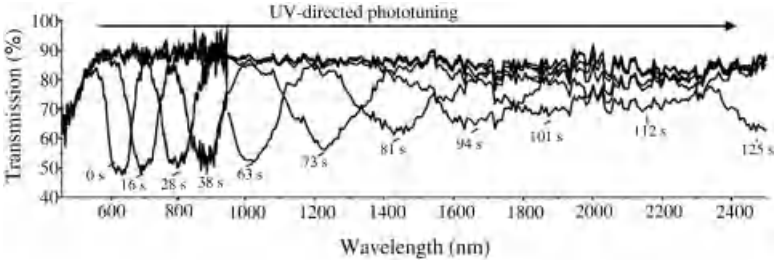

FIGURE 6.12 Transmission spectra of 6 wt% **11** in LC1444 during phototuning for 5 μm thick cell. Used with permission from Ref. [51].

the CLC phase regardless of intensity or duration of exposure. The time necessary for the complete restoration of the original spectral properties (position, bandwidth, baseline transmission, and reflectivity) of **11**-based CLC is dramatically reduced from days to a few minutes by polymer stabilization of the CLC helix.

Green et al. reported two light-driven chiral molecular switches **15** and **16** with tetrahedral and axial chirality (Figure 6.13) [52]. When chiral switch **15** was doped in nematic LC host E31 at 15 wt% concentration, phototuning the reflection color over the entire visible region was observed. An amazing feature of this photoresponsive CLC system is quick relaxation. After 1 min of exposure to bright white light, it has surprisingly returned to the original ambient color. Unfortunately, the mixture in such high concentration is near saturation level and visible signs of phase separation after several phototuning cycles were observed due to their poor solubility in LC host.

As noted before, light-driven switch **2** with axial chirality exhibited the highest HTP value for any light-driven switch reported so far [39]. The switch was found to be able to impart its chirality to a commercial nematic LC host, at low doping levels, to form a self-organized, optically tunable helical superstructure capable of fast and reversible phototuning of the structural reflection across entire visible region.

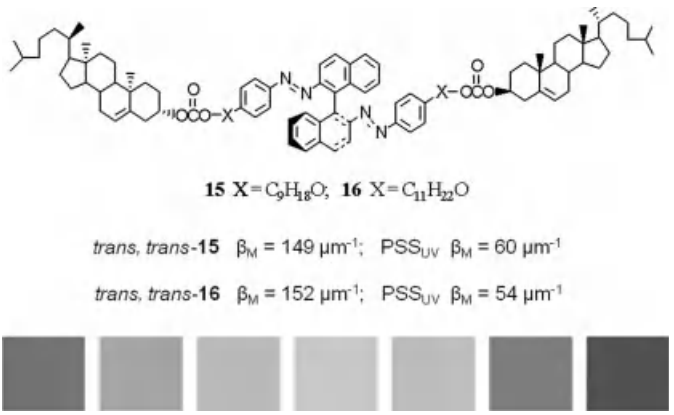

FIGURE 6.13 Molecular structures of light-driven molecular switches **15** and **16** with tetrahedral and axial chirality. Used with permission from Ref. [52].

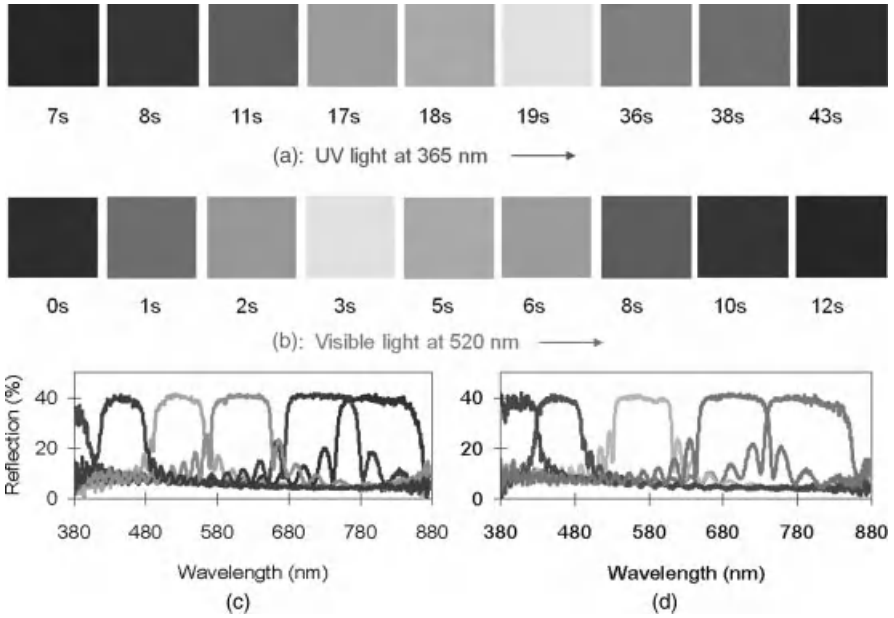

FIGURE 6.14 Reflection color images of 6.5 wt% chiral switch **2** in commercially available achiral LC host E7 in 5 μm thick planar cell. A: upon UV light at 365 nm (5.0 mW/cm^2) with different time; B: reversible back across the entire visible spectrum upon visible light at 520 nm (1.5 mW/cm^2) with different time. The colors were taken from a polarized reflective mode microscope. Reflective spectra of 6.5 wt% chiral switch **2** in LC E7 in a 5 μm thick planar cell at room temperature. C: under UV light at 365 nm wavelength (5.0 mW/cm^2) with different time (3 s, 8 s, 16 s, 25 s, 40 s, and 47 s, from left to right). D: under visible light at 520 nm wavelength (1.5 mW/cm^2) with different time (2 s, 5 s, 9 s, 12 s, and 20 s, from right to left). Used with permission from Ref. [39]. (*See the color version of this figure in Color Plates section.*)

This was the first report on reversible phototuning reflection color truly across entire visible region by employing light-driven chiral molecular switch or motor as the only chiral dopant in a LC media. For example, a mixture of 6.5 wt% **2** in nematic LC E7 was capillary filled into a 5 μm thick glass cell with a polyimide planar alignment layer and the cell was painted black on one side. The reflection wavelength of the cell was able to be tuned starting from UV region across the entire visible region to near infrared region upon UV irradiation at 365 nm (5.0 mW/cm^2) within approximately 50 s, whereas its reversible process starting from near infrared region across the entire visible region to UV region was achieved by visible light at 520 nm (1.5 mW/cm^2) or dark thermal relaxation. The reflection colors across the entire visible region were uniform and brilliant as shown in Figure 6.14A and B. Its ability to reversibly phototune the reflection color truly across entire visible region is further evidenced in Figure 6.14C and D. The reversible process with visible light is much faster than dark thermal relaxation. For instance, the phototuning time of 6.5 wt% **2** in E7 with a visible light at 520 nm (1.5 mW/cm^2) from near IR region back across entire visible region to UV region is within 20 s whereas its dark thermal relaxation back through

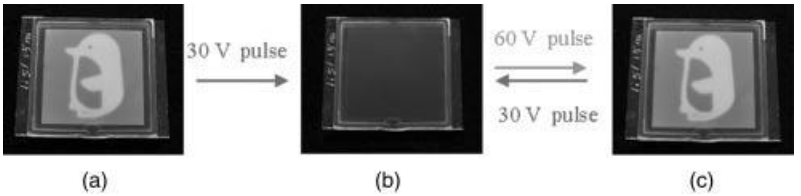

FIGURE 6.15 Images of 5 μm thick homeotropic alignment cell with 4 wt% chiral switch **2** in LC host E7. The image was recorded in a planar state through a photomask by a UV light (A). The image was hidden by a low voltage pulse in a focal conic state (B), which was reappeared by a high voltage pulse (C). The background color in the cell can be adjusted by light. Used with permission from Ref. [39]. (*See the color version of this figure in Color Plates section.*)

the entire visible region took approximately 10 h. Each reflection spectrum in Figure 6.14C and D has no drawback such as the dramatic change of the peak intensity and bandwidth compared with electric field-induced color tuning [53]. The reversible phototuning process was repeated many times without degradation. It is worth noting here that the reversible phototuning process across the entire visible region was achieved in seconds with the increase of light exposure intensity.

Furthermore, this chiral switch **2** was used in a color, photo-addressed liquid crystal display driven by light and hidden as well as fixed by application of an electric field from thermal degradation. Like conventional cholesteric LCs, the chiral switch doped in LC media is able to be electrically switched to bistable display by using polymer stabilized or surface stabilized chiral nematic texture. Even though the optically switched azo compounds are not thermally stable, an image can be made thermally stable and be retained indefinitely by electrically switching either the image or the image background to the focal conic state before it thermally relaxes. The image or its background is electrically selected by shifts in the electro-optic response curve that result from a change in the twisting power of the photosensitive chiral compound. An advantage of this display is that a thermally stable high resolution image can be captured without patterned electrodes or costly electronic drive and control circuitry, and retained indefinitely until electrically erased. Here such a light-driven device was made using the chiral switch **2**. The phototunable cholesteric layer sandwiched between two simple unpatterned transparent electrodes is sufficient. For example, an optical writing took place within seconds in a planar state through a photomask by a UV light. The reflective image (Figure 6.15A) can be hidden in focal conic texture by applying a 30 V pulse and revealed by applying a 60 V pulse (Figure 6.15C). Moreover, by applying a 30 V pulse to an optically written image so as to make the UV irradiated region going to the focal conic texture and the UV un-irradiated region going to the planar texture, an optically written image can be stored indefinitely because the planar and focal conic textures are stable even though the light-driven switch relaxes to the un-irradiated state.

Chiral cyclic azobenzene switches have also been used to investigate the light-driven twisting behaviors for CLC system [54–56]. It was reported that some chiral

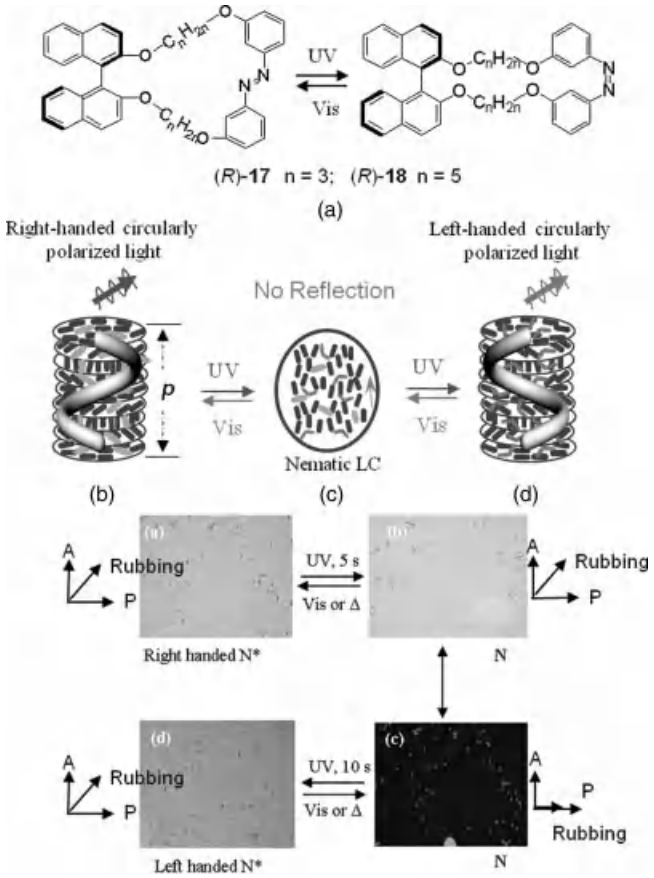

FIGURE 6.16 Top: Molecular structures of chiral cyclic azobenzenes (*R*)-**17** and (*R*)-**18** (A). Middle (B–D): Schematic mechanism of reflection wavelength tuning and handedness inversion of light-driven chiral molecular switch or motor in achiral nematic LC media reversibly and dynamically tuned by light. Bottom: Polarized optical photomicrographs of a planar aligned N* film containing 10 wt% (*R*)-**17** in ZLI-1132 at room temperature, showing reversible phase transitions occurring by light irradiation of the sample inside a 5 μm cell: (a) oily streak texture of the N* phase before irradiation; (b) N phase obtained by exposure of the sample to UV irradiation; (c) extinguishing orientation of the N cell by rotation between crossed polarizers; (d) regeneration of the oily streak texture of the N* phase upon continued irradiation (bottom–right). Used with permission from Ref. [56]. (*See the color version of this figure in Color Plates section.*)

cyclic compounds showed a reversible inversion in the handedness of CLC by means of their photoisomerization upon light. Manoj et al. recently reported a fast photon mode reversible handedness inversion of a self-organized helical superstructure, i.e., cholesteric LC phase, using light-driven chiral cyclic dopants (*R*)-**17** and (*R*)-**18** [56]. The two light-driven cyclic azobenzenophanes with axial chirality show photochemically reversible *trans* to *cis* isomerization in solution without

undergoing thermal or photoinduced racemization (Figure 6.16A). The switches exhibited good solubility, high HTP, and a large change in HTP due to photoisomerization in three commercially available structurally different achiral LC hosts. Therefore, reversible tuning reflection colors from blue to near IR by light irradiation from the induced CLC was observed. More interestingly, the different switching states of the two chiral cyclic dopants were found to be able to induce a helical superstructure of opposite handedness. For example, a typical CLC texture observed for the N* phase of the CLC mixture containing 10 wt% (*R*)-**17** in nematic LC ZLI-1132 under planar alignment conditions was quickly transformed into a planar N texture upon UV irradiation (Figure 6.16, A and B). As the sample in the N phase was rotated between fixed crossed polarizers, an extinguishing orientation of the cell was found when the orientation of the molecular director was along one of the polarizer directions (Figure 6.16C). This transient N phase was quickly transformed into an N* phase upon continued UV irradiation for a few more seconds (Figure 6.16D). The whole switching process was reversible with 440 nm irradiation. This provides clear evidence on the reversible handedness inversion upon light irradiation.

The induced helical pitch and photo-tunability of chiral cyclic dopants (*R*)-**17** and (*R*)-**18** in nematic LC media were measured using Cano's wedge method and the corresponding change in HTP values was summarized in Table 6.1. (*R*)-**17** in its *trans*-form shows a high HTP value in E7 and K15 while the corresponding value in ZLI-1132 was found to be low. Its analog (*R*)-**18** exhibits a lower HTP in E7 and K15 LC hosts compared to (*R*)-**17**. On the contrary, the HTP value of (*R*)-**18** in ZLI-1132 was found to be higher than what was obtained for its lower homologue compound. Compared with its analog at ortho-substitution, the chiral switch (*R*)-**17** with meta-substitution exhibited a higher HTP and a higher change in HTP, which might result from the intrinsic nature of its molecular structure and having a more dramatic geometrical change upon photoisomerization. Different LC hosts result in the different intermolecular associations between dopants and hosts. These results

TABLE 6.1 Helical twisting powers (β) of light-driven chiral molecular switches (*R*)-17 and (*R*)-18 in different nematic LC hosts as determined by Cano's wedge method and the observed change in values by irradiation. Positive and negative values represent right- and left-handed helical twists respectively

		β (wt%) μm^{-1}			
Dopant	Host NLC	Initial	PSS_{UV}	PSS_{vis}	$\Delta\beta$ [%][a]
(*R*)-**17**	E7	+40	+7	+30	83
	K15	+50	−10	+43	120
	ZLI-1132	+8	−26	+6	425
(*R*)-**18**	E7	+32	−10	+26	131
	K15	+12	−18	+8	250
	ZLI-1132	+32	−16	+24	150

[a] Percent change in β observed from initial to PSS_{UV}.

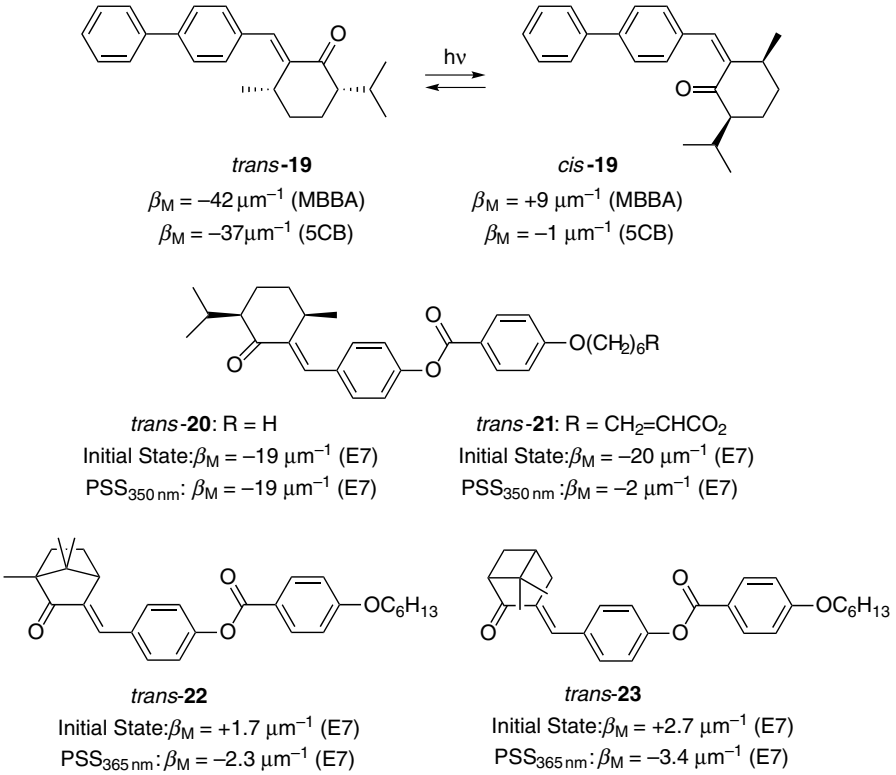

FIGURE 6.17 Menthone-based switchable chiral dopants.

clearly reveal the subtle dependence of HTP on the molecular structures of both the dopant and the NLC hosts. Interestingly, Kawamoto et al. reported that (*R*)-**17** can behave uniquely for non-destructive erasable chiroptical memory through its photoinduced switching in neat film [57].

6.3.2 Chiral Olefins as Dopants

Chiral olefins are the typical compounds with the capability of *trans–cis* isomerization similar to chiral azobenzenes, which can be used as light-driven chiral switches in LC media. Such compounds with exocyclic double bond should be chemically stable and do not form photo-dimers. However, to date only a few of these molecules have been reported to induce photoresponsive CLC system [58]. Yarmolenko et al. reported menthone-based chiral dopant **19** with high HTP and efficient cholesteric pitch modulation (Figure 6.17) [59]. Its *cis*-isomer was rather stable, and no thermally excited *cis–trans* isomerization was observed upon heating to 80°C, in contrast to azobenzene. As seen from Figure 6.17, the HTP value at its *trans*- and

cis-form exhibited a considerable difference, which results from their dramatically different shape, similar to the change observed in azobenzene isomers. Chiral dopant **19** doped in nematic host MBBA exhibited a handedness inversion upon light irradiation, whereas no such handedness inversion of the resulting CLC was observed when using 5CB instead of MBBA as the nematic host. These results clearly reveal the subtle dependence of HTP on the molecular structure of nematic LC host since different LC host results in the different intermolecular association between dopant **19** and its host. The high HTP of **19** is probably due to its better compatibility and interaction in the LC medium owing to its very similar structure to the host LC molecules. Later, Lub et al. synthesized menthone derivatives **20** and **21** and observed moderate HTP in E7 mixture [60]. Moreover, in order to investigate the effect of chemical structure on HTP two new photoisomerizable compounds that are structurally related to menthone derivative **20** were designed and synthesized (Figure 6.17). However, the *trans*-isomers of nopinone and camphor derivatives **22** and **23** exhibited much lower HTPs than **20**. It is possible that the chiral groups of the cage-like structure of **22** and **23** show less interaction with the LC host and hence lower HTP. It is interesting to note that the twist sense of the CLCs induced by **22** and **23** are opposite to the twist sense of **20**. Furthermore, the twist sense of *trans*- and *cis*-isomers of **22** and **23** are also opposite. Though the HTPs are less for these compounds, their studies led to better understanding of structure–property relationship of chiral photoisomerizable dopants.

Stilbene derivatives are another class of olefins which undergo *cis–trans* isomerization upon photoirradiation. Therefore by linking chiral moieties, stilbenes can be made photoresponsive chiral dopants to induce chiral nematic phase and the pitch of the resulting phase can be modulated upon photoirradiation owing to their photoisomerization. Lub and co-workers have reported several chiral stilbene derivatives **24**, **25** and **26** containing different chiral auxiliaries [61, 62]. Their structures and HTPs in achiral nematic liquid crystal hosts are shown in Figure 6.18.

Similar to menthone and stilbene derivatives, cinnamic esters are also capable of exhibiting photoinduced *cis–trans* isomerization and hence are potential candidates for photoswitchable dopants. Accordingly several chiral cinnamate esters **27–30** (Figure 6.19) containing isosorbide as the chiral moiety have been synthesized and investigated as efficient chiral dopants in nematic LC media [63, 64].

6.3.3 Chiral Diarylethenes as Dopants

Photochromic diarylethenes undergo a reversible 6-electron cyclization upon irradiation, leading to distinct change in structure and electronic configuration of the molecule [65]. This switching unit has been applied for reversible cholesteric to nematic transition and vice versa as well as photomanipulation of the cholesteric pitch [66–73]. Figure 6.20 shows some structures of these chiral diarylethenes. Feringa et al. reported the reversible cholesteric to nematic transition using open and closed form diarylethene **31** as shown in Figure 6.20 (top) [66]. When 1.4 wt% **31** in LC ZLI-389 was heated up under crossed polarizing microscope, a stable cholesteric

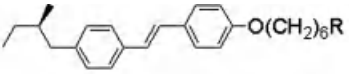

trans-**24** R = CH_2=CHCOO

Initial State: β_M = +5 μm^{-1} (ZLI4792), $PSS_{365\,nm}$: β_M = +3 μm^{-1} (ZLI4792)

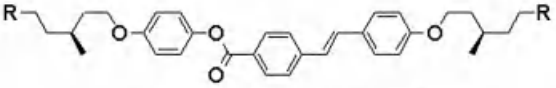

trans-**25** R = CH_2=CHCOO

Initial State: β_M = +7 μm^{-1} (E7), $PSS_{365\,nm}$: β_M = +3 μm^{-1} (E7)

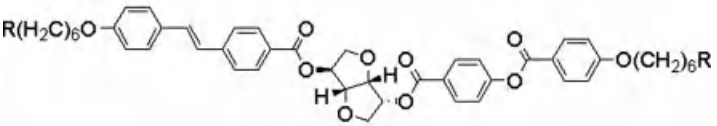

trans-**26** R = CH_2=CHCOO

Initial State: β_M = +48 μm^{-1} (E7), $PSS_{365\,nm}$: β_M = +20 μm^{-1} (E7)

FIGURE 6.18 Stilbene based switchable chiral dopants.

phase was observed close to the N–I transition temperature. When the temperature was kept within the range of 51–54°C, the cholesteric phase with identical fingerprint texture was stable (Figure 6.20A). When it was irradiated with UV light at 300 nm for 50 s, the cholesteric phase disappeared and a nematic phase texture was observed

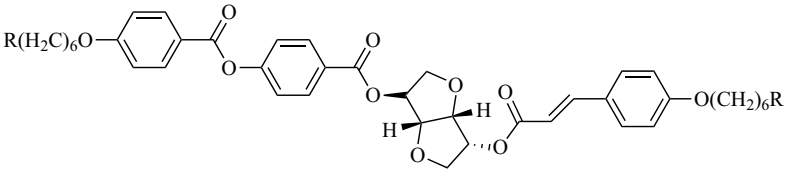

trans-**27**: R = H
Initial State: β_M = +56 μm^{-1} (E7)
$PSS_{350\,nm}$: β_M = +6 μm^{-1} (E7)

trans-**28**: R = CH_2 = CHCOO
Initial State: β_M = +42 μm^{-1} (E7)
$PSS_{350\,nm}$: β_M = +19 μm^{-1} (E7)

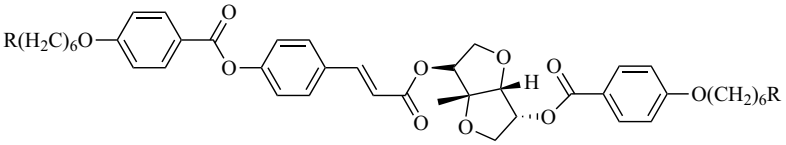

trans-**29**: R = H
Initial State: β_M = +54 μm^{-1} (E7)
$PSS_{350\,nm}$: β_M = +23 μm^{-1} (E7)

trans-**30**: R = CH_2 = CHCOO
Initial State: β_M = +38 μm^{-1} (E7)
$PSS_{350\,nm}$: β_M = +13 μm^{-1} (E7)

FIGURE 6.19 Cinnamic esters based switchable chiral dopants.

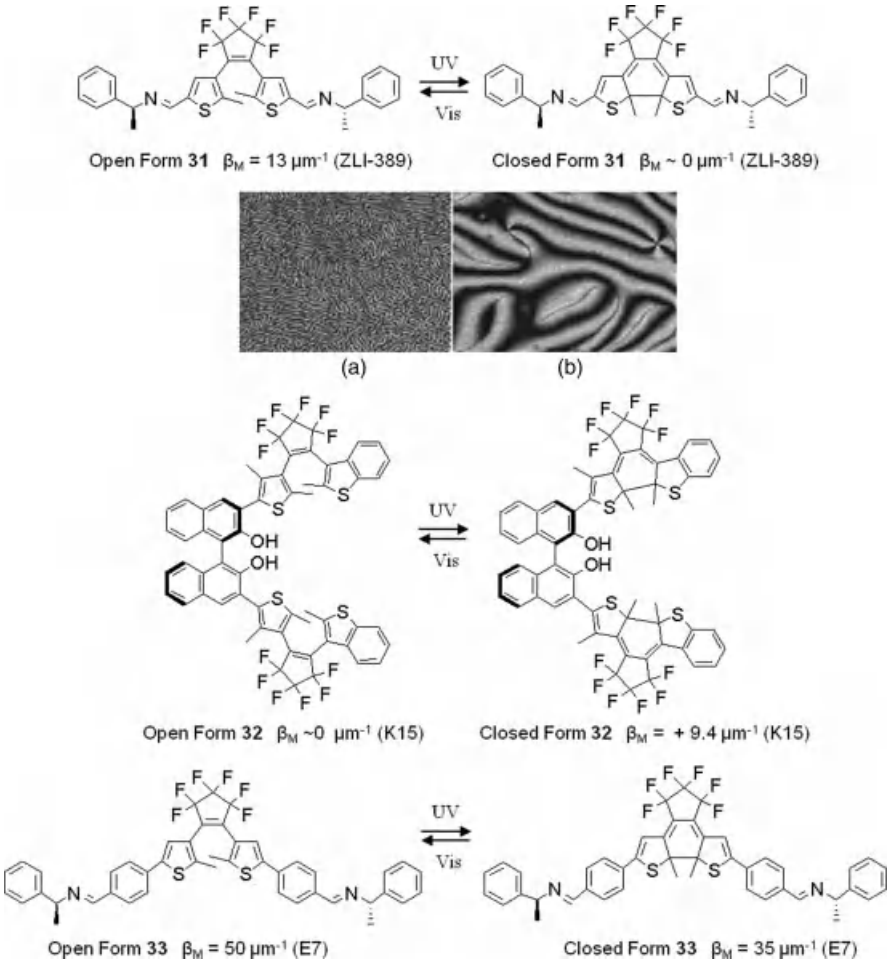

FIGURE 6.20 Top: Light-driven open-ring and closed-ring isomerization of photochromic chiral molecular switch **31**; cholesteric fingerprint texture (A) and nematic texture (B) of 1.4 wt% **31** in ZLI-389 at 52°C. Molecular structure and HTP of photochromic chiral molecular switches **32** and **23**. Used with permission from Ref. [66].

(Figure 6.20B). Irradiation of the sample with visible light for 30 s resulted in the reappearance of the cholesteric fingerprint texture. This results from the fact that the open form of chiral diarylethene **31** facilitates the formation of a stable cholesteric phase in ZLI-389, while its HTP in the closed form is too low to effectively stabilize a cholesteric phase. Yamaguchi et al. reported photochromic diarylethene **32** with axial chirality which can induce a stable photoswitching between the nematic and cholesteric phase due to its very weak HTP ($\beta_M \sim 0\,\mu m^{-1}$) at open form [68–72]. Cholesteric induction by this type of switch was supposed to be not very efficient

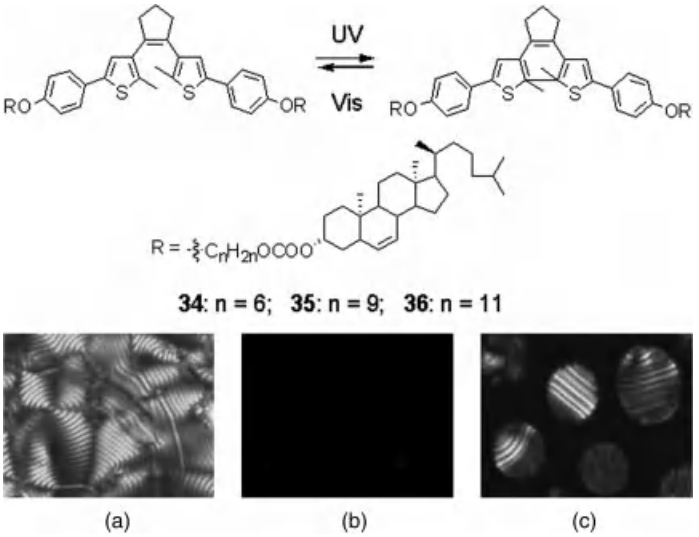

FIGURE 6.21 Molecular structures of chiral diarylethene **34–36** with tetrahedral chirality. Crossed polarized optical texture micrograph of 10 wt% of **34** in a nematic LC host 5CB before irradiation (A), after UV irradiation (B), and visible irradiation (C). Used with permission from Ref. [75].

because of extremely low HTP [74]. More recently, van Leeuwen et al. reported diarylethene **33** with a high HTP value of 50 μm^{-1} [73]. In contrast to the other diarylethene dopants reported previously, its ring-closed form **33** can induce CLC phase as well.

Rameshbabu et al. reported three photochromic chiral LC diarylethenes with tetrahedral chirality **34–36** which were found not only to be able to self-organize into a phototunable helical superstructure, but also to be able to induce a photoresponsive helical superstructure in an achiral LC host (Figure 6.21) [75]. For instance, 10 wt% **34** as a mesogenic dopant in a conventional achiral nematic 5CB exhibited a cholesteric polygonal fingerprint texture, as shown in Figure 6.21A. The transition from cholesteric to isotropic phase was observed. With UV irradiation at 310 nm (30 mW/cm^2) for 30 s, it transformed into isotropic phase (Figure 6.21B) whereas upon visible irradiation at 670 nm the reverse process was observed, as evidenced by the formation of the chiral nematic domain from isotropic phase appearing as droplet nucleation followed by coalescence (Figure 6.21C). The reverse process upon visible light irradiation was reached within 30 min.

Very recently Li et al. reported three light-driven dithienylcyclopentene switches (*S*,*S*)-**37**, (*R*,*R*)-**37**, and (*S*,*S*)-**38** (Figure 6.22) [76]. These chiral molecular switches with axial chirality were found not only to be able to act as a chiral dopant and induce a helical superstructure in an achiral nematic LC host, but also to be able to reversibly and dynamically tune the transmittance and reflection of the resulting cholesteric phase upon light irradiation. Light-driven chiral switch **37** exhibited an unusually

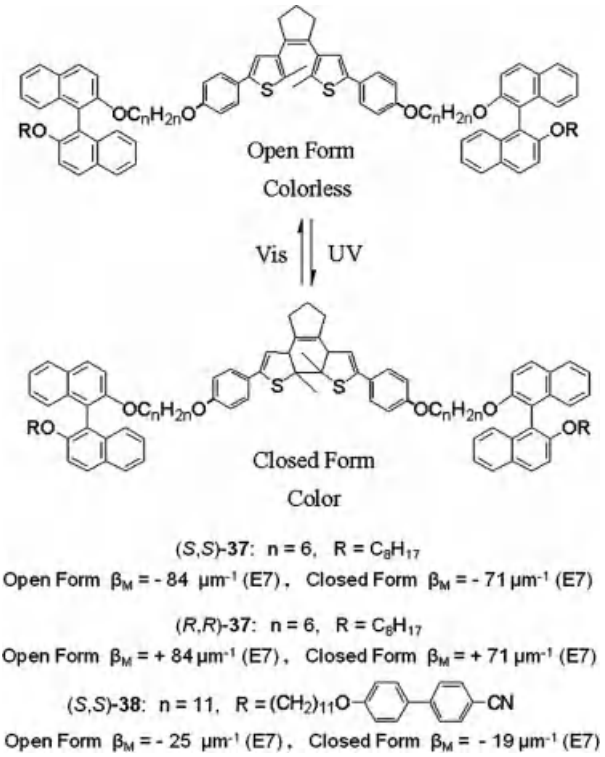

FIGURE 6.22 Diarylethenes **37** and **38** with axial chirality and their HTP values.

high HTP which is significantly larger than those of the known chiral diarylethenes reported so far.

6.3.4 Chiral Spirooxazines as Dopants

Spirooxazine has been known as a promising photochromic compound with good photo-fatigue resistance for a long time [77]. Typical examples of photochromic reactions of spirooxazines are the reversible photochemical cleavage of the C–O bond in the spirooxazine rings. Because the spiro-carbon of a spirooxazine molecule has potential as a chiral center, spirooxazines could be used as chiroptical molecular switches [78]. However, spirooxazines are usually racemic mixtures as shown in Figure 6.23. Therefore, if spirooxazines are to be used as chiroptical molecules in nematic LC system, modification of the spirooxazine with a chiral group is required. There are a few examples of spirooxazines used as the dopants in LC systems [78, 79]. Recently Jin et al. reported some novel thermally reversible photochromic axially chiral spirooxazines **40**–**43** [79]. These axially chiral spirooxazines showed ability to twist the nematic host LC E7 to form the cholesteric phases and the HTPs were

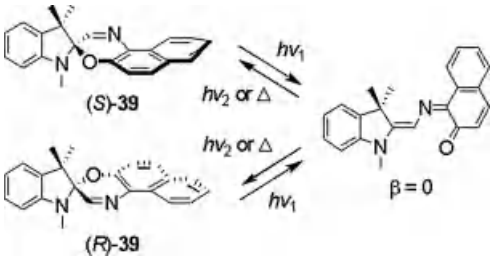

FIGURE 6.23 Schematic representation for the photochromic change of the spirooxazine **39**.

relatively high (Figure 6.24). Additionally, the result illustrated that the chiral spirooxazines containing bridged binaphthyl moiety exhibit higher HTP than the corresponding unbridged ones either for the initial state (ring-closed form) or for the photostationary state (ring-opened form, irradiated with 365 nm UV light).

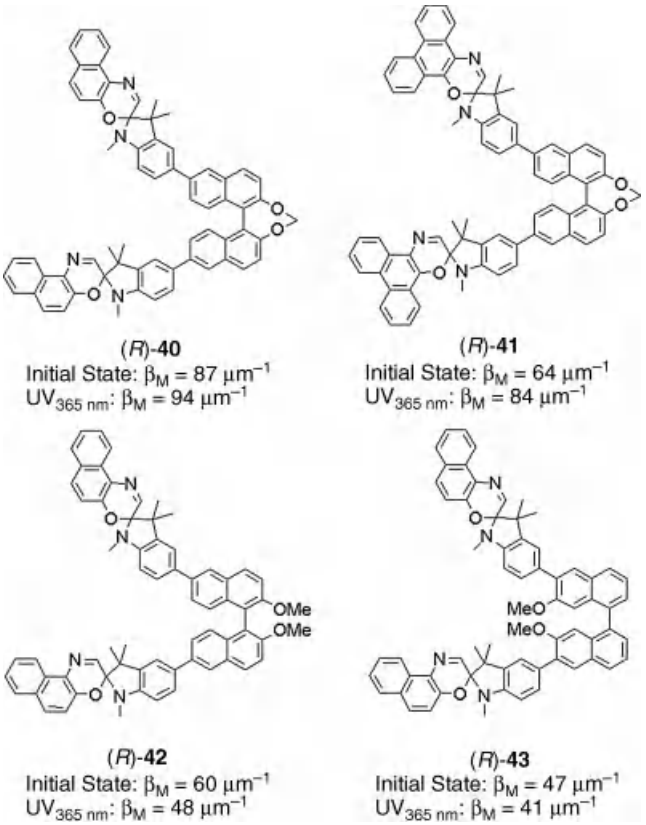

FIGURE 6.24 Molecular structures of light-driven spirooxazines with axial chirality **40–43** and their HTP values in E7.

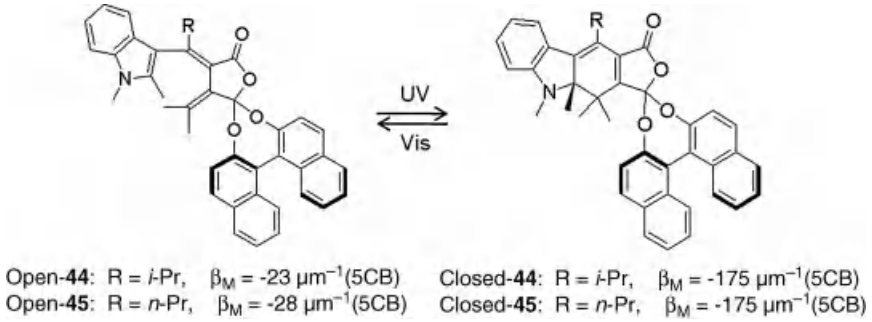

FIGURE 6.25 Molecular structures and photochromic reactions of indolylfulgides **44** and **45**.

Furthermore, this bifunctional system exhibited excellent thermally reversible photochromic behavior together with the chiral induction capability in LC hosts.

6.3.5 Chiral Fulgides as Dopants

Chiral fulgides are an interesting class of thermally irreversible photochromic materials with 6-electron cyclization upon light irradiation [80], which can be used as a light-driven trigger for LC systems. The photochromism of fulgides occurs between one of the colorless open forms and the photocyclized colored form. Yokoyama et al. reported that fulgides **44** and **45** with axial chirality acted as chiral dopants in nematic LC 5CB to induce cholesteric phase (Figure 6.25) [81–83]. The incorporation of an axially chiral binaphthol moiety into fulgide structure resulted in a bistable system with an enormous difference in HTP between the open and closed forms of the switch [81–83]. For example, chiral fulgide **45** at open form has a β_M of $-28.0\,\mu m^{-1}$ in 5CB whereas its ring-closed isomer has an impressive β_M of $-175\,\mu m^{-1}$. This allows photoswitching between cholesteric phases with a long and a short pitch, respectively, using small amounts of light-driven chiral dopant. The resulting CLC did not exhibit a handedness inversion upon light irradiation. However, this was circumvented with addition of non-photoresponsive chiral dopant (*S*)-dinaphtho[2,1-d:1′,2′-f][1,3]dioxepin with opposite HTP ($\beta_M = +92\,\mu m^{-1}$), resulting in reversible switching between a positive and negative handedness of cholesteric helix [83].

6.3.6 Chiral Overcrowded Alkenes as Dopants

Chiral overcrowded alkenes as dopants are much more likely to show inversion of the cholesteric helix sign upon switching. This kind of compounds is originally pioneered by Feringa and co-workers who continue to champion these materials for applications as molecular switches, molecular motors, and as enablers to photogenerate dynamic optical effects in CLCs. They reported some asymmetric overcrowded alkenes for chiroptical switches or motors [45, 84–87]. Take light-driven chiral motor **46** as example (Figure 6.26, top) [45, 87]. Its initial HTP at

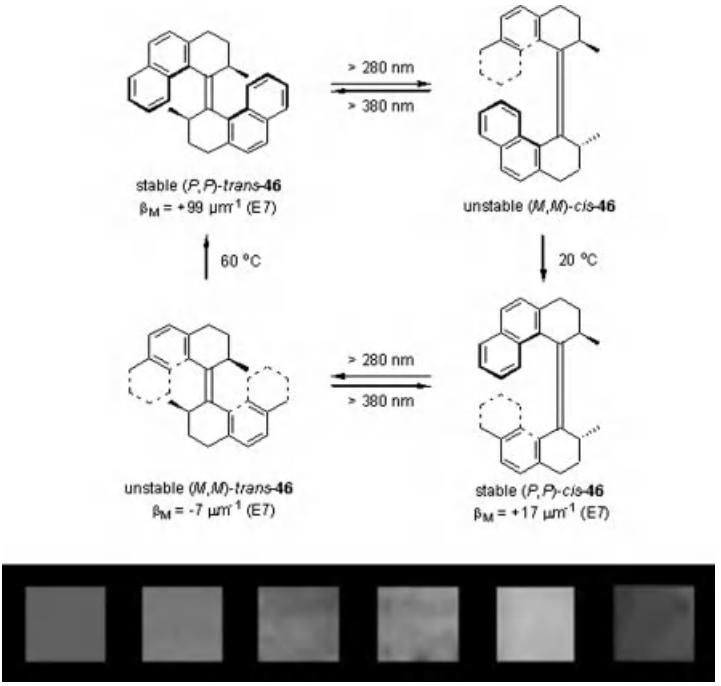

FIGURE 6.26 Unidirectional rotation of molecular motor **46** in a liquid crystalline host, and associated helical twisting powers (top); colors of **46** doped LC phase (6.16 wt% in E7) in time, starting from pure (*P*,*P*)-*trans*-**46** upon irradiation with >280 nm light at RT, as taken from actual photographs of the sample. The colors shown from left to right correspond to 0, 10, 20, 30, 40, and 80 s of irradiation time, respectively. Used with permission from Ref. [45].

(*P*,*P*)-*trans*-form in nematic E7 is $+99\,\mu m^{-1}$, but generation of a cholesteric helix with an opposite sign of similar pitch is impossible, as the (*M*,*M*)-*trans*-form possesses a minor negative HTP ($\beta_M = -7\,\mu m^{-1}$, E7). As a result of the high HTP at (*P*,*P*)-*trans*-form, colored LC films were easily generated using this dopant. Photochemical and thermal isomerization of the motor leads to irreversible color change in the LC film as shown in Figure 6.26 (bottom) [45].

A breakthrough in this area was achieved with the introduction of fluorene-derived molecular motors. Possibly due to the structural compatibility of the fluorene group with the LC host's biphenyl core, motor **47** was found to possess very large helical twisting powers for both stable and unstable forms (Figure 6.27, top). Moreover, these two forms induce cholesteric phases of opposite signs, making it possible to switch efficiently between cholesteric helicities. As the thermal isomerization step (from unstable to stable form) occurs readily at room temperature, these motors were found to be able to induce fully reversible color change of a liquid crystalline film across the entire visible spectrum [88, 89]. Moreover, switching of this molecular motor in a liquid crystalline environment induced an unprecedented rotational

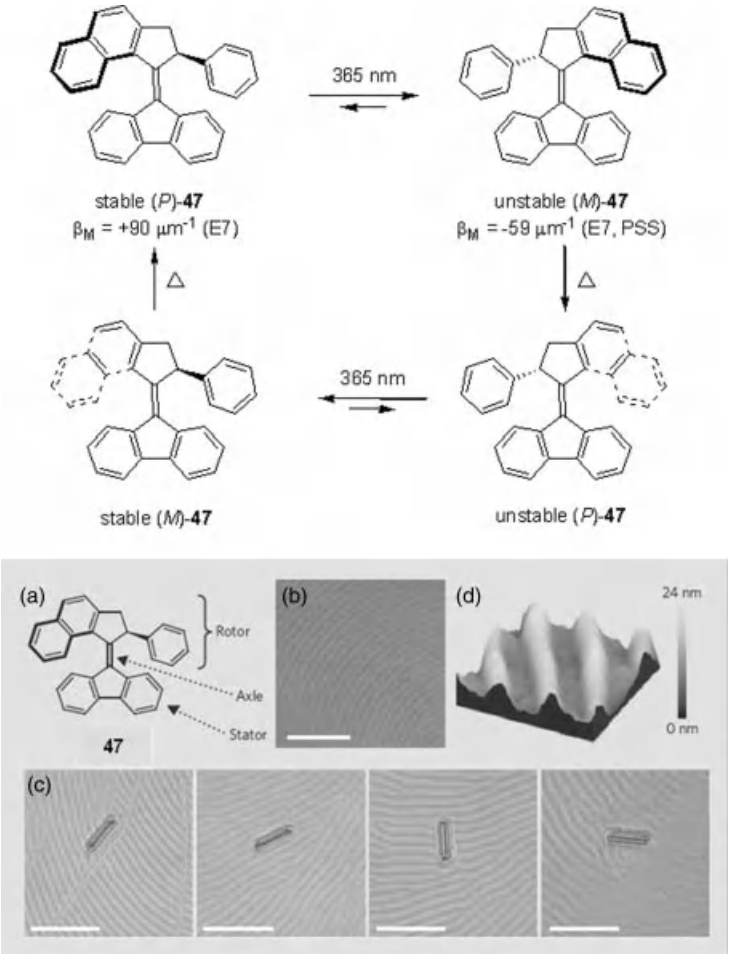

FIGURE 6.27 Features of a light-driven molecular motor: (a) Molecular structure of chiral motor **47**. (b) Polygonal texture of a LC film doped with 1 wt% chiral motor **47**. (c) Glass rod rotating on the LC during irradiation with ultraviolet light. Frames 1–4 (from left) were taken at 15-s intervals and show clockwise rotations of 28° (frame 2), 141° (frame 3), and 226° (frame 4) of the rod relative to the position in frame 1. Scale bars, 50 μm. (d) Surface structure of the LC film (atomic force microscopy image; 15 μm^2). Used with permission from Ref. [90]. (*See the color version of this figure in Color Plates section.*)

reorganization of the LC film, which was applied in the light-driven rotation of microscale glass rods (Figure 6.27, bottom) [90, 91].

Besides, other groups also reported some chiral overcrowded alkenes as the dopants in LC media [92, 93]. Bunning et al. showed the polarized optical microscopy (POM) images of light-driven chiral motor **47** in nematic LC media (Figure 6.28). As shown in Figure 6.28a, the CLC consisted of 4.2 wt% **47** in LC1444 exhibiting a characteristic Grandjean texture expected of a short-pitch CLC.

After exposure to 10 μW/cm^2 UV light, the texture of the CLC remained in this state but undergoes color change, indicating a change in pitch. As the CLC pitch unwinds, a texture shown in Figure 6.28b was observed for the nematic phase. Continued UV exposure generates the fingerprint texture apparented in Figure 6.28c, characteristic of a long-pitch CLC. With continued UV exposure, the CLC again shows the Grandjean texture (Figure 6.28d–g). As evident in these panels, the number of defects in the Grandjean texture was initially low and then became larger. Continued light exposure seemed to annihilate some of these defects, as evident in Figure 6.28f and g. After UV exposure, POM images were also captured in the dark. As expected, the texture of the CLC evolves from Grandjean (Figure 6.28h) to nematic (Figure 6.28i) to fingerprint (Figure 6.28j) as the helix inverts.

Furthermore, overcrowded alkenes have another pathway to show a switchable process in LC media which is caused by the chiral isomerization. This series of bistable switches of the overcrowded alkenes with an enantiomeric relationship between the two switch states can be interconverted by using circularly polarized light (CPL). It can be considered as a new type dopant, which exhibits the partial photoresolution under irradiating with CPL of one handedness. During the CPL process, the two enantiomers have different capability for absorbing the left-handed CPL (l-CPL) or right-handed CPL (r-CPL). As a result, one enantiomer is excited preferentially by either l-CPL or r-CPL within a racemic system, which will convert into the other enantiomer. However, this CPL being used has almost no effect to another enantiomer. On this occasion, the amount of the enantiomer will accumulate until an equilibrium or photostationary state (PSS) is reached. The enantiomeric excess (ee) value of this PSS (ee_{PSS}) at a certain wavelength of irradiation depends on the Kuhn anisotropy factor g_λ, defined as the ratio of the circular dichroism ($\Delta\varepsilon$) and the extinction coefficient (ε) (Eq. 6.1) [94].

$$ee_{PSS} = \frac{g_\lambda}{2} = \frac{\Delta\varepsilon}{2\varepsilon} \tag{6.1}$$

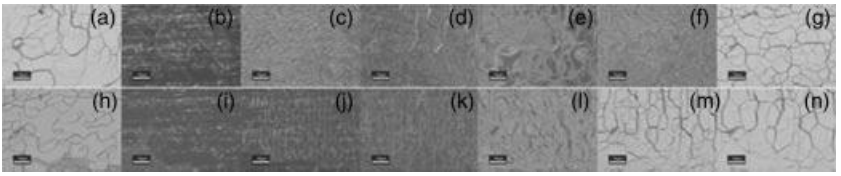

FIGURE 6.28 POM images of 4.2 wt% **47** in LC1444 during exposure to 365 nm UV light (15 mW/cm^2). The POM camera was filtered to 550 nm to avoid saturation with the UV light. (a) Grandjean texture before exposure (RCP, right-handed circularly polarized). (b) Formation of nematic during helical inversion. (c) Fingerprint texture after helical inversion. (d–g) Grandjean texture (LCP, left-handed circularly polarized) during UV exposure. (h) Defects disappear after UV light is removed. (i) Nematic phase during inversion. (j and k) Fingerprint texture after helical inversion. (l–n) Grandjean texture (RCP) restored in the dark. Used with permission from Ref. [93].

Normally, as g-value do not exceed 0.01, CPL photoresolution rarely leads to ee values over 0.5%. This ee values cannot be easily determined by the common methods. However, because the conversion from nematic to cholesteric is essentially thresholdless, theoretically these ee values are high enough to induce a nematic to cholesteric transition and can be determined from the cholesteric pitch via Equation 6.1. Similarly, the helicity of a cholesteric phase for this system can be controlled by only using the chiral information in the CPL. At last, the transition from cholesteric to nematic phase can be caused by irradiation with unpolarized light (UPL) or linearly polarized light (LPL), to lead to the racemization of chiral switch or motor [74].

Feringa et al. proved this concept by adopting the inherently dissymmetric overcrowded alkene **48** (Figure 6.29) [95]. They applied l-CPL irradiation at 313 nm to 20 wt% racemic **48** in a nematic LC K15 that can obtain the (*M*)-**48** with 0.07% ee as a cholesteric phase. Then, irradiating the (*M*)-**48** with LPL, the cholesteric LC phase gradually disappeared with the racemization. In the same way, the irradiation with r-CPL resulted in the cholesteric LC phase with opposite handedness, which still can go back to racemic state through LPL or UPL. Though the HTP (β) and the anisotropy factor (g) were both very low in this result, it did show the potential of this system for amplification of chirality via a chiral molecular switch to a macroscopic nematic to cholesteric phase transition by using a handedness CPL. In addition, this 3-stage LC switching system also presented how to control and develop between the positive and negative cholesteric LC phase.

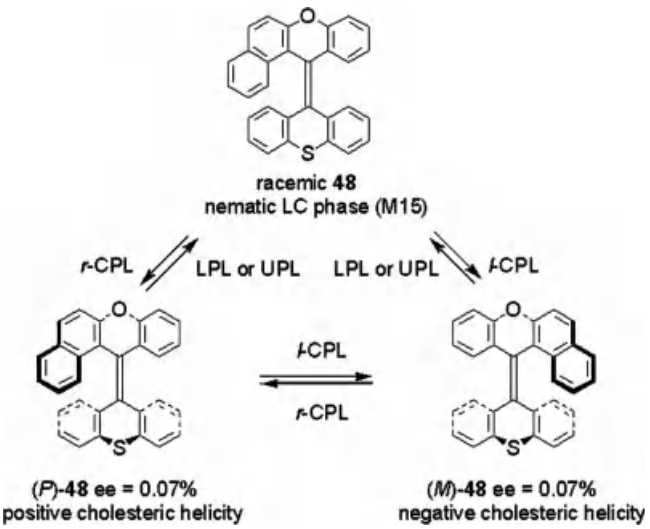

FIGURE 6.29 CPL-induced deracemization of overcrowded alkene-based switch **48** in NLC resulting in 3-stage LC switching. PL, linearly polarized light; UPL, unpolarized light.

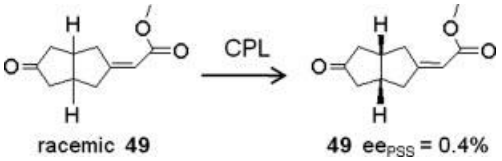

FIGURE 6.30 Deracemization of axially chiral bicyclic ketone **49** induced by CPL.

6.3.7 Axially Chiral Bicyclic Ketones as Dopants

Another series of reversible photoswitching of racemic bistable axially chiral bicyclic ketones irradiated by CPL, as mentioned previously in Section 6.3.6, was investigated by Schuster et al. [96–99]. Racemic axially chiral bicyclic ketone **49** was irradiated with l-CPL leading to the partial photoresolution (Figure 6.30) [96]. After irradiating for 6.7 h, a photostationary state was achieved with 0.4% ee, which is in good agreement with the calculated ee value from the anisotropy factor ($g_{305} = 0.0105$ at 305 nm). However, the enantiomeric enrichment cannot effectively cause the nematic to cholesteric phase transition, probably due to the low helical twisting power.

Several chiral bicyclic ketones **50–53** were designed as the photochemical molecular switches and applied as the triggers for the control of the LC phases (Figure 6.31) [96–99]. The structures of their rigid bicyclic core and ketone chromophore generally possess large g-values. Unfortunately, both the helical twisting power and solubility in nematic LC media are often low for most of them, which make it difficult to induce the nematic to cholesteric phase transition. Finally, they found the chiral bicyclic ketone **53** with a mesogenic unit, which resulted in a system capable of reversible nematic to cholesteric phase transition using the CPL resource (Figure 6.31) [99]. Ketone **53** contains a mesogenic moiety similar to the LC host

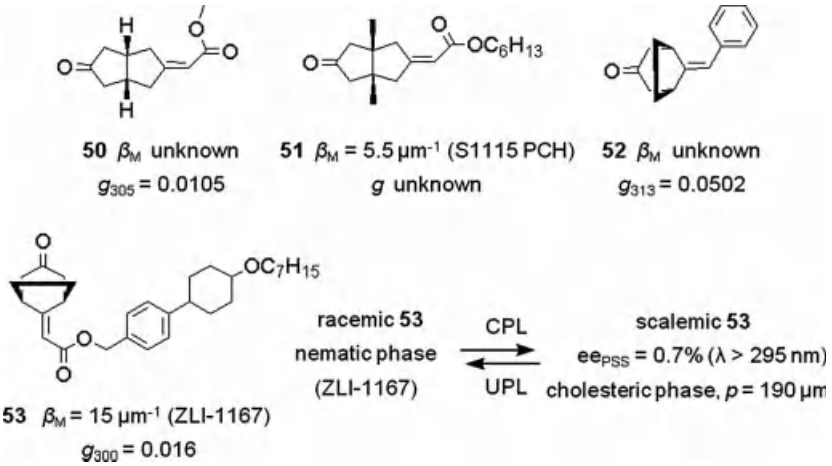

FIGURE 6.31 The examples of the chiral bicyclic ketones **50–53** designed by Schuster et al. and the process of nematic to cholesteric phase transition by CPL irradiation of the axially chiral bicyclic ketone **53**.

ZLI-1167 resulting in a helical twisting power of 15 μm^{-1}, a high g-value ($g_{300} =$ 0.016), and the good solubility. CPL irradiation ($\lambda > 295$ nm) of a nematic mixture containing 13 mol% racemic **53** resulted in a cholesteric phase with a pitch of 190 μm. This was more than twice the pitch obtained when a photo-resolved sample at the photostationary state was doped in the mesogenic host, probably due to scattering of the CPL by the LC mixture.

6.4 CONCLUSION

In this chapter, we have presented a brief overview about the dynamic behaviors and the properties of light-driven chiral molecular switches or motors in LC media. This kind of chiral molecular switches or motors doped into the LC media can be used as optical memory, optical display, and optical switching in the field of optical devices. As guest molecules, they can induce helical superstructures in an achiral LC host to obtain cholesteric LC and dynamically phototune the superstructures to achieve reversible reflection color or/and handedness inversion etc. Moreover, the phenomenon of cholesteric induction is a remarkable example of how the chiral information at the molecular level can be transmitted through amplification in self-organized stimuli-responsive soft matter. From the above discussions, it is clear that adding small quantities of chiral dopants to achiral liquid crystals have become the method of choice for helicity induction in liquid crystals. Furthermore, liquid crystals can serve as model systems in the development of supramolecular assemblies with controlled chiral architectures induced by stimuli-responsive chiral triggers.

The continuous efforts on finding new efficient photoswitchable and soluble chiral dopants are expected to provide better understanding of chiral induction in soft matter and could provide future smart materials and devices with improved properties and performance. Although the calamitic nematic phase has been largely exploited in this endeavor, the nematic phases exhibited by discotic and bent-core liquid crystals are still left to be explored. Finally the development of novel switchable chiral dopants with very high HTP in very small quantities as low as parts per million (ppm) and which can aid fast and reversible phototuning of reflection colors over the entire visible spectrum is urgently required to fully explore the potential of these intriguing materials. Open research fields also include other LC phases with induced chirality, like blue phases and smectic C^* phases, as well as chiral doped micelles.

ACKNOWLEDGMENTS

The preparation of this chapter benefited from the support to Quan Li by the Ohio Board of Regents under its Research Challenge program, the Air Force Office of Scientific Research (AFOSR FA9950-09-1-0193 and FA9950-09-1-0254), the Department of Energy (DOE DE-SC0001412), the Department of Defense Multidisciplinary University Research Initiative (AFOSR MURI FA 9550-06-1-0337 and FA9550-12-1-0037), and the National Science Foundation (NSF IIP 0750379).

REFERENCES

1. S. Kinoshita and S. Yoshioka. Structural colors in nature: the role of regularity and irregularity in the structure. *Chem Phys Chem* **2005**, *6*, 1442–1459.
2. S. Bertheier. *Iridescences: The Physical Color of Insects*, Springer, New York, 2007.
3. D. Graham-Rowe. Tunable structural color. *Nat. Photonics* **2009**, *3*, 551–553.
4. V. Sharma, M. Crne, J. Park, and M. Srinivasarao. Structural origin of circularly polarized iridescence in jeweled beetles. *Science* **2009**, *325*, 449–451.
5. B. L. Feringa. The art of building small: from molecular switches to molecular motors. *J. Org. Chem.* **2007**, *72*, 6635–6652.
6. K. Ichimura.In: H. Dürr and H. Bouas-Laurent, Eds., *Photochromism: Molecules and Systems*, Elsevier, Amsterdam, 1990.
7. M. Mathews, R. Zola, D. Yang, and Q. Li. Thermally, photochemically and electrically switchable reflection colors from self-organized chiral bent-core liquid crystals. *J. Mater. Chem.* **2011**, *21*, 2098–2103.
8. G. Heppke and F. Oestreicher. Bestimmung des helixdrehsinns cholesterischer phasen mit der Grandjean-Cano-methode. *Z. Naturforsch.* **1977**, *32*, 899–901.
9. G. Heppke and F. Oestreicher. Determination of the cholesteric screw sense. *Mol. Cryst. Liq. Lett.* **1978**, *41*, 245–249.
10. P. R. Gerber. On the determination of the cholesteric screw sense by the Grandjean–Cano-method. *Z. Naturforsch.* **1980**, *35*, 619–622.
11. I. Dierking. *Textures of Liquid Crystals*, Wiley-VCH, Weinheim, 2003.
12. G. Solladié and R. G. Zimmermann. Liquid crystals: a tool for studies on chirality. *Angew. Chem. Int. Ed.* **1984**, *23*, 348–362.
13. G. P. Spada and G. Proni. The nematic liquid crystal phase as a probe of the molecular shape helicity. *Enantiomer* **1998**, *3*, 301–314.
14. G. Proni and G. P. Spada. Doped nematic phases: a tool for amplifying and detecting chirality. *Enantiomer* **2001**, *6*, 171–179.
15. B. L. Feringa. *Molecular Switches*, Wiley–VCH, Germany, 2001.
16. N. Tamaoki. Cholesteric liquid crystals for color information technology. *Adv. Mater.* **2001**, *13*, 1135–1147.
17. S. Pieraccini, S. Masiero, A. Ferrarini, and G. P. Spada. Chirality transfer across length-scales in nematic liquid crystals: fundamentals and applications. *Chem. Soc. Rev.* **2011**, *40*, 258–271.
18. T. Ikeda. Photomodulation of liquid crystal orientations for photonic applications. *J. Mater. Chem.* **2003**, *13*, 2037–2057.
19. V. Balzani, A. Credi, F. M. Raymo, and J. F. Stoddart. Artificial molecular machines. *Angew. Chem. Int. Ed.* **2000**, *39*, 3348–3391.
20. The May 2000 issue of Chem. Rev.: Memories and Switches.
21. F. L. Carter, H. Siatkowski, and H. Wohltgen. *Molecular Electronic Devices*, Elsevier, Amsterdam, 1988.
22. E. Sackmann. Photochemically induced reversible color changes in cholesteric liquid crystals. *J. Am. Chem. Soc.* **1971**, *93*, 7088–7090.

23. D. Pijper and B. L. Feringa. Control of dynamic helicity at the macro- and supramolecular level. *Soft Matter* **2008**, *4*, 1349–1372.
24. K. Ichimura. Photoalignment of liquid-crystal systems. *Chem. Rev.* **2000**, *100*, 1847–1873.
25. T. Ikeda. Photomodulation of liquid crystal orientations for photonic applications. *J. Mater. Chem.* **2003**, *13*, 2037–2057.
26. M. Moriyama, S. Song, H. Matsuda, and N. Tamaoki. Effects of doped dialkylazobenzenes on helical pitch of cholesteric liquid crystal with medium molecular weight: utilisation for full-colour image recording. *J. Mater. Chem.* **2001**, *11*, 1003–1010.
27. S. Kurihara, T. Kanda, T. Nagase, and T. Nonaka. Photochemical color switching behavior of induced cholesteric liquid crystals for polarizer free liquid crystalline devices. *Appl. Phys. Lett.* **1998**, *73*, 2081–2083.
28. N. Tamaoki, S. Song, M. Moriyama, and H. Matsuda. Rewritable full-color recording in a photon mode. *Adv. Mater.* **2000**, *12*, 94–97.
29. S. V. Serak, E. O. Arikainen, H. F. Gleeson, V. A. Grozhik, J.-P. Guillou, and N. A. Usova. Laser-induced concentric colour domains in a cholesteric liquid crystal mixture containing a nematic azobenzene dopant. *Liq. Cryst.* **2002**, *29*, 19–26.
30. S. Tazuke, S. Kurihara, and T. Ikeda. Amplified image recording in liquid crystal. Media by means of photochemically triggered phase transition. *Chem. Lett.* **1987**, 911–914.
31. C. Ruslim and K. Ichimura. Conformational effect on macroscopic chirality modification of cholesteric mesophases by photochromic azobenzene dopants. *J. Phys. Chem. B* **2000**, *104*, 6529–6535.
32. C. Ruslim, M. Nakagawa, S. Morino, and K. Ichimura. Chiroptical properties of cholesteric liquid crystals induced by chiral photochromic 3,3′-dialkoxyazobenzenes. *Mol. Cryst. Liq. Cryst.* **2001**, *365*, 55–62.
33. T. Yoshioka, M. D. Z. Alam, T. Ogata, T. Nonaka, and S. Kurihara. Photochemical tuning of the helical structure of cholesteric liquid crystals by photoisomerization of chiral azobenzenes, and their structural effects. *Liq. Cryst.* **2004**, *31*, 1285–1291.
34. S. Kurihara, S. Nomiyama, and T. Nonaka. Photochemical switching between a compensated nematic phase and a twisted nematic phase by photoisomerization of chiral azobenzene molecules. *Chem. Mater.* **2000**, *12*, 9–12.
35. S. Kurihara, S. Nomiyama, and T. Nonaka. Photochemical control of the macrostructure of cholesteric liquid crystals by means of photoisomerization of chiral azobenzene molecules. *Chem. Mater.* **2001**, *13*, 1992–1997.
36. S. Pieraccini, G. Gottarelli, R. Labruto, S. Masiero, O. Pandoli, and G. P. Spada. The control of the cholesteric pitch by some azo photochemical chiral switches. *Chem. Eur. J.* **2004**, *10*, 5632–5639.
37. S. Pieraccini, S. Masiero, G. P. Spada, and G. Gottarelli. A new axially-chiral photochemical switch. *Chem. Commun.* **2003**, 598–599.
38. R. A. van Delden, T. Mecca, C. Rosini, and B. L. Feringa. A chiroptical molecular switch with distinct chiral and photochromic entities and its application in optical switching of a cholesteric liquid crystal. *Chem. Eur. J.* **2004**, *10*, 61–70.
39. J. Ma, Y. Li, T. White, A. Urbas, and Q. Li. Light-driven nanoscale chiral molecular switch: reversible dynamic full range color phototuning. *Chem. Commun.* **2010**, *46*, 3463–3465.

40. Q. Li, L. Li, J. Kim, H.-K. Park, and J. Williams. Reversible photoresponsive chiral liquid crystals containing cholesteryl moiety and azobenzene linker. *Chem. Mater.* **2005**, *17*, 6018–6021.
41. C. Ruslim and K. Ichimura. Conformation-assisted amplification of chirality transfer of chiral *Z*-azobenzenes. *Adv. Mater.* **2001**, *13*, 37–40.
42. C. Ruslim and K. Ichimura. Photoswitching in chiral nematic liquid crystals: interaction-selective helical twist inversion by a single chiral dopant. *J. Mater. Chem.* **2002**, *12*, 3377–3379.
43. T. Yoshioka, T. Ogata, T. Nonaka, M. Moritsugu, S.-N. Kim, and S. Kurihara. Reversible-photon-mode full-color display by means of photochemical modulation of a helically cholesteric structure. *Adv. Mater.* **2005**, *17*, 1226–1229.
44. R. A. van Delden, M. B. van Gelder, N. P. M. Huc, and B. L. Feringa. Controlling the color of cholesteric liquid-crystalline films by photoirradiation of a chiroptical molecular switch used as dopant. *Adv. Funct. Mater.* **2003**, *13*, 319–324.
45. R. A. van Delden, N. Koumura, N. Harada, and B. L. Feringa. Unidirectional rotary motion in a liquid crystalline environment: color tuning by a molecular motor. *Proc. Natl. Acad. Sci. U.S.A.* **2002**, *99*, 4945–4949.
46. Q. Li, L. Green, N. Venkataraman, I. Shiyanovskaya, A. Khan, A. Urbas, and J. W. Doane. Reversible photoswitchable axially chiral dopants with high helical twisting power. *J. Am. Chem. Soc.* **2007**, *129*, 12908–12909.
47. E. Montbath, N. Venkataraman, A. Khan, I. Shiyanovskaya, T. Schneider, J. W. Doane, L. Green, and Q. Li. Novel optically addressable photochiral displays. *SID Digest Tech. Pap.* **2008**, 919–922.
48. N. Venkataraman, G. Magyar, E. Montbath, A. Khan, T. Schneider, J. W. Doane, L. Green, and Q. Li. Thin flexible photosensitive cholesteric displays. *J. Soc. Information Display* **2009**, *17*, 869–873.
49. D.-K. Yang and J. W. Doane. Cholesteric liquid crystal/polymer gel dispersions: reflective display application. *SID Int. Symp. Digest Tech. Papers* **1992**, *23*, 759–761.
50. D.-K. Yang, J. L. West, L.-C. Chien, and J. W. Doane. Control of reflectivity and bistability in displays using cholesteric liquid crystals. *J. Appl. Phys.* **1994**, *76*, 1331–1333.
51. T. J. White, R. L. Bricker, L. V. Natarajan, N. V. Tabiryan, L. Green, Q. Li, and T. J. Bunning, Phototunable azobenzene cholesteric liquid crystals with 2000 nm range. *Adv. Funct. Mater.* **2009**, *19*, 3484–3488.
52. L. Green, Y. Li, T. White, A. Urbas, T. Bunning, and Q. Li. Light-driven molecular switches with tetrahedral and axial chirality. *Org. Biomol. Chem.* **2009**, *7*, 3930–3933.
53. J. Chen, S. M. Morris, T. D. Wilkinson, and H. J. Coles. Reversible color switching from blue to red in a polymer stabilized chiral nematic liquid crystals. *Appl. Phys. Lett.* **2007**, *91*, 121118.
54. M. Kawamoto, T. Aoki, and T. Wada. Light-driven twisting behaviour of chiral cyclic compounds. *Chem. Commun.* **2007**, 930–932.
55. M. Mathews and N. Tamaoki. Planar chiral azobenzenophanes as chiroptic switches for photon mode reversible reflection color control in induced chiral nematic liquid crystals. *J. Am. Chem. Soc.* **2008**, *130*, 11409–11416.
56. M. Mathews, R. S. Zola, S. Hurley, D.-K. Yang, T. J. White, T. J. Bunning, and Q. Li. Light-driven reversible handedness inversion in self-organized helical superstructures. *J. Am. Chem. Soc.* **2010**, *132*, 18361–18366.

57. M. Kawamoto, N. Shiga, K. Takashi, and T. Yamashita. Non-destructive erasable molecular switches and memory using light-driven twisting motions. *Chem. Commun.* **2010**, *46*, 8344–8346.

58. P. M. A. Bonaccorsi, D. A. Dunmur, and J. F. Stoddart. Cholesteric phases induced by chiral substituted cyclohexylidenemethanes. *New J. Chem.* **1988**, *12*, 83–85.

59. S. N. Yarmolenko, L. A. Kutulya, V. V. Vashchenko, and L. V. Chepeleva. Photosensitive chiral dopants with high twisting power. *Liq. Cryst.* **1994**, *16*, 877–882.

60. E. Mena, P. V. D. Witte, and J. Lub. Camphor and nopinone derivatives as new photosensitive chiral dopants. *Liq. Cryst.* **2000**, *27*, 929–933.

61. P. V. D. Witte, J. C. Galan, and J. Lub. Modification of the pitch of chiral nematic liquid crystals by means of photoisomerization of chiral dopants. *Liq. Cryst.* **1998**, *24*, 819–827.

62. J. Lub, A. Ferrer, C. Larossa, and B. Malo. Synthesis and properties of chiral stilbene diacrylates. *Liq. Cryst.* **2003**, *30*, 1207–1218.

63. J. Lub, W. P. M. Nijssen, R. T. Wegh, I. De Francisco, M. P. Ezquerro, and B. Malo. Photoisomerizable chiral compounds derived from isoserbide and cinnamic acid. *Liq. Cryst.* **2005**, *32*, 1031–1044.

64. J. Lub, W. P. M. Nijssen, R. T. Wegh, J. P. A. Vogels, and A. Ferrer. Synthesis and properties of photoisomerizable derivatives of isosorbide and their use in cholesteric filters. *Adv. Funct. Mater.* **2005**, *15*, 1961–1972.

65. M. Irie. Diarylethenes for memories and switches. *Chem. Rev.* **2000**, *100*, 1685–1716.

66. C. Denekamp and B. L. Feringa. Optically active diarylethenes for multimode photoswitching between liquid-crystalline phases. *Adv. Mater.* **1998**, *10*, 1080–1082.

67. T. van Leeuwen, T. C. Pijper, J. Areephong, B. L. Feringa, W. R. Browne, and N. Katsonis. Reversible photochemical control of cholesteric liquid crystals with a diamine-based diarylethene chiroptical switch. *J. Mater. Chem.* **2011**, *21*, 3142–3146.

68. T. Yamaguchi, H. Nakazumi, K. Uchida, and M. Irie. Photochromism of a chiral cyclohexane having two diarylethene chromophores. A large optical rotation change. *Chem. Lett.* **1999**, 653–654.

69. T. Yamaguchi, T. Inagawa, H. Nakazumi, S. Irie, and M. Irie. Photoswitching of helical twisting power of a chiral diarylethene dopant: pitch change in a chiral nematic liquid crystal. *Chem. Mater.* **2000**, *12*, 869–871.

70. T. Yamaguchi, T. Inagawa, H. Nakazumi, S. Irie, and M. Irie. Photoswitching of helical twisting power by chiral diarylethene dopants. *Mol. Cryst. Liq. Cryst.* **2001**, *365*, 861–866.

71. T. Yamaguchi, T. Inagawa, H. Nakazumi, S. Irie, and M. Irie. Phase transition of a liquid induced by chiral photochromic dopants. *Mol. Cryst. Liq. Cryst.* **2000**, *345*, 287–292.

72. T. Yamaguchi, T. Inagawa, H. Nakazumi, S. Irie, and M. Irie. Photoinduced pitch changes in chiral nematic liquid crystals formed by doping with chiral diarylethene. *J. Mater. Chem.* **2001**, *11*, 2453–2458.

73. T. van Leeuwen, T. C. Pijper, J. Areephong, B. L. Feringa, W. R. Browne, and N. Katsonis. Reversible photochemical control of cholesteric liquid crystals with a diamine-based diarylethene chiroptical switch. *J. Mater. Chem.* **2011**, *21*, 3142–3146.

74. R. Eelkema and B. L. Feringa. Amplification of chirality in liquid crystals. *Org. Biomol. Chem.* **2006**, *4*, 3729–3745.

75. K. Rameshbabu, A. Urbas, and Q. Li. Synthesis and characterization of thermally irreversible photochromic cholesteric liquid crystals. *J. Phys. Chem. B* **2011**, *115*, 3409–3415.

76. Y. Li, A. Urbas, and Q. Li. Synthesis and characterization of light-driven dithienylcyclopentene switches with axial chirality. *J. Org. Chem.* **2011**, doi: 10.1021/jo201139t.

77. B. L. Feringa, R. A. van Delden, N. Koumura, and E. M. Geertsema. Chiroptical molecular switches. *Chem. Rev.* **2000**, *100*, 1789–1816.

78. H. Hattori and T. Uryu. Photochromic chiral liquid crystalline systems containing spirooxazine with a chiral substituent II. Photoinduced behavior. *Liq. Cryst.* **2001**, *28*, 1099–1104.

79. L.-M. Jin, Y. Li, J. Ma, and Q. Li. Synthesis of novel thermally reversible photochromic axially chiral spirooxazines. *Org. Lett.* **2010**, *12*, 3552–3555.

80. Y. Yokoyama. Fulgides for memories and switches. *Chem. Rev.* **2000**, *100*, 1717–1739.

81. Y. Yokoyama and T. Sagisaka. Reversible control of pitch of induced cholesteric liquid crystal by optically active photochromic fulgide derivatives. *Chem. Lett.* **1997**, 687–688.

82. Y. Yokoyama, S. Uchida, Y. Yokoyama, T. Sagisaka, Y. Uchida, and T. Inada. Chiral photochromic compounds and control of functions. *Enantiomer* **1998**, *3*, 123–132.

83. T. Sagisaka and Y. Yokoyama. Reversible control of the pitch of cholesteric liquid crystals by photochromism of chiral fulgide derivatives. *Bull. Chem. Soc. Jpn.* **2000**, *73*, 191–196.

84. B. L. Feringa and H. Wynberg. Torsionally distorted olefins. Resolution of cis- and trans-4,4′-bi-1,1′,2,2′,3,3′,-hexahydrophenanthrylidene. *J. Am. Chem. Soc.* **1977**, 602–603.

85. B. L. Feringa, N. P. M. Huck, and H. A. V. Doren. Chiroptical switching between liquid crystalline phases. *J. Am. Chem. Soc.* **1995**, *117*, 9929–9930.

86. B. L. Feringa, W. F. Jager, B. De Lange, and E. W. Meijer. Chiroptical molecular switch. *J. Am. Chem. Soc.* **1991**, *113*, 5468–5470.

87. N. Koumura, R. W. J. Zijlstra, R. A. van Delden, N. Harada, and B. L. Feringa. Light-driven monodirectional molecular rotor. *Nature* **1999**, *401*, 152–155.

88. R. Eelkema and B. L. Feringa. Reversible full-range color control of a cholesteric liquid-crystalline film by using a molecular motor. *Chem. Asian J.* **2006**, *1*, 367–369.

89. A. Bosco, M. G. M. Jongejan, R. Eelkema, N. Katsonis, E. Lacaze, A. Ferrarini, and B. L. Feringa. Photoinduced reorganization of motor-doped chiral liquid crystals: bridging molecular isomerization and texture rotation. *J. Am. Chem. Soc.* **2008**, *130*, 14615–14624.

90. R. Eelkema, M. M. Pollard, J. Vicario, N. Katsonis, B. Serrano Ramon, C. W. M. Bastiaansen, D. J. Broer, and B. L. Feringa. Molecular machines: nanomotor rotates microscale objects. *Nature* **2006**, *440*, 163.

91. R. Eelkema, M. M. Pollard, N. Katsonis, J. Vicario, D. J. Broer, and B. L. Feringa. Rotational reorganization of doped cholesteric liquid crystalline films. *J. Am. Chem. Soc.* **2006**, *128*, 14397–14407.

92. C.-T. Chen and Y.-C. Chou. C_2-symmetric dibenzosuberane-based helicenes as potential chirochromic optical switches. *J. Am. Chem. Soc.* **2000**, *122*, 7662–7672.

93. T. J. White, S. A. Cazzell, A. S. Freer, D.-K. Yang, L. Sukhomlinova, L. Su, T. Kosa, B. Taheri, and T. J. Bunning. Widely tunable, photoinvertible cholesteric liquid crystals. *Adv. Mater.* **2011**, *23*, 1389–1392.

94. K. L. Stevenson and J. F. Verdieck. Photodestruction and photoresolution with CPL has been achieved. *J. Am. Chem. Soc.* **1968**, *90*, 2974–2975.

95. N. P. M. Huck, W. F. Jager, B. de Lange, and B. L. Feringa. Dynamic control and amplification of molecular chirality by circular polarized light. *Science* **1996**, *273*, 1686–1688.

96. M. Suarez and G. B. Schuster. Photoresolution of an axially chiral bicyclo[3.3.0]octan-3-one: phototriggers for a liquid crystal-based optical switch. *J. Am. Chem. Soc.* **1995**, *117*, 6732–6738.

97. Y. Zhang and G. B. Schuster. Chirochromism–photochromism by epimerization: search for a liquid crystal phototrigger. *J. Am. Chem. Soc.* **1994**, *116*, 4852–4857.

98. Y. Zhang and G. B. Schuster. Photoresolution of an axially chiral bicyclo[3.2.1]octan-3-one: phototriggers for a liquid crystal-based optical switch. *J. Org. Chem.* **1995**, *60*, 7192–7197.

99. K. S. Burnham and G. B. Schuster. Transfer of chirality from circularly polarized light to a bulk material property: propagation of photoresolution by a liquid crystal transition. *J. Am. Chem. Soc.* **1999**, *121*, 10245–10246.

CHAPTER 7

Liquid Crystal-Functionalized Nano- and Microfibers Produced by Electrospinning

JAN P. F. LAGERWALL

Graduate School of Convergence Science and Technology, Seoul National University, Gyeonggi-do, Korea

7.1 INTRODUCTION: WHY ELECTROSPINNING WITH LIQUID CRYSTALS?

Although electrospinning is actually a rather old invention, it is currently attracting rapidly increasing attention throughout the international research community [1–8]. Among the reasons is the potential of the technique for producing extremely thin polymer fibers, which can easily be functionalized by inorganic as well as organic non-polymeric additives. By including liquid crystals inside the fibers, or by spinning the fibers from liquid crystalline polymers, a number of interesting phenomena arise [9–15], inspiring new directions of academic research and holding potential for innovative applications. The extreme stretching during the spinning process aligns a main-chain liquid crystalline polymer very well along the fiber [15], and electrospinning a lyotropic cellulose-based chiral nematic phase results in helical fibers [14]. If a low molar mass liquid crystal is enclosed inside the polymer fiber the strong encapsulation in a cylindrical space with diameter in the nano-to micrometer range can have dramatic effects, e.g., expanding the liquid crystal phase sequence [12], inducing unusual structures of the director field or restricting normally continuously varying parameters to quantized values [10]. Compared to other approaches of studying liquid crystal confinement effects, electrospinning has the attractive property that the mesogenic material is incorporated at the time of producing the fiber; thus no time-consuming filling procedure is required. On the other hand the various types of unique properties of different liquid crystal phases—strong response function to applied fields or temperature changes, birefringence, photonic band gap,

Liquid Crystals Beyond Displays: Chemistry, Physics, and Applications, Edited by Quan Li.
© 2012 John Wiley & Sons, Inc. Published 2012 by John Wiley & Sons, Inc.

spontaneous polarization, etc.—can all be transferred to the polymer fiber, giving it a responsiveness and functionality that regular polymer fibers do not exhibit. This is wherein the main potential for applications lies, relevant in particular for the field of wearable electronics and smart textiles.

Liquid crystal electrospinning is a very young research field and it is presently studied by only a handful of groups around the world. Considering the numerous opportunities for curiosity-based as well as applied research and the simplicity and low investment costs of the experimental equipment a strong development in the near future can be expected. This chapter aims to introduce the concept, describe the basic practical requirements, and give some examples of current achievements as well as an outlook to where the field is heading, discussing also the application potential. It is the hope of the author that this will inspire new players to enter the field, taking it into new directions and initiating further original thrusts in the field. It is still largely unexplored and thus offers many attractive opportunities for innovative research.

7.2 WHAT IS ELECTROSPINNING?

Electrospinning provides a convenient means of producing exceptionally thin fibers from a variety of polymers. In contrast to standard spinning techniques the flow of the spinning solution is of secondary importance, the driving force in electrospinning not being mechanical but electrostatic. The physics and chemistry involved in the process are fascinating from a fundamental research point of view, and the produced fibers have considerable potential for new devices and composite materials as they can exhibit properties that are quite unique.

The first patents related to electrospinning are now more than a century old [16, 17], with the crucial patent by Anton Formhals appearing some 30 years later [18]. In recent years there has however been a strong revival of the interest in the technique, largely because it offers a number of attractive features which fit very well with today's focus on nano-, micro- and biotechnologies and advanced materials research. First, the technique allows easy fabrication of exceptionally thin continuous fibers with diameters down to some 3 nm in extreme cases, difficult if not impossible to achieve with other spinning techniques. Second, by using different variations of the basic set-up a range of different fibers with varying functionalities can be produced, including composite fibers with different materials in the core and in the sheath, and they can be collected aligned or unaligned, the latter resulting in non-woven textiles. Third, the equipment needed is of very small-scale and—compared to the equipment for standard spinning techniques—inexpensive, such that an electrospinning set-up can easily be incorporated in a standard research lab. Finally, the understanding of the electrospinning process has dramatically improved during the last 10–20 years, largely due to seminal works, e.g., from the groups of Darrel Reneker (University of Akron), Alexander Yarin (University of Illinois at Chicago), Joachim Wenndorf and Andreas Greiner (Universität Marburg), Gregory Rutledge (MIT), Seeram Ramakrishna (National University of Singapore) and Younan Xia (Georgia Institute of Technology). The modern development of electrospinning was recently well

summarized by Reneker and Yarin [3]: *Electrospinning has rapidly changed fiber making from a capital intensive, large scale process to a low cost, broadly applicable method that manufactures fibers on a laboratory bench, to serve diverse needs ranging from materials science and technology to life sciences and clinical medicine*.

The two key components of an electrospinning set-up are a high-voltage DC power supply and a syringe pump (or two or three of them) or microfluidics control unit. One further needs containers and tubing for the fluids to be spun (when a syringe pump is used a syringe can basically fill both purposes), a metal capillary that acts as the spinneret (the nozzle through which the fluid to be spun is ejected), a target electrode or combination of electrodes on which the fibers can be collected (while this is often referred to as the collector, fiber collection is in fact often done on an object inserted between the spinneret and the target electrode), and a construction for conveniently varying the distance between spinneret and target electrode. Finally, one generally closes off a volume of air in which the spinning takes place using, e.g., a plexiglass box, in order to have some control over the atmosphere in which the fibers are spun, the relative humidity being of particular importance. Figure 7.1 shows a picture of what an electrospinning set-up can look like as well as a scheme of the fundamentals of the process.

7.2.1 Polymers and Solvents Convenient for Electrospinning

As will be explained below, the fluid to be spun needs to be non-Newtonian. The typical choice is a polymer solution although also polymer melts can be spun successfully. The solvent evaporates during the spinning process, leaving the

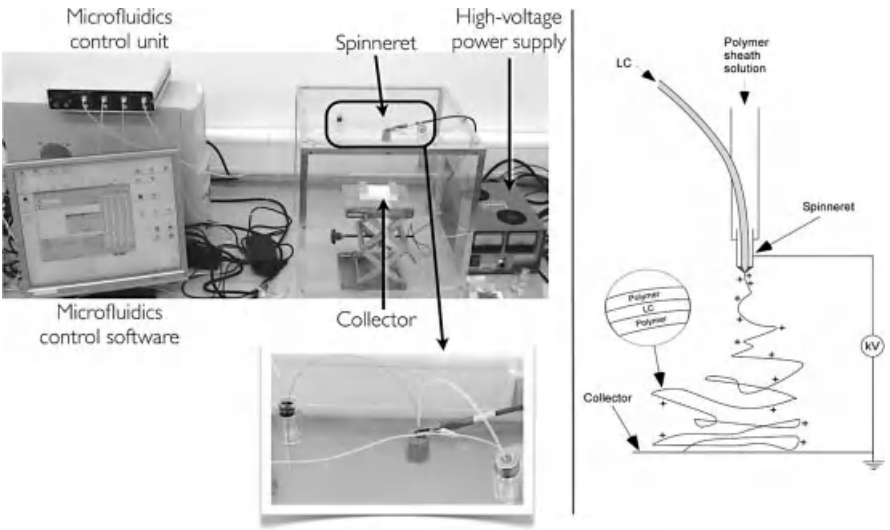

FIGURE 7.1 A set-up for coaxial electrospinning using a microfluidics control unit instead of syringe pumps (left) and a schematic drawing illustrating the process.

polymer or polymer blend to form the solid fiber. Also non-polymeric fluids or particles can be incorporated within the polymer fiber by using variations of the basic technique, something we will discuss in more detail once the basic electrospinning process has been introduced.

While many different polymers have been electrospun (some examples are presented in Table 7.1) using a variety of solvents, water- or ethanol-soluble polymers such as poly(ethylene glycol/oxide) (PEG/PEO), poly(vinyl pyrrolidone) (PVP), poly(vinyl alcohol) (PVA), and various cellulose derivatives are convenient to work with from a practical and environmental point of view. Fibers of poly(styrene) (PS), poly(acrylonitrile) (PAN), polylactide (PLA), and polyamides (PA) are also commonly produced by electrospinning, but they require organic solvents that may be less pleasant to work with. Molecular weights are typically in the range of 100,000 to several million and the polymer concentration is often around 5–30%, giving the spinning fluid a zero-shear viscosity similar to that of honey, about 3 Ns/m^2 [3].

7.2.2 The First Zone: Formation of the Taylor Cone

In contrast to ordinary spinning processes, the pressure on the spinning fluid is weak and the flow consequently becomes very slow in electrospinning. If no electric field is applied there will be a drop of the spinning fluid leaving the spinneret perhaps every 1–10 s. Thus, the flow is not a driving force in the spinning process; it is only required to constantly replenish the spinning solution at the spinneret. The driving force is instead an electric field applied to the fluid, typically by attaching the metal capillary to the hot pole of the DC power supply, whereas the ground is connected to the collector. The voltage applied to the capillary is very high, in the range of 10–20 kV, hence the power supply must be a rather special one (in fact, most groups doing electrospinning use the same brand of power supply: Gamma High Voltage Research). The current should however be very low (if not there is a short-circuit and something is severely wrong), hence the power supply will deliver only some hundred μA, rendering the set-up quite safe to work with. The distance between the spinneret and the collector is typically around 10 cm, so the applied field is on the order of kV/cm or 0.1 V/μm. It is thus comparable to the electric fields typically applied for switching liquid crystals, which may however also be even an order of magnitude or two higher.

The electric field leads to a separation of charges in the spinning fluid, e.g., the positive charges accumulating at the surface of the drop protruding from a positively charged spinneret (or negative charges for a negative spinneret voltage), as illustrated in Figure 7.2b. The charges in question are typically ions dissolved in the spinning solution, in some cases deliberately added in order to ensure sufficient charge density. With the application of the electric field a conflict between surface tension and electrostatic forces arises: while the former promotes a spherical droplet shape in order to minimize the surface of the liquid, the latter promotes a movement of the positive ions closer to the collector. The result is a deformation of the droplet into a cone shape (Figure 7.2c), referred to as the Taylor cone after the British physicist and mathematician Sir Geoffrey Ingram Taylor. Once the electric field is sufficiently high

TABLE 7.1 Examples of polymers and solvents (the list is nonexclusive, solvent mixtures often being used) commonly employed in electrospinning

Polymer	Abbreviation	Formula	Solvent	References
Poly(ethylene glycol/oxide)	PEG/PEO	$[-CH_2-CH_2-O-]_n$	water, ethanol	[19–21]
Poly(vinyl pyrrolidone)	PVP	$[-CH_2-CH(N{<}C{=}O)-]_n$	water, ethanol	[11, 12, 22–25]
Poly(vinyl alcohol)	PVA	$[-CH_2-CH(OH)-]_n$	water, ethanol	[26–32]
Poly(styrene)	PS	$[-CH_2-CH(C_6H_5)-]_n$	DMF, THF, $CHCl_3$, toluene	[33–39]
Polycarbonate	PC	$[-C_6H_4-C(CH_3)_2-C_6H_4-O-C(=O)-O-]_n$	THF, DMF, $CHCl_3$	[40–42]
Poly(acrylonitrile)	PAN	$[-CH_2-CH(CN)-]_n$	DMF, DMSO	[43–47]
Poly amides	PA	$[-NH-R_1-NH-C(=O)-R_2-C(=O)-]_n$	formic acid	[48–50]

(*Continued*)

TABLE 7.1 (*Continued*)

Polymer	Abbreviation	Formula	Solvent	References
Poly(methyl methacrylate)	PMMA		formic acid, DMF, $CHCl_3$	[33, 51–53]
Cellulose acetate	CA		acetone, ethanol, DMAc	[4, 54]
Polylactide	PLA		$CHCl_3$, CH_2Cl_2, acetone	[9, 50, 55]

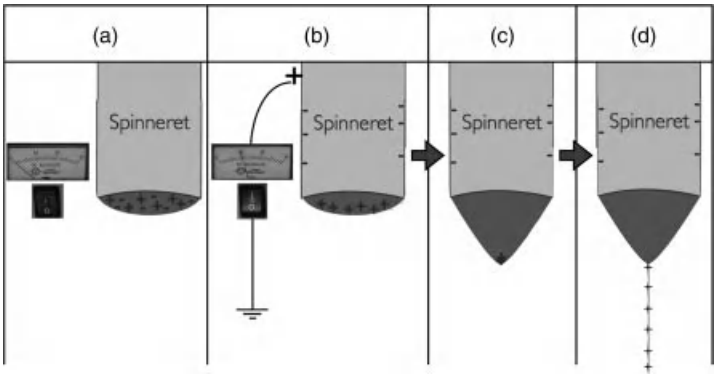

FIGURE 7.2 The different steps in the formation of the Taylor cone and jet ejection, the first stage of electrospinning. (a) The spinning fluid is slowly pumped through a capillary (the spinneret) until it protrudes slightly from the capillary orifice. (b) The electric voltage applied to the spinneret separates the ions in the fluid, those with the same charge as the voltage being repelled towards the boundary of the protruding drop. (c) These charges are attracted so strongly towards the collector that the drop deforms into a cone. (d) Eventually the self repulsion between the accumulated charges and their attraction towards the collector overwins the surface tension of the fluid, leading to the ejection of a thin jet of highly charged fluid from the cone tip towards the collector.

the electrostatic repulsion between the ions at the cone tip, and the attraction of the ions towards the collector, are so strong that they overcome the surface tension, leading to a liquid jet shooting out from the Taylor cone [3], as illustrated in Figure 7.2d. This is the basis of electrospinning (the region with the capillary orifice and the Taylor cone can therefore be called the first zone of electrospinning) as well as of a technique referred to as electrospray. We will say a few words about electrospray and the distinction from electrospinning below.

Some delay between field application and jet formation may occur, the magnitude depending on the rheological properties of the spinning solution. In typical cases, it is less than a second but with a highly viscoelastic spinning fluid such as a polymer melt the jet ejection can be delayed by as much as 90 s [3]. The size of the orifice has little impact on the jet diameter when it leaves the Taylor cone, as long as it is not so small that it leads to viscous flow restriction [3]. The optimum pumping flow rate is the one exactly equal to the rate at which the jet carries the fluid away from the capillary during spinning. As this increases with the applied electric field, the pumping flow rate must be adjusted accordingly if the voltage is changed.

7.2.3 The Second Zone: Jet Formation or Electrospray

If the spinning solution would be water or another ordinary Newtonian liquid, the jet would soon break up into droplets as a result of the Rayleigh instability (also referred to as capillary instability) that minimizes the surface energy of the liquid. When this happens we have electrospray, a technique that has become very important at the

sample preparation stage of mass spectrometry, in particular in the study of large biomolecules such as proteins (John B. Fenn was awarded the 2002 Nobel prize for chemistry for the introduction of "electrospray ionization" into the field of mass spectrometry). The division into droplets leads to rapid evaporation of liquid and a consequent strong increase in charge density within each droplet, quickly becoming so high that the initially formed droplets break up into much smaller ones, a process referred to as "atomization" (it is physically analogous to the initial formation of the Taylor cone).

Electrospray is something we wish to avoid in electrospinning and we do this by using non-Newtonian liquids as spinning solutions. As mentioned above they are most often solutions or melts of polymers with very high molecular weight. The viscoelastic properties of the polymer solution/melt counteract the separation into drops due to the Rayleigh instability and stabilize the jet, which thus stays intact and moves towards the collector. Nevertheless, the Rayleigh instability may be partially effective, producing a chain of regularly spaced drops (beads) along the fiber. This morphology is normally not desired and one must then modify the spinning parameters to regain continuous, smooth fibers. To some extent beading can be counteracted by increasing the feed rate of the spinning solution but more effective is to modify the composition of the solution. If one cannot switch to a polymer with higher molecular weight one can either raise the polymer concentration, although this will also give thicker fibers, or increase the conductivity of the solution, e.g., by salt addition. Since thin fibers are typically desired the latter option is often to prefer. The situation is graphically summarized in Figure 7.3.

Directly after leaving the Taylor cone the acceleration of the fluid in the electric field is so strong that the jet acquires translation velocities of about 5 m/s [3]. This should be contrasted with the typical drift speeds of the ions in the solution on the order of 0.1 m/s [56] and the very slow flow rate of the fluid(s) involved. This means that translational flow as well as charge translation within the jet can essentially be

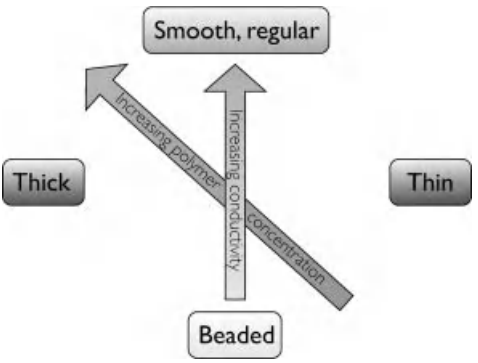

FIGURE 7.3 The character of the produced fibers can be tuned between "beads on a string" and smooth fibers with constant thickness by varying the composition of the spinning solution. The polymer concentration can be changed (thereby also influencing the fiber thickness) and/or the solution conductivity may be raised (e.g., by salt addition).

neglected from the point where the jet leaves the Taylor cone. In a first approximation, we can consider the electrospinning process as pure elongational flow and the relevant viscosities of the involved fluids are thus the elongational rather than the shear viscosities.

7.2.4 The Third Zone: Bending Instabilities and Fiber Stretching

On the way from the spinneret to the collector the jet is longitudinally stretched due to the repulsion between the like-charged ions that it carries with it. It also repeatedly experiences a second instability which is of great importance for the electrospinning process and the resulting fibers [3, 57]. This is a bending instability, also fundamentally resulting from the electrostatic repulsion between like-charged elements along the jet, but now in conjunction with a lateral fluctuation. As illustrated in a highly simplified way in Figure 7.4, considering only three charges distributed along a certain length of the jet, the electrostatic self repulsion will lead to no net force on the central element as long as the jet is absolutely straight. The forces from the upper and lower charges (F_u and F_d, respectively, with u for "up" and d for "down") are equal and oppositely directed; thus they compensate each other such that the net electrostatic force $F_r = 0$. But with a slight lateral fluctuation (Figure 7.4b) the forces are no longer balanced, yielding a nonzero lateral F_r. This amplifies the fluctuation and thus eventually giving rise to the bending instability, occurring when F_r is strong enough to overcome the elastic and viscous forces which promote the linear jet path (which is the shortest). The process is analogous to the Euler buckling process in mechanics (and thus also to the Frederiks transition, at the core of most electrooptic applications of liquid crystals), where a pillar compressed along its axis eventually breaks with a lateral movement as a lateral fluctuation is amplified by the axially applied force.

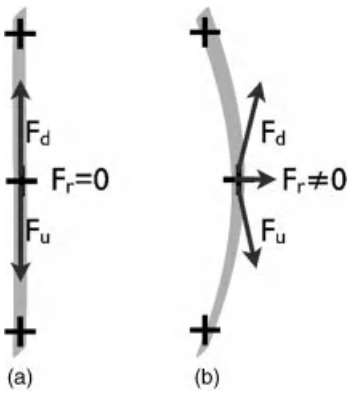

FIGURE 7.4 A simplified model for explaining the bending instability at the core of the exceptional stretching of the jet during electrospinning (see main text for explanation).

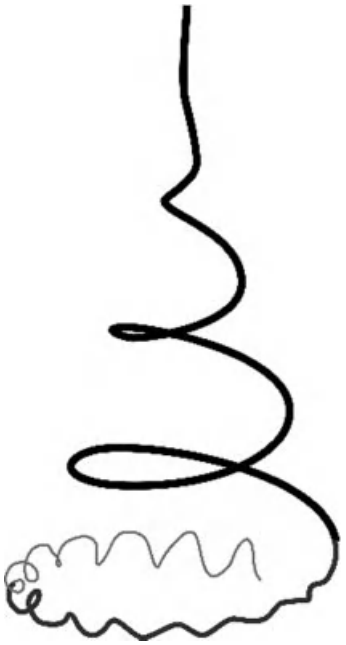

FIGURE 7.5 A simple cartoon of the envelope of the jet during electrospinning, characterized by multiple superposed spiral modulations due to subsequent electrostatically induced bending instabilities. Redrawn from [3].

The bending instability gives rise to a spiral-shaped continued path of the jet with a conical envelope, cf. Figure 7.5, first with a long pitch and relatively large (and increasing) spiral diameter. Eventually a second bending instability will typically appear, resulting in a smaller diameter spiral modulation of the jet, and this can go on to a third and fourth or even fifth hierarchical instability [3, 57]. The reason for the multiple bending instabilities is the continuously increasing charge density during the flight of the jet; although one might at first think that the substantial stretching would reduce the local charge density in the jet one must remember that the rapid evaporation of the solvent reduces the total jet volume, generally leading to a net increase in charge density. As a result of the multiple bending instabilities the jet follows a very complex path from the spinneret to the collector, with a path length that is orders of magnitude greater than the actual spinneret–collector distance, and the continuous stretching along this path renders the jet very much thinner at the end of the process than at the beginning. This is what allows such exceptionally thin fibers to be produced by electrospinning.

The elongation of the jet due to the multiple bending instabilities will normally continue until it hits the collector (or an object inserted in the spinning path) or until the polymer solidifies due to solvent evaporation or, in case of melt spinning, to cooling. During the elongation stage the jet experiences stretching ratios in the range

of 10^5 and stretching rates up to 10^5/s, values which are unmatched by other methods like fiber extrusion followed by mechanical stretching [6].

7.2.5 The Fourth and Final Zone: Fiber Collection

Just before the jet reaches the collector its translational speed is very high, often on the order of 40 m/s [6]. As it hits the collector the motion is abruptly stopped although the impact is not necessarily quite what one would expect considering the speed. Because of the bending instabilities during the jet flight the motion is largely lateral, in the plane of the collector, and the fiber can therefore be deposited as a relatively straight fiber. Depending on the vertical position of the collector, the impact of the jet may however be more or less head on, and in that case the buckling instability arising upon impact will lead to a characteristic small-diameter spiral pattern of the deposited fibers [3].

Normally one tries to optimize a set-up such that the jet solidifies just before or just after it hits the collector. If it is too wet the fiber morphology is not stable and deposited fibers will merge as a result of flow after deposition. If it is entirely dry then the decharging of the fiber via the contact with the grounded collector takes longer time. Since the fiber is still highly charged when it lands on the collector it repels the jet that approaches from above, which therefore moves laterally towards a different collection spot. As long as the charge on the deposited fiber is quickly neutralized this is fine; it results in a criss-cross deposition of fibers producing a characteristic open network mat structure, cf. Figure 7.6a. But if the decharging takes too long the repulsion of the incoming jet may be so strong so that the fibers are instead distributed in an uncontrolled way around the target area, building bridges between various surfaces around the collector.

In many cases an aligned collection of fibers is desired and a number of approaches have been developed to achieve this. The most obvious, but practically more involving, solution is to collect the fibers on a quickly rotating drum [58, 59], leading

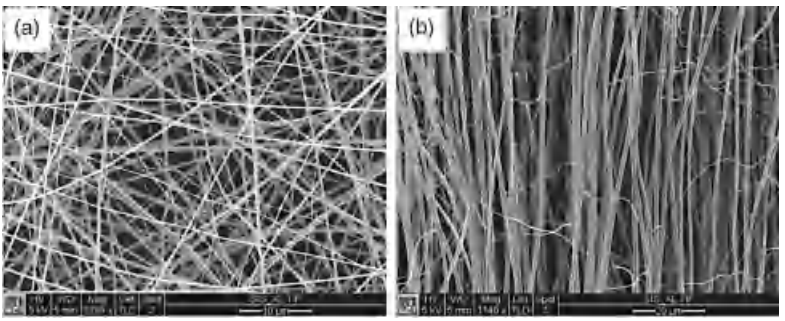

FIGURE 7.6 Scanning electron microscopy images of coaxially electrospun fibers with a nematic liquid crystal core and a composite sheath of PVP and TiO_2. The fibers were collected as a random non-woven mat (a) and aligned between the arms of a tweezer (b). Images courtesy of J. McCann and J. Lagerwall.

to fibers aligned perpendicular to the rotation axis. Quite well aligned fibers can however be achieved in a much easier way, simply by splitting up the collector electrode in two parallel grounded plates or wires [22, 50]. The electric field profile now has a horizontal component that promotes stretching of the fibers across the gap between the electrodes. Together with the repulsion between fibers that are suspended between the electrodes, thus only slowly discharged, this leads to an alignment of the fibers across the gap that can be quite good. The simplest way of realizing this type of alignment is to put a pair of metal tweezers on top of a flat collector electrode, resulting in the fiber jumping back and forth between the arms of the tweezers. The aligned fibers in Figure 7.6b were obtained in this way.

An interesting variation of this alignment technique was introduced recently by Yan et al. [60]. Rather than splitting up the target electrode in two, they placed two parallel blocks of a high permittivity dielectric material on top of the single grounded target electrode, again resulting in a lateral component of the electric field that stretches the fibers across the gap between the dielectric blocks. They demonstrated the concept with PVA fibers spun from aqueous solution onto water containers, blocks of wood, or ferrite, the latter yielding the best results.

If control of fiber alignment is much more critical than reduction of fiber diameter an attractive alternative can be to terminate the flight of the jet prior to the first bending instability, i.e., the third zone is eliminated from the process. Using this so-called near-field or high precision deposition electrospinning, in which the spinneret–collector distance is often only about a millimeter [61–63], excellent control of the position and alignment of the fibers can be achieved. Moreover, by using a collector substrate movable by an xy-translator very sophisticated patterns can be spun. (In principle also the spinneret could be moved but this is practically much more challenging since the spinneret is connected to the tubes for feeding with spinning solution as well as to the hot pole of the power supply.) This comes at the cost of somewhat thicker fibers and probably poorer alignment of the polymer chains within the fiber, since the extreme stretching induced by the multiple bending instabilities has been removed from the process. Moreover, the fibers may still be deposited with local spiral morphology due to a buckling instability at impact on the collector, especially for spinning distances greater than 1 mm [61].

7.2.6 Coaxial Electrospinning

A version of electrospinning that is particularly useful for incorporating low molar mass liquid crystals (or other liquids not amenable to spinning) is coaxial electrospinning, where one fluid is spun inside another one [64, 65]. As illustrated in Figure 7.1 a thin capillary is introduced inside the main tubing through which the polymer solution flows. This inner capillary runs almost coaxially with the main capillary until the orifice, where the two capillaries should end at the same height. They must be well centered at this point in order for the Taylor cone to form symmetrically, with the fluid pumped through the inner capillary uniformly surrounded by a layer of polymer solution. Since the introduction of the inner capillary through the wall of the main tubing often prevents perfect coaxial alignment of the

capillaries, one may need to slightly bend the metal capillary close to the orifice, such that they are well centered at the exit point of the spinneret. Alternatively, a special coaxial spinneret with dedicated inlets for the two fluids can be fabricated in a workshop.

The beauty of coaxial electrospinning is that any fluid with suitable viscosity that is immiscible with the polymer solution (jets produced with miscible fluids do not maintain the coaxial geometry throughout the electrospinning process [64]) can be spun into fibers by pumping this fluid through the inner capillary. The polymer forms a protective and confining cylindrical wall around the inner fluid. In other words, coaxial electrospinning produces fibers with a core–sheath structure, and because the sheath is a solid polymer the core can be a low molar mass liquid (it can of course also be a polymer), in our case a thermotropic liquid crystal. The inner fluid can give the composite fiber new functionality, e.g., special optical properties from a liquid crystal core (to be discussed in detail below). But even simple alkanes inside the fibers can functionalize the produced non-wovens into phase change materials useful for temperature stabilization [25].

Although we could in principle charge both or either liquid in coaxial electrospinning by using a metal capillary at the end of the inner tubing, upon connecting this to the hot pole of the power supply rather than the outer capillary (which in this case could be made of glass, for instance), the most common configuration is one where only the outer fluid is in direct contact with the electrode (the outer capillary, made of metal) and thus only this fluid gets charged. The inner fluid then does not experience the electrostatic forces that drive the electrospinning process, these being active only in the outer fluid. The jet core is instead stretched only by mechanical means as a secondary effect from the electrostatic stretching of the sheath [6]. This is advantageous when spinning living matter, such as cells, which may not survive the strong electrical charging, but it may also be a means of spinning highly conductive solutions, e.g., carbon nanotube suspensions or conductive polymers. These would short-circuit the set-up and thus terminate spinning as soon as the jet makes contact with the collector if spun as the outer (or only) fluid.

7.3 ELECTROSPINNING OF LIQUID CRYSTAL POLYMERS

The most straightforward approach to introduce liquid crystallinity to electrospinning is to work with liquid crystalline polymers for creating the fibers. These can be of thermotropic liquid crystal type, i.e., they form a liquid crystalline state after the solvent has evaporated or the isotropic melt has cooled down during the spinning process, resulting in a final fiber product that is liquid crystalline (possibly at elevated temperature). Also lyotropic liquid crystal polymers can be spun, in this case forming, e.g., a nematic phase during the spinning process, while the solvent is present. The final solvent-free fibers are then crystalline. Both approaches have been explored.

Canejo et al. investigated electrospinning from a lyotropic liquid crystalline solution of acetoxypropylcellulose (APC) in dimethylacetamide (DMAc) [14]. The concentration was 60 wt% concentration, rendering the mixture cholesteric,

yet this was near enough to the isotropic regime to ensure a viscosity that was not too high for spinning. The fiber product had some slightly unusual characteristics both on the large and the single-fiber scales. Rather than the typical criss-cross mat of reasonably long fibers that is usually obtained in electrospinning without alignment control, the fibers formed a web with an almost foam-like character of "cells" of varying sizes. Zooming in to the individual fibers, which were birefringent (revealing alignment of the polymer chains) and of a fairly large average diameter of just below 3 μm, the authors found these to be helically twisted. Interestingly, both right-and left-handed twists occurred (in a 3:1 ratio), hence the twisting is not a direct expression of the chirality of the polymer. Nevertheless, the theoretical analysis in the paper concludes that the chiral liquid crystalline state and its response to the electric field that drives the spinning process are at the core of the fiber twisting.

Solutions of a biphenyl-based smectic-forming thermotropic liquid crystalline main-chain polymer (molecular weight 29,000 g/mol) in hexafluoropropanol were electrospun by Nakashima et al. [66]. By adding the organic electrolyte pyridine at varying concentrations the team could modify the conductivity of the spinning solution, thereby tuning the diameter of the resulting fibers from about 100 nm to 5 μm. The internal polymer chain organization was characterized by X-ray scattering, revealing that fibers with a diameter greater than or equal to 220 nm exhibited a smectic structure. This was of a polydomain character in the thickest fibers but for a fiber diameter below 3 μm the layers were aligned perpendicular to the fiber axis. The thinnest fibers, with a diameter slightly above 100 nm, did not reveal any sign of chain ordering in the X-ray diffractograms.

Surprisingly, two different layer spacings were found for the smectic fibers, 24.0 Å and 17.0 Å. The authors explained this observation by the fact that the thermodynamically stable state of the polymer at the temperature of characterization is the SmC_a phase, characterized by tilted mesogen units, in opposite directions in adjacent layers. The tilt reduces the layer spacing compared to a non-tilted phase, like SmA, resulting in the smaller layer spacing of 17.0 Å. However, the strong stretching of the polymer chains in the electrospinning process promotes a metastable SmA state, yielding the larger 24.0 Å layer spacing. Annealing the fibers at 50°C (greater than the glass temperature $T_g = 30°C$) gradually transforms the SmA phase regimes to SmC_a and thus only the 17.0 Å layer spacing diffraction is observed after annealing.

The liquid crystalline polymer Vectra was melt-electrospun, thus without the use of solvent, by Ogata et al. [67]. Their modified set-up had a rod of Vectra being slowly translated towards the spinneret, where the rod tip was strongly heated by a triplet of CO_2 lasers, such that the viscosity of the polymer reached low enough values for electrospinning. The distance between spinneret and collector was rather small, only 2.5 cm. The small distance and the absence of solvent lead to relatively thick fibers, about 2.5 μm, but the chains were quite well aligned along the fibers, judging from the X-ray scattering diffractogram.

Considering the strong stretching during electrospinning, normally ensuring a highly uniform alignment of the director along the fiber, a very appealing concept is to produce liquid crystalline elastomer fibers by electrospinning, the crosslinking

taking place during or immediately after spinning for fixating the uniaxial order. By heating the fiber to the clearing point of the liquid crystalline elastomer, strong mechanical actuation effects could be expected. As the polymer chains acquire a more or less random coil conformation in the isotropic phase the fiber length should be reduced and the diameter increased [68]. In a joint effort by the Wendorff/Greiner and Finkelmann teams, Krause et al. explored this concept using a main chain copolymer comprising a mesogenic and a photocrosslinker monomer, respectively [15]. The polymer, with a molecular weight of $Mn \approx 44{,}000$ g/mol, was dissolved in chloroform at a concentration of about 7% by weight and spun with the relatively large spinneret–collector distance of 19 cm, at a consequent high voltage of about 25 kV.

The produced fibers, with an average diameter of about 1.5 μm, were birefringent, confirming the uniaxial alignment of the director along the fiber axis. Surprisingly, the report contains no discussion of the effect of heating the fibers above the clearing point. Obviously further studies along this interesting line of research are needed, but the lack of discussion of any actuation from the fibers gives a hint that the concept is not as straightforward as one may initially expect. Possibly the fact that the molecular weight is still rather low compared to typical polymer samples used for electrospinning renders the fiber production difficult.

The insufficient molar mass of the liquid crystalline polymer seems to have been the main reason for the difficulties encountered also in the study by Wu et al., investigating electrospinning of a polysiloxane backbone polymer with cholesteryl mesogen side chains [69]. Although the polymer concentration was very high (33% in chloroform), electrospinning did not succeed using this polymer on its own. Only upon addition of 5% of high molar mass poly ethylene oxide (PEO, $Mn = 1{,}000{,}000$), mixed into the chloroform solution of the liquid crystalline polymer, did high quality fibers result. The fiber diameter could be kept quite low, between 0.5 and 2 μm. Alternatively, some improvement of the fiber quality was obtained upon addition of low molar mass liquid crystal, an observation that is not so easy to explain. The improvement was however not sufficient and the fiber diameter also increased strongly in this way, rendering the mixing with PEO the better choice.

Interestingly, data from X-ray, scanning electron microscopy (SEM), and differential scanning calorimetry (DSC) investigations revealed no sign of phase separation between the liquid crystal polymer and the PEO, but they seem to have formed a homogeneous blend in the final fibers. Directly after electrospinning the polymer chains were aligned along the fibers, but not as well as might be expected, even worse than after conventional drawing. The authors attributed this observation to the fast solvent evaporation during spinning. By annealing the fibers for 20 min at 70°C the degree of chain orientational order went up considerably.

In summary, the experiments so far on electrospinning of liquid crystalline polymers show promise and interesting observations have been reported. Some problems still remain, however, most likely related primarily to the difficulties in realizing liquid crystalline polymers with very high molecular weight. By mixing the liquid crystalline polymer with regular, classically electrospinnable polymers, quite good results can nevertheless be achieved.

7.4 LOW MOLAR MASS LIQUID CRYSTALS INSIDE ELECTROSPUN FIBERS

Not only somewhat more complex but also much more versatile due to the immense catalog of available materials, is the spinning of low molar mass liquid crystals. The trick is to spin the non-polymeric, and thus "un-spinnable", liquid crystal as a core fluid contained inside a polymer sheath solution. The two approaches that have been explored for achieving this situation is to either mix polymer and liquid crystal in a common solvent and then rely on phase separation during the spinning process for obtaining the core–sheath structure [9], or to use coaxial electrospinning to establish the core–sheath geometry already at the starting point [10–12]. The resulting core–sheath fibers constitute an entirely new configuration for studying—and applying—low molar mass liquid crystals, opening possibilities very different from standard device configurations. The liquid crystal gives the fibers new functionality and responsiveness and the encapsulation of the liquid crystal in the narrow cylindrical fiber core allows easy investigation of 1D confinement effects. The fibers also have large application potential. While we are still at the very beginning of the research on development of liquid crystal-functionalized electrospun fibers and non-wovens one can envisage applying them in fields ranging from full spatial resolution temperature sensing, via dynamic camouflage clothing, to wearable electronics and displays. For simplicity we will in the following refer to low molar mass liquid crystals simply as "liquid crystals".

7.4.1 Non-Coaxial Electrospinning of Liquid Crystal Core Composite Fibers

Buyuktanir et al. devised an approach to liquid crystal electrospinning that is very attractive through its simplicity and the fact that a standard electrospinning set-up can be used. The commonly studied nematic liquid crystal 5CB was dissolved together with polylactide (PLA, $M_w = 186{,}000$ g/mol) in a chloroform–acetone solvent mixture (3:1 volume ratio), in proportions giving a PLA concentration of 7.3 wt%. This polymer concentration was kept fixed while the proportion of 5CB to PLA was varied in the range of 7–86%, spinnable solutions being those with 5CB concentrations below 70%. During the spinning process the 5CB phase separates from the polymer, forming the liquid crystal core of the fibers.

The phase separation between 5CB and PLA is however not complete but the fiber sheath actually becomes a mixture of PLA and 5CB. The authors found that phase separation started at 5CB to PLA ratios greater than 28 wt%, meaning that the excess 5CB then started forming a polymer-free liquid crystal core within the mixed composition sheath. Above this liquid crystal fraction the clearing transition enthalpy peak could be detected in differential scanning calorimetry measurements and the fibers appeared clearly birefringent for more than 40% 5CB, with the director generally aligned along the fibers as detected by polarizing microscopy. The morphology of the fibers (with diameters in the range of 0.5–2 μm) was however rather beaded for the liquid crystal-filled fibers.

7.4.2 Coaxial Electrospinning of Fibers with Solvent-Free Liquid Crystal Core Fluid: Practical Requirements

While the above approach is practically straightforward to realize, as only a single solvent-rich isotropic liquid phase is being spun, the degree of control is quite limited. The fiber beading in the report described above was also quite significant. It may thus be a worthwhile investment to modify a set-up for coaxial electrospinning to allow spinning of the pure liquid crystal as the core fluid, without addition of solvent, ensheathed by the outer polymer–solvent solution. While it should be possible to spin both thermotropic and lyotropic liquid crystals in this way the experiments carried out so far have been restricted to thermotropics. With lyotropics the situation obviously gets more complex as solvent is then a critical component of the liquid crystal phase, hence both sheath and core fluids contain solvent which may or may not evaporate during or after the spinning.

Generally, the coaxial approach to liquid crystal electrospinning requires the basic set-up to be extended with a tailored temperature regulation system, allowing the user to choose the phase adopted by the liquid crystalline material at the onset of spinning. While nematics can be relatively easy to electrospin, the shear viscosity η_2 in fact being even lower than the shear viscosity of the material heated to its isotropic phase, higher-ordered liquid crystal phases such as smectics or cholesterics are often (but not always) too viscous. It may be difficult to achieve continuous and smooth flow to the spinneret of a highly viscous fluid. Moreover, a large difference in elongational viscosity between inner and outer fluids complicates the spinning process such that a continuous filling of the fibers may be impossible. It is thus highly desirable to have the possibility to heat the material into the isotropic phase if we wish to prepare fibers with a core that eventually is in a high-ordered liquid crystalline state.

It is not trivial to realize a precise and versatile temperature control for electrospinning, since the substance to be heated is spatially distributed over the full length of tubing, the access for a heating system being very difficult in certain places. The simplest solution is to heat the whole system up to the spinneret with a heat gun. This method is readily accessible but obviously lacks precision, preventing true control of the spinning parameters and making repeatability challenging, and it also heats many components that would better stay at room temperature, such as the syringe pump in case this device is used. If instead a pneumatic microfluidics system is used for pumping the fluids this has the advantage that the vial from which the liquid crystal is pumped can easily be placed in a heating block for temperature control. This improves the situation but it is often not sufficient, since the large surface area of the tubing through which the liquid crystal flows renders temperature equilibration with the surrounding air very rapid. Despite heating the fluid while in the reservoir it may thus end up too cold once it reaches the spinneret. A design that proved quite effective is one where a heating block for the liquid crystal vials is combined with a heated air flow along the tubing. Even more efficient temperature control of the tubing may be realized by immersing it in a heated liquid bath, although this obviously places quite stringent requirements on sealing the liquid bath where the tubing leaves the bath, just before the spinneret and the electrical connection to the power supply.

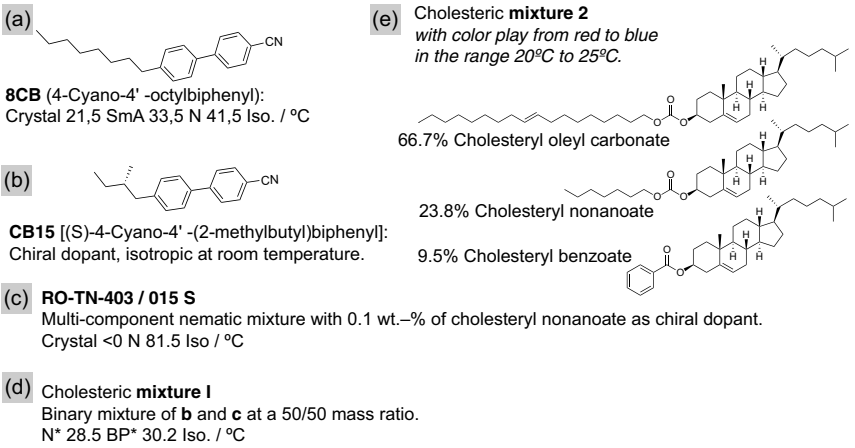

FIGURE 7.7 Key substances used for preparing the liquid crystal core materials in the electrospun composite fibers studied by the author's team.

For some liquid crystal substances the inner fluid can in fact sometimes be in a cholesteric or even smectic phase during spinning, rendering the heating requirements less critical. For instance, **8CB** (Figure 7.7a) could be spun at room temperature where the liquid crystal is in a SmA phase, close enough to the second-order N-SmA transition that the material still flows reasonably easily. Likewise, the short-pitch cholesteric formed by doping the commercial nematic mixture **RO-TN-403/015 S** with the chiral dopant **CB15** (see Figure 7.7b–d) had sufficiently low viscosity to be spun at room temperature. This mixture (in the following referred to as **mixture 1**) is much less viscous than the three-component cholesteryl ester **mixture 2** (Figure 7.7e) although both have about the same very short pitch of the director helix at room temperature.

With other liquid crystals strong heating is required for electrospinning, or one may have to resort to dissolving the liquid crystal in a solvent also in this case, being careful to use a solvent that is not miscible with the sheath solution and that will evaporate to a large extent during the spinning process. This is for instance the case when the clearing point is higher than the maximum spinning temperature of the sheath solution (often quite low due to the requirement to use reasonably volatile solvents in this solution) or when even the isotropic phase is too viscous, as can be the case for some discotic, bow-shaped, or oligomeric liquid crystals.

7.4.3 Sheath Morphology of Coaxially Spun Liquid Crystal Core Fibers

The first few experiments on coaxial liquid crystal core–polymer sheath electrospinning were carried out with an outer spinning solution containing not only just polymer but also a $Ti(OiPr)_4$ sol–gel precursor [12]. The result is a polymer–TiO_2 composite sheath that is particularly stable, making coaxial electrospinning with core fluids that are close to Newtonian relatively easy. The exact composition of the sheath

solution was in this case 3% PVP, 29% $Ti(OiPr)_4$, 48% ethanol, and 19% acetic acid, yielding a sheath where the polymer is in fact just a minority (27%, the rest TiO_2). While this gave very stable fibers with well-defined morphology (Figure 7.6) the fact that the sheath consists mainly of TiO_2 makes characterization of the liquid crystal core more challenging, and the optical properties of the liquid crystal are inaccessible behind this strongly scattering and birefringent sheath. The verification of the director alignment as well as the investigation of the phase sequence therefore had to be done with polarized Raman spectroscopy.

In later work the fibers were spun with a pure PVP sheath that is largely non-birefringent. This generally worked very well, fibers produced using a 12.5% PVP in ethanol solution as outer fluid appearing quite uniform in optical microscopy and the liquid crystal optical properties being easily detectable (these will be discussed below). The outer morphology of these fibers was investigated by SEM; some results were shown in Figure 7.8. The fibers were generally cylindrical although some examples of essentially flat ribbons were also found. Depending on the degree of liquid crystal filling, the outer diameter ranged between one and a few microns.

The fact that coaxial spinning with liquid crystal core and pure PVP sheath can produce stable fibers is actually somewhat surprising, because earlier attempts by Li and Xia to spin mineral oil coaxially inside a PVP ethanol solution failed due to structural breakdown of the coaxial jet. The result was complete separation into oil droplets and solid fibers of pure PVP [64]. The addition of the $Ti(OiPr)_4$ sol–gel precursor in the outer fluid was in their case required to stabilize the sheath. In the case with a liquid crystal in the core the situation is however somewhat different because the inner solution is also weakly non-Newtonian. Relatively long filaments can be drawn from liquid crystals, in contrast to isotropic Newtonian fluids where the Rayleigh instability more rapidly destabilizes a filament and separates the fluid into

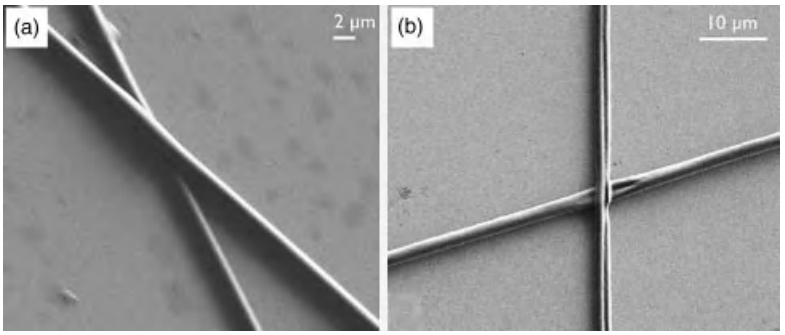

FIGURE 7.8 Scanning electron microscopy images (courtesy of G. Scalia and O. Calò) of pure PVP sheath fibers with cholesteric liquid crystal core (**mixture 1**, Figure 7.7d). Both samples were spun at room temperature with 25–35% relative humidity, 10 cm spinneret–collector distance, and 10 kV spinning voltage, with a 12.5% PVP in ethanol solution as the outer fluid. This was pumped at a flow rate of 1.8 mL/h while the inner fluid was pumped at flow rates of 0.14 mL/h (a) and 0.36 mL/h (b).

droplets. It thus seems that this property of the liquid crystal is beneficial for coaxial electrospinning, allowing us to use a simpler and in many respects practically preferable sheath solution than had the inner fluid been isotropic. This means that one should not heat the liquid crystal into its isotropic phase for spinning if it can be avoided. The nematic phase ought to be the optimum phase for spinning but unfortunately not all materials exhibit this phase.

The results of Li and Xia suggest that when encapsulating non-nematic materials a mechanically stronger sheath solution may be required to stabilize the coaxial jet. Different variations of the sheath solutions in this direction were therefore explored also for liquid crystal electrospinning, keeping the requirement that the sheath should be at least largely non-birefringent and transparent. One approach is to increase the polymer concentration, yielding fibers that are mainly cylindrical and intact, in some cases also yielding porous fiber sheaths. An alternative modification is to nevertheless add $Ti(OiPr)_4$ sol–gel precursor but at a rather small amount, just sufficient to stabilize the sheath but not so much that birefringence and scattering from TiO_2 grains become disturbing. The fibers formed with this sheath solution were truly excellent in terms of uniformity and cylindrical shape, cf. Figure 7.9, and the small amount of TiO_2 in the sheath did not prevent the liquid crystal from being visible through the fibers. A further interesting observation was that the TiO_2–PVP composite fibers were substantially thinner than those without TiO_2.

It is obviously of great interest to know also the internal structure of the fiber, the inner diameter being the most important parameter to establish. This is however not trivial to realize experimentally since the fibers are generally too thick for transmission electron microscopy (TEM) imaging. In addition, the similar electron density of the sheath polymer and the liquid crystal would lead to too weak contrast

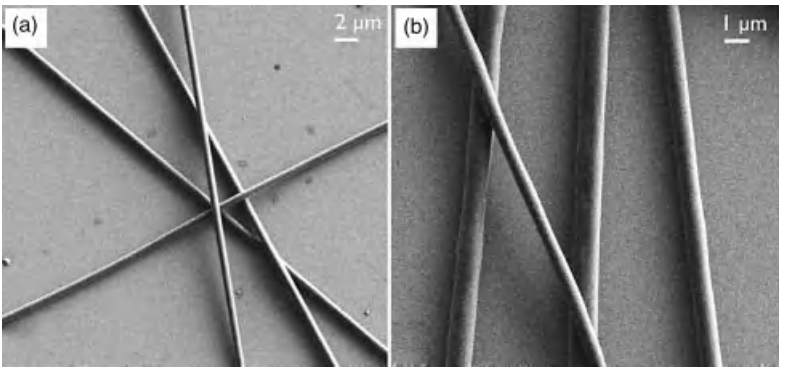

FIGURE 7.9 Scanning electron microscopy images (courtesy of G. Scalia and O. Calò) of fibers with composite sheath, consisting of 91% PVP and 9% TiO_2, and cholesteric core (**mixture 1**, Figure 7.7d). The ethanol-based sheath solution containing $Ti(OiPr)_4$ as sol–gel precursor in addition to 10% PVP was pumped at a flow rate of about 2 mL/h and the liquid crystal core fluid at 0.26 mL/h (a) and 0.80 mL/h (b), respectively. Both samples were spun at room temperature, with 25–35% relative humidity, 10 cm spinneret–collector distance and 10 kV spinning voltage.

for distinguishing the two regimes in TEM. One approach that has been successful in the characterization of similar systems is to carry out SEM on the fractured end surface of fibers that have been broken in two sections, at best after having dissolved the core fluid with a suitable solvent that does not affect the sheath. This however requires that the fiber sheath does not collapse during the fracture, something which turned out to be very difficult to avoid for pure PVP sheath fibers.

The approach that eventually brought success in imaging the internal structure was to use Focused Ion Beam (FIB) milling to cut sections through the fibers, either along or across them, and then image the dissected fiber using SEM or FIB. When exposed to the vacuum of the FIB chamber the low molar mass liquid crystal molecules of the core evaporate, leaving only the polymer sheath to form the image. As can be seen in Figure 7.10 this results in a very clear picture of the fiber morphology, internal as well as external. The channel that initially held the liquid crystal is easily seen. In this particular fiber, rather thick and with high degree of liquid crystal filling, the morphology is not cylindrical but rather one of a horizontal cylinder segment. Apparently the soft fiber sheath had collapsed when the fiber hit the substrate. The liquid crystal core channel has roughly the same cross-section as the fiber as a whole. The FIB characterization study is described in full detail in a paper soon to be published (authors E. Enz, V. La Ferrara, O. Calò, J. Lagerwall and G. Scalia).

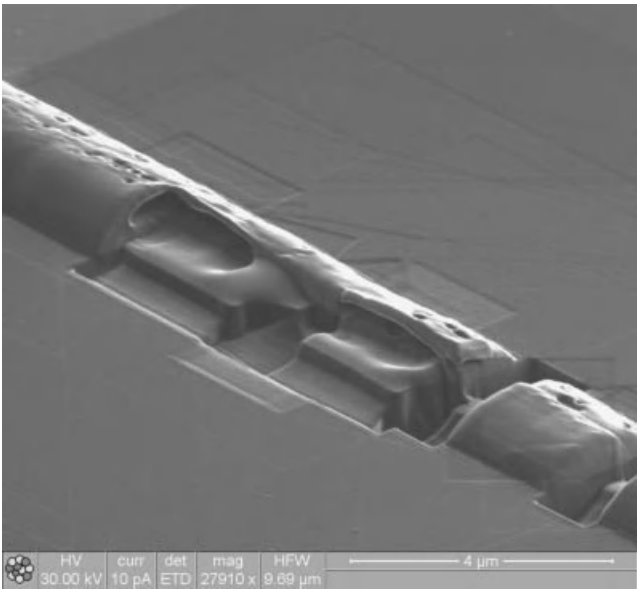

FIGURE 7.10 A richly filled fiber with pure PVP sheath and cholesteric liquid crystal core, dissected using FIB milling and imaged by the FIB. Upon hitting the substrate the fiber had collapsed from the normal cylindrical geometry into a horizontal cylinder segment morphology. The channel holding the liquid crystal can easily be seen in the regions where the FIB has cut away the sheath. Image courtesy of G. Scalia and V. La Ferrara.

7.4.4 How Does the Liquid Crystal Align inside the Fiber?

The cylindrical symmetry of the fiber (for simplicity we consider here only fibers with cylinder morphology) might intuitively suggest a director alignment along the fiber for a nematic phase but perpendicular for a SmA phase. In case of a nematic the minimum viscosity is along the director, hence an alignment along the fiber is to be expected considering the spinning conditions. Moreover, this alignment produces a defect-free director field within the cylindrical fiber, whereas homeotropic as well as planar but transverse alignment would yield very strong splay and bend, respectively, for the nematic confined in the narrow fiber core. The homeotropic alignment would on the other hand allow smectic layers to form concentrically along the fiber, compatible with easy shear flow on the way to the spinneret, promoting the hypothesis of this alignment for spinning in the smectic phase.

In case of clear and isotropic polymer sheaths the alignment of the director within the fibers is easily investigated with polarizing microscopy. Some fiber sheaths are however too scattering, or birefringent in themselves, such that this straightforward technique cannot be used for the purpose. For instance, the fibers with composite sheaths containing a large amount of TiO_2 are both strongly scattering and birefringent, rendering optical microscopy investigations useless for assessing the state of the liquid crystal core [12]. In this case, polarized Raman spectroscopy turned out to be highly useful since the liquid crystal has a very characteristic response spectrum that can easily be distinguished from that of the sheath. The strength of the liquid crystal peaks depends on the alignment of the director with respect to the polarization of the excitation laser, going to zero for perpendicular alignment and being maximal for parallel. This allows the director orientation and the effective degree of orientational order to be assessed also in such fibers.

In case the fibers have been spun with uniform fiber orientation they can also be placed in an X-ray scattering set-up, allowing the type of liquid crystal alignment in the fiber to be elucidated from the X-ray scattering diffractograms. This is particularly useful for smectic liquid crystal cores, since we can then study the director alignment and the layer formation independently. A convenient approach is to roll up an aligned and relatively dense fiber mat into a scroll, perpendicular to the fiber axis, which can then be inserted into an X-ray capillary for the experiment. An example of the result for a SmA-containing fiber is shown in Figure 7.11, the scroll production illustrated on the left and the resulting 2D X-ray pattern shown to the right.

It turns out that the assumption about the nematic orientation is correct (even for chiral nematics), but for smectics the layers do not form concentrically but perpendicular to the fibers. Even in the smectic phase planar alignment prevails, resulting in a stack of smectic layers along the fiber, each layer with a lateral extension no greater than the fiber diameter. The diffractogram in Figure 7.11 features clear small-angle smectic layer diffraction peaks along an axis perpendicular to the rolling direction, thus along the fiber axis. A more careful consideration of the situation makes this observation understandable. Since the flow during the actual spinning stage is of elongational type it is the elongational and not the shear viscosity that is relevant. For smectics the lowest shear viscosity is perpendicular to the director and along the

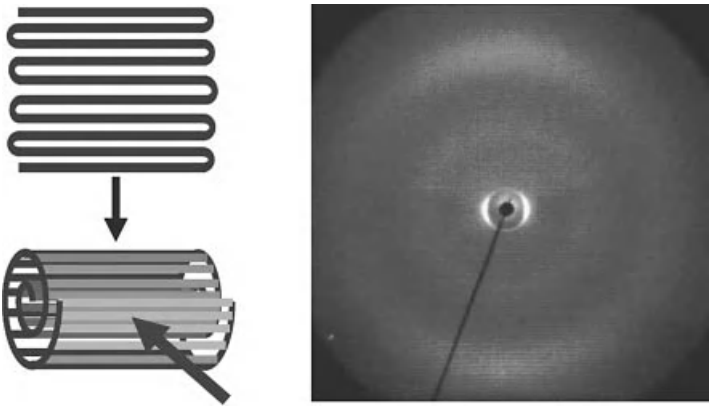

FIGURE 7.11 X-ray diffraction pattern (right) from **8CB** inside coaxially electrospun PVP fibers, rolled into a scroll (illustration on the left) and placed into a Mark capillary. From paper [11].

layers, since the layers can slide along each other. But the elongational viscosity in this direction can be expected to be rather high, since all layers are stretched together, without flow past each other, in elongational flow. Elongational flow along the director may be preferable since the elongation can easily be accommodated by making the lateral extension of each layer somewhat smaller and moving the molecules from the sides of the cylinder to the middle in order to form new interstitial layers. Finally, this smectic geometry may also be promoted by the fiber sheath imposing a strong planar director alignment at the boundary between liquid crystal and fiber sheath.

The lateral extension of the smectic layers is very small with this geometry, only the ≤ 1 μm diameter of the confined space inside the fiber. This size is smaller than the thickness of the thin cells typically used for preparing planar surface-stabilized ferroelectric liquid crystal (SSFLC) samples of very short-pitch chiral SmC* materials. In that case, a geometry with small lateral smectic layer extension, albeit only in one dimension, is secured by means of strong director anchoring at the sample boundaries. For the cylindrical symmetry of a core–sheath fiber the situation is however different, in a quite interesting way. While the geometry with the director along the fiber axis is unproblematic for a SmA phase, the tilted director of SmC* would lead to frustration. For a non-chiral SmC phase the requirement that each smectic layer should have uniform director tilting direction forces the layers to tilt in a uniform direction. Going to a chiral SmC* phase, however, this solution fails since the director tilt precesses along the layer normal in this phase, hence each layer would need to tilt in a direction slightly different from its neighbor layers above and below. Obviously this is incompatible with the stacking of the layers.

It is thus a very interesting question for future experiments to establish how an SmC* phase resolves this frustration. One may consider a number of scenarios. First, the SmC* phase may be replaced by SmA* in order to avoid the problem. Second, the

helix may be expelled as in flat SSFLC samples, but here all layers would be uniformly tilted as in the geometry expected for a non-chiral SmC phase within the fiber. This would yield the fiber spontaneously polarized with a component perpendicular to the fiber, probably with an impact on the actual spinning process in the electric field and obviously something that could be exploited in applications. Third, a modulation of the director tilt magnitude may occur on approaching the core perimeter, the tilt disappearing into a SmA-like geometry at the border of the fiber sheath. The larger part of the interior of each layer would then still be in SmC* geometry with a well-defined tilt direction within each layer (which would be perpendicular to the fiber axis) that precesses along the layer normal. Of course other scenarios are possible. In case of SmC* phases with high spontaneous polarization, the polarization may also play a role for the resulting alignment since the director field under confinement has been shown to be strongly influenced by high polarization values in case of planar cells [70].

7.4.5 Phase Sequence and Phase Transitions of Liquid Crystals Inside Electrospun Fibers

It is well known that the phase sequence of liquid crystals can be strongly affected by confinement [71–75], particularly sensitive phases such as the chiral smectic-C intermediate phases even disappearing completely already at relatively large surface spacings, on the order of 10 μm [72]. As the inner sample spacing in this latter case is an order of magnitude larger than the outer fiber diameter of typical electrospun fibers, we can clearly expect to see an influence from the encapsulation, even on more robust phases like nematic and SmA. Moreover, the cylindrical symmetry may have a particular effect, as already speculated above for SmC and SmC* phases and as will be further discussed for the case of chiral nematics and blue phases below.

In the first few experiments on coaxial electrospinning with a nematic liquid crystal mixture inside a composite PVP–TiO_2 sheath a dramatic increase of the clearing temperature by about 20°C compared to the bulk liquid crystal was found [12]. Moreover, the first-order character of the nematic–isotropic transition also seemed to have disappeared as a result of the strong confinement. In a series of elegant Atomic Force Microscopy investigations on liquid crystals in the vicinity of solid substrates, the team around Igor Musevic in Ljubljana demonstrated how liquid crystalline order prevails very near the surface even at temperatures well above the clearing temperature [76, 77]. In the electrospun fibers, where the liquid crystalline core is fully surrounded by a solid sheath with an inner diameter typically a few hundreds of nanometers the same phenomenon should occur. However, the molecules in the vicinity of the surface now constitute a much greater fraction of the whole liquid crystal volume than in usual samples. We may thus explain the observation of increased clearing point and the loss of first-order transition character as a result of a surface-induced stabilization of the liquid crystal phase that gets less effective on going from the sheath to the core. As we continue heating the fiber from the bulk clearing temperature the mixture gradually turns isotropic from the center, the ratio of nematic to isotropic phase continuously getting smaller until finally,

some 20°C above the bulk clearing temperature, even the surface layer has lost its orientational order. In this way the phase transition appears continuous to the outside world and liquid crystalline order is detectable at much higher temperatures than for bulk samples.

With relatively thick fiber mats prepared by coaxial electrospinning of **8CB** inside a pure PVP sheath, a sufficient amount of liquid crystal was contained to give a response in DSC experiments [11]. This allowed a study of the effect of encapsulation on the SmA-N and N-isotropic phase transitions. As expected, the phase transition peaks became weaker and more smeared out than for a bulk sample, and the two transitions approached each other upon increasing confinement, until they could no longer be resolved in the thinnest fibers, cf. Figure 7.12. The increase in clearing point was here less pronounced than in the previous study, most likely because the encapsulation was not as strong in these pure PVP sheaths as in case of the TiO_2–PVP composite fibers. The strong effect on the smectic–nematic transition temperature was explained as a result of an encapsulation-induced kinetic stabilization (superheating and -cooling) of whatever molecular arrangement that is in

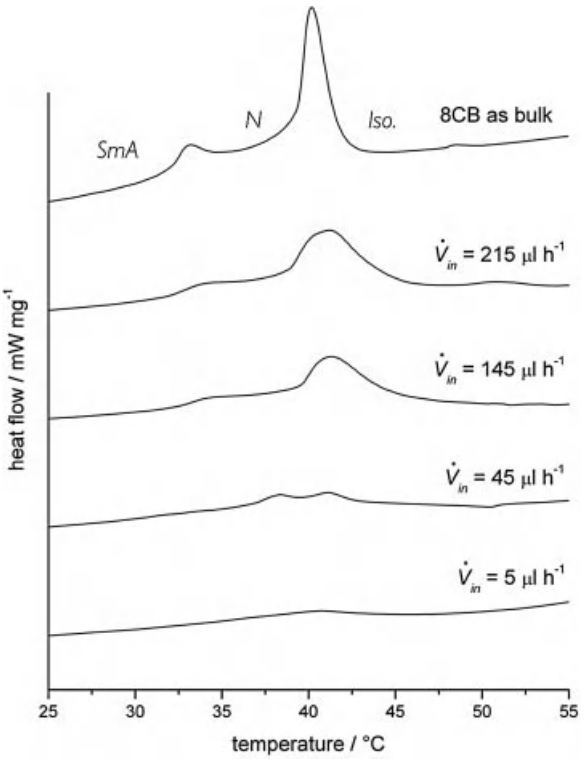

FIGURE 7.12 Differential scanning calorimetry curves on heating for **8CB** in electrospun PVP fibers, as a function of liquid crystal flow rate (lower rate yielding thinner fibers, with stronger confinement). From paper [11].

place. When first passing a certain phase transition temperature the mesogens at the inner surface of the polymer sheath are strongly anchored in an arrangement corresponding to the starting liquid crystal phase. This surface-stabilized cylindrical layer of molecules will counteract reorganization into a less or more ordered phase, leading to the strong supercooling/-heating effects.

A somewhat different type of modification of the phase sequence was observed when the chiral **mixture 1** was encapsulated in fibers. Here the phase transition between N^* and BP^* truly disappeared, on heating as well as on cooling. While also this effect was a consequence of the influence from the sheath on the liquid crystal structure formation, it was not a simple matter of kinetic stabilization. In fact, the two phases had become degenerate in the cylindrical confinement, as will be explained in the following.

7.4.6 The Optical Properties and Phase Behavior of Cholesteric and Blue Phases Inside Electrospun Fibers

Enz and Lagerwall prepared a series of PVP sheath fibers containing the short-pitch cholesteric liquid crystal **mixture 1**, reflecting a blue-green color when observed straight on [10]. In the experiments the liquid crystal flow rate as well as that of the sheath solution was varied. With increasing liquid crystal flow rate the fiber core, and thus the fiber, gets thicker and the sheath thinner (since the same volume of sheath solution must now surround the larger-diameter liquid crystal core). What was also apparent was that the continuity of liquid crystal filling depended strongly on the flow rate. At low flow rates the fibers were not only thinner but the liquid crystal was also distributed in elongated drops along the fiber rather than forming a continuous thin core. As in the fibers with a non-chiral nematic mixture [12] the clearing point went up, the more so the thinner the fiber. In the thinnest the clearing point was about 15 K higher than in the bulk liquid crystal.

The selective reflection color was visible in most fibers, in case of the thickest fibers easily detectable even by the naked eye. Such mats had the blue-green color of the cholesteric mixture. On the other hand, in fibers produced with lower liquid crystal flow rate, thus with smaller inner diameter, the color could be strikingly different. In many cases it varied between blue-green and yellow but in certain locations it could even reach the red end of the spectrum, cf. Figure 7.13 showing two mats with slightly different fiber diameters. This modulation and quantization of the cholesteric selective reflection color are a consequence of the cylindrical boundary conditions imposed by the fiber sheath on the cholesteric helix.

From the colored appearance of the fibers we can deduce that the director helix forms radially, compatible with a director aligned along the fiber at the boundary to the sheath. The geometry is illustrated in Figure 7.14. Note that this arrangement requires the director to be along the fiber axis also at the center of the fiber. This is the only central director orientation that is compatible with the cylindrical symmetry and allows a director distribution without a singular core (i.e., a disclination in which the core would be isotropic). In order to also fulfill the external boundary conditions, where the liquid crystal meets the polymer sheath, the inner diameter of the sheath

must thus be a multiple of the helix pitch. Because we have a certain variation of fiber diameters we therefore expect a variation in color, as the pitch must adjust to the actual fiber diameter. The situation is similar to that of the classic experiment with a Cano wedge cell, but the cylindrical geometry is twice as restrictive on the helical pitch as the standard flat geometry. While the substrate distance in the Cano cell must be a multiple of half the pitch, the cylindrical fiber diameter must be an integer number times the full pitch, since the central boundary condition must also be fulfilled. This gives a strong quantization of color, to the extent that in a thin fiber it is the fiber inner diameter that effectively determines the color, cf. the diagram in Figure 7.13.

In fibers with an inner diameter of about a micron or thicker the distortion away from the natural pitch will never be sufficient to account for the most extreme color changes, red reflection appearing from a cholesteric that is blue in its natural state. With a natural pitch p_0 of 300 nm (greenish blue natural color, $\lambda_0 = 450$ nm) we see in Figure 7.13 that red selective reflection would arise only if the inner fiber diameter is some 400 nm, allowing exactly one very extended helical pitch to fit in the fiber. This means that the fibers reflecting this color must in fact have an inner diameter of about this value. The majority of fibers are however more yellow-green, requiring an inner diameter that is either even thinner or somewhat thicker, around 650 nm. Having a most common inner diameter lower than some 400 nm in these fibers with micron-size outer diameter seems rather unlikely. It is thus possible to deduce from the colors that the fibers showing selective reflection have inner diameters in the range of 300–650 nm, most of them at the higher value. There were also several fibers in this

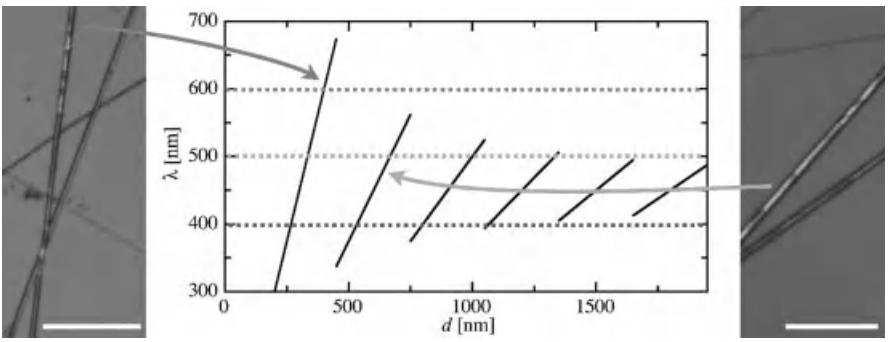

FIGURE 7.13 The confinement of the cholesteric liquid crystal **mixture 1** inside thin cylindrical fibers forces the director helix to expand or compress from its natural pitch, leading to a reflection color λ that depends on the inner fiber diameter d, as illustrated in the center diagram (black curve). The curve is calculated for a natural pitch $p_0 = 300$ nm, average refractive index 1.5, and a director field as in Figure 7.14 (see reference [10] for details). As a guide for the eye the wavelengths of blue, green, and red have been indicated with horizontal lines in the respective color. The red color of the fiber shown in the left example is possible only for a fiber with inner diameter of about 400 nm. The blue-green color shown on the right could occur for even thinner fibers, but more likely is a somewhat greater inner fiber diameter of about 640 nm. The scale bar is 50 μm. (*See the color version of this figure in Color Plates section.*)

study that did not show any visible selective reflection color. It is important to realize that this does not mean that they are unfilled or have the liquid crystal in a non-helical structure. The diagram in Figure 7.13 shows that the reflection wavelength of the cholesteric inside the fiber will lie in the UV range for many fiber diameters, hence no color can be seen from these fibers.

An important observation was that the transition between blue phase and cholesteric phase could no longer be detected for the liquid crystal in the fibers. This held for polarizing microscopy as well as DSC investigations, on heating as well as on cooling, and for all fibers regardless of their diameter. The reason is that the configuration in Figure 7.14 imposed by the cylindrical symmetry of the fiber, with a helical director twist in all directions perpendicular to the fiber axis, is unusual for a cholesteric phase in which the director normally twists only along a single direction. When confined inside the fiber the N^* phase is thus forced to adopt a configuration that is in fact nothing else than the double-twist cylinder configuration that is the basic building block for blue phases (see model at the bottom of Figure 7.14). The same situation, albeit on much larger scale, was achieved by Heinz Kitzerow and co-workers [78] by filling cholesteric liquid crystals into glass capillaries.

Considering the blue phase-like director configuration imposed onto the N^* phase by the cylindrical confinement, and the fact that the structural scale here is the same as that in bulk blue phases, it is easy to understand why the N^*-BP^* transition was not seen for **mixture 1** in the fibers: the cylindrical confinement of the N^* phase with strong surface director anchoring gives the N^* phase a BP^*-type structure, hence the two phases have become degenerate. For very thick fibers it should be possible to have a phase transition again, since multiple double-twist cylinders could then build up a cubic network in the BP^* phase once the cylindrical confinement is less strong.

Fibers, filled with **mixture 1** but with slightly sturdier sheath, achieved either by increasing the polymer concentration or by adding a small amount of the $Ti(OiPr)_4$ sol–gel precursor to the outer spinning solution, were also investigated. Also these fibers exhibited selective reflection but continuous filling was never seen in these

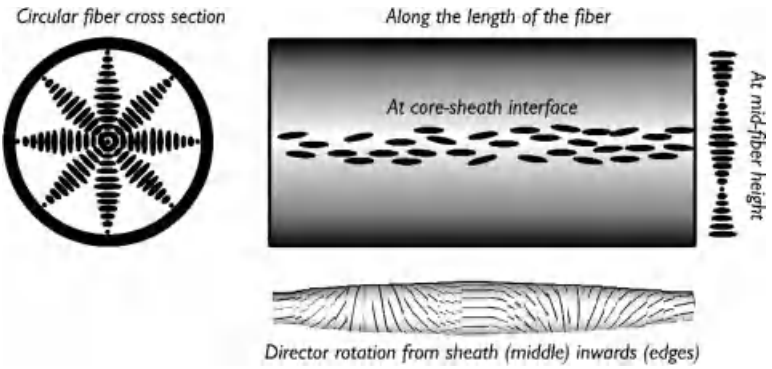

FIGURE 7.14 Schematic illustrations of the director field of a short-pitch cholesteric liquid crystal inside a cylindrical electrospun fiber.

fibers. Instead the cholesteric was separated into small droplets spaced quite regularly along the fiber. The main reason for the different encapsulation of the liquid crystal here, compared to the earlier described fibers, is most likely the mismatch in viscosity of the sheath and core solutions. From experiments in the Xia group with coaxial electrospinning of mineral oil [64] and octadecane [25], respectively, inside a PVP + $Ti(OiPr)_4$ sheath solution it is known that a change in viscosity of one of the fluids can have a dramatic impact on the continuity of the core. With the rather viscous mineral oil (viscosity about 70–80 mPa s) continuous and uniform filling of the fibers could easily be achieved with this sheath solution but in case of the much less viscous octadecane (heated to the liquid state prior to spinning, giving it a viscosity in the range of 2–4 mPa s) varicose break-up occurred inside the coaxial jet, resulting in regularly spaced drops of octadecane in the produced fibers.

7.5 APPLICATION POTENTIAL OF LIQUID CRYSTAL-CONTAINING ELECTROSPUN FIBERS

The addition of the responsiveness and functionality of liquid crystals to the nano-to-microscale fibers produced by electrospinning produces a new material that clearly has strong potential for application. While much work so far has been done with hygroscopic polymers such as PVP, convenient for academic studies but generally problematic in a device context, a switch to textile-grade sheath material will open the door to employing the fibers in non-woven smart textiles. If a convenient way of applying electric fields to the fibers can be found, for instance by using carbon nanotube-containing fibers [79, 80], wearable displays might be realized in this way.

The strongly colored selective reflection from short-pitch cholesterics renders these phases most attractive and the temperature dependence of the pitch makes it straightforward to apply cholesterics as temperature sensors. Since we see the color also in fibers containing the cholesteric, autonomous (not needing any power supply) fiber mat-integrated sensors could easily be produced by electrospinning. One could for instance spin a web of cholesteric-containing fibers over an apparatus of arbitrary shape, giving it a surface that continuously reveals the temperature at every part, with full spatial resolution. Alternatively, pipes or tubes can be coated with the fibers to monitor the temperature of liquids or gases flowing through a complex system in a cheap and efficient way, useful for monitoring the performance of a cooling water system. Finally, with the right type of polymer sheath the cholesteric phase could be incorporated into synthetic textiles that could find use in clothing. Such textiles could obviously provide a temperature read-out, but if the fibers in addition are spun with a porous sheath and if the cholesteric mixture has an adequate composition, the textile could even function as a chemical sensor [81–83], useful for people working in hazardous environments.

Electrospun fibers from liquid crystalline elastomers have obvious application potential in actuators. Judging from the lack of information on the actuation properties of the fibers produced so far [15] there are still problems to be addressed, but the concept is certainly very attractive and should be further explored. Many liquid crystal types have not yet been integrated into electrospun fibers, e.g., ferroelectric and

discotic liquid crystals. They would allow the production of new functional fibers for instance with spontaneous electric polarization or photoconductivity, opening for various new application possibilities, for instance in energy conversion [84–87]. The future looks bright for liquid crystal electrospinning and we can expect to see some very exciting developments in this field in the coming years.

REFERENCES

1. S. Agarwal and A. Greiner. Nanofibers by electrospinning. *Polymers Adv. Tech.* **2011**, *22*, 293–294.
2. X. Lu, C. Wang, and Y. Wei. One-dimensional composite nanomaterials: synthesis by electrospinning and their applications. *Small* **2009**, *5*, 2349–2370.
3. D. Reneker and A. Yarin. Electrospinning jets and polymer nanofibers. *Polymer* **2008**, *49*, 2387–2425.
4. J. Schiffman and C. Schauer. A review: electrospinning of biopolymer nanofibers and their applications. *Polymer Rev.* **2008**, *48*, 317–352.
5. G. Rutledge and S. Fridrikh. Formation of fibers by electrospinning. *Adv. Drug Deliv. Rev.* **2007**, *59*, 1384–1391.
6. A. Greiner and J. Wendorff. Electrospinning: a fascinating method for the preparation of ultrathin fibres. *Angew. Chem. Int. Ed.* **2007**, *46*, 5670–5703.
7. D. Li and Y. Xia. Electrospinning of nanofibers: reinventing the wheel? *Adv. Mater.* **2004**, *16*, 1151–1170.
8. Z. Huang, Y. Zhang, M. Kotaki, and S. Ramakrishna. A review on polymer nanofibers by electrospinning and their applications in nanocomposites. *Composites Sci. Tech.* **2003**, *63*, 2223–2253.
9. E. A. Buyuktanir, W. Frey, M. W. Margaret, and J. L. West. Self-assembled, optically responsive nematic liquid crystal/polymer core–shell fibers: formation and characterization. *Polymer* **2010**, *51*, 4823–4830.
10. E. Enz and J. Lagerwall. Electrospun microfibres with temperature sensitive iridescence from encapsulated cholesteric liquid crystal. *J. Mater. Chem.* **2010**, *20*, 6866–6872.
11. E. Enz, U. Baumeister, and J. Lagerwall. Coaxial electrospinning of liquid crystal-containing poly(vinyl pyrrolidone) microfibers. *Beilstein J. Org. Chem.* **2009**, *5*, doi: 10.3762/bjoc.5.58
12. J. P. F. Lagerwall, J. T. McCann, E. Formo, G. Scalia, and Y. Xia. Coaxial electrospinning of microfibres with liquid crystal in the core. *Chem. Commun.* **2008**, 5420–5422.
13. Y. Wu, Q. An, J. Yin, T. Hua, H. Xie, G. Li, and H. Tang. Liquid crystal fibers produced by using electrospinning technique. *Colloid Polymer Sci*. **2008**, *286*, 897–905.
14. J. Canejo, J. Borges, M. Godinho, P. Brogueira, P. Teixeria, and E. Terentjev. Helical twisting of electrospun liquid crystalline cellulose micro-and nanofibers. *Adv. Mater.* **2008**, *20*, 4821–4825.
15. S. Krause, R. Dersch, J. Wendorff, and H. Finkelmann. Photocrosslinkable liquid crystal main-chain polymers: thin films and electrospinning. *Macromol. Rapid Commun.* **2007**, *28*, 2062–2068.
16. J. F. Cooley. *US Patent* 692,631 (1902).

17. W. J. Morton. *US Patent* 705,691 (1902).
18. A. Formhals.Process and apparatus for preparing artificial threads. *US Patent* 1,975,504 (A) (1934).
19. J. Yu, S. Fridrikh, and G. Rutledge. The role of elasticity in the formation of electrospun fibers. *Polymer* **2006**, *47*, 4789–4797.
20. K. Arayanarakul, N. Choktaweesap, D. Aht-ong, C. Meechaisue, and P. Supaphol. Effects of poly(ethylene glycol), inorganic salt, sodium dodecyl sulfate, and solvent system on electrospinning of poly(ethylene oxide). *Macromol. Mater. Eng.* **2006**, *291*, 581–591.
21. S. Bhattarai, N. Bhattarai, H. Yi, P. Hwang, D. Cha, and H. Kim. Novel biodegradable electrospun membrane: scaffold for tissue engineering. *Biomaterials* **2004**, *25*, 2595–2602.
22. D. Li, Y. Wang, and Y. Xia. Electrospinning of polymeric and ceramic nanofibers as uniaxially aligned arrays. *Nano Lett*. **2003**, *3*, 1167–1171.
23. D. Li, Y. Wang, and Y. Xia. Electrospinning nanofibers as uniaxially aligned arrays and layer-by-layer stacked films. *Adv. Mater.* **2004**, *16*, 361–366.
24. J. McCann, D. Li, and Y. Xia. Electrospinning of nanofibers with core–sheath, hollow, or porous structures. *J. Mater. Chem.* **2005**, *15*, 735–738.
25. J. McCann, M. Marquez, and Y. Xia. Melt coaxial electrospinning: a versatile method for the encapsulation of solid materials and fabrication of phase change nanofibers. *Nano Lett*. **2006**, *6*, 2868–2872.
26. W. Salalha, J. Kuhn, Y. Dror, and E. Zussman. Encapsulation of bacteria and viruses in electrospun nanofibres. *Nanotechnology* **2006**, *17*, 4675–4681.
27. C. Zhang, X. Yuan, L. Wu, Y. Han, and J. Sheng. Study on morphology of electrospun poly (vinyl alcohol) mats. *Eur. Polym. J.* **2005**, *41*, 423–432.
28. Z. Jun, H. Hou, J. Wendorff, and A. Greiner. Poly(vinyl alcohol) nanofibres by electrospinning: influence of molecular weight on fibre shape. *E-polymers* **2005**, 038.
29. N. Li, X. Qin, E. Yang, and S. Wang. Effect on instability section of PVA electrospinning nanofibers by adding LiCl. *Mater. Lett.* **2008**, *62*, 1345–1348.
30. N. Li, X. Qin, L. Lin, and S. Wang. The effects of spinning conditions on the morphology of electrospun jet and nonwoven membrane. *Polymer Eng. Sci.* **2008**, *48*, 2362–2366.
31. D. He, B. Hu, Q. Yao, K. Wang, and S. Yu. Large-scale synthesis of flexible freestanding SERS substrates with high sensitivity: electrospun PVA nanofibers embedded with controlled alignment of silver nanoparticles. *ACS Nano* **2009**, *3*, 3993–4002.
32. H. Sun, H. Zhang, J. Zhang, H. Wei, J. Ju, M. Li, and B. Yang. White-light emission nanofibers obtained from assembling aqueous single-colored CdTe NCs into a PPV precursor and PVA matrix. *J. Mater. Chem.* **2009**, *19*, 6740–6744.
33. B. Sundaray, V. Subramanian, T. Natarajan, R. Xiang, C. Chang, and W. Fann. Electrospinning of continuous aligned polymer fibers. *Appl. Phys. Lett.* **2004**, *84*, 1222–1224.
34. S. Megelski, J. Stephens, D. Chase, and J. Rabolt. Micro- and nanostructured surface morphology on electrospun polymer fibers. *Macromolecules* **2002**, *35*, 8456–8466.
35. R. Sen, B. Zhao, D. Perea, M. Itkis, H. Hu, J. Love, E. Bekyarova, and R. Haddon. Preparation of single-walled carbon nanotube reinforced polystyrene and polyurethane nanofibers and membranes by electrospinning. *Nano Lett*. **2004**, *4*, 459–464.

36. C. Casper, J. Stephens, N. Tassi, D. Chase, and J. Rabolt. Controlling surface morphology of electrospun polystyrene fibers: effect of humidity and molecular weight in the electrospinning process. *Macromolecules* **2004**, *37*, 573–578.
37. S. Wang, Y. Li, J. Bai, Q. Yang, Y. Song, and C. Zhang. Characterization and photoluminescence studies of CdTe nanoparticles before and after transfer from liquid phase to polystyrene. *Bull. Mater. Sci.* **2009**, *32*, 487–491.
38. G. Eda and S. Shivkumar. Bead-to-fiber transition in electrospun polystyrene. *J. Appl. Polymer Sci.* **2007**, *106*, 475–487.
39. G. Eda, J. Liu, and S. Shivkumar. Flight path of electrospun polystyrene solutions: effects of molecular weight and concentration. *Mater. Lett.* **2007**, *61*, 1451–1455.
40. R. Krishnappa, K. Desai, and C. Sung. Morphological study of electrospun polycarbonates as a function of the solvent and processing voltage. *J. Mater. Sci.* **2003**, *38*, 2357–2365.
41. G. Kim, G. Michler, and P. Potschke. Deformation processes of ultrahigh porous multiwalled carbon nanotubes/polycarbonate composite fibers prepared by electrospinning. *Polymer* **2005**, *46*, 7346–7351.
42. S. Moon and R. Farris. The morphology, mechanical properties, and flammability of aligned electrospun polycarbonate (PC) nanofibers. *Polymer Eng. Sci.* **2008**, *48*, 1848–1854.
43. J. McCann, M. Marquez, and Y. Xia. Highly porous fibers by electrospinning into a cryogenic liquid. *J. Am. Chem. Soc.* **2006**, *128*, 1436–1437.
44. J. Liu, Z. Yue, and H. Fong. Continuous nanoscale carbon fibers with superior mechanical strength. *Small* **2009**, *5*, 536–542.
45. E. J. Ra, T. H. Kim, W. J. Yu, K. H. An, and Y. H. Lee. Ultramicropore formation in PAN/camphor-based carbon nanofiber paper. *Chem. Commun.* **2010**, *46*, 1320–1322.
46. C. Lai, Q. Guo, X. Wu, D. Reneker, and H. Hou. Growth of carbon nanostructures on carbonized electrospun nanofibers with palladium nanoparticles. *Nanotechnology* **2008**, *19*, 195303.
47. Q. Zhang, Z. Chang, M. Zhu, X. Mo, and D. Chen. Electrospun carbon nanotube composite nanofibres with uniaxially aligned arrays. *Nanotechnology* **2007**, *18*, 115611.
48. A. Bianco, G. Iardino, A. Manuelli, C. Bertarelli, and G. Zerbi. Strong orientation of polymer chains and small photochromic molecules in polyamide 6 electrospun fibers. *ChemPhysChem* **2007**, *8*, 510–514.
49. C. Mit-uppatham, M. Nithitanakul, and P. Supaphol. Ultrafine electrospun polyamide-6 fibers: effect of solution conditions on morphology and average fiber diameter. *Macromol. Chem. Phys.* **2004**, *205*, 2327–2338.
50. R. Dersch, T. Liu, A. Schaper, A. Greiner, and J. Wendorff. Electrospun nanofibers: internal structure and intrinsic orientation. *J. Polymer Sci. Part A: Polymer Chem.* **2003**, *41*, 545–553.
51. Y. Yao, Z. Gu, J. Zhang, C. Pan, Y. Zhang, and H. Wei. Fiber-oriented liquid crystal polarizers based on anisotropic electrospinning. *Adv. Mater.* **2007**, *19*, 3707.
52. X. Sui and H. Wagner. Tough nanocomposites: the role of carbon nanotube type. *Nano Lett*. **2009**, *9*, 1423–1426.
53. A. Bazilevsky, A. Yarin, and C. Megaridis. Co-electrospinning of core–shell fibers using a single-nozzle technique. *Langmuir* **2007**, *23*, 2311–2314.

54. P. L. Almeida, S. Kundu, J. P. Borges, M. H. Godinho, and J. L. Figueirinhas. Electro-optical light scattering shutter using electrospun cellulose-based nano-and microfibers. *Appl. Phys. Lett.* **2009**, *95*, 043501.
55. M. Acharya, G. Arumugam, and P. Heiden. Dual electric field induced alignment of electrospun nanofibers. *Macromol. Mater. Eng.* **2008**, *293*, 666–674.
56. D. Reneker and I. Chun. Nanometre diameter fibres of polymer, produced by electro-spinning. *Nanotechnology* **1996**, *7*, 216–223.
57. D. Reneker, A. Yarin, H. Fong, and S. Koombhongse. Bending instability of electrically charged liquid jets of polymer solutions in electrospinning. *J. Appl. Phys.* **2000**, *87*, 4531–4547.
58. P. Katta, M. Alessandro, R. Ramsier, and G. Chase. Continuous electrospinning of aligned polymer nanofibers onto a wire drum collector. *Nano Lett*. **2004**, *4*, 2215–2218.
59. L. Carnell, E. Siochi, N. Holloway, R. Stephens, C. Rhim, L. Niklason, and R. Clark. Aligned mats from electrospun single fibers. *Macromolecules* **2008**, *41*, 5345–5349.
60. H. Yan, L. Liu, and Z. Zhang. Alignment of electrospun nanofibers using dielectric materials. *Appl. Phys. Lett.* **2009**, *95*, 143114.
61. C. Hellmann, J. Belardi, R. Dersch, A. Greiner, J. Wendorff, and S. Bahnmueller. High precision deposition electrospinning of nanofibers and nanofiber nonwovens. *Polymer* **2009**, *50*, 1197–1205.
62. C. Chang, K. Limkrailassiri, and L. Lin. Continuous near-field electrospinning for large area deposition of orderly nanofiber patterns. *Appl. Phys. Lett.* **2008**, *93*, 123111.
63. D. Sun, C. Chang, S. Li, and L. Lin. Near-field electrospinning. *Nano Lett*. **2006**, *6*, 839–842.
64. D. Li and Y. Xia. Direct fabrication of composite and ceramic hollow nanofibers by electrospinning. *Nano Lett*. **2004**, *4*, 933–938.
65. Z. Sun, E. Zussman, A. Yarin, J. Wendorff, and A. Greiner. Compound core–shell polymer nanofibers by co-electrospinning. *Adv. Mater.* **2003**, *15*, 1929.
66. K. Nakashima, K. Tsuboi, H. Matsumoto, R. Ishige, M. Tokita, J. Watanabe, and A. Tanioka. Control over internal structure of liquid crystal polymer nanofibers by electrospinning. *Macromol. Rapid Commun.* **2010**, *31*, 1641–1645.
67. N. Ogata, N. Shimada, S. Yamaguchi, K. Nakane, and T. Ogihara. Meltelectrospinning of poly(ethylene terephthalate) and polyalirate. *J. Appl. Polymer Sci.* **2007**, *105*, 1127–1132.
68. W. Pisula, M. Zorn, J. Y. Chang, K. Muellen, and R. Zentel. Liquid crystalline ordering and charge transport in semiconducting materials. *Macromol. Rapid Commun.* **2009**, *30*, 1179–1202.
69. Y. Wu, Q. An, J. Yin, T. Hua, H. Xie, G. Li, and H. Tang. Liquid crystal fibers produced by using electrospinning technique. *Colloid Polymer Sci*. **2008**, *286*, 897–905.
70. P. Rudquist, J. P. F. Lagerwall, M. Buivydas, F. Gouda, S. T. Lagerwall, N. A. Clark, J. E. Maclennan, R. F. Shao, D. Coleman, S. Bardon, T. Bellini, D. R. Link, G. Natale, M. A. Glaser, D. M. Walba, M. D. Wand, and X. H. Chen. The case of threshold-less antiferroelectricity: polarization-stabilized twisted SmC* liquid crystals give V-shaped electro-optic response. *J. Mater. Chem.* **1999**, *9*, 1257–1261.
71. G. Iannacchione, G. Crawford, S. Qian, J. Doane, and D. Finotello. Nematic ordering in highly restrictive Vycor glass. *Phys. Rev. E* **1996**, *53*, 2402–2411.

72. J. P. F. Lagerwall, D. D. Parghi, D. Kruerke, F. Gouda, and P. Jagemalm. Phases, phase transitions and confinement effects in a series of antiferroelectric liquid crystals. *Liq. Cryst.* **2002**, *29*, 163–178.
73. R. Leheny, S. Park, R. Birgeneau, J. Gallani, C. Garland, and G. Iannacchione. Smectic ordering in liquid-crystal–aerosil dispersions. I. X-ray scattering. *Phys. Rev. E* **2003**, *67*, 011708.
74. T. Jin, B. Zalar, A. Lebar, M. Vilfan, S. Zumer, and D. Finotello. Anchoring and structural transitions as a function of molecular length in confined liquid crystals. *Eur. Phys. J. E* **2005**, *16*, 159–165.
75. M. Steinhart, S. Zimmermann, P. Goring, A. Schaper, U. Gosele, C. Weder, and J. Wendorff. Liquid crystalline nanowires in porous alumina: geometric confinement versus influence of pore walls. *Nano Lett*. **2005**, *5*, 429–434.
76. G. Carbone, R. Barberi, I. Musevic, and U. Krzic. Atomic force microscope study of presmectic modulation in the nematic and isotropic phases of the liquid crystal octylcyanobiphenyl using piezoresistive force detection. *Phys. Rev. E* **2005**, *71*, 051704.
77. K. Kocevar and I. Musevic. AFM study of forces in and structures of nematic liquid crystal interfaces on silanated glass. *Liq. Cryst.* **2001**, *28*, 599–606.
78. H. Kitzerow, B. Liu, F. Xu, and P. Crooker. Effect of chirality on liquid crystals in capillary tubes with parallel and perpendicular anchoring. *Phys. Rev. E* **1996**, *54*, 568–575.
79. L. Hu, M. Pasta, F. Mantia, L. Cui, S. Jeong, H. Deshazer, J. Choi, S. Han, and Y. Cui. Stretchable, porous, and conductive energy textiles. *Nano Lett*. **2010**, *10*, 708–714.
80. B. Shim, W. Chen, C. Doty, C. Xu, and N. Kotov. Smart electronic yarns and wearable fabrics for human biomonitoring made by carbon nanotube coating with polyelectrolytes. *Nano Lett*. **2008**, *8*, 4151–4157.
81. Y. Han, K. Pacheco, C. W. M. Bastiaansen, D. J. Broer, and R. P. Sijbesma. Optical monitoring of gases with cholesteric liquid crystals. *J. Am. Chem. Soc.* **2010**, *132*, 2961–2967.
82. D. Winterbottom, R. Narayanaswamy, and I. Raimundo. Cholesteric liquid crystals for detection of organic vapours. *Sen. Actuators B* **2003**, *90*, 52–57.
83. F. Dickert, A. Haunschild, and P. Hofmann. Cholesteric liquid-crystals for solvent vapor detection-elimination of cross-sensitivity by band shape-analysis and pattern-recognition. *Fresen. J. Anal. Chem.* **1994**, *350*, 577–581.
84. A. Jakli. Electro-mechanical effects in liquid crystals. *Liq. Cryst.* **2010**, *37*, 825–837.
85. J. Harden, M. Chambers, R. Verduzco, P. Luchette, J. T. Gleeson, S. Sprunt, and A. Jakli. Giant flexoelectricity in bent-core nematic liquid crystal elastomers. *Appl. Phys. Lett.* **2010**, *96*, 102907.
86. M. Chambers, R. Verduzco, J. T. Gleeson, S. Sprunt, and A. Jakli. Flexoelectricity of a calamitic liquid crystal elastomer swollen with a bent-core liquid crystal. *J. Mater. Chem.* **2009**, *19*, 7909–7913.
87. M. Chambers, R. Verduzco, J. T. Gleeson, S. Sprunt, and A. Jakli. Calamitic liquid-crystalline elastomers swollen in bent-core liquid-crystal solvents. *Adv. Mater.* **2009**, *21*, 1622.

CHAPTER 8

Functional Liquid Crystalline Block Copolymers: Order Meets Self-Assembled Nanostructures

XIA TONG and YUE ZHAO

Department of Chemistry, University of Sherbrooke, Québec, Canada

8.1 WHAT ARE FUNCTIONAL LIQUID CRYSTALLINE BLOCK COPOLYMERS?

Liquid crystalline block copolymers (LC-BCPs) are block copolymers of which one or more constituting polymers have mesogens either as side groups or in the main chain. The great interest of LC-BCPs has long been recognized. The most important feature is the interplay between two levels of order and self-assembly: the LC order formed by mesogens and the ordered nanostructures arising from the microphase separation of the blocks. There have been many studies on the mutual influence of the two levels of order in LC-BCPs [1–10]. A representative example was reported by Finkelmann and co-workers in 2000 [8]. It was found that when the microphase-separation occurred in the isotropic phase of a LC-BCP, the gyroid morphology was formed, while when the microphase separation was allowed to develop in a smectic phase, observed was a lamellar morphology. It is easy to picture that a layered smectic order of mesogens accommodates well a lamellar structure and thus can promote its formation.

In a broad sense, all LC-BCPs are functional and entitled with a combination of the characteristic properties of liquid crystalline polymers (LCPs) and BCPs: they can form LC phases and give rise to a variety of self-assembled nanostructures. However, what we mean by functional LC-BCPs in this chapter is different. A number of studies on LC-BCPs in recent years have explored the interplay of LC order and self-assembled nanostructures with the purpose to generate a specific new function. In other words, by rational LC-BCP design, an "active" interaction between two levels of order can be used to achieve something that otherwise is unachievable, rather than an effect of a "passive" interaction, which often is the consequence of the coexisting LC order and nanostructures. We focus our review and discussion only on

Liquid Crystals Beyond Displays: Chemistry, Physics, and Applications, Edited by Quan Li.
© 2012 John Wiley & Sons, Inc. Published 2012 by John Wiley & Sons, Inc.

representative studies that demonstrated a specific function as a result of the interaction between LC order and a self-assembled nanostructure.

8.2 MACROSCOPIC ORIENTATION OF NANODOMAINS

The most striking demonstration of new functions of LC-BCPs is the possibility of using the orientation of mesogens (LC order) on one block to align the nanodomains (nanocylinders or stripe-like domains) of another block at a macroscopic scale [11, 12]. In a study by Yu et al. [13], a thin film (~200 nm thick) of a diblock copolymer composed of poly(ethylene oxide) (PEO) and a polymethacrylate bearing azobenzene mesogenic side groups was spin-coated onto a glass slide coated with a rubbed polyimide layer; on slow cooling from the isotropic state into the smectic phases, surface-induced orientation of mesogens could bring microphase separated PEO cylindrical nanodomains (nanocylinders) to align in the same direction as mesogens. At room temperature, uniformly oriented crystalline PEO nanocylinders were found in an area of 12.4×3.1 μm by AFM imaging. An example of the reported results is shown in Figure 8.1, together with the chemical structure and phase transition temperatures of the used LC-BCP. This study shows clearly that the surface-induced orientation of the mesogens (a typical LC orientation method) builds an anisotropic matrix that imposes the orientation of PEO nanodomains. By this mechanism, the orientation of nanodomains can extend to the whole area of rubbed surface. This approach provides a valuable new means to control the order and organization of self-assembled nanostructures in BCPs, which often is a key requirement for enabling their applications [14, 15].

With azobenzene as the mesogens, the long-range LC orientation can be induced optically as a result of the trans–cis photoisomerization of the chromophore [16]. Yu et al. then used a similar LC-BCP and demonstrated that a macroscopic orientation of PEO nanodomains could also be obtained using the photo-induced LC orientation [17]. In this case, a film of about 100-nm thick, cast onto a non-rubbed glass slide, was exposed to linearly polarized visible light (488 nm, 100 mW/cm^2) at room temperature and then annealed at 140°C, yielding uniform, in-plane orientation of PEO nanocylinders in the same direction as azobenzene mesogens, that is, perpendicular to the polarization of the visible light, as shown in Figure 8.2. Using photo-induced LC orientation to align PEO nanodomains, the thermal annealing, which is required to enhance the LC orientation, should be carried out at a temperature where PEO is in the melted, fluid state in order to facilitate the orientation of the nanodomains under the effect of the LC matrix. In principle, the macroscopic orientation of PEO nanocylinders could be obtained in a large area whose size is basically determined by the light exposure process and conditions.

The use of light to direct the orientation of mesogens and thus the orientation of the nanodomains in LC-BCPs is not just about an orientation technique differing from surface rubbing, it offers appealing advantages associated with light. The most interesting may be the easy spatial control because the area of a thin film exposed to light can be chosen by using either a photomask or an interference pattern. Seki et al.

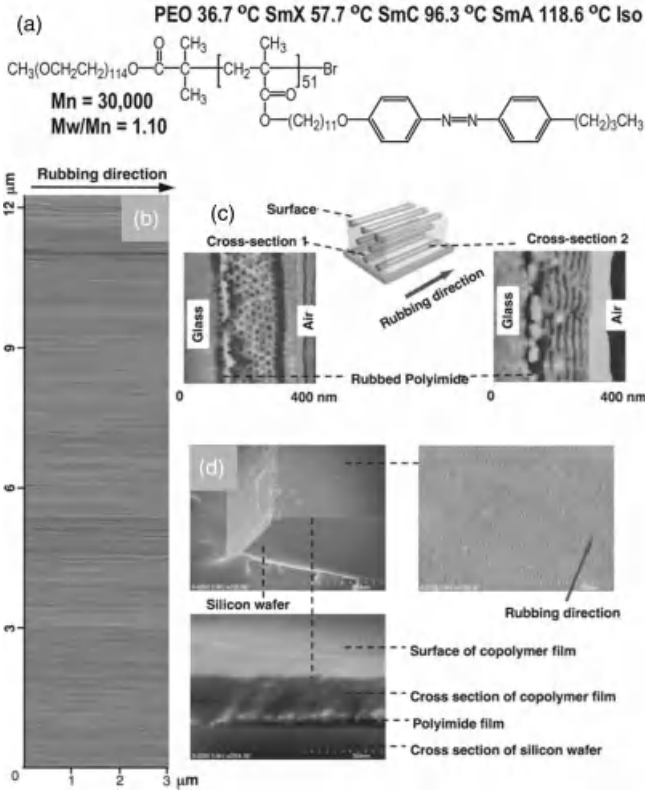

FIGURE 8.1 (a) Chemical structure and phase transition temperatures of the LC diblock copolymer. (b) Macroscopic orientation of PEO nanocylinders along the rubbing direction in an area of 12.4 × 3.1 μm. (c) AFM phase images. (d) SEM images of the cross sections of the film (the bright lines and dots in the SEM images are PEO blocks selectively stained by RuO_4). *Source*: Yu et al. (2006). Reprinted with permission. (*See the color version of this figure in Color Plates section.*)

exploited this possibility [18, 19]. Using a diblock copolymer composed of polystyrene (PS) and an azobenzene LCP, they exposed a thin film (thickness ~100 nm) containing vertically aligned PS nanocylinders to linearly polarized light through a photomask (10-μm period), and found alternating regions with PS nanocylinders oriented in-plane (in exposed regions) and perpendicularly to the substrate surface (in non-exposed regions) could be patterned, with a sharp transition of the orientational state at the interface [18]. An example of the results is shown in Figure 8.3. In principle, the photo-induced LC orientation could be explored to pattern or organize the orientation of nanodomains in LC-BCPs in a three-dimensional (3D) fashion.

Recently, our group extended the approach to π-conjugated polymers by demonstrating the use of LC orientation to obtain macroscopically aligned nanodomains of poly(3-hexylthiophene) (P3HT), which is one of the most studied conducting

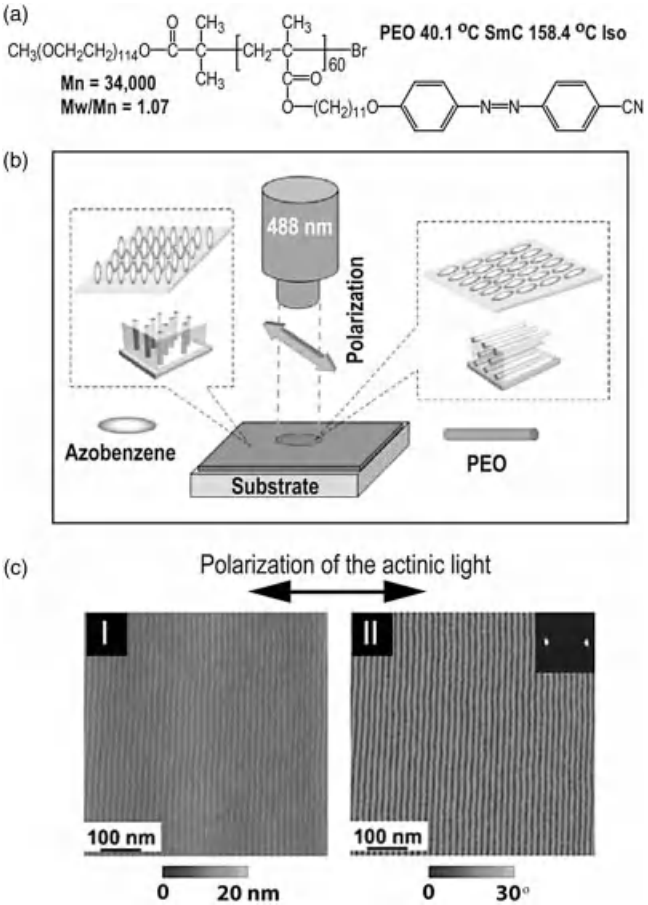

FIGURE 8.2 (a) Chemical structure and phase transition temperatures of the used LC diblock copolymer. (b) Schematic illustration of the orientation of azobenzene mesogens and the resulting alignment of microphase-separated nanocylinders in the irradiated and non-irradiated area of the block copolymer films. (c) AFM images of a film in an irradiated area: topological (I) and phase image (II). *Source*: Yu et al. (2006). Reprinted with permission.

polymers. There is growing interest in BCPs comprising one or more conducting polymers, because the microphase separation in BCPs provides a simple and effective way to generate a microstructure or morphology useful for their electronic and optoelectronic applications [20–22]. Macroscopically aligning self-assembled nanodomains of regioregular P3HT is challenging because it has a very high melting temperature T_m (>200°C), which means that its crystallization is the dominant event and competes with the self-assembly or an organization process [21]. We rationally designed and synthesized a diblock copolymer composed of P3HT and an azobenzene LCP of that the clearing (LC-to-isotropic transition) temperature is greater than the T_m of P3HT [23]. Under this condition, it is possible to anneal a thin film of

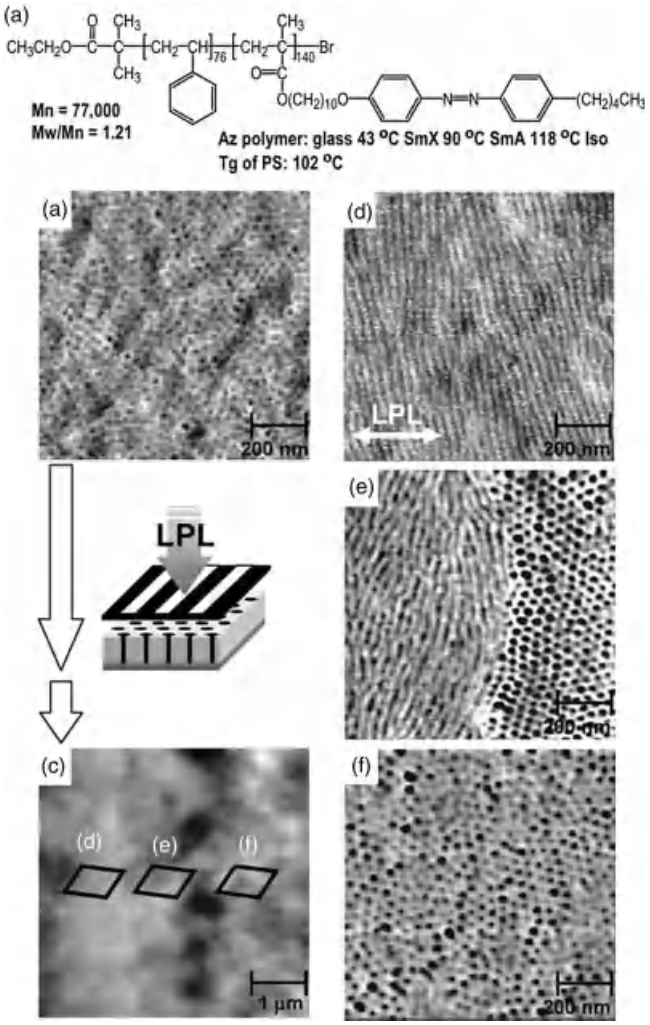

FIGURE 8.3 (a) Chemical structure and phase transition temperatures of the used LC diblock copolymer. (b) AFM phase image of the initial film showing that polystyrene nanocylinders are aligned perpendicularly to the substrate surface. (c) AFM topographical image after patterned irradiation with linearly polarized light. (d–f) AFM phase images recorded at irradiated area (d), boundary region (e) and non-irradiated area (f). *Source*: Morikawa et al. (2007). Reprinted with permission.

the LC-BCP in a LC phase to obtain surface-induced orientation of mesogens, while retaining P3HT in its melted state to allow the orientation of fluid P3HT nanodomains inside the oriented LC matrix. The results in Figure 8.4 shows that both surface and photo-induced orientation of azobenzene mesogens in the major phase of the LC-BCP could be used to impose a macroscopic orientation of stripe-like nanodomains of P3HT in the same direction as the mesogens. In the case of using

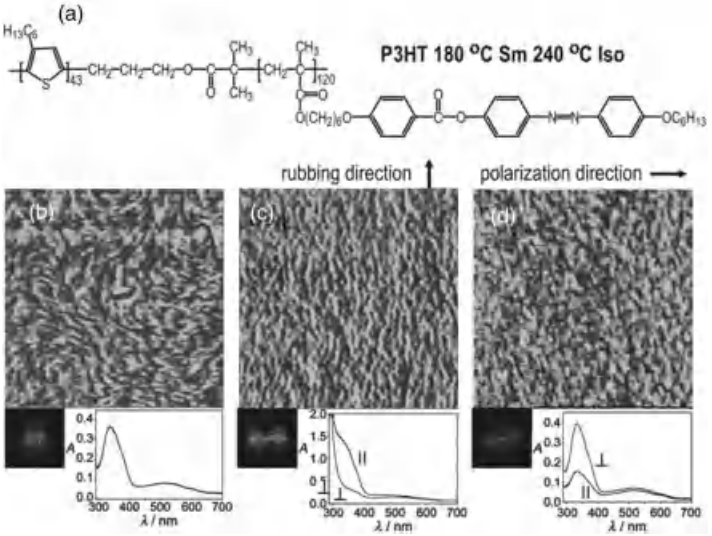

FIGURE 8.4 (a) Chemical structure and phase transition temperatures of the LC diblock copolymer. (b–d) AFM phase images (1×1 μm), fast Fourier transformations and polarized absorption spectra for thin films cast on a nonrubbed quartz plate (b), a rubbed glass plate for surface-induced orientation of the mesogens (c), and a nonrubbed quartz plate subjected to irradiation for photoinduced orientation of the mesogens (d). Absorption spectra were recorded with the beam of the spectrophotometer polarized to be parallel and perpendicular, respectively, to either the surface rubbing direction (c) or the polarization of the irradiating light (d). The surface- or photo-induced orientation of azobenzene mesogens can be noticed from the dichroism of the absorption band of trans azobenzene around 360 nm, while the absorption band near 540 nm is from crystallized P3HT chains. *Source*: Han et al. (2010). Reprinted with permission. (*See the color version of this figure in Color Plates section.*)

surface-induced LC orientation, a thin film (∼30 nm thick) cast on a glass slide with rubbed surface was first cooled from 260°C (isotropic state for both blocks) to 220°C (LC phase for the LCP block but isotropic phase for P3HT) for the orientation of both azobenzene mesogens and microphase separated P3HT strip-like domains, and then cooled to room temperature for the crystallization of P3HT. For photo-induced LC orientation, it was conducted at 45°C, and, prior to the analysis at room temperature, the film was annealed at 120°C. In view of the great ease of LC orientation and the variety of LC orientation methods, this study demonstrated a promising means for achieving and manipulating macroscopically ordered microstructure or morphology of π-conjugated polymer-based BCPs. As a future development, it would be interesting, and challenging, to know how to use this approach to induce macroscopic orientation of the nanodomains of both a donor and an acceptor polymer, which is required for photovoltaic applications. One possible strategy is to develop donor–acceptor diblock copolymers of which the two blocks are LCP.

8.3 SHAPE-MEMORY MATERIALS AND ELASTOMERS

LC thermoplastic elastomer represents another case where the interplay of LC order and a self-assembled BCP nanostructure can generate new functions. A thermoplastic elastomer can be obtained with an ABA-type triblock copolymer if the central B block is rubbery with a low T_g while the end A blocks are crystalline (or amorphous) with a high T_m (or T_g). The microphase separation could result in a network structure with the rubbery B blocks interconnected by rigid nanodomains of the A blocks; upon elongation, the extension (orientation) of B chains can be supported by the nanodomains of A acting as physical cross-links. The importance of this nanostructure has long been known and led to the development of commercialized thermoplastic elastomers like SBS (styrene-*b*-butadiene-*b*-styrene) or SIS (styrene-*b*-isoprene-*b*-styrene). Now, if one of the constituting polymers is LCP, the elastic deformation makes it easy to induce orientation of mesogens, and this could give rise to fascinating materials.

Such an example can be found in a study by Terentjev et al. [24]. They prepared a triblock copolymer whose middle block is a main-chain nematic LCP with a T_g at $\sim$40°C and whose end blocks are a short segment containing a semi-crystalline terphenyl moiety. With this LC-BCP, fiber could readily be drawn from the isotropic state; while upon subsequent cooling into the nematic phase, a uniform orientation of mesogens (monodomain) and the microphase separation was found to take place simultaneously, resulting in a network structure in which aggregated terphenyl moieties could act as multifunctional junction points and retain the orientation of mesogens. With mesogens incorporated into the main chain, the conformation of the chain backbone is strongly coupled with the ordering state of the mesogens. The resulting fiber exhibits a striking shape-memory effect. As shown in Figure 8.5, when the fiber is heated to above the clearing (nematic–isotropic) temperature, the order–disorder phase transition of the mesogens induces a conformational transition of chain backbone from an extended to a random coil state, the macroscopic manifestation of which is a nearly 500 percent contraction of the fiber. On cooling, the formation of the nematic phase restores the uniform orientation of mesogens and the fiber recovers its initial length. Since the reversible LC phase transition is responsible for the shape change, the large contraction and elongation of the fiber upon heating and cooling are reversible. This feature is unique to LC-BCPs, which contracts with conventional shape-memory polymers for which the temporary to permanent shape recovery occurs only once without reset of the temporary shape [25, 26].

Li et al. exploited this reversible shape-memory effect in a different way by targeting the fabrication of an artificial muscle [27]. Instead of using a main-chain nematic polymer, they used a side-on LCP that also exhibits a strong coupling between the LC order and the chain backbone [28]. The advantage of this design resides in the fact that controlled radical polymerization techniques such as atom transfer radical polymerization (ATRP) could be utilized for the synthesis of the LC-BCP with a low polydispersity. Their triblock copolymer consisted in a side-on LCP middle block and two rubbery end blocks (a random copolymer of n-butyl acrylate and an acrylate comonomer bearing a photo-polymerizable unit); by having an

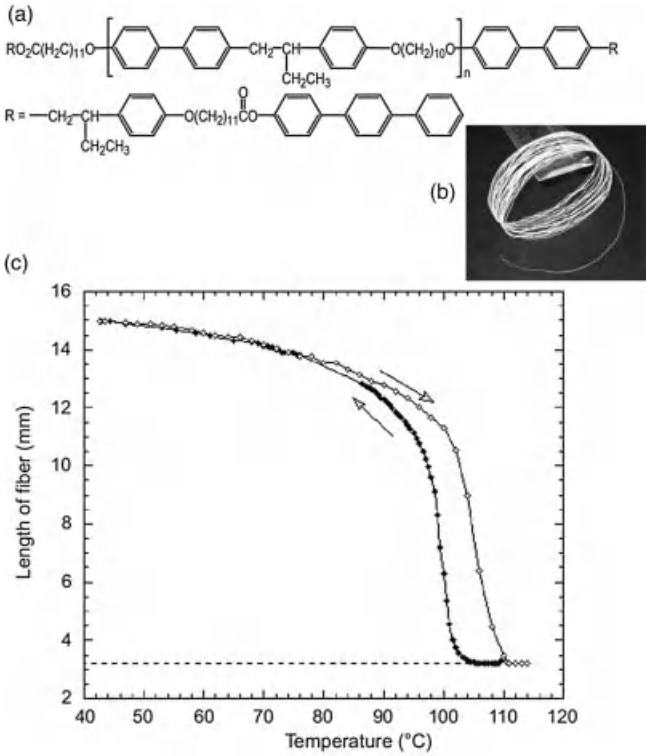

FIGURE 8.5 (a) Chemical structure of the used LC (telechelic) triblock copolymer. (b) Picture showing a roll of drawn fiber of the polymer. (c) Change in the length of a freely suspended fiber during a heating and cooling cycle, showing the reversible shape-memory effect. *Source*: Ahir et al. (2006). Reprinted with permission.

appropriate weight ratio of nematic to rubbery blocks (3:2), a lamellar structure was obtained with alternating LCP and rubbery nanodomains. LC elastomers with such a striated structure were proposed by De Gennes to behave like artificial muscle [29]. Li et al. used a magnetic field to induce a uniform orientation of mesogens in the LCP nanodomains while cross-lining the rubbery blocks, and observed a reversible contraction and elongation of a thick film (0.16 mm thickness) upon thermal LC-isotropic phase transition, as shown in Figure 8.6.

In addition to the use of LC triblock copolymers as shape-memory materials, they can also be designed to accomplish other functions. Kornfield et al. designed a triblock copolymer with polystyrene end blocks and a very long LC middle block [30]. When added in a small-molecule nematic LC, the BCP self-assemble into a network structure with the LCP block dissolved by the nematic solvent and PS chains microphase separated into micellar nanodomains acting as cross-linking points. Such LC gels were shown to display excellent electro-optical properties. In a study carried out by our group, a LCP with azobenzene mesogens was grafted

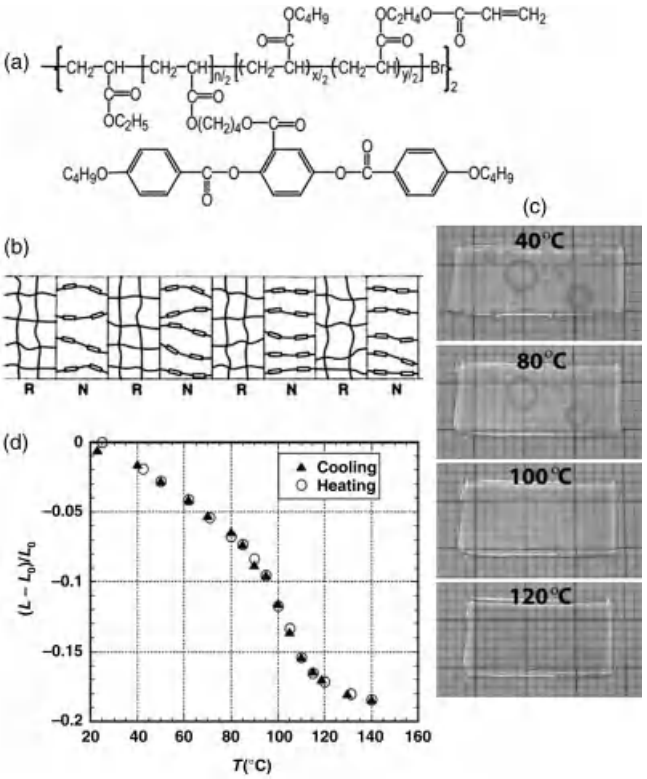

FIGURE 8.6 (a) Chemical structure of the used LC triblock copolymer. (b) A model of striated artificial muscles based on a microphase separated lamellar structure (N and R denote nematic polymer and cross-linked elastomer nanodomains, respectively). (c) Pictures of a sample taken at different temperatures showing a contraction upon the nematic-isotropic phase transition (near 110°C). (d) Fractional change in the length of the film during a heating and cooling cycle (L_0 and L are the initial and the changing lengths of the film, respectively). *Source*: Li et al. (2004). Reprinted with permission.

onto the rubbery polybutadiene block of SBS [31, 32]. The resulting thermoplastic elastomer, whose films can easily be prepared by solution-casting, could be used to record mechanically tunable diffraction gratings. Typically, when a film under strain with a uniform orientation of mesogens, is exposed to UV light through a grating photomask, a diffraction grating is formed as a result of the erasure of LC orientation in exposed areas. We showed that the period, diffraction efficiency and diffraction mode (between Raman-Nath and Bragg regimes) of such an elastic grating could be reversibly tuned upon elastic elongation or contraction of the film.

In all the above examples, a LCP is the active middle block, while it can also be used as the end blocks. We designed and synthesized a thermoplastic elastomer comprising poly(*n*-butyl acrylate) (PnBA) as the rubbery middle block and a LCP bearing azobenzene mesogens as the end blocks [33]. In this case, as the physical

cross-links were made with a LCP, new features emerged. When a film of this LC-BCP is stretched at $T < T_g$ of the LCP end blocks, the polymer acts as a conventional thermoplastic elastomer, with the elastic extension of PnBA chains supported by glassy cylindrical nanodomains of the LCP in which there is no long-range molecular orientation of mesogens. Interestingly, this elastomer can exhibit an intermediate elastic regime. As schematically illustrated in Figure 8.7, when a film is stretched with the LCP in its nematic phase, that is, above T_g but below the nematic–isotropic phase transition, the degree of elastic deformation of PnBA chains is reduced due to a deformation of the LCP nanodomains that induces a long-range orientation of mesogens. This LC orientation can be retained in the relaxed film at room temperature, giving rise to a thermoplastic elastomer containing glassy microdomains with oriented azobenzene mesogens. Subsequent deformation from this thermoplastic elastomer with anisotropic physical cross-links is reversible.

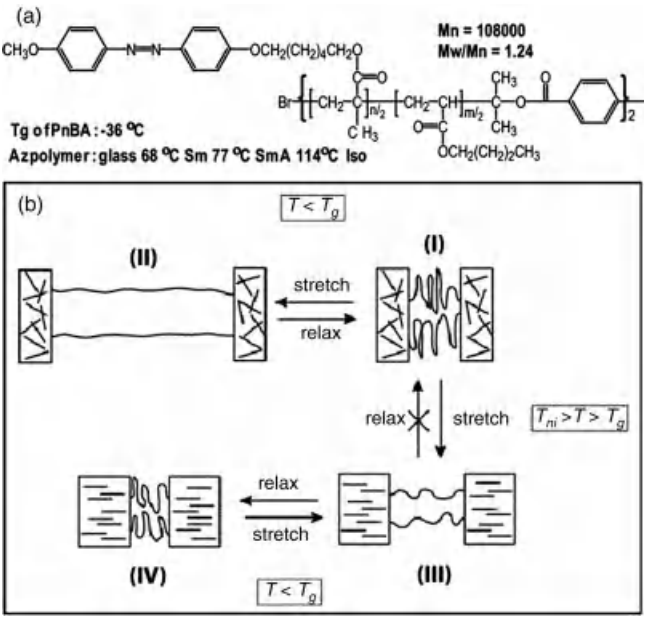

FIGURE 8.7 (a) Chemical structure and phase transition temperatures of the LC triblock copolymer. (b) Schematic illustration of the elasticity and orientation states in the thermoplastic elastomer: (I) initial film before stretching, showing no long-range orientation of mesogens in the microphase separated azo polymer nanodomains; (II) stretching at $T < T_g$ of the azo polymer (glassy microdomains), showing the conventional elasticity; (III) stretching at $T_{ni} > T > T_g$ of the azo polymer (LC microdomains), showing an intermediate elastomer state with deformed azo polymer nanodomains and induced LC orientation; (IV) relaxation at $T < T_g$ (glassy microdomains with oriented mesogens). The elastic recovery of the film is indicated by arrows. *Source*: Cui et al. (2004). Reprinted with permission.

8.4 STIMULI-RESPONSIVE VESICLES IN SOLUTION

LC order can also meet with self-assembled nanostructures in a solution. In principle, any LC-BCPs dissolved in a block-selective solvent could self-assemble into micelles or vesicles. Of particular interest are amphiphilic LC-BCPs built with a hydrophobic LCP and a hydrophilic polymer. They tend to form large vesicles with the LCP constituting the membrane (wall of the capsule) [34, 35]. This observation itself reflects the influence of the LC order on the self-assembled nanostructure as smaller curvature in a large membrane is more amenable to long-range order of mesogens than a spherical core of a core–shell micelle. BCP vesicles have attracted much attention over the last two decades or so as they could potentially be used as nanovectors for controlled drug delivery applications [36, 37]. Typically, a water-soluble agent can be loaded inside a BCP vesicle in aqueous solution, with the hydrophobic membrane providing a good protection. At the time of release (after the vesicle reaches a target site, for example), the vesicle membrane needs to be disrupted to allow the loaded agent to come out. For this reason, research on stimuli-responsive BCP vesicles has been increasingly active [38–40]. Basically, such a BCP vesicle can be designed to have its membrane to undergo a chemical reaction such as hydrolysis, or to respond to a signal such as a change in temperature or pH of the surrounding solution, or exposure to a magnetic field or light. It is clear that with a LC-BCP, if the membrane is formed by a LCP, the LC order and the mesophase transition can be exploited to make the resulting vesicle react to an external stimulus in a particular way. For this, rational LC-BCP design is the key.

Nassoy and coworkers made an elegant demonstration [41]. They designed and prepared giant asymmetric BCP vesicles (16 μm in diameter) of which the two leaflets are composed of two diblock copolymers that have the same hydrophilic poly (ethylene glycol) (PEG) but different hydrophobic polymer blocks. As depicted in Figure 8.8, the inner leaflet has polybutadiene that is not responsive to stimuli, while the outer leaflet has a side-on LCP with azobenzene mesogens in the membrane. Upon exposure to UV light inducing the trans–cis isomerization, a LC–isotropic phase transition occurs in the outer leaflet and the associated polymer chain conformational transition, from an extended to a coiled state, results in a contraction of the outer monolayer along the membrane thickness direction (similar to what happens in the shape-memory polymer as discussed above); the excess surface induces a curling instability that leads to the bursting of the vesicle membrane. The authors showed convincing experimental and theoretical results that support the proposed mechanism, for which a photo-induced LC–isotropic phase transition is at the origin.

Recently, by designing a new LC-BCP, our group investigated a different approach that makes use of a photo-plasticization effect to soften the vesicle membrane by light instead of bursting it [42]. As shown in Figure 8.9, the idea is to use an amphiphilic LC-BCP whose vesicle membrane-forming LCP bears randomly distributed biphenyl (in majority) and azobenzene mesogens (in minority); and upon absorption of UV light, the trans–cis isomerization of azobenzene could induce a LC–isotropic phase transition exerting a plasticization effect on the membrane. Using a diblock

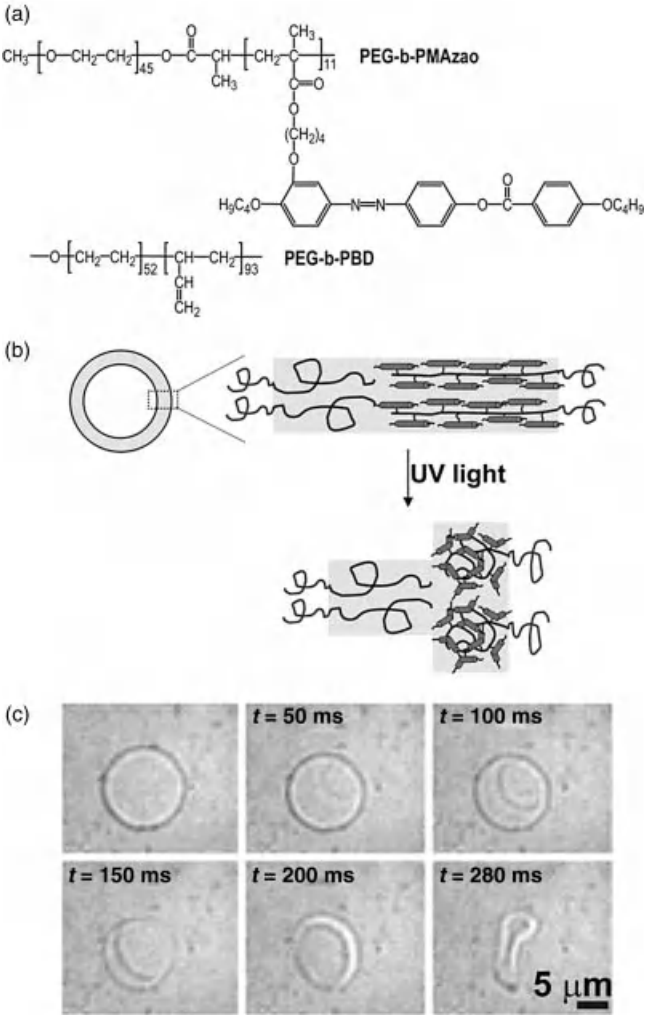

FIGURE 8.8 (a) Chemical structures of the two used amphiphilic diblock copolymers. (b) Schematic illustration of a giant asymmetric vesicle formed by the two polymers and the conformational changes within the bilayer membrane upon the trans–cis photoisomerization of azobenzene mesogens. (c) Snapshots showing the bursting of a giant vesicle upon UV light exposure (the first image shows the vesicle before illumination). *Source*: Mabrouk et al. (2009). Reprinted with permission.

copolymer comprising water-soluble poly(*N,N*-dimethylacrylamide) (PDMA) and a LC random copolymer containing a small amount of azobenzene mesogens (~12 mol% with respect to biphenyl mesogens), photo-optical measurements on a vesicle solution found evidence that a photo-induced LC order–disorder transition within the vesicle membrane occurred in aqueous solution. Moreover, using a pH-sensitive fluorescent probe, namely, 8-hydroxypyrene-1,3,6-trisulfonic acid

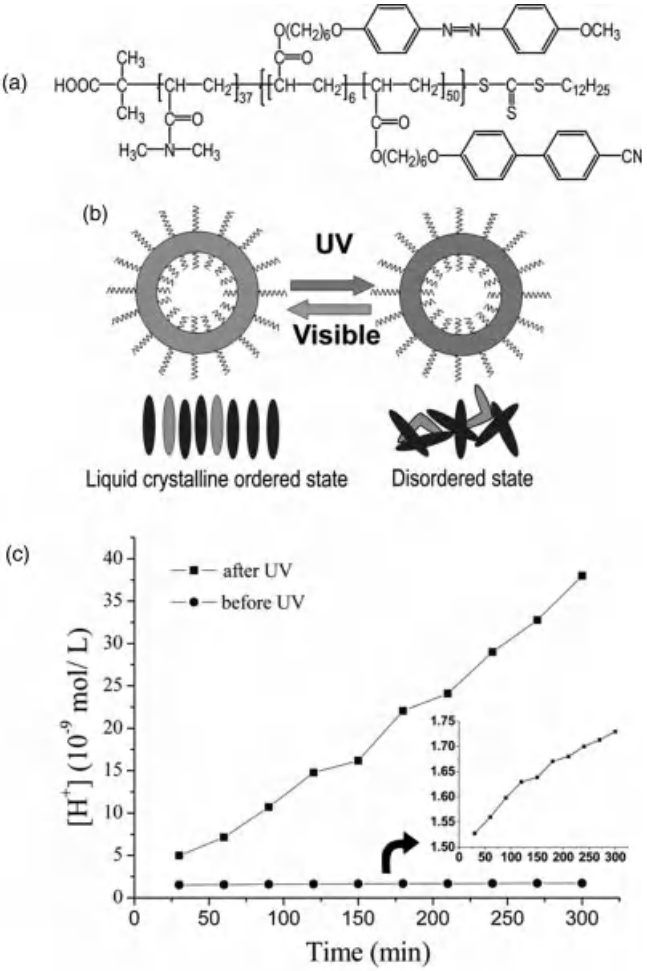

FIGURE 8.9 (a) Chemical structures of the amphiphilic LC diblock copolymer. (b) Schematic illustration of a vesicle whose LC membrane can undergo an order–disorder transition induced by the trans–cis photoisomerization of a small number of azobenzene mesogens as a result of the LC co-operative effect. (c) Plot of proton concentration $[H^+]$ vs. time for a vesicle solution with a pH gradient at room temperature; the inset is the rescaled result obtained with the solution without UV irradiation [the proton concentration is calculated from the excitation spectra of a pH-sensitive fluorescent probe, namely, 8-hydroxypyrene-1,3,6-trisulfonic acid trisodium salt (HPTS)]. *Source*: Yan et al. (2011). Reprinted with permission.

trisodium salt (HPTS), we found that softening of the vesicle membrane resulting from the photoisomerization led to an increase in the rate of proton diffusion from the interior to outside of the vesicle through the LCP membrane that is similar to plasticization of the vesicle membrane by adding a good solvent in aqueous solution [43].

8.5 OUTLOOK

This chapter highlights the representative examples of the research works in recent years that exploited the interplay of LC order and self-assembled nanostructures in LC-BCPs in such a way that a new function has been generated. Some common features are emerged from these studies. As LCPs, what can be exploited is mainly the great ease of long-range molecular orientation of mesogens. This has been used as an ordering template to induce a macroscopic orientation of cylindrical or strip-like nanodomains in BCPs, and for obtaining a uniform orientation in shape-memory polymers. The transition from an ordered to a disordered state (LC–isotropic phase transformation) is another feature that has been exploited for inducing a reversible polymer chain conformational switch required in shape-memory or actuator materials, and for disrupting the membrane of BCP vesicles. As for nanostructures in BCPs, they are mainly nanocylinders (for macroscopic orientation) and self-assembled network structures with micellar or lamellar nanodomains acting as physical cross-links (for shape-memory, actuator, and thermoplastic elastomers) in the solid state, and are vesicles in solution. In all cases, rational LC-BCP design played a key role in enabling the interaction of LC order and a given nanostructure to result in a target new function. Having identified these common features, it is safe to say that there is still much room for creative LC-BCP design for improving the demonstrated functions or for generating new properties.

LC order can be controlled or configured by an electric or magnetic field. It is conceivable that these external fields could also be exploited for organizing and manipulating the microphase separated structures in LC-BCPs through the stimuli-responsive orientation of mesogens. For instance, the lamellar structure in some BCPs have been investigated as photonic crystals [14] for selective reflection of light. If one domain contains mesogens, a change in their orientation induced by an electric or magnetic field could change the refractive index modulation of the alternating domains and thus result in a wavelength shift for the reflected light. Another possible way to develop novel LC-BCPs to take advantage of the active interaction between LC order and nanostructures would be to design more complex BCP structures. One example is the double LC-BCPs of which the two blocks are LCPs [44]. In the case of the use of a lamellar structure for artificial muscles [27], if the rubbery block is also a side-on or main-chain LCP containing azobenzene moieties (a low T_g is required), the thermally induced contraction and elongation may be more prominent.

REFERENCES

1. H. Fischer, S. Poser, M. Arnold, and W. Frank. On the influence of the morphological structure on the liquid crystalline behavior of liquid crystalline side chain block copolymers. *Macromolecules* **1994**, *27*, 7133–7138.
2. G. C. L. Wong, J. Commandeur, H. Fischer, and W. H. de Jeu. Orientational wetting in hybrid liquid crystalline block copolymers. *Phys. Rev. Lett.* **1996**, *77*, 5221–5224.

3. J. Sanger, W. Gronski, S. Maas, B. Stuhn, and B. Heck. Structural transition in a nematic LC block copolymer induced by the transition to the LC phase. *Macromolecules* **1997**, *30*, 6783–6787.
4. G. Mao, J. Wang, S. R. Clingman, and C. K. Ober. Molecular design, synthesis, and characterization of liquid. *Macromolecules* **1997**, *30*, 2556–2567.
5. M. Yamada, T. Iguchi, A. Hirao, S. Nakahama, and J. Watanabe. Side-chain liquid crystal block copolymers with well-defined structures prepared by living anionic polymerization I. Thermotropic phase behavior and structures of liquid crystal segment in lamellar type of microphase domain. *Polym. J.* **1998**, *30*, 23–30.
6. W. Y. Zheng, R. J. Albalak, and P. T. Hammond. Mesogen orientation within smectic C∗ side chain liquid crystalline diblock copolymers. *Macromolecules* **1998**, *31*, 2686–2689.
7. M. Anthamatten, W. Y. Zheng, and P. T. Hammond. A morphological study of well-defined smectic side-chain LC block copolymers. *Macromolecules* **1999**, *32*, 4838–4848.
8. A. Schneider, J.-J. Zanna, M. Yamada, H. Finkelmann, and R. Thomann. Competition between liquid crystalline phase symmetry and microphase morphology in a chiral smectic liquid crystalline–isotropic block copolymer. *Macromolecules* **2000**, *33*, 649–651.
9. K. K. Tenneti, X. Chen, C. Y. Li, X. Wan, X. Fan, Q. Zhou, L. Rong, and B. S. Hsia. Competition between liquid crystallinity and block copolymer self-assembly in core–shell rod–coil block copolymers. *Soft Matter* **2008**, *4*, 458–461.
10. E. Verploegen, T. Zhang, Y. S. Jung, C. Ross, and P. T. Hammond. Controlling the morphology of side chain liquid crystalline block copolymer thin films through variations in liquid crystalline content. *Nano Lett*. **2008**, *8*, 3434–3440.
11. Y. Zhao and J. He. Azobenzene-containing block copolymers: the interplay of light and morphology enables new functions. *Soft Matter* **2009**, *5*, 2686–2693.
12. H. F. Yu and T. Ikeda. Photocontrollable liquid–crystalline actuators. *Adv. Mater.* **2011**, *23*, 2149–2180.
13. H. Yu, J. Li, T. Ikeda, and T. Iyoda. Macroscopic parallel nanocylinder array fabrication using a simple rubbing technique. *Adv. Mater.* **2006**, *18*, 2213–2215.
14. C. Park, J. Yoon, and E. L. Thomas. Enabling nanotechnology with self assembled block copolymer patterns. *Polymer* **2003**, *44*, 6725–6760.
15. T. P. Lodge. Block copolymers: past successes and future challenges. *Macromol. Chem. Phys.* **2003**, *204*, 265–273.
16. A. Natansohn and P. Rochon. Photoinduced motion in azo-containing polymers. *Chem. Rev.* **2002**, *102*, 4139–4175.
17. H. Yu, T. Iyoda, and T. Ikeda. Photoinduced alignment of nanocylinders by supramolecular cooperative motions. *J. Am. Chem. Soc.* **2006**, *128*, 11010–11011.
18. Y. Morikawa, T. Kondo, S. Nagano, and T. Seki. Photoinduced 3D ordering and patterning of microphase-separated nanostructure in polystyrene-based block copolymer. *Chem. Mater.* **2007**, *19*, 1540–1542.
19. Y. Morikawa, S. Nagano, K. Watanabe, K. Kamata, T. Iyoda, and T. Seki. Optical alignment and patterning of nanoscale microdomains in a block copolymer thin film. *Adv. Mater.* **2006**, *18*, 883–886.
20. P. T. Wu, G. Ren, C. Li, R. Mezzenga, and S. A. Jenekhe. Crystalline diblock conjugated copolymers: synthesis, self-assembly, and microphase separation of poly(3-butylthiophene)-*b*-poly(3-octylthiophene). *Macromolecules* **2009**, *42*, 2317–2320.

21. B. W. Boudouris, C. D. Frisbie, and M. A. Hillmyer. Polylactide–polythiophene–polylactide triblock copolymers. *Macromolecules* **2010**, *43*, 3566–3569.
22. I. Botiz and S. B. Darling. Self-assembly of poly(3-hexylthiophene)-*block*-polylactide block copolymer and subsequent incorporation of electron acceptor material. *Macromolecules* **2009**, *42*, 8211–8217.
23. D. H. Han, X. Tong, Y. Zhao, and Y. Zhao. Block copolymers comprising p-conjugated and liquid crystalline subunits: induction of macroscopic nanodomain orientation. *Angew. Chem. Int. Ed.* **2010**, *49*, 9162–9165.
24. S. V. Ahir, A. R. Tajbakhsh, and E. M. Terentjev. Self-assembled shape-memory fibers of triblock liquid–crystal polymers. *Adv. Funct. Mater.* **2006**, *16*, 556–560.
25. A. Lendlein and S. K. Dr. Shape-memory polymers. *Angew. Chem. Int. Ed.* **2002**, *41*, 2034–2057.
26. M. Behl and A. Lendlein. Actively moving polymers. *Soft Matter.* **2007**, *3*, 58–67.
27. M.-H. Li, P. Keller, J. Yang, and P.-A. Albouy. An artificial muscle with lamellar structure based on a nematic triblock copolymer. *Adv. Mater.* **2004**, *16*, 1922–1925.
28. X.-F. Chen, Z. Shen, X.-H. Wan, X.-H. Fan, E.-Q. Chen, Y. Ma, and Q.-F. Zhou. Mesogen-jacketed liquid crystalline polymers. *Chem. Soc. Rev.* **2010**, *39*, 3072–3101.
29. P.-G. de Gennes. Un muscle artificiel sem-rapide. *C. R. 'Acad. Sci. Ser IIB: Mec Phys Chim Astron 2B* **1997**, *324*, 343–348.
30. M. D. Kempe, N. R. Scruggs, R. Verduzco, J. Lal, and J. A. Kornfield. Self-assembled liquid–crystalline gels designed from the bottom up. *Nat. Mater.* **2004**, *3*, 177–182.
31. S. Bai and Y. Zhao. Azobenzene-containing thermoplastic elastomers: Coupling mechanical and optical effects. *Macromolecules* **2001**, *34*, 9032–9038.
32. Y. Zhao, S. Bai, D. Dumont, and T. Galstian. Mechanically tunable diffraction gratings recorded on an azobenzene elastomer. *Adv. Mater.* **2002**, *14*, 512–514.
33. L. Cui, X. Tong, X. Yan, G. Liu, and Y. Zhao. Photoactive thermoplastic elastomers of azobenzene-containing triblock copolymers prepared through atom transfer radical polymerization. *Macromolecules* **2004**, *37*, 7097–7104.
34. J. Yang, D. Lévy, W. Deng, P. Keller, and M.-H. Li. Polymer vesicles formed by amphiphilic diblock copolymers containing a thermotropic liquid crystalline polymer block. *Chem. Commun.* **2005**, 4345–4347.
35. L. Jia, A. Cao, D. Lévy, B. Xu, P.-A. Albouy, X. Xing, M. J. Bowick, and M.-H. Li. Smectic polymer vesicles. *Soft Matter* **2009**, *5*, 3446.
36. L. Zhang, A. Eisenberg. Multiple morphologies of "crew-cut" aggregates of polystyrene-*b*-poly(acrylic acid) block copolymers. *Science* **1995**, *268*, 1728–1731.
37. B. M. Discher, Y.-Y. Won, D. S. Ege, J. C.-M. Lee, F. S. Bates, D. E. Discher, and D. A. Hammer. Polymersomes: tough vesicles made from diblock copolymers. *Science* **1999**, *284*, 1143.
38. A. Blanazs, S. P. Armes, and A. J. Ryan. Self-assembled block copolymer aggregates: from micelles to vesicles and their biological applications. *Macromol. Rapid Commun.* **2009**, *30*, 267–277.
39. K. Kita-Tokarczyk, J. Grumelard, T. Haefele, and W. Meier. Block copolymer vesicles-using concepts from polymer chemistry to mimic biomembranes. *Polymer* **2005**, *46*, 3540.
40. M. Li and P. Keller. Stimuli-responsive polymer vesicles. *Soft Matter* **2009**, *5*, 927–937.

41. E. Mabrouk, D. Cuvelier, F. Brochard-Wyart, P. Nassoy, and M.-H. Li. Bursting of sensitive polymersomes induced by curling. *PNAS* **2009**, *106*, 7294–7298.
42. B. Yan, X. Tong, P. Ayotte, and Y. Zhao.Light-responsive block copolymer vesicles based on a photo-softening effect. *Soft Matter*, **2011**, *7*, 10001–10009.
43. J. Wu and A. Eisenberg. Proton diffusion across membranes of vesicles of poly(styrene-*b*-acrylic acid) diblock copolymers. *J. Am. Chem. Soc.* **2006**, *128*, 2880–2884.
44. Y. Zhao, B. Qi, X. Tong and Y. Zhao. Synthesis of Double Side-Chain Liquid Crystalline Block Copolymers Using RAFT Polymerization and The Orientational Cooperative Effect. *Macromolecules* **2008**, *41*, 3823–3831.

CHAPTER 9

Semiconducting Applications of Polymerizable Liquid Crystals

MARY O'NEILL and STEPHEN M. KELLY
Department of Physics and Chemistry, University of Hull, UK

9.1 INTRODUCTION

Since the first demonstration of organic light-emitting diodes (OLEDs) based on conjugated small organics and main-chain polymers [1, 2], interest in the field of organic electronics has expanded enormously with applications in solar cells, plastic electronics as well as displays. Organic photovoltaics (OPVs) are being developed as low-cost, large-area, solar cells; organic field-effect transistors (OFETs) with performance comparable to amorphous silicon devices are expected to be used in flexible, or throwaway electronic applications, such as back-plates for rollable displays or radio-frequency identification (RFID) tags. While some applications remain a distant prospect, others have been commercially realized: OLEDs televisions have been demonstrated and white-light panels based on organic electroluminescence have found markets in architectural lighting. These devices are based on semiconducting and/or light-emitting conjugated organic materials. There is an incentive to develop low-cost and scalable processing methods so that the solution processing of materials is particularly attractive.

In an organic semiconductor, charge-carrier transport, and light-emission depend not only on the orbital energies and wavefunctions of the individual molecules or polymer chains, but also on intermolecular interactions, determined by the thin film morphology. Self-organization by the formation of liquid crystalline phases is considered a key strategy to control the order and packing of organic semiconductors [3]. Another advantage of liquid crystallinity is the ability to form monodomain samples without defects caused by grain barriers between neighbouring crystalline domains. The material may be annealed in the mesophase to give a high degree of molecular order and orientation. In liquid crystalline polymers the order is retained on cooling to

Liquid Crystals Beyond Displays: Chemistry, Physics, and Applications, Edited by Quan Li.
© 2012 John Wiley & Sons, Inc. Published 2012 by John Wiley & Sons, Inc.

room temperature by subsequent crystallization or glass formation. An excellent demonstration of the benefits of the self-assembly properties of liquid crystalline phases is the recent development of liquid crystalline, semiconducting, polymers, many of which contain thienothiophene groups, which show exceptionally high field-effect values of mobility up to 1 $cm^2 V^{-1} s^{-1}$ following annealing in the mesophase [4]. Polarized OLEDs have also been produced by the uniaxial alignment of main-chain polymers [5]. However, these polymers are highly viscous with high-temperature mesophases and also require high-temperature annealing for prolonged periods to optimize order. This chapter discusses an alternative method to produce ordered liquid crystalline polymers using low-temperature processing. Reactive mesogens are low mass liquid crystals with polymerizable groups separated from the core of the liquid crystal by spacer units [6–10]. They have low viscosity and can be designed with low temperature mesophases, so they can be easily ordered or macroscopically aligned in thin films at low temperatures. The order is then permanently fixed by cross-linking of adjacent molecules either by irradiation with ultraviolet light or thermal polymerization. The resulting polymer network is insoluble, so that further thin layers can be deposited on top using solution processing. This is an important advantage especially for OLEDs as multilayer devices give the best performance. Photopolymerization offers the further advantage of pixellation by photolithography: unexposed regions are simply removed by washing in the original spin-casting solvent.

Anisotropic polymer networks based on insulating and transparent reactive mesogens have been developed for many applications. For example, cholesteric polymer networks from reactive mesogens are used as color-flop pigments with a distinct viewing angle dependence of the color [11, 12]. They can also be used as broad band polarizers, by introducing a gradient in the pitch of the cholesteric helix, which broadens the reflection band [13]. Optical retarders based on nematic anisotropic networks have been used to improve the viewing angle of liquid crystal displays [14]. Liquid crystal elastomers are oriented rubbery networks that can reversibly contract, when the order is lost, for example by heating, or irradiating with light [15]. The molecular shape change is mirrored by changes in the mechanical shape of the solid.

In this chapter, we discuss the crosslinking of semiconducting reactive mesogens as well as their optical and electrical properties. The principles and applications of OLEDs are introduced and we report on the use of reactive mesogens to obtain polarized electroluminescence, with reference to methods to obtain uniform alignment of the mesogens. Photolithography is discussed as a technique to give a full color OLED incorporating reactive mesogens. Then, we outline the operating principle of OFETs and review the use of reactive mesogens in such devices. Finally, we assess the state of the art and make suggestions for its improvement.

9.2 MATERIAL PROPERTIES

9.2.1 Crosslinking of Reactive Mesogens

Figure 9.1 shows a schematic representation of the three parts of a semiconducting reactive mesogen. The central aromatic core forms the light-emitting or

FIGURE 9.1 Schematic of reactive monomer. The ellipse represents the aromatic core of the molecule. The zig–zag lines represent the aliphatic spacers and the squares represent the photoreactive end-groups.

charge-transporting chromophore. The reactive groups are separated from the aromatic core by flexible aliphatic spacers, which provide solubility and decouple the polymerization sites from the core. The material works as a negative photoresist and Figure 9.2 shows the processing steps leading to the formation of an anisotropic polymer network. Thin films of the monomers are formed by spin-casting, drop-casting, or another solution processing method. The liquid crystalline state may self-assemble spontaneously on the substrate surface as the solvent evaporates, or the sample is heated to attain the mesophase. The liquid crystalline molecules can be macroscopically oriented if there is an appropriate underlying alignment layer. Each monomer has two polymerizable end-groups so that an insoluble crosslinked polymer network is formed by photo- or thermal polymerization in the liquid crystalline phase, the former requiring irradiation with ultraviolet light with the opportunity for photopatterning. The crosslinks ensure that the polymerized network does not show any phase transitions and that it retains its liquid crystalline order through thermal cycling. Figure 9.3 shows a schematic representation of a cross-linked polymer network with nematic order.

Scheme 9.1 shows the general structures of the polymer backbones formed by polymerization of acrylate, methacrylate, diene, and oxetane reactive groups. The (meth)acrylate monomer polymerizes by a linear radical polymerization reaction to form a relatively flexible poly(meth)acrylate backbone. Cyclopolymerization of

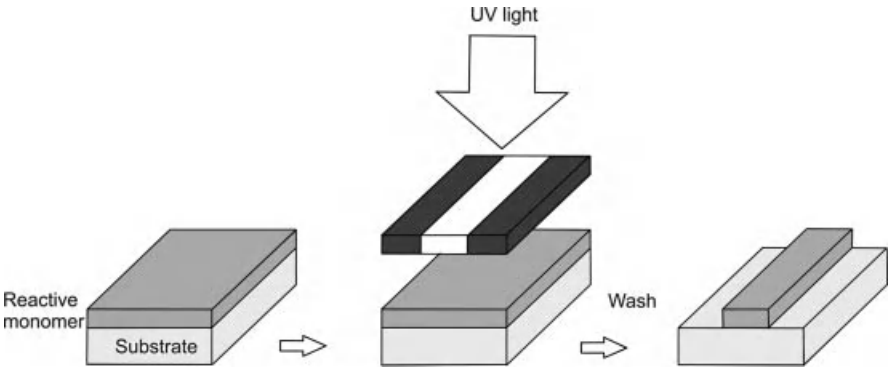

FIGURE 9.2 Schematic illustration of the photolithographic process. A thin film of reactive monomers is deposited by solution processing onto a substrate. The sample is irradiated with ultraviolet light through a mask. The irradiated material is photopolymerized and the remaining monomer is rinsed away by washing in the original solvent.

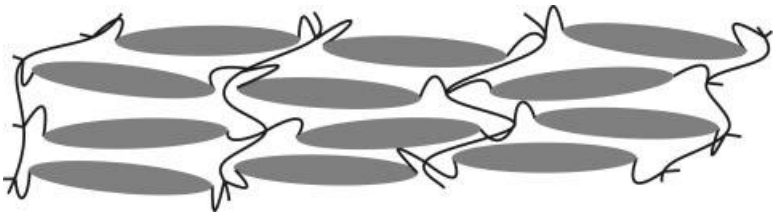

FIGURE 9.3 Schematic of a crosslinked polymer network with nematic order. The reactive mesogens have photopolymerizable groups attached via aliphatic spacers to each end of an extended aromatic core with semiconducting properties. The mesogens are deposited as a thin film by solution processing. They are polymerized and crosslinked either thermally or by irradiation with ultraviolet light.

the reactive diene group involves a sequential intra- and inter-molecular propagation: the double ring structure is first formed by reaction of the free radical with the second double bond of the diene group [16]. It provides a particularly rigid backbone. This reaction is sterically controlled and is generally slower than the polymerization of the (meth)acrylate compound. Radical photoinitiators, which decompose into free radicals, are necessary to start the polymerization. Usually these are added in very small quantities, normally 1 percent, although quantities as low as 10 ppm have been used [17]. However, the polymerization of some light-emitting reactive mesogens proceeds without a photo-initiator, so avoiding any possible trapping of carriers from the residual photo-initiator [18, 19]. The aromatic core of the reactive mesogen

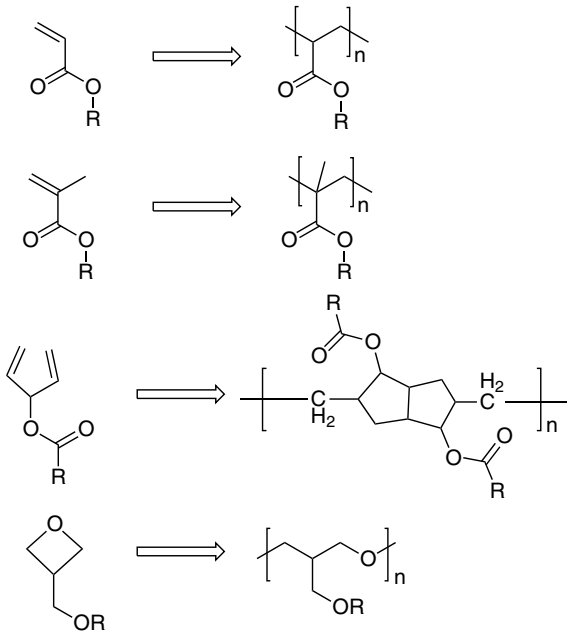

SCHEME 9.1 Polymerizable groups and the polymer backbones formed on polymerization.

absorbs the light and it is suggested that initiation occurs via thermally assisted energy transfer from the core to methacrylate group; the energy barrier for dissociating the C=C of the reactive group is reduced by 3.1 eV, the absorption energy of the aromatic core. Oxetanes are polymerized by a photocationic, ring-opening mechanism upon irradiation of the monomer doped with a suitable photosensitive catalyst. The protons (H+) released from the catalyst attack the electron-rich oxygen atom in the ring-strained oxetane ring and open it to form a linear poly(oxypropyl) polymer backbone. Free radical polymerization requires the absence of oxygen whereas cationic polymerization has the disadvantage of residual ionic impurities remaining in the crosslinked thin film.

Photo-differential scanning calorimetry has been used to investigate the extent of crosslinking of the semiconducting reactive mesogen, acrylic acid 6-[20]hexyl estermethyl substituted 1,4-phenylene-bis{4-[6-(acryloyloxy)-hexyloxy]benzoate} **1** (see Table 9.1) [17]. In this experiment the conversion of the photoreactive groups can be calculated from the enthalpy of polymerization. The acrylate end-groups of **1** showed a final conversion of 75 percent on polymerization in the smectic phase at 100 °C. Interestingly polymerization proceeds more slowly and with a lower conversion in the isotropic phase at 120 °C. This is attributed to the favorable alignment of the reactive groups in the smectic phase. Fourier transform infrared (FTIR) spectroscopy has also been used to confirm the crosslinking of reactive groups [18, 19]. However, it is difficult to unambiguously identify the extent of crosslinking because of overlapping FTIR resonances from other transitions in the molecules. As discussed

TABLE 9.1 Reactive mesogens 1 and 2 and polymerizable oligomer 3 used to study the extent or rate of photopolymerization

1

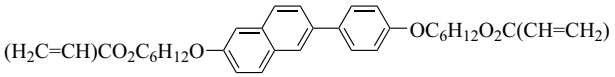

2

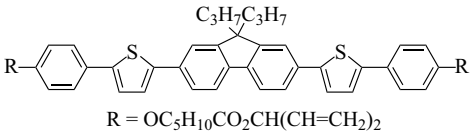

3

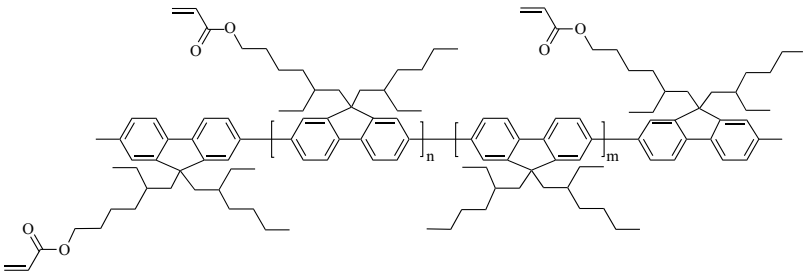

1: Cr-SmA = 85 °C; SmA-I = 111 °C; SmC- SmA = 66 °C; (acrylate).
2: Cr-N = 92 °C; N-I = 108 °C; t_g = 39 °C; (diene).
3: n = 0–100 percent; m = 0–100 percent; (acrylate).

above, one of the main advantages of the crosslinking of semiconducting reactive mesogens is to obtain an insoluble thin film, in order to make multilayer devices. The absorbance spectra of fluorene–thiophene reactive mesogens, for example **2** shown in Table 9.1, were measured before and after rinsing the thin film in the same solvent used for spin-casting the film [18, 19]. The absorbance decreased by 10 percent or less showing the removal of very little uncrosslinked material. There are wide variations in the time taken to crosslink semiconducting reactive mesogens, depending on the photo-initiator concentration, UV source temperature, etc. Thin films of oligofluorenes with variable acrylate content, compound **3** in Table 9.1, were crosslinked in a time of only 30 s [20].

9.2.2 Optical Properties of Calamitic Reactive Mesogens

Light is absorbed upon transfer of an electron from the highest occupied molecular orbital (HOMO) of a reactive mesogen to its lowest unoccupied molecular orbital (LUMO). These are localized on the aromatic core of the mesogen and have energy E_{HOMO} and E_{LUMO}. Excitons are neutral, bound electron–hole pairs and are formed by the coulombic interaction between the resulting electron and hole. The minimum absorption energy is the exciton energy,

$$E_{\mathrm{ex}} = E_{\mathrm{HOMO}} - E_{\mathrm{LUMO}} - E_{\mathrm{BE}}, \tag{9.1}$$

where E_{BE} is the exciton binding energy. Organic materials have large binding energies, $\approx$0.5 eV, because they are highly localized. The exciton recombines with the emission of a photon of energy $\approx E_{\mathrm{ex}}$. The emission spectrum is broadened and shows multiple peaks because of vibronic coupling. The oscillator strengths of the absorption and emission transitions are affected by intermolecular interactions that depend on the orientational and/or positional order of the mesogens. For example, the molecules of smectic liquid crystals are organized in parallel layers that represent the ideal configuration for the formation of H-aggregates [21–23]. Figure 9.4a shows the splitting of the excited state resulting from intermolecular coupling between a pair of molecules stacked head-to-head. In the lowest energy split state, the transition dipoles of neighboring molecules, indicated by arrows, are oriented in opposite directions so that the net transition dipole is zero and the lowest optical transition is optically forbidden [21]. Hence, H-aggregation gives a blue shift in absorption and can quench luminescence when the excitation relaxes to its lowest state before emission. The magnitude of the splitting varies with the intermolecular spacing that is influenced by the bulkiness of the aliphatic spacers and photoreactive groups. Similarly, as Figure 9.4b shows, the formation of J-aggregates (head-to-tail stacking) can lead to a red shift in absorption and enhanced emission. The formation of H- or J-aggregates depends on the relative displacements of neighboring molecules with nematics forming J aggregates when the longitudinal displacement of neighboring molecules is greater than half the molecular length. The positional order of smectics results in H aggregate formation so that nematics are more suitable light-emitting semiconductors than smectic liquid crystals.

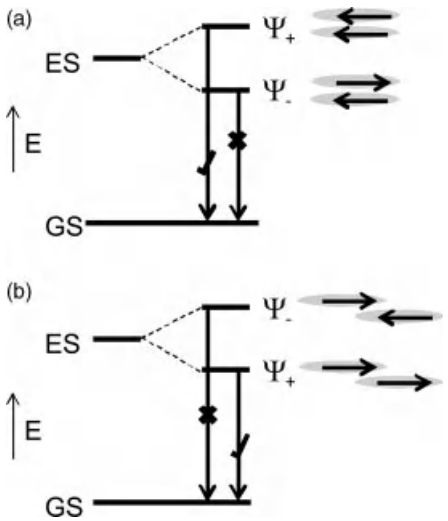

FIGURE 9.4 Illustration of the splitting of the lowest excited state of an isolated molecule when a (a) H and (b) J aggregates are formed. The combination of the transition dipoles makes the emission symmetry-allowed in the J-aggregate and forbidden in the H-aggregate. *Source:* Reprinted with permission from O'Neill and Kelly [3]. Copyright © 2010 WILEY-VCH.

There has been extensive research on nematic reactive mesogens for light emission. For example, the molecule **4**, see Table 9.2, has an extended backbone of conjugated fluorene–thipohene units. It absorbs in the near ultraviolet blue region of the spectrum and emits green light as shown in Figure 9.5. It has a photoluminescence quantum efficiency of 39 percent in solution and 35 percent as a thin film [24].

Experiments were carried to investigate whether the photopolymerization of reactive mesogens affects their emission properties [19]. The results depend critically

TABLE 9.2 Extended reactive mesogens 4 and 5 with nematic phases and a non-conjugated 1,4-pentadien-3-yl end-group at the terminus of the aliphatic spacers

4

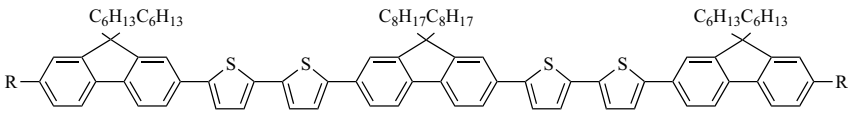

5

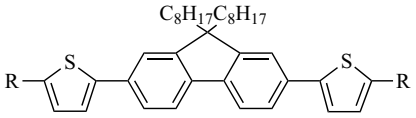

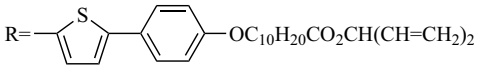

4: N-I = 188 °C; t_g = 26 °C; (diene with no observable melting point).
5: Cr-N = 52 °C; N-I = 143 °C; t_g = 0 °C; (diene).

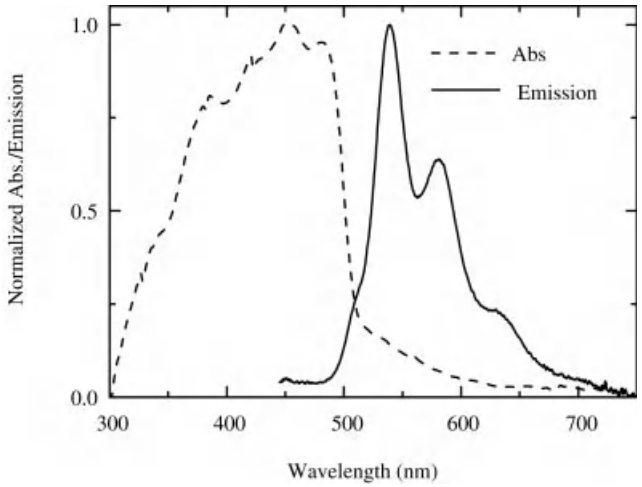

FIGURE 9.5 Absorption and emission spectra of a thin film of the reactive mesogen **4**.

on the conditions that the experiment was done. When the crosslinking was carried out by ultraviolet irradiation at 325 nm in a glove-box with <10 ppm of O_2 and water, the photoluminescence quantum efficiency was unchanged within the experimental error of 2 percent. However, photodegradation of the aromatic core was detected by FTIR and photoluminescence when photopolymerization was carried out in an environment containing air and oxygen.

The nematic reactive mesogens **2** and **4** have extended aromatic cores and are very highly birefringent [25, 26]. Figure 9.6 shows the birefringence Δn and refractive index of the extraordinary ray, n_e, of **2** and a nonpolymerizable homolog of **4** with

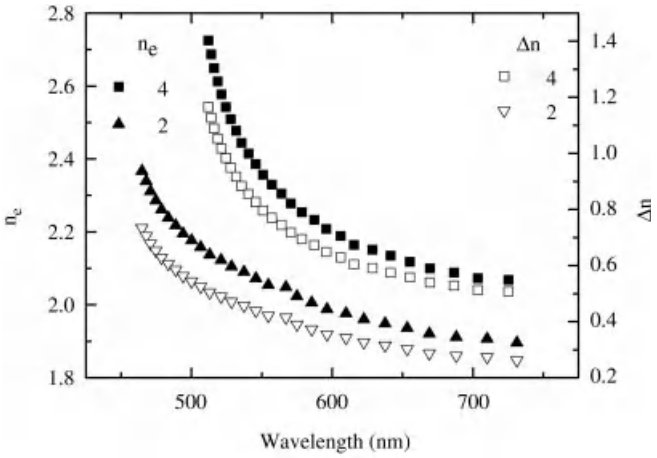

FIGURE 9.6 Birefringence, Δn, and refractive index of the extraordinary ray, n_e, of **2** and a nonpolymerizable homolog of **4**.

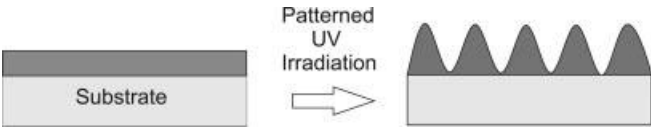

FIGURE 9.7 A nanostructured surface is spontaneously formed by patterned irradiation of a thin film of a polymerizable liquid crystal. The amplitude of the grating produced is often larger than the original thickness of the film. The material is not washed or etched.

six and fourteen aromatic rings, respectively, plotted as a function of wavelength. The highly dispersive nature of $n_e(\lambda)$ results from the $\pi-\pi^*$ absorption resonances, which peak at 395 nm and 452 nm for compounds **2** and **4**, respectively. The dipole moments of the transitions lie along the long axes of the molecules so that n_e rather than the ordinary refractive index n_o is affected by absorption. A maximum Δn value of 0.7 and 1.1 is obtained for the six and fourteen ring compounds, respectively, confirming the expected increase with molecular length. Hence, extremely large anisotropy is also expected in emission making this class of materials useful to obtain polarized electroluminescence, as discussed in Section 9.3.2.

The nanoscale patterning of the surfaces of organic semiconductors can significantly alter their emission properties. Current applications include the provision of distributed feedback in organic lasers [27, 28], and enhanced efficiency from OLEDs with corrugated structures [29]. Surface relief gratings were spontaneously formed by the patterned photopolymerization of thin films of reactive mesogen, as illustrated in Figure 9.7 [30]. Light from an ultraviolet HeCd laser was spatially modulated on transmission through a phase mask of period Λ_{PM} and incident to a thin film of the light-emitting, semiconducting reactive mesogen, **5**, which has a low melting point. The polymerization-induced change of chemical potential drives mass transfer from regions where there are troughs in irradiance toward the regions containing peaks. A surface grating of period Λ_{PM} or $\Lambda_{PM}/2$ is formed spontaneously with no development stage required [31]. Figure 9.8 shows an example of the morphology of a surface grating with period equal to Λ_{PM}. The mass transfer is enhanced by co-operative effects when the incident beam is polarized perpendicular to the grating grooves. Gratings deeper than the original film thickness were also created with a period as small as 265 nm. This period approaches that required, ≈250 nm [26], to make a second order distributed feedback structure for lasing near the emission peak of the material at 510 nm so that the photo-embossing process has major potential for applications in photonics. The mass transfer works well because the material has a nematic phase near room temperature. The compound **4**, which has a high clearing point of 188°C and is a nematic glass at room temperature, does not show appreciable mass transfer.

9.2.3 Electrical Properties of Calamitic Reactive Mesogens

Liquid crystals are relatively disordered compared to molecular crystals, so a coherent band-like description of charge-carrier transport in liquid crystals is inappropriate. Instead a thermally activated hopping model is used. The intersite hopping of electrons or holes occurs via π–π interactions between the sites, which usually

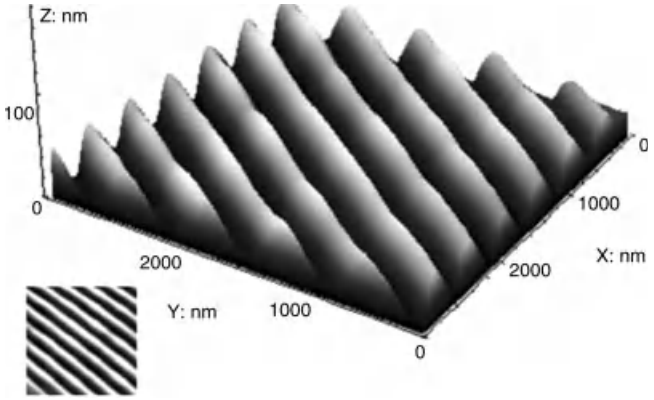

FIGURE 9.8 Image of surface grating formed by irradiation of a thin film through a phase mask of period 530 nm. The surface grating has the same period and average depth of ≈60 nm. The image was obtained using atomic force microscopy. *Source:* Reprinted with permission from Liedtke et al. [29]. Copyright © 2010 American Chemical Society.

are single molecules but may be traps [32]. The hopping rate depends on the strength of the electronic coupling between the HOMOs (LUMOs) of adjacent molecules, and exponentially decreases with intermolecular separation. Charge transport is characterized by the carrier mobility (μ), defined as the electron or hole velocity per unit electric field. Smectic reactive mesogens are expected to show high mobility in two dimensions because of their positional order and small intermolecular separation. Charge transport between the layers would be significantly slower. Disorder-based empirical models, for example that derived from the Monte-Carlo simulations of charge transport by Bässler et al. [33], have been used to discuss the temperature and electric field dependence of mobility for both smectic and nematic reactive mesogens [34–37]. The electronic density of states is broadened by disorder (see Figure 9.9) and may be represented by a Gaussian distribution, whose width depends on variations in the local conformation of the molecule, structural defects, dipolar disorder due to random orientation of polar groups, etc. The mobility increases with temperature as more energy is available to overcome the barriers for hopping between neighboring states created by energetic disorder. Positional disorder is caused by variations in the relative positions and orientations of molecules and results in a distribution of electronic couplings within the material. The mobility of smectic reactive mesogens is weakly temperature dependent, implying a small energetic disorder according to the Bässler model [34].

The charge carrier mobility in the plane of the device can be obtained from a field-effect transistor as explained in more detail in Section 9.4. Time-of-flight experiments are used to probe charge transport from top-to-bottom of a thin layer [36]. The molecules must be homogeneously aligned (in the plane of the film) so that intermolecular hopping can proceed in the right direction. The mobility of reactive mesogens (**6** and **7**, see Table 9.3) was studied at elevated temperatures in the smectic G phase and compared to a non-reactive analog, **8**. Ambipolar charge transport was observed.

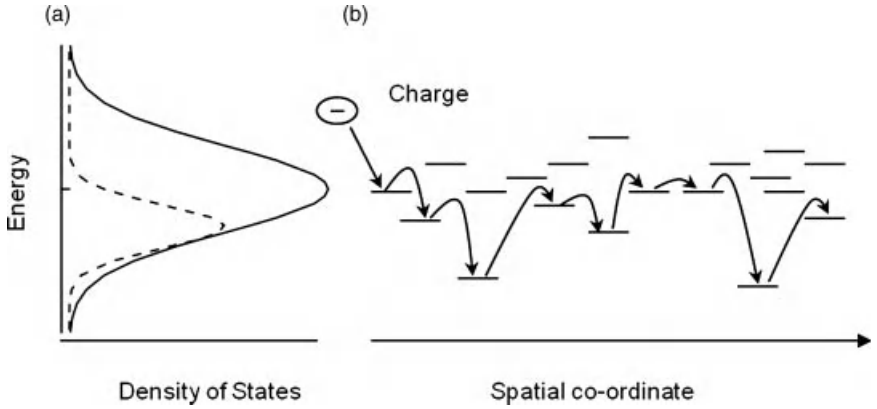

FIGURE 9.9 (a) The density of LUMO states (solid line) and occupied LUMO states (dashed line) for a disordered, liquid crystalline semiconductor. (b) The horizontal lines indicate energy levels of individual molecules in a disordered ensemble of molecules. The sequence of arrows shows an arbitrary pathway for an electron through the molecular ensemble. Hopping to a higher energy state requires activation energy and so is less likely than hopping to a lower energy state.

TABLE 9.3 Semiconducting reactive mesogens 6 and 7 with smectic phase and either a photopolymerizable oxetane or a non-conjugated 1,4-pentadien-3-yl end-group, respectively, at the terminus of the aliphatic spacers and their nonpolymerizable diheptyl-substituted homologue 8

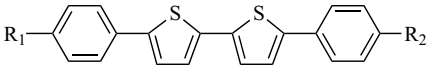

	R_1	R_2
6	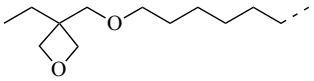 $[C_2H_5C(cycloCH_2OCH_2)CH_2OC_6H_{12}\text{-}]$	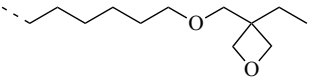 $[\text{-}C_6H_{12}OCH_2(cycloCH_2OCH_2)C_2H_5]$
7	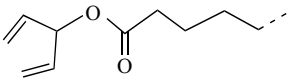 $[(H_2C{=}CH)_2CHO_2CC_4H_8\text{-}]$	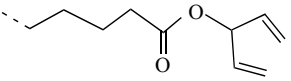 $-C_4H_8CO_2CH(CH{=}CH_2)_2$
8	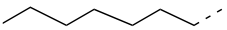 $[C_7H_{15}\text{-}]$	$[\text{-}C_7H_{15}]$

6: Cr-SmG = 83 °C; SmG-SmB = 93 °C; SmB-I = 144 °C; (oxetane)
7: Cr-SmG = 75 °C; SmG-I = 174 °C; (diene)
8: Cr-SmG = 140 °C; SmG-SmC = 225 °C; SmC-SmA = 229 °C; SmA-I = 234 °C; (nonpolymerizable aliphatic chains).

TABLE 9.4 Room temperature mobility of nematic compounds 2 and 9–11. Compounds 9–11 have the same aromatic core as 2 but different terminal groups as shown in the table. Compound 2 is a reactive mesogen and 9–11 have nonpolymerizable end-groups

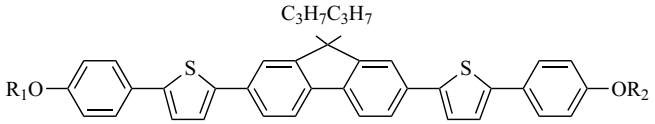

	R_1O-	-OR_2	Mobility $cm^2 V^2 S^{-2}$
2	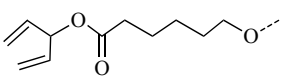	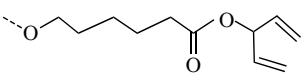	1.1×10^{-5}
9	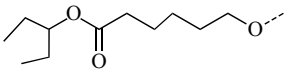	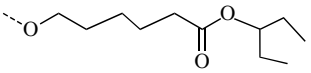	1.2×10^{-5}
10	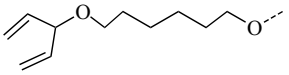	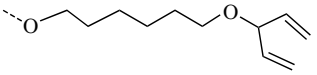	1.7×10^{-5}
11	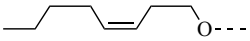	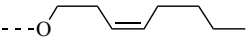	1.0×10^{-3}

2: Cr-N = 92 °C; N-I = 108 °C; t_g = 39 °C; (diene-ester).
9: Cr-N = 109 °C; N-I = 100 °C; t_g = 32 °C; (nonpolymerizable aliphatic-ester).
10: Cr-N = 92 °C; N-I = 116 °C; t_g = 19 °C; (diene-ether).
11: Cr-N = 153 °C; N-I = 146 °C; t_g = 32 °C; (nonpolymerizable alkene).

The diene and oxetane reactive mesogens have lower mobility and are less ordered than the non-reactive species, whose hole mobility is $0.044\,cm^2 V^{-1} s^{-1}$. On polymerization the mobility of the oxetane reactive mesogen **6**, increases, from $0.01\,cm^2 V^{-1} s^{-1}$ to $0.033\,cm^2 V^{-1} s^{-1}$ for holes, while that of the diene mesogen decreases. An experiment was carried out to check whether the polarizable nature of the ester or diene end-group significantly reduces the hole mobility of nematic mesogens. As shown in Table 9.4, compounds **2**, **9**, and **10** have the same aromatic core and branched end-group of similar length and shape, but have large differences in the polarizability of the end-group. All three compounds have very similar hole mobility values at room temperature. These values are almost 2 orders of magnitude smaller than that of compound **11**, which has unbranched end chains. This suggests that it is the shape of the end-group rather than its polarizable nature that limits the transport of holes.

9.3 OLEDs

9.3.1 Principle and Applications

Electroluminescence is the generation of light other than the black-body radiation by electrical excitation and was pioneered in molecular and polymeric thin film devices

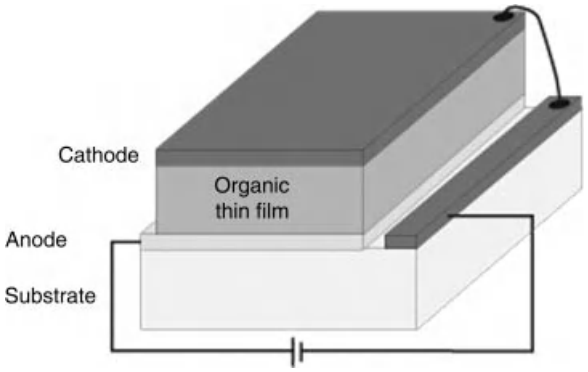

FIGURE 9.10 Schematic of an OLED consist a thin film of a light-emitting organic semiconductor sandwiched between cathode and anode. Light is emitted on application of a forward bias.

by groups in Kodak, and Cambridge [1, 2]. Figure 9.10 shows a schematic representation of an OLED containing a light-emitting semiconducting organic layer sandwiched between two dissimilar electrodes. An energy level diagram of the device is given in Figure 9.11, showing the built-in field originating from the difference in the work-functions of the two electrodes [38]. Electrons are injected from the cathode into LUMOs of the molecules at the interface. Similarly holes are injected from the anode into the HOMOs (electrons are removed from the HOMOs). The charged carriers drift in the applied field by thermally activated hopping from molecule-to-molecule, at a rate depending on the strength of the electronic coupling between the HOMOs (LUMOs) of adjacent molecules. The color of the emitted light can be tuned from blue to red by modification of E_{HOMO} and E_{LUMO} (see Eq. (9.1))

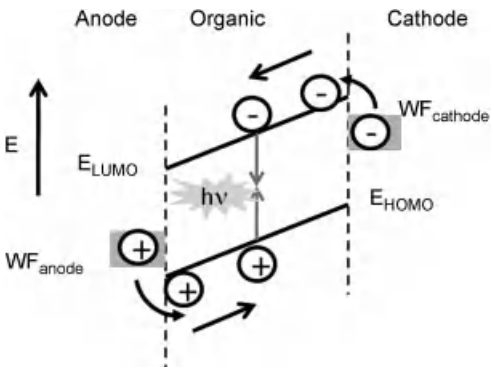

FIGURE 9.11 Energy level diagram of OLED showing the HOMO and LUMO energy levels, E_{HOMO} and E_{LUMO}, of an organic thin film sandwiched between anode and cathode of work-functions WF_{anode} and $WF_{cathode}$, respectively. The levels are tilted because of the built-in field. A photon of energy $h\nu$ is emitted as defined in Eq. (9.1).

using chemical design [39]: an electron donating group can be added to increase E_{HOMO} whereas electron-withdrawing groups decrease E_{LUMO}. The luminescence exits the device through one of the electrodes. Often the anode is made from indium tin oxide (ITO), which is transparent. The work-function of ITO is about 4.7 eV, which presents a large barrier for hole injection for most organic materials, when E_{HOMO} typically varies between 5.1 eV and 5.8 eV. Hence the conductive polymer poly-(3-4-ethylenedioxythiophene)/poly-(styrene sulfonate) (PEDOT:PSS), which has a work-function tunable over a limited range, is often inserted between the anode and the organic light-emitting film to improve the injection of holes [40]. Low work-function metals, for example Ca or Mg, are often used as cathodes to minimize the barrier for electron injection. However, these are unstable and must be capped with an inert metal, Al or Ag. Alternatively high work-function metals such as Al are used in conjunction with a thin insulating buffer layer, for example LiF or CsF, which improve electron injection by band bending [41]. Multiple organic layers are often used to stagger the injection barriers that are particularly large for blue emission. Hole/electron blocking layers at the cathode/anode may be introduced to confine carriers in the emission layer. Exciton blocking layers are used to prvent excitons from reaching the electrodes where they can be quenched. Multi-layer devices are easy to implement for small molecule OLEDs where the organic films are deposited by thermal evaporation in vacuo. Polymeric films are normally deposited by solution processing so that orthogonal solvents are needed to avoid layer mixing.

The exciton is formed from two independent charges of spin $\pm 1/2$ giving either an excited singlet ($S = 0$) or triplet ($S = 1$) state, as illustrated in Figure 9.12. The formation of exciton triplet states by electron–hole capture is three times more likely than singlet formation, if the process can be assumed to be spin independent. As discussed above, spin-allowed radiative emission (fluorescence) is from the

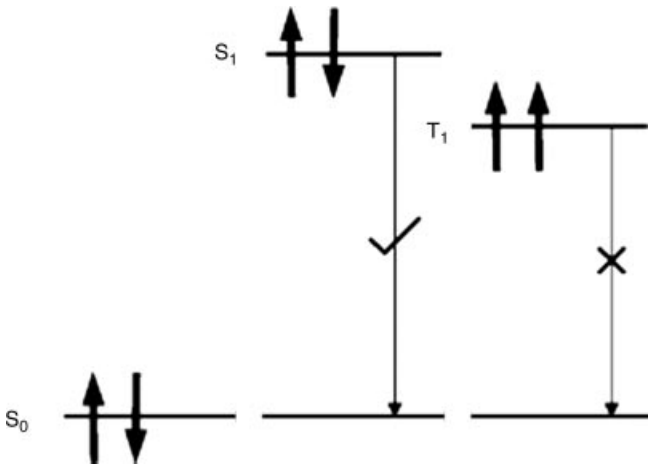

FIGURE 9.12 Schematic of ground singlet state (S_0), first excited singlet (S_1) and triplet (T_1), states. The $S_1 \rightarrow S_0$ transition is allowed and the $T_1 \rightarrow S_0$ transition is forbidden.

singlet only, so that the formation of triplets represents a significant energy loss, especially, when the exchange energy is large, inhibiting cross-over from the red-shifted triplet to the singlet. Triplet excitons can produce light by phosphorescence but this process is inefficient for organic materials. Metallo-organic complexes are often used as phosphorescent dopants in OLEDs [42]. The spin–orbit coupling produced by the heavy atom increases the rate of the forbidden transition from the triplet to the singlet ground state.

The external efficiency of the OLED is given by

$$\eta_{\mathrm{EL}} = \gamma \chi_S \, \eta_{\mathrm{PL}} \, \eta_{\mathrm{C}} \tag{9.2}$$

where γ is the ratio of the number of excitons within the device to the number of electrons in the external circuit; χ_S is the fraction of singlet excitons. η_{PL} is the photoluminescence quantum efficiency of the emitter; η_{C} is the fraction of photons coupled out of the device. There are many issues that affect the efficiency of an OLED. It is important to balance the injection of electron and holes and mobility should be high for both, so that space charge effects do not significantly impede charge injection. The luminescent material must have high quantum efficiency. Indeed the requirements for high mobility and high luminescent efficiency can be contradictory. Good charge transport require strong intermolecular coupling but the related aggregate may quench luminescence, as discussed in more detail in Section 9.2.2 [43]. The outcoupling efficiency of the OLED depends critically on the device configuration. The rear electrode acts as a mirror setting up standing waves so that optical mode pattern and recombination zone must be matched for efficient outcoupling of the light. η_{C} is also limited by total internal reflection that traps photons, emitted at large angles to the normal of the device, within the organic thin films and substrate. Finally, the materials must be photochemically, thermally, and electrochemically stable to maintain long-term operation.

The two main classes of OLEDs are based on conjugated small molecules and polymers, respectively. The more advanced technology, which is commercially widely available, involves small molecules that are deposited by thermal evaporation in vacuo. Shadow masks are used to define pixels. Polymer electroluminescence is less well-developed commercially but has potentially much lower fabrication costs because it uses solution processing. Ink jet printing can provide multi-colored displays. OLEDs are considered future competitors of LCD TVs particularly for high-end markets, because of their wider viewing angles, higher efficiency, very high contrast, and darker gray levels as well as their faster response times. OLEDs are gaining an increasing share in the market of small area displays for mobile phones, organizers, etc. The processing of large area displays has yet to be optimized and differential aging of the different color pixels remains a problem. Efficacies up to 70 cd A^{-1}, 28 cd A^{-1} and 8 cd A^{-1} have been achieved for green, red, and blue materials, respectively. White-light electrophosphorescence is now considered as a practical and efficient method for solid-state lighting [44]. Large area, color tunable, panels are anticipated and the first products are already available for specialized applications.

The initial interest in polarized EL was to provide a polarized OLED backlight for LCDs, eliminating the need for expensive polarizers, fluorescent tubes and diffusers/lightpipes. The polarization ratio R gives the ratio of the measured intensity of polarized light parallel and perpendicular to the alignment direction, as measured using an analyzer. It is used as a practical figure of merit. R values between 12 and 200 are required depending on the application, to avoid the use of a "clean-up" polarizer. This approach is considered as a useful market-entry product for OLEDs; a relatively unsophisticated unpixellated white-light or monochrome display is required when the image processing is carried out using the well-established addressing schemes of the liquid crystal display. High luminance levels are required from the OLED to compensate for losses through the display and filters. The compact nature of the OLEDs would give a slimmer display. A major potential market for OLEDs is in emissive displays for mobile phones, camcorders, and personal digital assistants. Many of these are viewed in bright sunshine and the image can be washed-out by reflection of sunlight transmitted into the display by the metal cathode. Linear polarizers at the output to the display are sometimes used to improve viewing in daylight since at least half of the incident sunlight is absorbed by the polarizer. The benefits of polarized OLEDs are obvious; the electroluminescent image has minimal loss on passage through the output polarizer.

9.3.2 Polarized Electroluminescence Using Reactive Mesogens

9.3.2.1 Introduction Polarized electroluminescence requires the uniform planar alignment of the light-emitting LC. This is normally obtained using an alignment layer located between the anode and the light-emitting film. Hence, the alignment layer must also be able to transport holes injected from the anode. Hole transport in disordered organic materials occurs by hopping between molecules with high values of E_{HOMO}. Intra- and inter-chain hopping occurs in conjugated polymers. The probability of hole transfer has an inverse exponential dependence on the intermolecular separation so that a reasonably high concentration of the hole transporting component is required. The alignment/charge transporting layer is normally deposited by spin-coating and uniaxial in-plane anisotropy is developed, either by mechanical rubbing in one direction or by photoalignment, as discussed below. It is thought that the rubbing of a polymer thin film results in the uniaxial orientation of the polymer chains near the surface of the film. The emission layer is then deposited on top and uniformly oriented in the direction imposed by the alignment layer by annealing in the liquid crystalline phase. The alignment is frozen-in by polymerization of the reactive mesogens either by annealing or by irradiation with UV light on cooling. Finally, a metallic cathode is deposited by thermal evaporation. The transition dipole moment of a calamitic liquid crystalline emitter is normally oriented along the long molecular axis. This determines the electric field direction of the emitted light so that the resulting polarization of the emission depends on the order parameter of the nematic [45]. The relationship is more complex than for absorption when the fluorescence tensor is of fourth order,

because it results from the product of two second rank tensors, namely the absorption and emission.

9.3.2.2 Photoalignment The process of mechanical rubbing produces dust and scratching, which can be expected to severely affect the yield and performance of thin layer OLEDs. These problems are expected to be more severe than in liquid crystal displays, because the electroluminescent film is typically about 50 nm thick. Mechanical damage may also result in short circuits and so-called "black-spots". These problems are avoided completely using non-contact photoalignment techniques first developed for LCDs [46, 47]. Illumination of the photoalignment film with polarized light generates a surface anisotropy in the alignment layer. When the LC film is deposited on top, the directors orient along with easy axis of the alignment layer, on annealing in the nematic phase. An added advantage is that the polarization direction of EL can be patterned photolithographically by patterning the polarization direction of the incident beam.

Coumarin side-chain polymers have been extensively used as photoalignment materials for nematic LCs for liquid crystal displays. On irradiation with linearly polarized light, the probability of a photochemical reaction is proportional to $\cos^2\phi$ where ϕ is the azimuthal angle between the polarization direction P of the incident beam and the transition dipole moment of the coumarin side-chain. According to Schadt et al. [48], the coumarin side-chains are depleted anisotropically by a $2+2$ cycloaddition, as illustrated in Scheme 9.2. The nematic liquid crystal is subsequently deposited and aligns homogeneously with its director-oriented parallel and perpendicular to P for weak and strong polarized UV illumination, respectively [49]. Spectroscopic analysis shows that the competition between two independent LC–surface interactions determines the resultant director orientation. Parallel LC alignment is determined by a short-range steric interaction with the dimerised cyclobutane side-chains. The LC alignment direction switches from parallel to perpendicular above a critical influence and subsequently the LC alignment is determined by a dispersive LC interaction with the intact side-chains in the bulk of the photoalignment layer. A key advantage of the use of side-chain coumarins as photoalignment polymers is their thermal stability resulting from crosslinking, especially in the parallel alignment regime.

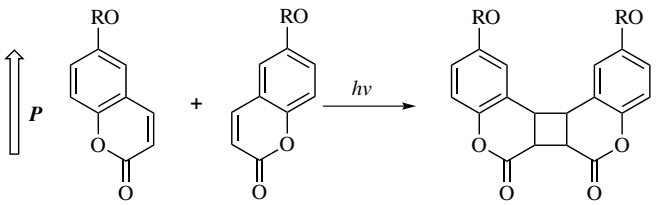

SCHEME 9.2 Chemical structures of coumarin group used for liquid crystal photoalignment before and after irradiation with polarized light. P indicates the polarization direction of the incident ultraviolet light.

9.3.2.3 Progress in RMs for Polarized OLEDs Polarized photoluminescence from an LC network was first demonstrated using a polymerizable mixture (Cr 116°C, N 150°C, I) of a photoinitiator, a thermal inhibitor dissolved in the non-luminescent reactive mesogen **12** and a guest luminescent diacrylate **13** shown in Table 9.5 [50]. The photoluminescence polarization ratio was 13:1. The acrylate **14** was synthesized by adding polymerizable acrylate end-groups to a light-emitting phenylenevinylene molecular fragment to form a similar reactive mesogen to the diacrylate **12** [51]. However, the acrylate **14** is luminescent due to the presence of the carbon–carbon double bonds [vinylene groups, –CH=CH–] in place of the carboxy groups [COO] in **12**. The former was aligned in the liquid crystalline state on a rubbed polyimide layer and then polymerized by heating up to a temperature of 180°C to form an anisotropic polymer network. The R value was only 3.5 using photoluminescence. This low polarization ratio could partly be attributed to a low

TABLE 9.5 Reactive mesogen 12, guest luminescent diacrylate 13, host reactive mesogen 14 and the polymerizable nematic oligomer 15 used for polarized luminescence

12

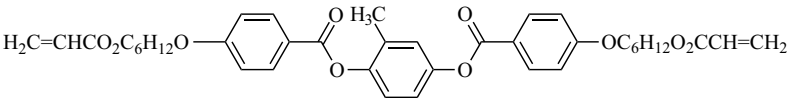

13

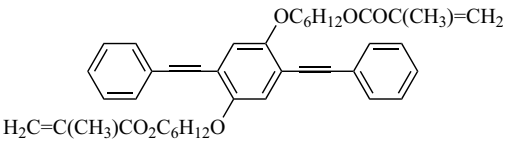

14

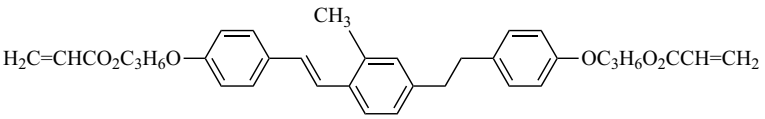

15

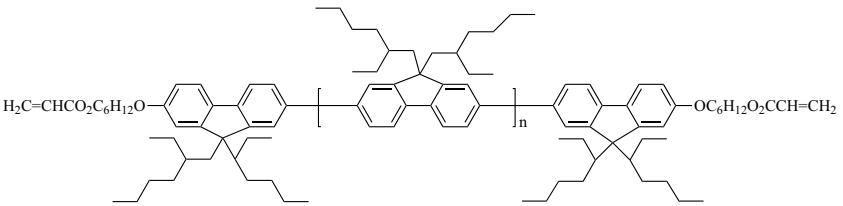

12: Cr-N = 86°C; N-I = 116 °C; t_g = 39°C; (host).
13: Cr-I = 80°C; (luminescent dopant).
14: Cr-SmA = 90°C, SmA-N = 144°C, N-I = 210°C.
15: N-I = 170°C; t_g = 80°C; (M_w = 600 g mol^{-1} by GPC; no melting point).

order parameter related to high temperature annealing, which was necessary because the acrylate **14** is crystalline at room temperature. Suitable molecular engineering allows the synthesis of reactive mesogens with much lower melting points and a nematic phase at room temperature. For example, the reactive mesogen **2** forms a nematic phase between 92°C and 108°C and maintains nematic order in a glassy state on cooling to room temperature. The compound has a glass transition temperature of 39°C. An efficient method was devised to prepare well-defined fluorene oligomeric blends with two acrylate end groups by end-capping [52]. For example, a blend **15** containing a mixture of fluorene trimers ($n = 1$), pentamers ($n = 3$), heptamers ($n = 5$), and nonamers ($n = 7$) forms supercooled nematic phases with no sign of crystallization upon cooling. The clearing point varies with molecular weight and was as low as 100°C.

Table 9.6 shows the coumarin phototalignment polymers (**16** and **17**) used to align reactive mesogens for polarized electroluminescence. The first polarized electroluminescent device using reactive mesogens was obtained by depositing **2** from solution by spin casting on a coumarin photoalignment polymer **16** that was previously irradiated with polarized UV light [53]. The photoalignment layer was doped with 4,4′,4″-tris(1-naphthyl)-*N*-phenyl-amino)-triphenylamine, **18** (see Table 9.7), to aid hole injection from the ITO electrode to the light-emitting film. The LC **2** was deposited, heated to 100°C and it was aligned spontaneously while slowly cooling to 20°C to form a nematic glass. The alignment was locked in by

TABLE 9.6 Coumarin polymers used to align reactive mesogens for polarized electroluminescence

16

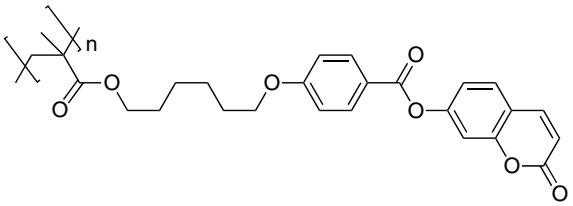

17

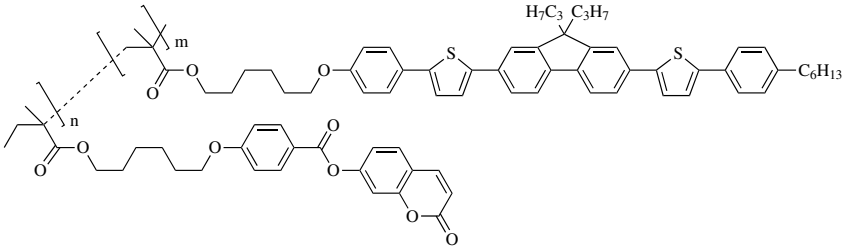

16: homopolymer $t_g = 60°C$.
17: copolymer n:m = 4:1; $t_g = 69°C$.

TABLE 9.7 4,4′,4″-tris[*N*-(1-naphthyl)-*N*-phenyl-amino]-triphenylamine used as a hole transporting dopant in the photoalignment layer 16

18

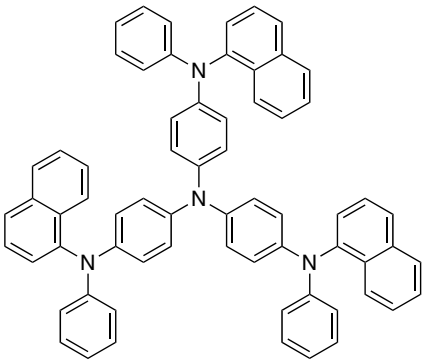

18: $t_g = 106^{o}C$; (triaryl amine dopant).

the formation of an anisotropic polymer network through photopolymerization at room temperature. Figure 9.13 shows the electroluminescent spectra for the orthogonal polarization directions. A maximum *R* value of 10:1 was obtained, limited by the order parameter of small molecules. The alignment direction was parallel to the polarization direction of the UV beam, independent of the irradiation conditions of the photoalignment layer. This implies that alignment is governed by the interaction of the LC with the coumarin photoproduct rather than the unreacted coumarin. However, R_{EL} depended on the fluence used to align the photopolymer as well as on the concentration of the hole transporting dopant, **18**. The latter has a

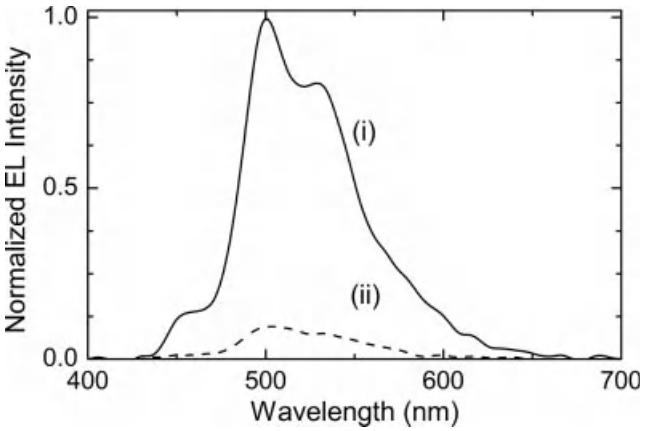

FIGURE 9.13 Polarized electroluminescence spectrum from a thin film of **2** taken (i) parallel and (ii) perpendicular to the alignment direction of a doped photoalignment layer. *Source:* Reprinted with permission from Contoret et al. [53]. Copyright © 2000 WILEY-VCH.

tetrahedral pyramidal shape and so inhibits the photogeneration of anisotropy in the photoalignment layer, so that high polarization ratios were only obtained when the **18**:**16** ratio was less than 30 percent. However, the maximum irradiance of 90 cd m^{-2} required an equal fraction of **18** and **16** in the alignment/hole transporting film.

Various strategies were investigated to optimize the alignment and hole injection properties of the alignment layers. A fluorene pentamer with polymerizable groups at the end of two aliphatic spacers is liquid crystalline at room temperature. It was aligned on a thin-rubbed polyphenylene vinylene (PPV) alignment layer and subsequently crosslinked to form a light-emitting polymer network with polarized emission [54]. PPV has a relatively low E_{HOMO} of 5.2 eV, facilitating hole injection. A R_{EL} value of 25 was obtained from a similar oligomer but the EL spectrum was broadened either by excimer emission or luminescence from the rubbed PPV alignment layer. Alternatively a copolymer with both coumarin and linear hole-transporting side-chains, polymer **17**, was developed as a photoaligning and hole injection film. The hole-injection unit has the same fluorene–thiophene aromatic core as the light-emitting mesogen, **2** [55, 56]. Both **2** and **17** have the same value of E_{HOMO}, equal to 5.6 eV, so that their hole injection properties are similar. However, the mobility of **17**, which could not be measured by time-of-flight, is expected to be much lower than that of **2**, equal to $1.1 \times 10^{-5}\,cm^2\,V^{-1}\,s^{-1}$, because of the low density of fluorene–thiophene side-chains (=20 percent) in the copolymer [36]. Polymer **17** was incorporated between the anode and the light-emitting film in a linearly polarized OLED. The light-emitter **5** had a longer thiophene–fluorene mesogen than **2**, to give a higher order parameter. The device had a luminance of 300 cd m^{-2} at 10 V and a maximum efficacy of 1.6 cd A^{-1}. R_{EL} had a maximum value of 13. Polarized electroluminescence with $R_{EL} = 31$ was obtained from extended liquid crystalline oligomers (non-polymerizable), which were aligned using a rubbed PEDOT/PSS layer [57].

As mentioned above, the alignment direction of the liquid crystalline emitter, and consequently the polarization direction of the emitted light, can be spatially patterned when photoalignment techniques are employed. This forms the basis of a three-dimensional display. The principle is illustrated in Figure 9.14. Each pixel can be subdivided into two subpixels having orthogonal polarization directions of emission simply by irradiating the adjacent subpixels of the photoalignment film with orthogonally polarized light. The two sets of subpixels create two separate images with orthogonal polarization. A three-dimensional effect is created when viewed through glasses having orthogonally polarized lenses; each eye sees a different image. This presents a low-cost solution for a three-dimensional display with applications in entertainment and medicine. The ability to pattern the polarization of electroluminescence may also have security applications as images can be generated that are only viewable through a polarizer. Figure 9.15 shows PL from a uniform layer of compound **5** deposited onto a photoalignment film of compound **17**, patterned by exposing adjacent squares with orthogonally polarized light. The photoluminescence image is viewed through a polarizer, and the green and dark regions are orthogonally aligned. Rotation of the polarizer by 90° changes the black

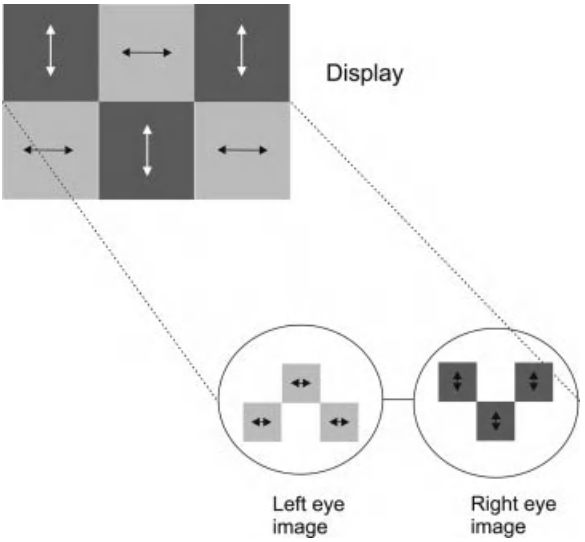

FIGURE 9.14 Illustration of principle of three-dimensional display using subpixels with orthogonally polarized emission. The symbols ↕ and ↔ represent vertically and horizontally polarized light, respectively.

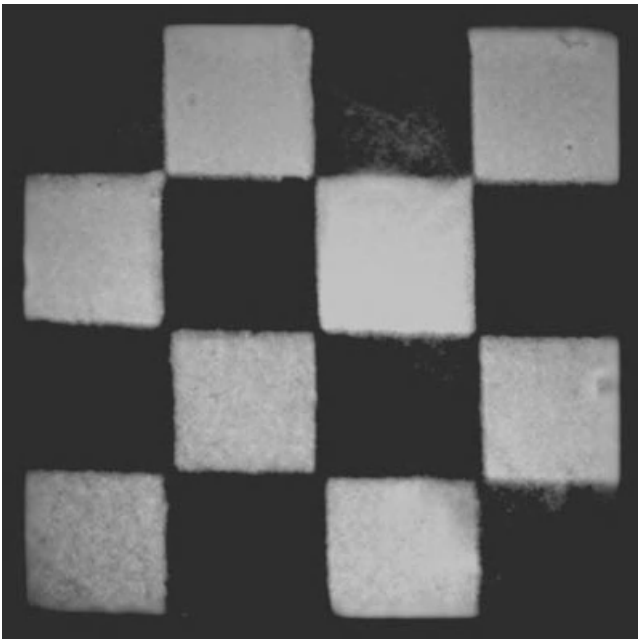

FIGURE 9.15 PL from compound **5** deposited onto a photoalignment film of compound **17**, patterned by exposing adjacent squares with orthogonally polarized light, viewed through a polarizer. The green and dark regions are aligned orthogonally. *Source:* Reprinted with permission from Aldred et al. [55]. Copyright © 2005 WILEY-VCH.

pixels to green and vice versa. This demonstrates the potential of the technology to make a three-dimensional display.

9.3.3 Pixellated Devices

Photolithography is the dominant patterning technique in the semiconductor industry, because of its high resolution, precise registration, fast throughput, and the ability to cover large areas. The photolithographic polymerization of light-emitting reactive mesogens is therefore a promising alternative route to ink-jet printing for a full-color display, with the added advantage of multi-layer capability; irradiation fixes the lower layer of a pixel before deposition of a second, this process is shown in Figure 9.16. A thin red-emitting film is deposited by solution processing, irradiated by UV light through a mask to define an insoluble pixel and the remaining materials removed by washing in chloroform. Pixels of the green and blue light-emitting materials are then sequentially formed in different regions by a similar process. It is important to deposit the red material first. Otherwise small quantities of the red-emitting material could

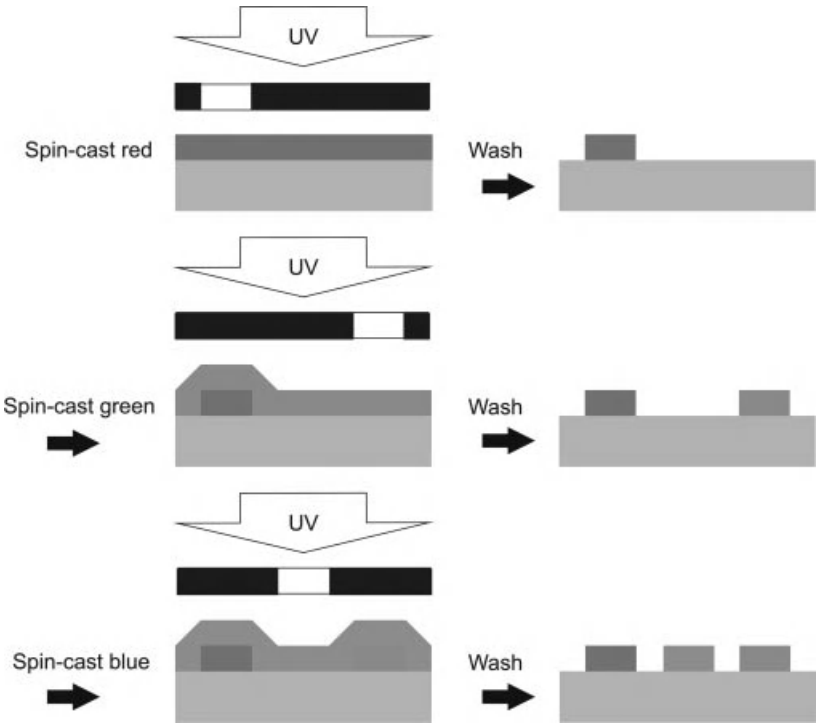

FIGURE 9.16 Photolithographic process to produce a red, green, and blue pixellated OLED. After patterned irradiation with ultraviolet light, the sample is washed with the solvent used for deposition, so that the unexposed regions are removed. (*See the color version of this figure in Color Plates section.*)

TABLE 9.8 Chemical structure of the blue and red-emitting reactive mesogens 19 and 20

19

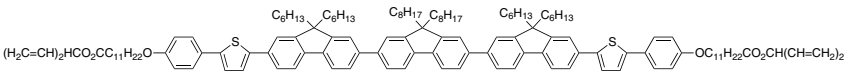

20

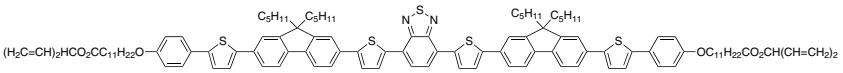

19: Cr-I = 80°C; N-I = 39°C; $t_g = -2$°C; (diene).
20: Cr-N = 142°C; N-I = 123°C; $t_g < 15$°C; (diene).

remain as a dopant in the green or blue pixel after washing. Energy transfer from the host to the dopant would result in some unwanted red emission from these pixels.

A pixellated red, green, and blue liquid crystal OLED was prepared by photolithography as described above [55]. Tables 9.2 and 9.8 show the chemical structures and transition temperatures of the blue, green, and red-emitting materials numbered **19**, **5**, and **20**, respectively. Their emission spectra are shown in Figure 9.17. Both compounds **19** and **5** are nematic reactive mesogens, which exhibit a metastable supercooled nematic phase for room temperature processing over long periods. Compound **20** is a nematic liquid crystal, which is a crystalline solid at room temperature and therefore it was used in a guest–host configuration to obtain a room temperature nematic phase. The red-emitter contained a blend of **20** in **5**, mixed in a ratio of 1:3. Red electroluminescence was observed because of efficient energy transfer from the host to the guest. The full color OLED with RGB pixels on the same substrate was fabricated as described above and is shown in Figure 9.18. UV light from a HeCd laser at 325 nm was used to photopolymerize the reactive mesogens. Figure 9.19 shows the irradiance and the efficacy of the three pixels as a

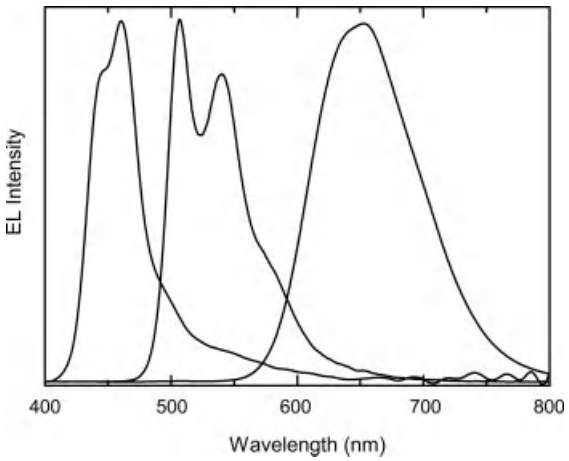

FIGURE 9.17 Electroluminescence spectrum of **19**, **5**, and **20**, respectively. *Source:* Reprinted with permission from Aldred et al. [55]. Copyright © 2005 WILEY-VCH.

FIGURE 9.18 A prototype OLED with a red, green, and blue pixel on the same substrate fabricated by sequential spin-coating and polymerization of the materials **20**, **5** blend, **5** and **19** onto a PEDOT:PSS film covering a patterned indium tin oxide (ITO) substrate. The pixels were defined by irradiation at 325 nm through a mask. Non-irradiated material was removed by washing with chloroform. The pixels were coated with a hole-blocking film of 3-(4-biphenylyl)-4-phenyl-5-*tert*-butylphenyl-1,2,4-triazole and capped with a LiF/Al electrode. *Source:* Reprinted with permission from Aldred et al. [55]. Copyright © 2005 WILEY-VCH. (*See the color version of this figure in Color Plates section.*)

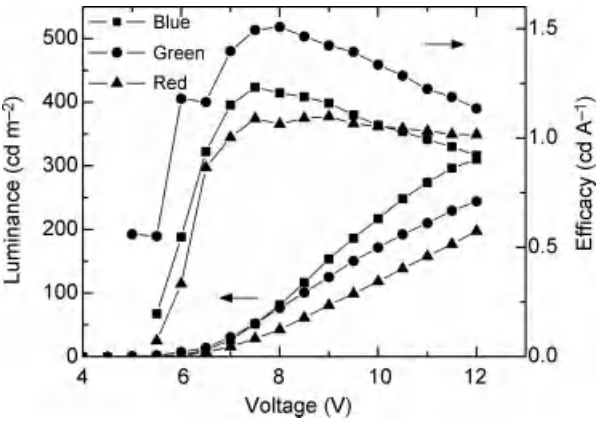

FIGURE 9.19 Luminance and efficacy from the blue, green and red pixels of the device shown in Figure 3.18.

function of voltage. Each pixel switched on at about 6 V. Electroluminescence was most efficient (1.5 cd A^{-1}) from the green pixel.

The photolithographic process can also give a new type of color-graded image using partial photopolymerization [25]. Figure 9.20 shows a photograph of an operating, single pixel, multicolor OLED, prepared by the sequential deposition of the red, green, and blue materials **20**, **5**, and **19**. The red material was deposited first, irradiated through a mask and washed to remove the unirradiated material. The green and blue materials were then processed similarly with the crosslinked green region partially overlapping the insoluble red film and the crosslinked blue partially overlapping the green. This results in blue–green and green–red emission, because there is some electroluminescence from both layers in the overlapping regions. A closer look at Figure 9.20 shows that the overlapping green–red region has two distinct zones giving yellow and orange EL. This arises because the red material in the overlapping region is not uniformly thick because the irradiation conditions were spatially varied to give nonuniform and incomplete polymerization resulting in partial removal of the film on washing. The photograph was taken at an operating

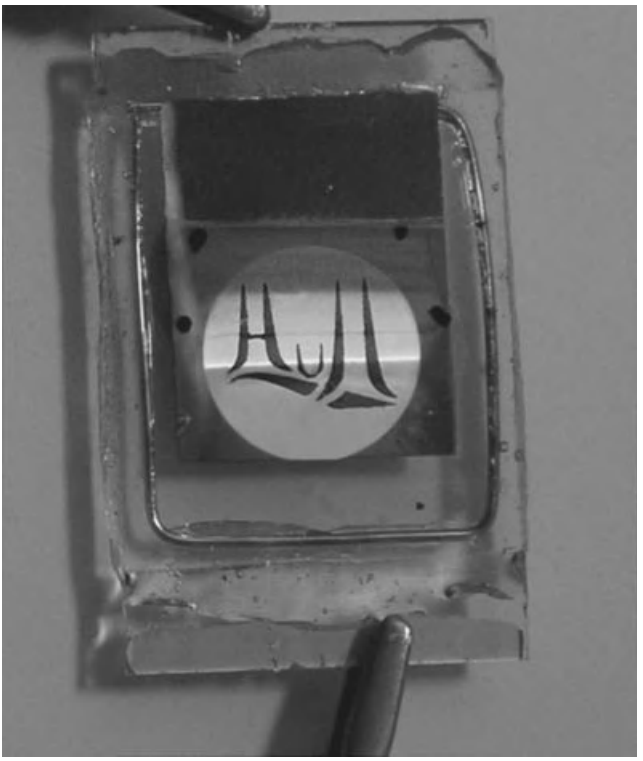

FIGURE 9.20 Photograph of graded-color single pixel OLED operating at 5 V. The logo represents the Humber Bridge located near Hull, England. This is one of the longest single span bridges in the world.

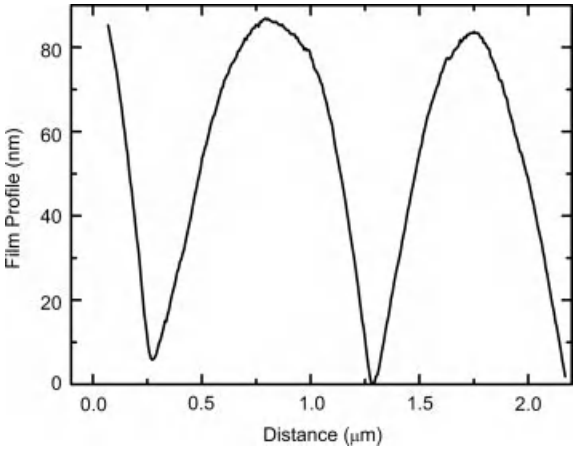

FIGURE 9.21 The surface profile, obtained using atomic force microscopy, of the washed polymer network film produced by irradiation of monomer **5** through a phase mask of period 1 μm. The period of the surface profile is equal to that of the phase mask.

voltage of 5 V. The threshold voltage for electroluminescence varied between 3.5 V and 4 V across the device.

Micron scale resolution is possible with the photolithographic process [20, 25], as shown by exposing a thin film of **5** through a phase mask of period 1 μm in soft-contact with the film. The phase mask produces a spatially modulated irradiance pattern with the same period as the phase mask; the exact spatial distribution of the irradiance depends on the relative intensity of the different diffraction orders of the grating [58]. The sample was then washed with chloroform to remove the soluble material. Figure 9.21 shows the surface profile of the washed film measured by atomic force microscopy. A surface relief grating is formed with a period equal to that of the phase mask. The non-crosslinked material in the minimally exposed regions is completely removed while the fully crosslinked material in the maximally exposed regions is retained. A grating thickness of ≈85 nm is obtained.

9.4 ORGANIC FIELD-EFFECT TRANSISTORS

9.4.1 Principle

Transistors are organic semiconductor devices use to amplify and switch electronic signals. In an OFET a voltage applied to the gate electrode controls the current between the source and drain electrodes [59, 60]. The construction of a typical OFET is shown in Figure 9.22. An insulator is placed between the gate and the organic semiconducting thin film. The source and drain electrode are separated using semiconducting channel of length L and width W. Ideally, when no gate voltage, V_G, is applied, the conductance of the semiconductor film is extremely low because there are no mobile charge carriers, that is, the transistor is "off". The application of V_G gives an electric field across the dielectric, which induces mobile charges in the

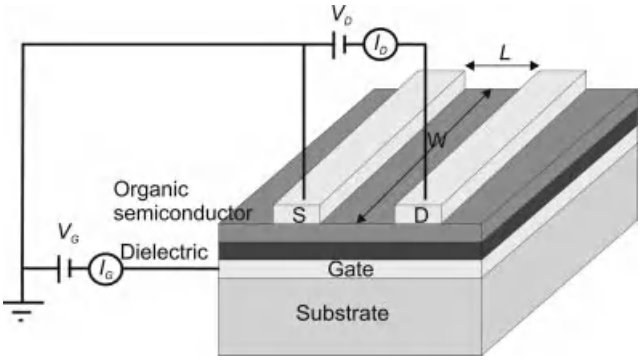

FIGURE 9.22 Schematic of an OFET. The gate electrode *G* is deposited on a substrate. The dielectric layer and p-type organic semiconducting film are deposited sequentially on top. The source *S* and drain *D* electrodes are photolithographically patterned to define a channel of width *W* and length *L*. The gate and drain voltages are V_G and V_D, respectively, with corresponding notation for current *I*.

semiconductor film. These move in response to the voltage, V_D, applied between the source and drain, that is, the transistor is "on". Figure 9.22 is an example of a bottom-gate, top-contact device configuration. The source and drain electrodes may be deposited between the dielectric and semiconducting thin film giving a bottom-gate, bottom-contact device. Alternatively the layers can be applied sequentially in the order: source and drain electrodes, semiconducting thin film, insulator, and gate electrode giving a top-gate configuration. Figure 9.22 also shows the circuit used to test the OFET. The source electrode is placed at ground. A hole (electron) drain current, I_D, is measured when a negative (positive) V_G is applied. V_G must be greater than a threshold value V_T, before current flows because the contacts may not be ohmic and charge-carrier traps must first be filled. Figure 9.23 shows the output characteristic curve of the transistor, that is, a plot of I_D versus V_D for different values of V_G. Two regions of the characteristic curve can be differentiated: I_D increases approximately linearly for low values of V_D, is when $V_D \ll (V_G - V_T)$. When $(V_G - V_T) > V_D$, I_D saturates. The physics underlying these characteristics is beyond the scope of this volume and is well explained elsewhere [60].

The charge-carrier mobility μ_{FET} is a key parameter obtained from the characteristics. It can be determined from the linear region using the equation

$$I_{\mathrm{D}} = \frac{WC}{L}\mu_{\mathrm{FET}}\left[(V_{\mathrm{G}} - V_{\mathrm{T}})V_{\mathrm{D}} - V_{\mathrm{D}}^2\right] \tag{9.3}$$

where C is the capacitance per unit area of the insulator. Alternatively, keeping V_{D} constant in the saturation region, μ_{FET} can be calculated from a plot of I_{D} versus $(V_{\mathrm{G}} - V_{\mathrm{T}})^2$ using the equation

$$I_{\mathrm{D}} = \frac{WC}{L}\mu_{\mathrm{FET}}(V_{\mathrm{G}} - V_{\mathrm{T}})^2 \tag{9.4}$$

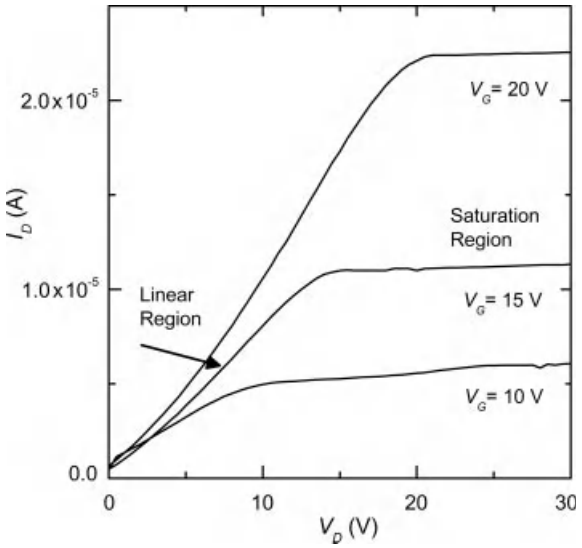

FIGURE 9.23 Output characteristics showing I_D versus V_D of a typical OFET.

It is desired to maximize the magnitude of μ_{FET} so that the operating voltage and power consumption of the transistor can be minimized. Another important parameter is the on/off ratio, equal to I_D (on)/I_D (off), which should be sufficiently large to define the states "0" and "1" in an electronic circuit.

Both the conjugated polymers, small molecules and blends of both material types are investigated as organic semiconductors and some materials show mobilities $>1\,\text{cm}^2\,\text{V}^{-1}\,\text{s}^{-1}$ [61, 62]. The market for organic electronics is at a very early stage with first products such as printed batteries and sensor on stream. Radio frequency identification (RFID) is a technology that allows all products to have a unique identifier, which is machine readable without line of sight. This gives a major impetus for the development of organic electronics because it requires very low-cost electronics. Electronic security provides another incentive for devices and systems that are easy to integrate, hard to simulate and simple to check. Smart packaging is expected to be another major application area with the potential to enhance the attractiveness of products.

9.4.2 Progress in Reactive Mesogens for OFETs

As discussed in Section 9.2.3, low-molar-mass smectics self-organize in layers with order in two dimensions. In the smectic A and C phases, the packing in the layers is fluid-like, while the more ordered, crystalline smectics, with hexatic, hexagonal, or herring-bone packing, facilitate greater π–π overlap. The resulting short intermolecular separations give large π–π coupling and the potential for fast intermolecular hopping. Silane-based surfactants are generally used to give the required homeotropic alignment to provide in-plane transport between the electrodes of OFETs

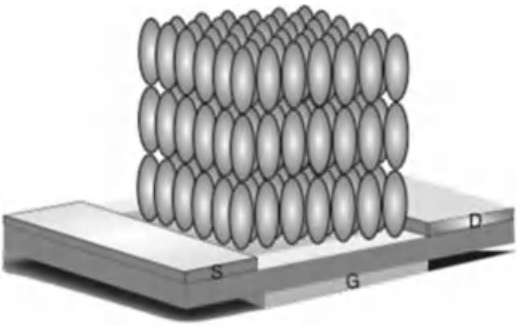

FIGURE 9.24 Schematic illustration of optimum orientation of smectic liquid crystals for OFET operation.

(see Figure 9.24). OFETs operate at room temperature so that materials are required with a smectic phase at room temperature and with an extended temperature range to ensure thermal stability. This is a considerable constraint on the design of suitable materials. An alternative way to ensure operating stability is to lock-in the smectic phase of a thin film of a reactive mesogen by polymerization. OFETs fabricated from both crosslinked and uncrosslinked thin films of the smectic reactive mesogens, compounds **6** and **7**, were studied [63–65]. The mobility of **7**, which has a diene reactive group, was 0.01 $cm^2 V^{-1} s^{-1}$ before crosslinking but decreased by a factor of 10 after photopolymerization in the high temperature crystalline smectic G phase. A similar trend was obtained elsewhere for an OFET constructed with the quaterthiophene acrylate **21**, whose structure is shown in Table 9.9 [65]. However, this result may not be general. The field-effect mobility of **6** increased after crosslinking, albeit from a very low value of $8 \times 10^{-5} cm^2 V^{-1} s^{-1}$. The same material showed time-of-flight mobility values, recorded at 140°C, of $1 \times 10^{-2} cm^2 V^{-1} s^{-1}$ before polymerization and $3 \times 10^{-2} cm^2 V^{-1} s^{-1}$ afterwards [66]. Crosslinking was also shown not to degrade charge transport in an OFET based on star-shaped molecules and in a nematic reactive mesogen with a diene photoreactive end-group studied with time-of-flight measurements [36, 67].

TABLE 9.9 Compounds 21 ($n = 4$, 6, and 8) and 22 with smectic phases used in OFETs

21

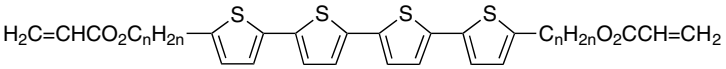

22

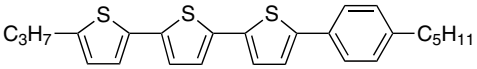

21: $n = 4$; Cr-I = 167°C; (acrylate).
21: $n = 6$; Cr-SmX = 157°C; SmX-I = 161°C; (acrylate).
21: $n = 8$; Cr-SmX1 = 145°C; SmX–SmX2 = 148°C; SmX2-I = 153°C; (acrylate).
22: Cr-SmX < –50°C; SmX-I = 57°C; (nonpolymerizable dialkane).

The minimum requirements for the OFET is a mobility $>10^{-2}\,cm^2\,V^{-1}\,s^{-1}$ with values $>1\,cm^2\,V^{-1}\,s^{-1}$ necessary for more sophisticated applications. The reduction in mobility of the best material following crosslinking may result from a disruption in the layer structure of the smectic mesogens, when the end-groups of the molecules form a covalently bonded polymer backbone. However, extrinsic issues are more likely because materials with good time-of-flight mobility are improved by crosslinking. The low mobility may also be associated with poor film quality and photo-induced dewetting. The OFET films were irradiated in a flowing nitrogen environment, which may have included oxygen and water vapour leading to some photodegradation. A solution-processed film of a non-reactive compound, **22**, which has a room temperature smectic phase, shows hole mobility values up to $0.04\,cm^2\,V^{-1}\,s^{-1}$ in an OFET when well aligned by a silane-based, self-assembled monolayer, and following annealing [68, 69]. Improved processing should ensure that reactive mesogens achieve similar or even better values.

9.5 DISCUSSION AND CONCLUSION

Reactive mesogens have not been as well researched as other organic semiconducting materials for OLEDs and OFETs and so have not reached the same level of performance. However, there are major incentives to expand interest in the technology. Reactive mesogens are compatible with solution processing, the preferred method for large scale manufacturing. This approach also solves one of the major problems of many solution based technologies: the poor thermal and temporal stability of material morphology. The polymerization of the reactive end-groups of the semiconducting monomers locks-in the optimized morphology. A significant development is the demonstration of a pixellated red, green, and blue liquid crystal OLED produced by photolithography. A similar device based on amorphous crosslinked polymers has also been made [70]. Indeed, photolithography can be used in conjunction with the printing of OLEDs for large-area manufacturing to enable sub-pixellation and the formation of multi-layer OLEDs. The ability to separately pattern the liquid crystal alignment direction and to pixellate the light-emitting/charge transporting material is a unique feature of reactive mesogens, which is very relevant with the current wide interest in three-dimensional displays. There are also many opportunities for new developments. For example, phosphorescent guest–host OLEDs are the most efficient class of OLEDs [71], but there has been little apparent effort to combine liquid crystalline hosts with phosphorescent light-emitting dopants. The inherent anisotropic gain of reactive mesogens and their potential for anisotropic feedback have hardly been exploited to reduce laser threshold and loss of organic thin film lasers [3]. These advantages may help overcome the challenges to reach continuous wave and/or electrically pumped lasing. A liquid crystal composite approach based on reactive mesogens has recently been used to provide a distributed interface to vertically separate electron-donating and electron-accepting films to give a novel organic photovoltaic device with much scope for further improvement [72, 73].

There are also many strategies available to improve the material and device performance of semiconducting reactive mesogens. Some developments made to improve the material properties of polymer and small molecule semiconductors can be transferred to reactive mesogens. For example, the performance of polymeric solar cells has been significantly enhanced by the use of "push–pull" copolymers as electron donors in phase-separated blends with fullerene-based electron acceptors. The copolymers have alternating electron-withdrawing and electron-donating components to increase the double bond character between the units resulting in a low band gap. These materials are linear and so could easily be incorporated into the aromatic cores of reactive mesogens. Sample processing has emerged as a critical factor that influences the electronic and optoelectronic properties of organic semiconductors and devices. For example, thermally evaporated smectics show higher values of mobility in OFETs than spin-cast ones. Zone and drop casting are alternate solution-based methods to obtain highly ordered thin films. Dip-casting might allow the anisotropic properties of reactive mesogens to be best exploited. Very often the liquid crystalline phases of reactive mesogens exist at high temperatures and annealing at these temperatures may not be compatible with efficient and cost-effective manufacturing processes. Alternatively, annealing may be carried out at lower temperatures using solvents as plasticisers to give lyotropic phases. Solvent vapour annealing at room temperature has produced samples of nematic oligomers with similar order parameters to those obtained by thermal annealing [74].

In summary, reactive mesogens that emit light and/or can transport electronic charge have been developed and applied to demonstrator OLEDs and OFETs. In these devices, the self-organization inherent to the liquid crystal phase gives an optimized morphology, which is locked-in by network formation on polymerization of the photoreactive end-groups of the monomers. Although material and processing improvements are required, the benefits of solution processing, photolithographic and multilayer capability, enhanced order, patterned photoalignment, excellent morphological stability, etc. should encourage continued research and development in the area.

REFERENCES

1. C. W. Tang and S. A. Vanslyke. Organic electroluminescent diodes. *Appl. Phys. Lett.* **1987**, *51*, 913–915.
2. J. H. Burroughes, D. D. C. Bradley, A. R. Brown, R. N. Marks, K. Mackay, R. H. Friend, P. L. Burns, and A. B. Holmes. Light-emitting diodes based on conjugated polymers. *Nature* **1990**, *347*, 539–541.
3. M. O'Neill and S. M. Kelly. Ordered materials for organic electronics and photonics. *Adv. Mater.* **2011**, *23*, 566–584.
4. I. McCulloch, M. Heeney, C. Bailey, K. Genevicius, I. MacDonald, M. Shkunov, D. Sparrowe, S. Tierney, R. Wagner, W. Zhang, M. L. Chabinyc, R. J. Kline, M. D. McGehee, and M. F. Toney. Liquid-crystalline semiconducting polymers with high charge-carrier mobility. *Nat. Mater.* **2006**, *5*, 328–333.

5. M. Grell, W. Knoll, D. Lupo, A. Meisel, T. Miteva, D. Neher, H. G. Nothofer, U. Scherf, and A. Yasuda. Blue polarized electroluminescence from a liquid crystalline polyfluorene. *Adv. Mater.* **1999**, *11*, 671–675.
6. R. A. M. Hikmet and J. Lub. Anisotropic networks and gels obtained by photopolymerisation in the liquid crystalline state: Synthesis and applications. *Prog. Poly. Sci.* (Oxford) **1996**, *21*, 1165–1209.
7. S. M. Kelly. Anisotropic networks, elastomers and gels. *Liq. Cryst.* **1998**, *24*, 71–82.
8. R. A. M. Hikmet, J. Lub, and D. J. Broer. Anisotropic networks formed by photopolymerization of liquid-crystalline molecules. *Adv. Mater.* **1991**, *3*, 392–394.
9. D. J. Broer, J. Boven, G. N. Mol, and G. Challa. *Makromol. Chem.* **1989**, *190*, 2255–2268.
10. S. M. Kelly. Anisotropic networks. *J. Mater. Chem.* **1995**, *5*, 2047–2061.
11. T. J. Bunning and F. H. Kreuzer. Cyclosiloxane-based liquid crystalline materials. *Trends Polym. Sci.* **1995**, *3*, 318–323.
12. T. Pfeuffer, D. Hanft, and P. Strohriegl. Vitrifying star-shaped liquid crystals: synthesis and application in cholesteric polymer networks. *Liq. Cryst.* **2002**, *29*, 1555–1564.
13. D. J. Broer, J. Lub, and G. N. Mol. Wide-band reflective polarizers from cholesteric polymer networks with a pitch gradient. *Nature* **1995**, *378*, 467–469.
14. M. Schadt, H. Seiberle, A. Schuster, and S. M. Kelly. Photo-generation of linearly polymerized liquid crystal aligning layers comprising novel, integrated optically patterned retarders and color filters. *Jpn. J. Appl. Phys.* **1995**, *34*, 3240–3249.
15. M. Warner and E. M. Terentjev. Nematic elastomers – a new state of matter? *Prog. Polym. Sci.* (Oxford) **1996**, *21*, 853–891.
16. A. W. Hall, D. Lacey, and P. I. Buxton. The use of photoinitiated free-radical cyclopolymerization in the preparation of novel side-chain liquid-crystalline polydienes. *Macromol. Rapid Commun.* **1996**, *17*, 417–425.
17. H. Thiem, P. Strohriegl, M. Shkunov, and I. McCulloch. Photopolymerization of reactive mesogens. *Macromol. Chem. Phys.* **2005**, *206*, 2153–2159.
18. A. E. A. Contoret, S. R. Farrar, M. O'Neill, and J. E. Nicholls. The photopolymerization and cross-linking of electroluminescent liquid crystals containing methacrylate and diene photopolymerizable end groups for multilayer organic light-emitting diodes. *Chem Mater.* **2002**, *14*, 1477–1487.
19. K. L. Woon, A. Liedtke, M. O'Neill, M. P. Aldred, S. P. Kitney, P. Vlachos, A. Bruneau, and S. M. Kelly. Photopolymerization studies of a light-emitting liquid crystal with methacrylate reactive groups for electroluminescence. In: *Proceedings of SPIE – The International Society for Optical Engineering* 2008, 70500E.
20. E. Scheler and P. Strohriegl. Tailoring fluorene-based oligomers for fast photopatterning. *J. Mater. Chem.* **2009**, *19*, 3207–3212.
21. J. Cornil, D. Beljonne, J. P. Calbert, and J. L. Brédas. Interchain interactions in organic π-conjugated materials: Impact on electronic structure, optical response, and charge transport. *Adv. Mater.* **2001**, *13*, 1053–1067.
22. S. Siddiqui and F. C. Spano. H- and J-aggregates of conjugated polymers and oligomers: A theoretical investigation. *Chem. Phys. Lett.* **1999**, *308*, 99–105.
23. J. Cornil, D. Beljonne, D. A. Dos Santos, J. P. Calbert, and J. L. Brédas. Intermolecular interactions in electroluminescent conjugated materials. *Thin Solid Films* **2000**, *363*, 72–75.

24. A. Liedtke. *Liquid crystals for light emitting diodes*. University of Hull, 2009.
25. K. L. Woon, A. E. A. Contoret, S. R. Farrar, A. Liedtke, M. O'Neill, P. Vlachos, M. P. Aldred, and S. M. Kelly. Material and device properties of highly birefringent nematic glasses and polymer networks for organic electroluminescence. *J. Soc. Inf. Disp.* **2006**, *14*, 557–563.
26. M. D. McGehee, M. A. Diaz-Garcia, F. Hide, R. Gupta, E. K. Miller, D. Moses, and A. J. Heeger. Semiconducting polymer distributed feedback lasers. *Appl. Phys. Lett.* **1998**, *72*, 1536–1538.
27. I. D. W. Samuel and G. A. Turnbull. Organic semiconductor lasers. *Chem. Rev.* **2007**, *107*, 1272–1295.
28. J. M. Ziebarth, A. K. Saafir, S. Fan, and M. D. McGehee. Extracting light from polymer light-emitting diodes using stamped Bragg gratings. *Adv. Funct. Mater.* **2004**, *14*, 451–456.
29. A. Liedtke, L. Chunhong, M. O'Neill, P. E. Dyer, S. P. Kitney, and S. M. Kelly. One-step photoembossing for submicrometer surface relief structures in liquid crystal semiconductors. *ACS Nano* **2010**, *4*, 3248–3253.
30. T. J. Trout, J. J. Schmieg, W. J. Gambogi, and A. M. Weber. Optical photopolymers: design and applications. *Adv. Mater.* **1998**, *10*, 1219–1224.
31. K. L. Woon, M. O'Neill, P. Vlachos, M. P. Aldred, and S. M. Kelly. Highly birefringent nematic and chiral nematic liquid crystals. *Liq. Cryst.* **2005**, *32*, 1191–1194.
32. J. F. Chang, H. Sirringhaus, M. Giles, M. Heeney, and I. McCulloch. Relative importance of polaron activation and disorder on charge transport in high-mobility conjugated polymer field-effect transistors. *Phys. Rev. B* **2007**, *76*, 205204.
33. P. M. Borsenberger, L. Pautmeier, and H. Bässler. Charge transport in disordered molecular solids. *J. Chem. Phys.* **1991**, *94*, 5447–5454.
34. R. J. Baldwin, T. Kreouzis, M. Shkunov, M. Heeney, W. Zhang, and I. McCulloch. A comprehensive study of the effect of reactive end groups on the charge carrier transport within polymerized and nonpolymerized liquid crystals. *J. Appl. Phys.* **2007**, *101*, 023713.
35. T. Kreouzis, R. J. Baldwin, M. Shkunov, I. McCulloch, M. Heeney, and W. Zhang. High mobility ambipolar charge transport in a cross-linked reactive mesogen at room temperature. *Appl. Phys. Lett.* **2005**, *87*, 172110.
36. S. R. Farrar, A. E. A. Contoret, M. O'Neill, J. E. Nicholls, G. J. Richards, and S. M. Kelly. Nondispersive hole transport of liquid crystalline glasses and a cross-linked network for organic electroluminescence. *Phys. Rev. B* **2002**, *66*, 125107.
37. K. L. Woon, M. P. Aldred, P. Vlachos, G. H. Mehl, T. Stirner, S. M. Kelly, and M. O'Neill. Electronic charge transport in extended nematic liquid crystals. *Chem. Mater.* **2006**, *18*, 2311–2317.
38. R. H. Friend, R. W. Gymer, A. B. Holmes, J. H. Burroughes, R. N. Marks, C. Taliani, D. D. C. Bradley, D. A. Dos Santos, and J. L. Brédas, M. Lögdlund, and W. R. Salaneck. Electroluminescence in conjugated polymers. *Nature* **1999**, *397*, 121–128.
39. A. C. Grimsdale, K. L. Chan, R. E. Martin, P. G. Jokisz, and A. B. Holmes. Synthesis of light-emitting conjugated polymers for applications in electroluminescent devices. *Chem. Rev.* **2009**, *109*, 897–1091.
40. A. M. Nardes, M. Kemerink, M. M. de Kok, E. Vinken, K. Maturova, and R. A. J. Janssen. Conductivity, work function, and environmental stability of PEDOT:PSS thin films treated with sorbitol. *Org. Electron.* **2008**, *9*, 727–734.

41. L. S. Hung, C. W. Tang, and M. G. Mason. Enhanced electron injection in organic electroluminescence devices using an Al/LiF electrode. *Appl. Phys. Lett.* **1997**, *70*, 152–154.

42. M. A. Baldo, D. F. O'Brien, Y. You, A. Shoustikov, S. Sibley, M. E. Thompson, and S. R. Forrest. Highly efficient phosphorescent emission from organic electroluminescent devices. *Nature* **1998**, *395*, 151–154.

43. A. Liedtke, M. O'Neill, S. M. Kelly, S. P. Kitney, B. Van Averbeke, P. Boudard, D. Beljonne, and J. Cornil. Optical properties of light-emitting nematic liquid crystals: A joint experimental and theoretical study. *J. Phys. Chem. B* **2010**, *114*, 11975–11982.

44. B. W. D'Andrade and S. R. Forrest. White organic light-emitting devices for solid-state lighting. *Adv. Mater.* **2004**, *16*, 1585–1595.

45. B. Schartel, V. Wachtendorf, M. Grell, D. D. C. Bradley, and M. Hennecke. Polarized fluorescence and orientational order parameters of a liquid-crystalline conjugated polymer. *Phys. Rev. B* **1999**, *60*, 277–283.

46. K. Ichimura. Photoalignment of liquid-crystal systems. *Chem. Rev.* **2000**, *100*, 1847–1873.

47. M. O'Neill and S. M. Kelly. Photoinduced surface alignment for liquid crystal displays. *J. Phys. D-Appl. Phys.* **2000**, *33*, R67–R84.

48. M. Schadt, H. Seiberle, and A. Schuster. Optical patterning of multidomain liquid-crystal displays with wide viewing angles. *Nature* **1996**, *381*, 212–215.

49. P. O. Jackson, M. O'Neill, W. L. Duffy, P. Hindmarsh, S. M. Kelly, and G. J. Owen. An investigation of the role of cross-linking and photodegradation of side-chain coumarin polymers in the photoalignment of liquid crystals. *Chem. Mater.* **2001**, *13*, 694–703.

50. A. P. Davey, R. G. Howard, and W. J. Blau. Polarised photoluminescence from oriented polymer liquid crystal films. *J. Mater. Chem.* **1997**, *7*, 417–420.

51. A. Bacher, P. G. Bentley, D. D. C. Bradley, L. K. Douglas, P. A. Glarvey, M. Grell, K. S. Whitehead, and M. L. Turner. Synthesis and characterisation of a conjugated reactive mesogen. *J. Mater. Chem.* **1999**, *9*, 2985–2990.

52. H. Thiem, M. Jandke, D. Hanft, and P. Strohriegl. Synthesis and orientation of fluorene containing-reactive mesogens. *Macromol. Chem. Phys.* **2006**, *207*, 370–381.

53. A. E. A. Contoret, S. R. Farrar, P. O. Jackson, S. M. Khan, L. May, M. O'Neill, J. E. Nicholls, S. M. Kelly, and R. J. Richards. Polarized electroluminescence from an anisotropic nematic network on a non-contact photoalignment layer. *Adv. Mater.* **2000**, *12*, 971.

54. M. Jandke, D. Hanft, P. Strohriegl, K. Whitehead, M. Grell, and D. D. C. Bradley. Polarized electroluminescence from photocrosslinkable nematic fluorene bisacrylates. In : *Proceedings of SPIE – the international society for optical engineering*, 2001, 338–347.

55. M. P. Aldred, A. E. A. Contoret, S. R. Farrar, S. M. Kelly, D. Mathieson, M. O'Neill, W. C. Tsoi, and P. Vlachos. A full-color electroluminescent device and patterned photoalignment using light-emitting liquid crystals. *Adv. Mater.* **2005**, *17*, 1368–1372.

56. M. P. Aldred, P. Vlachos, A. E. A. Contoret, S. R. Farrar, W. Chung-Tsoi, B. Mansoor, K. L. Woon, R. Hudson, S. M. Kelly, and M. O'Neill. Linearly polarised organic light-emitting diodes (OLEDs): synthesis and characterisation of a novel hole-transporting photoalignment copolymer. *J. Mater. Chem.* **2005**, *15*, 3208–3213.

57. S. W. Culligan, Y. Geng, S. H. Chen, K. Klubek, K. M. Vaeth, and C. W. Tang. Strongly polarized and efficient blue organic light-emitting diodes using monodisperse glassy nematic oligo(fluorene)s. *Adv. Mater.* **2003**, *15*, 1176–1180.
58. P. E. Dyer, R. J. Farley, and R. Giedl. Analysis of grating formation with excimer laser irradiated phase masks. *Opt. Commun.* **1995**, *115*, 327–334.
59. S. Allard, M. Forster, B. Souharce, H. Thiem, and U. Scherf. Organic semiconductors for solution-processable field-effect transistors (OFETs). *Angew. Chem. Int. Ed.* **2008**, *47*, 4070–4098.
60. C. R. Newman, C. D. Frisbie, D. A. da Silva, J. L. Bredas, P. C. Ewbank, and K. R. Mann. Introduction to organic thin film transistors and design of *n*-channel organic semiconductors. *Chem. Mater.* **2004**, *16*, 4436–4451.
61. R. Hamilton, J. Smith, S. Ogier, M. Heeney, J. E. Anthony, I. McCulloch, J. Veres, D. D. C. Bradley, and T. D. Anthopoulos. High-performance polymer-small molecule blend organic transistors. *Adv. Mater.* **2009**, *21*, 1166–1171.
62. H. Sirringhaus. Reliability of organic field-effect transistors. *Adv. Mater.* **2009**, *21*, 3859–3873.
63. I. McCulloch, M. Coelle, K. Genevicius, R. Hamilton, M. Heckmeier, M. Heeney, T. Kreouzis, M. Shkunov, and W. Zhang. Electrical properties of reactive liquid crystal semiconductors. *Jpn. J. Appl. Phys.* **2008**, *47*, 488–491.
64. I. McCulloch, W. Zhang, M. Heeney, C. Bailey, M. Giles, D. Graham, M. Shkunov, D. Sparrowe, and S. Tierney. Polymerisable liquid crystalline organic semiconductors and their fabrication in organic field effect transistors. *J. Mater. Chem.* **2003**, *13*, 2436–2444.
65. B. H. Huisman, J. J. P. Valeton, W. Nijssen, J. Lub, and W. Ten Hoeve. Oligothiophene-based networks applied for field-effect transistors. *Adv. Mater.* **2003**, *15*, 2002–2005.
66. R. J. Baldwin, T. Kreouzis, M. Shkunov, M. Heeney, W. Zhang, and I. McCulloch. A comprehensive study of the effect of reactive end groups on the charge carrier transport within polymerized and nonpolymerized liquid crystals. *J. Appl. Phys.* **2007**, *101*, 023713.
67. M. H. Hoang, M. J. Cho, D. C. Kim, K. H. Kim, J. W. Shin, M. Y. Cho, J. Joo, and D. H. Choi. Photoreactive π-conjugated star-shaped molecules for the organic field-effect transistor. *Org. Elec. Phys. Mater. Appl.* **2009**, *10*, 607–617.
68. F. Zhang, M. Funahashi, and N. Tamaoki. High-performance thin film transistors from semiconducting liquid crystalline phases by solution processes. *Appl. Phys. Lett.* **2007**, *91*, 063515.
69. F. Zhang, M. Funahashi, and N. Tamaoki. Thin-film transistors based on liquid-crystalline tetrafluorophenylter thiophene derivatives: thin-film structure and carrier transport. Organic Electronics: physics, materials, applications **2009**, *10*, 73–84.
70. C. D. Müller, A. Falcou, N. Reckefuss, M. Rojahn, V. Wiederhirn, P. Rudati, H. Frohne, O. Nuyken, H. Becker, and K. Meerholz. Multi-colour organic light-emitting displays by solution processing. *Nature* **2003**, *421*, 829–833.
71. S. Reineke, F. Lindner, G. Schwartz, N. Seidler, K. Walzer, B. Lüssem, and K. Leo. White organic light-emitting diodes with fluorescent tube efficiency. *Nature* **2009**, *459*, 234–238.
72. M. Carrasco-Orozco, W. C. Tsoi, M. O'Neill, M. P. Aldred, P. Vlachos, and S. M. Kelly. New photovoltaic concept: Liquid-crystal solar cells using a nematic gel template. *Adv. Mater.* **2006**, *18*, 1754.

73. W. C. Tsoi, M. O'Neill, M. P. Aldred, S. P. Kitney, P. Vlachos, and S. M. Kelly. Distributed bilayer photovoltaics based on nematic liquid crystal polymer networks. *Chem. Mater.* **2007**, *19*, 5475–5484.
74. L. Zeng, F. Yan, S. K. H. Wei, S. W. Culligan, and S. Chen. Synthesis and processing of monodisperse oligo(fluorene-co-bithiophene)s into oriented films by thermal and solvent annealing. *Adv. Funct. Mater.* **2009**, *19*, 1978–1986.

CHAPTER 10

Liquid Crystals of Carbon Nanotubes and Carbon Nanotubes in Liquid Crystals

GIUSY SCALIA

Department of Nanoscience and Technology, Seoul National University, Gyeonggi-do, Korea

10.1 INTRODUCTION

The combination of liquid crystals (LCs) and carbon nanotubes (CNTs) occupies a special place among the uses of liquid crystals in non-display applications because of the related intriguing scientific issues but also for the very appealing applications. Many articles have been published on different aspects of the topic and a few review articles have appeared [1–7].

Nanoparticles have attracted general attention and carbon nanotubes have come out from the mass for their peculiar and outstanding properties making them one of the most interesting materials of the century. LCs and CNTs seem to belong to two different worlds but they share more similitarities than expected. They are both anisotropic materials and as for LCs the macroscopic use of the nanotube properties relies on a macroscopic control of the tube alignment. This need brings these two worlds together but the interest of their combination goes well beyond.

The topic combines very different research fields bringing along their own specific issues and terminology. It is unavoidable in the early time of the meeting of these two worlds to find now and then in articles imprecise language or terminology from scientists from one community on the part related to the other community. However, this cross-fertilizing process brings new knowledge and applications creating a new research area of great breadth and with its own identity.

Let us first of all introduce carbon nanotubes: they are seamless cylinders of carbon atoms in a honey-comb arrangement. They can be visualized as formed by rolling up a graphene sheet. These tubes possess extremely high aspect ratio with

Liquid Crystals Beyond Displays: Chemistry, Physics, and Applications, Edited by Quan Li.
© 2012 John Wiley & Sons, Inc. Published 2012 by John Wiley & Sons, Inc.

diameters of the order of nanometers and variable length ranging from micrometer up to centimeters. If we consider a moderate length nanotube, let us say 1 micrometer long and with 1 nm diameter, its aspect ratio would correspond in our length-scale to an object with diameter of 1 m and length of 1 km! It is quite impressive to see that an object of such an aspect ratio is in fact stable. To be so it must possess superior mechanical properties.

The article by Ijima [8] in the early 90s boosted an enormous interest toward this nanoscale allotrope of carbon. The extreme aspect ratio makes CNTs quasi-one-dimensional objects, very interesting for basic science. Carbon nanotubes have also displayed exceptional properties [9] that together with their reduced dimensions make them very attractive for innovative applications. They can consist of a single wall, the single-wall CNTs (SWCNTs) or be composed of several concentric layers, a sort of Russian doll, the multi-wall CNTs (MWCNTs). In Figure 10.1 transmission electron microscopy (TEM) images of carbon nanotubes with one wall, single-wall (SWCNTs) on the left, and a MWCNT, on the right are reported. Because of the multiple walls that increase the diameter, MWCNTs typically have a lower aspect ratio than the SWCNTs. It is worth to point out that the progress in the synthesis of CNTs has allowed the realization of samples containing nanotubes with mainly two walls, thus introducing the concept of double-wall CNTs (DWCNTs).

Thanks to the graphitic structure CNTs have extraordinary mechanical properties. They are resilient against stresses with exceptional density-normalized Young's modulus and tensile strength. In SWCNTs those were found some 20 and 60 times, respectively, higher than those of steel [10]. According to the way the graphene layer is "rolled up" the nanotubes have different electronic properties. The identification of the type of nanotube is made via a couple of integer numbers usually indicated with the letters n and m respectively, cf. Figure 10.2. These are the coefficients in the base of the graphene unit vectors, defining the C vector that indicates how the CNT is

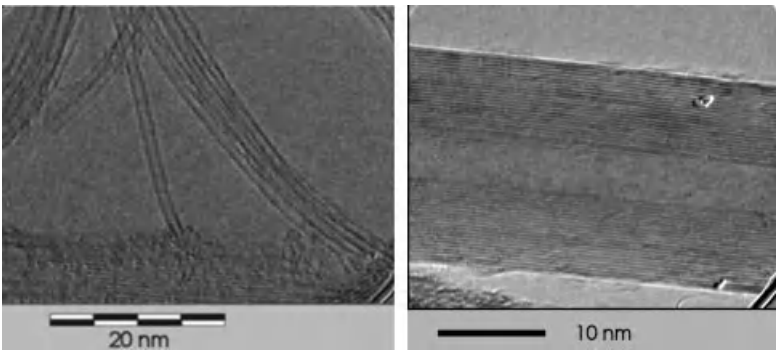

FIGURE 10.1 Images of CNTs by transmission electron microscopy (TEM). On the left an example of single-wall CNTs, produced through laser ablation by B. Hornbostel and imaged by J. Cech. On the right an example of MWCNTs, produced by arc-discharge by M. Haluska, imaged by J. Cech.

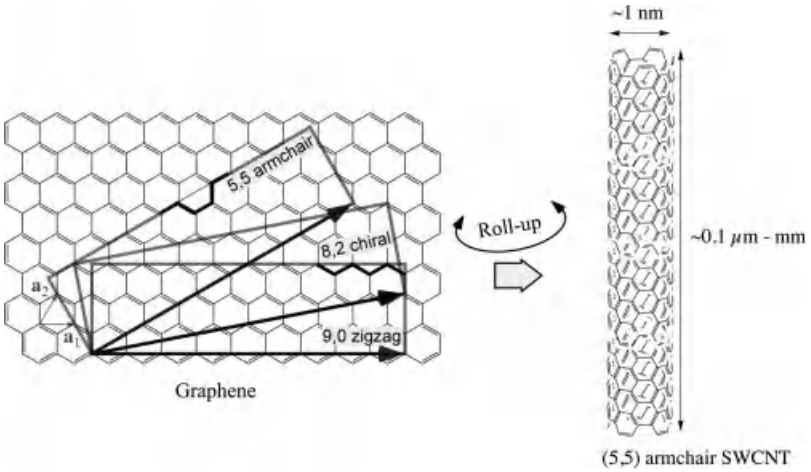

FIGURE 10.2 A single-wall carbon nanotube (SWCNT) can be viewed as a graphene sheet rolled up into a tube. Depending on the roll-up direction (n, m) the tube can be achiral (5.5 and 9.0 for examples, the former giving the armchair tube on the right) or chiral (any direction between the achiral ones allowing closure into a seamless tube, for example the 8.2).

rolled up. Since there are many different ways or directions of rolling up graphene into a tube, nanotubes with many different characteristics are present in ordinary samples. The nanotubes with $n = m$ are called as armchair from the profile of the arrangement of the carbon atoms on the tube circumference, perpendicular to the axis, while those with $m = 0$, for a similar reason, are called as zig–zag. These types based on their wall structures are not chiral. Among these two extreme structures a multitude of other arrangements can be obtained by rolling up at intermediate angles generating tubes that are instead chiral. All these intermediate forms have their own (n, m) indices and thus their own properties. In general, CNTs can be metallic or semiconducting, the two categories appearing at a ratio of 1:2, with the width of the band-gap of the semiconducting nanotubes proportional to the inverse of their diameter. The electrical conducting properties of CNTs are highly interesting. They exhibit an electron mobility of 100,000 cm^2/Vs, while the mobility in silicon is about 450 cm^2/Vs. They can carry a current density in the order of 10^{10} A/cm, orders of magnitude higher than copper with 10^6 A/cm^2. If the nanotubes have no defects the transport is ballistic, that means without scattering. The thermal conductivity is also remarkably high. In MWCNTs it has been measured to be more than 3 kW/mK [10], greater than that of natural diamond.

Because of their extraordinary properties many applications have been envisaged. The mechanical properties are attractive in composites or for realizing extra strong fibers. Metallic CNTs are attractive as nanowires in electronic circuits while the semiconducting can be used as transistors. Their use as heat sink in electronic circuits is also proposed together with the use as filler for improving the thermal properties of materials. Other potential uses are tips for AFM, thanks to their extreme aspect ratio and the ultra-small diameter, as actuators, as drug delivery system, others based on

their field emission properties and many more. In fact their excellent mechanical, electrical, and thermal properties together with their size make them ideal candidates in nanotechnology and for the realization of novel materials.

Despite the exceptional properties some issues need to be solved for their successful implementation in devices and materials. The presence of impurities and of defected tubes is a very important issue. Also there can be tubes not perfectly straight but bent, kinked, or branched. Defects in the tubes not only worsen their electrical, thermal, and mechanical properties but also influence their order in liquid crystals. As produced CNT samples contain, beside nanotubes, metal catalysts (if used for the CNT growth), amorphous carbon, or graphitic particles. Their presence can affect the properties of composites or the formation of LC phases. Caution must be taken about the presence of these by-products when using as-produced samples. Methods have been developed to purify CNTs and it is possible to purchase purified tubes of different grade or doing it in your own lab. Assessing the purity is not a trivial task and requires a combination of techniques but it is of key importance since the final performance and properties can be strongly affected by the presence of by-products. Ordinary samples contain nanotubes with different properties, different diameters, and also different length. This is a serious problem for carbon nanotube research because it brings a lack of control of the desired properties. The attempts to control the CNT type during growth, in order to have monodispersity and thus CNTs with specific properties, have so far not been successful. More promising are post-growth methods aimed to fractionate samples according to the tube length and diameter.

The CNT properties are excellent but mainly so along the nanotube axis, the extreme anisotropic shape of CNTs bringing strong anisotropy of their properties. The consequence is that the control of the CNT orientation is of great importance for the successful application of CNTs in devices or for the realization of new materials and for improving their performance [11–18]. The control of CNT alignment is thus an important issue and different approaches have been developed so far. Several review articles on the topic can be found in the literature, among them [19, 20]. The alignment methods can be divided into two major groups. The first is based on the realization of CNTs aligned during growth producing vertically aligned tubes referred as "forests" or CNTs planarly aligned on the substrate [21–24]. However, this approach has the disadvantage that CNTs with desired properties, degree of purification or sorted according to the size using the new wet-processing procedures cannot be chosen.

Diverse approaches have been used for obtaining post-growth alignment like application of electric, magnetic fields, mechanical stretching, or other types of directional forces [25–35]. Post-growth alignment methods are preferable to aligned growth because they can profit of the advances in purification and fractionation offering a final material with improved quality. The above mentioned methods of post-growth alignment are often bringing unsatisfactory results or being awkward or not applicable for all CNT types. An easy, versatile and general way of aligning CNTs is still lacking. In the quest of control of the orientation liquid crystal phases or liquid crystalline materials can play a crucial role. The liquid crystal route can be an effective and innovative alternative for manipulating and controlling the organization of the nanotubes.

Carbon nanotubes meet LCs also in other fields. CNTs can form transparent and conductive networks that have been proposed as replacement for ITO, for example in LCDs. They offer the advantage of better mechanical performance and flexibility making them compatible with flexible substrates. On the other hand, they were also used as alignment layer for LCs as first shown by Samulski and co-workers [36]. Carbon nanotubes have also been used as dopant for liquid crystals for enhancing the display related properties [37–46]. Although these topics are interesting and constitute another meeting point with liquid crystal science, they are related to display applications thus their treatment is out of the scope of this book.

In this chapter, the dispersion of CNTs will be discussed due to its key importance in any use of CNTs, giving also space to specific LC related issues. Then the LC phases formed by CNTs will be discussed followed by a short treatment of inclusions of CNTs in low-molar mass thermotropics, then CNTs in lyotropics and finally in polymeric systems. The vast majority of the works in the field have been of experimental nature with a few exceptions of theoretical articles [47–55].

10.2 DISPERSION OF CARBON NANOTUBES

One of the greatest challenges in any work on carbon nanotube suspensions is to efficiently separate the tubes and to keep them separated over long times within the intended host. Since carbon nanotubes are particles consisting entirely of carbon in an aromatic arrangement with an exceptional specific surface area they tend to aggregate very strongly due to very strong van der Waals interactions between adjacent tubes. There are extremely few organic solvents that can be considered useful as carbon nanotube hosts, although acceptable performance is provided by N-methylpyrrolidone (NMP) [56]. More recently, even better results were found with cyclohexylpyrrolidinone (CHP) [57]. The most common approach is otherwise to counteract nanotube aggregation by taking advantage of the hydrophobic effect, coating the nanotubes with low-molar mass surfactants [58] or amphiphilic polymers [59, 60] and use water as the dispersion medium. The amphiphiles adsorb onto the hydrophobic nanotube surface with their non-polar components, directing their polar groups outwards toward the aqueous host phase. This first of all renders the 'effective' nanotube surface, as experienced by the world outside the wrapped CNT, hydrophilic, second, the hydrophilic surfactant head groups or polymer chains introduce a repulsive force between the nanotubes, either of electrostatic type (for ionic head groups) or of entropic type (for flexible chains that get entangled in case of close nanotube contact, with a consequent entropy penalty), cf. Figure 10.3.

When the dispersion medium is a liquid crystal the amphiphile-based approach is useful for lyotropic liquid crystal hosts [61–73]. A potential problem is however that the large number of micelles present in a surfactant-based lyotropic liquid crystal phase can act as 'depletants', that is they may induce aggregation of the nanotubes by means of depletion attraction [74]. As the nanotube-free micelles are repelled from those containing nanotubes, the particles and their surroundings constitute excluded volumes (depleted regions) for the micelles. This leads to an entropy penalty that can

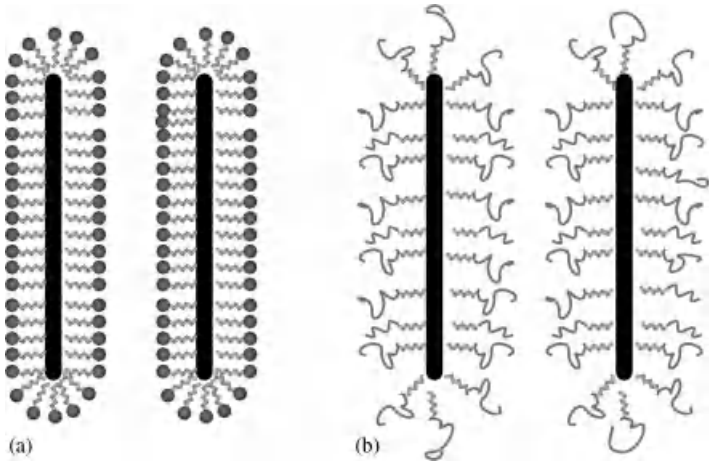

FIGURE 10.3 Schematic illustrations of how carbon nanotubes (black rods) are kept dispersed by adsorbed ionic (left) or nonionic (right) surfactants.

be relieved if the CNTs aggregate, giving rise to the depletion attraction phenomenon. It seems to be of particular importance when using the commonly employed anionic surfactant sodium dodecyl sulfate (SDS) for aiding the dispersion, whereas the cationic surfactant hexadecyl trimethylammonium bromide (CTAB) turns out to be much less susceptible to induce depletion attraction [75, 76]. In fact, the beautiful cryo-TEM work of Nativ-Roth and co-workers revealed that SWCNTs dispersed in CTAB tend to align uniformly within small clusters at intermediate surfactant concentrations, well above the critical micelle concentration but below the threshold for development of a macroscopically ordered liquid crystal phase. In their most recent work [77], they also showed that this type of local nanotube alignment occurs also in suspensions stabilized by anionic surfactants of intermediate concentrations, or in suspensions combining ionic and nonionic surfactants. The mechanism for this unexpected local ordering is not yet entirely clear but the authors propose that van der Waals interactions between nanotubes coated by surfactants that form a hemimicellar structure around the tubes, giving a periodically varying charge density, may be at the origin of the phenomenon.

Nevertheless, even when SDS is used CNTs can be kept well dispersed over fairly long time in the lyotropic host [69, 71], most likely due to the high viscosity of the host phase. Furthermore, improvement was achieved by combining anionic surfactants for dispersing the nanotubes with cationic surfactants for forming the liquid crystal phase: since the excess micelles of the host phase are then attracted rather than repelled from the nanotubes, they will act more as 'buffers' against aggregation than as depletants. Using sodium dodecyl benzene sulfonate (SDBS) for dispersing the tubes and CTAB for forming the liquid crystal phase very good results were obtained [61, 66, 67], as will be further discussed below. Furthermore, interesting alternatives for dispersing CNTs in water for example, DNA [59, 66, 78–86] and bile salts [87, 88].

For thermotropic hosts other solutions are required. The problem is here that both nanotubes and host are non-polar, hence it is difficult to design an appropriate amphiphilic molecule structure. On the other hand, many thermotropic liquid crystals are actually surprisingly good solvents for carbon nanotubes [89, 90]. For achieving a first rough dispersion of the CNTs in a thermotropic nematic it is in fact sufficient to just stir the sample over the time scale of an hour (for high-quality results sonication is, however, required). Scalia and co-workers also found using Raman spectroscopy that the commonly used cyanobiphenyl mesogens interact with carbon nanotubes, as evidenced by a shift in the Radial Breating Mode (RBM) wavenumber [91]. In the first systematic study of CNT dispersion in thermotropic liquid crystals, Schymura et al. found that the performance of the commonly used nematic mixture E7 is fully comparable with NMP and the negative anisotropy mesogen n-(4-methoxybenzylidene)-4-butylaniline (MBBA) was even somewhat better [90], as shown in Figure 10.4. However, the exact molecular structure of the mesogen is very important, dispersion for example, in pure 5CB (the majority component of E7) yielding much poorer results. This study also revealed that the nematic state is beneficial to dispersion, hence one should not heat a carbon nanotube-doped thermotropic liquid crystal to its isotropic state. The time to nanotube aggregation is then drastically reduced.

Despite the relatively good performance of some liquid crystals as CNT hosts, long-term stability of dispersions of pristine carbon nanotubes in a thermotropic liquid crystal has so far not been achieved. There is, thus, a clear need for new mediator substances that aid dispersion in non-aqueous solvents, specifically thermotropic liquid crystals. This approach is typically to combine a CNT 'anchor unit' with a moiety that interacts well with the host liquid, possibly through a spacer unit. The main difficulty lies in identifying an anchor unit that is truly effective in non-aqueous hosts, the most common choice being pyrene. Its similarity with a graphene sheet gives it the ability to adsorb strongly to the nanotube surface through aromatic interactions, minimizing the alteration of the electronic properties of CNTs. Meuer et al. used this moiety as anchor unit in their polymers tailor-designed for solubilizing MWCNTs in tetrahydrofuran (THF) [92]. The pyrene unit was attached with either a poly(methyl methacrylate) (PMMA) or a poly(ethylene glycol) (PEG) chain, rendering the nanotubes effectively 'hairy'. At high-nanotube concentration the PEG–pyrene-solubilized nanotubes even formed a liquid crystal phase. Pyrene was also used as CNT anchor in other polymer mediator molecules specifically designed for aiding CNT incorporation into polymeric hosts [93]. We will discuss this work below in the context of CNT-loaded liquid crystalline polymers.

A very recent and highly interesting approach for improving the dispersion of nanotubes in liquid crystals is to synthesize molecules specifically designed for mediating between the nanotube and the liquid crystal matrix. This route has so far been explored by Kühnast et al. [94], synthesizing low-molar mass mediator molecules where a pyrene CNT anchor unit was linked through an oligoethylene spacer with a cyanobiphenyl mesogen, and by Kimura et al., who used an oligo (phenylenevinylene) mediator molecule terminated at both ends with cyanobiphenyl moieties [95]. In [94] dramatic improvement of the stability of SWCNTs dispersed in

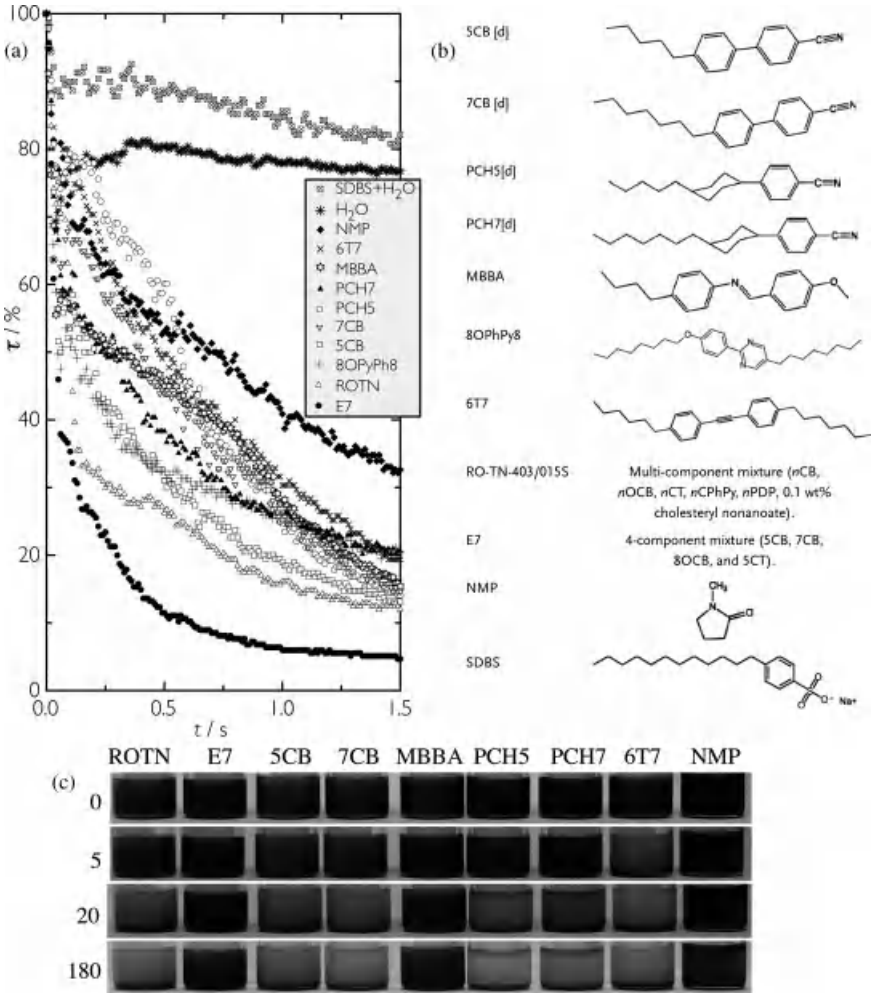

FIGURE 10.4 Thermotropic liquid crystals show surprisingly good performance in dispersing SWCNTs at the early stage of sonication, as shown in panel (a). The light transmitted through the sample is monitored at the beginning of the tip sonication process. Decrease of transmission indicates that more and more CNTs are getting into the host, thus, absorbing more light. Isotropic solvents including an aqueous SDBS solution are used as reference. In (b) the LC molecular structures employed in the study are shown. Suspensions of SWCNTs in different LCs and in the isotropic organic solvent NMP used as reference are shown in (c) for different centrifugation times. E7 and MBBA behave comparably well to NMP. For further details. Reprinted with permission from [90].

a standard commercial nematic thermotropic mixture was observed. The oligoethylene spacer unit turned out to be critical for the performance, mediator molecules with standard alkyl chains between pyrene and cyanobiphenyl units having almost no positive effect whatsoever. Most likely this difference is due to

the fact that alkyl chains tend to adsorb strongly on a graphite-like surface [96]. The oligoethylene chain cannot do this; hence it is efficient in separating the cyanobiphenyl unit from the nanotube as it should. The efficient mediators exhibit no liquid crystalline phase on their own, in contrast to the variations with alkyl spacers which exhibited nematic and/or smectic mesophases. Whether this difference plays a role for the difference in effectiveness is not yet clarified.

The longer mediator molecule synthesized by Kimura et al. [95] does exhibit liquid crystal phases, of smectic type. It does not contain an anchor group, such as pyrene, but instead the whole conjugated oligomer wraps in a helical fashion around the nanotube efficiently, with the cyanobiphenyl termini promoting spontaneous liquid crystalline organization of the system. With the help of these new mediator molecules added at minimum concentration (the suspension was filtered after sonication to remove excess oligomers) the team could achieve very good nanotube suspension in chloroform, stable over several months. Interestingly, when they added more of the oligomer to the suspension, phase separation occurred, the nanotubes slowly precipitating into a phase which turns out to have the same liquid crystalline phase sequence as the pure oligomer. In other words, the nanotubes are incorporated into the liquid crystal phase of the oligomer used for stabilizing the suspension. Although no large-scale aligned samples were reported, the work is certainly very interesting and holds promise for future extensions. Unfortunately no mention is given as to whether the oligomer can stabilize a CNT suspension in a regular low-molar mass thermotropic liquid crystal.

A polymer mediator was used also by Lee et al. for dispersing nanotubes in organic solvents [97]. In their case the conjugated polymer P3HT, commonly studied in the field of organic electronics, was used for stabilizing nanotube suspensions in dichlorobenzene. This approach resulted in very good dispersions, with a maximum SWCNT loading of 2.75 mg/mL. In fact, these suspensions were so good that they spontaneously formed a lyotropic nematic liquid crystal phase, an issue we will return to below.

An alternative and more drastic approach is to functionalize the CNTs covalently, oxidizing them and possibly attach tailored moieties for enhancing compatibility with the matrix [98]. This approach has been particularly important in the field of CNT–polymer composites and we will thus discuss this approach briefly when discussing liquid crystalline polymers as hosts for carbon nanotubes. A related approach is the use of superacids for solubilising CNTs and forming lyotropic phases as will be discussed later.

Related to the issue of nanotube dispersion is the procedure to purify the nanotubes. No synthesis-based method produces only carbon nanotubes and the vast majority in fact leads to a quite substantial fraction of impurities. Thus, it is imperative for many applications that the nanotubes are purified. Often this is done by chemical as well as mechanical treatment, the latter typically being dispersion followed by centrifugation. Better-dispersed nanotubes remain in suspension whereas large-scale aggregates and impurities are largely collected in the sediment. When doing work on CNT–liquid crystal composites it can be quite important to consider the possible effects of impurities because many experiments (e.g. conductivity measurements) do not necessarily distinguish CNTs from certain impurities.

10.3 LIQUID CRYSTAL PHASES OF CARBON NANOTUBES

An interesting processing route for obtaining ordered CNT materials is by induction of LC phases. This approach is technologically relevant because it is based on solution processing, quite attractive from an applicative point of view. The liquid crystalline phase is very important for the realization of extra-strong fibers of poly-(*p*-phenylenebenzobisoxazole), better known with its trademark name Kevlar. Therefore, LC phases can be useful for the realization of CNT materials with improved mechanical properties. Finally, CNTs can be used as model systems for studying the formation of LC phases of other anisotropic nanoparticles.

Carbon nanotubes, due to their elongated shape, are expected to form lyotropic liquid crystal phases when dispersed in liquids. The reason is based on the classical Onsager's theory of rigid rods forming liquid crystal phases at high-rod concentration [99, 100]. They indeed form LC phases as first shown by Windle and co-workers [101]. If the aspect ratio of the rods, that is, the ratio of the length and the diameter of the rods, and their concentration are high enough the free energy of the system is minimized if the rods form a liquid crystal phase. The loss in rotational freedom, that is, reduced orientational entropy, is compensated by a higher gain in translational entropy (the latter corresponds to a decrease of excluded volume). The formation of nematic lyotropic phases occurs above a threshold concentration, predicted by the Onsager theory being dependent on the dimension of the rods, specifically the volume fraction $v = 3.3\ d/L$, where d is the diameter of the rods and L is their length. Research on LC phases formed by CNTs have been developed mainly by the Windle [101–103], Poulin [74, 80, 104], and Smalley–Pasquali [105–107] and co-workers using multi-wall CNTs as well as single-wall CNTs. Based on Onsager's theory we can estimate the amount of SWCNTs needed considering a typical SWCNT density of 1.5 g/mL and a SWCNT d/L ratio of 10^{-3}. We would thus expect nematic phase formation already at about 0.5 wt.% loading. Since the aspect ratio of MWCNTs is lower than SWCNTs, we would expect for MWCNTs some ten times higher loading required. The reported experimental results show that only MWCNTs [101–103] come close to the theoretical predictions by Onsager, while higher loading of SWCNTs is needed for the formation of LC phases [80, 104] with some exceptions [104, 108] coming close to the theoretical prediction of 0.5 wt.%. There are several reasons that can influence the discrepancy between theory and experiments. One important problem is the difficulty in completely separating the nanotubes from each other: they tend to form ordered bundles that, as an overall, clearly possess a lower aspect ratio than isolated tubes. Thus, even if the average SWCNT d/L ratio may be on the order of 10^{-3}, the aspect ratio of bundles can be substantially lower affecting then the loading of nanotubes needed for the formation of the LC phase. When successful dispersion of individual tubes has been achieved, this has in almost all cases been at the cost of severe cutting of the tubes, a typical negative side effect of the high-power sonication or of aggressive chemical treatments required for breaking up the CNT aggregates or preventing their re-aggregation.

In the Onsager theory the rods are not interacting and the only interaction is of the steric type. This is absolutely untrue for carbon nanotubes that strongly attract each

others because of van der Waals forces. If the nanotubes are chemically treated or if there are surfactants or other type of molecules wrapping them up to counteract aggregation, the analysis of the forces entering into play becomes even more complex, not being usually possible to consider a balancing off with the attractive forces. The surfactants not only introduce repulsive electrostatic forces but also form a surrounding layer that together with the consequent double layer alter the effective dimension of the nanotube. Considering the diameter of the nanotubes, which is in the nanometer range, the "effective" diameter can be several times the original CNT diameter. On the one hand, the surfactant encapsulation increases the effective volume fraction considerably (at constant SWCNT weight fraction), on the other it does so at the expense of a great reduction in aspect ratio (a single surfactant molecule is typically twice as long as the SWCNT is thick).

The main result anyhow is that in general the interaction forces are all but negligible, playing a fundamental role in keeping the nanotubes apart or attracting them. Attractive forces exist in bare nanotubes promoting aggregation but repulsive forces are used in CNT dispersion for avoiding their reaggregation to achieve a high quality dispersion for example, a high loading with individual tube dispersion. Interestingly each of the three main groups active in the field has initially chosen its own approach for the dispersion of CNTs. Whereas Windle and co-workers oxidized their MWCNTs to make them water soluble [101–103] the Smalley and co-workers dispersed pristine SWCNTs in super acids [105–107, 109]. They have also used chlorosulfonic acid to dissolve SWCNTs, DWCNTs, and MWCNTs from different sources obtaining individual tube dispersions. They have observed that tubes with defects disperse worse and only the higher quality tubes were entering in the formation of LC phases [110]. Moreover, LC phases were also observed for longer SWCNTs as well MWCNTs (100 and 500 μm long, respectively) unlike other existing studies. The Poulin approach was instead to use DNA [80] or hyaluronic acid [104] for dispersing SWCNTs. In all cases nematic LC phases were achieved as verified by birefringent textures of the fluid suspensions detected in polarizing microscopy. Windle et al. also imaged disclinations in the nematic director field beautifully using scanning electron microscopy on samples from which the solvent had been evaporated [101, 103, 111]. The liquid crystalline structure remained intact upon drying. In this way they could have a closer look at the local arrangement and follow the director orientation visualizing almost the constituent building blocks of the LC phase. The authors found $\frac{1}{2}$ disclinations with both sign, namely $+1/2$ and $-1/2$ disclinations.

The Onsager theory was developed for monodisperse rods, meaning rods possessing the same dimension. This assumption is not valid for typical samples of CNTs. A treatment taking polydispersity into account reveals that at a certain rod concentration a biphase region isotropic + nematic appear with the rods of proper dimension and straightness forming the LC phase while the curved or too short rods will segregate into the isotropic region [100, 103], cf. Figure 10.5. This behaviour could be interesting to obtain size fractionation of the nanotubes according to the length [103]. After centrifugation the isotropic phase will be at the upper part while the nematic is on the bottom. The supernatant can then be removed and the procedure can be repeated several times leading to a narrower and narrower nanotube length distribution.

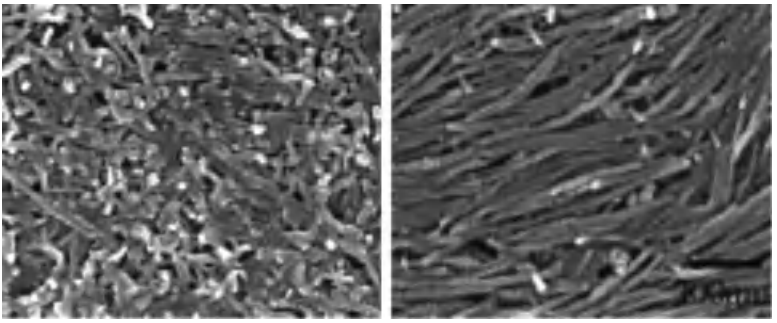

FIGURE 10.5 Size segregation of CNTs induced by phase separation. In the left image isotropic phase composed of shorter and probably more defected CNTs. On the right CNTs with dimension and quality suitable for the formation of LC phases. *Source*: Reprinted with permission from Zhang et al. [103]. Copyright (2006) American Chemical Society.

This procedure is feasible on lab scale and is scientifically very interesting, but it might be too complex and time consuming to be applied industrially.

The threshold value for the formation of the nematic LC phase was estimated by Song et al. [101] from the concentration of nanotubes needed for reaching percolation of droplets of nematic phase, within an isotropic background, to be around 4.3 vol.%. The transition from the isotropic to the liquid crystal phase was also studied for SWCNT suspensions [107]. The corresponding textures were again recognized by polarizing optical microscopy. A wide range of isotropic–nematic phase coexistence was observed by both groups. As discussed previously the reason for the bi-phase region lies in the polydispersity of size of carbon nanotubes [51, 112]. The higher the CNT polydispersity, the wider the region of phase coexistence.

Another important divergence from the theory is related with the rigidity: Onsager theory assumes perfect rod rigidity which is not at all true especially for long nanotubes. This would suggest that the formation of LC phases would not be realizable for very long and thin nanotubes. The relation between size of carbon nanotubes and formation of LC phases is investigated by Song and Windle [111]. Systematic studies with nanotubes of different length and diameters would be highly desirable but not currently feasible due to the lack of availability of such highly size-controlled samples. The authors investigated three samples of multi-walled CNTs not finding a straightforward relation between aspect ratio and threshold value of concentration for formation of LC phases. However, the texture and the density of defects of the resulting nematic phase were very different indicating a strong effect of the dimensions of the CNTs on the LC phase. They could distinctly observe that shorter and thicker CNTs, having also the lowest aspect ratio, aligned in a more continuous and packed way than the others, resembling ordinary nematics. Interestingly, for the other two cases, that is, MWCNTs with higher aspect ratio and with greater length, respectively, the authors observed a bending of the nanotubes themselves around the defects instead of the typical change of orientation of the director resulting from the almost continuous change of direction of straight rods.

The density of defects was also different in different samples. This outlines the importance of not only the aspect ratio but also of each dimension of the rods.

In terms of applicability, a drawback with the method of inducing LC phase behavior directly in CNT suspensions is the control of the director orientation, a prerequisite if one wants to use the method to deposit CNTs on a substrate along specific directions. The drying process can influence the alignment of CNTs as shown in Ref. [113] but even if scientifically interesting this does not appear straightforwardly usable for large scale alignment. Shear flow can induce alignment and this can be frozen in fibers with a high degree of alignment, as evidenced by the successful solution spinning of carbon nanotube fibers from a liquid crystal phase of CNTs [11, 51, 106, 109, 114, 115]. Zamora-Ledezma et al. [68] have shown that it is possible to impose a common unidirectional orientation in films also by shearing SWCNT lyotropic LCs, preserving the order parameter in the sample after drying. Their thorough analysis of the anisotropic properties demonstrates not only the achieved uniform alignment but also that their typical order parameters are in the order of 0.1–0.15. This value should be compared to the expected value from Onsager's theory at isotropic–nematic phase transition being <0.79. The much lower value observed experimentally outlines the high complexity of typical CNT systems and of SWCNTs in particular due to the possible formation of viscoelastic systems and to the tube "waviness" rather than rigidity.

The importance of the straightness and rigidity of SWCNTs for forming LC phases was further investigated by Puech et al. [108]. Initially their SWCNTs did not show a real tendency to form ordered phases because of the conformation of the starting SWCNTs comprising defected tubes with branches or kinks and long tube that would not keep themselves straight. After systematic sonication and centrifugation steps they obtained shorter tubes that formed LC phases with a dramatically improved order parameter. In dried samples they obtained a value of $S = 0.55$. In Figure 10.6a the tubes are shown after a first sonication and centrifugation treatment,

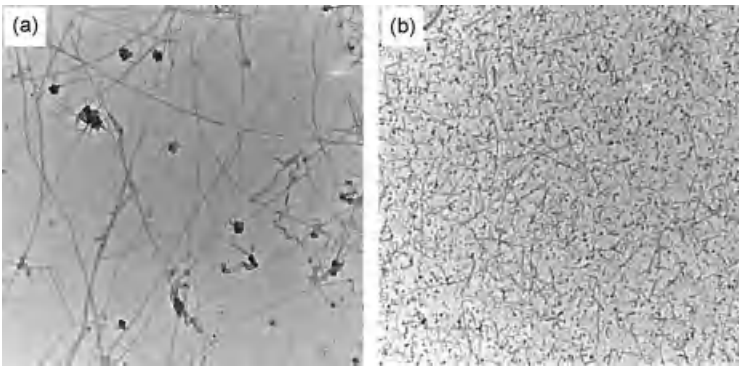

FIGURE 10.6 TEM images of CNTs. In (a) they were sonicated for 30 min and ultracentrifuged for 45 min while in (b) the sonication was performed for 3 h followed by 3 h of ultrascentrifugation. The size of the image is $1.5 \times 1.5\ \mu m^2$. *Source*: Reprinted with permission from Puech et al. [108]. Copyright (2011) American Chemical Society.

exhibiting branches and bending while in Figure 10.6b after long treatment they appear shorter, thinner, and straighter. Phase transitions can be used for sorting CNTs segregating the shorter or less straight and perfect into the isotropic phase. This strategy was used for further enriching the LC phase with tubes with size in the fluid phase and shape more suitable for building up LC phases. In this way the authors could measure the order parameter in the nematic regions, surrounded by the isotropic phase, forming droplets in shape resembling the tactoids, discussed theoretically in Ref. [88]. In these islands the order parameter was distinctly higher, reaching the value of 0.65, closer to the value predicted by Onsager theory. This work confirms the importance of the quality and dimension of the CNTs for being good "building blocks" of LC phases.

The above mentioned work by Lee et al., in which SWCNTs were suspended in dichlorobenzene with the help of the conjugated polymer P3HT [97] is interesting because it constitutes also a case of nematic lyotropic liquid crystal formation by the nanotubes where a uniform alignment could easily be achieved over a large monodomain by shearing. The authors could confirm the uniform alignment of the nanotubes by atomic force microscopy and polarized optical absorption spectroscopy. Moreover, they placed the thermotropic nematic liquid crystal 5CB in contact with a film prepared from the shear-aligned lyotropic CNT suspension, achieving uniform alignment of the 5CB director along the nanotubes, that is the nanotube film acts as alignment layer for the thermotropic nematic director.

A slightly different approach to achieving lyotropic liquid crystal formation from CNTs was presented by Islam et al. [116]. They prepared low-concentration nanotubes suspensions in an *N*-isopropyl acrylamide gel and then induced the ordering through a volume–compression transition. Although the resulting films are actually not fluid any more (they are in a gel state) they can be discussed in terms of nematic ordering. The ordering of the nanotubes can be quite impressive, reaching orientational order parameter values of about 0.8.

10.4 CARBON NANOTUBES ALIGNED BY THERMOTROPIC LIQUID CRYSTALS

Inclusions of rods with ferromagnetic properties, in thermotropic LCs where investigated first theoretically envisaging a possible improvement of the reorientational LC properties [117, 118]. These rods had all dimensions large enough compared with the LC molecules to be successfully described within the continuum theory. This situation is quite different from the inclusion of CNTs that have length much larger than the LC molecules but diameters in the nanometer range. Interestingly, the research on CNTs in thermotropics has evolved in the opposite way compared to the early seventies, starting, and developing mainly with experimental works, with some already mentioned theoretical exceptions.

The effect on phase transitions, optical, photorefractive, and electro-optic properties of LCs have been widely investigated [46, 89, 98, 119–140]. The vast majority of works in the field deals with nematics with some exceptions [29, 89, 130, 141–145]. In a recent series of experiments conducted by Rosenblatt and co-workers [142–144] multiwall carbon nanotubes were explored in their role as chiral dopants of liquid crystals. The authors found small but nevertheless clear-cut evidence of chirality transfer from the nanotubes to the liquid crystal both in smectic and nematic host phases. If the chiral species (here the nanotubes) is present with perfectly equal amounts of left- and right-handed enantiomers, that is, as a perfect racemate, such effects cannot occur. Usually carbon nanotube samples are considered as racemic because the synthesis procedures should not introduce any asymmetry and since any type of CNT chirality control is in fact extremely challenging. The results of the Rosenblatt team indicate, however, that at least this source of multiwall carbon nanotubes produces the tubes with a slight enantiomeric excess. Since, the scope of this book is non-display applications, we will hereby focus on the use of thermotropic liquid crystals for CNT organization. In fact, using thermotropic LCs as host the liquid crystalline organization can be transferred to the nanotubes. The transfer of order is a very interesting and effective way to align CNTs permitting to explore routes towards aligned.

CNTs are notoriously difficult to organize thus their control through a matrix is an attractive and innovative strategy. If arrays of aligned tubes are desired thermotropics can be more awkward to use even if attempts towards a matrix free use was made by Lynch and Patrick [146]. Alternatively thermotropics can open the route toward polymerized systems or CNT manipulation in fluid environment. Besides, the alignment of CNTs in LCs with the transfer of order is an intriguing scientific topic on its own.

The dispersion in thermotropics has some peculiar aspects in terms of the mechanism acting between tubes that can be beneficial for the dispersion [90]. In general thermotropics can accept lower concentrations of CNTs than lyotropics before aggregation. This disadvantage is compensated by the net advantage of well-developed alignment methods due to the display industry and an ease of uniform alignment and of reorientation. Thermotropics are therefore very attractive tools for manipulating carbon nanotubes.

The experimental studies have indicated so far an orientation of CNTs in nematics mainly along the director. Because of the exceptionally high electrical conductivity of the CNTs it is reasonable to investigate this property in the LC–CNT composite to infer information on the orientation of CNTs. The change in conductance, while switching the LC in a cell, was monitored and analyzed in Refs [147, 148]. Electrical investigations are, however, only an indirect proof of the CNT alignment and the data rely on the change of conductivity between undoped and doped samples solely due to CNTs. However, in normal samples, there are other impurities that can contribute substantially to the electrical response.

Because of the nanoscopic dimension of CNTs the direct assessment of their orientation is not trivial. Lynch and Patrick have shown unidirectional alignment of

CNTs in nematic LCs (5CB and E7) visualizing the alignment by atomic force microscope (AFM) after removal of the host [146], cf. Figure 10.7. They had deposited a composite of CNTs and nematic LC on a rubbed filter membrane. Through the porous membrane the excess of LC was removed leaving the CNTs on the substrate. The nanotubes could then be visualized by AFM showing a unidirectional alignment of the CNTs along the rubbing direction. Depositing electrodes they could induce an in-plane reorientation of the LC and also of the CNTs. From the orientational distribution of the MWCNTs they obtained a value for the orientational order parameter, evaluated for a 2D system (the CNTs are in the substrate plane) ranging between 0.7 and 0.9, a substantially higher value than for typical nematics. Their method has the advantage of removal of the matrix and the direct observation of the CNTs. However, it is desirable to investigate the alignment of CNTs also within the bulk monitoring the sole effect of LC ordering without any additional step or forces that could interfere with the process.

An unambiguous way to access the alignment of SWCNTs is through polarized Raman spectroscopy [149]. SWCNTs have a characteristic Raman spectrum that allows to recognize and distinguish the presence of SWCNTs. Because electronic transitions of SWCNTs are usually resonant with laser wavelengths, a decent Raman signal can be detected also from minute quantities of CNTs due to a resonance effect. The most intense mode in the SWCNT spectrum is the G-band, visible at a wavenumber of about $1590\,\mathrm{cm}^{-1}$, whose two main peaks are due to tangential vibrations parallel to the long axis and tangential to the circumferences respectively. If the tubes are defected or carbon impurities are present in the sample a band

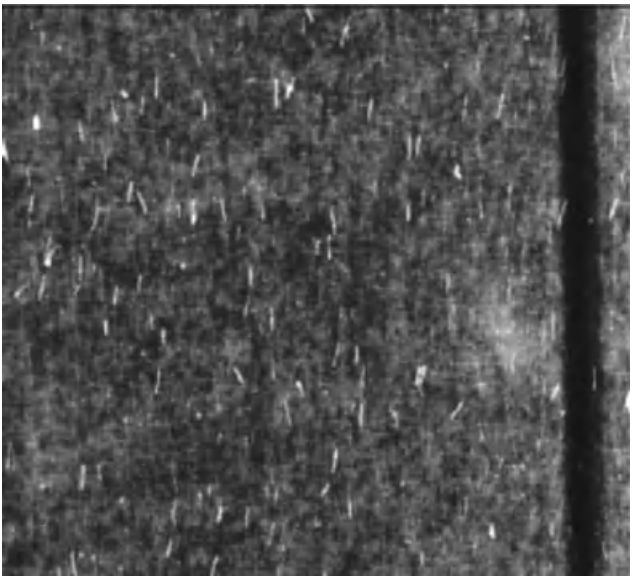

FIGURE 10.7 MWCNTs on a filter membrane aligned by the LC visualized by AFM after LC removal. *Source*: Reprinted with permission from Lynch and Patrick [146]. Copyright (2002) American Chemical Society.

designed with the letter D, at around 1350 cm^{-1}, becomes more pronounced. A mode specific of SWCNTs is the radial breathing mode (RBM) arising from the tubular structure and based on radial vibrations. It has been shown that by using polarized light it is possible, the first step in the Raman process, to discriminate the orientation of CNTs because the light absorption of CNTs is anisotropic, being much higher along the tube axis [149]. Thus, by monitoring the intensity of the Raman peaks it is possible to discriminate the orientation of the CNTs. Investigations in a standard LC cell filled with 5CB and SWCNTs of the HiPco type were performed analyzing the most intense peak, the G band, for polarization parallel and perpendicular (figure 10.8) to the LC director. The decrease of peak intensity from the first to the second case gives a clear, unambiguous proof of the alignment of SWCNTs along the LC director in the LC steady state [46, 150].

A difficulty might come from modes of some LC molecules, especially the ones with aromatic core, with peak positions very close to the G band. However, as shown in Figure 10.8, the G band can often be visualized despite the LC peaks when the peak positions are sufficiently separated. Raman spectroscopy is very informative concerning CNT quality, orientation, doping, bundling, interaction with the environment, etc. More information can be deduced by the Raman spectrum of SWCNTs but MWCNTs can be analyzed as well. The RBM is sensitive to the environment and can show a shift of its position also for noncovalent interactions like π–π stacking as shown in Figure 10.9b.

The interaction between LC molecules and CNTs is quite important because it could affect the reciprocal orientation and presumably the reciprocal degree of order. The direction of LC orientation and the strength of the anchoring onto surfaces is fundamental for the alignment of LCs in cells and it is expected to be relevant also for

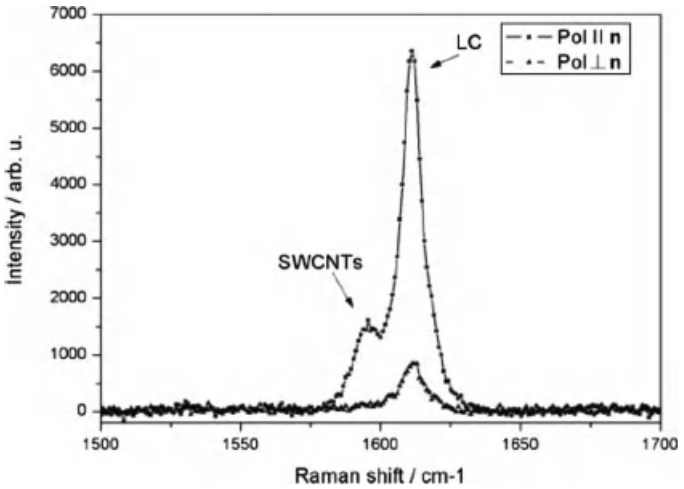

FIGURE 10.8 Alignment of SWCNTs probed by analyzing the change of intensity of the Raman modes for different directions of light polarization. *Source*: Reprint with permission from Scalia et al. [46].

the combination with CNTs. The graphitic structure seems quite suitable for the development of strong π–π interactions with aromatic LCs. From the dispersion study of Schymura et al. [90], it is clear that the aromaticity is not the only key aspect for the establishment of an interaction at the surface but the molecular structure of the LC on the whole indeed plays a role. The ease to disperse CNTs at the first stage of the mixing is not the only way to visualize the interaction. Around large aggregates of SWCNTs in 5CB an increase of stability of the nematic phase was observed at the nematic–isotropic phase transition [91], cf. Figure 10.9a. Vice versa, coming from the isotropic phase the nuclei of nematic phase appear at the tube interface. The CNT surfaces thus appear to be a suitable interface for LC anchoring. In addition the effect

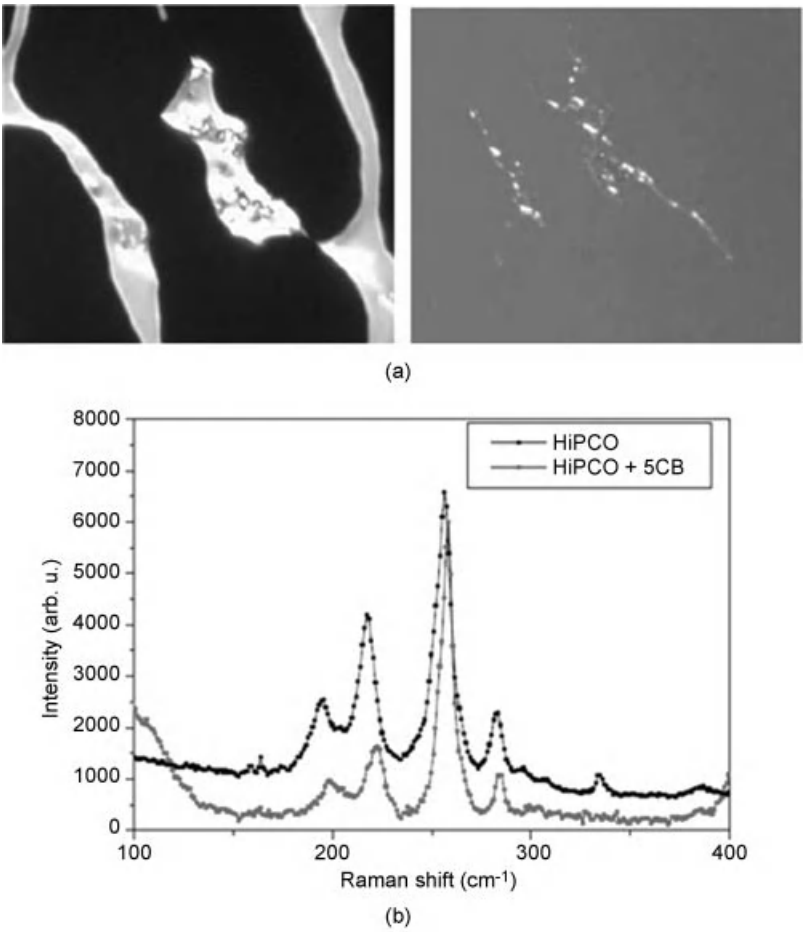

FIGURE 10.9 (a) Transition nematic–isotropic (left) and isotropic–nematic (right) around bundles of SWCNTs. (b) Shift of the position of RBMs between pristine and embedded in LC SWCNTs. *Source*: Reprinted permission from Scalia et al. [91].

of the interaction can be seen also from the shift of the Raman RBMs of the tubes between doped and undoped samples, cf. Figure 10.9b.

10.5 CARBON NANOTUBES ALIGNED BY LYOTROPIC LIQUID CRYSTALS

Kumar et al. [151], first reported the use of lyotropic liquid crystals as aligning hosts for carbon nanotubes, where poly(p-phenylene benzobisoxazole) (PBO) was synthesized by *in situ* polymerization in the presence of single-wall CNTs in poly (phosphoric acid) (PPA). The resulting solutions, with CNT to polymer concentrations of 0%, 5%, and 10%, form a nematic lyotropic liquid crystalline phase which the authors could spin into fibers. Optical microscopy images suggest good dispersion of the tubes (although the sole image shown is obtained with the sample between crossed polarizers, making it difficult to recognize nanotube aggregates) and the mechanical properties of the fibers were substantially enhanced by the presence of the CNTs. The tensile modulus, tensile strength, and elongation to break were found to be 20%, 60%, and 40% better, respectively, than for CNT-free PBO fibers. For instance, tensile strengths of pure PBO fibers were in the range 1.8–2.6 GPa whereas the fibers with 10% nanotubes showed tensile strengths in the range 2.9–4.2 GPa. Considering the rather large amount of nanotubes the improvement must still be regarded as a disappointment, probably due to insufficient dispersion quality (the nanotubes were pristine SWCNTs and no mediator was added) and/or to insufficient adhesion between the matrix polymer and the nanotube surfaces. No increase in electrical conductivity was measured for the fibers, a result that the authors attributed to the good alignment of the nanotubes, leading to a high-percolation threshold. However, the lack of electrical percolation, which is in fact quite surprising at such high-nanotube concentration, may equally well be due to insufficient dispersion quality, preventing a continuous conduction path through the polymer because the nanotubes are aggregated instead of well distributed throughout the sample. Indeed, later works on liquid crystalline polymers loaded with nanotubes (see below) report similar enhancements of mechanical properties at an order of magnitude lower nanotube concentration, suggesting that this early work did not represent optimum conditions.

Li et al. revisited the CNT–PBO system in 2006 [152], this time using oxidized MWCNTs and polymerizing *in situ* with the CNTs added to the PPA solvent together with the monomers. The oxidation of the CNTs allowed for better dispersion as well as covalent incorporation in the polymer during polymerization. Also in this work the authors spun fibers from the lyotropic nematic solutions, getting somewhat better results. Compared to the pure PBO fibers, composites with 2 wt.% MWCNTs had tensile strength improvements in the range 20–50%. The orientational order of the CNT-loaded fibers was, however, less than that of pristine PBO fibers, suggesting that the dispersion of the nanotubes was still not satisfactory.

A more recent paper that also used a polymer-based lyotropic liquid crystal host is that of Okano et al. [153]. In contrast to the work of Kumar et al. the system of Okano

and co-workers has the great advantage of being water-based, the polymer used for dispersing the nanotubes as well as for forming the lyotropic phase being sulfonated polyaramide (PPSA). This polymer forms a nematic phase already at a concentration of 0.6 wt.% and its anionic amphiphilic character gives it a good CNT dispersion capability: for a single-wall nanotube concentration of 1 mg/mL (0.1 wt.%) no CNT aggregates could be detected by optical microscopy in the lyotropic composite and the dispersions were reported to be stable for at least a year. The CNT-containing lyotropic system was spread on a substrate using a bar coater, inducing a uniform alignment of the liquid crystal director over a large area. An important aspect is that the water could be evaporated, leaving behind a solid system, without loss of the orientational order. The authors used polarized Raman spectroscopy to evaluate the orientational order of the nanotubes, finding a value for the order parameter of the SWCNTs of 0.48.

Most work on lyotropic liquid crystals as hosts for carbon nanotube dispersion and alignment has, however, been done using low-molar mass surfactants forming the host phase. This approach is attractive because one can use the surfactants employed as standard procedure for dispersing carbon nanotubes to form the lyotropic liquid crystal host phase. While composites of carbon nanotubes in thermotropic nematic are often done by introducing the nanotubes directly into the liquid crystal, this approach is rarely followed for the case of lyotropic host phases, which are typically inappropriate as host for carrying out the initial dispersion. Presumibly they are too viscous to achieve efficient sonication. Neither the surfactant nor the water has any dissolving power on the CNTs [90]. The surfactant wrapping and the water solvent simply keep the nanotubes dispersed, but the actual separation of the tubes must be done by mechanical methods, normally sonication.

The starting point for preparing a surfactant-based lyotropic liquid crystal–CNT composite is, thus, generally a high-quality isotropic CNT suspension in water, stabilized by a standard surfactant, such as SDS or CTAB. The transition to a lyotropic liquid crystal can then follow a number of different routes. In the earliest reports the isotropic CNT suspension was either mixed with a liquid crystalline surfactant solution of very high concentration, such that the desired surfactant concentration resulted in the final mixture [70], or dry surfactant and co-surfactant were added to the nanotube suspension to increase the surfactant concentration to the threshold for a nematic phase [69, 71]. In these first experiments on lyotropic liquid crystal-driven nanotube alignment the CNT concentration was rather low, rendering confirmation of the successful transfer of orientational order non-trivial. The first clear-cut evidence of alignment was provided by using polarized Raman spectroscopy [69, 71], giving unambiguous proof that SWCNTs were indeed oriented along the director of the lyotropic phase. The concept worked even upon addition of a chiral dopant rendering the host cholesteric (chiral nematic) with a pitch of its helical director modulation in the 100 μm range.

An important improvement was achieved by combining cationic and anionic surfactants, one for stabilizing the nanotube suspension, the other for forming the liquid crystal phase [67]. The cationic surfactant CTAB was added at sufficient concentration to form the desired liquid crystal host phase to a prepared high-quality

suspension of CNTs stabilized by anionic SDBS. In this way very high concentrations of nanotubes could be introduced to the liquid crystal phase with retained orientational order, such that the macroscopic phase behaved as a fluid polarizer, cf. Figure 10.10: the orientationally ordered nanotubes absorb light polarized along the tube axis, but not light with the perpendicular polarization. Thus, while the uniform alignment was corroborated with polarized Raman spectroscopy also in this work, the fact that the director of the liquid crystal phase could easily be uniformly aligned over square centimeter areas by shearing allowed the transfer of uniaxial orientational order to the nanotubes to be verified by simple inspection by eye through a linear polarizer. Importantly, the method combining cationic and anionic surfactants works equally well for single-wall CNTs [67] as well as for multi-wall CNTs [66], whereas other work with lyotropic liquid crystal hosts reported ordering only for single-wall but not for multi-wall nanotubes, presumably because the MWCNT diameter is much greater than that of the native lyotropic phase micelles [65, 75]. In the cationic system each nanotube is most likely surrounded by a 'buffer layer' of oppositely charged native micelles. This will reduce the risk of depletion attraction and probably improve the incorporation possibilities in the host phase, even when the nanotubes are of a different diameter than the host micelles.

The catanionic CNT suspension also exhibited very interesting rheological properties, with thin filaments in which the nanotubes are highly aligned being

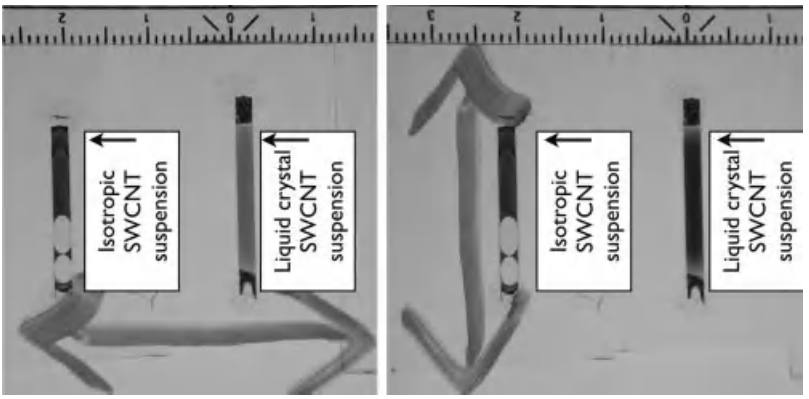

FIGURE 10.10 Two capillaries filled with single-wall carbon nanotube suspensions at the same concentrations, in one case in an isotropic host (left capillary) and in the other in a uniformly aligned liquid crystal host (right capillary, director along capillary axis). The samples are viewed with illumination from below through a linear polarizer held with its absorption direction (double arrow) perpendicular (left image) or parallel (right image) to the capillaries. For the isotropic sample this induces no change but the liquid crystal sample is much darker with the absorption direction parallel to the capillary than perpendicular. This is because the CNTs absorb preferentially light polarized along the tubes, that is, along the capillary in the liquid crystalline sample, leaving less light to go through the polarizer in the right image than in the left image. In the isotropic samples the nanotubes are randomly oriented, thus absorbing light equally strong for any polarization. A standard metric ruler is placed along the top edge of the photos to show the scale.

easy to draw from the phase [61, 67]. This phenomenon that occurs neither for the CNT-free liquid crystal phase nor for isotropic nanotube suspensions, can be understood as a percolation-like process where the micelle length diverges during elongational flow as a result of a positive feedback loop between orientational order, micelle stiffness, and length [61]. It happens for single-wall as well as multi-wall carbon nanotubes of different types but not for fullerenes and also not if the dispersion quality of nanotubes is insufficient. Recently, the rheological properties of nanotubes suspended in purely anionic SDS-based nematic lyotropic phases were investigated thoroughly by Tardani and Camillo [62]. They found significant viscoelastic behavior at nanotube loadings above 0.25%. The behavior was explained as a result of nanotube entanglement within the nematic matrix.

Xin et al. recently introduce an attractive alternative approach to forming the CNT-loaded lyotropic liquid crystal phase [63, 65]. As customary they started with an isotropic low-surfactant concentration suspension of nanotubes, stabilized either by nonionic dodecyl octaoxyethene monoether surfactant [65] or by an ionic surfactant (either CTAB or SDS) [63], but the liquid crystal phase formation was triggered by adding a large amount of polymer, inducing depletion attraction. For nonionically dispersed nanotubes nonioinic poly(ethylene glycol) (PEG) was added, while for CNTs stabilized by ionic surfactants a polyelectrolyte of the same charge as the surfactant was introduced. Due to the depletion attraction the surfactant-wrapped nanotubes aggregate, together with polymer and surfactant, forming a hexagonal columnar liquid crystal phase in which they are apparently still separated from each other. This phase separates from an essentially nanotube-free phase containing only polymer in water solution. The beautiful aspect of this approach is that the nanotube concentration in the liquid crystal phase is substantially raised compared to the initial suspension. An important question that remains to be addressed, however, is if the hexagonal phase can be aligned macroscopically. The pictures shown in these papers were from a polydomain sample, confirming the lyotropic liquid crystalline nature but not that the nanotubes were uniformly aligned. Moreover, the lack of high-magnification microscopy images taken without crossed polarizers precludes a true confirmation that no bundling of the nanotubes occurred.

Most work with lyotropic hosts has been done with aqueous solvents, although some exceptions exist, such as the already mentioned PPA-dissolved PBO. Another example is the report by Jiang et al. [154] where an ionic liquid was used as solvent for nanotubes dispersed with a nonionic polyoxyethylene surfactant. As in the works of Xin and co-workers the liquid crystal phase was of hexagonal columnar type. The same difficulty in obtaining a macroscopically uniform orientation of the host phase was probably the reason why no attempt to verify the alignment of the CNTs was reported in this work. The only case known to the author where a uniformly aligned purely hexagonal liquid crystal phase loaded with carbon nanotubes was prepared and investigated is the recent work of Mauter et al. [155] (The cationic system described by Scalia et al. [67] also formed a hexagonal columnar phase, as confirmed by X-ray scattering, but subsequent investigation showed that this phase occurs very close to a nematic phase, which probably prevails during shearing, making the uniform alignment by shearing of this phase possible.) As in the work of Scalia

et al. [67] a combination of cationic and anionic surfactants was used, here sodium taurodeoxycholate for suspending the CNTs and CTAB for forming the hexagonal columnar liquid crystal phase. The authors took great care in aligning the phase uniformly by cooling the mixture slowly from the isotropic temperature range to that of hexagonal columnar order in the presence of a 5T magnetic field. A very interesting aspect of this work is that the team polymerized the system after alignment, resulting in a solid film with integrated aligned nanotubes. Polarized Raman spectroscopy was used to verify that the nanotube orientation had not been lost in the process, and indeed the contrast between the responses for polarization parallel and perpendicular to the director was excellent. The nanotube concentration was rather low in this work (well below 0.1 wt.%), but if it can be increased in future work this approach holds great promise for manufacturing films profiting from well dispersed and uniformly aligned carbon nanotubes.

10.6 CARBON NANOTUBES IN LIQUID CRYSTALLINE POLYMERS OR POLYMERIZED LIQUID CRYSTALS

The alignment of the nanotubes imposed by liquid crystallinity is very useful in the context of polymeric matrices. In contrast to low-viscous and low-molar mass liquid crystal hosts that must be contained in vials or cells, a liquid crystalline polymer can be self-sustaining, often forming a glass with retained orientational order at room temperature. By spinning a fiber from the composite, impressive mechanical properties can be achieved. Compared to CNT composites with low-molar mass liquid crystals, a very important additional aspect in case of composites with liquid crystal polymers is—as in the case of any polymer–CNT composite—the adhesion between CNTs and polymer matrix, important for an efficient load transfer. Very often this is inadequate, resulting in nanotubes sliding within the matrix upon mechanical stress, thereby cancelling any beneficial mechanical effect from the CNT addition, regardless of the quality of their alignment and dispersion. Related to the use of liquid crystalline polymers is the approach to disperse the nanotubes in a reactive low-molar mass liquid crystal host and then polymerize the composite, resulting in a solid material with incorporated aligned carbon nanotubes.

As discussed above, dispersion is an immense challenge in preparing nanotube—liquid crystal composites, and the problems are if possible even greater when the host is polymeric. Simply mixing pristine nanotubes in a standard liquid crystalline polymer, molten or dissolved, will typically yield poor results, with substantial nanotube aggregation. Nevertheless, this approach was attempted by Choi et al., mixing up to 2 wt.% of pristine multiwall CNTs in the aromatic copolyester Vectra A950 using melt compounding [156]. The CNTs had no significant effect on the transition temperatures of the Vectra host, an observation that may be seen as a sign of weak interaction between the matrix and the filler particles. Despite the lack of CNT treatment to improve the compatibility with the host an improvement of mechanical properties was reported. With 2% of MWCNTs added the tensile strength increased from 62.3 MPa to 89.3 MPa (43.3% increase) and the modulus increased from

1.12 GPa to 1.79 GPa (59.8%). In principle the authors had expected even greater improvement and they attribute the limitations to insufficient dispersion of the nanotubes in the matrix. The authors did not assess the alignment of the tubes in the Vectra matrix. Another team attempted to polymerize the monomers *in situ* in the presence of pristine MWCNTs [157], yielding a nematic polymer–CNT composite. The characterization of this composite was not very detailed so it is difficult to judge if the *in situ* polymerization improved the situation compared to the approach to mix the CNTs directly with the pre-existing nematic polymer. Spectroscopy and microscopy studies suggest that the interactions between liquid crystal polymer and nanotubes were reasonably strong but further studies are required to assess the success of this approach.

There are essentially three different approaches that have been explored to circumvent the problems with dispersion of the CNTs in liquid crystalline polymers: (i) functionalize the nanotubes covalently for improved compatibility with the polymer; (ii) add a tailormade molecule that adsorbs noncovalently on the nanotube and mediates between filler and matrix; or (iii) modify the liquid crystal polymer for enhanced compatibility with the nanotubes. Although it generally impairs the properties of the nanotubes, at least for SWCNTs, the most common choice for realizing attractive CNT–liquid crystal polymer composites is the first one, to covalently functionalize the nanotubes. Either they are simply oxidized resulting in carboxylic acid groups attached to the CNT sidewalls [158, 159] or one grafts more complex moieties to the nanotubes, specifically designed to enhance compatibility with the host [158–160]. Sahoo et al. compared carboxylate group and hydroxyl benzoic acid (HBA)-functionalized MWCNTs for incorporation in a liquid crystalline polymer (the authors did not specify which phase the polymer formed) consisting of 80% HBA and 20% ethylene terphtalate (ET) [159]. The HBA-functionalized nanotubes are expected to be particularly easy to disperse because the covalently attached groups are identical to the majority component of the liquid crystal polymer. The nanotubes were introduced into the polymer at a concentration of 1 wt.% by mixing in a microcompounder, heated to a temperature above the melting point of the polymer. Absorbance spectroscopy revealed a non-negligible shift of the peaks for the two functionalized CNT types, in contrast to when raw MWCNTs were added to the polymer, indicating an enhanced interaction between the matrix and the nanotubes after these had been functionalized according to either route. The improved interaction was corroborated by scanning electron microscopy investigation of fractured surfaces, revealing nanotubes that had been broken upon fracture rather than pulled out of the matrix. Optical microscopy investigations also showed that the functionalized nanotubes were substantially better dispersed than the raw nanotubes, although all composites exhibited aggregates that were easily visible on the optical scale, that is, they were on the size of several microns. Mechanical testing of the composites also revealed a beneficial effect of the nanotube functionalization, the greatest improvement being seen for HBA–CNTs, as expected. Here the tensile strength increased from 87.5 MPa for the neat liquid crystal polymer to 123.5 MPa (41% increase) and the tensile modulus increased by 55%, from 2.9 GPa to 4.5 GPa. While the authors found substantially lower degree of improvement for the pristine

CNTs (6% and 28%) it is somewhat surprising that their reference values are much poorer than the above mentioned data for pristine nanotubes from Choi et al. [156]. Although the concentration of nanotubes differed by a factor of 2 between these studies the differences indicate that variations in the chemical structure of the polymer may be just as important as nanotube functionalization.

In the study of Lafuente et al. [158] three different functionalizations of single-wall CNTs were compared for integration into a nematic polyazomethine host. In addition to the standard carboxylate group attachment the authors prepared SWCNTs functionalized with $CONH(CH_2)_6NH_2$ amines or with 2-methyl-1,4-phenylenediamines. These two functionalizations are optimized for the target liquid crystal polymer host because the amine terminus can link covalently to the monomers of the host polymer. In fact, the 2-methyl-1,4-phenylenediamine constitutes one of the two monomers used for forming the liquid crystalline polymer. The SWCNTs were mixed at 1 wt.% concentration with the monomers and then the polymer was prepared by *in situ* polycondensation. For the two amine-functionalized CNT types this results in covalent attachment of the SWCNTs in the polymer, that is, the nanotubes become a fully integrated component of the polymer, in contrast to standard composites where they are simply dispersed in the host polymer. Obviously, this removes the risk of nanotubes sliding through the polymer and the approach should thus be highly beneficial for realizing CNT polymer composites with enhanced mechanical properties.

All composites prepared in the study exhibited a nematic phase and a glass transition temperature that is similar to that of the pure host polymer (about 55°C). The melting temperature was, however, raised by about 10°C upon nanotube addition. Although optical microscopy images reveal some large-scale aggregates the authors attribute these to impurities, maintaining that the nanotubes are well integrated into the polymer matrix. Fibers were extruded from composites as well as the pure polymer in the nematic phase. Electron microscopy and X-ray characterization of the fibers revealed a generally good, well-aligned fibrillar internal structure, for CNT-containing as well as pristine polymer. The fibers were subjected to mechanical testing, prior to and after thermal annealing. In particular, the samples with covalently integrated nanotubes showed substantial improvements of 80–100% in tensile strength (250 MPa or 270 MPa for the unannealed/annealed pristine polymer and 346 Mpa and 629 MPa for the unannealed/annealed composite with phenylenediamine-functionalized tubes) and up to 60% reduction of the elongation at break. The simple carboxylate-functionalized nanotubes also yielded an improvement compared to the pristine polymer, but of lower magnitude, 40% and 30%, respectively. The elastic modulus was improved from 7.1 GPa (no annealing) or 12.8 Gpa (annealed) for the pristine polymer to around 12 GPa (no annealing) or around 14 GPa (annealed) upon nanotube addition, in this case with very similar results for the carboxylate-functionalized tubes and the tubes that were covalently grafted to the polymer.

Hu et al. functionalized multiwall, poly{6-[4-(4-methoxyphenylazo)phenoxy] hexyl methacrylate carbon nanotubes covalently with side-chain azobenzene liquid crystalline polymer (PMMAZO) and studied the properties of the liquid crystal phase

formed by the resulting substance on its own [160]. The phase sequence of the CNT–PMMAZO is similar to that of pristine PMMAZO, with a nematic as well as a smectic phase in the mesophase temperature range, although the nematic–smectic transition peak picked up in DSC is substantially smaller for the nanotube-containing material than the pristine liquid crystalline polymer. Conductivity measurements under electric field suggest that the nanotubes are aligned to some extent, but this is in fact seen also when the system is in its isotropic phase. The results are thus somewhat inconclusive. Considering that the system contains a very high degree of carbon nanotubes more clear-cut results might be expected from a polarizing microscopy investigation of an aligned sample, relying on the anisotropic absorption of aligned nanotubes, as was previously done for nanotubes aligned in lyotropic liquid crystals [66, 67].

As discussed above the covalent modification of the nanotubes can in some cases be avoided by adding appropriate mediating molecules. These should adsorb non-covalently to the CNTs and provide it with an outer surface that integrates well with the liquid crystal polymer matrix. Among the best approaches is to use a mediating molecule that itself is a liquid crystal polymer. For instance, Ji et al. designed and synthesized a nematic main-chain liquid crystal polymer that was pyrene-terminated at both ends, providing anchor groups to carbon nanotubes [93]. The new polymer seems to provide a remarkable stabilization of nanotubes dispersed in organic solvents. According to the authors up to 12 mg/mL nanotubes can be dispersed, although there are no data for the dispersion quality and procedure for preparing the dispersion at such concentration. At 1 mg/mL concentration the authors find that simple stirring can produce a dispersion where the nanotube aggregates are below optical size. For better results sonication is however required. The pyrene-functionalized liquid crystal polymer was used for preparing mono-domain liquid crystal elastomer samples, which can work as actuators [15, 161, 162], with MWCNTs added at a concentration between 0.03 wt.% and 3 wt.%. No images of the resulting composites were shown, making it difficult to judge the quality of the dispersion, but the alignment of the nanotubes within the matrix was verified by terahertz spectroscopy. An anisotropic absorption was obtained for the higher carbon nanotube loadings, the absorption coefficient being almost twice as large for polarization along the director as for the perpendicular polarization, suggesting nanotube alignment along the director in the nematic elastomer. As the nanotube concentration is quite high in this work, the alignment of the nanotube actually ought to be easy to verify optically, just by studying the absorption of polarized light.

Liquid crystalline elastomers, extensively studied by the Terentjev's group, were the target host also in the work of Yang et al., where they used poly(*p*-phenyleneethynylene) as added mediator for dispersing single-wall carbon nanotubes without covalent modification [163]. In this work the alignment of the nanotubes was not a prime issue but scanning electron microscopy of the surface indicates a relatively uniform orientation along the liquid crystal director. The function of the CNTs was to absorb infrared light and to transfer the energy as heat to the elastomer matrix. The CNTs thus acted as tiny distributed heaters, rapidly taking the elastomer

above the nematic–isotropic transition temperature upon IR irradiation and thereby initiating the actuation.

An example of the third approach, where the liquid crystal polymer is tailored for compatibility with CNTs, is provided by Sordi et al. [164]. They incorporated sulfonate groups along the backbone of a liquid crystalline polyester in order to make it more compatible with carbon nanotubes or with nanodiamond. These nanoparticles were added under sonication at 1 wt.% to the polymer dissolved in a mixture of dichloromethane and trifluoracetic acid. Significant changes in the glass transition temperature upon addition of the nanoparticles to the sulfonated polymer indicate interactions between guests and hosts and some improvements of the mechanical properties were found, in particular with added nanodiamond. However, optical microscopy reveal very strong nanotube aggregation within the matrix, hence the procedure obviously calls for further optimization. Possibly *in situ* polymerization with the nanotubes added may lead to better results.

Cervini et al. explored a slightly different route, working with a low-molar mass liquid crystal host but of a polymerizable type [165]. This allowed them to turn the nanotube-liquid crystal composite into a solid film, with retained uniaxial orientation of the nanotubes. The multi-wall nanotubes had first been oxidized for adding hydroxy and carboxylic groups to their surfaces, allowing a subsequent attachment of aminopropyltriethoxysilane (APTES) moieties for improved incorporation in the liquid crystalline host and attachment to the glass substrate used for sample preparation. The authors point out that for multiwall nanotubes the oxidation may actually even be beneficial for the conductive properties, since sp^3 interwall connections are created in the process. The tubes were added at concentrations up to 5 wt.% into a mixture of polymerizable low-molar mass mesogens with acrylate side groups, with ethanol added as solvent, and dispersed by means of ultrasonication. After homogenization and alignment of the liquid crystal in a homeotropic geometry the sample was photopolymerized by UV light irradiation.

The APTES-functionalized nanotubes were much better dispersed than the tubes carrying only carboxylate groups. Electron microscopy and spectroscopy suggest that the tubes were well dispersed and aligned along the homeotropic liquid crystal director, although the description of the spectroscopy is not fully convincing. It is unclear how the measurements along and perpendicular to the director were made and if the data are really reliable because the sample alignment was hometropic and not with uniform in-plane director. This means that the light beam must have propagated along the film for the measurement with polarization parallel to the director but perpendicular for the other measurement. Apart from the difficulties in realizing such measurement geometries, the sample thickness for the two cases comes out dramatically different, hence it is not easy to compare the data. The description of the optical experiments is unfortunately rather bewildering and does not at all address these important details. More convincing is the study of the electrical properties which compares the in-plane and perpendicular conductivity of the composite film. The perpendicular conductivity is substantially greater than for the in-plane geometry, in particular above CNT concentrations of about 1 wt.%, which thus seems to constitute the percolation threshold. This indeed suggests that

the tubes were aligned homeotropically by the liquid crystal and that the alignment was not lost in the polymerization process.

10.7 CONCLUSIONS AND OUTLOOK

Liquid crystals have proven, and are continuously showing, to be very interesting for carbon nanotube research and for finding a way toward the application of this new nanoparticle class. The nanotube organization, critical for their successful, macroscopic use, can be achieved through the induction of LC phases from the CNTs or by mixing them with thermotropic or lyotropic LCs. Both classes of LCs have proven to be very efficient for aligning CNTs transferring their order. Solid materials can be realized with liquid crystal polymers or polymerizable LCs, enlarging the attractiveness of LCs.

The dispersion of CNTs is a critical issue for the CNT community, prerequisite for any further development. One way to solve it is with the use of surfactants. This approach makes lyotropic LCs phases particularly attractive for realizing composites with high loading of well dispersed CNTs. On the other hand tailored research has been devoted towards the dispersion of CNTs in thermotropics as well as polymer-based LCs finding suitable additives and/or evaluating the impact of the molecular structure on the quality of the dispersion. The encouraging results open new attractive ways for good dispersion of CNTs with these materials and call for more research on the topic. Improvements of the properties of composites can be expected but also novel uses. Furthermore, investigations are still required concerning the CNT–LC interaction and the properties of the combination. Interestring developments can come using tubes fractionated according to their type and dimensions, beneficial not only for the formation of LC phases from CNTs but also for the CNTs in the different LC matrices.

Liquid crystals, with their different types and the enormous variety of molecular structures or constituents provide a rich playground for creating new performing materials, devices or new superstructures based on CNTs, allowing to highlight their exceptional properties. The many diverse studies on LCs and CNTs have indicated the broadness of the subject that can be considered nowadays an autonomous research topic all around. The solid results and promising findings open new avenues of research and promise new exciting science and applications.

REFERENCES

1. J. P. F. Lagerwall and G. Scalia. Carbon nanotubes in liquid crystals (Feature article). *J. Mater. Chem.* **2008**, *18*, 2890–2898.
2. M. Rahman and W. Lee. Scientific duo of carbon nanotubes and nematic liquid crystals. *J. Phys. D-Appl. Phys.* **2009**, *42*, 063001.
3. G. Scalia. Alignment of carbon nanotubes in thermotropic and lyotropic liquid crystals. *ChemPhysChem* **2010**, *11*, 333–340.

4. P. Brochu and Q. Pei. Advances in dielectric elastomers for actuators and artificial muscles. *Macromol. Rapid Commun.* **2010**, *31*, 10–36.
5. H. K. Bisoyi and S. Kumar. Liquid-crystal nanoscience: an emerging avenue of soft self-assembly. *Chem. Soc. Rev.* **2011**, *40*, 306–319.
6. M. Supova, G. S. Martynkova, and K. Barabaszova. Effect of nanofillers dispersion in polymer matrices: A review. *Science Adv. Mater* **2011**, *3*, 1–25.
7. S. J. Zhang and S. Kumar. Carbon nanotubes as liquid crystals. *Small* **2008**, *4*, 1270–1283.
8. S. Iijima. Helical microtubules of graphitic carbon. *Nature* **1991**, *354*, 56–58.
9. R. Saito, M. S. Dresselhaus, and G. Dresselhaus. Physical Properties of Carbon Nanotubes. *Imperial College Press*, **1998**.
10. R. H. Baughman, A. A. Zakhidov, and W. A. de Heer. Carbon nanotubes – the route toward applications. *Science* **2002**, *297*, 787–792.
11. B. Vigolo, A. Penicaud, C. Coulon, C. Sauder, R. Pailler, C. Journet, P. Bernier, and P. Poulin. Macroscopic fibers and ribbons of oriented carbon nanotubes. *Science* **2000**, *290*, 1331–1334.
12. R. Haggenmueller, H.H. Gommans, A.G. Rinzler, J.E. Fischer, and K.L. Winey. Aligned single-wall carbon nanotubes in composites by melt processing methods. *Chem. Phys. Lett.* **2000**, *330*, 219–225.
13. E. S. Choi, J. S. Brooks, D. L. Eaton, M. S. Al-Haik, M. Y. Hussaini, H. Garmestani, D. Li, and K. Dahmen. Enhancement of thermal and electrical properties of carbon nanotube polymer composites by magnetic field processing. *J. Appl. Phys.* **2003**, *94*, 6034–6039.
14. M. Zhang, S. Fang, A. A. Zakhidov, S. B. Lee, A. E. Aliev, C. D. Williams, K. R. Atkinson, and R.H. Baughman. Strong, transparent, multifunctional, carbon nanotube sheets. *Science* **2005**, *309*, 1215–1219.
15. S. Ahir and E. M. Terentjev. Photomechanical actuation in polymer–nanotube composites. *Nature Mater.* **2005**, *4*, 491–495.
16. J. Guo, S. Hassan, A. Javey, G. Bosman, and M. Lundstrom. Assessment of high-frequency performance potential of carbon nanotube transistors. *IEEE Transactions on Nanotechnology* **2005**, *4*, 715–721.
17. H. Ko and V. Tsukruk. Liquid-crystalline processing of highly oriented carbon nanotube arrays for thin-film transistors. *Nano Lett*. **2006**, *6*, 1443–1448.
18. S. J. Kang, C. Kocabas, T. Ozel, M. Shim, N. Pimparkar, M. A. Alam, S. V. Rotkin, and J. A. Rogers. High-performance electronics using dense, perfectly aligned arrays of single-walled carbon nanotubes. *Nat. Nanotechnol.* **2007**, *2*, 230–236.
19. Iakoubovskii, K. Techniques of aligning carbon nanotubes. *Central Eur. J. Phys.* **2009**, *7*, 645–653.
20. T. Druzhinina, S. Hoeppener, and U. Schubert. Strategies for post-synthesis alignment and immobilization of carbon nanotubes. *Adv. Mater.* **2011**, *23*, 953–970.
21. S. M. Huang, L. M. Dai, and A. W. H. Mau. Patterned growth and contact transfer of well-aligned carbon nanotube films. *J. Phys. Chem. B* **1999**, *103*, 4223–4227.
22. S. Fan, M. G. Chapline, N. R. Franklin, T. W. Tombler, A. M. Cassell, and H. Dai. Self-oriented regular arrays of carbon nanotubes and their field emission properties. *Science* **1999**, *283*, 512.

23. S. M. Huang, X. Y. Cai, and J. Liu. Growth of millimeter-long and horizontally aligned single-walled carbon nanotubes on flat substrates. *J. Am. Chem. Soc.* **2003**, *125*, 5636–5637.
24. Y. Murakami, S. Chiashi, Y. Miyauchi, M. Hu, M. Ogura, T. Okubo, and S. Maruyama. Growth of vertically aligned single-walled carbon nanotube films on quartz substrates and their optical anisotropy. *Chem. Phys. Lett.* **2004**, *385*, 298–303.
25. K. Bubke, H. Gnewuch, M. Hempstead, J. Hammer, and M. Green. Optical anisotropy of dispersed carbon nanotubes induced by an electric field. *Appl. Phys. Lett.* **1997**, *71*, 1906–1908.
26. K. Yamamoto, S. Akita, and Y. Nakayama, Y. Orientation and purification of carbon nanotubes using ac electrophoresis. *J. Phys. D-Appl. Phys.* **1998**, *31*, L34–L36.
27. S. Gerdes, T. Ondarcuhu, S. Cholet, and C. Joachim. Combing a carbon nanotube on a flat metal–insulator–metal nanojunction. *Europhys. Lett.* **1999**, *48*, 292–298.
28. X. Chen, T. Saito, H. Yamada, and K. Matsushige. Aligning single-wall carbon nanotubes with an alternating-current electric field. *Appl. Phys. Lett.* **2001**, *78*, 3714–3716.
29. D. A. Walters, M. J. Casavant, X. C. Qin, C. B. Huffman, P. J. Boul, L. M. Ericson, E. H. Haroz, M. J. O'Connell, K. Smith, D. T. Colbert, and R. E. Smalley. In-plane-aligned membranes of carbon nanotubes. *Chem. Phys. Lett.* **2001**, *338*, 14–20.
30. T. Kimura, H. Ago, M. Tobita, S. Ohshima, M. Kyotani, and M. Yumura. Polymer composites of carbon nanotubes aligned by a magnetic field. *Adv. Mater.* **2002**, *14*, 1380–1383.
31. J. E. Fischer, W. Zhou, J. Vavro, C. Llaguno, C. Guthy, R. Haggenmueller, M. J. Casavant, D. E. Walters, and R. E. Smalley. Magnetically aligned single wall carbon nanotube films: Preferred orientation and anisotropic transport properties. *J. Appl. Phys.* **2003**, *93*, 2157–2163.
32. R. Krupke, F. Hennrich, H. von Lohneysen, and M. M. Kappes. Separation of metallic from semiconducting single-walled carbon nanotubes. *Science* **2003**, *301*, 344–347.
33. H. Wang, G. T. Christopherson, Z. Y. Xu, L. Porcar, D. L. Ho, D. Fry, and E. K. Hobbie. Shear-sans study of single-walled carbon nanotube suspensions. *Chem. Phys. Lett.* **2005**, *416*, 182–186.
34. C. Martin, J. Sandler, A. Windle, M. Schwarz, W. Bauhofer, K. Schulte, and M. Shaffer. Electric field-induced aligned multi-wall carbon nanotube networks in epoxy composites. *Polymer* **2005**, *46*, 877–886.
35. Q. W Li, Y. T. Zhu, I. A. Kinloch, and A. H. Windle. Self-organization of carbon nanotubes in evaporating droplets. *J. Phys. Chem. B* **2006**, *110*, 13926–13930.
36. J. M. Russell, S. J. Oh, I. LaRue, O. Zhou, and E. T. Samulski. Alignment of nematic liquid crystals using carbon nanotube films. *Thin Solid Films* **2006**, *509*, 53–57.
37. I. S. Baik, S. Y. Jeon, S. H. Lee, K. A. Park, S. H. Jeong, K. H. An, and Y. H. Lee. Electrical-field effect on carbon nanotubes in a twisted nematic liquid crystal cell. *Appl. Phys. Lett.* **2005**, *87*, 263110.
38. H. Y. Chen, W. Lee, and N. A. Clark. Faster electro-optical response characteristics of a carbon-nanotube-nematic suspension. *Appl. Phys. Lett.* **2007**, *90*, 033510.
39. H. Chen and W. Lee. Suppression of field screening in nematic liquid crystals by carbon nanotubes. *Appl. Phys. Lett.* **2006**, *88*, 222105.
40. C. Huang, C. Hu, H. Pan, and K. Lo. Electrooptical responses of carbon nanotube-doped liquid crystal devices. *Jpn. J. Appl. Phys.* **2005**, *44*, 8077–8081.

41. C. Huang and H. Pan. Comment on "electric-field effect on carbon nanotubes in a twisted nematic liquid crystal cell" [appl. Phys. Lett. 87, 263110 (2005)]. *Appl. Phys. Lett.* **2006**, *89*, 056101.
42. C. Huang, H. Pan, and C. Hsieh. Electrooptical properties of carbon–nanotube-doped twisted nematic liquid crystal cell. *Jpn. J. Appl. Phys.* **2006**, *45*, 6392–6394.
43. S. Y. Jeon, S. H. Shin, S. J. Jeong, S. H. Lee, S. H. Jeong, Y. H. Lee, H. C. Choi, and K. J. Kim. Effects of carbon nanotubes on electro-optical characteristics of liquid crystal cell driven by in-plane field. *Appl. Phys. Lett.* **2007**, *90*, 121901.
44. S. Y. Jeon, S. H. Shin, J. H. Lee, S. H. Lee, and Y. H. Lee. Effects of carbon nanotubes on nematic backflow in a twisted nematic liquid-crystal cell. *Jpn. J. Appl. Phys.* **2007**, *46*, 7801–7802.
45. W. Lee, C. Wang, and Y. Shih. Effects of carbon nanosolids on the electro-optical properties of a twisted nematic liquid-crystal host. *Appl. Phys. Lett.* **2004**, *85*, 513–515.
46. G. Scalia, J. P. F. Lagerwall, S. Schymura, M. Haluska, F. Giesselmann, and S. Roth. Carbon nanotubes in liquid crystals as versatile functional materials. *Physica Status Solidi B* **2007**, *244*, 4212–4217.
47. P. van der Schoot, V. Popa-Nita, and S. Kralj. Alignment of carbon nanotubes in nematic liquid crystals. *J. Phys. Chem. B* **2008**, *112*, 4512–4518.
48. W. Gwizdala, K. Gorny, and Z. Gburski. Molecular dynamics and dielectric loss in 4-cyano-4-n-pentylbiphenyl (5CB) mesogene film surrounding carbon nanotube - Computer simulation. *J. Mol. Structure* **2008**, *887*, 148–151.
49. F. R. Hung. Quadrupolar particles in a nematic liquid crystal: Effects of particle size and shape. *Phys. Rev. E* **2009**, *79*, 021705.
50. A. Dawid and W. Gwizdala. Dynamical and structural properties of 4-cyano-4-n-pentylbiphenyl (5CB) molecules adsorbed on carbon nanotubes of different chiralities: Computer simulation. *J. Non-crystalline Solids* **2009**, *355*, 1302–1306.
51. M. J. Green, A. N. G. Parra-Vasquez, N. Behabtu, and M. Pasquali. Modeling the phase behavior of polydisperse rigid rods with attractive interactions with applications to single-walled carbon nanotubes in superacids. *J. Chem. Phys.* **2009**, *131*, 084901.
52. V. Popa-Nita and S. Kralj. Liquid crystal-carbon nanotubes mixtures. *J. Chem. Phys.* **2010**, *132*, 024902.
53. A. Matsuyama. Biaxial nematic phase in mixtures of a liquid crystal and a rodlike polymer. *Mol. Cryst. Liq. Cryst.* **2011**, *540*, 42–49.
54. A. Matsuyama. Biaxial nematic phases in rod/liquid crystal mixtures. *Liq. Cryst.* **2011**, *38*, 729–736.
55. A. M. Somoza, C. Sagui, and C. Roland. Liquid crystal phases of capped carbon nanotubes. *Phys. Rev. B* **2001**, *63*, *81403*. (R).
56. S. Giordani, S. D. Bergin, V. Nicolosi, S. Lebedkin, M. M. Kappes, W. J. Blau, and J. N. Coleman. Debundling of single-walled nanotubes by dilution: Observation of large populations of individual nanotubes in amide solvent dispersions. *J. Phys. Chem. B.* **2006**, *110*, 15708–15718.
57. S. D. Bergin, Z. Y. Sun, D. Rickard, P. V. Streich, J. P. Hamilton, and J. N. Coleman. Multicomponent solubility parameters for single-walled carbon nanotube-solvent mixtures. *ACS Nano* **2009**, *3*, 2340–2350.
58. H. Wang. Dispersing carbon nanotubes using surfactants. *Curr. Opin. Colloid Interface Sci.* **2009**, *14*, 364–371.

59. M. Zheng, A. Jagota, E. D. Semke, B. A. Diner, R. S. Mclean, S. R. Lustig, R. E. Richardson, and N. G. Tassi. DNA-assisted dispersion and separation of carbon nanotubes. *Nature Mater.* **2003**, *2*, 338–342.
60. S. Park, H. S. Yang, D. Kim, K. Jo, and S. Jon. Rational design of amphiphilic polymers to make carbon nanotubes water-dispersible, anti-biofouling, and functionalizable. *Chem. Commun.* **2008**, 2876–2878.
61. S. Schymura, S. Dölle, J. Yamamoto, and J. Lagerwall. Filament formation in carbon nanotube-doped lyotropic liquid crystals. *Soft Matter* **2011**, *7*, 2663–2667.
62. F. Tardani and L. M. Camillo. Elasticity of dispersions based on carbon nanotubes dissolved in a lyotropic nematic solvent. *J. Phys. Chem. C* **2011**, *115*, 9424–9431.
63. X. Xin, H. Li, E. Kalwarczyk, A. Kelm, M. Fialkowski, E. Gorecka, D. Pociecha, and R. Holyst. Single-walled carbon nanotube/lyotropic liquid crystal hybrid materials fabricated by a phase separation method in the presence of polyelectrolyte. *Langmuir* **2010**, *26*, 8821–8828.
64. Y. S. Kwon, B. M. Jung, H. Lee, and J. Y. Chang. Preparation of polymeric SWNT-liquid crystal composites using a polymerizable surfactant. *Macromolecules* **2010**, *43*, 5376–5381.
65. X. Xin, H. Li, S. A. Wieczorek, T. Szymborski, E. Kalwarczyk, N. Ziebacz, E. Gorecka, D. Pociecha, and R. Holyst. Incorporation of carbon nanotubes into a lyotropic liquid crystal by phase separation in the presence of a hydrophilic polymer. *Langmuir* **2010**, *26*, 3562–3568.
66. S. Schymura, E. Enz, S. Roth, G. Scalia, and J. P. F. Lagerwall. Macroscopic-scale carbon nanotube alignment via self-assembly in lyotropic liquid crystals. *Synthetic Metals* **2009**, *159*, 2177–2179.
67. G. Scalia, C. von Bühler, C. Hägele, S. Roth, F. Giesselmann, and J. P. F. Lagerwall. Spontaneous macroscopic carbon nanotube alignment via colloidal suspension in hexagonal columnar lyotropic liquid crystals. *Soft Matter* **2008**, *4*, 570–576.
68. C. Zamora-Ledezma, C. Blanc, M. Maugey, C. Zakri, P. Poulin, and E. Anglaret. Anisotropic thin films of single-wall carbon nanotubes from aligned lyotropic nematic suspensions. *Nano Lett.* **2008**, *8*, 4103–4107.
69. J. P. F. Lagerwall, G. Scalia, M. Haluska, U. Dettlaff-Weglikowska, S. Roth, and F. Giesselmann. Nanotube alignment using lyotropic liquid crystals. *Adv. Mater.* **2007**, *19*, 359–364.
70. V. Weiss, R. Thiruvengadathan, and O. Regev. Preparation and characterization of a carbon nanotube-lyotropic liquid crystal composite. *Langmuir* **2006**, *22*, 854–856.
71. J. P. F. Lagerwall, G. Scalia, M. Haluska, U. Dettlaff-Weglikowska, S. Roth, and F. Giesselmann. Simultaneous alignment and dispersion of carbon nanotubes with lyotropic liquid crystals. *Phys. Status Solidi B* **2006**, *243*, 3046–3049.
72. O. Mondain-monval and P. Poulin. Mixed colloid-surfactant systems. *J. Phys. Condensed Matter* **2004**, *16*, S1873–S1885.
73. M. Zapotocky, L. Ramos, P. Poulin, T. C. Lubensky, and D. A. Weitz. Particle-stabilized defect gel in cholesteric liquid crystals. *Science* **1999**, *283*, 209–212.
74. C. Zakri and P. Poulin. Phase behavior of nanotube suspensions: From attraction induced percolation to liquid crystalline phases. *J. Mater. Chem.* **2006**, *16*, 4095–4098.
75. E. Nativ-Roth, R. Yerushalmi-Rozen, and O. Regev. Phase behavior and shear alignment in SWNT-surfactant dispersions. *Small* **2008**, *4*, 1459–1467.

76. E. Nativ-Roth, O. Regev, and R. Yerushalmi-Rozen. Shear-induced ordering of micellar arrays in the presence of single-walled carbon nanotubes. *Chem. Commun.* **2008**, 2037–2039.
77. E. Nativ-Roth, R. J. Nap, I. Szleifer, and R. Yerushalmi-Rozen. Order–disorder transition induced by surfactant micelles in single-walled carbon nanotubes dispersions. *Soft Matter* **2010**, *6*, 5289–5292.
78. N. Nakashima, S. Okuzono, H. Murakami, T. Nakai, and K. Yoshikawa. DNA dissolves single-walled carbon nanotubes in water. *Chem. Lett.* **2003**, *32*, 456–457.
79. M. Zheng, A. Jagota, M. S. Strano, A. P. Santos, P. Barone, S.G. Chou, B. A. Diner, M. S. Dresselhaus, R. S. McLean, G. B. Onoa, G. G. Samsonidze, E. D. Semke, M. Usrey, and D. J. Walls. Structure-based carbon nanotube sorting by sequence-dependent DNA assembly. *Science* **2003**, *302*, 1545–1548.
80. S. Badaire, C. Zakri, M. Maugey, A. Derre, J. N. Barisci, G. Wallace, and P. Poulin. Liquid crystals of DNA-stabilized carbon nanotubes. *Adv. Mater.* **2005**, *17*, 1673.
81. B. Gigliotti, B. Sakizzie, D. Bethune, R. Shelby, and J. Cha. Sequence-independent helical wrapping of singles-walled carbon nanotubes by long genomic DNA. *Nano Lett.* **2006**, *6*, 159–164.
82. H. Cathcart, S. Quinn, V. Nicolosi, J. M. Kelly, W. J. Blau, and J. N. Coleman. Spontaneous debundling of single-walled carbon nanotubes in DNA-based dispersions. *J. Phys. Chem. C* **2007**, *111*, 66–74.
83. A. N. Enyashin, S. Gemming, and G. Seifert. DNA-wrapped carbon nanotubes. *Nanotechnology* **2007**, *18*, 245702.
84. R. R. Johnson, A. T. C. Johnson, and M. L. Klein. Probing the structure of DNA–Carbon nanotube hybrids with molecular dynamics. *Nano Lett.* **2007**, *8*, 69–75.
85. X. Tu and M. Zheng. A DNA-based approach to the carbon nanotube sorting problem. *Nano Res.* **2008**, *1*, 185–194.
86. G. Y. Ao, D. Nepal, M. Aono, and V. A. Davis. Cholesteric and nematic liquid crystalline phase behavior of double-stranded DNA stabilized single-walled carbon nanotube dispersions. *ACS Nano* **2011**, *5*, 1450–1458.
87. W. Wenseleers, I. I. Vlasov, E. Goovaerts, E. D. Obraztsova, A. S. Lobach, and A. Bouwen. Efficient isolation and solubilization of pristine single-walled nanotubes in bile salt micelles. *Adv. Funct. Mater.* **2004**, *14*, 1105–1112.
88. N. Puech, E. Grelet, P. Poulin, C. Blanc, and P. van der Schoot. Nematic droplets in aqueous dispersions of carbon nanotubes. *Phys. Rev. E* **2010**, *82*, 020702.
89. J. P. F. Lagerwall, R. Dabrowski, and G. Scalia. Antiferroelectric liquid crystals with induced intermediate polar phases and the effects of doping with carbon nanotubes. *J. Non-crystalline Solids* **2007**, *353*, 4411–4417.
90. S. Schymura, M. Kühnast, V. Lutz, S. Jagiella, U. Dettlaff-Weglikowska, S. Roth, F. Giesselmann, C. Tschierske, G. Scalia, and J. Lagerwall. Towards efficient dispersion of carbon nanotubes in thermotropic liquid crystals. *Adv. Funct. Mater.* **2010**, *20*, 3350–3357.
91. G. Scalia, J. P. F. Lagerwall, M. Haluska, U. Dettlaff-Weglikowska, F. Giesselmann, and S. Roth. Effect of phenyl rings in liquid crystal molecules on SWCNTs studied by Raman spectroscopy. *Physica Status Solidi B* **2006**, *243*, 3238–3241.
92. S. Meuer, L. Braun, and R. Zentel. Solubilisation of multi walled carbon nanotubes by alpha-pyrene functionalised PMMA and their liquid crystalline self-organisation. *Chem. Commun.* **2008**, 3166–3168.

93. Y. Ji, Y. Y. Huang, R. Rungsawang, and E. M. Terentjev. Dispersion and alignment of carbon nanotubes in liquid crystalline polymers and elastomers. *Adv. Mater.* **2010**, *22*, 3436–3440.

94. M. Kühnast, C. Tschierske, and J. Lagerwall. Tailor-designed polyphilic promotors for stabilizing dispersions of carbon nanotubes in liquid crystals. *Chem. Commun.* **2010**, 6989–6991.

95. M. Kimura, N. Miki, N. Adachi, Y. Tatewaki, K. Ohta, and H. Shirai. Organization of single-walled carbon nanotubes wrapped with liquid-crystalline-conjugated oligomers. *J. Mater. Chem.* **2009**, *19*, 1086–1092.

96. S. Manne, J. Cleveland, H. Gaub, G. Stucky, and P. Hansma. Direct visualization of surfactant Hemimicelles by force microscopy of the electrical double-layer. *Langmuir* **1994**, *10*, 4409–4413.

97. H. W. Lee, W. You, S. Barman, S. Hellstrom, M. C. LeMieux, J. H. Oh, S. Liu, T. Fujiwara, W. M. Wang, B. Chen, Y. W. Jin, J. M. Kim, and Z. Bao. Lyotropic liquid-crystalline solutions of high-concentration dispersions of single-walled carbon nanotubes with conjugated polymers. *Small* **2009**, *5*, 1019–1024.

98. O. Trushkevych, N. Collings, T. Hasan, V. Scardaci, A. C. Ferrari, T. D. Wilkinson, W. A. Crossland, W. I. Milne, J. Geng, B. F. G. Johnson, and S. Macaulay. Characterization of carbon nanotube-thermotropic nematic liquid crystal composites. *J. Phys. D-Appl. Phys.* **2008**, *41*, 125106.

99. L. Onsager. The effects of shape on the interaction of colloidal particles. *Ann. N. Y. Acad. Sci.* **1949**, *51*, 627–659.

100. A. Donald, A. Windle, and S. Hanna. *Liquid Crystalline Polymers*. Cambridge University Press, 2006.

101. W. H. Song, I. A. Kinloch, and A. H. Windle. Nematic liquid crystallinity of multiwall carbon nanotubes. *Science* **2003**, *302*, 1363–1363.

102. W. Song and A. Windle. Isotropic-nematic phase transition of dispersions of multiwall carbon nanotubes. *Macromolecules* **2005**, *38*, 6181–6188.

103. S. J. Zhang, I. A. Kinloch, and A. H. Windle. Mesogenicity drives fractionation in lyotropic aqueous suspensions of multiwall carbon nanotubes. *Nano Lett*. **2006**, *6*, 568–572.

104. S. E. Moulton, M. Maugey, P. Poulin, and G. G. Wallace. Liquid crystal behavior of single-walled carbon nanotubes dispersed in biological hyaluronic acid solutions. *J. Am. Chem. Soc.* **2007**, *129*, 9452–9457.

105. V. Davis, L. Ericson, A. Parra-vasquez, H. Fan, Y. Wang, V. Prieto, J. Longoria, S. Ramesh, R. Saini, C. Kittrell, W. Billups, W. Adams, R. Hauge, R. Smalley, and M. Pasquali. Phase behavior and rheology of SWNTs in superacids. *Macromolecules* **2004**, *37*, 154–160.

106. L. M. Ericson, H. Fan, H. Peng, V. A. Davis, W. Zhou, J. Sulpizio, Y. Wang, R. Booker, J. Vavro, C. Guthy, A. N. Parra-Vasquez, M. J. Kim, S. Ramesh, R. K. Saini, C. Kittrell, G. Lavin, H. Schmidt, W. W. Adams, W. E. Billups, M. Pasquali, W. F. Hwang, R. H. Hauge, J. E. Fischer, and R. E. Smalley. Macroscopic, neat, single-walled carbon nanotube fibers. *Science* **2004**, *305*, 1447–1450.

107. P. Rai, R. Pinnick, A. Parra-vasquez, V. Davis, H. Schmidt, R. Hauge, R. Smalley, and M. Pasquali. Isotropic-nematic phase transition of single-walled carbon nanotubes in strong acids. *J. Am. Chem. Soc.* **2006**, *128*, 591–595.

108. N. Puech, C. Blanc, E. Grelet, C. Zamora-Ledezma, M. Maugey, C. Zakri, E. Anglaret, and P. Poulin. Highly ordered carbon nanotube nematic liquid crystals. *J. Phys. Chem. C* **2011**, *115*, 3272–3278.

109. V. A. Davis, A. N. G. Parra-Vasquez, M. J. Green, P. K. Rai, N. Behabtu, V. Prieto, R. D. Booker, J. Schmidt, E. Kesselman, W. Zhou, H. Fan, W. W. Adams, R. H. Hauge, J. E. Fischer, Y. Cohen, Y. Talmon, R. E. Smalley, and M. Pasquali. True solutions of single-walled carbon nanotubes for assembly into macroscopic materials. *Nat. Nanotechnol.* **2009**, *4*, 830–834.

110. A. N. G Parra-Vasquez, N. Behabtu, M. J. Green, C. L. Pint, C. C. Young, J. Schmidt, E. Kesselman, A. Goyal, P. M. Ajayan, Y. Cohen, Y. Talmon, R. H. Hauge, and M. Pasquali. Spontaneous dissolution of ultralong single- and multiwalled carbon nanotubes. *ACS Nano* **2010**, *4*, 3969–3978.

111. W. H. Song and A. H. Windle. Size-dependence and elasticity of liquid-crystalline multiwalled carbon nanotubes. *Adv. Mater.* **2008**, *20*, 3149–3154.

112. A. Speranza and P. Sollich. Isotropic–nematic phase equilibria in the Onsager theory of hard rods with length polydispersity. *Phys. Rev. E.* **2003**, *67*, 061702.

113. S. Zhang, Q. Li, I. A. Kinloch, and A. H. Windle. Ordering in a droplet of an aqueous suspension of single-wall carbon nanotubes on a solid substrate. *Langmuir* **2010**, *26*, 2107–2112.

114. R. Wang, J. Sun, and L. Gao. Liquid-crystal phase reinforced carbon nanotube fibers. *J. Phys. Chem. C* **2010**, *114*, 4923–4928.

115. S. J. Zhang, K. K. K. Koziol, I. A. Kinloch, and A. H. Windle. Macroscopic fibers of well-aligned carbon nanotubes by wet spinning. *Small* **2008**, *4*, 1217–1222.

116. M. Islam, A. Alsayed, Z. Dogic, J. Zhang, T. Lubensky, and A. Yodh. Nematic nanotube gels. *Phys. Rev. Lett.* **2004**, *92*, 088303.

117. F. Brochard and P.-G. de Gennes. Theory of magnetic suspensions in liquid crystals. *J. Phys. (Paris)* **1970**, *31*, 691–708.

118. S. V. Burylov and Y. L. Raikher. Orientation of a solid particle embedded in a monodomain nematic liquid crystal. *Phys. Rev. E* **1994**, *50*, 358–367.

119. I. C. Khoo, J. Ding, Y. Y. Zhang, K. Chen, and A. Diaz. Supra-nonlinear photorefractive response of single-walled carbon nanotube- and C60-doped nematic liquid crystal. *Appl. Phys. Lett.* **2003**, *82*, 3587.

120. W. Lee, H.-Y. Chen, and S.-L. Yeh. Surface-sustained permanent gratings in nematic liquid crystals doped with carbon nanotubes. *Opt. Express* **2002**, *10*, 482–487.

121. W. Lee and S.-L. Yeh. Optical amplification in nematics doped with carbon nanotubes. *Appl. Phys. Lett.* **2001**, *79*, 4488.

122. H. J. Shah, A. K. Fontecchio, D. Mattia, and Y. Gogotsi. Field controlled nematic-to-isotropic phase transition in liquid crystal–carbon nanotube composites. *J. Appl. Phys.* **2008**, *103*, 064314.

123. R. Basu and G. S. Iannacchione. Carbon nanotube dispersed liquid crystal: a nano electromechanical system. *Appl. Phys. Lett.* **2008**, *93*, 183105.

124. A. I. Goncharuk, N. I. Lebovka, L. N. Lisetski, and S. S. Minenko. Aggregation, percolation and phase transitions in nematic liquid crystal EBBA doped with carbon nanotubes. *J. Phys. D-Appl. Phys.* **2009**, *42*, 165411.

125. L. N. Lisetski, S. S. Minenko, A. V. Zhukov, P. P. Shtifanyuk, and N. I. Lebovka. Dispersions of carbon nanotubes in cholesteric liquid crystals. *Mol. Cryst. Liq. Cryst.* **2009**, *510*, 43–50.

126. R. Basu and G. S. Iannacchione. Nematic anchoring on carbon nanotubes. *Appl. Phys. Lett.* **2009**, *95*, 173113.

127. R. Basu and G. S. Iannacchione. Dielectric hysteresis, relaxation dynamics, and nonvolatile memory effect in carbon nanotube dispersed liquid crystal. *J. Appl. Phys.* **2009**, *106*, 124312.

128. V. Jayalakshmi and S. K. Prasad. Understanding the observation of large electrical conductivity in liquid crystal-carbon nanotube composites. *Appl. Phys. Lett.* **2009**, *94*, 202106.

129. P. Arora, A. Mikulko, F. Podgornov, and W. Haase. Dielectric and electro-optic properties of new ferroelectric liquid crystalline mixture doped with carbon nanotubes. *Mol. Cryst. Liq. Cryst.* **2009**, *502*, 1–8.

130. F. V. Podgornov, A. M. Suvorova, A. V. Lapanik, and W. Haase. Electrooptic and dielectric properties of ferroelectric liquid crystal/single walled carbon nanotubes dispersions confined in thin cells. *Chem. Phys. Lett.* **2009**, *479*, 206–210.

131. L. A. Dolgov, N. I. Lebovka, and O. V. Yaroshchuk. Effect of electrooptical memory in suspensions of carbon nanotubes in liquid crystals. *Colloid J.* **2009**, *71*, 603–611.

132. O. Yaroshchuk, S. Tomylko, L. Dolgov, T. Semikina, and O. Koyalchuk. Carbon nanotubes doped liquid crystals: robust composites with a function of electro-optic memory. *Diamond Relat. Mater.* **2010**, *19*, 567–572.

133. S. K. Shriyan and A. K. Fontecchio. Analysis of effects of oxidized multiwalled carbon nanotubes on electro-optic polymer/liquid crystal thin film gratings. *Opt. Express* **2010**, *18*, 24842–24852.

134. V. V. Ponevchinsky, A. I. Goncharuk, V. I. Vasil'ev, N. I. Lebovka, and M. S. Soskin. Cluster self-organization of nanotubes in a nematic phase: the percolation behavior and appearance of optical singularities. *JETP Lett.* **2010**, *91*, 241–244.

135. M. E. Abbasov, S. Ghosh, A. Quach, and G. O. Carlisle. Hybrid carbon nanotube and dye-doped liquid crystal material for holographic imaging. *J. Mater. Sci. Mater. Electron.* **2010**, *21*, 854–859.

136. S. Tomylko, L. Dolgov, T. Semikina, and O. Yaroshchuk. Liquid crystal–carbon nanotubes composites with the induced chirality: The way towards enhancement of electro-optic memory. *Mol. Cryst. Liq. Cryst.* **2010**, *527*, 130–136.

137. O. Buluy, S. Nepijko, V. Reshetnyak, E. Ouskova, V. Zadorozhnii, A. Leonhardt, M. Ritschel, G. Schoenhense, and Y. Reznikov. Magnetic sensitivity of a dispersion of aggregated ferromagnetic carbon nanotubes in liquid crystals. *Soft Matter* **2011**, *7*, 644–649.

138. L. N. Lisetski, S. S. Minenko, V. V. Ponevchinsky, M. S. Soskin, A. I. Goncharuk, and N. I. Lebovka. Microstructure and incubation processes in composite liquid crystalline material (5CB) filled with multi walled carbon nanotubes. *Materialwissenschaft Und Werkstofftechnik* **2011**, *42*, 5–14.

139. K. P. Sigdel and G. S. Iannacchione. Effect of carbon nanotubes on the isotropic to nematic and the nematic to smectic-A phase transitions in liquid crystal and carbon nanotubes composites. *Eur. Phys. J. E* **2011**, *34*, 34.

140. K. Won, R. Rajasekharan, P. Hands, Q. Dai, and T. W. Wilkinson. Adaptive lenticular lens array using a hybrid liquid crystal-carbon nanotube nanophotonic device. *Opt. Eng.* **2011**, *50*, 054002.

141. H. S. Jeong, Y. K. Ko, Y. H. Kim, D. K. Yoon, and H.-T. Jung. Self assembled plate-like structures of single-walled carbon nanotubes by non-covalent hybridization with smectic liquid crystals. *Carbon* **2010**, *48*, 774–780.

142. R. Basu, K. A. Boccuzzi, S. Ferjani, and C. Rosenblatt. Carbon nanotube-induced chirality in an achiral liquid crystal. *Appl. Phys. Lett.* **2010**, *97*, 121908.

143. R. Basu, R. G. Petschek, and C. Rosenblatt. Nematic electroclinic effect in a carbon-nanotube-doped achiral liquid crystal. *Phys. Rev. E* **2011**, *83*, 041707.

144. R. Basu, C.-L. Chen, and C. Rosenblatt. Carbon nanotube-induced macroscopic helical twist in an achiral nematic liquid crystal. *J. Appl. Phys.* **2011**, *109*, 083518.

145. S. Kumar and H. Bisoyi. Aligned carbon nanotubes in the supramolecular order of discotic liquid crystals. *Angew. Chem. Int. Ed.* **2007**, *46*, 1501–1503.

146. M. Lynch and D. Patrick. Organizing carbon nanotubes with liquid crystals. *Nano Lett.* **2002**, *2*, 1197–1201.

147. I. Dierking, G. Scalia, and P. Morales. Liquid crystal–carbon nanotube dispersions. *J. Appl. Phys.* **2005**, *97*, 044309.

148. I. Dierking, G. Scalia, P. Morales, and D. Leclere. Aligning and reorienting carbon nanotubes with nematic liquid crystals. *Adv. Mater.* **2004**, *16*, 865–869.

149. G. Duesberg, I. Loa, M. Burghard, K. Syassen, and S. Roth. Polarized Raman spectroscopy on isolated single-wall carbon nanotubes. *Phys. Rev. Lett.* **2000**, *85*, 5436–5439.

150. G. Scalia, M. Haluska, U. Dettlaff-Weglikowska, F. Giesselmann, and S. Roth. Polarized Raman spectroscopy study of SWCNT orientational order in an aligning liquid crystalline matrix. *AIP Conf. Proc.* **2005**, *786*, 114–117.

151. S. Kumar, T. Dang, F. Arnold, A. Bhattacharyya, B. Min, X. Zhang, R. Vaia, C. Park, W. Adams, R. Hauge, R. Smalley, S. Ramesh, and P. Willis. Synthesis, structure, and properties of pbo/swnt composites. *Macromolecules* **2002**, *35*, 9039–9043.

152. J. Li, X. Chen, X. Li, H. Cao, H. Yu, and Y. Huang. Synthesis, structure and properties of carbon nanotube/poly(p-phenylene benzobisoxazole) composite fibres. *Polym. Int.* **2006**, *55*, 456–465.

153. K. Okano, I. Noguchi, and T. Yamashita. Anisotropic carbon nanotube films fabricated from a lyotropic liquid-crystalline polymer. *Macromolecules* **2010**, *43*, 5496–5499.

154. W. Q. Jiang, B. Yu, W. M. Liu, and J. C. Hao. Carbon nanotubes incorporated within lyotropic hexagonal liquid crystal formed in room-temperature ionic liquids. *Langmuir* **2007**, *23*, 8549–8553.

155. M. S. Mauter, M. Elimelech, and C. O. Osuji. Nanocomposites of vertically aligned single-walled carbon nanotubes by magnetic alignment and polymerization of a lyotropic precursor. *ACS Nano* **2010**, *4*, 6651–6658.

156. H. J. Choi, J. Y. Kim, and S. H. Kim. Multi-wall carbon nanotube reinforced thermotropic liquid crystal copolyester nanocomposites. *Mol. Cryst. Liq. Cryst.* **2009**, *510*, 300–311.

157. X. Wang, J. Wang, W. Zhao, L. Zhang, X. Zhong, R. Li, and J. Ma. Synthesis and characterization of thermotropic liquid crystalline polyester/multi-walled carbon nanotube nanocomposites. *Appl. Surf. Sci.* **2010**, *256*, 1739–1743.

158. E. Lafuente, M. Pinol, M. T. Martinez, E. Munoz, L. Oriol, and J. L. Serrano. Preparation and characterization of nematic polyazomethine/single-walled carbon nanotube composites prepared by in situ polymerization. *J. Polym. Sci. Part A-Polym. Chem.* **2009**, *47*, 2361–2372.

159. N. G. Sahoo, H. K. F. Cheng, L. Li, S. H. Chan, Z. Judeh, and J. Zhao. Specific functionalization of carbon nanotubes for advanced polymer nanocomposites. *Adv. Funct. Mater.* **2009**, *19*, 3962–3971.

160. T. Hu, H. Xie, L. Chen, G. Zhong, and H. Zhang. Preparation and orientation behavior of multi-walled carbon nanotubes grafted with a side-chain azobenzene liquid crystalline polymer. *Polym. Int.* **2011**, *60*, 93–101.

161. C. Ohm, M. Brehmer, and R. Zentel. Liquid crystalline elastomers as actuators and sensors. *Adv. Mater.* **2010**, *22*, 3366–3387.

162. S. Courty, J. Mine, A. Tajbakhsh, and E. M. Terentjev. Nematic elastomers with aligned carbon nanotubes: New electromechanical actuators. *Europhys. Lett.* **2008**, *64*, 654–660.

163. L. Q. Yang, K. Setyowati, A. Li, S. Q. Gong, and J. Chen. Reversible infrared actuation of carbon nanotube-liquid crystalline elastomer nanocomposites. *Adv. Mater.* **2008**, *20*, 2271.

164. D. Sordi, C. De Ruijter, S. Orlanducci, S. J. Picken, E. J. R. Sudhoelter, M. L. Terranova, L. C. P. M. De Smet, and T. J. Dingemans. Sulfonated liquid crystalline polyesters as resin matrix for single wall carbon nanotube and nanodiamond composites. *J. Polym. Sci. Part A-Polym. Chem.* **2011**, *49*, 1079–1087.

165. R. Cervini, G. P. Simon, M. Ginic-Markovic, J. G. Matisons, C. Huynh, and S. Hawkins. Aligned silane-treated MWCNT/liquid crystal polymer films. *Nanotechnology* **2008**, *19*, 175602.

CHAPTER 11

Liquid Crystals in Metamaterials

AUGUSTINE M. URBAS and DEAN P. BROWN
Materials and Manufacturing Directorate, Air Force Research Laboratory WPAFB, OH, USA

11.1 INTRODUCTION

Poised to deliver advances in electromagnetic technologies, the field of metamaterials is rapidly expanding the range of electromagnetic properties available in materials by leveraging structured composites to generate targeted response outside of what is available in conventional materials. While novel and useful electromagnetic properties are the genesis of metamaterials research [1], the field has expanded to include acoustic/mechanical systems [2] and thermal materials [3, 4] as well. Structured electromagnetic materials have a long history in research [5] and this latest incarnation was spurred by the work of Pendry [6] and Smith et al. [7] on creating materials with artificial negative refractive index to demonstrate phenomena predicted by Veselago [8] decades ago. Many excellent references for a general understanding of metamaterials are available that describe the physics and research of these interesting and potentially useful systems in great detail and we direct readers to these references for background information in order to better cover the topic at hand. In short, metamaterial systems typically rely on sub-wavelength features or inclusions, sometimes called meta-atoms, with a structurally defined response, such as a shaped metallic or dielectric inclusion that possesses a resonance, which supplant the fundamental response of the atoms and molecules of the medium. Combined with secondary ordering which modifies the individual properties of the meta-atoms and introduces collective behavior, this meso-scale, local response to incident fields gives rise to a new effective bulk response of the system. When carefully composed, such systems can yield the target electromagnetic materials properties combinations, which are uniquely suited for a specific application. The most illustrative example of a metamaterial, and one of the first things to be called so, is the split ring resonator array. These can be simply a cubic lattice of metallic rings with a cut or gap in each ring. These arrays of shaped metal inclusions used to

Liquid Crystals Beyond Displays: Chemistry, Physics, and Applications, Edited by Quan Li.
© 2012 John Wiley & Sons, Inc. Published 2012 by John Wiley & Sons, Inc.

generate artificial magnetic media even though they are composed of non-magnetic component materials [9, 10]. The overall utility of metamaterials is enhanced by the ease with which gradients can be made by simple structural changes to the individual meta-atoms. This attribute is a fundamental enabler of the co-rising field of transformation optics which aims to change the way in which electromagnetic devices are conceived [11, 12]. Metamaterials also provide unique opportunities for tunable, active, and responsive materials since the fundamental unit, the meta-atom, can be loaded with small, dynamic components [13] or materials [14, 15] in order to change the overall system response. Indeed, the use of liquid crystals has been frequently suggested as a mode of tuning metamaterial response and key demonstrations have already shown significant potential in this area. Tunable metamaterials derived in this way will enable the design of highly nonlinear and dramatically responsive systems that are not possible in conventional materials and they will enable reconfigurable and dynamic antenna and aperture systems for optical and radio frequency (RF) applications.

11.2 METAMATERIALS BACKGROUND

Simple metamaterials are composed of meta-atoms or unit cells, such as split rings or metallic wires, in a periodic array. The properties of the meta-atoms define the overall response of the material. In order to modify both permeability ($\mu = \mathbf{H/B}$) and permittivity ($\varepsilon = \mathbf{E/D}$), susceptibilities for both magnetic and electric fields must be inherent to the meta-atom and material structure. In a basic example, a wire array and a split ring resonator array, both structured to give negative values at the same frequency of the permittivity and permeability, respectively, are combined to yield a negative index [10]. We will look closer at these simple independent media to see the key characteristics and how their properties can be tuned by the incorporation and control of LCs. Wire arrays have long been used as artificial dielectrics for RF frequencies [16]. A simple example is composed of long wires on a regular square lattice. The combination of wire size and spacing tunes both the density and effective mass of electrons in the medium. This in turn defines the new plasma frequency of the wire medium, creating an artificial response for a range of frequencies analogous to a Drude metal with the effective plasma frequency as shown in the equation below, for incident waves with electric field polarized along the wires [17].

$$\varepsilon_{eff} = 1 - \frac{2\pi c^2}{\omega^2 a^2 \ln(a/r)} = 1 - \frac{\omega_{eff}^2}{\omega^2} \tag{11.1}$$

A more characteristic example within metamaterials is that of the split ring resonator (SRR), initially proposed as a component of a negative index material by Smith et al [10]. A wide range of designs for resonant inclusions have since been explored, each having unique characteristic and advantages. In many cases, these can still be understood as one or more modified SRR units. In its simplest form the SRR is

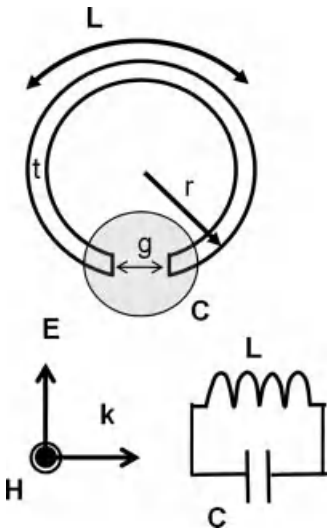

FIGURE 11.1 A simple split ring resonator where the structural features corresponding to equivalent circuit elements are indicated.

simply a cut loop as shown in Figure 11.1. As an inclusion, it can be understood as a free standing resonant circuit, by considering the gap as a capacitor with its plates shorted by the inductive ring. The effective inductance and capacitance of this structure combine to give its resonant frequency. The SRR couples to the magnetic component of an incident wave polarized along the axis of the ring. This induces current in the ring and drives oscillating fields whose magnitude depends on the incident frequency relative to the resonance of the ring giving the SRR an effective magnetic susceptibility. In a medium or array as shown in Figure 11.2, the response or effective permeability for a wave propagating through a medium composed of layers stacked out of the page with the magnetic field polarized along the axis of the ring is determined by the fill factor and geometric properties of the split ring units. The effective permeability of the SRR array can be written as:

$$\mu_{eff} = 1 - \frac{f\omega^2}{\omega^2 - \omega_0^2 + i\omega\Gamma} \tag{11.2}$$

after the notation of Smith et al. [10] and Pendry et al. [18] where $f = \pi r^2/a^2$ is the fill fraction of rings, ω is the incident frequency and $\omega_0 = 1/\text{LC}$ is the resonant frequency of the SRR unit. Coupling between neighboring meta-atoms [19, 20] and the spatial dispersion [21] play a significant role in the effective response and are widely discussed in the context of metamaterials. The resonant properties of the unit cell or meta-atom are also defined by the local dielectric or magnetic environment of the inclusion. In the split ring unit, for example, the effective value of the capacitive part of the structure is determined by the gap dielectric. If it is filled with a liquid

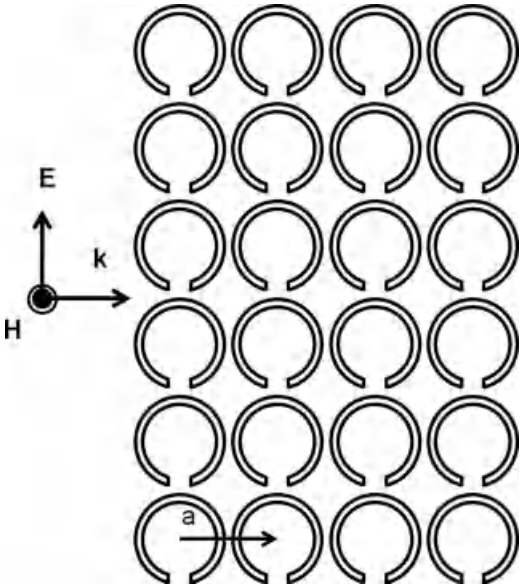

FIGURE 11.2 An artificial magnetic media made of an array of split ring resonators.

crystal material (LC material, not to be confused with the product of inductance and capacitance), then the resonant frequency of the SRR units is determined by the effective dielectric properties of the LC material and this in turn changes the effective medium properties of the array. This mechanism allows the overall structure to be sensitive to order and orientation of the LC material, or the properties of any material, within the gap which becomes the basis for tunable properties in metamaterials. Initial computational explorations and successful experimental demonstrations have been made specifically addressing liquid crystalline materials as the dynamic component in metamaterials systems.

Metamaterials were initially explored as effective bulk media where extended systems, built up from multiple layers of two dimensionally or three dimensionally patterned systems, are composed so as to deliver a new effective bulk response. This is an elusive goal and typically single effective media values for permeability, permittivity, or index can only be used to describe the behavior of these complex systems over some frequency range, incident angle range or under other specific conditions. Apart from effective bulk systems, in many applications, only a surface is needed to achieve the desired materials response [22]. This is clearly the case in frequency selective surfaces [23] or artificial magnetic conductors [24], which are typically planar periodic arrays of metallic features sometimes paired with and/or connected to an underlying ground plane. These planar systems have been incorporated into the larger understanding of metamaterials. It is no longer sensible to ascribe an effective bulk permittivity or permeability to this single layer, but the systems give useful response for some applications and in particular allow for the easy integration of liquid crystals as tunable media [25].

11.3 RF LC METAMATERIALS

Several key demonstrations of tunable RF metamaterials have been accomplished through the introduction of liquid crystals into typical RF metamaterials structures. A notable study demonstrated tunable magnetic permeability and in particular negative permeability in a split ring resonator type composite [26] and was followed up with tunable negative index in an Ω particle system [27] and fishnet type structures [28]. For more background on the Ω metamaterials see Simovski and He [29] or Huangfu et al. [30]. Tunable metamaterials at RF frequencies have been demonstrated in other ways, as well, relying on electronic components such as varactors (voltage tunable capacitors), [13, 31, 32] to change the resonant frequency of meta-atoms. Liquid crystals represent simple integration potential, however, and are beginning to be explored for RF applications [33, 34]. In several liquid crystal-based studies, standard metamaterial structures with resonant frequencies in the 10 s–100 GHz range were fabricated with alternating patterned metallic split rings or omega particles on Teflon substrates, which were sandwiched with spacers and infiltrated with liquid crystal materials. This has become a typical LC tunable metamaterial configuration due to the large field concentration between the closely spaced complementary patterns, ability to apply alignment fields and the convenience for introducing liquid crystal in a confined cell. As an example, the experimental structure implemented with split rings is by Zhang et al. [26] shown in Figure 11.3. The complementary pairs of split ring resonators are sandwiched facing one another with a layer of oriented liquid crystal between them in a two-dimensional array of standing pairs. The composite

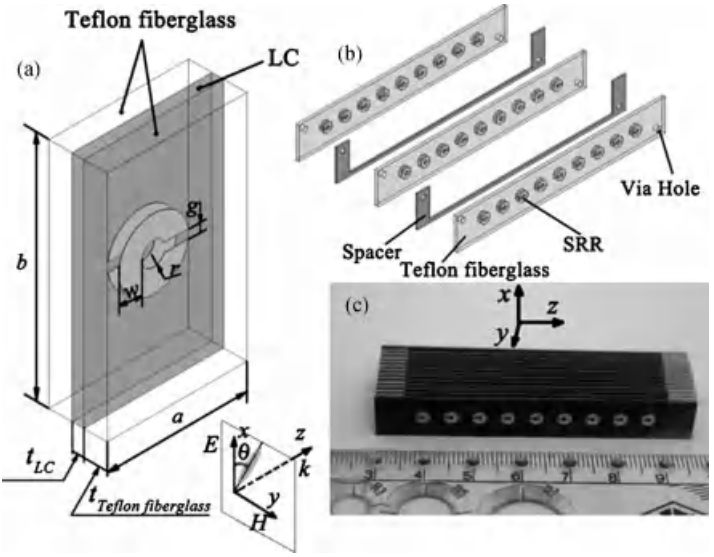

FIGURE 11.3 Experimental structure and arrangement of Zhang et al. indicating structural properties and the orientation of propagating fields. *Source*: Reprinted with permission from Zhang et al. *Applied Physics Letters*, American Institute of Physics.

was aligned so that pairs of meta-atoms overlaid one another and were separated by a thin layer of liquid crystal as shown in the diagram. In this configuration the fields coupling between the two complementary resonant elements are presumed to be largely perpendicular to their faces and most intense in the liquid crystal [35]. The orientation of the LC material was controlled with externally applied magnetic fields from permanent magnets. Using this scheme, Zhang et al. were able to provide two distinct orientations to the LC material, with the director either parallel or perpendicular to the planar meta-atoms. This presented a shift between effectively high and effectively low dielectric environments for the electric field coupling of the complementary structures. The coupling of the complementary rings is sensitive to the effective dielectric properties of the LC material between them which range from a low permittivity of 2.25 to a high permittivity of 2.82. Changes in the orientation of the LC director are shown to change the coupling of the rings and modify their effective resonant frequency. As is shown in Figure 11.4, a change of only a few percent in the center frequency of the resonance was experimentally demonstrated

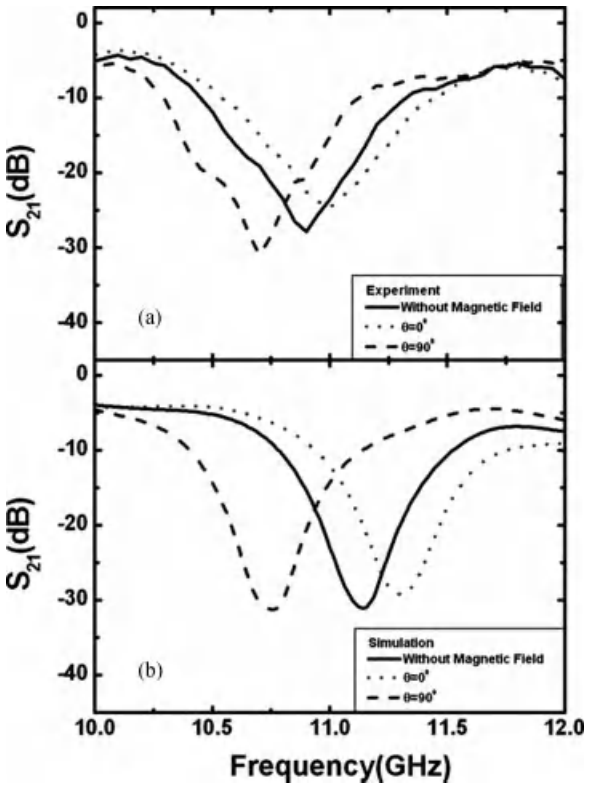

FIGURE 11.4 Experimental (a) and simulated (b) plots of the RF transmission of the metamaterial structure in Figure 11.3 showing the predicted and observed shift in resonance frequency with LC director orientation. *Source*: Reprinted with permission from Zhang et al. *Applied Physics Letters*, American Institute of Physics.

when compared with the roughly 20% shift of the dielectric properties of the LC. It is worth noting that the relative volume occupied by the LC was 1/3 of the overall unit cell. As shown above, the effective permittivity at a frequency depends on the separation from the resonance frequency. The shift in resonant frequency from the applied field provides a mechanism for tuning the effective properties of this material. Zhang et al. claimed to have tuned the band of negative permittivity. Though not explicitly shown in the report, it would have occurred very near resonance as was shown in an earlier report from the same group. In that study, a concentric complementary SRR structure exhibited tunable negative permeability but only over a very small frequency range [36]. These reports demonstrate uniform tuning of effective properties. The systems were, however, composed of only one or two layers of a two dimensional array. The use of magnetic fields, while effective, is likely to be impractical for larger systems and in many applications. Moreover, individually addressed, tunable unit cells may ultimately be more useful especially when considered for implementing dynamic transformation optics devices [37, 38].

11.4 RF TUNABLE "META-SURFACES" WITH LCs

Significant effort has been devoted to investigating tunable meta-surfaces for possible applications and tunable surfaces have received much of that focus. In addition to their inherent utility, this work can provide a "look ahead" at strategies and effects for bulk metamaterials systems. While, in general, liquid crystals have not received much attention in RF applications because of significant losses and response time limitations when compared with using electronic components for dynamic systems, they present a relatively simple and effective route for tunable systems and are being increasingly explored for components and tunable systems [39–41]. The advantages may be specifically suited to large area structures and for higher frequency applications (above 20 GHz) where electronic components become costly and performance is limited. This has made meta-surface-based studies a venue where useful demonstrations of LC tunable RF metamaterial based components and devices have been shown. Initial studies on tunable frequency selective surfaces (FSS) exhibited voltage tunable properties [42, 43]. The frequency selective surfaces used were composed of paired metal films with complementary or matching patterns, such as hole arrays to give resonant transmission or absorption windows at RF frequencies. The paired films were separated by a narrow cavity ($\sim$100 μm) that could be filled with LC. In general, FSSs have strong frequency dependent properties that vary considerably over spectral bands. The shape and size of the holes and properties of the surrounding dielectric determine the resonant frequency where transmission occurs. For paired films, coupling effects can also influence the overall properties. In an early study [42], paired FSS slot arrays were sandwiched around an LC cell containing BL037. The continuous FSSs were used as bias electrodes for the LC. When the LC director orientation was changed with applied voltage, the frequency of transmission shifted significantly (about 10%), which was consistent with predictions based on the expected properties of BL037. It is not clear from the reported analysis if the

shift in resonant frequency was simply related to the change in local dielectric around individual holes and if a change in coupling between films also played a role.

A subsequent experiment by Wenfei et al. [44, 45] utilized a more subtle aspect of meta-surfaces to create a tunable reflector. The meta-surface in this case was an array of square metal patches on a square two-dimensional lattice spaced over a metal ground plane as shown in Figure 11.5. In this configuration, isolated metal patches act as capacitive elements above the ground plane and possess a resonance based on their area or size. In this case, the patches were connected with thin bias lines to allow for electric field control of the liquid crystal filled between the upper metal film and lower ground plane, but minimally affected the RF properties. Applying a bias field changes the director orientation between the patch array and ground plane, as in a typical liquid crystal cell for display applications. This in turn tunes the effective capacitance of the patch and thereby its resonant frequency. The useful aspect of this, however, is that waves reflected from the surface acquire a phase shift. The phase shift of a given frequency depends on its displacement from the resonant frequency. By tuning the resonant frequency of the structure, the phase shift of the incident wave is changed. In this study, the patches were all biased in common and a single phase shift for the array was measured in a plane wave reflected from the surface. Phase shifts of nearly 165° and 130° were possible in regions of relatively low loss at 102 GHz and 130 GHz for separate structures. The same strategy was again used by Wenfei et al. [46], with a patterned array of diverse, different sized patches to generate a switchable beam pattern. Phase front synthesis requires more dynamically tunable phase control as shown in an example by Gaebler et al. [47]. Their demonstrations of a horn fed reflectarray based on a similar LC tunable meta-surface approach, where individual lines could be biased and subsequently, individual patches using a strategy similar to

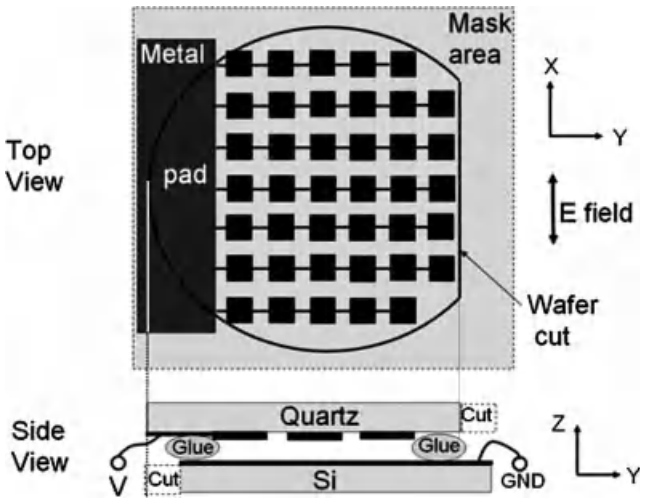

FIGURE 11.5 Tunable reflectarray configuration from Hu et al. showing bias and LC cell construction. *Source*: Reprinted with permission from Wenfei et al. *IEEE Transactions on Antennas and Propagation*, IEEE.

active LC displays, provided continuous scanning over $\pm 25^\circ$ along one plane for the line addressed and over a comparable cone angle for the fully addressable system with a bias of less than 15 V. It is important to point out that scanning is accomplished by the introduction of a predefined phase pattern, not simply by increasing bias voltage. More complex patterns can accomplish beam forming and other functions and require more precise control of phase fronts. Individual control of patches and sufficient area allow for complete control of beam shape and direction and ultimately could provide the significant utility, albeit with additional complexity. Losses from the LC material are comparable to those from scattering and dissipation in the metal structures. Significant power performance gains could be made with RF compatible, low loss LCs in this frequency range. These tunable surface arrays have been proposed as satellite-based antennas for RF communications [48]. The combination of large area, light weight and low operating power make them potentially appealing for this application.

11.5 LC TUNING OF META-ATOMS

The inherent leveraging of changes of a small volume of material to influence the effective bulk response of a metamaterial is a key characteristic that makes the intersection of metamaterials and liquid crystals intriguing and promising for research. Liquid crystals, of course, are an archetypal class of tunable materials which have been widely employed in changing the optical properties of devices, typically in displays and filters. The range that the properties of an LC system can be tuned over and the ease with which this is done by either temperature or applied fields, make them a material system of choice for devices and demonstrations of dynamic systems. In general, the bulk changes of dielectric properties that liquid crystals exhibit, either through phase changes (say from isotropic to nematic or between ordered phases) or by director orientation changes, such as from an applied field, are used directly. For example, in a liquid crystal display, polarization rotation is accomplished by a bulk layer of LC with appropriate alignment layers to give a texture through the layer which acts as an optical retarder. In essence, the whole optical path interacts with the LC in order for this device to function. In contrast, for a metamaterial system, the response of the system, e.g. of split rings, is determined by the resonant properties of the metallic meta-atom. For example, the split ring resonator we discussed before, this can be described as a resonant circuit with an inductive component (the ring) and a capacitive component (the split). The value of the capacitance is influenced by the dielectric properties of the material in and around the split. This has been studied in detail by Kowerdziej and coworkers [48–50] and by Zhang and coworkers [35]. Each has performed numerical analyses of different meta-atom designs that were loaded with LCs. The response of the system for different director orientations and as a function of the dielectric properties of the LC with temperature was predicted. Changes in resonance frequency, refractive index, and loss in bulk materials made from these unit cells were also done. Zhang et al. showed how the local fields within the meta-atom required that an accurate model of the

dielectric anisotropy and director orientation be used to predict accurate properties. Overall, significant shifts in resonant frequency and effective properties were shown, providing some promise for applications.

The studies of Zhang et al. and Kowerdziej et al. favored complementary meta-atom configurations, similar to those favored in experimental studies. Design studies aimed at enhancing the sensitivity of metamaterial structures to LC loading are still to be done. A simple series of calculations can show the sensitivity of a standard SRR to changes in LC orientation. The SRR design in Figure 11.6 was used for this purpose. A series of calculations was made with the structure immersed in BL006 (experimental data from Utsumi et al. [51] was used) with the director oriented perpendicular to the plane of the ring, along the y-axis. The incident wave was propagated in the z direction with the electric field polarized in the x direction and, as shown in Figure 11.7, the ring was found to have a resonance at 6.8 GHz. A comparison was made between this LC configuration and the LC director changed to the z orientation where the resonant frequency shifted minimally to $\sim$5 MHz higher frequency. In order to contrast this with the sensitivity of the structure to changes in the gap region alone, a calculation was made changing only the gap LC director to the z direction while leaving the ring immersed in the y oriented LC matrix. Interestingly, the resonance shifted to a significantly lower frequency of 6.73 GHz even though a much smaller volume of material was changed. Due to the complex fields surrounding the SRR structure, however, this counterintuitive behavior is not surprising. This shows the tremendous sensitivity to the gap dielectric that can be engineered into such systems, but clearly some care has to be taken to design the systems appropriately.

If we compare the volumetric sensitivities exhibited by the two cases in terms of frequency shift per unit volume-refractive index change there are six orders of magnitude difference between the gap only and all LC case, being 25 GHz/mm^3-RIU and 0.06 MHz/mm^3-RIU, respectively. Another way to think about this series of calculations is to consider the change in response of the resonant meta-atom to the

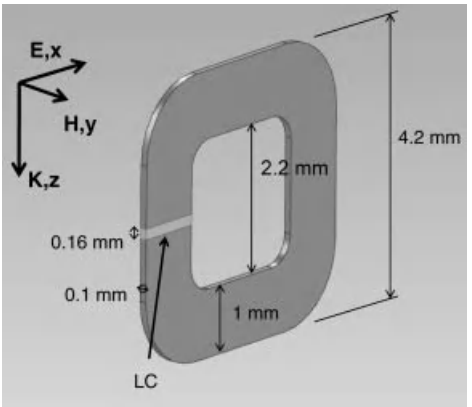

FIGURE 11.6 Split ring resonator diagram for LC sensitivity study indicating field orientations and alignment directions. The selectively oriented gap region is shaded gray.

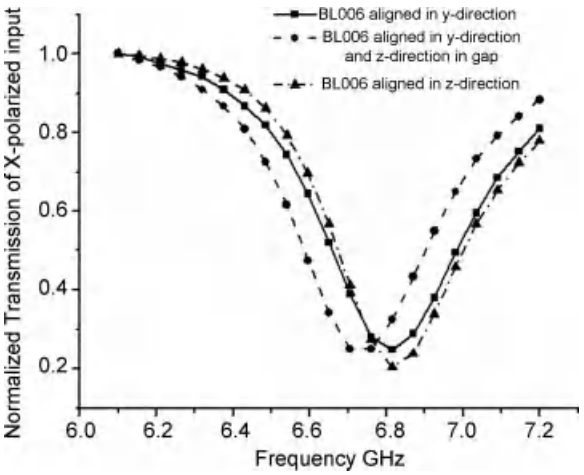

FIGURE 11.7 Calculated transmission spectra for the SRR medium in Figure 11.6 for various alignments of LC BL006.

change in LC director in the gap alone is comparable to the impact of the change due to the LC director orientation everywhere else (though the shifts counteract one another). Clearly there are significant advancements in unit cell design and polling field configuration possible to increase the tuning range and decrease potential losses of LC loaded cells. This may enhance the potential for more dramatic tuning and lower power requirements for tunable metamaterials compared with conventional bulk materials. The indirect loading of the SRR by the LC, which also can be understood as the coupling of the incident field to the LC via the metallic structure, is responsible for the overall change in effective response of the metamaterial. Although liquid crystals provide easy access to highly tunable properties and may be a system of choice for exploration of tunable properties in research and applications, there is nothing unique to LCs about the observed effects and the results are relevant to any tunable material used with a metamaterial. Indeed, in many meta-systems, the influence of the electromagnetic properties of a relatively small volume in the vicinity of the metallic or dielectric structure on the overall response of the structure and therefore the effective response of the composite metamaterial has been the proposed basis for sensor platforms [52], structural evaluations [53], highly nonlinear materials [54, 55], in addition to, tunable systems.

11.6 OPTICAL METAMATERIALS WITH LCs

The bulk of research in metamaterials falls in the RF frequency and LC metamaterials are no exception, although in both cases optical frequencies are actively and increasingly explored. Initial LC metamaterials work was mainly in the optical regime, an excellent exploration of which can be found here. In general, however,

metamaterials has followed the opposite course in research with initial demonstrations in RF followed by other frequency regimes, typically THz, infrared and then optical. As the frequency of the EM excitation increases, the character of the interaction between the structure and the electromagnetic field becomes more plasmonic in nature. Plasmons are collective oscillations of electron polarization at the interface between a metal and a dielectric [56]. Sub-wavelength metallic structures can exhibit localized surface plasmons at optical frequencies [57]. Plasmonic systems, which can still be effectively modeled with equivalent circuits to some extent, have been the basis for resonant metamaterials systems at optical frequencies and many key demonstrations, such as optical negative index, have been executed [58]. It is interesting to note the scaling and change of meta-atom structure and configuration as higher frequencies are explored. As we discussed above, the resonances within metamaterials can be modeled with equivalent circuits where structural inductances and capacitances are represented by the discrete equivalent circuit elements. The scaling with size of these two quantities and constituent materials properties is different as is highlighted by Soukoulis et al. [59]. At optical frequencies the structures used for negative index are modified to provide the correct balance of inductance and capacitance for the magnetic component and provide the effective permittivity response as well. One of the more popular configurations is the so called fishnet structure composed of a perforated multilayer, metal/dielectric film. The fishnet uniquely combines an electric and magnetic resonance in different structural elements at comparable frequencies as described by Zhang [60]. This structure has been widely explored as a negative index material over a range of frequencies [61]. Tunable fishnet structures for optical devices and modulators have been a long running goal of metamaterials research as well. Indeed, the infiltration of a fishnet structure with liquid crystal to provide tunable response was proposed shortly after the initial publication of the fishnet structure itself [25, 62, 63].

Liquid crystals have almost immediately been incorporated into materials at these higher frequencies in order to demonstrate tunable response due to the lack of other options and characterization difficulties of alternatives. The application of liquid crystals to optical metamaterials has been recently addressed by Diaz and Khoo [64], including excellent coverage of the underlying physics and phenomena. There are new and different challenges that arise here, however. They have both to do with the relatively small feature size of the metamaterials subunits at optical frequencies and with the difficulty in controlling the liquid crystal in regions where its orientation will alter the response of the overall metamaterials system. Bulk optical metamaterials are elusive due to loss and fabrication challenges. In thin or single layer metamaterials systems thermal response (tuning) has been demonstrated in a meta-magnetic system [65] and proposed in various configurations in an LC infiltrated fishnet structure. Electrical response has, to date, only been shown in single layer, 'meta-surface' configurations [66]. There is a substantial body of work on the interaction between LC's and plasmonic systems, which will be relevant in analyzing the current results and identifying future challenges.

A comparable study to the RF work above was explored, where LC was used in conjunction with a magnetic resonant grating to provide a tunable magnetic

metamaterial, a first step to tunable negative index. This grating structure is, in essence, analogous to the split ring component of a negative index metamaterial at RF frequencies and the study presented by Xiao et al. shows a clear parallel to this work. In brief, the structure in Figure 11.8 is composed of grating lines made of multilayered metal and dielectric materials. There are two metal films within each line separated vertically by a dielectric and capped with additional dielectric layers. For TM illumination, the magnetic component of the incident field excites circulating, anti-parallel currents in the metal films within each stripe yielding a magnetic resonance. A more detailed discussion can be found in the work of Cai et al. [67]. In the study by Xiao et al., the grating was infiltrated with LC and capped in a cell by a superstrate that had an applied PMMA alignment layer, as is shown in the diagram. The alignment layer had been rubbed so that the LC director would be aligned perpendicular to the grating lines, that is, the incident electric field was primarily

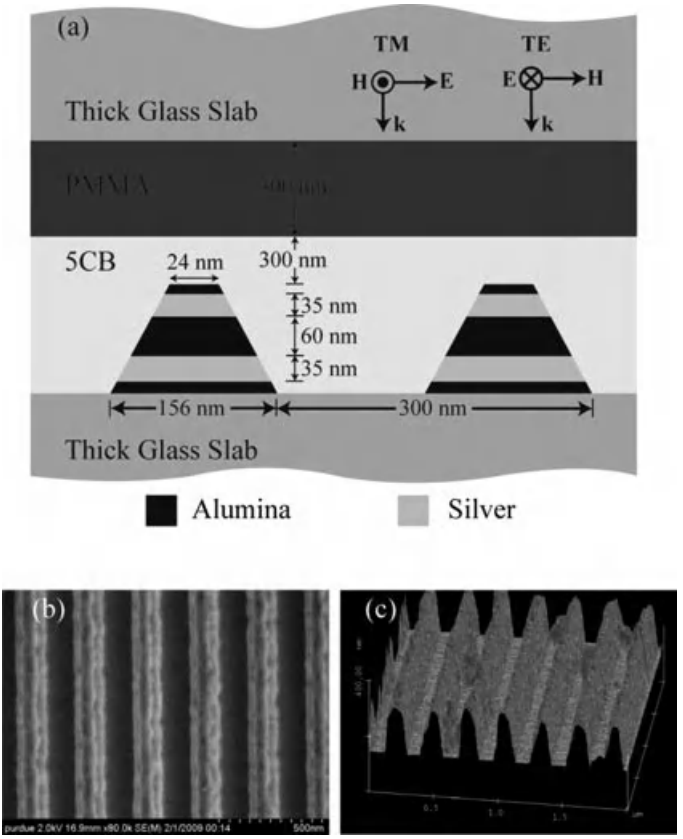

FIGURE 11.8 Diagram (a) of optical magnetic grating from Xiao et al. SEM image (b) and AFM (c) of experimentally characterized sample. *Source*: Reprinted with permission from Xiao et al., *Applied Physics Letters*, American Institute of Physics.

influenced by the extraordinary permittivity of the LC medium. The cell construction did not include provision for the application of field and so the only method of tuning the LC properties available was through temperature. It is likely that in the confined geometry, the local field profile and the ultimate effect on the director orientation field of the infiltrated LC from the applied field would be complex given the metal–dielectric composition of the film. The change in optical properties would be sensitive to this subtle configuration, but it is not intuitively clear what impact that would have on the properties. With the simpler temperature-based tuning of LC order, however, the structure did show a significant shift of the magnetic resonance center wavelength, about 50 nm shift in the center frequency, as is shown in Figure 11.9, as the sample was raised above the LC clearing temperature. The modeled results showed that the change was consistent with a change in index of 0.15 between the two states that is roughly consistent with the expected response of the structure and the 5CB liquid crystal used in the study. The authors, however, find that the effective extraordinary index of the LC appears to be lower than the literature values. This is attributed to air inclusions within the sample due to the complex structure. As noted above, in such a confined system there is likely to be a complex LC texture due to the structural influences and chemical anchoring changes influencing the LC director field. It is quite possible that the low effective index observed for the nematic state was caused by this director field which may have provided a more complex local orientation and distribution of the permittivity as it interacts with the plasmonic structure of the meta-magnetic grating than was accounted for in the model.

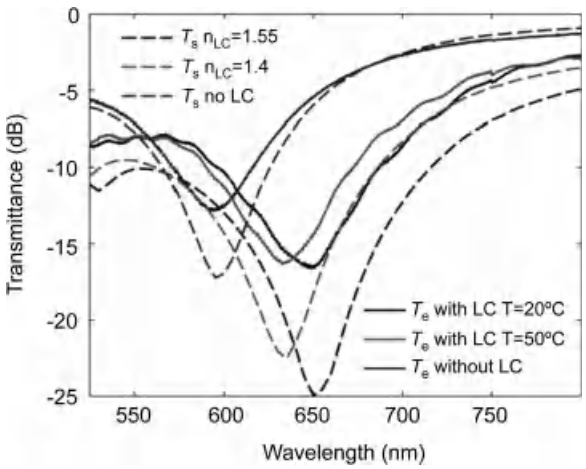

FIGURE 11.9 Measured (solid) and calculated (dashed) transmission spectrum of magnetic grating from Figure 11.8 without LC and with LC above and below the clearing temperature. *Source*: Reprinted with permission from Xiao et al. *Applied Physics Letters*, American Institute of Physics.

11.7 LC INTERACTION WITH PLASMONIC METAMATERIAL STRUCTURES

Dynamic plasmonic structures based on the interaction with LCs are a research field of their own that often crosses technically with optical metamaterials. There are a few interesting observations that can be made which highlight challenges that dynamic optical metamaterials using liquid crystals face. Many studies of changes in optical properties of plasmonic systems in response to liquid crystal order and orientation changes have been published. It is interesting to note the complex behavior observed in studies of single plasmonic particles and arrays. While switching of optical properties, typically observed as a change in the peak of the plasmon resonance, is observed roughly consistent with expectations based on the anisotropy of the LC, there are significant enhancements to shifts that have been attributed to field induced density fluctuations in the LC medium. A notable and early study by Muller et al. [68] explored the effect on an isolated spherical gold nanoparticle of immersion in LC and subsequent poling of the LC with an applied electric field. The shift in wavelength of the plasmon resonance peak for two orthogonal polarizations was shown to be in opposite directions, contrary to expectations. This is evidence of more complex field induced director textures around the particle or, as the authors suggest, possible density fluctuations induced by the field. A subsequent study by Chu et al. [69] on nanorods prepared in a similar fashion showed a clearer trend. In this study, while there was a clear difference between polarizations before applying the field, that is a dramatic splitting in the plasmons excited by two incident polarizations was observed [70, 71], which has been attributed to LC texture at the surface of the plasmonic particle. When field was applied, this splitting was dramatically reduced. The authors attributed this to possible density fluctuations, as Muller had, especially the pronounced red-shift of the cross polarized transverse mode.

In the simple model of liquid crystal orientation under applied field, this mode should only feel the low index in both the presence and absence of a poling field, as described by the authors. The reduced splitting in this and Muller's study can, however, be explained by the applied field acting to reduce anisotropy in the surface orientation of LC molecules close to the particle. Near the particle, a substantial component of the local electric field would be perpendicular to the particle surface as indicated in Figure 11.10 by the equipotentials curving around the central gold nanorod. This would direct the near surface orientation of LC director as illustrated by the dotted lines. In Chu's study, the LC near the surface of the particle would have the extraordinary axis oriented perpendicular to the surface. This would remove anisotropy that yields splitting in the plasmon modes. Notably, for the cross polarized transverse mode, it would result in a switch from the low index of the LC medium to the high index, being the dominant dielectric component. It is important to point out that at optical frequencies, the field associated with the surface plasmon decays rapidly away from the interface [72, 73], on the order of the particle size, and that surface orientation of LC molecules around plasmonic particles and resulting optical properties will dominate over bulk orientation. In the liquid crystal, the surface

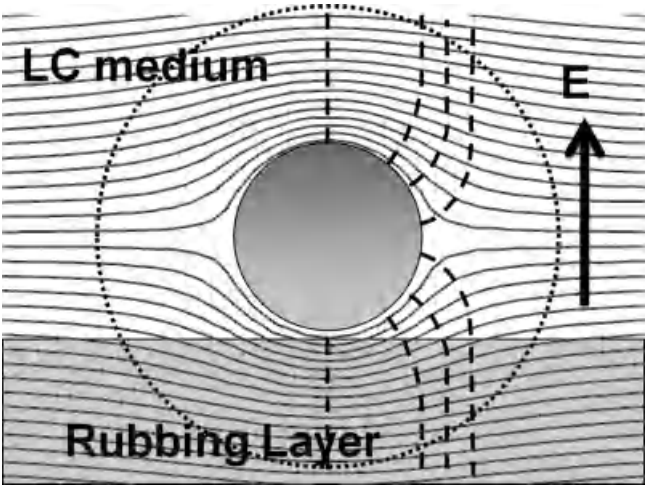

FIGURE 11.10 Equipotential curves (solid) surrounding a 14 nm diameter gold nanorod in an LC cell with polling field applied. Dashed lines indicate field profile and director orientation. LSPR field reaches approximately E/2 at the dotted line.

ordering effect extends into the bulk some distance related to the elastic properties of the LC medium and the surface interaction strength, as well as, the direction of electric fields at the particle surface. The complex interplay between surface ordering, orientation, and fields in and around particles is a rich area of study which may prove essentially enabling to optical metamaterials incorporating LCs. The complex interaction of surfaces and fields in the highly structured metallic systems that compose optical metamaterials will provide an interesting challenge for LC tuned plasmonic structures. The high optical field region close to the metallic inclusion is also the region where the LC is likely to see significantly altered applied poling fields and feel the most influence from surface ordering effects. This becomes particularly interesting in systems where the electromagnetic coupling between adjacent particles is mediated by an LC medium separating them. The small dimensions and confinement of LC systems has been studied for the variety of novel textures produced in such geometries. The complex dielectric textures created would certainly influence the coupling between plasmonic meta-atoms, for example, which may play a significant role in novel electromagnetically induced transparency (EIT) or Fano-type structures [74].

11.8 LIQUID CRYSTALS IN SELF-ASSEMBLED METAMATERIALS

Studies of tunable magnetic gratings and the RF SRR arrays represent the most direct intersection between metamaterials as they are basically understood and liquid crystals. This simple crossing of utilities can provide significant potential for

applications, but there are also novel approaches that leverage LC properties to uniquely exploit metamaterials concepts. Liquid crystals as dynamic materials are only one attribute that has been widely exploited in research and technology. Another is their use a structuring agent, or a structured system. Of course, their diverse and tunable optical and dielectric properties are directly resulting from the microstructures adopted by the LC molecules, but in some cases, the structure is directly relied on or used as a host to template a guest material. Two key examples are cholesteric LC Bragg reflectors and nano/micro particle template systems. In each case, secondary order arising from the LC texture generates longer length scale patterns. The LC is a critical component for providing the alignment or ordering forces, and the optical properties are secondary. Here too lies tremendous potential for liquid crystals in metamaterial systems. Since metamaterials typically rely on subwavelength inclusions ordered on a length scale also smaller than a wavelength, fabrication becomes a challenge as optical metamaterials move to shorter wavelengths and higher frequencies. Indeed, visible wavelength systems in this regime require inclusions of tens of nm in size spaced at only several times their size (often, very small gaps or separations are required between or inside of unit cells, as well). This becomes a fabrication challenge even under the best circumstances, and large area, three-dimensional patterning is beyond the reach of conventional techniques. LCs have potential for providing self-assembled templates for optical metamaterials in this range, where they could be used to structure functional inclusions in order to realize designed materials and their effective medium response.

Research directed at metamaterials fabricated though LC-mediated self-assembly is emerging rapidly to address the challenges of large area fabrication and small dimensions [1]. A wide range of self-assembly approaches are being considered and liquid crystals have been studied as hosts for structured effective media for some time. In contrast to their typical use for anisotropic electromagnetic and optical properties, in this venue, it is the mechanical and elastic anisotropies that are ultilized. Recently, results on the creation of ordered arrays of nanoparticles facilitated by liquid crystalline surface coatings have shown significant progress toward fabricating artificial dielectric materials at optical frequencies. Draper et al. [75] have recently published a study of inherently liquid crystalline gold nanoparticle materials which incorporate polar mesogenic corona molecules. The spherical particles adopt tactoidal shapes as the LC corona, or surface layer orders around hard central core. Potential for novel mesophase formation in neat material and blends is also discussed. These phases would order the gold nanoparticle cores with oriented and ordered LC phases separating them as shown in Figure 11.11. Significant potential for artificial dielectric properties at optical frequencies is possible via this route. Further, additional work on incorporating magnetic particles yields potential for novel magnetic materials following similar strategies. There is precedence for exploring these structures and initial experimental work on optical properties derived from structured nanoparticle composites. Khatua et al. [76] created closely packed structures from LC-coated gold nanoparticles. The ordered nanoparticles showed a significant, though small, shift in the plasmonic resonance between the nematic and

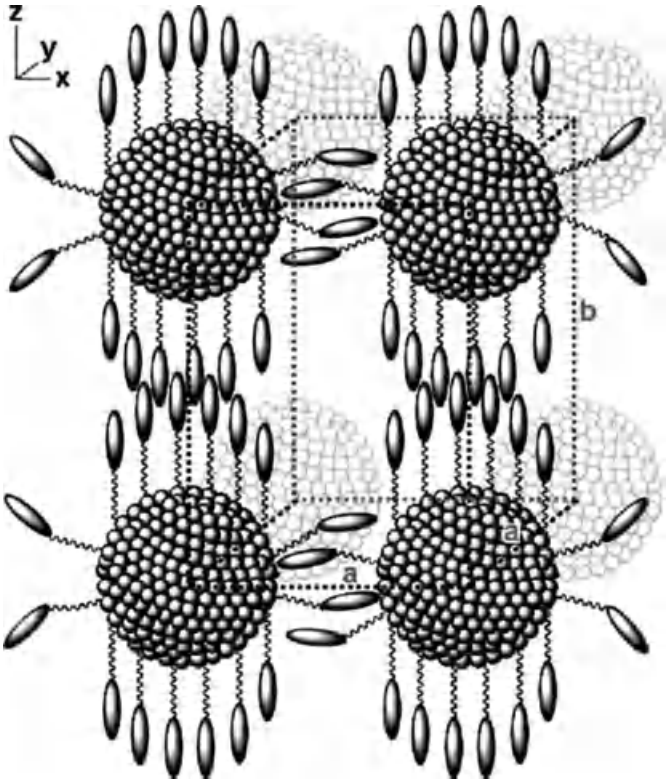

FIGURE 11.11 Cubic arrangements of gold nanoparticles in a square lattice co-ordinated by oriented surface layers of LC based mesogentic capping agents. *Source*: Reprinted with permission from Draper et al., *Advanced Functional Materials*, Wiley-VCH.

isotropic states of the surrounding LC. Other types of dynamic response from liquid crystal systems, such as photochromism [77], could also be employed in these systems. It is important to note that for this system, both the structuring and tunability were resulting from the LC corona/matrix. The change in plasmon resonance would translate into a shift in the effective properties of the system, though the authors of the study did not analyze the systems as such, others have proposed this [78, 79]. Following work on dipole arrays, the effective properties of this system could be extracted [80]. Significantly, no features indicating collective oscillation or coupling between particles were seen in contrast to a study by Augui and Barnes of lithographically fabricated nanorods [81] likely due to polydispersity in the particles and disorder. In addition, this approach has been applied to magnetic nanoparticle cores as well, which raises the potential of optically magnetic or magnetically tunable optical materials [82]. There are key observations needed in order demonstrate the capability to fabricate desired effective properties, but the potential is clear in these initial studies.

11.9 CHIRAL METAMATERIALS

Novel properties in meta-systems can also arise from extremely subwavelength structure in systems without a specific need for order. In particular, chiral metamaterials are an example where molecular scale chirality can influence the effective index of a material for a polarization and even reduce it below unity [83, 84]. In this case the molecular structure imparting the extreme chiral response can be $\lambda/200$ or smaller. Again, fabrication challenges for plasmonic chiral metamaterials at visible frequencies arise. Quantum chemical design efforts have yielded progress toward making extremely chiral systems for visible wavelengths. Molecular systems have the potential to provide low loss chiral subunits that can exhibit negative or extreme values of refractive index for one circular polarization [85]. Indeed cholesteric liquid crystal materials exhibit chiral structures, through the optical activity and dielectric anisotropy is too low to yield negative refractive index. However, the coupling of self-assembled liquid crystal based systems and plasmonic particles to make chiral metamaterials is a natural direction for research. Following the strategies above used by Khatua et al. [76], Draper et al. [75], and Demortière et al. [82] in combination with anisotropic particles and chiral host materials is a path with clear potential.

11.10 CONCLUSION OUTLOOK

While we have identified LCs as having some potential in tunable metamaterials and as a method of fabricating or structuring meta-systems, these approaches are just beginning to be explored. In addition, there is clearly a role which overlaps these two functions [78]. Liquid crystal components of meta-systems could guide assembly of meta-atoms yielding the desired effective response and provide a mechanism by which field tuning, optical response or other dynamic properties are possible. In this chapter, we explored current efforts at the intersection of LCs and metamaterials in the categories outlined above and looked forward to the potential in a variety of areas that have yet to be explored, or for which only basic results have been shown. Our goal in this work is to show were potential has been realized, where new topics exist and what fundamental limitations may play a role in the performance and utility of LC metamaterials. By reviewing current work, it is clear that the intersection of metamaterials and liquid crystals offers a variety of applications in dynamic electromagnetic properties of structured materials across the spectrum. There are many limitations which have already been encountered, as well as, areas where more research and development can be done to maximize the potential of this combination. One of the most critical is the development of novel liquid crystal systems for RF applications. This will alleviate the significant absorption related losses that show up in current experiments. Performance enhancements are possible in the short term through this and the formulation of LC mixtures with high dielectric anisotropy in the relevant frequency ranges. A second significant area is the design of unit cells or meta-atoms that best take advantage of the dielectric properties and changes available

from liquid crystals. To date, experiments have focused on loading well-known or typical meta-systems with LCs to observe tuning. Designing unit cells for interaction with LCs is sure to open up a wider range of available properties and will be essential for optical metamaterials where complex interactions can unlock new phenomena. The active research in this area is sure to yield interesting and useful results in the coming years.

REFERENCES

1. *Applications of Metamaterials*. In: F. Capolino, Ed., CRC Press, Boca Raton, 2009.
2. M.-H. Lu, L. Feng, and Y.-F. Chen. Phononic crystals and acoustic metamaterials. *Mater. Today* **2009**, *12*, 34–42.
3. Z. M. Zhang and B. J. Lee. Chapter 3 Theory of thermal radiation and radiative properties. In: B. K. T. Zhuomin, M. Zhang, and M. Graham, Eds, *Experimental Methods in the Physical Sciences*, Academic Press, 2009.
4. G. Chen, A. Narayanaswamy, and C. Dames. Engineering nanoscale phonon and photon transport for direct energy conversion. *Superlattices Microstruct*. **2004**, *35*, 161–172.
5. *Theory and Phenomena of Metamaterials*. In: F. Capolino, Ed., CRC Press, Boca Raton, 2009.
6. J. B. Pendry. Negative refraction makes a perfect lens. *Phys. Rev. Lett.* **2000**, *85*, 3966.
7. R. A. Shelby, D. R. Smith, and S. Schultz. Experimental verification of a negative index of refraction. *Science* **2001**, *292*, 77–79.
8. V. G. Veselago. The electrodynamics of substances with simultaneously negative values of permittivity and permeability. *Soviet Physics Uspekhi* **1968**, *10*, 6.
9. A. N. Lagarkov, V. N. Semenenko, V. A. Chistyaev, D. E. Ryabov, S. A. Tretyakov, and C. R. Simovski. Resonance properties of bi-helix media at microwaves. *Electromagnetics* **1997**, *17*, 213–237.
10. D. R. Smith, W. J. Padilla, D. C. Vier, S. C. Nemat-Nasser, and S. Schultz. Composite medium with simultaneously negative permeability and permittivity. *Phys. Rev. Lett.* **2000**, *84*, 4184.
11. U. Leonhardt and T. G. Philbin. Chapter 2 Transformation Optics and the Geometry of Light. In: *Progress in Optics*. E. Wolf, Ed., Elsevier, 2009.
12. J. Pendry. Metamaterials: Transformation optics. *New Scientist* **2011**, *209*, iv–v.
13. B. Kante, A. Ourir, S. N. Burokur, F. Gadot, and A. de Lustrac. Metamaterials for optical and radio communications. *Comptes Rendus Physique* **2008**, *9*, 31–40.
14. W. J. Padilla, A. J. Taylor, C. Highstrete, M. Lee, and R. D. Averitt. Dynamical electric and magnetic metamaterial response at terahertz frequencies. *Phys. Rev. Lett.* **2006**, *96*, 107401.
15. Y. Huang, X. Zhao, L. Wang, and C. Luo. Tunable left-handed metamaterial based on electrorheological fluids. *Prog. Nat. Sci.* **2008**, *18*, 907–911.
16. J. B. Birks, Ed., *Progress in Dielectrics*. Wiley, New York, 1960.
17. W. Rotman. Plasma simulation by artificial dielectrics and parallel-plate media. Antennas Propag. *IRE Trans. on* **1962**, *10*, 82–95.

18. J. B. Pendry, A. J. Holden, D. J. Robbins, and W. J. Stewart. Magnetism from conductors and enhanced nonlinear phenomena. Microwave Theory Tech. *IEEE Trans*. on **1999**, *47*, 2075–2084.
19. C. R. Simovski and S. A. Tretyakov. Local constitutive parameters of metamaterials from an effective-medium perspective. *Phys. Rev. B* **2007**, *75*, 195111.
20. D. R. Smith. Analytic expressions for the constitutive parameters of magnetoelectric metamaterials. *Phys. Rev. E* **2010**, *81*, 036605.
21. I. Nefedov, A. Viitanen, and S. Tretyakov. On reflection from interfaces with some spatially dispersive metamaterials. *J. Magn. Magn. Mater.* **2006**, *300*, 107–110.
22. L. Markley and G. V. Eleftheriades. Meta-screens and near-field antenna-arrays: a new perspective on subwavelength focusing and imaging. *Metamaterials* **2011**, *5*, 97–106.
23. B. A. Munk. *Frontmatter in Frequency Selective Surfaces*. John Wiley & Sons Inc., 2005.
24. R. E. Diaz and S. A. Clavijo. Artificial magnetic conductor. In: *Encyclopedia of RF and Microwave Engineering*, John Wiley & Sons Inc., 2005.
25. J. A. Bossard, L. Xiaotao, L. Ling, Y. Seokho, D. H. Werner, B. Weiner, T. S. Mayer, P. F. Cristman, A. Diaz, and I. C. Khoo. Tunable frequency selective surfaces and negative-zero-positive index metamaterials based on liquid crystals. *Antennas Propag. IEEE Trans. on* **2008**, *56*, 1308–1320.
26. F. Zhang, Q. Zhao, L. Kang, D. P. Gaillot, X. Zhao, J. Zhou, and D. Lippens. Magnetic control of negative permeability metamaterials based on liquid crystals. *Appl. Phys. Lett.* **2008**, *92*, 193104–193103.
27. F. Zhang, L. Kang, Q. Zhao, J. Zhou, X. Zhao, and D. Lippens. Magnetically tunable left handed metamaterials by liquid crystal orientation. *Opt. Exp.* **2009**, *17*, 4360–4366.
28. F. Zhang, W. Zhang, Q. Zhao, J. Sun, K. Qiu, J. Zhou, and D. Lippens. Electrically controllable fishnet metamaterial based on nematic liquid crystal. *Opt. Exp.* **2011**, *19*, 1563–1568.
29. C. R. Simovski and S. He. Frequency range and explicit expressions for negative permittivity and permeability for an isotropic medium formed by a lattice of perfectly conducting [Omega] particles. *Phys. Lett. A* **2003**, *311*, 254–263.
30. J. Huangfu, L. Ran, H. Chen, X.-M. Zhang, K. Chen, T. M. Grzegorczyk, and J. A. Kong. Experimental confirmation of negative refractive index of a metamaterial composed of Omega-like metallic patterns. *Appl. Phys. Lett.* **2004**, *84*, 1537–1539.
31. S. Larouche and D. R. Smith. A retrieval method for nonlinear metamaterials. *Opt. Commun.* **2010**, *283*, 1621–1627.
32. E. Poutrina, S. Larouche, and D. R. Smith. Parametric oscillator based on a single-layer resonant metamaterial. *Opt. Commun.* **2010**, *283*, 1640–1646.
33. F. Goelden, A. Lapanik, A. Gaebler, S. Mueller, W. Haase, and R. Jakoby. Systematic investigation of nematic liquid crystal mixtures at 30 GHz. *Digest of 2007 IEEE/LEOS Summer Topical Meetings*.
34. S. Mueller, M. Koeberle, F. Goelden, A. Penirschke, A. Gaebler, A. Lapanik, W. Haase, and R. Jakoby. *W-Band characterization of anisotropic liquid crystals at room temperature. 38th European Microwave Conference.*
35. F. Zhang, Q. Zhao, D. P. Gaillot, X. Zhao, and D. Lippens. Numerical investigation of metamaterials infiltrated by liquid crystal. *J. Opt. Soc. Am. B* **2008**, *25*, 1920–1925.

36. Q. Zhao, L. Kang, B. Du, B. Li, J. Zhou, H. Tang, X. Liang, and B. Zhang. Electrically tunable negative permeability metamaterials based on nematic liquid crystals. *Appl. Phys. Lett.* **2007**, *90*, 011112–011113.
37. N. Kundtz and D. R. Smith. Extreme-angle broadband metamaterial lens. *Nat. Mater.* **2010**, *9*, 129–132.
38. H. Chen, C. T. Chan, S. Liu, and Z. Lin. A simple route to a tunable electromagnetic gateway. *New J. Phys.* **2009**, *11*, 083012.
39. A. Gaebler, F. Goelden, A. Manabe, M. Goebel, S. Mueller, and R. Jakoby. Investigation of high performance transmission line phase shifters based on liquid crystal. 2009 *European Microwave Conference.*
40. A. Gaebler, F. Goelden, S. Mueller, and R. Jakoby. Modeling of electrically tunable transmission line phase shifter based on liquid crystal. *2008 Antennas and Propagation Society International Symposium, IEEE.*
41. N. Tentillier, F. Krasinski, R. Sauleau, B. Splingart, H. Lhermite, and P. Coquet. A liquid-crystal, tunable, ultra-thin Fabry-Perot resonator *in Ka band*. *Antennas Wireless Propag. Lett. IEEE* **2009**, *8*, 701–704.
42. H. Wenfei, R. Dickie, R. Cahill, H. Gamble, Y. Ismail, V. Fusco, D. Linton, N. Grant, and S. Rea. Liquid crystal tunable mm wave frequency selective surface. *Microwave Wireless Comp. Lett. IEEE* **2007**, *17*, 667–669.
43. F. Zhang, Q. Zhao, W. Zhang, J. Sun, J. Zhou, and D. Lippens. Voltage tunable short wire-pair type of metamaterial infiltrated by nematic liquid crystal. *Appl. Phys. Lett.* **2010**, *97*, 134103.
44. W. Hu, M. Y. Ismail, R. Cahill, H. S. Gamble, R. Dickie, V. F. Fusco, D. Linton, S. P. Rea, and N. Grant. Tunable liquid crystal reflectarray patch element. *Electronics Lett*. **2006**, *42*, 509–511.
45. H. Wenfei, R. Cahill, J. A. Encinar, R. Dickie, H. Gamble, V. Fusco, and N. Grant. Design and measurement of reconfigurable millimeter wave reflectarray cells with nematic liquid crystal. *Antennas Propag. IEEE Trans. on* **2008**, *56*, 3112–3117.
46. H. Wenfei, M. Arrebola, R. Cahill, J. A. Encinar, V. Fusco, H. S. Gamble, Y. Alvarez, and F. Las-Heras. 94 GHz Dual-reflector antenna with reflectarray subreflector. *Antennas Propag. IEEE Trans. on* **2009**, *57*, 3043–3050.
47. A. Gaebler, A. Moessinger, F. Goelden et al. Liquid crystal-reconfigurable antenna concepts for space applications at microwave and millimeter waves. *Int. J. Antennas Propag.* **2009**.
48. R. Kowerdziej, J. Parka, P. Nyga, and B. Salski. Simulation of a tunable metamaterial with nematic liquid crystal layers. *Liq. Cryst.* **2011**, *38*, 377–379.
49. R. Kowerdziej, J. Parka, and P. Nyga. Tunable liquid crystalline metamaterial structure in GHz range. *Mol. Cryst. Liq. Cryst.* **2011**, *545*, 91–95.
50. R. Kowerdziej, J. Parka and J. Krupka. Experimental study of thermally controlled metamaterial containing a liquid crystal layer at microwave frequencies. *Liq. Cryst.* **2011**, *38*, 743–747.
51. Y. Utsumi, T. Kamei, and R. Naito. Measurements of effective dielectric permittivity of microstrip-line-type liquid crystal devices using inductive coupled ring resonator. *Elect. Lett.* **2003**, *39*, 849–850.
52. I. A.I. Al-Naib, C. Jansen, and M. Koch. Thin-film sensing with planar asymmetric metamaterial resonators. *Appl. Phys. Lett.* **2008**, *93*, 083507–083503.

53. R. Melik, E. Unal, N. K. Perkgoz, C. Puttlitz, and H. V. Demir. Flexible metamaterials for wireless strain sensing. *Appl. Phys. Lett.* **2009**, *95*, 181105–181103.
54. D. Huang, E. Poutrina, and D. R. Smith. Analysis of the power dependent tuning of a varactor-loaded metamaterial at microwave frequencies. *Appl. Phys. Lett.* **2010**, *96*, 104104–104103.
55. I. V. Shadrivov, A. B. Kozyrev, D. W. van der Weide, and Y. S. Kivshar. Tunable transmission and harmonic generation in nonlinear metamaterials. *Appl. Phys. Lett.* **2008**, *93*, 161903–161903.
56. R. H. Ritchie. Plasma losses by fast electrons in thin films. *Phys. Rev.* **1957**, *106*, 874.
57. H. Kuwata, H. Tamaru, K. Esumi, and K. Miyano. Resonant light scattering from metal nanoparticles: practical analysis beyond Rayleigh approximation. *Appl. Phys. Lett.* **2003**, *83*, 4625–4627.
58. W. Cai and V. Shalaev. *Optical Metamaterials: Fundamentals and Applications*. Springer, New York, 2009.
59. C. M. Soukoulis, S. Linden, and M. Wegener. Negative refractive index at optical wavelengths. *Science* **2007**, *315*, 47–49.
60. S. Zhang, W. Fan, N. C. Panoiu, K. J. Malloy, R. M. Osgood, and S. R. J. Brueck. Experimental demonstration of near-infrared negative-index metamaterials. *Phys. Rev. Lett.* **2005**, *95*, 137404.
61. M. Kafesaki, I. Tsiapa, N. Katsarakis, T. Koschny, C. M. Soukoulis, and E. N. Economou. Left-handed metamaterials: The fishnet structure and its variations. *Phys. Rev. B* **2007**, *75*, 235114.
62. X. Wang, D.-H. Kwon, D. H. Werner, I.-C. Khoo, A. V. Kildishev, and V. M. Shalaev. Tunable optical negative-index metamaterials employing anisotropic liquid crystals. *Appl. Phys. Lett.* **2007**, *91*, 143122.
63. D. H. Werner, D.-H. Kwon, I.-C. Khoo, A. V. Kildishev, and V. M. Shalaev. Liquid crystal clad near-infrared metamaterials with tunable negative-zero-positive refractive indices. *Opt. Express* **2007**, *15*, 3342–3347.
64. A. K. Diaz, I. C. Khoo. Liquid-crystalline nanostructured optical metamaterials. In: D. Andrews, G. Scholes, and G. Wiederrecht, (Eds.), *Comprehensive Nanoscience and Technology*, Oxford Academic Press, 2011.
65. S. Xiao, U. K. Chettiar, A. V. Kildishev, V. Drachev, I. C. Khoo, and V. M. Shalaev. Tunable magnetic response of metamaterials. *Appl. Phys. Lett.* **2009**, *95*, 033115.
66. K. Iam Choon, A. Diaz, J. Liou, M. V. Stinger, H. Junbin, and M. Yi. Liquid crystals tunable optical metamaterials. *IEEE J. Select. Topic Quantum Elect.* **2010**, *16*, 410–417.
67. W. Cai, U. K. Chettiar, H.-K. Yuan, V. C. de Silva, A. V. Kildishev, V. P. Drachev, and V. M. Shalaev. Metamagnetics with rainbow colors. *Opt. Exp.* **2007**, *15*, 3333–3341.
68. J. Muller, C. Sonnichsen, H. von Poschinger, G. von Plessen, T. A. Klar, and J. Feldmann. Electrically controlled light scattering with single metal nanoparticles. *Appl. Phys. Lett.* **2002**, *81*, 171–173.
69. K. C. Chu, C. Y. Chao, Y. F. Chen, Y. C. Wu, and C. C. Chen. Electrically controlled surface plasmon resonance frequency of gold nanorods. *Appl. Phys. Lett.* **2006**, *89*, 103107.
70. S. Y. Park and D. Stroud. Splitting of surface plasmon frequencies of metal particles in a nematic liquid crystal. *Appl. Phys. Lett.* **2004**, *85*, 2920–2922.

71. S. Y. Park and D. Stroud. Surface-enhanced plasmon splitting in a liquid-crystal-coated gold nanoparticle. *Phys. Rev. Lett.* **2005**, *94*, 217401.

72. A. V. Whitney, J. W. Elam, S. Zou, A. V. Zinovev, P. C. Stair, G. C. Schatz, and R. P. Van Duyne. Localized surface plasmon resonance nanosensor: a high-resolution distance-dependence study using atomic layer deposition. *J. Phys. Chem. B* **2005**, *109*, 20522–20528.

73. P. M. Adam, L. Salomon, F. de Fornel, and J. P. Goudonnet. Determination of the spatial extension of the surface-plasmon evanescent field of a silver film with a photon scanning tunneling microscope. *Phys. Rev. B* **1993**, *48*, 2680.

74. B. Luk'yanchuk, N. I. Zheludev, S. A. Maier, N. J. Halas, P. Nordlander, H. Giessen, and C. T. Chong. The Fano resonance in plasmonic nanostructures and metamaterials. *Nat. Mater.* **2010**, *9*, 707–715.

75. M. Draper, I. M. Saez, S. J. Cowling, P. Gai, B. Heinrich, B. Donnio, D. Guillon, and J. W. Goodby. Self-assembly and shape morphology of liquid crystalline gold metamaterials. *Adv. Funct. Mater.* **2011**, *21*, 1260–1278.

76. S. Khatua, P. Manna, W.-S. Chang, A. Tcherniak, E. Friedlander, E. R. Zubarev, and S. Link. Plasmonic nanoparticles−Liquid crystal composites. *J. Phys. Chem. C* **2009**, *114*, 7251–7257.

77. Y. Li, D. Yu, L. Dai, A. Urbas, and Q. Li. Organo-soluble chiral thiol-monolayer-protected gold nanorods. *Langmuir* **2010**, *27*, 98–103.

78. Q. Liu, Y. Cui, D. Gardner, X. Li, S. He, and I. I. Smalyukh. Self-alignment of plasmonic gold nanorods in reconfigurable anisotropic fluids for tunable bulk metamaterial applications. *Nano Lett.* **2010**, *10*, 1347–1353.

79. A. B. Golovin, J. Xiang, Y. A. Nastishin, and O. D. Lavrentovich. *Electrically reconfigurable optical metamaterials based on orientationally ordered dispersions of metal nanorods in dielectric fluids*, SPIE, San Diego, California, USA, 2010.

80. K. Kempa, R. Ruppin, and J. B. Pendry. Electromagnetic response of a point-dipole crystal. *Phys. Rev. B* **2005**, *72*, 205103.

81. B. Augui and W. L. Barnes. Collective resonances in gold nanoparticle arrays. *Phys. Rev. Lett.* **2008**, *101*, 143902.

82. A. Demortière, S. Buathong, B. P. Pichon, P. Panissod, D. Guillon, S. Bégin-Colin, and B. Donnio. Nematic-like organization of magnetic mesogen-hybridized nanoparticles. *Small* **2010**, *6*, 1341–1346.

83. J. B. Pendry. A chiral route to negative refraction. *Science* **2004**, *306*, 1353–1355.

84. E. Plum, V. A. Fedotov, A. S. Schwanecke, N. I. Zheludev, and Y. Chen. Giant optical gyrotropy due to electromagnetic coupling. *Appl. Phys. Lett.* **2007**, *90*, 223113.

85. A. Baev, M. Samoc, P. N. Prasad, M. Krykunov, and J. Autschbach. A quantum chemical approach to the design of chiral negative index materials. *Opt. Exp.* **2007**, *15*, 5730–5741.

CHAPTER 12

Ferroelectric Colloids in Liquid Crystals

YURIY REZNIKOV

Institute of Physics, National Academy of Sciences of Ukraine, Kyiv, Ukraine

12.1 INTRODUCTION

For many years the science of liquid crystals mostly served the needs of liquid crystal display (LCD) industry; vast majority of funds and human resources were directed to development of numerous LCD modes in nematic liquid crystals (LCs). It was the needs of LCD industry that initiated rapid development of surface LC science, deep studies of correlation between the molecular structures and macroscopic properties of nematic LCs. Studies of more complicated LCs phases and composite LC materials to a large extent have also been initiated by numerous attempts to propose competitive alternative to the traditional nematic LCDs (e.g. PDLCs, bistable LCDs, ferroelectric LCDs). By the beginning of the last decade, the LCD industry has reached such a high level that its further progress has become determined mainly by development of the technology of non-LC components (for example, by fabrication of gigantic high-quality glass substrates for the last generation LCDs). This initiated some kind of rebooting of the scientific and mercantile interests of the LC scientific community. There are many sectors of hi-tech industry where LCs have great potentials, such as biotech, telecommunication, and optical processing. The new applications require new materials, sometimes with rather exotic properties, and new technologies. For example, LC materials for telecommunications usually require LCs with strong birefringence but low refractive index, adaptive LC optics needs materials with huge birefringence and low viscosity. Many promising applications of LC for terahertz region are suppressed by a strong absorption of LCs in this region; biotech needs replacement of thermotropic LCs to water-based lyotropic LCs. Tiny and precise patterning of LC alignment over the boundary surfaces becomes crucial for developing new optical elements. All of these new industry needs changed the priority points of LCs science; a number of LCD-related publications steadily decrease in expense of publications on application of LCs in photonics, optical processing, biosensors, and magneto-optics.

Liquid Crystals Beyond Displays: Chemistry, Physics, and Applications, Edited by Quan Li.
© 2012 John Wiley & Sons, Inc. Published 2012 by John Wiley & Sons, Inc.

One of the directions of the development of the modern LCs science is design and study of numerous LC composite materials. Long-distance orientation interaction in mesophase leads to extremely strong influence of a dispersed material on the mesogenic properties of the LC and vice versa; the LC matrix can effectively arrange the positional and translational ordering of the inclusions in the matrix. Therefore, combination of the orientational ordering and relative translation freedom in LCs with properties of the dispersed materials allows scientists to give unique properties to the composite, which are not inherent to its components. In order to obtain synergetic properties, part of the dispersion material in a LC matrix should not be high. Apparently, Brochard and de Gennes [1] first suggested that doping of a nematic LC with elongated submicron ferromagnetic particles in very low volume fraction ($f_v \leq 10^{-3}$) should result in drastic increase of the LC sensitivity to a magnetic field. In their picture, the magnetic moments of the particles are aligned by the magnetic field. The coupling between the magnetic particle and the liquid crystal molecule orientations then transfers the magnetic orientational effect onto the underlying liquid crystal matrix. After more than 30 years it was shown that doping of ferroelectric particles at low concentrations to a nematic introduces the ferroelectric properties inherent to the particles [2]. In particular, the nematic becomes sensitive to the sign of the applied electric field. Thus, one can say that the particles in tiny concentration may share their intrinsic properties with the LC matrix. It opens astonishing perspectives of low-concentrated LC nanocolloids for developing unique mesogenic materials and offers an innovative effective means to control precisely the physical properties of liquid crystals.

To realize application potential of the low-concentrated colloids the particles, there should be not only few enough particles but they also should be small enough in order not to disturb the director of a LC. To achieve this, the single particle should be so small that the anchoring parameter $\xi = \mathrm{WR}_{\mathrm{part}}/K$ would be much smaller than 1 (W is the anchoring energy of a LC with the surface of the particle, K is the elastic constant of a LC, $2R_{\mathrm{part}}$ is the characteristic size of the particles). The typical values of the anchoring energy are in the range of 10^{-4}–$10^{-6}\,\mathrm{J\,m^{-2}}$, $K \approx 10^{-11}$N. It means that $\xi \leq 1$, which corresponds to $R_{\mathrm{part}} \leq 100\,\mathrm{nm}$. When this condition is met, the particles do not substantially disturb the orientation of the LC director producing a macroscopically uniform alignment. One can say that the director does not "see" the particles, and the colloid appears similar to a pure LC with no readily apparent evidence of dissolved particles.

Despite the director is not disturbed by the nanoparticles, the interaction between them and LC molecules can essentially change the mesogenic properties of a LC. General description of the effect of nanoparticles on LC properties was proposed by Gorkunov and Osipov in the framework of molecular mean-field theory [3]. Effective anchoring potential between a nanoparticle and LC molecules can be written as

$$U_{\mathrm{part-LC}} = \bar{W}(\vec{a}_m * \vec{A}_n)^2 \tag{12.1}$$

where $\vec{a}$ is the long axis of the LC molecule m and $\vec{A}$ of the axis of the nanoparticles n. The particular expression for the constant $\bar{W}$ depends on the nature of a LC–nanoparticles interaction (dipole–dipole, van-der-Waals, etc.). The specific form of $\bar{W}$ determines the effect of the particles on the LC matrix. Even if the particle is isotropic and spherical ($\bar{W} = 0$), it changes the mesogenic properties of a LC effectively "diluting" it and decreasing the ordering and the clearing temperature T_c:

$$T_c = (1 - f_v)T_{c,0} \tag{12.2}$$

where $T_{c,0}$ is a clearing temperature of the LC host. For the low concentrated colloids this factor decreases T_c by tenth of degrees [4].

If the nanoparticles are anisotropic in shape, they are aligned by the LC matrix and improve the liquid crystal ordering due to the surface anchoring. It leads to the increase of T_c and softening of the first order nematic–isotropic transition. The shape anisotropy factor typically increases T_c also by tenth of degrees [5].

Other types of the anisotropic interactions between nanoparticles and a LC, such as the ones induced by intrinsic ferromagnetism and ferroelectricity of the particles, can lead to additional effect on a LC matrix and essentially change its basic parameters, such as ordering [6, 7], dielectric and conductive [8, 9], magnetic [10, 11], electro-optical [12, 13], and nonlinear optical [14, 15] properties.

When the actual size of the nanoparticles in LC, R_{part} becomes smaller than 100 nm, we enter the world of nano-science where the properties of the particles themselves can vary drastically. In sufficiently large colloidal particles, the ferromagnetic and ferroelectric materials form a polydomain structure that usually transforms into a single domain structure when the particles become smaller than 10–20 nm in the case of ferroelectrics [16] and 100–300 nm in the case of ferromagnetics. The further decrease of the size of the single domain ferromagnetics may result in their transition to a single domain superparamagnetic phase, which usually occurs when the particles get smaller than 20 nm [17]. As the size of single ferroelectric particles get smaller than 5 nm, the internal mean field becomes insufficiently high to maintain ferroelectric states, which results in loss of ferroelectricity [16]. The position of plasmon resonance of the noble metal nanoparticles also changes strongly as their size decreases [18]. If we remember about severe aggregation in a mesophase as well, it becomes evident how complex the physics of LC colloids is and how delicate the balance between the size and concentration of the particles in the LC matrix has to be in order to obtain reliable and predictable properties of the suspensions.

As we see, development and study of low-concentrated LC colloids promise us not only new astonishing applications of LCs, but also interesting and fundamental physics. Below we describe the main achievements in physics of low-concentrated LC colloids focusing on the colloids of ferroelectric materials in LCs. Despite the great interest, the detailed description of other types of particles (carbon nanotubes, fullerene dopings, quantum dots, ferromagnetic particles, aerosil, etc.) was left beyond the scope of this chapter.

12.2 PARTICLES INTERACTION AND THE PROBLEM OF COLLOID STABILITY

There have been no detailed studies of the stability of LC colloids published so far. We found only few brief mentions about the aggregation and sedimentation of the nanoparticles in LCs in the literature [19–22]. At the same time, these processes in thermotropic LC matrixes are very strong. Even if the colloid is visibly stable in the isotropic phase, the transition to the mesophase usually results in formation of visible aggregates, typically in the region of the transition interface. Usually the following attempts to break sedimintated particles and aggregates are not successful: after the refreshment of the dispersion visible aggregates and sedimintated particles appear again. The increased instability is inherent to all kinds of colloidal nanoparticles in LCs regardless the particles' nature (ferroelectric, ferromagnetic, dielectric, semiconductor, metal).

It is evident that the stability problem of LC colloids is directly related to the orientational ordering in a mesophase. The interaction of a nanoparticle with an LC matrix changes the arrangement of LC molecules around the particle disturbing both the order parameter and the director. It increases the free energy of the system, and aggregation of the particles is a mechanism of the compensation of these energy expenses. The trigger of the aggregation is a Brownian motion of the particles. By means of a random walk, the particles are brought at a critical distance l_{cr}, at which the interaction energy is stronger than the thermal energy k_BT. As a result, they begin to approach each other and form aggregates [23].

If the particles are so large that the anchoring parameter $\xi \gg 1$ (it usually corresponds to $R_{\text{part}} = 1\text{–}10\,\mu\text{m}$), the director is strongly disturbed around the particles down to creation of the point of orientational defects nearby [19]. In this case the particles interact as two effective dipoles due to elastic interaction and the critical distance l_{cr} is in the order of tens of microns or less.

For the particles with radius $R_{\text{part}} = 0.1\text{–}1\,\mu\text{m}$, the parameter ξ is usually less than 1. The strong director distortions require too much energy, and the distorted structure transforms into a smooth director deviation around the particle [24]. In this case the particles interact as quadruples, which is several times weaker than the dipoles. As a result, the distance, l_{cr} is in the order of 1 μm.

For the actual "nano"-particles ($R_{\text{part}} \leq 10\text{–}50\,\text{nm}$), $\xi \ll 1$ and the director does not "see" the particles at all. For this size of the particles, the interaction due the changes of the order parameter near the particles comes to the front [25, 26]. To compensate distortions of the order parameter, the particles begin approaching each other as long as they are at a distance l_{cr} of tens nanometers from each other. Thus, for any size of the particles and any type of interaction between the particles and a LC, the ordering of a mesophase encourages aggregation. Since a probability for the particles to be closer to each other is less than that to be further to each other, a time of the aggregation due to the mesogenic forces for small nanoparticles is much longer for the particles of micron size.

The direct interaction between particles may enhance the aggregation even further. It is clearly demonstrated for the case of carbon nanotubes. These almost

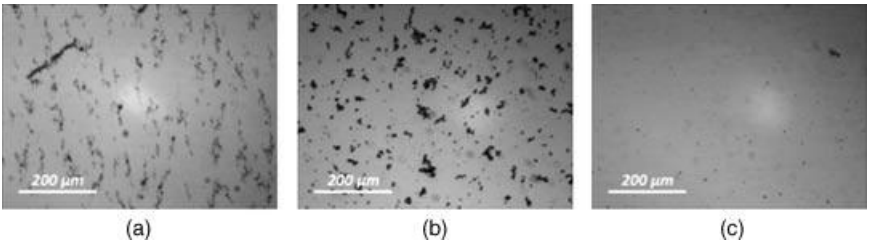

FIGURE 12.1 Photos of the suspensions in optical microscope. (a) Suspension of carbon nanotubes in LC 5CB ($f_w = 0.025\%$); scale. (b) Suspension of ferroelectric particles $Sn_2P_2S_6$ in LC 5CB ($f_w = 0.1\%$). (c) Suspension of ferromagnetic particles γ-Fe_2O_3 in LC 5CB ($f_w = 0.01\%$). Courtesy O. Buluy and O. Kurochkin.

one-dimensional objects have the diameters of several or tens of nanometers and the lengths of up to several microns. Strong anisotropy in the combination with great polarisability along the tube axis leads to a strong van-der-Waals interaction, U_{vdW}, between the nanotubes. The numerical calculation [22] has shown that for the radius of the nanotubes $R_{\text{tube}} = 50$ nm, and their length $l_{\text{tube}} = 5$ μm, the equilibrium spacing of two parallel nanotubes is around 100 nm and their interaction energy $U_{vdW}/k_BT \approx 6 \times 10^6$. This explains a tendency of a strong aggregation of the nanotubes in LCs. Herewith the anisotropy of LC matrix leads to formation of aggregates elongated to various degrees and predominantly oriented along the director of an LC [20, 22], Figure 12.1a.

The direct interaction is also important in the case of ferroelectric particles. For two ferroelectric particles, dipoles of which are antiparallel, the electrostatic interaction is

$$E_{el} \sim \frac{d_{part}^2}{4\pi\varepsilon_0 r^3} \tag{12.3}$$

where $d_{\text{part}} = P_{\text{part}} V_{\text{part}}$ is a permanent dipole moment of the particle, P is a polarization (dipole moment per volume unit), V_{part} is the particle volume. For typical ferroelectric material $BaTiO_3$, $P_{\text{part}} = 0.26\ \text{C/m}^2$ and the particles' size $R_{\text{part}} = 5$ nm, the value of E_{el} is equal to the thermal energy k_BT at $r = l_{cr} \approx 350$ nm and for $r = 100$ nm $E_{el}/k_BT \approx 40$. Thus, for ferroelectric particles the electrostatic interaction is larger than the interaction due to the ordering distortion. It determines strong aggregation of ferroelectric nanoparticles in a mesophase (Figure 12.1b).

For two ferromagnetic particles with antiparallel dipoles' arrangement the magnetic interaction is

$$E_{\text{mag}} \sim \frac{m_{part}^2}{4\pi\mu_0 r^3} \tag{12.4}$$

where $m_{\text{part}} = \mu_0 MV$, M is a magnetization of the material, $\mu_0 MV$ is a magnetic moment per unit volume. For the typical ferromagnetic material magnetite $M = 4.46 \times 10^5$ A/m and the particles' size $R_{\text{part}} = 5$ nm, the value E_{mag} at $r = l_{cr} \approx 3$ nm and

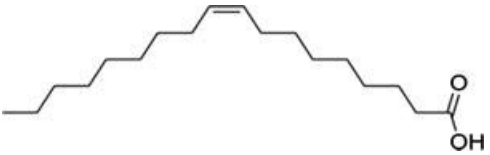

FIGURE 12.2 Chemical formula of oleic acid.

for $r = 100\,\text{nm}$ $E_{\text{mag}}/k_BT \approx 10^{-3}$. It means that the direct magnetic interaction is not crucial for ferromagnetic LC colloids and it is easier to get the stable colloids of such particles rather than of the ferroelectric ones (Figure 12.1c). The same concerns dielectric, semiconductor, and metal nanoparticles interacting mainly due to dipole-induced forces which turn out to be rather weak.

So, for the nanoparticles of the size less than tens of nanometers the aggregation is mainly caused by the direct interaction and the disturbance of the order parameter. In order to decrease the effect of these factors, the particles' surfaces are covered with surfactants. The role of a surfactant is to increase the excluded volume (in other words, to increase the steric repulsion radius) and to "smooth out" the disturbance of the order parameter of the LC around the particle, which is produced due to interaction of LC molecules with the particle' surface.

The most frequently used surfactants are long-chain carboxylic acids, especially an oleic acid (Figure 12.2), molecules of which contain strong polar groups and long hydrocarbon tails that fits well into a LC matrix. The molecules of the oleic acid are attached to the particles surfaces with the polar heads mainly by hydrogen bonds. To cover the particles by the oleic acid, the dispersion of the particles in a solvent (e.g. heptane) is prepared, and the molecules of the acid are spontaneously adsorbed on the particles surfaces with the polar heads. The oleic acid molecules are not too long ($l = 1.97$ nm) and do not increase the excluded volume much. At the same time, oleic acid is widely used in ferroelectric and ferromagnetic LC colloids, increasing stability of nanoparticles in LCs compared to the case of uncovered particles. Apparently, the oleic acid molecules, which are well embedded in a LC matrix, soften the disturbance of the order parameter in the particle–LC interface that decreases interparticles interaction.

The drawback of the oleic acid as a surfactant is that it is physically absorbed on the particle's surface and some equilibrium fraction of the oleic acid molecules end up in the bulk of a LC matrix decreasing its ordering and clearing temperature T_c. The ratio between the oleic acid molecules on the particles' surfaces and in the bulk can be monitored by IR spectroscopy [27], but the precise control of this ratio is difficult, which is a source of poor reproducibility of the colloid characteristics. Gupta et al. showed [28] that stearic acid gives suspensions that are more stable, but the deposition of material on the particles requires rather tricky treatment. Potentially much better results one can expect from surfactants that are chemically bonded to the surface (chemisorption) by changing the carboxylic function with $-SO_3H$ or with phosphorous containing acids [29–32]. In order to optimize interaction of the surfactant with a LC matrix, a mesogenic fragment is attached to the outer end

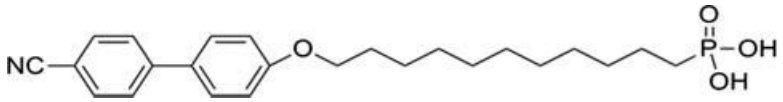

FIGURE 12.3 Chemical formula of the surfactant with the mesogenic group [33].

of long flexible hydrocarbon tails chemically bonded to the particle's surface. An example of such surfactant is presented in Figure 12.3 [33]. Application of this surfactant allowed getting stable suspension of elongated ferromagnetic nanoparticles γ-Fe_2O_3 (diameter, $d_{part} \approx 15$ nm, length, $l_{part} \approx 100$ nm, weight fraction, $f_w \approx 5 \times 10^{-3}\%$) in a LC 5CB with no aggregates visible in optical microscope.

The dendrite-like surfactant (Figure 12.4) provides a stable suspension with no visible aggregates of even larger elongated magnetic nanoparticles γ-Fe_2O_3 ($d_{part} =$ 10–25 nm, $l_{part} =$ 100–150 nm) in a smectic-C LC [34].

To optimize the interaction between the LC molecules and the surfactant, two-component surfactants are used. One of the components is a long flexible molecule (2–6 nm) that plays an "anti-aggregator" role. The second component consists of short (up to 1 nm), alkyl-containing molecules that cover a part of the particle (undercoating). This arrangement allows LC molecules to penetrate between the long flexible components and to "smooth out" the order parameter variation around the particles. The two-component surfactant depicted in Figure 12.5 [35] has allowed to get a stable suspension of golden nanoparticles ($d_{part} \approx 1.6$ nm) with the weight fraction $f_w = 1$ % in a LC E7 [36]. This suspension did not contain aggregates visible in optical microscope.

The results of the use of mesogenic surfactants chemically attached to the surface are very promising but the fact that the aggregates were not observed in optical microscope could not serve as a proof of single particles in a LC matrix. The first unambiguous proof that the dispersion of single particles can be produced in LC was obtained for the colloid of quantum dots CdSe/ZnS in a 5CB [37]. The dispersion of quantum dots covered with an organic shell consisting of oleic acid and

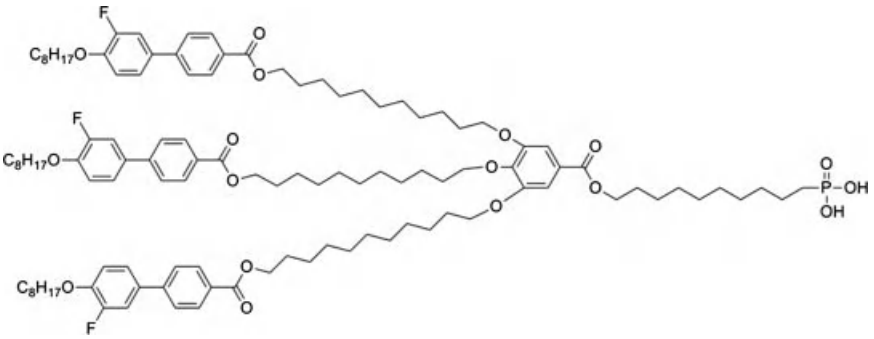

FIGURE 12.4 Chemical formula of the dendrite-like surfactant [34].

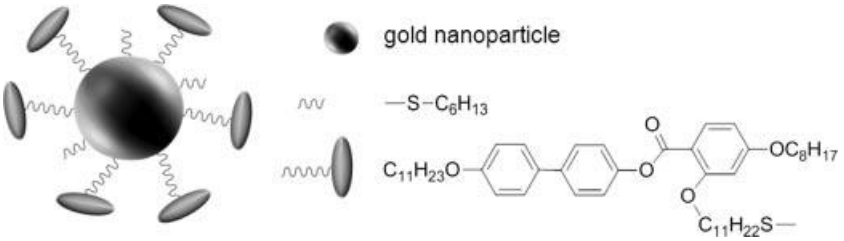

FIGURE 12.5 Gold nanoparticle attached with two-component surfactants [35].

trioctylphosphine oxide shows clearly visible aggregates with bright yellow luminescence in a fluorescent microscope (Figure 12.6a). In contrast, the quantum dots after site-exchange with mixture of dendron-like surfactant (Figure 12.3) and hexylphosponic acid in ratio 1:4 forms a stable dispersion in 5CB and homogeneously illuminated area is observed in a fluorescent microscope (Figure 12.6b).

12.3 PREPARATION OF THE FERROELECTRIC COLLOIDS

It is well known that the properties of nanoparticles can drastically differ from the properties of the macroscopic samples and this factor should be taken into account at the each stage of the LC suspensions preparation. It especially concerns ferroelectric particles, which can change or even lose their properties at the nano-scale. In sufficiently large colloidal particles, ferroelectric material is expected to form a polydomain structure. Macroscopic polarization of such particles is very small and working with single domain particles is preferable. The transition to a single domain structure occurs as the size of the particles decreases to approximately 15–20 nm [16]. At further decrease of the particles' size the ferroelectric mean field turns out to be insufficient to maintain a ferroelectric ground state. It usually

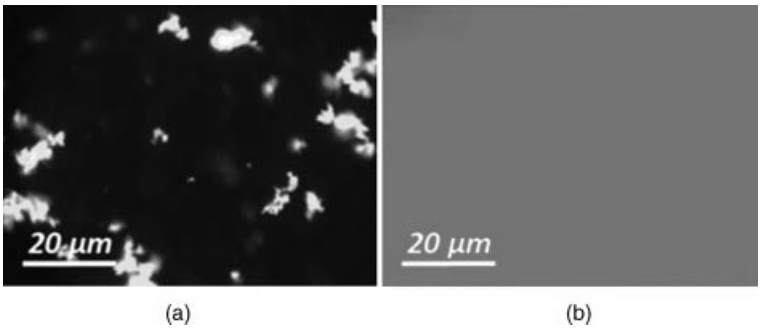

FIGURE 12.6 Fluorescence microscope images of CdSe/ZnS covered with different surfactants; (a) oleic acid based surfactant; (b) dendrite-like surfactant. Courtesy V. Vashchenko.

occurs for the particles smaller than 5 nm. For this reason, in order to get the maximum output of the permanent polarization, the optimal size of the particles in LC colloids should be in the range of 10–100 nm. At the same time, to get the stable colloid with no director disturbance, it is preferable to have the smallest particles possible. This means that the preferable size of the particle should be close to 10 nm. Therefore, only very narrow region of the particles' size can provide efficient influence of the ferroelectric particles. If one also takes into account that the electric charges which always are in a LC bulk can considerably screen the permanent dipole moment of the particles, producing of stable and reliable ferroelectric LC nanocolloids can be a real challenge.

Common techniques of fabrication of nanoparticles by chemical precipitation and spark plasma technique do not work in the case of ferroelectric nanoparticles in LCs, because these techniques usually give either the particles with not-ferroelectric cubic structure or they are too small to have strong ferroelectric properties. Therefore, the primary technique of ferroelectric particles producing is a mechanical grinding of ferroelectric materials [38].

Usually, the ferroelectric material is milled together with a surfactant in a nonionic liquid carrier. The most popular surfactant is oleic acid and heptanes or ethyl alcohol is taken as the carrier. In some modification of this technique, there is no carrier and only particles with a surfactant are being ground [2].

The final size of the nanoparticles is determined the milling time that in turn, strongly depends on the relative concentration of the components (surfactant, solvent, ferroelectric material), type of the mill (power of the mill, material, and weight of the jar and the ball(s) are important) and temperature of the milling. Depending on the type of the mill and the ferroelectric material, the time to get single domain ferroelectric particles varies from tens of minutes to hundreds of days.

The optimal parameters of the milling also strongly depend on the material being ground. For instance, due to the impact of the balls of planetary ball mill PM200 manufactured by Retsch GmbH the material $St_2P_3S_6$ is decomposed during the milling and a low powerful mill (e.g. Pulverisette 7 by Fritsch GmbH) should be used for this material. Moreover, the impact of the balls can be so strong that some material from the jar can be dislodged and get incorporated in the ferroelectric powder. This leads to the contamination of the ferroelectric.

All listed factors show how delicate the mechanical grinding technique is. Each combination of the milling machine and the material being ground requires a specific recipe to produce the single domain ferroelectric particles. The optimization of the grinding parameters for a particular material is a long and laborious process, but once it is established the results are very reliable.

Even the optimal grinding parameters do not guarantee the maximum possible polarization of the nanoparticles. Due to the size dispersion, electric charges in the solvent, presence of the particles with the cubic symmetry and other factors only a part of the produced nanoparticles have an essential polarization. This greatly complicates producing the efficient and reliable colloids. The breakthrough in solving this problem was done by Cook et al. [39]. They proposed a technique of harvesting ferroelectric nanoparticles to separate polar and nonpolar particles in the

FIGURE 12.7 The part of the harvesting unit made by G. Cook and D. Evans according to according to Cook et al. [39]. One can see the central wire with the harvested particles on it. Photo of Yu. Reznikov.

suspension and pick up single domain ferroelectrics particles only. The idea of the technique was to use gradient electric field to selectively harvest ferroelectric nanoparticles with the strongest dipole moments from bulk nanoparticle preparations. The harvesting was performed in a small sealed glass container with the dispersion of ferroelectric particles and surfactant in non-ionic and non-conducting solvent (usually heptanes) (Figure 12.7). There was a thin inner wire electrode at the center of the container and an external radial foil electrode that wrapped around the container. The inner wire electrode was put within a thin-walled sealed glass capillary tube. A high DC potential (typically 10–20 kV in a 2 cm diameter vial) was applied to the inner wire electrode while the outer foil electrode was grounded. When the DC-field was applied, which produced a large field gradient, the harvested nanoparticles with permanent dipoles were accumulated on the inner wire electrode and nonpolar particles without dipole moments were either rejected and accumulated on the outer glass wall or remained within the fluid.

Using the harvesting technique, authors of [39] were able to pick up 9 nm nanoparticles of $BaTiO_3$ and showed that the harvesting essentially enhances the effect of the particles on the characteristics of the LC (decreases the Freedericksz transition voltage and amplifies the photorefraction response). Another important

result was that the authors of Ref. [39] were unable to harvest nanoparticles fabricated by direct chemical synthesis, which resulted in nanoparticles' not having dipole moments. At the same time, harvesting can sometimes be successful even when the initial material for the grinding process was produced chemically and had a cubic symmetry. It allowed the authors of Ref. [39] to suggest that the stress and strain in nanoparticles that are produced during the grinding is an important factor in obtaining single ferroelectric domains at the nanometer scale. Moreover, recent experiments of the same group have shown that the ferroelectric properties of small nanoparticles (< 10 nm) are enhanced with respect to the large nanoparticle [40].

Our experience has shown that chemically the same ferroelectric materials (e.g. $BaTiO_3$) obtained from different sources or treated differently have an absolutely different harvesting efficiency. Therefore, a prior harvesting is a necessary procedure for the preparation of the reliable ferroelectric LC colloids.

After the grinding the produced nanoparticles need to be transferred to the LC matrix. In order to do this, the suspension of the nanoparticles in a solvent (preferably after the harvesting) is mixed with an LC and carefully dispersed by ultrasonication. Then, the solvent (usually heptanes) is slowly evaporated at slightly elevated temperature and atmosphere pressure. Typically this process lasts around 10 h at 60°C.

It should be noted that even small residuals of the solvent deteriorate the ordering of the LC matrix and mask the effect of the particles. Therefore, the evaporation process should be carefully controlled and monitored, for example, by the precise weighting of the mixture. Special attention should be paid to the solvent evaporation in a case of many-component LC mixtures because this process may cause a change in the matrix composition due to evaporation of low-weight components [7]. The consequent changes of the mesogenic properties of the matrix (average order parameter, $\bar{S}$, clearing temperature, T_c, dielectric anisotropy, ε_a, birefringence, n_a) can be incorrectly interpreted as the effect of nanoparticles. Specifically, evaporation of the heptanes from the mixture of MLC-6609, nanoparticles $BaTiO_3$ and oleic acid at low pressure and elevated temperature led to loss of low-weight components of MLC-6609 mixture that resulted in increase of T_c by several degrees.

It should be underlined that each new combination of the ferroelectric material, surfactant, and LC matrix requires their own fabrication recipe and we described only the principles of the producing of ferroelectric colloids. More detailed information about preparation of some specific colloids are available in the papers [2, 38, 39, 41].

12.4 ORIENTATIONAL ORDERING IN FERROELECTRIC LIQUID CRYSTAL COLLOIDS

The primary factor that distinguishes ferroelectrics from dielectric and semiconductor materials is a spontaneous electrical polarization. This polarization is a consequence of a the ions shift in the crystal lattice below the Curie temperature T_{Curie}, or an ordering of the microscopic dipoles at $T < T_{\text{Curie}}$. Obviously that it is the permanent dipoles of the ferroelectric nanoparticles that determine the specific

properties of the ferroelectric LC colloids. The permanent dipole induces a field in the surrounding isotropic medium.

$$\vec{E}_{part} = \frac{R_{part}^3}{3\varepsilon_0}\left(3\frac{\left(\vec{P}_{part}\cdot\vec{r}\right)\vec{r}}{r^5} - \frac{\vec{P}_{part}}{r^3}\right) \tag{12.5}$$

This field is very strong and is of the same order of magnitude that are the fields dealt with in a nonlinear optics; it is also comparable to the intermolecular fields. For the particles of $BaTiO_3$ with $d_{\text{part}} = 10\,\text{nm}$, $\vec{E}_{\text{part}} \approx 10^6\text{Vm}^{-1}$. The estimation of the ratio of the electrostatic interaction associated with this field to the thermal energy, U_{part}/k_BT gives the number of the order of 10^4 [42]. Therefore, even if the anisotropic part of the electrostatic interaction is small, one can expect that most of the dipole moments of the particles will be aligned parallel or antiparallel to the local director, $\vec{n}$, of a matrix and effective anchoring energy $\bar{W}$ that describes the coupling between the particles dipole moment and the local director can be considered strong. If the particle is elongated with the dipole moment parallel to the long axis and the LC molecules are parallel to their surfaces (planar alignment conditions), the orientational coupling between the particles and LC is further strengthened and long axis of the elongated particles is also aligned along the director of an LC (Figure 12.8).

Besides the orientational coupling between the LC matrix and the dipoles, the electric field $\vec{E}_{\text{part}}$ strongly polarizes the surrounding LC molecules, thereby

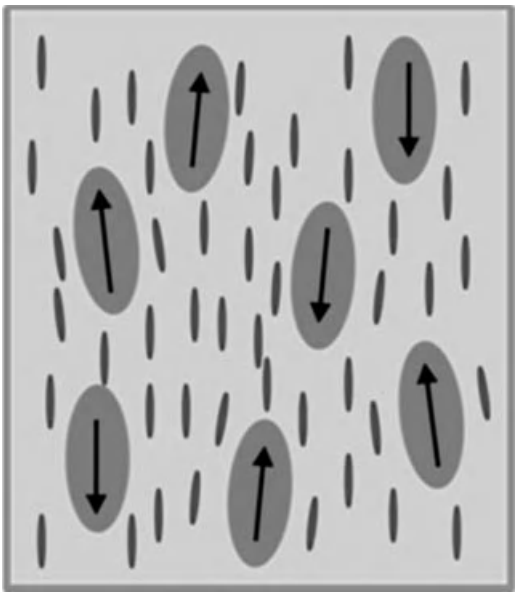

FIGURE 12.8 Schematic illustration of ferroelectric nanoparticles suspended in a liquid crystal. The permanent dipole moments of the nanoparticles have a distribution of orientations coupled with the distribution of orientation of LC molecules.

increasing intermolecular interaction [6]. According to the classic Mayer-Saupe mean field theory, this leads to the increase of the order parameter nearby the particles and, in turn, to the increase of the average order parameter of an LC with the particles, $\vec{S}_{\text{col}}$, and its clearing temperature, T_c. According to Li et al. [6], the shift of T_c does not depend on the size of the particles at the fixed volume fraction f_v and is proportional to $\vec{P}^2_{\text{part}}$:

$$\Delta T_c = \frac{Z f_v N_{\text{LC}} \beta_\alpha^2}{36\pi\varepsilon_o l_{m-m} 4.54 k_B} \vec{P}^2_{\text{part}} \tag{12.6}$$

where Z is nearest neighbour molecules separated by distance l_{m-m}, N_{LC} is the LC molecular concentration, β_a is the anisotropy of molecular polarisability. Substitution of the characteristic values in Eq. (12.6) gives the value of $\Delta T_c \approx (1\text{–}10)^{\circ}\text{C}$, that is, the effect of the particles should be strong.

With the approach by Li et al. [6], it was implicitly assumed that the dipole moments of all the particles were perfectly aligned in one direction. Lopatina and Selinger [43] considered interaction of the orientational order parameter of the dipoles with the orientational ordering of the liquid crystals. Using Landau theory, which suggested a small order parameter of both a LC and nanoparticles, they showed that it also stabilized the nematic phase and increased T_c. The problem of the application of this theory arises when the order parameter of nanoparticles is not small due to a strong interaction between nanoparticles and liquid crystal molecules. More adequate description of the suspension with interacting order parameters, S_{LC} and S_{part} was proposed in the other paper of the same authors [44]. The Mayer-Saupe theory that do not limit the value of S_{LC}, was applied. In this case

$$\Delta T_c = \frac{1.03 f_v \varepsilon_a}{135 \rho_{\text{LC}} k_B \varepsilon_0 \varepsilon^2} \vec{P}^2_{\text{part}} \tag{12.7}$$

The estimation according to Eq. (12.7) predicts the shift of $T_c \approx 1^{\circ}$. As one can see, the difference between Eqs (4) and (5) is that ΔT_c scales as β_a^2 in Eq. (12.4) but according to Eq. (12.5) it should scale linearly with ε_a. This difference arises because in the theory of Li et al. the additional interaction between the molecules is a consequence of the polarization of the neighboring molecules by the electric field $\vec{E}_{\text{part}}$ which is proportional to β_a. This polarization result in additional intermolecular interaction which scales as β_a^2. In the theory of Lopatina and Selinger the direct influence of the nanoparticles' electric field which scales linearly with ε_a is considered. At the present stage it is difficult to be sure which model is closer to reality but in any case, both approaches suggested in Refs [6] and [44] predict a notable increase of the order parameter and clearing temperature of the colloid.

The rise of $\bar{S}_{\text{col}}$ and T_c should be accompanied by the corresponding increase of all the parameters of a mesophase that are determined by the LC ordering, such as dielectric anisotropy, $\varepsilon_a(\bar{S}_{\text{col}})$, birefringence, $n_a(\bar{S}_{\text{col}})$, Frank constants, $K(\bar{S}^2_{\text{col}})$, etc. The systematic experiments carried out with the colloid of ferroelectric nanoparticles $Sn_2P_2S_6$ in a classic one-component LC pentyl-cianobiphenyl (5CB) [45] confirmed

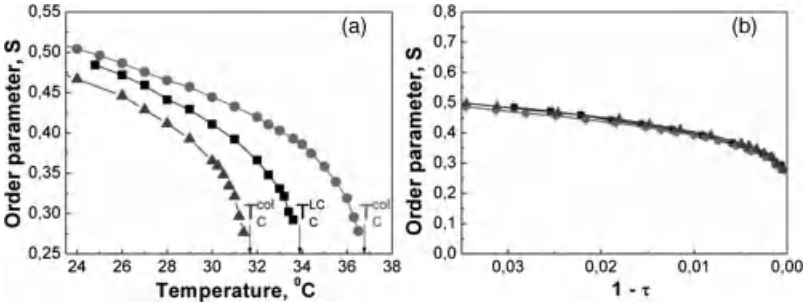

FIGURE 12.9 (a) Temperature dependences of the order parameter of the pure 5CB (black line), suspension with the increased T_c (red line), suspension with the decrease T_c (blue line). (b) The same dependences in the reduced temperature coordinates [45].

these predictions. In Figure 12.9a the temperature dependencies of the order parameter of 5CB doped with $f_w \approx 0.3\%$ of $Sn_2P_2S_6$ are shown. One can see the evident increase of T_c ($\Delta T_c \approx 3°$) and the order parameter $\bar{S}_{col}$ in the colloid compared to the pure LC 5CB. The measurements of the temperature dependencies $\varepsilon_a(T)$ and $n_a(T)$ showed the corresponding increase of these values.

It should be noted that the magnitude and sometimes even the sign of ΔT_c and the corresponding changes of $\varepsilon_a(T)$ and $n_a(T)$ could vary from sample to sample despite the same producing recipe. The causes of the poor reproducibility of these values are discussed below. The maximum positive shift of T_c was 11° that caused the strong increase of ε_a and n_a even at room temperature (Figures 12.10a and b).

The important point here is that despite the magnitude and even the sign of the changes of the order parameter and clearing temperature vary from sample to sample, in all cases $S_{LC}(\tau)$ and $\bar{S}_{col}(\tau)$ plotted as a function of the reduced temperature $\tau = (T + 273°)/(T_c + 273°)$ fit perfectly (Figure 12.9b). Moreover, the temperature dependencies $\varepsilon_{II,\perp}(\tau)$ and $n_a(\tau)$ also fit in the reduced coordinates (Figures 12.10b and 12.11b). It means that all observed changes in the characteristics

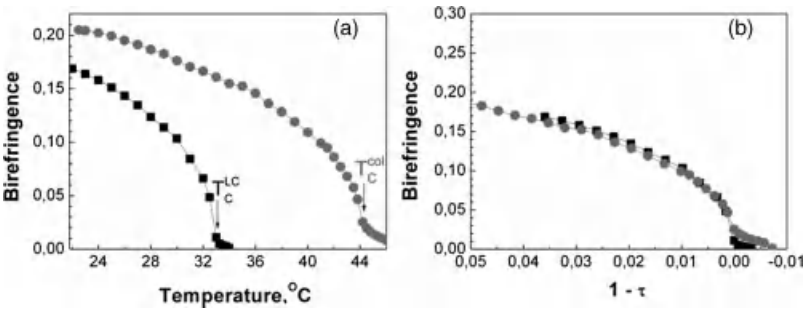

FIGURE 12.10 (a) Temperature dependences of the order parameter of the pure 5CB (black line), suspension with the increased T_c (red line), suspension with the decrease T_c (blue line). (b) The same dependences in the reduced temperature coordinates [45].

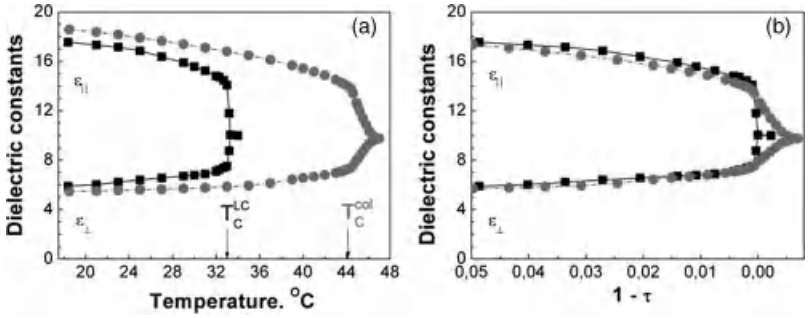

FIGURE 12.11 (a) Temperature dependences of the dielectric constants of the pure 5CB (black line) and the suspension with the increased T_c (red line). (b) The same dependences in the reduced temperature coordinates [45].

of the single component LC 5CB can be fully explained by the changes of the order parameter of the LC host due to the presence of the particles. All other possible mechanisms of the changes of the values $\varepsilon_{II,\perp}$ and n_a give only small contribution, if any at all. For instance, it concerns the direct contribution of the dipole moment and polarisability of the particles to $\varepsilon_{II,\perp}$ and n_a. It is also seen from the comparison of the Freedericksz transition voltage in a planar cell filled with a pure 5CB to the one filled with the colloid. The transition voltage for a pure LC is determined by the expression [46]:

$$U_{Fr} = \pi\sqrt{\frac{K_{11}\left(S_{LC}^2\right)}{\varepsilon_0\varepsilon_{a,LC}(S_{LC})}} \tag{12.8}$$

The value $\varepsilon_a, \ \propto S_{\mathrm{LC}}$, and the elastic constant $K_{11} \propto S_{\mathrm{LC}}^2$ [46]. Therefore, if the effect of the particles is reduced to a change of the LC ordering, one can expect a slight increase of the transition voltage $U_{Fr} \propto \sqrt{\bar{S}_{\mathrm{col}}}$ due to increase of the order parameter of the colloid, $\bar{S}_{\mathrm{col}}$. For the experimental data depicted in Figure7a, at room temperature $\varepsilon_{a,\mathrm{LC}}/\varepsilon_{a,\mathrm{col}} = S_{\mathrm{LC}}/\bar{S}_{\mathrm{col}} = 0.86$, $K_{11,\mathrm{LC}}/K_{11,\mathrm{col}} = S_{\mathrm{LC}}^2/\bar{S}_{\mathrm{col}}^2 = 0.79$ and $U_{\mathrm{col}} \approx 1.04U_{\mathrm{LC}}$ are expected. Experimental results confirmed this estimation; it was found that for an AC-field ($v = 1$ kHz) the transition voltage $U_{LC} = 1.84 \pm 0.02$ V and $U_{\mathrm{col}} = 1.87 \pm 0.02$ V.

Thus, one can state that for single-component LC, such as 5CB, the properties of the suspensions are mainly determined by the influence of the particles on the ordering of a LC matrix. Such behavior of the ferroelectric nanoparticles is reminiscent of the behavior of low-molecular weight molecular dopants in nematics. Chen and Luchkhrust as far back as in 1969 concluded that the temperature dependence $\bar{S}(\tau)$, $\tau = T/(T_c + 273°)$, for a nematic LC with impurities is the universal function of the reduced temperature [47]. It was also shown that the function $\bar{S}(\tau)$ did not depend on the chemical structure of the impurities and coincided with the dependence $\bar{S}_0(\tau)$ for the pure LC matrix. Later, Pinkevich et al. [48] showed that this universality follows from the standard Grandjean–Maier–Saupe (GMS)

molecular field theory. The sign of the shift of τ is determined by the relationship between the amplitude of inter-molecular interaction of LC molecules, G_{lc-lc}, and the amplitude of interaction "LC molecule—impurity molecule", G_{lc-imp}. In the case of non-mesogenic impurities, $G_{lc-lc} > G_{lc--imp}$, the local order parameter around the impurity is less than the one in a pure LC, and the shift of the clearing temperature, $\Delta T_c < 0$. Mesogenic dopants can interact with liquid crystal molecules more strongly than liquid crystal molecules with themselves, $G_{lc-lc} < G_{lc-imp}$. Therefore, mesogenic impurities can increase the local ordering and increase the clearing temperature.

Exactly the same behavior is observed in the colloid of ferroelectric nanoparticles in 5CB. Therefore, one can suggest that the ferroelectric nano-particles, $Sn_2P_2S_6$, in LC 5CB can act like molecular dopants, and the change of the order parameter of the LC is the dominant mechanism that determines the difference between the properties of the colloid and pure single component LC.

To understand why such big macroscopic object as ferromagnetic nano-particle, volume of which is 100–1000 times larger than the volume of molecule, can work as a virtual molecular dopant, Reshetnyak considered a ferroelectric LC colloid as LC host with undisturbed order parameter, S_{LC}, with clusters of LC molecules, having order parameter S_{cl} that differs from S_{LC} due to the presence of ferroelectric nano-particles [49]. In this case in the framework of Maier-Saupe model, he obtained universality of the function $\bar{S}_{\mathrm{col}}(\tau)$. The important point is that in this model the universality of the function $\bar{S}_{\mathrm{col}}(\tau)$ is the consequence of the Maier-Saupe formalism that suggests the interaction between LC molecules due to long-range dispersion forces. Therefore, the experiments show that the ferroelectric nano-particles do not change a character of the intermolecular interaction in the LC host, and their influence reduces the enhancement ($\Delta T_c > 0$) or depressing ($\Delta T_c < 0$) of this interaction, which leads to a change of the host order parameter value.

Finalizing the description of the effect of the ferroelectric nanoparticles on the ordering of LCs, we cannot avoid the question of poor reproducibility of the results in these systems. First of all, one can state that the effect of the increase of the ordering exists unambiguously, and that was independently confirmed by the measurements of the dichroism of dye molecules embedded to the colloid of $St_2P_3S_6$ in 5CB matrix [45], by the characteristic Raman scattering bands of 5CB molecules in the colloid of $BaTiO_3$ particles in 5CB [41] and by the dichroism of the characteristic functional groups of the nematic matrix components of the suspension of $BaTiO_3$ particles in a MLC-6609 [6]. The question of why in some experiments SL_c and T_c decreases, requires additional studies. There are several causes that can mask the effect of the permanent polarization of the particles and lead to a reduction of S_{LC} and T_c.

(1) *Screening of the polarization by external charges.* There are always free charges in an LC. Typical concentration of the charges in commercially available 5CB is $c_e = 10^{20}$–$10^{22}\,\mathrm{m}^{-3}$ and the concentration of the particles is $c_{\mathrm{part}} = 10^{19}$–$10^{21}\,\mathrm{m}^{-3}$. The estimations are according to Lopatina and Selinger [43] show that at concentration of charges $c_e = 10^{20}$–$10^{22}\,\mathrm{m}^{-3}$ the

Debye screening length, $k_D^{-1} \sim 300 - 2$ nm can be comparable to the size of the particles and the screening effect can be strong. To decrease the screening effect, weakly conductive LC is preferable. For example, the ferroelectric colloids based on LC–TL 205 which is characterized by extremely low conductivity, reveal reliable characteristics [39].

(2) *Influence of surfactants.* A surfactant changes the order parameter of the LC near the particle's surface. Usually surfactants deteriorate the ordering which causes the decrease of T_c. It is also true that the oleic acid, coating of which induces homeotropic alignment of 5CB, disturbs the order parameter of the LC in the vicinity of the spherical nanoparticles. Also, Atkuri et al. showed that oleic acid presents as a dimer, monomer, or complex conjugate with $BaTiO_3$ particles [27] and some part of oleic acid in a dimeric form is always present in the bulk of LC, decreasing the LC ordering. The relationship between these components strongly depends on the time of the particles' milling, particles' size and concentration of the oleic acid and particles in an LC. It is very difficult to control all these parameters during preparation of an LC and their final contribution to the decrease of S_{LC} and T_c can vary from experiment to experiment. At the same time, this contribution can be large. For instance, only 0.5 wt.% of oleic acid dissolved in 5CB, decreases the clearing temperature by $\Delta T_c \approx -1.6^{\circ}$C.

(3) *The particles' size dispersion.* This factor can also be very important. The particles' size dispersion strongly depends on the milling time, parameters of the mill and concentration of the milled components. Taking into account the narrow range of the particles sizes that provide single domain structure (5–20 nm) and a strong permanent polarization, it is clear how sensitive the characteristics of the final suspension are to the details of the grinding process. The typical distribution of the ferroelectric particles after the milling is presented in the chart in Figure 12.12. One can see that only small part of all the numbers of the particles can work effectively works.

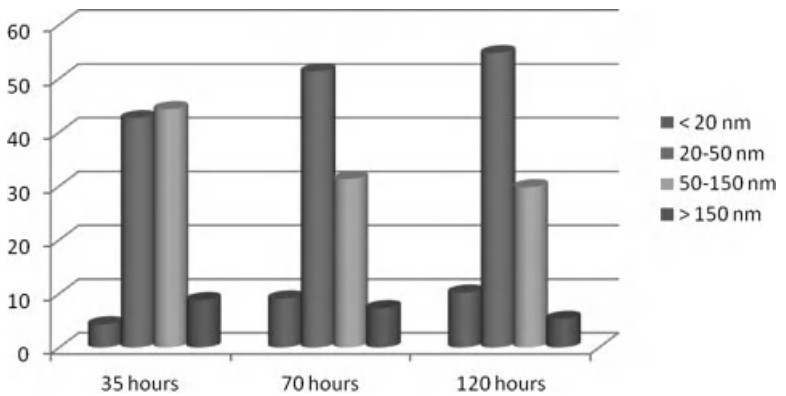

FIGURE 12.12 Distribution of the $St_2P_2S_6$ at the different times of milling. Courtesy O. Kurochkin.

12.5 DIELECTRIC AND REORIENTATIONAL PROPERTIES OF FERROELECTRIC LC COLLOIDS

In the previous chapter, we considered the effect of the particles on the properties of a LC matrix due to the mechanism of the orientational coupling enhancement between LC molecules and showed that this mechanism is responsible for the observed properties of a LC 5CB doped with nanoparticles $Sn_2P_2S_6$. At the same time, we must not forget that the ferroelectrics themselves have the unique dielectric properties. Ferroelectric materials possess spontaneous polarization, their dielectric constants can vary in a wide range $\varepsilon = 100$–10,000. Polarization of ferroelectrics nonlinearly depends on the electric field, it is reversed by the change of the direction of the field and reveals strong hysteresis. In addition, while being in a liquid matrix, ferroelectric nanoparticles can rotate and align according to the sign and the direction of external electric field. All of this must necessarily affect the dielectric properties of an LC and, as a consequence, on the characteristics of reorientational electro-optical effects, that is, determined by dielectric anisotropy of a LC.

There are several experimental evidences of the undoubtful influence of the dielectric properties of the particles on the dielectric and reorientation properties of a LC. First, this is a linear dielectric response of the nematic colloid; when a weak bias electric field is applied to the cell, the director of the colloid is reoriented along the direction of the applied low-frequency ($\nu = 200$ Hz) electric AC-field, $\vec{E}$, also following the sign of the field [2]. This effect is explained by formation of the polar ordering of the particles' permanent dipoles by the bias field and following collective intact reorientation of the strongly coupled particles and the director with the alternation of the AC-field.

Further, the electrical Freedericksz transition voltage in a DC-field strongly depends on electrical history of the cells with the ferroelectric LC colloid. Cook et al. observed that in a cell with the colloid of $BaTiO_3$ nanoparticle in LC TL205 the voltage of the Freedericksz transition decreased or increased, depending on the polarity of the applied voltage, giving a net 1.6 V Freedericksz threshold asymmetry [50]. This polarization hysteresis indicates that the cell behaves as a ferroelectric material that is, explained in line with [2] by orientation of the particles' dipole moments in a DC-field according to the sign of the field. The interesting fact is that in the experiments of Cook et al. the cell "remembered" the sign of the applied field, sometimes even after overheating of the cell above clearing point. It means that once aligned, the dipole moments may keep their alignment for rather long time, unlike in the case described by Reznikov et al. [2], where the polarization of the cell disappeared during few milliseconds after the bias electric field was switched off.

One more evident contribution of the ferroelectricity to the dielectric properties of the colloids is repeatedly observed strong increase (by several times) of the LCs dielectric anisotropy and birefringence after doping it with ferroelectric particles [2, 28, 41, 51, 52]. In some experiments, this increase was observed despite decrease of T_c in the colloid and cannot be explained by the increase of the LC matrix order parameter [28].

The most developed theory of dielectric properties of ferroelectric LC suspension was recently published by Shelestiuk et al. [42]. The authors generalized the Maxwell-Garnet approach considering anisotropic in shape and dielectric polarisability nanoparticles in a dielectrically anisotropic LC matrix. The particles possess a permanent dipole moment, a strong orientational coupling between the particles and LC is suggested and no interaction between the particles is assumed.

One of the conclusions of the classic Maxwell-Garnet theory is that adding dielectric particles with high dielectric permittivity $\varepsilon_{\text{part}}$ to a dielectric matrix with much smaller permittivity, ε_{LC} does not lead to a notable increase of the total effective dielectric permittivity of the suspension. The situation is different in the case of ferroelectric particles that possess permanent dipoles, however. Application of even a weak electric field breaks central symmetry of the dipoles' orientation and mean particle permanent polarization in the LC matrix becomes

$$\vec{P} = \vec{d}_{\text{part}}\vec{n}(\rho_+ - \rho_-) \tag{12.9}$$

where ρ_+ and ρ_- are the fractions of the particles aligned, respectively, parallel and antiparallel to the local director $\vec{n}$. The fractions ρ_+ and ρ_- are described by the Boltzmann distribution in electric field $\vec{E}$ and lead to the mean value of $\vec{P} = (d^2_{\text{part}}V_{\text{part}}/k_BT)\vec{n}(\vec{n}\vec{E})$, which contributes to the expressions for effective permittivities of the suspension. The analytical, although rather complicated, expressions of $\varepsilon_{II}$and $\varepsilon_{\perp}$can be found in the article [42]. They show that the presence of the permanent dipole moment does increase the value of ε_{II} and accordingly, the dielectric anisotropy ε_a. Unfortunately, the uncertainty of many experimental parameters (P, V_{part}, f_v, etc.) makes the quantitative comparison of the calculations with the experimental data difficult at this stage.

The effect of the ferroelectric particles on the dielectric properties of a LC is closely related to repeatedly observed decrease of the Freedericksz transitions voltages in AC-field [2, 28, 41]. Typically, the transition voltage U_{Fr} drops by 1.3–2.5 times. These values are too high to be explained by possible disordering of the LC matrix, which results in slight decrease of $U_{Fr} \propto \sqrt{S}$. The problem about the Freedericksz transitions in the ferroelectric LC suspension was consistently resolved in [42]. The important result of this work is that the effective permittivity as it appears in the expression for free energy of the colloid in a cell does not coincide with the expressions for $\varepsilon_{II}^{\text{col}}$ and $\varepsilon_{\perp}^{\text{col}}$ which are obtained in the frame of generalized Maxwell-Garnett picture. Therefore, the formula for the Freedericksz transitions voltage is given by

$$U_{Fr} = \pi\sqrt{\frac{K_{11}}{\varepsilon_o\varepsilon_{a,\text{eff}}^{\text{col}}}} \tag{12.10}$$

where $\varepsilon_{a,\text{eff}}^{\text{col}} \neq \varepsilon_a^{\text{col}}$. Since $\varepsilon_{a,\,\text{eff}}^{\text{col}} > \varepsilon_a^{\text{LC}}$, the Freedericksz transition voltage decreases in the suspension. The variance between $\varepsilon_{a,\,\text{eff}}^{\text{col}}$ and $\varepsilon_a^{\text{col}}$ can be serious, and difference in the calculations of the Freedericksz transition voltage reduction is essential.

It should be noted that the experimental data described in this chapter were obtained for multi-component LC mixtures and this circumstance was not taken into account in the theories of dielectric properties and Freedericksz transition of ferroelectric colloids. At the same time, the presence of different components with different molecular masses and dipole moments may seriously affect the final properties of the suspensions. Indeed, an electric field $\vec{E}_{\text{part}}$ decreases quickly (as r^{-3}) with a distance from the particles. Therefore, the local electrical field is very inhomogeneous in a LC, even if it is partially compensated by free charges which are always there in an LC. Motion of the polar molecules with various dipole moments and various molecular weights in the gradient of the local electric field, as well as various different adsorption affinities of various mixtures' molecular components on the particle's surface can lead to a spatial redistribution of the individual components of the LC matrix. Obviously, the resulting micro/nano-separation of the mixture should affect the macroscopic properties of the colloid. Micro-separation probably provides additional contribution to the changes of the dielectric and reorientation properties in the ferroelectric colloids based on many-component LCs and masks the effect of the orientation amplification, clearly observed in a single-component matrix 5CB.

The effect of the ferroelectric particles on the dielectric and reorientation properties of ferroelectric LC is of special interest because interaction between the permanent polarization of the particles and macroscopic polarization of the LC can be expected. There are only few papers on this topic [54, 55] till now, but they point to a strong effect of the particles. Liang et al. [54] reported on almost doubling of the spontaneous polarization, enhancement of dielectric properties and faster response time in a ferroelectric LC CS1024 (Chisso) doped with $BaTiO_3$ ($\sim$30 nm size) in a small concentration. Unlike them, Mikułko et al. [55] observed only slightly lower spontaneous polarization and lower relative dielectric permittivity for the nanocomposite of $BaTiO_3$ ($\sim$30 nm size) in another ferroelectric LC LAHS9. At the same time, as in the work of Liang et al., faster response time of the nanocomposite was reported.

12.6 CONCLUSIONS

The science of LC ferroelectric colloids is very young and many of its technological and scientific problems are yet to be solved, many issues are under hot discussions and the general description of these materials is far from completion. Nevertheless, summarizing the knowledge obtained since the first publication on the properties of ferroelectric LC colloids, one can list the following main results:

- Strong permanent polarization of the ferroelectric nanoparticles results in unique properties of the LCs doped with these nanoparticles, such as sensitivity to the sign of the electric field, enhanced dielectric anisotropy, and birefringence of nematic LCs.

- There are two main mechanisms of the particles' effect: the increase of the orientation coupling between LC molecules and the direct contribution of the permanent polarization of the particles to the dielectric properties of the LC mixture. The latter is the primary factor in the case of multi-component LC mixtures and the enhancement of the orientation coupling dominates in a single-component LC 5CB. In the last case, the ferroelectric nanoparticles can be considered as effective molecular impurities with giant dipole moments.
- Only narrow range of the particles' sizes, approximately from 5–8 to 10–20 nm, results in providing effective influence of the particles. Together with screening of the permanent polarization by free electric charges, it makes it still difficult to produce reliable colloids. The harvesting of the ferroelectric nanoparticles helps to improve the reliability and efficiency of the particles impact.

These basic results established a solid platform for the following fundamental studies and application of ferroelectric LC colloids. We believe that after development of highly reliable methods of the producing stable ferroelectric LC colloids, they will offer an innovative simple and effective means to control precisely the physical properties of liquid crystalline materials and find its important place among LC materials for electro-optical, nonlinear optical, and telecommunication LC devices.

ACKNOWLEDGMENTS

I am grateful to my close collaborators, D. Evans, A. Glushchenko, V. Reshetnyak, T. Sluckin, J. West, and their teams for long-term collaboration in the field of LC colloids, and for numerous useful discussions which have helped us to agree on a joint view of ferroelectric LC colloid physics. I also acknowledge the help and advice from O. Buchnev, O. Buluy E. O. Kurochkin, B. Lev, L. Lopatina, A, Morozovskaya, M. Reznikov, V. Zadorozhnyi, and V. Vashchenko. I thank Ch. Rosenblatt for reviewing the manuscript and the valued advice.

REFERENCES

1. F. Brochard and P. G. de Gennes. Theory of magnetic suspensions in liquid crystals. *J. de Phys.* **1970**, *31*, 691–706.
2. Yu. Reznikov, O. Buchnev, O. Tereshchenko, V. Reshetnyak, A. Glushchenko, and J. West. Ferroelectric nematic suspension. *Appl. Phys. Lett.* **2003**, *82*, 1917.
3. M. Gorkunov and M. Osipov. Mean-field theory of a nematic liquid crystal doped with anisotropic nanoparticles. *Soft Matter* **2011**, *7*, 4348–4356.
4. F. Haraguchi, K. Inoue, N. Toshima, S. Kobayashi, and K. Takatoh. Reduction of the threshold voltages of nematic liquid crystal electrooptical devices by doping inorganic nanoparticles. *Jpn. J. Appl. Phys.* **2007**, *46*, L796–L797.

5. H. Duran, B. Gazdecki, A. Yamashita, and T. Kyi. Effect of carbon nanotubes on phase transition of nematic liquid crystals. *Liq. Cryst.* **2005**, *32*, 815–821.
6. F. Li, O. Buchnev, C. Cheon, A. Glushchenko, V. Reshetnyak, Yu. Reznikov, T. Sluckin, and J. West. Orientational coupling amplification in ferroelectric nematic colloids. *Phys. Rev. Lett.* **2006**, *97*, 147801/ 1–4.
7. F. Li, O. Buchnev, C. Cheon, A. Glushchenko, V. Reshetnyak, Yu. Reznikov, T. Sluckin, and J. West. Erratum: Orientational coupling amplification in ferroelectric nematic colloids. *Phys. Rev. Lett.* **2006**, *97*, 147801/1-4. *Phys. Rev. Lett.* 99, 219901.
8. R. Basu and G. S. Iannacchione. Nematic anchoring on carbon nanotubes. *Appl. Phys. Lett.* **2009**, *95*, 173113/ 1–3.
9. I. Dierking, G. Scalia, and P. Morales. Liquid crystal–carbon nanotube dispersions. *J. Appl. Phys.* **2005**, *97*, 044309/ 1–5.
10. P. Kopčanský, N. Tomašovičová, M. Koneracká, V. Závišová, M. Timko, A. Džarová, A. Šprincová, N. Éber, K. Fodor-Csorba, T. Tóth-Katona, A. Vajda, and J. Jadzyn. Structural changes in the 6CHBT liquid crystal doped with spherical, rodlike, and chainlike magnetic particles. *Phys. Rev. E* **2008**, *78*, 011702/ 1–5.
11. N. Podoliak, O. Buchnev, O. Buluy, G. D'Alessandro, M. Kaczmarek, Yu. Reznikov, and T. J. Sluckin. Macroscopic optical effects in low concentration ferronematics. *Soft Matter* **2011**, *7*, 4742–4749.
12. O. Kurochkin, O. Buchnev, A. Iljin, S. K. Park, S. B. Kwon, O. Grabar, and Yu. Reznikov. A colloid of ferroelectric nanoparticles in a cholesteric liquid crystal. *J. Opt. A: Pure Appl. Opt.* **2009**, *11*, 024003/ 1–5.
13. M. Kaczmarek, O. Buchnev, I. Nandhakumar. Ferroelectric nanoparticles in low refractive index liquid crystals for strong electro-optic response. *Appl. Phys. Lett.* **2008**, *92*, 103307/ 1–3.
14. O. Buchnev, A. Dyadyusha, M. Kaczmarek, V. Reshetnyak, and Yu. Reznikov. Enhanced two-beam coupling in colloids of ferroelectric nanoparticles in liquid crystals. *J. Opt. Soc. Am. B* **2007**, *24*, 1512–1516.
15. G. Cook, A. V. Glushchenko, V. Reshetnyak, A. T. Griffith, M. A. Saleh, and D. R. Evans. Nanoparticle doped organic-inorganic hybrid photorefractives. *Opt. Express* **2008**, *16*, 4015–4022.
16. E. Erdem, H.-C. Semmelhack, R. Bottcher, H. Rumpf, J. Banys, A. Matthes, H.-J. Glase, D. Hirsch, and E. Hartmann. Study of the tetragonal-to-cubic phase transition in PbTiO3 nanopowders. *J. Phys.: Condens. Matter* **2006**, *18*, 3861–3874.
17. D. S. Mathew and R.-S. Juang. An overview of the structure and magnetism of spinel ferrite nanoparticles and their synthesis in microemulsions. *Chem. Eng. J.* **2007**, *129*, 51–65.
18. S. Y. Park and D. Stroud. Splitting of surface plasmon frequencies of metal particles in a nematic liquid crystal. *Appl. Phys. Lett.* **2004**, *85*, 2920–2922.
19. H. Stark. Physics of colloidal dispersions in nematic liquid crystals. *Phys. Rep.* **2001**, *351*, 387–474.
20. E. Ouskova, O. Buluy, C. Blanc, H. Dietsch, and A. Mertel. Enhanced magneto-optical properties of suspensions of spindle type mono-dispersed hematite nano-particles in liquid crystal. *Mol. Cryst. Liq. Cryst.* **2010**, *525*, 104–111.
21. V. V. Ponevchinsky, A. I. Goncharuk, V. I. Vasil'ev, N. I. Lebovka, and M. S. Soskin. *JETP Lett.* **2010**, *91*, 241–244.

22. O. Buluy, S. Nepijko, V. Reshetnyak, E. Ouskova, V. Zadorozhnii, A. Leonhardt, M. Ritschel, G. Schönhense, and Yu. Reznikov. Magnetic sensitivity of a dispersion of aggregated ferromagnetic carbon nanotubes in liquid crystals. *Soft Matter* **2011**, *7*, 644–649.
23. S. Chandtasekhar. Stochastic problems in physics and astronomy. *Rev. Mod. Phys.* **1943**, *15*, 1–89.
24. O. V. Kuksenok, R. W. Ruhwandl, S. V. Shiyanovskii, and E. M. Terentjev. Director structure around a colloid particle suspended in a nematic liquid crystal. *Phys. Rev. E* **1996**, *54*, 5198–5203.
25. P. Galatola and J.-B. Fournier. Nematic-wetted colloids in the isotropic phase: Pairwise interaction, biaxiality, and defects. *Phys. Rev. Lett.* **2001**, *86*, 3915–3918.
26. S. Chernyshuk, B. Lev, and H. Yokoyama. Paranematic interaction between nanoparticles of ordinary shape. *Phys. Rev. E* **2005**, *71*, 062701/ 1–4.
27. H. Atkuri, K. Zhang, and J. West. Fabrication of paraelectric nanocolloidal liquid crystals. *Mol. Cryst. Liq. Cryst.* **2009**, *508*, 183–190.
28. M. Gupta, I. Satpathy, A. Roy, and R. Pratibha. Nanoparticle induced director distortion and disorder in liquid crystal-nanoparticle dispersions. *J. Colloid Interf. Sci.* **2010**, *352*, 292–298.
29. A. Szilágyi, G. Fetter, and M. Zrínyi. Thermotropic behaviour of the complex liquid crystal system containing 8CB [4-cyano-4'-(n-octylbiphenyl)] and organic ferrofluid. *J. Therm. Anal. Calorim.* **2005**, *82*, 525–530.
30. A. B. Bourlinos, A. Bakandritsos, V. Georgakilas, and D. Petridis. Surface modification of ultrafine magnetic iron oxide particles. *Chem. Mater.* **2002**, *14*, 3226–3228.
31. T. Fried, G. Shemer, G. Markovich. Ordered two-dimensional arrays of ferrite nanoparticles. *Adv. Mater.* **2001**, *13*, 1158.
32. C. Yee, G. Kataby, A. Ulman, T. Prozorov, H. White, A. King, M. Rafailovich, J. Sokolov, and A. Gedanken. Self-assembled monolayers of alkanesulfonic and phosphonic acids on amorphous iron oxide nanoparticles. *Langmuir* **1999**, *15*, 7111–7115.
33. M. Kolosov, A. Krivoshey, M. Prodanov, O. Buluy, Yu. Reznikov, O. Semenenko, J. Goodby, and V. Vashchenko. Dispersion of magnetic nano rods in nematic liquid crystals. 23rd International Liquid Crystal Conference 2010, July 11–16, 2010, Krakow, Poland, Abstract Book.
34. M. Prodanov, A. Fedoryako, M. Kolosov, A. Krivoshey, J. Goodby, V. Vashchenko, E. Pozhidaev, and S. Gamzaeva. Rotational viscosity of dispersion of magnetic nano particles in ferroelectric liquid crystals. 23rd International Liquid Crystal Conference, July 11-16 2010, Krakow, Poland, Abstract Book, p. 742.
35. L. Cseh and G. H. Mehl. The design and the investigation of room temperature thermotropic nematic gold nanoparticles. *J. Am. Chem. Soc.* **2006**, *128*, 13377–133786.
36. E. Ouskova, D. Lysenko, S. Ksondzyk, L. Cseh, G. H. Mehl, V. Reshentnyak, and Yu. Reznikov. Strong cubic optical nonlinearity of gold nanoparticles suspension in nematic liquid crystal. *Mol. Cryst. Liq. Cryst.* **2011**, *545*, 123–132.
37. M. Prodanov, N. Pogorelova, A. Kurochkin, A. Kryshtal, A. Krivoshey, Yu. Reznikov, J. Goodby, and V. Vashchenko. Dispersion of quantum dots in nematic liquid Crystals. 6th International Chemistry Conference Toulouse-Kiev, May 30–June 1, 2011, Abstrats Book.
38. H. Atkuri, G. Cook, D. R. Evans, C.-I. Cheon, A. Glushchenko, V. Reshetnyak, J. West, and K. Zhang. Preparation of ferroelectric nanoparticles for their use in liquid crystalline colloids. *J. Opt. A: Pure Appl. Opt.* **2009**, *11*, 024006/ 1–5.

39. G. Cook, J. L. Barnes, S. A. Basun, D. R. Evans, R. F. Ziolo, A. Ponce, V. Yu. Reshetnyak, A. Glushchenko, and P. P. Baneerje. Harvesting single ferroelectric domain stressed nanoparticles for optical and ferroic applications. *J. Appl. Phys.* **2010**, *108*, 064309/ 1–5.
40. D. R. Evans, S. A. Basun, G. Cook, I. P. Pinkevych, and V. Yu. Reshetnyak. Electric field interactions and aggregation dynamics of ferroelectric nanoparticles in isotropic fluid suspensions. *Phys. Rev. B* **2011**, *84*, 174111/1-9.
41. J.-F. Blach, S. Saitzek, C. Legrand, L. Dupont, J.-F. Henninot, and M. Warnghem. $BaTiO_3$ ferroelectric nanoparticles dispersed in 5CB nematic liquid crystal: Synthesis and electro-optical characterization. *J. Appl. Phys.* **2010**, *107*, 074102/ 1–7.
42. S. Shelestiuk, V. Reshetnyak, and T. Sluckin. Fredericks transition in ferroelectric liquid-crystal nanosuspensions. *Phys.Rev. E* **2011**, *83*, 041705/ 1–13.
43. L. M. Lopatina and J. V. Selinger. Theory of ferroelectric nanoparticles in nematic liquid crystals. *Phys. Rev. Lett.* **2009**, *102*, 197802–197804.
44. L. M. Lopatina and J. V. Selinger. Maier-Saupe-type theory of ferroelectric nanoparticles in nematic liquid crystals. *Phys. Rev. E.* **2011**, *84*, 141703/1-7.
45. O. Kurochkin, H. Atkuri, O. Buchnev, A. Glushchenko, O. Grabar, R. Karapinar, V. Reshetnyak, J. West, and Y. Reznikov. Nano-colloids of Sn2P2S6 in nematic liquid Crystal. *Cond. Matt. Phys.* **2010**, *13*, 33701/ 1–9.
46. P. G. de Gennes and J. Prost. *The Physics of Liquid Crystals*. Oxford University Press, New York, 1994.
47. D. Chen and G. Luchkhrust. Electron resonance study of the perturbation of the order in a nematic mesophase by a second component. *Trans. Faraday Soc.* **1969**, *65*, 656–664.
48. I. P. Pinkevich, Yu. Reznikov, V. Y. Reshetnyak, and O. V. Yaroshchuk. Conformational optical nonlinearity of nematic liquid crystals. *Int. J. Nonlinear Opt. Phys.* **1992**, *1*, 447–472.
49. Private communication
50. G. Cook, V. Reshetnyak, R. F. Ziolo, S. A. Basun, P. P. Banerjee, D. R. Evans. Asymmetric Freedericksz transitions from symmetric liquid crystal cells doped with harvested ferroelectric nanoparticles. *Opt. Express* **2010**, *18*, 17339–17345.
51. M. Kaczmarek, O. Buchnev, and I. Nandhakumar. Ferroelectric nanoparticles in low refractive index liquid crystals for strong electro-optic response. *Appl. Phys. Lett.* **2008**, *92*, 103307/ 1–3.
52. O. Kurochkin, O. Buchnev, A. Iljin, S. K. Park, S. B. Kwon, O. Grabar, and Yu. Reznikov. A colloidofferroelectricnanoparticlesin a cholestericliquidcrystal. *J. Opt. A: Pure Appl. Opt.* **2009**, *11*, 024003/ 1–5.
53. O. Buchnev, A. Dyadyusha, M. Kaczmarek, V. Reshetnyak, Yu. Reznikov. Enhanced two-beam coupling in colloids of ferroelectric nanoparticles in liquid crystals. *J. Opt. Soc. Am. B* **2007**, *24*, 1512–1516.
54. H.-H. Liang, Y.-Z. Xiao, F.-J. Hsh, C.-C. Wu, and J.-Y. Lee. Enhancing the electro-optical properties of ferroelectric liquid crystals by doping ferroelectric nanoparticles. *Liq. Cryst.* **2010**, *37*, 255–261.
55. A. Mikułko, P. Arora, A. Glushchenko, A. Lapanik, and W. Haase. Complementary studies of $BaTiO_3$ nanoparticles suspended in a ferroelectric liquid-crystalline mixture. *Europhys. Lett.* **2009**, *87,27009/* 1–4.

CHAPTER 13

Fact or Fiction: Cybotactic Groups in the Nematic Phase of Bent Core Mesogens

BHARAT R. ACHARYA
Platypus Technologies, Madison, WI, USA

SATYENDRA KUMAR
Department of Physics, Kent State University, Kent, OH, USA

13.1 INTRODUCTION

A defect-free crystalline solid possesses long-range bond-orientational and positional- order and, therefore, has low symmetry. Lattices of crystalline solids are invariant under symmetry operations corresponding to a specific *space group* and the *basis* of the crystal [1]. Isotropic liquids, on the other hand, exhibit positional–order correlations that extend over a very short distance, typically only up to few nearest neighbors. As a consequence, the isotropic (I) liquid is invariant under any (translational, rotational, or other) symmetry operation (Figure 13.1a). Some materials with non-spherical building blocks (e.g., rods, discs, parallelepipeds, and bent rods) exhibit a number of intermediate phases between the crystalline solid and isotropic liquid. These are collectively known as liquid crystals (LCs). The anisotropic shape of their building blocks effectively leads to anisotropic interaction potentials and to the development of long-range orientational order. Depending on specific molecular organization and the nature of interactions, a variety of LC phases with different (short or long) range of bond-orientational or positional order along different spatial directions have been predicted and observed [2].

Among the various LC phases, the simplest is the nematic (N) phase in which the symmetry axis of the constituent entities, for example, long axes of cylindrical molecules, are on average aligned along a common direction, known as the director ($\vec{n}$), as shown in Figure 13.1b. The measure of orientational order, that is, the degree

Liquid Crystals Beyond Displays: Chemistry, Physics, and Applications, Edited by Quan Li.
© 2012 John Wiley & Sons, Inc. Published 2012 by John Wiley & Sons, Inc.

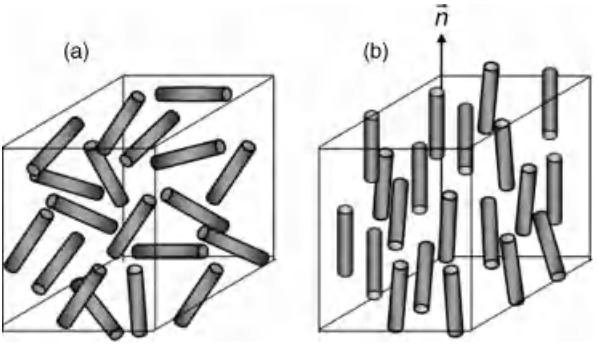

FIGURE 13.1 Molecular organization in the (a) isotropic and (b) nematic phases of rod like molecules.

to which molecules are parallel to each other, is given by the nematic order parameter $S = \frac{1}{2} < 3\cos^2\theta - 1 >$, where θ is the average angle that individual molecules make with $\vec{n}$ and the brackets represent ensemble average. The N phase does not possess any translational order and its existence requires anisotropic interactions between anisotropic objects. This is generally achieved by designing molecules with a rigid core (to provide anisotropic interaction) and flexible end-groups (to render the interactions weak enough to prevent crystallization). Based on these criteria, a number of LCs have been designed, synthesized, and are widely used in commercial applications. Most of the molecules that form the N phase are cylindrically symmetric and the resulting N phase possesses uniaxial symmetry. In this chapter, we describe properties of the uniaxial N phase followed by the recent advances in understanding the structural properties of the biaxial nematic phases of bent-core molecules.

13.2 NEMATIC PHASE OF ROD-LIKE MOLECULES

When a LC material is cooled from the I phase toward the N–I transition temperature (T_{NI}), small nematic volumes begin to spontaneously form and disappear as a consequence of nematic thermal fluctuations in the isotropic phase. In these correlated regions the nematic order parameter (OP), S, is non-zero and a fraction of the incident light energy is scattered due to miniscule turbidity in the proximity of the N phase. The orientation of local director of different clusters is uncorrelated and the cluster sizes are small. Within these clusters, the molecules exhibit *local* short-range orientational correlation that may extend up to 20–50 molecular dimensions [3]. Therefore, the isotropic phase optically appears dark between crossed polarizers. Typical time scale of the nematic OP fluctuations in the isotropic phase is in the range of *micro-* to *milli*-seconds [4].

At T_{NI}, the system enters the N phase via a weakly first order phase transition. The N phase is characterized with three (Bent, Splay, and Twist) deformations with corresponding elastic constants. At the temperatures of interest, the energy needed to spontaneously affect a long wavelength deformation can be lower than or comparable

to $\frac{1}{2}K_BT$. Consequently, the local director $\vec{n}(\mathbf{r})$ fluctuates with a relaxation time that depends on the values of relevant elastic and viscosity coefficients. In a bulk nematic LC, and in the absence of external boundary conditions, these domains are randomly distributed. As a consequence, measurements of any macroscopic physical parameters, such as refractive index and dielectric constant, in an unaligned nematic LC yield an average contribution from these randomly oriented domains. Therefore, a uniformly aligned mono-domain, needed for fundamental studies or applications that exploit anisotropic physical properties of NLC is generally achieved by subjecting these microscopic domains to external fields, such as surface anchoring, magnetic, or electric fields.

As the temperature of the N phase is lowered toward an underlying smectic phase, the effect of the underlying phases starts to emerge in the vicinity of the transition temperature in the form of small correlated volumes having the properties and order belonging to the more ordered smectic phase [5]. Depending on the underlying phase, these local correlations can be short-range SmA or SmC like. These pre-transitional correlated volumes once were believed to be characteristics of a new thermodynamically stable phase [6]. The SmA/SmC fluctuations, with the molecules arranged perpendicular/oblique to smectic layers, are referred to as SmA/SmC *cybotactic groups* and *skew–cybotactic groups*, respectively. Molecular organization in these cybotactic groups is shown in Figure 13.2. The nature of intermolecular interactions and distance from the transition temperature determine the size and time scale of pre-transitional smectic fluctuations in the nematic matrix.

In most cases, the smectic cybotactic groups are present within a few degrees from the transition temperature [7] whereas in other systems they may persist over almost the entire nematic range of as much as 100°C [8]. In both cases, these smectic pre-transitional fluctuations in the N phase grow in size as the transition to lower phase is approached. As a consequence, physical parameters related to their effective size also show strong temperature dependence. For example, if the underlying phase is the SmA phase, both longitudinal and transverse correlation lengths (i.e., parallel and perpendicular to $\vec{n}$) diverge with a power law at the transition [9], as depicted in

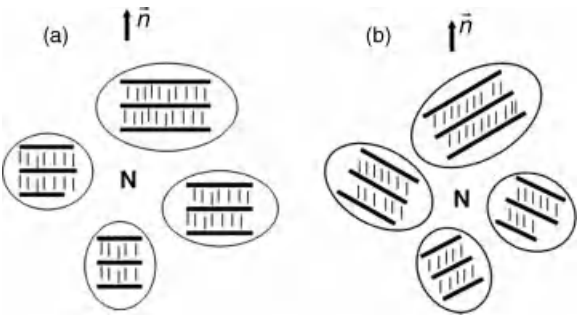

FIGURE 13.2 Cybotactic clusters in a nematic (N) matrix with (a) SmA-type and (b) SmC-type fluctuations. The LC molecules within the fluctuating smectic cluster are aligned parallel to the director, adapted from Ref. [5].

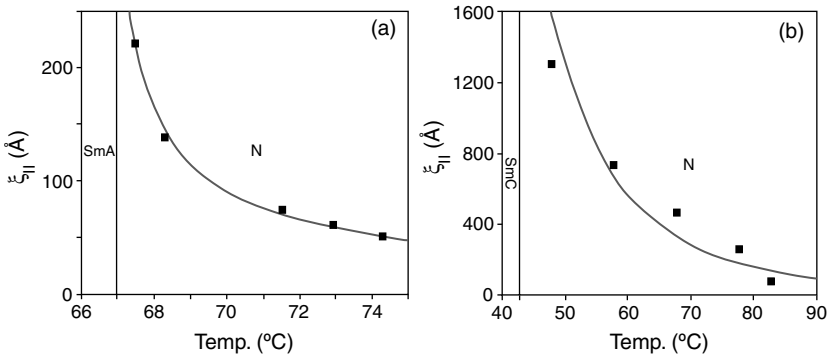

FIGURE 13.3 Variation of longitudinal correlation length with temperature in the N phase of LCs (a) 8OCB and (b) 6OO8 possessing underlying SmA and SmC phases, respectively. The correlation length in the nematic phase grows as the underlying SmA or SmC phase is approached. The correlation lengths for 6OO8 were replotted from the values in Ref. [35].

Figure 13.3a. The evolution of SmC type (i.e., skew) cybotactic groups is reflected in (a) the divergence of the two correlation lengths (Figure 13.3b), (b) an increase in tilt angle, and (c) a decrease in layer spacing with decreasing temperature [10]. As extensive X-ray results [9, 11, 12] accumulated over the past three decades show, the area and the number of layers in correlated volumes increase with decreasing temperature. Since the first use of the term "cybotactic groups" by de Vries [6] and its adoption by McMillan [7], it has been synonymous with pretransitional fluctuations. There was little use of this term over the past 25 years. However, it has recently been used to describe the X-ray diffraction patterns from the thermotropic biaxial N phase in bent-core mesogens. In this chapter, we examine recent uses of the term cybotactic groups against the above listed expectations and the validity of their reported sightings.

13.3 X-RAY SCATTERING

X-ray diffraction (XRD) is an ideal non-destructive tool for extracting the static and dynamical structural information about a system. XRD has been used to identify phases [2], quantitatively investigate critical phenomena [5, 11], and to obtain the structural information of solid and liquids [13]. For a system of N molecules, the total scattered intensity at any point in the $\vec{q}$-space is given by the average over all molecules and their relative orientations [11],

$$I(\vec{q}) = N\langle|f(\vec{q})|^2\rangle + \left\langle \sum_{j\neq k} f_j(\vec{q}) f_k^*(\vec{q}) \exp\left[i(\vec{r}_j - \vec{r}_k).\vec{q}\right) \right\rangle$$

where, $f_i(\vec{q}) = \int_V \rho_i(\vec{r}) \exp\,(\vec{q}.\vec{r}) d\vec{r}$ is the Fourier transform of the electron density $\rho_i(\vec{r})$ of ith atom in a molecule, $< >$ represents ensemble average, and $\vec{q}$ is the X-ray

momentum transfer vector. In general, the scattered intensity is expressed as a product of two terms: the form factor $F(\vec{q}) = \langle |f(\vec{q})|^2 \rangle$ that depends primarily on the molecular structure and conformation, and the structure factor $S(\vec{q})$ that includes both spatial and orientational correlations:

$$I(\vec{q}) = NF(\vec{q}) \times S(\vec{q})$$

The structural factor depends on the relative positions and orientation of two neighboring anisotropic molecules and is given by [9],

$$S(\vec{q}) = 1 + \frac{1}{NF(\vec{q})} \left\langle \sum_{j \neq k} f_j(\vec{q}) f_k^*(\vec{q}) \exp\left[i(\vec{r}_j - \vec{r}_k).\vec{q}\right) \right\rangle$$

In a system with infinitely narrow instrumental resolution function, the observed intensity in $\vec{q}$-space is given by $I(\vec{q}) = F(\vec{q}) \times S(\vec{q})$.

This formulism with appropriate approximations for the *form* and *structure* factors has been used to understand the structure of different phases. In the liquid phase of isotropic molecules, the correlations are mostly limited only to the nearest neighbors and $S(\vec{q})$ can be approximated by the Fourier transform of the pair correlation function. Therefore, the diffraction pattern exhibits a diffuse ring in the reciprocal space that corresponds to the length scale associated with average nearest neighbor separation [13]. In the I phase of anisotropic (e.g., rod like) molecules, there are two length scales (length and the width) associated with nearest neighbor correlations. Therefore, two diffused rings corresponding to the two length scales are observed. The ring at the small (large) angle corresponds to the length (width) of the molecules. For a uniformly aligned (i.e., monodomain) N phase, the diffraction pattern reflects its symmetry. Consequently, the two diffuse rings in the isotropic phase condense into two pairs of diffuse crescents, one at small angle along $\vec{n}$ and the other along the orthogonal direction (Figure 13.4).

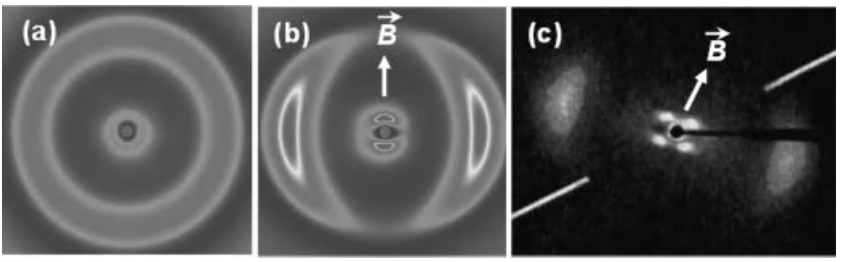

FIGURE 13.4 Two dimensional X-ray diffraction pattern from (a) isotropic and (b) nematic phases of 4-cyano-4′-pentylbiphenyl (5CB) and (c) cybotactic smectic C phase of nematic phase of bis-(4′-n-octyloxybenzal)-2-chlor1o,4-phenylenediamine. Vector $\vec{B}$ represents the direction of external magnetic field while the white line in (c) denotes the direction of the capillary axis. *Source*: Reprinted with permission from de Vries [8], Copyright 1970, Gordon Breach Science Publishers. (*See the color version of this figure in Color Plates section.*)

In the case of SmA cybotactic groups, the diffraction pattern is very similar to that of the ordinary N phase except that the inner diffuse peaks are sharper owing to stronger scattering from enhanced pre-transitional fluctuations. The "correlated volume" (or, cybotactic group size) diverges as temperature approaches the transition. Scattered intensity in these systems has been modeled using a Lorentzian-like structure factor combined with a slowly decaying function of q around $q = 0$. The form factor has been analytically calculated for the rod-like molecules to appropriately describe the observed intensity distribution [14]. The SmC fluctuations in the N phase give rise to four diffuse small angle peaks as a result of the degeneracy of smectic layer orientation with respect to $\vec{n}$ which is along the field direction (Figure 13.2b). Experiments performed in the N phase with or without an underlying SmC phase have established that the correlation lengths in these systems increase, the apparent tilt angle increases, and the layer spacing, d, decreases as the temperature is lowered [7–12].

13.4 NEMATIC PHASE OF BENT CORE MESOGENS

Since the pioneering work of Niori et al. [15], it has become clear that the LC phases exhibited by bent-core mesogens possess properties not observed in calamitic mesogens. They have emerged as a new sub-field of LC science [16]. In the I phase, the bent core molecules are randomly distributed while in N phase, their molecular biaxiality leads to two different possibilities. When the long axes of molecules are aligned parallel to the primary director $\vec{n}$, and the planes of the molecules are randomly distributed around $\vec{n}$, one obtains the well-known uniaxial N phase (Figure 13.5a). On the other hand, a biaxial N phase forms when the planes of the molecules are aligned parallel to the secondary director $\vec{m}$ (Figure 13.5b). XRD pattern from the I phase of bent-core LC consists of two diffuse rings corresponding to the effective length and width of molecules (Figure 13.6a). The XRD pattern from

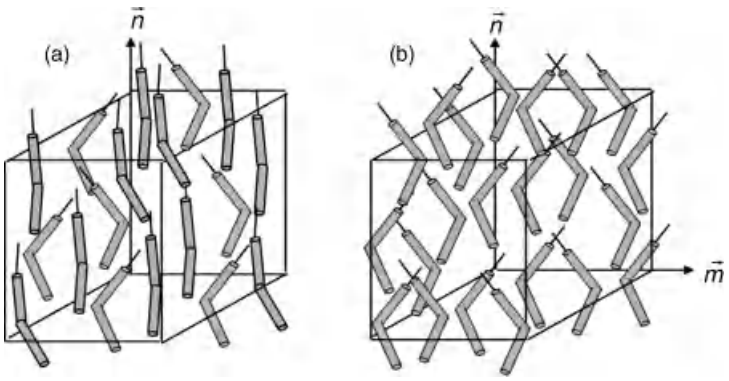

FIGURE 13.5 Molecular organization in (a) uniaxial and (b) biaxial nematic phase of bent-core molecules.

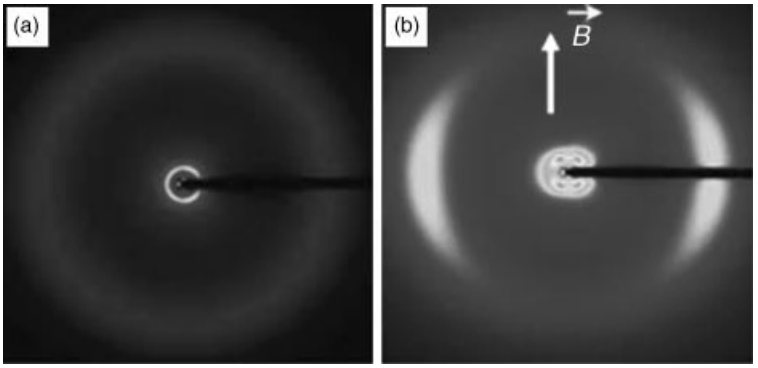

FIGURE 13.6 The 2D XRD from (a) isotropic and (b) the nematic phases of bent-core molecules. The diffraction at small angle in the N phase depends on the alignment of secondary director.

the nematic phase of these materials, however, depends on the ordering of the directors $\vec{n}$ and $\vec{m}$ (see below).

Among various bent-core molecules synthesized over the past decade, mesogens with rigid oxadiazole core exhibit a stable nematic phase [17]. The first attempt to investigate their structural properties in the nematic phase using XRD was carried out on three compounds (Figure 13.7) [18, 19]. An aligned nematic phase of these materials exhibited four small angle diffuse peaks very similar to that of SmC type cybotactic groups. However, the measured values of correlation lengths were comparable to molecular dimensions and independent of temperature over the entire N phase as has been independently confirmed by several research groups [20, 21]. Based on the very weak thermal dependence of correlation lengths, the possibility of pronounced pretransitional SmC fluctuations, i.e., the existence of large cybotactic groups can be categorically ruled out. Conventional approximations used in the analysis of X-ray diffraction patterns were not sufficient to fully describe the LC phases formed by these molecules. By sandwiching a thin film of LC between two rubbed polyimide-coated substrates and applying an external electric filed, the structure of the nematic phase in the two orthogonal directions in the plane perpendicular to $\vec{n}$, was also investigated. Two-dimensional XRD from the surface-aligned sample exhibited distinct patterns in the two orthogonal directions as shown in Figure 13.8 [18, 19].

To describe these XRD patterns, a simple model of the nematic phase was developed. Bent-core molecules were approximated by two rigid cylinders with a fixed angle between them, a widely accepted approximation [22, 23]. Both, the form and the structure factors were used to calculate the scattering intensity for an aligned mono-domain nematic phase [14]. The calculated X-ray intensity distribution exhibited distinct patterns in the two orthogonal directions in the plane perpendicular to $\vec{n}$, in *qualitative* agreement with the experimental observation. This led to the discovery of theoretically predicted biaxial nematic phase in a low-molar mass oxadiazole-based

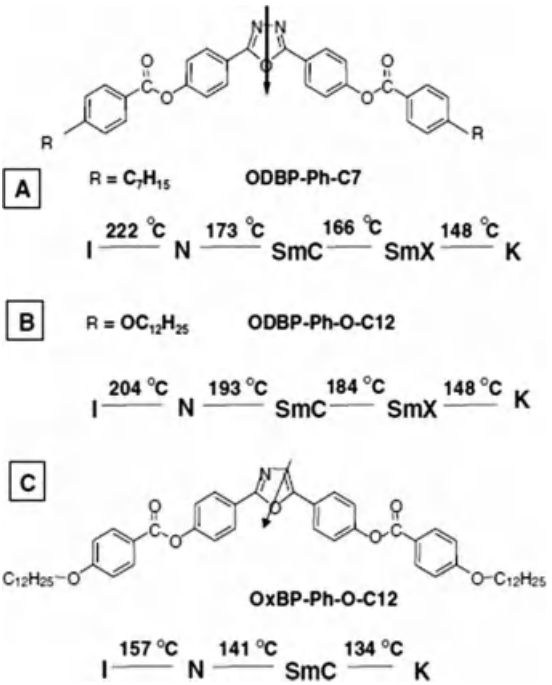

FIGURE 13.7 Molecular structures of oxadiazole-based compounds exhibiting four diffuse XRD peaks at small angle.

bent core thermotropic LC [18, 19, 24, 25]. *It should be noted that the claim of biaxial nematic phase was based on the observation of two distinct diffraction patterns in two orthogonal planes* (Figure 13.8) *and NOT just on mere existence of four diffuse peaks as has been erroneously stated* [27] *by some researchers.*

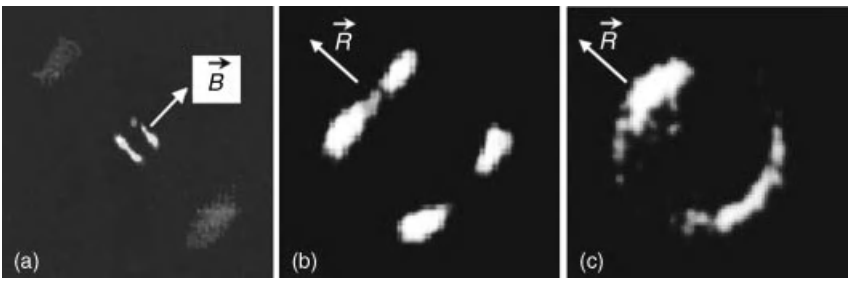

FIGURE 13.8 Two-dimensional XRD pattern from the nematic phase of (a) compound **A** at 195°C inside a capillary tube in the presence of magnetic field $\vec{B}$, (b) compound **B** between two beryllium plates coated with polyimide film and rubbed along $\vec{R}$, and (c) sample in (b) in the presence of external electric field perpendicular to the substrates. Panels (b) and (c) show only the small angle diffraction for clarity.

To incorporate orientational fluctuations of $\vec{n}$ and $\vec{m}$, Mayer-Saupe type temperature dependent distribution function was introduced. Based on the parameters (e.g., the temperature and the interaction potential) of the distribution function, the model can predict isotropic and both uniaxial and biaxial nematic phases. The model was used to interpret the XRD pattern observed in the N phase of azo-based bent core LCs and to predict the presence of uniaxial and biaxial nematic phases [14, 26]. According to this model, origin of the four diffuse peaks in XRD pattern is the geometrical structure (i.e., the form factor) of the bent-core molecule and not the presence of cybotactic clusters. The model predicts that the XRD pattern from the N phase of mesogens that maintain the bent structure in the statistical ensemble, consists of four diffuse peaks independently of the underlying phase. The uniaxial N phase has identical diffraction patterns while the biaxial nematic phase must exhibit distinct patterns in the two orthogonal directions perpendicular to $\vec{n}$.

Since the discovery of the biaxial N phase in oxadiazole-based bent-core LCs, different experimental techniques have been used to investigate these and other bent-core materials. Southern et al. [20] have studied, using XRD and polarized Raman scattering [PRS], biaxial order in oxadiazole-based bent core LC C_5–Ph–OC_{12} with asymmetric alkyl chains (Figure 13.9). XRD from the nematic phase of these molecules exhibited four diffused peaks similar to the symmetric compounds [18]. While no attempt was made to align the planes of the molecules with a second field to extract the information on the biaxiality using XRD, the PRS measurements supported the existence of both uniaxial and biaxial nematic phases.

One of the most important results of this study was the temperature independence of the end-to-end (or, longitudinal) correlation length that was found to be comparable to the molecular dimension over the entire nematic range of more than 50°C (Figure 13.10). Also, angular separation between two XRD peaks slowly increased and saturated at ~15°C below T_{NI}. These results, clearly demonstrate that the four diffuse peaks are not the result of SmC fluctuations but must arise from the changes in the bend angle of the core.

A group in Japan [16] conducted XRD study of a thiazole-based bent core LC with a 13°C wide N phase and an underlying SmC phase (Figure 13.11). Four diffuse peaks at small angles characterize the XRD patterns of this phase. They reported that

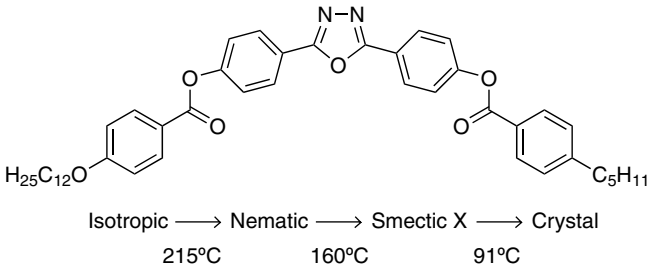

FIGURE 13.9 Molecular structure of compound C_5-Ph-OC_{12} and the transition temperatures. *Source*: Reprinted with permission from Southern et al. [20]. Copyright 2008 EPLA.

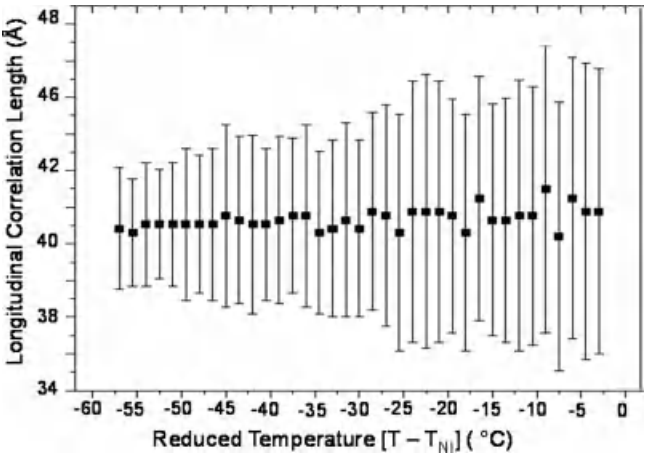

FIGURE 13.10 Temperature dependence of correlation length of C_5-ODBP-ph-OC_{12}. *Source*: Reprinted with permission from Southern et al. [20]. Copyright 2008 EPLA.

the *coherence length* increased at lower temperatures suggesting the presence of cybotactic groups.

Vaupotič et al. [27], investigated bent-core LCs based on 3,4-benzothiophene (BTP) and 1,3 dimethoxybenzene (DMB) (compounds **1** and **2** in Figure 13.12). Two-dimensional XRD patterns from the LC phase of the BTP molecule having asymmetric arms exhibited four diffused peaks at small angle in the N phase above the SmC phase. The mesogen with hexyl group attached to the central DMB core is the first known bent-core system to exhibit a stable N phase above the SmA phase. XRD

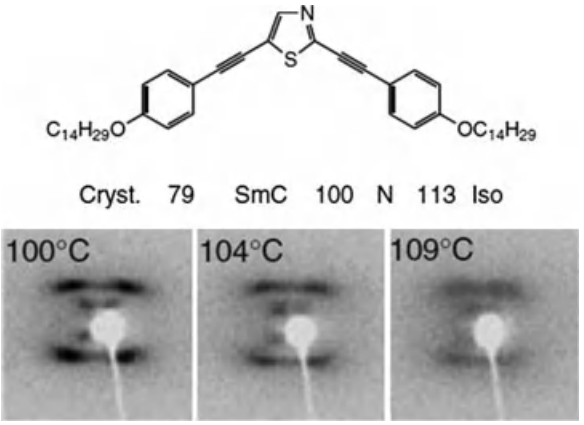

FIGURE 13.11 Molecular structure and X-ray diffraction patterns from molecules with long alkyl chains. *Source*: Reprinted with permission from Takazoe and Takanishi [16]. Copyright 2006, Japan Society of Applied Physics.

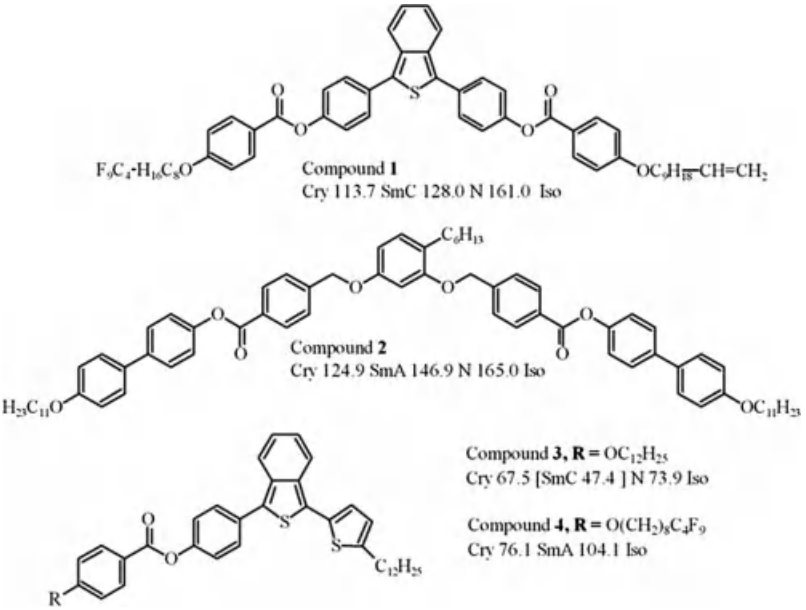

FIGURE 13.12 Bent-core molecules used to establish that the four diffuse XRD peaks arise from SmC type fluctuations. *Source*: Reprinted with permission from Vaupotič et al. [27]. Copyright 2009, The American Physical Society.

patterns of the DMB mesogen consist of two diffuse peaks at small angle. Similarly, a mixture of two bent-core molecules (compounds **3** and **4** in Figure 13.12), exhibiting the SmA and SmC phase, gave a stable N phase with underlying SmA phase and had only two small angle diffuse peaks. Based on these observations, the authors concluded that the four diffuse peaks at the small angle were due to pre-transitional SmC fluctuations (or, the skewed cybotactic groups) and not due to the architecture of bent-core molecules. The presence of an underlying SmC phase was considered a prerequisite for the formation of skew cybotactic groups. We believe this requirement to be *ad hoc* and can be true only for second order transitions. But the N to SmC phase transition is almost always found to be first order. A nematic phase may appear to be headed for a second order transition to the SmC phase at lower temperatures, but other more ordered phases can intervene and preempt the expected transition via a first order transition. In those systems, the SmC phase may not be observable. Thus, as the temperature is lowered and depending on the nature of molecules and intrinsic interactions, the pretransitional fluctuations may be of a different nature than of the lower temperature phase if the transition is first order. Whether a mesogen would show SmA-like or SmC-like pretransitional fluctuations in the N phase can, to some extent, be inferred from the behavior of its homologs. In fact, in early seventies when de Vries introduced the term "cybotactic" to describe the pretransitional fluctuations, one of the homologous series of rod-like molecules exhibited skewed cybotactic groups while the underlying phase was a crystalline solid [8]. Other homologs of the

same material actually showed SmC-like pretransitional phenomena in the N phase above the SmC phase. Recently, new bent core LCs with a stable N phase above the SmA phase exhibiting four diffuse peaks in XRD have been reported (see below).

A random distribution of the cybotactic groups around the director was used in this study to model the average structure factor to represent the observed scattered X-ray intensity [27]. Although the temperature dependence of the correlation length or the tilt angle was not measured, the correlation lengths at a temperature few degrees above the smectic transition temperature was found to be five molecular lengths/widths along the directions longitudinal/transverse to $\vec{n}$. On the basis of limited reported information, it is not possible to conclude whether the changes in their diffraction patterns arose from thermal evolution of the structure factor (i.e., cybotactic groups) or from the changes in the molecular form factor arising from changes in molecular conformation or the bend-angle.

In another experiment [28], structural investigations of asymmetric 3,5-bis-{4-[4-(nonyloxy)benzoyloxy]phenyl}-1,2,4-oxadiazoles (9BPO) were conducted under the influence of surface anchoring and an applied electric field. This LC material exhibits the SmC phase below the N phase (Figure 13.13). The two-dimensional X-ray diffraction pattern from magnetic field aligned sample in the N phase reveals four diffuse peaks at small angle. The longitudinal and transverse correlation lengths increase with decreasing temperature as expected for skewed cybotactic group (Figure 13.14). Response to an applied electric field and the observed ferroelectric behavior both suggest that these molecules form SmC type polar cybotactic clusters that are randomly distributed in an unaligned N phase. Application of external electric field aligns these clusters along the field direction. Molecular dynamics simulations based on Gay-Berne dipolar model, where the bent-core molecule was approximated by three ellipsoids, supported the observed field-switching behavior. Although this explanation appears convincing at a first glance, it raises several serious questions.

Firstly, the long dimension of these clusters (i.e., the longitudinal correlation length) is almost one molecular dimension under high magnetic field even close to the N – SmC transition! The transverse correlation length ranges from 2–4 molecular dimensions. If these polar cybotactic clusters do exist in this system, the correlated volumes is comprised of 4–16 molecules, a number very small for pretransitional fluctuations close to the N – SmC transition. Incidentally, if one assumes free rotation

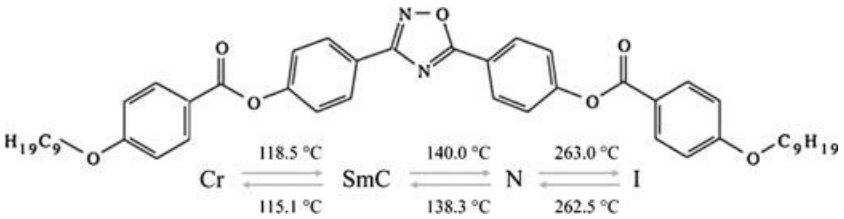

FIGURE 13.13 Chemical structure and phase sequence of oxadiazole based compound (9BPO) showing ferroelectric nematic phase. *Source*: Reprinted with permission from Francesangeli et al. [28]. Copyright 2009 WILEY-VCH Verlag GmbH & Co. KGaA, Weinheim.

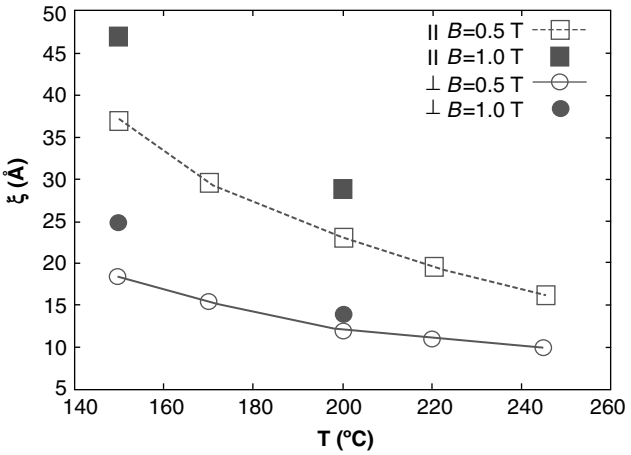

FIGURE 13.14 Correlations lengths of 9BPO at different magnetic field strengths as a function of temperature. Reprinted with permission from Francesangeli et al. [28], Copyright 2009 WILEY-VCH Verlag GmbH & Co. KGaA, Weinheim.

of the molecule about its long axis in the uniaxial N phase at 200°C, the transverse correlation length (∼10 Å) turns out to be the average molecular width calculated using the 46 Å length and 132° bend angle [29]. Under this assumption, the transverse correlation length remains approximately 1–2 molecular lengths, thus contradicting the presence of cybotactic groups.

Second, when a thin film of LC is filled between SiO_2 deposited glass substrates, the director aligns parallel to the deposition direction and four diffuse XRD peaks are observed [28]. However, in the presence of an electric field, molecular dipole moments (perpendicular to $\vec{n}$) of the clusters rotate to become parallel to the electric field. It is inconceivable that $\vec{n}$ of these clusters previously aligned parallel to the rubbing direction become randomly oriented in the presence of the electric field! Perhaps a stronger field (surface or magnetic) that does not couple with macroscopic polarization of the clusters will produce an aligned monodomain of ferroelectric biaxial nematic phase to resolve this ambiguity.

A systematic temperature dependent small angle XRD from magnetically aligned N phase of the diester of 2,5-bis-(*p*-hydroxyphenyl)-1,3,4-oxadiazole (ODBP-Ph-O-C_4H_9) (Figure 13.15), which has no underlying SmC phase, has recently been

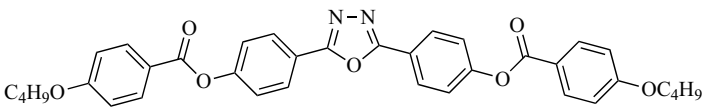

FIGURE 13.15 Structure of ODBP-ph-O-C_4-H_9, a homolog of ODBP-ph-OC_{12}. Source: Reprinted with permission from Francesangeli and Samulski [30]. Copyright 2010, The Royal Society of Chemistry.

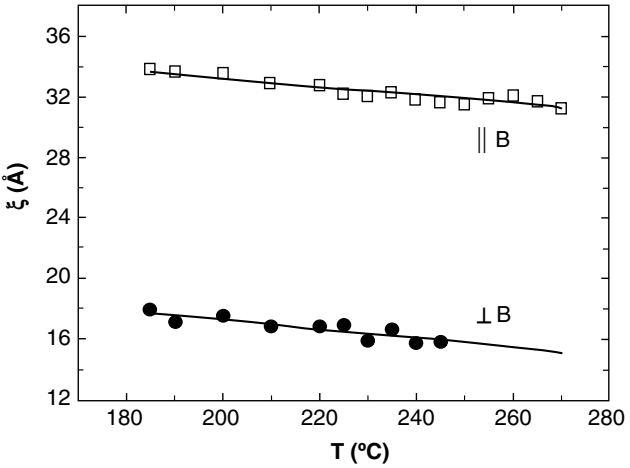

FIGURE 13.16 Measured correlation lengths in two orthogonal directions in ODBP-ph-O-C_4H_9. Reprinted with permission from Francesangeli and Samulski [30], Copyright 2010, The Royal Society of Chemistry.

performed [30]. The XRD pattern of this material consists of four diffuse peaks as reported by de Vries in a calamitic LCs [8] without an underlying SmC phase. This rules out the interpretation of the four diffuse XRD peaks as being indicative of the underlying pretransitional SmC cybotactic groups. XRD results from this material shows a "layer spacing" significantly lower than the actual molecular length (27.8 vs. 36 Å) leading to an estimated molecular tilt angle of 40.8°C at 210°C. Subsequently, a supramolecular structural model based on the SmC cybotactic clusters in a nematic host was proposed. X-ray scattering intensity profiles show very little peak sharpening with decreasing temperature. The calculated correlation lengths in two orthogonal directions are of the order of molecular dimensions and essentially independent of temperature over the entire nematic range (Figure 13.16). More importantly, the splitting of four small angle diffuse peaks is strongly temperature dependent. The origin of this change in splitting was attributed to the change in the tilt angle of the cybotactic groups. However, in the absence of any increase in SmC correlations (and thus the structure factor), the source of the splitting must be the changes in the form factor, very likely arising from changes in the bent-angle. Other investigations of such materials have shown a change in the bend angle as high as 27° [31, 32]. Again, if one assumes that molecules are free to rotate around their long axis as in the uniaxial N phase, the transverse correlation lengths corresponds to the diameter of the rotational volume of the molecule. Even with restricted rotation in cybotactic clusters, the number of molecules inside one correlated volume close to the transition remains ~10, inconsistent with the pretransitional cybotactic clusters which are known to diverge in size (Figure 13.3).

The N phase of ODBP-Ph-O-C_4H_9, between two substrates providing planar boundary conditions with provision to apply orthogonal electric and magnetic fields, has also been reported [30]. As observed earlier [18, 19] in the absence of external

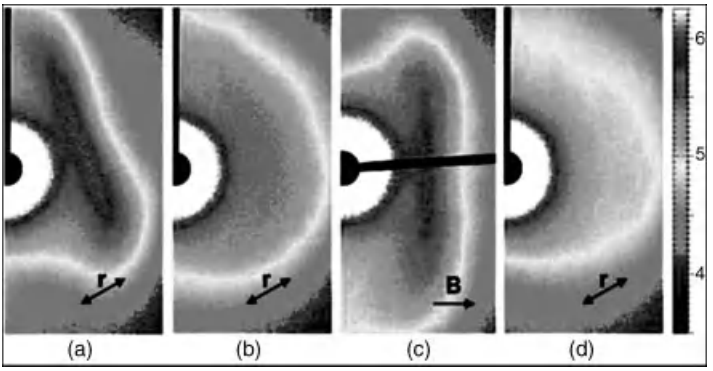

FIGURE 13.17 The 2D XRD patterns from nematic phase of ODBP-ph-O-C_4H_9 between two surfaces under different fields "r" represents the rubbing direction. (a) $E = 0$, $B = 0$: two peaks are evident from the two lobes seen in the outline of the reflection, (b) $E = 4$ V/μm, $B = 0$: the peaks nearly disappear as $\vec{n}$ becomes parallel to $\vec{E}$, (c) $E = 4$ V/μm, $B = 1$ T: lobes disappear as the two reflections become one and $\vec{n}$ orients ∥ to $\vec{B}$, $\vec{m}$∥ to $\vec{E}$, and (d) $E = 5$V/μm, $B = 1$ T: higher electric field reorients $\vec{n}$ parallel to the electric field and the small angle peak disappears. *Source*: Reprinted with permission from Francesangeli and Samulski [30]. Copyright 2010, The Royal Society of Chemistry.

fields, the XRD shows four diffuse peaks [two of which are shown in Figure 13.17 (a)]. When an external electric field is applied perpendicular to the cell, the diffraction pattern exhibits weak diffuse peaks approximately along the rubbing direction [Figure 13.17(b)]. With an in-plane magnetic field perpendicular to the electric field, the four small-angle diffuse peaks merge into two [Figure 13.17(c) shows one] with the maximum intensity along the magnetic field direction $\vec{B}$. These results suggest that $\vec{n}$ is aligned along $\vec{B}$ while $\vec{m}$ is oriented parallel to the electric field. These observations are qualitatively the same as earlier reported [18, 19] for the ODBP mesogens (Figure 13.8) to prove the nematic phase's biaxiality. These results, in particular, the correlation length remaining comparable to molecular dimensions over the entire nematic range and the change of four diffuse peaks into two upon application of two crossed fields strongly suggest that the origin of the four diffuse peaks in XRD patterns from these materials are not cybotactic clusters. Clearly, the four nematic peaks originate from the molecular structure of the mesogens per the model previously developed for ODBP [18, 19].

Structural investigations of ODBOP-ph-OC12 and ODBP-Ph-C7 also revealed [21] four diffuse peaks at small angle. Although the effect of crossed fields was not investigated, measured values of the correlation lengths confirmed that they remained comparable to molecular dimensions and were independent of temperatures. The tilt angle calculated from XRD shows a decrease of $\sim 5°$ and $7°$ for ODBOP-ph-OC_{12} and ODBP-Ph-C_7, respectively. The skewed cybotactic clusters were invoked to describe the observed four diffuse peaks. *Meta-cybotactic structure*, a more complex clustering than skewed cybotactic groups [33], was also suggested.

Based on results from different research groups on ODBP-based bent-core LCs, it can be concluded that (i) the nematic phase of these materials exhibits four diffuse peaks at small angle independently of the underlying phase, (ii) the separation between the peaks or the apparent tilt angle decreases with temperature, (iii) the "layer spacing" increases with temperature, and (iv) the positional order (or smectic) correlation lengths in these systems are of the order of molecular dimensions over the entire nematic temperature range. Under these conditions, thermal evolution of the tilt angle can only be explained by assuming some change in molecular bend angle and therefore the effective length of the molecules. These results provide strong evidence against the presence of the skewed cybotactic clusters as introduced by de Vries and McMillan, and subsequently adopted by de Gennes and others to describe the pretransitional fluctuations.

Keith et al. [34] have performed a systematic investigation of structural–property relationship in the N phase of a homologous series of bent-core molecules derived from 4-cyanoresorcinol with terminal alkyl chains of different lengths (Figure 13.18). Some of the homologs also have a smectic phase at lower temperatures. All members of the series exhibit four XRD diffuse peaks at small angles. The results also show that molecular organization in their N phase depends strongly on the length of the alkyl chains. For the two shortest ($m = n = 2$ and 4) homologs, the splitting between small-angle XRD peaks decreases with increasing temperature. In contrast, for all other homologs, the splitting increases and the layer spacing decreases with increasing temperature, a drastically different result from the ODBP-based bent core molecules. The layer spacing increases as a function of the number of alkyl chains but it is always smaller than the calculated molecular length (Figure 13.19(c)). Structural properties of the nematic phase of these materials reveal a transformation from a nematic phase having only the nearest neighbor correlations (for short chain molecules) as in ordinary nematics to large cybotactic clusters (for long chain molecules). LC materials with medium sized clusters (e.g., $n = 9$) have strong temperature dependent cluster sizes and therefore exhibit temperature dependent structural transformation. For shorter chain mesogens, the four diffuse peaks clearly arise from the molecular form factor (i.e., changes in the bend-angle) while for the longer chain LCs, the changes in the four diffuse peaks may originate from changes in tilt angle within the cybotactic clusters. It is expected that the bend-angle in all cases would change with temperature. However, clustering may overshadow it for larger

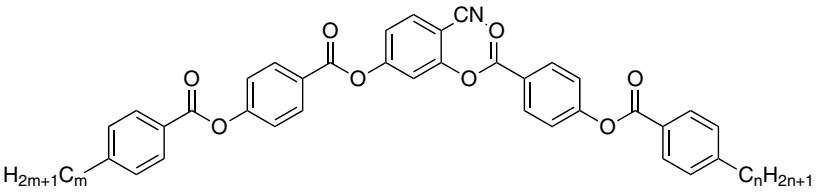

FIGURE 13.18 Molecular structure of cyanoresorcinol-based bent core molecules. The values of m and n was varied from 2 to 14. *Source*: Reprinted with permission from Keith et al. [34]. Copyright 2010, The Royal Society of Chemistry.

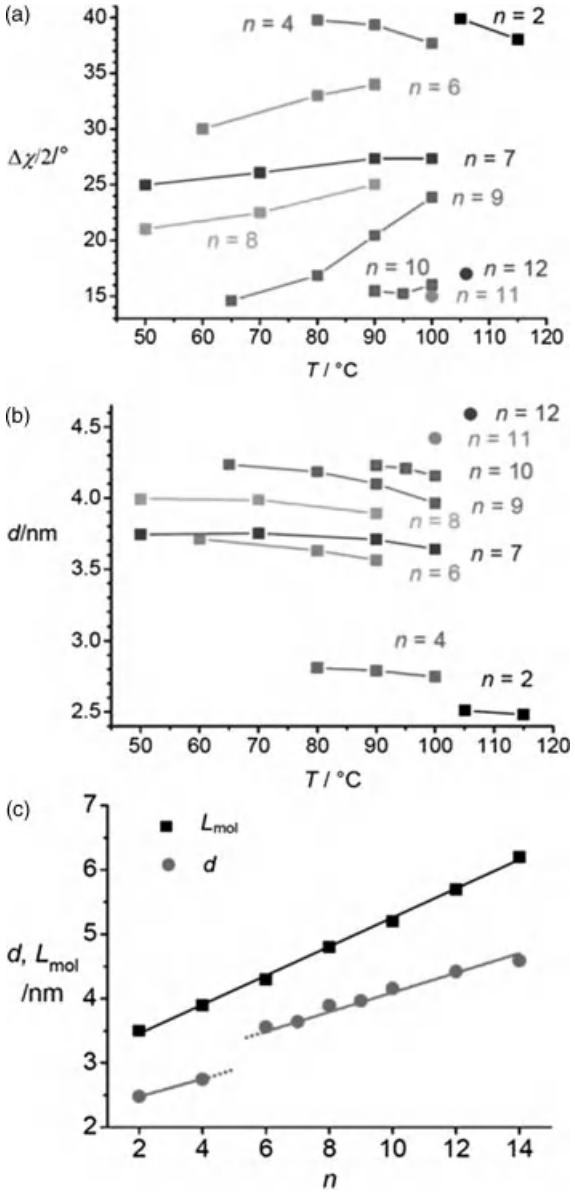

FIGURE 13.19 Temperature and chain length dependence of structural parameters of cyanoresorcinol based bent-core masogens. $\Delta\chi$ is the angular separation between diffuse peaks, d is the layer spacing and L_{mol} is molecular length. *Source*: Reprinted with permission from Keith et al. [34]. Copyright 2010, The Royal Society of Chemistry.

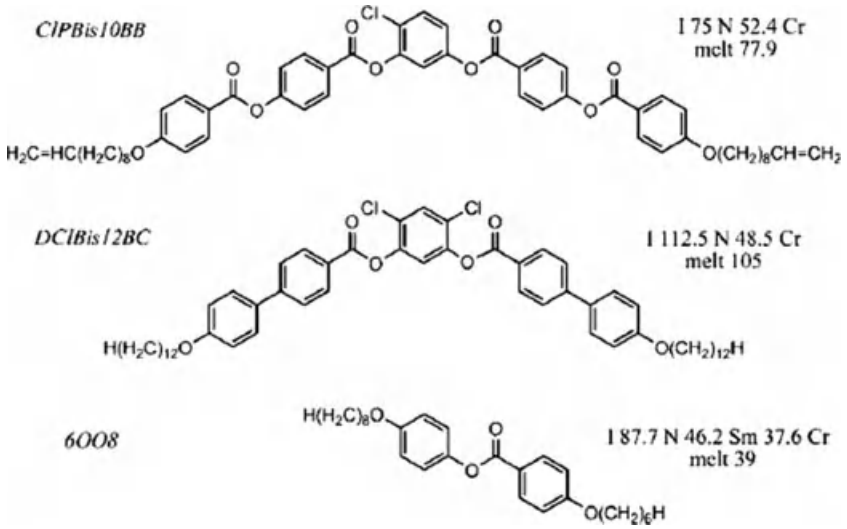

FIGURE 13.20 Molecular structure and the transition temperatures of bent core molecules exhibiting unusual viscoelastic properties. 6OO8, a LC material exhibiting SmC phase below N phase, was studied for comparison. *Source*: Reprinted with permission from Hong et al. [35]. Copyright 2010, The Royal Society of Chemistry.

molecules. For medium chain lengths, the changes in the four diffuse peaks can arise from changes in both the bend-angle (molecular geometry) and the molecular tilt angle within cybotactic clusters. Therefore, the organization of molecules in the N phase of bent core molecules is governed by detailed molecular structures, intermolecular interactions, geometrical factors, and clustering.

A different class of bent core molecules such as 4-chloro-1,3-phenylene bis-4-[40-(9-decenyloxy)benzoyloxy]benzoate (ClPbis10BB) and 4,6-dichloro-1,3-phenylene bis-4-[40(dodecyloxy)) biphenyl] carboxylate (DClPbis12BC) [35] is based on chlorophenylene at the center that defines the bend angle (Figure 13.20). These molecules are particularly attractive because they do not have any underlying smectic phase and, more importantly, they exhibit an unusually large flexoelectric effect [36] and flow viscosities [37]. XRD patterns of these compounds show two small angle arcs close to T_{NI} that gradually transforms into four diffuse peaks in a manner similar to the other bent core systems. Quite interestingly, the length scales (i.e., layer spacing) are significantly smaller than the molecular lengths (32 Å vs. 45 Å). The observed XRD patterns are described on the basis of the existence of short-range SmC type correlations. Assuming that local director of these clusters follows Mayer-Saupe type distribution function, the experimentally observed diffraction patterns at small angle have been qualitatively reproduced. The longitudinal and transverse correlation lengths were found to be a few molecular dimensions and insensitive to temperature (Figure 13.21). For comparison, the correlation lengths for 6OO8, a molecule with structure similar to one of the arms of ClPbis10BB, is also plotted in

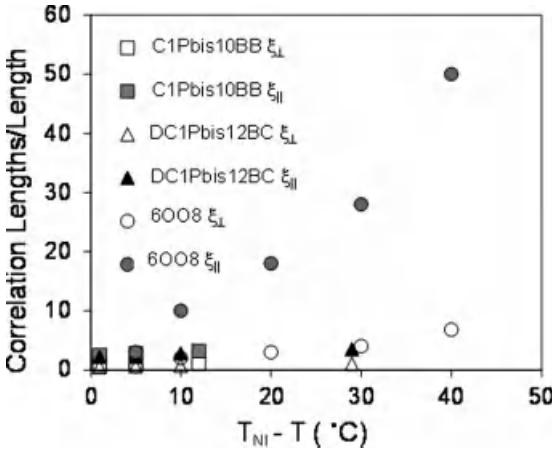

FIGURE 13.21 Temperature dependence of transverse and longitudinal correlation lengths (normalized with respective length of molecules) for ClPbis10BB, DClPbis12BC and 6OO8. The correlated lengths are plotted using the data from Table 1 in Ref. [35].

Figure 13.21. Compound 6OO8 has the SmC phase below the N phase and is known to exhibit pretransitional fluctuations. The results clearly show that the correlation lengths (normalized with respect to the length of the molecules) are almost independent of temperatures for both bent core molecules while they are strongly temperature dependent for 6OO8. This clearly indicates that de Vries skewed cybotactic cluster model introduced to describe the pretransitional phenomena does not describe the four XRD diffuse peaks in this system. However, intermolecular correlations do exist in the N phase which extends up to several molecular dimensions in both directions. Supramolecular structures that involve a few molecules with smectic like correlations are most likely responsible for the observed XRD pattern in these systems.

13.5 SUMMARY

We have reviewed several reports on different forms of cybotactic clustering in the nematic phase of bent core molecules published since the discovery of the biaxial nematic phase [17, 18]. We have attempted to interpret results with the same criteria applied to all and commented on the validity of the interpretation of experimental results. It is made clear that the molecular organization/association in these systems is rather complex in the N phase. Depending on the specific molecular architecture, flexibility, and intermolecular interactions, the nematic phase of bent core molecules may behave like an ordinary nematic or as a nematic with self-organized nanoscopic clusters. While the XRD pattern in the first case can be explained by simple geometrical considerations, the interpretations of the second case requires the formation of supramolecular structures that might be responsible for unusual

properties, such as ferroelectricity, giant flexoelectric effect, and anomalous visco-elastic coefficient. In either case, the correlation lengths appear to be independent of temperature for a number of bent core molecules. This suggests that the terminology "cybotactic groups" that has conventinoally been used to represent pretransitional phenomena, to describe statistical clustering of a few molecules which persist even into the isotropic phase appears to be misleading. This work was supported by Basic Energy Sciences, Office of Science, the US Department of Energy grant # DE-SC0001412. The authors thanks Dr. D. M. Agra-Kooijman for her sharing correlation length data.

REFERENCES

1. C. Kittel. *Introduction to Solid State Physics*, 8th ed., John Wiley & Sons, 2005.
2. S. Kumar, Ed. *Liquid Crystals: Experimental Study of Physical Properties and Phase Transitions*, Cambridge University Press, 2001.
3. G. W. Stewart. X-ray diffraction intensity of the two liquid phases of para-azoxyanisol. *J. Chem. Phys.* **1936**, *4*, 231–236.
4. T. W. Stintson and J.D. Litster. Temperature dependence of normal modes in a nematic liquid crystals. *Phys. Rev. Lett.* **1970**, *25*, 503–506.
5. P. G. de Gennes. *The Physics of Liquid Crystals*, Oxford University Press, 1974.
6. A. de Vries. Evidence for the existence of more than one type of nematic phase. *Mol. Cryst. Liq. Crys.* **1970**, *10*, 31–37.
7. W. McMillan. Measurement of smectic-A-phase order-parameter fluctuations in the nematic pahse of *p*-n-Octyloxybenzylidene-p′-toluidine. *Phys. Rev. A* **1973**, *7*, 1673–1678.
8. A. de Vries. X-ray photographic studies of liquid crystals I: a cybotactic nematic phase. *Mol. Cryst. Liq. Cryst.* **1970**, *10*, 219–236.
9. A. Primak, M. Fisch, and S. Kumar. Critical behavior at the nematic-to-smectic-*A* transition in a strong magnetic field. *Phys. Rev. Lett.* **2002**, *88*, 035701–1-4.
10. A. de Vries. X-ray diffraction studies of structure of skewed cybotactic nematic pahse: A review of the literature. *J. Mol. Liq.* **1986**, *31*, 193–202.
11. J. Als-Nielsen, R. J. Birgeneau, M. Kaplan, J. D. Litster, and C. R. Safinya. High-resolution x-ray study of a second-order nematic-smectic-*A* phase transition. *Phys. Rev. Lett.* **1977**, *39*, 352–355.
12. J. Als-Nielsen, J. D. Litster, R. J. Birgeneau, M. Kaplan, C. R. Safinya, A. Lindegaard-Andersen, and S. Mathiesen. Observation of algebraic decay of positional order in a smectic liquid crystal. *Phys. Rev. B* **1980**, *22*, 312–320.
13. P. M. Chaikin and T. C. Lubensky. *Principles of Condensed Matter Physics*, Cambridge University Press, Cambridge, 1997.
14. B. R. Acharya, S. W. Kang, V. Prasad, and S. Kumar. Role of molecular structure on x-ray diffraction in uniaxial and biaxial phases of thermotropic liquid crystals. *J. Phys. Chem. B* **2009**, *113*, 3845–3852.
15. T. Niori, T. Sekine, J. Watanabe, T. Furukawa, H. Takezoe. Distinct ferroelectric smectic liquid crystals consisting of banana shaped achiral molecules. *J. Mater. Chem.* **1996**, *6*, 123–1233.

16. H. Takazoe and Y. Takanishi. Distinct ferroelectric smectic liquid crystals consisting of banana shaped achiral molecules. *Jpn. J. Appl. Phys.* **2006**, *45*, 597–625.
17. T. J. Dingemans and E. T. Samulski. Distinct ferroelectric smectic liquid crystals consisting of banana shaped achiral molecules. *Liq. Cryst.* **2000**, *27*, 131–136.
18. B. R. Acharya, A. Primak, T. J. Dingemans, E. T. Samulski, and S. Kumar. The elusive thermotropic biaxial nematic phase in rigid bent-core molecules. *Pramana* **2003**, *61*, 231–237.
19. B. R. Acharya, A. Primak, and S. Kumar. Biaxial nematic phase in bent-core thermotropic mesogens. *Phys. Rev. Lett.* **2004**, *92*, 145506-1-4.
20. C. D. Southern, P. D. Brimicomb, S. D. Siemianowski, S. Jaradat, N. Roberts, V. Gortz, J. W. Goodby, and H. F. Gleeson. Thermotropic biaxial nematic order parameters and phase transitions deduced by Raman scattering. *EPL* **2008**, *82*, 56001-1-6.
21. O. Francesangeli, F. Vita, C. Ferrero, T. Dingemans, and E. T. Samulski. Cybotaxis dominates the nematic phase of bent-core mesogens: a small-angle diffuse X-ray diffraction study. *Soft Matter* **2011**, *7*, 895–901.
22. D. R. Link, G. Natale, R. Shao, J. E. Maclennan, N. A. Clark, E. Korblova, and D. M. Walba. Spontaneous formation of macroscopic chiral domains in a fluid smectic phase of achiral molecules. *Science* **1997**, *88*, 1924–1927.
23. M. A. Bates. Influence of flexibility on the biaxial nematic phase of bent core liquid crystals: A Monte Carlo simulation study. *Phys. Rev. E* **2006**, *74*, 061702-1-11.
24. L. A. Madsen, T. J. Dingemans, M. Nakata, and E. T. Samulski. Thermotropic biaxial nematic liquid crystals. *Phys. Rev. Lett.* **2004**, *92*, 145505-1-4.
25. J. Palaez and M. R. Wilson. Atomistic simulations of a thermotropic biaxial liquid crystal. *Phys. Rev. Lett.* **2006**, *97*, 267801-1-4.
26. V. Prasad, S. W. Kang, K. A. Suresh, L. Joshi, Q. B. Wang, and S. Kumar. Thermotropic uniaxial and biaxial nematic and smectic phases in bent-core mesogens. *J. Am. Chem. Soc.* **2005**, *127*, 17224–17227.
27. N. Vaupotič, J. Szydlowska, M. Salamonczyk, A. Kovarova, J. Svoboda, M. Osipov, D. Pociecha, and E. Gorecka. Structure studies of the nematic phase formed by bent-core molecules. *Phys. Rev. E* **2009**, *80*, 030701(R)-1-4.
28. O. Francesangeli, V. Stanic, S. I. Torgova, A. Strigazzi, N. Scaramuzza, C. Ferrero, I. P. Dolbnya, T. M. Weiss, R. Berardi, L. Muccioli, S. Orlandi, and C. Zannoni. Ferroelectric response and induced biaxiality in the nematic phase of a bent-core mesogen. *Adv. Funct. Mat.* **2009**, *19*, 2592–2600.
29. S. I. Torgova, T. A. Geivandova, O. Francesangeli, and A. Strigazzi. Banana-shaped 1,2, 4-oxadiazoles. *Pramana* **2003**, *61*, 239–248.
30. O. Francesangeli and E. T. Samulski. Insights into the cybotactic nematic phase of bent-core molecules. *Soft Matter* **2010**, *6*, 2413.
31. R. Y. Dong and A Marini. Conformational study of a bent-core liquid lrystal: C-13 NMR and DFT computation approach. *J. Phys. Chem. B* **2009**, *113*, 14062–14072.
32. A. Eremin, H. Nadasi, G. Pelzl, S. Diele, H. Kresse, W. Weissflog, and S. Grande. Paraelectric–antiferroelectric transitions in the bent-core liquid-crystalline materials. *Phys. Chem. Chem. Phys.* **2004**, *6*, 1290–1298.
33. E. T. Samulski. Meta-cybotaxis and nematic biaxiality. *Liq. Cryst.* **2010**, *37*, 669–678.
34. C. Keith, A. Lehmann, U. Baumeister, M. Prehm, and C. Tschierske. Nematic phases of bent-core mesogens. *Soft Matter* **2010**, *6*, 1704–1721.

35. S. H. Hong, R. Verduzco, J. C. Williams, R. J. Twieg, E. DiMasi, R. Pindak, A. Jakli, J. T. Gleeson, and S. Sprunt. Short-range smectic order in bent-core nematic liquid crystals. *Soft Matter* **2010**, *6*, 4819–4827.
36. J. Harden, B. Mbanga, N. Éber, K. Fodor-Csorba, S. Sprunt, J. T. Gleeson, and A. Jákli. Giant flexoelectricity of bent-core nematic liquid crystals. *Phys. Rev. Lett.* **2006**, *97*, 157802-1-4.
37. S. Stojadinovic, A. Adorjan, and S. Sprunt. Giant flexoelectricity of bent-core nematic liquid crystals. *Phys. Rev. E* **2002**, *66*, 060701-1-4 (R).

CHAPTER 14

Lyotropic Chromonic Liquid Crystals: Emerging Applications

HEUNG-SHIK PARK and OLEG D. LAVRENTOVICH
Liquid Crystal Institute, Kent State University, Kent, OH, USA

14.1 INTRODUCTION

Over the last 10 years since the early work of Attwood, Lydon, Tiddy, and co-workers [1–3] there has been a growing interest in a distinct family of lyotropic liquid crystals (LCs), the so-called lyotropic chromonic liquid crystals (LCLCs). LCLCs represent a broad but not well-understood class of soft matter in which the reversible self-assembled aggregates formed by non-amphiphilic molecules show liquid crystalline phases [4–7]. The range of materials which forms chromonic LC phases includes drugs [2, 3, 8–10], dyes [11–14], and DNA nucleotides, such as guanosine derivatives [15, 16]. The name "chromonic" was suggested by Lydon to carry connotations of dyes and chromosomes and of the bis-chromone structure of disodium cromoglycate (DSCG), also known as an anti-asthmatic drug cromolyn or INTAL, one of the first studied LCLCs [3, 5].

The LCLC molecules have a plank-like or disk-like polyaromatic central core with polar groups at the periphery. The geometry of the basic structural unit in LCLCs is different from spherical or cylindrical micelles and bilayers formed by amphiphilic molecules in the conventional lyotropic LCs. In water, the chromonic molecules typically stack on top of each other face-to-face (the so-called H-aggregation) to minimize the areas of unfavorable contact with water and leaving the ionic solubilizing groups at the aggregate–water interface. This structure has been proven by X-ray diffraction studies and polarized UV–vis spectroscopic measurements for many LCLCs [10, 14, 17–21]. The typical separation between the adjacent molecules along the stacking direction in H-aggregates is about 0.33–0.34 nm as measured by X-ray diffraction [10, 14, 19]. This value of the stacking distance does not depend on the chromonic concentration and the phase of solution, and represents a basic feature

Liquid Crystals Beyond Displays: Chemistry, Physics, and Applications, Edited by Quan Li.
© 2012 John Wiley & Sons, Inc. Published 2012 by John Wiley & Sons, Inc.

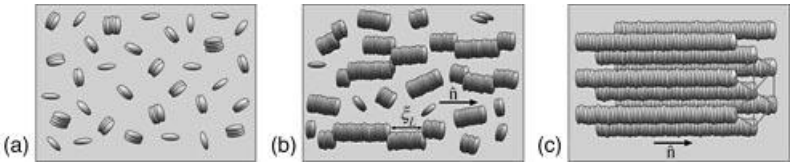

FIGURE 14.1 Schematic illustration of LCLC aggregates in (a) I phase, (b) N phase, and (c) C phase.

of the chromonic aggregates. When the polar groups are fully ionized, the line density of electric charge along the aggregate can be very high, for example, $\sim 6e$/nm (e is the electron's charge) for the LCLC molecules with two ionic groups. The stacking distance and the line charge make LCLC aggregates similar to the double-strand B-DNA molecules. The important difference is that in LCLCs, there are no chemical bonds to fix the length of aggregates.

The underlying mechanism of aggregate self-assembly in LCLCs is analogous to the process resulting in worm-like micelles formed by surfactant molecules in solutions and the so-called "living" polymerization. The aggregate would grow indefinitely if it were not for the entropy that decreases when the number of aggregates decreases. The balance of the "end" energy E of an aggregate (also called the scission energy, that is, the energy needed to cut an aggregate into two), and the entropy gained by producing more "ends", results in the prediction of the broadly polydisperse system with an average aggregation number:

$$\langle n \rangle \propto \sqrt{\phi} \exp \frac{E}{2k_B T} \tag{14.1}$$

determined by the volume fraction ϕ of the solute and strongly dependent on E and the absolute temperature T, for example, Refs [22, 23]. As the concentration of a chromonic material increases, the aggregates multiply, elongate, and align parallel to the common direction, called the director $\hat{\mathbf{n}}$. The two most commonly met phases are the uniaxial nematic (N) phase and the hexagonal columnar (C) phase, Figure 14.1. In earlier publications, one often finds the term "M phase", where "M" stands for "middle." We use the term "C phase" instead of "M phase" whenever the presence of a hexagonal columnar phase with aggregates forming a hexagonal lattice in the plane perpendicular to $\hat{\mathbf{n}}$, is established [19, 24].

The aggregates' length depends not only on the concentration, but also on the specific details of molecular interactions, temperature [4, 25], ionic content [8, 19, 26–29], pH of the solution [19], and type of the side groups [4, 30]. The LCLCs, thus, represent an interesting self-assembled system with an orientational and positional order that is highly sensitive to a number of factors.

The recognition of LCLCs as a fascinating and distinct class of lyotropic LCs was not widespread just a few years ago. As one of the pioneers in this field, Lydon [5] wrote, "A single large-scale commercial application of chromonics will of course change this picture overnight . . . the continuing discovery of unique properties and

versatility of these systems promises much." Recently, there have been several studies demonstrating the potential of chromonics for applications in functional materials and devices, such as optical polarizers [31, 32], optically anisotropic films [12, 33–35], biosensor [36, 37], micro-patterned films [38], nano-fabrication materials [39, 40], and organic electronics [41]. In this review, we focus on the recent studies of LCLCs and their potential applications.

14.2 STRUCTURES AND PHASE PROPERTIES OF LCLCs

Even in the dilute isotropic (I) solutions, chromonic molecules have a strong tendency to stack into aggregates. The balance of energy gained by placing a chromonic molecule inside the aggregate and the entropy term promoting a larger number of aggregates produces a polydisperse system of linear aggregates [22, 23] that can arrange themselves into ordered LC phases as a function of concentration and temperature. The techniques commonly used to determine the phase behavior of LCLCs include polarizing optical microscopy, X-ray diffractometry, and NMR spectroscopy. Other techniques, such as dynamic light scattering, small-angle neutron scattering, transmission electron microscopy, and rheological measurement have also been used to characterize the aggregates of LCLCs.

14.2.1 Food Dye Sunset Yellow as LCLCs

Several previous studies demonstrated the aggregate structures and phase behavior of sunset yellow (SSY), one of the most typical LCLCs. SSY is a food coloring azo dye, having the chemical name disodium salt of 6-hydroxy-5-[(4-sulfophenyl)azo]-2-naphthalenesulfonic acid, Figure 14.2(a)–(b). SSY contains central aromatic groups, phenyl and naphthyl rings linked via an azo group with two solubilizing sulfonate groups attached to either end of the molecule. The liquid crystalline properties of SSY have been studied by Ormerod [42], Luoma [43], and recently by Horowitz et al. [14], Park et al. [19, 29], Edwards et al. [20], and Chami and Wilson [44]. Compared with other LCLCs, the aggregate structure of SSY has been somewhat better established. Most significantly, it has been shown that the stacks of SSY in water contain only one molecule in cross section and the SSY molecules are on average perpendicular to the aggregate axis [14, 19, 20, 44]. The average diameter d_{SSY} of the aggregate, according to Edwards et al. [20], is about 1 nm, while Luoma [43] found $d_{SSY} = 1.4$ nm.

The phase diagram of SSY [19] shows the I, N, and C phases with broad coexistence regions, Figure 14.2(c). The N phase produces Schlieren textures with disclinations (characterized by two dark brushes of extinction) and point defects-boojums (with four brushes of extinction), Figure 14.2. The columnar phase shows characteristic "developable" domains [45].

14.2.1.1 X-ray Diffraction Measurement of SSY Water Solutions X-ray diffraction measurement is an important technique not only for the phase

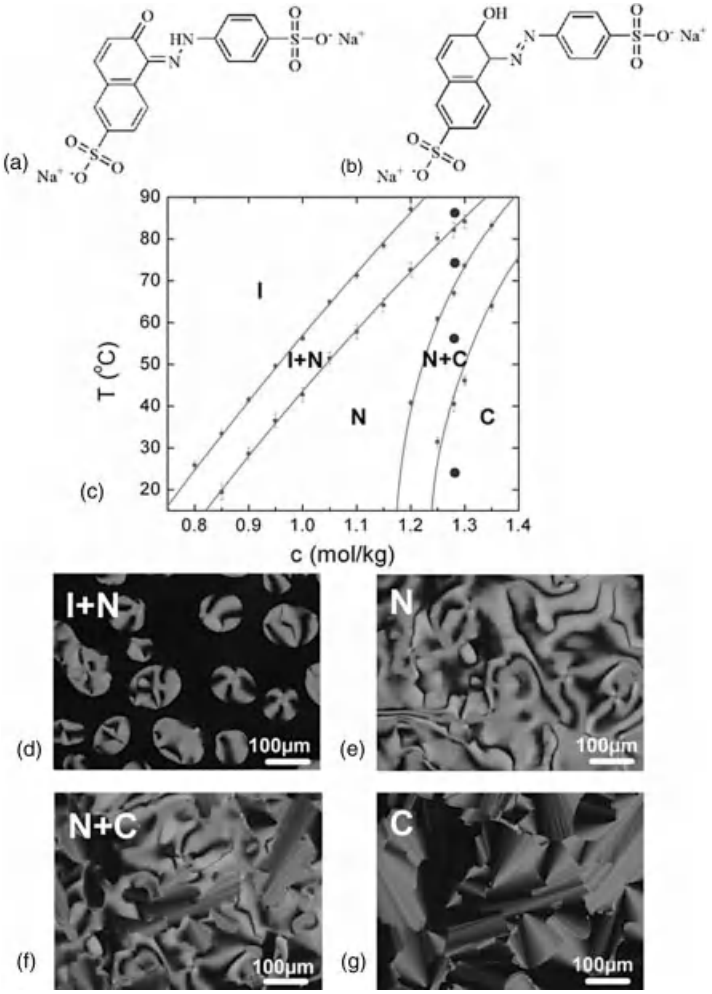

FIGURE 14.2 The molecular structure of two forms of SSY, (a) NH hydrazone tautomer: prevailing form in aqueous solution [19, 20] and (b) OH azo tautomer. Phase diagram (c) and polarizing micrographs (d)–(g) of SSY water solutions. The error bars represent the difference between the data taken on heating (upper end of the bar) and cooling (lower end of the bar). The filled circles at the vertical line indicate the temperatures at which the pictures (d)–(g) were taken.

identification but also for the characterization of LCLC aggregates. Several previous studies used X-ray measurements to characterize SSY aggregate structures [14, 19, 24]. Figure 14.3 shows the typical X-ray diffraction patterns of the I phase of 0.7 mol/kg, N phase of 0.9 mol/kg, and C phase of 1.36 mol/kg SSY solutions [19]. In the I phase of SSY solution, $c_{SSY} = 0.7$ mol/kg, the aggregates have no orientational order, Figure 14.3(a). Since SSY molecules possess positive

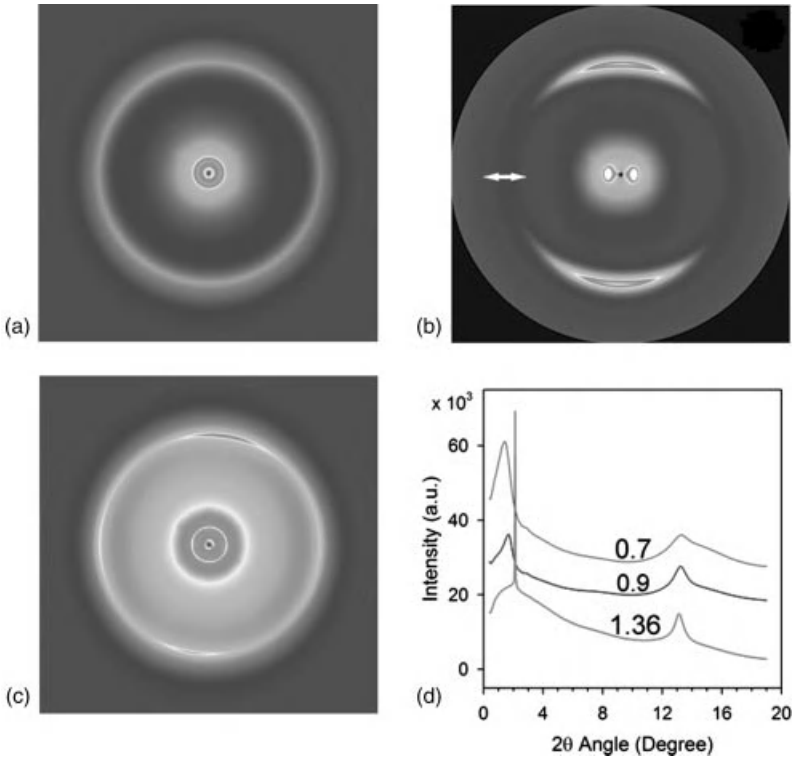

FIGURE 14.3 Typical X-ray patterns (a)–(c) of SSY water solutions at different concentrations SSY c: (a) I phase, SSY $c = 0.7$ mol/kg; (b) N phase, SSY $c = 0.9$ mol/kg; (c) C phase, SSY $c = 1.36$ mol/kg. The arrow in (b) represents the direction of the magnetic field; (d) diffractographs of SSY water solutions at different concentrations SSY c : 0.7 mol/kg (green), 0.9 mol/kg (blue), and 1.36 mol/kg (red). (Redrawn from Park et al. [19].)

anisotropic magnetic susceptibility, they orient parallel to the direction of the magnetic field. Consequently, the director $\hat{\mathbf{n}}$, the common direction of aggregates, aligns perpendicularly to the magnetic field. The walls of circular capillaries containing the sample for X-ray studies assist in a uniform alignment of $\hat{\mathbf{n}}$ along the axis of the capillary, so that the magnetic field is typically directed perpendicularly to the sample. The diffraction pattern of the aligned N phase has two pairs of arcs in orthogonal directions, Figure 14.3(b). This feature supports the model of H-aggregation [46], with the molecules stacked on top of each other, being on average perpendicular to $\hat{\mathbf{n}}$. One pair of arcs in the vertical direction at the large angle ($2\theta = 13.2°$) ascribed to the stacking distance ($a_z = 0.33$ nm) along $\hat{\mathbf{n}}$ remains the same in the I and C phases, indicating that the space between chromonic molecules within an aggregate is not altered by the concentration of SSY. Another pair of arcs in the horizontal direction is from the small angle diffraction, related to the average distance between the SSY aggregates.

TABLE 14.1 X-ray diffraction data for four different concentrations of SSY in water, expressed in molal c_{SSY} (mol/kg) and volume fraction ϕ_{SSY} units. The temperature is fixed at 28.4°C

c_{SSY}	ϕ_{SSY}	d (nm)	D (nm)	$\xi_{D,SSY}$ (nm)	$\xi_{L,SSY}$ (nm)	Phase
0.7	0.184	3.11	–	4.42	2.4	I
0.9	0.225	2.63	–	5.56	3.5	N
1.14	0.269	2.34	–	8.56	4.8	N
1.36	0.305	2.07	2.39	104.72	13.4	C

$D = 2d_1/\sqrt{3}$ in the C phase. $\xi_{D,SSY}$ was calculated from the FWHM of a small angle peak at $2\theta = 1.45 \sim 2.12°$. $\xi_{L,SSY}$ was calculated from the FWHM of a large angle peak at $2\theta = 13.2°$.

One can determine the correlation length $\xi_{L,SSY}$ corresponding to the stacking repeat distance, that is, inversely proportional to the full width at half maximum (FWHM) of the scattering wave vector peak. One finds that $\xi_{L,SSY}$ increases with the concentration of SSY [19, 24]. However, $\xi_{L,SSY}$ is much smaller than the true (average) length $\langle L \rangle$ of aggregates. For example, the correlation length for 0.9 mol/kg N phase SSY is $\xi_{L,SSY} = 3.5$ nm [19]. This quantity is much smaller than the minimum length L_{min} of aggregates capable to form an N phase in the Onsager model of identical thin rods, $L_{min} \approx 4d_{SSY}/\phi_{SSY} \approx 20$ nm [47]. Park et al. [19] have suggested that the chromonic aggregates may possess defects and branches, in which case the X-ray coherence can be lost but a physical connection remains, Figure 14.1(b). Recent measurement by Renshaw and Day [48] of the diffusion coefficients by NMR spectroscopy also demonstrated that the length of SSY aggregates is larger than the correlation length measured by X-ray diffraction.

The X-ray of a $c_{SSY} = 1.36$ mol/kg C phase at small angle $2\theta = 2.1°$ shows a strong sharp diffraction line and three faint, but sharp diffraction lines d_2, d_3, d_4 whose diffraction spacings are in the ratio of $1 : 1/\sqrt{3} : 1/\sqrt{4} : 1/\sqrt{7}$, characteristic of the hexagonal structure, Figure 14.3(c) [10, 17]. The inter-aggregate axis-to-axis distance D can be directly related to these diffraction lines, $D = 2d/\sqrt{3}$, Table 14.1. The correlation length $\xi_{D,SSY}$, associated with the positional order transverse to the aggregate axes determined from the FWHM of the peak at $2\theta = 2.1°$ is much larger than the corresponding value in the N phase, Table 14.1.

14.2.2 Anti-Asthmatic Drug DSCG as LCLCs

Disodium cromoglycate (DSCG) is widely known as an antiasthmatic drug. It is one of the most extensively studied LCLC materials. However, the details about the aggregate structure of DSCG are still the subject of discussion. Hartshorne and Woodard [10] assumed that there is one molecule in the cross-section of the cylindrical aggregate of DSCG. They estimated the cylinder diameter to be about 1.6 nm. Later, Lydon [3, 5] proposed that the aggregate is shaped like a hollow square

cylinder with four molecules in cross-section, linked by electrostatic salt bridges. Recently, Dickinson et al. [21] calculated from X-ray scattering experiments that there are two DSCG molecules in the cross-section of the aggregate. They comprehensively analyzed both past and recent X-ray and absorption data concerning the different chromonic LCs and concluded that the aggregate structures of many chromonic systems are very simple, consisting of one or two molecules in a cross-section of aggregate. If the charged groups of the chromonics are located on opposite sides of the molecules, then the aggregates have one molecule in their cross-section. But if the charged groups are on the same side of the molecules, then two molecules can be arranged in the cross-section of the aggregate with the charged groups far away from each other [21].

Most of the structural data on LCLCs formed by DSCG indicate that the DSCG molecules are arranged into H-stacks, with the molecules being on average perpendicular to the aggregate long axis, to the director and thus to the optic axis. Recently, Wu et al. [49] suggested an alternative thread-like model of side-by-side stacking for DSCG and similar solutions. However, a direct verification of molecular orientation in the dry films of DSCG by soft X-ray microscopy [50, 51] and in fully hydrated bulk LCLC samples by measurements of optical birefringence [51] and behavior in the magnetic field [52] show that the molecular cores are on average perpendicular to the director and the optic axis, which is consistent with the H-type "face-to-face" molecular stacking.

Figure 14.4 shows the phase diagram of pure DSCG water solution [53]. At room temperature (23°C), as the concentration of DSCG increases, the aqueous solution of DSCG shows the I phase at $c_{\mathrm{DSCG}} < 0.22$ mol/kg (10 wt.%) followed by a biphasic state of coexisting N and I phases, N phase, coexisting N and C phases, and a homogeneous C phase at $c_{\mathrm{DSCG}} > 0.52$ mol/kg (21 wt.%). We note that highly concentrated DSCG solutions show a phase transition sequence with increasing temperature that is different from the case of SSY solutions. For example, 0.62 mol/kg of DSCG, being in the homogeneous C phase at room temperature, transforms into the N + C biphasic state, then the I + N biphasic state, and then the I + C biphasic state as the temperature increases, Figure 14.4. In SSY, the phase diagram is much simpler and the homogeneous C phase transforms into less ordered N + C, N, and I + N states upon heating, Figure 14.2.

14.2.2.1 X-Ray Diffraction Measurement of DSCG Water Solutions

The X-ray diffraction patterns of a DSCG solution are similar to those from SSY solution. The X-ray diffraction pattern for a $c_{\mathrm{DSCG}} = 0.344$ mol/kg (15 wt.%) N sample in the magnetic field directed horizontally shows two pairs of arcs, Figure 14.5(a) [53]. One pair of arcs centered along the vertical axis corresponds to the stacking repeat distance ($a_z = 0.34$ nm) between the DSCG molecules in the aggregate. Another pair of arcs centered along the horizontal axis is related to the average distance between the DSCG aggregates. The X-ray diffraction patterns of the C phase of DSCG is similar to the C phase of SSY, showing a strong sharp diffraction line at the small angle $2\theta \approx 1.1 \sim 1.5°$ and three faint diffraction lines,

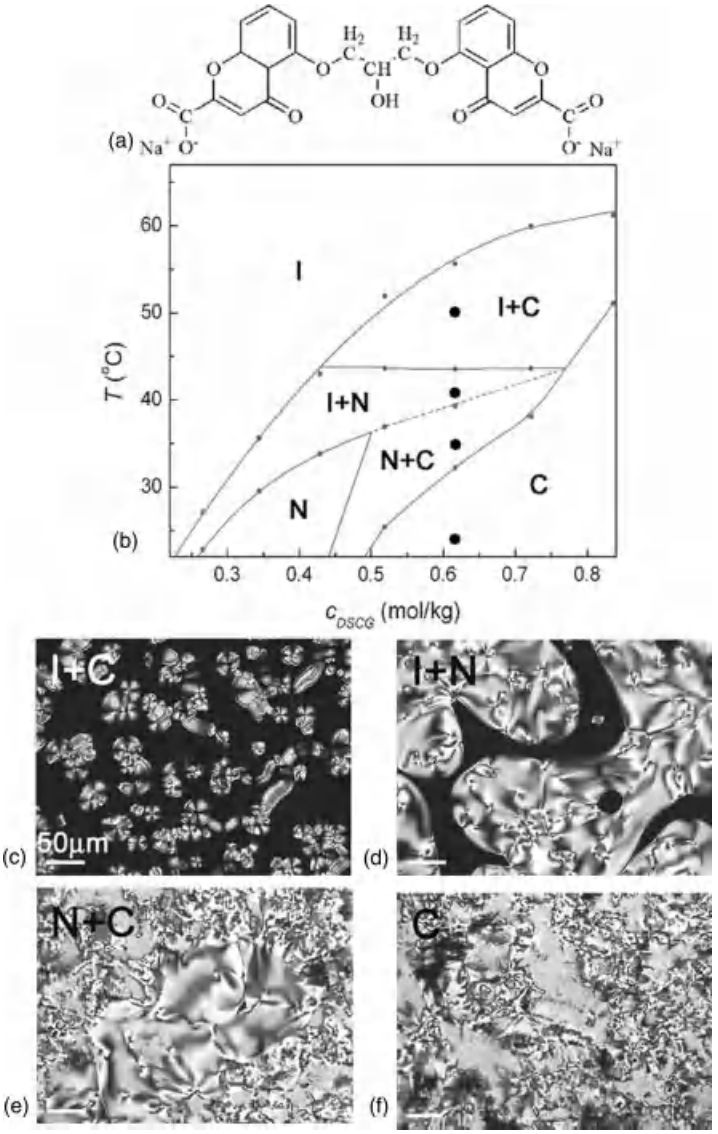

FIGURE 14.4 The molecular structure of DSCG (a). Phase diagram (b) and polarizing micrographs (c)–(f) of DSCG water solutions; I + C biphasic state (c), I + N biphasic state (d), N + C biphasic state (e), and C phase (f). The filled circles at the vertical line indicate the temperatures at which the pictures were taken.

which arise from the long-range hexagonal packing of the columns in the plane perpendicular to $\hat{\mathbf{n}}$. The inter-aggregate axis-to-axis distance D decreases as c_{DSCG} increases, Table 14.2. The stacking distance $a_z = 0.34$ nm is not changed, but $\xi_{\mathrm{L,DSCG}}$ is larger than that in the N phase, Table 14.2.

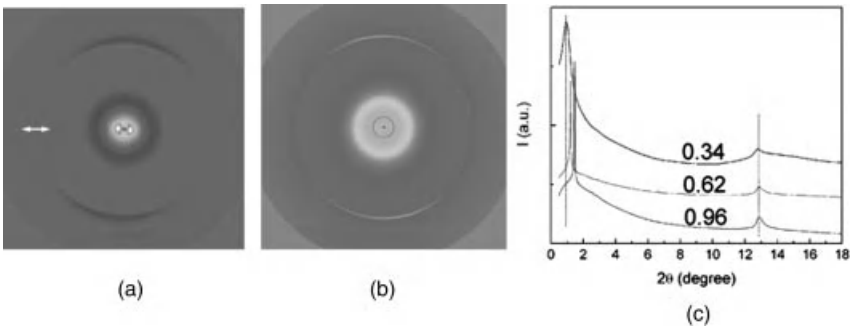

FIGURE 14.5 X-ray patterns of DSCG water solutions; (a) N phase, DSCG $c = 0.34$ mol/kg; (b) C phase, DSCG $c = 0.96$ mol/kg. The arrow in (a) represents the direction of the magnetic field. (c) Diffractographs of DSCG water solutions at different concentrations of DSCG: 0.34 mol/kg, 0.62 mol/kg, and 0.96 mol/kg. All data are taken at 28.4°C. (Reprinted with permission from Park [53].)

14.2.3 Effects of Molecular Structure on Phase Diagrams of LCLCs

The molecular structure–property relationships of LCLCs present an interesting question, but they are not clearly understood because most of the studies of LCLCs have been performed on a few available materials. Recently, Tam-Chang and coworkers synthesized several derivatives of rylenebis(dicarboximide) dye and described the effect of the structures of the counterions, side chains, and core ring systems on the LC properties of these compounds, Figure 14.6 [13, 30, 54]. They demonstrated that replacing the side-chain, $CH_2CH_2NH(CH_3)_2$, in a perylenebis(dicarboximide), dye (a) in Figure 14.6, with a bulky alkyl chain, $CH_2CMe_2CH_2NH(CH_3)_2$, dye (b) in Figure 14.6, destabilizes the N phase by lowering the transition temperatures $T_{N \to N+I}$ and $T_{N+I \to I}$ [13, 30]. They also showed that replacing the chloride ions by tosylate ions, dye (c) in Figure 14.6, formed the I + C biphase at high concentration instead of homogeneous N or C

TABLE 14.2 X-ray diffraction data for four different concentrations of DSCG in water, expressed in molal c_{DSCG} (mol/kg) and volume fraction ϕ_{DSCG} units. The temperature is fixed at 28.4°C

c_{DSCG}	ϕ_{DSCG}	d (nm)	D (nm)	$\xi_{D,DSCG}$ (nm)	$\xi_{L,DSCG}$ (nm)	Phase
0.103	0.033	3.99	–	–	1.5	I
0.344	0.102	4.68	–	–	5.2	N
0.616	0.169	3.63	4.19	69.8	11.2	C
0.961	0.241	3.01	3.48	74.8	12.1	C

$D = 2d_1/\sqrt{3}$ in the C phase. $\xi_{D,DSCG}$ was calculated from the FWHM of a small angle peak at $2\theta = 0.95 \sim 1.46°$. $\xi_{L,DSCG}$ was calculated from the FWHM of a large angle peak at $2\theta = 12.8°$.

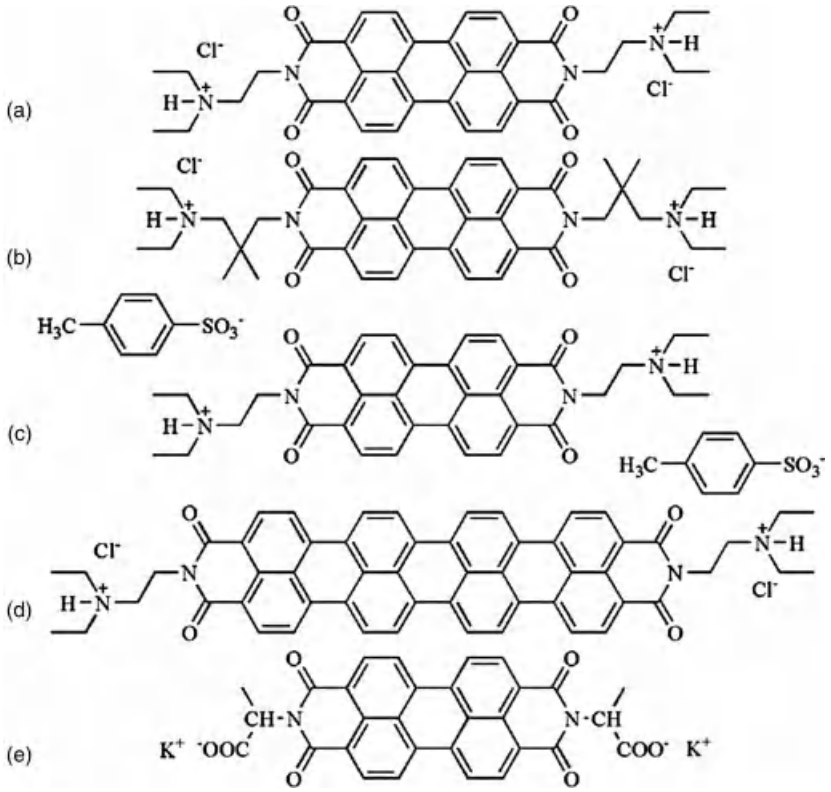

FIGURE 14.6 (a)–(e) Molecularly designed rylenebis(dicarboximide) dyes prepared by Tam-Chang et al. [13, 30, 54].

phases [30]. The effect of the aromatic ring structures was investigated by comparing the properties of perylenebis(dicarboximide), dye (a) in Figure 14.6 and quaterrylenebis(dicarboximide), dye (d) in Figure 14.6 [13, 30]. Dye (d) in Figure 14.6 was only soluble in acidic solutions, such as HCOOH or H_2SO_4 aqueous solution, but not in water. The maximum of absorption peak, λ_{max}, of dye (d) in Figure 14.6, is red-shift by ~300 nm compared to λ_{max} of dye (a) in Figure 14.6, as a result of a more extended molecular core.

The introduction of a chiral center in a side-chain results in a cholesteric phase, as evidenced by the characteristic fingerprint texture associated with a helical twist of the director, dye (e) in Figure 14.6 [54]. A cholesteric phase can also be attained by adding an amino acid with a chiral center such as alanine and glucose, to the N phase LCLCs [9]. Figure 14.7 shows a micrograph of cholesteric phase formed in 14 wt.% DSCG solution doped with 10 wt.% L-alanine.

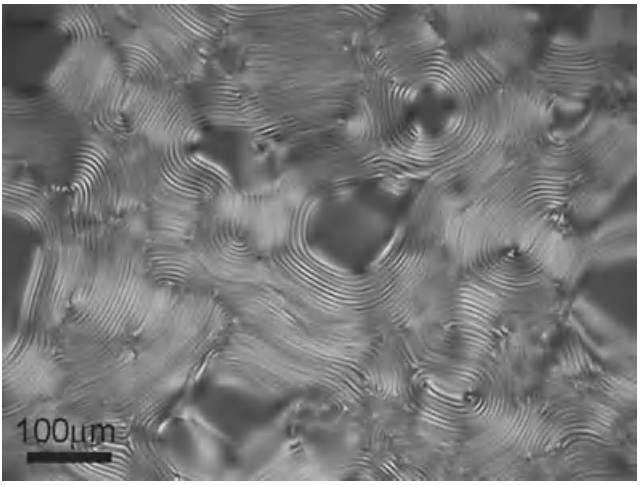

FIGURE 14.7 Polarizing micrograph of cholesteric phase formed in 14 wt.% DSCG solution doped with 10 wt.% L-alanine. The texture shows fingerprint regions with helical axis in the plane of the cell.

14.2.4 Effect of Additives on Phase Diagrams of LCLCs

Aggregation and the subsequent self-assembly of LCLC molecules into the N and C phases depend on a number of factors. (a) The intra-aggregate interactions responsible for the monomer stacking and reversible aggregation are determined mainly by non-covalent attractive forces such as π–π interaction and repulsive electrostatic forces between the ionized groups, such as sulfonate and carboxylate. The extent of ionization of these groups depends on the pH of the solution. (b) The inter-aggregate interactions are mainly controlled by the excluded volume effects, as in the Onsager model of nematic order [47]; electrostatic forces, usually of a repulsive nature; and repulsive hydration forces (i.e., forces derived from the work needed to dehydrate the hydrophilic lateral surfaces of the aggregates [55, 56]). Several previous studies have demonstrated how the phases of LCLCs are affected by additives, either charged, such as salts [8, 19, 26–29], or non-charged, such as neutral polymers [29, 51, 57, 58].

14.2.4.1 Ionic Additive Effect on LCLCs Exploration of the electrostatic effects started with the observation made by Yu and Saupe [8] that the addition of a salt NaCl to DSCG solution, increases the temperature $T_{N \to N+I}$ at which the homogeneous N phase transforms into the biphasic N–I coexistence region, as well as the temperature $T_{N+I \to N}$ of the complete melting. Kostko et al. [26] supported this conclusion of the salt-induced increasing of $T_{N \to N+I}$ and $T_{N+I \to I}$ for the case of salts with small cations, Na^+, K^+, but also found an opposite effect of destabilization of the N phase by salts with large organic cations, such as tetraethylammonium bromide and tetrabutylammonium bromide. A study by Prasad

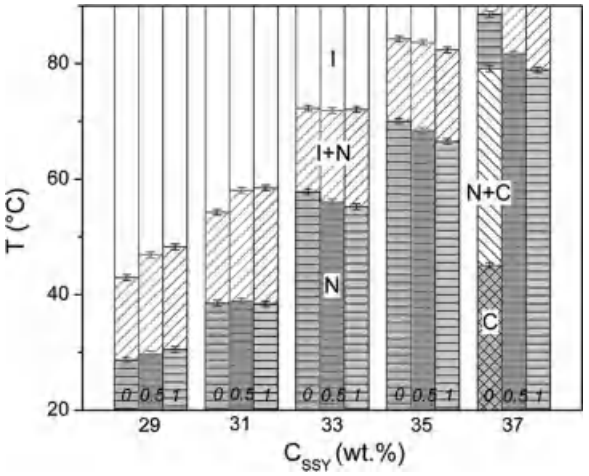

FIGURE 14.8 Phase behavior of SSY solution in the presence of NaCl, 0; 0.5; and 1 mol/kg. The transition temperatures were determined upon cooling [29].

et al. [27] showed that NaCl increases the viscosity of SSY solution, but did not find any change in the transition temperatures.

Recently, Park et al. [29] explained a strong effect of a monovalent salt NaCl on phase diagrams that is different for high and low concentrations of SSY, Figure 14.8. The salt promotes the orientational order at low concentrations of SSY and suppresses it at high concentrations; the later behavior is in agreement with the earlier studies of the Tiddy and co-workers [28]. Moreover, in highly concentrated SSY solutions, the salt is capable of melting the positionally ordered C phase into the positionally disordered N phase. Park et al. [29] suggested that these experimental findings are caused by the salt-induced screening of electrostatic repulsion among the charged SSY molecules within and between the aggregates. The screening leads to (1) increase of the scission energy and elongation of aggregates and (2) decrease of their persistence length. The two tendencies (1) and (2) have an opposite effect on the ordered phases, as (1) promotes the stability of the N and C orders, while (2) suppresses both orientational and positional orders.

14.2.4.2 Nonionic Additive Effect on LCLCs Recently, several studies showed that the effects of the neutral non-adsorbing polymer on LCLCs. Simon et al. [57] demonstrated that some water-soluble polymers added to isotropic DSCG solutions cause the formation of birefringent droplets. Tortora et al. [51, 58] showed that polyethylene glycol (PEG) can condense DSCG solutions into orientationally and positionally ordered domains of various morphologies, such as tactoids of the N phase, and toroids of the C phase. In the condensed region, the LCLC director was shown to be tangential to the I–N and I–C interfaces.

In the classic picture, the excluded volume effects are considered for colloidal dispersions of particles with a fixed shape, say, rigid rods of constant length and

diameter. In this picture, an added depletion agent, such as neutral spheres, forces the rods to pack more closely, as the spheres, and rods cannot penetrate each other. The volume available for both species is maximized when these two are spatially separated [59, 60]. One of the most efficient depletion agents is the neutral non-adsorbing polymer PEG. In water, a PEG molecule behaves as a random coil that can be approximated by a sphere of a certain radius of gyration r_g. PEG-induced "depletion attraction" has been observed for a variety of systems, including the solutions of DNA [61–64].

Park et al. [29] demonstrated that PEG added to the isotropic or nematic solutions of SSY causes a strong condensing effect on SSY, triggering phase separation and condensation of the LC phases, either of the N type or the C type, Figure 14.9. The role of PEG is primarily in condensing the SSY into more densely packed regions with a higher concentration of SSY in which the system can acquire an orientational order (forming the N phase from the original I phase) or even a positional order (forming the C phase). Since the main structural unit of LCLC is a self-assembled aggregate rather than an individual molecule, the excluded volume effects are expected to occur at two different levels: for dilute system with short aggregates, the effect is mostly in the increase of the aggregate length, while for the longer aggregates in more concentrated solutions, the effect is in a denser lateral packing with an ensuing orientational and positional order, Figure 14.10. PEG also decreases the inter-aggregate separation in the condensed regions [29].

14.2.4.3 pH Effect on LCLCs The ionic groups of chromonic molecules, such as sulfonate and carboxylate groups, play an important role in water solubility as they are easily ionized in the broad range of pH. For example, at the neutral pH, SSY in water is negatively charged with the molecular charge $\sim 2e$, caused by the ionization of two sulfonate groups. However, at a high pH, SSY molecules increase their negative charge as a result of the additional ionization of either OH or NH groups in the central part of the molecules [65–67]. Using the values of the acid dissociation constants $pK_a = 10.4$ from Ref. [67], one can estimate the relative population of two species, the -3 charged form and the -2 charged form, in water solutions as a function of pH. At the neutral pH (in the range between ~ 5 and 8), most of SSY molecules exist in the -2 charged form. As pH increases, SSY becomes more charged; above pH = 12.4, more than 99% of SSY molecules have a charge -3. The high negative charge of SSY at high pH weakens aggregation, decreasing the scission energy E, see Eq. (14.1). A study by Gooding et al. [66] showed that the aggregation of SSY in dilute solutions ($c_{SSY} < 0.1$ mol/kg) and found that at pH ≥ 13, SSY does not aggregate at all.

Taylor and Herzfeld [68] demonstrated that when E decreases, the N phase disappears, giving rise to the coexisting I + C phases. At a very low E, the system might even crystallize. All these predictions are in qualitative agreement with the experimental results [19]. Namely, at low concentrations c_{NaOH} of the added base NaOH, the increased pH narrows the temperature range of the N phase. At higher c_{NaOH}, the base promotes biphasic regions I + N, I + C, and then a complete isotropization of the solution with precipitation of a crystalline phase, Figure 14.11.

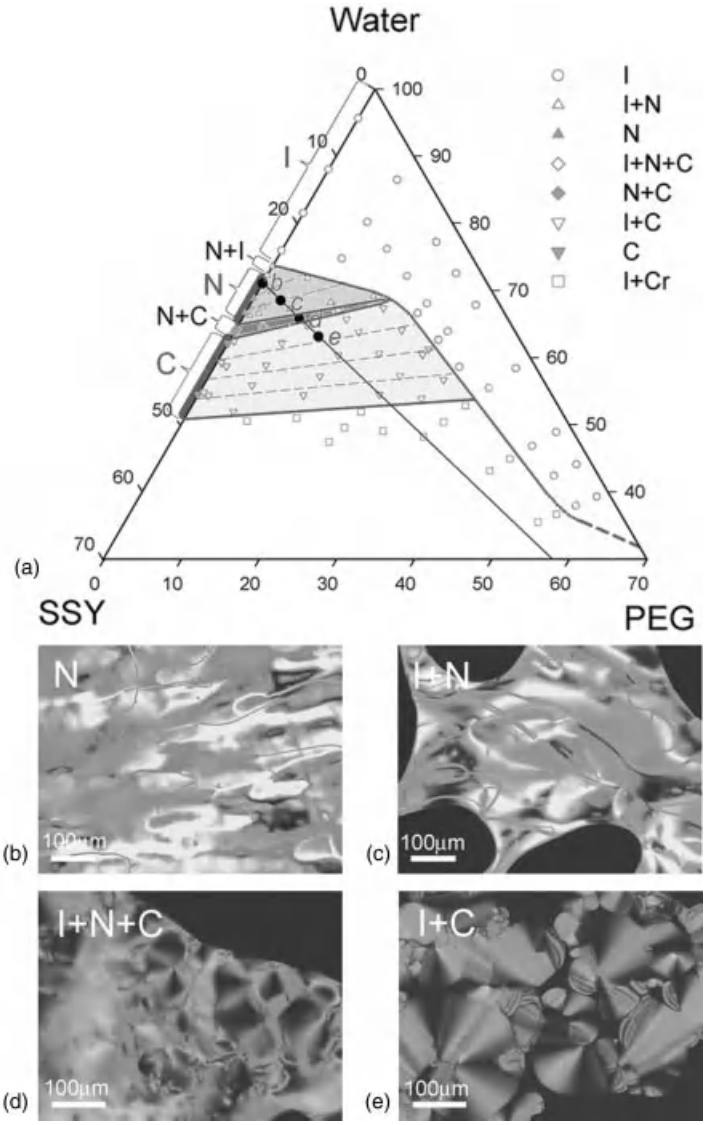

FIGURE 14.9 The ternary phase diagram (a) and polarizing micrographs of SSY and PEG water mixtures; N phase (b), I + N phase (c), I + N + C phase (d), and I + C phase (e). See Ref. [29] for more details.

14.3 EMERGING APPLICATIONS OF LCLCs

Chromonic molecules are self-assembled through noncovalent thus relatively weak interactions, such as π–π attraction into the ordered structures, which depends on many factors such as ionic content, pH, temperature, concentration, and molecular structures. They can be used for the control of supramolecular entities in LCLCs to

FIGURE 14.10 Schematic illustration of the excluded volume effect of the increasing concentration of PEG and chromonics: elongation of short aggregates (a), followed by parallel arrangement in the N phase (b) and C phase (c).

generate functional materials and devices. Here, we summarize the recent development of the potential applications of LCLCs. Two primary areas of applications are presented: anisotropic dried films formed from the aligned LCLC precursors by evaporating water and LCLCs in their fully hydrated bulk state.

14.3.1 Applications of LCLCs in the Form of Dry Films

The first relatively well-studied application of LCLCs is the fabrication of the highly ordered thin films with anisotropic properties for optical elements [13, 31, 69–75], such as linear polarizers, retarders, security tags, and optical compensators. All these applications take advantage of the fact that the structure of chromonic materials in the LC state is orientationally ordered. As a result, the LCLCs show useful structural and optical properties, such as birefringence and polarization-dependent absorption.

The planar alignment of LCLCs with aggregates parallel to one particular direction in the plane of substrate can be achieved by mechanical shearing [12, 31], or by a specially treated alignment layer [18]. Once the aligned structure of LCLCs is created in the LC state, it can be "frozen" by evaporating the solvent. The resulting dry film still preserves an orientational order and, thus, anisotropic optical properties. Preserved in-plane long-range orientational order has been demonstrated not only for micron-thick films but also for nano-thick films prepared by a layer-by-layer electrostatic deposition and composed of one or few stacked LCLC monolayers [12, 35]. Note that the N and C phases in contact with their own isotropic melt, align the director in the plane of the interface (tangential orientation) [29, 51, 58].

An alternative homeotropic alignment of LCLCs with aggregates being perpendicular to the substrates is much harder to achieve. So far, there is only one reported technique for water-based LCLCs, based on glass plates treated with weak water solutions of N,N-dimethyl-N-octadecyl-3-aminopropyl-trimethoxysilyl chloride (DMOAP) [52]. A study by Tolkki et al. [76] showed that an LCLC formed with organic solvents can be aligned homeotropically on a layer of fullerene C_{60}.

To the best of our knowledge, there are no reports on the tilted alignment of LCLCs, except an observation that such an alignment can be achieved in very small domains of the LCLCs surrounded by the I phase [29]. This might be related with the fact that the tilted alignment is not compatible with the aggregated nature of building units.

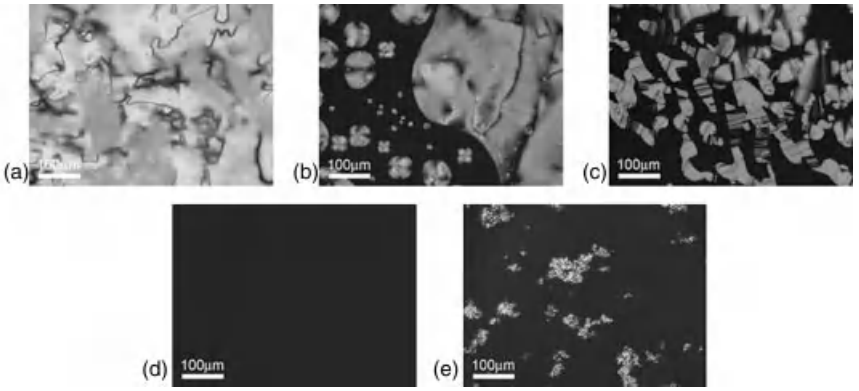

FIGURE 14.11 Polarizing micrographs for $c = 1.14$ mol/kg SSY solution doped with NaOH at different concentrations: (a) $c_{NaOH} = 0$ mol/kg, pH = 6.5, homogeneous N phase; (b) $c_{NaOH} = 0.1$ mol/kg, pH = 11.6, coexisting N and I phases; (c) $c_{NaOH} = 0.2$ mol/kg, pH = 11.9, coexisting C and I phases; (d) $c_{NaOH} = 0.5$ mol/kg, pH = 12.5, homogeneous I phase; (e) $c_{NaOH} = 2$ mol/kg, pH = 13.2, precipitate.

14.3.1.1 Polarizers The conventional dichroic polarizers are used as external polarizers for LCDs, which are usually assembled with glass substrates. The display market demands flexible, light-weight, unbreakable, and cheap displays. The plastic substrate is a solution to meet these demands; however, most plastics are birefringent, which leads to serious shortcomings when the external polarizers are used. The oriented LCLC film can be used as internal polarizers because of their anisotropic absorption. The chromonic internal polarizers, thus, allow one to use inexpensive birefringent easy-to-process plastics for the development of flexible LCDs.

The first claim of the LCLC-based polarizer was made by Dreyer [69, 70]. An orientationally ordered film can be prepared using a suitably treated (rubbed) surface or by applying an external field. Crowley et al. [77] showed the shear-induced alignment of azo dye, CI acid red 266 and cyanine dye. Shear-induced alignment is an easy and useful technique for aligning chromonic LCs. A study by Iverson and Tam-Chang [78] showed that shear-induced orientation of the synthesized rylenebis (dicarboximide) dye followed by evaporation of solvent led to polarizing films with dichroic ratio as high as 30. Sergan et al. [31] built the twisted nematic (TN) LCD with plastic substrates and chromonic internal polarizing layers which provided the contrast ratio of at least 70:1. They also demonstrated that the chromonic dye films can provide uniform planar alignment for rod-like thermotropic LCs, Figure 14.12. The chromonic polarizing films are effective over the range of absorption wavelength of the particular chromonic dyes, which is related with the structure of molecule; see the previous section. Using these properties, Tam-Chang et al. [13] showed that a synthesized chromonic dye with a large conjugated aromatic core, such as quaterrylenebis(dicarboximide) can be used for near-IR polarizing materials. Tam-Chang et al. [13] demonstrated that a broad spectrum polarizing film

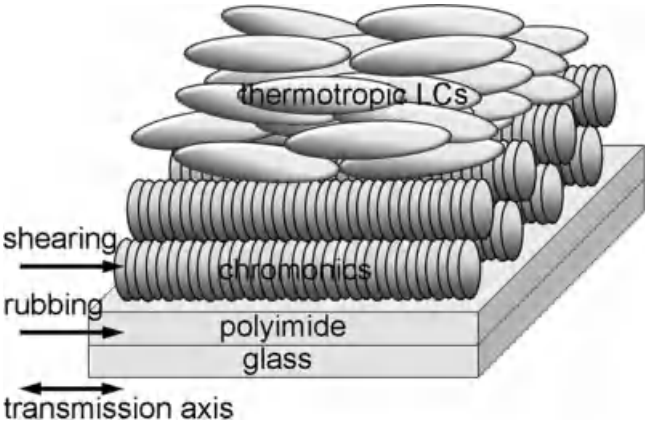

FIGURE 14.12 Schematic illustration of alignment of thermotropic LC molecules on chromonic dye layer.

can be made by using a mixture of molecularly designed chromonic dyes which absorbs over almost the entire visible range.

One of the major problems for practical uses is that the dry chromonic films develop undesirable periodic stripe patterns that are often called "tiger stripes" or "herringbone textures" because of their characteristic textures under the polarizing microscope. X-ray microscopy and near edge X-ray spectra (NEXAFS) spectroscopy of texture formation in dry chromonic films revealed that these periodic patterns are formed by nearly sinusoidal or in some cases zig–zag undulations of the chromonic columns [50]. Kaznatcheev et al. [50] proposed that the undulations and the related "tiger stripes" and "herringbone" textures are caused by the decrease of the inter-columnar separation upon evaporation of water. When the separation between the columns decreases, they need to form a periodic tilted structure to fill the space available, as the effective separation between the tilted aggregates is larger than a separation measured along the normal to the aggregates. The effect is similar to the well-known Helfrich–Hurault effect in smectic LCs, see, for example [45].

Schneider et al. [34] demonstrated that the stripe textures can be eliminated by adding a certain block copolymer to the LCLC formulation, which dramatically improves the polarizing efficiency of the films. The exact mechanisms behind this empirical recipe will remain unclear until we learn much more about the visco-elasticity of LCLCs. A study by Yaroshchuk et al. [79] showed that the ion/plasma beam treatment of polyimide-covered substrates significantly improves the alignment of LCLCs in the form of fully hydrated mesomorphic solutions and in the form of dry films.

Recently, Bae et al. [80] demonstrated a technique to prepare thin polarizing films using non-aqueous LCLCs. They prepared a photocurable organic solution of red-colored chromonic dye, bis-(N,N-diethylaminoethyl)perylene-3,4,9,10-tetracarboxylic diimide in a photo-polymerizable solution composed with acrylic acid and small amount of photoinitiator with a multifunctional monomer (pentaerythritol tetraacrylate). The solution was in the N phase. They coated this photocurable LCLC

organic solution onto a glass or plastic substrate with mechanical shearing and then irradiated with UV light for polymerization. This polymerized polarizing film from an organic-based LCLC solution showed better surface hardness, adhesion to substrates, and solvent resistance than the polarizing films form aqueous LCLCs. Park et al. [81] also described that the polymer-stabilized chromonic thin film shows good mechanical stability and chemical stability. They prepared the N phase solution of chromonic dye, water, and acrylic acid and then coated this solution onto the substrates. After evaporation of water, they polymerized thin film by UV irradiation.

14.3.1.2 Layer-by-Layer Deposition of LCLCs A different technique to prepare in-plane oriented molecular mono- and multi-layered films of chromonic materials with nanometer thickness is the electrostatic layer-by-layer deposition of the LCLCs and polycations [12, 35, 82]. A glass or mica substrate was modified with a polycation, poly(diallyldimethyammonium chloride) (PDDA) and then the N phase of chromonic solution, Violet 20 (V20), was deposited onto the PDDA layer with mechanical shearing. The excess of LCLCs was rinsed off to produce the chromonic monolayer [12]. Using atomic force microscopy and X-ray photoelectron spectroscopy, Schneider et al. [35] demonstrated that the orientationally ordered chromonic aggregates are preserved within the monolayer of a dry LCLC film with aggregates aligned parallel to the substrate, Figure 14.13.

Using the electrostatic layer-by-layer deposition technique, Boiko et al. [82] reported the film comprised alternative layers of positively and negatively charged chromonic LCs, Figure 14.14.

14.3.1.3 Micro-Patterned Chromonic Films One of the versatile approaches for aligning LCLCs is the use of orienting surfaces made from photo-aligned polymer films [72, 83–87]. Compared with other aligning techniques, this technique has an advantage of producing multiple orientations of LCLCs on a single film. Photoalignment using photoisomerizable molecules such as azobenzene is based on their anisotropic reorientation produced by the polarized light irradiation. The orientational order of azobenzene compounds can be effectively transferred to the photochemically inactive LCLCs, such as DSCG [72] and C.I. Direct Blue 67 [83, 84]. Matsunnaga et al. [85] demonstrated that micropatterns of chromonic materials can be fabricated using this photoalignment technique. They spin-coated a polyamide with a photoresponsive dimethylaminoazobenze (MNC10-PAM) on a glass substrate, irradiated the polyamide film with linearly polarized light, and then irradiated again with 90° rotated linearly polarized light through a photomask to reorient azobenzene components in the exposed regions. An aqueous solution of 5 wt.% of C.I. Direct Blue 67 was applied on the photo-aligned layer and then dried to produce a micro-patterned film, Figure 14.15.

Another approach to generate micro-patterned chromonic elements is to use the micro-patterned template. A study by Tam-Chang et al. [38] showed the fabrication of micro-patterns of anisotropic materials using a template with micro-scaled line features. An isotropic solution of a synthesized perylenebis(dicarboximide) was introduced between a cover glass slide and polydimethylsiloxane (PDMS) template

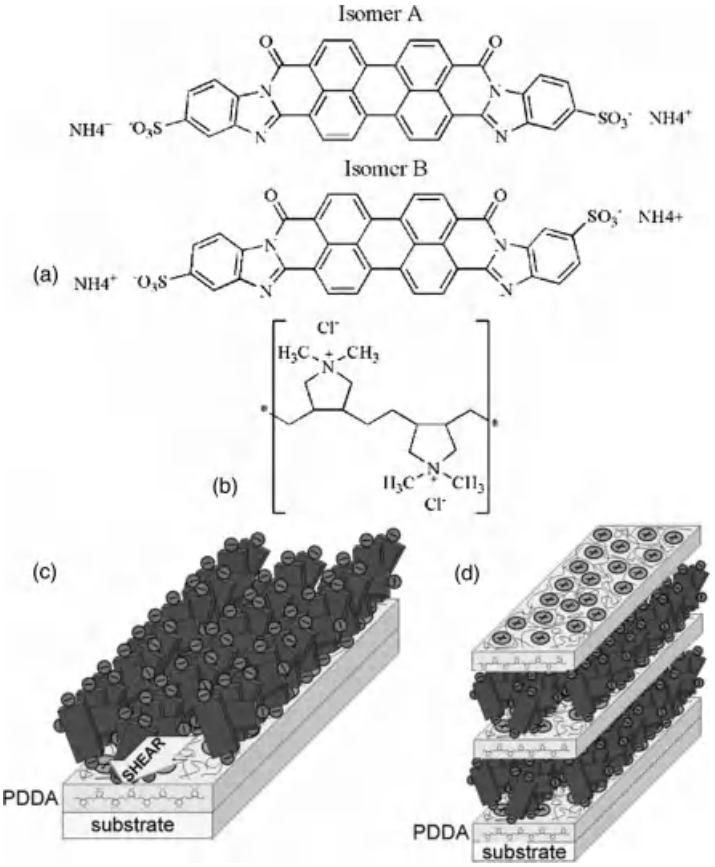

FIGURE 14.13 Molecular structure of violet 20 (a) and PDDA (b). Schematic diagrams showing the plausible geometry of (c) monolayer of chromonics onto the layer of PDDA and (d) multilayered structure of PDDA/chromonics. (Redrawn from Schneider and Lavrentovich [12] and Schneider et al. [35].)

with regular line features of ~9 μm wide, ~2 μm deep, and ~11 μm apart. The chromonic solution became more concentrated into the LC phase by slow evaporation of solvent. After the sample was dried, the PDMS template was peeled off, leaving an array of parallel stripes of aligned dry chmononics, Figure 14.16.

Nastishin et al. [88] reported a photo-induced alignment of the LCLCs by polarized light acting directly on the LCLC slab rather through the effects in the aligning substrates. In the experiment, a uniform planar texture of an LCLC was shown to realign by as much as 90° under irradiation with a linearly polarized laser beam. The effect was observed for LCLC materials, such as dye Blue 27 that absorbs light. For transparent LCLCs, such as DSCG, the photo-induced realignment is not observed, but once the material is doped with a light absorbing agent, the LCLC acquires the ability to realign in the polarized light.

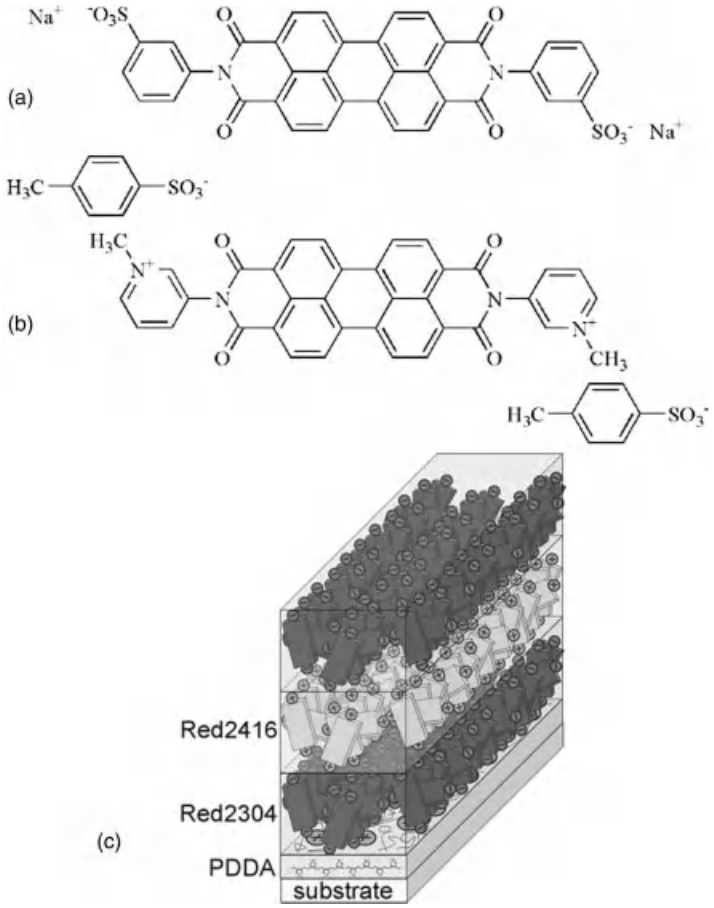

FIGURE 14.14 Molecular structure of negatively charged dye Red 2304 (a) and positively charged dye Red 2416 (b), and (c) schematic diagram of the multilayer structure of PDDA/Red 2304/Red 2416. (Redrawn from Boiko et al. [82].)

14.3.1.4 Organic Electronics The field of organic electronics has gained considerable attention because of the emerging applications in flexible displays and electronics such as light-emitting-diodes (LEDs), photovoltaic cells, and filed effect transistors (FETs). Among the various conductive organic materials, LCs are currently viewed as an attractive candidate for organic electronics because of their long-range orientational order and adaptive structure that heal local defects [89–92]. Recently, several studies showed the electro-optical properties of π-stacked LCLCs [41, 76, 93]. LCLCs are good for processing devices since the orientational order of LCLCs with dense packing is preserved when the aggregates are transferred from the LC solution into thin films by drying. LCLCs can adopt two characteristic orientations required for electronic devices; the planar alignment which is needed for FET to ensure the charge migration between the source and

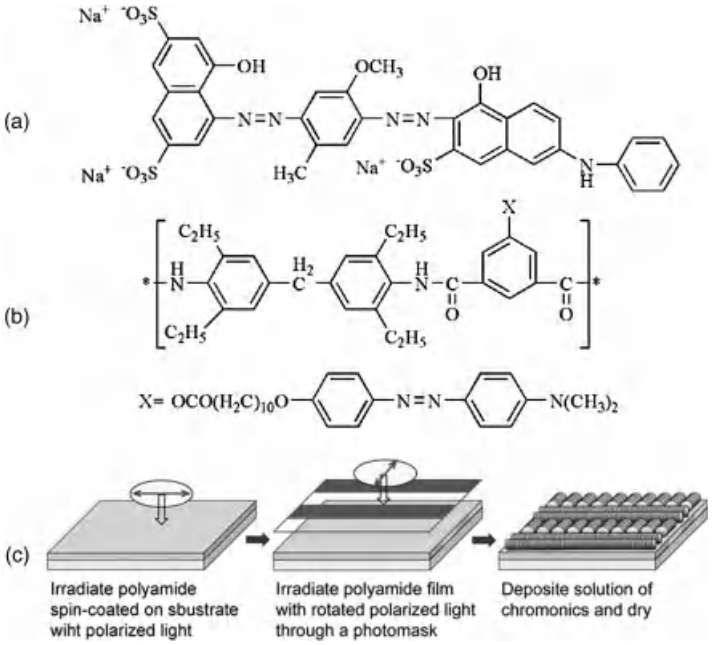

FIGURE 14.15 The molecular structure of C.I. Drirect Blue 67 (a) and polyamide with a photoresponsive dimethylaminoazobenze (MNC10-PAM) (b). Schematic diagram illustrating the procedure for fabricating micro-patterned polarizing films (c). (Redrawn from Matsunaga et al. [85].)

the drain, and the homeotropic alignment which is beneficial for the performance in LED or photovoltaic cell.

Nazarenko et al. [41] demonstrated that aligned dry films of LCLCs exhibit semiconducting properties with anisotropic mobility of charge carries caused by the directional π–π interactions. They deposited LCLCs on the glass substrates either parallel or perpendicular to the gap of two gold electrodes separated by 15 μm and determined the charge carrier mobilities, $\mu_{\parallel} = 5 \times 10^{-3}\,\mathrm{cm^2\,V^{-1}\,s^{-1}}$ and $\mu_{\perp} = 3 \times 10^{-5}\,\mathrm{cm^2\,V^{-1}\,s^{-1}}$, Figure 14.17(a) and (b). The electronic delocalization in two dimensions is a characteristic feature of LCLCs, which is not observed in linear conductive polymers. The electric properties of LCLCs depend strongly upon their aggregate structure and the orientation of aggregates on the substrate.

A study by Tolkki et al. [76] showed that the aggregation of chromonic dye, N,N-di(3,4,5-tridodecylphenyl)-perylene-3,4,9,10-tetracarboxylic acid diimide (PDI12) exhibits the long fluorescence lifetime, ~40 ns, in both solution and thin dry film. They prepared the double-layer system with homeotropic aligned PDI12 layer on top of layer of fullerene C_{60} and presented fluorescence quenching and photo-induced voltage caused by the interaction between PDI12 and C_{60}, Figure 14.18. The homeotropic aligned PDI12 film with the thickness of 10 nm was prepared by the Langmuir–Schaeffer method. They explained that chromonic dye PDI12 acts as an

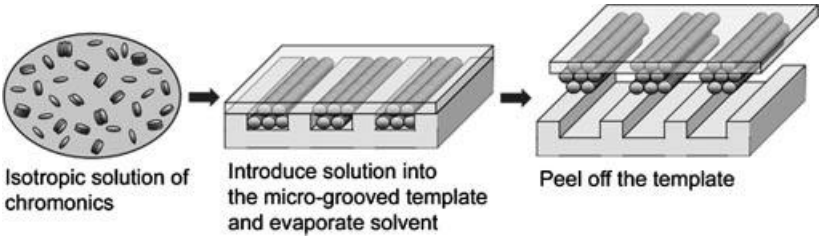

FIGURE 14.16 Schematic diagram illustrating the template-guided organization of LCLCs leading to a micropattern of anisotropically ordered solid. (Redrawn from Tam-Chang et al. [38].)

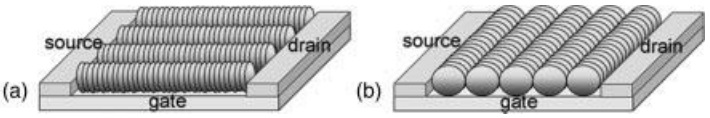

FIGURE 14.17 Schematic diagrams of FET; LCLC aggregates aligned parallel (a) and perpendicular (b) to the gap of two gold electrodes, source and drain, on a gate substrate. (Redrawn from Nazarenko et al. [41].)

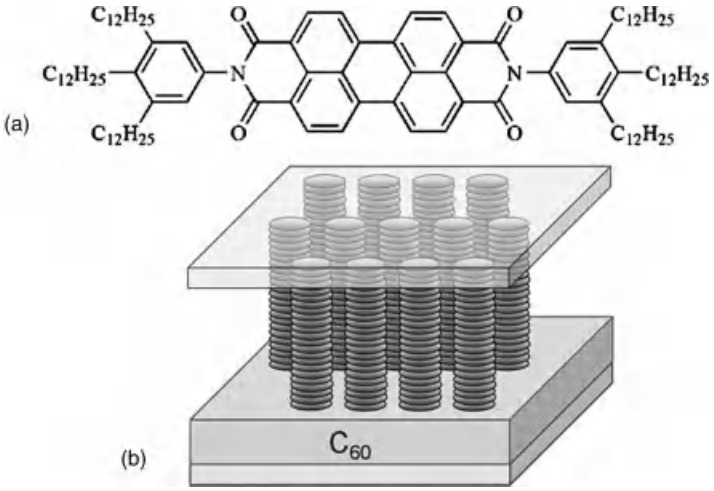

FIGURE 14.18 Molecular structure of PDI12 (a) and schematic diagram (b) of the double-layer system with homeotropic aligned PDI12 layer on top of layer of C60. (Redrawn from Tolkki et al. [76].)

electron acceptor and C_{60} as an electron donor showing promising photoelectric properties.

14.3.1.5 Vertically Aligned Graphene Layers Prepared by LCLCs Graphene, a plat monolayer of carbon atoms tightly packed into a two-dimensional honeycomb lattice, has been attracting much attention owing to its fascinating physical properties, such as quantum electronic transport, tunable band gap, extremely high mobility, and high elasticity [94–97]. Since the discovery of the first isolated graphene prepared by mechanical exfoliation of graphite crystals, many chemical approaches to synthesize graphene have been developed. Graphene monolayers typically deposit themselves flat on substrates or associate face-to-face to form stacked multilayers parallel to the substrates.

Recently, Guo et al. [40] demonstrated that LCLCs can be used to fabricate vertically aligned graphene layer arrays (VAGLAs) with heights from 50 to 800 nm and with two-dimensional in-plane orientational order. Several different sulfonated chromonic dye solutions (such as Blue 27, Violet 20, and Bordeaux dye) were applied on substrates by mechanical shearing. The chromonic films were then dried at room temperature and carbonized by directly heating in nitrogen at 700°C. It was suggested that during the carbonization process, the orientation of the disk-like molecules on substrates becomes stabilized through edge-to-edge polymerization reactions, in which neighboring molecular disks cross-link and merge into vertical graphene layers, Figure 14.19. They also demonstrated that the local shear force can be used to

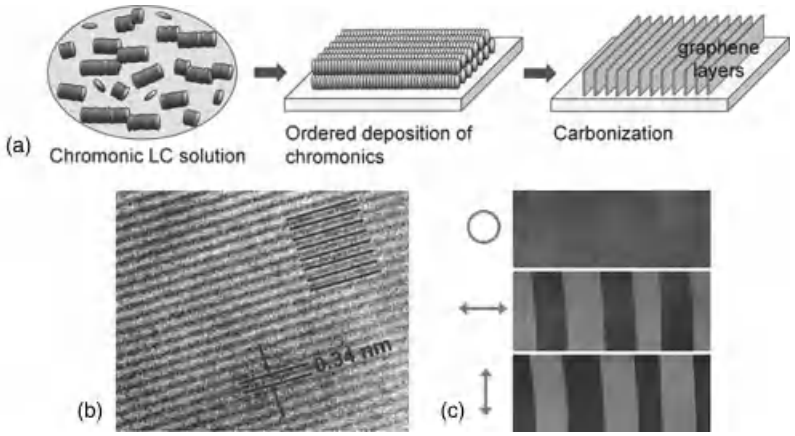

FIGURE 14.19 Schematic diagram illustrating the formation of vertically aligned graphene layer arrays (a). HR-TEM image showing the full fringe field in *Z*-axis projection, indicating vertical graphene layer orientation (b). An optically imbedded VAGLAs pattern on quartz (25×75 mm) with two orthogonal directions by the microshear technique (c). The arrow indicates the polarization direction of light and the circle indicates unpolarized light. (Reprinted with permission from Guo et al. [40].) (*See the color version of this figure in Color Plates section.*)

make polarization-active patterns or imbedded lettering apparent only under polarized light, Figure 14.19 [40].

14.3.2 Applications of LCLCs in the Form of Aqueous Solutions

14.3.2.1 Biosensor Anisotropic optical properties of LCLCs such as birefringence can be used for enhancing optical images for biosensors. LCLCs are not toxic to many microbial species [98] and antibody–antigen binding is not altered by LCLCs [99], which are also important conditions for using them in biological sensing. Lavrentovich and coworkers explored the use of LCLCs in biosensors [36, 37, 98, 100]. They filled a mixture of the N phase DSCG, antigen-coated (streptavidin) microbe (latex beads of diameter $\sim$0.6 μm), and corresponding antibody (anti-streptavidin) into a cell consisted of two glass plates coated with rubbed polyimide for a planar alignment of DSCG aggregates, Figure 14.20.

The idea of LCLC-based detection is as follows. Each microbe has characteristic molecular groups-antigens at the surface, to which a corresponding antibody can bind, thus "recognizing" and "detecting" it. Each antibody molecule has two binding sites; thus this binding often results in the formation of an aggregate of microbes, namely, an immune complex. A director distortion of LCLCs is used to amplify the recognition and detection of immune complex. If such a complex grows in the LCLC bulk and becomes larger than some critical size $d_c \sim K/W \sim 1$ μm, then it should cause director distortions and optical distinction by placing the sample between two

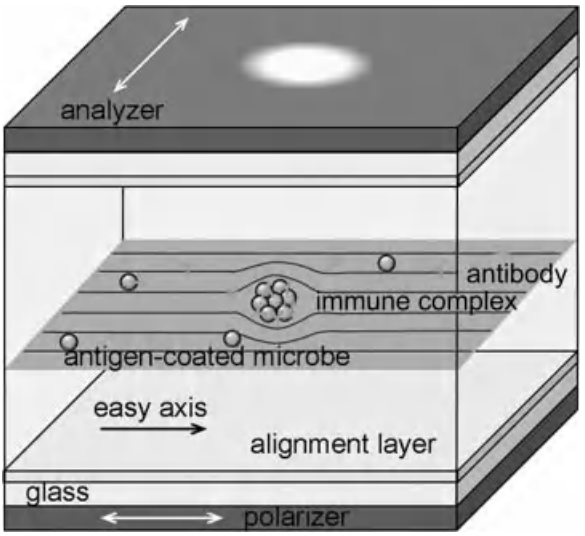

FIGURE 14.20 The scheme of the LCLC biosensor for the detection of immune complexs. (Redrawn from Shiyanovskii et al. [37].) (*See the color version of this figure in Color Plates section.*)

crossed polarizers. Here K is the typical Frank elastic constant and W is the polar anchoring coefficient at the LC–particle interface [36, 37].

The biological selectivity of detection is guaranteed by the selectivity of antibody–antigen binding. Helfinstine et al. [100] also used this scheme for detecting *Bacillus atrophaeus* (BA) spore by anti-BA endospore antibody. The biosensor would function in real time to determine the formation of immune complexes since the director distortion at length scales (0.1–10 μm) occur faster than 0.1 s [37].

14.3.2.2 Optical Compensators It is known that the twisted nematic (TN) LCD has a problem of narrow viewing angle. Light leakage in the dark state and uneven retardation change along the viewing angle cause the asymmetric distribution of light intensity in gray scale. One of the most successful ways to solve this intrinsic problem is to use the optical compensation films. Polymer films with negative birefringence are usually used to counteract the positive birefringence of the nematic LC cells.

There are two geometries in TN LCD with two polarizers placed either parallel ('normally black' or NB mode) or perpendicular ('normally white' or NW mode) to each other. The NB mode is in the dark state when the LC director undergoes a 90° twist between two paralleled polarizers. The NW mode shows dark state when the applied field transforms the LC director from 90° twisted state to a homeotropic state between the crossed polarizers. Lavrentovich et al. [73, 74] demonstrated that the N phase LCLC cells can be used as compensating plates in TN LCD. To match the twist director of the cell in the dark state in the NB mode, they used the twisted chromonic LC cell doped with L-alanine (see previous section) or the combination of the twisted chromonic cell and planar chromonic cell, Figure 14.21. The compensating chromonic cells provide achromatic dark sate and contrast ratio up to 50:1 at all directions within a 40° come of viewing angle [73].

In the dark state of the NW mode TN cell shows the homeotropic director configuration in the middle of the cell, but it shows the splay deformed director configuration near the bounding plates. To compensate the dark state of the NW mode of TN LCD, the uniaxial planar chromonic cell can be used together with a discotic nematic film with negative birefringence and splay optic axis configuration developed by Fuji photo film, Figure 14.22, [73]. Sergan and Kelly [33] also demonstrated that chromonic dry film can be used for compensation of the dark state of the TN LCD combined with commercially available optical retarders. The range of retardation can be easily controlled by the film thickness and concentration of the chromonic solution.

14.3.2.3 Functional Material for Nano-Fabrications Metal nanorods (NRs) show potential for numerous practical applications ranging from molecular [101] and biological sensors [102] to solar energy conversion [103] and the construction of optical cloaking devices [104–106]. One of the most challenges of nanotechnology today is to develop simple and reliable techniques to produce the complex arrangements and assemblies of NRs which are the key to the successful application of the nanoparticle-based devices. The assemblies of metallic NRs show dramatic modification of their optical and electric properties as compared to those of

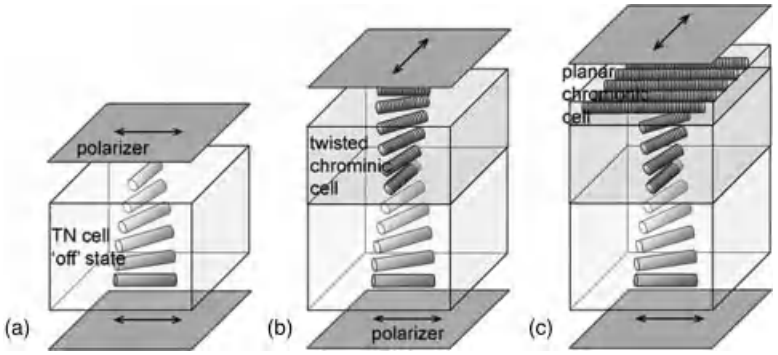

FIGURE 14.21 The configuration of a NB mode of TN LCD: (a) a uncompensated TN cell; (b) a TN cell compensated with a twisted N^* phase chromonic cell; (c) a TN cell compensated with a twisted N^* phase cell and a planar chromonic cell. (Redrawn from Lavrentovich et al. [73].)

individual NRs [107, 108] and consequently can be used as the "building units" for more complex architectures.

Recently, Park et al. [39] described a technique for assembling metallic NRs utilizing the anisotropic attractive forces between the NRs and aggregated stacks of chromonic materials. They used DSCG aggregates, as the linking agent for NR assembly. As described above, DSCG molecules stack face-to-face, leaving the charged groups, carboxylate, at the aggregate–water interface with counterions, Na^+. The stacks thus represent self-assembled macroions with the ability to interact with other charged species, such as gold NRs covered with ionic surfactants,

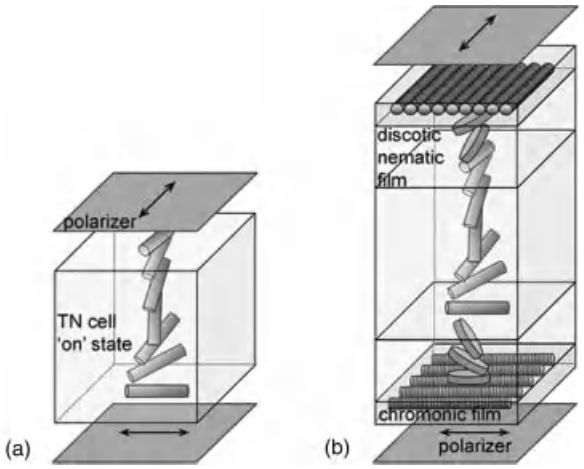

FIGURE 14.22 The configuration of a NW mode of TN LCD: (a) a uncompensated NW TN cell; (b) a NW TN cell compensated with a negative birefringence discotic nematic film and a planar chromonic cell with optic axis in the plane of the film (negative A-plate). (Redrawn from Lavrentovich et al. [73].)

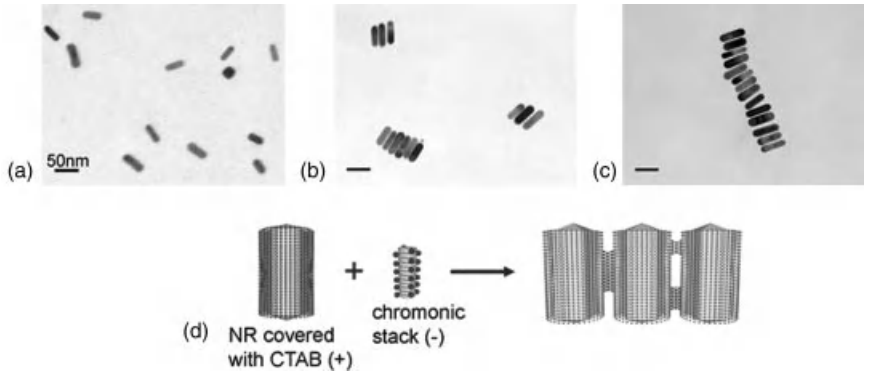

FIGURE 14.23 Side-by-side assembly of gold NRs induced by 0.8 mM DSCG solution mixed with ~2 nM gold NR solution, in 1:1 ratio. (a) TEM image of the control sample, no DSCG; (b) and (c) assembled structures of gold NRs formed after the addition of DSCG solution. (d) Schematic representation of the side-by-side assembly of positively charged gold NRs mediated by negatively charged stacks of DSCG serving as self-assembled multivalent counter ions. (Redrawn from Park et al. [39].)

hexadecyltrimethylammonium bromide (CATB). CTAB is a cationic surfactant that forms a double layer around each gold NR. The anisotropic electrostatic interaction between the chromonic stacks and NRs produces the different geometries of NR assembly by changing the surface charge of NRs, and thus changing the nature of their electrostatic interactions with DSCG stacks. When the positively changed gold NRs are mixed with DSCG solution, the negatively charged DSCG stacks easily attach on the lateral surface of the gold NR producing side-by-side assembled gold NR structures, Figure 14.23. When the isolated gold NRs are coated with poly(acrylic acid) (PAA) to screen the positive charges on the lateral surface, the DSCG stacks effectively bind on the ends of gold NRs producing end-to-end assembled gold NR structures, Figure 14.24. The unique feature of this technique is that the assembly of NRs can be controlled by many parameters since the structure of the linkage agent chromonic stacks is not fixed and depends strongly on temperature, concentration, and pH of the solution. The process of NR assembly can be quenched by the dilution of the solution and by adding a polyelectrolyte to the solution of NRs and DSCGs.

Park et al. [39] also demonstrated that the LCLC-assisted assembly of gold NRs is reversible, which represents an important improvement as compared to many other known techniques of NRs assembly, such as covalent binding. For example, side-by-side assembled NR structures can be disassembled through the increase of pH. As already indicated, high pH increases the negative charge of the DSCG molecules and leads to shortening of the DSCG stacks, rendering them less capable of linking the NRs [39].

14.3.2.4 Chromonic LCs Formed by Biomolecules Mundy et al. [109] examined the solution of ethidium bromide (EB) in DSCG water system. EB is a widely used nucleic acid stain which becomes fluorescent when intercalated into

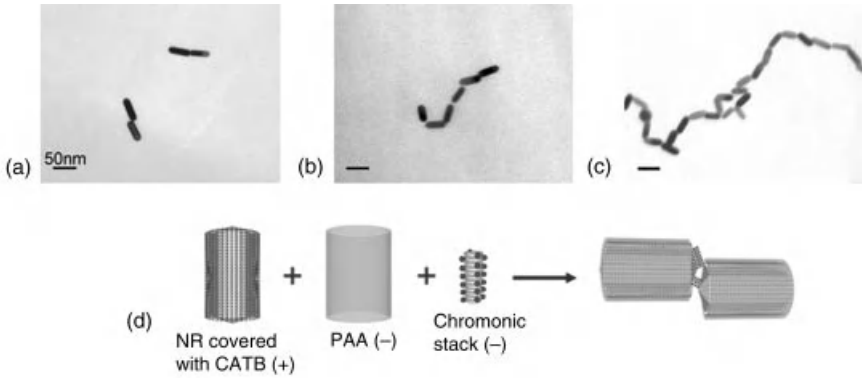

FIGURE 14.24 End-to-end assembly of Au NRs with CTAB and PAA coating, induced by 0.2 M DSCG added to ~2 nM NR solution in 1:1 ratio. TEM images of the end-to-end chains were taken about 2 h (a), 5 h (b), and 24 h (c) after the mixture preparation. (d) Schematic representation of the end-to-end assembly. (Redrawn from Park et al. [39].)

DNA. They demonstrated that the pattern of interaction of EB with a DSCG solution is analogous to its interaction with DNA, suggesting that the stacking of bases in DNA can be regarded as being similar to the chromonic stacking.

Recently, Clark and coworkers investigated the mesomorphic behavior of relatively short strands of oligomeric DNA and RNA [110–112]. Nakata et al. [110] found that relatively short complementary B-form DNA oligomers, only 6–20 base pairs in length, are capable to exhibit N and C phases in water solutions. At first sight, such a finding is very surprising, as the duplexes are very short and lack the shape anisotropy needed to establish the orientationally ordered phases. It turned out that the mechanism of mesophase formation is directly related to the chromonic-like stacking of DNA duplexes on top of each other, similar to the H-aggregation of individual chromonic molecules considered above. Further experiments were performed on mixtures of single-stranded and double-stranded oligomers. When the concentrations are large enough, duplex oligomers are phase-separated into LC droplets from an isotropic background rich in single strands. This phase separation is explained by a combination of depletion-type entropic forces, attributable to flexibility mismatch, and energy gained upon stacking [112]. The effects of LCLC condensation by additives such as PEG described above are thus similar to the effects in the systems formed by biomolecules.

Spindler and coworkers showed that guanosine, one of the four DNA nucleotides, can self-assemble into highly ordered columnar structures in aqueous solutions [15, 16]. Four guanosine molecules assemble to form a planar disk-shaped tetramer and then tetramers stack into an elongated aggregate in the same way as other chromonics do. The stacking distance of the disk-shaped tetramer is 0.34 nm, same as the distance of chromonic stacking [16]. They also described that the addition of monovalent salt such as potassium ion can promote the self-assembly of guanosine tetramers, leading to the formation of the LC phase when enough salt is

added. These experiments suggest that the chromonic family embraces a wide range of biomaterials.

14.4 CONCLUSIONS

Recently, there has been an increasing interest in LCLCs, not only because chromonic materials represent a distinct class of soft matter showing unique properties different from the conventional lyotropic LCs, but also because they have shown promise for new applications, such as the preparation of optically anisotropic films, micro-pattering, biosensing, and functional materials for nano-fabrication, as described above. Deeper understanding of the properties of LCLCs, including details of aggregation, molecular structure–property relationship, role of concentration, temperature, and ionic content is important not only for the basic research but also for the development of new applications. We hope that this review provides a basic understanding of phase behavior and the physical properties of the self-assembled chromonic materials and expands the opportunities for practical applications of LCLCs.

REFERENCES

1. T. K. Attwood, J. E. Lydon, and F. Jones. The chromonic phases of dyes. *Liq. Cryst.* **1986**, *1*, 499–507.
2. T. K. Attwood, J. E. Lydon, C. Hall, and G. J. T. Tiddy. The distinction between chromonic and amphiphilic lyotropic mesophases. *Liq. Cryst.* **1990**, *7*, 657–668.
3. J. E. Lydon. Chromonic liquid crystal phases. *Curr. Opin. Colloid Interface Sci.* **1998**, *3*, 458–466.
4. D. J. Edwards, A. P. Ormerod, G. J. T. Tiddy, A. A. Jaber, and A. Mahendrasingham. Aggregation and lyotropic liquid crystal formation of anionic azo dyes for textile fibres. In: *Physico-Chemical Principles of Colour Chemistry; Advances in Color Chemistry Series*. A. T. Peters and H. S. Freeman,Ed., Springer-Verlag, New York, 1996.
5. J. E. Lydon. Chromonic mesophases. *Curr. Opin. Colloid Interface Sci.* **2004**, *8*, 480–489.
6. S.-W. Tam-Chang and L. Huang. Chromonic liquid crystals: properties and applications as functional materials. *Chem. Commun.* **2008**, 1957–1967.
7. J. E. Lydon. Chromonic review. *J. Mater. Chem.* **2010**, *20*, 10071–10099.
8. L. J. Yu and A. Saupe. Deuteron resonance of nematic disodium cromoglycate-water systems. *Mol. Cryst. Liq. Cryst.* **1982**, *80*, 129–143.
9. H. Lee and M. M. Labes. Lyotropic cholesteric and nematic phases of disodium cromoglycate in magnetic fields. *Mol. Cryst. Liq. Cryst.* **1982**, *84*, 137–157.
10. N. H. Hartshorne and G. D. Woodard. Mesomorphism in the system disodium chromoglycae–water. *Mol. Cryst. Liq. Cryst.* **1973**, *23*, 343–368.
11. G. J. T. Tiddy, D. L. Mateer, A. P. Ormerod, W. J. Harrison, and D. J. Edwards. Highly ordered aggregates in dilute water–dye systems. *Langmuir* **1995**, *11*, 390–393.

12. T. Schneider and O. D. Lavrentovich. Self assembled monolayers and multilayered stacks of lyotropic chromonic liquid crystalline dyes with in-plane orientational order. *Langmuir* **2000**, *16*, 5227–5230.
13. S.-W. Tam-Chang, W. Seo, I. K. Iverson, and S. M. Casey. Ionic quaterrylenebis (dicarboximide): a novel mesogen and long-wavelength polarizing material. *Angew. Chem. Int. Ed.* **2003**, *42*, 897–900.
14. V. R. Horowitz, L. A. Janowitz, A. L. Modic, P. A. Heiney, and P. J. Collings. Aggregation behavior and chromonic liquid crystal properties of an anionic monoazo dye. *Phys. Rev. E* **2005**, *72*, 041710.
15. L. Spindler, I. Drevensek-Olenik, M. Copic, R. Romih, J. Cerar, J. Skerjanc, and P. Mariani. Dynamic light scattering and ^{31}P NMR spectroscopy study of the self-assembly of deoxyguanosine 5′-monophosphate. *Eur. Phys. J. E* **2002**, *7*, 95–102.
16. P. Mariani, F. Spinozzi, F. Federiconi, H. Amenitsch, L. Spindler, and I. Drevensek-Olenik. Small angle x-ray scattering analysis of deoxyguanosine 5′-monophosphate self-assembling in solution: nucleation and growth of G-quadruplexes. *J. Phys. Chem. B* **2009**, *113*, 7934–7944.
17. D. Goldfarb, Z. Luz, N. Spielberg, and H. Zimmermann. Structural and orientational characteristics of the disodium cromoglycate–water mesophases by deuterium NMR and x-ray diffraction. *Mol. Cryst. Liq. Cryst.* **1985**, *126*, 225–246.
18. Y. A. Nastishin, H. Liu, T. Schneider, V. G. Nazarenko, R. Vasyuta, S. V. Shiyanovskii, and O. D. Lavrentovich. Optical characterization of the nematic lyotropic chromonic liquid crystals: light absorption, birefringence, and scalar order parameter. *Phys. Rev. E* **2005**, *72*, 041711.
19. H.-S. Park, S.-W. Kang, L. Tortora, Y. Nastishin, D. Finotello, S. Kumar, S., and O. D. Lavrentovich. Self-assembly of lyotropic chromonic liquid crystal Sunset Yellow and effects of ionic additives. *J. Phys. Chem. B* **2008**, *112*, 16307–16319.
20. D. J. Edwards, J. W. Jones, O. Lozman, A. P. Ormerod, M. Sintyureva, and G. J. T. Tiddy. Chromonic liquid crystal formation by Edicol Sunset Yellow. *J. Phys. Chem. B* **2008**, *112*, 14628–14636.
21. A. J. Dickinson, N. D. LaRacuente, C. B. Mckitterick, and P. J. Collings. Aggregate structure and free energy changes in chromonic liquid crystals. *Mol. Cryst. Liq. Cryst.* **2009**, *509*, 9–20.
22. M. E. Cates and S. J. Candau. Statics and dynamics in worm-like surfactant micelles. *J. Phys.: Condens. Matter* **1990**, *2*, 6869–6892.
23. W. M. Gelbart and A. Ben-Shaul. The "new" science of "complex fluids." *J. Phys. Chem.* **1996**, *100*, 13169–13189.
24. L. Joshi, S.-W. Kang, D. M. Agra-Kooijman, and S. Kumar. Concentration, temperature, and pH dependence of sunset-yellow aggregates in aqueous solutions: an X-ray investigation. *Phys. Rev. E* **2009**, *80*, 041703.
25. Y. A. Nastishin, H. Liu, S. V. Shiyanovskii, O. D. Lavrentovich, A. F. Kostko, and M. A. Anisimov. Pretransitional fluctuations in the isotropic phase of a lyotropic chromonic liquid crystal. *Phys. Rev. E* **2004**, *70*, 051706.
26. A. F. Kostko, B. H. Cipriano, O. A. Pinchuk, L. Ziserman, M. A. Anisimov, D. Danino, and S. R. Raghavan. Salt effects on the phase behavior, structure, and rheology of chromonic liquid crystals. *J. Phys. Chem. B* **2005**, *109*, 19126–19133.

27. S. K. Prasad, G. G. Nair, G. Hegd, and V. Jayalakshmi. Evidence of wormlike micellar behavior in chromonic liquid crystals: rheological, X-ray, and dielectric studies. *J. Phys. Chem. B* **2007**, *111*, 9741–9746.
28. J. W. Jones, L. Lue, A. P. Ormerod, and G. J. T. Tiddy. The influence of sodium chloride on the self-association and chromonic mesophase formation of Edicol Sunset Yellow. *Liq. Cryst.* **2010**, *37*, 711–722.
29. H.-S. Park, S.-W. Kang, L. Tortora, S. Kumar, and O. D. Lavrentovich. Condensation of self-assembled lyotropic chromonic liquid crystal Sunset Yellow in aqueous solutions crowded with polyethylene glycol and doped with salt. *Langmuir* **2011**, *27*, 4164–4175.
30. S.-W. Tam-Chang, J. Helbley, and I. K. Iverson. A study of the structural effects on the liquid-crystalline properties of ionic perylenebis(dicarboximide)s using UV-vis spectroscopy, polarized light microscopy, and NMR spectroscopy. *Langmuir* **2008**, *24*, 2133–2139.
31. T. Sergan, T. Schneider, J. Kelly, and O. D. Lavrentovich. Polarizing-alignment layers for twisted nematic cells. *Liq. Cryst.* **2000**, *27*, 567–572.
32. Y. Bobrov, C. Cobb, P. Lazarev, P. Bos, D. Bryant, and H. Wonderly. Lyotropic thin film polarizers. Digest of technical papers at 2001 Society for Information Display international symposium 2001, 1102–1107.
33. T. Sergan and J. Kelly. Negative uniaxial films from lyotropic liquid crystalline material for liquid crystal display application. *Liq. Cryst.* **2000**, *27*, 1481–1484.
34. T. Schneider, A. Golovin, J. C. Lee, and O. D. Lavrentovich. Lyotropic chromonic liquid crystals in aligned films for applications as polarizing coatings. *J. Inform. Display* **2004**, *5*, 27–38.
35. T. Schneider, K. Artyushkova, J. E. Fulghum, L. Broadwater, A. Smith, and O. D. Lavrentovich. Oriented monolayers prepared from lyotropic chromonic liquid crystal. *Langmuir* **2005**, *21*, 2300–2307.
36. S. V. Shiyanovskii, O. D. Lavrentovich, T. Schneider, T. Ishikawa, I. I. Smalyukh, C. J. Woolverton, G. D. Niehaus, and K. J. Doane. Lyotropic chromonic liquid crystals for biological sensing applications. *Mol. Cryst. Liq. Cryst.* **2005**, *434*, 259–270.
37. S. V. Shiyanovskii, T. Schneider, I. I. Smalyukh, T. Ishikawa, G. D. Niehaus, K. J. Doane, C. J. Woolverton, and O. D. Lavrentovich. Real-time microbe detection based on director distortions around growing immune complexes in lyotropic chromonic liquid crystals. *Phys. Rev. E* **2005**, *71*, 020702R.
38. S.-W. Tam-Chang, J. Helbley, T. D. Carson, W. Seo, and I. K. Iverson. Template-guided organization of chromonic liquid crystals into micropatterned anisotropic organic solids. *Chem. Commun.* **2006**, 503–505.
39. H.-S. Park, A. Agarwal, N. A. Kotov, and O. D. Lavrentovich. Controllable side-by-side and end-to-end assembly of Au nanorods by lyotropic chromonic materials. *Langmuir* **2008**, *24*, 13833–13837.
40. F. Guo, A. Mukhopadhyay, B. W. Sheldon, and R. H. Hurt. Vertically aligned graphene layer arrays from chromonic liquid crystal precursors. *Adv. Mater.* **2011**, *23*, 508–513.
41. V. G. Nazarenko, O. P. Boiko, M. I. Anisimov, A. K. Kadashchuk, Y. A. Nastishin, A. B. Golovin, and O. D. Lavrentovich. Lyotropic chromonic liquid crystal semiconductors for water-solution processable organic electronics. *Appl. Phys. Lett.* **2010**, *97*, 263305.

42. A. P. Ormerod. The Formation of Chromonic Liquid Crystals by Water Soluble Azo Dyes [dissertation]. Salford, UK: University of Salford, **1995**.
43. R. J. Luoma. X-ray Scattering and Magnetic Birefringence Studies of Aqueous Solutions of Chromonic Molecular Aggregates [dissertation]. Waltham, MA: Brandeis University, **1995**.
44. F. Chami and M. R. Wilson. Molecular order in a chromonic liquid crystal: a molecular simulation study of the anionic azo dye Sunset Yellow. *J. Am. Chem. Soc.* **2010**, *132*, 7794–7802.
45. M. Kleman and O. D. Lavrentovich. *Soft Matter Physics: An Introduction*. Springer, New York, 2003.
46. A. H. Herz. Aggregation of sensitizing dyes in solution and their adsorption onto silver halides. *Adv. Colloid Interface Sci.* **1977**, *8*, 237–298.
47. L. Onsager. The effects of shape on the interaction of colloidal particles. *Ann. N.Y. Acad. Sci.* **1949**, *51*, 627–659.
48. M. P. Renshaw and I. J. Day. NMR characterization of the aggregation state of the azo dye Sunset Yellow in the isotropic phase. *J. Phys. Chem. B* **2010**, *114*, 10032–10038.
49. L. Wu, J. Lal, K. A. Simon, E. A. Burton, and Y.-Y. Luk. Nonamphiphilic assembly in water: polymorphic nature, thread structure, and thermodynamic incompatibility. *J. Am. Chem. Soc.* **2009**, *131*, 7430–7443.
50. K. V. Kaznatcheev, P. Dudin, O. D. Lavrentovich, and A. P. Hitchcock. X-ray microscopy study of chromonic liquid crystal dry film texture. *Phys. Rev. E* **2007**, *76*, 061703.
51. L. Tortora, H.-S. Park, S.-W. Kang, V. Savaryn, S.-H. Hong, K. Kaznatcheev, D. Finotello, S. Sprunt, S. Kumar, and O. D. Lavrentovich. Self-assembly, condensation, and order in aqueous lyotropic chromonic liquid crystals crowded with additives. *Soft Matter* **2010**, *6*, 4157–4167.
52. V. G. Nazarenko, O. P. Boiko, H.-S. Park, O. M. Brodyn, M. M. Omelchenko, L. Tortora, Y. A. Nastishin, and O. D. Lavrentovich. Surface alignment and anchoring transitions in nematic lyotropic chromonic liquid crystal. *Phys. Rev. Lett.* **2010**, *105*, 017801.
53. H.-S. Park. Self-assembly of lyotropic chromonic liquid crystals: effects of additives and applications [dissertation]. Kent, OH: Kent State University, **2010**.
54. S.-W. Tam-Chang, W. Seo, and I. K. Iveson. Synthesis and studies of the properties of a liquid-crystalline quaterrylenebis(dicarboximide) by ^{1}H NMR and UV−vis spectroscopies. *J. Org. Chem.* **2004**, *69*, 2719–2726.
55. D. C. Rau, B. Lee, and V. A. Parsegian. Measurement of the repulsive force between polyelectrolyte molecules in ionic solution: hydration forces between parallel DNA double helices. *Proc. Natl. Acad. Sci. USA* **1984**, *81*, 2621–2625.
56. P. Mariani, F. Ciuchi, and L. Saturni. Helix-specific interactions induce condensation of guanosine four-stranded helices in concentrated salt solutions. *Biophys. J.* **1998**, *74*, 430–435.
57. K. A. Simon, P. Sejwal, R. B. Gerecht, and Y.-Y. Luk. Water-in-water emulsions stabilized by non-amphiphilic interactions: polymer-dispersed lyotropic liquid crystals. *Langmuir* **2007**, *23*, 1453–1458.
58. L. Tortora and O. D. Lavrentovich. Chiral symmetry breaking by spatial confinement in tactoidal droplets of lyotropic chromonic liquid crystals. *Proc. Natl. Acad. Sci. USA* **2011**, *108*, 5163–5168.
59. S. Asakura and F. Oosawa. Interaction between particles suspended in solutions of macromolecules. *J. Polym. Sci.* **1958**, *33*, 183–192.

60. R. Tuinier, J. Rieger, and C. G. de Kruif. Depletion-induced phase separation in colloid polymer mixtures. *Adv. Colloid Interface Sci.* **2003**, *103*, 1–31.

61. L. S. Lerman. A transition to a compact form of DNA in polymer solutions. *Proc. Nat. Acad. Sci. U.S.A.* **1971**, *68*, 1886–1890.

62. V. V. Vasilevskaya, A. R. Khokhlov, Y. Matsuzawa, and K. Yoshikawa. Collapse of single DNA molecule in poly(ethylene glycol) solutions. *J. Chem. Phys.* **1995**, *102*, 6595–6602.

63. V. A. Bloomfield. DNA condensation. *Curr. Opin. Structural Biology* **1996**, *6*, 334–341.

64. J. E. B. Ramos, R. de Vries, and J. R. Neto. DNA ψ-condensation and reentrant decondensation: effect of the PEG degree of polymerization. *J. Phys. Chem. B* **2005**, *109*, 23661–23665.

65. J. J. Gooding, R. G. Compton, C. M. Brennan, and J. H. Atherton. The mechanism of the electro-reduction of some azo dyes. *Electroanalysis* **1996**, *8*, 519–523.

66. J. J. Gooding, R. G. Compton, C. M. Brennan, and J. H. Atherton. A new electrochemical method for the investigation of the aggregation of dyes in solution. *Electroanalysis* **1997**, *9*, 759–764.

67. M. Perez-Urquiza and J. L. Beltran. Determination of the dissociation constants of sulfonated azo dyes by capillary zone electrophoresis and spectrophotometry methods. *J. Chromatogr. A* **2001**, *917*, 331–336.

68. M. P. Taylor and J. Herzfeld. Shape anisotropy and ordered phases in reversibly assembling lyotropic systems. *Phys. Rev. A* **1991**, *43*, 1892–1905.

69. J. F. Dreyer. Optical device and method and manufacture thereof. *US Patent* 2,400,877, **1946**.

70. J. F. Dreyer. Dichroic light-polarizing sheet materials and the like and the formation and use thereof. *US Patent* 2,544,659, **1951**.

71. J. F. Dreyer. The fixing of molecular orientation. *J. Phys. Colloid Chem.* **1948**, *52*, 808–810.

72. T. Fujiwara and K. Ichimura. Surface-assisted photoalignment control of lyotropic liquid crystals. Part 2. Photoalignment of aqueous solutions of a water-soluble anti-asthmatic drug as lyotropic liquid crystals. *J. Mater. Chem.* **2002**, *12*, 3387–3391.

73. M. Lavrentovich, T. Sergan, and J. Kelly. Planar and twisted lyotropic chromonic liquid crystal cells as optical compensators for twisted nematic displays. *Liq. Cryst.* **2003**, *30*, 851–859.

74. M. Lavrentovich, T. Sergan, and J. Kelly. Lyotropic chromonic liquid crystals for optical applications: an optical retardation plate for twisted nematic cells. *Mol. Cryst. Liq. Cryst.* **2004**, *409*, 21–28.

75. S.-W. Tam-Chang, W. Seo, K. Rove, and S. M. Casey. Molecularly designed chromonic liquid crystals for the fabrication of broad spectrum polarizing materials. *Chem. Mater.* **2004**, *16*, 1832–1834.

76. A. Tolkki, E. Vuorimaa, V. Chukharev, H. Lemmetyinen, P. Ihalainen, J. Peltonen, V. Dehm, and F. Wurthner. Langmuir-Schaeffer films from a π–π stacking perylenediimide dye: organization and charge transfer properties. *Langmuir* **2010**, *26*, 6630–6637.

77. T. L. Crowley, C. Bottrill, D. Mateer, W. J. Harrison, and G. J. T. Tiddy. Lyotropic chromonic liquid crystals: neutron scattering studies of shear-induced orientation and reorientation. *Colloids Surf. A* **1997**, *129–130*, 95–115.

78. I. K. Iverson and S.-W. Tam-Chang. Cascade of molecular order by sequential self-organization, induced orientation, and order transfer processes. *J. Am. Chem. Soc.* **1999**, *121*, 5801–5802.

79. O. Yaroshchuk, R. Kravchuk, S. Gubarev, I. Protsenko, A. Golovin, and O. D. Lavrentovich. Plasma beam alignment of lyotropic chromonic liquid crystals. Digest of technical papers at 2011 Society for Information Display international symposium, 15–20 May 2011, Los Angeles, California.

80. Y.-J. Bae, H.-J. Yang, S.-H. Shin, K.-U. Jeong, and M.-H. Lee. A novel thin film polarizer from photocurable non-aqueous lyotropic chromonic liquid crystal solutions. *J. Mater. Chem.* **2011**, *21*, 2074–2077.

81. S.-K. Park, S.-E. Kim, D.-Y. Kim, S.-W. Kang, S. Shin, S.-W. Kuo, S.-H. Hwang, S. H. Lee, M.-H. Lee, and K.-U. Jeong. Polymer-stabilized chromonic liquid-crystalline polarizer. *Adv. Funct. Mater.* **2011**, *21*, 2129–2139.

82. O. Boiko, O. Komarov, R. Vasyuta, V. Nazarenko, Y. Slominskiy, and T. Schneider. Nano-architecture of self-assembled monolayer and multilayer stacks of lyotropic chromonic liquid crystalline dyes. *Mol. Cryst. Liq. Cryst.* **2005**, *434*, 305–314.

83. K. Ichimura, M. Momose, K. Kudo, and H. Akiyama. Surface-assisted photolithography to form anisotropic dye layers as a new horizon of command surfaces. *Langmuir* **1995**, *11*, 2341–2343.

84. K. Ichimura, T. Fujiwara, M. Momose, and D. Matsunnaga. Surface-assisted photo-alignment control of lyotropic liquid crystals. Part 1. Characterisation and photoalignment of aqueous solutions of a water-soluble dye as lyotropic liquid crystals. *J. Mater. Chem.* **2002**, *12*, 3380–3386.

85. D. Matsunnaga, T. Tamaki, H. Akiyama, and K. Ichimura. Photofabrication of mcro-patterned polarizing elements for stereoscopic displays. *Adv. Mater.* **2002**, *14*, 1477–1480.

86. D. Matsunnaga, T. Tamaki, and K. Ichimura. Azo-pendant polyamides which have the potential to photoalign chromonic lyotropic liquid crystals. *J. Mater. Chem.* **2003**, *13*, 1558–1564.

87. C. Ruslim, M. Hashimoto, D. Matsunnaga, T. Tamaki, and K. Ichimura. Optical and surface morphological properties of polarizing films fabricated from a chromonic dye by the photoalignment technique. *Langmuir* **2004**, *20*, 95–100.

88. Y. A. Nastishin, O. P. Boiko, R. M. Vasyuta, V. P. Pergamenshchik, V. G. Nazarenko, and O. D. Lavrentovich. Photoinduced reorientation of light-absorbing lyotropic chromonic liquid crystal. *Ukr. J. Phys.* **2009**, *54*, 82–88.

89. V. Percec, M. Goldde, T. K. Bera, Y. Miura, I. Shiyanovskaya, K. D. Singer, V. S. K. Balagurusamy, P. A. Heiney, I Schnell, A. Rapp, H.-W. Spiess, S. D. Hudson, and H. Duan. Self-organization of supramolecular helical dendrimers into complex electronic materials. *Nature* **2002**, *419*, 384–387.

90. J. Tant, et al. Liquid crystalline metal-free phthalocyanines designed for charge and exciton transport. *J. Phys. Chem. B* **2005**, *109*, 20315–20323.

91. K. Oikawa, H. Monobe, K. Nakayama, T. Kimoto, K. Tsuchiya, B. Heinrich, D. Guillon, Y. Shimizu, and M. Yokoyama. High carrier mobility of organic field-effect transistors with a thiophene–naphthalene mesomorphic semiconductor. *Adv. Mater.* **2007**, *19*, 1864–1868.

92. S. Sergeyev, W. Pisula, and Y. H. Geerts. Discotic liquid crystals: a new generation of organic semiconductors. *Chem. Soc. Rev.* **2007**, *36*, 1902–1929.
93. S. K. Lee, Y. Zu, A. Herrmann, Y. Geerts, K. Mullen, and A. J. Bard. Electrochemistry, spectroscopy and electrogenerated chemiluminescence of perylene, terrylene, and quaterryle diimides in aprotic solution. *J. Am. Chem. Soc.* **1999**, *121*, 3513–3520.
94. K. S. Novoselov, A. K. Geim, S. V. Morozov, D. Jiang, Y. Zhang, S. V. Dubonos, I. V. Grigorieva, and A. A. Firsov. Electric field effect in atomically thin carbon films. *Science* **2004**, *306*, 666–669.
95. A. K. Geim and K. S. Novoselov. The rise of graphene. *Nature Mater.* **2007**, *6*, 183–191.
96. A. K. Geim. Graphene: status and prospects. *Science* **2009**, *324*, 1530–1534.
97. K. S. Kim, Y. Zhao, H. Jang, S. Y. Lee, J. M. Kim, K. S. Kim, J. H. Ahn, P. Kim, J.-Y. Choi, and B. H. Hong. Large-scale pattern growth of graphene films for stretchable transparent electrodes. *Nature* **2009**, *457*, 706–710.
98. C. J. Woolverton, E. Gustely, L. Li, and O. D. Lavrentovich. Liquid crystal effects on bacterial viability. *Liq. Cryst.* **2005**, *32*, 417–423.
99. Y. Y. Luk, C. H. Jang, L. L. Cheng, B. A. Israel, and N. L. Abbott. Influence of lyotropic liquid crystals on the ability of antibodies to bind to surface-immobilized antigens. *Chem. Mater.* **2005**, *17*, 4774–4782.
100. S. L. Helfinstine, O. D. Lavrentovich, and C. J. Woolverton. Lyotropic liquid crystal as a real-time detector of microbial immune complexes. *Lett. Appl. Microbiol.* **2006**, *43*, 27–32.
101. Z. Tang, N. A. Kotov, S. Magonov, and B. Ozturk. Nanostructured artificial nacre. *Nat. Mater.* **2003**, *2*, 413–418.
102. X. Huang, I. H. El-Sayed, W. Qian, and M. A. El-Sayed. Cancer cells assemble and align gold nanorods conjugated to antibodies to produce highly enhanced, sharp, and polarized surface Raman spectra: a potential cancer diagnostic marker. *Nano Lett.* **2007**, *7*, 1591–1597.
103. J. Lee, A. O. Govorov, J. Dulka, and N. A. Kotov. Bioconjugates of CdTe nanowires and Au nanoparticles: plasmon-exciton interactions, luminescence enhancement and collective effects. *Nano Lett.* **2004**, *4*, 2323–2330.
104. W. S. Cai, U. K. Chettiar, A. V. Kildishev, and V. M. Shalaev. Optical cloaking with metamaterials. *Nat. Photon.* **2007**, *1*, 224–227.
105. A. B. Golovin and O. D. Lavrentovich. Electrically reconfigurable optical metamaterial based on colloidal dispersion of metal nanorods in dielectric fluid. *Appl. Phys. Lett.* **2009**, *95*, 254104.
106. A. B. Golovin, J. Xiang, H.-S. Park, L. Tortora, Y. A. Nastishin, S. V. Shiyanovskii, and O. D. Lavrentovich. Eletro-optic effects in colloidal dispersion of metal nano-rods in dielectric fluid. *Mater.* **2011**, *4*, 390–416.
107. K. L. Kelly, E. Coronado, L. L. Zhao, and G. C. Schatz. The optical properties of metal nanoparticles: the influence of size, shape, and dielectric environment. *J. Phys. Chem. B* **2003**, *107*, 668–677.
108. L. M. Liz-Mrzan. Tailoring surface plasmons through the morphology and assembly of metal nanoparticles. *Langmuir* **2006**, *22*, 32–41.
109. K. Mundy, J. C. Sleep, and J. E. Lydon. The intercalation of ethidium bromide in the chromonic lyotropic phases of drugs and nucleic acids. *Liq. Cryst.* **1995**, *19*, 107–112.

110. M. Nakata, G. Zanchetta, B. D. Chapman, C. D. Jones, J. O. Cross, R. Pindak, T. Bellini, and N. A. Clark. End-to-end stacking and liquid crystal condensation of 6-to-20-base pair DNA duplexes. *Science* **2007**, *318*, 1276–1279.

111. G. Zanchetta, T. Bellini, M. Nakata, and N. A. Clark. Physical polymerization and liquid crystallization of RNA oligomers. *J. Am. Chem. Soc.* **2008**, *130*, 12864–12865.

112. G. Zanchetta, M. Nakata, M. Buscaglia, T. Bellini, and N. A. Clark. Phase separation and liquid crystallization of complementary sequences in mixtures of nano DNA oligomers. *Proc. Natl. Acad. U.S.A.* **2008**, *105*, 1111–1117.

CHAPTER 15

Liquid Crystal-Based Chemical Sensors

JACOB T. HUNTER and NICHOLAS L. ABBOTT

Department of Chemical and Biological Engineering, University of Wisconsin, Madison, WI, USA

15.1 INTRODUCTION

This chapter presents an overview of recent advances in the use of liquid crystals (LCs) for sensing of small organic molecules from vapors (chemical sensing). The fundamental phenomenon underlying the approach to LC-based sensors addressed in this chapter is an adsorbate-driven anchoring transition in a film of LC, a phenomenon that has been known since the pioneering studies in the early 1990s by Pieranski and Jerome [1–4]. Recent studies have sought to realize chemical sensors based on LCs by using combinations of chemically tailored surfaces and LCs in order to engineer highly selective adsorbate-induced ordering transitions in the LCs. We also note that cholesteric LCs have been used for chemical sensing (with a change of pitch occurring upon absorption of an analyte), but approaches to chemical sensing based on cholesteric LCs lie beyond the scope of this chapter [5–14]. Finally, a number of studies with LCs as biological sensors have been reported over the past decade; however, we do not attempt to address those advances but rather refer the interested reader to relevant literature [15–24].

Figure 15.1 depicts two examples of adsorbate-driven ordering transitions that have been utilized as the basis of chemical sensors. In the first example, intermolecular interactions between the chemically functionalized surface and the LC lead to an initial azimuthal orientation of the LC on the surface (Figure 15.1A). Binding of the targeted analyte to the surface disrupts the intermolecular interactions of the surface with the LC, resulting in an azimuthal ordering transition of the LC to an orientation that is orthogonal to the initial orientation, as dictated by an anisotropic topography engineered into the chemically functionalized surface (Figure 15.1B).

Liquid Crystals Beyond Displays: Chemistry, Physics, and Applications, Edited by Quan Li.
© 2012 John Wiley & Sons, Inc. Published 2012 by John Wiley & Sons, Inc.

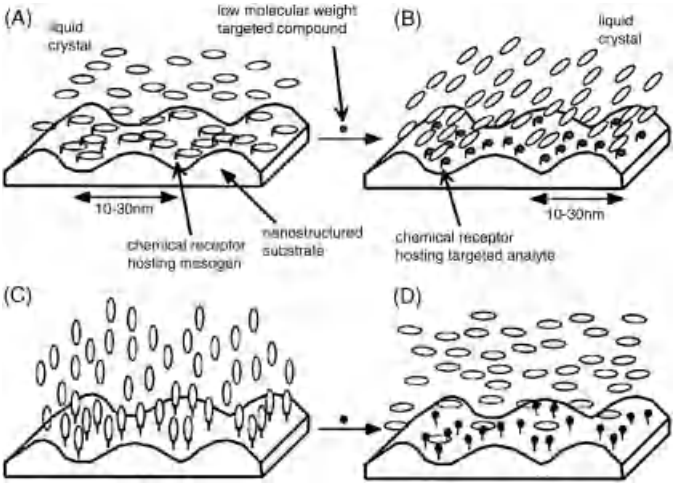

FIGURE 15.1 Schematic illustration of the competitive interaction between a LC and a low molecular weight targeted compound for a molecular receptor hosted on a surface with nanometer-scale topography. (A) Before exposure to a targeted compound, the molecules forming the LC mesogens bind with the molecular receptor and thereby anchor the LC in an azimuthal orientation that is orthogonal to the topography of the surface. (B) Binding of the targeted analyte to the surface-immobilized receptors displaces the LC from its interaction with the receptor shown in panel (A), and the LC orients along the topography. (C) A receptor-induced orientation of a LC that is perpendicular to a surface. (D) Binding of a targeted analyte to the surface-immobilized receptors displaces the LC from its interaction with the receptor shown in panel (A), and the LC tilts away from the surface normal. Reprinted with permission from Shah and Abbott [25]. Copyright 2001 AAAS.

As discussed later in this chapter, this type of azimuthal, adsorbate-induced ordering transition in a LC can lead to the detection of organoamine compounds. As shown in Figure 15.2A, prior to binding of the organoamine, a LC with a nitrile group (e.g. 4′-pentyl-4-biphenyl-carbonitrile, 5CB) will assume a uniform azimuthal orientation on a surface presenting oriented, carboxylic acid groups due to hydrogen bonding between the nitrile groups of the LC and the carboxylic acids. Upon exposure of the system to organoamines, the stronger acid-based interaction of the amine and carboxylic acid will displace the nitrile group from its hydrogen bonded state on the surface: this loss of hydrogen bonding results in an azimuthal ordering transition of the LC. As noted above, the final azimuthal orientation of the LC is dictated by topography of the surface [25–28].

The second class of ordering transitions to be discussed in this chapter as the basis of chemical sensors are those that involve a change in the out-of-plane orientation of the LC (Figure 15.1C and D). In this case, the intermolecular interactions between the chemical functionality presented by the surface and the LC lead to an initial homeotropic orientation of the LC. Upon binding of the adsorbate to the surface, the loss of these intermolecular interactions results in a tilting of the LC away from the homeotropic orientation. As detailed in the next section, a number of studies have

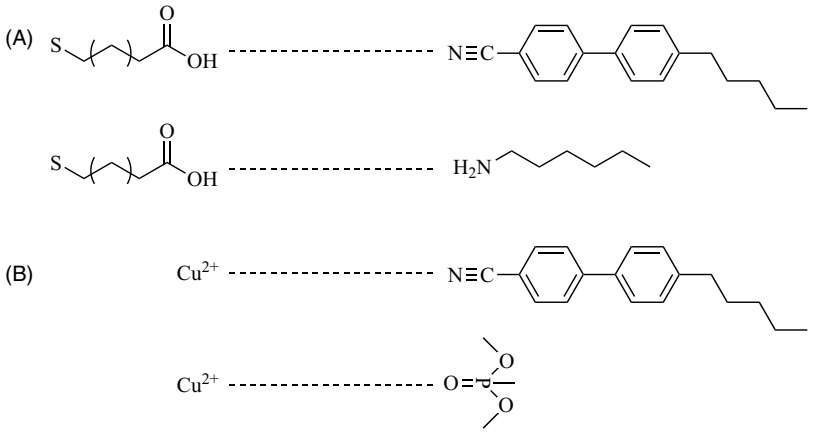

FIGURE 15.2 Schematic illustration of the intermolecular interactions that occur between chemically functionalized surfaces and either mesogens (top) or analytes (bottom) to create chemically responsive LC systems.

revealed that surfaces decorated with metal salts that coordinate with the nitrile groups of LCs, can be used to achieve the initial homeotropic orientation of the LC (Figure 15.2B). Upon exposure of the system to an analyte that coordinates to the metal ions with an affinity that is greater than the nitrile group (e.g., a molecule with a phosphoryl group), the nitrile–metal ion coordination interaction is lost, resulting in an ordering transition of the LC toward a planar orientation [25, 29–39].

The remainder of the chapter is as follows. In Section 15.2, we present design principles for chemically functionalized surfaces that can be used to create chemical sensors based on adsorbate-driven ordering transitions in LCs. In Section 15.3, we describe the analytic characteristics of LC sensors for detection of coordinating compounds. Section 15.4 addresses principles for LC sensors designed using acid–base interactions, and Section 15.5 presents some concluding perspectives.

15.2 DESIGN OF CHEMICALLY FUNCTIONALIZED SURFACES FOR USE IN LC-BASED CHEMICAL SENSORS

15.2.1 Surfaces Decorated with Metal Salts

As described in Section 15.1, surfaces that are decorated with metal salts represent a promising class of surfaces for chemical sensing because choice of the metal cation of the salt can be used to tune the selectivity of the LC-based sensor. In this section, we describe enabling studies of the orientations of LCs on surfaces decorated with metal salts, and summarize evidence that coordination interactions between the nitrile group of LCs and the metal cation play a central role in determining the orientations of the LCs.

The effect of varying the type of metal perchlorate salt on the LC orientation of nematic 5CB is shown in Figure 15.3. The figure shows polarized light micrographs

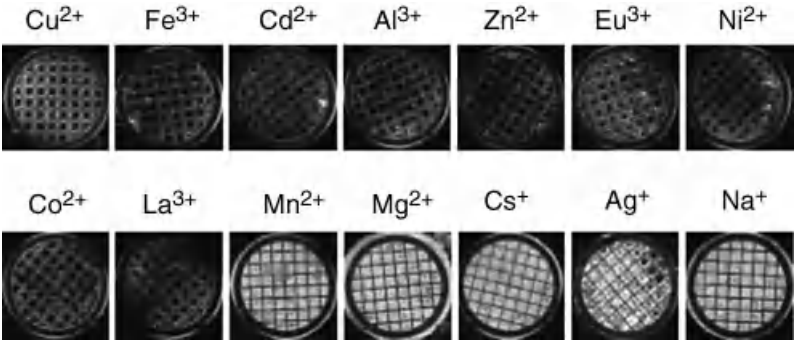

FIGURE 15.3 Optical images (crossed polars) of gold grids impregnated with 5CB supported on metal perchlorate salts. Each grid is 3 mm in diameter. Reprinted with permission from Yang et al. [38]. Copyright 2004 American Chemical Society.

(crossed polars) of nematic 5CB, placed into the pores of 20-μm-thick metallic grids, supported on metal perchlorate salt-decorated surfaces. Because the easy axis of the nematic phase of 5CB at the air interface is homeotropic, images that appear dark between crossed polars indicate that the anchoring of the 5CB on the metal salt surface was homeotropic. Thus, it is apparent from Figure 15.3 that the perchlorate salts of Cu^{2+}, Fe^{3+}, Cd^{2+}, Al^{3+}, Zn^{2+}, Eu^{3+}, Ni^{2+}, Co^{2+}, and La^{3+} all cause homeotropic anchoring whereas Mn^{2+}, Mg^{2+}, Cs^{+}, Ag^{+}, and Na^{+} lead to bright micrographs between cross polars, indicating a tilted or planar orientations of the LC at the metal salt decorated surfaces [38].

The results described in Figure 15.4A provide insight into the origins of the cation-dependent orientation of the LCs seen in Figure 15.3. These results reveal that the alignment of 5CB in contact with the metal perchlorate salts is dependent on the electron affinity of the metal cation, where metal cations with a high-electron affinity cause homeotropic orientations of the nematic phase of 5CB whereas metal cations with a low electron affinity cause planar or tilted orientations. Because the electron affinity of an ion is a measure of the ability of the ion to accept electrons from electron-donating ligands (e.g., nitrile groups), the correlation between the orientation of the LC and electron affinity of the metal ions suggests that the orientations of the LC result from the binding of the nitrile groups of the nematic phase of 5CB with the metal ions presented at these surfaces. This proposition is supported by infrared (IR) spectroscopy (Figure 15.4B). Whereas free nitrile groups give rise to a peak in the vibrational spectrum at $\sim 2227\ cm^{-1}$, a new peak is evident in the IR spectrum for surfaces presenting metal ions with high electron affinity. For example, for Cu^{2+} a peak is apparent at $\sim 2287\ cm^{-1}$, consistent with formation of a nitrile–Cu^{2+} complex [40–42]. We note that while the LC used in the IR studies shown in Figure 15.4B and C is 8CB, it possesses the same nitrile chemical functionality as 5CB [38].

Overall, these results along with similar results reported in the literature [31, 38] provide strong support for the proposition that metal salts can be used to prepare a class of chemically functionalized surfaces at which LCs can be oriented through

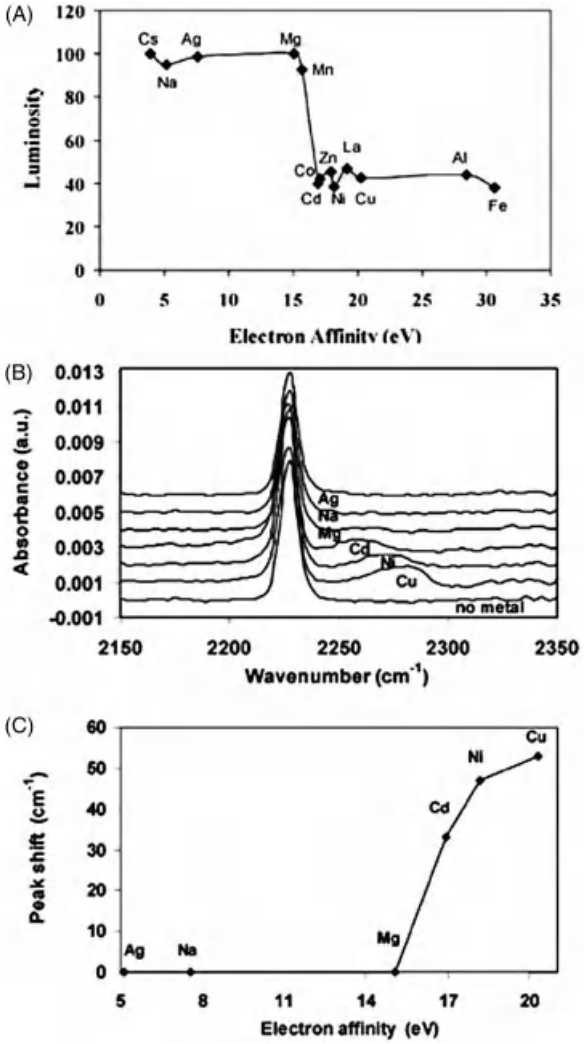

FIGURE 15.4 Characterization of the ordering of LCs on metal ion-decorated surfaces, and IR spectroscopy of those surfaces. (A) Intensity of light (crossed polars) transmitted through 5CB supported on various metal perchlorate salts as a function of the electron affinities of the metal ions. (B) and (C) IR spectra of films of 8CB spin coated onto surfaces presenting metal ions. The peak at 2227 cm^{-1} corresponds to the stretching vibration of the nitrile groups of 8CB in bulk. Reprinted with permission from Yang et al. [38]. Copyright 2004 American Chemistry Society.

metal ion–LC coordination interactions involving the nitrile group of the LC. As discussed below, these coordination interactions can be disrupted by targeted chemical analytes, thus leading to a class of LC-based sensors for coordinating compounds.

15.2.2 Surfaces Decorated with Carboxylic Acids

The principles underlying the design of LC-based sensors, as shown in Figure 15.1A and B, can be applied to surfaces with a wide range of chemical functionality. As a second example, we briefly mention the use of surfaces that present carboxylic acid groups [25, 26, 28]. As described in Section 15.3 such surfaces are useful for detecting basic analytes, such as organoamines.

The utility of carboxylic acid-functionalized surfaces for chemical sensing is the capacity of these surfaces to participate in hydrogen bonding with chemical functional groups present on the LC [27, 28]. As evidence that hydrogen bonding between the nitrile group of 5CB and a carboxylic acid-functionalized surface can orient a nematic phase, Figure 15.5 shows that conversion of a carboxylic acid into a sodium carboxylate group on a surface can trigger an azimuthal ordering transition in nematic 5CB. The carboxylic acid can serve as a hydrogen bond donor to the nitrile group of the LC whereas the carboxylate group cannot participate in a hydrogen bond with a nitrile group, consistent with a role for hydrogen bonding in the observed ordering transition. We note here that the surfaces presenting the carboxylic acid/carboxylate species in Figure 15.5 also possess an anisotropic topography. Thus, in the absence of hydrogen bonding, the azimuthal orientation of the LC was dominated by the influence of the topography of the surface [27].

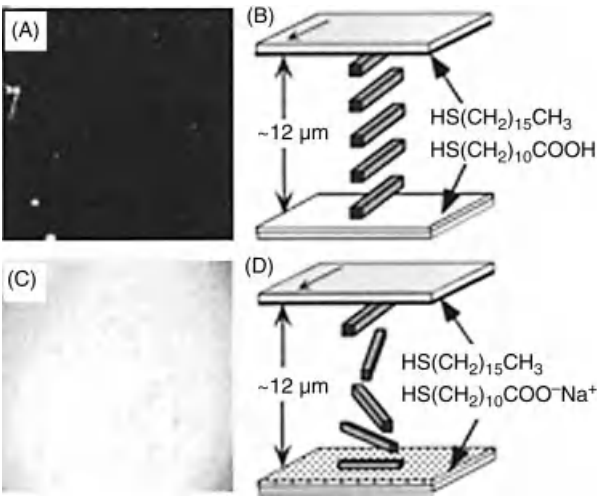

FIGURE 15.5 (A) and (C) Optical textures (crossed polars) formed by nematic 5CB within optical cells prepared with one surface supporting a self-assembled monolayer (SAM) formed from $H_3C(CH_2)_{15}SH$ and an opposing surface supporting a SAM formed from $HOOC(CH_2)_{10}SH$ that was pretreated at pH 3.2 (A) or 10.6 (C). (B) and (D) Schematic illustrations of the orientations of the LCs interpreted from the optical textures shown in panels (A) and (C), respectively. The arrows indicate the direction of deposition of gold onto the substrate. Reprinted with permission from Shah and Abbott [27]. Copyright 1999 American Chemical Society.

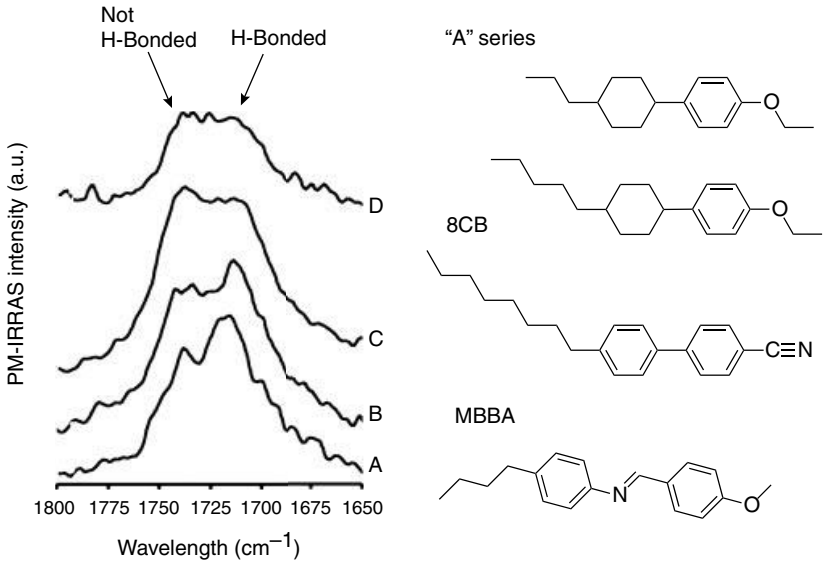

FIGURE 15.6 IR spectra of carboxylic acid-terminated SAMs before and after contact with LCs. SAMs formed from $HS(CH_2)_{11}COOH$ on gold (A), coated with the LC "A" series (B), 8CB (C), and MBBA (D). Also shown are the molecular structures of the mesogen. Reprinted with permission from Luk et al. [26]. Copyright 2004 Elsevier.

Additional spectroscopic evidence for hydrogen bonding is found in the IR spectra as shown in Figure 15.6. Figure 15.6A shows the IR spectra of the carboxylic acid-terminated surface prior to contact with one of three LCs. Inspection of Figure 15.6A reveals evidence of carbonyl groups within the monolayer in two environments (i.e., two peaks in the IR spectrum). These two peaks correspond to hydrogen bonded and non-hydrogen bonded carbonyl groups, with the hydrogen bonding occurring laterally within the monolayer. Contact of the "A" series LC (Figure 15.6B) with the carboxylic acid-terminated monolayer leads to very little change in the IR spectrum. This indicates that the "A" series LC does not form hydrogen bonds of sufficient strength to disrupt the intra-monolayer hydrogen bonding. In contrast, the IR spectra in (Figure 15.6C and D) indicate that both 5CB and MBBA do form hydrogen bonds with the carboxylic acid groups of the monolayer and thus disrupt the lateral network of hydrogen bonds between adjacent carboxylic acid groups on the surface [26]. Additional discussion regarding the interpretation of the IR spectra can be found in Ref. [26].

15.3 LC-BASED SENSORS FOR COORDINATING COMPOUNDS

The results presented in Section 15.2.1 clearly demonstrate that surfaces presenting metal cations can orient nitrile-containing LCs through metal ion–nitrile coordination

interactions. As discussed below, this type of surface presents the opportunity to trigger ordering transitions in LC films through exposure of the system to analytes that coordinate with metal cations more strongly than the nitrile groups of the LC. Figure 15.7 shows a first example of a LC-based chemical sensor for an organophosphonate compound, dimethylmethylphosphonate (DMMP). DMMP is a common simulant for chemical nerve agents and pesticides, and possesses a phosphoryl group that coordinates strongly to a range of transition metal cations (see Figure 15.2B). As shown in Figure 15.7A–D, prior to exposure to a vapor of DMMP, the film of nematic 5CB assumes a homeotropic orientation on the surface decorated with copper perchlorate, consistent with coordination between the Cu^{2+} ions and the nitrile groups of the LC. Following exposure to a vapor of DMMP, however, the LC film was observed

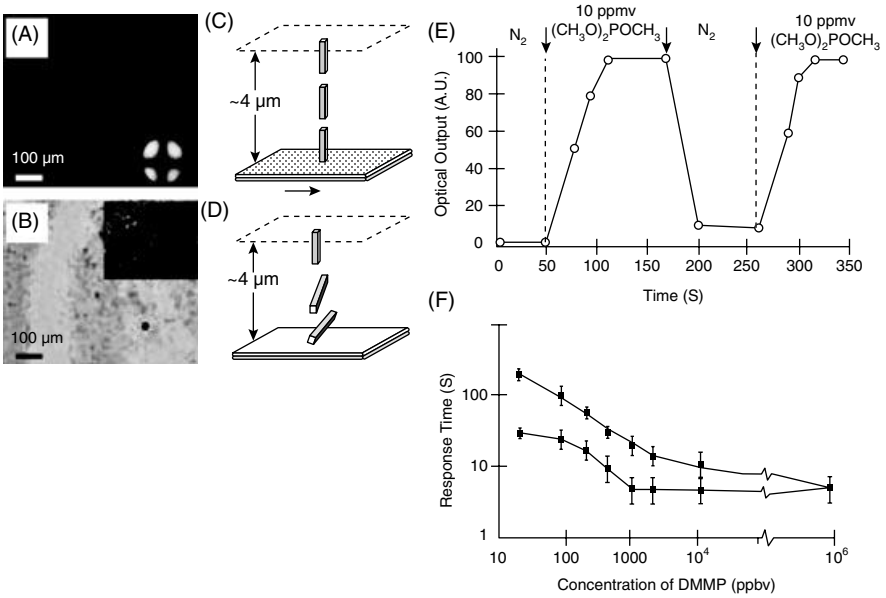

FIGURE 15.7 Optical textures (crossed polars) formed by a film of nematic 5CB on a surface that was (A) pretreated with 100 mM $Cu(ClO_4)_2$ and (B) pretreated as in panel (A) and subsequently exposed to a vapor concentration of 900 ppmv $(CH_3O)_2POCH_3$ (viewed at maximum transmission). The inset in panel (B) shows the optical texture at maximum extinction. (C) and (D) Schematic illustrations of the orientations of the LCs interpreted from the optical textures are shown in panels (A) and (B), respectively. The arrow in panel (C) indicates the direction of deposition of gold onto the substrate. (E) Reversibility of the optical brightness of a film of 5CB supported on a SAM formed from $HOOC(CH_2)_{10}SH$ that was pretreated as shown in panel (A) and exposed sequentially to 10 ppmv $(CH_3O)_2POCH_3$ and N_2. (F) Response times of films of 5CB (thickness 4 μm) supported on surfaces presenting Cu^{2+} that were exposed to $(CH_3O)_2POCH_3$ convected to the surface from a nozzle that was placed 2 mm (closed circle) or 3 mm (closed square) above the film of 5CB. The response time is defined as the time at which the onset of reorientation of the LC was visible to the naked eye. Reprinted with permission from Shah and Abbott [25]. Copyright 2001 AAAS.

to undergo an orientational transition that was driven by a change in anchoring of the LC at the metal salt-decorated surface. This response is consistent with displacement of the nitrile group of 5CB from its coordination interaction with Cu^{2+}, driven by competitive binding of DMMP (see below for spectroscopic evidence that supports this interpretation) [25].

Several key characteristics of the DMMP-induced ordering transitions are described in Figures 15.7E and F. Firstly, Figure 15.7E demonstrates that the DMMP-induced ordering transitions are reversible [25, 31, 33, 36, 39]. Secondly, Figure 15.7F reveals that the LC responds to concentrations of DMMP that are in the 10s of parts-per-billion range [25]. These ordering transitions are not limited to nematic 5CB, but smectic thin films of 8CB heated to a temperature very close to the nematic–smectic phase transition, when supported on Cu^{2+}-decorated surfaces, also undergo ordering transitions upon exposure to DMMP (Figure 15.8) [39]. In addition, the dynamics of the response of the film of smectic LC is dependent on the concentration of DMMP in the vapor phase that passes above the film of LC. Here we also note that the quantitative response of the LC sensor is strongly dependent on the geometry of the system, and that variations in the thickness of the LC film likely contribute to the scatter in the experimental data as shown in Figure 15.8 [39].

A key attribute of a chemical sensor is selectivity-detection of the targeted compound but not other compounds found in the sampling environment. Figure 15.9 shows an example of the selective response of LC-based chemical sensors to DMMP

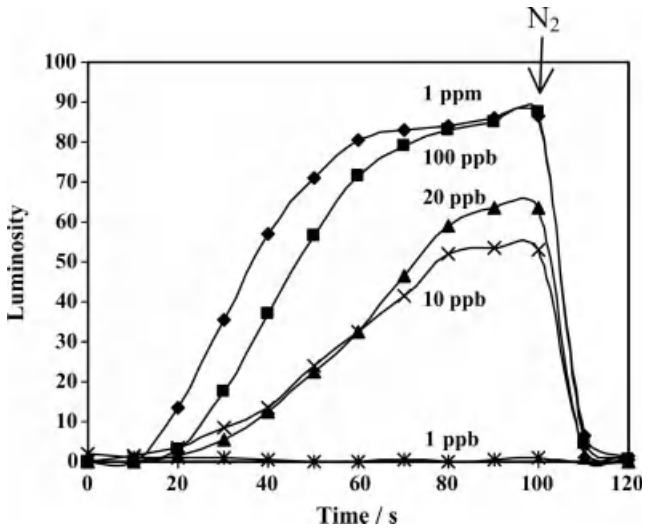

FIGURE 15.8 Time-dependent change in the intensity of light transmitted through a thin film of 8CB (thickness 900 nm) supported on Cu^{2+}-decorated surfaces following exposure to various concentrations of DMMP. Reprinted with permission from Yang et al. [39]. Copyright 2005 Elsevier.

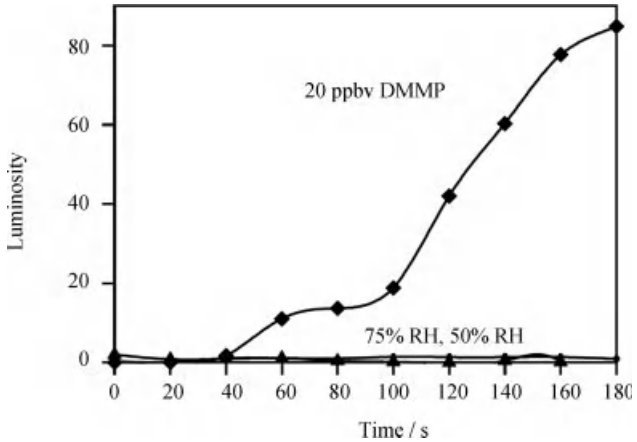

FIGURE 15.9 Effect of relative humidity (RH) on the visual appearance of a film of 8CB supported on Cu^{2+}-decorated surfaces. No change in luminosity was observed when the sample was exposed to pure N_2 with RH of 50% and 75%, respectively, whereas a 20 ppbv DMMP vaporous stream leads to an observable color change in the 8CB film in 60 s. Reprinted with permission from Yang et al. [39]. Copyright 2005 Elsevier.

as compared to water. Water is commonly problematic in chemical sensing because it is present in many sampling environments in high yet variable concentrations. Because water does not coordinate with Cu^{2+} with sufficient strength to displace the nitrile group of 8CB from its coordination with Cu^{2+}, the results in Figure 15.9 show that a LC sensor based on 8CB and Cu^{2+}-decorated surfaces does not respond to water present in air at concentrations that correspond to relative humidities of 50% or 75% [39].

The proposition that the ordering transitions shown in Figures 15.7–15.9 result from ligand exchange reactions at the metal ion-decorated surfaces is supported by IR spectroscopy [38]. Prior to exposure to DMMP, two nitrile absorption peaks are evident in the IR spectrum (Figure 15.10A, bottom curve). As discussed above, the peak at 2227 cm^{-1} corresponds to free nitrile groups and the peak at 2287 cm^{-1} corresponds to nitrile groups coordinated with Cu^{2+}. Following exposure to DMMP (Figure 15.10A, middle curve), the peak at 2287 cm^{-1}, present prior to exposure, disappears. The loss of this peak is consistent with displacement of the nitrile group of the 8CB from its coordination with the Cu^{2+} due to competitive binding of DMMP with the Cu^{2+} ion. Finally, following a nitrogen purge of the system the nitrile peak corresponding to the coordinated state of the nitrile group reappears in the IR spectrum (Figure 15.10A, top curve). The reappearance of this peak is consistent with the reversible response of the LC film to DMMP, as shown in Figures 15.7 and 15.8. The connection proposed between the ordering transitions of nitrile containing LCs and IR spectroscopy is further strengthened by the IR spectra shown in Figure 15.10B, obtained using surfaces presenting Ni^{2+} ions. Whereas Ni^{2+}-decorated surfaces cause homeotropic orientations of nitrile-containing LCs

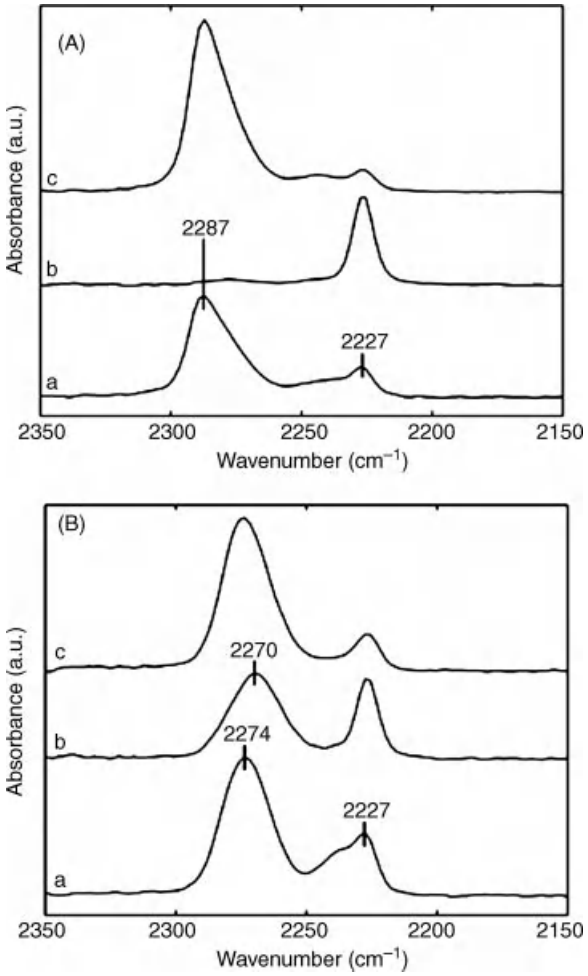

FIGURE 15.10 Infrared spectroscopy characterizing the response of 8CB supported on surfaces decorated with Cu^{2+} or Ni^{2+} ions to DMMP. (A) IR spectra of a thin film of 8CB on a surface presenting Cu^{2+} perchlorate salts (a) before and (b) during exposure to 10 ppm DMMP, and (c) after a 30-min air purge. (B) IR spectra of a thin film of 8CB on a surface supporting Ni^{2+} perchlorate salts (a) before and (b) during exposure to 10 ppm DMMP, and (c) after a 30-min air purge. Reprinted with permission from Cadwell et al. [31]. Copyright 2006 American Chemical Society.

(see Figure 15.3), such films of LCs do not undergo ordering transitions upon exposure to DMMP. These observations are consistent with the IR spectra in Figure 15.10B, where exposure of a film of 8CB to DMMP does not result in elimination of the peak corresponding to the coordinated state of the nitrile group. That is, the Ni^{2+}–nitrile coordination complex is not disrupted by DMMP to the extent that is observed with Cu^{2+}-decorated surfaces. Overall, these results and

others reported in the literature [31, 32, 38, 40–42] support our conclusion that ligand exchange reactions underlie the sensitive and selective ordering transitions of LCs that can be observed on surfaces decorated with metal ions.

15.4 LC SENSORS DESIGNED TO REPORT ACID–BASE INTERACTIONS

To illustrate the generality of LC-based sensors that use chemically functionalized surfaces, we next describe a class of sensors that report acid–base interactions [25, 26, 28]. Such sensors can report important classes of compounds such as organoamines compounds that can be used, for example, to indicate the freshness of foods [25, 28]. As discussed in the context of Figures 15.5 and 15.6, past studies have provided evidence that hydrogen bonding between carboxylic acid-functionalized surfaces and nitrile-containing LCs can lead to preferred azimuthal orientations of supported LC films [26, 27]. The binding of an alkylamine to these surfaces, which results from an acid–base reaction between the amine and carboxylic acid, leads to the disruption of the initial hydrogen bonded state of the LC and thus an azimuthal ordering transition (Figure 15.11). As noted above, in the absence of the hydrogen

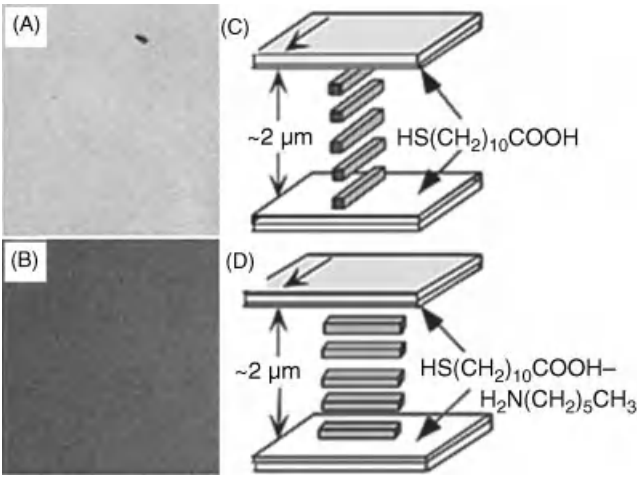

FIGURE 15.11 (A) and (B) Interference color of a film of nematic 5CB supported on a SAM formed from $HOOC(CH_2)_{10}SH$ before (A) and after (B) exposure to n-$H_2N(CH_2)_5CH_3$. (C) Schematic illustration of the orientation of the LC in contact with a carboxylic acid monolayer that is consistent with interference colors shown in panel (A). The bold arrow indicates the direction of deposition of gold onto the substrate. (D) Schematic illustration of the orientation of the LC in contact with the hexylamine-reacted carboxylic acid monolayer that is consistent with the interference colors shown in panel (B). Reprinted with permission from Shah and Abbott [28]). Copyright 2003 American Chemical Society. (*See the color version of this figure in Color Plates section.*)

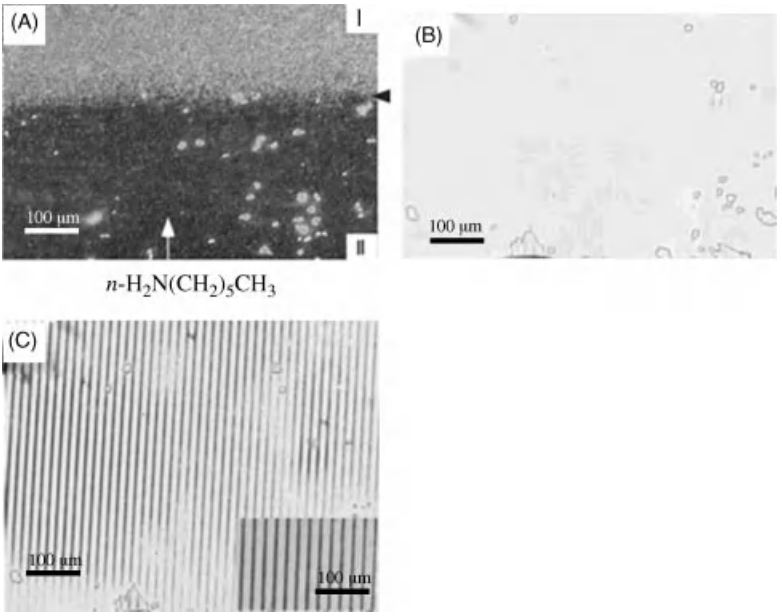

FIGURE 15.12 Optical images formed by 5CB within optical cells (12 μm) fabricated with surfaces presenting carboxylic acid. The cells were exposed to 750 ppmv n-$H_2N(CH_2)_5CH_3$ at the edge shown at the bottom of the image. Panel (A) shows the optical textures of 5CB during diffusion of n-$H_2N(CH_2)_5CH_3$ across the cell. In region I, the presentation of carboxylic acid causes a 90° twist distortion in the LC. In region II, n-$H_2N(CH_2)_5CH_3$ bound to the carboxylic acid groups results in a uniform orientation of the LC. The arrow indicates the limit of the diffusion front of n-$H_2N(CH_2)_5CH_3$. (B) and (C) Optical textures (cross polars) formed by nematic 5CB within optical cells (12 μm) prepared with one surface supporting a SAM formed from $H_3C(CH_2)_{14}SH$ and an opposing surface supporting a SAM patterned using HOOC $(CH_2)_{10}SH$ and $H_3C(CH_2)_{11}SH$ pretreated at pH 3.2 (B) prior to exposure to n-$H_2N(CH_2)_5CH_3$ and (C) after exposure for 8 min to 750 ppmv of n-$H_2N(CH_2)_5CH_3$. The inset in panel (C) is a magnified region showing the formation of the patterned region upon exposure to the analyte. Reprinted with permission from Shah and Abbott [28]. Copyright 2003 American Chemical Society.

bonding interactions, the topographical features of the surface define the azimuthal orientation of the LC [28].

Exposure of a film of LC confined between two surfaces presenting carboxylic acids groups, when exposed to a vapor of hexylamine, can cause an ordering transition that propagates laterally across the film of LC (Figure 15.12A). If the surface is patterned with stripes of carboxylic acids groups that are separated by methyl-terminated areas, the ordering transition triggered by the hexylamine can lead to patterned orientations of the LC and a diffraction grating (Figure 15.12B and C) [28]. Figure 15.13 illustrates the progression of the ordering transition across the LC sample is consistent with diffusion of the hexylamine laterally across

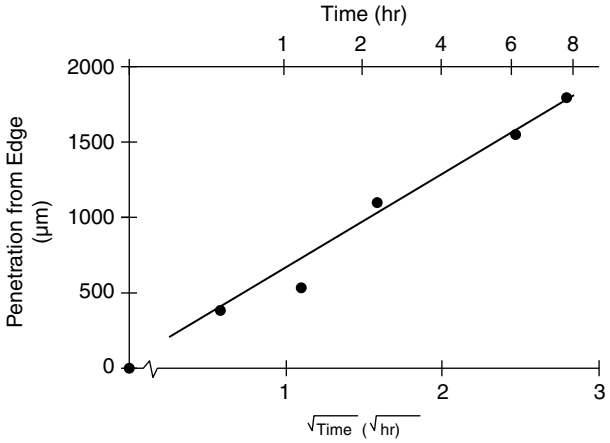

FIGURE 15.13 Penetration distance (from the edge of a LC cell) of n-$H_2N(CH_2)_5CH_3$ as a function of exposure time and as a function of the square root of exposure time. Reprinted with permission from Shah and Abbott [28]. Copyright 2003 American Chemical Society.

the film. The LC film, thus, provides a diffusion cell in which transport of the gas across the cell is readily visualized via an ordering transition that is induced in the LC [28].

15.5 CONCLUDING COMMENTS

We end this chapter by making several additional observations regarding the promise and opportunity defined by LC-based sensors. Firstly, whereas many of the results presented above were obtained using a model organophosphonate compound, we have also demonstrated that the principles described above can be extended to live nerve agents, which are also organophosphonates [25, 31, 38]. As shown in Figure 15.14, using surfaces presenting Al^{3+}, Zn^{2+}, and Fe^{3+}, it is possible to use LCs to detect the nerve agents GB, GD, GA, and VX [32]. Secondly, we comment that there exists a substantially unexplored opportunity to design LCs that are tailored for chemical sensing. The experiments described above were largely based on commercially available LCs that were designed largely with a view to application in LC displays, and there is little reason to believe that they represent optimal designs for LC-based chemical sensors. As a first example of an attempt to tailor the design of a mesogen for chemical sensing, we show in Figure 15.15 results obtained using a mesogen that was synthesized to contain two nitrile groups [34]. The incorporation of two coordinating nitrile groups into a mesogen resulted in observations of homeotropic orientations of the LC on surfaces presenting low densities of Cu^{2+} ions (densities that did not cause homeotropic orientation of 5CB) (Figure 15.15). However, the strong coordination of the mesogens to the

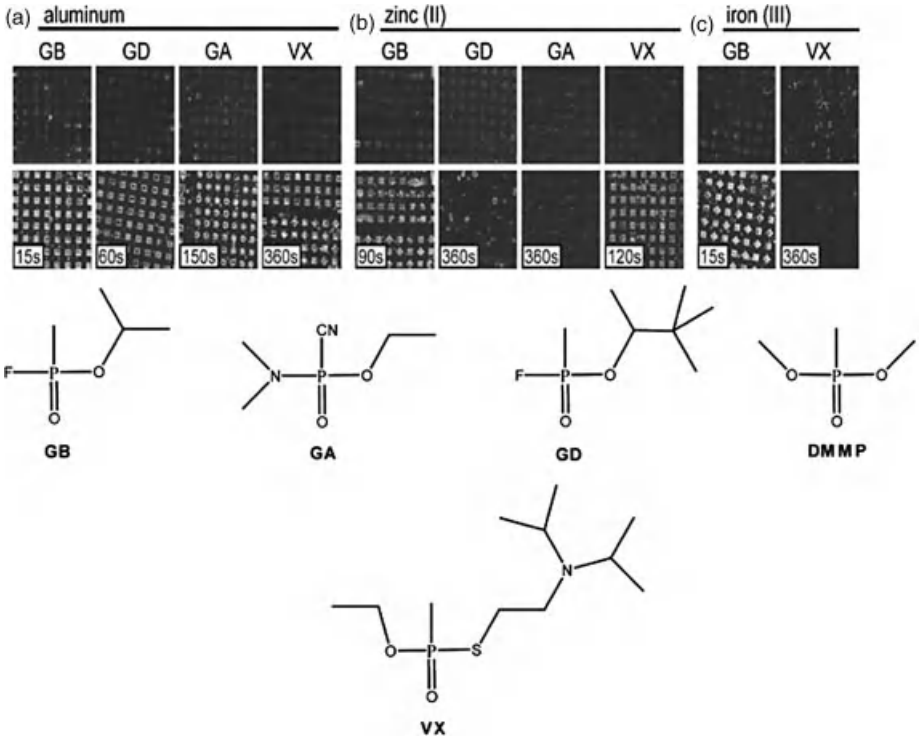

FIGURE 15.14 Optical images (crossed polars) of the nitrile containg LC E7 supported on perchlorate salts of (a) aluminum(III), (b) zinc(II), and (c) iron(III) before (top row) and after (bottom row) exposure to organophosphorous nerve agents. The duration of agent exposure is indicated. Imaged areas are approximately 7.5 mm by 7.5 mm. Reprinted with permission from Cadwell et al. [32]. Copyright 2007 Elsevier.

Cu^{2+}-decorated surface also inhibited ordering transitions triggered by DMMP, that is, DMMP was not able to readily displace the dinitrile-based mesogens from coordination with the Cu^{2+} (Figure 15.16). This example serves to illustrate how the attributes of LC-based sensors can be potentially improved through the tailoring of the design of mesogens [34]. Finally, we comment that the realization of practical LC-based sensors requires that the systems be stable over long periods of time. We have recently reported on the time-dependent behaviors of LC sensors at surfaces decorated with metal salts (Figure 15.17) [33]. Those studies revealed that the stability of the sensor is strongly dependent on the amount of metal salt present on the surface. We have also found evidence that partial dissolution of the metal salt into the LC leads to formation of an electrical double layer that can influence the response of the LC-based sensor [33]. Such phenomena at these complex LC interfaces are not yet fully understood and define a fertile territory for future investigations.

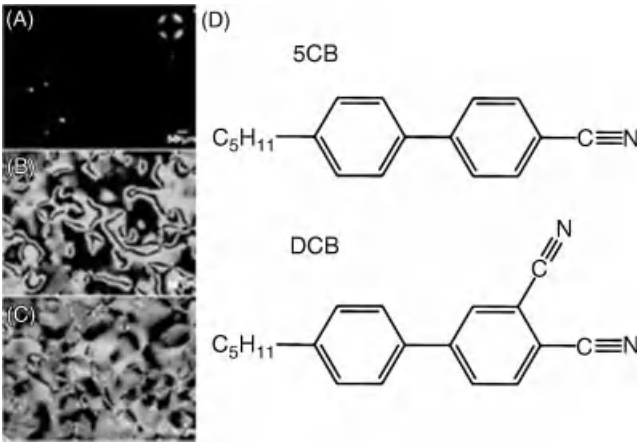

FIGURE 15.15 (A) Optical micrographs (crossed polars) of a thin film of nematic LC mixture containing 2 wt.% DCB (D, lower structure) in 5CB (D, upper structure) confined between SAMs formed from $HOOC(CH_2)_{10}SH$ that were pretreated sequentially with aqueous solution of 0.01 (N) NaOH and 50mM$Cu(ClO_4)_2$, followed by a thorough rinse with ethanol. The inset in panel (A) is a conoscopic image indicating homeotropic alignment. (B) and (C) Optical micrographs (crossed polars) of LCs containing 2 wt.% DCB in 5CB confined within optical cells with surfaces prepared from either (B) SAMs formed from $HOOC(CH_2)_{10}SH$ or (C) SAMs formed from $HOOC(CH_2)_{10}SH$ and pretreated with 0.01 (N) NaOH. Reprinted with permission from Pal et al. [34]. Copyright 2010 American Chemical Society.

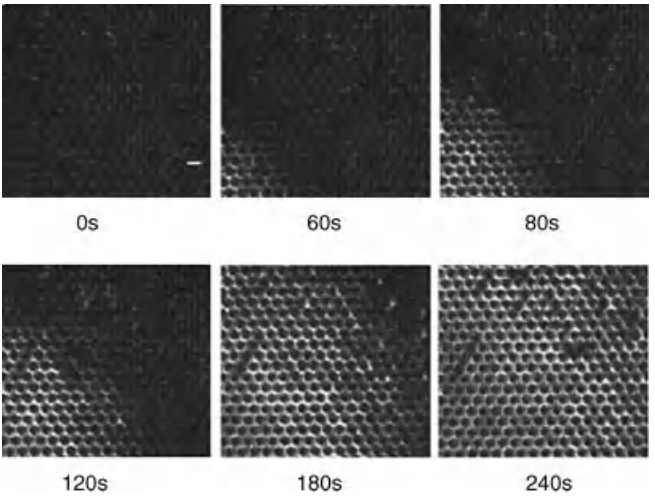

FIGURE 15.16 Optical images (crossed polars) of a mixture of 5CB containing 2.0 wt.% DCB (see Figure 15.15) showing the time-dependent response of the LCs hosted in micropillar arrays to a vapor of DMMP (Scale bar = 50 μm). Reprinted with permission from Pal et al. [34]. Copyright 2010 American Chemical Society.

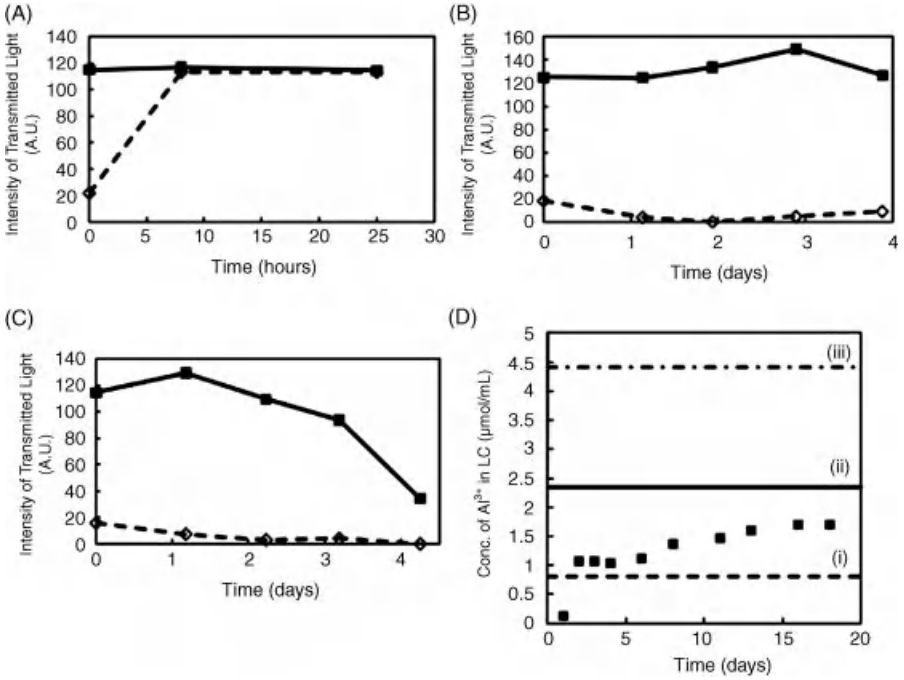

FIGURE 15.17 (A) Quantification of the optical response of a film of nematic 5CB supported on a surface decorated with 0.39 ng/mm^2 Al perchlorate. The solid data points indicate the response of the LC to exposure to 5 ppm DMMP; the open data points show the optical response of the LC prior to exposure to DMMP. (B) Quantification of the optical response of a film of nematic 5CB supported on a surface decorated with 1.13 ng/mm^2 Al perchlorate. The solid data points indicate the response of the LC to exposure to 5 ppm DMMP; the open data points show the optical response of the LC prior to exposure to DMMP. (C) Quantification of the optical response of a film of nematic 5CB supported on a surface decorated with 2.14 ng/mm^2 Al perchlorate. The solid data points indicate the response of the LC to exposure to 5 ppm DMMP; the open data points show the optical response of the LC prior to exposure to DMMP. (D) Concentration of Al^{3+} dissolved in 5CB as a function of time of contact of the LC with excess Al perchlorate salt. The horizontal lines indicate the concentration of Al^{3+} that would be present in a 20 μm thick film of LC if all metal salt on the surface dissolved into the LC; (i) 0.39 ng/mm^2 Al perchlorate, (ii) 1.13 ng/mm^2 Al perchlorate, and (iii) 2.14 ng/mm^2 Al perchlorate. Reprinted with permission from Hunter et al. [33]. Copyright 2010 American Chemical Society.

ACKNOWLEDGMENTS

This study was funded by the Army Research Office through Grants W911NF-07-1-0446 and W911NF-10-1-0181 as well as by the National Science Foundation through grants DMR-0520527 and DMR-0602570.

REFERENCES

1. P. Pieranski, B. Jerome, and M. Gabay. Adsorption-induced anchoring transitions. *Mol. Cryst. Liq. Cryst. Incorporating Nonlinear Optics* **1990**, *179*, 285–315.
2. B. Jerome and Y. R. Shen. Anchoring of nematic liquid crystals on mica in the presence of volatile molecules. *Phys. Rev. E* **1993**, *48*, 4556.
3. J. Bechhoefer, J. L. Duvail, L. Masson, B. Jérme, R.M. Hornreich, and P. Pieranski. Critical behavior in anchoring transitions of nematic liquid crystals. *Phys. Rev. Lett.* **1990**, *64*, 1911.
4. J. Bechhoefer, R. M. Hornreich, B. Jérme, and P. Pieranski. Systematic studies of the anchoring transition in nematic liquid crystals. *Phys. Rev. A*, **1990**, *41*, 3187.
5. T. J. Novak, E. J. Poziomek, and R. A. Mackay. Use of anisotropic materials as chemical detectors. *Anal. Lett.* **1972**, *5*, 187–192.
6. E. J. Poziomek, T. J. Novak, and R. A. Mackay. Transparency characteristics of several cholesteryl esters. *Mol. Cryst. Liq. Cryst.* **1972**, *15*, 283–295.
7. F. L. Dickert, A. Haunschild, P. Hofmann, and G. Mages. Molecular recognition of organic solvents and ammonia: shapes and donor properties as sensor effects. *Sensors and Actuators B: Chemical* **1992**, *6*, 25–28.
8. F. L. Dickert, A. Haunschild, and P. Hofmann, Cholesteric liquid crystals for solvent vapour detection — Elimination of cross sensitivity by band shape analysis and pattern recognition. *Fresenius' J. Anal. Chem.* **1994**, *350*, 577–581.
9. A. D. Rey. Theory and simulation of gas diffusion in cholesteric liquid crystal films. *Mol. Cryst. Liq. Cryst.* **1997**, *293*, 87–109.
10. D. A. Winterbottom, R. Narayanaswamy, and I. M. Raimundo. Cholesteric liquid crystals for detection of organic vapours. *Sensors and Actuators B: Chemical* **2003**, *90*, 52–57.
11. N. Kirchner, L. Zedler, T. G. Mayerhofer, and G. J. Mohr. Functional liquid crystal films selectively recognize amine vapours and simultaneously change their colour. *Chem. Commun.* **2006**, 1512–1514.
12. L. Sutarlie, H. Qin, and K.-L. Yang, Polymer stabilized cholesteric liquid crystal arrays for detecting vaporous amines. *Analyst* **2010**, *135*, 1691–1696.
13. L. Sutarlie, J. Y. Lim, and K.-L. Yang, Cholesteric liquid crystals doped with dodecylamine for detecting aldehyde vapors. *Anal. Chem.* **2011**, *83*, 5253–5258.
14. E. J. Poziomek, T. J. Novak, and R. A. Mackay. Use of liquid crystals as vapor detectors. *Mol. Cryst. Liq. Cryst.* **1974**, *27*, 175–185.
15. Y. Bai and N. L. Abbott. Recent advances in colloidal and interfacial phenomena involving liquid crystals. *Langmuir* **2011**, *27*, 5719–5738.
16. X. Bi, S. L. Lai, and K.-L. Yang. Liquid crystal multiplexed protease assays reporting enzymatic activities as optical bar charts. *Anal. Chem.* **2009**, *81*, 5503–5509.
17. J. M. Brake, M. K. Daschner, Y.-Y. Luk, and N. L. Abbott. Biomolecular interactions at phospholipid-decorated surfaces of liquid crystals. *Science* **2003**, *302*, 2094–2097.
18. T. Govindaraju, P. J. Bertics, R. T. Raines, and N. L. Abbott. Using measurements of anchoring energies of liquid crystals on surfaces to quantify proteins captured by immobilized ligands. *J. Am. Chem. Soc.* **2007**, *129*, 11223–11231.
19. V. K. Gupta, J. J. Skaife, T. B. Dubrovsky, and N. L. Abbott. Optical amplification of ligand–receptor binding using liquid crystals. *Science* **1998**, *279*, 2077–2080.

20. C.-H. Jang, L.-L. Cheng, C. W. Olsen, and N. L. Abbott. Anchoring of nematic liquid crystals on viruses with different envelope structures. *Nano Lett*. **2006**, *6*, 1053–1058.
21. C.-H. Jang, M. L. Tingey, N. L. Korpi, G. J. Wiepz, J. H. Schiller, P. J. Bertics, and N. L. Abbott. Using liquid crystals to report membrane proteins captured by affinity microcontact printing from cell lysates and membrane extracts. *J. Am. Chem. Soc.* **2005**, *127*, 8912–8913.
22. A. D. Price and D. K. Schwartz. DNA hybridization-induced reorientation of liquid crystal anchoring at the nematic liquid crystal/aqueous interface. *J. Am. Chem. Soc.* **2008**, *130*, 8188–8194.
23. S. V. Shiyanovskii, T. Schneider, I. I. Smalyukh, T. Ishikawa, G. D. Niehaus, K. J. Doane, C. J. Woolverton, and O. D. Lavrentovich. Real-time microbe detection based on director distortions around growing immune complexes in lyotropic chromonic liquid crystals. *Phys. Rev. E* **2005**, *71*, 020702.
24. L. S. Birchall, R. V. Ulijn, and S. J. Webb. A combined SPS-LCD sensor for screening protease specificity. *Chem. Commun.* **2008**, 2861–2863.
25. R. R. Shah and N.L. Abbott. Principles for measurement of chemical exposure based on recognition-driven anchoring transitions in liquid crystals. *Science* **2001**, *293*, 1296–1299.
26. Y. Y. Luk, K. L. Yang, K. Cadwell and N. L. Abbott. Deciphering the interactions between liquid crystals and chemically functionalized surfaces: Role of hydrogen bonding on orientations of liquid crystals. *Surf. Sci.* **2004**, *570*, 43–56.
27. R. R. Shah and N. L. Abbott. Using liquid crystals to image reactants and products of acid-base reactions on surfaces with micrometer resolution. *J. Am. Chem. Soc.* **1999**, *121*, 11300–11310.
28. R. R. Shah and N.L. Abbott. Orientational transitions of liquid crystals driven by binding of organoamines to carboxylic acids presented at surfaces with nanometer-scale topography. *Langmuir* **2003**, *19*, 275–284.
29. X. Bi and K.-L. Yang. Real-time liquid crystal-based glutaraldehyde sensor. *Sens. Actuators B: Chem.* **2008**, *134*, 432–437.
30. M. L. Bungabong, P. B. Ong, and K.-L. Yang. Using copper perchlorate doped liquid crystals for the detection of organophosphonate vapor. *Sens. Actuators B: Chem.* **2010**, *148*, 420–426.
31. K. D. Cadwell, M. E. Alf, and N. L. Abbott. Infrared spectroscopy of competitive interactions between liquid crystals, metal salts, and dimethyl methylphosphonate at surfaces. *J. Phys. Chem. B* **2006**, *110*, 26081–26088.
32. K. D. Cadwell, N. A. Lockwood, B. A. Nellis, M. E. Alf, C. R. Willis, and N. L. Abbott. Detection of organophosphorous nerve agents using liquid crystals supported on chemically functionalized surfaces. *Sens. Actuators B: Chem.* **2007**, *128*, 91–98.
33. J. T. Hunter, S. K. Pal, and N. L. Abbott. Adsorbate-induced ordering transitions of nematic liquid crystals on surfaces decorated with aluminum perchlorate salts. *ACS Appl. Mater. Interf.* **2010**, *2*, 1857–1865.
34. S. K. Pal, C. Acevedo-Vélez, J. T. Hunter, and N. L. Abbott. Effects of divalent ligand interactions on surface-induced ordering of liquid crystals. *Chem. Mater.* **2010**, *22*, 5474–5482.
35. A. Sen and B. R. Acharya. Alignment of nematic liquid crystals at inorganic salt-liquid crystal interfaces. *Liq. Cryst.* **2011**, *38*, 495–506.

36. S. S. Sridharamurthy, K. D. Cadwell, N. L. Abbott, and H. Jiang. A microstructure for the detection of vapor-phase analytes based on orientational transitions of liquid crystals. *Smart Materials & Structures* **2008**, *17*, 4.
37. H. J. VanTreeck, D. R. Most, B. A. Grinwald, K. A. Kupcho, A. Sen, M. D. Bonds, and B. R. Acharya. Quantitative detection of a simulant of organophosphonate chemical warfare agents using liquid crystals. *Sens. Actuators B: Chem.* **2011**, *158*, 104–110.
38. K. L. Yang, K. Cadwell, and N. L. Abbott. Mechanistic study of the anchoring behavior of liquid crystals supported on metal salts and their orientational responses to dimethyl methylphosphonate. *J. Phys. Chem. B* **2004**, *108*, 20180–20186.
39. K. L. Yang, K. Cadwell, and N. L. Abbott. Use of self-assembled monolayers, metal ions and smectic liquid crystals to detect organophosphonates. *Sens. Actuators B: Chem.* **2005**, *104*, 50–56.
40. E. Escalona Platero, M. Peñarroya Mentruit, and C. Morterra. Fourier transform infrared spectroscopy study of CD3CN adsorbed on pure and doped γ-alumina. *Langmuir* **1999**, *15*, 5079–5087.
41. Y. Marcus. Preferential solvation of silver(I), copper(I) and copper(II) ions in aqueous acetonitrile. *J. Chem. Soc., Dalton Trans.* **1991**, 2265–2268.
42. A. G. Pelmenschikov, R. A. van Santen, J. Janchen, and E. Meijer. Acetonitrile-d3 as a probe of Lewis and Broensted acidity of zeolites. *J. Phys. Chem.* **1993**, *97*, 11071–11074.

CHAPTER 16

Polymer Stabilized Cholesteric Liquid Crystal for Switchable Windows

DENG-KE YANG

Chemical Physics Interdisciplinary Program and Liquid Crystal Institute, Kent State University, Kent, OH, USA

16.1 INTRODUCTION

Liquid crystals (LCs) have been used to make switchable windows. The state-of-the-art technologies are polymer dispersed liquid crystals (PDLCs) and polymer stabilized cholesteric texture (PSCT) light shutters [1–4], which were developed at Kent State University. In PDLCs, liquid crystals exist in micron size droplets which are dispersed in an isotropic polymer. The concentration of the polymer is comparable to that of the liquid crystal. The polymer forms a continuous medium and the liquid crystal droplets are isolated from one another. The rod-like liquid crystal exhibits optical birefringence: ordinary refractive index n_o for light polarized perpendicular to the liquid crystal and extraordinary refractive index n_e for light polarized parallel to the liquid crystal. The polymer is optically isotropic with the refractive index n_P. The materials are chosen in such a way that $n_P = n_o < n_e$. In the absence of an electric field, either the droplet director orients randomly throughout the PDLCs or the liquid crystal director inside the droplet orients in all directions as shown in Figure 16.1a. When light propagates through a LC droplet, the encountered effective refractive index n_{eff}, which is between n_o and n_e, is different from the refractive index n_P of the polymer. Therefore light is scattered. When a sufficiently high electric field is applied across the PDLC film, the LC is aligned uniformly along the applied field (film normal direction) as shown in Figure 16.1b. For normal incident light, when it propagates through the LC droplet, the encountered effective refractive index is n_o which is matched to the refractive index n_P of the polymer. Therefore light is transmitted.

In a PSCT, the concentration of the cholesteric liquid crystal (ChLC) is usually much higher than that of the polymer. The liquid crystal forms a continuous medium

Liquid Crystals Beyond Displays: Chemistry, Physics, and Applications, Edited by Quan Li.
© 2012 John Wiley & Sons, Inc. Published 2012 by John Wiley & Sons, Inc.

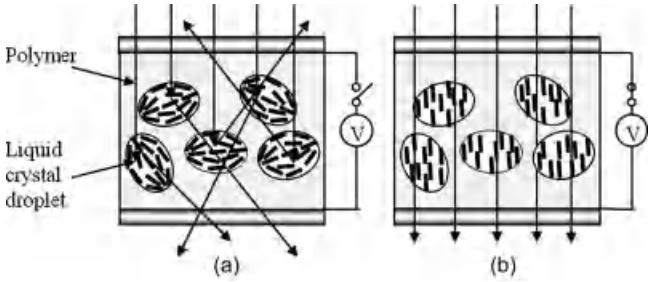

FIGURE 16.1 Schematic diagram of the PDLC switchable window: (a) scattering state in the absence of electric field and (b) transparent state in the presence of electric field.

while the polymer forms a network dispersed in the liquid crystal. Because of its helical structure, the ChLC exhibits three states: planar texture, focal conic texture, and homeotropic texture. The planar and homeotropic textures are uniform single domain structures and transmit light in broad wavelength regions. The focal conic texture is a poly-domain structure and scatters light. The dispersed polymer network stabilizes one or two of the three states in the absence of an electric field. An externally applied electric field can switch the PSCT between a scattering state and a transparent state.

There are many research papers, review papers, and books dedicated to PDLCs [5–9]. Since PSCTs have some superior optical properties, such as higher transmittance and larger viewing angle than the counterpart PDLC, this monograph will not discuss PDLCs further. Instead, it will concentrate on PSCT switchable windows.

Scattering liquid crystal materials have been used for displays as well as for switchable windows because of the properties listed below. First, they do not use polarizers, and therefore they have high transmittance (~90%) and are compatible with flexible substrates with non-uniform birefringence. Second, they can be manufactured in large formats using a roll-to-roll process. Third, they have fascinating visual effects, no mechanically moving parts and instant switching. They can be used to make switchable windows to control not only privacy but also energy flow. In many situations privacy control is needed. Use in bathroom windows is such an example. The window usually should be transparent for open view and opaque occasionally for privacy. Figure 16.2 shows a liquid crystal switchable window manufactured by Polytronix Inc. Contemporary office buildings and residential houses have many windows. On bright sunny days, sunlight entering the buildings through windows attributes a lot to heating, which costs a significant amount of energy in air conditioning. Liquid crystal switchable windows can be used as architectural windows to control energy flow. When internal temperature is low (such as a cold winter day), the window is switched to the transparent state to allow sunlight to warm the building. In a hot summer day, the window is switched to the scattering state to stop sunlight entering the building, which reduces the heating effect. Also on a cold winter night, the window is switched to the scattering state to stop heat leakage

FIGURE 16.2 Photographs of liquid crystal switchable office window manufactured by Polytronix Inc. Photo courtesy of Polytronix Inc.

by blackbody radiation out of the window. Figure 16.3 shows an experimental greenhouse with switchable liquid crystal window.

16.2 CHOLESTERIC LIQUID CRYSTAL

A ChLC possesses a helical structure where the liquid crystal twists around a helical axis as shown in Figure 16.4a [10–13]. The distance over which the liquid crystal rotates 360° is the pitch P. Depending on the orientations of the liquid crystal and the helical axis, the ChLC has three different states with different optical properties as shown in Fig. 16.4. In the planar texture, the LC possesses the helical structure with the helical axis parallel to the cell normal. In this state the liquid crystal exhibits a reflection band located at the wavelength $\lambda_o = [(n_e + n_o)/2]P$ with the bandwidth $\Delta\lambda = (n_e - n_o)P$. Outside of the reflection band, the material is transparent. In the focal conic texture, the helical structure is preserved. The orientation of the helical

FIGURE 16.3 Photographs of green house with liquid crystal switchable window in Cleveland Botanic Garden. Photo courtesy of Cleveland Botanic Garden. (*See the color version of this figure in Color Plates section.*)

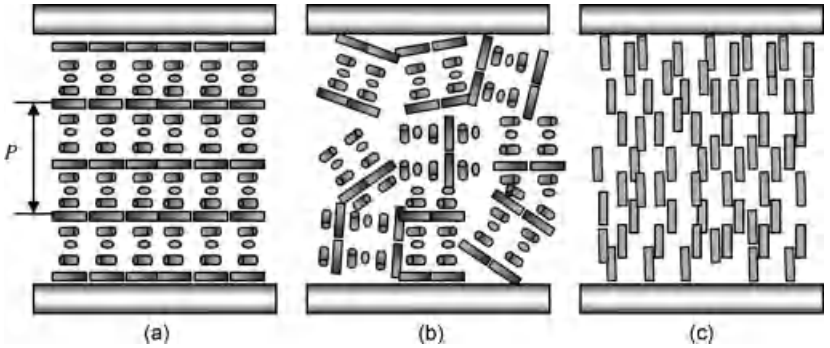

FIGURE 16.4 Cholesteric textures: (a) planar texture, (b) focal conic texture, and (c) homeotropic texture.

axis, however, becomes random as shown in Figure 16.4b. The material has a polydomain structure and scatters light, because the refractive index changes discontinuously from domain to domain. In the homeotropic texture, the helical structure is unwound by an external field, such as an electric field, and the liquid crystal is uniformly aligned as shown in Figure 16.4c. The liquid crystal is transparent.

16.3 POLYMER STABILIZATION

Polymer stabilized liquid crystals are composites of liquid crystal and polymer [14, 15]. They are constructed from a mixture of liquid crystal and monomers. The monomers usually have a rigid core and flexible tails like liquid crystal molecules as shown in Figure 16.5a. The concentration of the monomers is usually less than 10%. The monomers are directly dissolved in the liquid crystals as shown in Figure 16.5b. Although any type of polymerization method can be used, photo-initiated polymerization is fast and is usually used. The monomers are usually acrylate or methyl-acrylate because of their fast reaction rate. In order to form stable polymer networks, the (average) functionality of the monomers must be larger than 1. A small amount of photo-initiator, such as benzoin methyl ether, is added to the mixture. The concentration of the photo-initiator is typically 1–5% of the monomer. When irradiated under UV light, the photo-initiator produces free radicals which react with the double bonds of the monomer and initiate the chain reaction of polymerization. The UV intensity is usually a few mW/cm^2 and the irradiation time is in the order of minutes.

Before polymerization, the mixture of the monomer and the liquid crystal is in a liquid crystal phase. The polymerization environment is anisotropic due to the aligning effect of the liquid crystal on the monomer and the anisotropic diffusion of the monomer in the liquid crystal. Anisotropic fiber-like polymer networks, which mimic the structure of the liquid crystal during polymerization, are usually formed [14–17]. Figure 16.6 is an SEM (Scanning Electron Microscope) picture of a polymer network formed in the nematic phase. The lateral size of the polymer

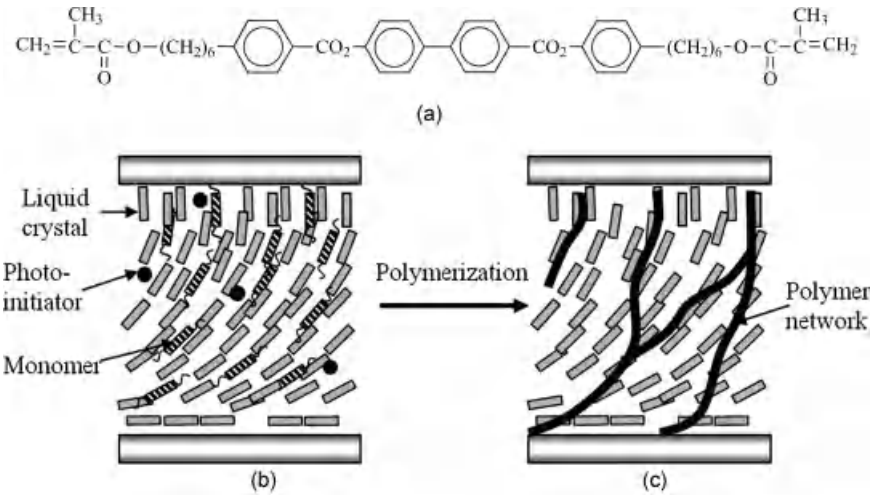

FIGURE 16.5 Schematic diagram of polymer stabilized liquid crystal: (a) chemical structure of monomer 4,4′-bis-{4-[6-(acryloyloxy)-hexyloxy]benzoate}-1,1′-biphenylene, (b) before polymerization, and (c) after polymerization.

network is usually in the sub-micron region. Because the mixture of the liquid crystal and monomer is in a liquid crystal phase during polymerization, external fields and surface alignment techniques can be applied to create various polymer network structure, thereby achieving many fascinating structures.

The morphology of the polymer network plays an important role in the performance of polymer stabilized cholesteric texture materials. In order to fabricate PSCTs with long-term stability, the monomers inside the network must be highly cross-linked and the lateral size of the network must be big enough [18]. The factors affecting the morphology are the structure of the monomer, UV intensity,

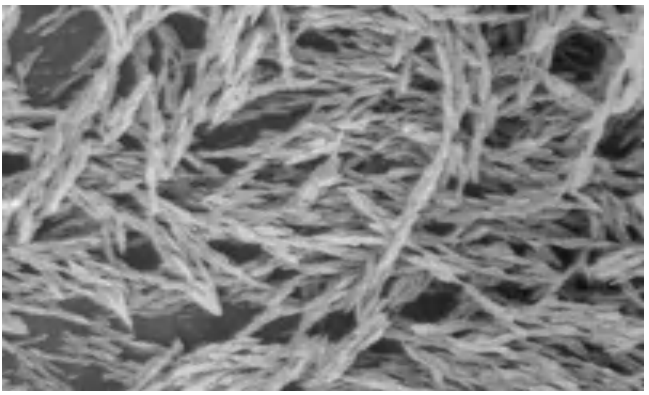

FIGURE 16.6 SEM picture of the polymer network formed in homogenous aligned nematic phase. The picture was obtained by splitting the LC cell, immersing the cell in a solvent to remove the liquid crystal, evaporating the solvent and coating gold on the sample.

photo-initiator type and concentration, and the temperature [16, 18]. Monomers with rigid core and two flexible tails usually form strong polymer networks which can withstand perturbation of external fields and temperature variations. Polymer networks formed by monomers without a rigid core usually reorient with liquid crystals when external electric fields are applied. The lateral size of polymer networks is determined by the polymerization rate, mobility, and concentration of monomers. Polymer networks with larger lateral sizes are obtained with lower polymerization rates which can be achieved with lower UV intensities or lower photo-initiator concentrations in photo-polymerization. Polymer network with larger lateral sizes are also obtained with high mobility of monomers, which can be achieved with higher polymerization temperature. When monomers are polymerized in the isotropic phase, the formed polymers have isotropic bead-like structures.

After polymerization, the anisotropic polymer networks formed affect the orientation of liquid crystals. They tend to keep the liquid crystal in the state (where the liquid crystal is parallel to the polymer network) during the polymerization [14, 15, 18–22]. The aligning effect of the polymer network on the liquid crystal can be considered as the anchoring imposed by the polymer network surface. The strength of the aligning effect depends on the structure of the monomer, the orientation order of the monomer in the polymer network, and the surface area of the polymer network. When the monomers in the polymer network are highly orientationally ordered, the aligning strength is strong; this can be achieved by polymerizing the monomers at a temperature much lower than the liquid crystal–isotropic transition temperature. The aligning strength is approximately linearly proportional to the polymer concentration. It is also linearly proportional to the surface area of the polymer network in per unit volume. Under a fixed polymer concentration, the surface area density is higher with smaller polymer network lateral size, and thus the aligning strength is stronger.

16.4 POLYMER STABILIZED CHOLESTERIC TEXTURE

PSCT materials can be operated in a variety of modes, depending on the curing condition, cholesteric pitch, polymer concentration, and dielectric anisotropy. The modes are normal mode, reverse mode, and bistable mode [23–25]. The normal mode PSCT material is scattering in the absence of voltage and becomes transparent when a voltage is applied across it. In contrast, the reverse mode PSCT material is transparent in the absence of voltage and becomes scattering when a voltage is applied cross it. The bistable PSCT material can be either scattering or transparent in the absence of voltage, depending on the history of voltage application. It can be switched between the scattering and transparent states by voltage pulses.

16.4.1 Normal Mode Polymer Stabilized Cholesteric Texture

The normal mode polymer stabilized cholesteric texture material is made from a mixture of a ChLC with a positive dielectric anisotropy ($\Delta\varepsilon > 0$) and a small amount

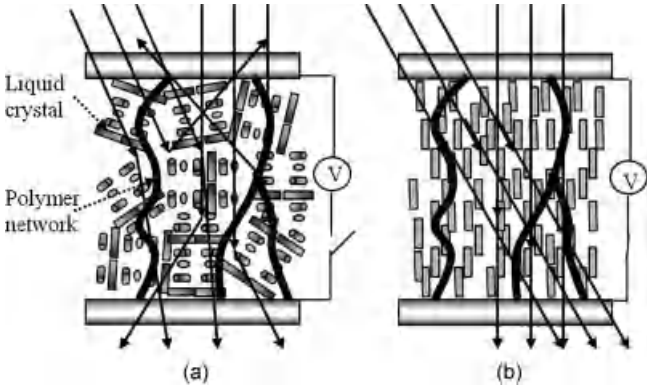

FIGURE 16.7 Schematic diagram showing how the normal mode polymer stabilized cholesteric texture switchable window works.

of monomers [22, 23, 26–28]. The pitch of the ChLC is a few microns (~0.5–5 μm). No special cell surface treatment is needed. The substrates have a transparent ITO (Indium Tin Oxide) electrode. When the monomers are polymerized, the mixture is in the homeotropic texture in the presence of an external field in the cell normal direction. The polymer network formed is perpendicular to the cell surface as shown in Figure 16.7.

After the polymerization, the inter-molecular interaction between liquid crystal molecules tends to form the helical structure while the interaction between the liquid crystal and the polymer network tends to keep the liquid crystal in the unwound homeotropic texture. The competition between these two interactions results in the focal conic texture as shown in Figure 16.7a. In this texture, the ChLC forms many micron-size domains. In each domain, the LC is in the twisted Ch structure along a helical axis. The orientation of the helical axis, however, changes from domain to domain. The refractive index changes abruptly from domain to domain. When a light (incident normally or obliquely) propagates through the PSCT material, it is scattered away from the original incident direction and the material is opaque. Without the polymer network, the ChLC may relax to the planar texture or the focal conic domain size may change gradually, and become less scattering. The polymer network stabilizes the focal conic texture at zero voltage and maximizes the scattering. When a sufficiently high voltage is applied across the cell, the liquid crystal ($\Delta\varepsilon > 0$) is switched to the homeotropic texture as shown in Figure 16.7b, because the liquid crystal tends to orient parallel to the applied electric field direction. The PSCT material is in the uniform aligned state and therefore it becomes transparent. Because the concentration of the polymer is low and both the liquid crystal and the polymer are aligned in the cell normal direction, the normal mode PSCT material is transparent at any viewing angle. The photograph of a normal mode PSCT switchable window is shown in Figure 16.8.

Figure 16.9 shows the transmittance of a normal mode PSCT switchable window [29]. The cell thickness is 15 μm. The helical pitch is about 0.8 μm. The

FIGURE 16.8 Photographs of normal mode polymer stabilized cholesteric texture switchable window: (a) scattering focal conic texture in the absence of voltage and (b) transparent homeotropic texture in the presence of voltage. Photo courtesy of Kent Optronics Inc.

monomer is RM257 (from Merck) which is bifunctional. The concentration of the monomer is 2.0 wt%. The light source for the measurement is a He–Ne green laser at wavelength of 543.5 nm. The full linear collection angle of a circular photo detector for measurement is 9.5°. At 0 V, the PSCT material is in the focal conic texture and the transmittance of the PSCT material is less than 2%. As the applied voltage is gradually increased, the liquid crystal is tilted toward the cell normal direction. The domain size increases and the effective birefringence decreases. Therefore the transmittance increases. When the voltage is increased above 40 V (the driving voltage), the helical structure is unwound and the liquid crystal is uniformly aligned in the cell normal direction (so is the polymer network). The maximum transmittance of 87% is reached. The transmittance is normalized to the incident light. The light loss is due to the reflections from the two air–glass interfaces and ITO–glass interfaces. The PSCT material is very transparent. When the voltage is gradually

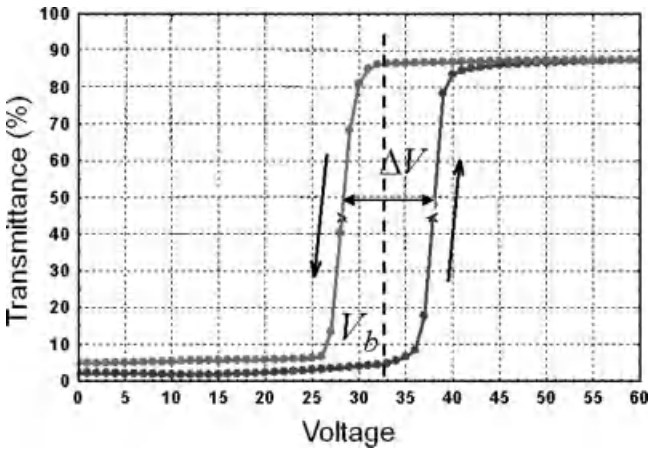

FIGURE 16.9 Transmittance as a function of applied voltage of the normal mode PSCT switchable window.

decreased, the PSCT material relaxes back to the focal conic texture and its transmittance decreases. It is worth noting that the transmittance at 0 V is about 5%, different from the initial transmittance at 0 V. This difference is caused by the fact that the focal conic domain size depends on how the applied voltage is removed. The scattering of the PSCT material depends on how close the domain size is to the wavelength of light. If the applied high voltage is removed suddenly, smaller domains form and the transmittance of 2% is obtained. If the applied high voltage is removed gradually, larger domains form and the transmittance of 5% is obtained.

Also note in Figure 16.9 that there is a hysteresis in the transition between the focal conic state and the homeotropic state. With increasing voltage, the transmittance of $\{[(87\% + 2\%)/2] = 44.5\%\}$ is obtained at 38 V while with decreasing voltage, the same transmittance is obtained at 28 V. The hysteresis is $\Delta V = 38\ \text{V} - 28\ \text{V} = 10\ \text{V}$. On one hand, the normal mode PSCT is not suitable for gray scale operation because of the hysteresis. On the other hand, the hysteresis can be used to make multiplexed switchable window on a passive matrix [25, 30]. The PSCT material is bistable at the bias voltage $V_b = (38\ \text{V} + 28\ \text{V})/2 = 33\ \text{V}$. When the applied voltage is increased from 0 V to 33 V, the PSCT material is scattering. When the applied voltage is decreased from 50 V to 33 V, the PSCT material is transparent. The hysteresis can be enhanced by the polymer network. Figure 16.10 shows the transmittance–voltage curves of normal mode PSCT windows made with a variety of polymer concentrations. When the polymer concentration is increased from 2.5% to 4.5%, the hysteresis ΔV increases from 8 V to 16 V. When the polymer concentration is increased, the voltage to switch the PSCT material to the transparent homeotropic state decreases slightly, while the voltage at which the material relaxes to the scattering focal conic state decreases greatly. When the polymer concentration is sufficiently high, the

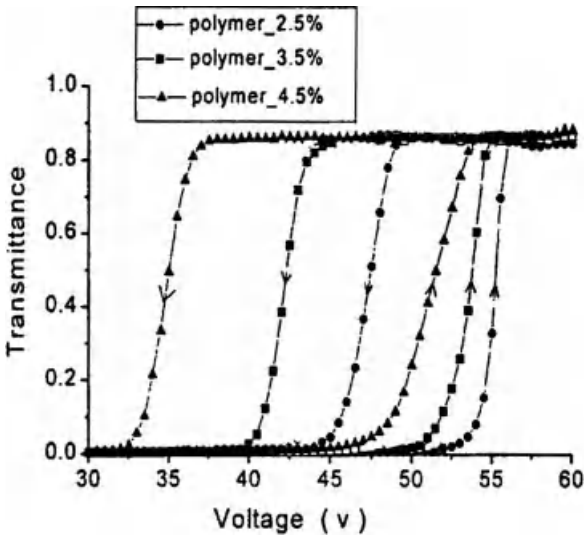

FIGURE 16.10 Transmittance as a function of applied voltage of the normal mode PSCT window with different polymer concentrations.

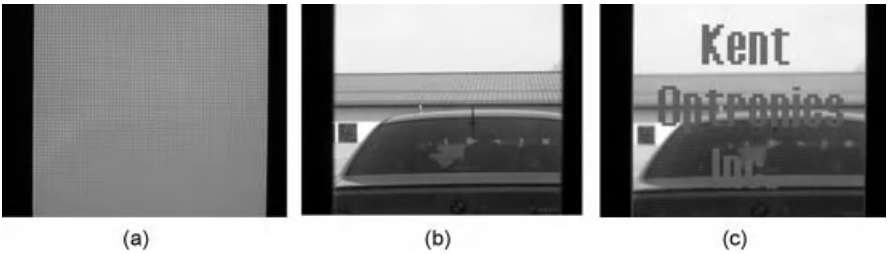

FIGURE 16.11 Photographs of PSCT multiplexed display on a passive matrix developed by Kent Optronics Inc. (KOI): (a) scattering state at zero voltage, (b) transparent state at high voltage, and (c) bistable states at bias voltage. Photo courtesy of KOI.

PSCT material will remain in the homeotropic texture even when the applied voltage is completely removed. We will discuss this phenomenon in more detail in the bistable mode PSCT window. Figure 16.11 shows photos of normal mode PSCT multiplexed display on a passive matrix made by Kent Optronics Inc.

In order to scatter visible light strongly, the focal conic domain size of the PSCT material in the scattering state has to be around the wavelength of the light. The main factors affecting the domain size are helical pitch, polymer concentration, and curing UV intensity. The trend is that smaller domains are obtained with shorter helical pitch, higher polymer concentrations, higher photo-initiator concentrations, and higher curing UV intensities. The scattering of the focal conic texture also is stronger with larger birefringence and thicker cell thickness.

The driving voltage of a normal mode PSCT window is the voltage needed to obtain 90% of the maximum transmittance, determined by helical pitch, dielectric anisotropy of the liquid crystal, twist elastic constant, and polymer concentration. Without the polymer network, the driving voltage is governed by the equation (in SI unit) $V_d = \pi^2(h/P)\sqrt{K_{22}/\varepsilon_0\Delta\varepsilon}$, where h is the PSCT cell thickness, P is the helical pitch, K_{22} is the twist elastic constant, and $\Delta\varepsilon$ is the dielectric anisotropy [10]. The polymer network tends to align the LC in the cell normal direction, the same as the applied electric field. Therefore the driving voltage decreases with increasing polymer concentration as shown in Figure 16.10.

The normal mode PSCT switchable window has quite different rising and falling times. The rising time τ_r (from the scattering focal conic texture to the transparent homeotropic texture) is in the order of 10 ms when the applied voltage is 1.5 times higher than the driving voltage. The rising time can be dramatically reduced by applying higher voltage. It has a small dependence of the helical pitch and is independent of the polymer concentration. The falling time τ_f (from the transparent state to the scattering state) is in the order of ms. It can be dramatically reduced by using ChLC with shorter pitches, because the energy difference between the unwound state (homeotropic texture) and the twisted state (focal conic texture) is bigger for ChLCs with shorter pitches. The relation between them can be approximately described by $\tau_f = \gamma P^2/(4\pi^2 K_{22})$, where γ is the rotational viscosity coefficient. In contrary, the falling time increases with increasing polymer

concentration, because the polymer network tends to keep the PSCT material in the homeotropic texture.

16.4.2 Reverse Mode Polymer Stabilized Cholesteric Texture

The reverse mode PSCT switchable window is also made from a mixture of cholesteric liquid crystal ($\Delta\varepsilon > 0$) and a small amount of monomers [22, 23, 31]. The pitch of the liquid crystal is a few microns (~3–15 μm). The mixture is filled into a cell with homogeneous alignment layers. The mixture is in the planar texture in the absence of voltage because of the alignment layers. The monomers are polymerized in the planar texture. The polymer network formed is parallel to the cell surface, as shown in Figure 16.12.

After polymerization, the PSCT material is stabilized in the planar texture in the absence of voltage, as shown in Figure 16.12a. Because the pitch is in the infrared region, the material is transparent for visible light incident in all directions. When a sufficiently high voltage is applied across the cell, the field tends to align the liquid crystal in the cell normal direction while the polymer network tends to keep the liquid crystal in the planar texture. As a result of the competition between these two forces, the liquid crystal is switched to the poly-domain focal conic texture as shown in Figure 16.12b, and the material becomes scattering. When the applied voltage is removed, the PSCT material returns to the planar texture. A photograph of reverse mode PSCT switchable window is shown in Figure 16.13.

The transmittance–voltage curves of two reverse mode PSCT switchable window are shown in Figure 16.14 [29]. The cell thickness is 10 μm and the pitch length is about 4 μm. The light source is a He–Ne green laser and the light is incident normally on the PSCT cells. The full linear collection angle of a circular photo detector for measurement is 9.5°. The concentration of the bifunctional monomer is about 5%. The transmittance is normalized to the incident light. At 0 V, the PSCT material is in the transparent planar texture with the transmittance about 85%. The main light loss is due to the reflection from the air–glass interfaces and ITO–glass interfaces. A small

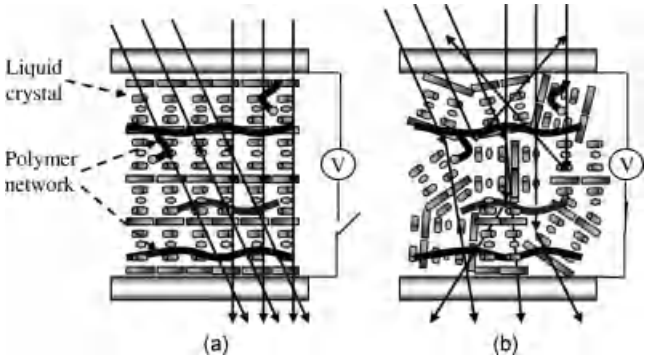

FIGURE 16.12 Schematic diagram showing how the reverse mode polymer stabilized cholesteric texture switchable window works.

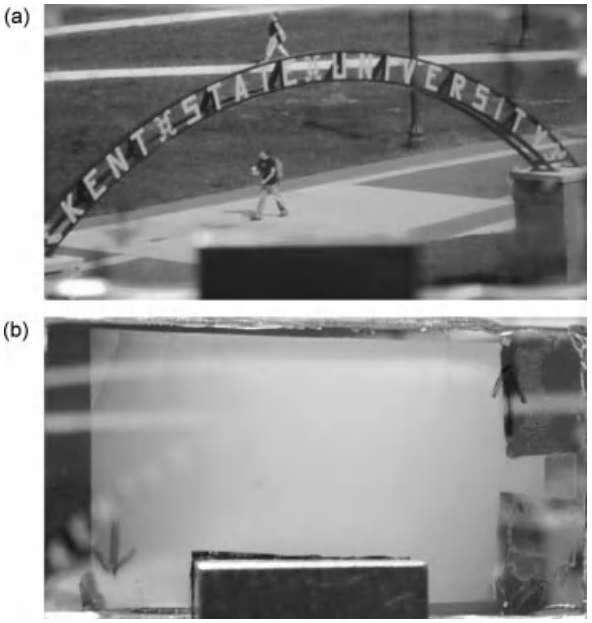

FIGURE 16.13 Photographs of normal mode polymer stabilized cholesteric texture switchable window: (a) transparent planar texture in the absence of voltage and (b) scattering focal conic texture in the presence of voltage.

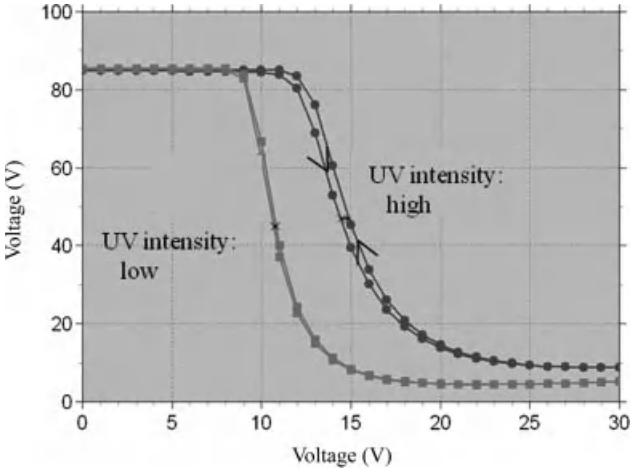

FIGURE 16.14 Transmittance as a function of applied voltage of the reverse mode PSCT switchable window.

amount of the lost light is due to the residual scattering caused by the refractive index mismatch between the liquid crystal and the polymer network. When a voltage about a threshold value V_t is applied, the liquid crystal begins to tilt away from the cell plane. The material is gradually switched to the scattering focal conic texture and the transmittance decreases. The transmittance becomes a minimum when an appropriate voltage V_m is applied. When the applied voltage is increased further, the transmittance increases slightly, because the liquid crystal tilts too much to the cell normal direction and the effective birefringence start to decreases. When the applied voltage is decreased from V_m, the material relaxes back to the planar texture and the transmittance increases. It is worth to point out that in reverse mode PSCT, the polymer network must be strong. When the liquid crystal reorients under the influence of the applied electric field, it exerts a force on the polymer network. If the polymer network is not strong, it will reorient with the liquid crystal. When the applied electric field is removed, the polymer network may not be able to relax to the direction parallel to the cell surface, which will result in a residual scattering.

In order to scatter visible light, the focal conic domain size should be close to the wavelength of the light. The domain size is determined by the polymer concentration, morphology, and helical pitch. The trend is that the domain size becomes smaller with higher polymer concentration, higher curing UV intensity, and shorter pitch. As shown in Figure 16.14, the PSCT material cured under the high UV intensity has a lower scattering efficiency, because the domain size is too small. Higher scattering efficiency can be achieved with larger birefringence and thicker cell.

Reverse mode PSCT materials have fast response time. When the applied voltage is 1.5 times higher than the minimum transmittance voltage V_m, the falling time τ_r (from the planar texture to the focal conic texture) is about a few ms. The rising time τ_r (from the focal conic texture to the planar texture) is also about a few ms. The rising time can be reduced by increasing the polymer concentration, decreasing the helical pitch, and using low curing UV intensity.

In some applications, such as bathroom window, the window needs to be transparent most of the time, and opaque (scattering) occasionally. The reverse mode PSCT material is more suitable for this type of application. It is also more desirable for safety reason. For example, it can be used for automobile windows which will be transparent when electric power is lost.

16.4.3 Bistable Mode Polymer Stabilized Cholesteric Texture

The liquid crystal switchable windows (PDLC, normal, and reverse mode PSCT) discussed so far are mono-stable. They are opaque (optical scattering) at one voltage condition and transparent at another voltage condition. A voltage must be applied to sustain one of the optical states. Although liquid crystals are dielectric media, in reality their conductivities are not zero because of impurities. Therefore the switchable windows consume some energy when a voltage must be applied in prolonged periods. A bistable window is highly desirable, in which both the opaque and transparent states are stable in the absence of voltage; and window can be switched between the two states by a voltage pulse.

The bistable mode PSCT switchable window is based on the normal mode PSCT material [25]. As shown in Section 16.4.1, for the PSCT material with sufficiently high polymer concentration, it is switched from the scattering focal conic texture to the transparent homeotropic texture when a sufficiently high voltage is applied; it remains in the homeotropic texture when the applied voltage is removed. Therefore the PSCT material has two stable states in the absence of voltage: the scattering focal conic texture and the transparent homeotropic texture. What is needed now is a means to switch the material between the two states. Dual frequency liquid crystal can be used to accomplish this task. Under a low frequency electric field, it has a positive dielectric anisotropy and tends to align parallel to the electric field while under a high frequency electric field, it has a negative dielectric anisotropy and tends to align perpendicular to the electric field. When a dual frequency LC is used in the bistable mode PSCT, a low frequency voltage switches the material from the focal conic texture to the homeotropic texture and a high frequency voltage switch the material from the homeotropic texture to the focal conic texture.

Figure 16.15 shows the response of the bistable mode PSCT window to applied voltages [28]. The dielectric anisotropy of the material is about $+2.2$ at 100 Hz and -2.0 at 20 kHz. The pitch of the material is about 1.6 μm. The concentration of a bi-functional acrylate monomer is 8.0%. The cell thickness is 10 μm. The switchable window is prepared in the same way as the normal mode PSCT window. The formed polymer network is perpendicular to the cell surface and tends to align the material in the homeotropic texture. In the electro-optical measurement, a white light from an arc lamp was used. The collection angle of the detection was 4.7°. Figure 16.15a shows the response of the bistable mode material to the applied voltage with a frequency of 100 Hz. It is initially in the focal conic texture with a low transmittance less than 10%. When the voltage is increased, the material is switched to the homeotropic texture with a high transmittance about 87%. When the voltage is removed, it remains in the homeotropic texture with the high transmittance. In the homeotropic texture, the liquid crystal molecules are parallel to the polymer network and the strong aligning force of the polymer prevents the liquid crystal from reorienting away from the polymer network direction when the applied voltage is removed. Figure 16.15b

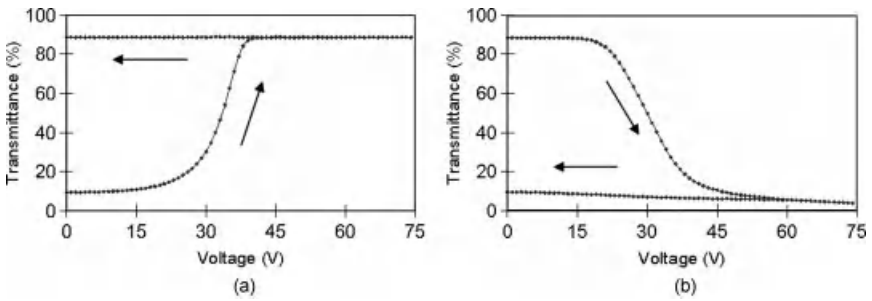

FIGURE 16.15 Response of the bistable mode PSCT switchable window to applied voltages with different frequencies: (a) 100 Hz and (b) 20 kHz.

shows the response of the bistable mode PSCT window to the applied voltage with a frequency of 20 kHz. The material is initially in the homeotropic texture with the high transmittance. When the voltage is increased, it is switched to the focal conic texture with the low transmittance. When the voltage is removed, the material remains in the focal conic texture and the transmittance remains low. In the focal conic texture, the orientation of the liquid crystal molecules with respect to the polymer network is more or less random and the aligning force of the polymer network cannot unwind the helical structure. It is worth to point out that the concentration of the polymer must be properly chosen. If the polymer concentration is too low, its aligning effect will be weak and cannot hold the PSCT material in the homeotropic texture when the low frequency voltage is removed. If the polymer concentration is too high, its aligning effect will be strong and will pull the PSCT material from the focal conic texture to the homeotropic texture when the high frequency voltage is removed.

In the absence of voltage, the bistable mode PSCT switchable window can be either in the focal conic texture with low transmittance or the homeotropic texture with high transmittance. Voltage pulses with different frequencies can be used to switch it back and forth. Figure 16.16a shows the response of the PSCT material initially in the homeotropic texture to a 500 ms wide high frequency voltage pulse [25]. The amplitude of the pulse is 50 V and the frequency is 20 kHz. Before the pulse the material is in the homeotropic texture with high transmittance. When the high frequency voltage pulse is applied, the material is switched to the focal conic texture and the transmittance decreases. After the pulse, the material remains in the focal conic texture except for a small reorientation of the LC as indicated by the slight increase of the transmittance. Figure 16.16b shows the response of the PSCT material initially in the focal conic texture to a 500 ms wide low frequency voltage pulse. The amplitude of the pulse is 50 V and the frequency is 100 Hz. Before the pulse, the material is in the focal conic texture with low transmittance. When the low frequency voltage pulse is applied, the material is switched to homeotropic texture and the transmittance increases. After the pulse, the material remains in the homeotropic texture with high transmittance. If the voltage pulse is short, it will not be able to

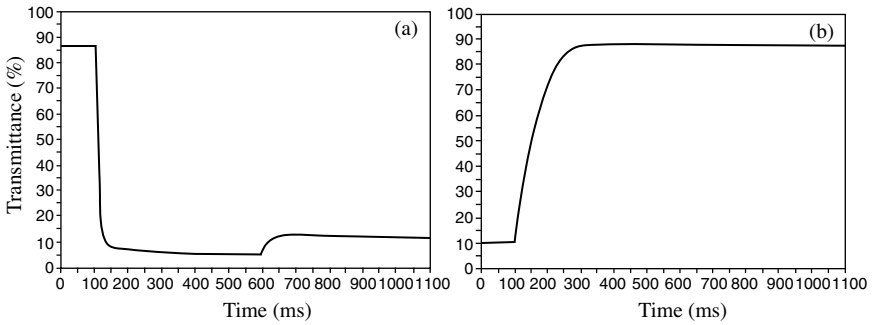

FIGURE 16.16 Response of the bistable mode PSCT switchable window to voltage pulses with different frequencies: (a) 20 kHz and (b) 100 Hz.

FIGURE 16.17 Photographs of the bistable mode PSCT switchable window in the absence of voltage: (a) opaque state and (b) transparent state.

switch the PSCT material into the maximum or minimum transmittance states. Gray scale is possible by varying the pulse width because of the multi-domain structure of the PSCT cell.

Figure 16.17a shows a photograph of the bistable mode PSCT switchable window in the absence of voltage after being switched to the focal conic texture by the high frequency voltage pulse [25]. The light shutter is scattering and blocks the scene behind. Figure 16.17b shows a photograph of the PSCT window in the absence of voltage after being switched to the homeotropic texture by the low frequency voltage pulse. The window is transparent and the scene behind is visible.

The PSCT windows are used for privacy control. They can be used to control energy flow through architectural windows. Contemporary office buildings and resident houses have many windows. In a hot summer day, sunlight entering the buildings through windows heats the building and air conditioning the buildings costs a great amount of energy. It is desirable to have smart windows that can automatically block sunlight when the temperature inside the building increases to a preset value. It is indeed possible to develop this type of smart window, which is switched to the transparent homeotropic texture by applied voltage and is switched to the scattering focal conic texture by ambient temperature.

The smart window is also based on the normal mode PSCT material and prepared in the same way as the normal mode window [24]. The cholesteric liquid crystal has a positive dielectric anisotropy and the helical pitch about 1 μm. The cholesteric to isotropic transition temperature is about 50°C. The used monomer is bifunctional and its concentration is 5%. In the electro-optical measurement, a white light from an arc lamp is used. The collection angle of the detection was 4.7°. The voltage applied to the cells is AC voltage with the frequency of 1 kHz. The formed polymer network is perpendicular to the cell substrates and tends to align the LC into the homeotropic texture. Both the focal conic and homeotropic textures are stable in the absence of voltage.

Figure 16.18a shows the response of the smart PSCT material to applied voltage. Initially, it is in the scattering focal conic texture with a low transmittance of 2%. When the applied voltage is increased, it is gradually switched to the homeotropic texture with a high transmittance of 87%. When the voltage is removed, it remains in

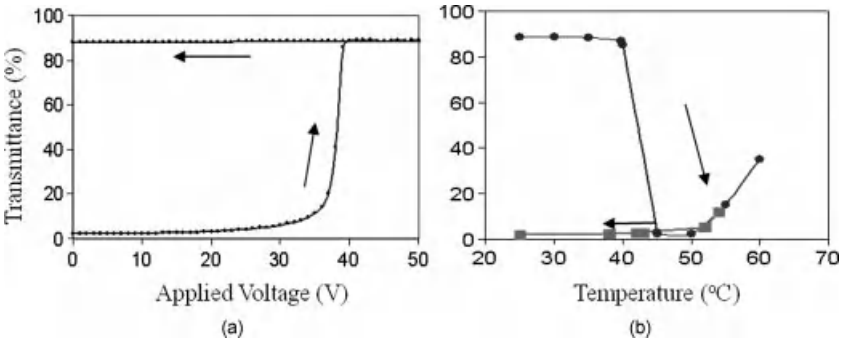

FIGURE 16.18 Response of the smart bistable mode PSCT switchable window to applied voltage and temperature: (a) 1 kHz voltage and (b) temperature.

the homeotropic texture with the high transmittance, due to the strong aligning effect of the polymer network.

Figure 16.18b shows the transmittance of the smart PSCT material as a function of temperature. It is initially in the transparent homeotropic texture. It remains in the transparent state at temperature below 40°C. When the temperature is increased above that, the PSCT material transforms into the scattering focal conic texture and its transmittance decreases. The physics behind the transition is the decrease of the aligning force of the polymer network with increasing temperature. When the temperature is sufficiently high, the polymer network is no longer able to hold the liquid crystal in the homeotropic texture. The transmittance remains low until the cholesteric–isotropic transition. When the liquid crystal starts to transform into the isotropic state, transmittance of the PSCT material increases. Once the PSCT material is in the focal conic texture or isotropic state, it will remain in the focal conic texture with the low transmittance when the ambient temperature is decreased.

Figure 16.19 shows photographs of the smart PSCT window in the absence of voltage and at 25°C [24]. The PSCT window is bistable. Figure 16.19a show the photograph of the PSCT window in the scattering focal conic texture. It blocks the scene behind. Figure 16.19b shows the photograph of the window in the homeotropic texture. It is transparent and the scene behind is visible.

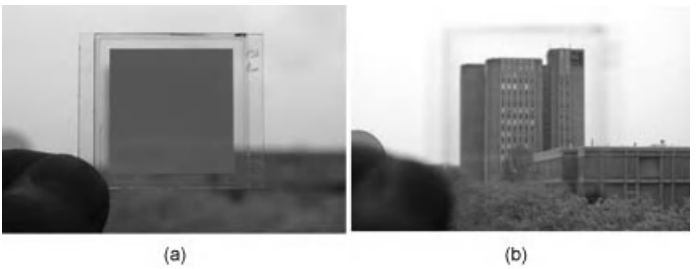

FIGURE 16.19 Photographs of the smart bistable mode PSCT switchable window in the absence of voltage: (a) opaque state and (b) transparent state.

16.5 CONCLUSION

Polymer stabilized cholesteric texture materials are used to make switchable windows for privacy control. They can be operated in normal mode, reverse mode, and bistable mode, depending on the polymer concentration, helical pitch, and curing condition. Polymer stabilized cholesteric texture switchable windows have the advantages of high transmittance transparent state, large viewing angle, and instant switching (in a few ms). They are good candidates for switchable architectural and greenhouse windows to control light energy flow. Research is underway to maximize the backward scattering in the scattering state.

REFERENCES

1. J. W. Doane, N. A. Vaz, B.-G. Wu, and S. Zumer. Field controlled light scattering from nematic microdroplets. *Appl. Phys. Lett.* **1996**, *48*, 269.
2. P. S. Drzaic. Polymer dispersed nematic liquid crystal for large area displays and light valves, *J. Appl. Phys.* **1986**, *60*, 2142.
3. J. L. Fergason. Polymer encapsulated nematic liquid crystals for scattering and light control applications. *SID Int. Symp. Digest Tech. Papers* **1985**, *16*, 68.
4. D.-K. Yang, L. C. Chien, and J. W. Doane. Cholesteric liquid crystal/polymer gel dispersion for haze-free light shutter. *Appl. Phys. Lett.* **1992**, *60*, 3102.
5. P. S. Drzaic. *Liquid Crystal Dispersions*, World Scientific, NJ, 1995.
6. G. P. Crawford and S. Zumer. *Liquid Crystals in Complex Geometries*, Taylor & Francis, London, 1996.
7. J. W. Doane. Polymer dispersed liquid crystal displays. In: B. Bahadur, Ed., *Liquid Crystals, Applications and Uses*, vol. 1, World Scientific, Singapore, 1990, Chapter 14.
8. H.-S. Kitzerow. Polymer-dispersed liquid crystals, from the nematic curvilinear aligned phase to ferroelectric films. *Liq. Cryst.* **1994**, *16*, 1.
9. G. P. Crawford, J. W. Doane, and S. Zumer. Polymer dispersed liquid crystals: nematic droplets and related systems. In: P. J. Collings and J. S. Patel, Eds., *Handbook of Liquid Crystal Research*, Oxford University Press, New York, 1997, Chapter 9.
10. P. G. de Gennes and J. Prost. *The Physics of Liquid Crystals*, Oxford University Press, New York, 1993.
11. S. Chandrasekhar. *Liquid Crystals*, 2nd Edition, Cambridge University Press, New York, 1997.
12. D.-K. Yang and S.-T. Wu. *Fundamentals of Liquid Crystal Devices*, John Wiley & Sons, 2006.
13. S.-T. Wu and D.-K. Yang. *Reflective Liquid Crystal Displays*, John Wiley & Sons, Ltd., 2001.
14. D. J. Broer. Liquid crystalline networks formed by photoinitiated chain cross-linking. In: G. P. Crawford and S. Zumer, Eds., *Liquid Crystals in Complex Geometries*, Taylor & Francis, London, 1996.
15. R. A. M. Hikmet. Anisotropic gels obtained by photopolymerization in the liquid crystal state. In: G. P. Crawford and S. Zumer, Eds., *Liquid Crystals in Complex Geometries*, Taylor & Francis, London, 1996.

16. Y. K. Fung, D.-K. Yang, Y. Sun, L. C. Chien, S. Zumer, and J. W. Doane. Polymer networks formed in liquid crystals. *Liq. Cryst.* **1995**, *19*, 797.
17. G. A. Held, L. L. Kosbar, I. Dierking, A. C. Lowe, G. Grinstein, V. Lee, and R. D. Miller. Confocal microscopy study of texture transitions in a polymer stabilized cholesteric liquid crystal. *Phys. Rev. Lett.* **1997**, *79*, 3443.
18. R. Q. Ma and D.-K. Yang. Freedericksz transition in polymer stabilized nematic liquid crystals. *Phys. Rev. E* **2000**, *61*, 1576.
19. Y. K. Fung, A. Borstnik, S. Zumer, D.-K. Yang, and J. W. Doane. Pretransitional nematic ordering in liquid crystals with dispersed polymer networks. *Phys. Rev. E* **1997**, *55*, 1637.
20. P. Bos, J. Rahman, and J. Doane. *SID Digest Tech. Pap.* **1993**, *XXIV*, 887.
21. H. Kikuchi, M. Yokota, Y. Hisakado, H. Yang, and T. Kajiyama. Polymer-stabilized liquid crystal blue phases. *Nat. Mater.* **2002**, *1*, 111.
22. R. E. Kraig, P. L. Taylor, R. Q. Ma, and D.-K. Yang. Nematic order in polymer stabilized liquid crystal. *Phys. Rev. E* **1998**, *58*, 4594.
23. D.-K. Yang, L.-C. Chien, and Y. K. Fung. Polymer stabilized cholesteric textures: materials and applications. In: G. P. Crawford and S. Zumer, Eds., *Liquid Crystals in Complex Geometries*, Taylor & Francis, London, 1996.
24. R. Bao, C.-M. Liu, and D.-K. Yang. Smart bistable polymer stabilized cholesteric texture light shutter. *Appl. Phys. Express* **2009**, *2*, 112401.
25. J. Ma, L. Shi, and D.-K. Yang. Bistable polymer stabilized cholesteric texture light shutter. *Appl. Phys. Express* **2010**, *3*, 021702.
26. R. Sun, W. Jang, and D.-K. Yang. Optimization of polymer stabilized cholesteric texture materials for high-brightness projection displays. *SID Int. Symp. Digest Tech. Papers* **1999**, *XXX*, 652.
27. S. Hurley, J. Ma, and D.-K. Yang. A flexible display using dye-doped PSCT. *SID Int. Symp. Digest Tech. Papers* **2009**, *XXXX*, 1520.
28. J. Ma, S. Hicks, S. Hurley, and D.-K. Yang. Effect of pressure on polymer stabilized cholesteric. *SID Int. Symp. Digest Tech. Papers* **2009**, *XXXX*, 1532.
29. S. Hurley.Liquid crystal displays for pixelated glare shielding eyewear, Dissertation, Kent State University Publication, 2010.
30. F. Zhang and D.-K. Yang. Polymer stabilized cholesteric dichroic dye displays. *SID Int. Symp. Digest Tech. Papers* **2002**, *XXXIII*, 469.
31. R. Q. Ma and D.-K. Yang. Polymer stabilized cholesteric texture reverse-mode light shutter: cell design. *J. SID* **1998**, *6*, 125.

CHAPTER 17

Liquid Crystals for Nanophotonics

TIMOTHY D. WILKINSON and R. RAJESEKHARAN
Electrical Engineering Division, University of Cambridge, Cambridge, UK

17.1 INTRODUCTION

Integrating nanotechnology and liquid crystals (LCs) opens up a new area of hybrid research, which enables the realization of novel photonic devices and displays [1–7]. A study by Yeung et al. [1] showed the possibility of using nano-structured alignment surfaces based on a random distribution of vertical and horizontal polyimide domains (inhomogeneous layer) to align LC molecules for display applications. It was observed from the experiment that if the inhomogeneity was submicron in size, then there was no visible defect in the LCD and also that the layer takes on interesting properties that can be controlled by the properties of the domains. The nano-structured alignment surfaces can provide any pretilt angles between 0° and 90° and are useful for realizing zero-bias voltage π cells and bistable bend splay displays. Another major example of the application of nanotechnology to LCDs is the addition of nanoparticles to the LC [3–7]. Depending on the optical properties of the nanoparticles, which may be metallic, semiconducting or dielectric, the LC can take on different dispersive properties.

In this chapter, carbon nanotubes and LCs are integrated together to realize novel photonic devices to exploit the drastic size difference between the LC molecules (1–2 nm) and carbon nanotubes (a few nano to micro meters). This interaction can be interpreted as an interaction through the optical anisotropy of the LC [8, 9]. Hence, vertically grown carbon nanotubes electrodes in a LC can be used to form defect centers in the LC which then can be manipulated by applying an external electric field. The electric field confinement of the nanotube is of the same order as its height. So carbon nanotubes in the array are usually spaced at a distance twice their height to minimize electrostatic field shielding from the adjacent neighbors and to avoid the distortion of the photonic elements formed. The vertical height of the multi-wall carbon nanotubes in these arrays was typically 2–5 μm, which implies that the

Liquid Crystals Beyond Displays: Chemistry, Physics, and Applications, Edited by Quan Li.
© 2012 John Wiley & Sons, Inc. Published 2012 by John Wiley & Sons, Inc.

distance between two carbon nanotubes had to be at least 10 μm to ensure that there was no electrostatic repulsion between the field profiles of adjacent nanotubes to avoid distortion in the phase modulation.

This technology offers completely new ways of controlling molecules in LCs, allowing the crystals to move in a variety of directions to create optical components, such as nanophotonic lens arrays. LC molecules are shaped so that they naturally align with each other if put into a cell to form an optically active pixel. In a LC display device the LC pixel is used to change the polarization of the light passing through it and the degree of change (seen as contrast) is done through an applied voltage on electrodes at the top and bottom of the cell. The applied voltage makes the LC molecules rotate in the cell and changes their orientation with respect to the light passing through the cell. This cell geometry limits the ways in which the light can interact with the LC molecules on a two-dimensional (2D) plane. When a three-dimensional (3D) element is added to the lower electrode, it is possible to change the way in which the voltage interacts with the LC molecules to make a 3D optical structure. This means that it is possible to have a resolution of over 10^6 optical elements such as multi-wall carbon nanotubes up to 5 μm high on a 10×10 mm chip. For shorter multi-wall carbon nanotubes, even greater density nano and micro-optical arrays are possible within a very small volume.

17.2 CARBON NANOTUBES

Carbon is the most versatile element in the periodic table because of the different arrangements of electrons around the nucleus of the atom and hence the number of bonds it can form with other elements. There exists three allotropic forms of carbon; graphite, diamond, and buckminsterfullerene. Graphite consists of layered planar sheets of sp^2 hybridized carbon atoms bonded together in a hexagonal network. Diamond has a crystalline structure where each sp^3 hybridized carbon atom is bonded with four others in a tetrahedral arrangement. The third allotrope buckminsterfullerene or fullerene (C60) is made up of spheroidal or cylindrical molecules with all the carbon atoms sp^2 hybridized [10]. Smalley and co-workers [11] proposed the existence of a tubular form of fullerene termed a carbon nanotube. The experimental evidence of the existence of carbon nanotubes was discovered by Iijima [12] by imaging multi-walled carbon nanotubes using transmission electron microscopy. Iijima discovered single-walled carbon nanotubes as well two years later. A single-walled carbon nanotube can be considered as a rolled graphene sheet. Carbon nanotubes are one of the most promising materials for device fabrication because of their excellent electrical, thermal, and mechanical properties in addition to high aspect ratio and high resistance to chemical and physical attack.

Carbon nanotubes are metallic or semiconducting based on the exact way the carbon nanotubes are wrapped. Multi-wall carbon nanotubes are metallic in most cases as there are so many layers and the probability is very high of having one wrapped layer in the group to being metallic.

17.3 UNIFORM PATTERNED GROWTH OF MULTI-WALL CARBON NANOTUBES

Carbon nanotubes find applications in the areas, such as micro electronics, field emission displays, X-ray sources, and gas sensors. Single- and multi-walled carbon nanotubes can be grown using high-pressure arcs, laser ablation, and chemical vapor deposition. It is essential to develop a process which enables high yield, highly uniform, perfectly aligned nanotubes at precise locations on the substrate in order to utilize their unique properties. The plasma-enhanced chemical vapor deposition (PECVD) technique was used [13] to grow uniform, perfectly aligned nanotubes on a Si substrate. The process of using PECVD along with lithographic patterning without the deposition of amorphous carbon (a–C) has been largely ignored in the literature. A study by Teo et al. [14] showed the impact of the C_2H_2:NH_3 ratio in the growth of the carbon nanotubes and a–C deposition in the conventional PECVD technique. The plasma is not necessary for the nucleation and growth of nanotubes, but the electric field induced by the plasma is required for the alignment of the nanotubes. The C_2H_2 provides carbon for the growth of the nanotubes, while the NH_3 etches the carbon and hence a balance between the growth of the tubes and removal of a–C is achieved. The C_2H_2:NH_3 ratio was varied from 15% to 75% in order to investigate the influence of the gas composition on the formation of a–C. The chemical composition of the unpatterned Si areas was investigated by Auger electron spectroscopy (using an in situ 2 keV Ar–ion gun). When the C_2H_2 ratio increased beyond 30%, a–C deposition also increased and they found a peak when it crossed 50%. An interface region of Si, C, N_2, and O_2 formed for all C_2H_2 concentrations. It was found that the optimal C_2H_2 ratio for clean nanotubes deposition lies between 15% and 30%. The thickness of the Ni thin film catalyst controls the diameter, height, and density of the nanotubes. The spacing between the nanotubes can be controlled through lithography and the height of the nanotubes by the deposition time of the tip growth mechanism. This pattern and growth method was used for growing uniform, patterned, multi-wall nanotubes in the nanophotonic devices.

Where V the voltage is applied across the electrodes and d is the gap spacing between the electrodes. If one of the electrodes is replaced by a sharp protrusion or a carbon nanotube, then d is interpreted as the minimum distance between the electrodes. So the local field (within 1–2 nm of the surface atoms) is much higher than the applied field. So the field is very high close to the tip and causes field emission of electrons above a threshold value. The shape of the electric field that spawns from the carbon nanotube in vacuum is also found to be near Gaussian [15].

17.4 PROPERTIES OF LCs EXPLOITED IN NANOPHOTONIC DEVICES

The main properties that are used in our device developments are birefringence, dielectric anisotropy, and fluid viscosity.

$$\text{Microscopic Anisotropy} + \text{ordering} \rightarrow \text{Macroscopic Anisotropy}$$
$$\text{Fluidity} \rightarrow \text{Permits reorganization.}$$

The speed of light in a medium is a direct function of the refractive index of that medium. Birefringent materials have refractive indices that are direction dependent. If the refractive indices for parallel and perpendicular polarized light are different within a material, then the light will travel at different velocities depending on its polarization (the orientation of the electric field) through the birefringent medium. Interaction between the light waves polarized parallely and perpendicular to the molecular axis, depends on the wavelength and gives rise to different colors when viewed through an optical microscope with white light. Dielectric anisotropy of LCs may be defined as the difference between the dielectric permittivities parallel and perpendicular to the director. Interaction of a LC with the external electric field is very much dependent on their dielectric properties.

17.5 THE OPTICS OF NEMATIC LIQUID CRYSTALS

The nematic mesophase is one of the most common calimatic (rod-like) LC mesophases [16]. A large birefringence and a low control voltage distinguish the nematic phase from other electro optical materials. The molecules in the nematic phase only have long range order and no longitudinal order (i.e. do not form layers). This is the least ordered mesophase before the isotropic. The calimatic molecular shape gives order in the nematic phase, which means that on the average the molecules spend slightly less time spinning about their long axis than they do about their light short axis.

The optical indicatrix or index ellipsoid of a LC is a 3D structure to represent the variation of the velocity of light passing through it with respect to the molecular director. When light enters a birefringent material like a LC, its electric field is split into two orthogonal components termed ordinary and extra ordinary rays corresponding to the ordinary refractive index (n_o) and extra ordinary refractive index (n_e) as shown in Figure 17.1. In the case of uniaxial samples, one of the components lies on the equatorial plane and always has the same value, called ordinary component.

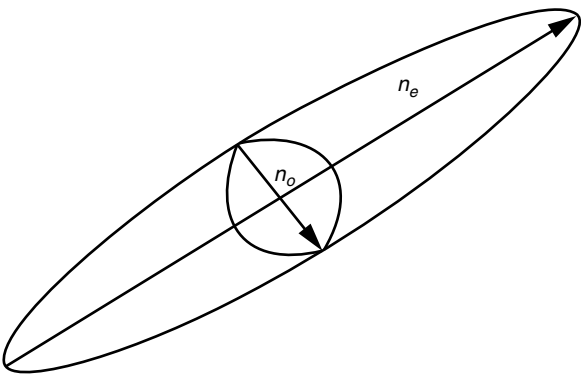

FIGURE 17.1 Refractive indicatrix of a nematic LC molecule.

The other component varies with the angle of incidence and is known as the extra ordinary component. All these parameters are bulk parameters, which are estimated by taking the statistical average across billions of individual molecules.

If the optical indicatrix is oriented at an angle θ to the plane of the cell such as the plane of the glass walls and ITO electrodes, then the refractive index seen by light passing perpendicular to the cell wall is given by

$$n(\theta) = \frac{n_e n_o}{[n_e^2 \sin^2 \theta + n_o^2 \cos^2 \theta]^{1/2}} \tag{17.1}$$

From the above equation, the optical retardance Γ can be calculated for a given sample of thickness d and at a wavelength λ when the material is oriented at an angle θ to the light polarization direction.

$$\Gamma = \frac{2\pi d(n(\theta) - n_o)}{\lambda} \tag{17.2}$$

17.6 LC HYBRID SYSTEMS DOPED WITH NANOTECHNOLOGY

Commercial manufacturer of LC displays use a mixture of 5–10 LC compounds in order to have the appropriate physical properties. The performance of a LC device mainly depends on the LC materials used. Therefore, much effort has been made to improve the electro-optical properties of the LC by introducing dopants, such as dyes and nano-particles [17]. Carbon-based nano particles (nanotubes) have been found promising because of the excellent electrical properties and strong interaction with the aromatic mesogenic groups of LCs. Alternatively, it was observed that, due to high electron affinity and large mobility of π electrons along the tubular axis of the nanotubes, there was an extremely high anisotropy of polarizibility, electrical, and electro-optic properties of the nematic LC/carbon nanotube suspensions. These are much closer to the desired properties for LC displays than the LC alone. Threshold voltage and response time are also critical concerns for a LC device. Low threshold voltage and fast response time result in a better performance for the optical device. Adding a small amount of high aspect ratio carbon nanotubes into the rod like LC mixture yields a good guest–host effect, and hence predictably modifies the absolute dielectric anisotropy as well as the viscosity of the LC–carbon nanotube mixture. These two parameters significantly affect the electro-optical effects of a LC device. Fuelled by both scientific interest and potential applications, carbon nanotube and LC-based suspensions are still of great interest.

The electro-optic properties of a LC can be modified by introducing nano-particles [3]. A study by Jeong et al. [4] showed the formation of unusual double four-lobe nematic textures in a multi-wall carbon nanotube doped LC under the application of an external voltage from 120 to 160 V_{rms} at 1 Hz. The LC cell was prepared using two glass substrates with inner ITO electrode coatings filled with Merck (MJ951160, positive dielectric anisotropy) and a cell gap of 60 μm. Multi-wall

carbon nanotubes having diameters around 3–6 nm and lengths of around 250 nm were first dissolved (10^{-3} wt.%) in dichloroethane and then mixed with the nematic LC. The prepared cell was characterized between crossed polarizers under the application of an external electric field. A perfect dark state was observed at low voltages. When the voltage increased, light started leaking through the crossed polarizers. A four-lobe texture appeared at 60 V_{rms} threshold voltage due to the director deformation inside the LC caused by the motion of the carbon nanotubes.

A study by Baik et al. [5] showed the local deformation of the LC director introduced by translational motion of carbon nanotubes in a plane field. The LC molecules were homogeneously aligned in the cell. Single wall carbon nanotubes having diameter less than 3 nm with a bundle size of tens of nanometers were doped (5×10^{-4} wt.%) in a LC medium. Inter-digitated opaque aluminum electrodes were placed on the bottom substrate, having width and thickness of 10 μm and 30 μm, respectively. The cell was observed between crossed polarizers under an external applied voltage. Two vertical stripes started to appear after a threshold voltage of around 60 V_{rms} due the motion of the carbon. The motion of the carbon nanotubes is explained below. The carbon nanotubes can hold a net charge due to a permanent dipole moment. This net charge can overcome the LC director field locally and hence the movement of the nanotubes.

The electro-optical characteristics of carbon nanotube doped LC devices were investigated by Huang et al. [6]. The threshold voltages and switching behavior of the device were measured and discussed. The measured results revealed that anisotropic carbon nanosolids modified the dielectric anisotropy and the viscosity of the LC–carbon nanotube mixture which changed the threshold voltage and the switching behavior of the LC device. Carbon nanotube doped LC devices with two complementary structures were considered; twisted nematic (TN) and chiral homeotropic LC (CHLC).

17.7 CARBON NANOTUBES AS ELECTRODE STRUCTURES

A traditional device structure such as a LC display pixel is based on a parallel plate capacitor design with top and bottom electrodes aligned to give a uniform electric field profile across the LC cell. Vertically grown multi-wall carbon nanotubes allow us to break this uniform structure and create a true 3D electric field profile. If a MWCNT is grown with more than three concentric skins of grapheme then there is a 99.999% chance that it will be conducting. A typical MWCNT used here would be 50 m in diameter which equates to roughly seven skins, hence we can assume that all of the tubes will be conductors and act as very fine wires grown vertically from the substrate. Using the PECVD process [14] arrays of electrodes have been made from individual vertically aligned multi-wall carbon nanotubes which are then used to address a layer of nematic LC. The nanotube electrodes create a near-Gaussian electric field profile which is used to reorient a planar aligned nematic LC. The variation in refractive index within the LC layer acts like a graded index optical element which can be varied by changing the applied electric field to the carbon nanotube.

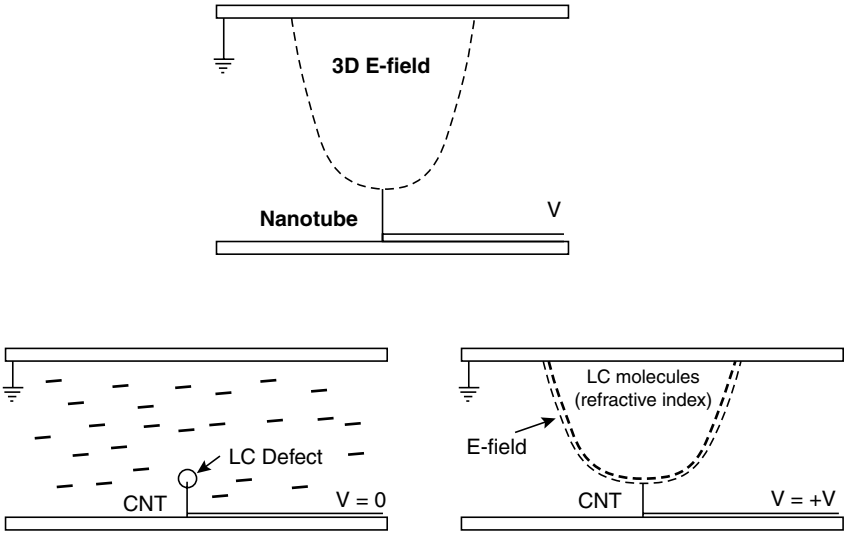

FIGURE 17.2 (a) Electric field profile of a single nanotube electrode within a vacuum. (b) A nanotube electrode in a LC cell with no external field applied. (c) A nanotube electrode within a LC cell with an external voltage V.

When individual MWCNTs are subjected to an applied electrical potential, they form an electric field profile from the tube tip to the ground plane which is approximately Gaussian in shape [15] as indicated by the dotted line in Figure 17.2(a). If the nanotube electrodes are immersed in a planar aligned nematic LC material as shown in Figure 17.2(b) with no field applied, then the LC molecules would align parallel to the upper substrate surfaces due to the planar alignment provided by rubbing a surface coating, such as a thin film of polyimide. When an electric field is applied to the cell shown in Figure 17.2(c), then the molecules of the LC align to the electric field due to their dielectric anisotropy and freedom to flow. The electric field profile is approximately Gaussian in shape and the LC molecules will align to this field (assuming in this case a positive dielectric anisotropy) creating a torque about the long molecular axis which causes them to rotate. The final orientation of the LC is quite complex due to the Gaussian field profile combined with the surface effects of the alignment layer applied to the upper substrate of the cell. The resulting combination of these two effects creates a varying (or graded) refractive index profile across the cell. The profile formed is in effect a micro-optical element due to the gradient index profile across the reoriented LC. If the graded index were Gaussian, then this would form a microlens capable of focussing an applied light wave. More importantly, the micro-optical elements can be tuned by varying the applied field and therefore reorienting the LC and varying the optical properties of the microlens. The optical element formed is similar to modal LC lenses formed with wire electrodes [18] but with a much higher density and element resolution.

The device in Figure 17.2 shows a nanotube on the lower electrode and an upper electrode acting as an earth plane for the electric field. This upper electrode is made of

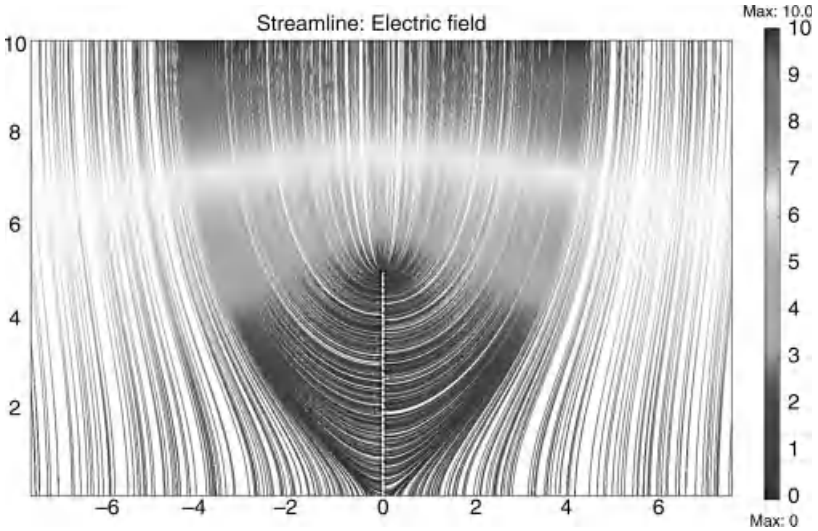

FIGURE 17.3 Simulated electrical field profile surrounding the single carbon nanotube (10 μm high) with an applied field of 1 Vm^{-1}.

transparent conducting material, indium tin oxide (ITO), on glass. A multi-wall carbon nanotube can be likened to a conductive metal rod of nanometer dimensions. When it is embedded between two plane electrodes in a sandwich structure, the nanotube changes the ideal plane electrostatic field profile. A theoretical study on the electrical field effects of carbon nanotubes has been carried out using the finite element method. A COMSOL finite element simulation of the electric field profile of the device structure, in Figure 17.2(a), is shown in Figure 17.3. The simulation assumes a conducting MWCNT in a vacuum and a good ohmic contact with the substrate underneath.

The ideal electrical field of a pair of parallel conducting plates is modified by the nanotube. The effective distance of the field from the nanotube is of the same order as the height of the CNT. The 2D model of a single nanotube has also been extended into 3D showing that the field profile is circularly symmetric about the centre of the nanotube. The curved electrical field profile in 3D can be used to control the behavior of the LC molecules as the field intensity is strong enough to reorient them with an applied field of 1 Vm^{-1}. Varying the applied voltage changes the intensity of the field, the area over which the electric field extends, and hence the alignment of LCs within the area concerned. This makes the fabrication of a focus-tunable lens possible.

Figure 17.4 shows the 2D electrical field around a carbon nanotube array. Carbon nanotubes are spaced at a distance twice their height to minimize electrostatic field shielding from adjacent ones. Typical vertical multi-wall carbon nanotubes in arrays are 2–5 μm in height, which implies that the distance between two carbon nanotubes has to be at least 10 μm to ensure there is no electrostatic interaction between one another. This means that the LC micro lens array in a 10-by-10-mm chip would have a resolution of 1000×1000 lenslets for MWCNTs up to 5 μm high. For shorter

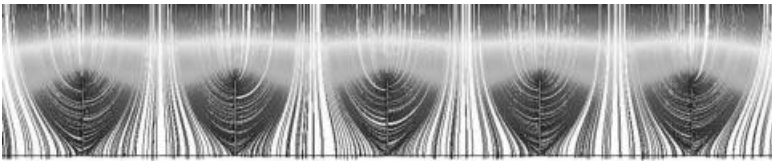

FIGURE 17.4 Simulated field profile of an array of nanotube electrodes at 1 Vm^{-1}.

MWCNTs, even greater density micro-optical arrays are possible. One of the main limitations of the microlenses formed in this structure is that they have a very tight aperture due to the localization of the electric field around the nanotube electrodes.

A typical array of individual nanotubes is shown in the electron microscope image of Figure 17.5(a) with a higher magnification view in Figure 17.5(b). In this case the nanotubes were patterned in small groups of 4 with 1 μm spacing between the nanotubes and 10 μm spacing between the groups.

The sparse array in Figure 17.5 was then fabricated into a LC device. In order to make the device both reflective and also to provide a common electrical connection to all the nanotubes, 400 nm of aluminum was cold sputtered onto the array. The array was then assembled with a top electrode containing ITO on 0.5 mm thick borosilicate glass into a LC cell with a 20 μm cell gap set by spacer balls in UV glue. No alignment layer was applied to the nanotube array, but the top glass electrode was coated with AM4276 LC alignment layer and rubbed in the horizontal direction to give planar alignment. The cell was then capillary filled with BLO48 (positive dielectric anisotropy) nematic LC.

The assembled device was then viewed under horizontally polarized light on an optical microscope. The arrays of nanotubes were clearly visible as black dots as each 50 nm nanotube tip was the site for a defect in the nematic LC. Individual nanotubes with their groups of 4 could be seen at 40× magnification. Figure 17.6(a) shows the sparse array at zero applied electric field. The array of CNT groups can be clearly seen as defects in the image. As the applied field was increased, the nanotube electrodes were seen to begin switching at 1.8 Vm^{-1}, which corresponds to the equivalent of a Freedrickzs transition. Figure 17.6(b) shows the nanotube array at 2.2 Vm^{-1} applied field and the nanotubes are now all fully switched. The distortion in the LC director can be seen in this image as visible contrast, with an analyzer in the horizontal direction, centred on each nanotube group. The irregular distortion structure seen in Figure 17.6(b) if not perfectly circularly symmetric due to the fact that the LC is horizontally aligned on the top substrate. The LC reorients to the field of the nanotube electrode in a complex manner, forming a twisted structure centered on each nanotube group.

The distortion in the LC can also be seen without any polarizer or analyzer under the microscope as shown in Figure 17.7. Each feature is based around a group of 4 CNTs in the array and can be switched on and off with the applied electric field. Each feature resembles a roughly circular defect surrounding the CNT group.

The lensing properties of these micro-optical elements were tested under the same microscope at 40×. Due to the limited depth of focus of the high magnification it

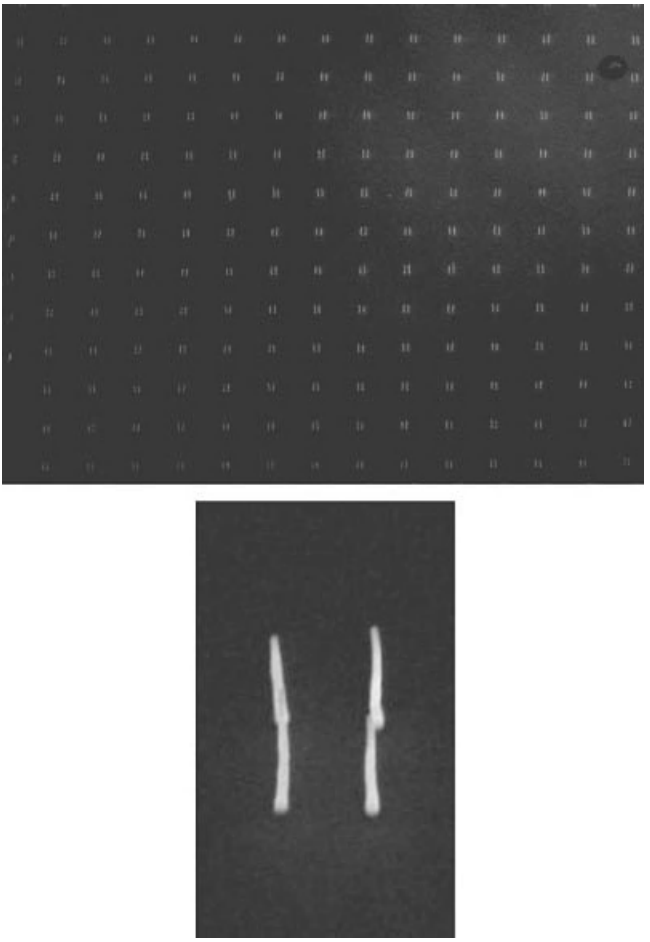

FIGURE 17.5 Sparse array of nanotubes in groups of 4. (a) Array view with group spacing of 10 μm. (b) View of a single group with nanotube spacing or 1 μm.

should be possible to switch the CNT tip in and out of focus with an applied electric field. Figure 17.8(a) shows the array with 0 Vm^{-1} applied field and the microscope adjusted to be out of focus. The image in Figure 17.8(b) is the same area with an applied field of 2.1 Vm^{-1}. The lensing function of the LC can be seen as the LC defect state at the tip of the nanotubes now appear in focus and are visible as a cluster of black dots at the centre of each lenslet.

17.8 NANOPHOTONIC DEVICE CHARACTERIZATION

The microscopic phase profile of each lenslet is of interest as it decides the real modulation capability and applications of the device. The experimental set-up is

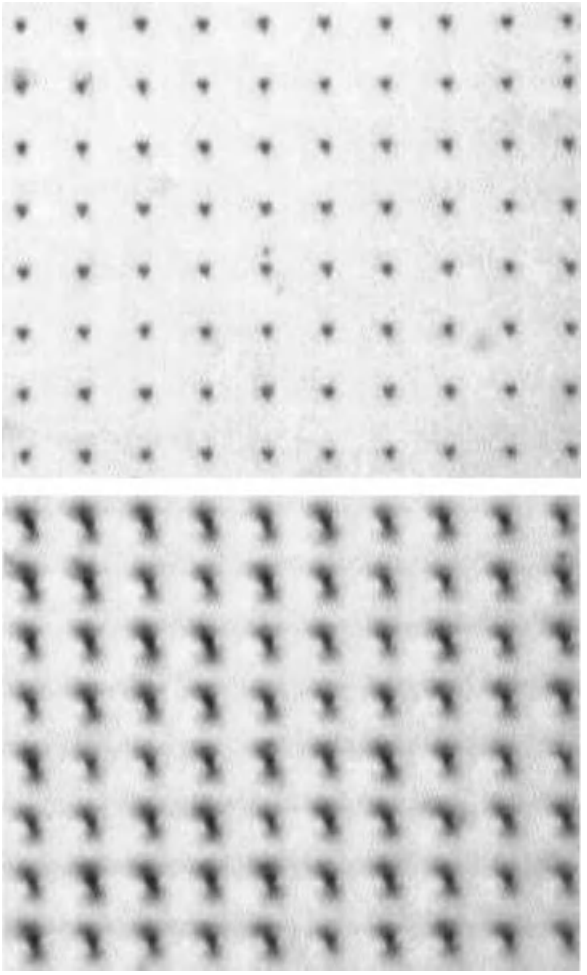

FIGURE 17.6 Sparse nanotube array in a LC at 20× optical magnification under a polarizing microscope with the analyzer aligned parallel to the rubbing direction of the LC (horizontal). (a) 0 Vm^{-1} applied field, (b) 2.2 Vm^{-1} applied AC field.

shown in Figure 17.9. An optical microscope was used to detect the beam in reflective mode and for capturing the interference fringes. The setup consisted of a He–Ne laser along with a beam expander as the illuminating source. An objective having a magnification of 20× was used in the microscope. The device was mounted on a fine three axis tilting stage and attached to the microscope in reflective mode. The rubbing direction of the device was kept at 45° to the polarizer. The interference fringes were formed due to the interference between the ordinary and extra-ordinary beams being combined by an analyzer which was crossed with the polarizer [19]. A rotating diffuser (transparent plastic sheet) was used to average out speckle noise. The fringes were captured by a CCD camera and frame grabber. A white light source was used to

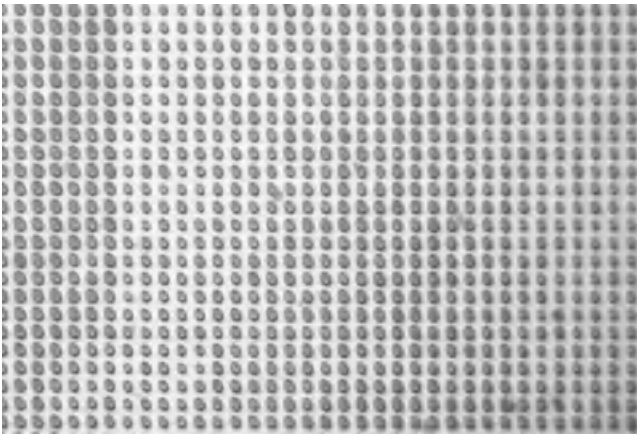

FIGURE 17.7 Image of the LC–CNT array at 2.2 Vm^{-1} taken at 20× with no polarizer or analyzer on the microscope.

see the device and to help in alignment. A voltage source was used to study the variation of interference fringes at different applied voltages. The interferogram, retrieved unwrapped phase profiles of an array of lenslet and one lenslet at different voltages are shown Figure 17.9.

It was found that in the absence of an external voltage circular fringes were observed, which showed an alignment deformation of the LC molecules near the carbon nanotubes even though the macroscopic alignment was planar [Figure 17.10(a)]. The change in phase modulation (the phase difference between the center and circumference of each lenslet) was bigger at lower voltages than at higher voltages as shown in Figure 13.10 because the molecular alignment was more or less homeotropic at higher voltages. This resulted in a diminishing of the interference fringes. The phase profile was distorted at 0 V_{rms}, but became symmetric at 1 V_{rms} and distortion again started from 3 V_{rms} upwards for the device [20]. The focal length was calculated as follows

$$f = \frac{r^2}{2\lambda N} \tag{17.3}$$

where r is the radius of the lenslet, N the number of observed fringes and λ the wavelength of light. The above equation for the focal length can be written in terms of phase difference as

$$f = \frac{r^2}{2\text{OPD}} \; [56, 57] \tag{17.4}$$

where OPD is the peak-to-valley optical path difference from the center to the edge, and r is the radius of the test area (5 μm). The variation in the focal length of a single lenslet and averaged over lenslets in a particular area of the device with

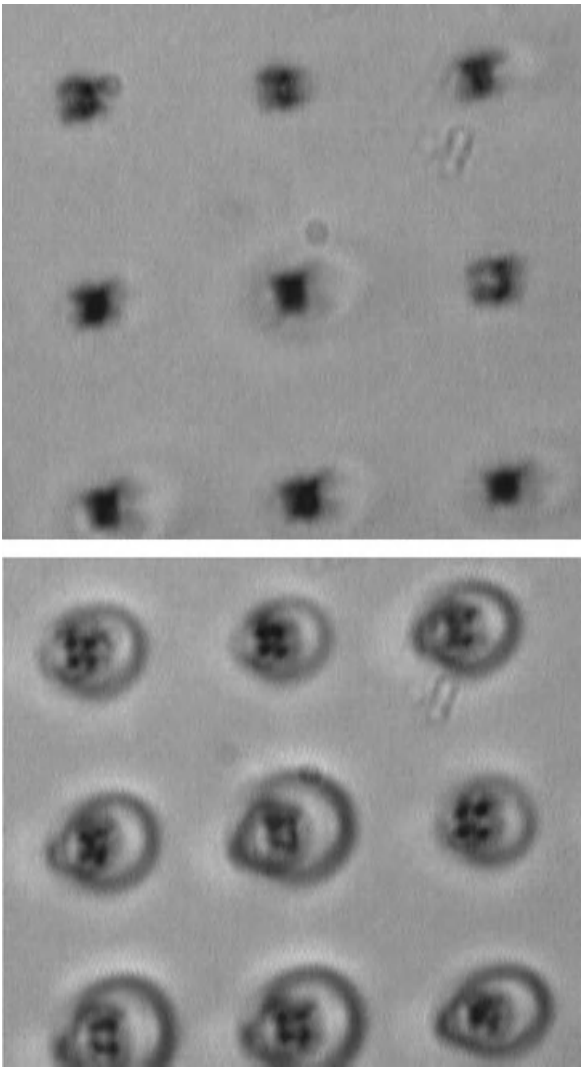

FIGURE 17.8 Defocus of the nanotube lenslet array at 40×. (a) Defocused image of the array at $0\,\mathrm{Vm}^{-1}$ applied field. (b) Array brought into focus with $2.1\,\mathrm{Vm}^{-1}$ applied field.

respect to voltage is shown in Figure 17.11(b). The focal length of each lenslet at $0\,\mathrm{V_{rms}}$ is randomly varied. It was observed that the focal length increased with respect to the voltage and hence the lenslets were concave in nature. The focal length variation was in agreement with the simulation results (Figure 17.4), where the Gaussian profile gave maximum alignment at the centre of each lenslet compared to the circumference. An average focal length over the lenslets were calculated because, the focal length variation was found to be random after $3\,\mathrm{V_{rms}}$

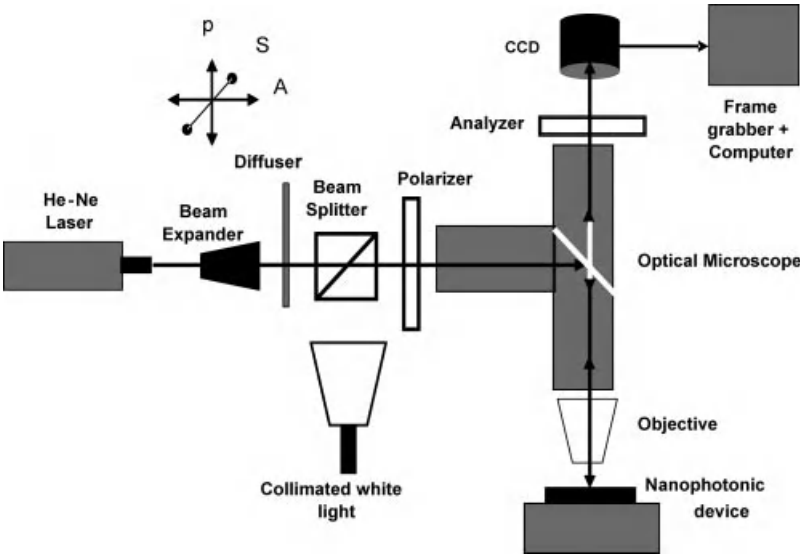

FIGURE 17.9 Experimental set for recording interference fringes from the nanophotonic device in reflective mode.

for many lenslets and also a slight change in focal length between each lenslet below 3 V_{rms} in some areas of the device. The random behavior after 3 V_{rms} was because of the complicated electric field profile due to different ohmic contacts for each CNT.

The phase profile of the device was also dependent on the alignment of the LC in the device. A device with better LC alignment gives more phase modulation than a device with poor alignment. Figure 17.12 shows the focal length variation of two devices with different alignment qualities. The focal length variation was from 11 μm to 15 μm for the voltage range 0 V_{rms} to 4 V_{rms} for a reflective device with poor alignment compared to 12–27 μm for a reflective device with good alignment.

Reflective nano-photonic devices can be useful in display related applications such as when making high-resolution displays where each nanotube electrode addresses the LC molecules and hence the nanotube position acts as a single pixel. The advantage of the silicon device is that electronics can be easily integrated with the silicon using standard silicon fabrication technologies. Another application is displaying complicated holograms for 3D displays and as an electrically reconfigurable optical diffuser. Optical diffusers change the angular divergence of incident light as well as act as a random phase modulator. The current device acts as a grating at the same time because of the periodically arranged CNTs with 10 μm separation and microlensing due to the LC graded index. The device can be used for homogenous illumination that is reconfigurable with an external voltage. The device has over 10^6 lenslets within the 10 mm^2 area. From a geometric optics perspective, the greater the number of elements in the lens array, the finer the separation of the

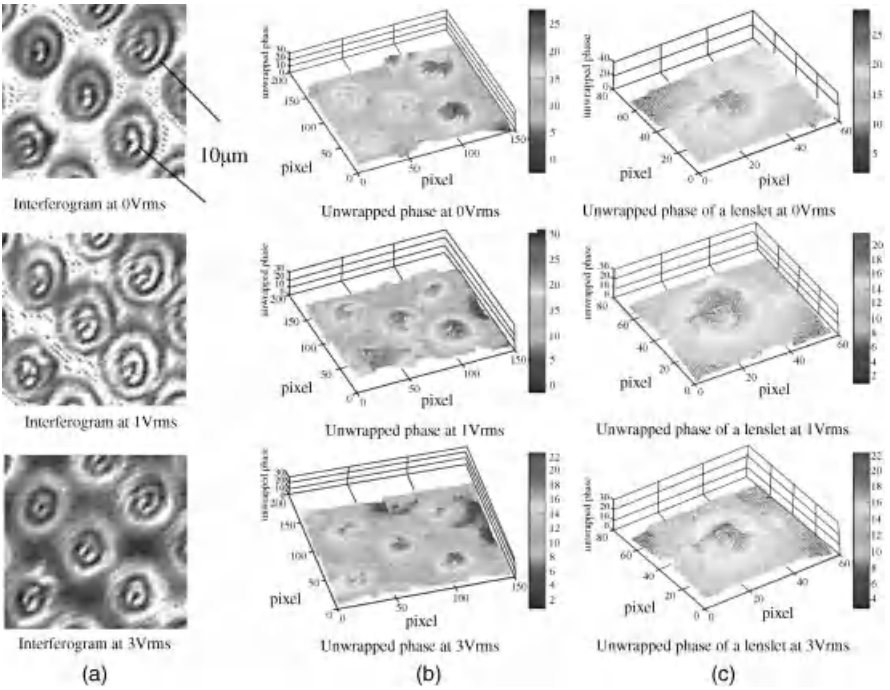

FIGURE 17.10 3D microscopic phase profile of an array at 0 V_{rms}, 1 V_{rms} and 3 V_{rms} (a) an array of interferograms, (b) unwrapped phase of the array, and (c) unwrapped phase of a lenslet.

incident beam and hence the more uniform the illumination [21]. The lenslets in the device are not completely identical in performance, which helps to suppress multiple beam interference patterns due to the spots generated by each lenslet. This can further enhance the uniformity of illumination.

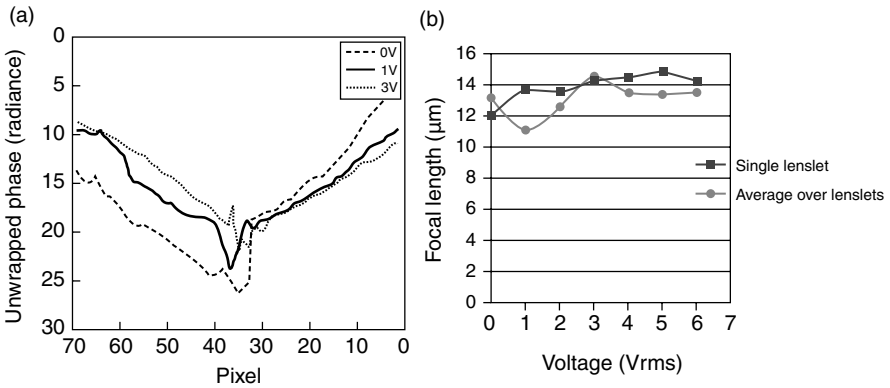

FIGURE 17.11 (a) 2D unwrapped phase profile at 0 V_{rms}, 1 V_{rms}, and 3 V_{rms}; (b) focal length variation with respect to external voltage.

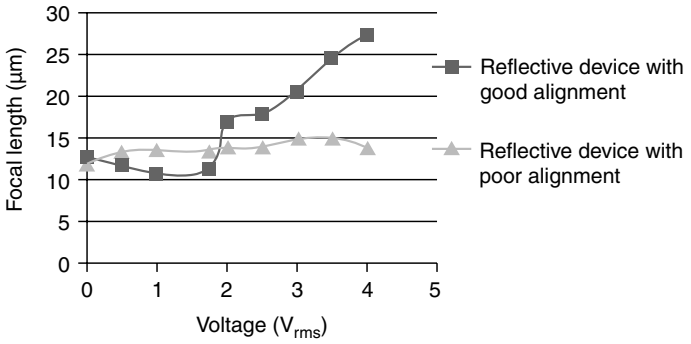

FIGURE 17.12 Focal length variation with respect to external voltage for the devices with different alignments.

17.9 CARBON NANOTUBE ELECTRODE OPTIMIZATION IN THE DEVICE

In order to find out a suitable nanotube electrode geometry in the nanophotonic device, the electrode number, and geometry was varied mainly from one, three, four, and five. The period of the nanotubes group was kept at 10 μm and separation between each nanotube at 1 μm. All other parameters such as thickness of the cell and alignment were also kept constant for all the device geometries. The results were obtained from both electric field simulations and experimentally.

The resultant electric field widens as the number of nanotubes per group increases. For device applications, the resultant electric field needs not only to be wide but also symmetric. The number of nanotubes and separation between each nanotube in a group decided the symmetry of the resultant electric field. The electrostatic simulations were carried out by varying the number and geometries of the nanotube electrodes per group. Figure 17.13 shows the electric field profile generated by one, three, four, and five nanotubes per group with each nanotube separated by 1 μm. The group was repeated at 10 μm intervals. It was clear from the simulation that one nanotube electrode generated a symmetric field profile. But the resultant field was narrower than the other geometries. The three nanotube group electric field profile was not symmetric compared to all other geometries. Four and five nanotubes generated wider resultant electric field profiles than the other geometries. By considering the symmetry and minimum number of nanotubes per group, four nanotubes was found to be most suitable for micro-lens applications. The higher numbers of nanotubes per group were also considered such as six and eight. The six nanotube geometry is also suitable for micro-lens array applications with wider lenslet apertures as shown in Figure 17.14. Figures 17.15 and 17.16 show the 3D resultant electric field simulation for one, three, four, five, and six nanotubes groups. The simulation results were experimentally verified by fabricating devices with some of the different geometries.

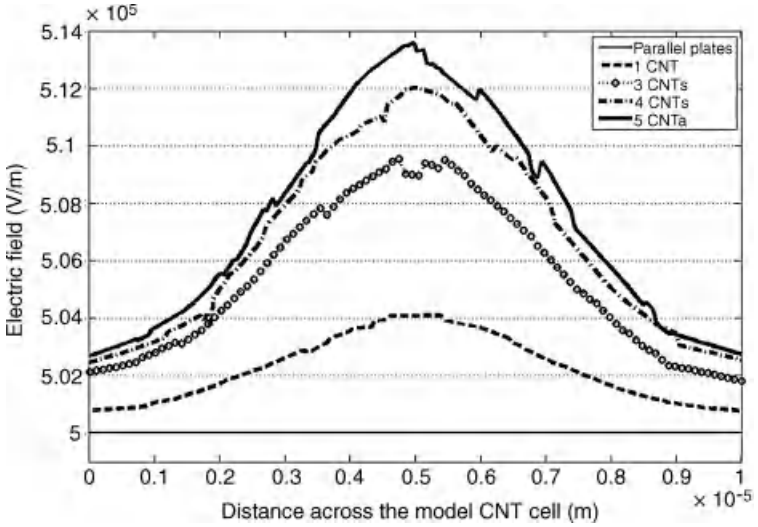

FIGURE 17.13 Modeled 2D electric field profile produced by a group of one, three, four, and five carbon nanotubes placed 1 μm apart.

17.10 CARBON NANOTUBE ELECTRODE OPTIMIZATION: EXPERIMENTAL RESULTS

Based on the simulation results, devices with different number of nanotubes and geometries were fabricated such as one, three, four, and five. The experimental results matched the electric field simulations. The phase profile of each nanotube element

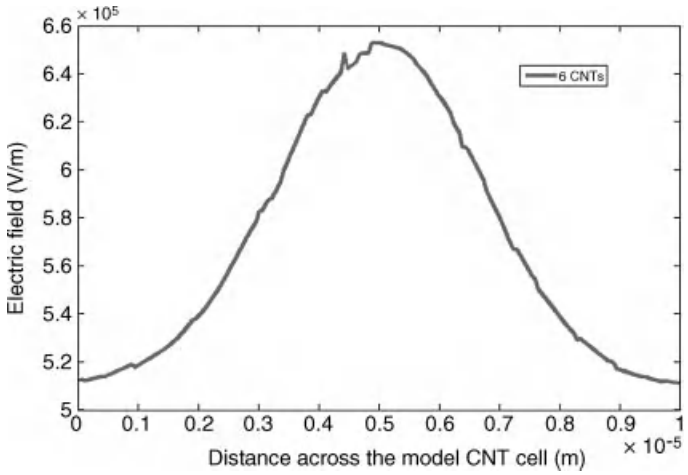

FIGURE 17.14 Modeled 2D electric field profile produced by a group of six nanotubes.

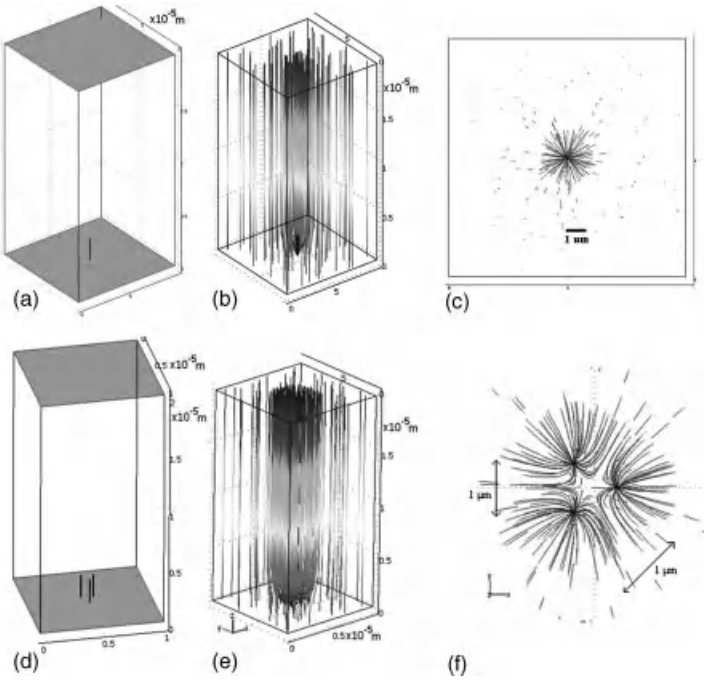

FIGURE 17.15 3D models for the groups of (a) one nanotube and (d) three nanotubes, in free space, connected 1 μm apart. Streamline view of the simulated E Fields generated by the groups of (b) one nanotube and (e) three nanotubes. (c) and (f) present the same in the *x*–*y* plane, respectively. The direction of E-Field lines indicates the repulsion present due to neighboring nanotubes.

(lenslet) was recovered to study refractive index profile, resultant phase modulation capabilities and focal length variation of the device.

Figure 17.17 shows SEM picture of an array of single nanotube electrodes on silicon substrate. The electrodes were separated by 10 μm. The height of the nanotube electrode was around 4–6 μm. The device was fabricated using a planar alignment on the top electrode as discussed in the previous sections.

Figure 17.18 shows interference fringes recorded from the device at different applied voltages using the interference setup shown in Figure 17.9. It was found that fringes were observed at 0 V_{rms} because the nanotube distorted the planar alignment of the LC molecules around it. The fringes were symmetric and wide at around 1.3 $V_{rms.}$ The fringes disappeared as the voltage increased above 3 $V_{rms.}$ This is because the LC molecules aligned almost homeotropically at higher voltages. Figure 17.19 shows the unwrapped phase profile of one lenslet. The unwrapped phase became symmetric and wider at around 1.3 V_{rms} and distorted as the voltage increased. The maximum phase modulation observed was 4π. The one nanotube electrode geometry gives a symmetrical phase profile and is suitable for lens array applications. However, the field profile is narrow which results in small diameter

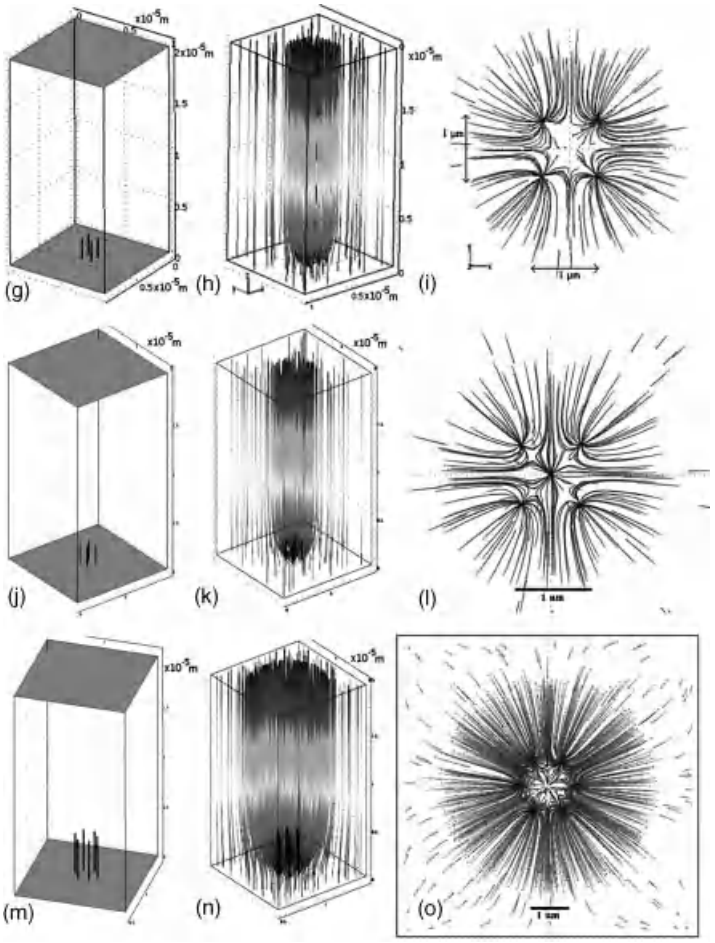

FIGURE 17.16 3D models for the groups of (g) four nanotubes, (j) five nanotubes, and (m) six nanotubes, in free space, connected 1 μm apart. Streamline view of the simulated E fields generated by the groups of (h) four nanotubes, (k) five nanotubes, and (n) six nanotubes. (i), (l), and (o) present the same in the *x*–*y* plane, respectively. The direction of E-field lines indicates the repulsion present due to neighboring nanotubes.

lenslets and hence the lensing is weak. But the single nanotube electrodes are suitable for high-resolution display applications where each nanotube site acts as a pixel with minimum fringing field effects.

Three nanotube electrodes were grown on silicon substrate as shown in Figure 17.20. Each nanotube was separated by 1 μm in the group and the group repeated in 10 μm. The fabrication method was same as in Section 17.7.

Figure 17.21 shows the interference fringes obtained from the device using an interference setup. It was clear from the interferogram that the fringes are asymmetric and distorted. The unwrapped phase profile was recovered to understand the phase

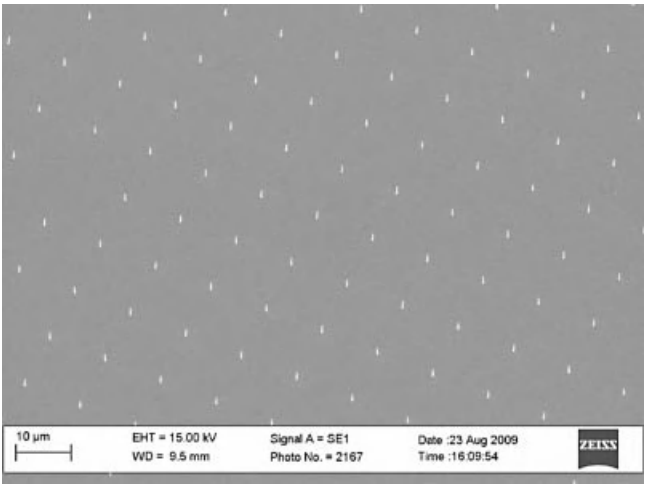

FIGURE 17.17 Scanning electron microscope (SEM) image of single nanotube electrode on silicon substrate.

modulation and symmetry in detail. The lenslet diameter increased with voltage and there was more overlapping between lenslets at around 1.3 V_{rms}. Three nanotubes electrode was not best suited for lensing applications as the interference fringes were not circular and phase profile distorted.

Figure 17.22 shows SEM picture of a four nanotubes electrode on the silicon substrate. All other device parameters were same as the previous devices. Figure 13.22 shows interference fringes from the device at different applied voltages such as 0 V_{rms}, 1.3 V_{rms}, and 3 V_{rms}. The fringes were wider at around 1 V_{rms} with maximum phase modulation capability as shown in Figure 17.23. The fringes disappeared at higher voltages as discussed for the previous geometries. The unwrapped phase became almost symmetric and widest at around 1 V_{rms} and distorted as the voltage increased. The four nanotubes electrode geometry gave an almost symmetrical phase profile with wide resultant field and was suitable for a lens array.

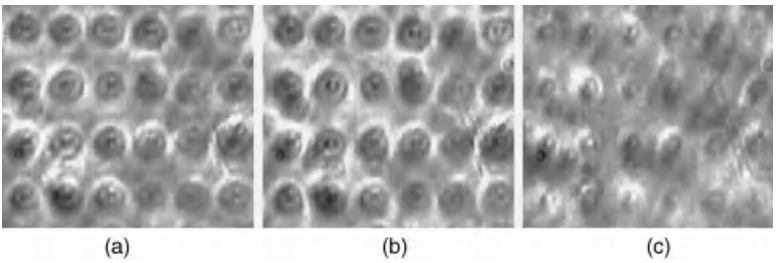

FIGURE 17.18 Interference fringes at different voltages from one nanotube device. (a) 0 V_{rms}, (b) 1.3 V_{rms}, and (c) 3.5 V_{rms}.

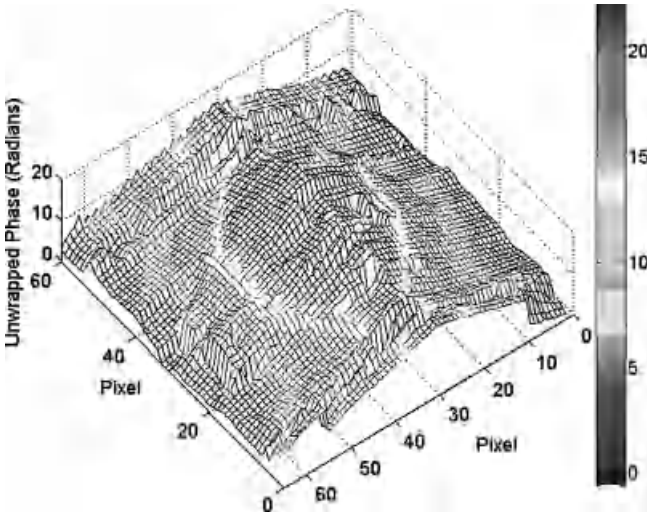

FIGURE 17.19 Unwrapped phase of a one nanotube lenslet at 1.3 V_{rms}.

Five nanotube electrodes were grown on silicon substrate as shown in Figure 17.24. The fabrication parameters were same as the previous devices.

Figure 17.25 shows interference fringes recovered from the device at different applied voltages. The fringes are almost symmetrical with a small distortion at the center of the fringes. This is due to the centre nanotube in the five group distorting the refractive index profile and gradient at the center of each lenslet. This was further studied by recovering the unwrapped phase from the fringes. The lenslet phase profile was distorted. Though the fringes were almost symmetrical for the five nanotube

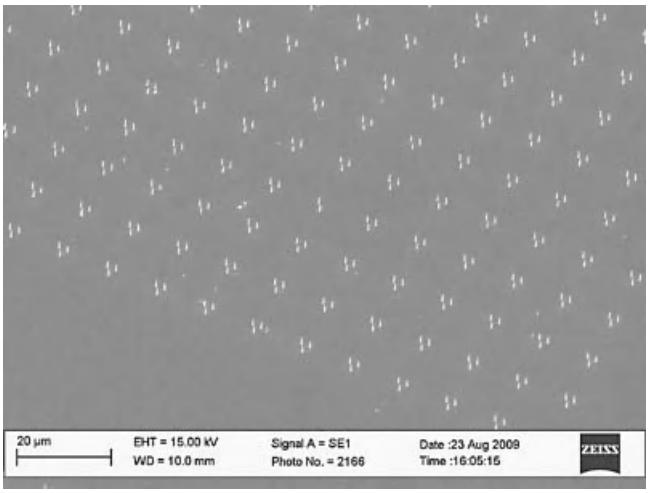

FIGURE 17.20 SEM image of three nanotubes electrode on silicon substrate.

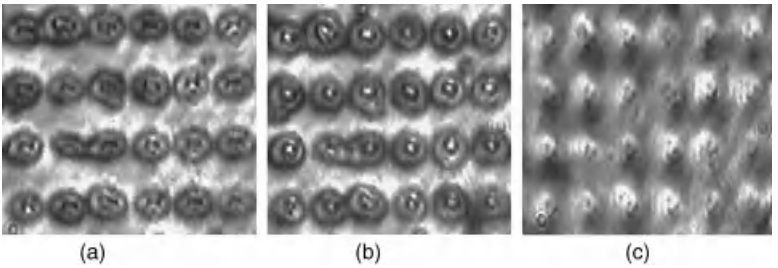

FIGURE 17.21 Interference fringes at different voltages from 3CNT device. (a) 0 V_{rms}, (b) 1.3 V_{rms}, and (c) 3.5 V_{rms}.

geometry, there was distortion at the centre of each lenslet and was not suitable for lens array applications.

17.11 TRANSPARENT NANOPHOTONIC DEVICE

The nanophotonic devices discussed so far operate in a reflective mode [8]. The reflective devices were fabricated on silicon substrate and were made reflective by providing a thin layer of aluminum on the silicon which also acted as a common electrode. Such devices are useful for display applications or for displaying complicated 3D holograms because electronics could easily be integrated with the silicon. In this section, characteristics of the transparent nanophotonic device are presented. The transparent nanophotonic device was fabricated on a quartz substrate and covered with nematic LC to give light modulation capabilities [30]. The device has proven ideal for making voltage dependent high resolution nanophotonic lens arrays, a wave front sensor, diffuser and grating. Figure 17.26 shows a transparent nanophotonic device where nanotubes are grown vertically on the lower electrode

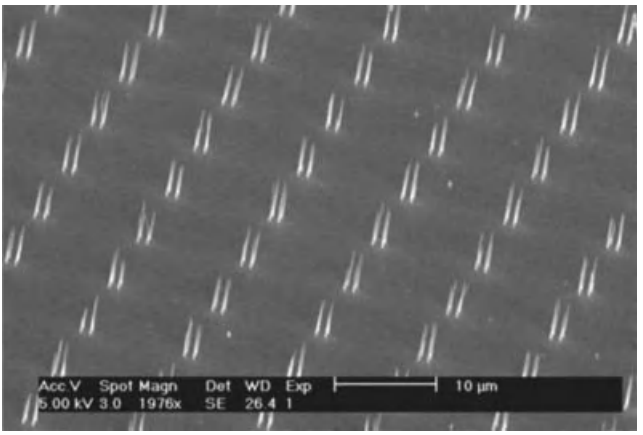

FIGURE 17.22 SEM image of four nanotubes electrode on silicon substrate.

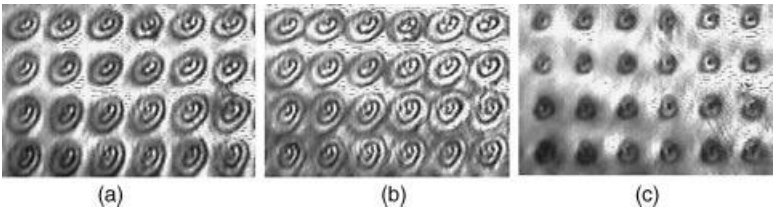

FIGURE 17.23 Interference fringes at different voltages from 3CNT device. (a) 0 V_{rms}, (b) 1.3 V_{rms}, and (c) 3.5 V_{rms}.

and an upper electrode is acting as an earth plane for the electric field. The lower electrode was made from a quartz substrate with a 100-nm thick titanium nitride layer for an electric contact and the upper electrode with ITO on 0.5-mm thick borosilicate glass. The cell gap was set at 20 μm using spacer balls in UV glue and was filled with a nematic liquid, BL048 from Merck. The top electrode alone was given a planar alignment layer by rubbing a thin film of polyimide (AM4276) and hence the resultant alignment of the device was hybrid.

In the current device, the nanotubes were patterned in small groups of six with a 1-μm spacing between the nanotubes and a 10 μm spacing between the groups to increase the resultant electric field and hence the diameter of each phase modulating element as shown in Figure 17.27.

The transparent device was viewed under a polarized optical microscope in transmission mode at different voltages. The device started switching at 0.75 V_{rms}, which corresponds to the equivalent of a Freedrickzs transition. The light focused at each nanotube site (lenslet) of the device was clearly visible when viewed under the microscope. Figure 17.28 shows the device switching at 1.1 V_{rms}.

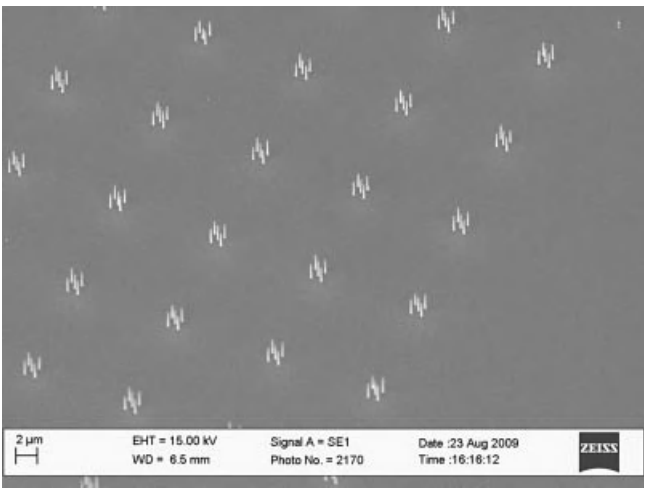

FIGURE 17.24 SEM image of five nanotube electrodes on a silicon substrate.

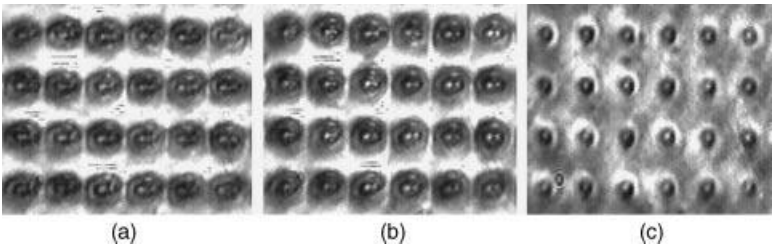

FIGURE 17.25 Interference fringes at different voltages from 5CNT device. (a) 0 V_{rms}, (b) 1.3 V_{rms}, and (c) 3.5 V_{rms}.

The phase modulating capabilities of the transparent device were studied at different voltages experimentally. The set-up consisted of a He–Ne laser along with a beam expander as the illuminating source similar to that in Figure 17.9. An optical microscope was used to detect the beam in transmission mode and for capturing the image. An eyepiece having a magnification of 20× was used in the microscope. The device was mounted on a fine three-axis tilting stage and attached to the microscope in transmission mode. The rubbing direction of the device was kept at 45° to the polarizer. The interference fringes were formed owing to the interference between the ordinary and extraordinary beams being combined by an analyzer that was crossed with the polarizer [19]. A rotating diffuser (transparent plastic sheet) was also used to average out speckle noise. The fringes were captured by a CCD camera and frame grabber. A voltage source was used to study the variation of interference fringes at different applied voltages. The interferogram of four lenslets and retrieved unwrapped phase profile of one lenslet at 0 V_{rms}, 1.1 V_{rms}, and 6 V_{rms} of the transparent device with a six-nanotube group with each nanotube separated by

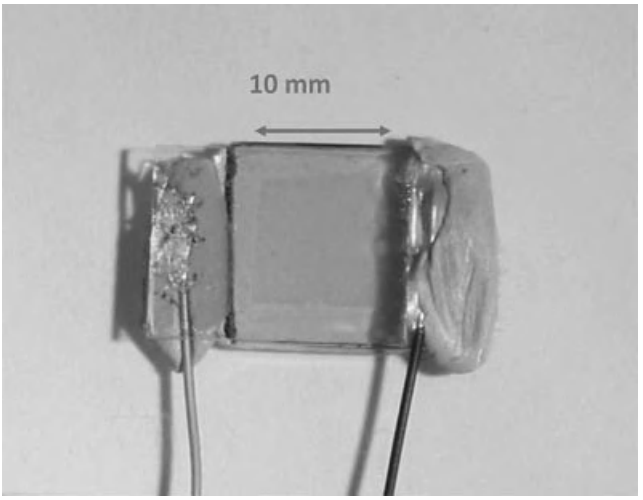

FIGURE 17.26 Carbon nanotube and LC-based transparent nanophotonic device.

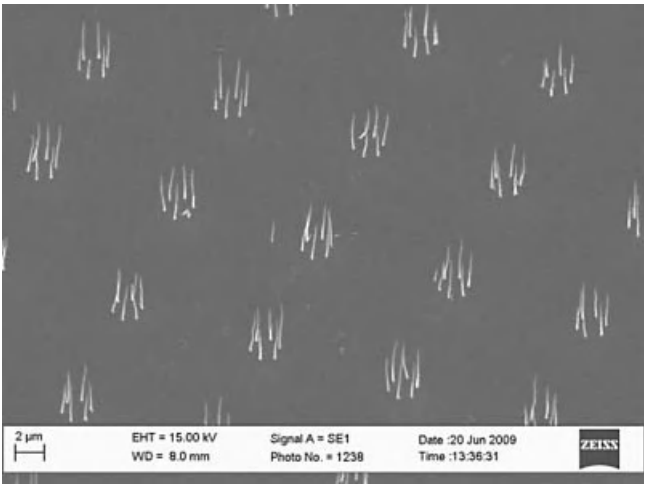

FIGURE 17.27 Electron microscope image of multi-wall carbon nanotube electrodes on a quartz substrate.

1 µm and a period of 10 µm are shown in Figure 17.29. The fringes were observed at 0 V_{rms} due to the alignment of the LC molecules by the carbon nanotubes even though the top electrode was given a planar alignment. The interference fringes were more or less circular and clear at lower voltages. As the voltage increased, the circular fringes became rectangular in shape due to repulsion of electric field from each of the carbon nanotube groups. The fringes started to disappear at around 2.5 V_{rms} and a black spot was observed at the position of each lenslet. The phase modulation was 2.86π at 0.98 V_{rms} with distorted phase profile. The phase profile became smooth and

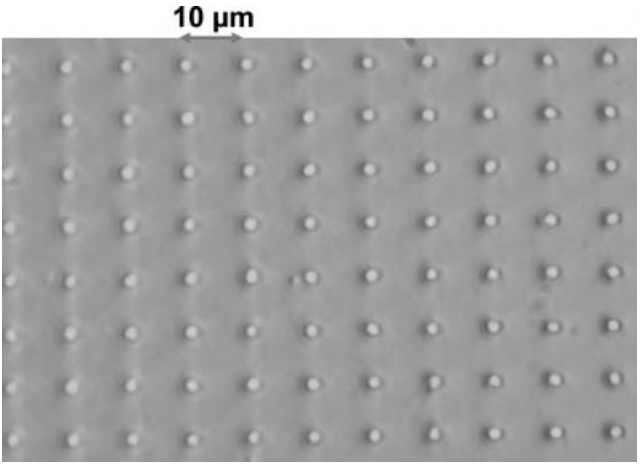

FIGURE 17.28 The transparent device at 1.1 V_{rms} under optical microscope (50× magnification).

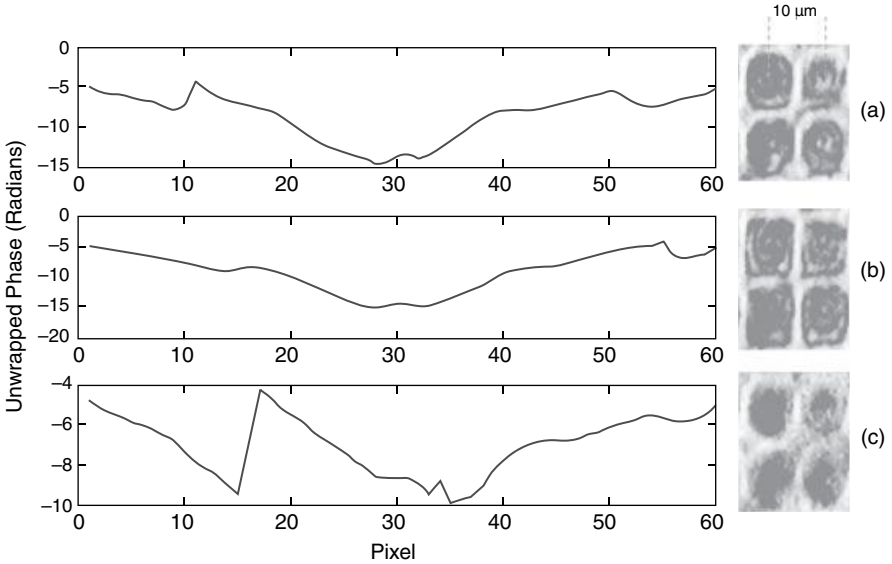

FIGURE 17.29 Unwrapped phase of a single lenlet and interference fringes from the nanophotonic device (four lenslets) at 0.98 V_{rms}. (a) 1.1 V_{rms} and (b) 2.5 V_{rms}.

parabolic at voltages below 2 V_{rms} with phase modulation of 3π–4.2π. The phase modulation decreased with the distortion in phase profile as the voltage increased.

Light intensity and focal length variation of the device at each nanotube group site (lenslet) were studied to understand the imaging characteristics of the device. These parameters are also needed for making suitable applications using the device. In order to study the light intensity profile from each lenslet, the device was fixed in a polarized microscope where the objective was focused on to the top of each nanotube position. The image of the device was recorded on a CCD at different voltages. The light focusing effect at different voltages is shown in Figure 17.30(a)–(f). The nanotubes distort the planar orientation of the LC around the nanotube which results in a graded refractive index profile. At 0 V_{rms}, the light focusing was not uniform for all the lenslets because the LC distortion was different for each nanotube position as shown in Figure 17.30(a). The focusing started improving as the voltage increased from 0 V_{rms}. The light focusing at 0.75 V_{rms} is shown in Figure 17.30(b). The focusing of light became most uniform at around 1.1 V_{rms} and light intensity increased at each lenslet position as shown in Figure 17.30(c). The focusing effect reduced with further increase in the applied voltage. This can be seen in the images at 1.8 V_{rms} and 2 V_{rms}, as shown in Figures 17.30(d) and (e), respectively. As the voltage increased above 2 V_{rms}, the light intensity at each lenslet position started decreasing and finely disappeared at higher voltages as shown in Figure 17.30(f). Figure 17.31 shows one-dimensional (1D) cross section of the intensity profile across five lenslets at 0, 1.1, 2.2, and 3 V_{rms}. It was clear that at 0 V_{rms} the light intensity was more at the nanotube positions compared to that remaining in the area of the device. But the light intensity between each of the nanotube groups was not uniform and hence created an

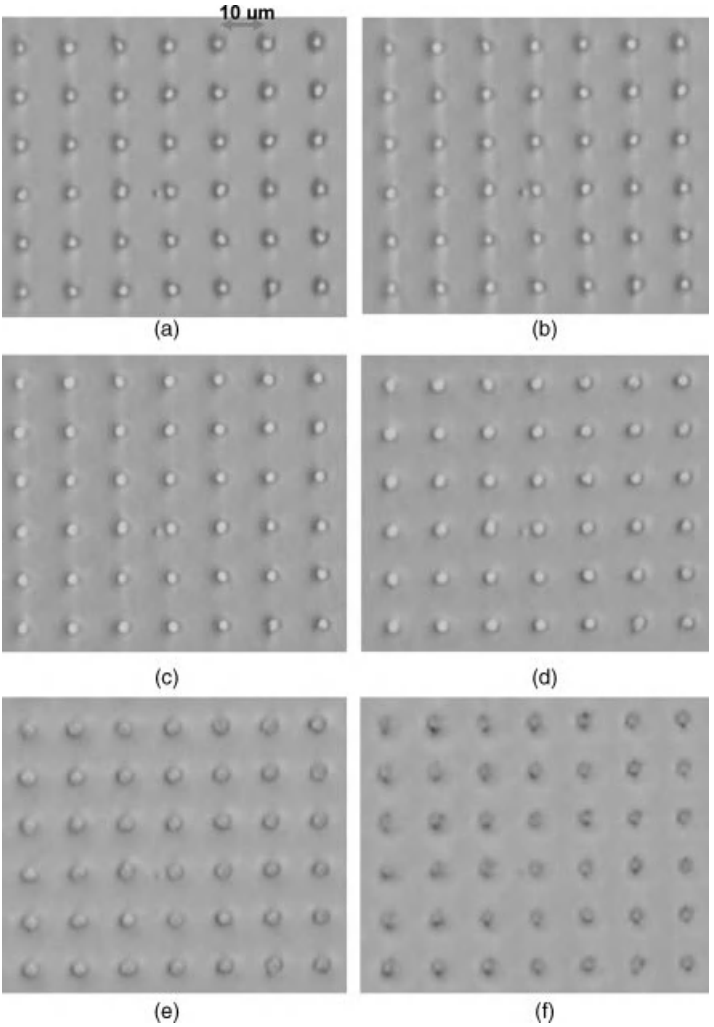

FIGURE 17.30 The nanophotonic lens array focusing the light at (a) 0 V_{rms}, (b) 0.75 V_{rms}, (c) 1.1 V_{rms}, (d) 1.8 V_{rms}, (e) 2 V_{rms}, and (f) 4 V_{rms}.

aberrated lens array. When the voltage was 1.1 V_{rms}, the light intensity was maximum at these nanotube positions with a wider profile. The light intensity was also smooth and uniform between the nanotube groups. The device acted as a lens array with least aberration at around 1.1 V_{rms}. Further increase in the voltage distorted the light intensity profile and there was no proper lensing above 1.8 V_{rms}.

The focal length of each lenslet was calculated using the Eqs (17.3) and (17.4). The focal length varied with respect to the applied voltage as shown in Figure 17.32. Further increase in the voltage distorted the orientation of the LC molecules in the device and hence no focusing was observed. The nanophotonic device was, however,

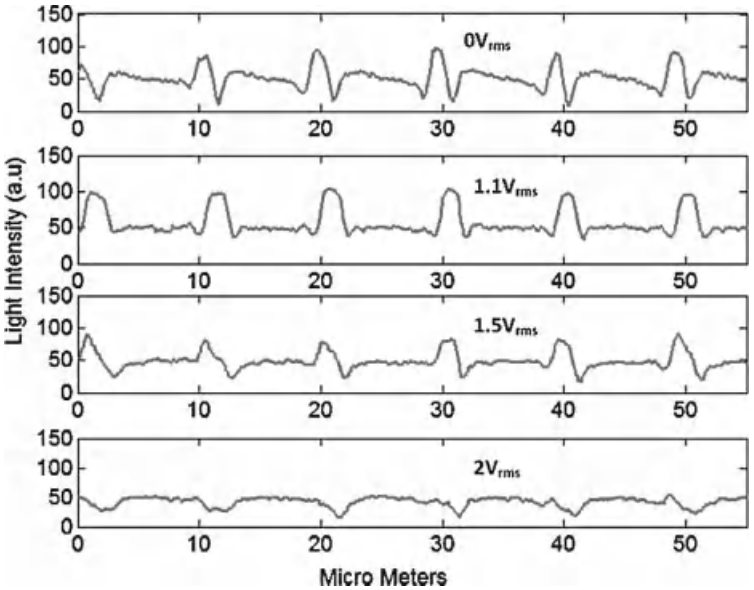

FIGURE 17.31 The 1D light intensity profile across six lenslets at (a) 0 V_{rms}, (b) 1.1 V_{rms}, (c) 1.5 V_{rms}, and (d) 2 V_{rms}.

acting like a voltage reconfigurable lens array at lower voltages. The focal length variation was due to the change in phase profile with respect to the applied voltage. The focal length varied from 10 μm (0 V_{rms}) to 36 μm (2.2 V_{rms}) and hence the lens array became more concave in nature with increased applied voltage. The lensing nature of the lens arrays disappeared after 3 V_{rms} because the LC molecules aligned randomly at higher electric fields. The focal length variation was slightly better for the transparent sample because the light was incident normal to the device surface

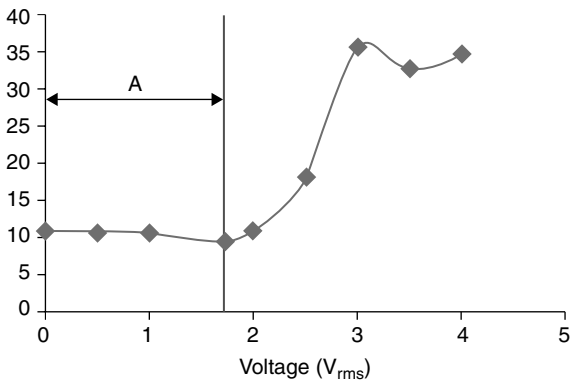

FIGURE 17.32 Focal length variation of one lenslet with respect to applied voltage. Region 'A' represents the useful region for imaging.

and there was no double pass of light through each micro lenslet as in the case of the reflective device. Only the transparent device can be used for imaging applications because of the easy integration with rest of the optical components and lower distortion in the image.

The light intensity variation across the lenslet in the device and focal length variation with respect to the applied field was calculated to find the useful range for imaging applications. Though the focal length varied from 10 μm to 36 μm, the useful region for imaging was found to be from 10 μm to 14 μm which corresponds to the voltage range 0–1.8 V_{rms}. There were distorted interference fringes above 1.84 V_{rms} and hence the focal length variation.

From the light intensity studies it was clear that the light focusing ability of the device considerably decreased from 1.8 V_{rms} upwards. This was due to the fact that as the voltage increased above 1.8 V_{rms}, the alignment of LC molecules got distorted and further increased in the voltage forced the molecules at each nanotube site to align homeotropically. Figure 13.32 shows the focal length verses voltage graph where the region 'A' is most useful for imaging. The focal length varied until 4 V_{rms} because the interference fringes were present up till this voltage. The number of fringes decreased as the voltage increased above 1.8 V_{rms}.

17.12 NANOPHOTONIC COMPOUND EYE-BASED 3D VISION SENSOR

Large vertabrates like humans have large single aperture eyes. The eyes are optimized to provide high resolution, large field of view, focusing ability, color detection, and a very large dynamic range to see both in the bright sunshine and in the dark night. Small invertebrates on the other hand cannot afford large single heavy aperture eyes that consume a lot of metabolic energy. They have instead compound eyes, where the image capturing is distributed amongst a matrix of small eye sensors. Miniaturized imaging systems based on artificial compound-eye vision have been examined experimentally by several groups [22, 23]. Little attention has been paid to the optical imaging system compared to the comparatively large effort in the electronics, and the burden of the extraordinarily complex image processing. This has prevented the realization of a fully functional, miniaturized high-resolution compact camera. Their optical performance has also been limited by inadequate fabrication and assembly technologies for the individual components. This chapter presents the development of a nanophotonic 3D sensor system for high resolution 2D imaging, and 3D video by overcoming the diffraction barrier. The key component for achieving this goal is the imaging optics itself. We have developed a novel nanophotonic micro-lens array as discussed in Chapter 4 suitable for a compound eye based high-resolution imaging sensor. We apply integral imaging to enable 3D video/display in the sensor to give advantages such as continuous view points, full parallax, no convergence-accommodation conflict and no need for any special glass to evoke the 3D image.

Integral imaging is based on integral photography, which was proposed by Lippmann [24]. Integral imaging is a 3D image display technique that produces

true 3D images. The advantages of integral imaging compared to other 3D image systems include continuous view points, full parallax, no convergence accommodation conflict and no special viewing glasses are required to see the 3D image [25–28]. It is an auto stereoscopic technique where the 3D object is sampled by a micro-lens array or a pinhole. Each micro lenslet picks up a particular perspective of the object which is called an elemental image. Reconstruction of a 3D image of the object from 2D elemental images is a reverse of the pickup process. The 3D image is reconstructed from all the elemental images using a lens array.

Figure 17.33 shows the block diagram of the camera and display stage. The camera stage is the capture stage. The captured image is transmitted as electrical signals and converted back into optical signal in the display stage.

The integral imaging system can be divided into camera stage (pick up stage) and display stage (3D image reconstruction stage). Figure 17.34 shows the principle of the pickup method by a camera. The 3D object is sampled by a micro-lens array. An inverted real image (for a convex lens array) of the object is created by each micro lenslet behind the micro-lens array. The image formed by each lenslet is called the elemental image. Each elemental image is formed from a different perspective of the object. Then all the elemental images are recorded on a CCD camera.

We define the following parameters, W_L is the width of the lens array, W_S is the width of the pickup device, f_C is the focal length of the camera lens in front of CCD to demagnify all the elemental images down to the size of the CCD, and Z_{MC} is the distance between the lens array and the camera lens [27].

$$\frac{W_L}{Z_{MC}} \cong \frac{W_S}{f_C} \tag{17.5}$$

$$W_L = W_M N \text{ and } W_S = \text{NMP}_C \tag{17.6}$$

Also W_M is the pitch of the microlenses, N is the number of micro lenslets, M is the number of pixels in the elemental image, and P_C is the pitch of the pickup device. It is clear from the above equations that the number of pixels in the pickup device is the product of the number of micro lenses and pixels in the elemental image. The resolution of the reconstructed 3D image is given by the number of micro lenses. The number of pixels per elemental image is related to the viewing zone, or the resolution, of the reconstructed 3D image. It has been experimentally observed that at least ten pixels per elemental image in the vertical and horizontal directions are required for minimum clarity in the reconstructed 3D image.

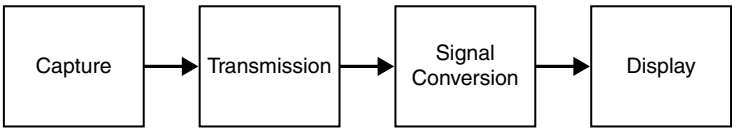

FIGURE 17.33 Block diagram of camera (pick up) and display stage.

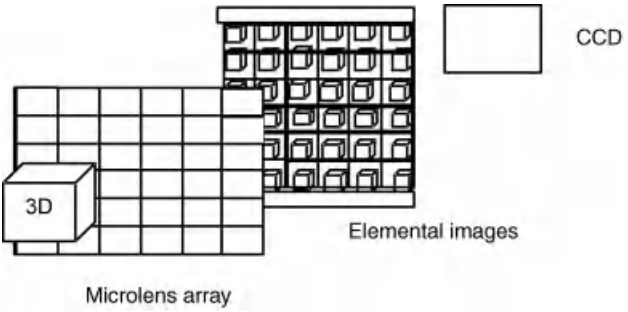

FIGURE 17.34 Block diagram of the camera stage.

The 3D image can be reconstructed from the elemental images by two methods, namely computational reconstruction or optical reconstruction. Computational reconstruction uses pixel mapping techniques to get 3D/2D image. In optical reconstruction, the reconstruction is done using a LCD and lens array in real time, and is useful for 3D video and microscopy. Real time or computational 2D reconstruction of the image from the elemental images is used for compound eye-based imaging systems. Integral imaging technique provides a 3D image from the elemental images and that aspect is explored further in this chapter.

17.13 OPTICAL RECONSTRUCTION TECHNIQUE

In the optical reconstruction stage, the set of elemental images is displayed on a LCD in front of a second lens array [28, 29]. The light rays from these elemental images then go through the lens array, reconstructing the image of the object at the same position as the object as shown in Figure 17.35. Note that although all the elemental images are imaged by the corresponding lenslet into the same plane or the reference image plane, the 3D scene is reconstructed in the image space by the intersection of the ray bundles emanating from each of the lenslets. This method allows viewers to observe a reconstructed 3D image in real time floating in air. Here also the resolution of the reconstructed 3D image is given by the number of lenslets in the lens array. The viewing angle and the depth of the reproduced 3D images depend on the focal length of the convex lenses. The viewing angle Φ is expressed as [28]

$$\Phi = 2\tan^{-1}\left(\frac{P}{2g}\right) \tag{17.7}$$

where P is the pitch of the elemental image and g is the distance between the principle plane and elemental images on the LCD.

The main resolution limitation of this 3D imaging sensor lies in the resolution of the micro-lens array. Miniaturization strategies that have been applied with great success to electronics cannot be simply transferred to optical imaging systems. We have started to exploit nanophotonics and integral imaging technologies to

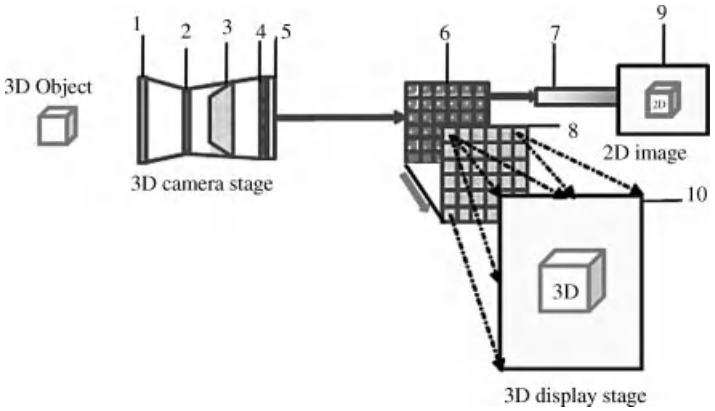

FIGURE 17.35 Schematic diagram of the proposed 3D vision sensor. 1 – imaging lens, 2 – nanophotonic lens array, 3 – pinhole array (optional), 4 – CMOS/CCD sensor, 5 – control electronics, 6 – LCD, 7 – pixel mapping/image processing, 8 – large lens array, 9 – out put 3D image, 10 – output: 2D image (compound eye sensor).

overcome these issues. In the designed sensor, the above mentioned problems of imaging optics, resolution, and miniaturization issues of the sensor system are addressed by introducing the transparent nanophotonic lens array, where each lenslet radius is of the order of 5 μm which is much smaller compared to any commercially available fixed lens array and the focal length is voltage reconfigurable. Applications of this type sensor are mainly in miniaturized 3D camera, 3D microscopy, and endoscopy. Figure 13.35 shows the general architecture of the sensor.

The sensor head (camera stage) has an imaging lens (convex lens). The imaging lens is used to demagnify the image of a far away object to a suitable scale. The voltage dependant lenses also give us an option to get real and virtual 3D image capture by changing the focal length. Without this lens the operating distance of the sensor is limited to millimeters and field of view is very small. When multiple objects are present at a large distance, without this imaging lens only nearby objects get clarity in the image plane and other images will be out of focus. The 3D images near the lens array for reproduction have a higher resolution than those farther away from the lens array. These problems can be solved by incorporating a suitable imaging lens. The imaging lens focuses the image in front (for real 3D) or behind (for virtual 3D) of the nanophotonic micro-lens array to generate many elemental images. The elemental images are recorded on a high resolution CCD/CMOS recording device.

The display stage has a high-resolution LCD where all the elemental images recorded by the CCD are displayed. The large lens array to reconstruct the 3D image was fabricated from crossed lenticular sheet with 10 lines per in inch (10 LPI). In the lenticular lens array, two lenticular sheets (10 LPI acrylic sheets with refractive index 1.49) were crossed at right angles. The lens side of the two lenticular sheets was contacted together in this scheme. Since the focal length of the lens is determined only by the lens side, the two lens arrays have the same focal length when crossed at

right angle. The fabricated lens array is shown in Figure 13.36. The light focusing capability of the lens array was studied using a white light source. The lens array focused light in the back focal plane as shown in Figure 17.36. The focal length of the array was experimentally measured at 3.9 mm from the center of the lens array.

Calibration of the 3D vision sensor was performed using a standard micro-lens array (suss micro-optics, circular lenses, quadratic grid: lens pitch 110 μm, ROC 0.817 mm, numerical aperture 0.03, size 15 mm × 15 mm × 0.9 mm) in the camera

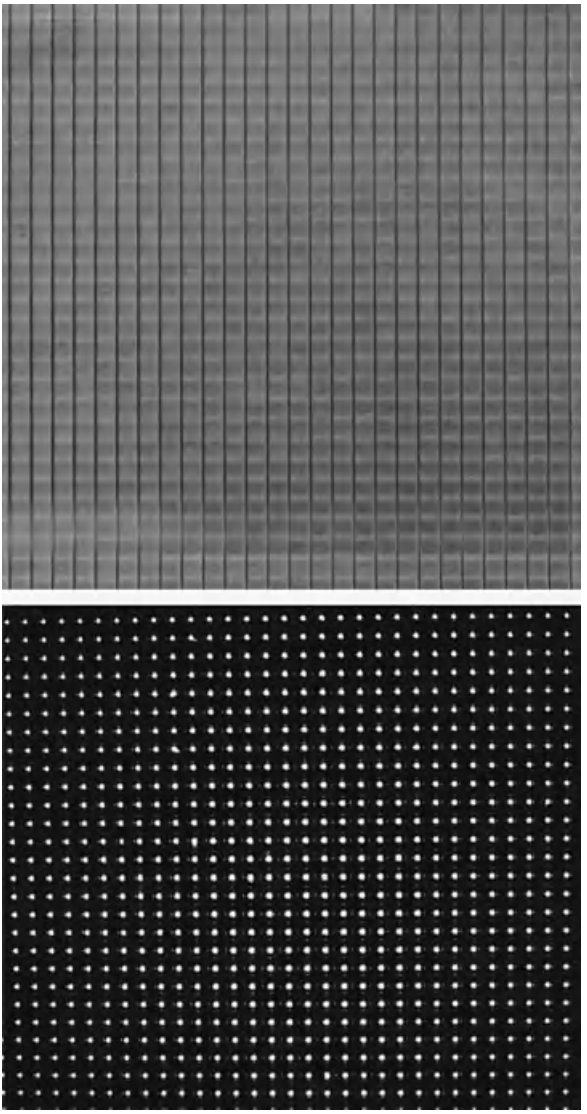

FIGURE 17.36 Left, lens array fabricated from two lenticular sheets having pitch 2.5 mm; right, light focused by the lenticular lens array.

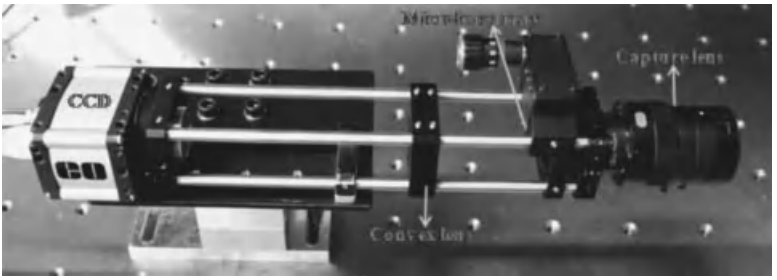

FIGURE 17.37 The 3D vision sensor camera stage developed. (*See the color version of this figure in Color Plates section.*)

stage to fix system parameters. Figure 17.37 shows the 3D vision sensor camera stage developed for calibrating the system parameters including the display stage and the lens array fabricated with two lenticular sheets. The sensor consists of capture lens (imaging lens) to demagnify the image of a far away object to a suitable scale followed by the standard micro-lens array to sample the image and CCD with a convex lens to record the elemental images. We used a very high resolution CMOS color camera (EO-10012C $\frac{1}{2}$ inch CMOS Color GigE) to record the elemental images with pixel resolution 3840×2748 and pixel size $1.67 \times 1.67\,\mu m$ in the camera stage.

The 3D display stage for the sensor was fabricated using the crossed lenticular lens array and silicon graphics 1600SW, 17 in. LCD monitor as shown in Figure 13.38. The dot pitch of the display was 0.23 mm for high resolution. The separation between the display and the lens array was adjustable for improving the quality of the 3D image reconstructed. The size of the lens array was 15×15 cm. Computationally simulated elemental images of the number 3D was used to calibrate [29] the display as shown in Figure 17.38. The inverted version of the image was used in experiment. All the elemental images were displayed on the display and the lenticular lens array was kept 4 mm away (the distance measured from centre of the lens array to the display). Figure 17.39 shows the reconstructed 3D image in the display from two different angles (top view and bottom view). The 'D' moved with respect to the '3' in top and bottom view. This shows that there was a full parallax in the reconstructed 3D image. Each elemental images was displayed using 10×10 pixels on the LCD and each elemental was covered by a single lenslet of size 2.5 mm on the lenticular lens array. This experiment helped to fix the distance between the lenticular lens array and the display stage.

17.14 IMAGING USING THE NANOPHOTONIC LENS ARRAY

The imaging characteristics of the nanophotonic lens array were studied for calibration. US air force (USAF) test pattern was used an object. A transmission microscope with a CCD camera was used to capture the images from the nanophotonic device at different voltages. The number 3 (100 μm) in the USAF pattern was used for imaging.

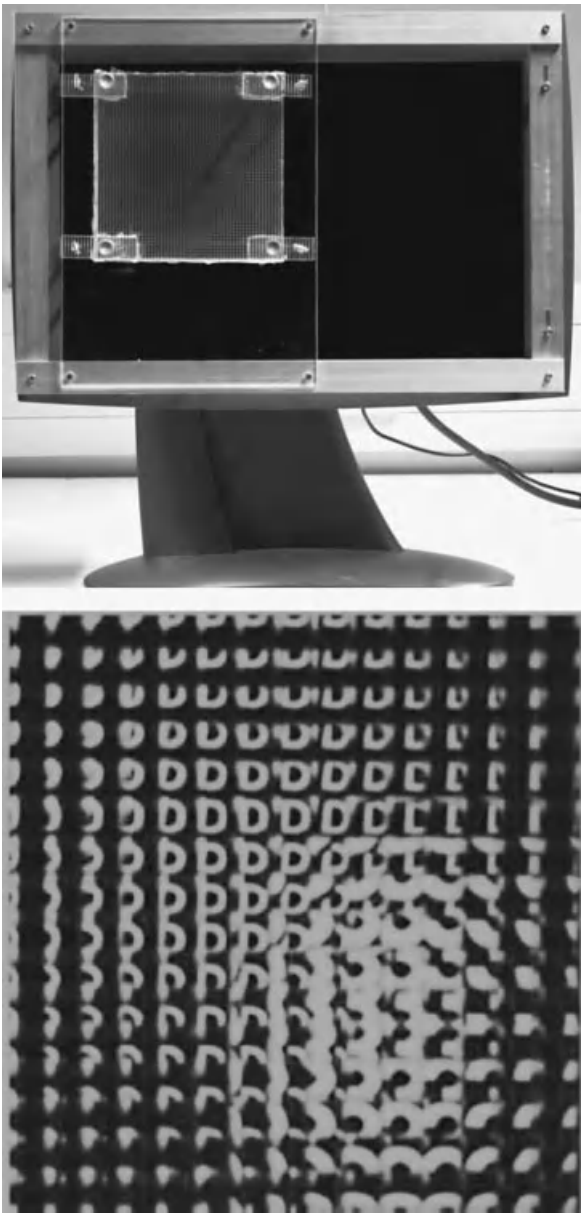

FIGURE 17.38 Fabricated 3D display stage using crossed lenticular lens array and silicon graphics 1600 SW, 17 in. LCD monitor, the elemental images of 3&D [29].

The images formed from the nanophotonic lens array was not clear at zero volts because of the less ordered alignment of the LC molecules around the nanotubes and hence created a non uniform gradient refractive index profile. This matched the interference experiments where fringes were observed at zero volts as discussed in

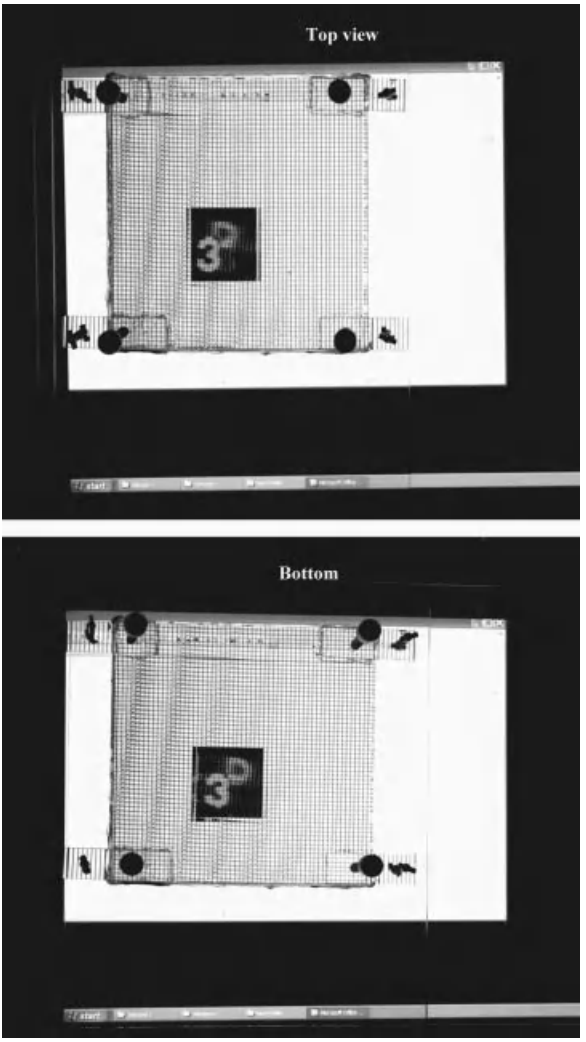

FIGURE 17.39 The reconstructed 3D image in the developed 3D display from all the elemental images viewed from top and bottom. (*See the color version of this figure in Color Plates section.*)

Section 17.8. The images became very clear at 1.1 V_{rms} and started disappearing with increase in the applied voltage. The performance exactly matched with the focal length study. Figure 17.40 shows the image formed from the nanophotonic lens array at different voltages.

The focal length variation and the phase profile with respect to the applied voltage of the nanophotonic lens array were as discussed previously. The focal length increased with respect to the applied voltage and hence the concave nature increased. The behavior of the lens array at 0 V_{rms} and close to 0 V_{rms} was not clear from the

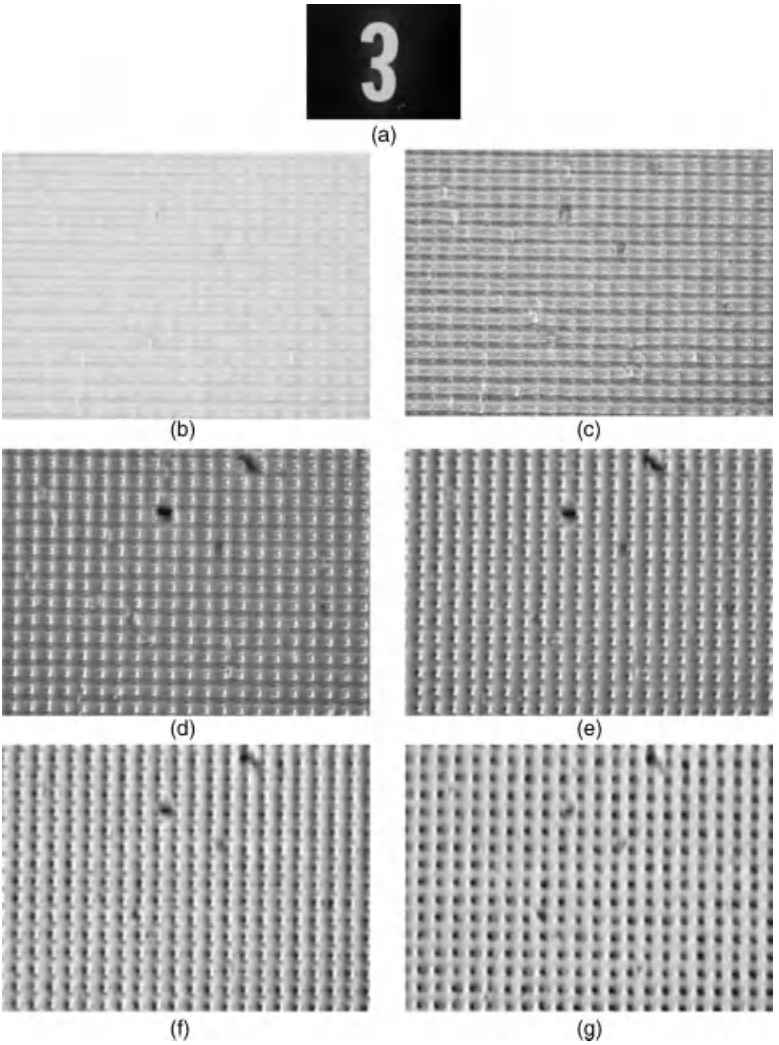

FIGURE 17.40 Object used and captured elemental images from the nanophotonic lens array at different voltages (a) object, (b) images at 0 V_{rms}, (c) images at 0.75 V_{rms}, (d) images at 1.1 V_{rms}, (e) images at 1.8 V_{rms}, (f) images at 2.2 V_{rms}, and (g) images at 3.5 V_{rms}.

previous results. The image formation at various distances from the nanophotonic lens array was used to find the behavior of the lens array at 0 V_{rms}. Figure 17.41 shows the images captured of the object '3' at different images planes. In Figure 17.41(b), the image plane was 10 μm away from the plane at Figure 17.41(a).

It was clear from the images that the image size reduced with distance as well as the fact that the images were non-inverted and hence both planes were before the focal plane. When the distance increased by another 30 μm from the previous plane, the focal plane was reached as shown in Figure 17.42. When the distance increased by

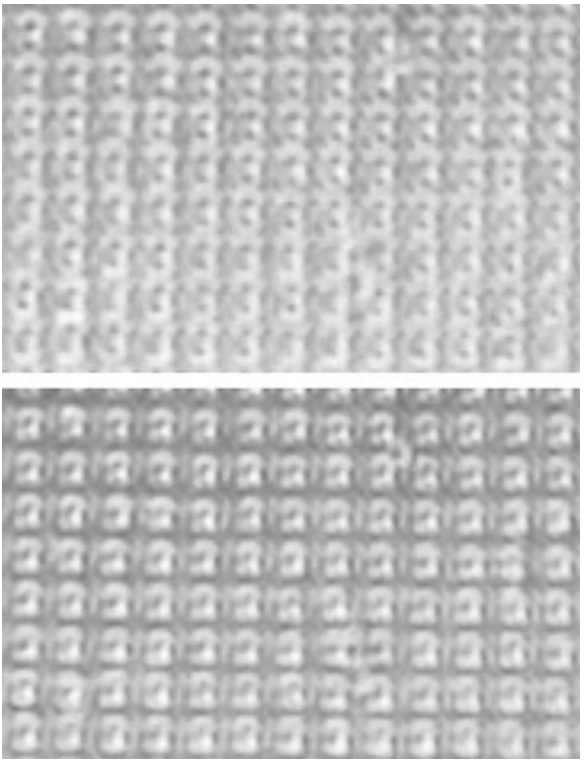

FIGURE 17.41 The images formed at two different focal planes (b) the focal plane is 10 μm away from the image focal plane (a).

another 41 μm from the focal plane, the inverted images appeared and hence the image plane was after the focal plane as shown in Figure 17.43(a). With a further increase in distance of 5 μm, the image size increased as shown in Figure 17.43(b). Hence the refractive index profile created a distorted convex lens at 0 V_{rms} and the convex nature reduced (concave nature increased) with respect to the applied voltage. In some part of the lens array, the convex nature slightly increased at very lower voltages just after 0 V_{rms} and then concave nature increased with further increase in voltage. The nanophotonic lens array is useful for imaging just before the concave nature increases. This is because when the concave nature increases, there is more distortion in the refractive index profile. The optimum voltage for the imaging was around 1.1 V_{rms}.

17.15 CONCLUSIONS AND DISCUSSION

In this chapter we have presented a nanophotonic device based on a hybrid combination of multi-wall carbon nanotubes and LCs. The carbon nanotube

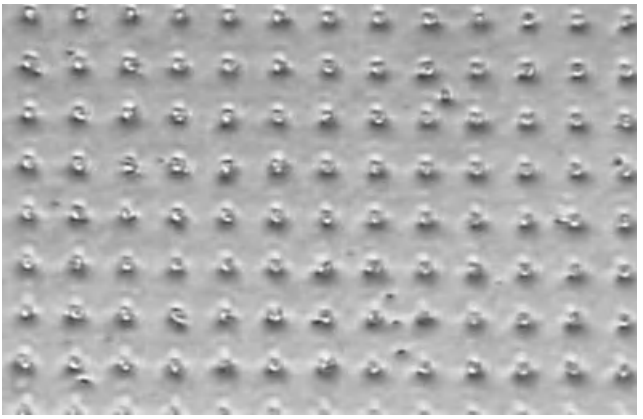

FIGURE 17.42 An image plane near to the focal plane.

electrode arrays were grown on silicon substrate (reflective device) and on quartz (transparent device) by plasma enhanced chemical vapor deposition after employing e-beam lithography and covered with nematic LC. The multi-wall carbon nanotubes act as individual electrode sites that spawn an electric-field profile, dictating the refractive index profile within the LC and hence creating a series of graded index profiles, which form various photonic elements. The device was analyzed under an optical microscope and it was found that photonic element was formed at each nanotube site and the photonic elements switched with respect to the applied voltage. This has led to the conclusion that micro/nano regions in the device interact with light.

The phase profile from micro region in the device was recovered using an interference set-up attached with an optical microscope. Each nanotube site acted like a lenslet. The phase profile was more or less parabolic at lower voltages and hence acted like a voltage reconfigurable nanophotonic lens array. The effect of nanotube electrode geometry in the phase profile and the lenslet diameter has been studied using electric field simulation followed by fabricating the devices with one, three, four, and five nanotube groups. The four nanotube group was found to be optimum for lens array applications and one nanotube for display applications. However, a larger number of nanotubes per group could be used for increasing the lenslet diameter.

A transparent nanophotonic device was also discussed where the nanotube electrodes were grown on a quartz substrate. The device is suitable for lens array applications because of the easy alignment with other optical components and there was no double pass of light through the device. The electrode geometry used had six nanotubes per group in a hexagonal pattern. The phase profile and focal length were calculated and found that the device acted as nanophotonic lens array at lower voltages. The light focusing was also studied at different voltages to understand the focusing properties of the device. The light intensity profile at each lenslet was smooth and maximum at a lower voltage and at the same voltage the phase profile was

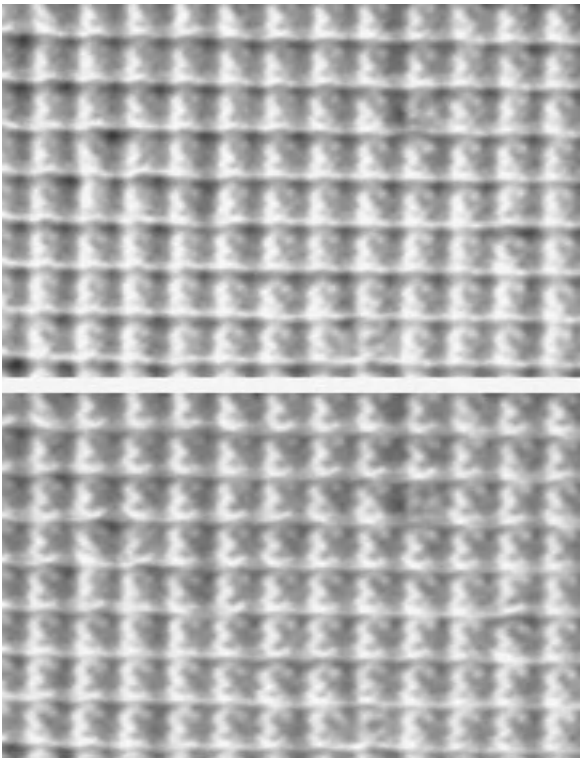

FIGURE 17.43 The images formed at two different focal planes (b) the focal plane is 5 μm away from the image focal plane (a).

parabolic like. The useful voltage range of the device for imaging application was obtained from the studies of phase profile, phase aberrations, intensity profile, and focal length variation. Electro-optic characteristics, such as transmission voltage characteristic, response time and the contrast ratio of the device were studied to optimize the device performance for different applications. These analyses showed that the device finds application as a nanophotonic lens array, reconfigurable hologram, and grating at lower voltages in addition to the suitability of the device for display application at higher voltages.

This chapter also presented a 3D vision sensor realized using the nanophotonic lens array. The imaging characteristic of the lens array was studied using USAF test pattern at different voltages. The useful voltage range for imaging obtained from the imaging experiments were matched with previously obtained voltage range from the intensity profile. An insect eye-based imaging system was developed first where each nanophotonic lenslet captured a particular perspective of an object called the elemental image. The number of elemental images was equal to number of lenslets. One pixel from each elemental image was extracted to get a 2D image of the object as in the case of compound eye imaging system of an insect. This imaging system was then extended using integral imaging techniques to realize a 3D vision sensor.

The pick up stage (camera stage) and display stage were developed and integrated together. The 3D sensor was then calibrated using a standard micro-lens lens array, plastic objects and simulated elemental images. The sensor was also modified into a 3D microscope for analyzing microscopic objects. Since the focal length of the nanophotonic lens array was in micro meters range, the elemental images formed was just before the diffraction effect predominated and hence over came the limitation imposed by diffraction. The concept of the 3D microscope can be extended to realize a 3D endoscope where the image floats in the air with full parallax. The advantage of the current technique is that it can give very high resolution of the specimen under observation and the endoscope can be realized in a small foot print. Another advantage is that the 3D image can be seen without any glasses to many viewers with full parallax.

The potential applications of this type of nanophotonic device range from 3D cameras through to wavefront sensors. Furthermore other structures can be made using the ebeam patterning system to locate the CNTs from holograms and gratings [31] through to photonic bandgap metamaterials [32]. The spacing of the tubes can be set down to 500 nm as has been recently demonstrated in work on CNT-based metamaterials [33]. By controlling lattice structures and defects, filters, lenses, and waveguides can all be fabricated using these principles. Their operation can then be further enhanced with the inclusion of a variable refractive index material such as a LC into these novel 3D nano-structures.

REFERENCES

1. F. S. Yeung, J. Y. Ho, Y. W. Li, F. C. Xie, O. K. Tsui, P. Sheng, and H. S. Kwok. Variable liquid crystal pretilt angles by nanostructured surfaces. *Appl. Phys. Lett.* **2004**, *85*, 513.
2. J. T. K. Wan, O. K. C. Tsui, H.-S. Kwok, and P. Sheng. Liquid crystal pretilt control by inhomogeneous surfaces. *Phys. Rev. E* **2005**, *72*, 021711.
3. O. Trushkevych, N. Collings, T. Hasan, V. Scardaci, A. C. Ferrari, T. D. Wilkinson, W. A. Crossland, W. I. Milne, J. Geng, B. F. G. Johnson, and S. Macaulay. Characterization of carbon nanotube–thermotropic nematic liquid crystal composites. *J. Phys. D: Appl. Phys.* **2008**, *41*, 125106.
4. S. J. Jeong, P. Sureshkumar, K.-U. Jeong, A. K. Srivastava, S. H. Lee, S. H. Jeong, Y. H. Lee, R. Lu, and S.-T. Wu. Unusual double four-lobe textures generated by the motion of carbon nanotubes in a nematic liquid crystal. *Opt. Exp.* **2007**, *15*, 11698–11705.
5. I.-S. Baik, S. Y. Jeon, S. J. Jeong, S. H. Lee, K. H. An, S. H. Jeong, and Y. H. Leeb. Local deformation of liquid crystal director induced by translational motion of carbon nanotubes under in-plane field. *Jpn. J. Appl. Phys.* **2006**, *100*, 074306-1-5.
6. C.-Y. Huang, C.-Y. Hu, H.-C. Pan, and K.-Y. Lo. Electrooptical responses of carbon nanotube-doped liquid crystal devices. *Jpn. J. Appl. Phys.* **2005**, *44*, 8077–8081.
7. W. Lee, C.-Y. Wang, and Y.-C. Shih. Effects of carbon nanosolids on the electro-optical properties of a twisted nematic liquid-crystal host. *Appl. Phys. Lett.* **2004**, *85*, 513.
8. T. D. Wilkinson, X. Wang, K. B. K. Teo, and W. I. Milne. Sparse multiwall carbon nanotube electrode arrays for liquid-crystal photonic devices. *Adv. Mater.* **2008**, *20*, 363–366.

9. W. Lee, C.-Y. Wang, and Y.-C. Shih. Effects of carbon nanosolids on the electro-optical properties of a twisted nematic liquid-crystal host. *Appl. Phys. Lett.* **2004**, *85*, 513.
10. M. J. O. Connell. *Carbon Nanotubes, Properties and Application*. Taylor & Francis Group, 2006.
11. H. W. Kroto, J. R. Heath, S. C. Obrien, R. F. Curl, and R. E. Smalley. C-60 Buckminsterfullerene. *Nature* **1985**, *318*, 162–163.
12. S. Iijima. Helical microtubules of graphitic carbon. *Nature* **1991**, *354*, 56–58.
13. T. Kawano, H. C. Chiamori, M. Suter, Q. Zhou, B. D. Sosnowchik, and L. Lin. An electrothermal carbon nanotube gas sensor. *Nano Lett*. **2007**, *7*, 3686–3690.
14. K. B. K. Teo, M. Chhowalla, G. A. J. Amaratunga, W. I. Milne, D. G. Hasko, G. Pirio, P. Legagneux, F. Wyczisk, and D. Pribat. Uniform patterned growth of carbon nanotubes without surface carbon. *Appl. Phys. Lett.* **2001**, *79*, 1534–1536.
15. W. I. Milne, K. B. K. Teo, M. Chhowalla, G. A. J. Amaratunga, S. B. Lee, D. G. Hasko, H. Ahmed, O. Groening, P. Legagneux, L. Gangloff, J. P. Schnell, G. Pirio, D. Pribat, M. Castignolles, A. Loiseau, V. Semet, and V. T. Binh. Electrical and field emission investigation of individual carbon nanotubes from plasma enhanced chemical vapour deposition. *Diamond and Related Materials* **2003**, *12*, 422–428.
16. P. J. Collings and M. Hird. *Introduction to Liquid Crystals, Chemisrty and Physics*. Taylor & Francis Group, 1998.
17. C. Y. Huang, C.-Y. Hu, H. C. Pan, and K.-Y. Lo. Electrooptical response of carbon nanotube-doped liquid crystal devices. *Jpn. J. Appl. Phys.* **2005**, *44*, 8077–8081.
18. A. F. Naumov, M. Y. Loktev, I. R. Guralnik, and G. V. Vdovin. Liquid-crystal adaptive lenses with modal control. *Opt. Lett.* **1998**, *243*, 992–994.
19. M. Ye, Y. Yokoyama, and S. Sato. Liquid crystal lens prepared utilizing patterned molecular orientations on cell walls. *Appl. Phys Lett.* **2006**, *89*, 141112.
20. H. Ren and S. T. Wu. Liquid crystal lens with large focal length tunability and low operating voltage. *Opt. Express* **2007**, *15*, 11328.
21. X. Deng, X. Liang, Z. Chen, W. Yu, and R. Ma. Uniform illumination of large targets using a lens array. *Appl. Opt.* **1986**, *25*, 377.
22. R. Volkel, M. Eisner, and K. J. Weible. Miniaturized imaging systems. *Microelectronic Eng*. **2003**, *67–68*, 461–472.
23. J. S. Sanders and C. E. Halford. Design and analysis of apposition compound eye optical sensors. *Opt. Eng*. **1995**, *34*, 222–235.
24. M. G. Lippmann. Epreuves reversibles donnant la sensation durelief. *J. Phys.* **1908**, *7*, 821–825.
25. F. Okano, H. Hoshino, J. Arai, and I. Yuyama. Real-time pickup method for a there-dimensional image based on integral photography. *Appl. Opt.* **1997**, *36*, 1598–1603.
26. H. Hoshino, F. Okano, H. Isono, and I. Yuyama. Analysis of resolution limitation of integral photography. *J. Opt. Soc. Am. A* **1998**, *15*, 2059–2065.
27. L. Erdmann and K. J. Gabriel. High-resolution digital integral photography by use of a scanning microlens array. *Appl. Opt.* **2001**, *40*, 5592–5599.
28. F. Okano, J. Arai, H. Hoshino and I. Yuyama. Three-dimensional video system based on integral photography. *Opt. Eng*. **1999**, *38*, 1072–1077.

29. J.-S. Park, D.-C. Hwang, D.-H. Shin, and E.-S. Kim. Enhanced-resolution computational integral imaging reconstruction using an intermediate view reconstruction technique. *Opt. Eng.* **2006**, *45*, 117004.
30. Q. Dai, R. Rajesekharan, H. Butt, K. Won, X. Wang, G. Amaratunga, and T. D. Wilkinson. Transparent liquid crystal based microlens array using vertically aligned carbon nanofibre electrodes on quartz substrates. *Nanotechnology* **2011**, *22*, 115201.
31. K. Won, R. Rajesekharan, P. J. W. Hands, Q. Dai, and T. D. Wilkinson. Adaptive lenticular lens array using a hybrid liquid crystal–carbon nanotube nanophotonic device. *Opt. Eng.* **2011**, *50*, 054002.
32. H. Butt, Q. Dai, P. Farah, T. Butler, T. D. Wilkinson, J. J. Baumberg, and G. A. J. Amaratunga. Metamaterial high pass filter based on periodic wire arrays of multiwalled carbon nanotubes. *Appl. Phys. Lett.* **2010**, *97*, 163102.
33. H. Butt, Q. Dai, G. A. J. Amaratunga, and T. D. Wilkinson. Photonic crystals and metamaterial filters based on 2D arrays of silicon nanopillars. *Prog. Electromagnet. Res.* **2011**, *113*, 179–194.

INDEX

ambipolar 33,
ambipolar charge transport 312
amphiphilic 62, 295–297, 345, 347, 360, 449

biaxial 16, 118, 131, 145, 432, 441
biaxial nematic phase 428, 430, 433–435, 445
bilayer 43, 44, 57, 58, 65, 298, 449
bilayer OLED 67, 68
birefringence 58, 160, 164, 251, 270, 310, 403, 413, 415, 420, 422, 455, 463, 472, 473, 474, 505, 506, 512, 514, 517, 527, 528
blue phase (BP) 20, 115, 158, 167, 168, 198, 243, 274, 276, 278
bulk heterojunction (BHJ) 44, 65, 66
block copolymer 285–297, 465
boojum 451

C_{60} 50, 51, 65, 463, 469–471, 526
calamitic 30, 31, 49, 56, 113, 130, 131, 134, 173, 243, 308, 311, 318, 432, 440
carbon nanotube 55, 263, 279, 341–347, 349, 350, 353–355, 359, 360, 362, 365–368, 405–407, 526, 527, 529, 530, 536, 540, 541, 548, 549, 562, 563
carbon nanotube (CNT) 341–368, 530–534, 538, 546–548, 565
charge-carrier mobility 31, 33, 37–39, 44, 45, 56, 60, 70, 312, 330
charge-carrier transport 33, 34, 303, 311
chemical potential 311
chemical vapor deposition (CVD) 527, 530, 563
chiral homeotropic LC (CHLC) 530
cholesteric 21, 115, 119, 145, 217, 218, 220, 230–235, 237, 238, 240–243, 263, 267, 268, 270, 276, 279, 360, 505, 508, 509, 510, 511, 512, 516, 517, 521, 522
cholesteric LC (CLC) 1, 213, 214, 215, 216, 222, 227, 228, 241, 269, 271, 276–278, 395, 397, 458, 459, 484, 507, 515, 520
cholesteric polymer 304
columnar 30, 31, 33, 38, 39, 40, 43–45, 47–50, 53–59, 61, 62, 65, 67, 69, 70, 87, 88, 90, 91, 94, 95, 115, 131–133, 142, 145, 158, 167, 168, 173, 174, 198, 362, 363, 450, 451, 465, 476
conduction band 33
π-conjugated aromatic core 29, 65
conoscopic 61, 500
correlation 37, 39, 132, 165, 179, 213, 403, 413, 415, 420, 422, 427–429, 431, 440, 442, 444, 488
correlation length 430, 432, 433, 435, 438–442, 445, 446, 454
crystal engineering 84
current-voltage (I-V) 36, 69
cyclic voltammetry (CV) 40

defect-free 44, 56, 70, 272, 427
diblock copolymer 286–288, 290, 290, 296, 297
dielectric 4, 6, 15, 36, 69, 85, 179, 180, 187–190, 193, 195, 196, 262, 329, 330,'379, 380–382, 384–392, 395, 405, 406, 408, 413, 415, 420–423, 510, 514, 517, 518, 520, 525, 527–531, 533

Liquid Crystals Beyond Displays: Chemistry, Physics, and Applications, Edited by Quan Li.

© 2012 John Wiley & Sons, Inc. Published 2012 by John Wiley & Sons, Inc.

dielectric constant 36, 112, 120, 176, 179, 181, 185, 417, 420, 429
dielectric material 262, 391, 395, 397
disodium cromoglycate (DSCG) 449, 454–460, 466, 467, 472, 474–476
differential scanning calorimetry (DSC) 31, 97, 130, 175, 265, 266, 275, 278, 307, 366
dipole-dipole interaction 37, 101, 116, 145
discotic liquid crystal (discotic LC, DLC) 29, 31, 33–35, 37–41, 43, 45–47, 53–57, 59, 60, 62, 63, 65–67, 69, 70, 88, 94, 105, 113, 280
dispersion 196, 345, 347, 349–351, 355, 358–360, 362–364, 366, 368, 381, 404, 406, 408–412, 418, 419, 460
dispersion relation 1, 2, 4, 20
DNA 213, 346, 351, 449, 450, 461, 476
donor-acceptor complex 50
donor-acceptor diblock copolymer 290
donor-acceptor ensembles 52
donor-acceptor group 134, 135

electroluminescence (EL) 66, 303, 304, 311, 314, 317, 318, 321–323, 326, 328, 329
electromagnetic 7, 379, 380, 389, 390, 394, 395, 397
electron-acceptor 40, 50, 65, 66, 112, 124, 126, 139, 145, 334, 471
electron-donating 316, 333, 334, 488
electron-transport 40, 67
electrostatic 35, 36, 252, 254, 257, 259, 260, 263, 345, 351, 407, 414, 455, 459, 463, 466, 475, 525, 526, 532, 540
exciton diffusion length 31, 64, 65, 70
exciton-binding energy 64, 308

face-to-face 449, 455, 474,
ferroelectricity 89, 90, 103, 104, 113, 114, 116–119, 133, 142, 145, 193, 405, 420, 446
Fermi's Golden Rule 3
field-effect transistor (FET) 28, 36, 37, 45, 62, 468, 470
fill factor (ff) 381
focal conic 170, 227, 506–508, 511–521
fourier transform 290, 307, 593, 594
fullerene 49–52, 334, 362, 405, 463, 469, 526

Gaussian 527, 530, 531, 537
Gaussian distribution 139, 312
Grandjean-Cano 216

hexabenzocoronene (HBC) 35, 45–47, 49, 58, 62, 65, 69
hexagonal columnar (Col_h) 30, 31, 40, 43, 48, 50, 57, 58, 145, 362, 363, 450
highest occupied molecular orbital (HOMO) 32, 33, 37, 40, 64, 65, 67, 308, 312, 315
hole-transporting 67
homeotropic alignment 44, 49, 50, 56–58, 60, 65, 122, 130, 141, 180, 181, 196, 227, 272, 331, 367, 419, 463, 469, 470, 473, 486, 487, 492, 494, 498, 500, 506, 508, 511, 514, 518, 519, 521, 536, 542, 553
homeotropic cell 122, 123, 145
homogeneous 13, 62, 91, 97, 133, 265, 312, 319, 410, 455, 457, 459, 464, 515, 530
hydrogen bonding 37, 47–49, 51, 142, 170, 174, 175, 408, 486, 490, 491, 496

indium tin oxide (ITO) 57, 58, 65–68, 316, 321, 327, 345, 511, 512, 515, 529, 532, 533, 547
π-π stacking 37, 357
π-π interaction 358
inhomogeneous 84, 100, 101, 104, 422, 525
interface 21, 36, 62, 64, 67, 69, 132, 176, 177, 287, 315, 333, 358, 390, 393, 406, 408, 449, 460, 463, 473, 474, 488, 499, 512, 515, 527
irreversible 169, 237, 238

kinetic 175, 176, 179–181, 183, 275, 276
Kossel 171

Langmuir-Blodgett (LB) 60, 62, 63, 69, 112, 141
liquid crystal display (LC display, LCD) 227, 304, 318, 319, 387, 526, 529, 530
light scattering 451
light-emitting diode (LED) 29, 40, 56, 66, 67, 303–305, 311, 314–319, 323, 468

lowest unoccupied molecular orbital (LUMO) 32, 33, 37, 40, 64, 65, 67, 308, 312, 313, 315

magnetic 60, 62, 70, 83–105, 185, 188, 214, 217, 292, 295, 298, 344, 354, 363, 380–385, 390–392, 396
mesogenic 49, 57, 62, 131, 134, 135, 139–141, 195, 219, 234, 243, 251, 265, 286, 395, 404, 405, 408, 409, 413, 418, 529
mesogenicity 126
mesomorphic 48, 141, 157, 160, 163, 465, 476
monodomain 44, 51, 56, 59, 62, 291, 303, 354, 366, 431, 439
monolayer 60, 62, 63, 197, 295, 333, 463, 466, 467, 471, 490, 491, 496
Monte-Carlo simulation 312
morphology 70, 146, 258, 261, 262, 266, 268, 269, 271, 272, 285, 288, 290, 509, 517
multi-walled carbon nanotube (multi-wall CNT, MWCNT) 342, 343, 347, 350, 356, 357, 359, 361, 363, 364, 530–533

n-type 33, 39–41, 44, 65, 68
nonlinear optic (NLO) 104, 111–146, 405, 414, 423
non-amphiphilic 449
non-mesogenic 418
nucleation 58, 61, 220, 234, 527

one-dimensional 1, 33, 38, 39, 56, 115, 139, 407, 550
open circuit voltage 64
optical path difference (OPD) 536
π-orbital overlap 30, 33, 37
order parameter 5, 11, 125, 160, 165, 172, 175, 191, 197, 318, 321–323, 334, 353, 354, 356, 360, 406, 408, 409, 413, 415–420, 428
organic field-effect transistor (OFET) 36, 37, 45, 56, 60, 63, 68, 69, 303, 304, 329–334
organic light-emitting diode (OLED) 40, 41, 43, 56, 63, 66–68, 303, 304, 311, 314–320, 323, 325–328, 333, 334
organic photovoltaic (OPV) 50, 65, 330

paramagnetic liquid crystal (PLC) 83, 84, 95, 97, 105, 177, 178
perylene 41, 43, 65, 68–70
perylene diimide (PDI) 41–43, 70
6,6-phenyl-C_{61}-butyric acid methyl ester (PCBM or $PC_{61}BM$) 50, 66
photonic bandgap (PBG) 1, 3–8, 10–12, 18, 19
photostationary state (PSS) 229, 230, 232, 240
photovoltaic (PV) 29, 43–46, 52, 56, 57, 63, 65, 113, 290, 303, 333, 468, 469
phthalocyanine 38, 43, 44, 50, 52, 53, 57–59, 62, 65, 69, 88
phthalocyanine-C_{60} dyad 50
planar alignment 4, 21, 56, 57, 60, 62, 226, 229, 272, 318, 414, 472, 463, 464, 468, 472, 531
plasma-enhanced chemical vapor deposition (PECVD) 527, 530
polarizing optical microscopy (POM) 31, 97, 100, 164, 239, 240
poly(acrylonitrile) (PAN) 254, 255
polyactide (PLA) 254, 256, 266
polyamide (PA) 197, 254, 255, 466, 469
polycyclic aromatic hydrocarbon (PAH) 45–47
poly(diallyldimethyammonium chloride) (PDDA) 466–468
poly(*N*,*N*-dimethylacrylamide) (PDMA) 296
polydimethylsiloxane (PDMS) 466, 467
poly(3,4-ethylenedioxythiophene) (PEDOT) 66
poly(3,4-ethylenedioxythiophene)/poly (styrenesulfonate) (PEDOT/PSS) 316, 323
poly(ethylene glycol) (PEG) 254, 255, 295, 347, 362, 461, 463, 476
poly(ethylene oxide) (PEO) 254, 255, 265, 286, 287
poly(3-hexylthiophene) (P3HT) 40, 288–290, 349, 354
polymer dispersed liquid crystal (PDLC) 176, 403, 505, 506, 517
polymeric cholesteric liquid crystal (PCLC) 8, 9, 19
polymer sacrificial layer 58

polymer stabilized cholesteric texture (PSCT) 505–521
poly(methyl methacrylate) (PMMA) 256, 347, 391
poly(*p*-phenylene benzobisoxazole) (PBO) 359, 362
poly(*para*-phenylene vinylene) (PPV) 323
poly(phosphoric acid) (PPA) 359, 362
poly(tetrafluoroethylene) (PTFE) 60, 62
poly(vinyl alcohol) (PVA) 7, 8, 19, 254, 255, 262
poly(vinyl pyrrolidone) (PVP) 254, 274–276, 279
porphyrin 29, 38, 43, 49–53, 57, 58, 60, 65–66
poly(styrene) (PS) 254–255
power conversion efficiency (PCE) 44, 65, 66, 533, 542, 547, 549
p-type 33, 39, 40, 65, 67
pulse-radiolysis time-resolved microwave conductivity (PR-TRMC) 34, 35, 37–41, 43, 44
pyroelectric liquid crystal polymer (PLCP) 118, 123, 124

quasi-boolshelf (QBS) 123
quaterrylene diimide (QDI) 43

radial breathing mode (RBM) 347, 357–359
radio frequency (RF) 380, 383–387, 389, 390, 391, 394, 397
radio-frequency identification (RFID) 303, 331
red-green-blue (RGB) 18–20, 223, 326
relative humidity (RH) 494
roll-to-roll 506

saturated calomel electrode (SCE) 44
scanning electron microscopy (SEM) 265, 269, 271, 542, 544–547
scanning tunnelling microscope (STM) 188
second harmonic generation (SHG) 104, 111–113, 118–124, 126–128, 130, 133, 134, 137–142, 145
self-assembled monolayers (SAM) 60, 490–492, 496, 497, 500
single crystal 85, 112
single-molecule magnet (SMM) 84, 88–90, 92
single-walled carbon nanotube (SWCNT) 342, 343, 346–354, 356–360, 364, 365, 526
smectic (Sm) 1–2, 6, 87, 88, 93, 100, 115–117, 123, 124, 128, 131, 133, 145, 158, 167, 168, 170–174, 183, 184, 186, 188, 191, 193, 198, 243, 264, 267, 268, 272–275, 285, 286, 307, 308, 312, 331–334, 349, 355, 366, 409, 429, 432, 436, 438, 442, 444–445, 465, 493
sodium dodecyl benzene sulfate (SDBS) 346, 348, 361
sodium dodecyl sulfate (SDS) 346, 360, 362
solar cell 40, 41, 44, 45, 56, 63–66, 303, 334
space charge-limited current (SCLC) 35–37
split ring resonator (SRR) 380–382, 385, 388, 389, 394
steric interaction 193, 319
styrene-*b*-butadiene-*b*-styrene (SBS) 291, 293
styrene-*b*-isoprene-*b*-styrene (SIS) 291
sunset yellow (SSY) 451–455, 460–462, 464
surface-stabilized ferroelectric liquid crystal (SSFLC) 116, 124, 273, 274

terrylene diimide (TDI) 43
thermal annealing 30, 50, 57, 58, 286, 334, 365
thermal back relaxation (TBR) 160, 177–180
time of flight or time-of-flight (TOF) 33–35, 37–40
transmission electron microscopy (TEM) 270, 271, 342, 346, 353
triblock copolymer 291–294
triphenylene 38–41, 43, 47, 49, 54, 57–59, 62, 65, 67, 68
triphenylene-gold nanoparticle (TP-GNP) 55, 56
twist grain boundary (TGB) 2, 115, 168, 169
twisted nematic (TN) 464, 473, 474, 530
unpolarized light (UPL) 167, 241

van der Waals (VdW) 346, 351, 405, 407
variable temperature X-ray diffraction (VT-XRD) 97
very-large-scale integration (VLSI) 113, 145

wet-processing 344
whispering gallery mode (WGM) 21

XRD (X-ray diffraction) 31, 59, 61, 97, 185, 188, 273, 430, 431, 436, 438, 440, 449, 451, 452, 454, 455, 457

zone casting 60, 62, 69